PUBLICATIONS 2021

T. Pradeep

INDIAN INSTITUTE OF TECHNOLOGY MADRAS

सिद्धिर्भवति कर्मजा

Contents

Journal Papers Published in 2021*

Publications from our group

1. Gas phase ion chemistry of titanium-oxofullerene with ligated solvents, Jayoti Roy, Papri Chakraborty, Ganesan Paramasivam, Ganapati Natarajan, and Thalappil Pradeep, *Phys. Chem. Chem. Phys.*, 2021 (DOI: 10.1039/D1CP04716G).
2. Assembling atomically precise noble metal nanoclusters using supramolecular interactions, Abhijit Nag, and Thalappil Pradeep, *ACS Nanoscience Au*, 2021 (DOI:10.1021/acsnanoscienceau.1c00046).
3. Direct imaging of lattice planes in atomically precise noble metal cluster crystals using a conventional transmission electron microscope, Ananthu Mahendranath, Biswajit Mondal, Korath Sivan Sugi, and Thalappil Pradeep, *Chem. Comm.*, 2021 (DOI: 10.1039/D1CC05643C).
4. Desorption-induced evolution of cubic and hexagonal ices in an ultrahigh vacuum and cryogenic temperatures, Gaurav Vishwakarma, Jyotirmoy Ghosh, and Thalappil Pradeep, *Phys. Chem. Chem. Phys.*, 23 (2021) 24052 (DOI: 10.1039/D1CP03872A).
5. Light-activated intercluster conversion of an atomically precise silver nanocluster, Arijit Jana, Madhuri Jash, Ajay Kumar Poonia, Ganesan Paramasivam, Md Rabiul Islam, Papri Chakraborty, Sudhadevi Antharjanam, Jan Machacek, Sundargopal Ghosh, Kumaran Nair Valsala Devi Adarsh, Tomas Base, and Thalappil Pradeep, *ACS Nano*, 15 (2021) 15781–15793 (DOI: 10.1021/acsnano.1c02602).
6. Interference of phosphate in adsorption of arsenate and arsenite over confined metastable two-line ferrihydrite and magnetite, Chennu Sudhakar, Sritama

Mukherjee, Avula Anil Kumar, Ganesan Paramasivam, P. Karthigai Meena, Nonappa, and Thalappil Pradeep, *J. Phys. Chem. C*, 125 (2021), 22502-22512 (DOI: 10.1021/acs.jpcc.1c04317).

7. Aminoclay-graphene oxide composite for thin-film composite reverse osmosis membranes with unprecedented water flux and fouling resistance, Md Rabiul Islam, Pratishtha Khurana, Pillalamarri Srikrishnarka, Ankit Nagar, Madhuri Jash, Shantha Kumar Jenifer, Mohd Azhardin Ganayee, Mathava Kumar, and Thalappil Pradeep, *Adv. Mater. Interfaces*, 8 (2021) 2100533 (DOI: 10.1002/admi.202100533).
8. Cellulosic ternary nanocomposite for affordable and sustainable fluoride removal, Moses Egor, Avula Anil Kumar, Tripti Ahuja, Sritama Mukherjee, Amrita Chakraborty, Chennu Sudhakar, Pillalamarri Srikrishnarka, Sandeep Bose, Swathy Jakka Ravindran, and Thalappil Pradeep, *ACS Sustainable Chem. Eng.*, 9 (2021), 12788-12799 (DOI: 10.1021/acssuschemeng.1c03272).
9. Isotopic exchange of atomically precise nanoclusters with materials of varying dimensions: From nanoscale to bulk, Papri Chakraborty, Paulami Bose, Jayoti Roy, Abhijit Nag, Biswajit Mondal, Amrita Chakraborty, and Thalappil Pradeep, *J. Phys. Chem. C*, 125 (2021) 16110–16117 (DOI: 10.1021/acs.jpcc.1c02264).
10. Triboelectric generators for sustainable reduction leading to nanoparticles and nanoclusters, Vishal Kumar, Pillalamarri Srikrishnarka, Jyoti Sarita Mohanty, Murugesan Kannan, Ramamurthy Nagarajan, and Thalappil Pradeep, *ACS Sustainable Chem. Eng.*, 9 (2021) 7431-7436 (DOI: 10.1021/acssuschemeng.1c01586).
11. Gold cluster-loaded dendritic nanosilica: single particle luminescence and catalytic properties in the bulk, Jyoti Sarita Mohanty, Ayan Maity, Tripti Ahuja, Kamalesh Chaudhari, Pillalamarri Srikrishnarka, Vivek Polshettiwar, and Thalappil Pradeep, *Nanoscale*, 13 (2021) 9788-9797 (DOI: 10.1039/d1nr00619c).
12. Transformation of nanodiamonds to onion-like carbons by ambient electrospray deposition, Deeksha Satyabola, Tripti Ahuja, Sandeep Bose, Biswajit Mondal, Pillalamarri Srikrishnarka, Murugesan Kannan, B. Krishnamurthy Spoorthi, and Thalappil Pradeep, *J. Phys. Chem. C*, (2021) (DOI: 10.1021/acs.jpcc.1c00166).

13. Ambient microdroplet annealing of nanoparticles, Angshuman Ray Chowdhuri, B. K. Spoorthi, Biswajit Mondal, Paulami Bose, Sandeep Bose, and Thalappil Pradeep, *Chem. Sci.*, 12 (2021) 6370–6377 (DOI: 10.1039/d1sc00112d).
14. Molecular materials through microdroplets: Synthesis of protein-protected luminescent clusters of noble metals, Sandeep Bose, Amit Chatterjee, Shantha Kumar Jenifer, Biswajit Mondal, Pillalamarri Srikrishnarka, Debasmita Ghosh, Angshuman Ray Chowdhuri, M. P. Kannan, Sailaja Elchuri, and Thalappil Pradeep, *ACS Sustainable Chem. Eng.*, 9 (2021) 4554–4563 (DOI: 10.1021/acssuschemeng.0c09145).
15. Facile crystallization of ice I_h via formaldehyde hydrate in ultrahigh vacuum under cryogenic conditions, Jyotirmoy Ghosh, Gaurav Vishwakarma, Subhadip Das, and Thalappil Pradeep, *J. Phys. Chem. C*, 125 (2021) 4532–4539 (DOI: 10.1021/acs.jpcc.0c10367).
16. 2D-Molybdenum disulfide-derived ion source for mass spectrometry, Pallab Basuri, Sourav Jana, Biswajit Mondal, Tripti Ahuja, Keerthana Unni, Md Rabiul Islam, Subhashree Das, Jaydeb Chakrabarti, and Thalappil Pradeep, *ACS Nano*, 15 (2021) 523-531 (DOI: 10.1021/acsnano.0c09985).
17. Scalable drop-to-film condensation on a nanostructured hierarchical surface for enhanced humidity harvesting, Ankit Nagar, Ramesh Kumar, Pillalamarri Srikrishnarka, Tiju Thomas, and Thalappil Pradeep, *ACS Appl. Nano Mater.*, 4 (2021) 1540-1550 (DOI: 10.1021/acsanm.0c03032).
18. Toward vibrational tomography of citrate on dynamically changing individual silver nanoparticles, Tripti Ahuja, Kamalesh Chaudhari, Ganesan Paramasivam, Gopi Ragupathy, Jyoti Sarita Mohanty, and Thalappil Pradeep, *J. Phys. Chem. C*, 125 (2021) 3553-3566 (DOI: 10.1021/acs.jpcc.0c09981).
19. Hierarchical assembly of atomically precise metal clusters as a luminescent strain sensor, Debasmita Ghosh, Mohd Azhardin Ganayee, Anirban Som, Pillalamarri Srikrishnarka, Nidhi Murali, Sandeep Bose, Amrita Chakraborty, Biswajit Mondal, Pijush Ghosh, and Thalappil Pradeep, *ACS Appl. Mater. Interfaces*, 125 (2021) 3256–3267 (DOI: 10.1021/acsami.0c19239).

20. Near-infrared chiral plasmonic microwires through precision assembly of gold nanorods on soft biotemplates, Amrita Chakraborty, Nonappa, Biswajit Mondal, Kamalesh Chaudhari, Heikki Rekola, Ville Hynninen, Mauri Kostiainen, Robin Ras, and Thalappil Pradeep, *J. Phys. Chem. C*, 125 (2021) 3256-3267 (DOI: 10.1021/acs.jpcc.0c11512).
21. Selective extraction of gold by niacin, Abhijit Nag, Md Rabiul Islam, and Thalappil Pradeep, *ACS Sustainable Chem. Eng.*, 9 (2021) 2129–2135 (DOI: 10.1021/acssuschemeng.0c07409).

Publications with other groups

22. Design of a waste paper-derived chemically 'reactive' and durable functional material with tailorable mechanical property following an ambient and sustainable chemical approach, Arpita Shome, Adil Rather, Angana Borbora, Pillalamarri Srikrishnarka, Avijit Baidya, Thalappil Pradeep, and Uttam Manna, *Chem. Asian J.*, 16 (2021) 1988-2001 (DOI: 10.1002/asia.202100475).
23. Kinetics of inter-cluster reactions between atomically precise noble metal clusters $[Ag_{25}(DMBT)_{18}]$-and $[Au_{25}(PET)_{18}]$- in room temperature solutions, Marco Neumaier, Ananya Baksi, Patrick Weis, Erik Schneider, Papri Chakraborty, Horst Hahn, Thalappil Pradeep and Manfred Kappes, *J. Am. Chem. Soc.*, 143 (2021) 6969–6980 (DOI: 10.1021/jacs.1c01140).

*Some of these papers will appear in 2022. Some were listed in publications of 2020 without page numbers, but appeared in 2021.

Editorials

24. Guest editorial on Special Issue on “Nanoclusters”: A Glimpse into the Efforts to Redefine Matter at the Nanoscale, Thalappil Pradeep, *Small*, 17 (2021) 2102931. (DOI:10.1002/smll.202102931).
25. Expectations for perspectives in ACS Sustainable Chemistry & Engineering, David T. Allen, D. Julie Carrier, Jingwen Chen, Nicholas Gathergood, Jinlong Gong, Hongxian Han, King Kuok (Mimi) Hii, Bing-Joe Hwang, Asha Liza James, Peter Licence, Michael Meier, Audrey Moores, Ryuhei Nakamura, Thalappil Pradeep, Bert Sels, Bala Subramaniam, Michael K. C. Tam, Lin Zhang, Julio F. Serrano, *ACS Sustainable Chem. Eng.*, 9 (2021) 16528–16530. (DOI:10.1021/acssuschemeng.1c07865).
26. Nanotechnology for Sustainability in ACS Sustainable Chemistry & Engineering: Some Pointers,Thalappil Pradeep, Zhenxing Li and Rafael Luque, *ACS Sustainable Chem. Eng.*, 9 (2021) 14327–14329. (DOI:10.1021/acssuschemeng.1c07031).
27. ACS Sustainable Chemistry & Engineering Welcomes Manuscripts on Advanced E-Waste Recycling, Lingen ZhangLingen Zhang, More by Lingen Zhang, Thalappil Pradeep, Peter Licence, Bala Subramaniam, and David T. Allen, *ACS Sustainable Chem. Eng.*, 9 (2021) 3624–3625. (DOI: 10.1021/acssuschemeng.1c01344).
28. The Power of the United Nations Sustainable Development Goals in Sustainable Chemistry and Engineering Research, Paul Anastas, Marcelo Nolasco, Francesca Kerton, Mary Kirchhoff, Peter Licence, Thalappil Pradeep, Bala Subramaniam, and Audrey Moores, *ACS Sustainable Chem. Eng.*, 9 (2021) 8015-8017. (DOI: 10.1021/acssuschemeng.1c03762).
29. Lab to Market: Where the Rubber Meets the Road for Sustainable Chemical Technologies, Bala Subramaniam, David Allen, King Kuok (Mimi) Hii, Juan Colberg, and Thalappil Pradeep, *ACS Sustainable Chem. Eng.*, 9 (2021) 2987-2989. (DOI: 10.1021/acssuschemeng.1c00980).

General Articles

1. Personal news, Sanjay Bajpai (1965–2021), Ashutosh Sharma, Rajiv, K. Tayal Akhilesh Gupta, Neelima Alam, G. V. Raghunath Reddy, Vineet Saini, J. B. V. Reddy, Ranjith Krishna Pai, Ligy Philip, Prasada Raju, and T. Pradeep, Current Science, 120 (2021) 1790-1791.
2. A popular science article: Sritama Mukherjee and T. Pradeep, Water security through advanced materials, Emerging Technology Insight 2021, published by the Commonwealth Security Group, London. Available at: https://www.commonwealthsecurity.org/emerging-technology-insight-2021, pages 66-68.
3. Popular science article in Malayalam, *Keralam jnanasamoohathilekku valarumbol*, T. Pradeep, Deshabhimani Weekly, 30 (52) (2021) 8-13, December 5, 2021.

Book Chapter

1. Nanosensors for water quality monitoring, Tanvi Gupte and Thalappil Pradeep, Separations of Water Pollutants with Nanotechnology, Satinder Ahuja (Ed), Elsevier (2022) (ISBN: 9780323907637)

Journal Papers

Publications from our group

PCCP

ROYAL SOCIETY OF CHEMISTRY

PAPER

View Article Online
View Journal

Check for updates

Cite this: DOI: 10.1039/d1cp04716g

Gas phase ion chemistry of titanium–oxofullerene with ligated solvents†

Jayoti Roy,‡[a] Papri Chakraborty,‡[a] Ganesan Paramasivam,[a] Ganapati Natarajan[b] and Thalappil Pradeep *[a]

Received 15th October 2021,
Accepted 23rd December 2021

DOI: 10.1039/d1cp04716g

rsc.li/pccp

We investigated the gas phase fragmentation events of highly symmetric fullerene-like (FN-like) titanium oxo-cluster anions, $[H_{12}Ti_{42}O_{60}(OCH_3)_{42}(HOCH_3)_{10}(H_2O)_2]^{2-}$ (**1**) and $[H_7Ti_{42}O_{60}(OCH_3)_{42}(HOCH_3)_{10}(H_2O)_3]^{1-}$ (**2**). These oxo-clusters contain a closed cage $Ti_{42}O_{60}$ core, protected by a specific number of methoxy, methanol, and water molecules acting as ligands. These dianionic and monoanionic species were generated in the gas phase by electrospray ionization of the $H_6[Ti_{42}(\mu^3\text{-}O)_{60}(O^iPr)_{42}(OH)_{12}]$ (TOF) cluster in methanol. Collision induced dissociation studies of **1** revealed that upon increasing the collision energy, the protecting ligands were stripped off first, and $[Ti_{41}O_{58}]^{2-}$ was formed as the first fragment from the $Ti_{42}O_{60}$ core. Thereafter, systematic TiO_2 losses were observed giving rise to subsequent fragments like $[Ti_{40}O_{56}]^{2-}$, $[Ti_{39}O_{54}]^{2-}$, $[Ti_{38}O_{52}]^{2-}$, *etc.* Similar fragments were also observed for monoanionic species **2** as well. Systematic 23 TiO_2 losses were observed, which were followed by complete shattering of the cage. We also carried out computational studies using density functional theory (DFT) to investigate the structures and fragmentation mechanism. The fragmentation of TOF was comparable to the fragmentation of C_{60} ions, where systematic C_2 losses were observed. We believe that this is a consequence of topological similarity. The present study provides valuable insights into the structural constitution of TOF clusters and stability of the parent as well as the resulting cage-fragments in the gas phase.

1 Introduction

Titanium dioxide (TiO_2) has drawn significant research interest since the last few decades, owing to its intrinsic physicochemical properties and wide range of applications in energy, catalysis, and environmental sciences.[1,2] Molecular analogues of TiO_2 semiconducting materials are Ti–oxo clusters (TOCs), also known as polyoxo–titanium clusters (PTCs).[3–6] PTCs are one of the emerging classes of inorganic metal–oxo nanoparticles. PTCs show photocatalytic activity and find enormous applications in solar energy conversion, degradation of environmental pollutants, wastewater treatment, and other photochemical processes.[7,8] Energy-states and detailed structure–property relationships of PTCs have also been studied in the literature.[9–11] In the recent past, a wide variety of PTCs, such as Ti_6O_3,[7] Ti_6O_4,[12] $Ti_{13}O_{10}$,[13] $Ti_{17}O_{24}$,[14] $Ti_{18}O_{27}$,[15] $Ti_{25}O_{26}$,[16] $Ti_{28}O_{48}$,[17] $Ti_{34}O_{50}$,[18] $Ti_{52}O_{74}$,[14] *etc.*, have been synthesized, by varying O-containing ligands as well as other secondary ligands, with distinct molecular formulae.

Most of the reported PTCs are composed of Ti atoms bonded with O-donor ligands like carboxylates, alkoxides, *etc.* Apart from O-donor ligands, P-donor ligands like phosphonate, phosphinate and phenyl phosphonate (Phen-PO_3) as well as N-donor ligands like 2-amino-ethylphosphonate, 1,10-phenanthroline, *N*,*N*-dimethylformamide (DMF), *N*,*N*-dimethylacetamide (DMA), pyridine, *etc.*, exhibit a strong binding affinity with Ti. Fang *et al.* reported $Ti_{52}(\mu\text{-}OH)_2(\mu\text{-}O)_{14}(\mu^3\text{-}O)_{50}(\mu^4\text{-}O)_8(PA)_{34}(O^iPr)_{28}$ (where PA is propionic acid), which is a PTC with the highest nuclearity reported to date. It consisted of a stepwise layered assembly of smaller units of $Ti_6(\mu^3\text{-}O)_4(BDC)_2(PA)_2(O^iPr)_{10}$ clusters where BDC represents benzenedicarboxylate.[14] Other PTCs containing noble metals $[Ag(CH_3CN)]_2[Ag_6Ti_{16}(\mu_3\text{-}O)_{18}(\mu_2\text{-}O)_4(\text{benzoate})_{26}(CH_3CN)_2]$ (PTC-47) and $[Ag_6Ti_{16}(\mu_3\text{-}O)_{16}(\mu_2\text{-}O)_4(\text{benzoate})_{24}(CH_3COO)_4(CH_3CN)_2$ (PTC-48) with Ag–O–Ti bonds are also known.[19]

On the other hand, a great variety of fullerene-like (FN-like) inorganic cluster systems with well-established synthetic protocols and structural details have been reported.[20–26] They can be grouped into various classes based on the atomic construction of their metal core, metal–metal bonding, ligands and

---

[a] *DST Unit of Nanoscience (DST UNS) & Thematic Unit of Excellence (TUE), Department of Chemistry, Indian Institute of Technology Madras, Chennai 600036, India. E-mail: pradeep@iitm.ac.in*

[b] *International Centre for Clean Water (ICCW), IIT Madras Research Park, Taramani, Chennai 6000113, India*

† Electronic supplementary information (ESI) available: UV-vis absorption, additional ESI-MS, CID-MS data, and theoretically optimized structures (PDF). See DOI: 10.1039/d1cp04716g

‡ These authors contributed equally.

polyoxometalate building units. Several of them contain regular polyhedral cluster-like structures with higher molecular symmetry, like As_{20} which was reported by Moses *et al.*[20] and $Mo_{132}O_{372}$ which was reported by Müller *et al.*[26] A sphere-like $Mo_{72}Fe_{30}$ cluster, with high solution phase stability and pH-dependent tunable size, was reported by Liu *et al.*[27]

Despite the progress in research interest in the bottom-up synthetic strategies and various applications of PTCs, their gas phase behaviours are often unclear. A few Ti–oxo clusters like $[Ti_{17}(\mu^2\text{-}O)_2(\mu^3\text{-}O)_{18}(\mu^4\text{-}O)_2(PA)_8(O^iPr)_{16}]$,[14] $[Ti_{52}(\mu\text{-}OH)_2(\mu\text{-}O)_{14}(\mu^3\text{-}O)_{50}(\mu_4\text{-}O)_8(PA)_{34}(O^iPr)_{28}]$,[14] $[Eu_{24}Ti_8(L)_{31}(HL)_{42}(CH_3CN)_{11}(H_2O)_8]\cdot nH_2O$,[24] ($H_2L$ = salicylic acid, $n \sim 50$), $[Ti_6O_5(OCH_3)_4(C_5N_3O_2H_7)_4K_2H_5(H_2O)_5]^-$ have been characterized by electrospray ionization mass spectrometry (ESI MS) to understand their composition in the solution phase.[28]

A system of particular importance is titanium-oxofullerene (Ti–oxoFN), $Ti_{42}O_{60}$. Gao *et al.* established its crystal structure and revealed its composition as $H_6[Ti_{42}(\mu^3\text{-}O)_{60}(O^iPr)_{42}(OH)_{12}]$ (TOF), where O^iPr is an isopropoxide ligand.[29] This cluster consists of a $Ti_{42}O_{60}$ core that exhibits an icosahedral (I_h) symmetry, similar to that of C_{60}. Facile ionization of the cluster from solution allowed its gas phase characterization by ESI MS. Until now, there have been a few reports on gas phase dissociation studies of small $Ti_xO_y^+$ ions, produced by laser ablation Ti in the presence of oxygen, but studies on larger Ti–O clusters, synthesized in the solution or solid phase, remain unexplored.[30,31]

In this paper, we present a study of the gas phase dissociation mechanism of the TOF cluster to understand its structural constitution. We show that upon increasing the collision energy, first, the loss of the peripheral ligands occurred, followed by the dissociation of the metal–oxo cage. TiO_2 units were lost systematically from the Ti–oxo (Ti–O) cage with increasing collision energy (CE) followed by a complete rupture of its structure. This may be compared with the case of fullerenes (FNs), where C_2 loss occurred systematically. Thus, gas phase fragmentation events of TOF are shown to have similarities with the gas phase fragmentation of FNs. The dissociation events of TOF were also modelled using density functional theory (DFT) to understand the structures resulting from the fragmentation of the parent $Ti_{42}O_{60}$ core. We note that understanding advanced materials through mass spectrometry is an important direction of research as demonstrated here.[32]

2 Experimental section

2.1 Reagents and materials

All the reagents were commercially available and were used without further purification. Titanium(IV) isopropoxide ($Ti(O^iPr)_4$, 99.9%, was purchased from Avra Synthesis Private Limited. Analytical grade formic acid (HCOOH), isopropyl alcohol ($(CH_3)_2CHOH$) and HPLC grade toluene and methanol ($HOCH_3$) were used.

2.2 Synthesis of TOF

TOF was synthesized by slightly modifying the reported method.[29] In ∼5.5 mL of isopropyl alcohol, 0.92 mL $Ti(O^iPr)_4$ (3.0 mmol), and 5 drops of formic acid were added at room temperature. The solution was refluxed at 100 °C for 4 days and then cooled to room temperature. The solution of the as-synthesized cluster was then slowly evaporated at room temperature. Colourless crystals of TOF were obtained after a few days and used for further studies.

2.3 Instrumentation

UV-Vis studies were performed using a PerkinElmer Lambda 25 UV-vis spectrometer. All ESI MS studies were performed using a Waters Synapt G2-Si high definition mass spectrometer (HDMS). The mass spectrometric measurements were performed in the negative ion mode. For ESI MS studies, TOF was dissolved in a toluene–$HOCH_3$ mixture at a concentration of $\sim 1\ \mu g\ mL^{-1}$. Capillary voltage, cone voltage, and source offset were kept at 2 kV, 0 V, and 0 V, respectively, to obtain a well resolved mass spectrum of TOF. The source temperature and desolvation temperature were maintained at 100 and 150 °C, respectively. Desolvation gas flow of 400 L h^{-1} was used. In the Synapt G2-Si instrument, the mass-selected ions pass through trap, ion mobility and transfer cells before entering the time-of-flight analyser. In the trap and transfer cells, the precursor ions can be collided with Ar gas for collision-induced dissociation (CID) studies. In our experiments, we carried out CID in both trap and transfer cells, while the IMS cell was kept off. No extra voltages were applied in the IMS cell to avoid additional fragmentation of the ions. In trap, the collision energy (CE) was varied between 0 and 200 CE (CE is expressed in instrumental units). Further increase of CE was attained by increasing the voltages in the transfer cells. As the IMS cell did not contribute any effect on the applied collision voltages, the total CE is considered as the sum of the trap and transfer CEs. A simplified view of the instrumental set-up is presented in Scheme 1. DFT calculations were performed with the grid-based projector-augmented wave (GPAW) method. All structures were optimized using the Perdew–Burke–Ernzerhof (PBE) functional along with the DZP (double-ζ plus polarization) basis set in a linear combination of atomic orbitals (LCAO) formalism. Additional details are provided in the ESI† (see SI1).

3 Results and discussion

The TOF was synthesized following the reported method[29] as described in the experimental section. It was dissolved in toluene and characterized by UV-vis as shown in Fig. S1 (ESI†). The solution phase absorption spectrum was similar to the reported solid-state UV-vis spectrum.[29] The structure of TOF, modelled using the co-ordinates of its crystal structure,[29] is presented in Fig. 1(A). The metal–oxo core of the cluster consists of 42 Ti atoms, among which 12 Ti atoms, labelled as {Ti1} are seven co-ordinated and the remaining 30 Ti atoms, labelled as {Ti2} are five co-ordinated. These 12 {Ti1} atoms form a platonic $\{Ti_{12}\}$ icosahedron which is further capped by a $\{Ti_{30}\}$ icosidodecahedron. This $\{Ti_{30}\}$ icosidodecahedron is constituted by five co-ordinated Ti atoms {Ti2}. These 42 Ti

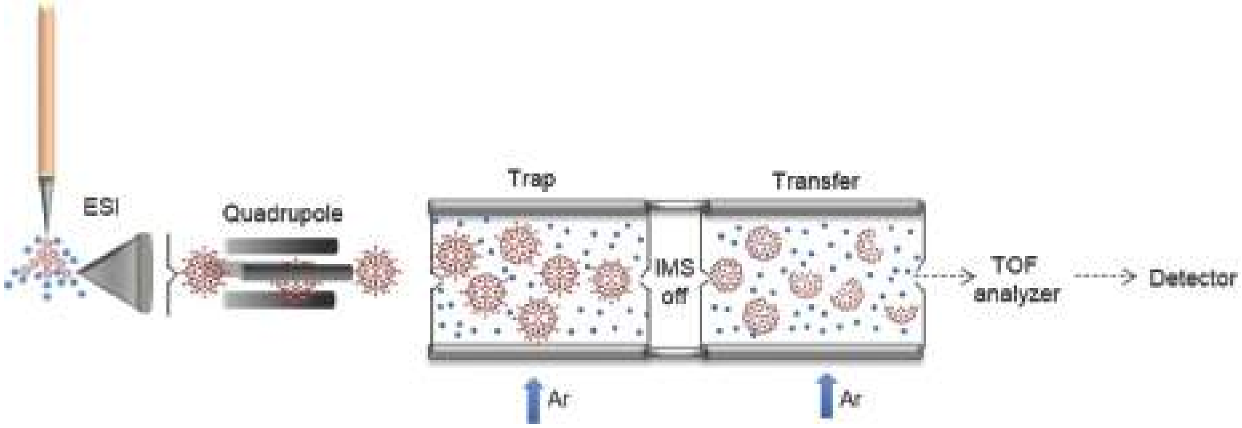

Scheme 1 Schematic representation of the instrumental setup used for collision-induced dissociation studies. Collisions occurred in the trap and transfer cells, after mass-selection of the ions using the quadrupole mass filter.

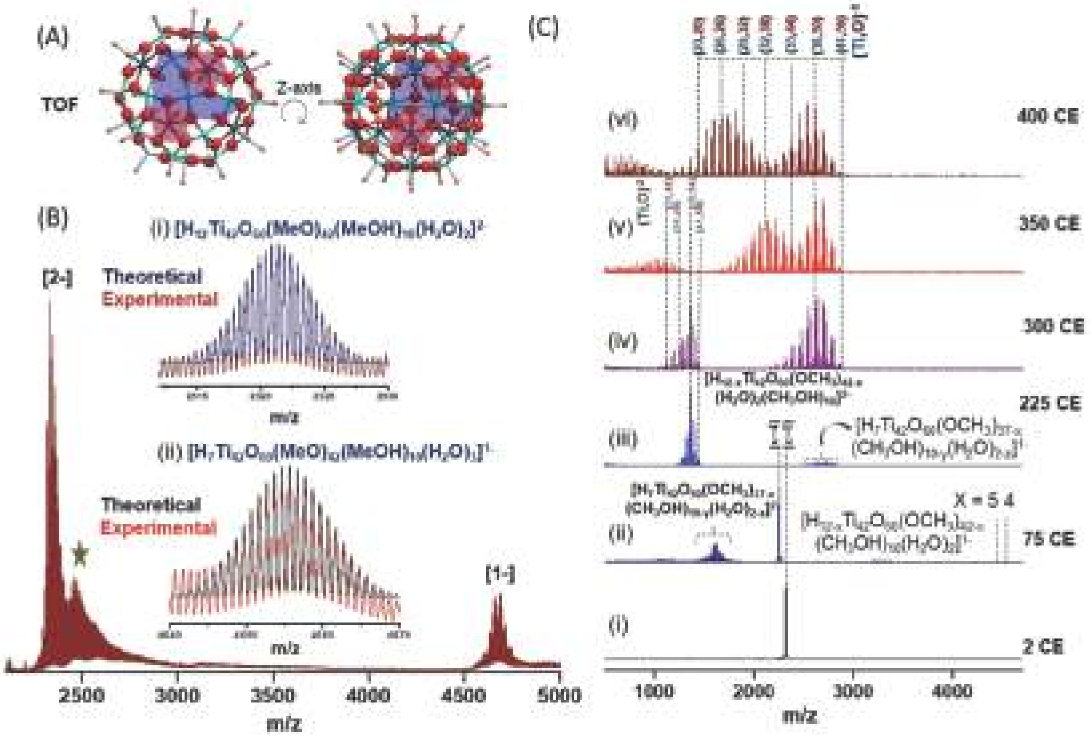

Fig. 1 (A) Molecular structures of TOF, which was modelled using the co-ordinates of its reported crystal structure. Colour codes: Deep blue, {Ti1}; cyan, {Ti2}; red, cage oxygen; blush red, ligand oxygen. (B) ESI MS of TOF. Insets (i) and (ii) show the theoretical and experimental isotopic distributions of the mass spectrum of $\{H_{12}Ti_{42}O_{60}(OCH_3)_{42}(HOCH_3)_{10}(H_2O)_2\}^{2-}$ (**1**) and $\{H_7Ti_{42}O_{60}(OCH_3)_{42}(HOCH_3)_{10}(H_2O)_3\}^{1-}$ (**2**), respectively. (C) CID mass spectra of **1**. For clarity, the spectra are shown for certain CEs only. (Detailed CID spectra are in Fig. S3 and S4, ESI†). Some of the peaks are labelled as (*x*,*y*) where *x* and *y* correspond to the number of Ti and O atoms of the Ti–O cage fragments, respectively.

atoms are connected by 60 μ^3-O^{2-} ions, and the overall structure exhibits a FN-like $\{O_{60}\}$ arrangement. Specifically, the $\{O_{60}\}$ cage of the cluster core is comprised of $\{O_5\}$ pentagonal rings and $\{O_6\}$ distorted hexagonal rings, arranged in a fashion similar to the C_{60} cage. The {Ti1} atoms stabilize the 12 $\{O_5\}$ rings of the $\{O_{60}\}$ cage, giving an overall I_h symmetry to the cluster, thus establishing its structural analogy with C_{60}.

ESI MS was performed using a toluene solution of TOF, further diluted with methanol. ESI MS of TOF is presented in Fig. 1(B). The peripheral isopropoxide ligands of TOF were exchanged with methoxy ligands and the cluster was ionized in dianionic and monoanionic states during ESI MS. A similar phenomenon was observed in the reported mass spectrum of TOF also.[29] The compositions of the cluster ions were confirmed by comparing the experimental isotopic distributions with the calculated ones (Fig. 1(B)(i and ii)). The peaks at *m*/*z* 2321 and 4655 were assigned to $\{H_{12}Ti_{42}O_{60}(OCH_3)_{42}(HOCH_3)_{10}(H_2O)_2\}^{2-}$(1) and $\{H_7Ti_{42}O_{60}(OCH_3)_{42}(HOCH_3)_{10}(H_2O)_3\}^{1-}$ (2) ions, respectively. We presumed that the isolated hydrogen atoms $\{H_{12}\}$ and $\{H_7\}$ are present at the periphery of cluster ions **1** and **2** respectively but their exact positions are unknown. However, the peaks for these parent cluster ions were also associated with a bunch of other peaks in the *m*/*z* range of 2300–2550 and 4525–4800, respectively. Expanded views of these *m*/*z* ranges are presented in Fig. S2 (ESI†) which revealed that these peaks originated due to the exchange between isopropoxide and methoxy ligands, occurring in solution.

We primarily focused on CID studies of the doubly charged precursor ion **1**. The precursor ion **1** was selected and collided with Ar gas in the trap and transfer cells. By understanding its fragmentation pathway, we attempted to resolve the structural stability and subunits that constituted the FN-like Ti–O cage.

3.1 CID of TOF

CID is a well-established technique of fragmentation of ions by collision with gas molecules.[33–35] Here, CID of the molecular ion of interest, *i.e.* (*m*/*z* 2321, TOF in 2− charge state) was studied over a range of activation energies, from 2 to 400 CE (Fig. 1(C)). Ion **1** was subjected to collisions with Ar gas inside the trap by gradually increasing energy from 0 to 200 CE. The intensities of the parent and fragmented product ions were monitored carefully. Ion **1** is surrounded by methoxy groups from outside and $HOCH_3$ and H_2O ligands from inside the Ti–O cage.[29] With increase in energy from 2 to 20 CE, fragmented ions were seen resulting from the neutral loss of *m*/*z* 32. These losses can be attributed to either neutral $HOCH_3$ loss or loss of a $-OCH_3$ ligand along with a H. As the –OMe ligands protected the outer surface of the Ti–O cage, whereas the neutral $HOCH_3$ ligands were confined inside the cage, it is likely that loss of an -OMe ligand along with a H (–OMe/H) will be preferred. As discussed above, these additional Hs are present in the periphery of the ion **1**, although their exact positions are unknown. The first two $-OCH_3$/H loss resulted in the fragmented ions at *m*/*z* 2305 and 2289 (see Fig. S3(C), ESI† with molecular formulae $\{H_{11}Ti_{42}O_{60}(OCH_3)_{41}(HOCH_3)_{10}(H_2O)_2\}^{2-}$ and $\{H_{10}Ti_{42}O_{60}(OCH_3)_{40}(HOCH_3)_{10}(H_2O)_2\}^{2-}$, respectively).

With the gradual increase of energy from 20 to 50 CE, two more similar $-OCH_3$/H (*m*/*z* 32) losses were observed and the subsequent fragmented ions were detected at *m*/*z* 2273 and 2257, respectively (see Fig. S3(C), ESI†). With further increase in CE, the intensities of these peaks decreased. After 50 CE, the parent ion **1** was completely converted to fragmented ions and $\{H_8Ti_{42}O_{60}(OCH_3)_{38}(HOCH_3)_{10}(H_2O)_2\}^{2-}$ appeared as the most abundant species (see Fig. S3(C), ESI†).

At CE 65, the peak for $\{H_8Ti_{42}O_{60}(OCH_3)_{38}(HOCH_3)_{10}(H_2O)_2\}^{2-}$ started to fragment and a bunch of peaks of 2− charge state appeared in the *m*/*z* range of 1580 to 1830 (Fig. S3(A)(iv), ESI†). The intensities of these ions increased with increase in CE up to 175 CE (Fig. S3 and S4(i), ESI†). With the increase in CE, *m*/*z* values of the fragment ions moved to 1240–1580. These bunch of peaks appeared with small *m*/*z* differences of 7, 8, or 9 between the adjacent peaks. However, these were not well resolved. Also, as the formation of all these ions happened simultaneously, it was difficult to identify any systematic fragmentation here. These mass losses were probably due to the loss of the ligands, OCH_3, $HOCH_3$, and H_2O occurring simultaneously. Thus, it appeared that in the range of 65 to 175 CE, the ligands of the oxo-cage were lost preferentially.

Above 175 CE, these bunches of doubly charged peaks in the *m*/*z* range of 1280–1450 were resolved (see Fig. S4, ESI†) and their *m*/*z* values and isotopic patterns suggested that at this stage all the ligands of TOF were stripped off. Subsequently, fragmentation of the cage, which contained the $Ti_{42}O_{60}$ core, was observed in the mass spectrum. In the trap cell, the maximum accelerating voltage could be increased to 200 CE. At CE 200, the fragments observed were $[Ti_{41}O_{58}]^{2-}$ (*m*/*z* 1445), $[Ti_{40}O_{56}]^{2-}$(*m*/*z* 1405), $[Ti_{39}O_{54}]^{2-}$ (*m*/*z* 1365), $[Ti_{38}O_{52}]^{2-}$ (*m*/*z* 1325), $[Ti_{37}O_{50}]^{2-}$ (*m*/*z* 1285) and $[Ti_{36}O_{48}]^{2-}$ (*m*/*z* 1245) with successive neutral losses of *m*/*z* 40, *i.e.* TiO_2 (see Fig. S4, ESI†). $(TiO_2)_n^{+}$ losses were also observed during photofragmentation or CID of smaller $Ti_xO_y^{+}$ clusters, produced by the laser ablation technique in the gas phase.[30,31] All the $HOCH_3$ and H_2O ligands, which were confined inside the Ti–O cage, were also lost prior to the formation of the first cage fragment, *i.e.* $[Ti_{41}O_{58}]^{2-}$, see Fig. S3(B) (ESI†) and Fig. 1C(v). At 200 CE also, limited fragmentation of the Ti–O core was observed (see Fig. S4(ii), ESI†), and it was evident that the Ti–O cage exhibited high gas phase stability and required more energy to undergo complete fragmentation. Further energy required for the fragmentation of the cage was supplied by increasing CE in the transfer cell. In the transfer cells, an additional 0–200 CE was applied. As discussed earlier in the instrumental section, we are referring to the total CE as a sum of the trap and transfer energies. With further increase of CE in the transfer cells, more TiO_2 fragments were lost from the cage. At 300 CE (Fig. 1(C)(iv) and Fig. S4(iv), ESI†), fragment ions such as $[Ti_{35}O_{46}]^{2-}$ (*m*/*z* 1205), $[Ti_{34}O_{44}]^{2-}$ (*m*/*z* 1165), $[Ti_{33}O_{42}]^{2-}$ (*m*/*z* 1125) and $[Ti_{32}O_{40}]^{2-}$ (*m*/*z* 1085) were observed in ESI MS. All these peaks appeared due to the systematic loss of TiO_2 (Fig. 1(C)(iv and v)) and the fragmentation continued until $[Ti_{29}O_{34}]^{2-}$ (*m*/*z* 965) was formed. Thus, collisional excitation resulted in a systematic loss of TiO_2 subunits, which probably constituted the primary building blocks of the Ti–O cage of TOF. However, after CE 350, again a bunch of poorly resolved peaks appeared in the range below *m*/*z* 950 due to further fragmentation of the cage (Fig. 1(C)(v and vi)) which indicated that the cluster core was disrupted completely. The CID mass spectra for the entire range of CEs from 2 to 400 CE are shown in the ESI† (Fig. S3 and S4).

However, apart from this fragmentation channel of the ions in the 2− charge state, another pathway of fragmentation from ion **1** was also observed. At 65 CE, a singly charged peak at *m*/*z* 4530 appeared which was assigned to $\{H_7Ti_{42}O_{60}(OCH_3)_{38}(HOCH_3)_{10}(H_2O)_3\}^{1-}$ (see Fig. S3(iv) and S5(A and B), ESI†). A comparison of the isotopic distribution of the theoretical and experimental peaks at *m*/*z* 4530 is shown in Fig. S4(C) (ESI†).

With the gradual increase in energy from 65 to 150 CE, a series of singly charged peaks also appeared in the *m*/*z* range of 2900–3400 (see Fig. S3(A)(iv–vi), ESI†). Similar to the fragment ions in 2− charged state, here also, the bunch of peaks, appearing mostly due to the loss of the peripheral ligands, were not well-resolved until 175 CE. The monoanionic fragment ions, $[Ti_{41}O_{57}]^{1-}$, $[Ti_{40}O_{55}]^{1-}$, $[Ti_{39}O_{53}]^{1-}$, $[Ti_{38}O_{51}]^{1-}$, $[Ti_{37}O_{49}]^{1-}$ and $[Ti_{36}O_{47}]^{1-}$ were detected at 250 CE, which differed by *m*/*z* 80 (see Fig. S4(iii), ESI†). These were also formed by systematic loss of TiO_2, similar to the case of the dianionic cage fragments. At around 300 CE, further fragmentation occurred in the monoanionic state too and more TiO_2 units were lost from the cage. Thus, the species $[Ti_{35}O_{45}]^{1-}$, $[Ti_{34}O_{43}]^{1-}$, $[Ti_{33}O_{41}]^{1-}$ and $[Ti_{32}O_{39}]^{1-}$ were formed at 300 CE (see Fig. S4(iv), ESI†). At 400 CE, $[Ti_{19}O_{13}]^{1-}$ was observed at *m*/*z* 1116. The CE could not be increased further in the current instrumental set-up. An expanded view of the CID mass spectrum at 400 CE is shown in Fig. 2, which revealed the presence of another systematic fragmentation pathway for the monoanionic fragmented ions. Each of the above-mentioned monoanionic anions was accompanied by another peak at a slightly lower *m*/*z* value with a difference of 16. This was attributed to the loss of an O atom from the respective monoanionic fragments. The molecular compositions of these Ti–O cage fragments were confirmed by comparing the calculated mass spectrum with the experimental ones. Thus, these additional fragment ions were assigned to $[Ti_{41}O_{56}]^{1-}$, $[Ti_{40}O_{54}]^{1-}$, $[Ti_{39}O_{52}]^{1-}$, $[Ti_{38}O_{50}]^{1-}$, $[Ti_{37}O_{48}]^{1-}$, $[Ti_{36}O_{46}]^{1-}$, $[Ti_{35}O_{44}]^{1-}$, $[Ti_{34}O_{42}]^{1-}$, $[Ti_{33}O_{40}]^{1-}$, $[Ti_{32}O_{38}]^{1-}$, $[Ti_{31}O_{36}]^{1-}$, $[Ti_{30}O_{34}]^{1-}$, $[Ti_{29}O_{32}]^{1-}$ and $[Ti_{28}O_{30}]^{1-}$ (see Fig. S6, ESI†). In Fig. 2(B), the expanded mass spectrum in the range of *m*/*z* 2448–2485 is shown and theoretical and experimental mass spectrum of $[Ti_{36}O_{46}]^{1-}$ and $[Ti_{36}O_{47}]^{1-}$ are compared. Isotopic distributions of other fragments are shown in the ESI† (see Fig. S7). For simplicity, we categorize the fragmentation in the monoanionic charge state into two fragmentation channels: path-I which produced fragment ions containing an odd number of O atoms and path-II which produced fragment ions containing an even number of O atoms. Thus, the systematic loss of neutral TiO_2 was the predominant dissociation pathway of the Ti–O cage in both 2− and 1− charge states. These fragmentation events of the Ti–O cage of TOF are comparable to the dissociation of FN molecules where a systematic loss of C_2 units occurred.[36] Similar fragmentation study of the intact monoanionic parent ion **2** (*m*/*z* 4655, detected in ESI MS as shown in Fig. 1(B)) was also performed. CID spectra with increasing laboratory CE for **2** are shown in Fig. S8 (ESI†). Species **2** also showed a loss of ligands from the cluster with the gradual increase in CE. The fragmentation of species **2** was observed around 400 CE as shown in Fig. S8 and S9 (ESI†).

3.2 Collision energy-resolved fragmentation curves

CE resolved fragmentation curves were constructed by plotting the relative intensities of a particular ion as a function of the applied CE.[32,37] The relative intensities of ions were calculated using the following formula:

$$I_{\mathrm{r}} = \frac{I_{\mathrm{p}}}{I_{\mathrm{t}}}$$

where I_{r} refers to the relative intensity of a particular ion, I_{p} refers to the actual intensity of the particular ion and I_{t}

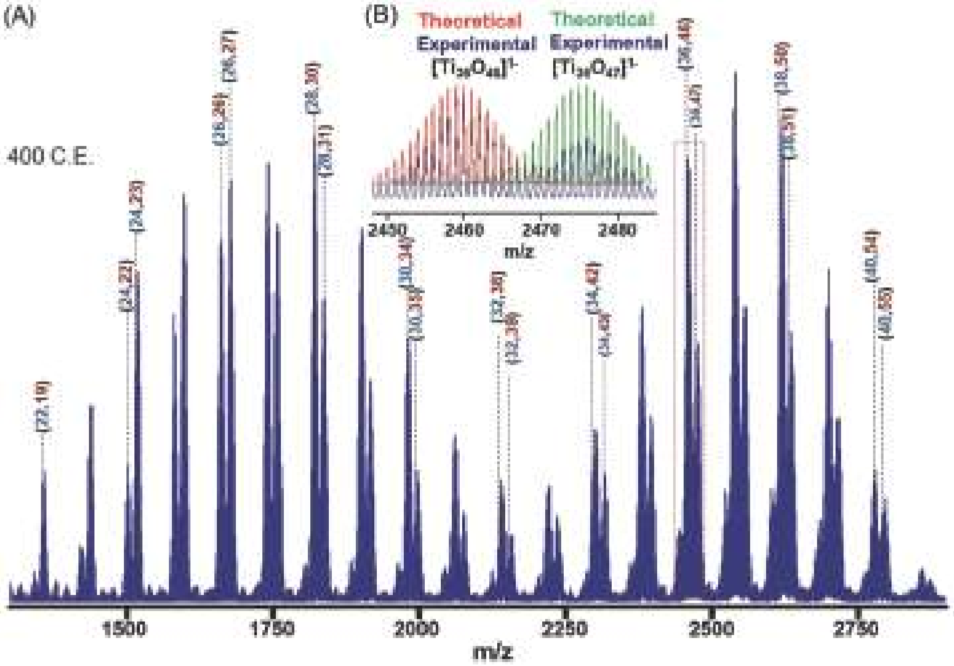

Fig. 2 (A) Expanded CID mass spectrum of TOF at 400 CE showing the monoanionic cage fragment ions. Alternative peaks are assigned with (*x*,*y*) where *x* denotes the no. of Ti and *y* denotes the no. of O atoms. Detailed assignments are shown in Fig. S6(B) (ESI†). (B) Theoretical and experimental isotopic distributions of one set of fragment ions, *i.e.* $[Ti_{36}O_{46}]^{1-}$ and $[Ti_{36}O_{47}]^{1-}$.

refers to the sum of the intensities of parent and all the fragment ions. CE resolved curves are helpful in understanding the correlation between the yield of the fragment ions and their internal energy distribution.[38,39]

In Fig. 3, CE-resolved dissociation curves for the fragmentation of the dianionic species **1**, are presented. Such energy-resolved curves explained the extent of energy demand for the dissociation processes and also presented the various parallel and successive fragmentation events of the Ti–O cage as a function of applied CE. CE-resolved curves of the precursor ion **1** and all the mono- and dianionic fragments resulting from it are presented in Fig. 3(A). Fig. 3(A)(i) shows an expanded view of the relative abundance *vs.* CE of all the above-mentioned fragmented ions. The product ions with relative abundance below 0.01 were neglected in these plots. The curves for the dianionic fragment ions are presented separately in Fig. 3(B). In Fig. 3(C)(i and ii), similar fragmentation curves for the monoanionic anions are shown. The energy-resolved fragmentation curve of the parent dianion **1** exhibited a sigmoidal decay pattern. The intermediate species formed due to the loss of ligands of **1** have been ignored in the energy-resolved studies as those peaks were poor in resolution and also our primary objective was to investigate the fragmentation mechanism of the Ti–O cage. From Fig. 3(A), it is clear that the parent ion **1** was dissociated completely beyond 50 CE. The fragmentation of FN-like cage started around 200 CE, which suggested that though the loss of the peripheral ligands was facile, the Ti–O cage was highly stable in the gas phase and needed high energy to undergo fragmentation. From Fig. 3(B) and (C), it is clear that the loss of TiO_2 occurred in a systematic fashion. In Fig. 3(B), the fragmentation efficiency curves for the dianionic cage fragments of $[Ti_{34}O_{44}]^{2-}$, $[Ti_{33}O_{42}]^{2-}$, $[Ti_{32}O_{40}]^{2-}$, $[Ti_{31}O_{38}]^{2-}$, $[Ti_{30}O_{36}]^{2-}$ and $[Ti_{29}O_{34}]^{2-}$ are shown. Fragmentation curves for these selected dianionic fragments alone are shown due to their greater abundance in comparison with other dianionic fragments.

From Fig. 3(B), it appears that the fragments $[Ti_{34}O_{44}]^{2-}$, $[Ti_{33}O_{42}]^{2-}$, $[Ti_{32}O_{40}]^{2-}$, $[Ti_{31}O_{38}]^{2-}$, *etc.* were produced simultaneously. This may be due to the fact that for a given CE, there will be a broad internal energy distribution leading to different fragmentation outcomes. Initially, these ions increased in

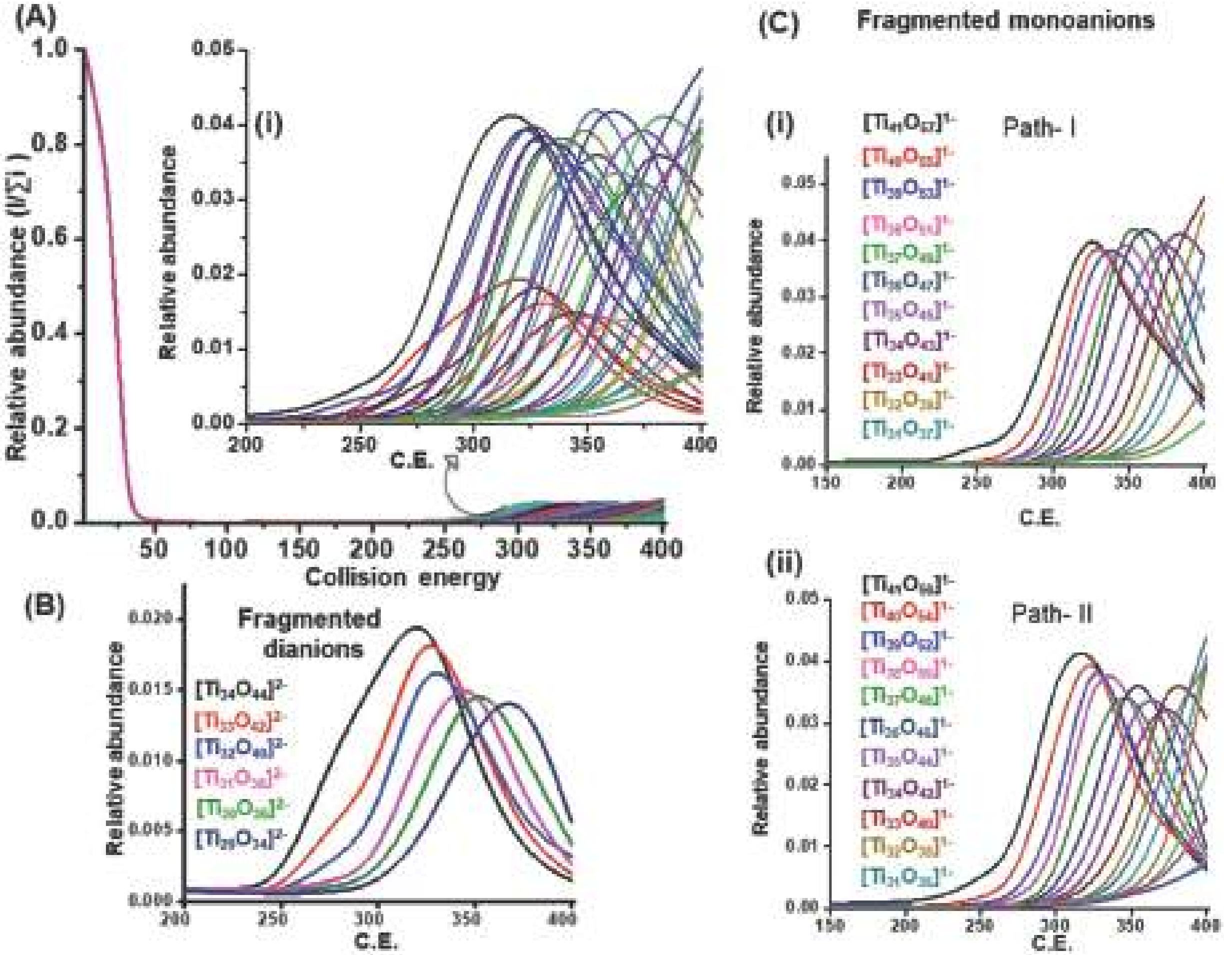

Fig. 3 Collision energy-resolved relative abundances of parent and fragment ions of **1** as a function of collision energy (CE). (A) Relative abundance *vs.* CE plot of the precursor ion **1**, and anionic Ti–O cage fragment units are shown. In the inset (A)(i), expanded views of curves for the fragment ions in the range of 200–400 CE. (B) Relative abundance *vs.* CE plot of dianionic fragment ions, $[Ti_{34}O_{44}]^{2-}$, $[Ti_{33}O_{42}]^{2-}$, $[Ti_{32}O_{40}]^{2-}$, $[Ti_{31}O_{38}]^{2-}$, $[Ti_{30}O_{36}]^{2-}$ and $[Ti_{29}O_{34}]^{2-}$. (C) (i) and (ii) show the relative abundance *vs.* CE plots for monoanionic cage fragment ions of paths I and II.

intensity and after reaching a threshold energy, they started to undergo further fragmentation. The ions $[Ti_{34}O_{44}]^{2-}$, $[Ti_{33}O_{42}]^{2-}$, $[Ti_{32}O_{40}]^{2-}$, $[Ti_{31}O_{38}]^{2-}$, $[Ti_{30}O_{36}]^{2-}$ and $[Ti_{29}O_{34}]^{2-}$ started dissociating after 320, 325, 330, 345, 352 and 367 CE, respectively, as observed from Fig. 3(B). Thus, the energy required for dissociation of each of these fragment ions was different suggesting a change in the inherent stability of the cage after systematic TiO_2 loss.

Similar graphs of monoanionic fragments produced from precursor **1** are presented in Fig. 3(C). The CE resolved graphs for the ions $[Ti_{41}O_{57}]^{1-}$, $[Ti_{40}O_{55}]^{1-}$, $[Ti_{39}O_{53}]^{1-}$, $[Ti_{38}O_{51}]^{1-}$, $[Ti_{37}O_{49}]^{1-}$, $[Ti_{36}O_{47}]^{1-}$ and $[Ti_{35}O_{45}]^{1-}$ formed by path-I (see Fig. 3(C)(i)) and $[Ti_{41}O_{56}]^{1-}$, $[Ti_{40}O_{54}]^{1-}$, $[Ti_{39}O_{52}]^{1-}$, $[Ti_{38}O_{50}]^{1-}$, $[Ti_{37}O_{48}]^{1-}$, $[Ti_{36}O_{46}]^{1-}$ and $[Ti_{35}O_{44}]^{1-}$ formed by path-II (see Fig. 3(C)(ii)), showed a similar trend of fragmentation to the dianionic species. The yield of ions beyond 400 CE was not monitored. Thus, it was clear that the systematic loss of TiO_2 was observed from the Ti–O cage and the fragments obtained in the subsequent stages exhibited different internal energy distribution. A sequential fragmentation mechanism of **1** is proposed in Fig. 4 based on the detection of CID mass spectra and nature of CE resolved curves of fragment ions.

The fragmentation events of the Ti–O FN cage, $\{Ti_{42}O_{60}\}$, of (**1**) can be correlated with the fragmentation events of carbon FNs.[40,41] The simplified stepwise dissociation scheme of the FN-like cage of TOF is shown in Scheme 2, which ultimately dissociated into Ti–O fragments. Electron impact ionization (EI) and higher energy (8 keV) CID/mass-analysed ion kinetic energy spectra of C_{60}^{+} (*m*/*z* 720) under single collision condition was reported and the fragmentation process resulted in corresponding losses of C_2 molecules, yielding smaller even-numbered carbon cluster fragment ions.[40,42,43] Fragmentation of various FNs and sequential C_2 loss mechanisms were also studied by low- and high-energy CID and surface impact at different energies.[44] Likewise, fast-atom bombardment (FAB) of multicharged C_{60}^{z+} (z = 1–4) with He also resulted in multicharged fragment ions by neutral losses of C_2.[45,46] There are several such mass spectrometric reports.[47–49] Thus, the dissociation mechanism of the Ti–O cage and carbon FNs are comparable.

3.3 Computational study

We have modelled the structure of the parent ion $[H_{12}Ti_{42}O_{60}(OCH_3)_{42}(HOCH_3)_{10}(H_2O)_2]^{2-}$ (**1**) based on the reported crystal structure of TOF,[29] $[H_6[Ti_{42}(\mu^3\text{-}O)_{60}(O^iPr)_{42}(OH)_{12}]]$ and optimized the structure of **1** and that of its major fragments using DFT (details of methods are in the experimental section). In the structure of **1**, for simplicity, we neglected all the 12 hydrogens (H_{12}) as their precise positions are unknown from experiment. However, we continue to write the number of extra hydrogens associated with the cluster in the structural formula for clarity, even though they are not included in our structural models.

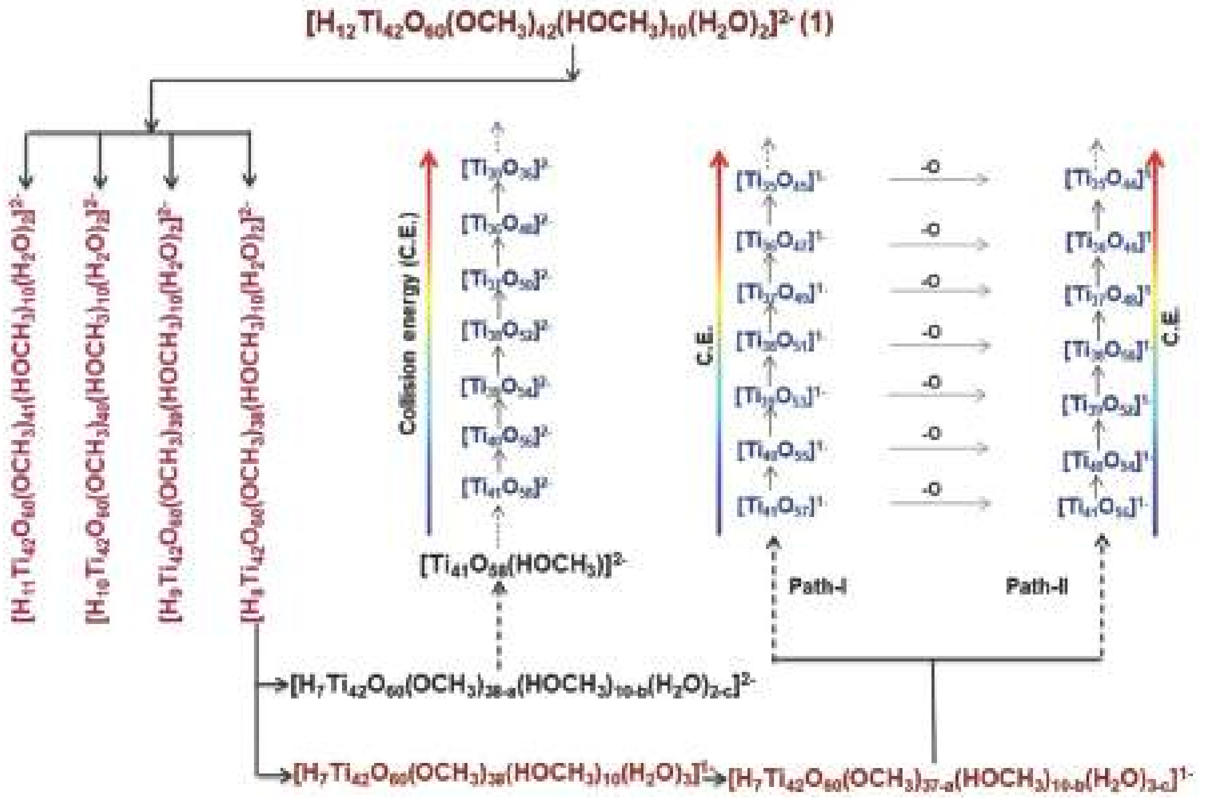

Fig. 4 Fragmentation pathways of targeted molecular ion **1**; a ($0 \leq a < 38$), b ($0 < b < 10$), and c ($0 \leq c < 3$) labels in molecular formulae represent the losses of OCH_3, $HOCH_3$, H_2O ligands, respectively in the fragmentation process.

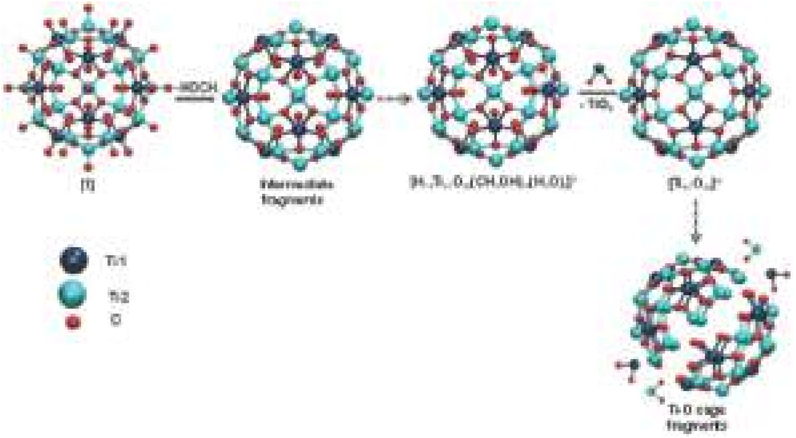

Scheme 2 Schematic representation of the fragmentation mechanism of TOF.

In the first step, all the peripheral ligands, *i.e.*, the forty-two isopropyl groups of TOF, were exchanged with methyl groups ($-CH_3$) and the preliminary structure of $H_6[Ti_{42}O_{60}(OCH_3)_{42}(OH)_{12}]$ was optimized (see in Fig. S9 and Table S1, ESI†). The charge state of $[Ti_{42}O_{60}(OCH_3)_{42}(OH)_{12}]$ is -6 with no extra hydrogens. Here, the hydrogens are weakly interacting with the cluster unit in the crystalline phase and would not be involved in charge transfer.

In the second step, we made internal ligand substitutions by replacing ten of the –OH groups by ten $-(OH)CH_3$ groups and the remaining two –OH groups were replaced by two H_2O-groups to give an initial geometry of **1** which we attempted to optimize in the -2 charge state. In the course of DFT optimization of **1**, we found that convergence could not be obtained, and we then repeated the optimization by increasing the total charge in units of one starting from -6 to +6, and out of all of these charge states, the DFT calculation converged only in the +4 charge state. In DFT calculations, there is a long-standing charge-delocalization issue and electronic states tend to be more delocalized than found experimentally.[50] As a result, charges from DFT calculations generally do not reproduce numerically the oxidation numbers of atoms, but the geometries from DFT simulations can often reproduce the structure and bonding configurations of molecules and materials in those oxidation states.

The positive charge could be qualitatively understood if we assume that the twelve hydrogen atoms donate electrons as ligands to clusters **1** and **2** so that in their absence, the clusters are effectively more positively charged. For clusters **1** and **2** in the gas phase, the surface hydrogen atoms may be more closely bound and could donate electrons to the cluster. Therefore, the charge of -2 observed in the mass spectrum for **1** is more negative than in the deprotonated state used in DFT calculations with a charge of +4. The resulting optimized structure of $[Ti_{42}O_{60}(OCH_3)_{42}(OHCH_3)_{10}(H_2O)_2]^{4+}$ is equivalent to that of $[H_{12}Ti_{42}O_{60}(OCH_3)_{42}(HOCH_3)_{10}(H_2O)_2]^{2-}$ as shown in Fig. 5(A)(a).

The optimized structure of **1** and its charge state calculation including the constituent species such as $\{Ti1\}O_7$, $\{Ti2\}O_5$, OCH_3, $(HO)CH_3$, H_2O are shown in Fig. S10 and in SI2 (ESI†), respectively. Note that {Ti1} and {Ti2} refer to distinct coordination types of Ti atoms in the structure. For the methanol ligands, we observed an average $\{Ti1\}-HO(CH_3)$ bond larger by 0.3 Å (15%) compared to the {Ti1}-OH bond distance found in $[Ti_{42}O_{60}(OCH_3)_{42}(OH)_{12}]^{6-}$, indicating only weak covalent Ti–O bonds with methanol. Furthermore, the two $-OH_2$ groups are completely detached from {Ti1} sites as two separate water molecules with non-covalent {Ti1}–O bonding distances of 2.53 Å and 2.60 Å, with the variation being dependent on the space available near the particular water moiety. The separation of methanol and water molecules from {Ti1} sites within the cage leaves the total structure with more cationic charges. Thus, the weakly bound methanol and free water molecules are confined in a highly cationic charged cage because fewer electrons are donated by these ligand groups compared to OH groups, which are closely bound to the cage.

On the other hand, it was observed that the bonding interaction of the peripheral methoxide ligands attached to seven-coordinated {Ti1} atoms was greatly strengthened as indicated by the contraction in the {Ti1}-O bond distance by 0.15 Å (6.3%). Similarly, it was noticed that the interaction of methoxide ligands bonded to the five-coordinated {Ti2} atoms were also strengthened as shown by a bond contraction of 0.11 Å (5.9%).

While the overall charge of TOF can be obtained using a standard organometallic electron counting procedure (see Table S1, ESI†), we found that application of simplistic electron counting to cluster ion **1** did not yield the correct charge state, which may be attributed to partial charge transfer. To better understand the partial charge transfer processes which stabilize cluster **1**, Bader charge analysis of structure **1** was carried out (see in Tables S2–S4, ESI†). The average charge of ten methanol molecules was $-0.028e^-$ and that of the two water molecules was $-0.006e^-$. This analysis indicated that there is no significant charge transfer from caged methanol and water molecules to the seven-coordinated {Ti1} centres. Thus, the molecules may be considered free in the sense that they are subject only to supramolecular interactions. As a result of this, the {Ti1} atoms have stronger interaction with the methoxide

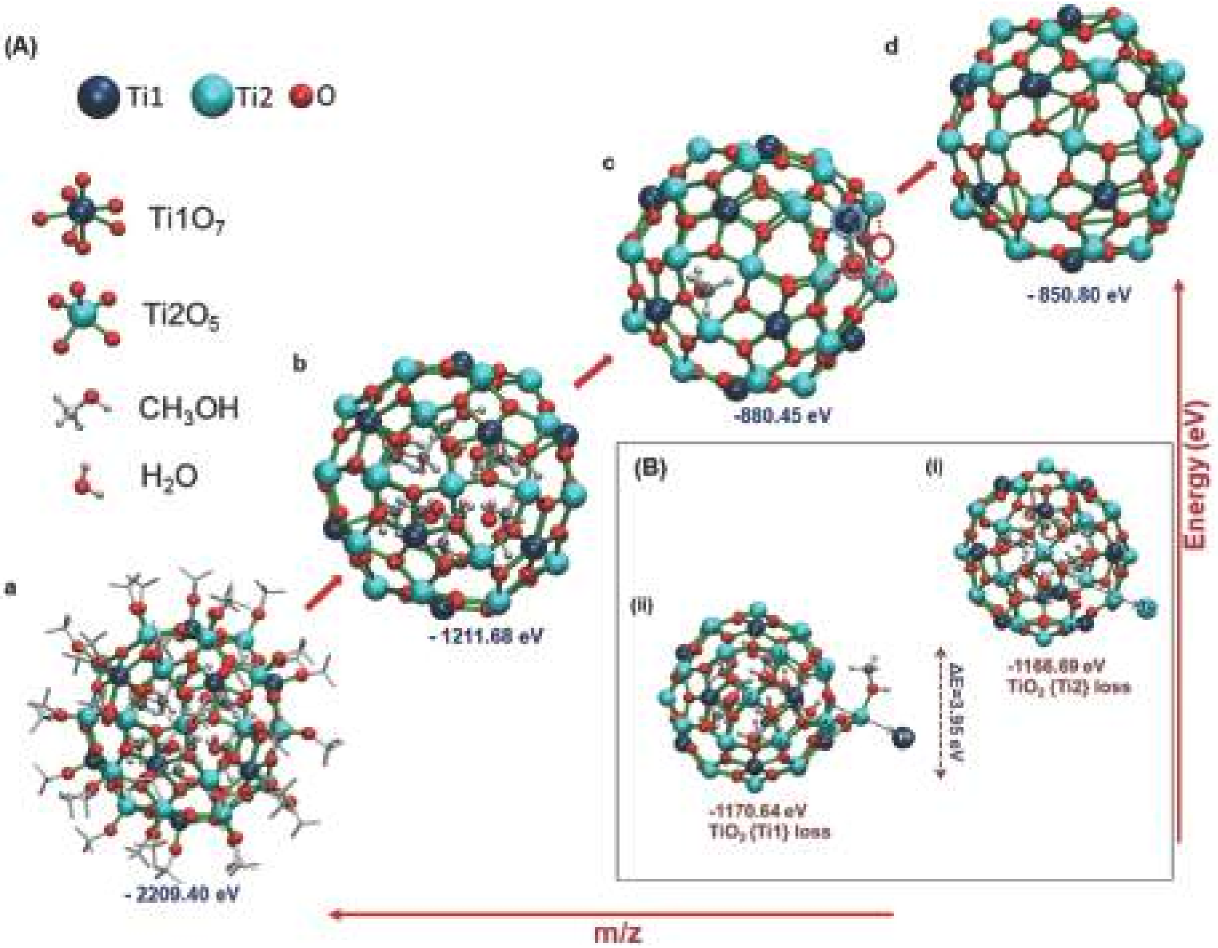

Fig. 5 (A) The DFT-optimized structures of (a) $[H_{12}Ti_{42}O_{60}(OCH_3)_{42}(HOCH_3)_{10}(H_2O)_2]^{2-}$, (b) $[H_{12}Ti_{42}O_{60}(OHCH_3)_{10}(H_2O)_2]^{2-}$, (c) $[Ti_{41}O_{58}(HOCH_3)]^{2-}$ and (d) $[Ti_{41}O_{58}]^{2-}$. (B) Comparison between free energy changes of cages (i and ii) due to loss of TiO_2 with {Ti1} (deep blue colour) and {Ti2} (light blue colour) sites. Colour of oxygen, carbon, and hydrogen atoms are red, dark grey and grey respectively). The twelve hydrogen atoms have been not included in the structures as described in the text.

ligands, since the DFT-optimized structure for cluster **1** compared to TOF shows the reduction of the average {Ti1}–O(CH_3) bond length from 1.90 to 1.8 Å, and a more positive average charge on the methoxide ligands bonded to {Ti1} centre ($-0.37e^-$), compared to {Ti2} centres ($-0.42e^-$). These results suggest the possibility of greater electron donation (loss of negative charge) from methoxide ligands to {Ti1} centres in cluster **1**. DFT study of average charges on OCH_3 ligands in TOF indicates a slightly more positive value ($-0.56e^-$) at {Ti1} centres in TOF ($-0.56e^-$) compared to that at {Ti2} centres ($-0.57e^-$), which supports our finding of greater partial charge transfer from OCH_3 ligands at {Ti1} centers compared to {Ti2} centers in cluster **1**. This increase in partial charge transfer may contribute to stabilizing the {Ti1}-centres when molecules are free in the cage. Such charge transfer differences at different {Ti1} sites may be understood as polarization effects on the Ti–O(CH_3) bond caused by the methanol and water molecules inside the cage as shown in Fig. S11 (ESI†). The strength of this effect would be stronger for methanol molecules than water molecules due their closer position to the {Ti1} centre. Furthermore, since the polarization effect is not present for {Ti2} centres, they attract less charge from the methoxide ligands. In reality, the cluster **1** may also be further stabilized *via* charge transfer with the hydrogen ions.

We computationally investigated all the intermediate stages of the cluster fragmentation as observed in the experiments such as loss of peripheral ligands, cleavage of the Ti–O cage, release of the ligands from inside the cage and finally the fragmentation of the Ti–O cage in detail. The structures of the major ions identified in MS such as the parent ion and major fragmented product ions were optimized and stacked as shown in Fig. 5. The structure of **1** was optimized after removing twelve peripheral -OCH_3 ligand groups from {Ti1} sites (see Fig. S12(A), ESI†). However, the Ti–O bonding interaction at {Ti1} sites along the wall of the cage underwent a significant bond elongation up to 4.4% and {Ti2}–O bonding reorganization at {Ti2} sites led to {Ti2}–O bond distances increase on average by 1.3%. The local geometry around {Ti1} atoms become more distorted with different bond lengths for different neighbouring bridging O atoms. The bond strains due to the {Ti1} attraction to the methanolic O atoms. The {Ti2}–O pentagonal bonding geometry remained unaltered due to the removal of twelve OCH_3 ligand groups, since there are no strong internal bonding interactions for {Ti2} compared to {Ti1} atoms. These observations may be explained by the higher bond strain at {Ti1} sites compared to {Ti2} sites. Theoretically optimized structures of intermediates $[H_{12}Ti_{42}O_{60}(CH_3O)_{30}(CH_3OH)_{10}(H_2O)_2]^{2-}$ and $[H_{12}Ti_{41}O_{58}(CH_3OH)_{10}(H_2O)_2]^{2-}$ formed during gas phase fragmentation are shown in Fig. S13 (ESI†).

In the second intermediate structure shown in Fig. 5(A)(b)), all the remaining thirty $-OCH_3$ peripheral ligands were lost from {Ti2} sites and the bonding interaction of Ti–O were seen to have strengthened in the cage and the local geometry around Ti became asymmetric. To understand the preferential site for TiO_2 fragment loss, first, we removed fragments containing {Ti1} and {Ti2} atoms from the surface of the methoxy ligand-free cluster. The cage fragment structures were optimized after removing one TiO_2 unit each attached to the {Ti1} and {Ti2} sites and they are shown in Fig. 5(B)(i and ii), respectively. Based on the relative ordering of the total energies of the two different open cage shell structures, it was confirmed that TiO_2 removal from a {Ti1} site is energetically favourable than from a {Ti2} site.

It is interesting to observe that the total energy of the structure with a $\{Ti1\}O_2$ unit loss in Fig. 5B(i) is 3.95 eV lower than the total energy of the structure with a $\{Ti2\}O_2$ unit loss of Fig. 5B(ii). This relative energetic ordering, $E(\{Ti1\}O_2 \text{ loss}) < E(\{Ti2\}O_2 \text{ loss})$, is due to the increased bond strain around {Ti1} atoms compared to that around {Ti2} atoms, as discussed earlier. Therefore, a $\{Ti1\}O_2$ unit loss leads to a greater structural relaxation, as the potential energy stored in the strained bonds is released. Moreover, in the $\{Ti1\}O_2$ removed structure, *i.e.*, Fig. 5B(i), a new bond appears between a {Ti2} atom on the edge of the cage opening and the O atom of the methanol which had been previously bonded to the {Ti1} atom of the lost $\{Ti1\}O_2$ unit. During structural relaxation, this methanol unit rotates from the inside to the outside of the cage while being anchored to the {Ti2} atom which protrudes like a lip to the cage opening as seen in Fig. 5B(i). However, such stabilization by methanol rotating out of the cage while being hinged is not possible in the case of $\{Ti2\}O_2$, which leaves behind six-coordinated {Ti1} atoms that are more rigid and the methanol units remain tightly bonded inside the cage. There could be additional weak interactions arising from hydrogen bonds contributing to these.

The opening of cage with TiO_2 loss at {Ti1} sites left a hole with dimensions of ~ 7.2 Å × 7.0 Å and the edges of the opening were puckered due to {Ti2} atoms interacting with methanol. In contrast, for the cage opening with TiO_2 loss from {Ti2} sites, it was noted that the opening remained unaltered during optimization apart from a slight contraction of the cage opening after the complete removal of ligands from the cage. Loss of all ligands makes $[Ti_{41}O_{58}]^{2-}$ and subsequent fragmentation is expected from this cluster.

4 Conclusions

We performed detailed CID studies on a Ti–oxo cluster protected by ligands, referred to as TOF. Upon increasing the CE, after the ligands were stripped off, a systematic loss of TiO_2 was observed during the fragmentation of the FN-like cluster core. Firstly, all the peripheral ligands along with the ligands inside the cluster-core were lost from TOF leading to the formation of $[Ti_{41}O_{58}]^{2-}$. From this species, up to 23 systematic TiO_2 losses were observed, and finally $[Ti_{19}O_{13}]^{1-}$ was formed. Beyond this stage, upon further increase of energy, the structure collapsed completely. The fragmentation pathway was comparable to that of C_{60} and the other FNs where systematic C_2 losses were seen up to $C_{30}{}^+$, which was followed by shattering of the cage.[51–53] Expanding such studies to other metal oxoFNs[26,27,54–57] would provide greater insights into the science of such structures.

Author contributions

T. P. proposed the project. J. R. and P. C. performed the experiments. J. R. prepared the samples. J. R. and P. C. performed mass spectrometric measurements. G. P. and G. N. carried out theoretical calculations. J. R. and P. C. wrote the first draft of the manuscript, and the final version of the manuscript was prepared through the contributions of all authors. All authors have given approval to the final version of the manuscript.

Conflicts of interest

There are no conflicts to declare.

Acknowledgements

J. R. acknowledges IIT Madras for an institute doctoral fellowship. P. C. also acknowledges IIT Madras for an institute postdoctoral fellowship. We thank Dr Kartheek Joshua for his help in computational studies. We thank the Department of Science and Technology, Government of India, for the continuous support of our research program.

References

1 A. Kubacka, M. Fern Andez-García and G. Col, Advanced Nanoarchitectures for Solar Photocatalytic Applications, *Chem. Rev.*, 2012, **112**, 1555–1614.

2 Y. Gao, W. Nie, Q. Zhu, X. Wang, S. Wang, F. Fan and C. Li, The Polarization Effect in Surface-Plasmon-Induced Photocatalysis on Au/TiO_2 Nanoparticles, *Angew. Chem.*, 2020, **132**, 18375–18380.

3 C. Wang, C. Liu, L. Jiao Li and Z.-M. Sun, Synthesis, Crystal Structures, and Photochemical Properties of a Family of Heterometallic Titanium Oxo Clusters, *Inorg. Chem.*, 2019, **58**, 6312–6319.

4 S. Chen, W.-H. Fang, L. Zhang and J. Zhang, Atomically Precise Multimetallic Semiconductive Nanoclusters with Optical Limiting Effects, *Angew. Chem., Int. Ed.*, 2018, **57**, 11252–11256.

5 L. Rozes and C. Sanchez, Titanium oxo-clusters: Precursors for a Lego-like construction of nanostructured hybrid materials, *Chem. Soc. Rev.*, 2011, **40**, 1006–1030.

6 P. Coppens, Y. Chen and E. Trzop, Crystallography and Properties of Polyoxotitanate Nanoclusters, *Chem. Rev.*, 2014, **114**, 9645–9661.

7 W.-H. Fang, L. Zhang and J. Zhang, Synthetic strategies, diverse structures and tuneable properties of polyoxo-titanium clusters, *Chem. Soc. Rev.*, 2018, **47**, 404–421.

8 R. Chen, Z.-F. Hong, Y.-R. Zhao, H. Zheng, G.-J. Li, Q.-C. Zhang, X.-J. Kong, L.-S. Long and L.-S. Zheng, Ligand-Dependent Luminescence Properties of Lanthanide–Titanium Oxo Clusters, *Inorg. Chem.*, 2019, **58**, 15008–15012.

9 X. Fan, J. Wang, K. Wu, L. Zhang and J. Zhang, Isomerism in Titanium-Oxo Clusters: Molecular Anatase Model with Atomic Structure and Improved Photocatalytic Activity, *Angew. Chem., Int. Ed.*, 2019, **58**, 1320–1323.

10 Y.-Z. Yu, Y.-R. Zhang, C.-H. Geng, L. Sun, Y. Guo, Y.-R. Feng, Y.-X. Wang and X.-M. Zhang, Precise and Wide-Ranged Band-Gap Tuning of Ti6-Core-Based Titanium Oxo Clusters by the Type and Number of Chromophore Ligands, *Inorg. Chem.*, 2019, **58**, 16785–16791.

11 S. Pike, T. Krämer and F. Tuna, Photo-redox reactivity of titanium-oxo clusters: Mechanistic insight into a two-electron intramolecular process, and structural characterisation of mixed-valent Ti(III)/Ti(IV) products, *Chem. Sci.*, 2019, **10**, 6886–6898.

12 M. Czakler, C. Artner and U. Schubert, Two new hexanuclear titanium oxo cluster types and their structural connection to known clusters, *New J. Chem.*, 2018, **42**, 12098–12103.

13 J. Le Hou, W. Luo, Y. Y. Wu, H. C. Su, G. L. Zhang, Q. Y. Zhu and J. Dai, Two Ti13-oxo-clusters showing non-compact structures, film electrode preparation and photocurrent properties, *Dalton Trans.*, 2015, **44**, 19829–19835.

14 W.-H. Fang, L. Zhang and J. Zhang, A 3.6 nm Ti52–Oxo Nanocluster with Precise Atomic Structure, *J. Am. Chem. Soc.*, 2016, **138**, 7480–7483.

15 G. Zhang, C. Liu, D.-L. Long, L. Cronin, C.-H. Tung and Y. Wang, Water-Soluble Pentagonal-Prismatic Titanium-Oxo Clusters, *J. Am. Chem. Soc.*, 2016, **138**, 11097–11100.

16 Y. Chen, E. Trzop, J. D. Sokolow and P. Coppens, Direct Observation of the Binding Mode of the Phosphonate Anchor to Nanosized Polyoxotitanate Clusters, *Chem. – Eur. J.*, 2013, **19**, 16651–16655.

17 N. Narayanam, W.-H. Fang, K. Chintakrinda, L. Zhang and J. Zhang, Deep eutectic-solvothermal synthesis of titanium-oxo clusters protected by π-conjugated chromophores, *Chem. Commun.*, 2017, **53**, 8078–8080.

18 J. D. Sokolow, E. Trzop, Y. Chen, J. Tang, L. J. Allen, R. H. Crabtree, J. B. Benedict and P. Coppens, Binding modes of carboxylate- and acetylacetonate-linked chromophores to homodisperse polyoxotitanate nanoclusters, *J. Am. Chem. Soc.*, 2012, **134**, 11695–11700.

19 S. Chen, W. H. Fang, L. Zhang and J. Zhang, Atomically Precise Multimetallic Semiconductive Nanoclusters with Optical Limiting Effects, *Angew. Chem., Int. Ed.*, 2018, **57**, 11252–11256.

20 M. J. Moses, J. C. Fettinger and B. W. Eichhorn, Interpenetrating As20 fullerene and Ni12 icosahedra in the onion-skin $[As@Ni_{12}@As_{20}]^{3-}$ ion, *Science*, 2003, **300**, 778–780.

21 T. Guo, M. D. Diener, Y. Chai, M. J. Alford, R. E. Haufler, S. M. McClure, T. Ohno, J. H. Weaver, G. E. Scuseria and R. E. Smalley, Uranium Stabilization of C28: A Tetravalent Fullerene, *Science*, 1992, **257**, 1661–1664.

22 L. Qin, G.-J. Zhou, Y.-Z. Yu, H. Nojiri, C. Schröder, R. E. P. Winpenny and Y.-Z. Zheng, Topological Self-Assembly of Highly Symmetric Lanthanide Clusters: A Magnetic Study of Exchange-Coupling "Fingerprints" in Giant Gadolinium(III) Cages, *J. Am. Chem. Soc.*, 2017, **139**, 16405–16411.

23 S.-T. Zheng and G.-Y. Yang, Recent advances in paramagnetic-TM-substituted polyoxometalates (TM = Mn, Fe, Co, Ni, Cu), *Chem. Soc. Rev.*, 2012, **41**, 7623–7646.

24 H. Zheng, M.-H. Du, S.-C. Lin, Z.-C. Tang, X.-J. Kong, L.-S. Long and L.-S. Zheng, Assembly of a Wheel-Like Eu24Ti8 Cluster under the Guidance of High-Resolution Electrospray Ionization Mass Spectrometry, *Angew. Chem., Int. Ed.*, 2018, **57**, 10976–10979.

25 X.-J. Kong, L.-S. Long, Z. Zheng, R.-B. Huang and L.-S. Zheng, Keeping the Ball Rolling: Fullerene-like Molecular Clusters, *Acc. Chem. Res.*, 2009, **43**, 201–209.

26 R. W. Pow, W. Xuan, D.-L. Long, N. L. Bell and L. Cronin, Embedding alkenes within an icosahedral inorganic fullerene $\{(NH_4)_{42}[Mo_{132}O_{372}(L)30(H_2O)72]\}$ for trapping volatile organics, *Chem. Sci.*, 2020, **11**, 2388–2393.

27 T. Liu, B. Imber, E. Diemann, G. Liu, K. Cokleski, H. Li, Z. Chen and A. Müller, Deprotonations and Charges of Well-Defined $\{Mo_{72}Fe_{30}\}$ Nanoacids Simply Stepwise Tuned by pH Allow Control/Variation of Related Self-Assembly Processes, *J. Am. Chem. Soc.*, 2006, **128**, 15914–15920.

28 S. S. Passadis, S. Hadjithoma, A. G. Kalampounias, A. C. Tsipis, S. Sproules, H. N. Miras, A. D. Keramidas and T. A. Kabanos, Synthesis, structural and physicochemical characterization of a new type Ti6-oxo cluster protected by a cyclic imide dioxime ligand, *Dalton Trans.*, 2019, **48**, 5551–5559.

29 M.-Y. Gao, F. Wang, Z.-G. Gu, D.-X. Zhang, L. Zhang and J. Zhang, Fullerene-like Polyoxotitanium Cage with High Solution Stability, *J. Am. Chem. Soc.*, 2016, **138**, 2556–2559.

30 M. Jadraque, B. Sierra, A. Sfounis and M. Velegrakis, Photofragmentation of mass-selected titanium oxide cluster cations, *Appl. Phys. B: Lasers Opt.*, 2010, **100**, 587–590.

31 M. Velegrakis, M. Massaouti and M. Jadraque, Collision-induced dissociation studies on gas-phase titanium oxide cluster cations, *Appl. Phys. A: Mater. Sci. Process.*, 2012, **108**, 127–131.

32 P. Chakraborty, A. Baksi, E. Khatun, A. Nag, A. Ghosh and T. Pradeep, Dissociation of Gas Phase Ions of Atomically Precise Silver Clusters Reflects Their Solution Phase Stability, *J. Phys. Chem. C*, 2017, **121**, 10971–10981.

33 M. T. Rodgers and P. B. Armentrout, *Comprehensive Coordination Chemistry II*, Elsevier Ltd, 2004, vol. 2, pp. 141–158.

34 S. A. McLuckey, Principles of collisional activation in analytical mass spectrometry, *J. Am. Soc. Mass Spectrom.*, 1992, **3**, 599–614.

35 A. G. Harrison, Energy-resolved mass spectrometry: a comparison of quadrupole cell and cone-voltage collision-induced dissociation, *Rapid Commun. Mass Spectrom.*, 1999, **13**, 1663–1670.

36 F. Lépine, B. Climen, M. A. Lebeault and C. Bordas, Time-dependent delayed electron spectra: A direct measurement of total decay rate as a function of internal energy, *Eur. Phys. J. D*, 2009, **55**, 627–635.

37 R. W. Kirschbaum, M. Hausmann, O. V. Boltalina, S. H. Strauss and T. Drewello, Energy-dependent gas-phase fragmentation of fluorofullerene multiply charged anions (MCAs), *Phys. Chem. Chem. Phys.*, 2015, **17**, 23052–23058.

38 J. S. Klassen and P. Kebarle, Collision-Induced Dissociation Threshold Energies of Protonated Glycine, Glycinamide, and Some Related Small Peptides and Peptide Amino Amides, *J. Am. Chem. Soc.*, 1997, **119**, 6552–6563.

39 A. Kafle, C. Nwokolo, L. Sanchez and P. B. Armentrout, Threshold Collision-Induced Dissociation of Hydrated Thorium(IV) Trihydroxide Cation: Experimental and Theoretical Investigation of the Binding Energies for $Th(OH)_3$ + $(H_2O)n$ Complexes (n = 1–4), *J. Phys. Chem. A*, 2020, **124**, 3090–3100.

40 I. N. Ioffe, O. N. Mazaleva, L. N. Sidorov, S. Yang, T. Wei, E. Kemnitz and S. I. Troyanov, Cage Shrinkage of Fullerene via a C_2 Loss: from IPR $C_{90}(28)Cl_{24}$ to Nonclassical, Heptagon-Containing $C_{88}Cl_{22/24}$, *Inorg. Chem.*, 2013, **52**, 13821–13823.

41 H. Shen, P. Hvelplund, D. Mathur, A. Bárány, H. Cederquist, N. Selberg and D. C. Lorents, Fullerene-fullerene collisions: Fragmentation and electron capture, *Phys. Rev. A: At., Mol., Opt. Phys.*, 1995, **52**, 3847–3851.

42 E. E. B. Campbell, T. Raz and R. D. Levine, Internal energy dependence of the fragmentation patterns of C_{60} and $C_{60}{}^{+}$, *Chem. Phys. Lett.*, 1996, **253**, 261–267.

43 T. Pradeep and R. G. Cooks, C_{60} inflation: production of C_{62}, C_{64}, …, *Int. J. Mass Spectrom. Ion Process.*, 1994, **135**, 243–247.

44 R. D. Beck, J. Rockenberger, P. Weis and M. M. Kappes, Fragmentation of $C_{60}{}^{+}$ and higher fullerenes by surface impact, *J. Chem. Phys.*, 1996, **104**, 3638–3650.

45 J. H. Gross, S. Giesa and W. Krätschmer, Negative-ion low-temperature fast-atom bombardment mass spectrometry of monomeric and dimeric [60]fullerene compounds, *Rapid Commun. Mass Spectrom.*, 1999, **13**, 815–820.

46 R. J. Doyle and M. M. Ross, Dissociations of singly and multiply charged fullerene ions, *J. Phys. Chem.*, 2002, **95**, 4954–4956.

47 V. Y. Markov, A. Y. Borschevsky and L. N. Sidorov, MALDI mass spectrometry of fullerene derivatives, *Int. J. Mass Spectrom.*, 2012, **325–327**, 100–112.

48 G. C. Vougioukalakis, M. M. Roubelakis and M. Orfanopoulos, Open-cage fullerenes: Towards the construction of nanosized molecular containers, *Chem. Soc. Rev.*, 2010, **39**, 817–844.

49 H. Zettergren, Interactions of energetic ions with fullerenes, PAHs, and their weakly bound clusters, *Nucl. Instruments Methods Phys. Res. Sect. B Beam Interact. Mater. Atoms*, 2017, **408**, 9–15.

50 A. J. Cohen, P. Mori-Sánchez and W. Yang, Insights into current limitations of density functional theory, *Science*, 2008, **321**, 792–794.

51 D. R. Luffer and K. H. Schram, Electron ionization mass spectrometry of synthetic C_{60}, *Rapid Commun. Mass Spectrom.*, 1990, **4**, 552–556.

52 K. Hata, M. Ariff, K. Tohji and Y. Saito, Selective formation of C20 cluster ions by field evaporation from carbon nanotubes, *Chem. Phys. Lett.*, 1999, **308**, 343–346.

53 R. Ehlich, P. Landenberger and H. Prinzbach, Coalescence of C20 fullerenes, *J. Chem. Phys.*, 2001, **115**, 5830–5835.

54 D. Schröder, Applications of Electrospray Ionization Mass Spectrometry in Mechanistic Studies and Catalysis Research, *Acc. Chem. Res.*, 2012, **45**, 1521–1532.

55 L. Suber, M. Bonamico and V. Fares, Synthesis, Magnetism, and X-ray Molecular Structure of the Mixed-Valence Vanadium(IV/V)–Oxygen Cluster $[VO_4 \subset (V_{18}O_{45})]$9-, *Inorg. Chem.*, 1997, **36**, 2030–2033.

56 H. Zheng, M.-H. Du, S.-C. Lin, Z.-C. Tang, X.-J. Kong, L.-S. Long and L.-S. Zheng, Assembly of a Wheel-Like Eu 24 Ti 8 Cluster under the Guidance of High-Resolution Electrospray Ionization Mass Spectrometry, *Angew. Chem., Int. Ed.*, 2018, **57**, 10976–10979.

57 J. Lin, N. Li, S. Yang, M. Jia, J. Liu, X.-M. Li, L. An, Q. Tian, L.-Z. Dong and Y.-Q. Lan, Self-Assembly of Giant Mo_{240} Hollow Opening Dodecahedra, *J. Am. Chem. Soc.*, 2020, **142**, 13982–13988.

Electronic Supplementary Information

Gas Phase Ion Chemistry of Titanium-Oxofullerene With Ligated Solvents

Jayoti Roy[‡]*, Papri Chakraborty*[‡]*, Ganesan Paramasivam, Ganapati Natarajan*[$]*, and Thalappil Pradeep**

DST Unit of Nanoscience (DST UNS) & Thematic Unit of Excellence (TUE), Department of Chemistry, Indian Institute of Technology Madras, Chennai 600036, India.

International Centre for Clean Water (ICCW), IIT Madras Research Park, Taramani, Chennai 6000113, India.

Table of Contents

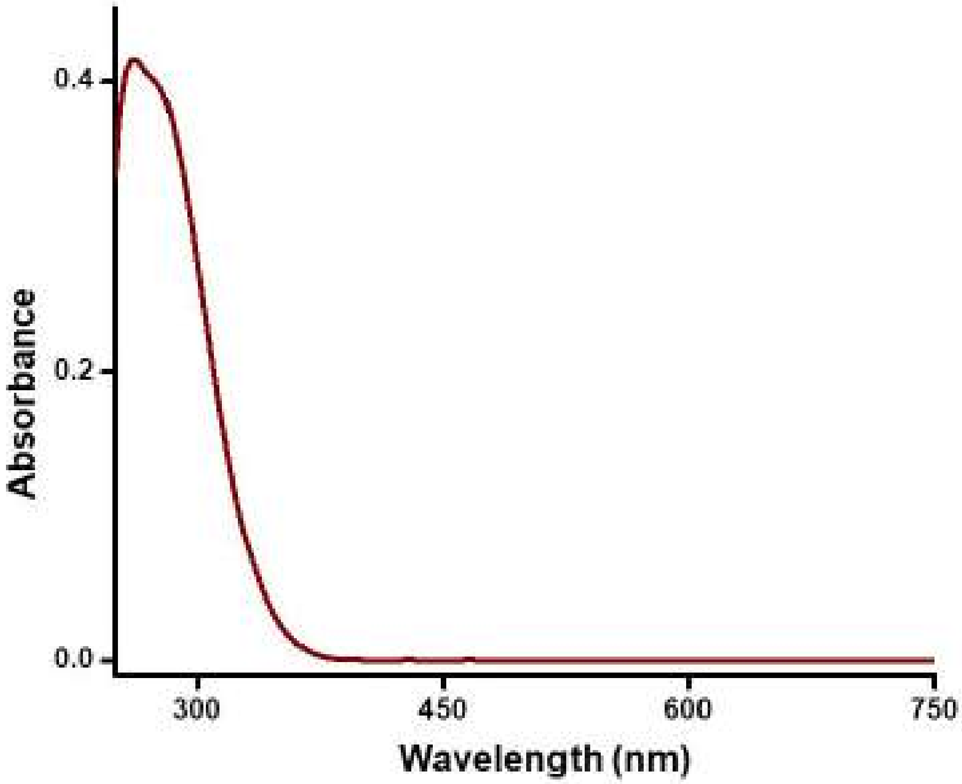

Fig. S1 Solution phase UV-vis absorption spectrum of TOF in toluene.

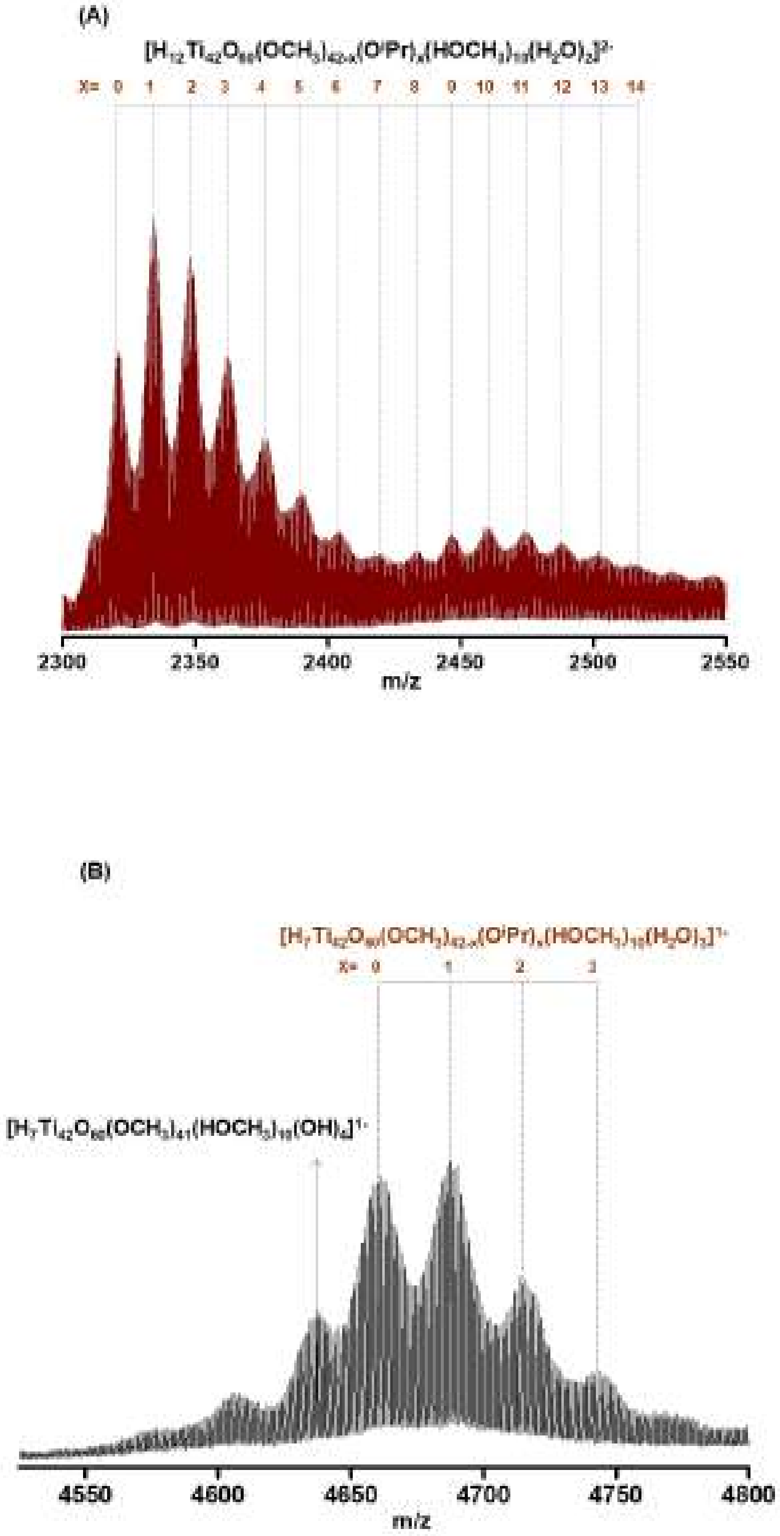

Fig. S2 Expanded view of ESI MS of TOF in the range (A) m/z 2330-2550 and (B) m/z 4525-4800.

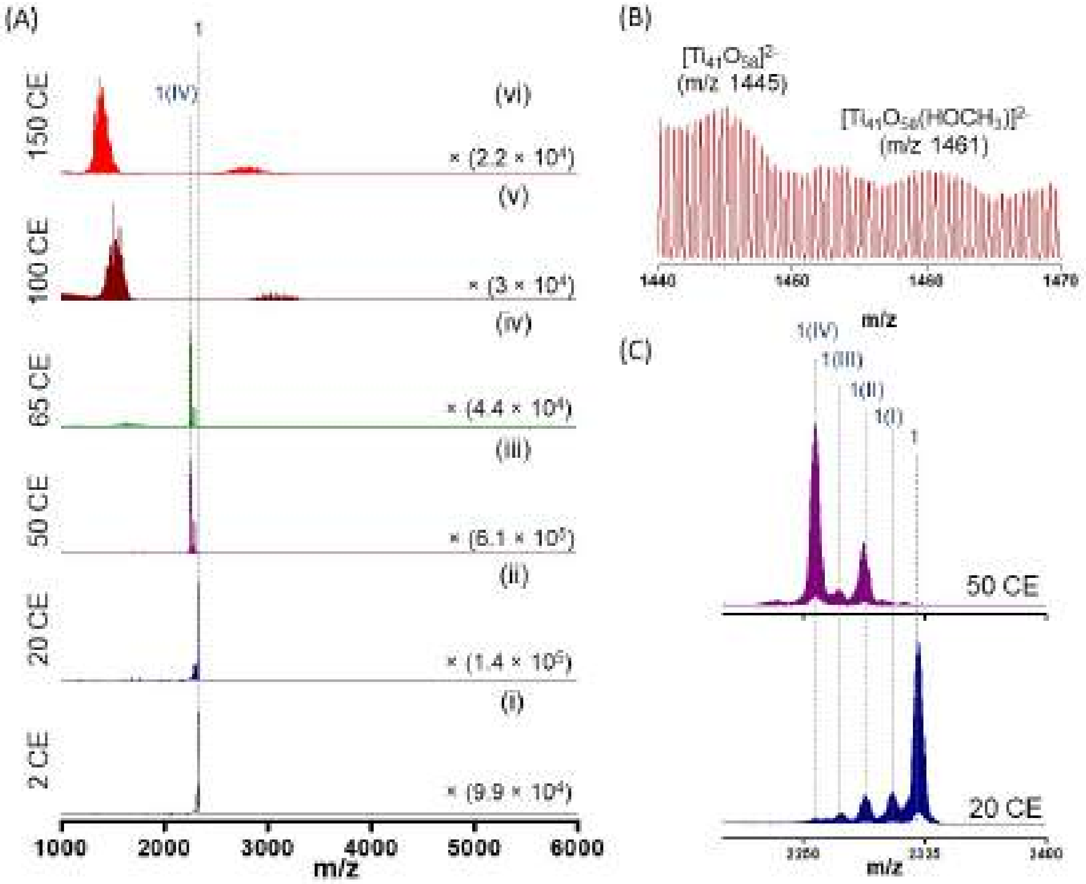

Fig. S3 Detailed CID mass spectrum of $[H_{12}Ti_{42}O_{60}(OCH_3)_{42}(HOCH_3)_{10}(H_2O)_2]^{2-}$ (**1**) with gradual increase of collision energy. (A) MS/MS spectra from 2-150 CE. (B) shows the expanded view of the spectrum at 150 CE in the m/z range of m/z 1440-1470. Mass spectrum of $[Ti_{41}O_{58}]^{2-}$ and $[Ti_{41}O_{58}(HOCH_3)]^{2-}$ are labeled at m/z 1445 and m/z 1461 respectively. (C) shows the expanded spectra in m/z range of 2200-2400 at 20 CE and 50 CE. 1(I), 1(II), 1(III) and 1(IV) correspond to one, two, three, and four methanol loss species from the precursor ion **1**, with molecular formulae $[H_{11}Ti_{42}O_{60}(OCH_3)_{41}(HOCH_3)_{10}(H_2O)_2]^{2-}$, $[H_{10}Ti_{42}O_{60}(OCH_3)_{40}(HOCH_3)_{10}(H_2O)_2]^{2-}$, $[H_9Ti_{42}O_{60}(OCH_3)_{39}(HOCH_3)_{10}(H_2O)_2]^{2-}$, $[H_8Ti_{42}O_{60}(OCH_3)_{38}(HOCH_3)_{10}(H_2O)_2]^{2-}$, respectively.

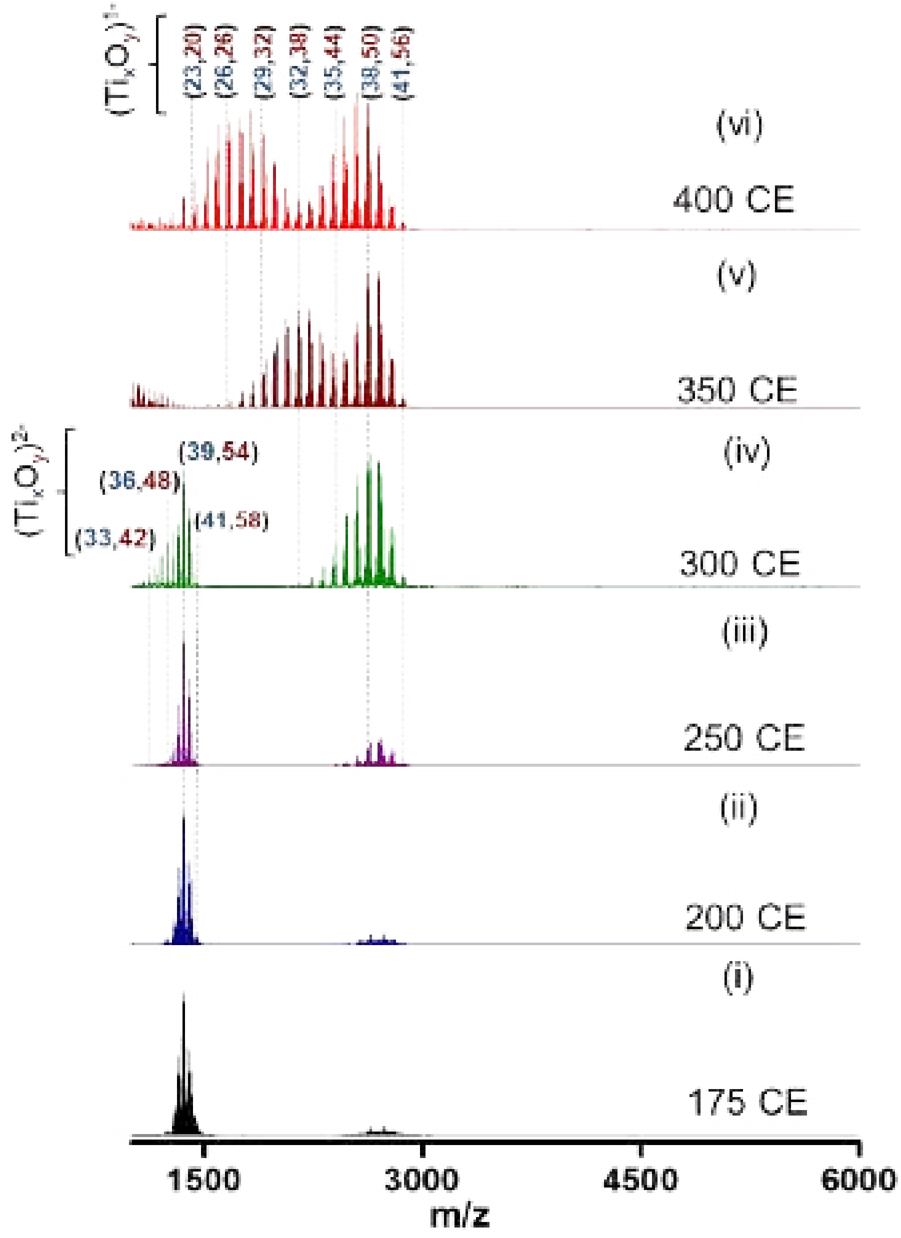

Fig. S4 Detailed CID mass spectrum of $[H_{12}Ti_{42}O_{60}(OCH_3)_{42}(HOCH_3)_{10}(H_2O)_2]^{2-}$ (**1**) with the gradual increase of CE from 175- 400 CE.

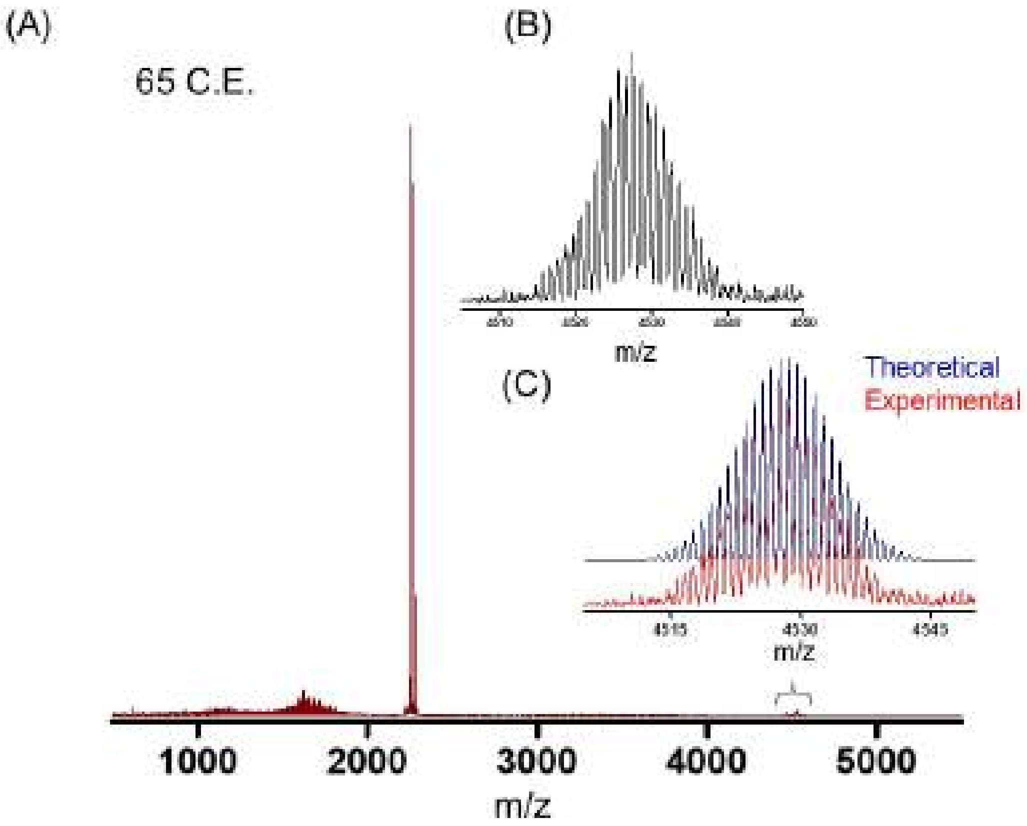

Fig. S5 (A). CID mass spectrum of $[H_{12}Ti_{42}O_{60}(OCH_3)_{42}(HOCH_3)_{10}(H_2O)_2]^{2-}$ at 65 C.E. (B) Expanded view of mass spectrum of $[H_7Ti_{42}O_{60}(OCH_3)_{38}(HOCH_3)_{10}(H_2O)_3]^{1-}$. (C) Theoretical and experimental mass spectrum of $[H_7Ti_{42}O_{60}(OCH_3)_{38}(HOCH_3)_{10}(H_2O)_3]^{1-}$.

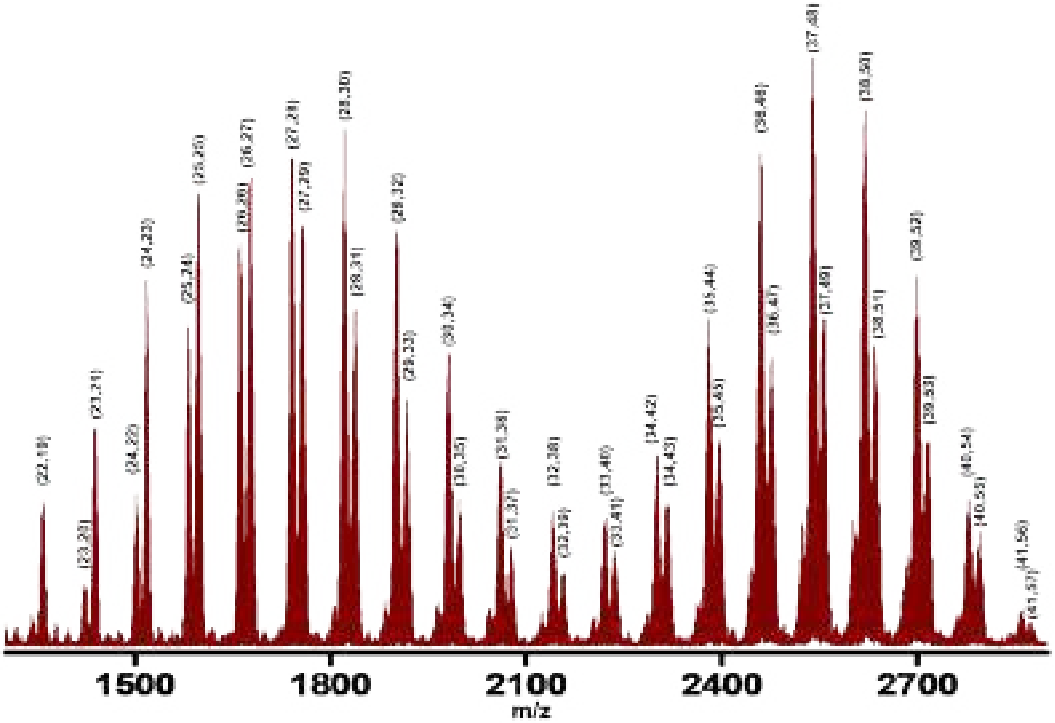

Fig. S6 CID mass spectrum of $[H_{12}Ti_{42}O_{60}(OCH_3)_{42}(HOCH_3)_{10}(H_2O)_2]^{2-}$ at 400 C.E. A cascade of Ti-oxo cage fragments were generated. The peaks are labeled as (x,y) where x and y represent the number of Ti and O atoms present in the cage fragments.

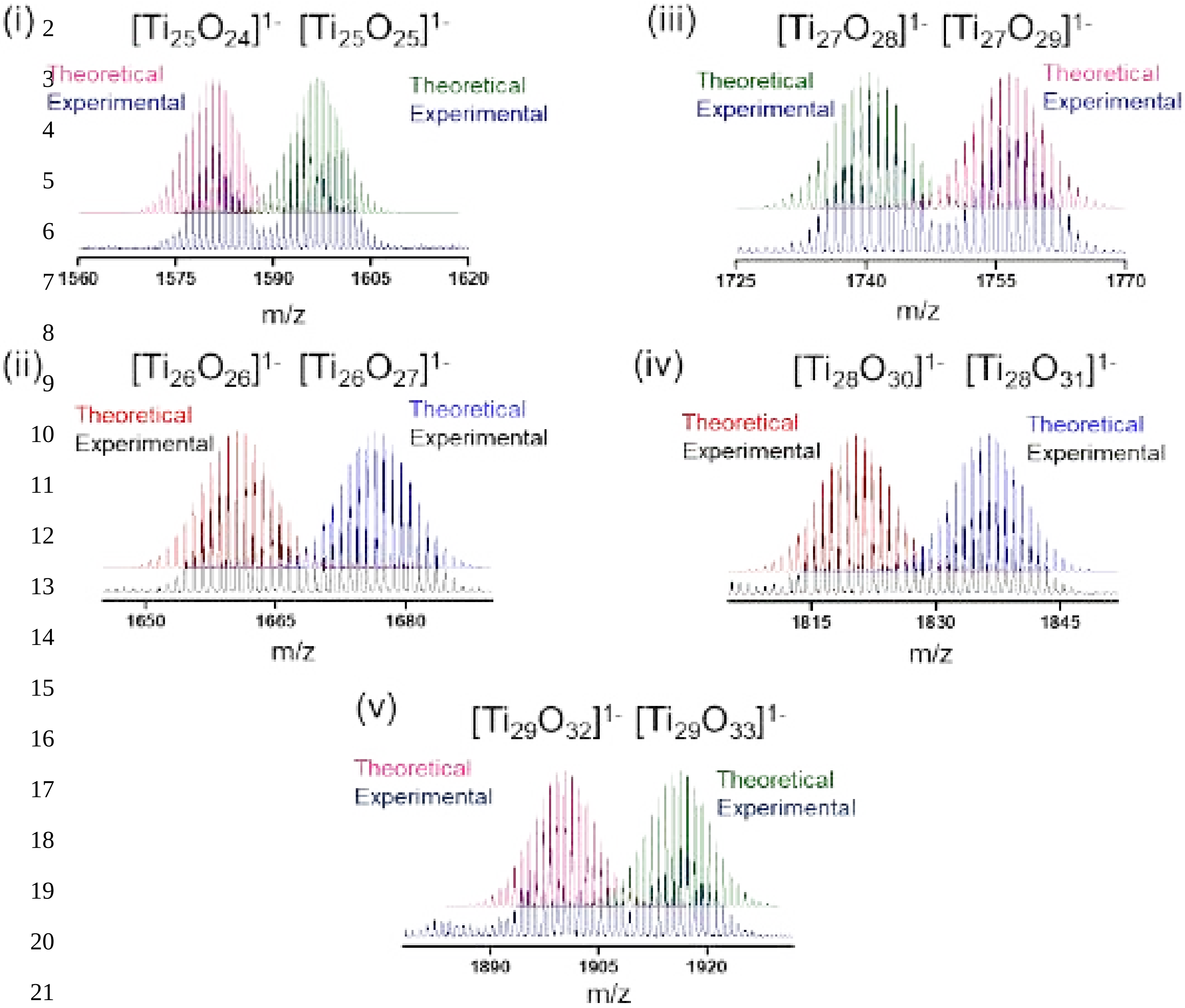

Fig. S7 Expanded views of the calculated and experimental isotopic distributions of (i) $[Ti_{25}O_{24}]^{1-}$, $[Ti_{25}O_{25}]^{1-}$; (ii) $[Ti_{26}O_{26}]^{1-}$, $[Ti_{26}O_{27}]^{1-}$; (iii) $[Ti_{27}O_{28}]^{1-}$, $[Ti_{27}O_{29}]^{1-}$; (iv) $[Ti_{28}O_{30}]^{1-}$, $[Ti_{28}O_{31}]^{1-}$ and (v) $[Ti_{29}O_{32}]^{1-}$, $[Ti_{29}O_{33}]^{1-}$.

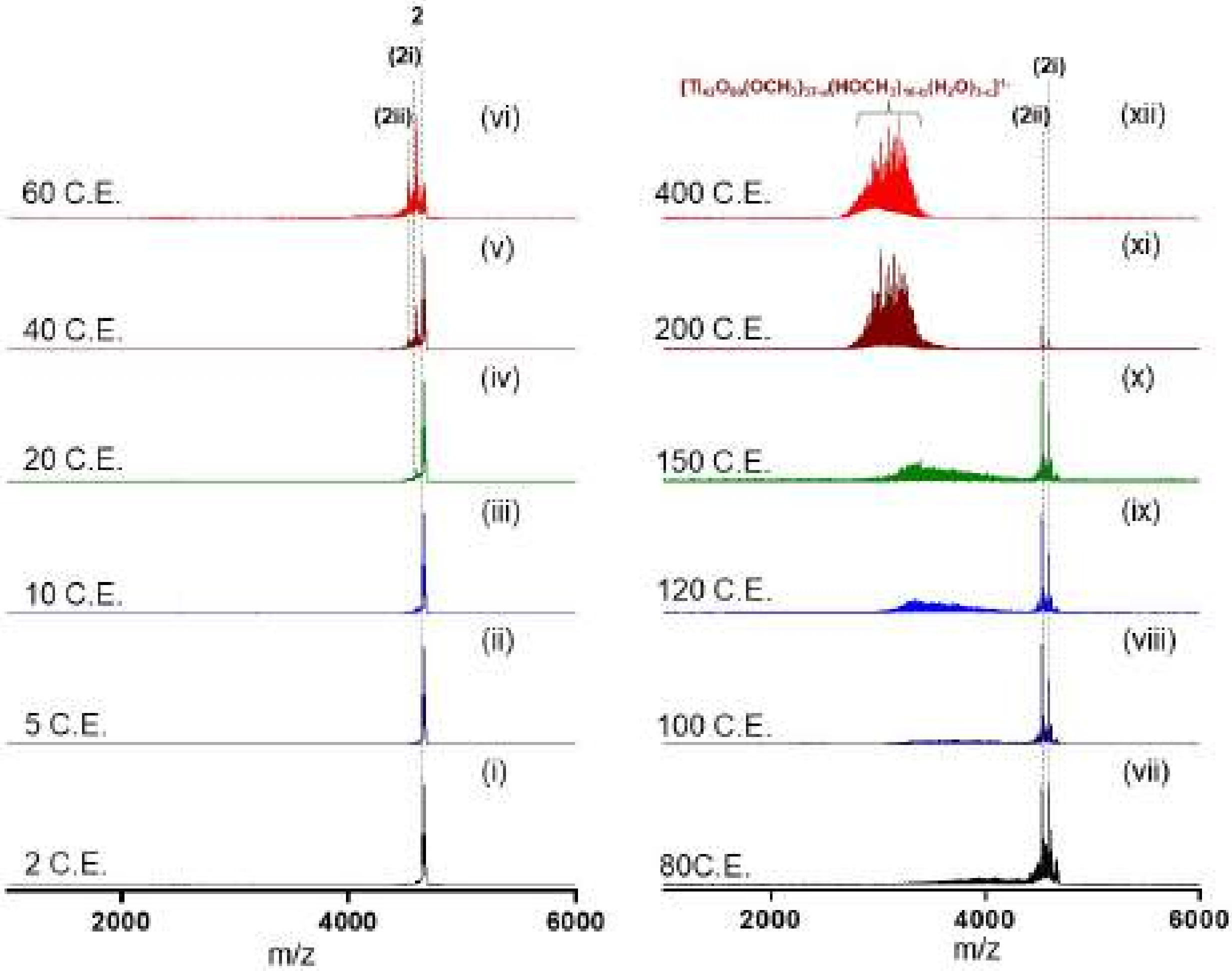

Fig. S8 CID mass spectra of $[H_7Ti_{42}O_{60}(OCH_3)_{42}(HOCH_3)_{10}(H_2O)_3]^{1-}$(**2**) with gradual increase of collision energy from 2 C.E. to 400 C.E. **2i** and **2ii** indicate two and four methanol loss species, respectively from **2**.

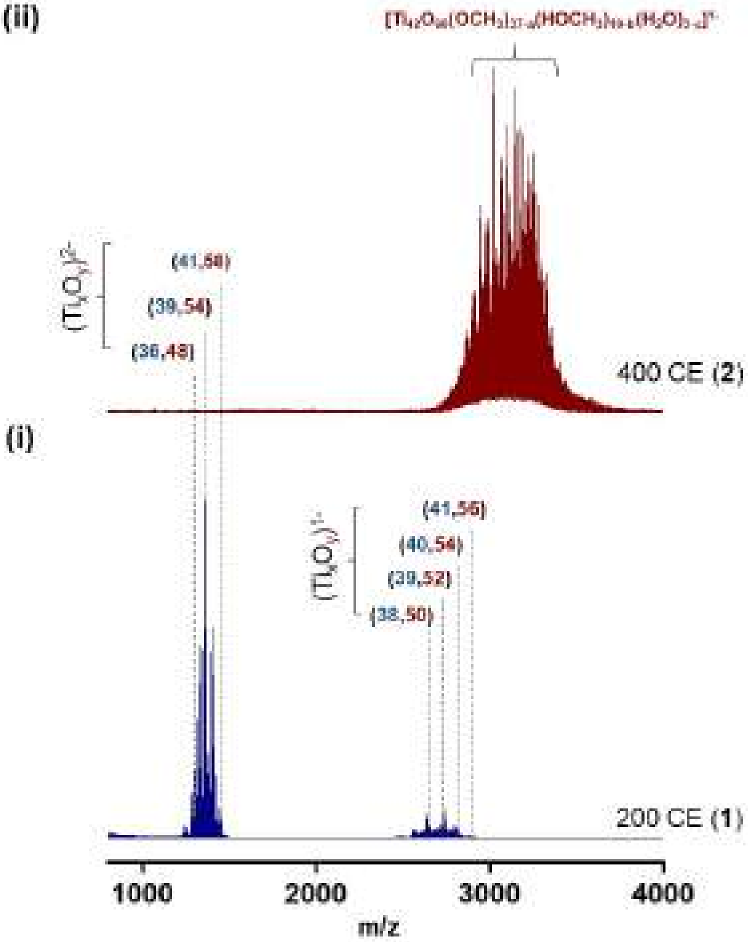

Fig. S9 Stacked mass spectra of parent ions, **1** at 200 CE (i) and **2** at 400 CE (ii).

SI1 Additional details of computational study – DFT calculations were performed with the GPAW method. The atom PAW setups were used as Ti ($3s^2 4s^2 3p^6 3d^2$), O ($2s^2 2p^4$), C ($2s^2 2p^2$), and H($1s^1$) to denote the adequate valance electronic interactions in the calculations. The initial structure of **1** was optimized by taking the crystal structure of TOF, as reported by Gao et al and removing its 6Hs.[1] All geometry optimizations were carried out with a grid spacing of 0.2 A˚ and standard force minimization conditions. PBE exchange functional and double zeta polarization (DZP) basis set were used only because these are accurate enough to give reasonably accuracy for metal cluster systems and are widely used combination in atomic-orbital DFT simulations for nanoclusters.[2–4]

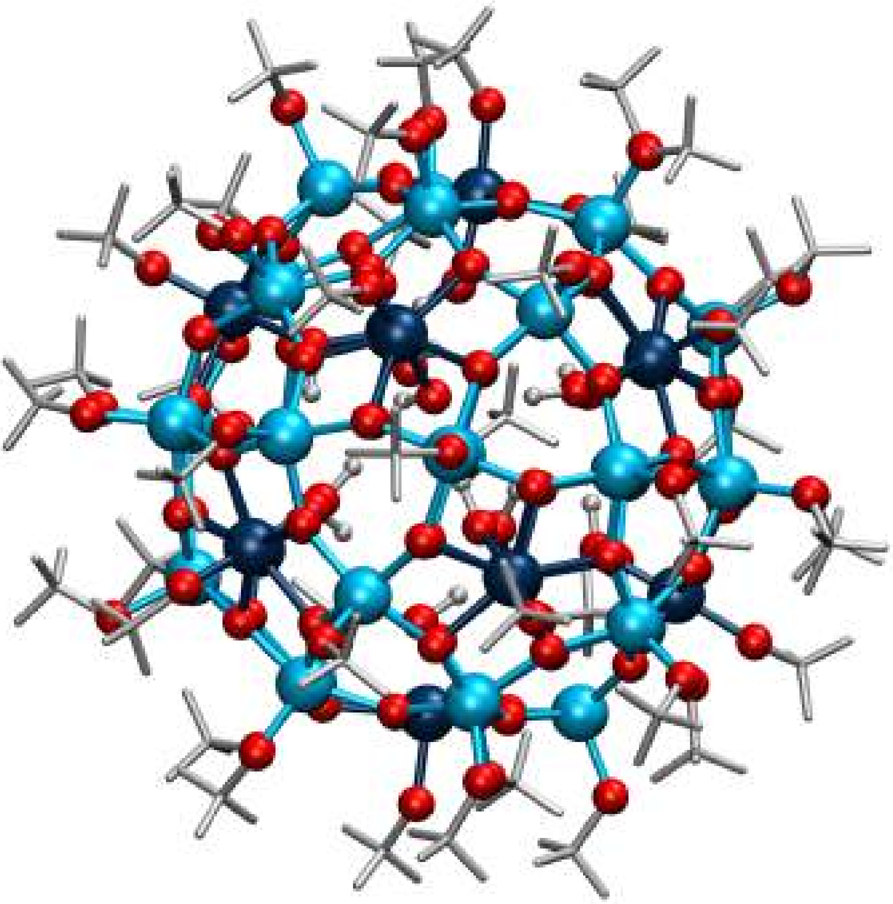

Fig. S10 Theoretically optimized structure of $H_6[Ti_{42}O_{60}(OCH_3)_{42}(OH)_{12}]$, E = -2204.21 eV.

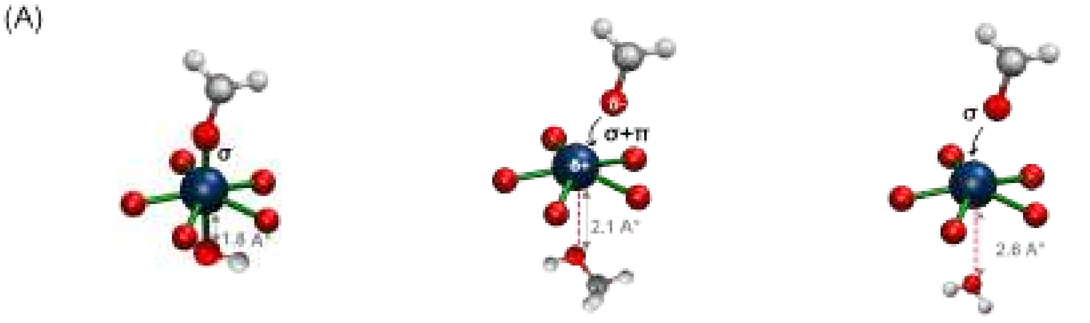

(i) Ti1 centre of TOF

(ii) Ti1 centre nearest to methanol in Cluster **1**

(iii) Ti1 centre near to H_2O in Cluster **1**

Fig. S11 Various binding modes and types of electron donation of the methoxide ligand with the Ti1 centre, obtained from DFT models. (i) Sigma bonding between methoxide and Ti1 centre of TOF, (ii) sigma and pi electron donation from methoxide ligand to Ti1 atom which is near to methanol molecules in cluster **1** and (iii) only sigma bonding between methoxy and Ti1 centre which is near to the cage-H_2O molecules.

SI2 Explanation of difference in charges between protonated and unprotonated $[Ti_{42}O_{60}(MeO)_{42}(MeOH)_{10}(H_2O)_2]^{-2}$

It is likely that in the gas phase the hydrogen atoms are strongly bonded to the bridging O sites on the surface of the cage, while in the crystal and solution phase the extra hydrogen atoms are more loosely bound to the cluster. This being the case we may treat the twelve H atoms as additional acceptor atoms to the ligands of the cluster. We know from the crystal structure of TOF that there are six preferential sites octahedrally arranged for the six hydrogen atoms though we do not know their exact placement and when we have twelve hydrogen atoms due to symmetry considerations, they will be bonded to the bridging O atoms as six pairs of hydrogen atoms at these six octahedral sites with each H atom donating 1*e*.

We verified that the single-electron donation of H to Ti indeed yields the overall cluster -2 charge according to the standard textbook rules for calculating the charges of organometallic complexes and we only assumed that the two water molecules and ten methanol molecules inside the cage do not donate electrons to Ti. Assuming an oxidation state of 4 for Ti the number of charges on Ti atoms is 42*4*e* = 168*e*. Twelve H atoms are in +1 oxidation state, so electrons accepted by Hs are 12*1*e* = 12*e*. The charges donated by ligands are as following the 10 -OMe ligands (connected to Ti1, close to MeOH) (10x3*e* = 30*e*), 2 -OMe ligands (connected to Ti1, close to H_2O)2*1*e* = 2*e*. Remaining 30 -OMe (Ti2 site) ligands and 60 μ_3-bridging atoms donate (30*1*e*) = 30*e*, (60x2*e*) = 120*e* respectively to the Ti atoms. Therefore, total charges donated by ligands is (30+2+30+120)*e* = 182*e* to Ti. Therefore, the charge on the cluster is 168+12-182 = -2.

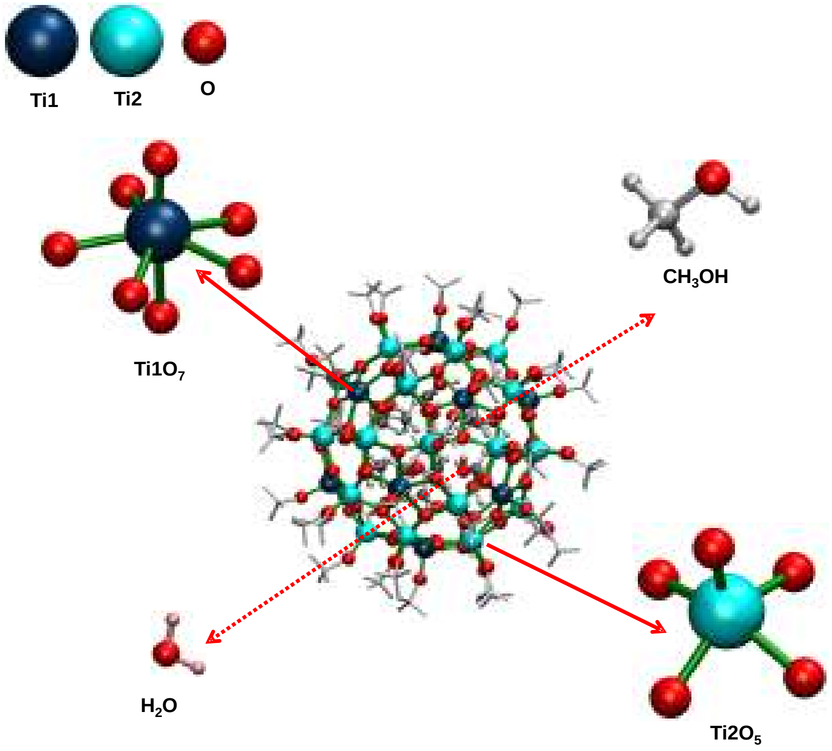

Fig. S12 Theoretically optimized structure of $[H_{12}Ti_{42}O_{60}(CH_3O)_{42}(CH_3OH)_{10}(H_2O)_2\}^{2-}$ (**1**) All constituent molecules such as $Ti1O_7$, $Ti2O_5$, CH_3OH, H_2O are labelled.

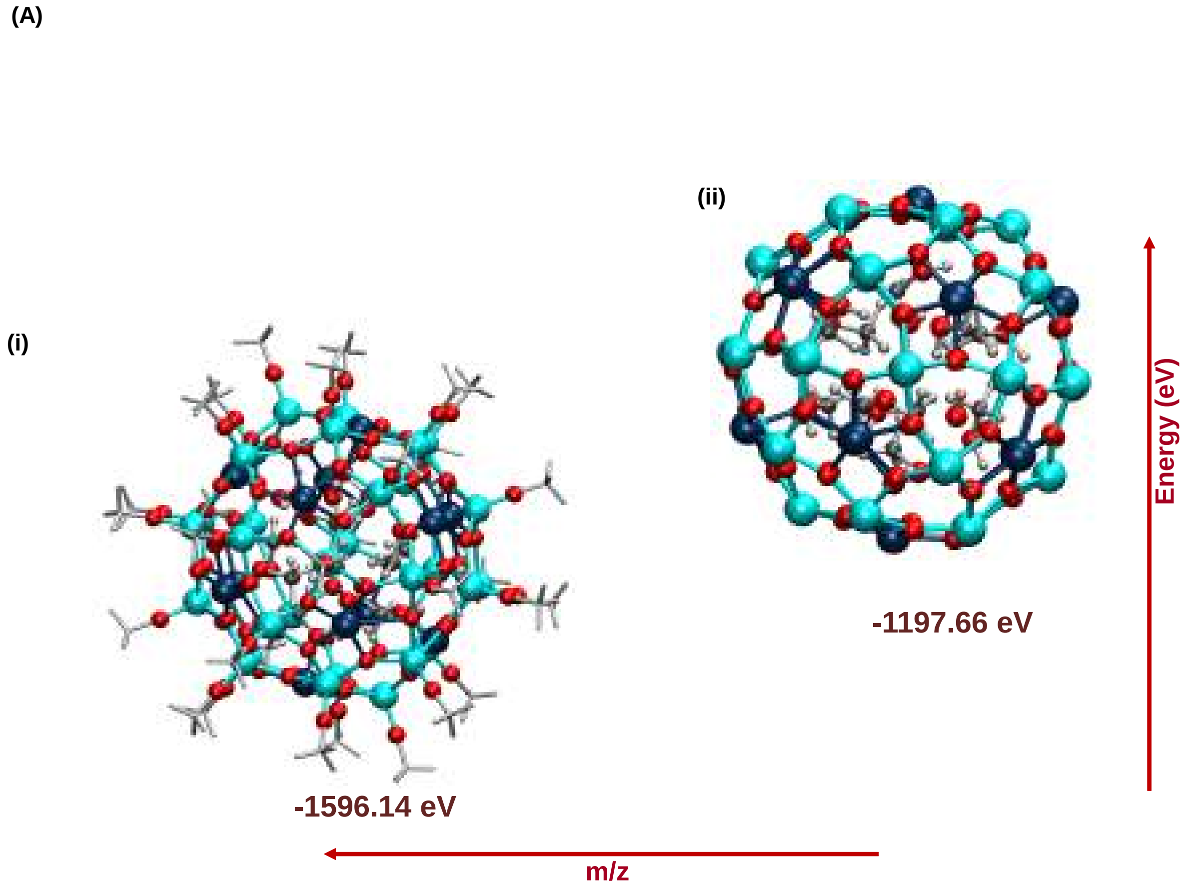

Fig. S13 Theoretically optimized structures of intermediates (i) $[H_{12}Ti_{42}O_{60}(CH_3O)_{30}(CH_3OH)_{10}(H_2O)_2]^{2-}$ (ii) $[H_{12}Ti_{41}O_{58}(CH_3OH)_{10}(H_2O)_2]^{2-}$ formed during gas phase fragmentation.

Table S1 Electron count for various constituents of **1**.

Formula	**No. of electrons donated / lost by each atom**	**No. of ligands/metal atoms**	**Total of charge of electron contribution**	**Total charge (e^-)**
Ti1	4	12	48	180
Ti2	4	30	120	
H	1	12	12	
MeO (Ti1 site close to MeOH)	3	10	-30	-182
MeO (Ti1 site close to H2O)	1	2	-2	
MeO(Ti2 site)	1	30	-30	
μ_3-O	2	60	-120	
$CH_3(OH)$	0	10	0	
H_2O	0	2	0	
Total charge				-2

Table S2: Comparison of Bader charges of the caged methanol molecules in cluster **1**. Labels 1, 2, 3, 4, 5, 6, 7, 8, 9 and 10 refer to each of the 10 methanol molecules.

Atoms	**Isolated methanol (e-)**	**In cluster 1 (e-)**	**Sum of each methanol (e-)**
1) O	-1.073469	-1.125902	
H	0.550502	0.580965	
C	0.405900	0.374355	
H	0.053647	0.122978	
H	0.014493	0.059993	
H	0.048936	-0.018294	-0.005905
2) O		-1.158572	
H		0.612039	
C		0.395603	
H		0.082344	
H		0.000059	
H		0.056760	-0.011767
3) O		-1.143032	
H		0.580766	
C		0.381641	
H		0.005621	
H		0.058059	
H		0.089870	-0.027075
4) O		-1.130505	
H		0.572016	

C		0.341842	
H		0.101267	
H		0.020504	
H		0.086536	-0.00834
5) O		-1.151216	
H		0.590230	
C		0.382089	
H		0.062989	
H		-0.030719	
H		0.090837	-0.05579
6) O		-1.147379	
H		0.589789	
C		0.307513	
H		-0.012398	
H		0.109244	
H		0.095780	-0.057451
7) O		-1.141296	
H		0.581964	
C		0.352674	
H		0.057328	
H		0.024900	
H		0.086162	-0.038268
8) O		-1.151764	
H		0.594026	
C		0.321497	
H		0.105723	
H		0.073583	
H		0.038504	-0.018431
9) O		-1.101824	

Atoms	**Isolated water (e-)**	**In cluster 1 (e-)**	**Sum of each water (e-)**
1) O	-1.094402	-1.174572	
H	0.547159	0.569319	
H	0.547249	0.615906	0.053807
H		0.564074	
C		0.368489	
H		0.019425	
H		0.046601	
10) O		-1.157097	
H		0.602332	
C		0.369650	
H		0.015565	
H		0.040704	
H		0.098016	-0.03083
		Total charge on ten methanol molecules	-0.282348

Table S3: Comparison of Bader charges of caged water molecules in the isolated molecule case and in cluster **1**.

2) O		-1.173333	
H		0.573600	
H		0.576726	-0.023007
		Total charge on both water molecules	-0.012354

Table S4: Average Bader charges of ligated molecules in [$Ti_{42}(\mu^3\text{-}O)_{60}(OCH_3)_{42}(OH)_{12}]^{6-}$ [computed structure for (TOF)] and in cluster **1**.

Atoms	**Average charges in TOF (e-)**	**Average charges in cluster ion 1 (e-)**
OCH_3(Ti1 bonded)	-0.57638	-0.36619
OCH_3(Ti2 bonded)	-0.57511	-0.41631
OH	-0.57386	-
$HOCH_3$	-	-0.0282348
H_2O	-	-0.012354

References

1 M.-Y. Gao, F. Wang, Z.-G. Gu, D.-X. Zhang, L. Zhang and J. Zhang, Fullerene-like Polyoxotitanium Cage with High Solution Stability, *J. Am. Chem. Soc.*, 2016, **138**, 2556–2559.

2 A. H. Larsen, M. Vanin, J. J. Mortensen, K. S. Thygesen and K. W. Jacobsen,

Localized atomic basis set in the projector augmented wave method, *Phys. Rev. B - Condens. Matter Mater. Phys.*, 2009, **80**, 195112.

3 P. Chakraborty, A. Nag, B. Mondal, E. Khatun, G. Paramasivam and T. Pradeep, Fullerene-Mediated Aggregation of $M_{25}(SR)_{18}^{-}$(M = Ag, Au) Nanoclusters, *J. Phys. Chem. C*, 2020, **124**, 14891–14900.

4 A. Nag, P. Chakraborty, G. Paramasivam, M. Bodiuzzaman, G. Natarajan and T. Pradeep, Isomerism in Supramolecular Adducts of Atomically Precise Nanoparticles, *J. Am. Chem. Soc.*, 2018, **140**, 13590–13593.

ACS NANOSCIENCE Au
AN OPEN ACCESS JOURNAL OF THE AMERICAN CHEMICAL SOCIETY

Assembling Atomically Precise Noble Metal Nanoclusters Using Supramolecular Interactions

Abhijit Nag and Thalappil Pradeep*

Cite This: https://doi.org/10.1021/acsnanoscienceau.1c00046 Read Online

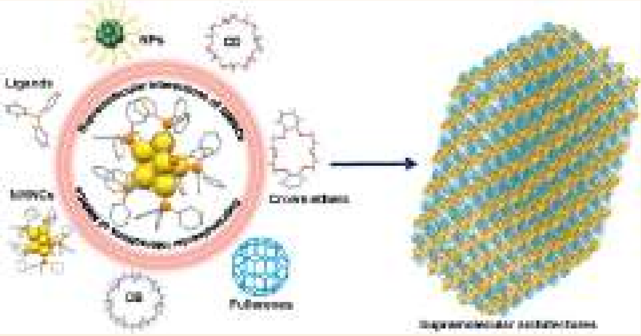

ABSTRACT: Supramolecular chemistry (SC) of noble metal nanoclusters (NMNCs) is one of the fascinating areas of contemporary materials science. It is principally concerned with the noncovalent interactions between NMNCs, as well as between NMNCs and molecules or nanoparticles. This review focuses on recent advances in the supramolecular assembly of NMNCs and applications of the resulting structures. We have divided the topics into four distinct subgroups: (i) SC of NMNCs in gaseous and solution phases, (ii) supramolecular interactions of NMNCs in crystal lattices, (iii) supramolecular assemblies of NMNCs with nanoparticles and NMNCs, and (iv) SC of NMNCs with other molecules. The last explores their interactions with fullerenes, cyclodextrins, cucurbiturils, crown ethers, and more. After discussing these topics concisely, various emerging properties of the assembled systems in terms of their mechanical, optical, magnetic, charge-transfer, etc. properties and applications are presented. SC is seen to provide a crucial role to induce new physical and chemical properties in such hybrid nanomaterials. Finally, we highlight the scope for expansion and future research in the area. This review would be useful to those working on functional nanostructures in general and NMNCs in particular.

KEYWORDS: *supramolecular chemistry, noncovalent interactions, nanoclusters, assemblies, functional nanostructures*

1. INTRODUCTION

Supramolecular chemistry (SC) deals with the creation of structures and associated functions through noncovalent interactions between molecules. These reversible interactions originating from hydrophobic forces, van der Waals (vdWs) forces, hydrogen bonds, and metal−ligand binding are crucial to understand self-assembling systems and various biological processes as well as to design molecular machines. SC has developed into a prominent interdisciplinary research area including biology, chemistry, nanotechnology, materials science, and physics. It has also led to some of the important advancements in molecular science. Research in this area is advancing at an accelerated pace, and all the frontier journals present these fascinating directions. Jean-Marie Lehn, Charles J. Pedersen, and Donald J. Cram have shared the Nobel Prize in chemistry (1987) for their research on "host−guest" assemblies. In 2016, Ben Feringa, Fraser Stoddart, and Jean-Pierre Sauvage were awarded the Nobel Prize in chemistry for their work on the design and synthesis of tiny molecular machines, utilizing principles of supramolecular chemistry. It is worth noting that supramolecular assemblies could be designed to carry out specific functions. Today, such assemblies are possible with noble metal nanoclusters (NMNCs), although many of the functions of such assemblies are yet to be explored.

NMNCs are emerging materials due to their unique physical and chemical properties.[1,2] They are made of a metal core connected by staple motifs, further stabilized by a monolayer of ligands such as thiolates, phosphines,[3−5] carbenes,[2] alkynyls,[6,7] or a mixture of ligands.[8−10] Atomically precise NMNCs such as $[Au_{25}(SR)_{18}]^-$ (refs 11 amd 12), $[Au_{102}(SR)_{44}]$,[13] $[Au_{144}(SR)_{60}]$,[14,15] $[Au_{52}(TBBT)_{32}]$,[16] $[Au_{38}(SR)_{24}]$,[17] $[Ag_{29}(S_2R)_{12}]^{3-}$ (ref 18), $[Ag_{25}(SR)_{18}]^-$ (ref 19), $[Ag_{44}(SR)_{30}]^{4-}$ (ref 20), and $[PdAu_{24}(SR)_{18}]$[21] (SR- a thiolate ligand) have precise molecular formulas, could be charged or uncharged, and exhibit unusual molecular properties. Examples include well-defined optical absorption and emission due to quantized energy levels, electrochemical properties, chirality, and chemical reactivity.[1,2,22−27] Limited investigations have been performed on their collective

Received: October 25, 2021
Revised: December 20, 2021
Accepted: December 21, 2021

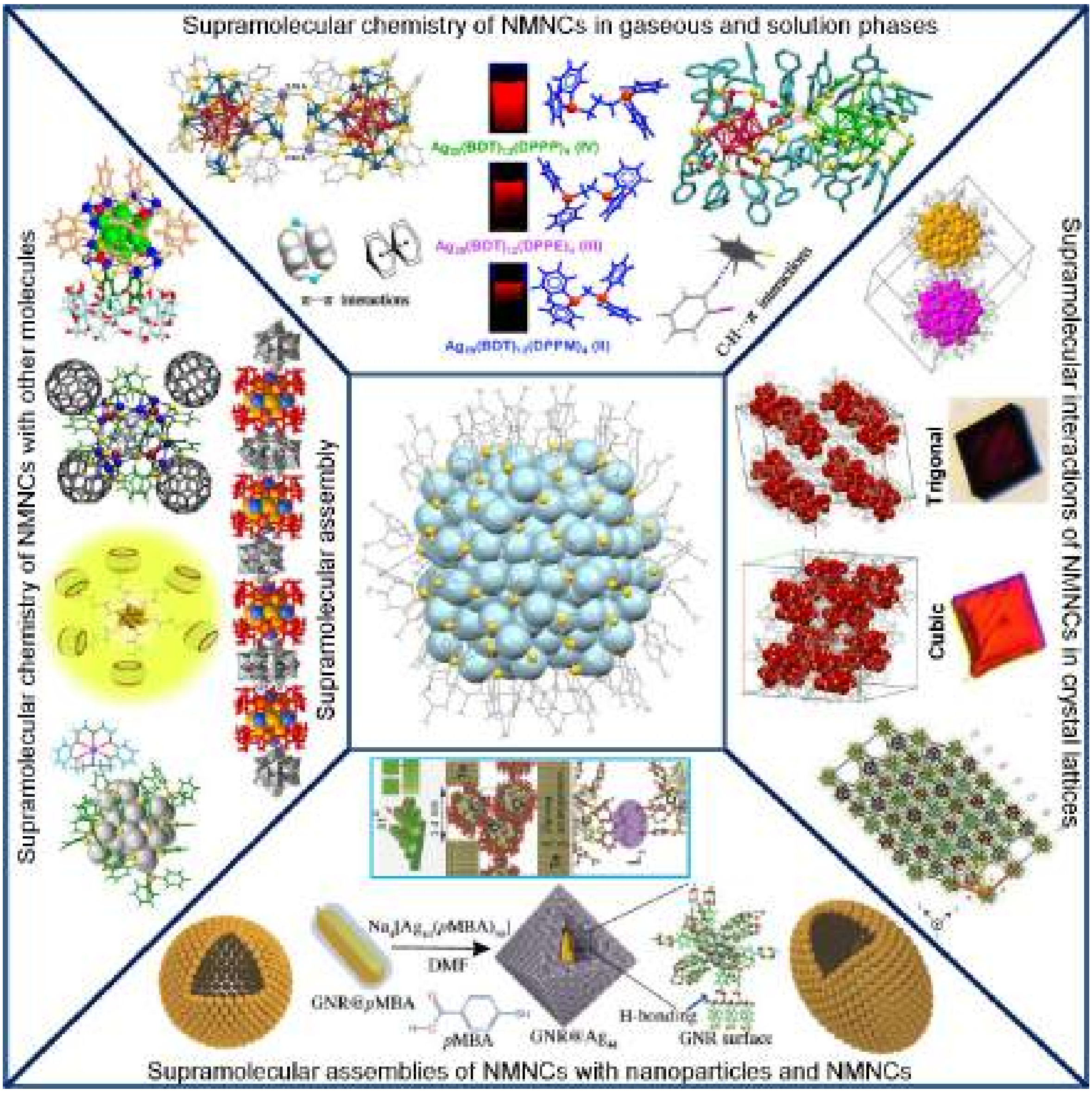

Figure 1. Various kinds of supramolecular assemblies of atomically precise NCs. Individual structures have been gathered from refs 20, 38, 43, 44, 46, 48, 53, 64, 65, 67, 69, 81, 82, 86, and101. At the center, an isolated ligand-protected cluster has been redrawn from ref 47.

properties such as magnetism. The presence of various kinds of ligands on the metal core enables the possibility of making specific noncovalent interactions with NMNCs, nanoparticles (NPs), and other molecules.[28−31] There are also possibilities of forming inclusion complexes of ligands acting as guests with suitable hosts for the SC of NMNCs. Examples of this branch of NMNCs-assembled materials are beginning to be available. As a result, the rich diversity in this category of materials is definite to make a lasting impact on materials science. In this context, we wish to present a review of the area reflecting on the past and present potential directions for the future.

Here, we focus on various possibilities of supramolecular assemblies of NMNCs and categorize them into the following specific topics (Figure 1):

1. SC of NMNCs in gaseous and solution phases
2. Supramolecular interactions of NMNCs in crystal lattices
3. Supramolecular assemblies of NMNCs with nanoparticles and NMNCs
4. SC of NMNCs with other molecules

In gaseous and solution phases, physical interactions such as vdWs, $\pi\cdots\pi$, $\pi\cdots$H−C, electrostatic, etc. can be present. But in the crystalline state, combinations of these interactions exist. SC of NMNCs is largely arising from interactions of the ligands, and the energy involved in them is 1−2 orders lower than in typical covalent bonds. Therefore, the resulting structures will follow the general trends of supramolecular interactions of organic molecules in gaseous, solution, and crystalline states. Additional properties could arise in the case of NMNCs when a highly ordered self-assembly is formed using SC. Such examples are also discussed below. While there are several sources of excitement, there are many challenges too; we will point to a few of them in the last section of the review. A key point to bear in mind is that the structures of most of the NMNCs lattices are not completely resolved with counterions and solvents to understand all the supramolecular interactions in detail as in organic crystals.

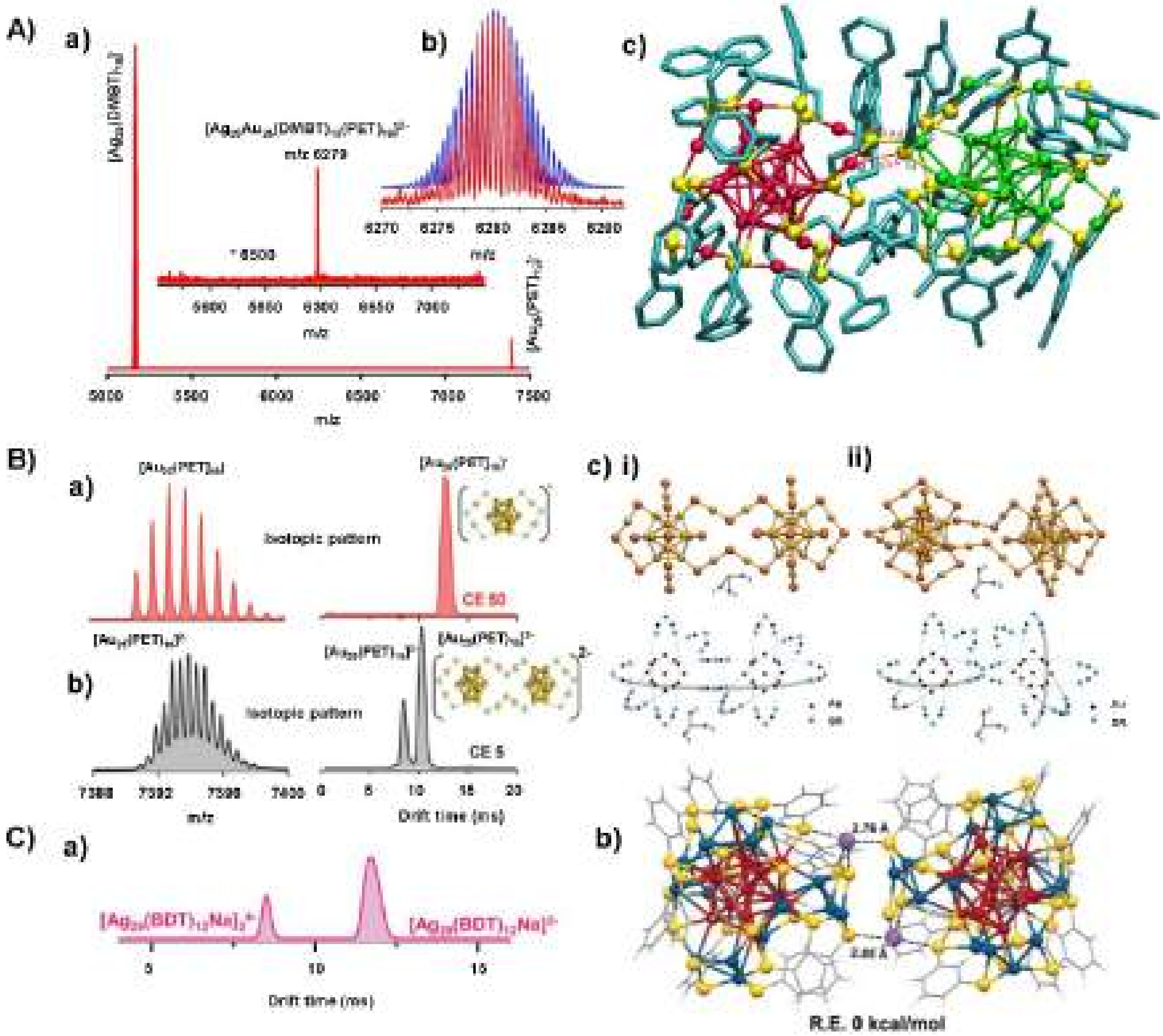

Figure 2. (A) (a) Formation of $[Au_{25}Ag_{25}(PET)_{18}(DMBT)_{18}]^{2-}$ heterodimer via intercluster reaction between $[Ag_{25}(DMBT)_{18}]^{1-}$ and $[Au_{25}(PET)_{18}]^{1-}$. (b) Experimental and calculated isotopic patterns for the dimer confirming the charge state of 2^-. (c) DFT optimized structure of the adduct $[Au_{25}Ag_{25}(PET)_{18}(DMBT)_{18}]^{2-}$. Color codes: white, H; yellow, S; red, Au; green, Ag; cyan, C. (Reproduced from ref 38. Copyright 2016 Nature Publishing Group.) (B) (a and b) Isotopic patterns and mobility distributions of $[Au_{25}(PET)_{18}]^{1-}$ and $[Au_{50}(PET)_{36}]^{2-}$ at the collision energies (CEs) 30 and 5 eV, respectively. With the increase of CE, the dimer is converted to a monomer. (c) DFT optimized structure and Borromean ring model of $[Au_{50}(PET)_{36}]^{2-}$. Color codes: pale red, S; orange, Au. (Adopted from ref 39. Copyright 2016 Royal Society of Chemistry.) (C) (a) Mobility distributions of $[Ag_{29}(S_2R)_{12}Na]^{2-}$ and $[Ag_{29}(S_2R)_{12}Na]_2^{4-}$ with different drifts (S_2R = BDT: 1,3-benzenedithiol). (b) DFT optimized structure of $[Ag_{29}(S_2R)_{12}Na]_2^{4-}$. Color codes: yellow, S; blue and red, Ag; purple, Na; white, H; gray, carbon. (Adopted from ref 43. Copyright 2016 Royal Society of Chemistry.)

2. SC OF NMNCS IN GASEOUS AND SOLUTION PHASES

SC of NMNCs in gaseous and solution phases was studied mainly using mass spectrometry (MS). In this context, intercluster reactions, dimerization of NMNCs, and ligand−NMNCs interactions are discussed below. We note that intercluster reaction and dimerization of NMNCs are the outcomes of supramolecular interactions.

2.1. Intercluster Chemistry of NMNCs

Alloying of NMNCs can be achieved easily via intercluster reactions.[32−36] Reaction between two well-known NMNCs, $[Ag_{44}(SR_1)_{30}]^{4-}$ and $[Au_{25}(SR)_{18}]^-$ (where SR_1 and SR_2 were 4-fluorothiophenol and 2-phenylethanethiol, respectively), led to the alloy NMNCs $[Ag_yAu_{44-y}(SR_1)_{30-n}(SR_2)_n]$ and $[Au_xAg_{25-x}(SR_2)_{18-m}(SR_1)_m]$.[37] Another example is the intercluster reaction between $[Ag_{25}(DMBT)_{18}]^-$ and $[Au_{25}(PET)_{18}]^-$, and alloying of NMNCs occurred keeping their $[M_{25}(SR)_{18}]^-$ structure and topology intact, via the dianionic adduct, $[Au_{25}Ag_{25}(PET)_{18}(DMBT)_{18}]^{2-}$ (Figure 2Aa and b).[38] All these studies were principally based on MS. Density functional theory (DFT) calculation and molecular docking studies suggested that $\pi\cdots\pi$, $\pi\cdots$H−C, and metallophilic interactions were the main reasons for such intercluster reactions to be initiated (Figure 2Ac). It may seem that there could be a repulsive force between the two anionic NMNCs when they approach each other. However, the overall charges of these NMNCs, $[Ag_{25}(SR)_{18}]^-$ and $[Au_{25}(SR)_{18}]^-$, are not confined but distributed over all the atoms in their staples, core, and ligands. As a result, the two NMNCs do not feel reasonable repulsive interactions between them. vdWs interactions between the NMNCs are playing a key role for such intercluster reactions as the atom exchange gets initiated

https://doi.org/10.1021/acsnanoscienceau.1c00046
ACS Nanosci. Au XXXX, XXX, XXX−XXX

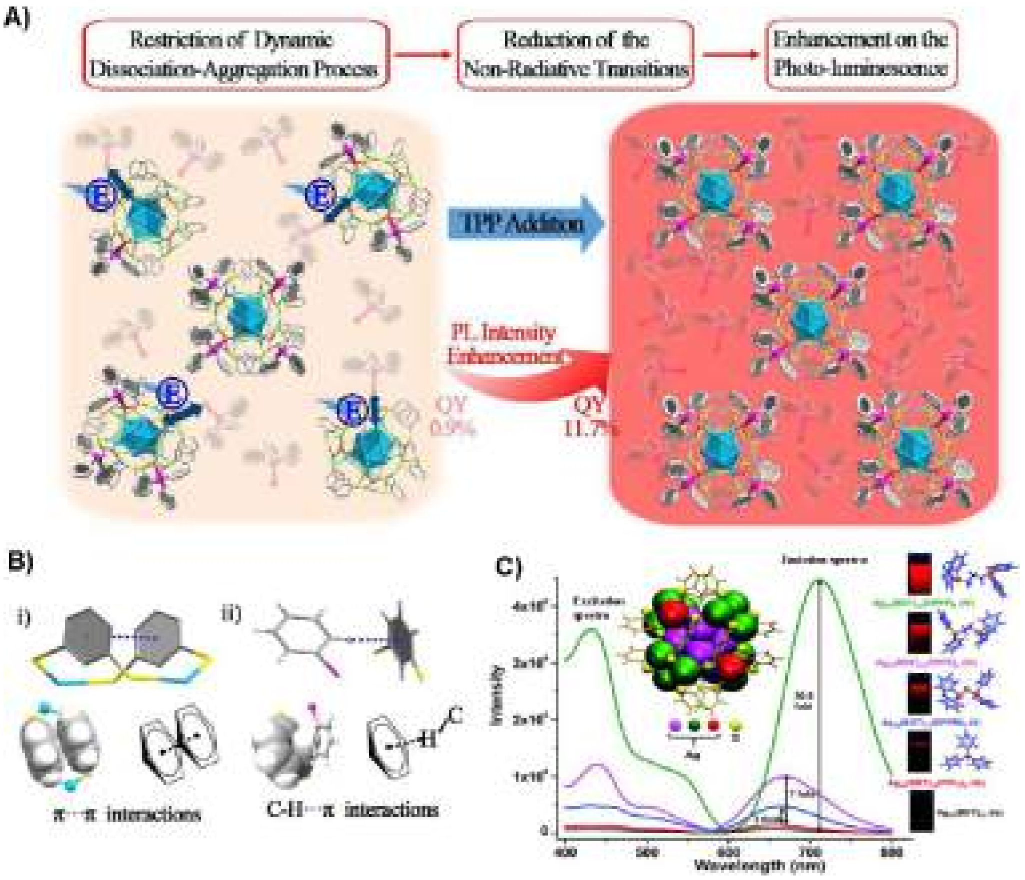

Figure 3. (A) Schematic representation of the luminescent enhancement of $[Ag_{29}(S_2R)_{12}(TPP)_4]$ in solution by the dissociation−aggregation process (S_2R = BDT). (B) (i) $\pi\cdots\pi$ interaction between S_2R ligands and (ii) $\pi\cdots H{-}C$ interaction between S_2R and TPP ligands, respectively. (Reproduced from ref 44. Copyright 2018 Royal Society of Chemistry.) (C) Emission and excitation spectra of NCs with different secondary ligands; each set is presented using the same color code. The DFT optimized structure of $[Ag_{29}(S_2R)_{12}]$ is presented in the inset. About 30 times enhancement in PL intensity related to its parent NMNC, $[Ag_{29}(S_2R)_{12}(TPP)_4]$, was confirmed when TPP was replaced with DPPP. (Reproduced from ref 46. Copyright 2018 Royal Society of Chemistry.)

by the formation of intercluster adducts,[34,35] which have been detected by MS (Figure 2A).

2.2. Dimerization of NMNCs

Dimerization and aggregation of NMNCs occurred due to the presence of noncovalent interactions. Our group reported the aggregation of $[Au_{25}(SR)_{18}]^-$ in the gas phase using ion mobility (IM) MS.[39] The trimer, dimer, and monomer of $[Au_{25}(SR)_{18}]^-$ were separated because of their difference in collision cross sections. As a result, different drift times were observed for them in the mobility distribution. The isotopic patterns and mobility distributions of $[Au_{25}(PET)_{18}]^{1-}$ and $[Au_{50}(PET)_{36}]^{2-}$ at the collision energies (CEs) 30 and 5 eV are presented in Figure 2Ba and b, respectively. DFT calculations revealed that noncovalent and aurophilic interactions are the primary causes for the gas-phase aggregation of $[Au_{25}(SR)_{18}]^-$ (Figure 2Bc). However, despite having a similar structure, $[Ag_{25}(SR)_{18}]^-$ did not produce such a dimer in the gas phase. Bidentate thiol ligand can play a crucial role to assemble thiolated NMNCs into multimers. Recently, Bodiuzzaman et al. reported a covalently linked dimer of $[Ag_{25}(SR)_{18}]^-$ which was also confirmed using MS and supported by DFT calculations and other techniques.[40] Dimers of $[Au_{25}(S\text{-}tBu)_{18}]^-$ were obtained using bidentate benzene-1,4-dithiol as a ligand.[41] Similarly, Lahtinen et al. confirmed the formation of a dimer of $[Au_{102}(SR)_{44}]$ and $[Au_{250}(SR)_n]$ using transmission electron microscopy (TEM) where biphenyldithiols (BPDTs) were used as a linker.[42]

In another report, dimerization of $[Ag_{29}(S_2R)_{12}]^{3-}$ induced by alkali metal ions was investigated using IM MS in the gas phase.[43] The proton affinity of the same metal cluster was also studied. Dimers induced by H^+ and Li^+ were not detected because these cations are smaller in size. Na^+, K^+, Rb^+, and Cs^+ induced dimer formations were studied using IM MS. The mobility distributions of $[Ag_{29}(S_2R)_{12}Na]^{2-}$ and $[Ag_{29}(S_2R)_{12}Na]_2^{4-}$ with different drift times are shown in Figure 2Ca. The dimerization process was assisted by the interactions between the sulfur of the NMNCs and the cations (Figure 2Cb).

2.3. Interactions of NMNCs with Ligands

Ligand−ligand and NMNC−ligand interactions play a crucial role to build the SC of NMNCs in gaseous and solution phases. In this context, Zhu and co-workers reported a novel mechanism of aggregation induced emission where the restriction of the "dissociation−aggregation pattern" of ligands is explained using $[Ag_{29}(S_2R)_{12}(TPP)_4]$ (TPP: triphenylphosphine) (termed as Ag_{29}) as an example (Figure 3A).[44] To prove the dissociation−aggregation process, different concentrations of TPP molecules were added to the nondissociative $[Ag_{28}Pt_1(Adm)_{18}(TPP)_4]$[45] (termed as $Ag_{28}Pt_1$) (Adm: 1-adamantanethiol) and dissociative Ag_{29} solution. The photo-

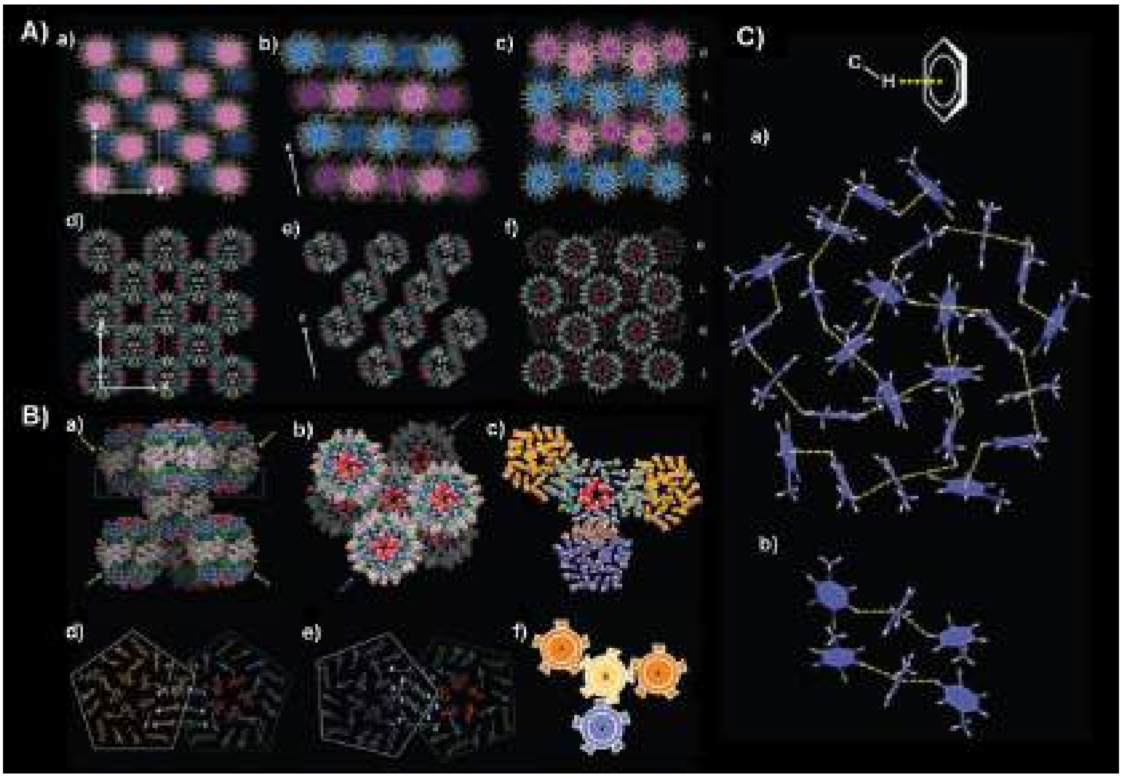

Figure 4. (A) Packing of $[Au_{246}(p\text{-MBT})_{80}]$ in the unit cell. Views from the (a) *z*-direction, (b) *y*-direction, (c) and *x*-direction. Color codes: $[Au_{246}(p\text{-MBT})_{80}]$ with different chirality, gold, blue, and magenta; sulfur, yellow; carbon, gray. (d–f) Arrangement of ligands of $[Au_{246}(p\text{-MBT})_{80}]$ along the *z*-, *y*-, and *x*-directions. Color codes: ligands positioned at the middle of $[Au_{246}(p\text{-MBT})_{80}]$, gray, red, blue, and green; ligands positioned at the extremes, green, blue, and red. (B) Intercluster self-assembly generated by the ligands. (a and b) Coordination geometry of $[Au_{246}(p\text{-MBT})_{80}]$ in the unit cell: side view (a) and top view (b). (c) Interactions among the intercluster ligands. (d) Side-by-side assembly of the ligands in $[Au_{246}(p\text{-MBT})_{80}]$ with the same chirality. (e) Point-to-point assembling of the ligands in $[Au_{246}(p\text{-MBT})_{80}]$ with opposite chirality. (f) Schematic representation of the directional packing of $[Au_{246}(p\text{-MBT})_{80}]$. (C) Various $\pi\cdots$H–C interactions between the ligands of NMNC: (a) rotational and (b) parallel patterns. (Reproduced from ref 47. Copyright 2016 American Association for the Advancement of Science.)

luminescence (PL) intensity of Ag_{29} was improved 13 times by the addition of TPP into *N,N* dimethylformamide (DMF) solution of the NMNC. But the PL intensity of nondissociative $Ag_{28}Pt_1$ remained almost the same after the addition of TPP. A temperature-dependent PL study of Ag_{29} NC showed two stages of intensity increase.[44] This confirmed that both the quenched thermal vibration process and the restriction of the TPP dissociation–aggregation process were involved in Ag_{29}. However, only the thermal vibration process was observed for $Ag_{28}Pt_1$. The $\pi\cdots\pi$ and $\pi\cdots$H–C interactions between the ligands are shown in Figure 3B.

In a subsequent study, Khatun et al. demonstrated that systematic replacement of the TPP with other secondary ligands resulted in an enhancement of PL intensity of Ag_{29} in the NIR (near-infrared) region.[46] Secondary ligands also play a vital role to enhance the photoluminescence of NMNCs. About 30 times enhancement in PL intensity related to the parent NMNC, $[Ag_{29}(S_2R)_{12}(TPP)_4]$, was confirmed when TPP was replaced with 1,3-bis(diphenylphosphino)propane (DPPP) (Figure 3C). DFT calculations of the NMNC with different secondary ligands suggested that the emission was due to a LMCT (ligand to metal charge transfer). Enhancement of the luminescence was because of restricted intramolecular rotation (RIR). The rigidity of the NMNC surface was increased when TPP was replaced with DPPP because of the presence of a greater number of noncovalent interactions ($\pi\cdots\pi$ and $\pi\cdots$H–C interactions) in DPPP capped NMNCs. The rigidity of the NC promoted the radiative transitions by allowing RIR. A similar type of result was also observed for $[Ag_{51}(S_2R)_{19}(TPP)_3]$.[46]

3. SUPRAMOLECULAR ASSEMBLIES OF NMNCS IN CRYSTAL LATTICES

Supramolecular interactions could play an important role in the systematic organization of NMNCs in crystal lattices. Well-organized assembly of NMNCs is present in their unit cells. An understanding of the packing arrangement of NMNCs in a crystal lattice could provide new insights into the NMNC-assembled patterns, structures, and properties. In this section, supramolecular interactions of NMNCs via intercluster and intracluster fashions in crystal lattices are presented.

3.1. Ligand Induced Supramolecular Assemblies of NMNCs in Crystal Lattices

Supramolecular interactions among ligands present in a crystal lattice generate various unique patterns, structures, and properties. In this section, we will focus on various supramolecular interactions among ligands leading to different symmetries and patterns.

For example, Jin and co-workers determined the structure of $[Au_{246}(p\text{-MBT})_{80}]$ (*p*-MBT = *p*-methylbenzenethiolate) at the atomic, molecular, and nanoscale levels using SCXRD (single crystal X-ray diffraction).[47] The ligands generated complex patterns on the NMNC surfaces similar to structures of biomolecules. The density and symmetry of the surface

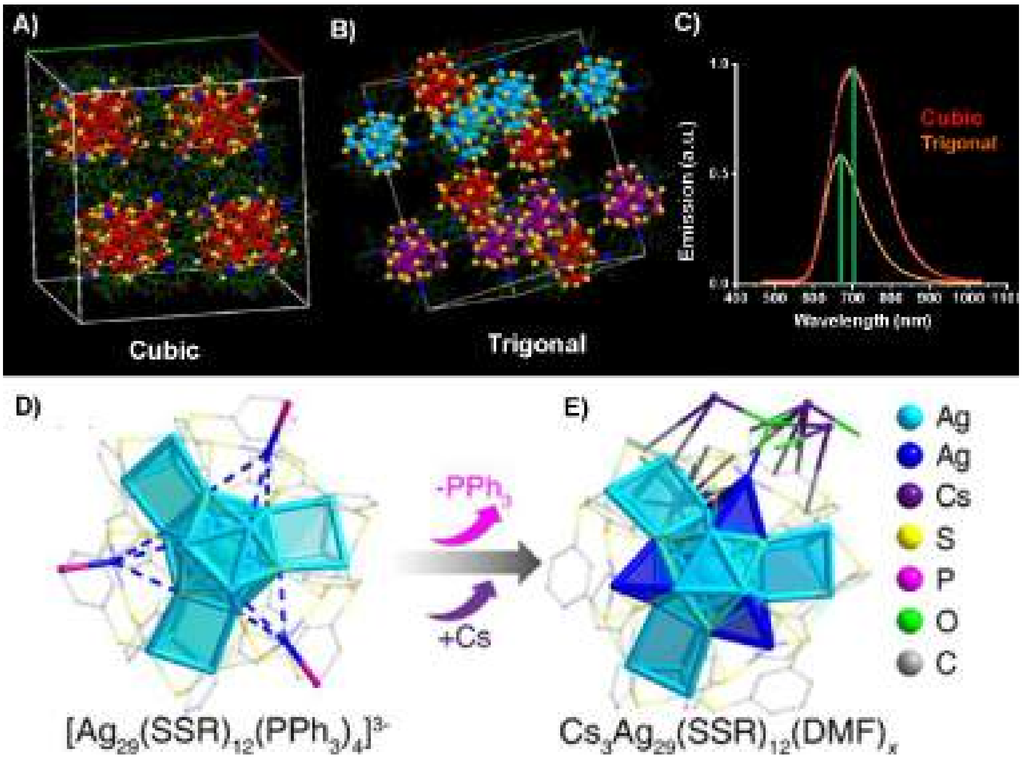

Figure 5. (A) Cubic unit cell and (B) trigonal unit cell of Ag_{29} NMNC. (C) Emission spectra of the cubic and trigonal crystals of the NMNC. (Adopted from ref 53. Copyright 2018 Royal Society of Chemistry.) (D) Structure of Ag_{29} NMNC. (E) Crystal structure of $[Ag_{29}Cs_3(S_2R)_{12}(DMF)_m]$ ($m = 5, 6$). (Adopted from ref 58. Copyright 2019 American Chemical Society.)

patterns further guided the packing of NMNCs into lattices with rotational, orientational, and translational order. $[Au_{246}(p\text{-}MBT)_{80}]$ NMNCs are presented with a square configuration in Figure 4Aa, akin to the packing mode in the [100] plane of fcc metals. The NMNCs are stacked obliquely along the [001] direction (Figure 4Ab). The packing density of the NMNCs is 60%, which is less than the fcc lattice (74%). The consequence of specific intercluster interactions of the monoclinic packing is correlated to the alignment of the ligands on the NMNCs (Figure 4Ad−f). The crystal lattice was verified to possess an ABAB type of arrangement, wherein $[Au_{246}(p\text{-}MBT)_{80}]$ makes up the A layer and isomeric NMNCs are the B layer (i.e., (R-NC)A@(L-NC)B@(R-NC)A@(L-NC)B), shown in Figure 4Ac. To realize the intercluster assembly of $[Au_{246}(p\text{-}MBT)_{80}]$, the coordination environment of the surface ligands was also examined (Figure 4Ba−f). Each NMNC is surrounded by six neighboring NMNCs. Four of them have the same chirality as the central one (Figure 4Ba, yellow arrows). They are organized within the same square layer. The other two are of the opposite chirality in different layers (Figure 4Bb, purple arrows). The peripheral ligands of a NMNC interacted with other ligands from three neighboring NMNCs, and five pairs of interacted ligands contributed to each interaction (Figure 4Bc). Intermolecular $\pi \cdots H{-}C$ interactions play a key role to stabilize the surface patterns on the NMNCs. The C−H bonds of the methyl groups or phenyl rings interact with the π electrons (Figure 4Ca and b). The ligand's rotational and parallel self-assembled surface patterns are comparable to the structural complexity of biomolecules such as the α-helix and β-sheet in proteins.

Similarly, $[Au_{144}(PMT)_{60}]$[48] (PMT = S-CH_2Ph) and $[Au_{133}(PET)_{52}]$[49] (SR = S-C_2H_4Ph) NMNCs are arranged with an ABAB packing mode (i.e., (R-NC)A@(L-NC)B@(R-NC)A@(L-NC)B) like the above-mentioned $[Au_{246}(p\text{-}MBT)_{80}]$. The asymmetric arrangement of the surface structures results in isomerism in NMNCs. Intercluster interactions were observed between the two neighboring $[Au_{144}(PMT)_{60}]$ NMNCs. The optical isomers (R and L) were stacked layer by layer with a hexagonal pattern in the (001) plane and a square configuration in the (100) and (010) planes. Each $[Au_{144}(PMT)_{60}]$ was surrounded by six $[Au_{144}(PMT)_{60}]$ NMNCs with the opposite chirality in the crystal lattice. Various kinds of supramolecular interactions such as $\pi \cdots H{-}C$ (2.80 Å) and $H \cdots H$ (2.54 Å) between the ligands of neighboring NMNCs lead to the formation of compact and ordered crystal structures.

The ABAB (e.g., $[Au_{246}(p\text{-}MBT)_{80}]$, $[Au_{133}(PET)_{52}]$, and $[Au_{144}(PMT)_{60}]$) and the ABCD (e.g., $[Au_{92}(SR)_{44}]$)[50] are the two well-known packing fashions of the NMNC system. Recently, a third mode of packing—ABCDEF (6H packing mode)—was reported for $[Au_{60}S_6(PMT)_{36}]$ by Gan et al.[51] In their work, Gan et al. incorporated a sulfur atom on $[Au_{60}S_6(PMT)_{36}]$ and converted it into $[Au_{60}S_7(PMT)_{36}]$ by heating. As a consequence, the ABCDEF (6H packing mode) arrangement in $[Au_{60}S_6(PMT)_{36}]$ was converted into the ABAB mode for $[Au_{60}S_7(PMT)_{36}]$, although the crystallization conditions were identical. The difference in the packing in the unit cell was reflected in the optical properties. The PL intensity of the $[Au_{60}S_6(PMT)_{36}]$ (ABCDEF-6H packing mode) crystal lattices is weaker compared to $[Au_{60}S_7(PMT)_{36}]$ (ABAB packing mode) in the amorphous state. $[Ag_{46}S_7(SR)_{24}]$ (SR = S-PhMe_2) packed with the ACB@ACB mode (simple translational symmetry) in the crystal lattice.[52] Each NMNC is connected with four other NMNCs in other planes. $C{-}H \cdots \pi$ interactions (intracluster) between adjacent ligands resulted in

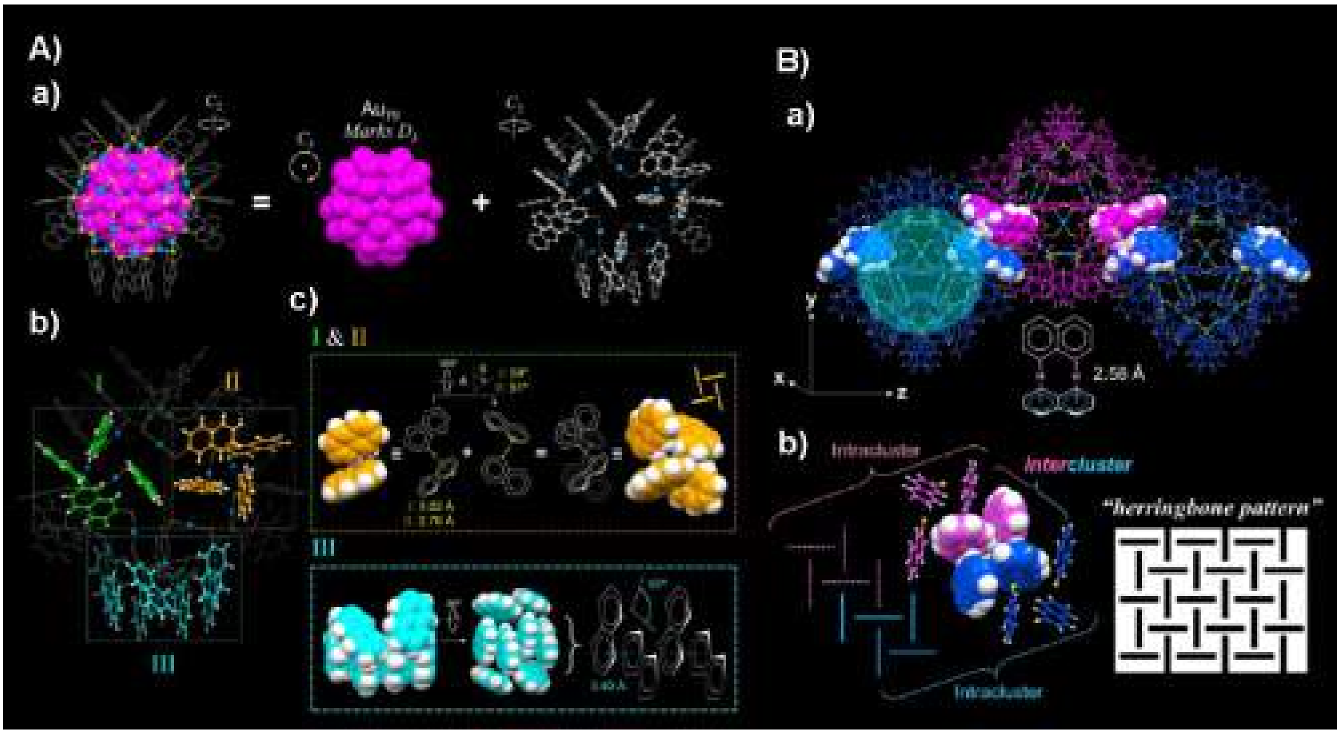

Figure 6. (A) (a) Crystal structures of the $[Au_{103}S_2(S\text{-}Nap)_{41}]$ NMNC, Au_{79} (middle), and ligands (right). Color codes: magenta and blue, Au; yellow, S; white, H. (b) Intracluster interactions via ligands. (c) T-shaped arrangement adopted a "herringbone pattern" via $\pi\cdots H{-}C$. (B) (a) Intercluster interactions ($\pi\cdots H{-}C$) in the crystal lattice of Au_{103} NMNC. (b) Intercluster and intracluster interactions resulted in the "herringbone pattern". (Adopted from ref 54. Copyright 2017 American Chemical Society.)

the systematic organization of the ligands on the NMNC surface.

Supramolecular interactions can be tuned to generate a polymorphic NMNC crystal lattice.[53] In this context, a cubic lattice (C) of $[Ag_{29}(S_2R)_{12}(TPP)_4]$ was obtained using the drop-casting method (Figure 5A). $[Ag_{29}(S_2R)_{12}(TPP)_4]$ adopted the trigonal lattice (T) when the vapor diffusion method was used (Figure 5B). The T unit cell was composed of three different orientations of the NMNCs (highlighted in different colors), whereas only one type of orientation of the NMNCs was confirmed in the C unit cell (Figure 5A and B). The difference in the intercluster interactions of TPP and S_2R resulted in two polymorphic crystals. The $\pi\cdots H{-}C$ interactions of TPP were more favored in a C lattice compared to a T lattice. The greater numbers of $\pi\cdots H{-}C$ interactions resulted in a greater rigidity in the C system relative to the T system. This is why the cubic crystals gave rise to a greater PL intensity compared to trigonal crystals (Figure 5C).

In another study, the SCXRD of $[Au_{103}S_2(NPT)_{41}]$ (NPT = 2-naphthalenethiol) revealed the "intercluster assembly" of NMNCs (Figure 6Aa).[54] The surfaces of the NMNCs are highly stabilized through intracluster noncovalent interactions, such as $H\cdots H$ and $\pi\cdots H{-}C$ interactions. Intercluster and ligand−ligand interactions resulted in highly dense assembly in the unit cell (Figure 6Ab). Naphthalene thiols on the NMNC surface created local tetramers through noncovalent interactions of $\pi\cdots\pi$ and $\pi\cdots H{-}C$ stacking (Figure 6Ac). The outer surfaces of the ligands of neighboring NMNCs are interlinked via T-shaped $C{-}H\cdots\pi$ interactions with an average distance of 2.58 Å to yield intercluster assembly (Figure 6Ba). Such an orderly T-shaped arrangement adopted a "herringbone pattern" via intercluster interactions (Figure 6Bb). These types of patterns have resulted in a linearly connected zigzag arrangement in the unit cell.

Recently, Khatun et al. reported an assembly of NMNCs coprotected by diphosphine and thiol, $[Ag_{22}(SR)_{12}(DPPE)_4Cl_4]^{2+}$ (SR = 2,5-dimethylbenzenethiol; DPPE = 1,2-bis(diphenylphosphino)ethane).[55] The NMNC consisted of an Ag_{10} core and $[Ag_{12}(DPPE)_4(2,5\text{-}DMBT)_{12}Cl_4]$ shell. The $[Ag_{12}(SR)_{12}(DPPE)_4Cl_4]$ shell encapsulated the Ag_{10} core. Electrospray ionization (ESI) MS study also supported the SCXRD data. An unusual crystallization induced luminescence enhancement was confirmed for this NMNC as the emission was weak in the amorphous states and solution. However, about 12 times luminescent enhancement was observed in the case of the crystalline state relative to the amorphous state. As the NMNC is protected by DPPE and DMBT, the well-organized noncovalent interactions ($\pi\cdots H{-}C$ and $\pi\cdots\pi$) between the ligands throughout the crystal lattice led to the enhancement in luminescence.

Negishi and co-workers reported some essential factors for the assembly of NMNCs and the functions and properties of such assembled structures.[56] $[Au_4Pt_2(SR)_8]^0$ was used for the study, and the following four points were mentioned about the NMNCs: (1) $[Au_4Pt_2(SR)_8]^0$ could be utilized as a building block to generate one-dimensional connected structures (1D-CS) via intercluster gold−gold bonds (aurophilic bond). (2) The intra-NC ligand interactions differed subject to the ligand structure having a similar structure of $[Au_4Pt_2(SR)_8]^0$. Consequently, the distribution of the ligands varied depending on the structure of the ligand in $[Au_4Pt_2(SR)_8]^0$. (3) The inter-NC ligand interactions were influenced by the changes in the distributions of the ligands. (4) The band gap of the NMNCs was reduced by the formation of 1D-CS. This study established

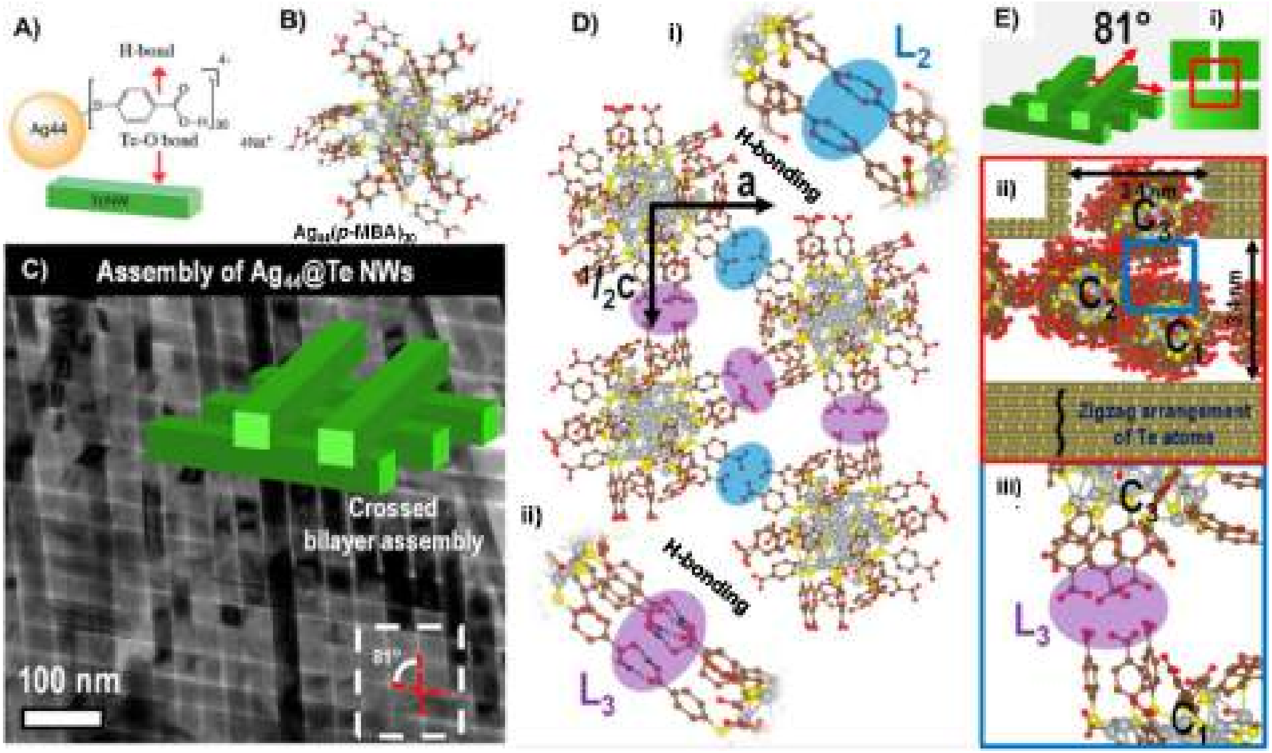

Figure 7. (A) Schematic representation of the interactions between $[Ag_{44}(SR)_{30}]$ and Te NWs. (B) Total structure of $[Ag_{44}(p\text{-MBA})_{30}]$. (C) Formation of the crossed-bilayer assembly (CBA) of Ag44@Te NWs shown via TEM images. (D) H-bonding between the carboxylic group of the ligand of adjoining. The adjoining NCs' network via H-bonding with L_2 (i) and L_3 (ii) fashion. (E) (i) Schematic representation of the CBA. (ii) Zoom in view of the area shown in (i). Further zoom in view is presented in (iii). Different NCs are labeled as C_1, C_2, and C_3. (Reproduced from refs 28, 64, and 68. Copyright 2019 American Chemical Society, 2016 and 2017 Wiley.)

that intracluster ligand interactions need to be created to yield 1D-CS with desired functionalities.

Supramolecular interactions were also reported for heterocyclic carbene-protected Au superatom NMNCs $[Au_{13}(NHC^{Bn})_9Cl_3]^{2+}$ (NHCs N-heterocyclic carbenes).[57] The NMNC was synthesized by the reduction of precise Cl−Au−NHC complexes. The NMNC consisted of an icosahedral Au_{13} core protected by nine NHCs and three chlorides in an ordered fashion. SCXRD revealed that the NMNCs were assembled via multiple noncovalent interactions ($\pi\cdots H{-}C$ and $\pi\cdots\pi$) which made the surfaces of the ligands rigid. As a result, a high quantum yield (QY) up to 16.0% was observed. The QY is considerably higher than other reported Au_{13} superatom NMNCs.

Hydrogen bonding interactions among ligands were also studied. The complete structure of $[Ag_{44}(SR)_{30}]$ (SR = p-mercaptobenzoic acid) was resolved using X-ray crystallography.[20] The crystal lattice consisted of two kinds of Ag_{44} NMNCs (α and β) stacked in a fcc lattice. They are correlated by a mirror reflection symmetry. The ACB layers were arranged in order in a six-layer sequence—Aα-Cβ-Bα-Aβ-Cα-Bβ—due to the presence of $\alpha-\beta$ mirror symmetry. $[Ag_{44}(SR)_{30}]$ produced a self-assembled structure throughout the crystal lattice through the establishment of strong H-bonds between the carboxyl groups of neighboring NMNCs. The ligands were interconnected via double and triple bundles. Intralayer H-bonding between neighboring NMNCs ($\alpha\alpha$ or $\beta\beta$) resulted in a doubly bundled ligand arrangement, whereas the interlayer H-bonding between neighboring NMNCs ($\alpha\beta$) gave rise to the triply bundled ligand arrangements.[21]

3.2. Ion Induced Supramolecular Assemblies of NMNCs in Crystal Lattices

Ion induced supramolecular interactions such as electrostatic, cation$\cdots\pi$, and anion$\cdots\pi$ interactions take crucial part in nature, particularly in molecular recognition, protein structure, and enzyme catalysis. Similarly, ions could also play an important role to assemble NMNCs via ion induced supramolecular interactions. Pradeep and co-workers reported the gas-phase adducts of $[Ag_{29}(S_2R)_{12}]$ with alkali metals as discussed above.[43] Recently, Zhu and his co-workers resolved the structure of Cs^+ attachment with $[Ag_{29}(S_2R)_{12}(TPP)_4]$ using X-ray crystallography and studied the supramolecular assembly of the NMNCs.[58] The addition of Cs^+ peeled the TPP off from the NMNC surface and resulted in a neutral Cs−NMNC complex, $[Ag_{29}Cs_3(S_2R)_{12}(DMF)_m]$ ($m = 5, 6$) (Figure 5D and E). The formation of such a complex was driven by the electrostatic attraction between $[Ag_{29}(S_2R)_{12}(TPP)_4]^{3-}$ and Cs^+ and was facilitated by $Cs\cdots\pi$ and Cs−S interactions. The capture of Cs^+ induced changes on the $[Ag_{29}(S_2R)_{12}]$ unit. Interactions among $[Ag_{29}(S_2R)_{12}(TPP)_4]^{3-}$, Cs^+, and DMF gave rise to a 1D self-assembled structure in the crystal lattice. The optical properties of $[Ag_{29}Cs_3(S_2R)_{12}(DMF)_m]$ were changed remarkably compared to the parent NC due to such types of intercluster interactions. Similarly, hydrophobic NMNCs $[Ag_{29}(S_2R)_{12}(PPh_3)_4]^{3-}$ were made water-soluble using solvent-conjoined Na^+ by the same group.[59]

In a subsequent study, Hyeon and co-workers reported a simple synthesis of an assembly of highly fluorescent AuNCs. In particular, Zn^{2+} induced precise assembly of Au_4 NCs exhibited a QY of ~90% in water.[60] This is the highest QY reported for NMNCs until date. Zn^{2+} induced distinctive aurophilic interaction (gold(I)−gold(I), d^{10}−d^{10}) among Au_4 NCs, resulting in such a highly greenish-blue fluorescence. This bright fluorescence came from the Zn^{2+} induced rigidified environment due to the delay in vibrational relaxation. This NMNC assembly may be used for the drug delivery by monitoring the reassembly and disassembly processes reversibly, by the readdition and extraction of metal ions.

Counter ions also assist in the packing arrangement of NMNC in a unit cell. The Jin group reported the variation in packing for Au_{23}, Au_{21}@Cl, and Au_{21}@$AgCl_2$ NMNCs because of their differences in surface structures and counterions.[61] X-ray diffraction studies revealed the hierarchical assembly in the crystal lattice. Au_{21} NCs were systematically organized into one-dimensional (1D) nanofibrils via various noncovalent interactions (π···anion, π···π, and aryl Cl···H−C interactions) facilitated by site-specific surface hooks. Further, these 1D nanofibrils resulted in 3D crystals which gave rise to the hierarchical assembly. Modification of the packing arrangements of Au_{21} NCs by modifying the counterions influenced the electrical transport properties by 2 orders of magnitude.

4. SUPRAMOLECULAR ASSEMBLIES OF NMNCS WITH NANOPARTICLES AND NMNCS

Supramolecular interactions of NMNCs with NPs and NMNCs could result in self-assembled superstructures. The interactions of $[Ag_{32}(SG)_{19}]$[62] with 1D tellurium nanowires (Te NWs) were introduced by Pradeep and co-workers.[63] The reaction between Ag NPs and ions with 1D Te NWs resulted in AgTe NWs. But a different reactivity toward Te NWs was evidenced for NMNCs which lead to the formation of Ag islands at different locations on the Te NWs. Inspired by this result, Som et al. further studied the interactions between Te NWs and $[Ag_{44}(p\text{-MBA})_{30}]$ (MBA = S-PhCOOH) (termed as Ag_{44}) (Figure 7A and B).[64] After dispersing Ag_{44}@Te NWs in 1-butanol, the sample was kept for solvent evaporation. These hybrid material Ag_{44}@Te NWs resulted in a crossed-bilayer structure, whereas a monolayer assembly was formed when the NMNC was absent (Figure 7C). TEM data revealed that the hybrid Ag_{44}@Te NWs formed a woven-fabric-like structure, where the NWs were arranged in parallel fashion in the same layer but, in the adjacent layer, they were organized with an unusual angle of 81^o between them. The Ag_{44} NCs were attached onto the Te NWs' surface by Te−O interactions. Computational study demonstrated that the organization of the Te NWs between two adjacent layers with an angle of 81^o assisted the formation of the strongest H-bonding because of the three pairs (L_3) of H-bonding between the neighboring Ag_{44} NCs layered over Te NWs (Figure 7D and E). To support these data, another NC $[Au_{102}(SR)_{44}]$ was also used in the study. In this case, a similar structure was noticed, but the angle between the two adjacent layers was 77°. Such a difference in angles (81° and 77°) was due to the difference in orientation of the ligands on the two NMNC surfaces.

Recently, Chakraborty et al. explored the supramolecular assembly of $[Ag_{44}(SR)_{30}]$ with gold nanorods (GNRs) through H-bonding interactions.[65] They employed p-MBA ligands to functionalize Au GNRs at neutral pH. Then, the functionalized GNRs were utilized for the assembly of $[Ag_{44}(SR)_{30}]$ in DMF for 20 h. H-bonds were generated between the carboxyl groups of nearby *p*-MBA ligands for both the GNRs and Ag_{44} NCs during this process. This resulted in a multilayer shell that encapsulated the individual GNRs. As a result, the GNRs transformed into cagelike nanostructures. The morphology of the composite nanostructures formed was octahedral.[65] Similarly, the p-MBA-functionalized Au nanorods were used for reactions with NMNCs such as $[Au_{102}(SR)_{44}]$[13] and $[Au_{250}(SR)_n]$[42] in a parallel way to generalize the process. But here less dense encapsulation of GNRs was noticed. It was suggested that some of these *p*-MBA-stabilized Au NCs would be deprotonated (i.e., S-PhCOONa) in the formation of the assembly. As a result, a few of the *p*-MBA ligands of these two NMNCs do not take part in the formation of H-bonds.

In yet another study, Bose et al. reported the reaction between a NMNC, $[Au_{25}(SR)_{18}]$ (SR = 2-phenylethanethiol), and polydispersed silver NPs (~4 nm) capped with the same ligand.[66] The reaction produced alloyed NPs under ambient conditions. HRTEM study revealed that such type of reaction gave rise to highly monodisperse superlattices of 2D Au−Ag alloy NPs. Such reactions are highly dependent upon the nature of the capping ligands since reaction did not proceed when 4-(*tert*-butyl)benzyl mercaptan was used as a protecting ligand for the Au NCs.

Supracolloidal self-assembly of NMNCs, especially $[Au_{102}(p\text{-MBA})_{44}]$ under aqueous conditions, was studied by Nonappa and co-workers.[67,68] Monodisperse gold NCs were preferred for the formation of template-free 2D nanosheets and closed spherical capsids. Such supracolloidal self-assembly of $[Au_{102}(p\text{-MBA})_{44}]$ was obtained due to the presence of the spontaneous and inherent arrangement of the H-bonding interactions of *p*-MBA ligands. Dialysis of $[Au_{102}(p\text{-MBA})_{44}]$ (SR = S-PhCOOH or S-PhCOONa) from soluble water to insoluble methanol led to the formation of spontaneous self-assembly of such NMNCs into monolayer 2D sheets. The slow dialysis offered enough time for the NMNCs to assemble in the hexagonal close-packed structure as the geometry facilitates the formation of the maximum number of H-bonds. However, the rapid injection of dispersed partially deprotonated (in water) $[Au_{102}(p\text{-MBA})_{44}]$ into methanol resulted in spherical superstructures of an average diameter of 200 nm. The tomographic reconstruction data revealed that these superstructures were hollow. These hollow spherical superstructures were formed based on shape-defined NMNC subunits. These spherical superstructures were named “colloidal capsids” (see Figure 1 and section 4). The fusion of two capsids was also observed. The H-bonding interactions between two adjacent capsids could result in the fusion of two capsids. Ellipsoidal capsids were also formed either due to the rearrangement of defects upon assembly or fusion of two capsids. However, the forming mechanisms and how the ellipsoidal capsid shells can be tuned are currently unknown.

5. SC OF NMNCS WITH OTHER MOLECULES

SC of NMNCs with other molecules such as fullerenes, cyclodextrins, cucurbiturils, crown ether, etc. is composed of special structural compatibility and host−guest interactions. In this section, we discuss such interactions one by one.

5.1. SC of NMNCs with Fullerenes

Fullerenes are considered one of the important classes of molecules to explore SC because of their size, shape, rich π-electron cloud, and electron-accepting properties. Recently, Chakraborty et al. described the supramolecular functionalization of silver NMNCs with fullerenes.[69] Reaction between $[Ag_{29}(S_2R)_{12}]^{3-}$ with C_{60} at room temperature resulted in the generation of $[Ag_{29}(S_2R)_{12}(C_{60})_n]^{3-}$ (n = 1−9). $[Ag_{29}(S_2R)_{12}]^{3-}$ and four equivalents of C_{60} gave rise to

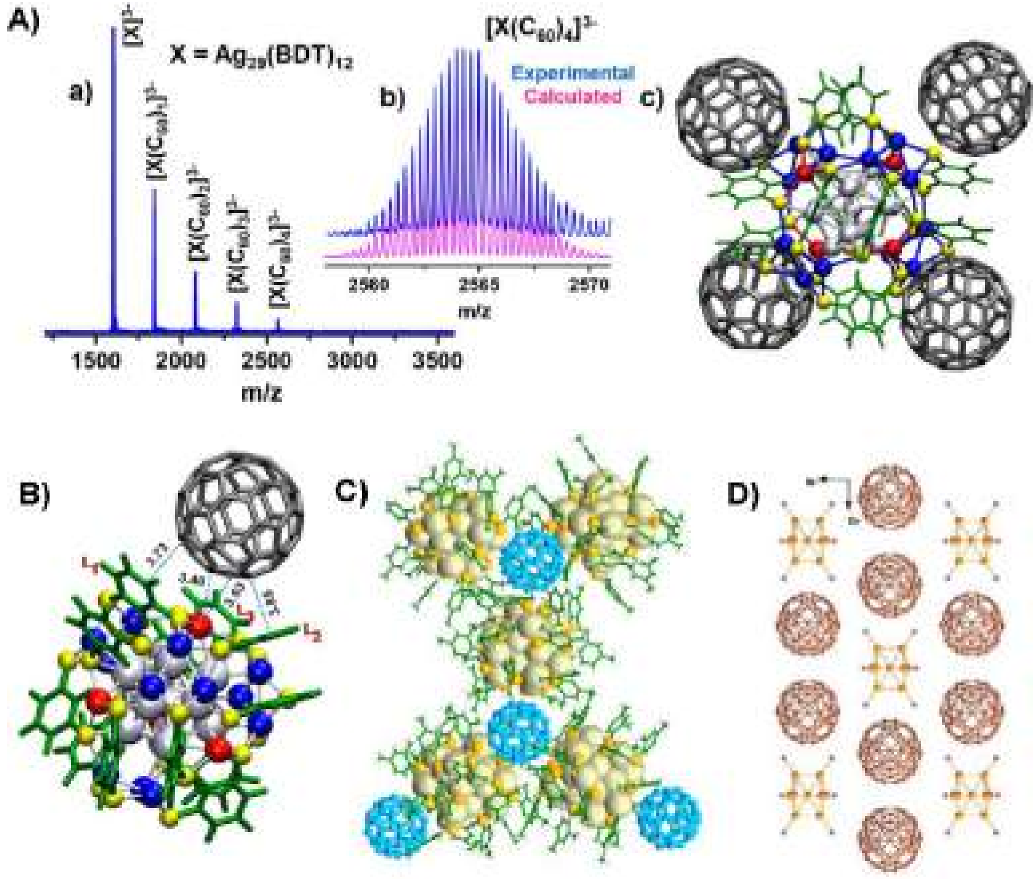

Figure 8. (A) (a) ESI-MS of $[Ag_{29}(S_2R)_{12}(C_{60})_n]^{3-}$ (n = 1−4) adducts. (b) Theoretical and experimental isotopic patterns of $[Ag_{29}(S_2R)_{12}(C_{60})_1]^{3-}$. (c) DFT optimized structure of $[Ag_{29}(S_2R)_{12}(C_{60})_4]^{3-}$. (B) Strong noncovalent interactions between the NMNC and C_{60}. (Reproduced from ref 69. Copyright 2018 American Chemical Society.) (C) Fullerene (C_{60}) induced aggregation of $[Ag_{25}(SR)_{18}]^-$. (Adopted from the ref 70. Copyright 2020 American Chemical Society.) (D) Assembly of $[Au_8(TPP)_8(C_{60})_2]$ along the (001) plane. (Reproduced from the ref 71. Copyright 2008 Wiley.)

$[Ag_{29}(S_2R)_{12}(C_{60})_n]^{3-}$ (n = 1−4) complexes, which were detected by ESI-MS (Figure 8A). The ligand surfaces of the NMNC are organized in such a fashion to form a cavity, allowing the π-electrons of the surface of fullerenes to interact. Such host−guest complexations were enabled by this structural compatibility (Figure 8B). The structures of $[Ag_{29}(S_2R)_{12}(C_{60})_n]^{3-}$ (n = 1−4) adducts were predicted using molecular docking and DFT calculation. The non-covalent interactions such as $\pi\cdots$H−C, $\pi\cdots\pi$, and vdWs interactions between the aromatic rings of S_2R of the NC and the aromatic surface of the fullerene were the main reason for the formation of such assemblies. Similar results were obtained when C_{70} was used in place of C_{60}. Similarly, fullerene (C_{60} and C_{70}) based aggregation of $[M_{25}(SR)_{18}]^-$ NCs (-SR= thiolate ligand, M = Ag or Au) was also studied using ESI-MS.[70] The nature of the complexation witnessed in the case of $[Ag_{29}(S_2R)_{12}]^{3-}$ was different compared to fullerene adducts of $[M_{25}(SR)_{18}]^-$. Multiple fullerenes interacted on the ligand surface of a single NMNC, in the case of $[Ag_{29}(S_2R)_{12}]^{3-}$. But multiple NMNCs interacted on the surface of a fullerene in the case of $[M_{25}(SR)_{18}]^-$ (Figure 8C).

In another study, Schulz-Dobrick et al. reported the crystal structure of fullerides with Au NCs in 2008.[71] Single crystals were obtained via the layering method where slow interdiffusion of $[(Au_8(TPP)_8)(NO_3)_2]$ in acetonitrile and KC_{60} in THF resulted in black crystals containing AuNCs and fullerides (Figure 8D). By this method, two different complexes, $[(Au_7(TPP)_7)C_{60}\cdot THF]$ and $[(Au_8(TPP)_8)(C_{60})_2]$, were obtained. Electrostatic attraction between fullerides and positively charged NMNCs and intermolecular interactions resulted in such intercluster building blocks. This kind of intercluster building block could bring in highly exciting properties such as electronic transport.

5.2. SC of NMNCs with Cyclodextrins

Cyclodextrin (CD) is a family of cyclic oligosaccharides containing a macrocyclic ring of glucose subunits (GS) connected by α-1,4 glycosidic bonds. The three most studied CDs are α-CD (connected by six GS), β-CD (connected by seven GS), and γ-CD (connected by eight GS). CD has a hydrophilic external surface and an inherent hydrophobic internal cavity. Due to these properties, it is known to produce supramolecular host−guest complexes.[72] In this section, we will mainly focus on the SC of CDs with NMNCs.

The supramolecular interaction between $[Au_{25}(SBB)_{18}]$ (SBB = 4-(*tert*-butyl)benzyl mercaptan) and β-CDs was investigated by Pradeep and co-workers.[72] There were a maximum of four CDs on a single NC surface which were established by ESI-MS. Formation of such adducts is shown in Figure 9A. The supramolecular adducts, $[Au_{25}(SBB)_{18}\cap\beta\text{-}CD_n]$ (n = 1−4), are presented in Figure 9B. DFT calculations suggested that host−guest interactions were favored through the finer rim of the CDs which was further recognized by

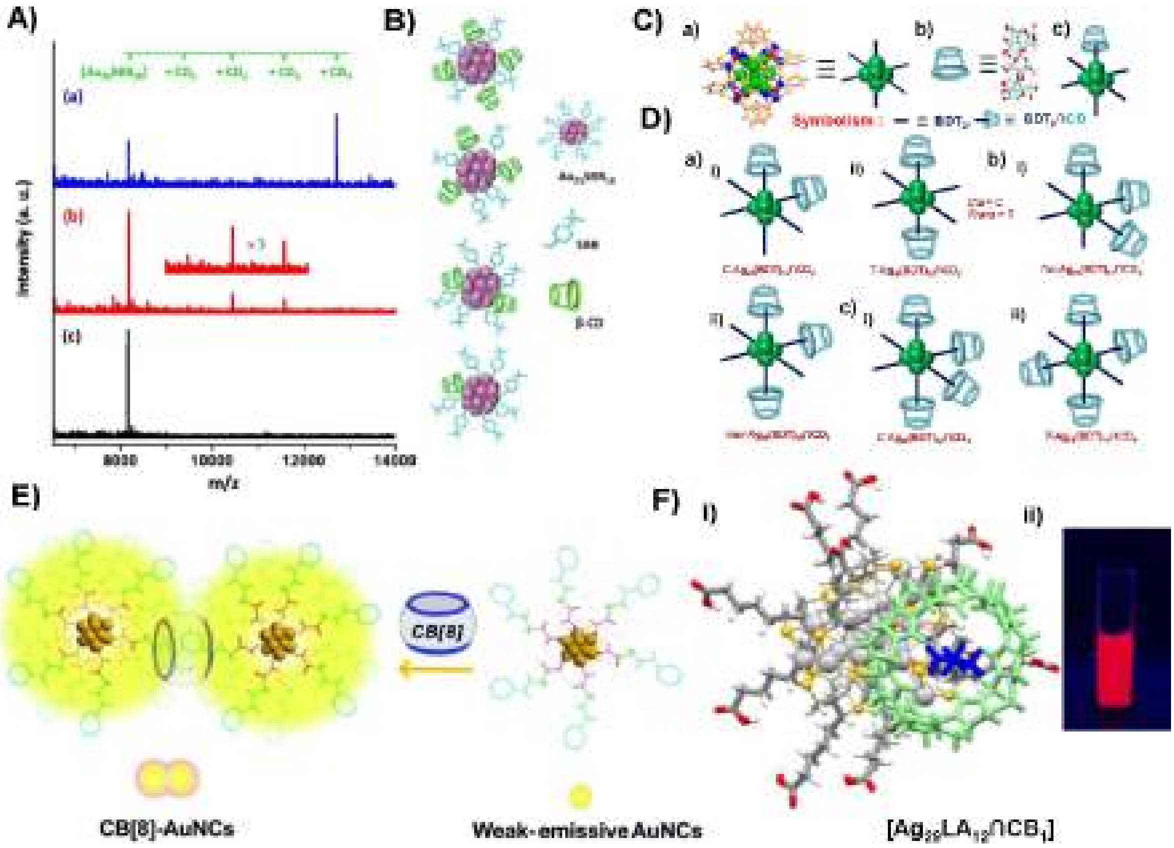

Figure 9. (A) ESI-MS of the $[Au_{25}SBB_{18}\cap CD_n]$ (n = 1−4) adducts. (B) Schematic presentation of the $[Au_{25}(SBB)_{18}\cap(\beta\text{-CD})_n]$ (n = 1−4) adducts. (Adopted from ref 72. Copyright 2014 American Chemical Society.) (C) Schematic presentation of (a) $[Ag_{29}(S_2R)_{12}]$ where S_2R is BDT and (b) β-CDs. (D) Simple presentation of the isomers of $[Ag_{29}(S_2R)_{12}\cap(CD)_n]$ (n = 2 to 3). (Reproduced from ref 81. Copyright 2018 American Chemical Society). (E) Supramolecular interactions of CB[8] with AuNCs resulted in enhancement in luminescence. (Adopted from ref 82. Copyright 2020 Royal Society of Chemistry.) (F) (i) DFT optimized structure of $[Ag_{29}(LA)_{12}CB[7]_1]$. (ii) Highly luminescent $[Ag_{29}(LA)_{12}CB[7]]$ complexes in water. (Reproduced from ref 85. Copyright 2020 American Chemical Society.)

optimizing the structure of HSBB∩β-CD in DFT. The DFT optimized structure of $[Au_{25}(SBB)_{18}\cap(\beta\text{-CD})_4]$ revealed that the four β-CDs were attached with tetrahedral symmetry on the NMNC surface, reducing the steric hindrance among β-CDs. vdWs interactions between the SBB ligands and the β-CD were the main reason for the formation of such a complex. The noncovalent interactions between SBB and β-CD gave rise to an improvement of the luminescence and stability of the NMNC.

Similarly, Li and co-workers investigated the surface modification of $[Au_{38}S_2(SR)_{20}]$ (SR/Adm = 1-adamantanethiolate) with α-, β-, and γ-CDs using MS and UV−vis techniques.[73] Among all the CDs, only β-CDs were selectively chemisorbed onto the NMNC surface to form $[Au_{38}S_2(Adm)_{20}\cap(\beta\text{-CD})_1]$ and $[Au_{38}S_2(Adm)_{20}\cap(\beta\text{-CD})_2]$ complexes. The structures of these complexes were deciphered using molecular dynamics simulations where two β-CDs were attached at the two corners of the Au_{38} NC, reducing their mutual steric hindrance. The functionalization of β-CDs onto the NC surface resulted in stability. Similarly, Bhunia et al. also studied the supramolecular interactions of Au NCs capped by glutathione with α-, β-, and γ-CDs.[74]

Isomerism in NMNCs is a highly interesting research theme.[75−80] In this context, supramolecular complexes, $[Ag_{29}(S_2R)_{12}\cap(CD)_n]$ (n = 1 to 6), were synthesized through the reaction between the as-prepared $[Ag_{29}(S_2R)_{12}]$ and α-, β-, and γ-CDs in DMF.[81] ESI-MS and NMR study confirmed the formation of supramolecular adducts. Molecular docking study and DFT calculations were carried out to obtain the lowest energy structures of $[Ag_{29}(S_2R)_{12}\cap(CD)_n]$ (n = 1 to 6) complexes which showed that a pair of S_2R ligands were encapsulated by CD. The $\pi\cdots$H−C, hydrogen bonding, weak ionic Ag⋯O, and vdWs interactions play a crucial role to form such supramolecular adducts. More significantly, the geometries of these supramolecular complexes resembled the octahedral complexes of transition metals, giving rise to different isomers. A simple representation of the isomers is presented in Figure 9C and D. Such kind of isomers were separated using IM MS.[81]

5.3. SC of NMNCs with Cucurbiturils

Cucurbiturils are supramolecular macrocyclic molecules consisting of glycoluril ($=C_4H_2N_4O_2=$) monomers connected by methylene bridges ($-CH_2-$). The crystal structures of cucurbiturils revealed that the O atoms are situated along the edges and tilted inward, creating a partly enclosed cavity. The name of this molecule is derived from its resemblance with a pumpkin of the Cucurbitaceae family. Cucurbiturils are generally written as cucurbit[n]uril, where n is the number of glycoluril ($=C_4H_2N_4O_2=$) units. Two simple abbreviations are CB[n] and CB$_n$. These compounds are suitable hosts for an array of neutral and cationic species through hydrophobic interactions and cation−dipole interactions, respectively. Here, we discuss mainly the supramolecular complexes of CBs with NMNCs.

Recently, Jiang et al. developed a method to reversibly brighten and enhance the emission of a gold NC, $[Au_{22}(FGGC)_{18}]$ (N-terminal Phe-Gly-Gly-Cys peptide = FGGC), using supramolecular complexation between FGGC peptides and CB[n] (n = 7, 8) in water (Figure 9E).[82] This is the first report of supramolecular complexation of a NMNC with CBs. The approach of supramolecular complexation effectively enhanced the emission of AuNCs by rigidifying the ligand surface of an NMNC. As a result, an effective restriction of the nonradiative transition and elevation of the radiative transition occurred which was confirmed using an ultrafast spectroscopy study. The supramolecular interaction between the NMNCs and CBs resulted in a high QY of 51% for CB[7] and 39% for CB[8] in water at room temperature, respectively.

In another study, Pradeep and co-workers investigated the formation of supramolecular host–guest complexation of $[Ag_{29}(LA)_{12}]$[83,84] (LA = α-lipoic acid) with CB[7] in an aqueous medium at room temperature (Figure 9F).[85] Molecular docking study and DFT calculations were used to support the experimental results. This study demonstrated the encapsulation of LA ligands by CB[7]. Here also, inclusion complexation leads to improved luminescence of about 1.25 times compared to the parent NMNC.

5.4. SC of NMNCs with Crown Ethers

Crown ethers are heterocyclic compounds containing several ether groups. They were highly used to form supramolecular host–guest complexes. The hydrophilic cavity created by ether oxygen atoms is highly efficient to capture alkali and alkaline earth metal ions. The cavity size is highly specific for a specific metal ion. For example, 18-crown-6, 15-crown-5, and 12-crown-4 have a high affinity for potassium cation, sodium cation, and lithium cation, respectively. The hydrophilic cavity is surrounded by the hydrophobic ethylenic groups. Crown ethers are well-known for the ion transport mechanism and phase-transfer catalysis. They are used as building blocks for supramolecular architectures.

Pradeep and co-workers reported the first crystal structure of a supramolecular assembly of a silver NC, $[Ag_{29}(S_2R)_{12}(TPP)_4]^{3-}$ (Ag_{29}), with dibenzo-18-crown-6 ($DB_{18}C_6$) using SCXRD (Figure 10A).[86] The crystallization induced self-arrangement of $DB_{18}C_6$ molecules produced a hexamer cagelike structure in the interstitial spaces of the crystal lattice of trigonal Ag_{29} (Ag_{29}T) NCs. Such insertion of hexameric cages in the crystal lattice gave rise to an anisotropic expansion of the Ag_{29}T lattice along its z-axis. The presence of intermolecular $\pi\cdots$H–C interactions between $DB_{18}C_6Na^+$ and the TPP and S_2R ligands of the NC and electrostatic interaction between 3 $DB_{18}C_6Na^+$ and the negatively charged Ag_{29} NC was the main reason for such self-organized assemblies (Figure 10B). The distance between the sodium ions is also provided in Figure 10C. This structure resembles a new family of "lattice inclusion" complexes in NMNCs. Assembly of NMNCs with $DB_{18}C_6Na^+$ is presented in Figure 10D. Such supramolecular interactions resulted in ~3.5 times improvement in luminescence compared to the parent crystals, Ag_{29}T. Such kind of study delivers an approach for building new NC-assembled hybrid materials with enhanced properties.

5.5. Other Supramolecular Interactions of NMNCs

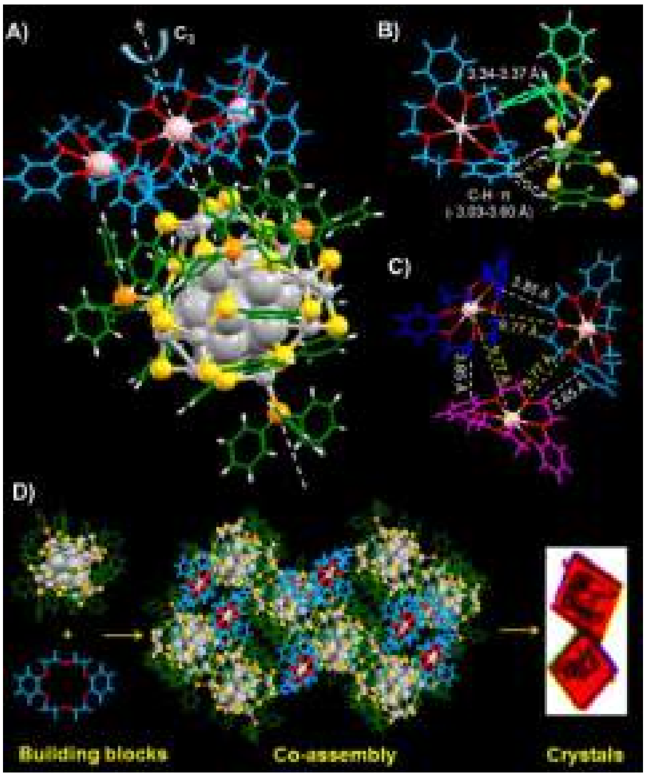

Figure 10. (A) Crystal structure of $[Ag_{29}(S_2R)_{12}(TPP)_4]^{3-}$ with dibenzo-18-crown-6. (B) Supramolecular interaction between one of the $DB_{18}C_6Na^+$ and S_2R and TPP of the NMNC. (C) Zoomed in view of the three $DB_{18}C_6Na^+$ molecules connected to the NMNC. Color codes: Ag, gray; S, yellow; P, orange; O, red; C of TPP and S_2R, green; H of TPP and S_2R, white; H and C of $DB_{18}C_6$, light blue; Na, pink. Color codes in part C: C and H of the three $DB_{18}C_6Na^+$ molecules, light blue, dark blue, and purple, respectively. (D) Formation of coassembly of $[Ag_{29}(S_2R)_{12}(TPP)_4]^{3-}$ with dibenzo-18-crown-6 via supramolecular interactions. (Adopted from ref 86. Copyright 2019 American Chemical Society.)

Muhammed and co-workers recently functionalized AgNCs with a pillar[5]arene based host ligand (P_5) $[Ag_{29}(LA-P_5)_{12}(TPP)_2]$ (LA- Lipoic acid).[87] The AgNCs were synthesized in two different ways: (i) via direct synthesis using silver nitrate salt ($AgNO_3$), LA-P_5, and TPP and (ii) via the reaction between $[Ag_{18}H_{16}(TPP)_{10}]_2^+$ (ref 88) and LA-P_5 (Figure 11A). The pillar[5]arene based NMNCs $[Ag_{29}(LA-P_5)_{12}(TPP)_2]$ showed a reversible host–guest interaction with neutral alkylamines and cationic quaternary ammonium guests (Figure 11B). This supramolecular interaction resulted in the formation of spherical assemblies with a dramatic enhancement of luminescence by ~2000-fold. This is the highest luminescence enhancement data reported in the literature to date for NMNCs.

In another study, Mohammed and co-workers explored the charge-transfer dynamics between the positively charged 5,10,15,20-tetra(1-methyl-4-pyridino)-porphyrin tetra(p-toluene sulfonate) (TMPyP) and negatively charged undoped and Au-doped Ag_{29} NMNCs.[89] Transient absorption (TA) spectroscopic study revealed that the interfacial charge transfer, the triplet state lifetime, and the intersystem crossing of porphyrin can be altered by the doping of gold in Ag_{29} NCs. Moreover, the electrostatic interaction between the negatively charged NMNCs and the positively charged TMPyP played a key role in the complex formation and subsequently facilitated the transfer process.

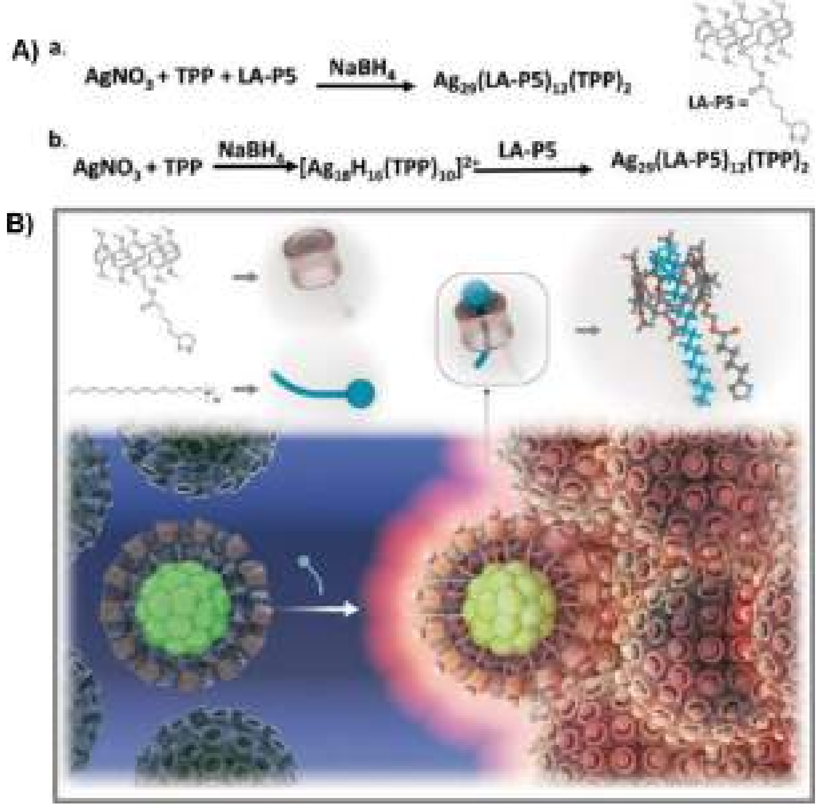

Figure 11. (A) Synthesis of $[Ag_{29}(LA\text{-}P_5)_{12}(TPP)_2]$ via two methods: (i) direct synthesis and (ii) ligand exchange. (B) Schematic representation of host−guest interaction between $[Ag_{29}(LA\text{-}P_5)_{12}(TPP)_2]$ and CTAB leading to self-assembly and luminescence enhancement. (Reproduced from ref 87. Copyright 2019 Wiley.)

6. PROPERTIES OF SUPRAMOLECULAR ASSEMBLIES OF NMNCS

Supramolecular complexes generally should have the following basic properties:

(1) Structural complementarity: The geometric structure and electronic properties of the host and guest are mutually complementing. Complementarity permits the host to accomplish a selective binding of the guest of a specific structure only. This phenomenon is termed as "molecular recognition" in supramolecular chemistry.

(2) Supramolecular complexes have a high structural orientation because of the presence of a large number of noncovalent interactions.

(3) The supramolecular interactions could result in self-assembled structures. In this process, small molecular species spontaneously interact together and result in much larger and complex assemblies. As a result, the entropy of the system reduces, or $\Delta S < 0$. However, the process is spontaneous, so the Gibbs energy is negative: $\Delta G = \Delta H - T\Delta S < 0$. This must be true if $\Delta H < 0$ and $|\Delta H| > |T\Delta S|$. So, self-assembly is accompanied by the release of large amounts of heat.

Apart from all these basic properties, many other properties are also evidenced for the supramolecular complexes of NMNCs which are discussed below.

6.1. Mechanical

The mechanical properties of NMNC-assembled solids generated from the supramolecular self-assembly are beginning to be explored. Pradeep and co-workers explored the mechanical properties of single crystals of NMNCs such as Ag_{29} polymorphs (Ag_{29} C and Ag_{29} T, respectively), monothiol-protected Ag_{46}, and its cocrystal with Ag_{40} crystallizing in trigonal and monoclinic lattices (Ag_{46} T and $Ag_{40/46}$ M), respectively (Figure 12A).[90] The acquired Young's modulus (Er) values of the NC-assembled solids were comparable to those of zeolitic imidazolate frameworks (ZIFs). The data exhibited the following trend: Ag_{29} T > Ag_{29} C > $Ag_{40}/_{46}$ M > Ag_{46} T. The viscoelastic properties of all of the four NC-assembled solids were evaluated, and the value of the tan δ/damping factor of Ag_{46} T was higher than those of other systems. The study concluded that the supramolecular interactions of the NMNCs' surfaces playing a key to influencing the mechanical properties.

6.2. Luminescence

Supramolecular complexation of NMNCs could result in enhancement of luminescence. Enhancement of luminescence was evidenced for CBs, CDs, and crown ethers when they formed supramolecular adducts with NMNCs.[85,86] Due to the presence of strong noncovalent interactions between the host and guest, the whole system becomes highly rigid. As a result, the whole system experienced a high luminescence. Similar luminescence enhancement was observed for Ag_{29} C compared to Ag_{29} T.[53]

6.3. Charge Transfer

There could be charge transfer between the guest and host if they differ in their electronic properties. This phenomenon was evidenced in the case of $[Ag_{29}(S_2R)_{12}(C_{60})_n]^{3-}$, where NMNC has three negative charge states.[69] Collision induced dissociation (CID) study revealed that the NMNC transferred

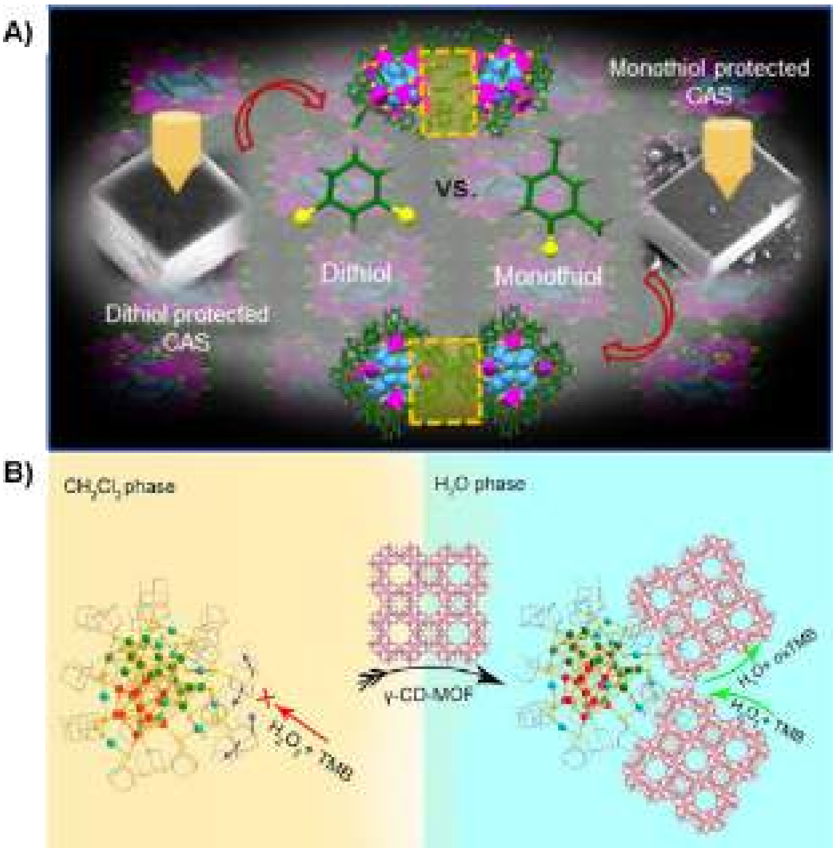

Figure 12. (A) Study of the mechanical properties of single crystals of NMNCs such as dithiol-protected Ag_{29} polymorphs (C and T), monothiol-protected Ag_{46}, and its cocrystal with Ag_{40}. (Reproduced from ref 90. Copyright 2020 American Chemical Society.) (B) γ-CD-MOF induced water solubility of $[Au_{40}(S\text{-}Adm)_{22}]$ NMNCs. This water-soluble hybrid component activated gold NCs for the horseradish peroxidase (HRP)-mimicking catalysis. (Adopted from ref 98. Copyright 2020 American Chemical Society.)

an electron to C_{60}. Similarly, the reducing NC $[Ni_9Te_6(PEt_3)_8]$ is known to form a charge-transfer complex with the fullerene.[91] Microcrystals of $Au_{32}({}^{n}Bu_3P)_{12}Cl_8$ NCs containing highly ordered self-assembly ($\sigma = 1.56 \times 10^{-4}$ S/m) exhibited enhanced charge carrier transport by 2 orders of magnitude compared to polycrystalline thin films ($\sigma \approx 1 \times 10^{-6}$ S/m).[92]

6.4. Magnetic

The magnetic property of the NC is a very recent emerging field. Supramolecular complexes of NCs could result in an enhancement in the magnetic property. Binary assemblies of fullerenes with $[Ni_9Te_6(PEt_3)_8]$ transition metal NCs experienced magnetic properties at low temperatures.[91]

7. APPLICATIONS OF SUPRAMOLECULAR ASSEMBLIES OF NMNCS

Various applications of supramolecular complexes of NMNCs are pointed out in the following:

7.1. Sensing

Sensing is one of the fundamental applications of NMNCs. Supramolecular complexes of $[Ag_{29}LA_{12}]$ with CDs displayed red luminescence. In recent studies, Nag et al. have developed a method to sense dopamine at a concentration as low as 10 nM using $[Ag_{29}LA_{12}@CD_n]$ (n = 1−3).[85] Supramolecular complexes of $[Ag_{29}LA_{12}]$ with CDs are highly red luminescent. The dopamine molecules were encapsulated by the vacant cavity of CD, which resulted in quenching of the luminescence. Recently, the rapid and cyclic detection of explosives such as nitrobenzene (NB) was performed using a hybrid polymer membrane generated from $[Ag_{12}(StBu)_6(CF_3COO)_6(NH_2\text{-}bpz)_3]_n$-MOF $[NH_2\text{-}Ag_{12}bpz]$.[93] The chiral recognition of D- and L-Trp (Trp = tryptophan) was reported using the assembled enantiomeric $[Au_{14}(MPA)_6(D/L\text{-}Trp)_4]$ NMNCs generated by Zn^{2+} coordination (MPA = 3-mercaptopropionic acid).[94]

7.2. Cell Imaging

Live cell imaging is one of the fascinating applications of supramolecular complexes of NMNCs. Recently, supramolecular complexes of $[Au_{22}(FGGC)_{18}]$ with CB[7] exhibited exceptional imaging of cancer A549 cells.[82] Also, cancer cell imaging, targeted delivery, and photothermal/photodynamic therapies were reported using $[Pt_1Ag_{28}]$ NC assembly.[95] Further, a folic acid based $[Au_{22}(SG)_{18}]$ NMNC assembly has been utilized to study the cancer cells.[96]

7.3. Photocatalytic Activity

Xie and co-workers introduced a hybrid material, consisting of per-6-thio-β-cyclodextrin (SH-β-CD) capped gold NCs and TiO_2 NPs.[97] This hybrid material displayed improved photocatalytic performance over TiO_2 NPs. The hybrid material exhibited enhanced effects on photocatalytic decomposition of organic pollutants via host−guest complexation. This hybrid TiO_2 system had better efficiency (∼98%) compared to only TiO_2 NPs (∼47%).

7.4. Catalytic Activity

Zhao et al. recently generated a hybrid material using adamantanethiolate-protected [$Au_{40}(S\text{-}Adm)_{22}$] NMNCs and γ-CD-MOF.[98] This hybrid material exhibited excellent water solubility and catalytic activity which is different from the parent [$Au_{40}(S\text{-}Adm)_{22}$] NMNCs (Figure 12B). This water-soluble hybrid component activated gold NCs for the horseradish peroxidase (HRP)-mimicking catalysis.

7.5. Other Applications

Cluster-assembled solids have been utilized to generate multicolor light-emitting diodes (LEDs), where NMNCs' assembly acts as a color conversion layer. Wu et al. effectively established the construction of LEDs using an assembly of [$Cu_{14}(DT)_{10}$] (DT-1-dodecanethiol).[99] Fabrication of a WLED (white light-emitting diode) using a Zn-coordinated NMNCs' assembly [Zn-Au@SG] was reported (SG = glutathiolate).[100]

8. CONCLUSIONS AND FUTURE PERSPECTIVES

This Review highlights the various supramolecular assemblies of NMNCs in gaseous, solution, and solid states. Intercluster reaction, dimerization, cation induced dimerization, and ligand−NC interactions were discussed in the context of supramolecular interactions of NMNCs in gaseous and solution phases. In the solid state, interactions, chirality, and symmetry were studied in crystal lattices. These were mostly studied by SCXRD and electron microscopy. This work also presented the SC of NMNCs with molecules such as (i) fullerenes, (ii) CDs, (iii) CBs, and (iv) crown ethers. Structural compatibility between the NMNCs and such molecules favors host−guest complexes.

There are many challenges in this field. In the initial stages of NMNC research, understanding the core, ligands, and total structures of clusters themselves was of interest to the community rather than the understanding of NMNC−NMNC interactions. It is natural that science in this area evolved this way. Nowadays, the community is interested in exploring NMNC assemblies of such large molecules in greater detail within their crystal lattices. However, the nature of supramolecular interactions in NMNC crystals is difficult to be understood at the same level of precision as in the case of organic molecules as most structures are solved by excluding counterions and solvents. In many cases, solvent molecules are not present in the solved crystal structures. Even finding a counterion is very difficult.[18] They are often observed in other studies such as infrared spectroscopy or mass spectrometry. Although such supramolecular interactions in crystal structures are not studied in greater detail, in $Ag_{44}(MBA)_{30}$, for example, such interactions between ligands have been shown to be the fundamental reason for crystal assembly.[20] Generally, the resolution of such molecular crystals is lower than that of small organic and inorganic molecules.[13,54] It is clear that the dynamic nature of NMNCs makes it difficult to form stable directional assemblies in most of them. Besides, each NMNC is stable only in a few specific solvents. Thus, exploring crystallization under common conditions cannot be attempted for all NMNCs.

Supramolecular interactions of NMNCs are largely about the interactions of ligands. One can find supramolecular interactions in all condensed phases. However, in the case of NMNCs, new properties such as luminescence enhancement, mechanical properties, electrical conductivity, etc. may arise due to such supramolecular assemblies. With the help of such supramolecular assemblies one can develop new hybrid nanomaterials allowing noncovalent interactions. It is a highly interdisciplinary research area. Much emphasis on the crystal structures was given in many studies to understand the systems properly. Such assemblies lead to highly complex structures, and some of the structures are comparable to α-helices and β-sheets of proteins.[47]

Noble metals such as silver and gold are highly expensive. However, some of the luminescent NMNCs are biocompatible and are used for cell imaging.[1,2] Some of them are well-known for catalysis.[1,2] Recently, there is interest in synthesizing copper NCs which may turn out to be cheaper.

Despite these limitations, there are many possibilities for future work:

(i) Intercluster assembly could induce new properties such as mechanical, optical, and magnetic properties as well as gas sensing and storage.

(ii) CD, CB, and porphyrins based NMNC-assembled solids can be potential candidates for gas storage and sensing. NC based host−guest interactions are still a growing research area compared to intracluster growth and intercluster assembly. Noncovalent interactions between hosts and guests could alter the electronic and geometric structures and properties of individual NMNCs. Till now only very few examples have been reported. Supramolecular interactions could result in the enhancement of luminescence.

(iii) Although some of the supramolecular complexes were characterized as a mixture of adducts in the solution and gas phases, isolation of these complexes in the solid state can give rise to a new class of NMNC-assembled solids. Moreover, separation of the isomers of these supramolecular complexes due to the different binding modes of NMNCs is challenging. Such isomerism could result in various novel properties such as chirality, self-assembly, etc.

(iv) There are large possibilities to extend these supramolecular complexes to NMNC-assembled metal−organic frameworks and polyoxometalates.[101] Such kind of supramolecular complexes may give rise to new examples of magnetic and conductive luminescent materials.

(v) Supramolecular complexes of NMNCs with CDs and CBs could be utilized as drug delivery agents and for bioimaging.

(vi) Studies such as dynamic light scattering, small angle X-ray scattering, small angle neutron scattering, etc. could be used to analyze the supramolecular complexes of NMNCs in the immediate future.

(vii) Roy et al. demonstrated a binary assembly of fullerenes with transition metal NCs.[91,102,103] Similar kinds of studies can be performed for other atomically precise NC systems such as metal oxides, polyoxometalates, metal peroxides, boron oxides, and boron clusters, which are also atomically precise.

(viii) CDs, CBs, and fullerenes can be used as linkers between NCs and other atomically precise NC systems such as metal oxides, polyoxometalates, metal peroxides, boron oxides, and boron clusters. This could result in hybrid nanomaterials with enhanced properties.

It is clear that these and other related aspects will enrich the area in the years to come.

AUTHOR INFORMATION

Corresponding Author

Thalappil Pradeep − *DST Unit of Nanoscience (DST UNS) and Thematic Unit of Excellence, Department of Chemistry, Indian Institute of Technology Madras, Chennai 600036, India;* orcid.org/0000-0003-3174-534X;
Email: pradeep@iitm.ac.in; Fax: +91-44 2257-0545

Author

Abhijit Nag − *DST Unit of Nanoscience (DST UNS) and Thematic Unit of Excellence, Department of Chemistry, Indian Institute of Technology Madras, Chennai 600036, India;* Present Address: A.N.: University of Edinburgh, Joseph Black Building, David Brewster Road, Edinburgh EH93FJ, Scotland

Complete contact information is available at:
https://pubs.acs.org/10.1021/acsnanoscienceau.1c00046

Notes

The authors declare no competing financial interest.

ACKNOWLEDGMENTS

We thank the Department of Science and Technology, Government of India for constantly supporting our research program on nanomaterials. A.N. thanks IIT Madras for a Postdoctoral fellowship. T.P. acknowledges support from the Centre of Excellence on Molecular Materials and Functions under the Institution of Eminence scheme of IIT Madras.

REFERENCES

(1) Chakraborty, I.; Pradeep, T. Atomically Precise Clusters of Noble Metals: Emerging Link between Atoms and Nanoparticles. *Chem. Rev.* **2017**, *117* (12), 8208−8271.

(2) Jin, R.; Zeng, C.; Zhou, M.; Chen, Y. Atomically Precise Colloidal Metal Nanoclusters and Nanoparticles: Fundamentals and Opportunities. *Chem. Rev.* **2016**, *116* (18), 10346−10413.

(3) Takano, S.; Ito, S.; Tsukuda, T. Efficient and Selective Conversion of Phosphine-Protected (MAu8)2+ (M = Pd, Pt) Superatoms to Thiolate-Protected (MAu12)6+ or Alkynyl-Protected (MAu12)4+ Superatoms via Hydride Doping. *J. Am. Chem. Soc.* **2019**, *141* (40), 15994−16002.

(4) Hirata, K.; Chakraborty, P.; Nag, A.; Takano, S.; Koyasu, K.; Pradeep, T.; Tsukuda, T. Interconversions of Structural Isomers of [PdAu8(PPh3)8]2+ and [Au9(PPh3)8]3+ Revealed by Ion Mobility Mass Spectrometry. *J. Phys. Chem. C* **2018**, *122* (40), 23123−23128.

(5) Ghosh, A.; Bodiuzzaman, M.; Nag, A.; Jash, M.; Baksi, A.; Pradeep, T. Sequential Dihydrogen Desorption from Hydride-Protected Atomically Precise Silver Clusters and the Formation of Naked Clusters in the Gas Phase. *ACS Nano* **2017**, *11* (11), 11145−11151.

(6) Ito, S.; Takano, S.; Tsukuda, T. Alkynyl-Protected Au22(C≡CR)18 Clusters Featuring New Interfacial Motifs and R-Dependent Photoluminescence. *J. Phys. Chem. Lett.* **2019**, *10* (21), 6892−6896.

(7) Guan, Z.-J.; Hu, F.; Li, J.-J.; Wen, Z.-R.; Lin, Y.-M.; Wang, Q.-M. Isomerization in Alkynyl-Protected Gold Nanoclusters. *J. Am. Chem. Soc.* **2020**, *142* (6), 2995−3001.

(8) Alhilaly, M. J.; Bootharaju, M. S.; Joshi, C. P.; Besong, T. M.; Emwas, A.-H.; Juarez-Mosqueda, R.; Kaappa, S.; Malola, S.; Adil, K.; Shkurenko, A.; Häkkinen, H.; Eddaoudi, M.; Bakr, O. M. [Ag67(SPhMe2)32(PPh3)8]3+: Synthesis, Total Structure, and Optical Properties of a Large Box-Shaped Silver Nanocluster. *J. Am. Chem. Soc.* **2016**, *138* (44), 14727−14732.

(9) Ghosh, A.; Ghosh, D.; Khatun, E.; Chakraborty, P.; Pradeep, T. Unusual reactivity of dithiol protected clusters in comparison to monothiol protected clusters: studies using Ag51(BDT)19(TPP)3 and Ag29(BDT)12(TPP)4. *Nanoscale* **2017**, *9* (3), 1068−1077.

(10) Bodiuzzaman, M.; Ghosh, A.; Sugi, K. S.; Nag, A.; Khatun, E.; Varghese, B.; Paramasivam, G.; Antharjanam, S.; Natarajan, G.; Pradeep, T. Camouflaging Structural Diversity: Co-crystallization of Two Different Nanoparticles Having Different Cores But the Same Shell. *Angew. Chem., Int. Ed.* **2019**, *58* (1), 189−194.

(11) Zhu, M.; Aikens, C. M.; Hollander, F. J.; Schatz, G. C.; Jin, R. Correlating the Crystal Structure of A Thiol-Protected Au25 Cluster and Optical Properties. *J. Am. Chem. Soc.* **2008**, *130* (18), 5883−5885.

(12) Heaven, M. W.; Dass, A.; White, P. S.; Holt, K. M.; Murray, R. W. Crystal Structure of the Gold Nanoparticle [N(C8H17)4][Au25(SCH2CH2Ph)18]. *J. Am. Chem. Soc.* **2008**, *130* (12), 3754−3755.

(13) Jadzinsky, P. D.; Calero, G.; Ackerson, C. J.; Bushnell, D. A.; Kornberg, R. D. Structure of a Thiol Monolayer-Protected Gold Nanoparticle at 1.1 Å Resolution. *Science* **2007**, *318* (5849), 430.

(14) Qian, H.; Jin, R. Controlling Nanoparticles with Atomic Precision: The Case of Au144(SCH2CH2Ph)60. *Nano Lett.* **2009**, *9* (12), 4083−4087.

(15) Fields-Zinna, C. A.; Sardar, R.; Beasley, C. A.; Murray, R. W. Electrospray Ionization Mass Spectrometry of Intrinsically Cationized Nanoparticles, [Au144/146(SC11H22N(CH2CH3)3+)x(S(CH2)5CH3)y]x+. *J. Am. Chem. Soc.* **2009**, *131* (44), 16266−16271.

(16) Zeng, C.; Chen, Y.; Liu, C.; Nobusada, K.; Rosi, N. L.; Jin, R. Gold tetrahedra coil up: Kekulé-like and double helical superstructures. *Sci. Adv.* **2015**, *1* (9), e1500425.

(17) Qian, H.; Eckenhoff, W. T.; Zhu, Y.; Pintauer, T.; Jin, R. Total Structure Determination of Thiolate-Protected Au38 Nanoparticles. *J. Am. Chem. Soc.* **2010**, *132* (24), 8280−8281.

(18) AbdulHalim, L. G.; Bootharaju, M. S.; Tang, Q.; Del Gobbo, S.; AbdulHalim, R. G.; Eddaoudi, M.; Jiang, D.-e.; Bakr, O. M. Ag29(BDT)12(TPP)4: A Tetravalent Nanocluster. *J. Am. Chem. Soc.* **2015**, *137* (37), 11970−11975.

(19) Joshi, C. P.; Bootharaju, M. S.; Alhilaly, M. J.; Bakr, O. M. [Ag25(SR)18]−: The "Golden" Silver Nanoparticle. *J. Am. Chem. Soc.* **2015**, *137* (36), 11578−11581.

(20) Yoon, B.; Luedtke, W. D.; Barnett, R. N.; Gao, J.; Desireddy, A.; Conn, B. E.; Bigioni, T.; Landman, U. Hydrogen-bonded structure and mechanical chiral response of a silver nanoparticle superlattice. *Nat. Mater.* **2014**, *13* (8), 807−811.

(21) Tofanelli, M. A.; Ni, T. W.; Phillips, B. D.; Ackerson, C. J. Crystal Structure of the PdAu24(SR)180 Superatom. *Inorg. Chem.* **2016**, *55* (3), 999−1001.

(22) Takano, S.; Tsukuda, T. Chemically Modified Gold/Silver Superatoms as Artificial Elements at Nanoscale: Design Principles and Synthesis Challenges. *J. Am. Chem. Soc.* **2021**, *143* (4), 1683−1698.

(23) Chakraborty, P.; Pradeep, T. The emerging interface of mass spectrometry with materials. *NPG Asia Mater.* **2019**, *11* (1), 48.

(24) Bodiuzzaman, M.; Dar, W. A.; Pradeep, T. Cocrystals of Atomically Precise Noble Metal Nanoclusters. *Small* **2021**, *17* (27), 2003981.

(25) Khatun, E.; Pradeep, T. New Routes for Multicomponent Atomically Precise Metal Nanoclusters. *ACS Omega* **2021**, *6* (1), 1−16.

(26) Krishnadas, K. R.; Sementa, L.; Medves, M.; Fortunelli, A.; Stener, M.; Fürstenberg, A.; Longhi, G.; Bürgi, T. Chiral Functionalization of an Atomically Precise Noble Metal Cluster: Insights into the Origin of Chirality and Photoluminescence. *ACS Nano* **2020**, *14* (8), 9687−9700.

(27) Zeng, Y.; Havenridge, S.; Gharib, M.; Baksi, A.; Weerawardene, K. L. D. M.; Ziefuß, A. R.; Strelow, C.; Rehbock, C.; Mews, A.; Barcikowski, S.; Kappes, M. M.; Parak, W. J.; Aikens, C. M.; Chakraborty, I. Impact of Ligands on Structural and Optical Properties of Ag29 Nanoclusters. *J. Am. Chem. Soc.* **2021**, *143* (25), 9405−9414.

(28) Chakraborty, P.; Nag, A.; Chakraborty, A.; Pradeep, T. Approaching Materials with Atomic Precision Using Supramolecular Cluster Assemblies. *Acc. Chem. Res.* **2019**, *52* (1), 2−11.

(29) Rival, J. V.; Mymoona, P.; Lakshmi, K. M.; Nonappa; Pradeep, T.; Shibu, E. S. Self-Assembly of Precision Noble Metal Nanoclusters: Hierarchical Structural Complexity, Colloidal Superstructures, and Applications. *Small* **2021**, *17* (27), 2005718.

(30) Bonacchi, S.; Antonello, S.; Dainese, T.; Maran, F. Atomically Precise Metal Nanoclusters: Novel Building Blocks for Hierarchical Structures. *Chem.—Eur. J.* **2021**, *27* (1), 30−38.

(31) Li, Y.; Zhou, M.; Song, Y.; Higaki, T.; Wang, H.; Jin, R. Double-helical assembly of heterodimeric nanoclusters into supercrystals. *Nature* **2021**, *594* (7863), 380−384.

(32) Krishnadas, K. R.; Baksi, A.; Ghosh, A.; Natarajan, G.; Som, A.; Pradeep, T. Interparticle Reactions: An Emerging Direction in Nanomaterials Chemistry. *Acc. Chem. Res.* **2017**, *50* (8), 1988−1996.

(33) Krishnadas, K. R.; Baksi, A.; Ghosh, A.; Natarajan, G.; Pradeep, T. Manifestation of Geometric and Electronic Shell Structures of Metal Clusters in Intercluster Reactions. *ACS Nano* **2017**, *11* (6), 6015−6023.

(34) Huang, B.; Pei, Y. On the mechanism of inter-cluster alloying reactions: two-stage metal exchange of [Au25(PET)18]− and [Ag25(DMBT)18]− clusters. *J. Mater. Chem. A* **2020**, *8* (20), 10242−10251.

(35) Chakraborty, P.; Nag, A.; Natarajan, G.; Bandyopadhyay, N.; Paramasivam, G.; Panwar, M. K.; Chakrabarti, J.; Pradeep, T. Rapid isotopic exchange in nanoparticles. *Sci. Adv.* **2019**, *5* (1), eaau7555.

(36) Neumaier, M.; Baksi, A.; Weis, P.; Schneider, E. K.; Chakraborty, P.; Hahn, H.; Pradeep, T.; Kappes, M. M. Kinetics of Intercluster Reactions between Atomically Precise Noble Metal Clusters [Ag25(DMBT)18]− and [Au25(PET)18]− in Room Temperature Solutions. *J. Am. Chem. Soc.* **2021**, *143* (18), 6969−6980.

(37) Krishnadas, K. R.; Ghosh, A.; Baksi, A.; Chakraborty, I.; Natarajan, G.; Pradeep, T. Intercluster Reactions between Au25(SR)18 and Ag44(SR)30. *J. Am. Chem. Soc.* **2016**, *138* (1), 140−148.

(38) Krishnadas, K. R.; Baksi, A.; Ghosh, A.; Natarajan, G.; Pradeep, T. Structure-conserving spontaneous transformations between nanoparticles. *Nat. Commun.* **2016**, *7* (1), 13447.

(39) Baksi, A.; Chakraborty, P.; Bhat, S.; Natarajan, G.; Pradeep, T. [Au25(SR)18]22−: a noble metal cluster dimer in the gas phase. *Chem. Commun.* **2016**, *52* (54), 8397−8400.

(40) Bodiuzzaman, M.; Nag, A.; Pradeep Narayanan, R.; Chakraborty, A.; Bag, R.; Paramasivam, G.; Natarajan, G.; Sekar, G.; Ghosh, S.; Pradeep, T. A covalently linked dimer of [Ag25(DMBT)18]−. *Chem. Commun.* **2019**, *55* (34), 5025−5028.

(41) Sels, A.; Salassa, G.; Cousin, F.; Lee, L.-T.; Bürgi, T. Covalently bonded multimers of Au25(SBut)18 as a conjugated system. *Nanoscale* **2018**, *10* (26), 12754−12762.

(42) Lahtinen, T.; Hulkko, E.; Sokołowska, K.; Tero, T.-R.; Saarnio, V.; Lindgren, J.; Pettersson, M.; Häkkinen, H.; Lehtovaara, L. Covalently linked multimers of gold nanoclusters Au102(p-MBA)44 and Au ∼ 250(p-MBA)n. *Nanoscale* **2016**, *8* (44), 18665−18674.

(43) Chakraborty, P.; Baksi, A.; Mudedla, S. K.; Nag, A.; Paramasivam, G.; Subramanian, V.; Pradeep, T. Understanding proton capture and cation-induced dimerization of [Ag29(BDT)12]3− clusters by ion mobility mass spectrometry. *Phys. Chem. Chem. Phys.* **2018**, *20* (11), 7593−7603.

(44) Kang, X.; Wang, S.; Zhu, M. Observation of a new type of aggregation-induced emission in nanoclusters. *Chem. Sci.* **2018**, *9* (11), 3062−3068.

(45) Ghosh, A.; Mohammed, O. F.; Bakr, O. M. Atomic-Level Doping of Metal Clusters. *Acc. Chem. Res.* **2018**, *51* (12), 3094−3103.

(46) Khatun, E.; Ghosh, A.; Chakraborty, P.; Singh, P.; Bodiuzzaman, M.; Ganesan, P.; Nataranjan, G.; Ghosh, J.; Pal, S. K.; Pradeep, T. A thirty-fold photoluminescence enhancement induced by secondary ligands in monolayer protected silver clusters. *Nanoscale* **2018**, *10* (42), 20033−20042.

(47) Zeng, C.; Chen, Y.; Kirschbaum, K.; Lambright, K. J.; Jin, R. Emergence of hierarchical structural complexities in nanoparticles and their assembly. *Science* **2016**, *354* (6319), 1580.

(48) Yan, N.; Xia, N.; Liao, L.; Zhu, M.; Jin, F.; Jin, R.; Wu, Z. Unraveling the long-pursued Au144 structure by x-ray crystallography. *Sci. Adv.* **2018**, *4* (10), eaat7259.

(49) Zeng, C.; Chen, Y.; Kirschbaum, K.; Appavoo, K.; Sfeir, M. Y.; Jin, R. Structural patterns at all scales in a nonmetallic chiral Au133(SR)52 nanoparticle. *Sci. Adv.* **2015**, *1* (2), e1500045.

(50) Liao, L.; Chen, J.; Wang, C.; Zhuang, S.; Yan, N.; Yao, C.; Xia, N.; Li, L.; Bao, X.; Wu, Z. Transition-sized Au92 nanoparticle bridging non-fcc-structured gold nanoclusters and fcc-structured gold nanocrystals. *Chem. Commun.* **2016**, *52* (81), 12036−12039.

(51) Gan, Z.; Chen, J.; Liao, L.; Zhang, H.; Wu, Z. Surface Single-Atom Tailoring of a Gold Nanoparticle. *J. Phys. Chem. Lett.* **2018**, *9* (1), 204−208.

(52) Liu, X.; Chen, J.; Yuan, J.; Li, Y.; Li, J.; Zhou, S.; Yao, C.; Liao, L.; Zhuang, S.; Zhao, Y.; Deng, H.; Yang, J.; Wu, Z. A Silver Nanocluster Containing Interstitial Sulfur and Unprecedented Chemical Bonds. *Angew. Chem., Int. Ed.* **2018**, *57* (35), 11273−11277.

(53) Nag, A.; Chakraborty, P.; Bodiuzzaman, M.; Ahuja, T.; Antharjanam, S.; Pradeep, T. Polymorphism of Ag29(BDT)12(TPP)43− cluster: interactions of secondary ligands and their effect on solid state luminescence. *Nanoscale* **2018**, *10* (21), 9851−9855.

(54) Higaki, T.; Liu, C.; Zhou, M.; Luo, T.-Y.; Rosi, N. L.; Jin, R. Tailoring the Structure of 58-Electron Gold Nanoclusters: Au103S2(S-Nap)41 and Its Implications. *J. Am. Chem. Soc.* **2017**, *139* (29), 9994−10001.

(55) Khatun, E.; Bodiuzzaman, M.; Sugi, K. S.; Chakraborty, P.; Paramasivam, G.; Dar, W. A.; Ahuja, T.; Antharjanam, S.; Pradeep, T. Confining an Ag10 Core in an Ag12 Shell: A Four-Electron Superatom with Enhanced Photoluminescence upon Crystallization. *ACS Nano* **2019**, *13* (5), 5753−5759.

(56) Hossain, S.; Imai, Y.; Motohashi, Y.; Chen, Z.; Suzuki, D.; Suzuki, T.; Kataoka, Y.; Hirata, M.; Ono, T.; Kurashige, W.; Kawawaki, T.; Yamamoto, T.; Negishi, Y. Understanding and designing one-dimensional assemblies of ligand-protected metal nanoclusters. *Mater. Horiz.* **2020**, *7* (3), 796−803.

(57) Narouz, M. R.; Takano, S.; Lummis, P. A.; Levchenko, T. I.; Nazemi, A.; Kaappa, S.; Malola, S.; Yousefalizadeh, G.; Calhoun, L. A.; Stamplecoskie, K. G.; Häkkinen, H.; Tsukuda, T.; Crudden, C. M. Robust, Highly Luminescent Au13 Superatoms Protected by N-Heterocyclic Carbenes. *J. Am. Chem. Soc.* **2019**, *141* (38), 14997−15002.

(58) Wei, X.; Kang, X.; Yuan, Q.; Qin, C.; Jin, S.; Wang, S.; Zhu, M. Capture of Cesium Ions with Nanoclusters: Effects on Inter- and Intramolecular Assembly. *Chem. Mater.* **2019**, *31* (13), 4945−4952.

(59) Kang, X.; Wei, X.; Xiang, P.; Tian, X.; Zuo, Z.; Song, F.; Wang, S.; Zhu, M. Rendering hydrophobic nanoclusters water-soluble and biocompatible. *Chem. Sci.* **2020**, *11* (18), 4808−4816.

(60) Chang, H.; Karan, N. S.; Shin, K.; Bootharaju, M. S.; Nah, S.; Chae, S. I.; Baek, W.; Lee, S.; Kim, J.; Son, Y. J.; Kang, T.; Ko, G.; Kwon, S.-H.; Hyeon, T. Highly Fluorescent Gold Cluster Assembly. *J. Am. Chem. Soc.* **2021**, *143* (1), 326−334.

(61) Li, Q.; Russell, J. C.; Luo, T.-Y.; Roy, X.; Rosi, N. L.; Zhu, Y.; Jin, R. Modulating the hierarchical fibrous assembly of Au nanoparticles with atomic precision. *Nat. Commun.* **2018**, *9* (1), 3871.

(62) Udayabhaskararao, T.; Bootharaju, M. S.; Pradeep, T. Thiolate-protected Ag32 clusters: mass spectral studies of composition and insights into the Ag−thiolate structure from NMR. *Nanoscale* **2013**, *5* (19), 9404−9411.

(63) Som, A.; Samal, A. K.; Udayabhaskararao, T.; Bootharaju, M. S.; Pradeep, T. Manifestation of the Difference in Reactivity of Silver Clusters in Contrast to Its Ions and Nanoparticles: The Growth of Metal Tipped Te Nanowires. *Chem. Mater.* **2014**, *26* (10), 3049−3056.

(64) Som, A.; Chakraborty, I.; Maark, T. A.; Bhat, S.; Pradeep, T. Cluster-Mediated Crossed Bilayer Precision Assemblies of 1D Nanowires. *Adv. Mater.* **2016**, *28* (14), 2827−2833.

(65) Chakraborty, A.; Fernandez, A. C.; Som, A.; Mondal, B.; Natarajan, G.; Paramasivam, G.; Lahtinen, T.; Häkkinen, H.; Nonappa; Pradeep, T. Atomically Precise Nanocluster Assemblies Encapsulating Plasmonic Gold Nanorods. *Angew. Chem., Int. Ed.* **2018**, *57* (22), 6522−6526.

(66) Bose, P.; Chakraborty, P.; Mohanty, J. S.; Nonappa; Ray; Chowdhuri, A.; Khatun, E.; Ahuja, T.; Mahendranath, A.; Pradeep, T. Atom transfer between precision nanoclusters and polydispersed nanoparticles: a facile route for monodisperse alloy nanoparticles and their superstructures. *Nanoscale* **2020**, *12* (43), 22116−22128.

(67) Nonappa; Lahtinen, T.; Haataja, J. S.; Tero, T.-R.; Häkkinen, H.; Ikkala, O. Template-Free Supracolloidal Self-Assembly of Atomically Precise Gold Nanoclusters: From 2D Colloidal Crystals to Spherical Capsids. *Angew. Chem., Int. Ed.* **2016**, *55* (52), 16035−16038.

(68) Nonappa; Ikkala, O. Hydrogen Bonding Directed Colloidal Self-Assembly of Nanoparticles into 2D Crystals, Capsids, and Supracolloidal Assemblies. *Adv. Funct. Mater.* **2018**, *28* (27), 1704328.

(69) Chakraborty, P.; Nag, A.; Paramasivam, G.; Natarajan, G.; Pradeep, T. Fullerene-Functionalized Monolayer-Protected Silver Clusters: [Ag29(BDT)12(C60)n]3− (n = 1−9). *ACS Nano* **2018**, *12* (3), 2415−2425.

(70) Chakraborty, P.; Nag, A.; Mondal, B.; Khatun, E.; Paramasivam, G.; Pradeep, T. Fullerene-Mediated Aggregation of M25(SR)18− (M = Ag, Au) Nanoclusters. *J. Phys. Chem. C* **2020**, *124* (27), 14891−14900.

(71) Schulz-Dobrick, M.; Jansen, M. Intercluster Compounds Consisting of Gold Clusters and Fullerides: [Au7(PPh3)7]C60· THF and [Au8(PPh3)8](C60)2. *Angew. Chem., Int. Ed.* **2008**, *47* (12), 2256−2259.

(72) Mathew, A.; Natarajan, G.; Lehtovaara, L.; Häkkinen, H.; Kumar, R. M.; Subramanian, V.; Jaleel, A.; Pradeep, T. Supramolecular Functionalization and Concomitant Enhancement in Properties of Au25 Clusters. *ACS Nano* **2014**, *8* (1), 139−152.

(73) Yan, C.; Liu, C.; Abroshan, H.; Li, Z.; Qiu, R.; Li, G. Surface modification of adamantane-terminated gold nanoclusters using cyclodextrins. *Phys. Chem. Chem. Phys.* **2016**, *18* (33), 23358−23364.

(74) Bhunia, S.; Kumar, S.; Purkayastha, P. Gold Nanocluster-Grafted Cyclodextrin Suprastructures: Formation of Nanospheres to Nanocubes with Intriguing Photophysics. *ACS Omega* **2018**, *3* (2), 1492−1497.

(75) Chen, Y.; Liu, C.; Tang, Q.; Zeng, C.; Higaki, T.; Das, A.; Jiang, D.-e.; Rosi, N. L.; Jin, R. Isomerism in Au28(SR)20 Nanocluster and Stable Structures. *J. Am. Chem. Soc.* **2016**, *138* (5), 1482−1485.

(76) Kang, X.; Zhu, M. Structural Isomerism in Atomically Precise Nanoclusters. *Chem. Mater.* **2021**, *33* (1), 39−62.

(77) Xu, W. W.; Zeng, X. C.; Gao, Y. The structural isomerism in gold nanoclusters. *Nanoscale* **2018**, *10* (20), 9476−9483.

(78) Matus, M. F.; Malola, S.; Kinder Bonilla, E.; Barngrover, B. M.; Aikens, C. M.; Häkkinen, H. A topological isomer of the Au25(SR)18− nanocluster. *Chem. Commun.* **2020**, *56* (58), 8087−8090.

(79) Qin, Z.; Zhang, J.; Wan, C.; Liu, S.; Abroshan, H.; Jin, R.; Li, G. Atomically precise nanoclusters with reversible isomeric transformation for rotary nanomotors. *Nat. Commun.* **2020**, *11* (1), 6019.

(80) Baksi, A.; Ghosh, A.; Mudedla, S. K.; Chakraborty, P.; Bhat, S.; Mondal, B.; Krishnadas, K. R.; Subramanian, V.; Pradeep, T. Isomerism in Monolayer Protected Silver Cluster Ions: An Ion Mobility-Mass Spectrometry Approach. *J. Phys. Chem. C* **2017**, *121* (24), 13421−13427.

(81) Nag, A.; Chakraborty, P.; Paramasivam, G.; Bodiuzzaman, M.; Natarajan, G.; Pradeep, T. Isomerism in Supramolecular Adducts of Atomically Precise Nanoparticles. *J. Am. Chem. Soc.* **2018**, *140* (42), 13590−13593.

(82) Jiang, T.; Qu, G.; Wang, J.; Ma, X.; Tian, H. Cucurbiturils brighten Au nanoclusters in water. *Chem. Sci.* **2020**, *11* (13), 3531−3537.

(83) van der Linden, M.; Barendregt, A.; van Bunningen, A. J.; Chin, P. T. K.; Thies-Weesie, D.; de Groot, F. M. F.; Meijerink, A. Characterisation, degradation and regeneration of luminescent Ag29 clusters in solution. *Nanoscale* **2016**, *8* (47), 19901−19909.

(84) Black, D. M.; Robles, G.; Lopez, P.; Bach, S. B. H.; Alvarez, M.; Whetten, R. L. Liquid Chromatography Separation and Mass Spectrometry Detection of Silver-Lipoate Ag29(LA)12 Nanoclusters: Evidence of Isomerism in the Solution Phase. *Anal. Chem.* **2018**, *90* (3), 2010−2017.

(85) Nag, A.; Chakraborty, P.; Thacharon, A.; Paramasivam, G.; Mondal, B.; Bodiuzzaman, M.; Pradeep, T. Atomically Precise Noble Metal Cluster-Assembled Superstructures in Water: Luminescence Enhancement and Sensing. *J. Phys. Chem. C* **2020**, *124* (40), 22298−22303.

(86) Chakraborty, P.; Nag, A.; Sugi, K. S.; Ahuja, T.; Varghese, B.; Pradeep, T. Crystallization of a Supramolecular Coassembly of an Atomically Precise Nanoparticle with a Crown Ether. *ACS Mater. Lett.* **2019**, *1* (5), 534−540.

(87) Muhammed, M. A. H.; Cruz, L. K.; Emwas, A.-H.; El-Zohry, A. M.; Moosa, B.; Mohammed, O. F.; Khashab, N. M. Pillar[5]arene-Stabilized Silver Nanoclusters: Extraordinary Stability and Luminescence Enhancement Induced by Host−Guest Interactions. *Angew. Chem., Int. Ed.* **2019**, *58* (44), 15665−15670.

(88) Bootharaju, M. S.; Dey, R.; Gevers, L. E.; Hedhili, M. N.; Basset, J.-M.; Bakr, O. M. A New Class of Atomically Precise, Hydride-Rich Silver Nanoclusters Co-Protected by Phosphines. *J. Am. Chem. Soc.* **2016**, *138* (42), 13770−13773.

(89) Almansaf, A. A.; Parida, M. R.; Besong, T. M. D.; Maity, P.; Bootharaju, M. S.; Bakr, O. M.; Mohammed, O. F. The impact of Au doping on the charge carrier dynamics at the interfaces between cationic porphyrin and silver nanoclusters. *Chem. Phys. Lett.* **2017**, *683*, 393−397.

(90) Sugi, K. S.; Bandyopadhyay, P.; Bodiuzzaman, M.; Nag, A.; Hridya, M.; Dar, W. A.; Ghosh, P.; Pradeep, T. Manifestation of Structural Differences of Atomically Precise Cluster-Assembled Solids in Their Mechanical Properties. *Chem. Mater.* **2020**, *32* (18), 7973−7984.

(91) Roy, X.; Lee, C.-H.; Crowther, A. C.; Schenck, C. L.; Besara, T.; Lalancette, R. A.; Siegrist, T.; Stephens, P. W.; Brus, L. E.; Kim, P.; Steigerwald, M. L.; Nuckolls, C. Nanoscale Atoms in Solid-State Chemistry. *Science* **2013**, *341* (6142), 157.

(92) Fetzer, F.; Maier, A.; Hodas, M.; Geladari, O.; Braun, K.; Meixner, A. J.; Schreiber, F.; Schnepf, A.; Scheele, M. Structural order enhances charge carrier transport in self-assembled Au-nanoclusters. *Nat. Commun.* **2020**, *11* (1), 6188.

(93) Wang, Y.-M.; Zhang, J.-W.; Wang, Q.-Y.; Li, H.-Y.; Dong, X.-Y.; Wang, S.; Zang, S.-Q. Fabrication of silver chalcogenolate cluster hybrid membranes with enhanced structural stability and luminescence efficiency. *Chem. Commun.* **2019**, *55* (97), 14677−14680.

(94) Basu, S.; Hajra, A.; Gayen, C.; Paul, A. Zinc-Ion-Induced Aggregation of Gold Clusters for Visible-Light-Excitation-Based Fluorimetric Discrimination of Geometrical Isomers. *ChemPhysChem* **2020**, *21* (8), 809−813.

(95) Yang, Y.; Wang, S.; Zhou, Y.; Wang, X.; Liu, X.; Xie, A.; Shen, Y.; Zhu, M. Structurally accurate lipophilic Pt1Ag28 nanoclusters based cancer theranostic micelles for dual-targeting/aggregation enhanced fluorescence imaging and photothermal/photodynamic therapies. *Colloids Surf., B* **2020**, *196*, 111346.

(96) Zhang, C.; Zhang, A.; Hou, W.; Li, T.; Wang, K.; Zhang, Q.; de la Fuente, J. M.; Jin, W.; Cui, D. Mimicking Pathogenic Invasion with the Complexes of Au22(SG)18-Engineered Assemblies and Folic Acid. *ACS Nano* **2018**, *12* (5), 4408−4418.

(97) Zhu, H.; Goswami, N.; Yao, Q.; Chen, T.; Liu, Y.; Xu, Q.; Chen, D.; Lu, J.; Xie, J. Cyclodextrin−gold nanocluster decorated TiO2 enhances photocatalytic decomposition of organic pollutants. *J. Mater. Chem. A* **2018**, *6* (3), 1102−1108.

(98) Zhao, Y.; Zhuang, S.; Liao, L.; Wang, C.; Xia, N.; Gan, Z.; Gu, W.; Li, J.; Deng, H.; Wu, Z. A Dual Purpose Strategy to Endow Gold Nanoclusters with Both Catalysis Activity and Water Solubility. *J. Am. Chem. Soc.* **2020**, *142* (2), 973−977.

(99) Wu, Z.; Liu, J.; Gao, Y.; Liu, H.; Li, T.; Zou, H.; Wang, Z.; Zhang, K.; Wang, Y.; Zhang, H.; Yang, B. Assembly-Induced Enhancement of Cu Nanoclusters Luminescence with Mechanochromic Property. *J. Am. Chem. Soc.* **2015**, *137* (40), 12906−12913.

(100) Huang, H.-Y.; Cai, K.-B.; Talite, M. J.; Chou, W.-C.; Chen, P.-W.; Yuan, C.-T. Coordination-induced emission enhancement in gold-nanoclusters with solid-state quantum yields up to 40% for eco-friendly, low-reabsorption nano-phosphors. *Sci. Rep.* **2019**, *9* (1), 4053.

(101) Moussawi, M. A.; Leclerc-Laronze, N.; Floquet, S.; Abramov, P. A.; Sokolov, M. N.; Cordier, S.; Ponchel, A.; Monflier, E.; Bricout, H.; Landy, D.; Haouas, M.; Marrot, J.; Cadot, E. Polyoxometalate, Cationic Cluster, and γ-Cyclodextrin: From Primary Interactions to Supramolecular Hybrid Materials. *J. Am. Chem. Soc.* **2017**, *139* (36), 12793−12803.

(102) Ong, W.-L.; O'Brien, E. S.; Dougherty, P. S. M.; Paley, D. W.; Fred Higgs, C., III; McGaughey, A. J. H.; Malen, J. A.; Roy, X. Orientational order controls crystalline and amorphous thermal transport in superatomic crystals. *Nat. Mater.* **2017**, *16* (1), 83−88.

(103) Pinkard, A.; Champsaur, A. M.; Roy, X. Molecular Clusters: Nanoscale Building Blocks for Solid-State Materials. *Acc. Chem. Res.* **2018**, *51* (4), 919−929.

ChemComm

ROYAL SOCIETY OF CHEMISTRY

COMMUNICATION

View Article Online
View Journal

Check for updates

Cite this: DOI: 10.1039/d1cc05643c

Received 6th October 2021,
Accepted 22nd November 2021

DOI: 10.1039/d1cc05643c

rsc.li/chemcomm

Direct imaging of lattice planes in atomically precise noble metal cluster crystals using a conventional transmission electron microscope†

Ananthu Mahendranath,[abc] Biswajit Mondal,[ab] Korath Shivan Sugi[ab] and Thalappil Pradeep *[ab]

Imaging finer structural details of atomically precise noble metal cluster crystals has been difficult with electron microscopy, owing to their extreme beam sensitivity. Here we present a simple method whereby lattice planes in single crystals of nanoclusters can be observed using a conventional transmission electron microscope, enabling further expansion of cluster research.

Atomically precise noble metal clusters (APNMCs) belong to an emerging class of materials with unusual properties.[1–3] Over one hundred nanocluster molecules have been understood with single crystal diffraction leading to their atomic structures.[4–11] Consequently, the application of quantum chemical simulations has allowed us to unravel their spectroscopic properties.[12] A large number of other clusters are known today with their compositions being determined by advanced mass spectrometry.[13] While spectroscopy,[14,15] chemistry,[16–18] catalysis,[19,20] and applications[21,22] of all of them are intensely pursued, absence of precise structures makes a thorough understanding of their properties difficult.

Single crystal diffraction, the preeminent tool for structural elucidation, requires high quality single crystals. While microcrystal electron diffraction and single particle reconstruction coupled with computer modelling have revealed the structures of many molecules including clusters,[23–26] they are still not commonly used in cluster science, excepting the report on Au_{68}.[24] The traditional transmission electron microscope (TEM), available in most of the research institutions, is generally not adequate for routine characterization of APNMCs and their crystals, in view of the extreme beam sensitivity of fragile clusters, which transforms them to nanoparticles instantaneously upon electron beam exposure.[27] A method to observe clusters under such conditions for precise determination of their lattice parameters would facilitate the growth of cluster science.

In this communication, we present a simple way to image cluster crystals using a traditional transmission electron microscope where beam induced damage is minimized. Through this methodology, we have successfully imaged various lattice planes in three APNMCs

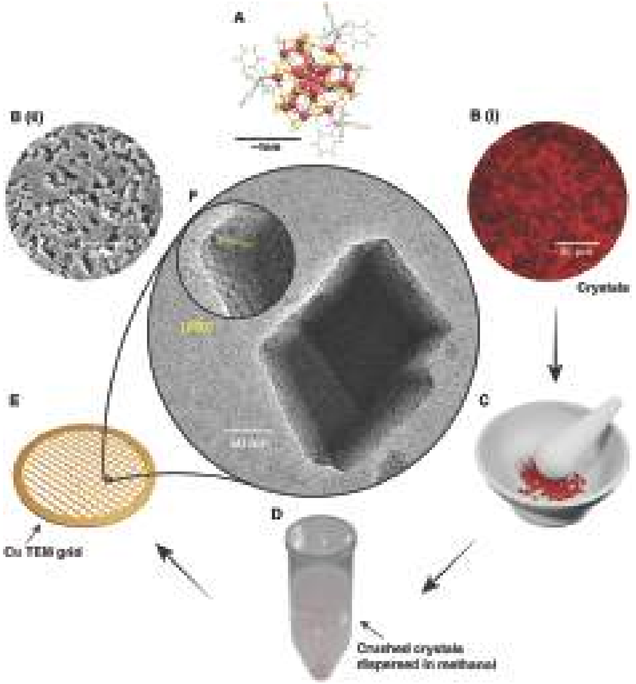

Fig. 1 (A) Single crystal X-ray structure of $[Ag_{29}BDT_{12}TPP_4]^{3-}$ cluster. B(i) represent optical image and B(ii) SEM image of the as crystalized Ag_{29} crystals prepared by solvent evaporation. (C–E) Schematic of the process involved in sample preparation. (F) Shows TEM image of $Ag_{29}C$ crystallites. Inset of (F) shows an expanded view of the (200) lattice plane of $Ag_{29}C$.

---

[a] *DST Unit of Nanoscience and Thematic Unit of Excellence, Department of Chemistry, Indian Institute of Technology Madras, Chennai 600036, India. E-mail: pradeep@iitm.ac.in*

[b] *Centre of Excellence on Molecular Materials and Functions, Indian Institute of Technology Madras, Chennai, 600036, India*

[c] *Department of Metallurgical and Materials Engineering, Indian Institute of Technology Madras, Chennai, 600036, India*

† Electronic supplementary information (ESI) available. See DOI: 10.1039/d1cc05643c

whose structure has been solved previously using single crystal X-ray diffraction, namely – cubic (C) $[Ag_{29}(BDT)_{12}(TPP)_4]^{3-}$ (ref. 7), it's trigonal (T) polymorph,[28] and $[Ag_{25}(DMBT)_{18}]^-$ (ref. 9), where BDT, TPP, and DMBT are 1,3-benzenedithiol, triphenylphosphine, and 2,4-dimethylbenzenethiol, respectively. The method is schematically illustrated in Fig. 1 with $[Ag_{29}(BDT)_{12}(TPP)_4]^{3-}$ (abbreviated as $Ag_{29}C$, C refers to cubic polymorph) as a model. We start with $Ag_{29}C$ single crystals of edge length varying from around 0.1 μm to 80 μm, which are routinely crystalized in the laboratory by solvent evaporation (see the experimental section in ESI† for further details). All the clusters discussed here were fully characterized using UV-Vis spectroscopy, and ESI MS (Fig. S1–S3, ESI†). Results were in agreement with the reported data. The single crystal morphology was as per literature and the structural parameters were checked with SCXRD (Tables S2 and S3, ESI†). About 100 such single crystals weighing around 0.5 mg were carefully transferred from a glass slide used for crystal growth and were ground thoroughly with a mortar and pestle, to make a powder composed of 0.02 μm to 0.7 μm particles (see ESI† Fig. S4, for further details and an optical micrograph of the powder). This cluster crystal powder was suspended in methanol, in which the cluster was insoluble, and was sonicated for 10 s. About 10 μl of this suspension was drop-casted on a carbon coated 300 mesh copper grid. After drying for 2 h, the sample was imaged under 100 kV electron beam using a JEOL 3010 TEM, with a LaB_6 filament, having 1.2 Å point-to-point resolution. Cluster crystals were noticed immediately under the electron beam while continuous exposure of more than 60 s damages the crystals. This time may be used to optimize parameters for better imaging. By moving the beam to an adjacent crystal, it was possible to collect more than 10 images without beam induced damage.

While examining such crystallites, we observe the various lattice structures of $Ag_{29}C$, as shown in Fig. 2(A–C). These correspond to (110), (111), and (200) planes with lattice constants of 2.42 nm, 1.97 nm and 1.71 nm, respectively. Due to the cubic symmetry of $Ag_{29}C$, these may also correspond to equivalent planes in other directions (ESI† Table S4). Several other adjacent $Ag_{29}C$ crystallites on the grid are also presented in the ESI† (Fig. S5). These lattice parameters match well with the crystallographic data reported by AbdulHalim, *et al.*[8] We compare the TEM images with the crystal structures in Fig. 2(D–F).

Once beam induced damage sets in, nanoclusters coalesce to form larger nanoparticles. To understand the optimum time during which measurements can be done, before beam induced damages occur, we exposed the sample to the electron beam for an extended period of time. As mentioned previously, images can be collected for about 60 s from one crystallite,

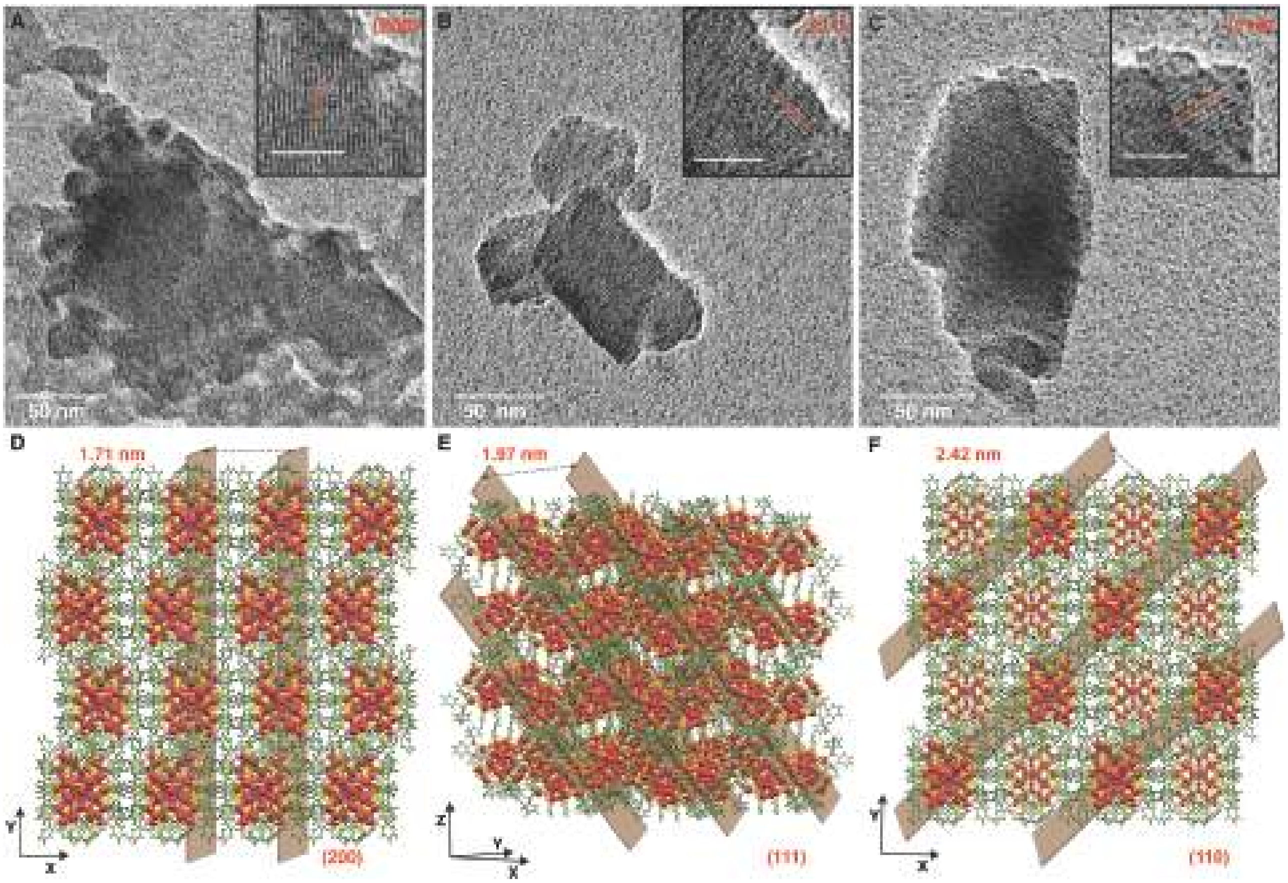

Fig. 2 TEM images of $Ag_{29}C$ crystallites representing various lattice planes (A–C). The insets show expanded views of the corresponding lattice planes. (D–F) are representative images of a 2 × 2 × 2 unit cell of $Ag_{29}C$. Scale bars in insets are 25 nm. Early signs of beam induced damage are seen in B.

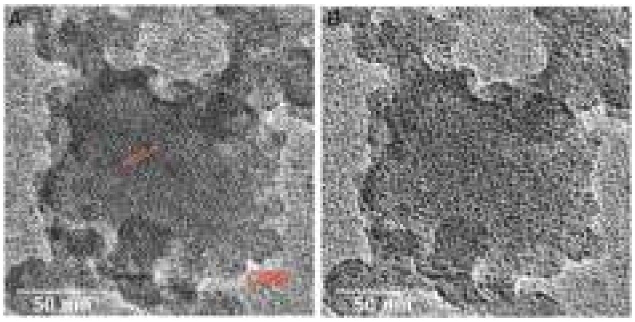

Fig. 3 (A) TEM image of an $Ag_{29}C$ crystallite imaged without any noticeable damages. (B) Nanoparticle growth that happened over the region, after an exposure of nearly 56 s.

without noticeable beam induced damage, during which approximately 10 images could be collected for each area. However, beam induced damages set in the course of time and the lattice transforms continuously after 60 s. The systematic transformation is captured in ESI† (Fig. S6 and S8), and two of those images are presented in Fig. 3. As observed, beyond 60 s (Fig. S8, ESI†), the sample undergoes permanent changes and lattice planes are no more visible. Particles up to approximately 3.8 nm diameter were observed till 56 s (Fig. S7, ESI†). Bigger particles (>10 nm) were formed up on exposure beyond ~ 2 min (Fig. S9, ESI†). It is to be noted that the direction of growth of these particles is not yet clear and is beyond the scope of experiments discussed here. In this methodology, by reducing the accelerating voltage, we have managed to delay the damges happening to APNMCs. This creates a time window to image lattice planes, before beam induced damges become predominant. We believe that the success of this imaging methodology is also related to the thickness of the sample as well as the relative orientation of crystals on the TEM grid, with enhanced thermal contact with the grid. Therefore, removing those crystallites without proper contact by gentle tapping or inverting the grid, after drying the sample on the grid, can enhance the success of imaging. Improving thermal contact may be possible with grids such as ultra thin carbon film, microgrid, and those with supports such as molybdenum mesh and gold mesh. Thicker crystallites were opaque to electron beam (Fig. S10, ESI†). Note that images were collected at room temperature. When an acceleration potential greater than 100 kV was used, the crystallites got damaged sooner and the very first images showed signs of particle formation. With 100 kV voltage, all our attempts were successful in obtaining high quality images. The conditions used for imaging are presented as Table S1 in ESI.†

In order to ensure that this methodology is applicable for other crystals, we examined trigonal single crystals of $[Ag_{29}(BDT)_{12}(TPP)_4]^{3-}$ cluster (abbreviated as $Ag_{29}T$), which was a polymorph reported by our group.[28] The images correlated exactly to the single crystal structure of crystal of $Ag_{29}T$, as seen in Fig. 4(A–D). The lattice planes observed were (011) and (012) with interplanar spacings of 2.12 nm and 1.68 nm, respectively. Additional images from adjacent $Ag_{29}T$ crystallites

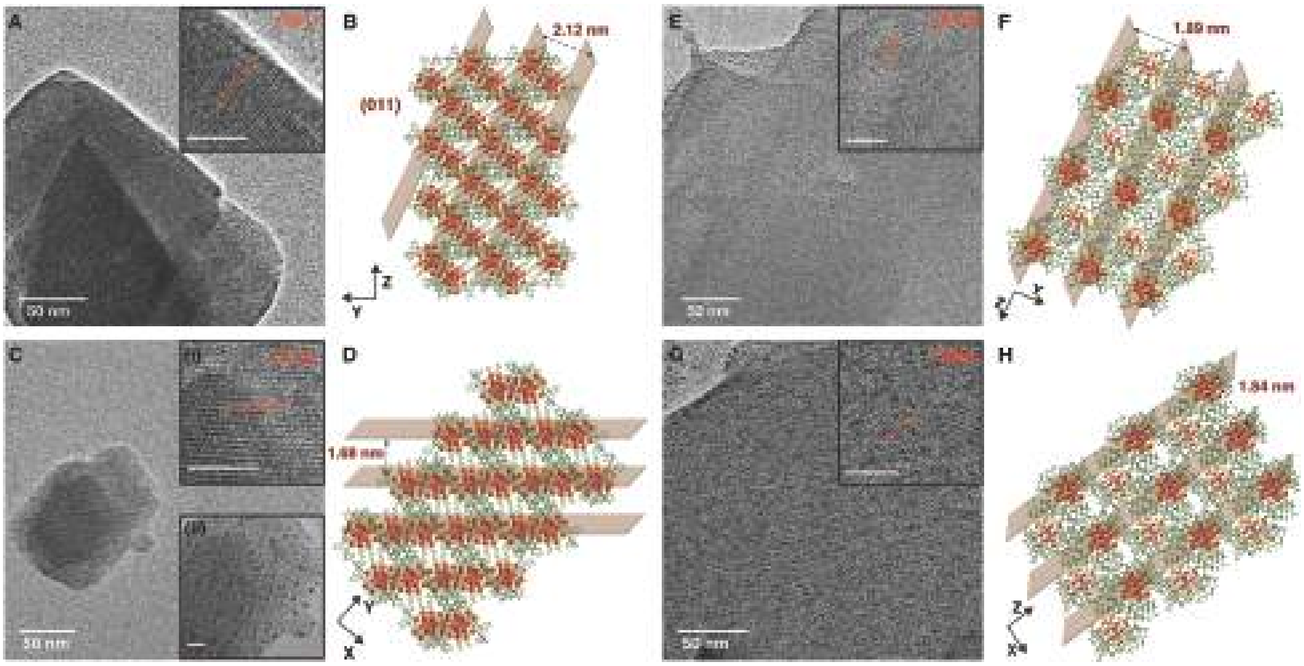

Fig. 4 TEM images of various crystallites representing different lattice planes of $Ag_{29}T$ and Ag_{25}. (A and C) represent TEM images of $Ag_{29}T$ crystallites and (B and D) are representative images of corresponding planes in a $2 \times 2 \times 2$ unit cell of the same crystal. Inset in A represents the expanded image of the crystallite. Insets (i and ii) show an expanded area of the crystallite and beam induced damage from another area after nearly 60 s of exposure. (E and G) represent TEM images from Ag_{25} crystallites and (F and H) are representative images of corresponding planes in a $3 \times 3 \times 3$ unit cell. Insets in (E and G) show expanded views of the crystallites. The scale bars in all insets are 25 nm, except for (ii), where it is 10 nm.

and beam induced damages on one of them are presented in ESI† as Fig. S11 and S12, respectively. $Ag_{29}T$ shows beam induced damage after 60 s of beam exposure (Fig. C(ii)).

Furthermore, we observed single crystals of $[Ag_{25}(DMBT)_{18}]^-$ (abbreviated as Ag_{25}) as well. The lattice spacings observed in these images were consistent with the expected distances in Ag_{25} crystallites, which are triclinic, as depicted in Fig. 4(E–H). Additional images of the Ag_{25} crystallites are presented as Fig. S13 (ESI†). Ag_{25} also shows beam induced damage, as shown in the inset of Fig. 4G. As in the case of $Ag_{29}C$, the planes may correspond to equivalent ones in other directions, due to the trigonal and triclinic symmetries of $Ag_{29}T$ and Ag_{25}, respectively (Tables S5–S6, ESI†).

We had also performed this experiment by using water as a solvent to disperse the cluster crystal powder. Both $Ag_{29}C$ and $Ag_{29}T$ are insoluble in water. While using water as a solvent, the grid was dried for an extended period of 6 h before imaging. Similar results were obtained and are presented as Fig. S14 in the ESI.† Detailed analysis followed for obtaining the lattice spacing in the crystallites, is described in ESI† (Tables S4–S6 and Fig. S15).

In conclusion, we show that a simple methodology can make cluster crystals observable with regular transmission electron microscopes available in most research laboratories. Generally, APNMCs grow in size and their structure gets transformed upon exposure to electron beam. We demonstrate that with careful sample preparation and optimized imaging parameters, finer structural details of nanocluster single crystals can be obtained, without causing damages, using electron microscope models that are employed for routine imaging. This will ensure more details of such fragile materials to be examined in many labs across the world. If this methodology were to be applied with improved instrumentation like low-dose imaging, cryo-cooling, *etc.*, we anticipate that even the ligands will be observable. Consequently, we hope that crystal structures of unknown clusters will be determined more routinely.

A. M, thanks Ministry of Education, Government of India, and IIT Madras for his fellowship. We thank Ms. Jayoti Roy and Ms. Anagha Jose, for assisting with mass spectrometric analysis. T. P. acknowledges funding for the Centre of Excellence on Molecular Materials and Functions under the Institution of Eminence scheme of IIT Madras. We thank the Department of Science and Technology, Government of India, for supporting our research programme.

Conflicts of interest

There are no conflicts to declare.

References

1 I. Chakraborty and T. Pradeep, *Chem. Rev.*, 2017, **117**, 8208–8271.

2 R. Jin, C. Zeng, M. Zhou and Y. Chen, *Chem. Rev.*, 2016, **116**, 10346–10413.

3 X. Kang, Y. Li, M. Zhu and R. Jin, *Chem. Soc. Rev.*, 2020, **49**, 6443–6514.

4 P. D. Jadzinsky, G. Calero, C. J. Ackerson, D. A. Bushnell and R. D. Kornberg, *Science*, 2007, **318**, 430–433.

5 M. Bodiuzzaman, A. Ghosh, K. S. Sugi, A. Nag, E. Khatun, B. Varghese, G. Paramasivam, S. Antharjanam, G. Natarajan and T. Pradeep, *Angew. Chem., Int. Ed.*, 2019, **58**, 189–194.

6 D. Crasto, S. Malola, G. Brosofsky, A. Dass and H. Häkkinen, *J. Am. Chem. Soc.*, 2014, **136**, 5000–5005.

7 M. W. Heaven, A. Dass, P. S. White, K. M. Holt and R. W. Murray, *J. Am. Chem. Soc.*, 2008, **130**, 3754–3755.

8 L. G. AbdulHalim, M. S. Bootharaju, Q. Tang, S. Del Gobbo, R. G. AbdulHalim, M. Eddaoudi, D. Jiang and O. M. Bakr, *J. Am. Chem. Soc.*, 2015, **137**, 11970–11975.

9 Y. Li and R. Jin, *J. Am. Chem. Soc.*, 2020, **142**, 13627–13644.

10 C. P. Joshi, M. S. Bootharaju, M. J. Alhilaly and O. M. Bakr, *J. Am. Chem. Soc.*, 2015, **137**, 11578–11581.

11 S. Lee, M. S. Bootharaju, G. Deng, S. Malola, W. Baek, H. Häkkinen, N. Zheng and T. Hyeon, *J. Am. Chem. Soc.*, 2020, **142**, 13974–13981.

12 M. Zhu, C. M. Aikens, F. J. Hollander, G. C. Schatz and R. Jin, *J. Am. Chem. Soc.*, 2008, **130**, 5883–5885.

13 P. Chakraborty and T. Pradeep, *NPG Asia Mater.*, 2019, **11**, 1–22.

14 Y. Lin, P. Charchar, A. J. Christofferson, M. R. Thomas, N. Todorova, M. M. Mazo, Q. Chen, J. Doutch, R. Richardson, I. Yarovsky and M. M. Stevens, *J. Am. Chem. Soc.*, 2018, **140**, 18217–18226.

15 M. Neumaier, A. Baksi, P. Weis, E. K. Schneider, P. Chakraborty, H. Hahn, T. Pradeep and M. M. Kappes, *J. Am. Chem. Soc.*, 2021, **143**, 6969–6980.

16 K. R. Krishnadas, A. Ghosh, A. Baksi, I. Chakraborty, G. Natarajan and T. Pradeep, *J. Am. Chem. Soc.*, 2015, **138**, 140–148.

17 K. R. Krishnadas, A. Baksi, A. Ghosh, G. Natarajan, A. Som and T. Pradeep, *Acc. Chem. Res.*, 2017, **50**, 1988–1996.

18 Q. Yao, Z. Wu, Z. Liu, Y. Lin, X. Yuan and J. Xie, *Chem. Sci.*, 2021, **12**, 99–127.

19 X. Du and R. Jin, *ACS Nano*, 2019, **13**, 7383–7387.

20 Y. Du, H. Sheng, D. Astruc and M. Zhu, *Chem. Rev.*, 2019, **120**, 526–622.

21 Y. Li, S. Li, A. V. Nagarajan, Z. Liu, S. Nevins, Y. Song, G. Mpourmpakis and R. Jin, *J. Am. Chem. Soc.*, 2021, **143**, 11102–11108.

22 X.-R. Song, N. Goswami, H.-H. Yang and J. Xie, *Analyst*, 2016, **141**, 3126–3140.

23 C. G. Jones, M. W. Martynowycz, J. Hattne, T. J. Fulton, B. M. Stoltz, J. A. Rodriguez, H. M. Nelson and T. Gonen, *ACS Cent. Sci.*, 2018, **4**, 1587–1592.

24 M. Azubel, J. Koivisto, S. Malola, D. Bushnell, G. L. Hura, A. L. Koh, H. Tsunoyama, T. Tsukuda, M. Pettersson, H. Häkkinen and R. D. Kornberg, *Science*, 2014, **345**, 909–912.

25 M. Azubel, A. L. Koh, K. Koyasu, T. Tsukuda and R. D. Kornberg, *ACS Nano*, 2017, **11**, 11866–11871.

26 S. Vergara, D. A. Lukes, M. W. Martynowycz, U. Santiago, G. Plascencia-Villa, S. C. Weiss, M. J. de la Cruz, D. M. Black, M. M. Alvarez, X. López-Lozano, C. O. Barnes, G. Lin, H.-C. Weissker, R. L. Whetten, T. Gonen, M. J. Yacaman and G. Calero, *J. Phys. Chem. Lett.*, 2017, **8**, 5523–5530.

27 P. Ramasamy, S. Guha, E. S. Shibu, T. S. Sreeprasad, S. Bag, A. Banerjee and T. Pradeep, *J. Mater. Chem.*, 2009, **19**, 8456–8462.

28 A. Nag, P. Chakraborty, M. Bodiuzzaman, T. Ahuja, S. Antharjanam and T. Pradeep, *Nanoscale*, 2018, **10**, 9851–9855.

Supplementary Information

Direct Imaging of Lattice Planes in Atomically Precise Noble Metal Cluster Crystals Using a Conventional Transmission Electron Microscope

Ananthu Mahendranath,[a,b,c] Biswajit Mondal, [a,b] Korath Shivan Sugi [a,b] and Thalappil Pradeep[a,b,*]

[a] *DST Unit of Nanoscience and Thematic Unit of Excellence, Department of Chemistry, Indian Institute of Technology Madras, Chennai 600036, India.*

[b] *Centre of Excellence on Molecular Materials and Functions, Indian Institute of Technology Madras, Chennai 600036, India.*

[c] *Department of Metallurgical and Materials Engineering, Indian Institute of Technology Madras, Chennai 600036, India.*

*Email: pradeep@iitm.ac.in

Table of Contents

Experimental Section

Chemicals. Sodium borohydride ($NaBH_4$, 99.99% metal basis), triphenylphosphine (TPP), tetraphenylphosphonium bromide, benzene-1,3-dithiol (BDT), and 2,4-dimethylbenzenethiol (DMBT) were purchased from Sigma-Aldrich. Silver nitrate ($AgNO_3$, 99%) was purchased from RANKEM India. All solvents including methanol, dichloromethane (DCM), and dimethylformamide (DMF) were of analytical grade.

Synthesis of $[Ag_{29}(BDT)_{12}TPP_4]^{3-}$ nanocluster. Synthesis of Ag_{29} nanocluster was performed by following a previously reported procedure.[1] 20 mg of $AgNO_3$ was dissolved in 5 mL of methanol. To this, 10 mL of DCM and 13.5 μL of BDT were added. The solution changed to turbid yellow color on addition of BDT. After stirring for about 2 min, 200 mg of TPP (dissolved in 1 mL of DCM) was added. The turbid yellow color changed to colorless immediately after addition of TPP. After 15 min, 10.5 mg of $NaBH_4$ in 500 μL of cold deionized (DI) water was added. The stirring was continued for 3 h under dark conditions. The resulting solution was centrifuged, and the supernatant was discarded. The residue was repeatedly washed with methanol to remove excess thiols and thiolates, and was subsequently dispersed in DMF. This DMF dispersion on centrifugation gave cluster alone in the supernatant, and any resulting precipitate was discarded. This purified cluster solution in DMF was dried over glass slides, under dark conditions.

Synthesis of $[Ag_{25}(DMBT)_{18}]^-$ nanocluster. Synthesis of Ag_{25} nanocluster was performed by following a previously reported procedure.[2] ∼38 mg of $AgNO_3$ was dissolved in 2 mL of methanol. To this, ∼90 μL of DMBT was added that produced a thick yellow mixture. Next, 17 mL of DCM was added to the vial and stirred for 20 minutes under an ice-bath. A freshly prepared solution of ∼6 mg tetraphenylphosphonium bromide in 0.5 mL methanol was added before the drop-wise addition of 0.5 mL of ice-cold water containing ∼15 mg $NaBH_4$. Color of the reaction mixture changed to light yellow and then to dark. This solution was allowed to stir for 6 h and aged overnight at 4 ℃. Afterward, the dark solution was centrifuged and thus obtained supernatant was concentrated to 5 mL by solvent evaporation in a rotavapor. The cluster was precipitated in methanol, and subsequently washed a couple times in the same solvent. The precipitate obtained was then dissolved into DCM that produced a yellowish Ag_{25} clusters.

Crystallization of Ag_{29}C nanocluster. The purified cluster powder (~10 mg) was dissolved in 1 ml of DMF and filtered using a syringe filter. This concentrated cluster solution was drop-casted on a microscope glass slide and was left to evaporate slowly in a dark box, at room temperature. After 2−3 days, luminescent red crystals suitable for SCXRD were obtained.

Crystallization of Ag_{29}T nanocluster. The purified cluster powder (~5 mg) was dissolved in 500 µl of DMF and filtered using a syringe filter. The concentrated cluster solution was kept for vapor diffusion with methanol (1.5 ml). After almost 2 months, luminescent red crystals suitable for SCXRD were obtanied.

The crystals were also confirmed by monitoring the birefringence using a polarization microscope, for a faster assortment. Trigonal crystals alone showed strong birefringence.

Crystallization of Ag_{25} nanocluster. The purified cluster powder (~30 mg) was dissolved in 1 ml of DCM and filtered using a syringe filter. The concentrated cluster solution was layered with hexane and kept at 4 ℃, under dark conditions. After few days, thick rectangular-shaped black crystals suitable for SCXRD were obtained.

Instrumentation

UV−Visible absorption spectra of all samples were collected using a PerkinElmer Lambda 25 spectrometer.

Electrospray Ionization Mass Spectrometry (ESI MS) of samples were measured using a Waters Synapt G2-Si high-resolution mass spectrometer.

Optical micrograph images were taken on a Leica DM750 P microscope (transmission mode) and Keyence VHX-950F digital microscope (reflection mode).

Scanning Electron Microscopy (SEM) was done using the Helios G4 UX DualBeam microscope.

Single-Crystal X-ray Diffraction (SCXRD) of the nanocluster single crystals were performed on a Bruker D8 VENTURE APEX3 CMOS diffractometer using Cu Kα (λ= 1.54178 Å) radiation.

Transmission electron microscopy (TEM) images were taken on a JEOL 3010 microscope. Details are presented below.

Table S1 Instrument specifications and conditions used for TEM imaging

Instrument Model	JEOL 3010 (instrument was purchased in 2004)
Accelerating voltage	100 kV
Beam Current	39 µA
Frame exposure	0.1 s
Filament	LaB_6
Camera	Gatan Orius SC200 CCD camera (2K x 2K)
Vaccum	10^{-5} to 10^{-6} Pa
Resolution	1.4 Å lattice, 1.2 Å point-to-point
Objective lens	Focal length 2.5mm, Cs 0.6mm, Cc 1.3mm, minimum focus step 1 nm

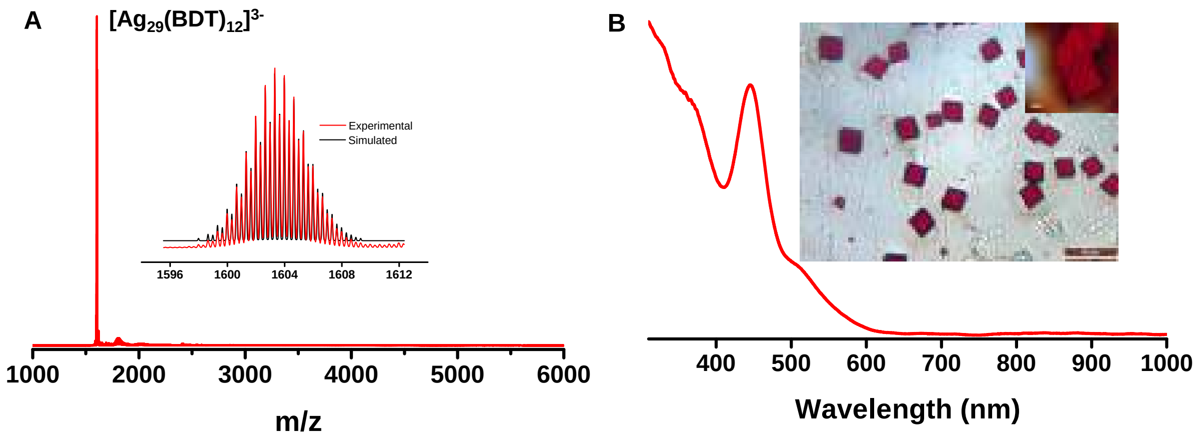

Fig. S1 Characterization of cubic Ag$_{29}$ clusters. (A) Negative mode ESI MS of [Ag$_{29}$(BDT)$_{12}$(TPP)$_4$]$^{3-}$. Inset shows a comparison between experimental and simulated isotopic distributions of the main peak. (B) UV-Vis absorption spectrum of [Ag$_{29}$(BDT)$_{12}$(TPP)$_4$]$^{3-}$, dispersed in DMF. Inset shows optical micrograph images taken from a batch of Ag$_{29}$C crystals.

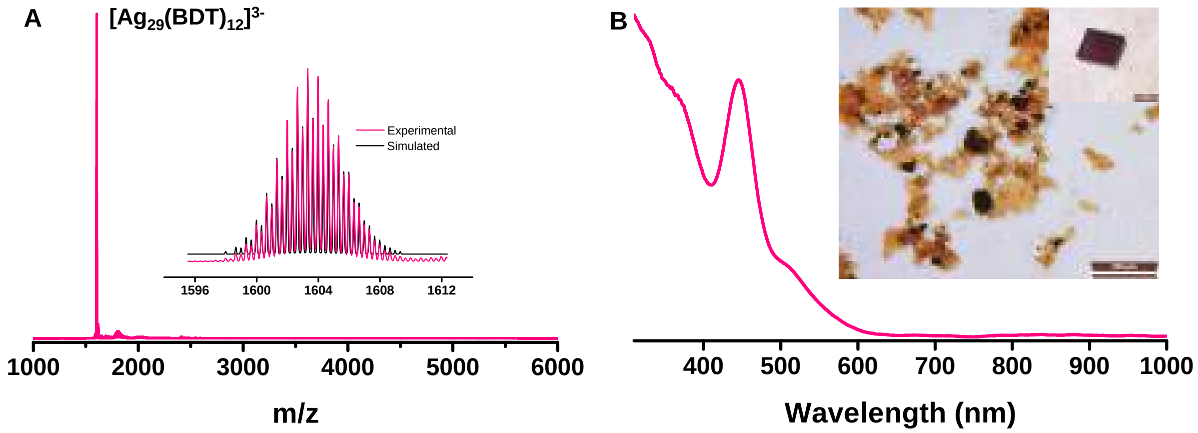

Fig. S2 Characterization of trigonal Ag$_{29}$ clusters. (A) Negative mode ESI MS of [Ag$_{29}$(BDT)$_{12}$(TPP)$_4$]$^{3-}$. Inset shows a comparison between experimental and simulated isotopic distributions of the main peak. (B) UV-Vis absorption spectrum of [Ag$_{29}$(BDT)$_{12}$(TPP)$_4$]$^{3-}$, dispersed in DMF. Inset shows an optical micrograph taken from a batch of Ag$_{29}$T crystals.

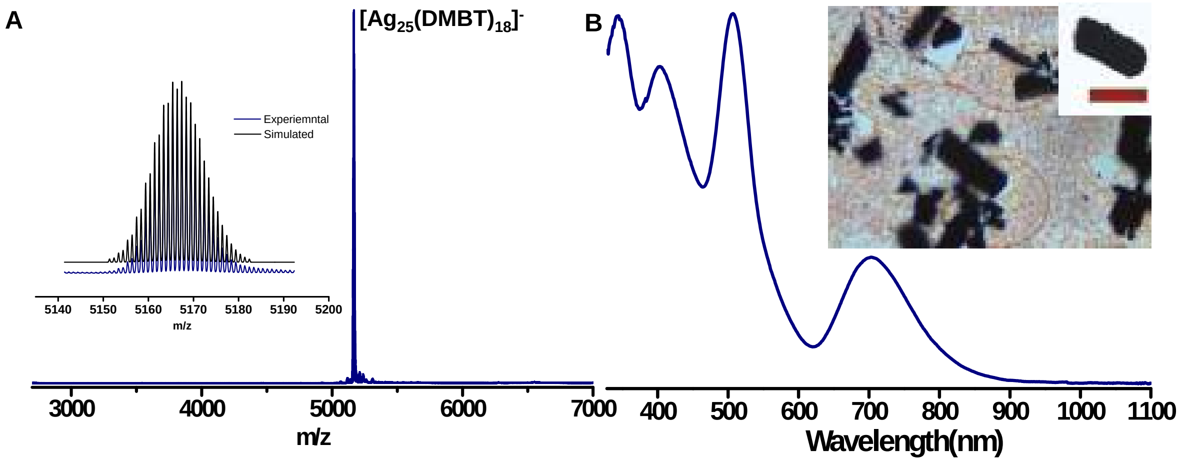

Fig. S3 Characterization of Ag_{25} clusters. (A) Negative mode ESI MS of $[Ag_{25}(DBMT)_{18}]^-$. Inset shows a comparison between experimental and simulated isotopic distributions of the peak. (B) UV-Vis absorption spectrum of $[Ag_{25}(DBMT)_{18}]^-$, dispersed in DCM. Inset shows optical micrograph images taken from a batch of Ag_{25} crystals.

Table S1 Structural parameters of $Ag_{29}C$ crystal from SCXRD

Crystal system	Cubic	
Space group	P a -3	
Unit cell dimensions	a = 34.72 Å	α= 90°
	b = 34.72 Å	β= 90°
	c = 34.72 Å	γ = 90°
Volume	41841 Å^3	

Table S2 Structural parameters of $Ag_{29}T$ crystal from SCXRD

Crystal system	Trigonal	
Space group	R -3 H	
Unit cell dimensions	a = 27.39 Å	α= 90°
	b = 27.39 Å	β= 90°
	c = 47.66 Å	γ = 120°
Volume	30967 Å^3	

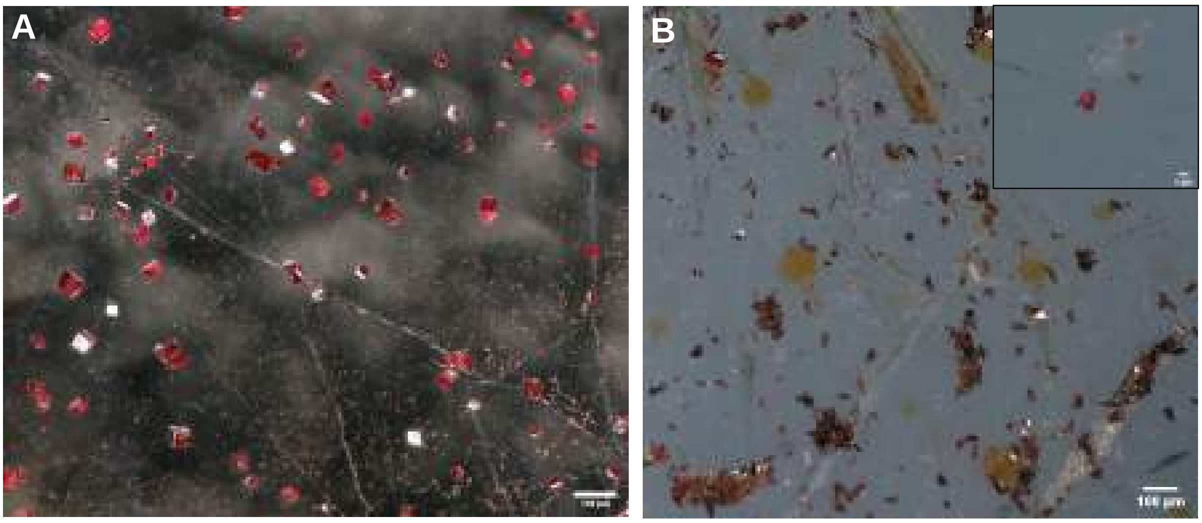

Fig. S4 Optical images of sample preparation. (A) $Ag_{29}C$ crystals before crushing and (B) crushed $Ag_{29}C$ crystallites in the mortar. Inset shows one of the crystallites. The images were recorded in reflection mode.

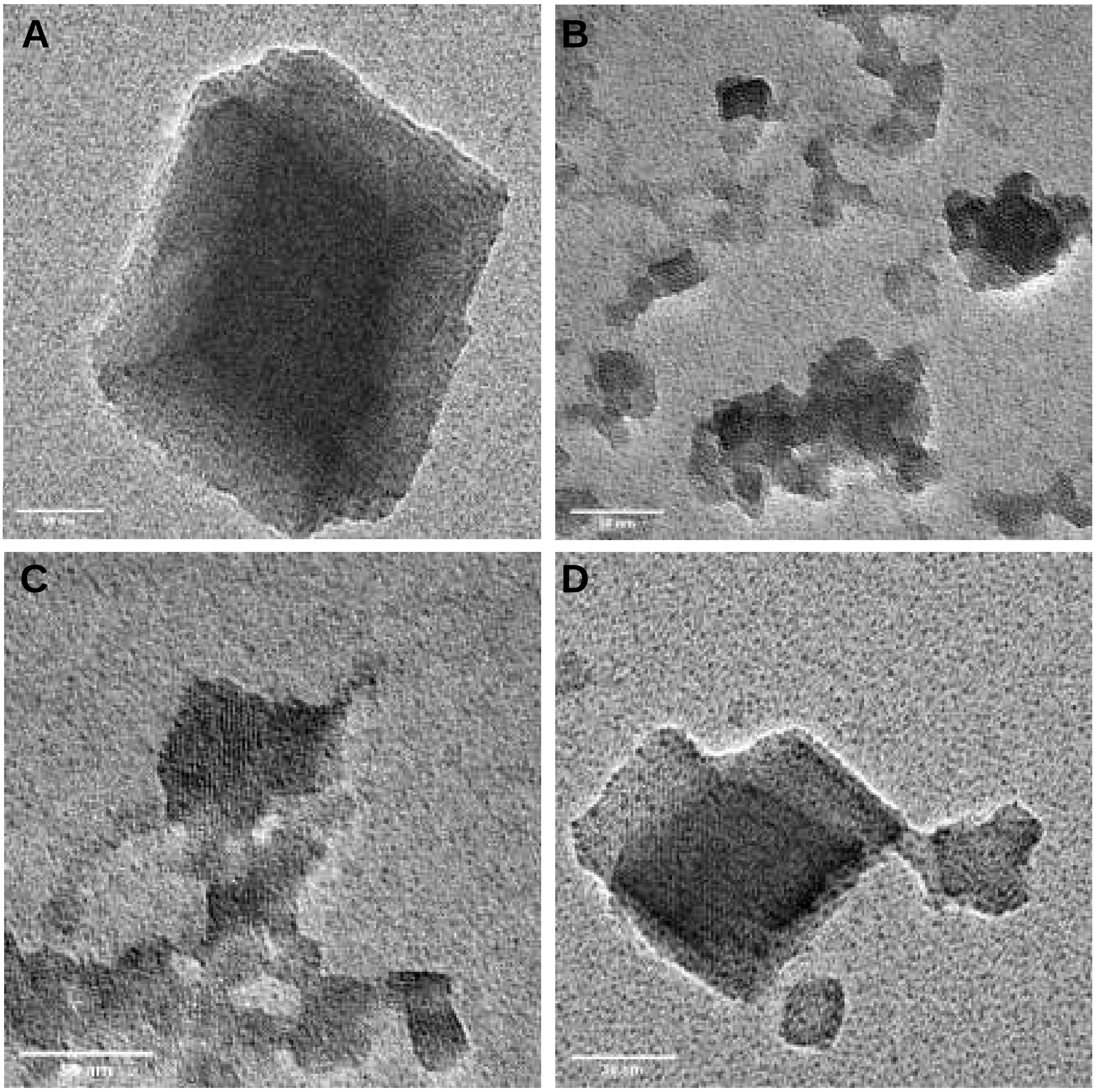

Fig. S5 TEM images from $Ag_{29}C$ crystallites. Early signs of beam induced nanoparticle formation can be seen in D.

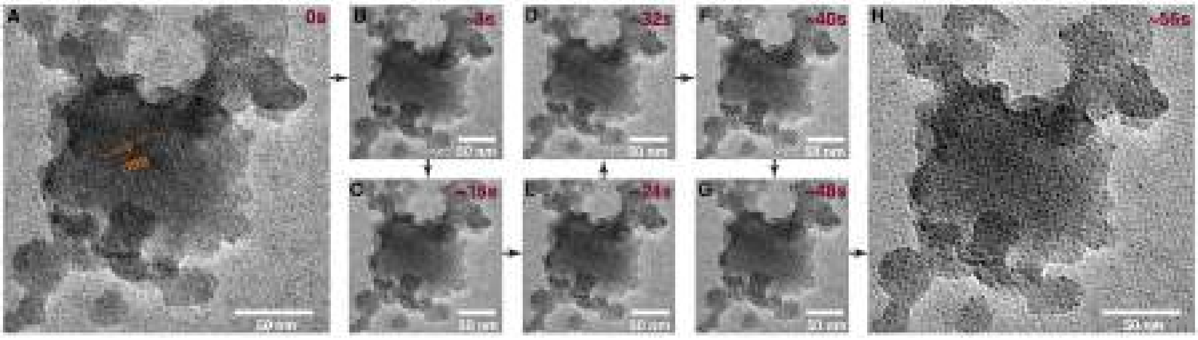

Fig. S6 Systematic transformation in a piece of $Ag_{29}C$ crystal, during extended exposure. Time of exposure is mentioned on the images.

At the beginning of imaging there is hardly any noticeable particle growth on the crystallites. As the experiment advanced, the time through which the crystallite is exposed to the electron beam increases, and we start seeing noticeable particle growth on the crystallites. After approximately 56s, there is considerable particle growth.

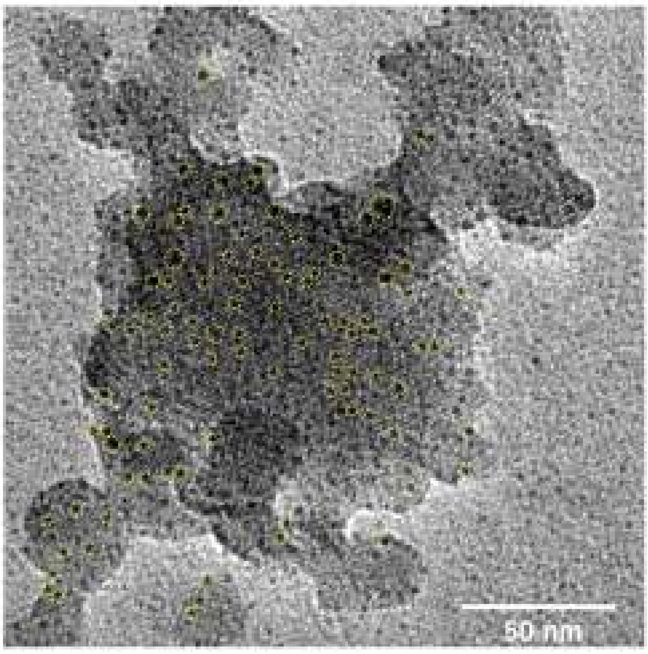

Fig. S7 TEM image of a crystallite after approximately 56s exposure to electron beam. A few of the particles are highlighted. Particles of different sizes, varying from 0.2 nm to 3.8 nm are visible.

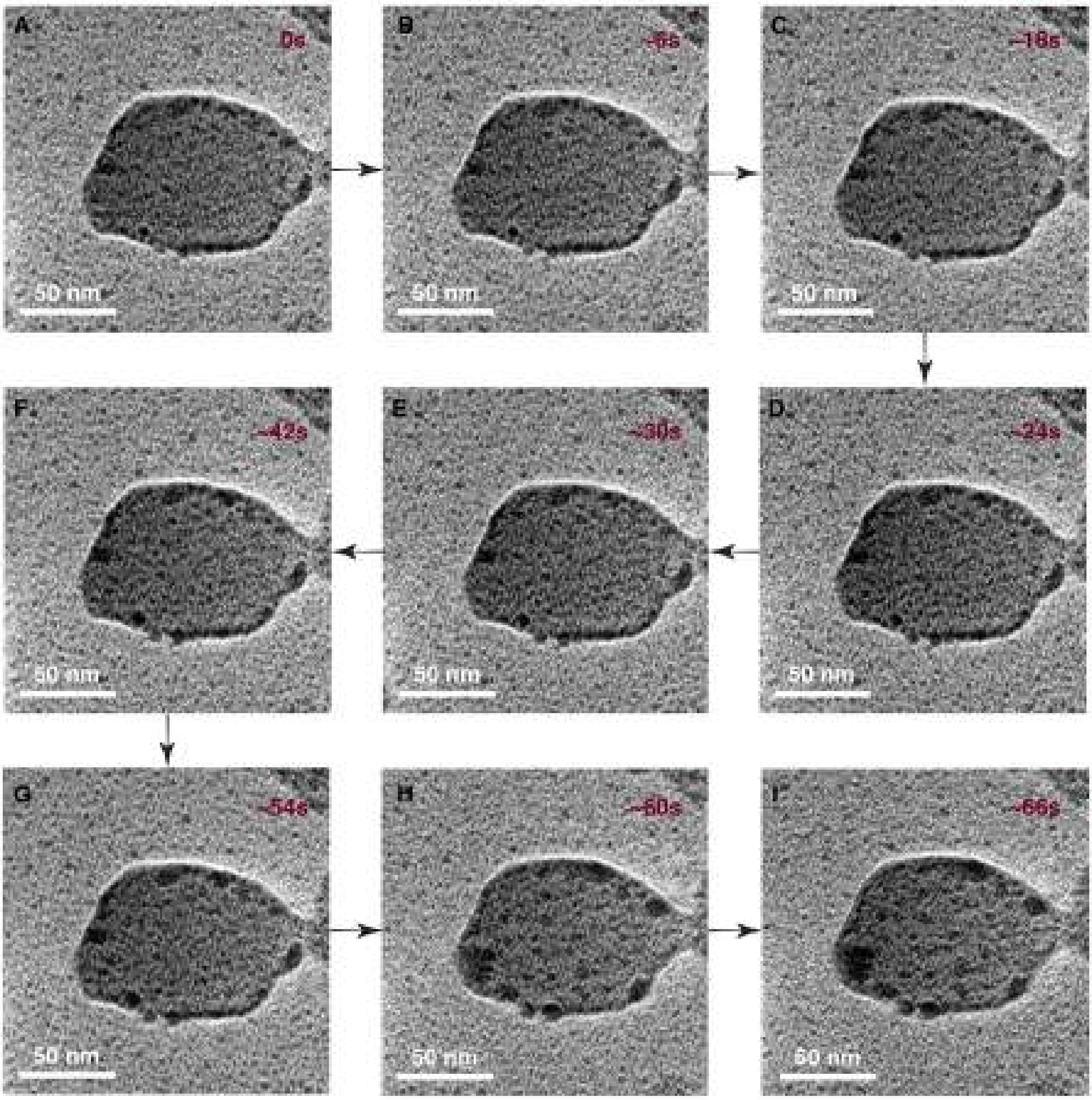

Fig. S8 Systematic transformation in another $Ag_{29}C$ crystallite, during extended exposure. Time of exposure is mentioned on the images.

Beyond approximately 60s, the particle growth becomes predominant and lattice planes of cluster crystals are no more imageable.

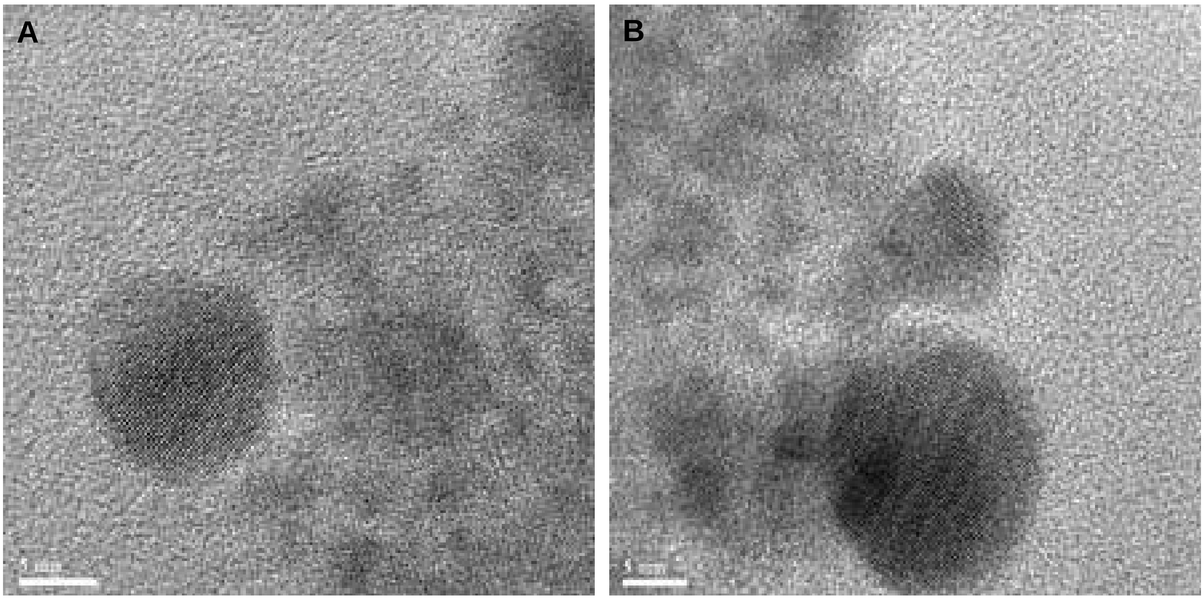

Fig. S9 Fused nanoparticles formed upon exposure beyond ~2 min, showing lattice resolution.

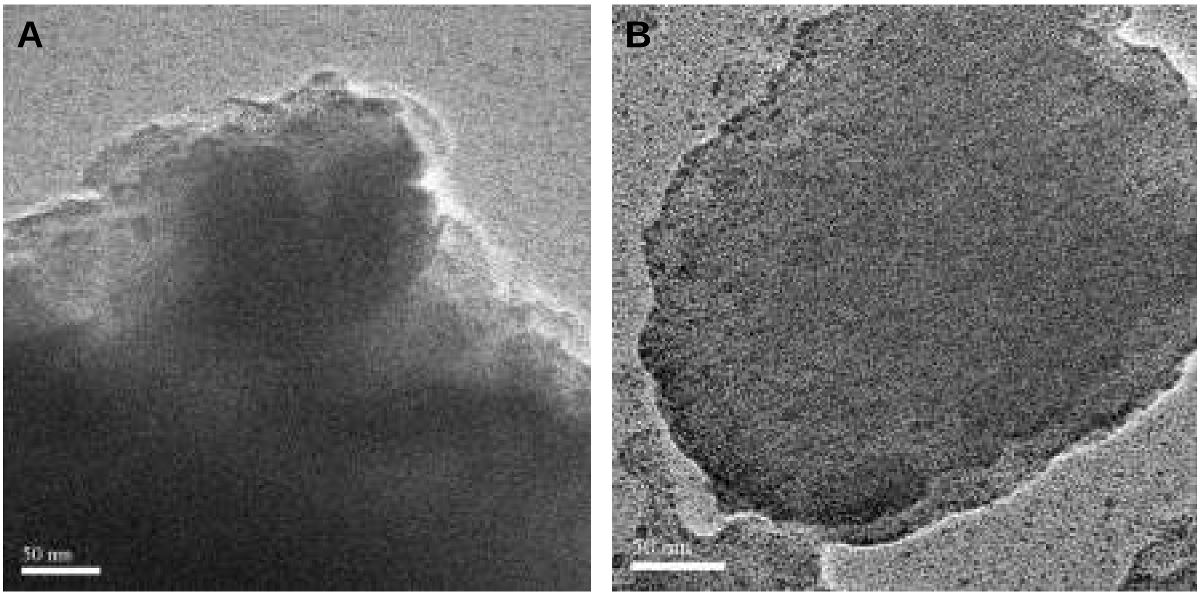

Fig. S10 TEM images from thicker $Ag_{29}C$ crystallites. The electron beam was opaque to these crystallites.

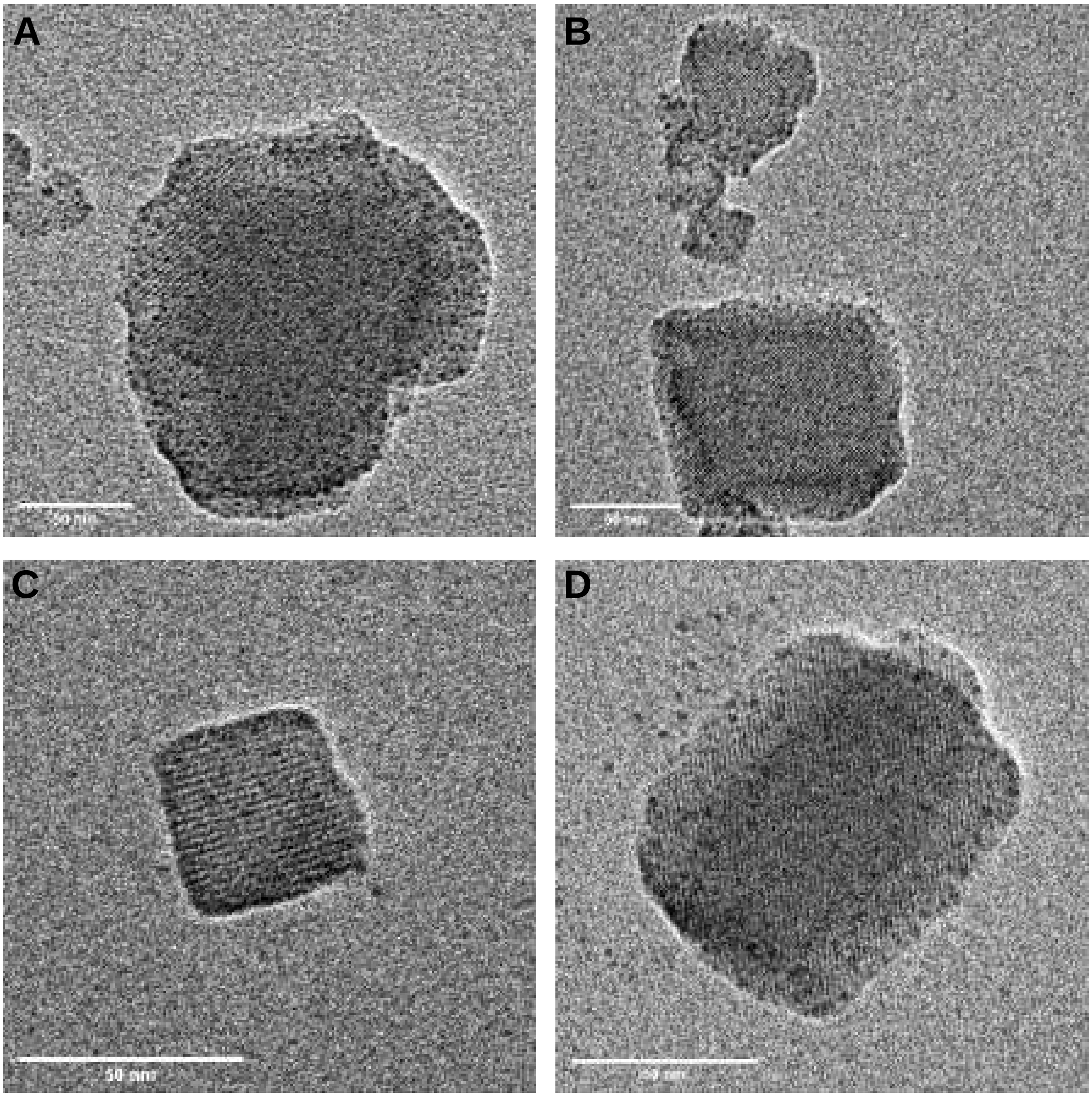

Fig. S11 TEM images from $Ag_{29}T$ crystallites. Early signs of beam induced nanoparticle formation can be seen in all crystallites.

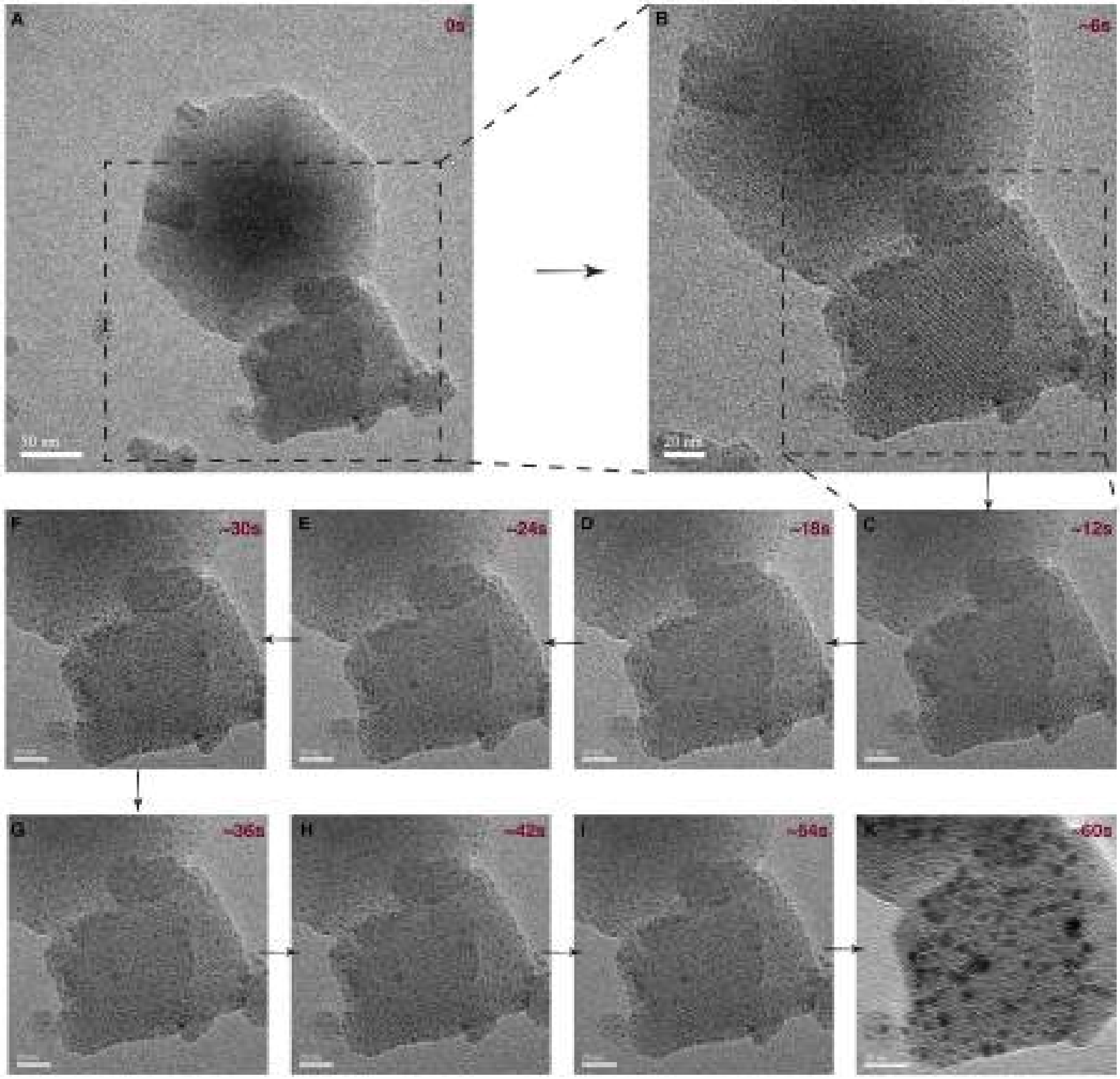

Fig. S12 Systematic transformation happening to an $Ag_{29}T$ crystallite, during extended exposure.

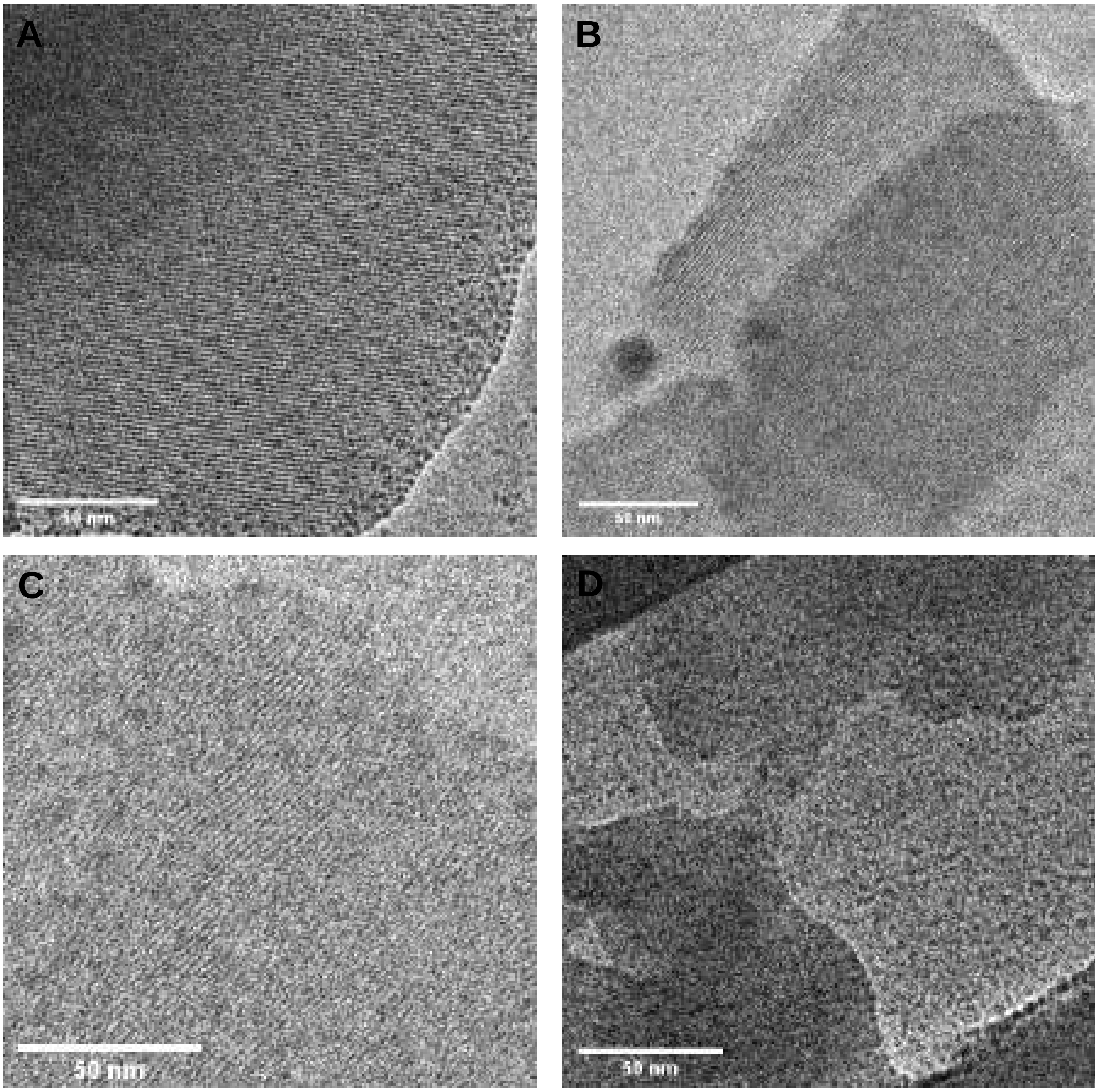

Fig. S13 TEM images from Ag_{25} crystallites. Early signs of beam induced nanoparticle formation can be seen in (A) and (D).

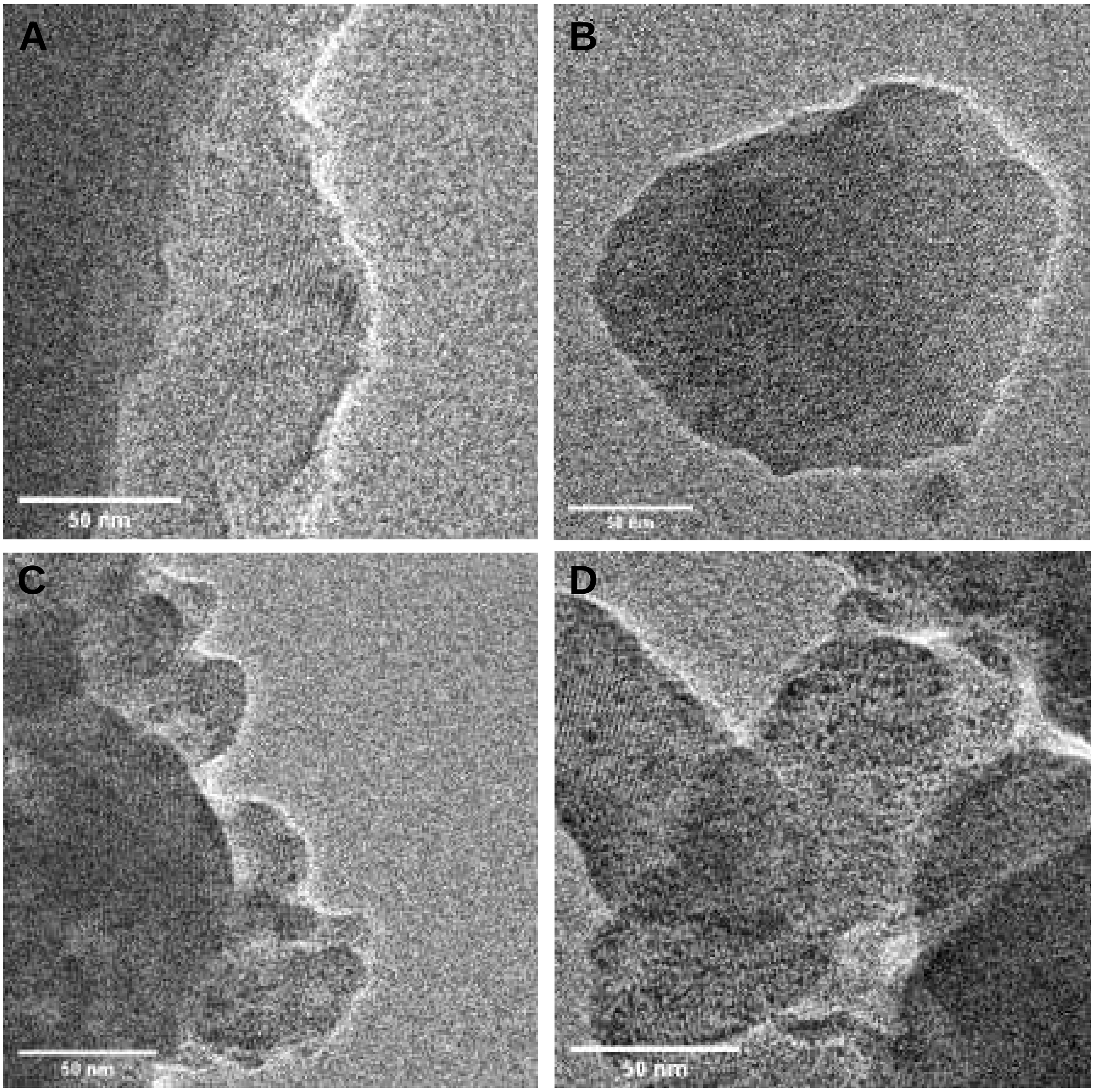

Fig. S14 TEM images of $Ag_{29}C$ crystallites dispersed in water. Beam induced damage is seen in D.

Calculation of theoretical lattice spacing for various planes

The theoretical lattice spacing in various planes in $Ag_{29}C$, $Ag_{29}T$ and Ag_{25} were calculated from the standard formula corresponding to their crystal symmetry.

$Ag_{29}C$ has a cubic symmetry, so the following formula was used:

$$\frac{1}{d^2} = \frac{h^2 + k^2 + l^2}{a^2}$$

The following crystal parameters, as reported,[1] were use:

a = b = c = 34.2011 Å

$\alpha = \beta = \gamma = 90°$

Table S4 Lattice spacing of some selected planes in $Ag_{29}C$

(hkl)	d (nm)
(100), (010), (001), ($\bar{1}00$), ($0\bar{1}0$), ($00\bar{1}$)	3.42
(110), (101), (011), ($\bar{1}10$), ($\bar{1}01$), ($01\bar{1}$), ($1\bar{1}0$), ($10\bar{1}$), ($0\bar{1}1$), ($\bar{1}\bar{1}0$), ($\bar{1}0\bar{1}$), ($0\bar{1}\bar{1}$)	2.42
(111), ($\bar{1}\bar{1}\bar{1}$), ($\bar{1}11$), ($1\bar{1}1$), ($11\bar{1}$), ($\bar{1}\bar{1}1$), ($\bar{1}1\bar{1}$), ($1\bar{1}\bar{1}$)	1.97
(200), (020), (002), ($\bar{2}00$), ($0\bar{2}0$), ($00\bar{2}$)	1.71
(210), (201), (021), (120), (102), (012), ($\bar{2}10$), ($\bar{2}01$), ($01\bar{2}$), ($\bar{1}20$), ($\bar{1}02$), ($02\bar{1}$), ($2\bar{1}0$), ($20\bar{1}$), ($02\bar{1}$), ($0\bar{1}2$), ($\bar{2}\bar{1}0$), ($\bar{2}0\bar{1}$), ($0\bar{2}\bar{1}$), ($\bar{1}\bar{2}0$), ($\bar{1}0\bar{2}$), ($0\bar{1}\bar{2}$)	1.52

$Ag_{29}T$ has a trigonal symmetry, so the following formula for a hexagonal lattice was used:

$$\frac{1}{d^2} = \frac{4}{3}\left(\frac{(h^2 + hk + l^2)}{a^2}\right) + \frac{l^2}{c^2}$$

The following crystal parameters, as reported,[3] were used:

a = b = 27.46 Å

c = 46.65 Å

$\alpha = \beta = 90°$

$\gamma = 120°$

Table S5 Lattice spacing of some selected planes in $Ag_{29}T$

(hkl)	d (nm)
(100), (010), ($\bar{1}00$), ($0\bar{1}0$),	2.38
(011), (101), ($0\bar{1}\bar{1}$), ($\bar{1}0\bar{1}$), ($0\bar{1}1$), ($\bar{1}01$)	2.12
(012), ($10\bar{2}$), ($\bar{1}0\bar{2}$), ($0\bar{1}\bar{2}$), ($\bar{1}02$), ($0\bar{1}2$), ($10\bar{2}$), ($01\bar{2}$)	1.66
(110), ($\bar{1}\bar{1}0$), ($2\bar{1}0$), ($\bar{1}20$), ($\bar{2}10$), ($1\bar{2}0$)	1.373

Ag_{25} has a triclinic symmetry, so the following formula was used:

$$\frac{1}{d^2} = \frac{1}{V^2}(S_{11}h^2 + S_{22}k^2 + S_{33}l^2 + 2S_{12}hk + 2S_{23}kl + 2S_{13}hl)$$

where

$$S_{11} = b^2c^2sin^2\alpha$$

$$S_{22} = a^2c^2sin^2\beta$$

$$S_{33} = a^2b^2sin^2\gamma$$

$$S_{12} = abc^2(\cos\alpha\cos\beta - \cos\gamma)$$

$$S_{23} = a^2bc(\cos\beta\cos\gamma - \cos\alpha)$$

$$S_{13} = ab^2c(\cos\gamma\cos\alpha - \cos\beta)$$

The following crystal parameters, as reported,[2] were used

a = 19.0634 Å

b = 19.5919 Å

c = 26.7981 Å

$\alpha = 93.424°$

$\beta = 90.859°$

$\gamma =$ 104.756°

V = 9656.7 $Å^3$

Table S6 Lattice spacing of some selected planes in Ag_{25}

(hkl)	d (nm)
(010), $(0\bar{1}0)$	1.89
$(\bar{1}00)$, (100)	1.84
$(0\bar{1}1)$, $(01\bar{1})$	1.59

$(10\bar{1}), (\bar{1}01)$	1.53

Calculation of experimental lattice spacing for various planes

The TEM images were analysed using ImageJ software. The scale bar is calibrated from the value obtained from TEM. Following this, a fast Fourier transform (FFT) pattern was generated from the area where lattice planes were observed. An inverse FFT pattern was generated by selecting an appropriate spot from the FFT pattern. In this inverse FFT pattern, the lines correspond to the lattice planes. A plot profile corresponding to a line drawn perpendicular to the pattern can be generated from which lattice distance was calculated.

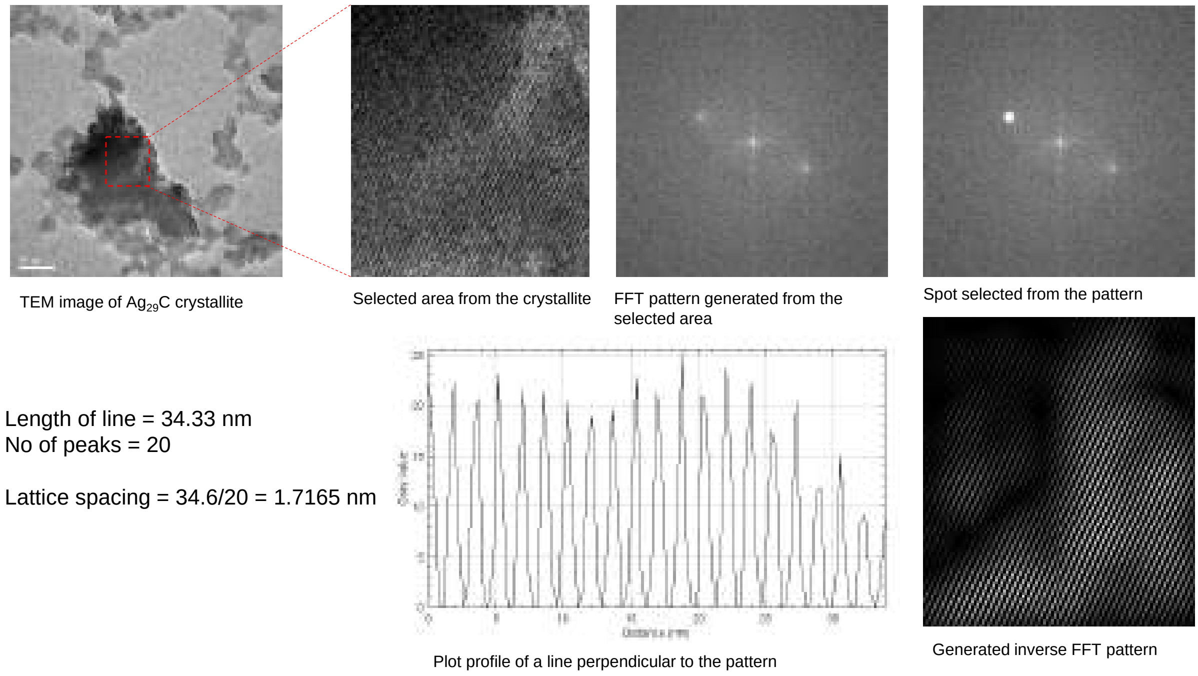

TEM image of $Ag_{29}C$ crystallite

Selected area from the crystallite

FFT pattern generated from the selected area

Spot selected from the pattern

Length of line = 34.33 nm
No of peaks = 20

Lattice spacing = 34.6/20 = 1.7165 nm

Plot profile of a line perpendicular to the pattern

Generated inverse FFT pattern

Fig. S15 Method used for calculating lattice distances from the experimental data.

References

1 L. G. AbdulHalim, M. S. Bootharaju, Q. Tang, S. Del Gobbo, R. G. AbdulHalim, M. Eddaoudi, D. Jiang and O. M. Bakr, *J. Am. Chem. Soc.*, 2015, **137**, 11970–11975.

2 C. P. Joshi, M. S. Bootharaju, M. J. Alhilaly and O. M. Bakr, *J. Am. Chem. Soc.*, 2015, **137**, 11578–11581.

3 A. Nag, P. Chakraborty, M. Bodiuzzaman, T. Ahuja, S. Antharjanam and T. Pradeep, *Nanoscale*, 2018, **10**, 9851–9855.

PCCP

ROYAL SOCIETY OF CHEMISTRY

PAPER

View Article Online
View Journal | View Issue

Check for updates

Cite this: *Phys. Chem. Chem. Phys.*, 2021, **23**, 24052

Received 24th August 2021,
Accepted 5th October 2021

DOI: 10.1039/d1cp03872a

rsc.li/pccp

Desorption-induced evolution of cubic and hexagonal ices in an ultrahigh vacuum and cryogenic temperatures†

Gaurav Vishwakarma, Jyotirmoy Ghosh and Thalappil Pradeep *

Reflection absorption infrared spectroscopic investigations of multilayer films of acetonitrile (ACN) and water in an ultrahigh vacuum under isothermal conditions showed the emergence of cubic (ice I_c) and hexagonal (ice I_h) ices depending on the composition of the film. The experiments were conducted with a mixed film of 300 monolayers in thickness and the ACN : H_2O monolayer ratios were varied from 1 : 5 to 5 : 1. Mixed films were deposited at 10 K and warmed to 130–135 K, where ACN desorbed subsequently and IR spectral evolution was monitored continuously. While the emergence of ice I_c at 130 K has been reported, the occurrence of ice I_h at this temperature was seen for the first time. Detailed investigations showed that ice I_h can form at 125 K as well. Crystallization kinetics and activation energy (E_a) for the emergence of ice I_h were evaluated using the Avrami equation.

1 Introduction

The existence of water in diverse environments, as exotic as in space, is well known.[1–3] Water ice is known to exist in a number of amorphous as well as crystalline forms at different temperature and pressure conditions.[4–7] While ice I_h is the most dominant form in terrestrial conditions, it is known to exist above 150 K under an ultrahigh vacuum (UHV). The process of amorphous to crystalline transformation under UHV occurs generally by annealing the vapour deposited film, amorphous solid water (ASW), which involves multiple steps. At first, ASW is converted to ice I_c at temperatures between 100 and 150 K. This cubic form of ice is metastable in nature and is finally converted to the more stable ice I_h at temperatures higher than 150 K under an UHV,[8] a condition relevant to astrochemistry. However, ice I_c is, nowadays, termed as stacking-disordered ice (ice I_{sd}) as its structure contains cubic sequences interlaced with hexagonal sequences.[9,10]

Impurities/guest molecules lead to diverse phenomena in the host ice network ranging from hydrate formation[11–13] to varying phase behavior.[14,15] They also play a crucial role in the crystallization of water. For example, crystallization kinetics of H_2O can be enhanced by the addition of impurities like methanol, HCl and HNO_3. Different reasons have been suggested to explain these observations. While methanol-induced nucleation reduced the crystallization temperature,[16] excess proton (H^+) provided by HCl promoted the crystallization.[17] Minor amounts of HNO_3 also facilitated rapid crystallization.[18] Under high-pressure conditions, however, clathrate hydrates can be transformed to ice I_c upon their dissociation.[19–22] Mixed ices can be warmed to form gas hydrates in an UHV; our earlier studies showed that clathrate hydrates of acetone and formaldehyde formed by such methods were converted to ice I_c and ice I_h, respectively, in the range of 130–135 K.[12,23] In such conditions, however, the formation of both ice I_c and ice I_h was not shown from a single system. Crystallization of H_2O can also be achieved by several other methods such as annealing of amorphous ices,[24,25] supercooling of water droplets,[26–29] freezing of high-pressure ice phases followed by annealing[25,30–32] and freezing of water in confined geometries.[33–35] Hama *et al.*[36] showed that sublimation of a water/neon matrix leads to H_2O crystallization where sublimation of neon provided enough mobility to water molecules to cross the kinetic barrier of crystallization, even at 11–12 K. These studies suggest the rich diversity that is possible during the desorption of molecules from multicomponent ices.

ACN was detected in the molecular clouds Sgr B and Sgr A[37] and in comet Kohoutek.[38] Comets are condensed bodies of gas, ice and dust, and are known for their diversity in composition with H_2O as the most abundant species. But, in recent reports,[39–41] it was observed that comets (C/2016 R2 (Pan-STARRS) and 2I/Borisov) have a peculiar volatile composition with CO as the most abundant species. Volatiles are known to play a crucial role in the chemistry and physics of star

---

DST Unit of Nanoscience (DST UNS) and Thematic Unit of Excellence (TUE), Department of Chemistry, Indian Institute of Technology Madras, Chennai 600036, India. E-mail: pradeep@iitm.ac.in

† Electronic supplementary information (ESI) available: Isothermal time-dependent RAIR spectra, different crystallization parameters of H_2O, and TPD-MS spectra of ACN in different mixtures. See DOI: 10.1039/d1cp03872a

formation in such regions. The present work hints at the importance of the composition of volatiles on water-ice crystallization and thus may have a direct impact on catalysis,[8] cometary outbursts, and heat balance in the cometary bodies.[42] These phenomena can be modeled with the help of experiments conducted in an UHV under cryogenic conditions.

In the present study, we show that ice I_c and ice I_h can be formed selectively from mixed ices of ACN and H_2O by controlling their compositions. We found that a thin film with 1 : 5 ACN and H_2O mixture forms ice I_c while a thin film with 5 : 1 ACN and H_2O results in ice I_h after desorption of ACN from the ice film at 130–135 K. The existence of the two ice forms has been confirmed by using their unique IR spectral features. The rates of crystallization of the films were studied using the Avrami equation. The activation energy for the formation of ice I_h under this condition was slightly lower than the value reported earlier. The creation of different crystallographic forms of ices by composition control presents new possibilities for structural diversity in interstellar ice analogues.

2 Experimental section

2.1 Experimental setup

All the experiments were performed in an ultrahigh vacuum (UHV) chamber with a base pressure of $\sim 5 \times 10^{-10}$ mbar, discussed in detail elsewhere.[43] Briefly, the instrument is composed of three stainless steel UHV chambers: an ionization chamber, an octupole chamber, and a scattering chamber, used for low energy ion scattering of mass selected ions.[44–47] The instrument is equipped with reflection absorption infrared spectroscopy (RAIRS) and temperature-programmed desorption (TPD) mass spectrometry. Experiments were performed in the scattering chamber, fitted with a precision x–y–z–θ sample manipulator on which a closed-cycle helium cryostat (Coldedge Technologies) was mounted from the top, along with various probes focusing on the substrate. These vacuum chambers were pumped using a turbomolecular pumps, which were backed by several diaphragm pumps. A cold cathode gauge controlled using a MaxiGauge controller (Pfeiffer, Model TPG 256 A) monitored the vacuum in these chambers.

A highly polished Ru(0001) single crystal was used as substrate. The substrate was attached to a copper holder which in turn was connected at the tip of a closed-cycle helium cryostat (Zephyr HC-4A air-cooled compressor). The substrate temperature could be varied in a wide range of 8–1000 K with a temperature accuracy/uncertainty of 0.5 K. Different temperature sensors (K-type thermocouple and a platinum sensor) and a resistive heater (25 Ω) were connected to a temperature controller (Lakeshore, Model 336).

2.2 Sample preparation

Before preparing the sample, the metal substrate was heated to 400 K multiple times to ensure the cleanness of the surface. The substrate was polished and annealed at 1000 K prior to the present set of experiments. As the experiments were of multilayers and the results were insensitive to the impurities on the very top of the surface, detailed cleaning procedures were not necessary. ACN (RANKEM, 99.9%) and Millipore water (H_2O of 18.2 MΩ resistivity) were taken in a vacuum-sealed test tube (glass-to-metal seal) and further purified by several freeze–pump–thaw cycles. The samples were vapour-deposited on Ru(0001) using high-precision all-metal leak valves, one each exclusively for ACN and H_2O. The sample lines were kept near to the substrate for uniform growth of the thin ice films. During vapour deposition, mass spectra were recorded simultaneously to verify the purity, and to measure the ratio of the ACN and water vapours. Preparation of ice thin film was controlled through a leak valve and the coverage is expressed in monolayers (MLs), assuming 1.33×10^{-6} mbar s = 1 ML, which was estimated to contain $\sim 1.1 \times 10^{15}$ molecules cm^{-2}, as outlined in several reports.[11,48,49]

2.3 Experimental procedure

Thin films of 300 MLs of ACN and H_2O were created by backfilling the vacuum chamber at a total pressure of $\sim 5 \times 10^{-7}$ mbar for 10 minutes. Different ratios of ACN and H_2O (1 : 1, 1 : 5, and 5 : 1) were prepared at 10 K by keeping the total pressure constant and varying the inlet pressure of ACN and H_2O accordingly. For example, for the co-deposition (referred to as ACN : H_2O) of ACN and H_2O at a 1 : 1 ratio, the inlet pressure of ACN was $\sim 2.5 \times 10^{-7}$ mbar and that of H_2O was $\sim 2.5 \times 10^{-7}$ mbar. For the other ratios, the inlet pressures of ACN and H_2O were varied accordingly. Here, exposures were measured as the product of the dosing time and the increase in total chamber pressure for the dose. We followed a similar method of surface coverage to one reported previously.[48–50] However, the actual composition of the mixture may be different upon considering ionization sensitivity factors. The accepted sensitivity factor for water and ACN are 1.0 and 2.0, respectively.[51] For time-dependent as well as temperature-dependent studies, as prepared thin films were warmed at a rate of 5 K min^{-1} to the desired temperatures.

2.4 RAIRS setup

RAIR spectra were collected in the 4000–550 cm^{-1} range with a spectral resolution of 2 cm^{-1} using a Bruker Vertex 70 FT-IR spectrometer. The IR beam was taken out of the spectrometer using a gold-plated mirror and focused on the sample at an incident angle of 80° ± 7° through a ZnSe viewport. The reflected IR beam from the sample was re-focused using another gold-plated mirror to a liquid N_2 cooled mercury cadmium telluride (MCT) detector. The IR beam outside of the vacuum chamber was purged with dry N_2 to avoid background noise. To ensure better signal-to-noise ratio, each RAIR spectrum was averaged over 512 scans.

3 Results and discussion

We performed our study starting with the desorption behavior of ACN from 1 : 1 ice mixtures of ACN : H_2O in the range of 125–

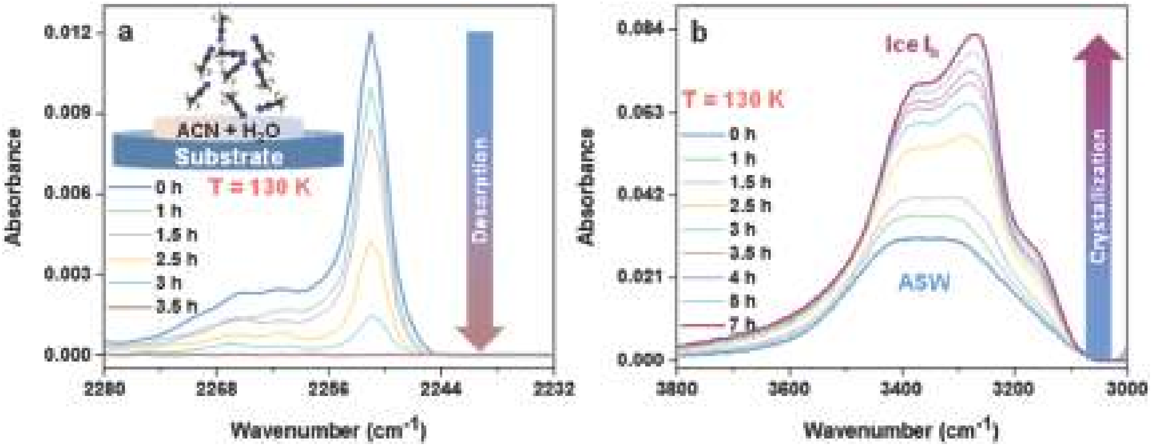

Fig. 1 Desorption induced ice crystallization. Isothermal time-dependent RAIR spectra of 300 MLs of 1 : 1 ACN : H_2O at 130 K in the (a) C≡N stretching region and (b) O–H stretching region. The film was co-deposited on Ru(0001) at 10 K and then heated at a rate of 5 K min^{-1} to 130 K. The C≡N stretching band at 2251 cm^{-1} vanished due to desorption of ACN which transformed the broad O–H stretching band centered at ~3350 cm^{-1} into ice I$_h$. The inset in (a) shows the desorption of ACN from an ice mixture at 130 K.

135 K. As mentioned in the experimental section, the ratios are in terms of molar concentrations, assuming the same sticking coefficient for both the species. Fig. 1 shows the time-dependent RAIR spectra of 300 MLs of 1 : 1 ACN : H_2O at 130 K. For this, mixed ice was co-deposited on Ru(0001) at 10 K and warmed to 130 K. The ice mixture was held at 130 K under vacuum for 7 h. Fig. 1a and b show time-dependent RAIR spectra at 130 K in the C≡N and O–H stretching regions, respectively. We will mainly focus on the C≡N stretch (2232–2280 cm^{-1}) and O–H stretch (3000–3800 cm^{-1}) where major changes were observed for the ACN : H_2O films. The spectra of 150 MLs of pure ACN and of 300 MLs of ACN : H_2O films with different ratios (1 : 1, 1 : 5, and 5 : 1) at 10 K are shown in Fig. S1A (ESI†) and the peak assignments for these are consistent with previous reports.[52,53] In Fig. 1a, at 0 h, corresponding to the first spectrum when the temperature equilibrates at 130 K, the C≡N stretching band shows a peak at 2251 cm^{-1} which is the characteristic peak of pure ACN at 130 K. This peak is due to the phase separation of ACN from the H_2O matrix as shown in Fig. S2b (ESI†), where the broad peak (2264 cm^{-1}, attributed to hydrogen-bonded ACN with H_2O)[44,54] at 10 K was reduced in intensity and shifted to 2251 cm^{-1} (attributed to pure ACN) at 130–135 K, as reported in our previous study.[44] This was further confirmed by comparing the RAIR spectra of 150 MLs of pure ACN (Fig. S3, ESI†) with the spectra in Fig. 1a. The 2251 cm^{-1} peak disappeared within 3.5 h due to the desorption of ACN from the ice mixture and is comparable to the desorption of 150 MLs of pure ACN within 3 h from the substrate, as shown in Fig. S3b (ESI†). The desorption behavior of ACN can be seen in the TPD mass spectra shown in Fig. S1B (ESI†), for different mixtures.

In Fig. 1b, the O–H stretching band showed a major change due to the desorption of ACN with time, at 130 K. At 0 h, the broad peak centered at ~3350 cm^{-1} (after the phase separation of ACN from the ice mixture), is a distinctive feature of ASW. At 130 K, ACN desorbed gradually from the ice matrix and the broad peak centered at ~3350 cm^{-1} was red-shifted, manifesting an increase in order and number of H-bonded H_2O molecules.[55] The peak gradually became sharp and was spilt within 7 h. Sharpening and splitting of the O–H stretching band were attributed to the crystallization of the ice film. The band splits, giving three peaks positioned at 3375, 3275, and 3165 cm^{-1}, were assigned to ice I$_h$. These assignments were confirmed by comparing the O–H stretching band of the ice film left after desorption of ACN at 130 K and of pure crystalline ice I$_h$, as shown in Fig. S4a (ESI†). Both the bands are equivalent, which confirmed the formation of ice I$_h$ after desorption of ACN at 130 K. However, as shown in Fig. S4a (ESI†), the high-frequency shoulder at ~3380 cm^{-1} increases in amplitude slightly for pure crystalline ice I$_h$ (red trace) compared to ice *I*$_h$ obtained from mixed ice (black trace) and this rise is attributed to the presence of grain-boundary water in the former case.[56] Furthermore, to confirm that ice crystallization is a desorption assisted process, we carried out two experiments. First, we performed an isothermal time-dependent RAIR study of 300 MLs of ACN : H_2O in a 1 : 1 ratio at 120 K as shown in Fig. S8 (ESI†). Desorption of ACN (shown in Fig. S8b, ESI†) was not complete even after 51 h as the peak at 2251 cm^{-1} did not vanish completely. In turn, the broad peak at ~3350 cm^{-1} of the O–H stretching band shown in Fig. S8a (ESI†) remained broad, suggesting no crystallization. Also, we performed an isothermal time-dependent RAIR experiment of 150 MLs of solid H_2O film at 130 K, as shown in Fig. S9 (ESI†). Self-crystallization of a solid H_2O film was not observed even after 19 h. This proved that desorption of ACN from an ice mixture assists in crystallization of ice at a lower temperature than its normal crystallization temperature of 155 K.

Ice I$_h$ was formed *via* ACN desorption from 1 : 1 ACN : H_2O films even at 125, 127, and 135 K as shown in Fig. S5–S7 (ESI†). We observed that with decreasing temperature, the time required for the desorption of ACN and crystallization of ice increased. Here, it was evident that desorption assisted ice I$_h$

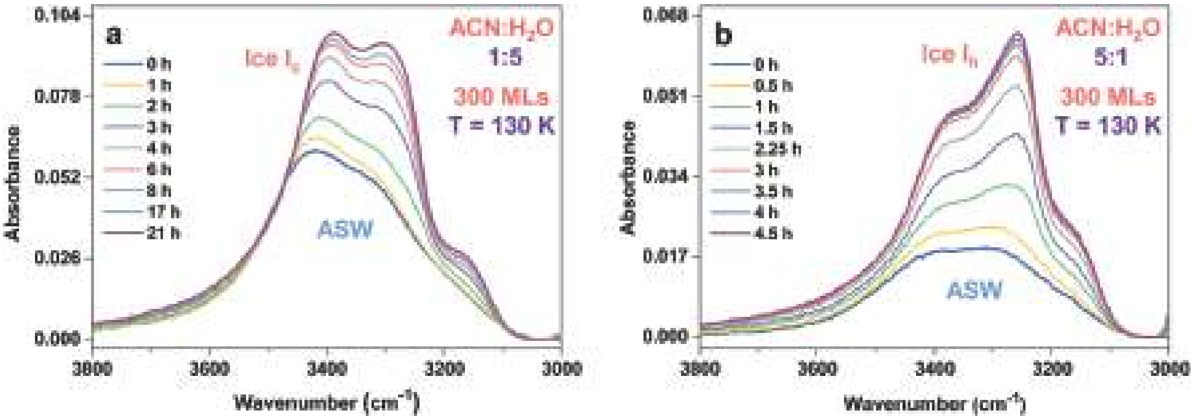

Fig. 2 (a) Time-dependent RAIR spectra of 300 MLs of 1 : 5 ACN : H_2O film at 130 K in the O–H stretching region. The film was co-deposited on Ru(0001) at 10 K and then heated at a rate of 5 K min^{-1} to 130 K. The first spectrum (*t* = 0 h) is from a completely amorphous film and the last spectrum (*t* = 21 h) is from a completely crystallized ice film. (b) Time-dependent RAIR spectra of 300 MLs of the 5 : 1 ACN : H_2O film at 130 K in the O–H stretching region. The film was co-deposited on Ru(0001) at 10 K and then heated at a rate of 5 K min^{-1} to 130 K. The first spectrum (*t* = 0 h) is from a completely amorphous film and the last spectrum (*t* = 4.5 h) is from a completely crystallized ice film.

crystallization follows certain kinetics. The crystallization kinetics of ice formation is of major importance for both terrestrial as well as extraterrestrial science. Isothermal time-dependent RAIR spectra of 1 : 1 ACN : H_2O films at 125, 127, 130, and 135 K were used to evaluate the crystallization kinetics. These data are described in the Crystallization Kinetics section. Furthermore, the effect of the composition of the ice film on ice crystallization was also studied for ACN : H_2O ratios of 1 : 5 and 5 : 1. The larger the fraction of ACN molecules in the ASW film, the faster the desorption of ACN and consequently the diffusion of H_2O molecules. Fig. 2a shows the isothermal time-dependent RAIR spectra in the O–H stretching region of 300 MLs of 1 : 5 ACN : H_2O film at 130 K. The associated desorption behavior of ACN from the ice film is shown in Fig. S10a (ESI†), where the C$\equiv$N stretching band consists of two types of peaks, attributed to hydrogen-bonded ACN (broad peak around 2266 cm^{-1})[54] and free ACN (peak at 2251 cm^{-1}), respectively, at 130 K at 0 h. At 130 K, while the ACN phase separated for an ACN : H_2O ratio of 1 : 1, the occurrence of a broad peak at 2266 cm^{-1} for 1 : 5 ACN : H_2O was surprising. Here, ACN could not phase-separate completely from the ice film even at 130 K because the number of ACN molecules was less and most of them were trapped in the ASW matrix. Several theoretical studies suggest[57–59] that ACN molecules can form a hydrate cluster (CH_3CN)-$(H_2O)_n$ ($n > 1$) with varying number of H_2O molecules which could also be a reason for ACN not being phase-separated at 130 K for the 1 : 5 ACN : H_2O film. Because of the cluster formation between ACN and H_2O, complete desorption of ACN from the ice film took a longer time of 4 h than the 1 : 1 ACN : H_2O film. This restricted ACN desorption can also be seen in the TPD mass spectra shown in Fig. S1B (ESI†). The marked (with red star) desorption hump around 132 K along with the main desorption peak at ~140 K are attributed to the restricted ACN desorption from the 1 : 5 ACN : H_2O film during annealing. On the other hand, the O–H stretching region showed (in Fig. 2a) a prominent change with the restricted desorption of ACN from the film. The ASW feature at 0 h gradually became sharp and split into three peaks namely, 3395, 3290 and 3165 cm^{-1}, with time. These features of the O–H stretching band correspond to ice I_c, (Fig. S4b, ESI†) and are consistent with previous studies[12,60,61] including our earlier study[12] where we correlated the RAIRS and reflection high-energy electron diffraction (RHEED) data under similar experimental conditions. Limited (due to the smaller amount of ACN in the 1 : 5 ACN : H_2O film) and obstructed (due to the cluster formation) desorption of ACN molecules from the ice film gave restricted mobility to the H_2O molecules. In turn, ASW was restricted to metastable ice I_c even after 21 h at 130 K. We performed similar isothermal time-dependent RAIR experiments for the 1 : 5 ACN : H_2O film at 133 and 135 K and obtained similar results leading to ice I_c as shown in Fig. S11, and S12, respectively (ESI†).

We performed another isothermal time-dependent experiment of 300 MLs with 5 : 1 ACN : H_2O at 130 K. The O–H stretching region is shown in Fig. 2b and the associated ACN desorption behavior is shown in Fig. S10b (ESI†). At 0 h, the C$\equiv$N stretching band at 2251 cm^{-1} (the same as obtained for the 1 : 1 ACN : H_2O film) shown in Fig. S10b (ESI†) obtained after phase separation of ACN from the ice mixture at 130 K vanished within 3 h due to rapid desorption of the ACN molecules. The desorption of a large number of ACN molecules from the ice matrix provided a sufficiently high mobility to the H_2O molecules. These mobile H_2O molecules arranged most stably and resulted in ice I_h within 4.5 h. It is evident that the ice I_h formation from the 5 : 1 ACN : H_2O film was faster than that of the 1 : 1 ACN : H_2O film as expected due to bulk desorption of ACN in the former case. We obtained a similar result for the 5 : 1 ACN : H_2O films at 133 and 135 K, shown in Fig. S13 and S14 (ESI†). Thus, we can form ice I_c and ice I_h selectively depending on the ice film compositions.

Formation of crystalline ice requires a sufficiently high mobility of water molecules for diffusion and molecular rearrangement.[36] When ACN and water are co-deposited at 10 K, it forms a well-mixed system. Upon warming above 100 K, ACN molecules were phase-separated from water-ice[44] but they remain in the ice matrix. We suggest that during phase separation, ACN being a larger molecule, will increase the mobility/diffusion of water molecules, which will be further increased by the subsequent desorption of ACN after keeping the mixture at a given temperature for several hours. This desorption of the ACN molecules is the trigger for the diffusion/mobility of water that leads to the accelerated crystallization. In the case of the 1 : 5 mixture, due to the phase separation of smaller quantities of ACN and their desorption, ASW crystallization is restricted to metastable ice I_c.

The present study and earlier reports on methanol,[16] acetone[12] and formaldehyde[23] show that the kinetics of crystallization is affected by the specific additives that are incorporated in the ASW film and a specific reason has been given for each. There may be one or several effects that might be causing the lowering of the onset temperature of crystallinity; it could be the desorption temperature, size, chemical nature or morphology of the co-deposited molecules. In the present case, it is the desorption (temperature) of the co-adsorbed molecule, which is affecting the crystallization kinetics of ASW. It may require additional theoretical as well as experimental investigations to correlate the effect of different molecules on ASW crystallization.

Crystallization kinetics

Time-dependent RAIR spectra of 1 : 1 ACN : H_2O films were utilized to evaluate the crystallization of ASW under isothermal conditions at the corresponding temperatures (125, 127, 130, and 135 K, shown in Fig. 1b and Fig. S5–S7, ESI†). The volatile O–H stretching bands of RAIRS were utilized to estimate the crystallization kinetics of ASW crystallization in previous reports.[12,17,23,62,63] Here, we adopted a similar approach.

Fig. 3(a) shows the time-dependent RAIR spectra for 300 MLs of 1 : 1 ACN : H_2O film kept at 127 K. The first spectrum (0 h trace) in Fig. 3a is from a completely amorphous film and the last spectrum (21 h) is from a completely crystalline film. The intermediate spectra represent the progress of crystallization and are a combination of pure amorphous and pure crystalline spectra. The vertical dashed line at a fixed wavenumber (3268 cm^{-1}) was used to evaluate the crystallization fraction for each temperature.

Fig. 3b shows the crystallization fraction *versus* time obtained from vertical cuts through the time series spectra of O–H starching bands for a set of isothermal time-dependent experiments (shown in Fig. S5a, S6a and S7a, ESI†), analogous to those shown in Fig. 3a at different temperatures. The crystallization fraction, $x(t)$ was calculated by eqn (1),

$$x(t) = \frac{\Delta A(1)}{\Delta A(2)} \tag{1}$$

where $\Delta A(1)$ is the difference in the absorbance at a particular time t and that at time zero, and $\Delta A(2)$ is the difference in absorbance of a completely crystallized film and that of a completely amorphous film.

In Fig. 3b the change of the shape of the curve from sigmoidal to an exponential, manifests an increase in crystallization kinetics with increasing temperature.[12,17] Various crystallization parameters for ASW were evaluated by fitting the crystallization fraction to the Avrami equation[64,65] at different temperatures. The Avrami equation is

$$x(t) = 1 - \exp\,(-k{\cdot}t)^n \tag{2}$$

where k is the rate constant, t is time, and n is an exponent. For all temperatures, n can hold close to integer values between 1 to 4 and this predicts the nature of the crystallization process. After arranging eqn (2) in linear form, the equation becomes

$$\ln(-\ln[1 - x(t)]) = n\ln(t) + n\ln k \tag{3}$$

Fig. 4a shows $\ln(-\ln[1 - x(t)])$ *versus* $\ln(t)$ plotted for different temperatures using eqn (3). The slope and intercept of linearly fitted lines were utilized to estimate the value of n and k for different temperatures. The obtained values of n and

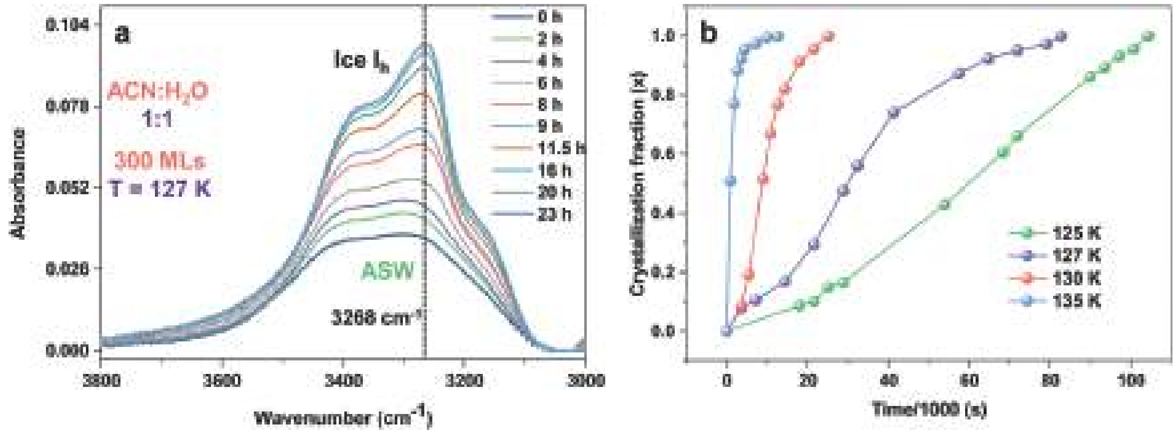

Fig. 3 (a) Time-dependent RAIR spectra of 300 MLs of the 1 : 1 ACN : H_2O film at 127 K in the O–H stretching region. The film was co-deposited on Ru(0001) at 10 K and heated at a rate of 5 K min^{-1} to 127 K. (b) Crystallization fraction *versus* time for 300 MLs of the 1 : 1 ACN : H_2O film obtained from isothermal RAIR measurements at 125, 127, 130, and 135 K. The crystallization fraction was calculated from a vertical cut at 3268 cm^{-1} in the O–H stretching band for a set of time-dependent RAIRS spectra shown in Fig. 1a and Fig. S5a, S6a, and S7a (ESI†).

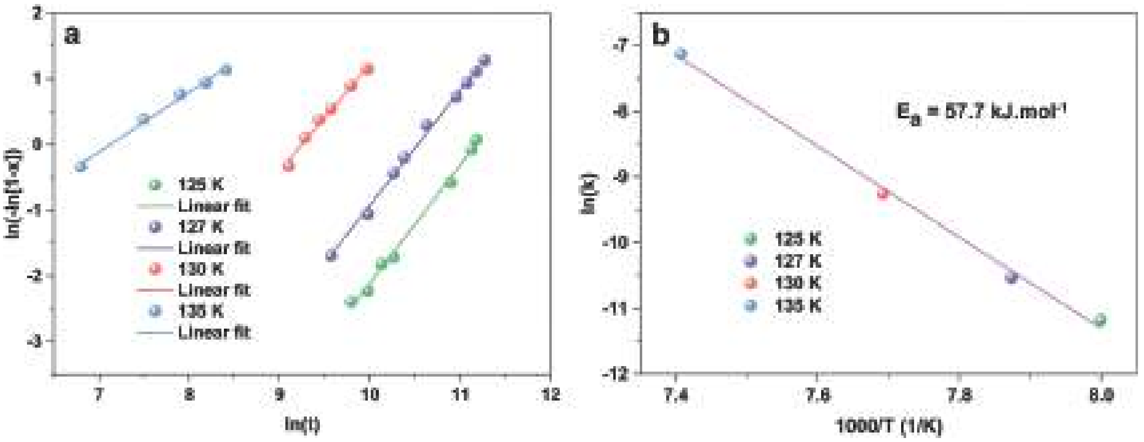

Fig. 4 A plot of the linearized form of the Avrami equation for ASW crystallization. Plots of ln(−ln[1 − x]) *vs.* ln(t) at different temperatures of 125, 127, 130, and 135 K were made using the O–H stretching bands. The obtained data points were fitted using the Avrami equation. (b) Arrhenius plot of ln k *versus* (1/T), achieved from the analysis the slope and intercept of the linearly fitted lines of plot (a) for different temperatures. The activation energy (E_a) of ice crystallization was calculated from the slope of the linearly fitted straight line of plot (b).

k are listed in Table S1 (ESI†). The estimated value of k in this study is larger than the previously reported values estimated in similar experimental conditions,[23,62] which, further, presents evidence for accelerated crystallization.

The value obtained for n was between 1.80 to 0.90 for different temperatures. With the input of previous studies we note that for the evaluated value of n, crystallization kinetics is a diffusion-controlled phenomenon with particles growing into predominantly spherical geometry,[12,23,62,63,66–68] and it is evident that ACN desorption from an ice mixture provides enough mobility for water volatile molecules for rearrangement and crystallization. However, crystallization of ASW gives an n value equal to ∼4, and suggests three-dimensional growth and random nucleation.[62,69,70] Our values of n are, however, lower and suggest low dimensional growth. This is reasonable because ACN is undergoing phase separation but within the ice-matrix in the form of small domains. These domains can be present at bulk and at interfaces in the ice-matrix. When the ACN molecules desorbed form such domains, they will induce (diffusion/mobility) crystallization and will prevent three-dimensional growth.[12,23] The activation energy (E_a) of ice crystallization was estimated from the slope of the linearly fitted line of the Arrhenius plot (Fig. 4b, ln k *versus* (1/T)). The evaluated activation energy in this study was ∼57.7 kJ mol^{-1} and it is comparable with that of the previously reported value for the crystallization of pure ASW.[17,62,69,71,72] Here, early ice I_h crystallization from 1 : 1 ACN : H_2O films can be attributed to the desorption assisted mobility of H_2O molecules. Due to sufficient mobility, H_2O molecules occupied the thermodynamically most stable sites and resulted in ice I_h at a lower temperature (125–135 K) than the usual ice I_h crystallization temperature.

4 Conclusions

We have established an isothermal route for the formation of either ice I_c and ice I_h, induced by the desorption of ACN from ice mixtures depending upon their compositions at 130–135 K in an UHV. We were also able to form ice I_h at 125 K which is a much lower temperature than the usual crystallization temperature in UHV conditions. Associated crystallization kinetics for ice I_h and the activation energy of crystallization were evaluated by using isothermal time-dependent RAIR spectra at 125–135 K for a 1 : 1 ACN : H_2O film. We assumed that the extent of desorption of ACN and relative (simultaneous) diffusion of H_2O molecules played an important role in ice crystallization at low temperatures. Such studies will be of importance in astrophysical environments or ISM.

Author contributions

T. P. proposed the project and supervised the progress. G. V. designed and performed the experiments. G. V and J. G. analyzed the results. The manuscript was written through contributions of all the authors.

Conflicts of interest

The authors declare no competing financial interests.

Acknowledgements

We acknowledge the Science and Engineering Research Board (SERB), Department of Science and Technology (DST), Government of India for research funding. We thank Dr Bhalamurugan Sivaraman and Dr Rabin Rajan J. Methikkalam for helpful comments and discussions. We also thank Mr Bijesh Malla, Mr Chandan Bhat, Mr Pillalamarri Srikrishnarka, and Dr Tripti Ahuja for their valuable input in relation to this work. G. V. thanks IITM for his research fellowship. J. G. acknowledges IIT Madras for an institute postdoctoral fellowship.

References

1 A. C. Cheung, D. M. Rank, C. H. Townes, D. D. Thornton and W. J. Welch, Detection of water in interstellar regions by its microwave radiation, *Nature*, 1969, **221**, 626–628.

2 E. L. Gibb, D. C. B. Whittet, A. C. A. Boogert and A. G. G. M. Tielens, Interstellar Ice: The Infrared Space Observatory Legacy, *Astrophys. J., Suppl. Ser.*, 2004, **151**, 35–73.

3 W. J. Gillett and F. C. Forrest, Spectra of the Becklin-Neugebauer point source and the Kleinmann-Low nebula from 2.8 to 13.5 microns, *Astrophys. J.*, 1973, **179**, 483–491.

4 T. Bartels-Rausch, V. Bergeron, J. H. E. Cartwright, R. Escribano, J. L. Finney, H. Grothe, P. J. Gutié Rrez, J. Haapala, W. F. Kuhs, J. B. C. Pettersson, S. D. Price, I. Sainz-Díaz, D. J. Stokes, G. Strazzulla, E. S. Thomson, H. Trinks and N. Uras-Aytemiz, Ice structures, patterns, and processes: A view across the ice-fields, *Rev. Mod. Phys.*, 2012, **84**, 885.

5 C. A. Angell, Amorphous Water, *Annu. Rev. Phys. Chem.*, 2004, **55**, 559–583.

6 T. Loerting, K. Winkel, M. Seidl, M. Bauer, C. Mitterdorfer, P. H. Handle, C. G. Salzmann, E. Mayer, J. L. Finney and D. T. Bowron, How many amorphous ices are there?, *Phys. Chem. Chem. Phys.*, 2011, **13**, 8783–8794.

7 C. G. Salzmann, P. G. Radaelli, B. Slater and J. L. Finney, The polymorphism of ice: Five unresolved questions, *Phys. Chem. Chem. Phys.*, 2011, **13**, 18468–18480.

8 N. Watanabe and A. Kouchi, Ice surface reactions: A key to chemical evolution in space, *Prog. Surf. Sci.*, 2008, **83**, 439–489.

9 W. F. Kuhs, C. Sippel, A. Falenty and T. C. Hansen, Extent and relevance of stacking disorder in 'ice Ic', *Proc. Natl. Acad. Sci. U. S. A.*, 2012, **109**, 21259–21264.

10 T. L. Malkin, B. J. Murray, C. G. Salzmann, V. Molinero, S. J. Pickering and T. F. Whale, Stacking disorder in ice I, *Phys. Chem. Chem. Phys.*, 2014, **17**, 60–76.

11 J. Ghosh, R. R. J. Methikkalam, R. G. Bhuin, G. Ragupathy, N. Choudhary, R. Kumar and T. Pradeep, Clathrate hydrates in interstellar environment, *Proc. Natl. Acad. Sci. U. S. A.*, 2019, **116**, 1526–1531.

12 J. Ghosh, R. G. Bhuin, G. Vishwakarma and T. Pradeep, Formation of Cubic Ice via Clathrate Hydrate, Prepared in Ultrahigh Vacuum under Cryogenic Conditions, *J. Phys. Chem. Lett.*, 2020, **11**, 26–32.

13 J. Ghosh, R. G. Bhuin, G. Ragupathy and T. Pradeep, Spontaneous Formation of Tetrahydrofuran Hydrate in Ultrahigh Vacuum, *J. Phys. Chem. C*, 2019, **123**, 16300–16307.

14 J. Ghosh, Propane and propane – water interactions: a study at cryogenic temperatures †, *Phys. Chem. Chem. Phys.*, 2018, **20**, 1838–1847.

15 R. G. Bhuin, R. R. J. Methikkalam, S. Bag and T. Pradeep, Diffusion and Crystallization of Dichloromethane within the Pores of Amorphous Solid Water, *J. Phys. Chem. C*, 2016, **120**, 13474–13484.

16 R. Souda, Effects of methanol on crystallization of water in the deeply supercooled region, *Phys. Rev. B: Condens. Matter Mater. Phys.*, 2007, **75**, 184116.

17 D. H. Lee and H. Kang, Acid-Promoted Crystallization of Amorphous Solid Water, *J. Phys. Chem. C*, 2018, **122**, 24164–24170.

18 S. M. McClure, E. T. Barlow, M. C. Akin, P. L. Tanaka, D. J. Safarik, T. M. Truskett and C. B. Mullins, Effect of dilute nitric acid on crystallization and fracture of amorphous solid water films, *J. Phys. Chem. C*, 2007, **111**, 10438–10447.

19 A. Falenty, T. C. Hansen and W. F. Kuhs, Cubic Ice Formation and Annealing during CO2 Clathrate Hydrate Decomposition at Low Temperatures, *Phys. Chem. Ice*, 2010, 411.

20 A. Falenty and W. F. Kuhs, 'Self-Preservation' of CO2 Gas Hydrates-Surface Microstructure and Ice Perfection, *J. Phys. Chem. B*, 2009, **113**, 15975–15988.

21 W. F. Kuhs, G. Genov, D. K. Staykova and T. Hansen, Ice perfection and onset of anomalous preservation of gas hydrates, *Phys. Chem. Chem. Phys.*, 2004, **6**, 4917–4920.

22 S. Takeya, T. Uchida, J. Nagao, R. Ohmura, W. Shimada, Y. Kamata, T. Ebinuma and H. Narita, Particle size effect of CH4 hydrate for self-preservation, *Chem. Eng. Sci.*, 2005, **60**, 1383–1387.

23 J. Ghosh, G. Vishwakarma, S. Das and T. Pradeep, Facile Crystallization of Ice I h via Formaldehyde Hydrate in Ultrahigh Vacuum under Cryogenic Conditions, *J. Phys. Chem. C*, 2021, **125**, 4532–4539.

24 L. G. Dowell and A. P. Rinfret, Low-temperature forms of ice as studied by X-ray diffraction, *Nature*, 1960, **188**, 1144–1148.

25 J. A. McMillan and S. C. Los, Vitreous ice: Irreversible transformations during warm-up, *Nature*, 1965, **206**, 806–807.

26 E. Mayer and A. Hallbrucker, Cubic ice from liquid water, *Nature*, 1987, **325**, 601–602.

27 T. L. Malkin, B. J. Murray, A. V. Brukhno, J. Anwar and C. G. Salzmann, Structure of ice crystallized from supercooled water, *Proc. Natl. Acad. Sci. U. S. A.*, 2012, **109**, 1041–1045.

28 B. J. Murray, D. A. Knopf and A. K. Bertram, The formation of cubic ice under conditions relevant to Earth's atmosphere, *Nature*, 2005, **434**, 202–205.

29 B. J. Murray and A. K. Bertram, Formation and stability of cubic ice in water droplets, *Phys. Chem. Chem. Phys.*, 2006, **8**, 186–192.

30 Y. P. Handa, D. D. Klug and E. Whalley, Energies of the phases of ice at low temperature and pressure relative to ice Ih, *Can. J. Chem.*, 1988, **66**, 919–924.

31 J. E. Bertie, L. D. Calvert and E. Whalley, Transformations of ice II, Ice III, and ice v at atmospheric pressure, *J. Chem. Phys.*, 1963, **38**, 840–846.

32 V. Petrenko and R. Whitworth, *Physics of ice*, Oxford, 2002.

33 J. C. Dore, M. Dunn and P. Chieux, Neutron diffraction studies of ice nucleation in porous silica, *J. Phys., Colloq.*, 1987, **48**, 457–463.

34 D. C. Steytler, J. C. Dore and C. J. Wright, Neutron diffraction study of cubic ice nucleation in a porous silica network, *J. Phys. Chem.*, 1983, **87**, 2458–2459.

35 J. M. Baker, J. C. Dore and P. Behrens, Nucleation of ice in confined geometry, *J. Phys. Chem. B*, 1997, **101**, 6226–6229.

36 T. Hama, S. Ishizuka, T. Yamazaki, Y. Kimura, A. Kouchi, N. Watanabe, T. Sugimoto and V. Pirronello, Fast crystalline ice formation at extremely low temperature through water/neon matrix sublimation, *Phys. Chem. Chem. Phys.*, 2017, **19**, 17677–17684.

37 P. M. Solomon, K. B. Jefferts, A. A. Penzias and R. W. Wilson, Detection of Millimeter Emission Lines from Interstellar Methyl Cyanide, *Astrophys. J.*, 1971, **168**, L107.

38 B. L. Ulich and E. K. Conklin, Detection of methyl cyanide in Comet Kohoutek, *Nature*, 1974, **248**, 121.

39 A. J. McKay, M. A. DiSanti, M. S. P. Kelley, M. M. Knight, M. Womack, K. Wierzchos, O. H. Pinto, B. Bonev, G. L. Villanueva, N. Dello Russo, A. L. Cochran, N. Biver, J. Bauer, R. J. Vervack, E. Gibb, N. Roth and H. Kawakita, The peculiar volatile composition of co-dominated comet C/2016 R2 (PanSTARRS), *Astron. J.*, 2019, **158**, 128.

40 M. A. Cordiner, S. N. Milam, N. Biver, D. Bockelée-Morvan, N. X. Roth, E. A. Bergin, E. Jehin, A. J. Remijan, S. B. Charnley, M. J. Mumma, J. Boissier, J. Crovisier, L. Paganini, Y. J. Kuan and D. C. Lis, Unusually high CO abundance of the first active interstellar comet, *Nat. Astron.*, 2020, **4**, 861–866.

41 D. Bodewits, J. W. Noonan, P. D. Feldman, M. T. Bannister, D. Farnocchia, W. M. Harris, J. Y. Li, K. E. Mandt, J. W. Parker and Z. X. Xing, The carbon monoxide-rich interstellar comet 2I/Borisov, *Nat. Astron.*, 2020, **4**, 867–871.

42 J. Klinger, Extraterrestrial Ice. A Review, *J. Phys. Chem.*, 1983, **87**, 4209–4214.

43 S. Bag, R. G. Bhuin, R. R. J. Methikkalam, T. Pradeep, L. Kephart, J. Walker, K. Kuchta, D. Martin and J. Wei, Development of ultralow energy (1-10 eV) ion scattering spectrometry coupled with reflection absorption infrared spectroscopy and temperature programmed desorption for the investigation of molecular solids, *Rev. Sci. Instrum.*, 2014, **85**, 1–7.

44 R. G. Bhuin, R. R. J. Methikkalam, B. Sivaraman and T. Pradeep, Interaction of Acetonitrile with Water-Ice: An Infrared Spectroscopic Study, *J. Phys. Chem. C*, 2015, **119**, 11524–11532.

45 R. G. Bhuin, R. R. J. Methikkalam, S. Bag and T. Pradeep, Diffusion and Crystallization of Dichloromethane within the Pores of Amorphous Solid Water, *J. Phys. Chem. C*, 2016, **120**, 13474–13484.

46 R. R. J. Methikkalam, R. G. Bhuin, J. Ghosh, B. Sivaraman and T. Pradeep, Interaction of Acetonitrile with Alcohols at Cryogenic Temperatures, *J. Phys. Chem. C*, 2017, **121**, 2822–2835.

47 R. Rajan, J. Methikkalam, J. Ghosh, R. Gobinda Bhuin, S. Bag, G. Ragupathy and T. Pradeep, Iron assisted formation of CO 2 over condensed CO and its relevance to interstellar chemistry †, *Phys. Chem. Chem. Phys.*, 2020, **22**, 8491.

48 H. Kang, T. H. Shin, S. C. Park, I. K. Kim and S. J. Han, Acidity of hydrogen chloride on ice, *J. Am. Chem. Soc.*, 2000, **122**, 9842–9843.

49 Y. Kim, E. S. Moon, S. Shin and H. Kang, Acidic water monolayer on ruthenium(0001), *Angew. Chem., Int. Ed.*, 2012, **51**, 12806–12809.

50 J. E. Schaff and J. T. Roberts, Toward an understanding of the surface chemical properties of ice: Differences between the amorphous and crystalline surfaces, *J. Phys. Chem.*, 1996, **100**, 14151–14160.

51 J. E. Bartmess and R. M. Georgiadis, Empirical methods for determination of ionization gauge relative sensitivities for different gases, *Vacuum*, 1983, **33**, 149–153.

52 E. L. Pace and L. J. Noe, Infrared Spectra of Acetonitrile and Acetonitrile-d3, *J. Chem. Phys.*, 1968, **49**, 5317–5325.

53 M. P. Marzocchi and S. Dobos, Infrared spectra and crystal structure of CH3CN and CD3CN. Polarization and intensity measurements, *Spectrochim. Acta, Part A*, 1974, **30**, 1437–1444.

54 J. E. Schaff and J. T. Roberts, Interaction of Acetonitrile with the Surfaces of Amorphous and Crystalline Ice, *Langmuir*, 1999, **15**, 7232–7237.

55 E. H. G. Backus, M. L. Grecea, A. W. Kleyn and M. Bonn, Surface crystallization of amorphous solid water, *Phys. Rev. Lett.*, 2004, **92**, 236101.

56 T. Kondo, H. S. Kato, M. Kawai and M. Bonn, The distinct vibrational signature of grain-boundary water in nanocrystalline ice films, *Chem. Phys. Lett.*, 2007, **448**, 121–126.

57 A. Chaudhari and S. L. Lee, Density Functional study of hydrogen-bonded acetonitrile-water complex, *Int. J. Quantum Chem.*, 2005, **102**, 106–111.

58 D.-S. Ahn and S. Lee, Computational Study of σ-and π-type Hydrogen Bonding in Acetonitrile-Water Clusters, *Bull. Korean Chem. Soc.*, 2003, **24**, 545.

59 R. Gopi, N. Ramanathan and K. Sundararajan, Acetonitrile-water hydrogen-bonded interaction: Matrix-isolation infrared and ab initio computation, *J. Mol. Struct.*, 2015, **1094**, 118–129.

60 W. Hagen, A. G. G. M. Tielens and J. M. Greenberg, The infrared spectra of amorphous solid water and ice Ic between 10 and 140 K, *Chem. Phys.*, 1981, **56**, 367–379.

61 E. Whalley, A detailed assignment of the O–H stretching bands of ice I, *Can. J. Chem.*, 1977, **55**, 3429–3441.

62 R. S. Smith, J. Matthiesen, J. Knox and B. D. Kay, Crystallization kinetics and excess free energy of H2O and D2O nanoscale films of amorphous solid water, *J. Phys. Chem. A*, 2011, **115**, 5908–5917.

63 R. S. Smith, N. G. Petrik, G. A. Kimmel and B. D. Kay, Thermal and nonthermal physiochemical processes in nanoscale films of amorphous solid water, *Acc. Chem. Res.*, 2012, **45**, 33–42.

64 M. Avrami, Kinetics of phase change. I: General theory, *J. Chem. Phys.*, 1939, **7**, 1103–1112.

65 M. Avrami, Kinetics of phase change. II Transformation-time relations for random distribution of nuclei, *J. Chem. Phys.*, 1940, **8**, 212–224.

66 W. Hage, A. Hallbrucker, E. Mayer and G. P. Johari, Crystallization kinetics of water below 150 K, *J. Chem. Phys.*, 1994, **100**, 2743–2747.

67 R. H. Doremus, *Rates of phase transformations*, Academic Press, New York, 1985.

68 C. N. R. Rao and K. J. Rao, *Phase transitions in solids: an approach to the study of the chemistry and physics of solids*, McGraw-Hill, New York, 1978.

69 T. Kondo, H. S. Kato, M. Bonn and M. Kawai, Deposition and crystallization studies of thin amorphous solid water films on Ru(0001) and on CO-precovered Ru(0001), *J. Chem. Phys.*, 2007, **127**, 094703.

70 Z. Dohnálek, G. A. Kimmel, R. L. Ciolli, K. P. Stevenson, R. S. Smith and B. D. Kay, The effect of the underlying substrate on the crystallization kinetics of dense amorphous solid water films, *J. Chem. Phys.*, 2000, **112**, 5932–5941.

71 D. J. Safarik and C. B. Mullins, The nucleation rate of crystalline ice in amorphous solid water, *J. Chem. Phys.*, 2004, **121**, 6003–6010.

72 C. Yuan, R. S. Smith and B. D. Kay, Communication: Distinguishing between bulk and interface-enhanced crystallization in nanoscale films of amorphous solid water, *J. Chem. Phys.*, 2017, **146**, 031102.

Supplementary information

Desorption-induced Evolution of Cubic and Hexagonal Ices in Ultrahigh Vacuum and Cryogenic Temperatures

Gaurav Vishwakarma,† Jyotirmoy Ghosh,† and Thalappil Pradeep†*

†DST Unit of Nanoscience (DST UNS) and Thematic Unit of Excellence (TUE), Department of Chemistry, Indian Institute of Technology Madras, Chennai 600036, India

AUTHOR INFORMATION

Corresponding author

*Email: pradeep@iitm.ac.in

Table of Content

Supplementary Information 1A:

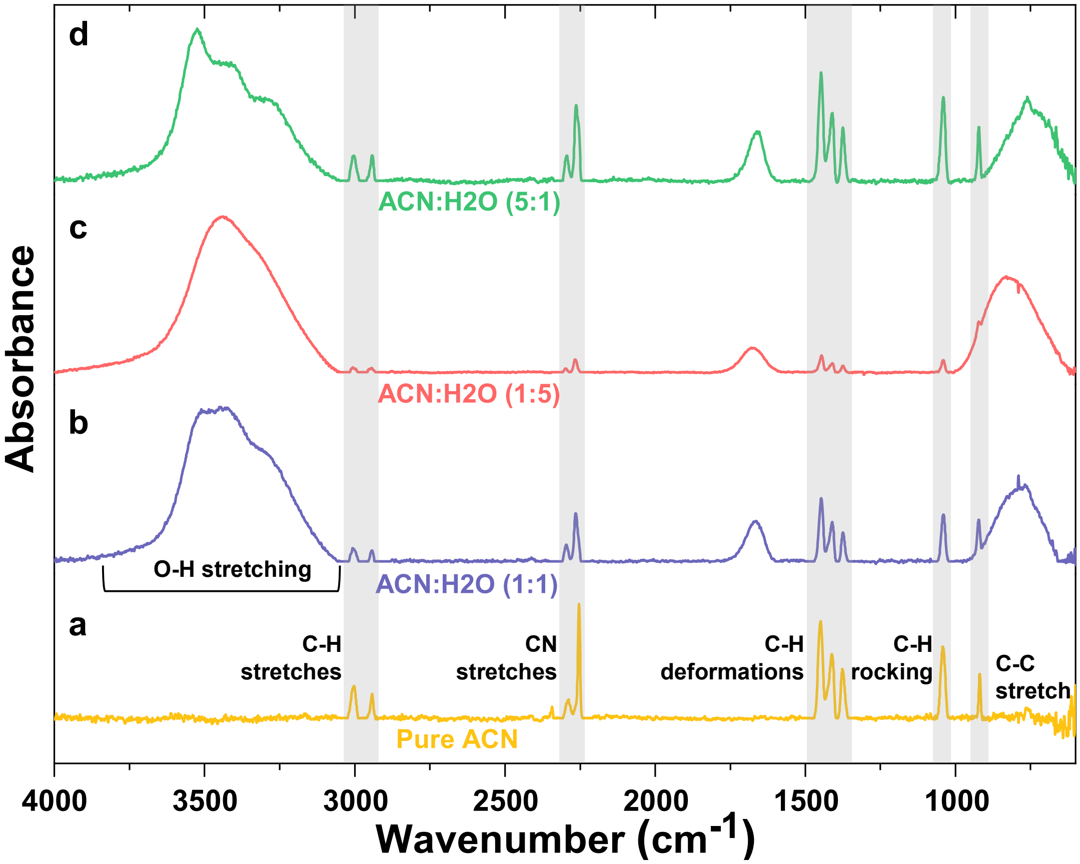

Fig. S1A RAIR spectra of (a)150 MLs of ACN, (b) 300 MLs of 1:1 ACN:H_2O, (c) 300 MLs of 1:5 ACN:H_2O, (d) 300 MLs of 5:1 ACN:H_2O at 10 K.

Supplementary Information 1B:

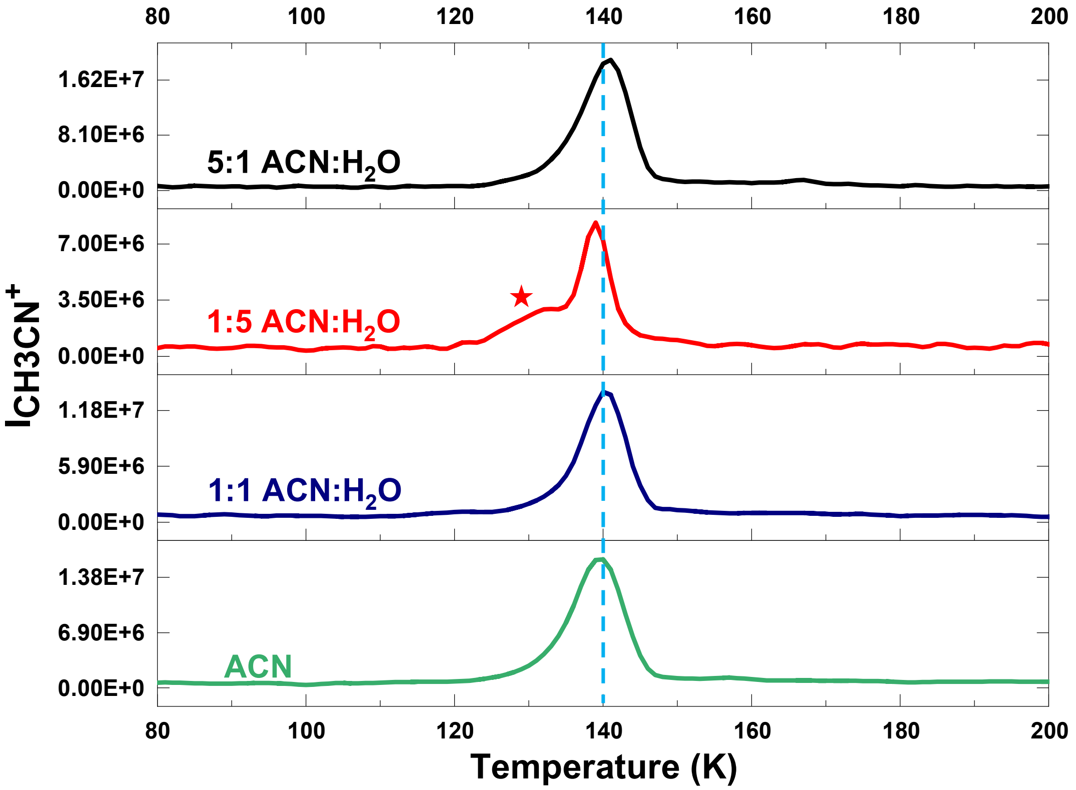

Fig. S2B TPD-MS spectra of 150 MLs of pure ACN (green), 300 MLs of 1:1 ACN:H_2O (blue), 300 MLs of 1:5 ACN:H_2O (red), and 300 MLs of 5:1 ACN:H_2O (black). Ramping rate = 10 K.min^{-1}. Here, the intensities of CH_3CN^+ (m/z = 41) under these conditions are plotted. The marked desorption (*) hump is due to the restricted ACN desorption from 1:5 ACN:H_2O film during annealing.

Supplementary information 2:

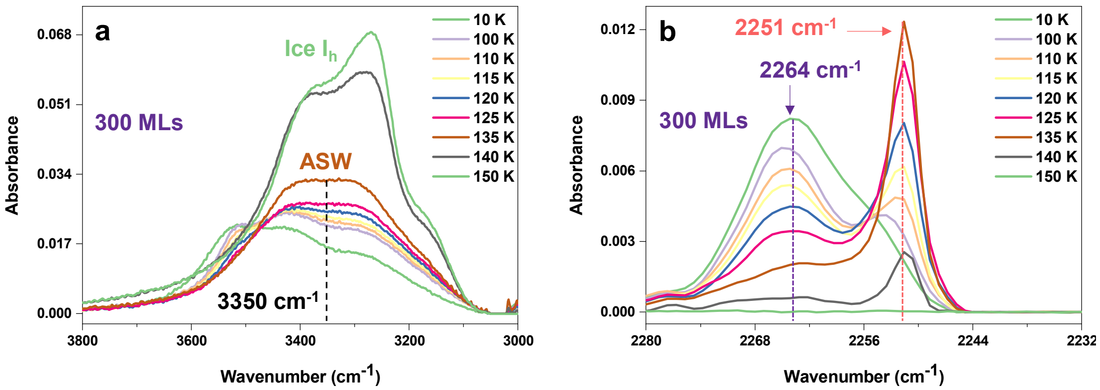

Figure S3 Temperature-dependent RAIR spectra of 300 MLs of 1:1 ACN:H_2O film co-deposited on Ru(0001) at 10 K and heated at a rate of 5 K min^{-1}. (a) O-H stretching region (b) C≡N stretching region.

Supplementary information 3:

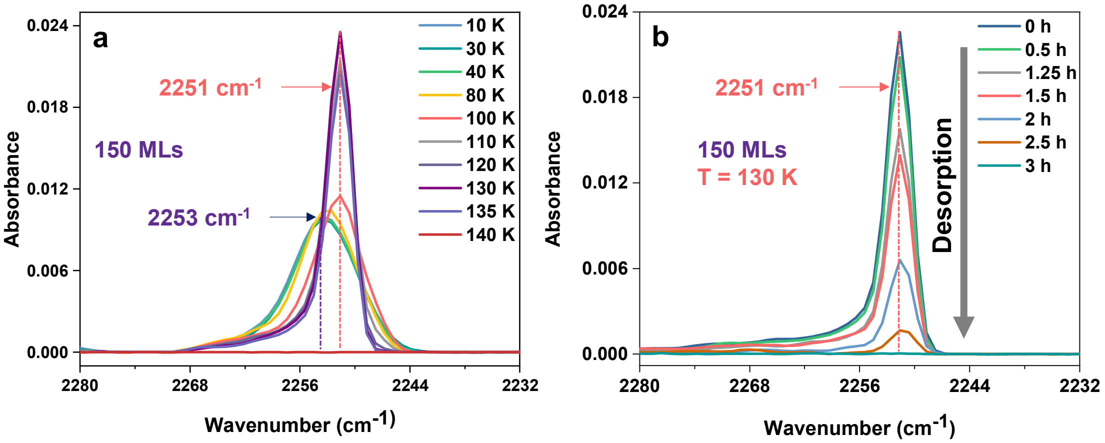

Fig. S4 RAIR spectra of 150 MLs of pure ACN in the C≡N stretching region. (a) Temperature-dependent spectra taken after ACN deposited at 10 K and heated at a rate of 5 K min^{-1} to the desorption temperature of ACN. ACN was found in two phases, where a low temperature amorphous phase (broad peak at ~ 2253 cm^{-1}) converted into crystalline phase (sharp peak at 2251 cm^{-1}) after 100 K.[1,2] (b) Isothermal time-dependent spectra at 130 K. The ACN vapour was deposited at 10 K and heated at a rate of 5 K min^{-1} to and kept at 130 K. ACN desorbed from substrate within 3 h.

Supplementary Information 4:

(a) Hexagonal Ice

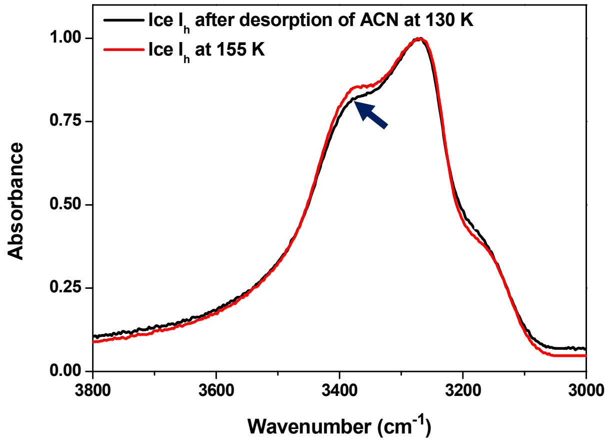

Fig. S5a RAIR spectra of Ice I$_h$ obtained after desorption of ACN from 300 MLs of 1:1 ACN:H_2O film at 130 K (black trace) and Ice I$_h$ obtained after heating 150 MLs of pure solid H_2O at 155 K (red trace) in the O-H stretching region. The spectra were normalized by the integral intensity of the absorbance. ACN:H_2O (1:1) film of 300 MLs and pure H_2O film of 150 MLs were prepared by depositing at 10 K and heating at a rate of 5 K min^{-1} to the mentioned temperatures. Both the spectrum were almost identical and confirms the formation of Ice I$_h$ after desorption of ACN from 1:1 ACN:H_2O film.

(b) Cubic Ice

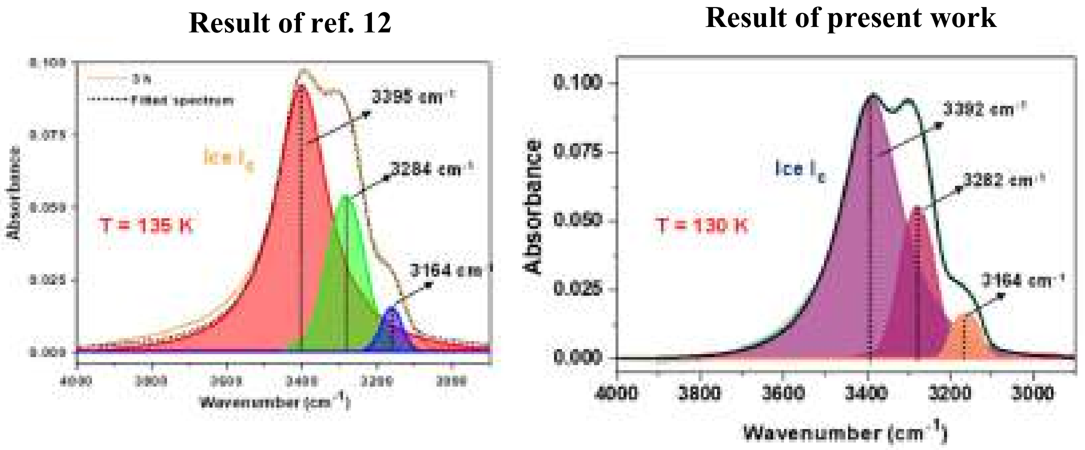
Result of ref. 12

Result of present work

Fig. S4b The deconvoluted features of IR data of ref. 12 (J. Phys. Chem. Lett. vol. 11 (2020) p. 26) and the current work. In ref. 12, Ice I$_c$ via acetone hydrate was prepared by annealing a co-deposited ~300 MLs acetone:H_2O (1:1) film to 135 K and maintaining it there in UHV for 3 h.

Supplementary Information 5:

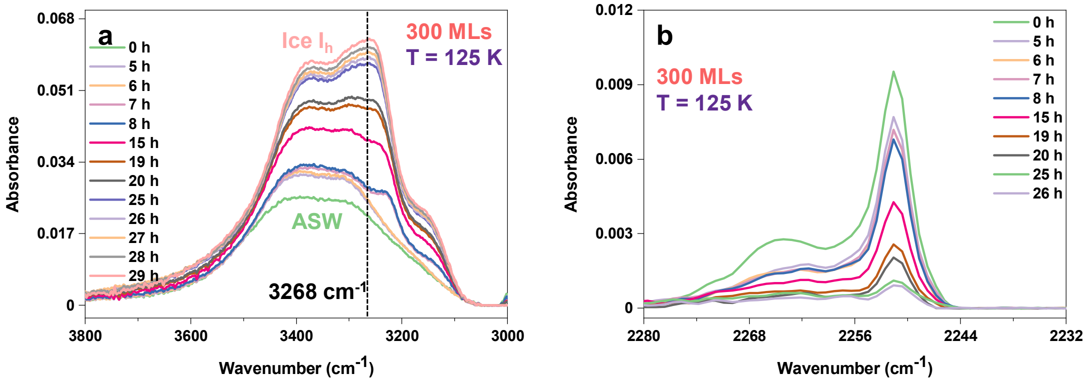

Fig. S6 Isothermal time-dependent RAIR spectra of 300 MLs of 1:1 ACN:H_2O film at 125 K in the (a) O-H stretching region and, (b) C≡N stretching region. Mixed film was prepared by vapour deposition on Ru(0001) at 10 K and heated to 125 K at a rate of 5 K min^{-1}.

Supplementary Information 6:

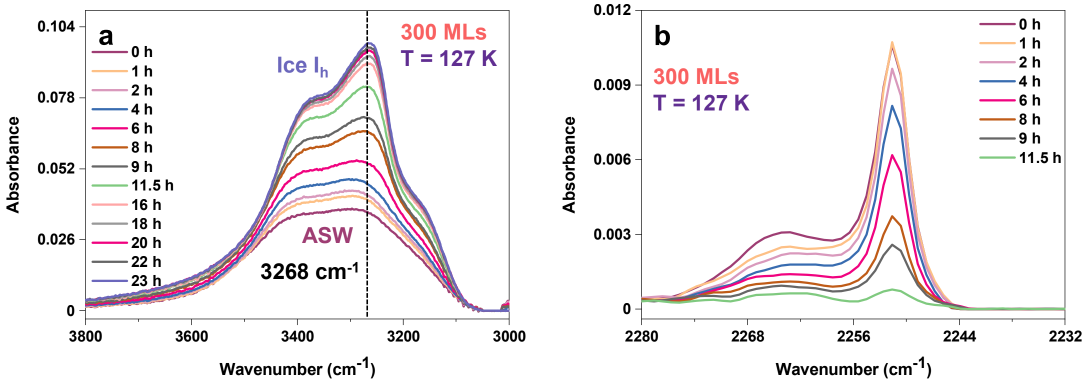

Fig. S7 Isothermal time-dependent RAIR spectra of 300 MLs of 1:1 ACN:H_2O film at 127 K in the (a) O-H stretching region and, (b) C≡N stretching region. Mixed film was prepared by vapour deposition on Ru(0001) at 10 K and heated to 127 K at a rate of 5 K min^{-1}.

Supplementary Information 7:

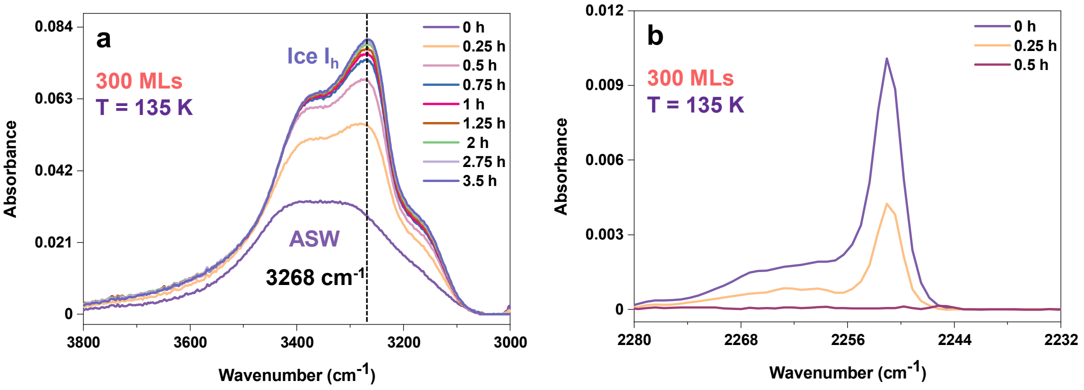

Fig. S8 Isothermal time-dependent RAIR spectra of 300 MLs of 1:1 ACN:H_2O film at 135 K in the (a) O-H stretching region and, (b) C≡N stretching region. Mixed film was prepared by vapour deposition on Ru(0001) at 10 K and heated to 135 K at a rate of 5 K min^{-1}.

Supplementary Information 8:

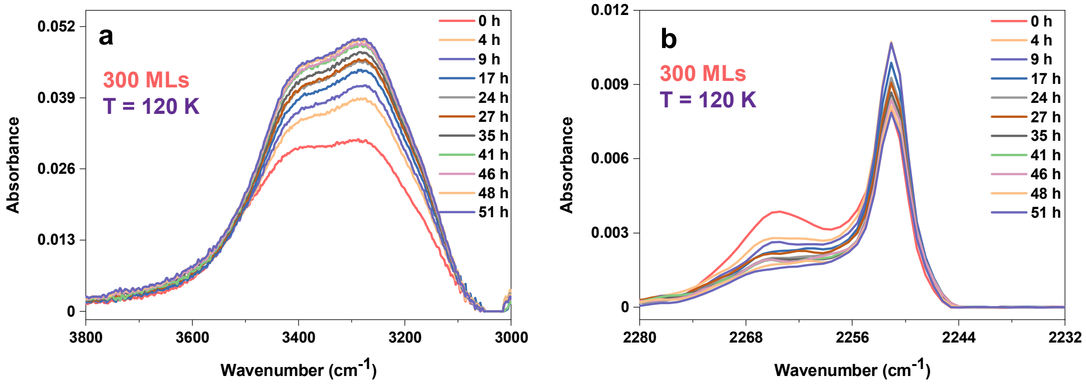

Fig. S9 Isothermal time-dependent RAIR spectra of 300 MLs of 1:1 ACN:H_2O film at 120 K in the (a) O-H stretching region and, (b) C≡N stretching region. Mixed film was prepared by vapour deposition on Ru(0001) at 10 K and heated to 120 K at a rate of 5 K min^{-1}.

Supplementary Information 9:

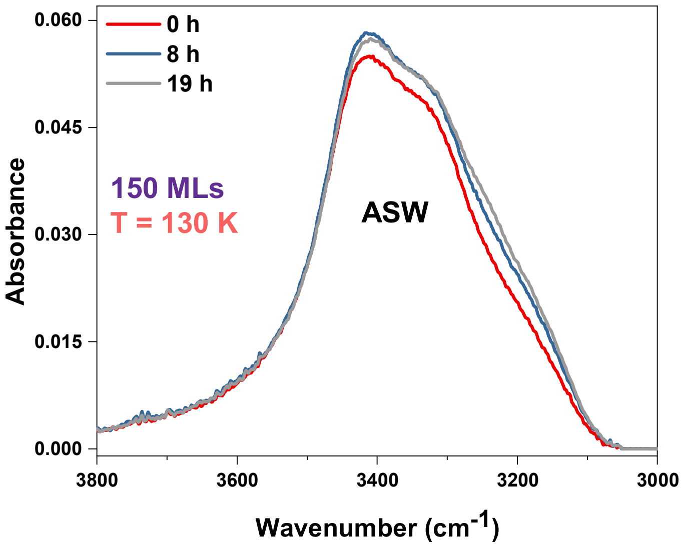

Fig. S10 Isothermal time-dependent RAIR spectra of 150 MLs of H_2O film at 130 K in the O-H stretching region. Thin film was prepared by vapour deposition on Ru(0001) at 10 K and heated to 130 K at a rate of 5 K min^{-1}.

Supplementary Information 10:

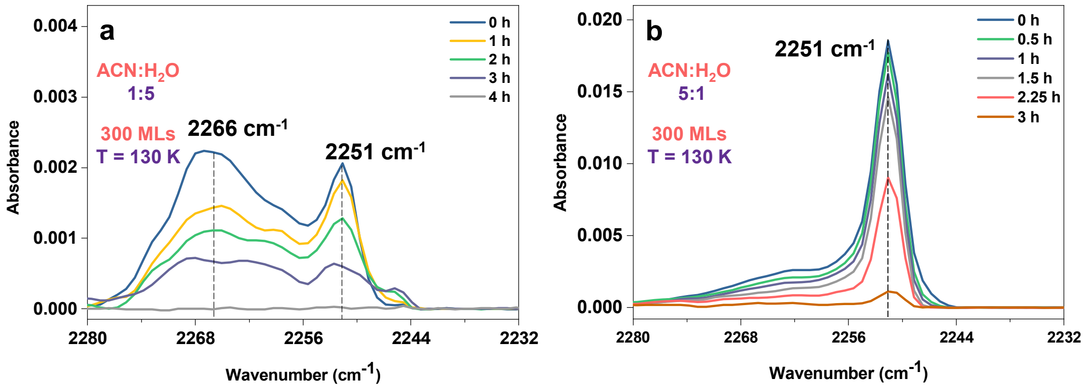

Fig. S11 (a) Isothermal time-dependent RAIR spectra of 300 MLs of 1:5 ACN:H_2O film at 130 K in the C≡N stretching region. (b) Isothermal time-dependent RAIR spectra of 300 MLs of 5:1 ACN:H_2O film at 130 K in the C≡N stretching region. Mixed film was prepared by vapour deposition on Ru(0001) at 10 K and heated to 130 K at a rate of 5 K min^{-1}.

Supplementary Information 11:

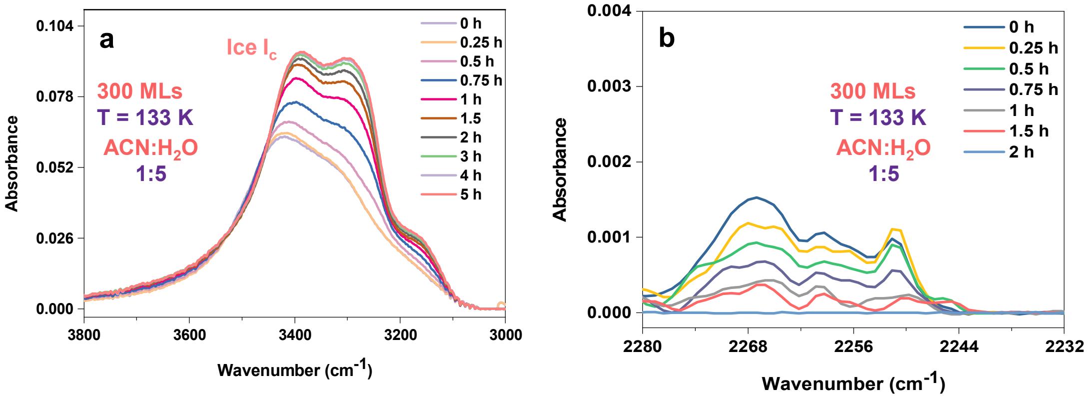

Fig. S12 Isothermal time-dependent RAIR spectra of 300 MLs of 1:5 ACN:H_2O film at 133 K in the (a) O-H stretching region and, (b) C≡N stretching region. Mixed film was prepared by vapour deposition on Ru(0001) at 10 K and heated to 133 K at a rate of 5 K min^{-1}.

Supplementary Information 12:

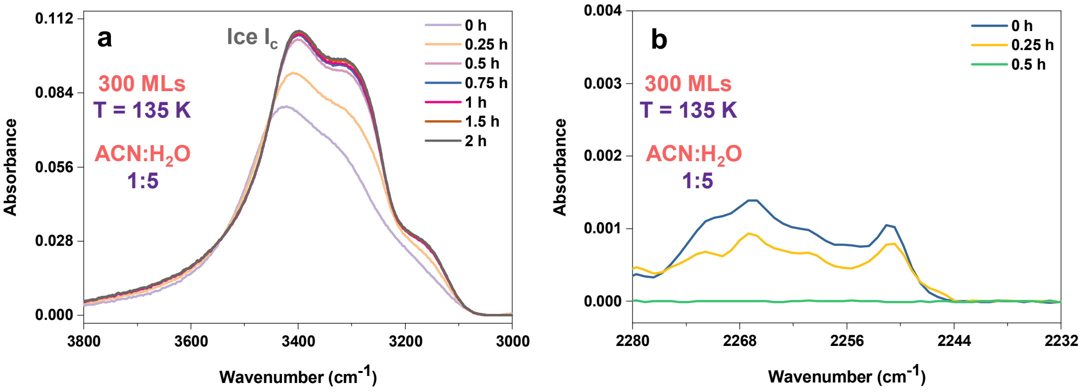

Fig. S13 Isothermal time-dependent RAIR spectra of 300 MLs of 1:5 ACN:H_2O film at 135 K in the (a) O-H stretching region and. (b) C≡N stretching region. Mixed film was prepared by vapour deposition on Ru(0001) at 10 K and heated to 135 K at a rate of 5 K min^{-1}.

Supplementary Information 13:

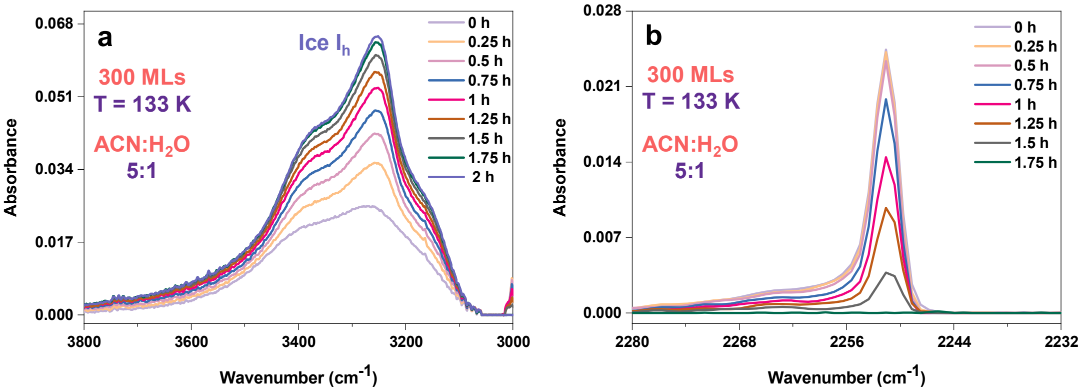

Fig. S14 Isothermal time-dependent RAIR spectra of 300 MLs of 5:1 ACN:H_2O film at 133 K in the (a) O-H stretching region and, (b) C≡N stretching region. Mixed film was prepared by vapour deposition on Ru(0001) at 10 K and heated to 133 K at a rate of 5 K min^{-1}.

Supplementary Information 14:

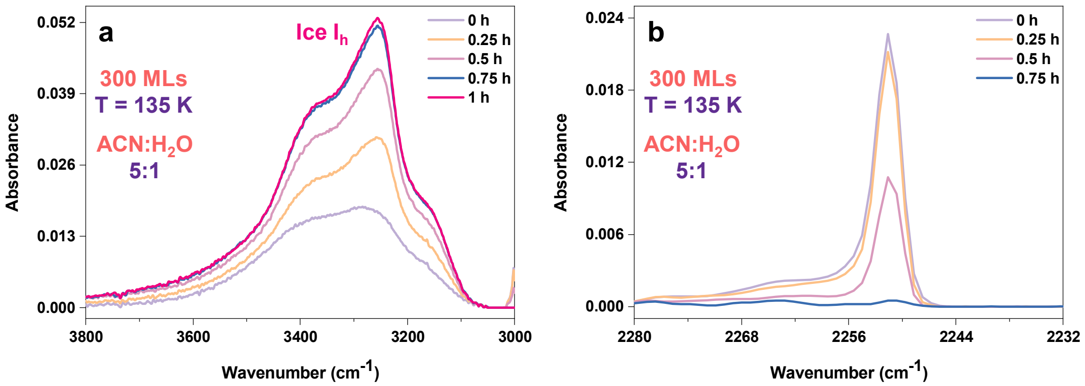

Fig. S15 Isothermal time-dependent RAIR spectra of 300 MLs of 5:1 ACN:H_2O film at 135 K in the (a) O-H stretching region and, (b) C≡N stretching region. Mixed film was prepared by vapour deposition on Ru(0001) at 10 K and heated to 135 K at a rate of 5 K min^{-1}.

Table S1 The parameters for crystallization of Ice I_h during the desorption of ACN from ice films at different temperatures.

	Temperature (K)	***n***	**Rate constant; *k* (s^{-1})**
O-H stretching	**125**	**1.80**	**1.39×10^{-05}**
	127	**1.75**	**2.66×10^{-05}**
	130	**1.63**	**9.60×10^{-05}**
	135	**0.91**	**8.05×10^{-04}**

References:

(1) Tizek, H.; Grothe, H.; Knözinger, E. Gas-Phase Deposition of Acetonitrile: An Attempt to Understand Ostwald's Step Rule on a Molecular Basis. *Chem. Phys. Lett.* **2004**, *383* (1–2), 129–133.

(2) Hudson, R. L.; Moore, M. H. Reactions of Nitriles in Ices Relevant to Titan, Comets, and the Interstellar Medium: Formation of Cyanate Ion, Ketenimines, and Isonitriles. *Icarus* **2004**, *172* (2), 466–478.

ACS NANO

www.acsnano.org

Light-Activated Intercluster Conversion of an Atomically Precise Silver Nanocluster

Arijit Jana, Madhuri Jash, Ajay Kumar Poonia, Ganesan Paramasivam, Md Rabiul Islam, Papri Chakraborty, Sudhadevi Antharjanam, Jan Machacek, Sundargopal Ghosh, Kumaran Nair Valsala Devi Adarsh,* Tomas Base,* and Thalappil Pradeep*

Cite This: *ACS Nano* 2021, 15, 15781−15793

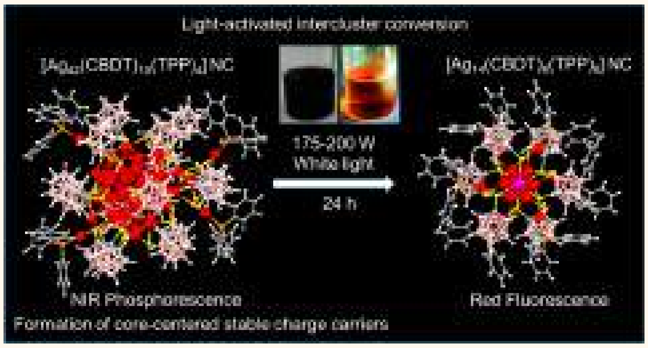

ABSTRACT: Noble metal nanoclusters protected with carboranes, a 12-vertex, nearly icosahedral boron−carbon framework system, have received immense attention due to their different physicochemical properties. We have synthesized *ortho*-carborane-1,2-dithiol (CBDT) and triphenylphosphine (TPP) coprotected $[Ag_{42}(CBDT)_{15}(TPP)_4]^{2-}$ (shortly Ag_{42}) using a ligand-exchange induced structural transformation reaction starting from $[Ag_{18}H_{16}(TPP)_{10}]^{2+}$ (shortly Ag_{18}). The formation of Ag_{42} was confirmed using UV−vis absorption spectroscopy, mass spectrometry, transmission electron microscopy, X-ray photoelectron spectroscopy, infrared spectroscopy, and multinuclear magnetic resonance spectroscopy. Multiple UV−vis optical absorption features, which exhibit characteristic patterns, confirmed its molecular nature. Ag_{42} is the highest nuclearity silver nanocluster protected with carboranes reported so far. Although these clusters are thermally stable up to 200 °C in their solid state, light-irradiation of its solutions in dichloromethane results in its structural conversion to $[Ag_{14}(CBDT)_6(TPP)_6]$ (shortly Ag_{14}). Single crystal X-ray diffraction of Ag_{14} exhibits Ag_8−Ag_6 core−shell structure of this nanocluster. Other spectroscopic and microscopic studies also confirm the formation of Ag_{14}. Time-dependent mass spectrometry revealed that this light-activated intercluster conversion went through two sets of intermediate clusters. The first set of intermediates, $[Ag_{37}(CBDT)_{12}(TPP)_4]^{3-}$ and $[Ag_{35}(CBDT)_8(TPP)_4]^{2-}$ were formed after 8 h of light irradiation, and the second set comprised of $[Ag_{30}(CBDT)_8(TPP)_4]^{2-}$, $[Ag_{26}(CBDT)_{11}(TPP)_4]^{2-}$, and $[Ag_{26}(CBDT)_7(TPP)_7]^{2-}$ were formed after 16 h of irradiation. After 24 h, the conversion to Ag_{14} was complete. Density functional theory calculations reveal that the kernel-centered excited state molecular orbitals of Ag_{42} are responsible for light-activated transformation. Interestingly, Ag_{42} showed near-infrared emission at 980 nm (1.26 eV) with a lifetime of >1.5 μs, indicating phosphorescence, while Ag_{14} shows red luminescence at 626 nm (1.98 eV) with a lifetime of 550 ps, indicating fluorescence. Femtosecond and nanosecond transient absorption showed the transitions between their electronic energy levels and associated carrier dynamics. Formation of the stable excited states of Ag_{42} is shown to be responsible for the core transformation.

KEYWORDS: *carboranes, silver nanoclusters, intercluster conversion, near-infrared emission, luminescence, ultrafast electron dynamics*

INTRODUCTION

Atomically precise nanoclusters (NCs) of noble metals with core dimension <3 nm, composed of a few tens to hundreds of atoms, are an emerging class of nanomaterials with specific properties, which represent a distinct category of materials between atoms and traditional nanoparticles.[1,2] Different noble metal based NCs, especially of gold, silver, copper, and platinum, protected by various types of surface ligands such as thiols, imine-thiols, phosphines, alkynes, sulfonates, DNAs, proteins, etc., have been synthesized by following different synthetic protocols.[3−13] Among different noble metal NCs, gold NCs have been prominent due to their facile synthesis and stability. Although silver NCs are reported less commonly, perhaps due to their higher reactivity, they have received increasing attention recently due to their functional proper-

Received: March 26, 2021
Accepted: September 27, 2021
Published: October 4, 2021

https://doi.org/10.1021/acsnano.1c02602

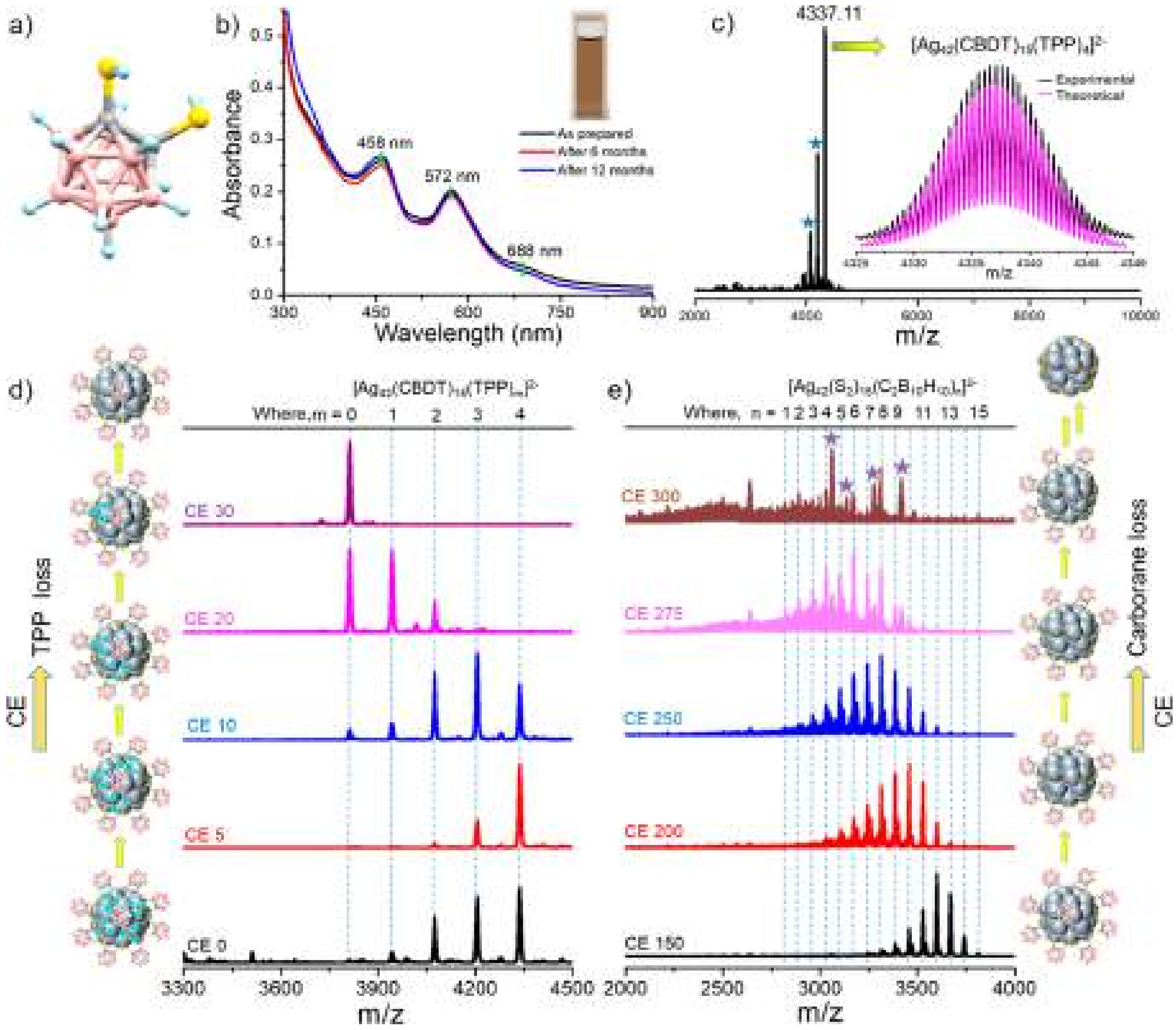

Figure 1. Synthesis and characterizations of Ag_{42} NC. (a) Molecular structure of the *ortho*-carborane 1,2-dithiol ligand. Color code for atoms: pink = boron, gray = carbon, yellow = sulfur, blue = hydrogen. (b) Time-dependent UV−vis absorption spectra of Ag_{42} NC in DCM indicating its stability. (inset) Photograph of the respective DCM solution. (c) Full range negative ion-mode ESI-MS spectrum of Ag_{42} NC. Two TPP losses were observed from the parent NC which are shown by the ☆ symbols. (inset) Exact matching of the isotopic distribution of the experimental and theoretical spectra. (d) Systematic losses of four TPP were observed from the peak at m/s 4337.11 with a charge state of 2− up to CE 30. (inset left) Schematic representation of TPP losses. (e) Fourteen sequential mass losses of carborane ($C_2B_{10}H_{10}$, M 142) units, along with a few silver sulfide loss peaks (marked as ☆). (inset right) Schematic representation of carborane losses.

ties.[14] Therefore, it is of interest to explore a family of stable silver NCs with tunable properties. Various physicochemical properties such as narrow energy gap and associated multiple electronic transitions, luminescence, chirality, etc., have been used in numerous fields, including optoelectronics, nanosensors, nonlinear optics, circularly polarized luminescence, and nanocluster sensitized solar cells, etc.[15−22] Different silver NCs have been characterized through mass spectrometric studies. However, some of them, such as Ag_6, Ag_9, Ag_{25}, Ag_{29}, Ag_{44}, Ag_{56}, Ag_{67}, and Ag_{141}, etc., with specific ligand structure and overall charge, have also been characterized structurally using single crystal X-ray diffraction.[23−30] Some recent studies have also reported synthesis and structural characterization of bimetallic and polymetallic NCs following coreduction of mixed metal precursors and intercluster reactions.[31−33] Different transition metal-doped silver NCs, especially Ti and Cd, with varying numbers of dopant atoms showed different electronic features in comparison to the undoped ones.[34,35] During crystallization of nanoclusters, more than one silver NC was crystallized within the same unit, forming cocrystals, such as Ag_{16}−Ag_{17}, Ag_{40}−Ag_{46}, Ag_{210}−Ag_{211}, etc.[36−38] A detailed understanding of their synthesis, and associated structures, and properties has become an important research direction.

Synthesis of specific nuclearity silver NCs with high purity is always challenging. Many factors such as pH, solvent, temperature, and ligand have profound roles in regulating nuclearity, shape, and surface activity of NCs.[39,40] Along with conventional coreduction of metal thiolates, other unconventional synthetic strategies such as solid-state gel-based mechanical grinding, microwave irradiation, and ligand exchange induced size focusing as well as fast purification using desalting column techniques were employed to scale up as well as purify NCs.[41−44] Shape tuning of nanoclusters based on their sensitivity or reactivity to an external solvent environment is possible, resulting in changes in the cluster core and composition.[45,46] Different photoirradiation methods

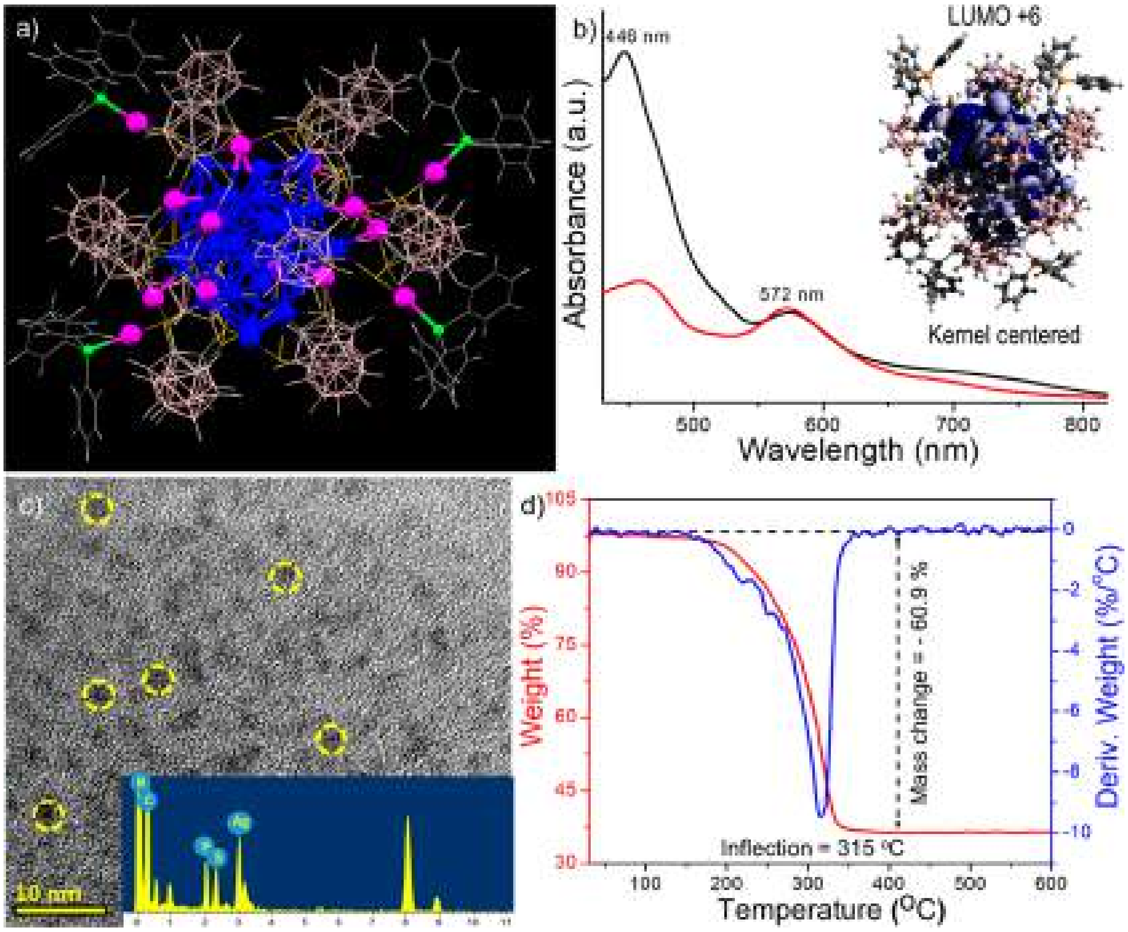

Figure 2. Structural studies and thermal stability of Ag_{42} NC. (a) DFT optimized structure of Ag_{42} NC. Atomic color code: blue = inner core Ag atoms, dark pink = outer core Ag atoms, green = phosphorus, pink = boron, yellow = sulfur, gray = carbon, white = hydrogen. (b) Comparison between theoretical and experimental UV−vis absorption spectra. (inset) Electron density map of kernel-centered LUMO + 6. (c) Large area TEM micrograph showing Ag_{42} NCs. (inset) EDS spectrum from such an area. (d) Thermogravimetric and differential thermal analysis data showing thermal stability up to 200 °C. The maximum mass change occurs at 315 °C.

are of interest due to their simplicity and effectiveness in shape engineering.[47] Various light sources such as UV lamps, sunlight, light emitting diodes (LEDs), fluorescent lamps, and lasers have been used for shape-tuning of nanoparticles and associated properties.[48,49] We have shown sunlight-mediated synthesis of stable silver nanoclusters in a gel matrix.[50] Although light-induced size growth was observed in gold nanoclusters, there has been no report of light-activated intercluster conversion of silver nanoclusters.[51] In view of the light sensitivity of silver nanostructures, we hypothesized that light may trigger the interconversion of NCs.

Carboranes (dicarba-*closo*-dodecaboranes of general formula $C_2B_{10}H_{12}$) are 12-vertex, nearly icosahedral carbon, and boron cage molecules with electrons delocalized over the molecular framework of CH and BH vertices as well as within the cage.[52] These types of molecules are promising candidates for synthesizing stable silver NCs with tunable electronic properties. Due to their rigid and robust three-dimensional architectures, chemical, and thermal stability as well as electronic structure, they possess an enormous potential to become key constituents of luminescent polymer materials, catalysts, hypergolic materials, surface-supported self-assembled entities, light-driven molecular nanomachines, etc.[53−58] Their tunable dipole moment and 3D pseudoaromatic character make carboranes' electronic properties tunable, unlike other organic counterparts.[59] There are a few reports of carborane-based metal nanoclusters and their extended framework solids (EFSs) with luminescence properties, but reports on the synthesis of higher nuclearity NCs are rare due to their poor stability and other synthetic limitations.[60−62]

In this work, we report the synthesis of Ag_{42} nanoclusters coprotected by *ortho*-carborane-1,2-dithiol (CBDT), and triphenylphosphine (TPP) ligands through the ligand-exchange induced structural transformation (LEIST) protocol. The formation of Ag_{42} was confirmed using different microscopic and spectroscopic studies. Although Ag_{42} is thermally stable up to 200 °C, it undergoes light-activated intercluster conversion to $[Ag_{14}(CBDT)_6(TPP)_6]$, through two sets of intermediate NCs. Single crystal X-ray diffraction (SC-XRD) confirmed the atomic structure of the as synthesized Ag_{14}. The Ag_{42} has a NIR emission centered around 980 nm, while as synthesized Ag_{14} showed red luminescence at 626 nm. Although the luminescence of Ag_{14} was weak at room temperature, there was >25-fold enhancement in emission with a slight red shift (17 nm) at 77 K. Time-dependent density-functional theory (TDDFT) calculations revealed the nature of orbitals responsible for their electronic transitions. To further understand the electronic transition of both the NCs, we have used femtosecond and nanosecond

https://doi.org/10.1021/acsnano.1c02602
ACS Nano 2021, 15, 15781−15793

transient absorption (fs-ns TA) pump−probe measurements, which probed their excited state charge transfer and relaxation dynamics. The Ag_{42} showed slow decay of excited state charge carriers (3.4 ± 0.6 and 24 ± 1 μs for 576 nm and 5.7 ± 0.4 and 70 ± 10 μs for 685 nm), in comparison to fast (85 ± 9 ps for 565 nm) decay in Ag_{14}.

RESULTS AND DISCUSSION

Synthesis and Characterization of Ag_{42} NC. We have synthesized *ortho*-carborane-1,2-dithiol, and triphenylphosphine coprotected Ag_{42} using a modified LEIST reaction from bipositively charged Ag_{18} nanocluster protected with 10 TPP and 16 hydride ligands. Details of synthesis and characterization of Ag_{18}, which has been reported previously, are presented in the Supporting Information along with UV−vis absorption and mass spectra (Figure S1).[63] Mass spectra of CBDT shown in Figure S2 exhibit characteristic isotopic distribution of the molecular ion at $m/z \sim 207.44$ and confirm its purity. A sequence of photographs showing the progression of the LEIST reaction is shown in Figure S3. In brief, following the addition of methanolic solution of CBDT to Ag_{18}, a white precipitate was formed initially. During the progress of the reaction, the precipitate got converted to a brown product in 4 h, indicating the formation of Ag_{42}.

It was first characterized using UV−vis absorption spectroscopy having a characteristic spectrum, as shown in Figure 1b. Three sharp absorption peaks at 688, 572, and 458 nm indicated the closely spaced molecule-like electronic states of the nanocluster. Absorption spectroscopic measurements of the cluster in different solvents (Figure S4) show characteristic spectral bands at 572 and 458 nm. We have observed broadening of the 572 nm peak in DMF and DMSO. The dipolar aprotic nature of these solvents, which leads to favorable interactions with the cluster, is the reason behind this spectral broadening. Long-term stability of the cluster was shown by identical UV−vis absorption features measured over a period of one year. Despite several attempts, we were unable to grow single crystals suitable for diffraction analysis. The grown black solids did not show prominent diffraction peaks in powder X-ray diffraction (Figure S5).

The molecular composition of the Ag_{42} was confirmed using high-resolution electrospray ionization mass spectrometry (HR-ESI-MS). Detailed instrumentation conditions and sample preparation details are given in the SI. Figure 1c shows the full-range mass spectrum of Ag_{42} in the negative ion-mode, with a characteristic isotopic distribution envelope of a dianionic (2−) cluster centered at m/z 4337.11. A peak separation of m/z 0.5 confirms the charge state as 2−. As no monoanionic species was detected, we assume that the charge state in solution is 2−. A mass of 8674.22 was assigned to the cluster, $[Ag_{42}(CBDT)_{15}(TPP)_4]^{2-}$. Isotopic distribution of the experimental spectrum is in exact agreement with the simulated one. Two other fragments, and their characteristic isotopic envelopes at m/z 4205.67 and 4074.21 indicate sequential losses of 262 amu, corresponding to TPP. In order to gain additional experimental evidence on the composition, we have studied MS/MS fragmentation of the ions derived from the parent cluster by varying the collision energy (CE). Figure 1d and e show the MS/MS fragmentation patterns of Ag_{42}. The parent Ag_{42} feature at m/z 4337.11 with 2− charge state was selected for the MS/MS fragmentation experiments. Sequential increase of CE from 0 to 30 (in instrumental units) led to four consecutive mass losses, each corresponding to one TPP (262) unit, which indicates the presence of four weakly bound TPP molecules on the cluster surface. The DFT optimized structure (shown in Figure 2a, to be discussed below) also revealed weak binding of monodentate TPP ligands as a secondary shell through Ag−P bonds on the cluster. Increasing the CE from 30 to 150 did not yield any other fragmentation. At the CE of 150, a set of fragments belonging to carborane ($C_2B_{10}H_{10}$, M 142) units started appearing, which indicate carborane loss from the NC. Further increase of the CE up to 300 showed a total of 15 mass losses of the carborane moiety. This is also supported by the previous results of desorption experiments and time-of-flight secondary ion mass spectrometry data of flat silver surfaces, both pointing at strong Ag−S bonds.[64,65] Along with the systematic loss of carborane fragments, other peaks in the lower mass range, shown in Figure S6, indicate the detachment of different silver-sulfide motifs during fragmentation. Spectral analysis reveals the formation of a few smaller carborane-thiolate silver clusters at m/z 1580.82, 1158.96, and 736.28 with the composition of $[Ag_7(C_2B_{10}H_{10}S_2)_4]^-$, $[Ag_5(C_2B_{10}H_{10}S_2)_3]^-$, and $[Ag_3(C_2B_{10}H_{10}S_2)_2]^-$, respectively. A gradual decrease of the intensity of these clusters was observed at higher collision energies. Along with these cluster species, there were several fragmented peaks at m/z 143.27, 175.26, 217.25, 250.20, 314.08, 326.24, 359.40, 391.41, 457.31, and 499.30 assigned to $[C_2B_{10}H_{11}]^-$, $[C_2B_{10}H_{11}S]^-$, $[Ag_2H_2]^-$, $[AgC_2B_{10}H_{10}]^-$, $[Ag(C_2B_{10}H_{10}S_2)]^-$, $[Ag_3H_3]^-$, $[Ag_2(C_2B_{10}H_{11}]^-$, $[Ag_2(C_2B_{10}H_{11}S)]^-$, $[Ag(C_2B_{10}H_{11}S)_2]^-$, and $[Ag_3(C_2B_{10}H_{11}S)]^-$, respectively. All of these peaks confirm the presence of different types of silver and CBDT arrangements present in the cluster.

In order to understand the structure, in the absence of single crystal data, theoretical modeling was undertaken. The optimized structure of Ag_{42} NC is shown in Figure 2a, protected with both CBDT and TPP ligands. We started the optimization from $[Ag_{46}(SPhMe_2)_{24}(TPP)_8]^{2+}$ NC, reported by the group by removing 4 silver atoms, 4 TPPs, and 24 thiolate ligands.[37] We have added 15 CBDT ligands to prepare a model of $[Ag_{42}(CBDT)_{15}(TPP)_4]^{2-}$. The optimized structure of Ag_{42} has a distinct core with 28 silver atoms and a shell of 14 silver atoms (shown in Figure S7). The core is distorted in nature, having Ag−Ag bond distances in the range 2.77−3.10 Å. The distortion of the core is mainly due to the spatial confinement of carboranes. Furthermore, a large number of CBDT ligands create voids between them to adjust their positions, and consequently, the distribution of Ag atoms in the shell is not even. The binding of carborane ligands with the silver core is through AgS_2, Ag_2S, and Ag_3S moieties, having Ag−S bond distances in the range 2.4−2.6 Å. The secondary TPP ligands bind with four Ag atoms with an average bond distance of 2.43 Å. The calculated UV−vis absorption features at 572 nm (shown in Figure 2b) match well with the experimental spectrum, indicative of an optimized structure. Density of states (DOS) calculations reveal that the absorption at 572 nm is due to the electronic transition from HOMOs (HOMO − 10 and HOMO − 9) having the energy of −0.74 eV to the LUMOs (LUMO + 5, LUMO + 6, and LUMO + 7) with the energy of 1.366, 1.43, and 1.576 eV, respectively (Figure S8a). Electron density plots show that the corresponding transitions are from ligand-centered HOMOs to kernel-centered LUMOs (shown in Figure 2b and S8b). We will come back to this aspect later in the text.

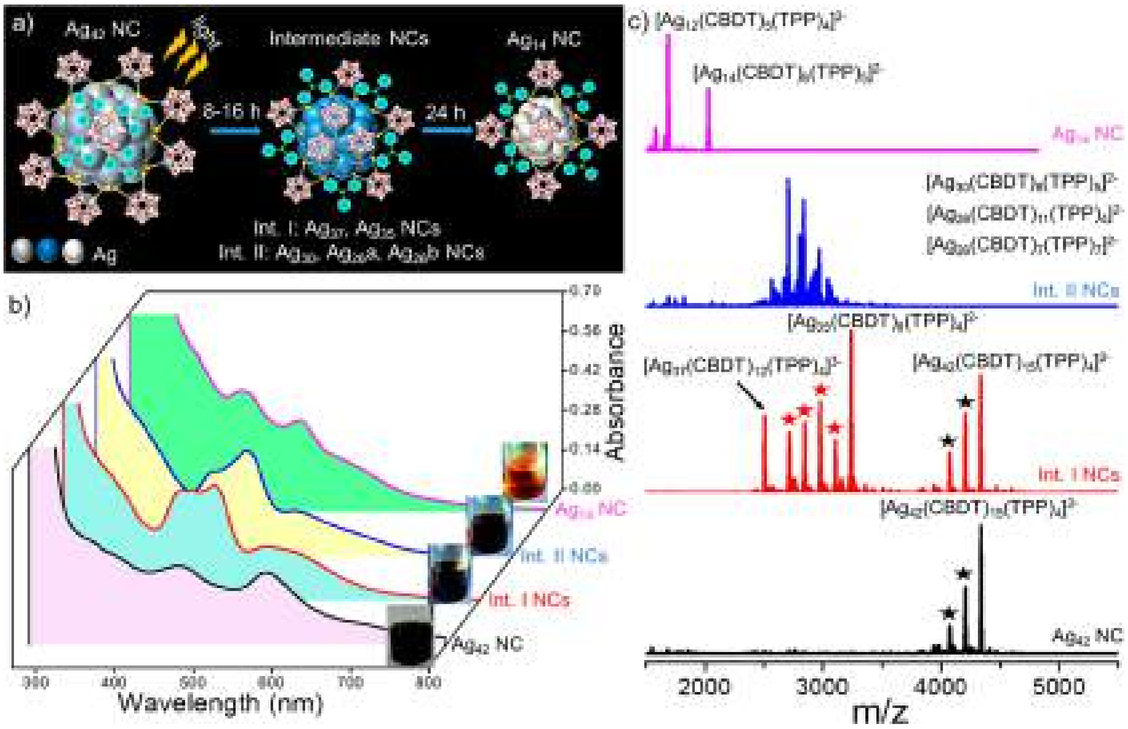

Figure 3. Studies of light-activated intercluster conversion. (a) Schematic representation of light-activated intercluster conversion of Ag_{42} to Ag_{14} through different intermediates. (b) UV−vis absorption spectra of both the NCs along with their mixed intermediate NCs. (inset) Photographic images of the color change during the light-irradiation. (c) Respective mass spectra showing the formation of intermediate nanoclusters during light exposure (each ☆ indicates TPP ligand loss from the respective parent NCs).

The Ag_{42} was further characterized by TEM. TEM micrographs are shown in Figures 2c, S9, and they show uniform particles in between 1.2 and 1.5 nm, confirming their cluster size. Although electron beam-induced damage is common in such clusters, individual clusters were readily seen in such images, possibly due to the high thermal stability of the system. The EDS spectrum confirmed the presence of B, C, P, S, and Ag with their atomic concentrations (%) of 41.83, 51.41, 2.22, 1.68, and 2.86, respectively. To further understand ligand binding, we studied multinuclear NMR spectra of the NC in $CDCl_3$. The ^{11}B NMR spectrum shown in Figure S10 displays four peaks at −10.32, −7.45, −3.35, and 20.23 ppm, which can be assigned to four nonequivalent boron atoms of the carborane ligands. The broadness of the peaks is due to the high electron density of the metallic core close to the carborane molecule. Furthermore, ^1H-decoupled ^{13}C NMR spectrum shown in Figure S11 exhibits two peaks at 53.45 and 58.49 ppm assigned to the carbon atoms of carborane ligands, along with several peaks characteristic of the TPP ligands in the range of 128.49−133.92 ppm. The ^{31}P NMR spectrum in Figure S12 shows a broad peak at 5.31 ppm, indicating TPP binding to the NC, in contrast to a free TPP exhibiting a sharp ^{31}P NMR signal at −5.66 ppm. XPS spectra of Ag_{42} in Figure S13 show the binding energy values of Ag $3d_{5/2}$ and $3d_{3/2}$ to be 368.5 and 374.6 eV, respectively. These values are close to the typical values of Ag(0). Other characteristic binding energy values of 162.2, 189.5, 284.8, 131.5 eV were correlated with S 2p, B 1s, C 1s, and P 2p spectral regions, respectively. To further understand ligand binding, the FT-IR spectrum of Ag_{42} was measured and compared with that of the free CBDT ligand, both shown in Figure S14. Two vibrational bands at 2601, and 2578 cm^{-1} for the free CBDT ligand, which got shifted to a single band at the lower frequency of 2561 cm^{-1} upon binding in the Ag_{42}, were observed. To comprehend these experimental data, we used DFT calculations to investigate the effect of silver binding to the CBDT ligand in this spectral region. The calculated IR spectra, shown in Figure S15, are dominated by the collective stretching modes of boron−hydrogen bonds. The stretching vibrations of the free SH groups of CBDT fall in this region too but produce only weak infrared lines covered by overlapping BH bands. The differences in the spectra of the free and Ag_{42}-bound CBDT ligand can therefore be attributed mainly to the specific way in which the individual BH bonds, and especially those that are adjacent to the vertices substituted by sulfur atoms, combine into the active vibrational modes. The shift of the band maximum of Ag_{42} to a lower wavenumber compared to free CBDT suggests chemically bound thiolate moieties.

Thermal Stability and Light-Activated Intercluster Conversion. To investigate the thermal stability, we have measured thermogravimetric analysis (TGA) of purified Ag_{42} powder. A detailed experimental procedure of the TGA measurement is presented in the SI. Figure 2d shows the TGA plot of Ag_{42}, which indicates thermal stability up to 200 °C and shows superior thermal stability compared to known silver NCs. To better understand the structural transformation in the solid state, we performed UV−vis absorption spectroscopy and differential scanning calorimetry (DSC) of the cluster during heating. Sample heated in the solid state was dissolved in DCM to measure the absorption spectra. Spectra shown in Figure S16 remained unchanged up to 125 °C, which supports structural stability. At 150 °C, the heated sample appears to have decomposed as the absorption spectrum shows no characteristic features except a background. In the DSC measurement (Figure S17), we observed a continuous exothermic heat flow up to 190 °C, which implies no

https://doi.org/10.1021/acsnano.1c02602

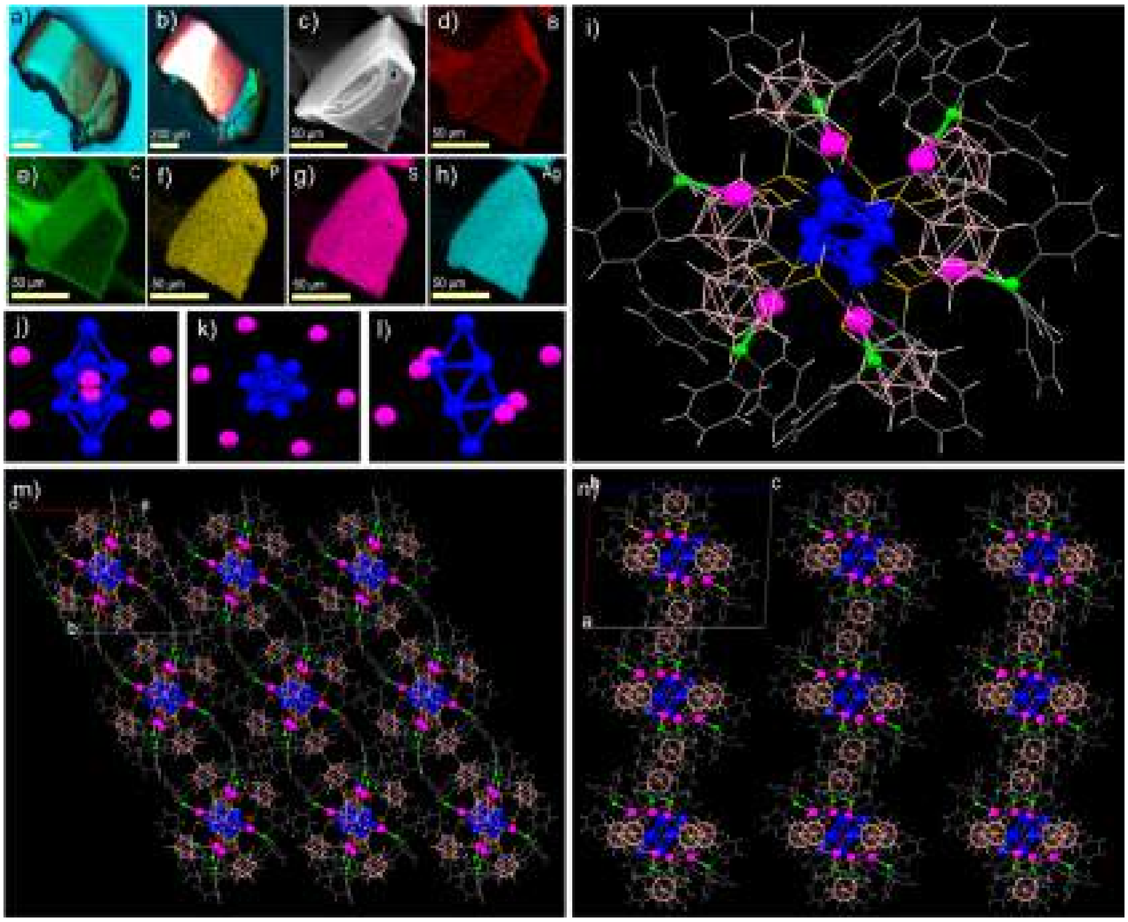

Figure 4. Single crystal structure of Ag_{14} NC. Optical micrographs of a single crystal (a) without a polarizer and (b) with a polarizer. (c−h) SEM-EDS elemental mapping of a single crystal proving the presence of all respective elements. (i) Single crystal structure of Ag_{14} nanocluster protected with six CBDT and six TPP ligands. (j−l) $Ag_8@Ag_6$ core−shell geometry from different orientations. (m, n) Supramolecular structure showing the packing of Ag_{14} in different orientations. The $[Ag_2S(TPP)_6]$ fragments are removed for clarity. Atomic color code: blue, dark pink = silver, yellow = sulfur, green = phosphorus, faint pink = boron, gray = carbon, white = hydrogen.

prominent phase transformation of the cluster below 200 °C. The continuous exothermic peak is attributed to ligand ordering, which also manifests a weak structural transition at 227 °C.

Nevertheless, we observed light-activated intercluster conversion from Ag_{42} to Ag_{14} in a DCM solution, accompanied by a visible color change from dark brownish to orange. Experimental details of light-triggered intercluster conversion are discussed in the SI. Figure 3a shows a schematic representation of the conversion. UV−vis absorption spectra and mass spectra measured after specific periods of light exposure (Xe arc lamp, 190 W) unveils that this intercluster conversion proceeds through several intermediate NCs. After 8 h of light exposure, the brownish Ag_{42} solution became dark reddish, and this change was accompanied by the decrease of the absorption peaks in the range from 500 to 700 nm, along with the appearance of other peaks at 418 and 463 nm, both arising from these intermediates. HR-ESI-MS spectrum (Figure 3c) shows two features at m/z 3239.64, with the charge state of 2−, and at m/z 2504.68, for 3−. These two spectral features correspond to $[Ag_{35}(CBDT)_8(TPP)_4]^{2-}$ and $[Ag_{37}(CBDT)_{12}(TPP)_4]^{3-}$, respectively. Figure S18 shows the exact matching of the experimental and calculated isotopic envelopes for both of these intermediate NCs. Light irradiation after 16 h leads to further changes in the UV−vis absorption spectra manifested by the appearance of a peak at 525 nm and another sharp peak at 462 nm. HR-ESI-MS measurements of the solution confirm the existence of a mixture of three primary NCs; $[Ag_{30}(CBDT)_8(TPP)_4]^{2-}$, $[Ag_{26}(CBDT)_{11}(TPP)_4]^{2-}$, and $[Ag_{26}(CBDT)_7(TPP)_7]^{2-}$ along with their fragmented peaks due to the loss of phosphine. Simulated isotopic distribution (shown in Figure S19) of these NCs matched well with experimental spectra. After 24 h of light irradiation, the solution became yellowish-orange with two distinct optical absorption peaks at 415 and 486 nm, and the mass spectrum confirmed the formation of Ag_{14} as an end product (Figure S20). Further exposure of light up to 48 h did not result in any significant change in the absorption features. To understand the effect of the lamp power on the conversion process, we have monitored the absorption features while varying the lamp power. Figures S21−S25 show the time-dependent UV−vis absorption spectra of the conversion at different lamp powers, namely 100, 125, 150, 175, and 200 W. We have observed complete conversion of Ag_{42} to Ag_{14} following a similar set of intermediate nanoclusters after 24 h of light exposure, at 175−200 W. Decreasing the lamp power below 150 W slowed down the conversion. For the lamp power of 100 W, the conversion was completed after 48 h. Lamp power below 100 W drastically reduced the rate of transformation.

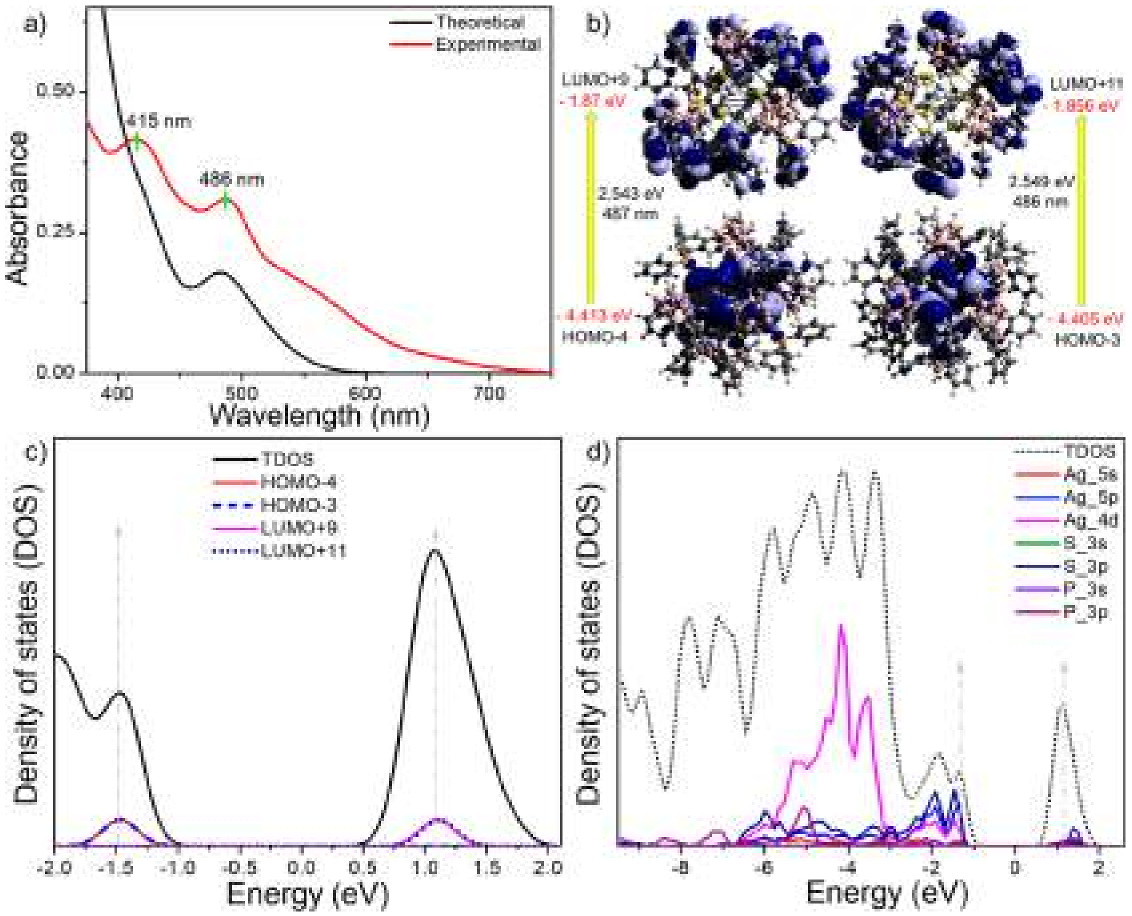

Figure 5. Theoretical electronic energy levels of Ag_{14} NC. (a) Experimental and theoretical UV−vis absorption spectra of Ag_{14}. (b) Frontier molecular orbitals responsible for the electronic transitions at 486 nm. (c) Total density of states in terms of molecular orbital contribution. (d) Total density of states in terms of atomic orbital contribution.

However, the absorption spectrum of Ag_{42} remained unchanged up to 100 °C. This confirms the thermal stability of the NC not only in its solid-state but also in solution. Figure S26 shows photographs of a DMF solution of Ag_{42} without any significant visible color change after heating to 100 °C. The superior thermal stability of Ag_{42} together with changes activated by light show possibilities leading potentially toward superstable silver NCs.

To better understand the structural stability, we have calculated the valence electrons of both the nanoclusters. According to the superatomic electron counting formula, $N\nu_A - M - Z$, the $[Ag_{42}(CBDT)_{15}(TPP)_4]^{2-}$ nanocluster has 14 free electrons (42 − 30 + 2) with the superatomic electronic configuration, $1S^2\ 1P^6\ 1D^6$ (where N = number of metal atoms, ν_A = atomic valence of the metal atoms, M = number of electron withdrawing ligands, and Z = overall charge of the cluster).[66−68] The unpaired electrons present in 1D nonspherical superatomic orbitals may generate paramagnetism in Ag_{42} clusters. In contrast, the $[Ag_{14}(CBDT)_6(TPP)_6]$ nanocluster has two free electrons (14 − 12 − 0), with an electronic configuration of $1S^2$. The superatomic closed shell electronic configuration may be a reason behind the formation of Ag_{14} as an end product upon light irradiation. Although due to the lack of closed shell electronic structure, the Ag_{42} nanocluster has less electronic stability, and it is stable over a longer time as well as upon heating, which is most probably due to the heat absorbing capacity of surrounding bulky carborane ligands.

Structure of the Product Ag_{14}. We were able to grow single crystals of Ag_{14}, which gave a detailed understanding of the structural details of the system. Around 50 mg of the product obtained from different sets of light-irradiation were used for the crystallization by slow diffusion of dry hexane into dichloromethane (dichloromethane:hexane = 2.5:1.5, v/v). Yellow cuboid crystals (an optical microscopy image of a single crystal is shown in Figures 4a and b) were obtained. The SEM image of a crystal shown in Figure 4c indicates its cuboid nature. Figures 4d−h shows the EDS elemental mapping of a single crystal, which proves the presence of the respective elements, i.e. B, C, P, S, and Ag in the single crystal.

The SC-XRD measurements show that Ag_{14} crystallizes in a triclinic crystal system with a cell volume of 7160 Å^3 under the space group of $P\bar{1}$ (detailed crystallographic information is presented in Table S1). The total structure of Ag_{14} (shown in Figure 4i) has diagonally opposite three pairs of carborane and three pairs of triphenylphosphine ligands. The further structural anatomy of the Ag_{14} core is shown in Figures 4j−l and S27, and it reveals the $Ag_8@Ag_6$ core−shell geometry. The Ag_8 core of the nanocluster is made by two tetrahedrons in a bicapped trigonal antiprismatic fashion along with an Ag_6S_{12} shell, which is further surrounded by six CBDT and TPP ligands. The CBDT and TPP act as the primary and secondary ligands, respectively. The six Ag atoms on the shell are bonded with the TPP ligands through Ag−P bonds. The average Ag−Ag bond distance of 2.6−2.7 Å of the Ag_8 core shown in Figure

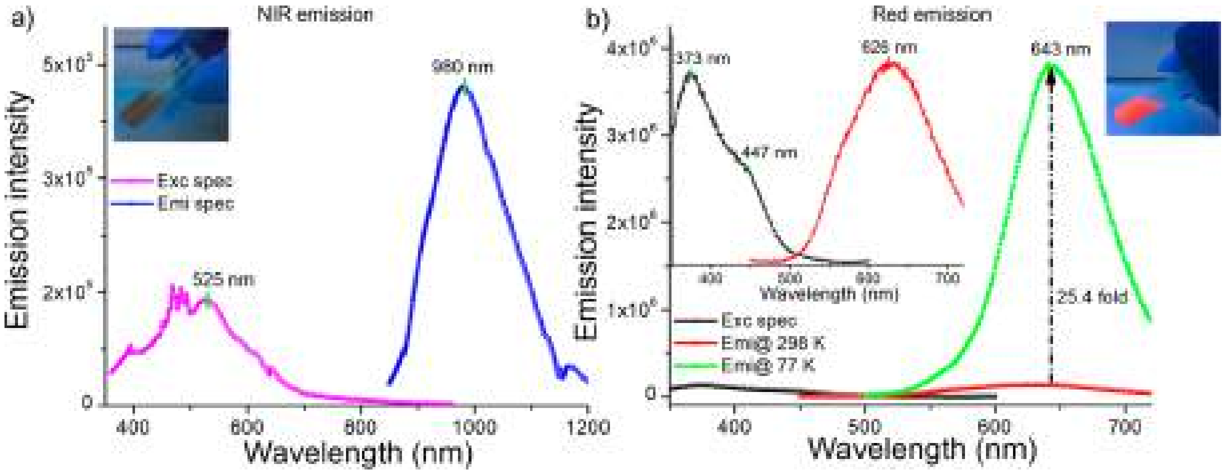

Figure 6. Emission properties of Ag_{42} and Ag_{14} NCs. (a) Excitation and emission spectra of the Ag_{42} indicate their NIR emission (inset) Image of the NC under 365 nm UV light, at room temperature. (b) >25-fold enhancement in the emission of the Ag_{14} upon cooling in LN_2, PL excitation, and emission spectra of Ag_{14} at room temperature. (left inset) Expanded spectra. (right inset) Red emission of the cluster under UV light. The sample was cooled under LN_2.

S28 is much shorter compared to the bond distance of 3.7−3.9 Å between the Ag_8 core and the six surrounding Ag atoms, clearly indicating a core−shell geometry. Careful analysis reveals that Ag_{14} has C_3 axial symmetry along with two capping Ag atoms of the Ag_8 core. Figures S29 and S30 show the C_3 axial symmetry of the structure from different orientations. The unit cell molecular packing of the crystal shown in Figure S31 reveals that four $[Ag_2S(TPP)_6]$ fragments are packed diagonally opposite to the cluster. Most probably, the $[Ag_2S(TPP)_6]$ fragments are generated from Ag_{42} during light irradiation, and they crystallize along with the Ag_{14} due to favorable interactions. The average distance of each $[Ag_2S(TPP)_6]$ fragment from the Ag_{14} centroid is in between 14.4 and 16.4 Å (Figure S31b). There is no covalent bonding between Ag_{14} and the $[Ag_2S(TPP)_6]$ fragments (Figure S32). Molecular packing of Ag_{14} along with $[Ag_2S(TPP)_6]$ fragments is shown in Figures 4m, n and S33 indicating lamellar packing of the cluster within the lattice. The binding force of Ag_{14} with $[Ag_2S(TPP)_6]$ fragments (shown in Figure S34) is due to the several intermolecular interactions such as CH-π, BH-π, B-CH, CH-BH, Ag-π, B-π, etc. To provide another independent view on Ag_{14}, we used TEM imaging (Figure S35), which displays uniform particle distribution. Extended beam irradiation produced Ag_2S with a lattice spacing of 2.8 Å, corresponding to the d_{110}. The EDS elemental analysis showed the presence of all the expected elements, i.e. B, C, P, S, and Ag with an atomic % of 38.86, 56.67, 1.54, 1.20, and 1.73, respectively. Figure S36 shows the ^{11}B NMR spectrum of the same with four peaks at −0.69, −7.32, −10.78, and −13.43 ppm in the shielded regions with nearly identical intensity, which was correlated with the symmetrical carborane binding of the Ag_{14} nanocluster. The proton decoupled ^{13}C NMR spectrum, shown in Figure S37, exhibits two peaks at 53.44 and 50.85 ppm assigned to carbon atoms of the carborane ligands, along with different characteristic peaks in the region of 128 to 134 ppm, corresponding to bonded TPP ligands. A broad ^{31}P NMR peak (shown in Figure S38) at 4.04 ppm indicates TPP binding with the nanocluster. To further confirm the chemical binding of different atoms in Ag_{14}, we performed XPS studies. The survey spectrum along with individual elements (Figure S39) confirm that the oxidation state of silver is close to Ag(0). The presence of B 1s and P 2p signatures at 189.8, and 131.5 eV, respectively, confirm the ligand binding in the solid state. FT-IR results (Figure S40) show changes in the BH stretching due to carborane binding with the metallic core.

Electronic Structure of Ag_{14} through TDDFT. TDDFT calculations were performed to understand the electronic energy levels and associated electronic transitions of Ag_{14}. Detailed structure optimization and details of calculations are presented in the SI. The DFT optimized structure and its anatomy are shown in Figures S41 and S42. The optical absorption spectrum was calculated using linear-response TDDFT and delta SCF methods, using the ground and excited state optimized structures of the NC. The calculated optical absorption spectrum in comparison with the experimental UV−vis spectrum is shown in Figure 5a. For both the spectra, not only the overall trend but also the distinct peak at 486 nm were matched well. The relevant molecular orbitals corresponding to this transition are plotted in Figure 5b. The transition is arising from two occupied molecular orbitals, i.e., HOMO − 4 and HOMO − 3, having energies of −4.413 and −4.405 eV to empty orbitals LUMO + 9 and LUMO + 11 with energies of −1.87 and −1.856 eV, respectively. This excitation is from core to surface states.

Additional density of state (DOS) calculation (shown in Figure 5c) reveals that both the HOMOs (HOMO − 4 and HOMO − 3) having the energy of −1.50 eV contributed equally to the transition to the LUMOs (LUMO + 9 and LUMO + 11) with the energy of 1.04 eV for this transition. The distribution of electron density of these molecular orbitals clearly shows that the metal core localized HOMOs transfer their charge to the delocalized LUMOs centered around the ligands. Therefore, the charge transfer is assigned as a metal core to ligand shell charge transfer (MLCT). However, the lowest transition (HOMO−LUMO gap) for this cluster is at 561 nm. The corresponding transition is taking place between HOMO and LUMO with a gap of 2.207 eV. To comprehend the hybridization of these molecular orbitals, the total and partial density of states were analyzed in the entire energy regime from −9.5 to 2 eV, as shown in Figure 5d. The middle of the gap was set at 0 eV for clarity. From Figure 5d, the doubly degenerate HOMO bands are mainly made up of 3p

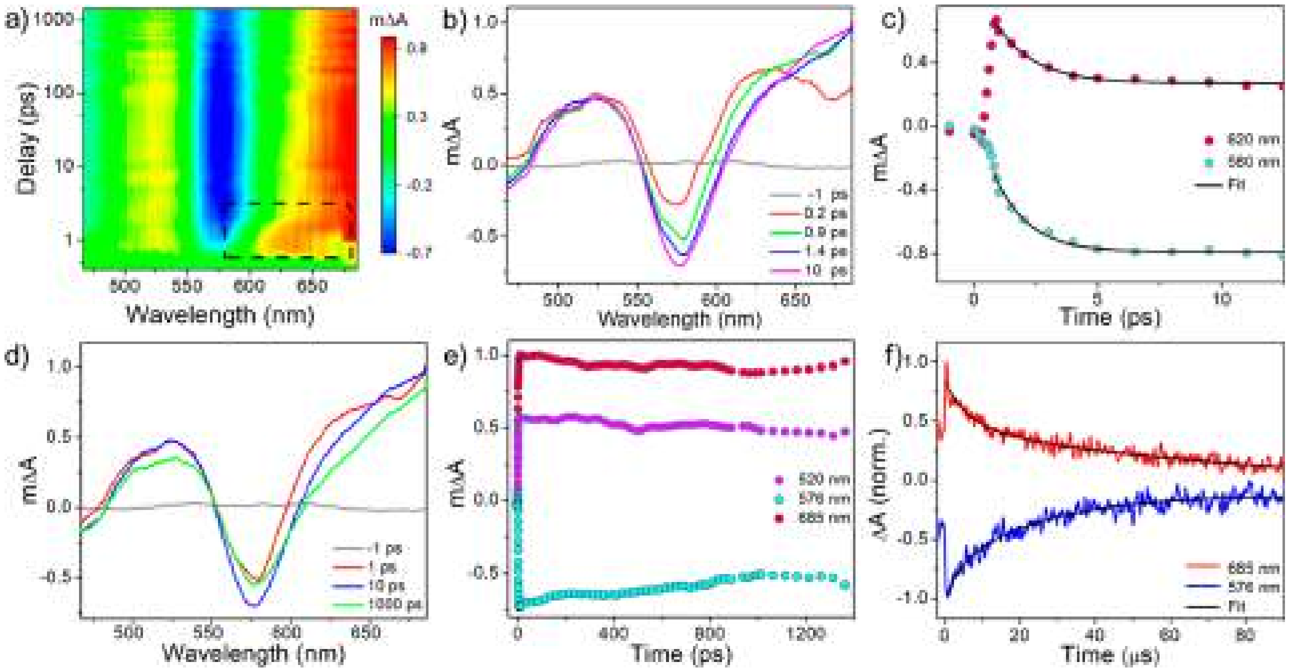

Figure 7. Femtosecond and ns-TA pump−probe spectra of Ag_{42} NC. (a) Contour plot, where the region enclosed by dashed lines indicates the photoinduced absorption arising from the Stark effect. (b) Spectral evolution of TA at an early time scale. (c) Formation and decay of bleach and PIA with time constants of 1.6 ± 0.1 and 1.4 ± 0.1 ps, showing close association of PIA with hot carriers. (d, e) Spectral and temporal evolution of TA for long time scales at different wavelengths. (f) Nanosecond time evolution recorded with ns laser flash photolysis.

AOs of S atoms and 5p and 4d AOs of Ag atoms, while the LUMO bands are dominated by 3p AOs of P atoms and 5p AOs of Ag atoms.

Luminescence Properties of Ag_{42} and Ag_{14} NCs. We have measured the photoluminescence spectra of Ag_{42} and Ag_{14} separately. Figure 6a and b shows the excitation and emission spectra of both the NCs. The former one exhibits a NIR emission maximum centered around 980 nm, corresponding to a broad excitation maximum centered around 525 nm. The lifetime of the NIR emission is >1.5 μs indicating that the emission is phosphorescence, originating from a triplet state (Figure S43). UV−vis absorption peak at 572 nm is close to the excitation maximum at 525 nm. Interestingly, Ag_{14} shows red luminescence at room temperature (25 °C) with an emission maximum at 626 nm, corresponding to the excitation maxima at 373 and 447 nm. The excitation maximum of the cluster present near to the broad absorption maximum is responsible for this emission at 626 nm. The emission feature of Ag_{14} enhances significantly upon cooling the sample in liquid nitrogen. The inseparable $[Ag_2S(TPP)_6]$ fragments present with the Ag_{14} cluster in solution may have a slight contribution in this aggregation process.

Luminescence spectral measurements show a 25.4-fold enhanced emission with 17 nm red-shift of the spectral profile. Luminescence enhancement with slight red-shift is due to the restriction of the nonradiative decay of the NCs, due to aggregation-induced emission, in liquid nitrogen matrix. Literature reports a similar type of emission enhancement in NCs due to enhanced rigidity of the NC in the presence of secondary ligands and lowering of the temperature.[69,70] Figure S44 presents images of Ag_{14} crystals under 365 nm UV excitation with clearly observable red emission.

Electron Dynamics of Ag_{42} and Ag_{14} through fs- and ns-TA. For better understanding the effect of light-activation to the electronic energy levels, and associated electronic transitions, we have measured femtosecond−nanosecond transient absorption (fs−ns-TA) of both the NCs. Details of the instrumental setup and measurements are given in the SI. The TA spectra of Ag_{42} are compiled in Figure 7. Upon photoexcitation using a 400 nm laser pump with a fluence of 250 μJ/cm^2, Ag_{42} showed ground-state photobleaching (GSPB), centered at 576 and 468 nm. The observed GSPB are at the positions of two states observed in the ground state optical absorption spectrum at 572 and 458 nm. It indicates the Pauli blocking of these two states by pump excited carriers, which reduces the absorption of probe pulse, generating GSPB signals. Along with it, other important features observed are a fast decaying photoinduced absorption (PIA) at 620 nm, red-shifted with respect to the GSPB at 576 nm and two nondecaying PIA signals at 685 and 520 nm.

In order to gain additional insight behind the origin of fast decaying PIA, we have plotted the spectral kinetics of TA and temporal profiles at 580 and 620 nm for the early time scales, in Figure 7b and c. From Figure 7b, we observe the simultaneous growth of the GSPB signal and the decrease of the PIA signal. The GSPB growth time generally relates to the time taken by the pump excited hot carriers to reach that state. The close association of GSPB growth with the PIA decay suggest that Coulomb interaction between the hot carriers causes the red shift of the 576 nm resonance. It causes the absorption of probe pulse into these levels, observed as red-shifted PIA. It disappears once all the pump-excited carriers reach that state. A similar effect, generally observed in semiconductors, is attributed as a Stark effect.[71] The observation of the Stark effect in our NCs suggests the close similarity of the electronic structure of NCs with semiconductors. The DFT optimized structure of Ag_{42} (shown in Figure 2a) reveals that it has a layer-like silver core (Ag_{12} and

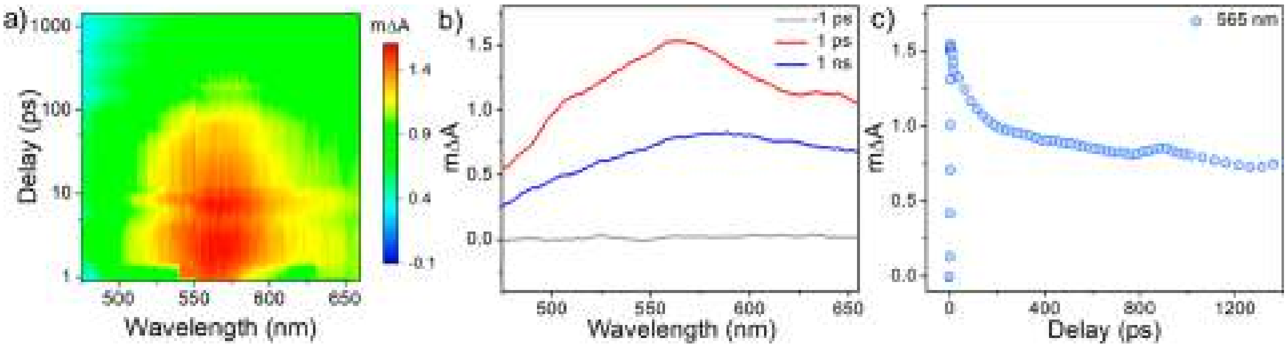

Figure 8. Femtosecond-TA pump−probe spectra of Ag_{14} NC. (a) Contour plot indicating a broad ESA. (b) Time evolution spectral profile of ESA features. (c) Fast decay time data of ESA corresponding to the 565 nm peak.

Ag_{30}) and surface CBDT and TPP ligand shells, making an anisotropic nature, which generates an inherent electric field gradient. Perturbation of the external electromagnetic field is due to this inherent electric field gradient. The literature shows that an anisotropic gold NC exhibits a similar type of Stark effect.[72] In order to analyze the lifetime of carriers, we have plotted the time evolution of GSPB and PIA features in Figure 7d and e. It shows almost similar kinetics for GSPB and PIA, not decaying in our fs-TA window, and this has an almost constant magnitude up to 1400 ps. It demonstrates the long lifetime of NC states. To determine their lifetime, we have further studied ns-TA decay kinetics using ns laser flash photolysis. The time evolution of ns-TA is shown in Figure 7f, with a very long lifetime, having average decay constants of 3.4 ± 0.6 and 24 ± 1 μs for 576 nm and 5.7 ± 0.4 and 70 ± 10 μs for 685 nm. The localized long-lived excited states of the silver core of the cluster, an element having inherent light sensitivity, are likely to be contributing to its light-induced core transformation (shown in Figures 2b and S6b).

In contrast to Ag_{42} NC, Ag_{14} did not show any type of photoinduced bleaching effects, the only feature observed was a broad PIA. Most probably, isotropic structure of Ag_{14} having C_3 axial symmetry (shown in Figures S29 and S30) did not have any inherent electric field gradient. Figure 8A shows the contour plot of Ag_{14} after 400 nm excitation at a fluence of 250 $\mu J/cm^2$. The TA spectral profile in Figure 8b did not show any GSB peaks; only it has a broad PIA in the range of 500 to 650 nm. The time evolution of PIA maximum centered around 565 nm is shown in Figure 8c, with the decay time of 85 ± 9 ps indicating fast relaxation, which is also in contrast to Ag_{42}, where we observed long lifetime of carriers.

CONCLUSION

In summary, we have presented the synthesis of *ortho*-carborane-1,2-dithiol and triphenylphosphine coprotected Ag_{42} NC using a LEIST reaction starting with Ag_{18}. This is a carborane-protected silver nanocluster with the highest number of Ag atoms reported so far. Numerous techniques have been used to probe the structure as well as electronic and photophysical properties of the Ag_{42}. Despite several efforts, molecular complexity limited us to get diffractable single crystals. Thermogravimetric measurements showed exceptional thermal stability in them, up to 200 °C. Although the cluster is thermally stable, irradiation with white light leads to a structural conversion to Ag_{14}. UV−vis absorption spectra indicate this structural conversion through some intermediate NCs. The mass spectrometric measurements suggested the interconversion through two sets of intermediate NCs. The first set of NCs were composed of $[Ag_{35}(CBDT)_8(TPP)_4]^{2-}$ and $[Ag_{37}(CBDT)_{12}(TPP)_4]^{3-}$, and the next had $[Ag_{30}(CBDT)_8(TPP)_4]^{2-}$, $[Ag_{26}(CBDT)_{11}(TPP)_4]^{2-}$, and $[Ag_{26}(CBDT)_7(TPP)_7]^{2-}$. Single crystal XRD confirms Ag_{14} had a Ag_8 bicapped trigonal antiprism core surrounded by six Ag surface atoms through Ag−S and Ag−P bonding. Six CBDT and TPP ligands coprotected the metallic core. TDDFT calculation of Ag_{14} reveals an electronic transition from the HOMO localized to Ag_{14} core to the LUMO centered on CBDT and TPP ligands. Interestingly, Ag_{42} showed a NIR phosphorescence in comparison to the red emitting Ag_{14}. Femtosecond TA measurements showed a very fast (lifetime of <1 ps) red-shifting of the ESA of Ag_{42} due to its anisotropic nature. Time-resolved (fs and ns)-TA confirms the slow decay (3.4 ± 0.6 and 24 ± 1 μs for 576 nm and 5.7 ± 0.4 and 70 ± 10 μs for 685 nm) features of Ag_{42}, in comparison to the fast decaying (85 ± 9 ps for 565 nm) ESA for Ag_{14}. This long time scale decay suggests slow vibrational relaxation, a potential reason for the observed light-induced core reduction. This work leads to the path toward a detailed understanding of light-triggered intercluster conversion of atomically precise metal nanoclusters and associated electron dynamics. We believe light-irradiated interconversion is a synthetic method to prepare other silver nanoclusters.

EXPERIMENTAL SECTION

Synthesis of Ag_{42} NCs. Ag_{42} was synthesized from hydride, and TPP coprotected Ag_{18} using the LEIST reaction. A detailed protocol for the synthesis of Ag_{18} is presented in the SI. In brief, a methanolic solution of Ag_{18} was reacted with CBDT, producing Ag_{42} as a brown precipitate, which was insoluble in common alcohols such as ethanol but soluble in chlorinated solvents. The crude NCs were purified using repeated washing by water, methanol, and ethanol solvents. The purified NCs in the solutions of dichloromethane (DCM), 1,2-dichlorobenzene (DCB), acetone, acetyl acetone (acac), methyl isobutyl ketone (MIBK), acetonitrile (ACN), tetrahydrofuran (THF), dimethylformamide (DMF), and dimethyl sulfoxide (DMSO) were used for further studies.

Synthesis of Ag_{14} NCs through Light-Irradiation. Ag_{14} was synthesized using light-irradiation of Ag_{42}. A DCM solution (5 mL) of purified Ag_{42} (10 mg) was degassed using argon bubbling prior to exposure to light. A 190 W solar simulator from Newport, India, was used as the source of light. After 24 h of light irradiation, Ag_{42} got transformed fully to Ag_{14}. There was no transformation Ag_{14} upon further irradiation. The reaction was accompanied by a change of color from dark brown (Ag_{42} NCs), to dark red (intermediate NCs), and to a final orange−yellow, typical of Ag_{14}. Diffraction quality single crystals of Ag_{14} were obtained by slow diffusion of dry hexane into the

https://doi.org/10.1021/acsnano.1c02602
ACS Nano 2021, 15, 15781−15793

concentrated cluster solution in DCM. The grown yellow cuboid crystals were used for single crystal X-ray diffraction.

Additional experimental details and instrumentations are presented in the Supporting Information.

ASSOCIATED CONTENT

Supporting Information

The Supporting Information is available free of charge at https://pubs.acs.org/doi/10.1021/acsnano.1c02602.

Experimental section, instrumentation, X-ray crystallographic details, computational details, and additional experimental data (PDF)

Single crystal X-ray data for Ag_{14} nanocluster (CIF)

AUTHOR INFORMATION

Corresponding Authors

Thalappil Pradeep − *DST Unit of Nanoscience (DST UNS), and Thematic Unit of Excellence (TUE), Department of Chemistry, Indian Institute of Technology, Madras, Chennai 600036, India;* orcid.org/0000-0003-3174-534X; Email: pradeep@iitm.ac.in

Tomas Base − *Department of Synthesis, Institute of Inorganic Chemistry, The Czech Academy of Science, 25068 Rez, Czech Republic;* orcid.org/0000-0003-2533-8705; Email: tbase@iic.acs.cz

Kumaran Nair Valsala Devi Adarsh − *Department of Physics, Indian Institute of Science Education, and Research Bhopal, Bhopal 462066, India;* orcid.org/0000-0002-6337-6545; Email: adarsh@iiserb.ac.in

Authors

Arijit Jana − *DST Unit of Nanoscience (DST UNS), and Thematic Unit of Excellence (TUE), Department of Chemistry, Indian Institute of Technology, Madras, Chennai 600036, India*

Madhuri Jash − *DST Unit of Nanoscience (DST UNS), and Thematic Unit of Excellence (TUE), Department of Chemistry, Indian Institute of Technology, Madras, Chennai 600036, India*

Ajay Kumar Poonia − *Department of Physics, Indian Institute of Science Education, and Research Bhopal, Bhopal 462066, India*

Ganesan Paramasivam − *DST Unit of Nanoscience (DST UNS), and Thematic Unit of Excellence (TUE), Department of Chemistry, Indian Institute of Technology, Madras, Chennai 600036, India*

Md Rabiul Islam − *DST Unit of Nanoscience (DST UNS), and Thematic Unit of Excellence (TUE), Department of Chemistry, Indian Institute of Technology, Madras, Chennai 600036, India*

Papri Chakraborty − *DST Unit of Nanoscience (DST UNS), and Thematic Unit of Excellence (TUE), Department of Chemistry, Indian Institute of Technology, Madras, Chennai 600036, India*

Sudhadevi Antharjanam − *Sophisticated Analytical Instruments Facility (SAIF), Indian Institute of Technology, Madras, Chennai 600036, India*

Jan Machacek − *Department of Synthesis, Institute of Inorganic Chemistry, The Czech Academy of Science, 25068 Rez, Czech Republic;* orcid.org/0000-0003-4723-0789

Sundargopal Ghosh − *DST Unit of Nanoscience (DST UNS), and Thematic Unit of Excellence (TUE), Department of Chemistry, Indian Institute of Technology, Madras, Chennai 600036, India;* orcid.org/0000-0001-6089-8244

Complete contact information is available at: https://pubs.acs.org/10.1021/acsnano.1c02602

Author Contributions

A.J. performed the synthesis, characterization, and most of the experimental studies. M.J. assisted A.J., especially in the crystallization of the samples. P.C. performed mass spectrometric studies. Md.R.I. conducted electron microscopic measurements. All the fs−ns time-resolved studies were conducted by A.K.P. in the laboratory of K.N.V.D.A. S.G. was involved in the discussion of experimental data. G.P. and J.M. performed computational studies. T.B. synthesized the carborane thiols used in this work and conducted all the work relating to those systems. The first draft of the manuscript was written by A.J., and all the authors contributed to improving it. T.P. suggested the problem, supervised the project, and finalized the manuscript. This work is a part of longer-term collaboration aimed at unlocking the potential of materials produced by combining metal nanoclusters and carborane ligands initiated by T.P. and T.B.

Notes

The authors declare no competing financial interest.

ACKNOWLEDGMENTS

The authors would like to acknowledge the Department of Science, and Technology, Govt. of India (DST-GOI), and the Ministry of Education, Youth, and Sports (MEYS) of the Czech Republic for their financial support to the bilateral research project registered under nos. DST/INT/Czech/P-16/2020 and LTAIN19152. K.N.V.D.A. gratefully acknowledges the Science and Engineering Research Board (SERB) for the grant, CRG/2019/002808. We would like to thank M. P. Kannan and Jayoti Roy for XPS and mass spectrometric measurements, respectively. A.J. thanks IIT Madras for his fellowship. T.P. acknowledges funding for the Centre of Excellence on Molecular Materials and Functions under the Institution of Eminence scheme of IIT Madras.

REFERENCES

(1) Jin, R.; Zeng, C.; Zhou, M.; Chen, Y. Atomically Precise Colloidal Metal Nanoclusters and Nanoparticles: Fundamentals and Opportunities. *Chem. Rev.* **2016**, *116*, 10346−10413.

(2) Chakraborty, I.; Pradeep, T. Atomically Precise Clusters of Noble Metals: Emerging Link between Atoms and Nanoparticles. *Chem. Rev.* **2017**, *117*, 8208−8271.

(3) Jadzinsky, P. D.; Calero, G.; Ackerson, C. J.; Bushnell, D. A.; Kornberg, R. D. Structure of a Thiol Monolayer−Protected Gold Nanoparticle at 1.1 Å Resolution. *Science (Washington, DC, U. S.)* **2007**, *318*, 430−434.

(4) Yang, H.; Wang, Y.; Chen, X.; Zhao, X.; Gu, L.; Huang, H.; Yan, J.; Xu, C.; Li, G.; Wu, J.; Edwards, A. J.; Dittrich, B.; Tang, Z.; Wang, D.; Lehtovaara, L.; Häkkinen, H.; Zheng, N. Plasmonic Twinned Silver Nanoparticles with Molecular Precision. *Nat. Commun.* **2016**, *7*, 1−8.

(5) Liu, X.; Astruc, D. Atomically Precise Copper Nanoclusters and Their Applications. *Coord. Chem. Rev.* **2018**, *359*, 112−126.

(6) Chakraborty, I.; Bhuin, R. G.; Bhat, S.; Pradeep, T. Blue Emitting Undecaplatinum Clusters. *Nanoscale* **2014**, *6*, 8561−8564.

(7) Yao, Q.; Chen, T.; Yuan, X.; Xie, J. Toward Total Synthesis of Thiolate-Protected Metal Nanoclusters. *Acc. Chem. Res.* **2018**, *51*, 1338−1348.

(8) Jana, A.; Chakraborty, P.; Dar, W. A.; Chandra, S.; Khatun, E.; Kannan, M. P.; Ras, R. H. A.; Pradeep, T. Dual Emitting Ag35 Nanocluster Protected by 2-Pyrene Imine Thiol. *Chem. Commun.* **2020**, *56*, 12550−12553.

(9) Jordan, A. J.; Lalic, G.; Sadighi, J. P. Coinage Metal Hydrides : Synthesis, Characterization, and Reactivity. *Chem. Rev.* **2016**, *116*, 8318−8372.

(10) Lei, Z.; Wan, X.-K.; Yuan, S.-F.; Guan, Z.-J.; Wang, Q.-M. Alkynyl Approach toward the Protection of Metal Nanoclusters. *Acc. Chem. Res.* **2018**, *51* (10), 2465−2474.

(11) Yang, S.; Chai, J.; Chong, H.; Song, Y.; Yu, H.; Zhu, M. Sulfonate, Sulfide and Thiolate Ligands into an Ultrasmall Nanocluster: [Ag40.13Cu13.87S19(tBuS)20(tBuSO3)12]. *Chem. Commun.* **2018**, *54*, 4314−4316.

(12) Cerretani, C.; Kanazawa, H.; Vosch, T.; Kondo, J. Crystal Structure of a NIR-Emitting DNA-Stabilized Ag16 Nanocluster. *Angew. Chem., Int. Ed.* **2019**, *58*, 17153−17157.

(13) Anand, U.; Ghosh, S.; Mukherjee, S. Toggling between Blue- and Red-Emitting Fluorescent Silver Nanoclusters. *J. Phys. Chem. Lett.* **2012**, *3*, 3605−3609.

(14) Yuan, P.; Zhang, R.; Selenius, E.; Ruan, P.; Yao, Y.; Zhou, Y.; Malola, S.; Häkkinen, H.; Teo, B. K.; Zheng, N. Solvent-Mediated Assembly of Atom-Precise Gold−Silver Nanoclusters to Semiconducting One-Dimensional Materials. *Nat. Commun.* **2020**, *11*, 1−8.

(15) Gell, L.; Lehtovaara, L.; Häkkinen, H. Superatomic S2 Silver Clusters Stabilized by a Thiolate-Phosphine Monolayer: Insight into Electronic and Optical Properties of Ag14(SC6H3F2)12(PPh3)8 and Ag16(SC6H3F2)14(DPPE)4. *J. Phys. Chem. A* **2014**, *118*, 8351−8355.

(16) Kang, X.; Zhu, M. Tailoring the Photoluminescence of Atomically Precise Nanoclusters. *Chem. Soc. Rev.* **2019**, *48*, 2422−2457.

(17) Liu, C.; Li, T.; Abroshan, H.; Li, Z.; Zhang, C.; Kim, H. J.; Li, G.; Jin, R. Chiral Ag23 Nanocluster with Open Shell Electronic Structure and Helical Face-Centered Cubic Framework. *Nat. Commun.* **2018**, *9*, 1−6.

(18) Abbas, M. A.; Kamat, P. V.; Bang, J. H. Thiolated Gold Nanoclusters for Light Energy Conversion. *ACS Energy Lett.* **2018**, *3* (4), 840−854.

(19) Subramanian, V.; Jena, S.; Ghosh, D.; Jash, M.; Baksi, A.; Ray, D.; Pradeep, T. Dual Probe Sensors Using Atomically Precise Noble Metal Clusters. *ACS Omega* **2017**, *2*, 7576−7583.

(20) Russier-Antoine, I.; Bertorelle, F.; Calin, N.; Sanader, Ž.; Krstić, M.; Comby-Zerbino, C.; Dugourd, P.; Brevet, P. F.; Bonacic-Koutecky, V.; Antoine, R. Ligand-Core NLO-Phores: A Combined Experimental and Theoretical Approach to the Two-Photon Absorption and Two-Photon Excited Emission Properties of Small-Ligated Silver Nanoclusters. *Nanoscale* **2017**, *9*, 1221−1228.

(21) Kumar, J.; Kawai, T.; Nakashima, T. Circularly Polarized Luminescence in Chiral Silver Nanoclusters. *Chem. Commun.* **2017**, *53*, 1269−1272.

(22) Wang, Y.; Liu, X.; Wang, Q.; Quick, M.; Kovalenko, S. A.; Chen, Q.; Koch, N.; Pinna, N. Insights into Charge Transfer at an Atomically Precise Nanocluster/Semiconductor Interface. *Angew. Chem.* **2020**, *132*, 7822−7828.

(23) Han, Z.; Dong, X.; Luo, P.; Li, S.; Wang, Z.; Zang, S.; Mak, T. C. W. Ultrastable Atomically Precise Chiral Silver Clusters with More than 95% Quantum Efficiency. *Sci. Adv.* **2020**, *6* (February), eaay0107.

(24) Xie, Z.; Sun, P.; Wang, Z.; Li, H.; Yu, L.; Sun, D.; Chen, M.; Bi, Y.; Xin, X.; Hao, J. Metal−Organic Gels from Silver Nanoclusters with Aggregation- Induced Emission and Fluorescence-to-Phosphorescence Switching. *Angew. Chem., Int. Ed.* **2020**, *59*, 9922−9927.

(25) Joshi, C. P.; Bootharaju, M. S.; Alhilaly, M. J.; Bakr, O. M. [Ag25(SR)18]-: The "Golden"Silver Nanoparticle. *J. Am. Chem. Soc.* **2015**, *137*, 11578−11581.

(26) AbdulHalim, L. G.; Bootharaju, M. S.; Tang, Q.; Del Gobbo, S.; AbdulHalim, R. G.; Eddaoudi, M.; Jiang, D. E.; Bakr, O. M. Ag29(BDT)12(TPP)4: A Tetravalent Nanocluster. *J. Am. Chem. Soc.* **2015**, *137*, 11970−11975.

(27) Desireddy, A.; Conn, B. E.; Guo, J.; Yoon, B.; Barnett, R. N.; Monahan, B. M.; Kirschbaum, K.; Griffith, W. P.; Whetten, R. L.; Landman, U.; Bigioni, T. P. Ultrastable Silver Nanoparticles. *Nature* **2013**, *501*, 399−402.

(28) Wang, Z.; Su, H. F.; Kurmoo, M.; Tung, C. H.; Sun, D.; Zheng, L. S. Trapping an Octahedral Ag6 Kernel in a Seven-Fold Symmetric Ag56 Nanowheel. *Nat. Commun.* **2018**, *9* (1), 1−8.

(29) Alhilaly, M. J.; Bootharaju, M. S.; Joshi, C. P.; Besong, T. M.; Emwas, A. H.; Juarez-Mosqueda, R.; Kaappa, S.; Malola, S.; Adil, K.; Shkurenko, A.; Häkkinen, H.; Eddaoudi, M.; Bakr, O. M. [Ag67-(SPhMe2)32(PPh3)8]3+: Synthesis, Total Structure, and Optical Properties of a Large Box-Shaped Silver Nanocluster. *J. Am. Chem. Soc.* **2016**, *138*, 14727−14732.

(30) Ren, L.; Yuan, P.; Su, H.; Malola, S.; Lin, S.; Tang, Z.; Teo, B. K.; Häkkinen, H.; Zheng, L.; Zheng, N. Bulky Surface Ligands Promote Surface Reactivities of [Ag141 × 12(S-Adm)40]3+ (X = Cl, Br, I) Nanoclusters: Models for Multiple-Twinned Nanoparticles. *J. Am. Chem. Soc.* **2017**, *139*, 13288−13291.

(31) Kang, X.; Zhou, M.; Wang, S.; Jin, S.; Sun, G.; Zhu, M.; Jin, R. The Tetrahedral Structure and Luminescence Properties of Bi-Metallic Pt1Ag28(SR)18(PPh3)4 Nanocluster. *Chem. Sci.* **2017**, *8*, 2581−2587.

(32) Bootharaju, M. S.; Kozlov, S. M.; Cao, Z.; Harb, M.; Maity, N.; Shkurenko, A.; Parida, M. R.; Hedhili, M. N.; Eddaoudi, M.; Mohammed, O. F.; Bakr, O. M.; Cavallo, L.; Basset, J. Doping-Induced Anisotropic Self-Assembly of Silver Icosahedra in [Pt2Ag23Cl7(PPh3)10] Nanoclusters. *J. Am. Chem. Soc.* **2017**, *139*, 1053−1056.

(33) Khatun, E.; Chakraborty, P.; Jacob, B. R.; Paramasivam, G.; Bodiuzzaman, M.; Dar, W. A.; Pradeep, T. Intercluster Reactions Resulting in Silver-Rich Trimetallic Nanoclusters. *Chem. Mater.* **2020**, *32* (1), 611−619.

(34) Gao, M. Y.; Wang, K.; Sun, Y.; Li, D.; Song, B. Q.; Andaloussi, Y. H.; Zaworotko, M. J.; Zhang, J.; Zhang, L. Tetrahedral Geometry Induction of Stable Ag-Ti Nanoclusters by Flexible Trifurcate TiL3 Metalloligand. *J. Am. Chem. Soc.* **2020**, *142*, 12784−12790.

(35) Bootharaju, M. S.; Chang, H.; Deng, G.; Malola, S.; Baek, W.; Häkkinen, H.; Zheng, N.; Hyeon, T. Cd12Ag32(SePh)36: Non-Noble Metal Doped Silver Nanoclusters. *J. Am. Chem. Soc.* **2019**, *141*, 8422−8425.

(36) Dar, W. A.; Bodiuzzaman, M.; Ghosh, D.; Paramasivam, G.; Khatun, E.; Sugi, K. S.; Pradeep, T. Interparticle Reactions between Silver Nanoclusters Leading to Product Cocrystals by Selective Cocrystallization. *ACS Nano* **2019**, *13*, 13365−13373.

(37) Bodiuzzaman, M.; Ghosh, A.; Sugi, K. S.; Nag, A.; Khatun, E.; et al. Camouflaging Structural Diversity : Co-Crystallization of Two Different Nanoparticles Having Different Cores but the Same Shell. *Angew. Chem., Int. Ed.* **2019**, *58*, 189−194.

(38) Liu, J. Y.; Alkan, F.; Wang, Z.; Zhang, Z. Y.; Kurmoo, M.; Yan, Z.; Zhao, Q. Q.; Aikens, C. M.; Tung, C. H.; Sun, D. Different Silver Nanoparticles in One Crystal: Ag210(iPrPhS)71(Ph3P)5Cl and Ag211(iPrPhS)71(Ph3P)6Cl. *Angew. Chem., Int. Ed.* **2019**, *58*, 195−199.

(39) Yuan, S.-F.; Guan, Z.-J.; Liu, W.-D.; Wang, Q.-M. Solvent-Triggered Reversible Interconversion of All-Nitrogen-Donor-Protected Silver Nanoclusters and Their Responsive Optical Properties. *Nat. Commun.* **2019**, *10*, 1−7.

(40) Chevrier, D. M.; Conn, B. E.; Li, B.; Jiang, D. E.; Bigioni, T. P.; Chatt, A.; Zhang, P. Interactions between Ultrastable Na4Ag44(SR)-30 Nanoclusters and Coordinating Solvents: Uncovering the Atomic-Scale Mechanism. *ACS Nano* **2020**, *14*, 8433−8441.

(41) Udayabhaskararao, T.; Pradeep, T. New Protocols for the Synthesis of Stable Ag and Au Nanocluster Molecules. *J. Phys. Chem. Lett.* **2013**, *4*, 1553−1564.

(42) Manno, R.; Ranjan, P.; Sebastian, V.; Mallada, R.; Irusta, S.; Sharma, U. K.; Van der Eycken, E. V.; Santamaria, J. Continuous Microwave-Assisted Synthesis of Silver Nanoclusters Confined in

Mesoporous SBA-15: Application in Alkyne Cyclizations. *Chem. Mater.* **2020**, *32*, 2874−2883.

(43) Booth""raju, M. S.; Burlakov, V. M.; Besong, T. M. D.; Joshi, C. P.; Abdulhalim, L. G.; Black, D. M.; Whetten, R. L.; Goriely, A.; Bakr, O. M. Reversible Size Control of Silver Nanoclusters via Ligand-Exchange. *Chem. Mater.* **2015**, *27*, 4289−4297.

(44) Yuan, X.; Yao, Q.; Yu, Y.; Luo, Z.; Dou, X.; Xie, J. Traveling through the Desalting Column Spontaneously Transforms Thiolated Ag Nanoclusters from Nonluminescent to Highly Luminescent. *J. Phys. Chem. Lett.* **2013**, *4* (11), 1811−1815.

(45) Yao, Q.; Fung, V.; Sun, C.; Huang, S.; Chen, T.; Jiang, D. E.; Lee, J. Y.; Xie, J. Revealing Isoelectronic Size Conversion Dynamics of Metal Nanoclusters by a Noncrystallization Approach. *Nat. Commun.* **2018**, *9* (1), 1−11.

(46) Booth""araju, M. S.; Joshi, C. P.; Alhilaly, M. J.; Bakr, O. M. Switching a Nanocluster Core from Hollow to Nonhollow. *Chem. Mater.* **2016**, *28* (10), 3292−3297.

(47) Stamplecoskie, K. G.; Scaiano, J. C. Light Emitting Diode Irradiation Can Control the Morphology and Optical Properties of Silver Nanoparticles. *J. Am. Chem. Soc.* **2010**, *132*, 1825−1827.

(48) Callegari, A.; Tonti, D.; Chergui, M. Photochemically Grown Silver Nanoparticles with Wavelength-Controlled Size and Shape. *Nano Lett.* **2003**, 3 (11), 1565−1568.

(49) Pietrobon, B.; Kitaev, V. Photochemical Synthesis of Monodisperse Size-Controlled Silver Decahedral Nanoparticles and Their Remarkable Optical Properties. *Chem. Mater.* **2008**, *20*, 5186−5190.

(50) Chakraborty, I.; Udayabhaskararao, T.; Deepesh, G. K.; Pradeep, T. Sunlight Mediated Synthesis and Antibacterial Properties of Monolayer Protected Silver Clusters. *J. Mater. Chem. B* **2013**, *1*, 4059−4064.

(51) Tang, L.; Kang, X.; Wang, S.; Zhu, M. Light-Induced Size-Growth of Atomically Precise Nanoclusters. *Langmuir* **2019**, *35*, 12350−12355.

(52) Núñez, R.; Tarrés, M.; Ferrer-Ugalde, A.; De Biani, F. F.; Teixidor, F. Electrochemistry and Photoluminescence of Icosahedral Carboranes, Boranes, Metallacarboranes, and Their Derivatives. *Chem. Rev.* **2016**, *116*, 14307−14378.

(53) Fister, T. T.; Vila, F. D.; Seidler, G. T.; Svec, L.; Linehan, J. C.; Cross, J. O. Local Electronic Structure of Dicarba-Closo-Dodecarboranes. *J. Am. Chem. Soc.* **2008**, *130*, 925−932.

(54) Nunez, R.; Romero, I.; Teixidor, F.; Vinas, C. Icosahedral Boron Clusters: A Perfect Tool for the Enhancement of Polymer Features. *Chem. Soc. Rev.* **2016**, *45*, 5147−5173.

(55) Fisher, S. P.; Tomich, A. W.; Lovera, S. O.; Kleinsasser, J. F.; Guo, J.; Asay, M. J.; Nelson, H. M.; Lavallo, V. Nonclassical Applications of Closo-Carborane Anions: From Main Group Chemistry and Catalysis to Energy Storage. *Chem. Rev.* **2019**, *119* (14), 8262−8290.

(56) Wang, Q.; Wang, J.; Wang, S.; Wang, Z.; Cao, M.; He, C.; Yang, J.; Zang, S.; Mak, T. C. W. O -Carborane Based and Atomically-Precise Metal Clusters as Hypergolic Materials. *J. Am. Chem. Soc.* **2020**, *142* (28), 12010−12014.

(57) Goronzy, D. P.; Staněk, J.; Avery, E.; Guo, H.; Bastl, Z.; Dušek, M.; Gallup, N. M.; Gün, S.; Kučeráková, M.; Levandowski, B. J.; Macháček, J.; Šícha, V.; Thomas, J. C.; Yavuz, A.; Houk, K. N.; Danlşman, M. F.; Mete, E.; Alexandrova, A. N.; Base, T.; Weiss, P. S. Influence of Terminal Carboxyl Groups on the Structure and Reactivity of Functionalized M-Carboranethiolate Self-Assembled Monolayers. *Chem. Mater.* **2020**, *32*, 6800−6809.

(58) Morin, J.-F.; Shirai, Y.; Tour, J. M. En Route to a Motorized Nanocar. *Org. Lett.* **2006**, *8*, 1713−1716.

(59) Poater, J.; Vinas, C.; Bennour, I.; Escayola, S.; Sola, M.; Teixidor, F. Too Persistent to Give Up: Aromaticity in Boron Clusters Survives Radical Structural Changes. *J. Am. Chem. Soc.* **2020**, *142*, 9396−9407.

(60) Wang, Z.; Wang, M.; Li, Y.; Luo, P.; Jia, T.; Huang, R.; Zang, S.; Mak, T. C. W. Atomically Precise Site-Specific Tailoring and Directional Assembly of Superatomic Silver Nanoclusters. *J. Am. Chem. Soc.* **2018**, *140*, 1069−1076.

(61) Li, Y.; Wang, Z.; Ma, X.; Luo, P.; Du, C.; Zang, S. Distinct Photophysical Properties in Atom-Precise Silver and Copper Nanocluster Analogues. *Nanoscale* **2019**, *11*, 5151−5157.

(62) Huang, J.; Wang, Z.; Zang, S.; Mak, T. C. W. Spontaneous Resolution of Chiral Multi-Thiolate-Protected Ag30 Nanoclusters. *ACS Cent. Sci.* **2020**, *6*, 1971−1976.

(63) Boothraju, M. S.; Dey, R.; Gevers, L. E.; Hedhili, M. N.; Basset, J. M.; Bakr, O. M. A New Class of Atomically Precise, Hydride-Rich Silver Nanoclusters Co-Protected by Phosphines. *J. Am. Chem. Soc.* **2016**, *138*, 13770−13773.

(64) Baše, T.; Bastl, Z.; Plzák, Z.; Grygar, T.; Plešek, J.; Carr, M. J.; Malina, V.; Šubrt, J.; Boháček, J.; Večerníková, E.; Kříž, O. Carboranethiol-Modified Gold Surfaces. A Study and Comparison of Modified Cluster and Flat Surfaces. *Langmuir* **2005**, *21*, 7776−7785.

(65) Vetushka, A.; Bernard, L.; Guseva, O.; Bastl, Z.; Plocek, J.; Tomandl, I.; Fejfar, A.; Baše, T.; Schmutz, P. Adsorption of Oriented Carborane Dipoles on a Silver Surface. *Phys. Status Solidi B* **2016**, *253* (3), 591−600.

(66) Lin, Z.; Slee, T.; Mingos, D. M. P. A Structural Jellium Model of Cluster Electronic Structure. *Chem. Phys.* **1990**, *142*, 321−334.

(67) Weerawardene, K. L. D. M.; Häkkinen, H.; Aikens, C. M. Connections between Theory and Experiment for Gold and Silver Nanoclusters. *Annu. Rev. Phys. Chem.* **2018**, *69*, 205−229.

(68) Walter, M.; Akola, J.; Lopez-Acevedo, O.; Jadzinsky, P. D.; Calero, G.; Ackerson, C. J.; Whetten, R. L.; Grönbeck, H.; Häkkinen, H. A Unified View of Ligand-Protected Gold Clusters as Superatom Complexes. *Proc. Natl. Acad. Sci. U. S. A.* **2008**, *105* (27), 9157−9162.

(69) Khatun, E.; Ghosh, A.; Chakraborty, P.; Singh, P.; Bodiuzzaman, M.; Ganesan, P.; Nataranjan, G.; Ghosh, J.; Pal, S. K.; Pradeep, T. Thirty-Fold Photoluminescence Enhancement Induced by Secondary Ligands in Monolayer Protected Silver Clusters. *Nanoscale* **2018**, *10*, 20033−20042.

(70) Wang, Z.; Su, H. F.; Tan, Y. Z.; Schein, S.; Lin, S. C.; Liu, W.; Wang, S. A.; Wang, W. G.; Tung, C. H.; Sun, D.; Zheng, L. S. Assembly of Silver Trigons into a Buckyball-Like Ag180 Nanocage. *Proc. Natl. Acad. Sci. U. S. A.* **2017**, *114* (46), 12132−12137.

(71) Aneesh, J.; Swarnkar, A.; Kumar Ravi, V.; Sharma, R.; Nag, A.; Adarsh, K. V. Ultrafast Exciton Dynamics in Colloidal CsPbBr3 Perovskite Nanocrystals: Biexciton Effect and Auger Recombination. *J. Phys. Chem. C* **2017**, *121* (8), 4734−4739.

(72) Li, Q.; Zhou, M.; So, W. Y.; Huang, J.; Li, M.; Kauffman, D. R.; Cotlet, M.; Higaki, T.; Peteanu, L. A.; Shao, Z.; Jin, R. A Mono-Cuboctahedral Series of Gold Nanoclusters: Photoluminescence Origin, Large Enhancement, Wide Tunability, and Structure-Property Correlation. *J. Am. Chem. Soc.* **2019**, *141* (13), 5314−5325.

Supporting Information

Light-Activated Intercluster Conversion of an Atomically Precise Silver Nanocluster

Arijit Jana[ξ], Madhuri Jash[ξ], Ajay Kumar Poonia[€], Ganesan Paramasivam[ξ], Md Rabiul Islam[ξ], Papri Chakraborty[ξ], Sudhadevi Antharjanam[δ], Jan Machacek [ψ], Sundargopal Ghosh[ξ], Kumaran Nair Valsala Devi Adarsh* [€], Tomas Base* [ψ], and Thalappil Pradeep* [ξ]

[ξ] DST Unit of Nanoscience (DST UNS), and Thematic Unit of Excellence (TUE), Department of Chemistry, Indian Institute of Technology, Madras, Chennai – 600036, India

[ψ] Department of Synthesis, Institute of Inorganic Chemistry, The Czech Academy of Science, 1001 Husinec-Rez, 25068, Czech Republic

[€]Department of Physics, Indian Institute of Science Education, and Research Bhopal, Bhopal-462066, India

[δ]Sophisticated Analytical Instruments Facility (SAIF), Indian Institute of Technology, Madras, Chennai – 600036, India

*Email: pradeep@iitm.ac.in, tbase@iic.acs.cz, adarsh@iiserb.ac.in

Table of contents:

Experimental section

Chemicals

Ortho-carborane-1, 2-dithiol (CBDT) was synthesized by following the previous literature.[1,2] As synthesized CBDT was further purified using crystallization from hot dichloromethane/hexane (1:1) solution. Silver nitrate ($AgNO_3$) was purchased from Rankem chemicals. Sodium borohydride ($NaBH_4$, 98%), and triphenylphosphine (TPP) were purchased from Aldrich chemicals. Solvent grade dichloromethane (DCM), chloroform ($CHCl_3$), n-hexane, N-N dimethyl-formamide (DMF), and methanol (99.5%) were purchased from Rankem chemicals and Finar, India. Milli-Q water was used for $[Ag_{18}H_{16}(TPP)_{10}]^{2+}$ NC synthesis purpose. Deuterated solvent, $CDCl_3$ (99.8 atom % D) was purchased from Sigma Aldrich. All the chemicals are commercially available and used as such without further purification.

Synthesis of $[Ag_{18}H_{16}(TPP)_{10}]^{2+}$ NC

Ag_{18} NC was synthesized by following the previous literatures.[3,4] Briefly, in room temperature, 20 mg of $AgNO_3$ was dissolve in 5 mL of methanol. After that, 70 mg of TPP was dissolved in 9 mL of $CHCl_3$ and was added to the reaction mixture under stirring condition. After 20 min of reaction, 6.5 mg $NaBH_4$, dissolved in 0.75 mL of milli-Q water was added to it. After addition of $NaBH_4$, reaction mixture becomes yellow solution, which gradually converted to dark brownish solution, and finally after 3.5 hours it becomes dark green color which indicates the formation of Ag_{18} NC. After completion of the reaction, mixed solvents were removed under reduced pressure. Dark greenish NC was dissolved in cold water to remove excess salts. Finally, the purified Ag_{18} NC was extracted using methanol. Formation of the NC was confirmed from their UV-vis absorption spectra and mass spectrometric results are shown in Figure S1. The yield of the reaction is 20% in terms of silver. The same NC was used for the synthesis of Ag_{42} NC.

Synthesis of $[Ag_{42}(CBDT)_{15}(TPP)_4]^{2-}$ NC

Ag_{42} was synthesized by following ligand exchange induced structural transformation (LEIST) reaction between Ag_{18}, and *ortho*-carborane-1, 2-dithiol (CBDT) ligand. During the synthesis, at first 5.5 mg of CBDT was dissolved in 1 mL of methanol. Then it was quickly added to the methanol solution of Ag_{18} (3 mg/mL) under 800 rpm stirring condition. Just after the addition of the ligand, a greenish-white precipitate was formed. After 4 hours of continuous reaction, the white precipitate was slowly converts to the brownish precipitate, which indicates the formation of Ag_{42}. After completion of the reaction, brownish precipitate was cleaned three times each using methanol and ethanol to remove the excess phosphines. Then the precipitate was vacuum dried, and Ag_{42} was extracted by dissolving the precipitate in dichloromethane or chloroform or dimethylformamide for further characterizations. Yield of the product is 60 to 65 % in terms of silver.

Thermal treatment of Ag_{42} NC

Thermal stability of the Ag_{42} cluster in its solid state was measured upon dropcasting 10 mg of purified cluster. After 24 h of heating, we have measured its UV-vis absorption spectrum upon dissolving the cluster in DCM. Figure S16 shows absorption spectrum of the cluster after each heating. To understand the thermal stability of the Ag_{42} in solution at ambient condition, 10 mg of NC soluble in 5 mL of DMF solvent was used for heat treatment. Each step of the heating experiment was performed for up to 24 hours at 600 rpm stirring condition. Photographs of the solution and the respective UV-vis absorption spectra of each step are shown in Figure S26.

Instrumentation

UV-vis absorption spectroscopy

UV-vis absorption spectra were measured using Perkin Elmer Lambda 365 UV-vis spectrometer in the wavelength region of 200 to 1100 nm.

ESI-MS

Mass spectrum of *ortho*-carborane-1, 2-dithiol was measured using Thermo Scientific LTQ XL Linear ion Trap Mass spectrometer. Mass spectra of all the nanoclusters were measured using Waters Synapt G2Si HDMS instrument. Ag_{18} NC mass spectrum was collected in positive ion mode, and Ag_{42}, Int. I, Int. II, Ag_{14} NCs mass spectra were collected in negative ion mode. All the MS/MS or fragmentation experiments were performed by varying the collision energy of the selected ions inside the trap cell using the G2Si instrument. An optimized condition of flow rate: 20 µL/min, capillary voltage: 2.5 - 3 kV, cone voltage: 0 V, source temperature: 70-100 ^{o}C were used to record these ESI-MS spectra measurements.

Photoluminescence spectroscopy

Photoluminescence spectra were measured using Jobin Yvon Nanolog fluorescence spectrometer.

X-ray photoelectron spectroscopy

X-ray photoelectron spectroscopy was recorded using ESCA probe TPD equipped with polychromatic Mg Kα X ray source (hγ = 1253.6 eV). Purified cluster solution made in DCM was drop casted on a sample grid for the measurements.

FT-IR spectroscopy

FT-IR spectra were recorded using JASCO FT-IR 4100 spectrometer after preparing sample pallets using potassium bromide.

NMR spectroscopy

Multinuclear NMR spectra of the samples were measured using Bruker 500 MHz FT-NMR spectrometer. Around 20-25 mg of NC soluble in 0.75 mL of $CDCl_3$ solvent was used for measurements. Spectra were processed using MestRe-Nova NMR software.

Powder XRD

Powder XRD of the Ag_{42} NC was measured using a D8 Advance Bruker instrument, using Cu Kα as the X-ray source (hγ = 8047.8 eV).

Thermogravimetric analysis (TGA) and derivative thermogravimetric (DTG), and differential scanning calorimetry (DSC) analysis

Thermogravimetric (TG) measurements of about 3.821 mg of NC sample in an alumina crucible were performed using a NETZSCH STA 449 F3 Jupiter instruments equipped with Proteus-6.1.0 software. The measurements were performed under nitrogen atmosphere at a flow rate of 20 mL/min in the temperature range of 30 to 600 °C with a heating rate of 10 °C/min. The DSC study was performed using the same instrument.

TCSPC measurements

The time-resolved PL lifetime measurements were performed using HORIBA DeltaFlex TCSPC lifetime spectrofluorometer. The spectrometer was coupled with ps pulses diode lasers (pulse width of 85 ps) with excitation wavelength centred at 530 nm and 400 nm for Ag_{42} and Ag_{14} NCs, respectively. For visible region HORIBA PPD-850 detector, and for NIR region HAMAMATSU PMT detector is employed. The instrument response function is shown in Figure S43.

Femtosecond pump-probe measurements

In fs-TA measurement, ultrafast short laser of pulse width 120 fs centred at 800 nm are generated by spectra physics Maitai oscillator with the energy of few hundreds of nJ. The output beam send to Ti: sapphire optical amplifier system to produce high energy pulses (4 mJ/pulses, pulse width 120 fs, repetition rate 1 kHz). The output beam is further split into two parts, the first high energy beam is used to produce the second harmonic using β-barium borate crystal. The obtained 400 nm pulses are employed to excite the sample with the intensity of 250 μJ/cm^2. Other weak part of beam is used to generate the white light continuum probe pulses by CaF_2 crystal (450-800 nm). The computer-controlled motion controller is used to create the delay between pump-probe. The absorbance changes in the probe beam due to pump is calculated using the equation-

$$\Delta A = \log[I_{ex}(s)/I_0(s)] - [I_{ex}(r)/I_0(r)]$$

Where r and s correspond to the reference and sample, I_{ex} and I_o are transmitted intensities of probe pulse after excitation and in ground state, respectively. The intensity of transmitted pulse are measured with the help of MS 2004 (600 lines/mm diffraction grating blazed at 600 nm) spectrometer, and Si linear photodiode arrays. To compensate for the group velocity dispersion, the obtained TA spectra are chirp corrected. The ethanol is used to measure the magnitude of chirp.

Nanosecond flash photolysis

In ns pump-probe measurement, we excite the sample using the second harmonic of Nd-YAG laser with pulse width of 5 ns (spectra physics). To monitor the change in absorbance the white light (500-800) is produced using Xenon-Arc lamp (150 W) which is aligned in cross beam configuration to the pulp laser beam. Laser flash photolysis spectrometer (LKS80Applied Photo physics) with the combination of oscilloscope (Agilent Infinium DSO9064A) is used to measure the change in absorbance.

Optical microscopy

Optical microscopic images of the crystals in 10X magnification were collected using LEICA optical microscope equipped with LAS V4.8 software. Polarizer, and without polarizer mode was used to collect the images.

Scanning electron microscopy (SEM)

SEM imaging was performed using FEI quanta environmental scanning electron microscope (ESEM) at high vacuum mode, at operating voltage of 30 kV. Energy dispersive X-ray analysis (EDS) spectra and elemental mapping were recorded using the same instrument.

Transmission electron microscopy (TEM)

TEM imaging and size analysis of the nanoclusters were performed using a JEOL 3010, 300 kV instrument at an accelerating voltage of 200 kV. The accelerating voltage was kept low to reduce beam-induced damage. Samples were prepared by drop casting the solution of the clusters on carbon-coated copper grids and dried under ambient conditions. EDS spectra were collected using the same instrument.

Crystallographic details

Single-crystal X-ray diffraction (SC-XRD) data collection was performed at 293 K using Bruker D8 VENTURE SC-XRD equipped with Mo Kα radiation source of wavelength 0.71073 Å, and a PHOTON 100 CMOS detector. A suitable crystal for SC-XRD analysis was mounted on a Kapton loop with the help of Paratone oil. The program APEX3-SAINT (Bruker, 2016) was used for integrating the frames. A multi-scan absorption correction was done using the program SADABS (Bruker, 2016). The structure was solved by SHELXT-2014 (Sheldrick, 2014), and refined by full-matrix least squares techniques using SHELXL-2018, (Sheldrick, 2018) computer program. Hydrogens on all carbon, and boron atoms were fixed at calculated positions, and refined as riding model with C—H = 0.93 Å, B-H = 1.10 Å, and $U_{iso}(H)$ = 1.2 Ueq(C) or 1.2 Ueq(B). The molecule is crystallized in triclinic crystal system with P-1 space group. The asymmetric unit contains half of Ag_{14} nanocluster (Ag_{14} NC) and half of Ag_2-S-(triphenylphosphie)$_2$ (shortly, Ag_2S@TPP) moieties. The solvent electron density could not be modelled satisfactorily due to difficulty in locating their position. The observed R_{int} was high due to very weak diffraction of crystal at higher Bragg's angles. Therefore a resolution cut at ~1.0 Å was made during data reduction process to get a reasonable integration parameters in values/error models. Reflections above $\theta = 18^0$ were omitted during refinement to improve R_{int} to a reasonable value. Due to very high thermal and vibrational/rotational disorder of triphenylphosphine as well as carborane moieties, several restraints (DFIX, SIMU, ISOR, DELU *etc.*) were applied to their bond distances, and thermal parameters (U_{ij}) values during refinement to maintain sensible molecular geometry as well as reasonable anisotropic displacement parameter (ADPs) values. Moreover, FLAT restraint is needed to be applied for atoms in the phenyl ring to lie in a common plane. These factors prevent to get a quality data for these type of crystals for a good R values. It is to be noted here that, there are some literature reports for metal-organic frameworks (MOFs), which has this type of high R values.[5-7]

Several attempts were made to grow a better quality crystal for SC-XRD studies, but all failed miserably, and this is the best crystal we could obtain for single crystal studies. Also, attempt to collect data at low temperature was not successful as we could not observe any diffraction peaks at simple scan stage itself. This may be caused due to the collapse of crystal lattice at low temperatures. Although refinement parameters such as R1 = 0.1869, wR2 = 0.4247, Rint = 0.2609, *etc.*, are high, the structure is presented here to show the formation of Ag_{14} nanocluster with the support of other experimental findings. A cif check report was made using the service of IUCR in which A and B level alerts were explained.

Computational details

The structural, electronic, and optical properties such as absorption spectra of the NCs are computationally studied using density functional theory (DFT) and time-dependent density functional theory (TDDFT) calculations. The atomic coordinates of its crystal structure were taken to initiate the geometric optimization using DFT and TDDFT as implemented in Grid-based Projector Augmented Wave method (GPAW) software package.[8,9] The exchange functional Pardew−Burke−Ernzerhof (PBE) functional was used in the real space grid to describe their optimized geometry and interactions in the cluster.[10] The grid spacing was kept at 0.2 Å. The atomic PAW setup describes the valence electrons for Ag ($4d^{10}$ $5s^1$ $5p^6$), S ($3s^2$ $3p^4$), P ($3s^2$ $3p^3$), C ($2s^2$ $2p^2$), B ($2s^2$ $2p^1$), and H ($1s^1$) with scalar-relativistic effects which were included for Ag. The convergence condition was to minimize the residual forces without any symmetry constraints by 0.05 eV/Å. The emission spectrum of the cluster was computed from the excited state optimized geometry of the cluster using delta SCF method.[11] All the structural visualizations of the NCs were done with visual molecular dynamics (VMD) software.

Ag_{14} NC structure optimization by DFT

The theoretically optimized structure of $[Ag_{14}(CBDT)_6(TPP)_6]$ NC in real space DFT was shown in Figure S41. The combination of TPP ligands with CBDT ligands restricts the TPP ligands to interact only at six edges of the cubic shell of the cluster. Here, the primary ligand is CBDT, and the secondary ligand is TPP. From the optimized structure, it is clear that the interaction of CBDT is responsible for the stability of the cluster. Further the primary ligand also controls the interaction of secondary ligand on the surface of the cluster. From Figure S42a, it is clear that with two sulfur atoms, the carborane ligand interacts with the core of the Ag_{14} cluster. However, the CBT ligands strongly interact with the Ag_6 core with the average bond distance of 2.56 Å rather than the shell. However, there is a significant distortion in the Ag(core)-S is found with the bond distances of 2.54 Å and 2.61 Å. Due to this interaction, the octahedral core is formed with two different Ag-Ag bond distances of 2.82 Å and 2.84 Å. The CBT ligands interaction with the cubic shell Ag atoms on the eight edges have two unique interactions, such as a strong interaction with the Ag-S bond distance of 2.63 Å on either Ag atom on the top and bottom of the cubic structure in which there is no secondary ligand interaction is observed. On the other hand, the Ag-S interaction with the Ag atom in which the P atom of the TPP ligands interacts is in general, a weak bonding interaction with the average bond distance of 2.67 Å starting from the bonding variation from 2.67 Å to 2.93 Å. It is noted from the geometry that the stabilization of the structure could be due to the asymmetric bonding interaction of S atoms of CBT ligands, and it may originate due to the two main things. One is the charge difference between two S atoms of the same CBT ligand, and the second thing is due to the strong interaction of Ag-P interaction with the bond distance of 2.56 Å. Furthermore, the conjunction of both primary and secondary ligands on the surface of the cluster also does not allow accommodation of two more TPP ligands on two Ag atoms of the cubic shell, which are only interacting with the primary CBT ligands. It is noted from the geometry that the stabilization of the structure could be due to the asymmetric bonding interaction of S atoms of CBT ligands, and it may originate due to the two main things. One is the charge difference between two S atoms of the same CBT ligand, and the second thing is due to the strong interaction of Ag-P interaction with the bond distance of 2.56 Å. Furthermore, the conjunction of both primary and secondary ligands on the surface of the cluster also does not allow accommodation of two more TPP ligands on two Ag atoms of the cubic shell, which are only interacting with the primary CBDT ligands.

Theoretical calculation of IR Spectra

Quantum chemistry calculations were performed by the NWChem package.[12] The geometries were optimized and vibrational frequencies were calculated by means of the density functional theory with the hybrid exchange–correlation functional PBE0.[13-15] Jensen's double–zeta basis PC-1 was used.[16] The translations and rotations were projected out of the nuclear hessian using the standard Eckart algorithm.[17] The calculated frequencies and normal modes were examined with the help of the visualisation program Gabedit.[18] The vibrational spectra were simulated with Gabedit by the simple application of Lorentzian line shape of uniform arbitrary half width. The half width values of 15 cm^{-1} and 30 cm^{-1} respectively were used, as indicated in the Figure S15.

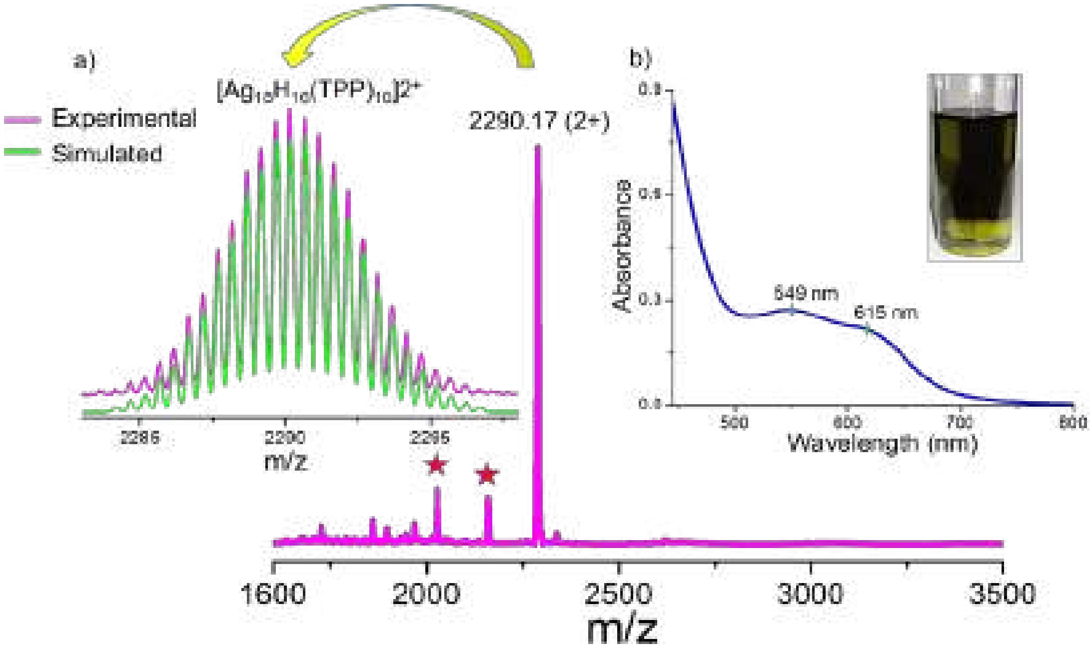

Figure S1. a) Positive ion-mode ESI-MS spectrum of the Ag_{18} NC. Each * indicates sequential TPP loss from the parent NC. Inset shows the exact matching of the isotopic distribution of the experimental and theoretical spectrum. b) UV-vis absorption spectrum of the Ag_{18} NC in methanol. Inset: photograph of the nanocluster in methanol.

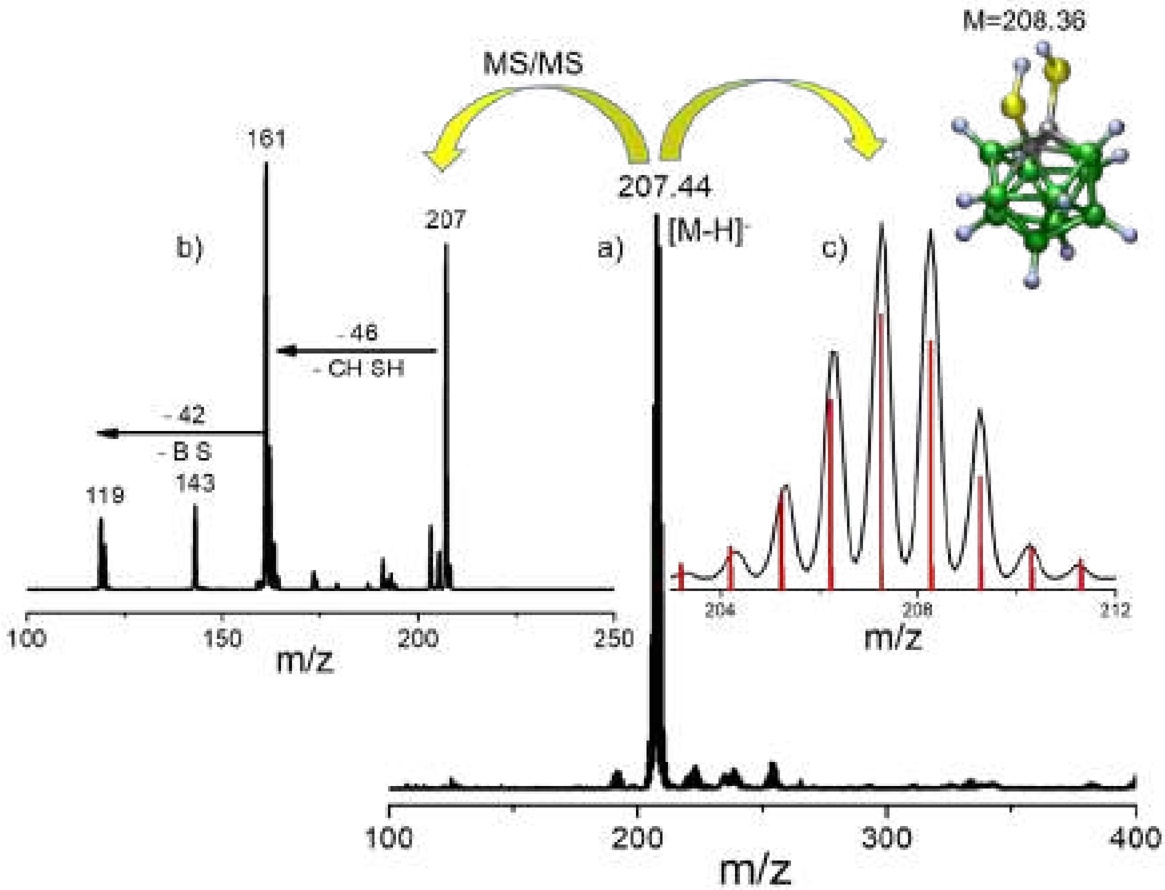

Figure S2. a) Negative ion-mode ESI-MS spectrum of the *ortho*-carborane-1, 2-dithiol ligand, b) MS/MS fragmentation pattern of the molecular ion peak at m/z 207.44, showing the loss of different fragments from the carborane moiety, c) exact matching of the isotopic distribution of the experimental spectrum with the theoretical spectrum.

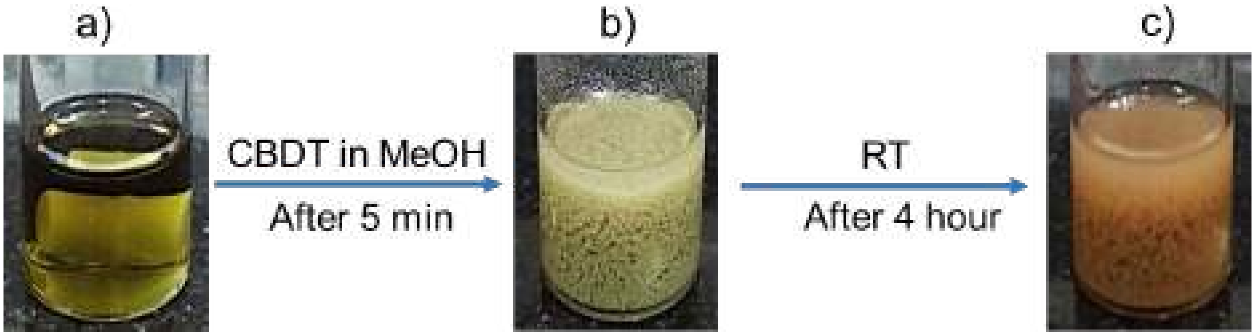

Figure S3. Digital photographs at the various stages of Ag_{42} synthesis; a) Ag_{18} in 5 ml methanol, b) after 5 min of the addition of the CBDT ligand, c) after 4 hours of the reaction at room temperature showed the color change during the reaction.

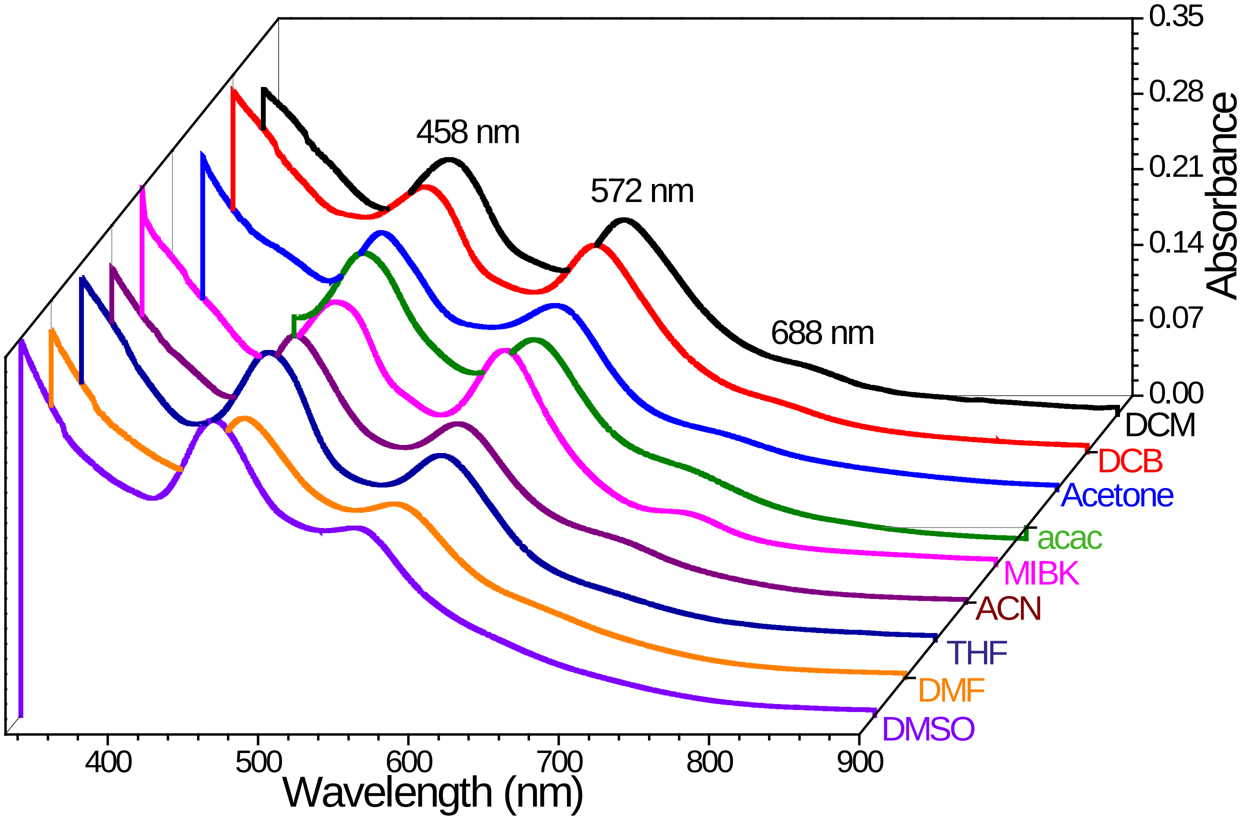

Figure S4. UV-vis absorption spectra of Ag_{42} nanocluster measured in different solvents. Broadening of absorption band at 572 nm was observed due to solvatochromic interaction with DMF, and DMSO. (Abbreviation: DCM = dichloromethane, DCB = 1, 2-dichlorobenzene, acac = acetyl acetone, MIBK = methyl isobutyl ketone, ACN = acetonitrile, THF = tetrahydrofuran, DMF = dimethyl formamide, DMSO = dimethyl sulfoxide).

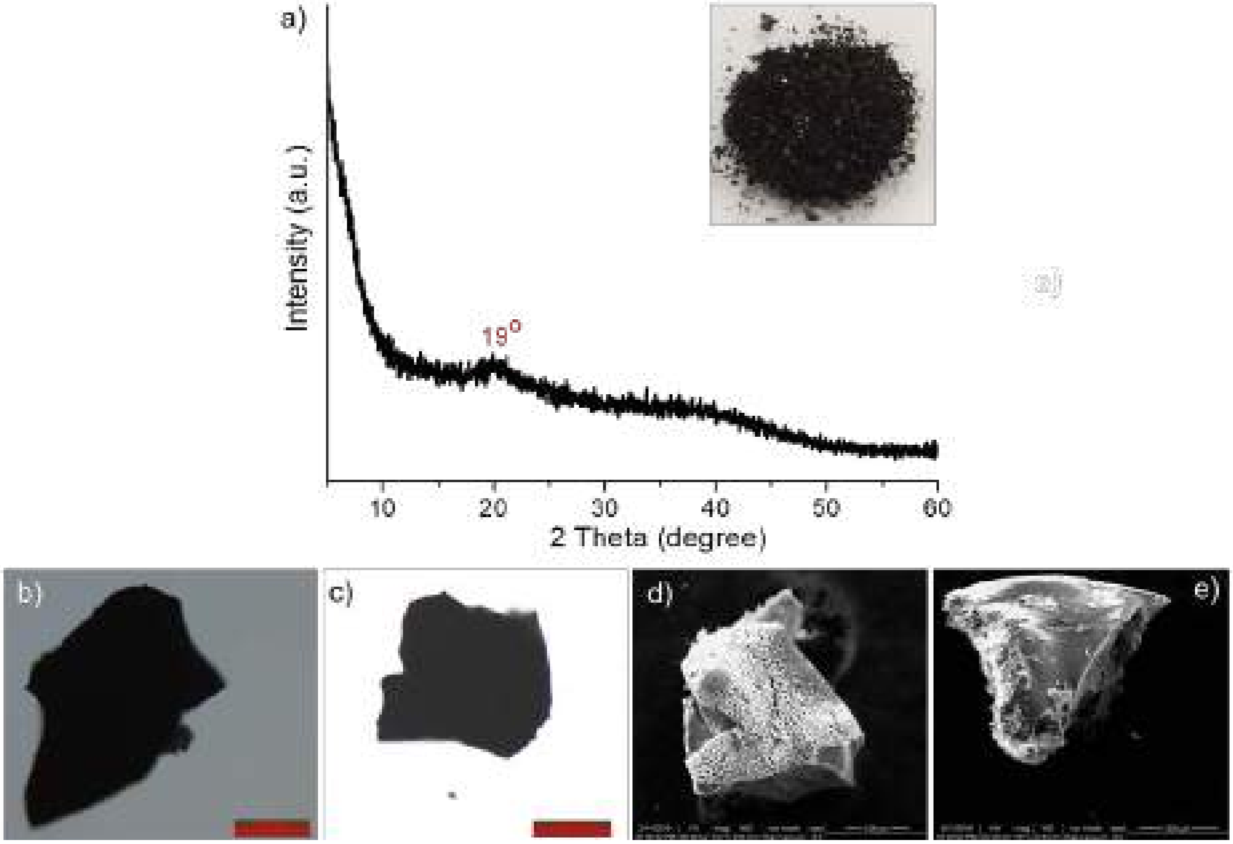

Figure S5. a) Powder XRD pattern of the Ag_{42}, which didn't show any significant diffraction peaks, indicating its weak crystallinity. Inset shows the optical image of powder of Ag_{42}. b, c) Optical microscopic images of the black color solids grown during crystallization. d, e) SEM images of the crystalline solids at different magnification.

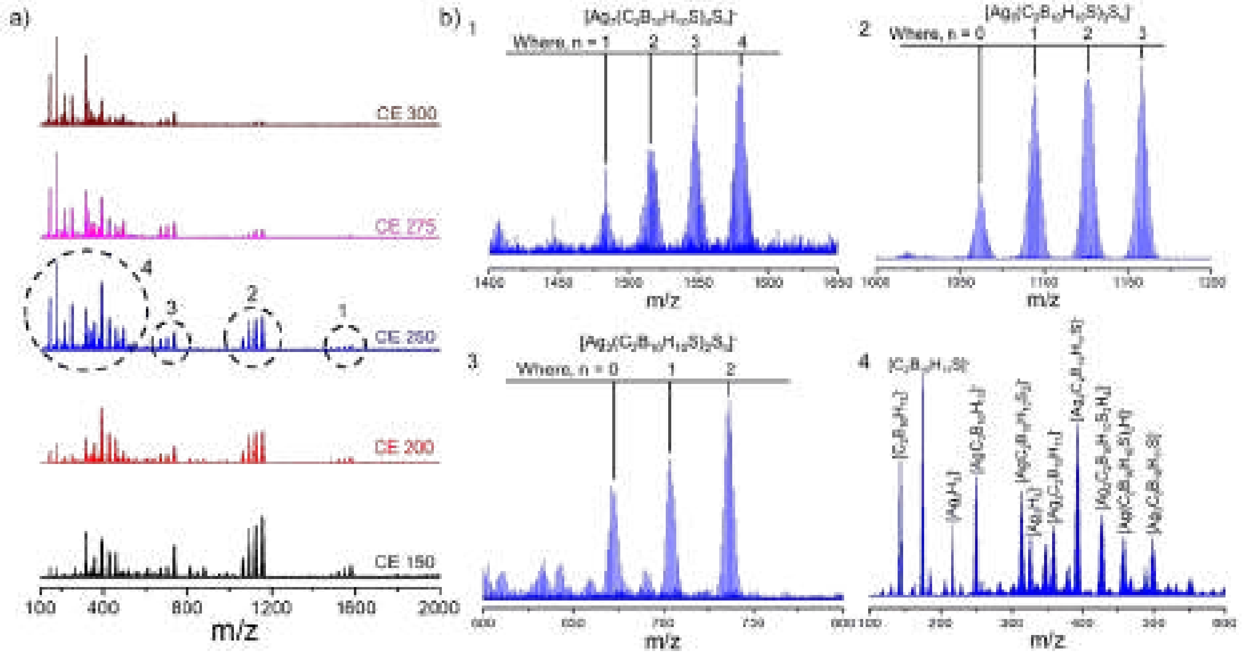

Figure S6. a) The collision energy dependent fragmentation patterns at lower mass range shows the formation of different silver thiolate species at higher collision energies. b) Expanded views of four different spectral regions having silver and carborane fragments.

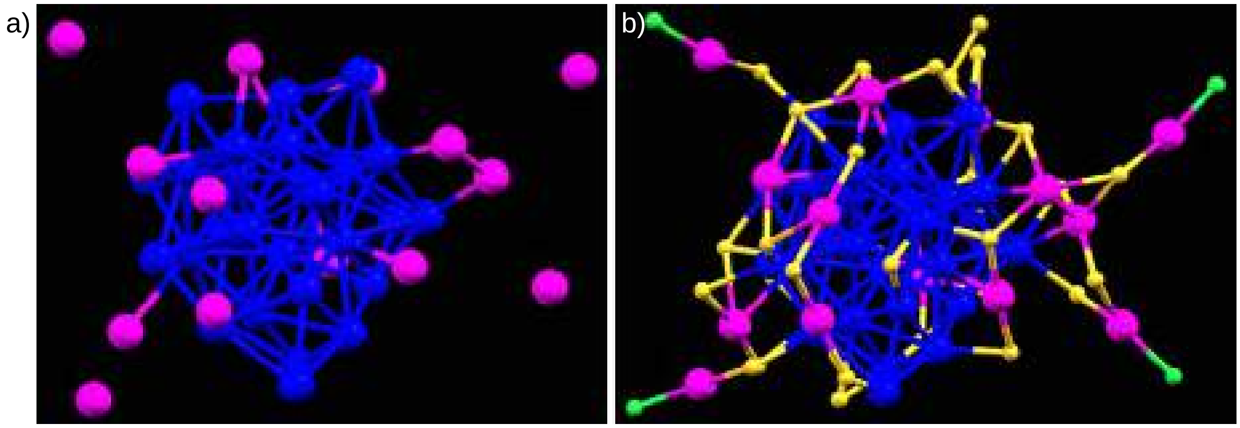

Figure S7. The DFT optimized core structure of Ag_{42}, a) the Ag_{42} core having Ag_{28} inner core, and Ag_{14} outer core, b) the same core connected with phosphorous and sulphur atoms. Ligands are removed for clarity. Atomic color codes as, blue = inner core 28 Ag atoms, pink = outer core 14 Ag atoms, yellow = sulphur, green = phosphorous.

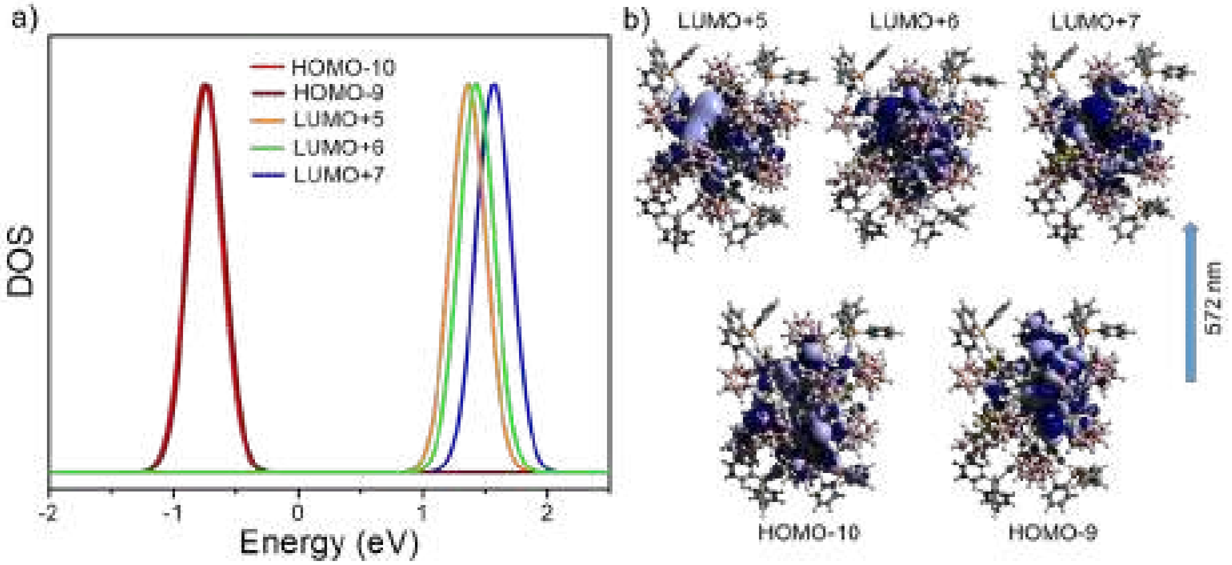

Figure S8. a) Density of states of Ag42 indicating the molecular orbitals contribution for the transition at 572 nm. b) Electron density plots of the respective molecular orbitals.

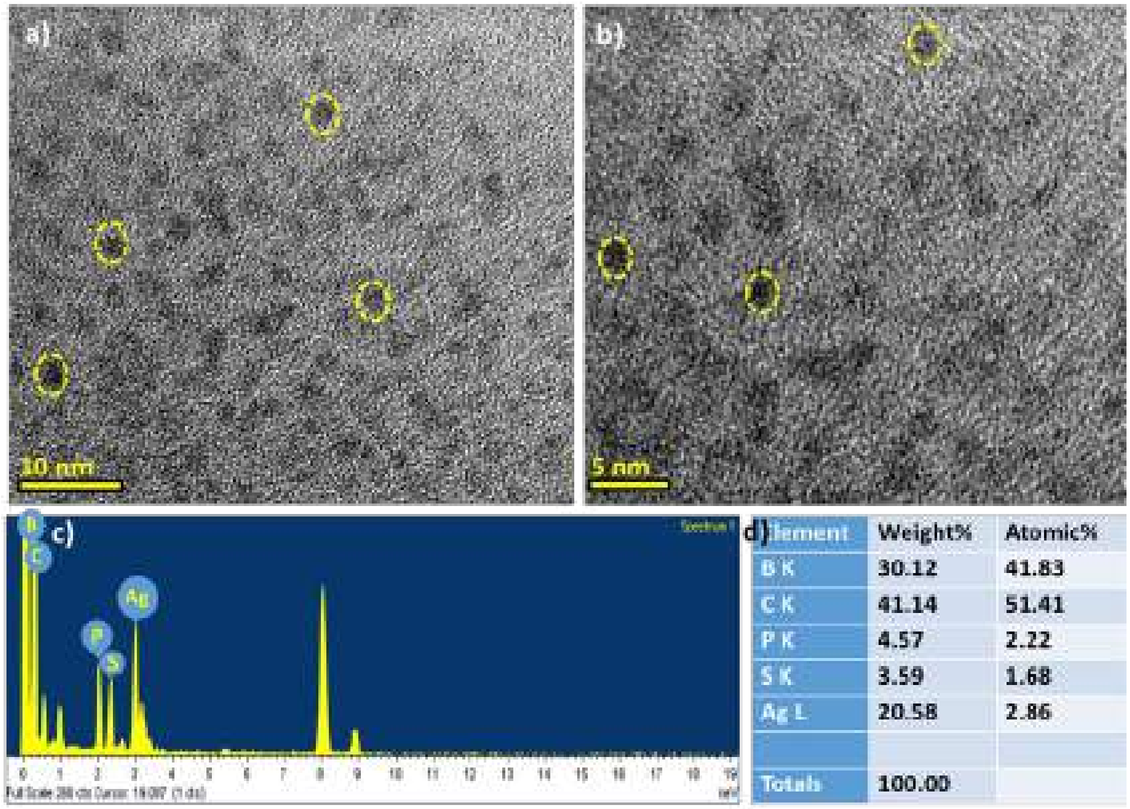

lement	Weight%	Atomic%
B K	30.12	41.83
C K	41.14	51.41
P K	4.57	2.22
S K	3.59	1.68
Ag L	20.58	2.86
Totals	100.00	

Figure S9. a-b) TEM images of the Ag42 in different magnification. c) EDS spectrum of the nanocluster showed the existing elements. d) Atomic % and weight % of the existing elements.

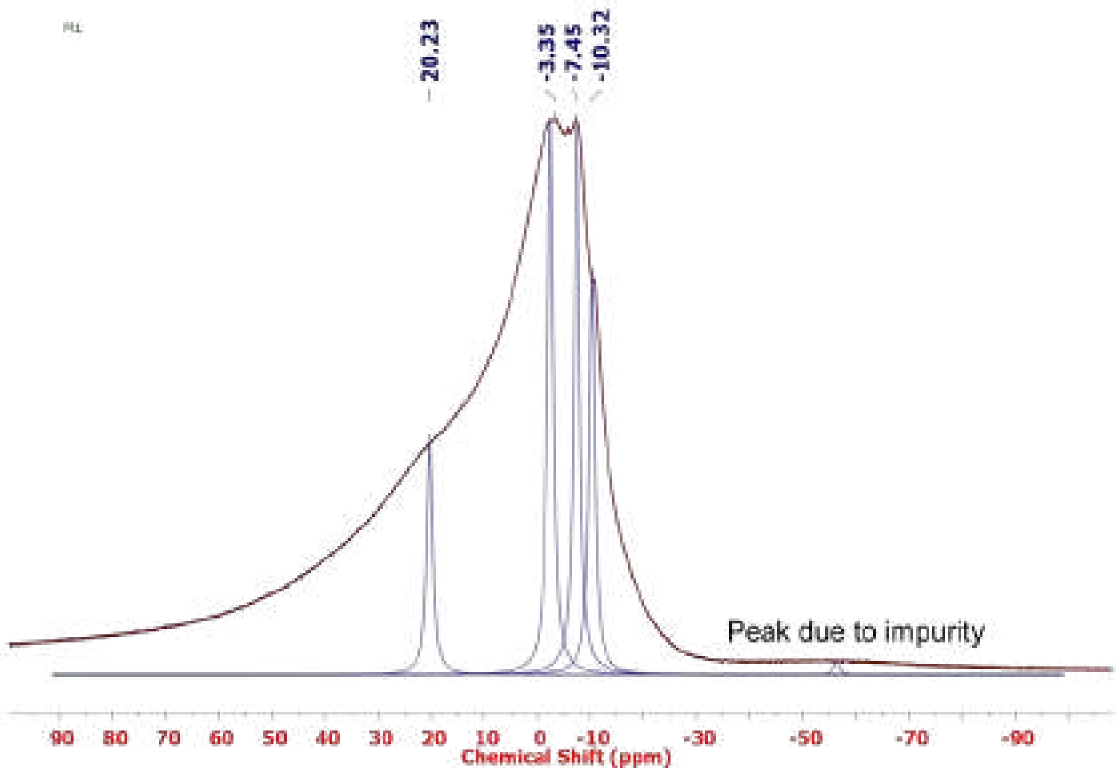

Figure S10. ^{11}B NMR spectrum of the Ag_{42} nanocluster in $CDCl_3$ solvent.

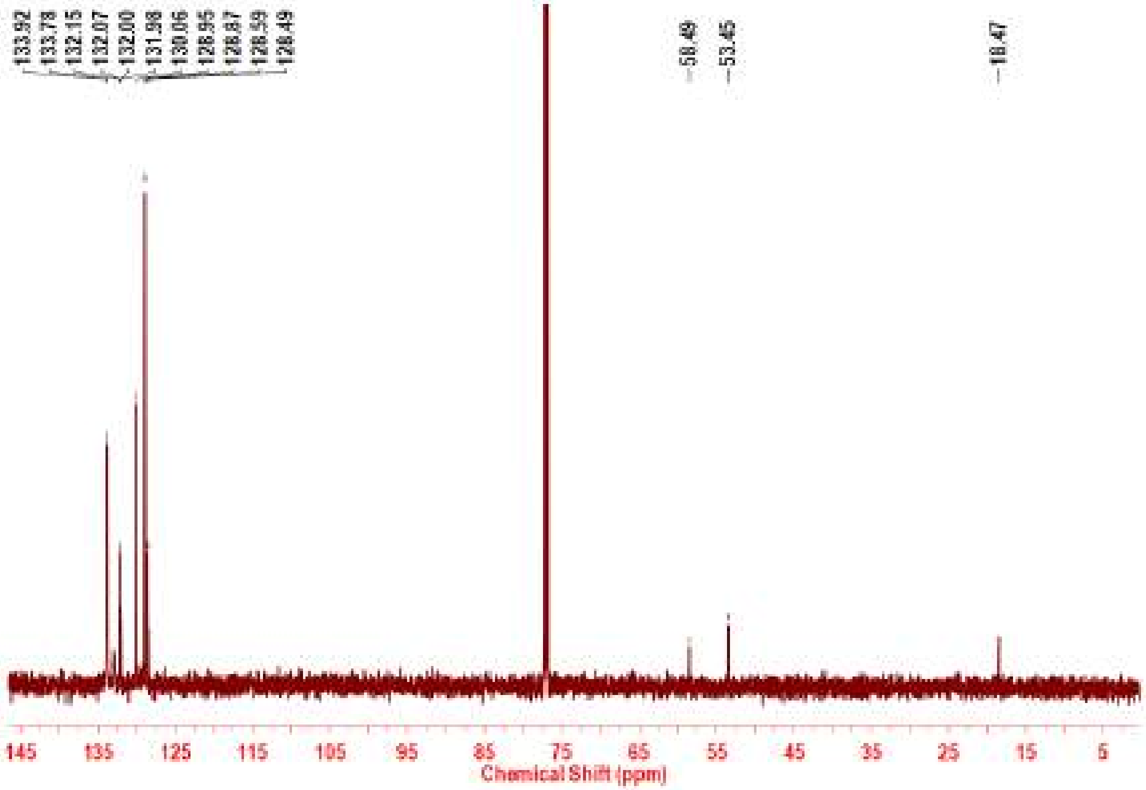

Figure S11. ^{13}C {^{1}H} NMR spectrum of the Ag_{42} nanocluster in $CDCl_3$ solvent.

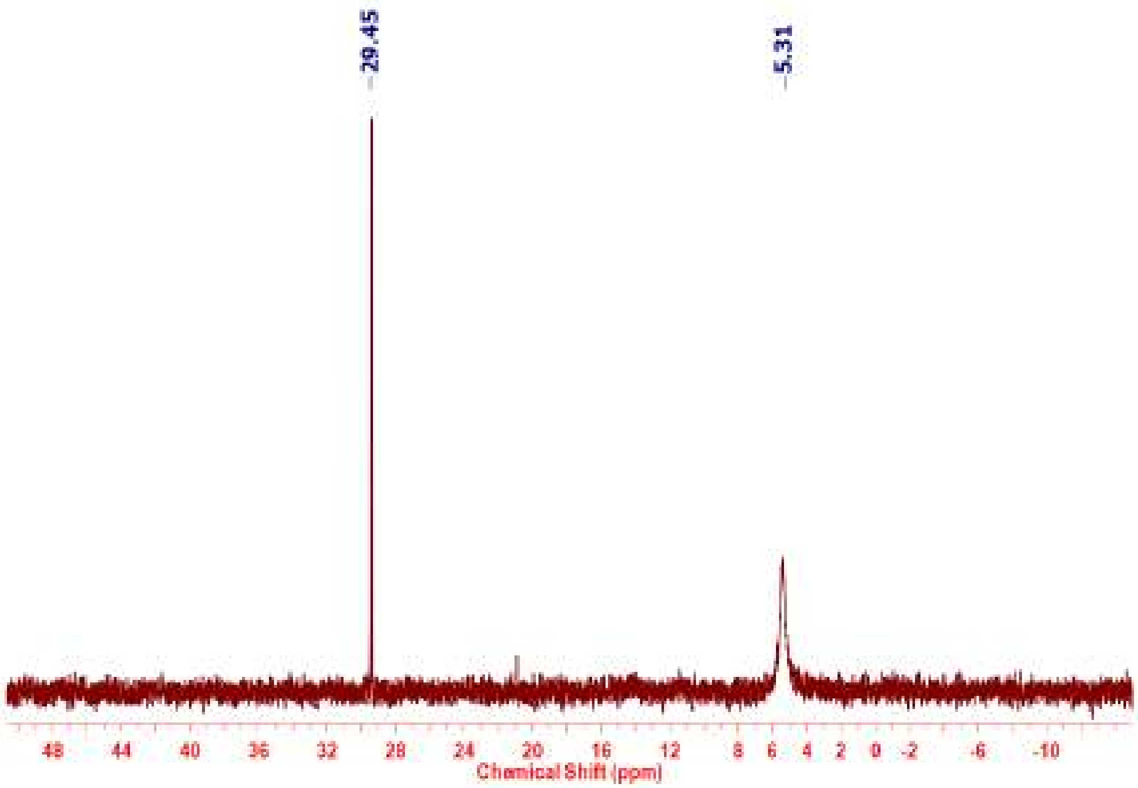

Figure S12. ^{31}P NMR spectrum of the Ag_{42} nanocluster in $CDCl_3$ solvent.

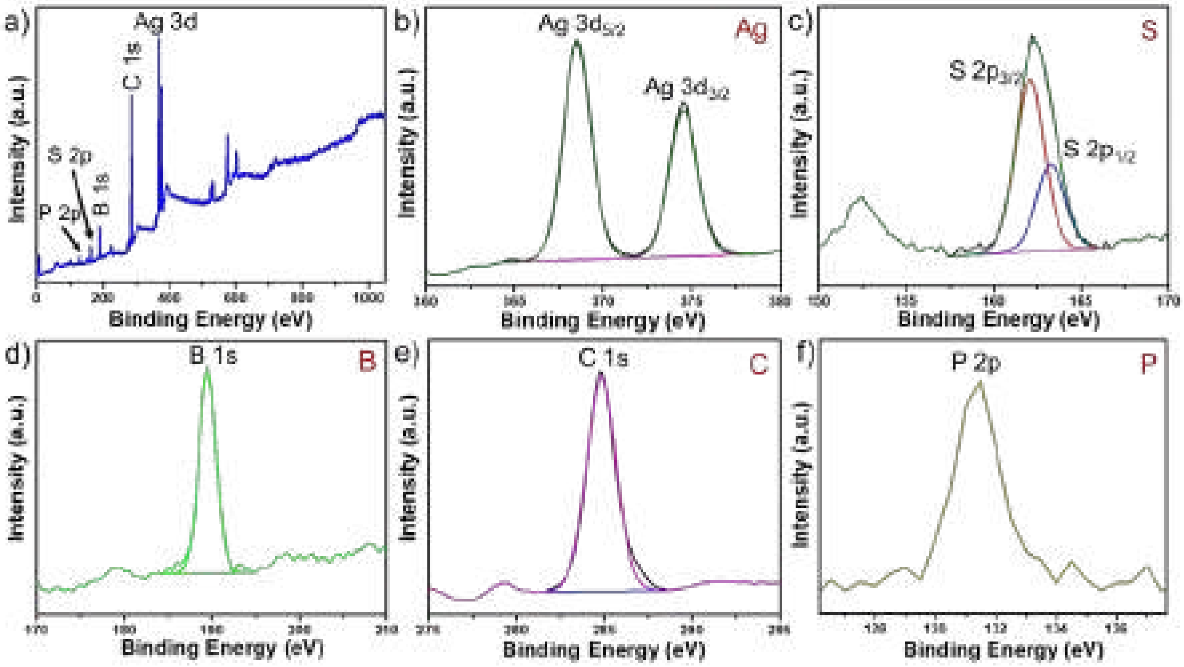

Figure S13. XPS spectra of Ag_{42}; a) XPS survey spectrum showed the signature peaks of the existing elements. Spectral fitting of b) Ag 3d region, c) S 2p region, d) B 1s region, e) C 1S region, f) P 2p region.

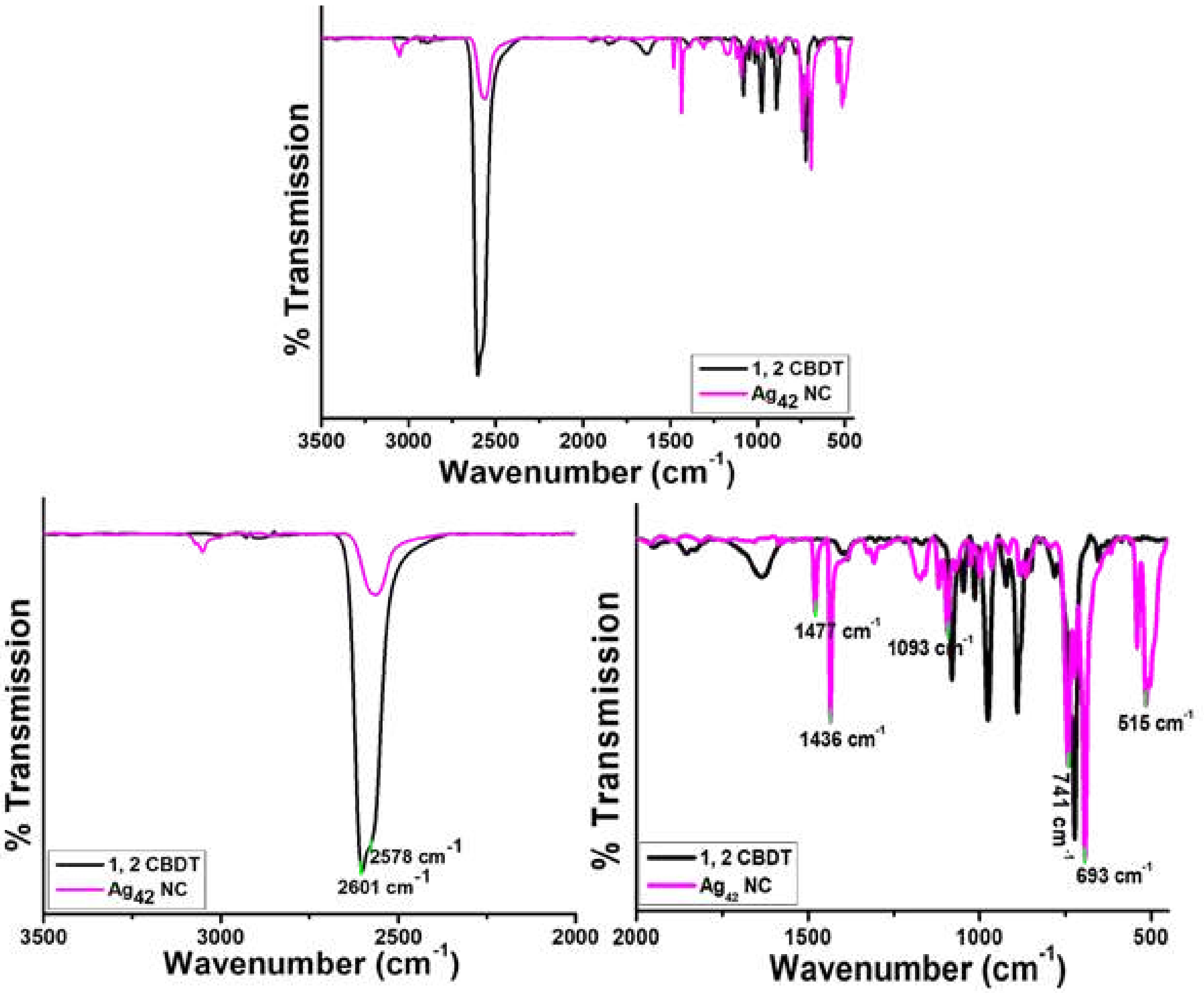

Figure S14. Combined FT-IR spectra of the *ortho*-carborane-1, 2-dithiol ligand, and Ag_{42} NC (top spectrum). Expanded view of the same spectra indicates the specific regions (bottom spectra).

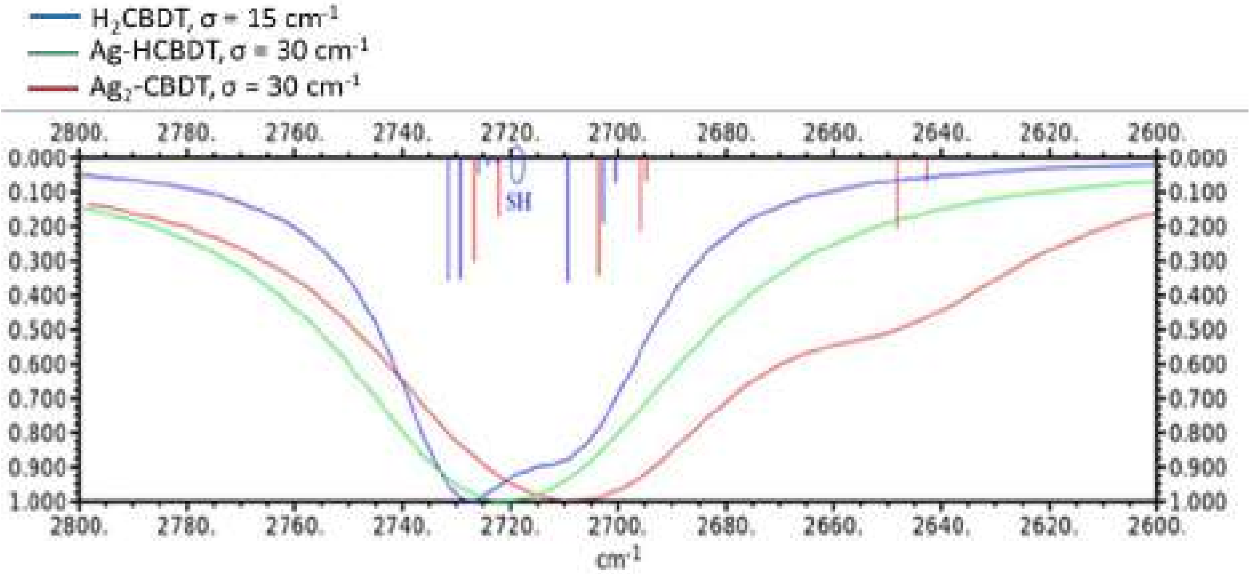

Figure S15. Calculated spectra of free CBDT (labelled as H2CBDT) and its respective bis-silver salt Ag2-CBDT. Circled is the area of SH vibrations.

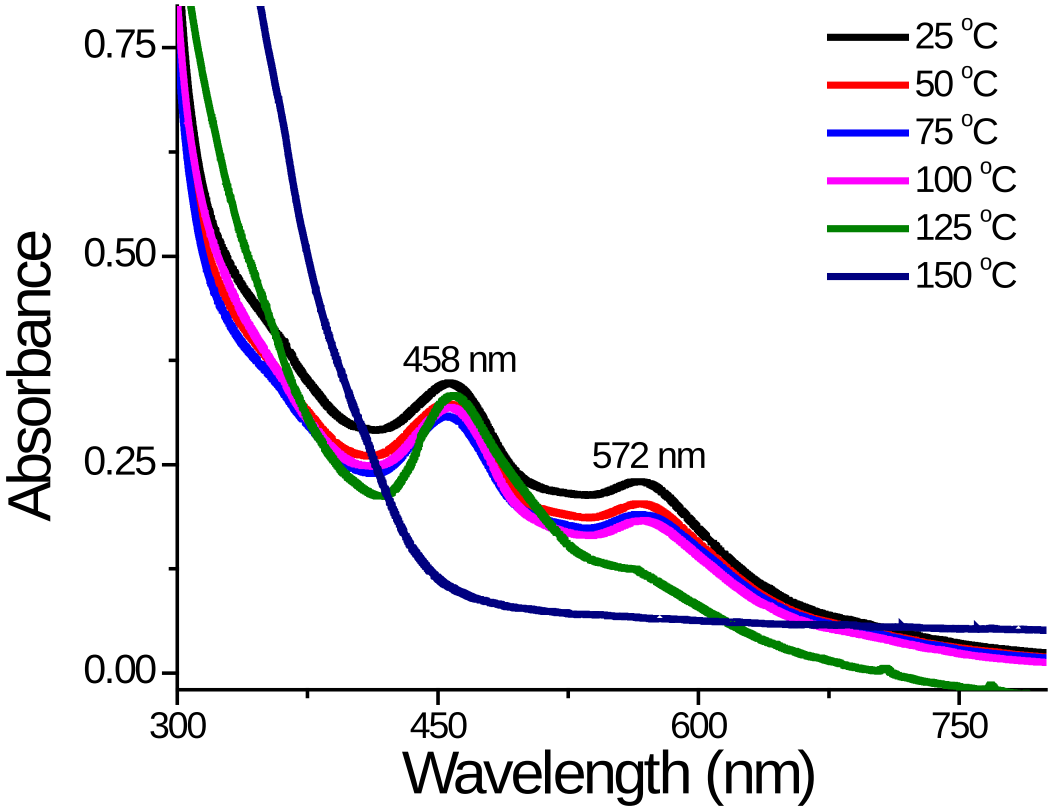

Figure S16. UV-vis absorption spectra of Ag42 cluster after heating at different temperatures in solid state.

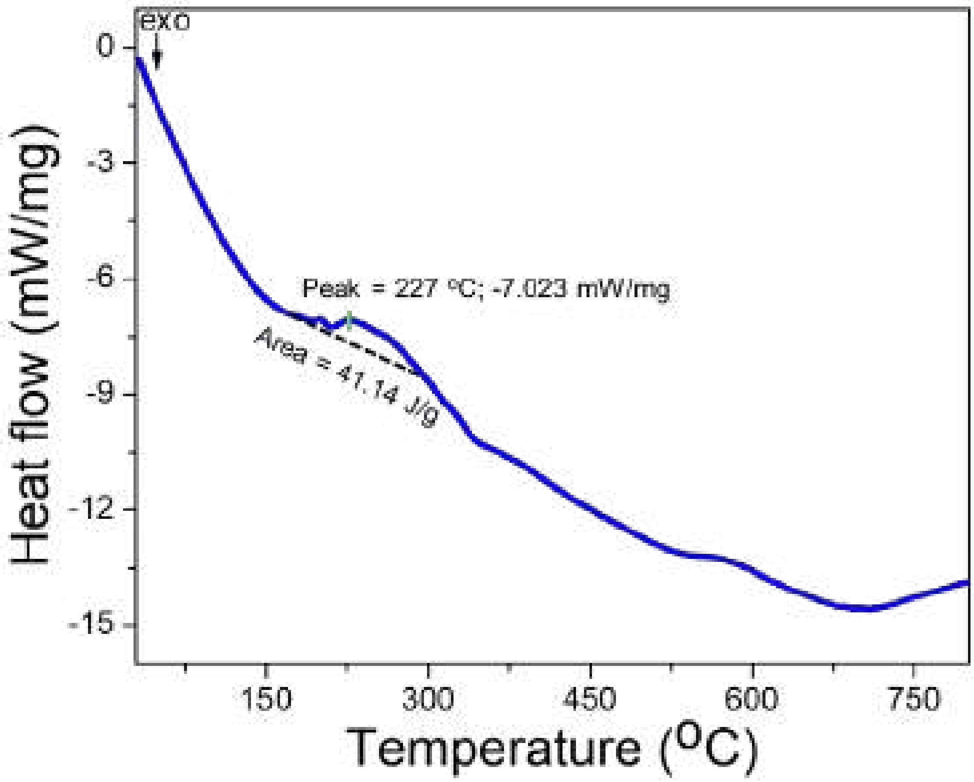

Figure S17. Differential scanning calorimetry data of Ag_{42} solid. No phase transition was observed up to 190 °C. The broad endothermic peak at 227 °C is attributed to a weak structural transformation, possibly due to ligand ordering.

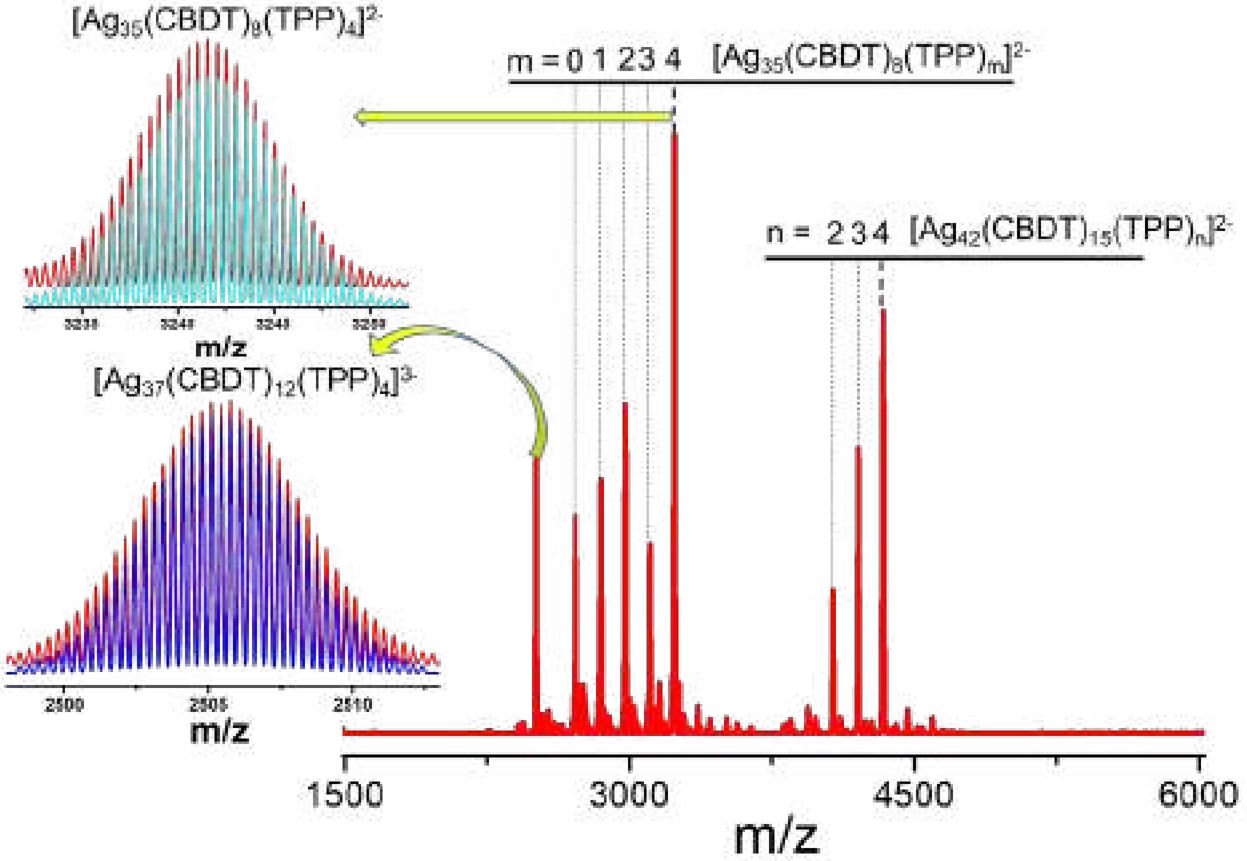

Figure S18. Negative ion-mode ESI-MS spectrum of the Int. I NCs indicating formation of $[Ag_{35}(CBDT)_8(TPP)_4]^{2-}$, and $[Ag_{37}(CBDT)_{12}(TPP)_4]^{3-}$ NCs. Inset: Exact matching of the isotopic distribution of the experimental and theoretical spectrum of the respective NCs. The subsequent TPP losses from their parent NC were observed.

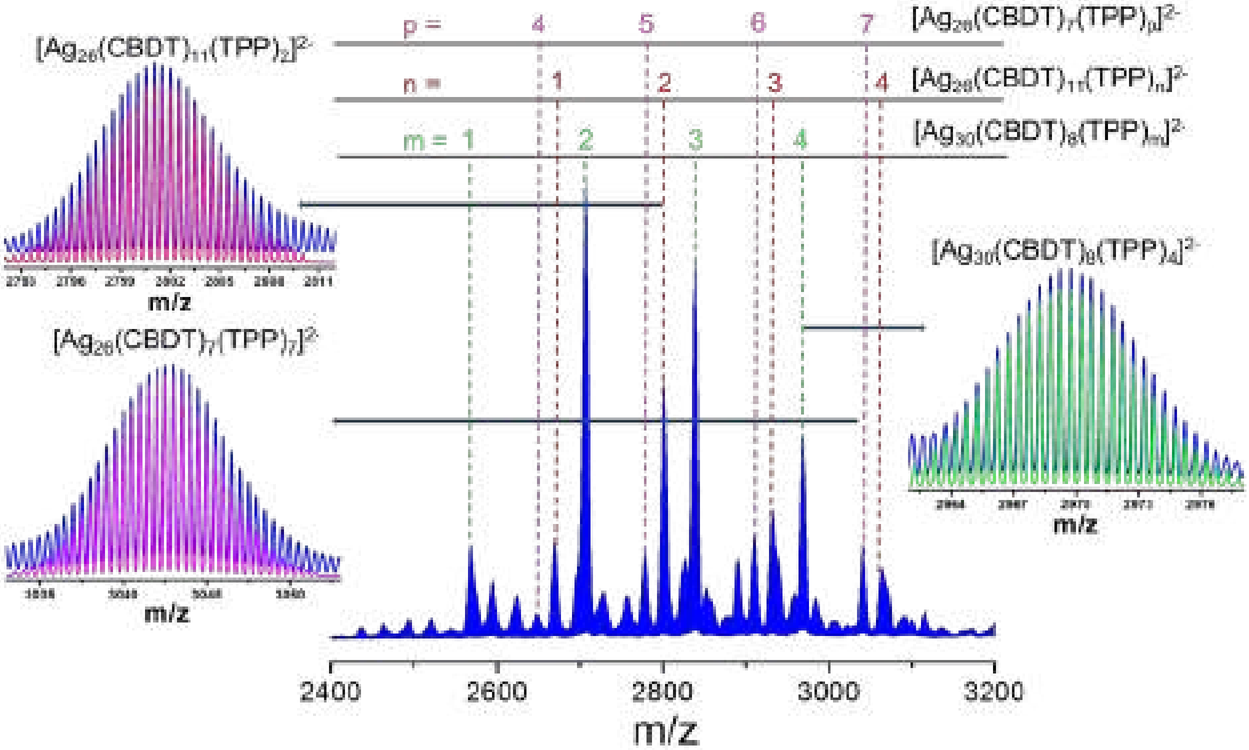

Figure S19. Negative ion-mode ESI-MS spectrum of Int. II NCs indicating the formation of $[Ag_{30}(CBDT)_8(TPP)_4]^{2-}$, $[Ag_{26}(CBDT)_{11}(TPP)_4]^{2-}$, and $[Ag_{26}(CBDT)_7(TPP)_7]^{2-}$ parent nanoclusters after 16 hr. light irradiation. Inset shows the exact matching of the isotopic distribution with the simulated spectra. The subsequent TPP losses from their parent nanoclusters were observed.

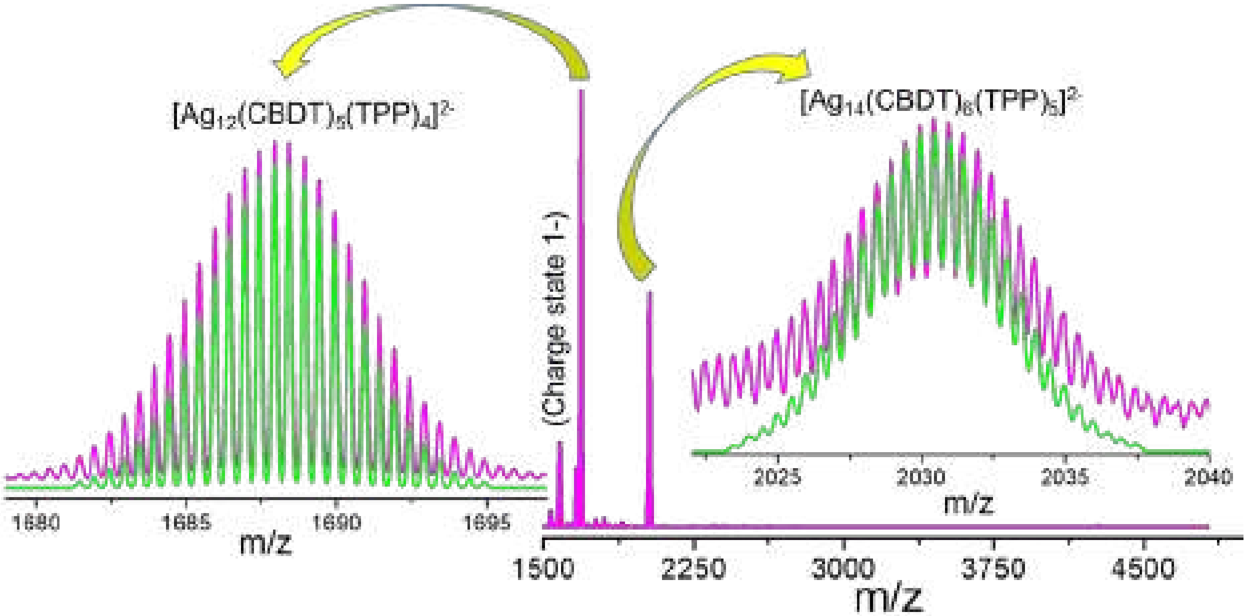

Figure S20. Negative ion-mode ESI-MS spectrum of the as synthesized Ag_{14} after 24 hr. light irradiation. $[Ag_{12}(CBDT)_5(TPP)_4]^{2-}$ peak also observed due to $[Ag_2(CBDT)(TPP)_2]$ fragment loss from the original Ag_{14} NC. Inset shows the exact matching of the isotopic distribution with the respective theoretical spectrum.

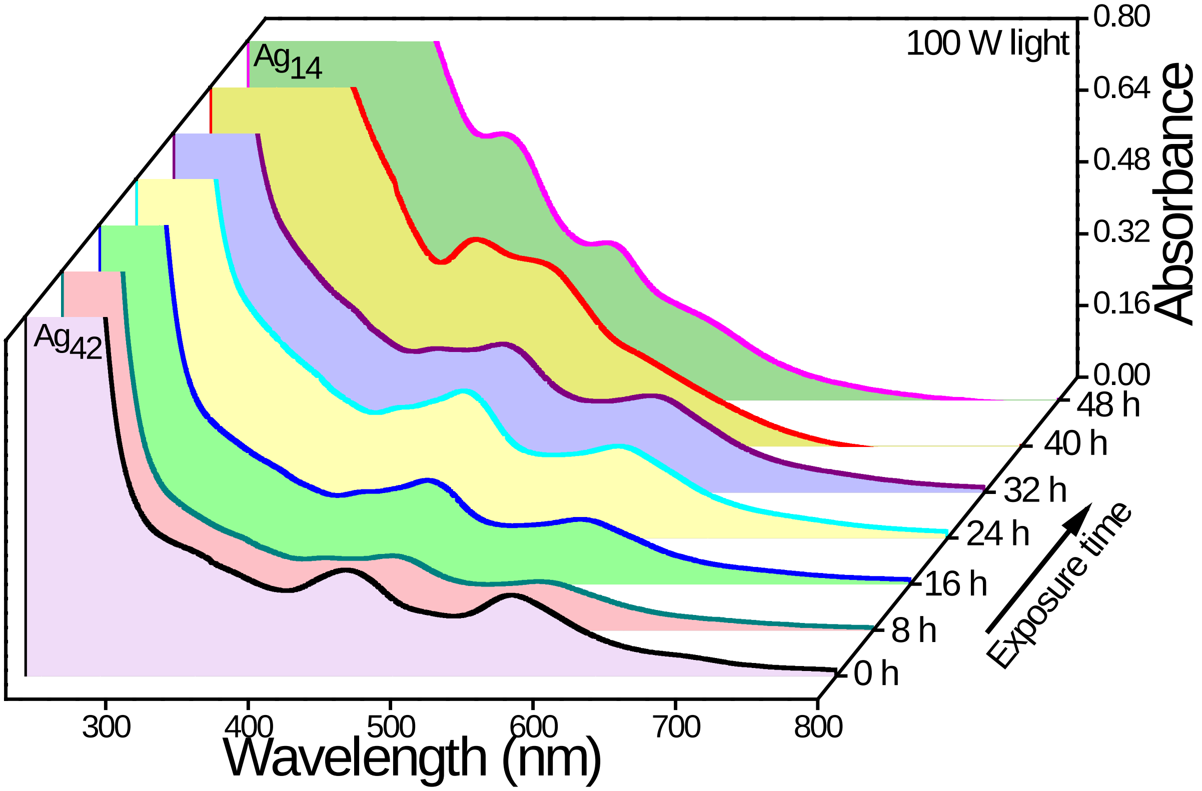

Figure S21. Time-dependent interconversion of Ag_{42} to Ag_{14} at an irradiation power of 100 W.

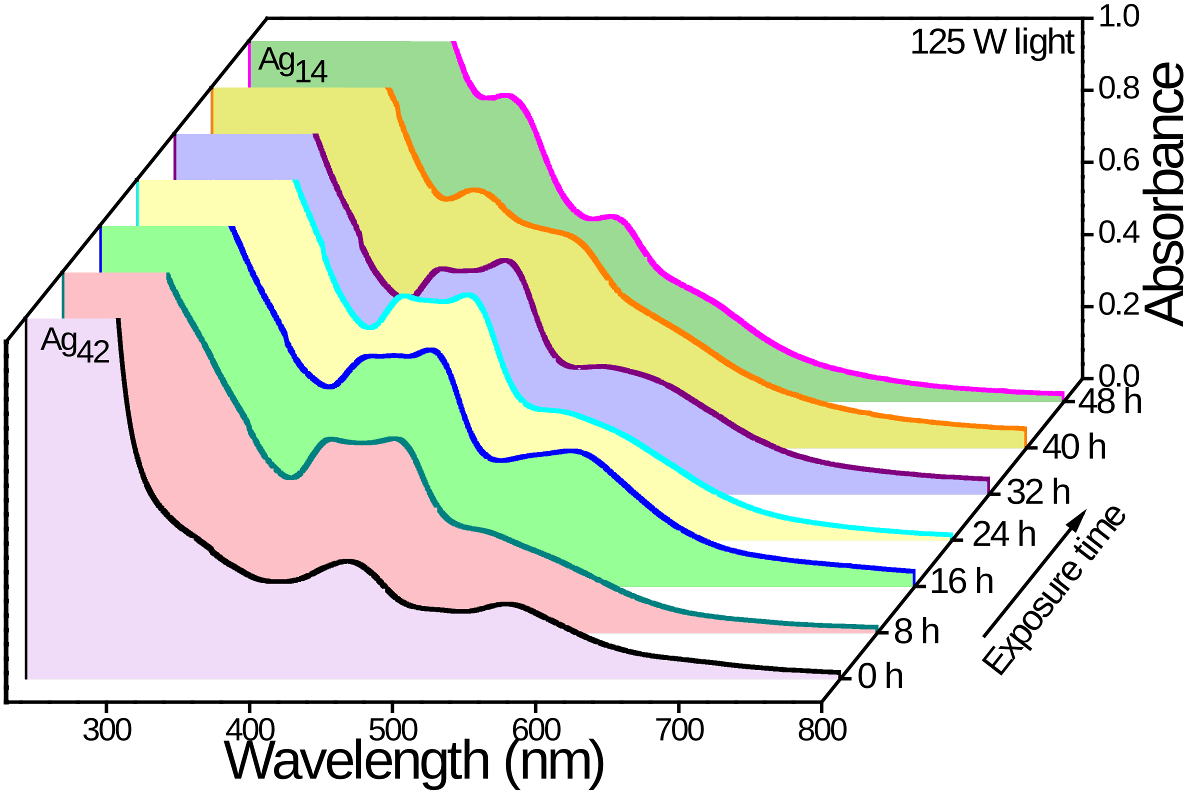

Figure S22. Time-dependent interconversion of Ag$_{42}$ to Ag$_{14}$ at an irradiation power of 125 W.

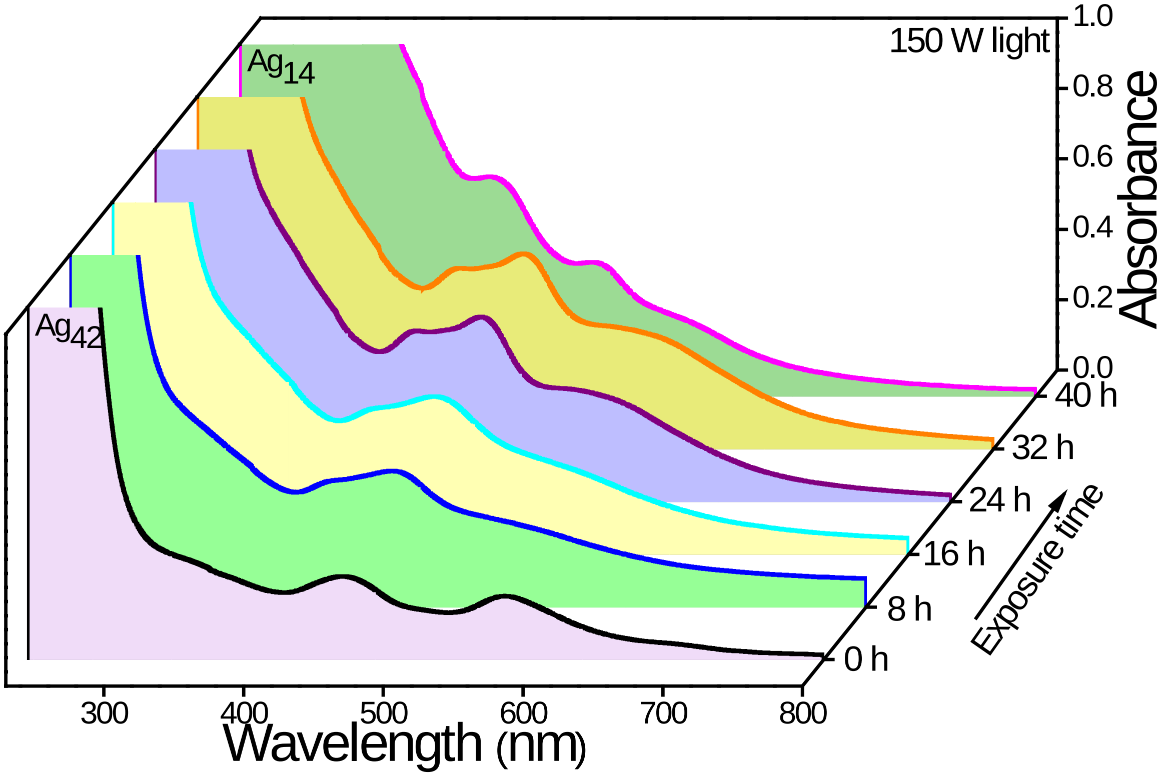

Figure S23. Time-dependent interconversion of Ag$_{42}$ to Ag$_{14}$ at an irradiation power of 150 W.

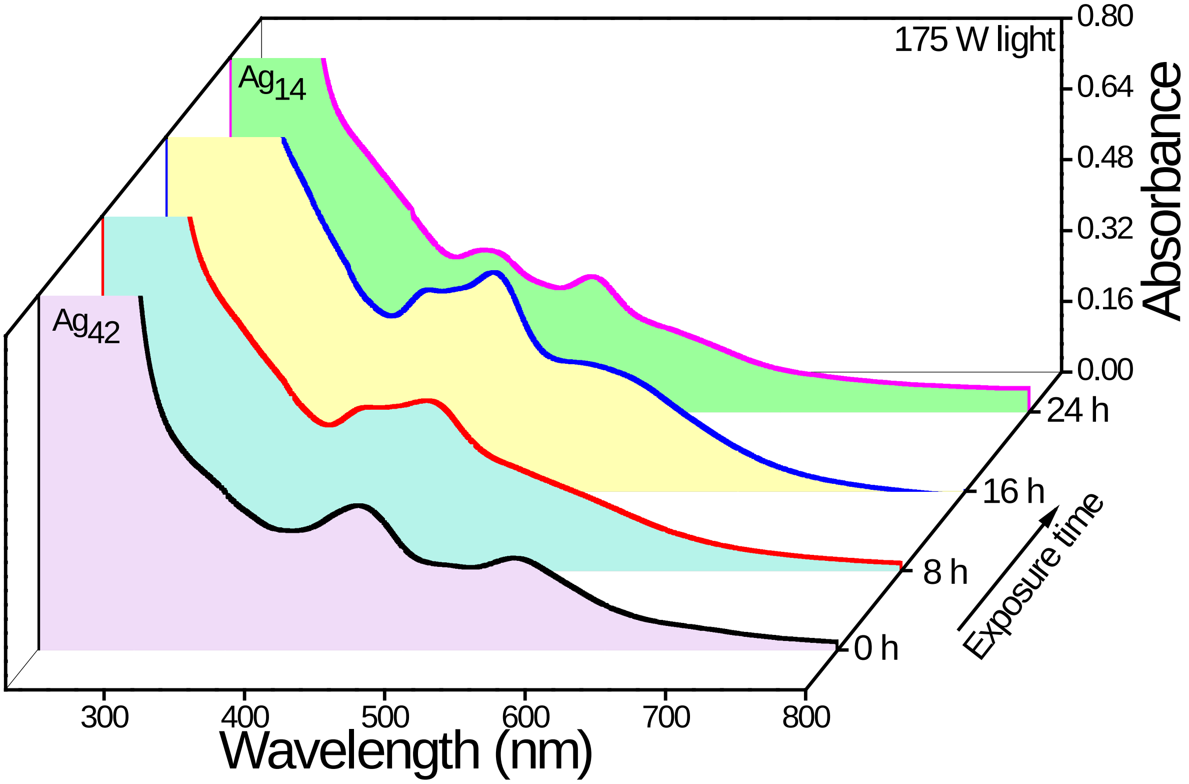

Figure S24. Time-dependent interconversion of Ag_{42} to Ag_{14} at an irradiation power of 175 W.

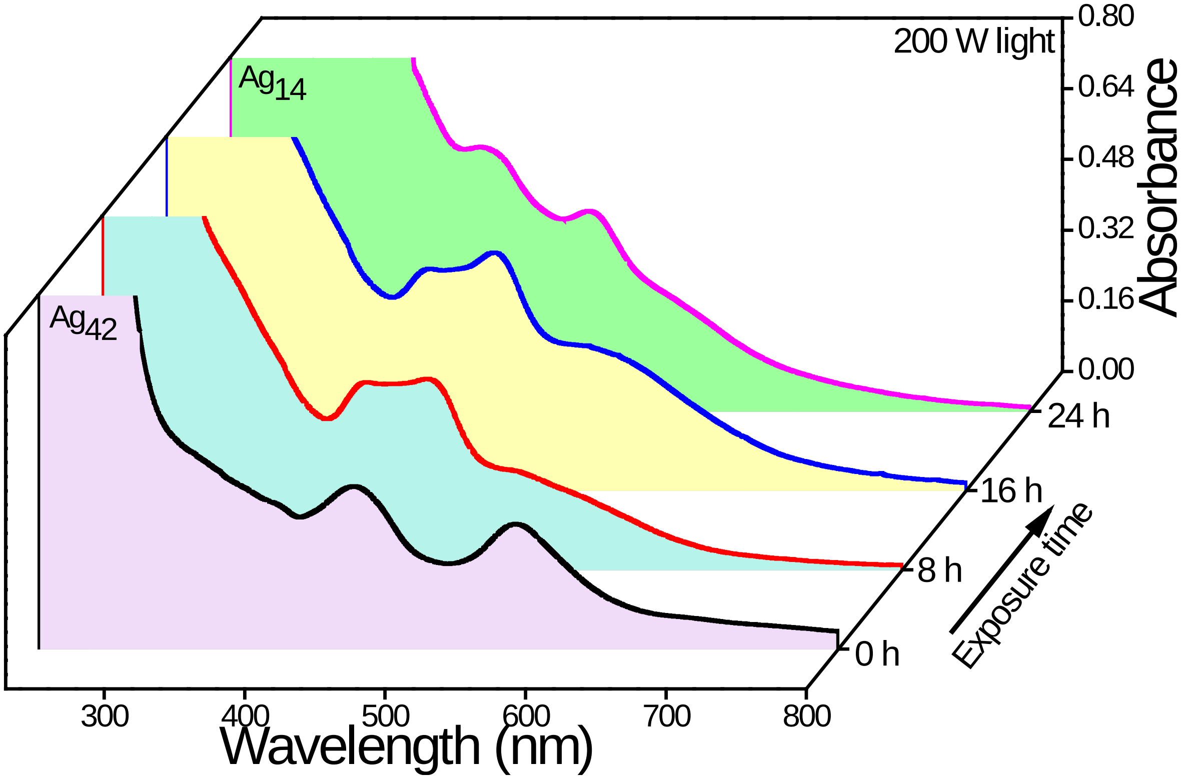

Figure S25. Time-dependent interconversion of Ag_{42} to Ag_{14} at an irradiation power of 200 W.

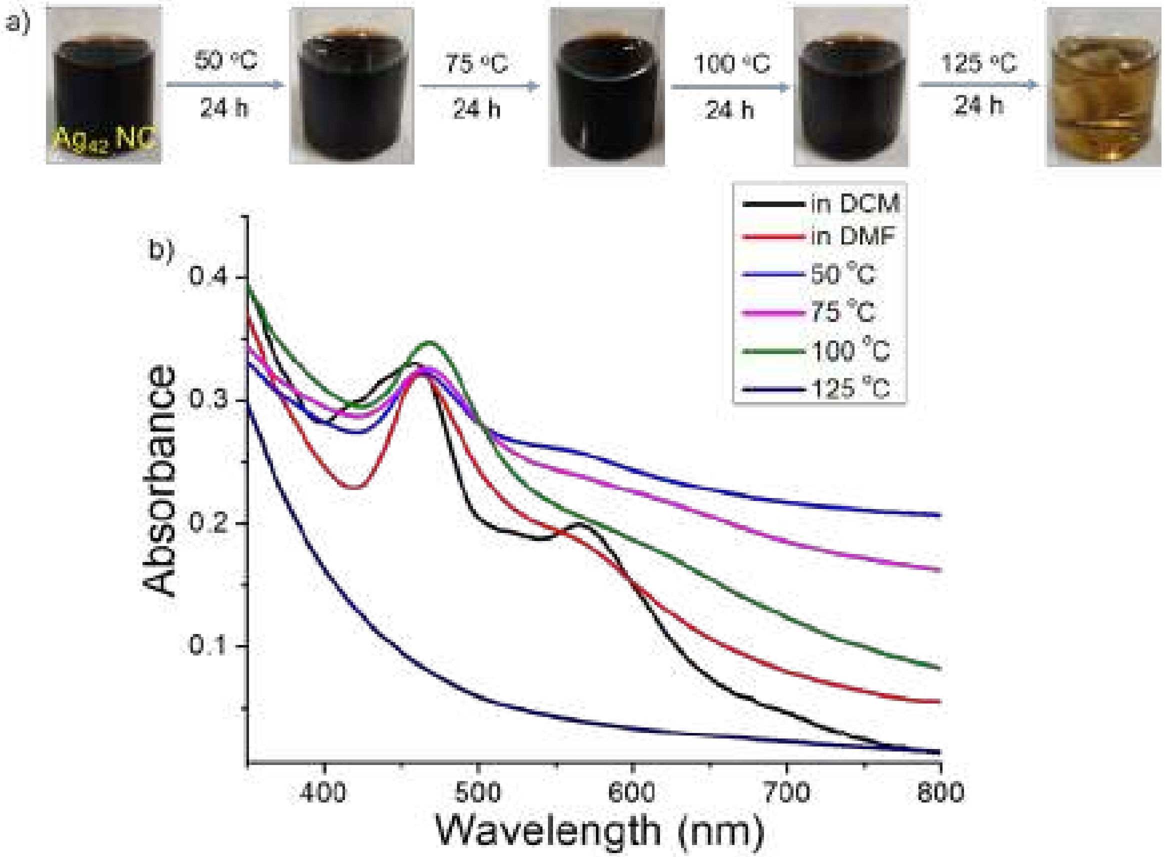

Figure S26. a) Photographs of the Ag_{42} in DMF during the heating of different temperatures, b) UV-vis absorption spectra were recorded for heating at above mentioned temperatures, which showed its stability up to 100 °C.

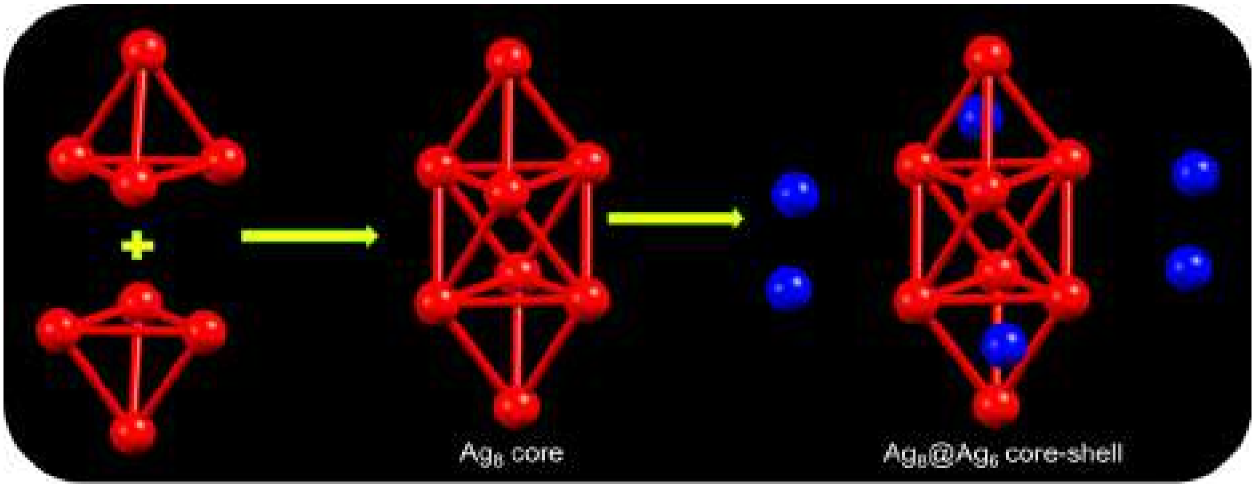

Figure S27. Atomic packing of the Ag_{14} as Ag_8 bicapped trigonal antiprism core, and Ag_6 surface silver atoms. All of the atoms are silver here. Red atoms indicate the inner Ag_8 core, blue atoms are for the outer six silver atoms.

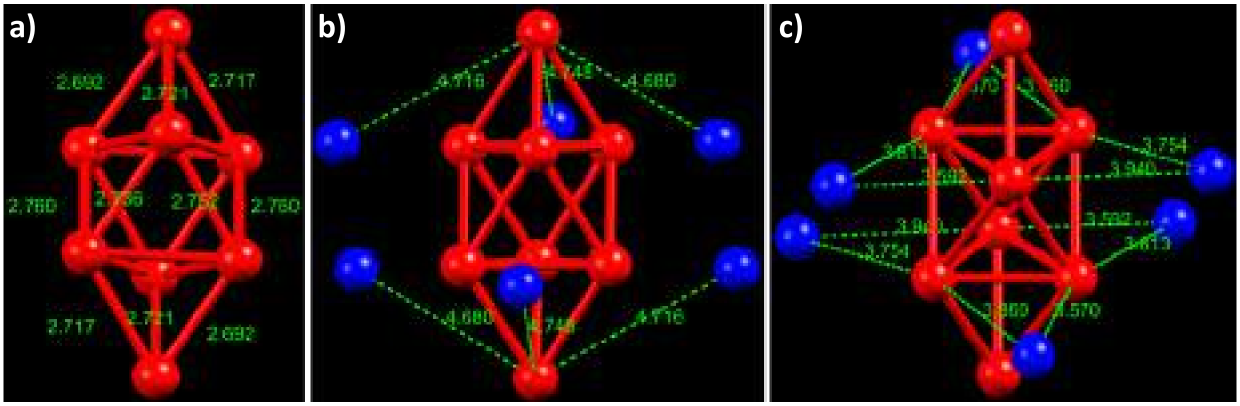

Figure S28. a) Interatomic Ag-Ag distances within Ag_8 bicapped trigonal antiprism core, b-c) interatomic distance of outer 6 Ag atoms from their nearest Ag atoms. All of the atoms are silver here.

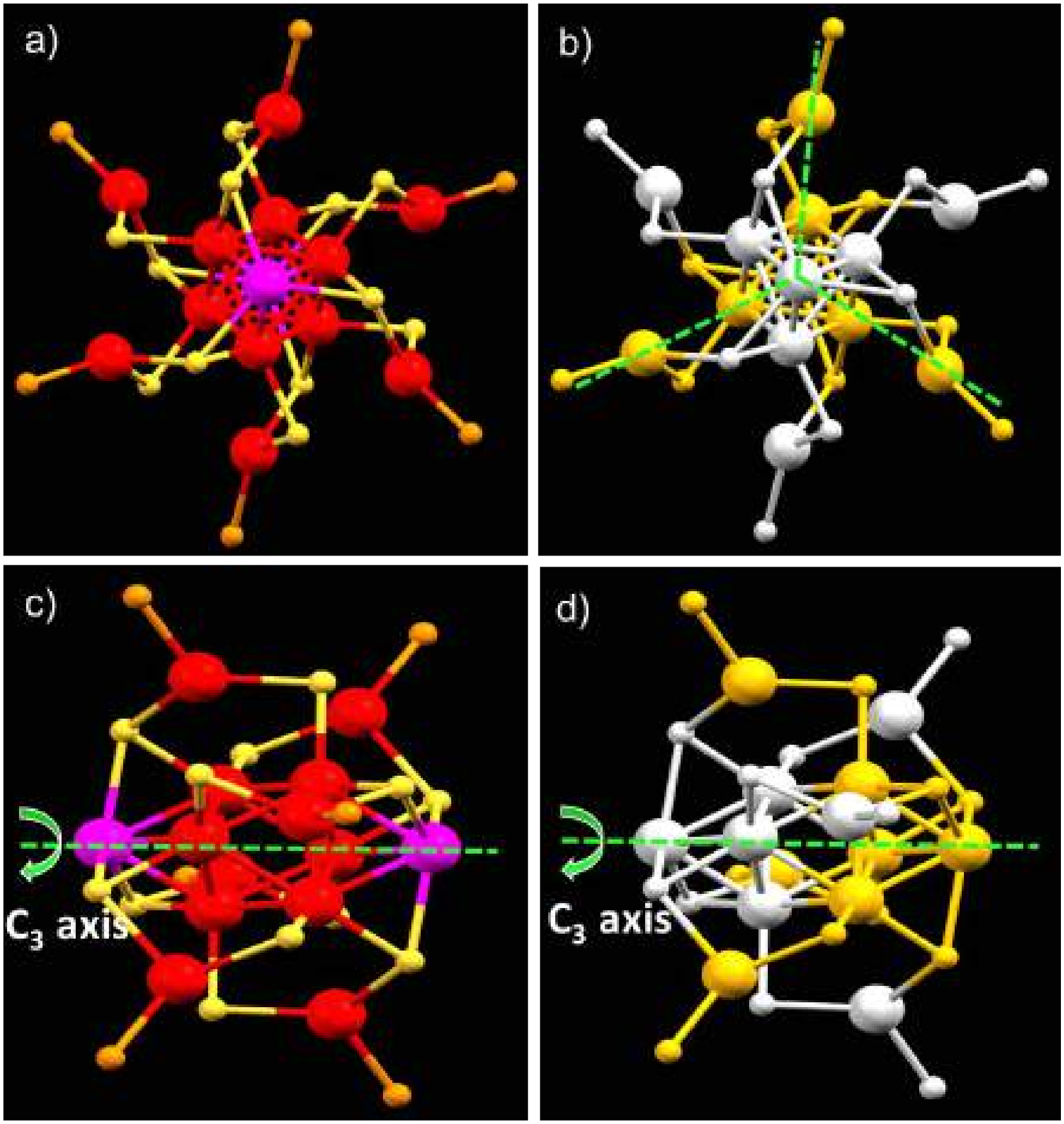

Figure S29. a-d) Single crystal structure of Ag14 core without CBDT, and TPP ligands with C3 axial symmetry in a different orientation, a, c) atomic color codes as red, pink = silver, yellow = sulphur, brown = phosphorous, b, d) the same atomic arrangements with symmetry oriented colors in ball and stick model.

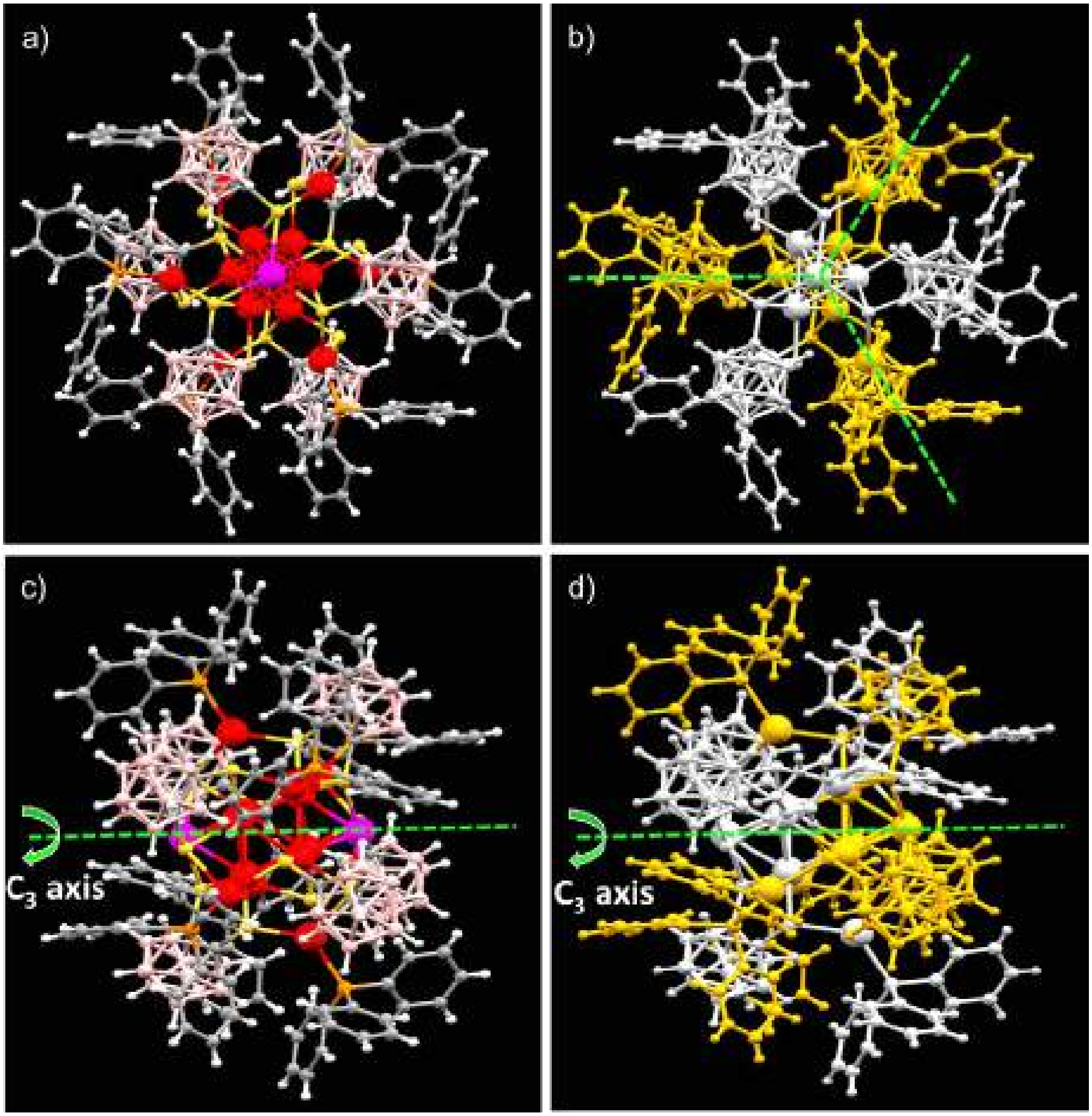

Figure S30. a-d) Full structure of the Ag_{14} having C_3 axial symmetry from two different orientation (a, c atoms are in their respective colors; b, d symmetry colors).

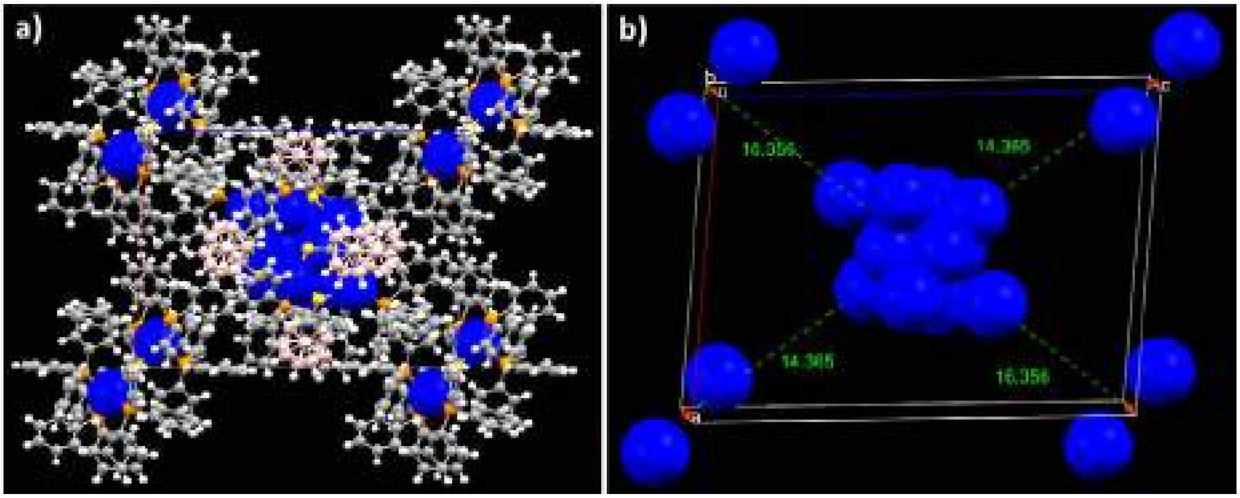

Figure S31. a) Full structure molecular packing of the Ag_{14} shows four $[Ag_2S(TPP)_6]$ units packed surrounding the Ag_{14}, b) distance between the centroids of four $[Ag_2S(TPP)_6]$ fragments from the centroids of Ag_{14} core.

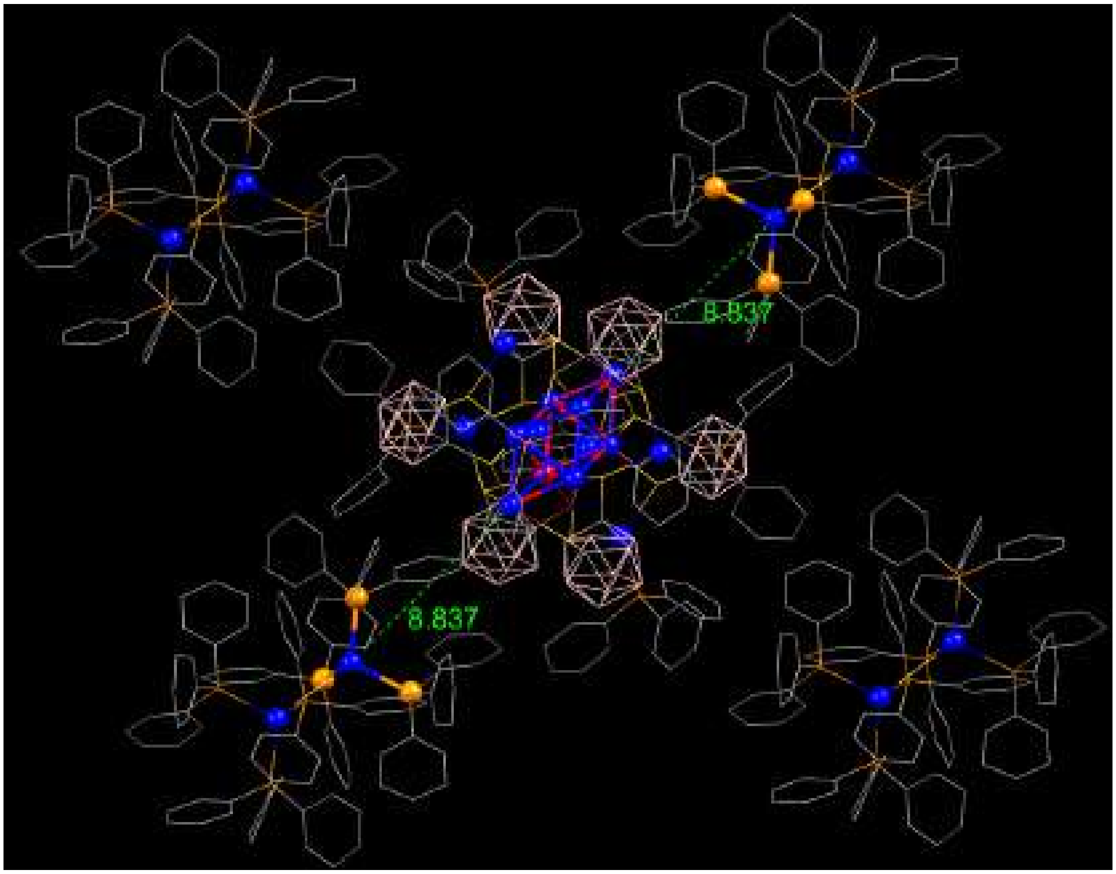

Figure S32. Single-crystal molecular packing of the Ag_{14} shows two capped silver atoms on the bicapped trigonal antiprism Ag_{14} core was shielded by the nearest TPP unit of $[Ag_2S(TPP)_6]$ (hydrogen atoms are removed for clarity).

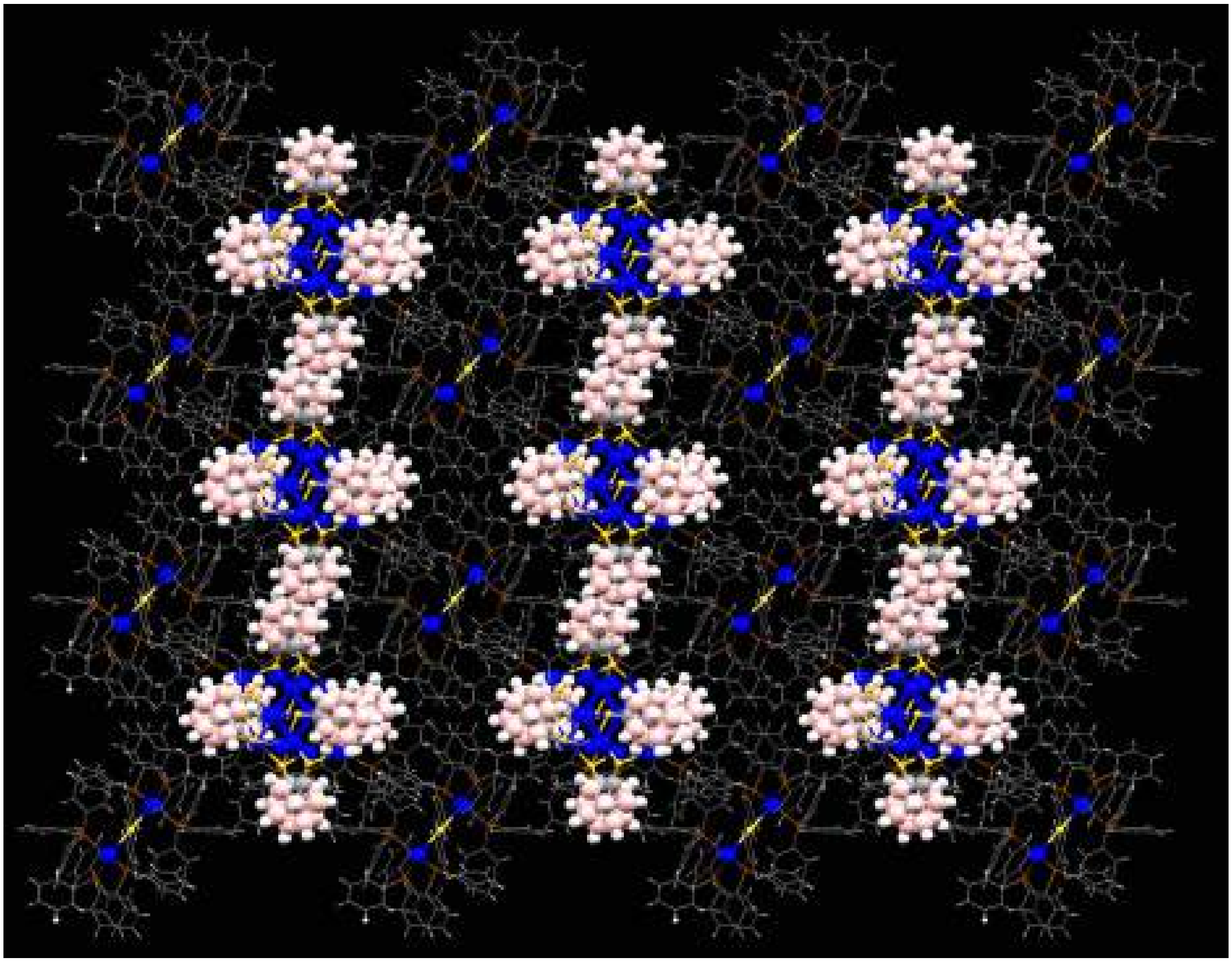

Figure S33. Extended molecular packing of the same NC showed repeating lamellar packing of $[Ag_{14}(CBDT)_6(TPP)_6]$ and $[Ag_2S(TPP)_6]$ units.

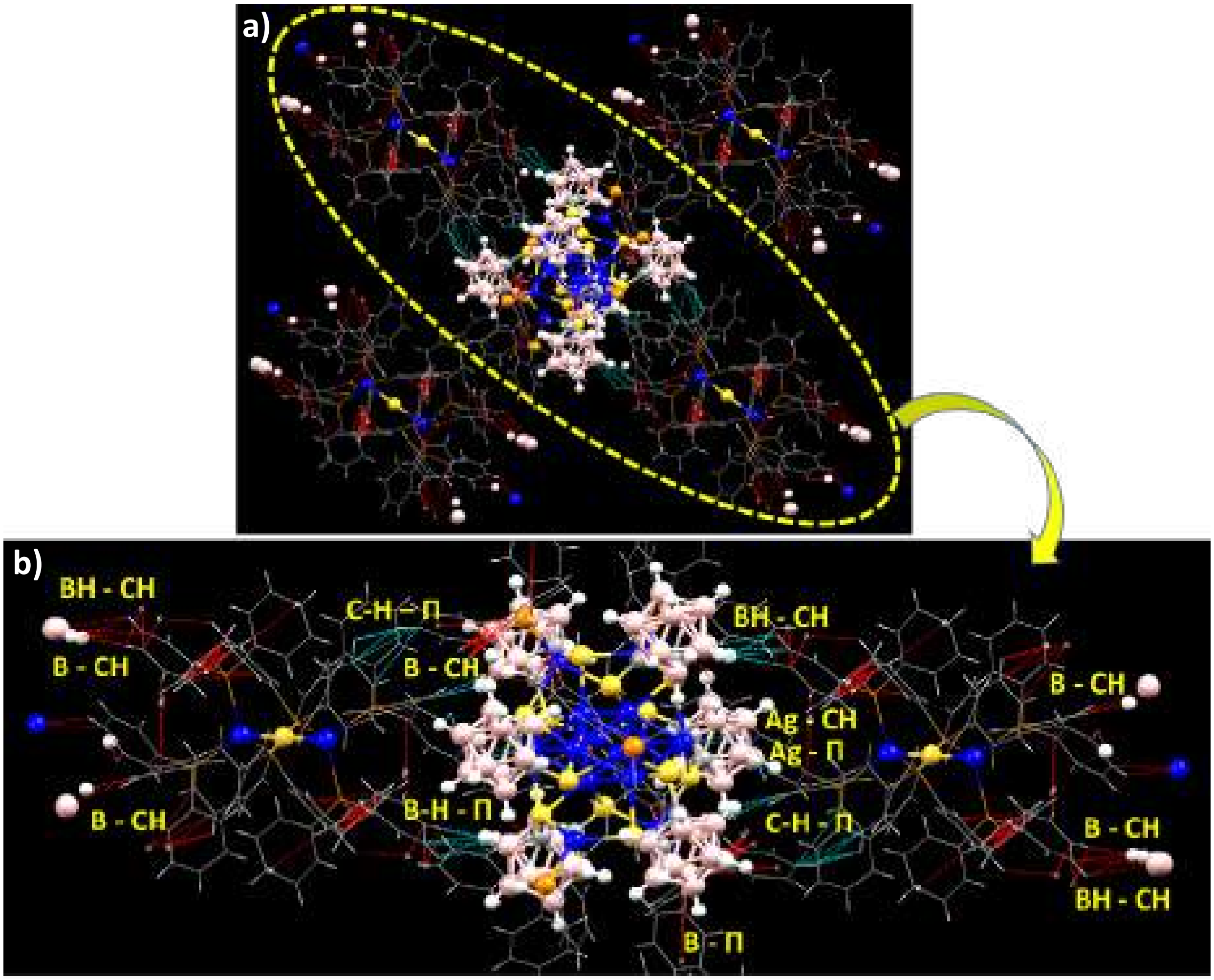

Figure S34. a-b) Intercluster packing due to different intermolecular interaction such as CH-π, BH- π, B-CH, BH-CH, Ag- π, Ag-CH, B-π of Ag_{14} with $[Ag_2S(TPP)_6]$ unit.

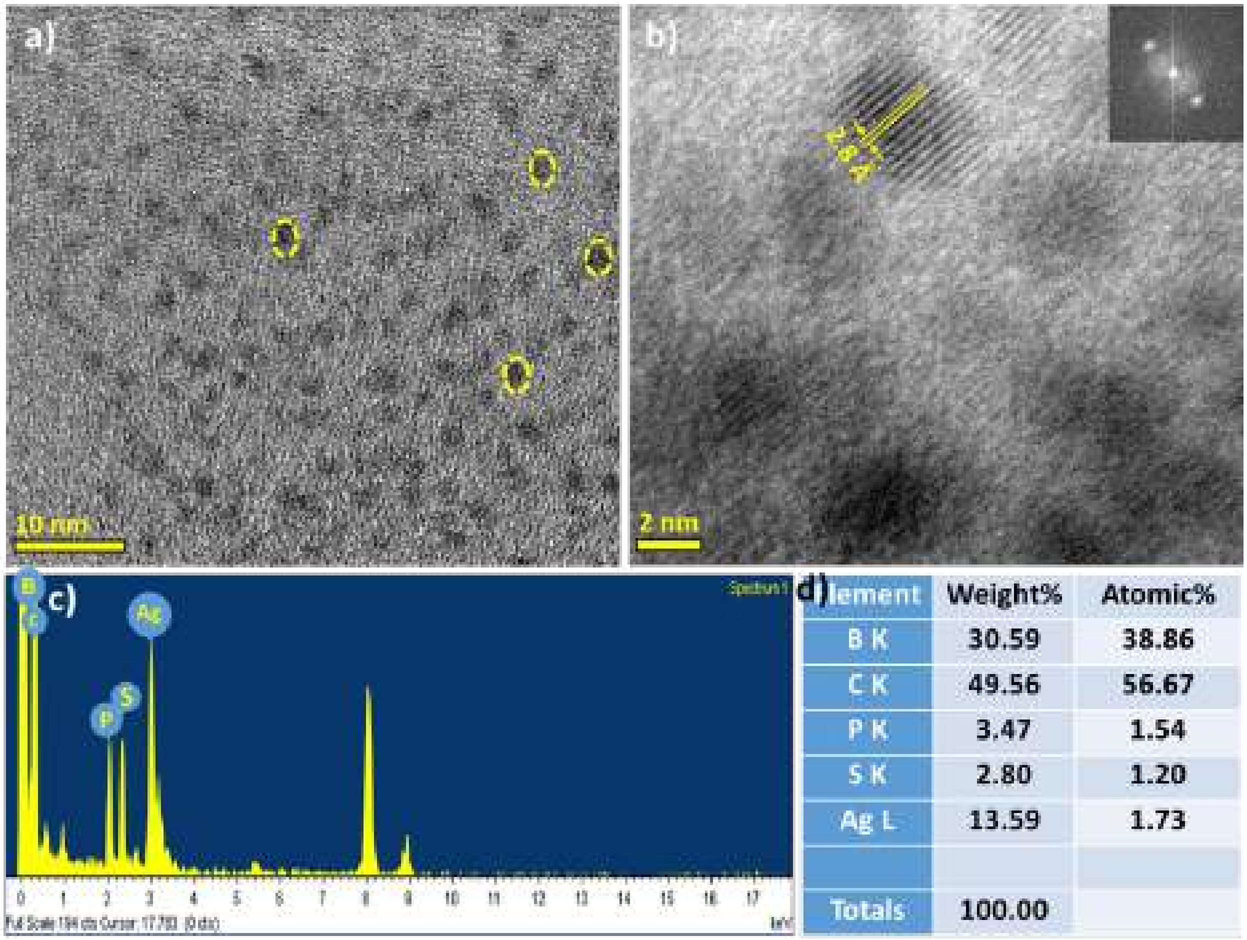

Element	Weight%	Atomic%
B K	30.59	38.86
C K	49.56	56.67
P K	3.47	1.54
S K	2.80	1.20
Ag L	13.59	1.73
Totals	100.00	

Figure S35. a) TEM image of the Ag_{14}, b) HRTEM image of the NCs having lattice spacing of 2.8 Å after 5 min beam irradiation, c-d) EDS spectrum of the NC with the quantification of the respective elements.

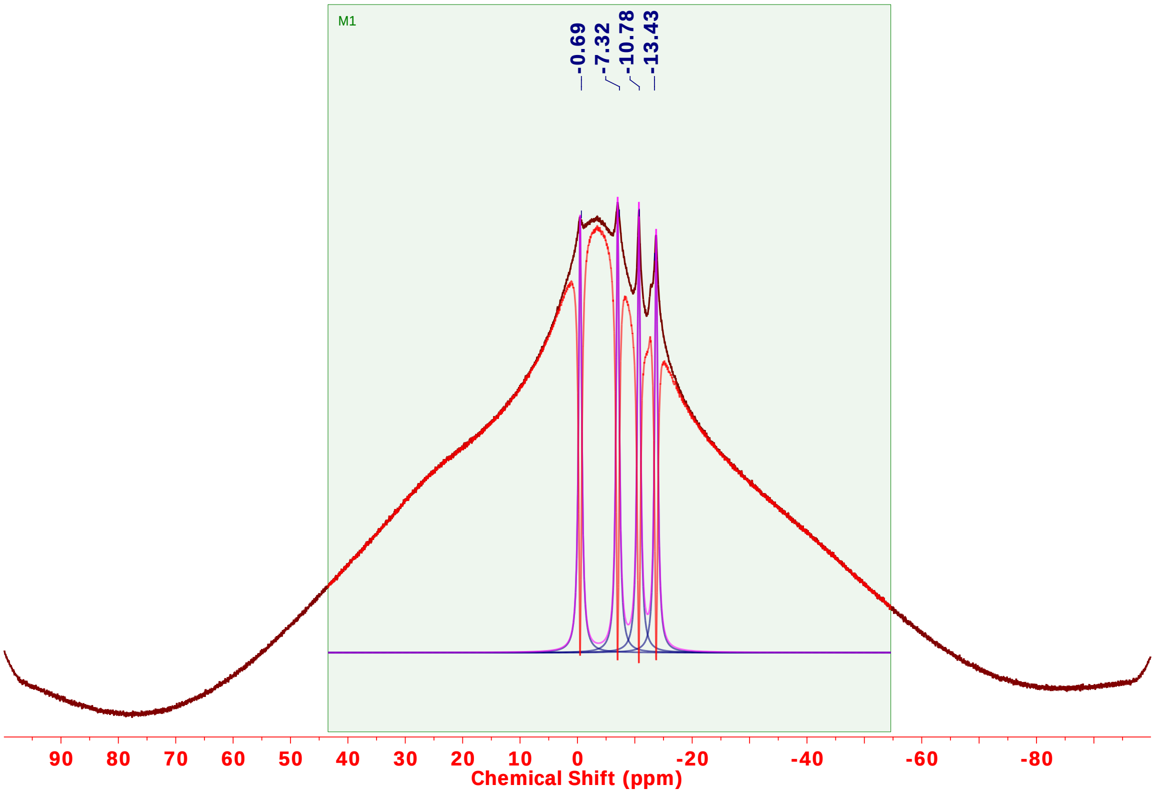

Figure S36. ^{11}B NMR spectrum of the Ag_{14} nanocluster in $CDCl_3$ solvent.

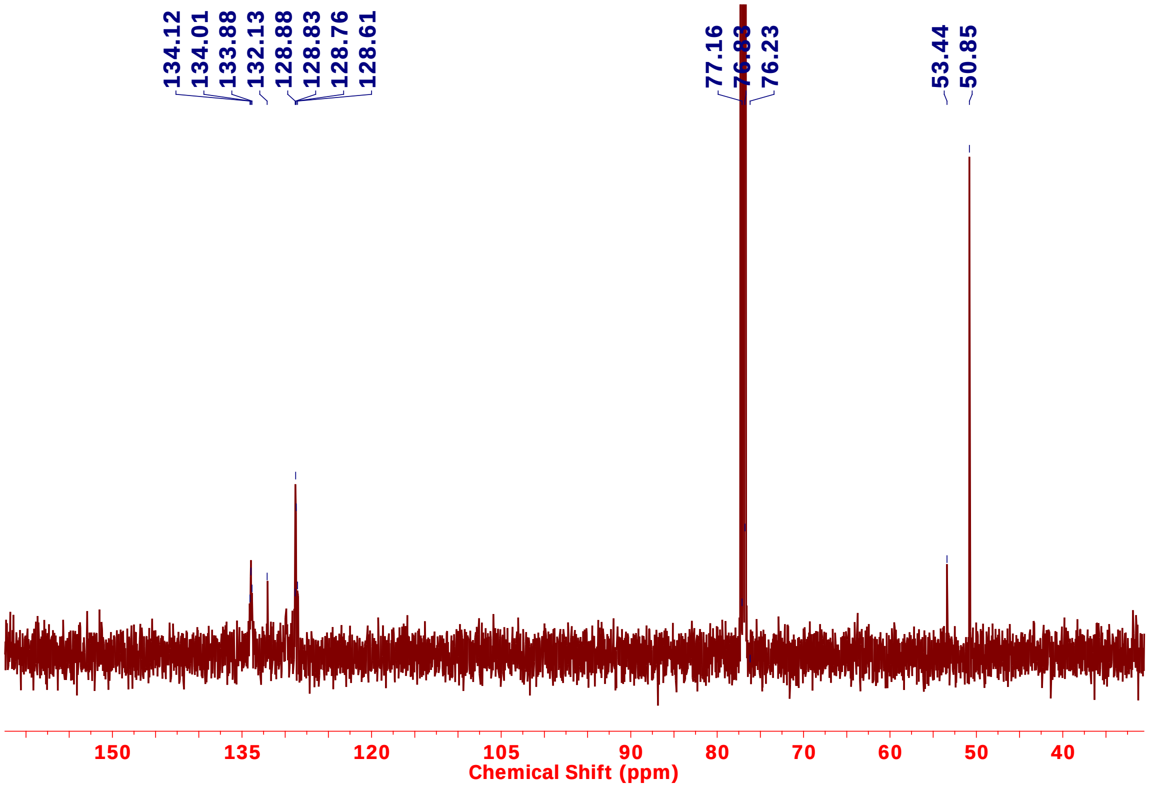

Figure S37. ^{13}C {^{1}H} NMR spectrum of the Ag_{14} nanocluster in $CDCl_3$ solvent.

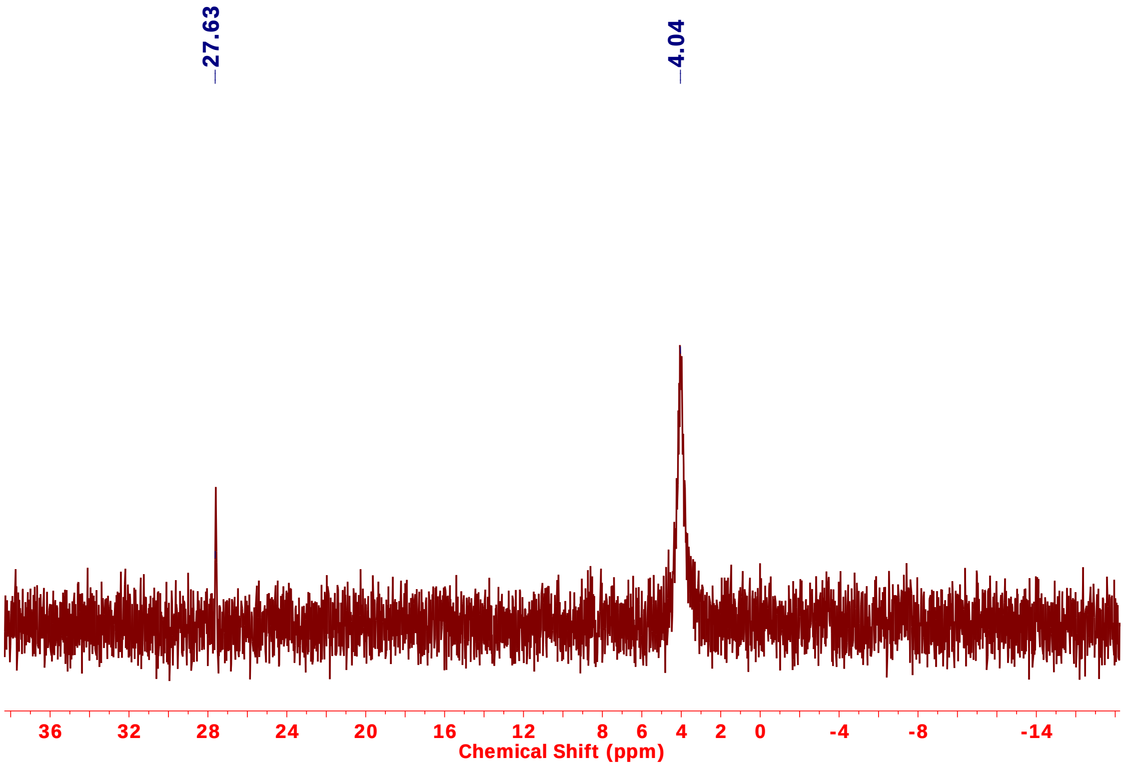

Figure S38. ^{31}P NMR spectrum of the Ag_{14} nanocluster in $CDCl_3$ solvent.

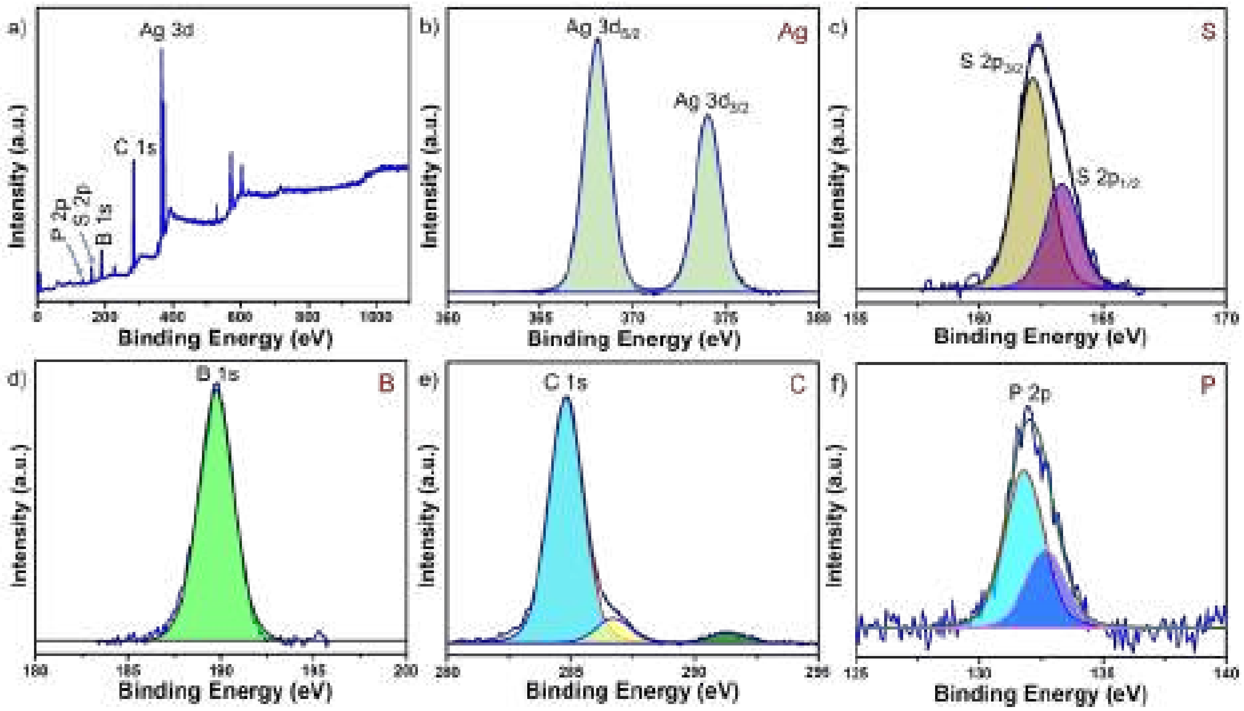

Figure S39. XPS spectra of Ag_{14}; a) XPS survey spectrum showed the signature peaks of existing elements. Spectral fitting of b) Ag 3d region, c) C 1S region, d) S 2p region, e) B 1S region, f) P 2p region.

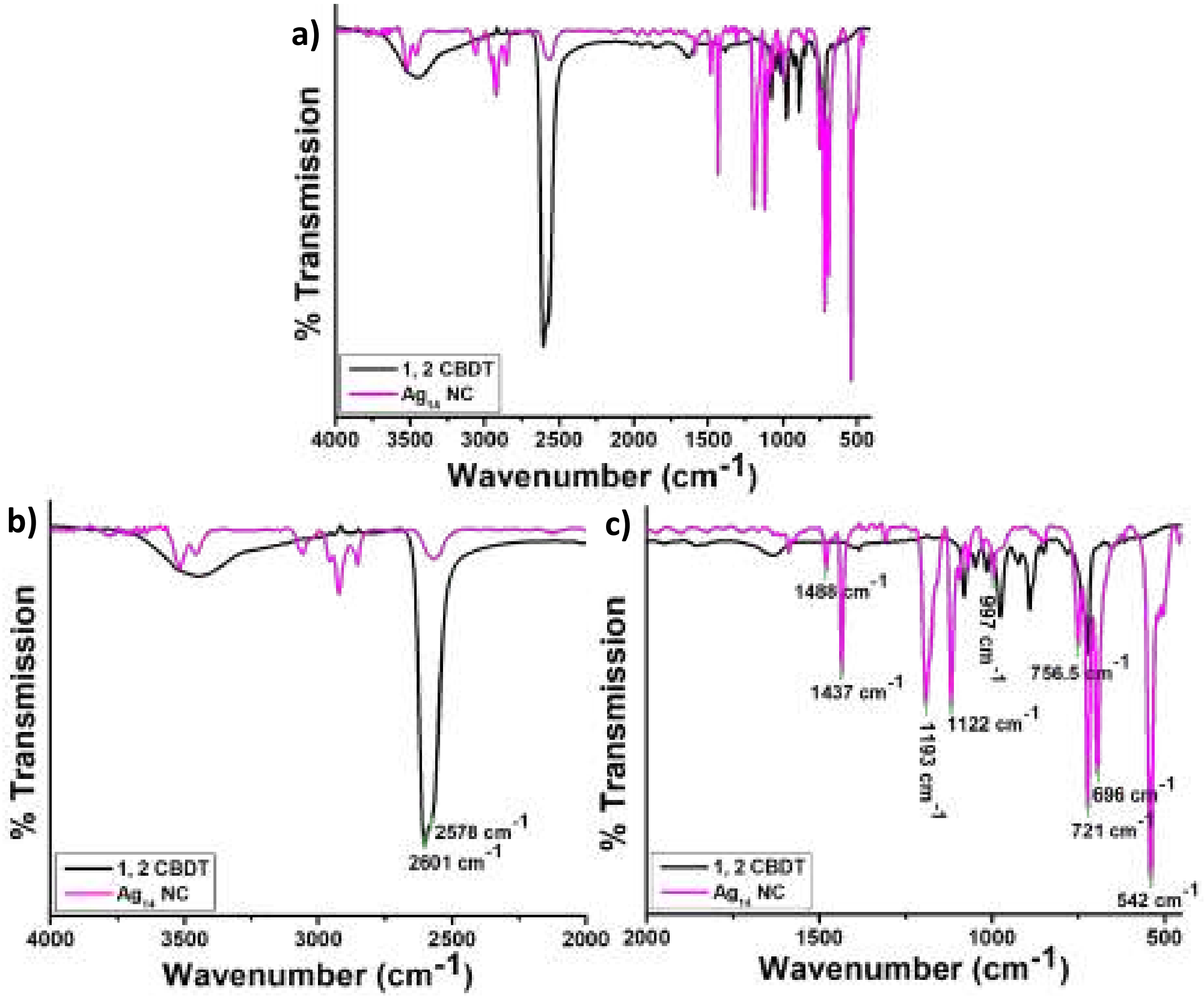

Figure S40. a) Combined FT-IR spectra of the *ortho*-carborane-1, 2-dithiol ligand, and Ag_{14} NC, b, and c) expanded view of the same spectra with peak assignments.

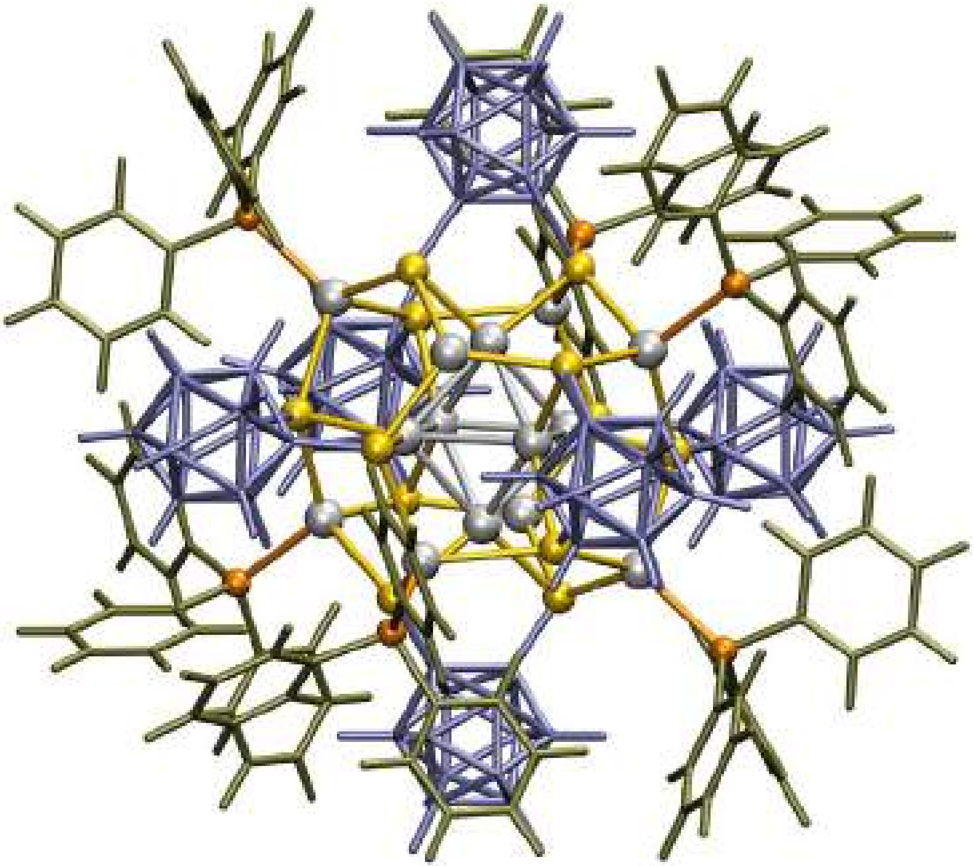

Figure S41. The DFT optimized structure of the Ag_{14} with all ligands; (color code of the atoms, grey: silver, yellow: sulphur, orange: phosphorous, blue: carborane, brown: phenyl).

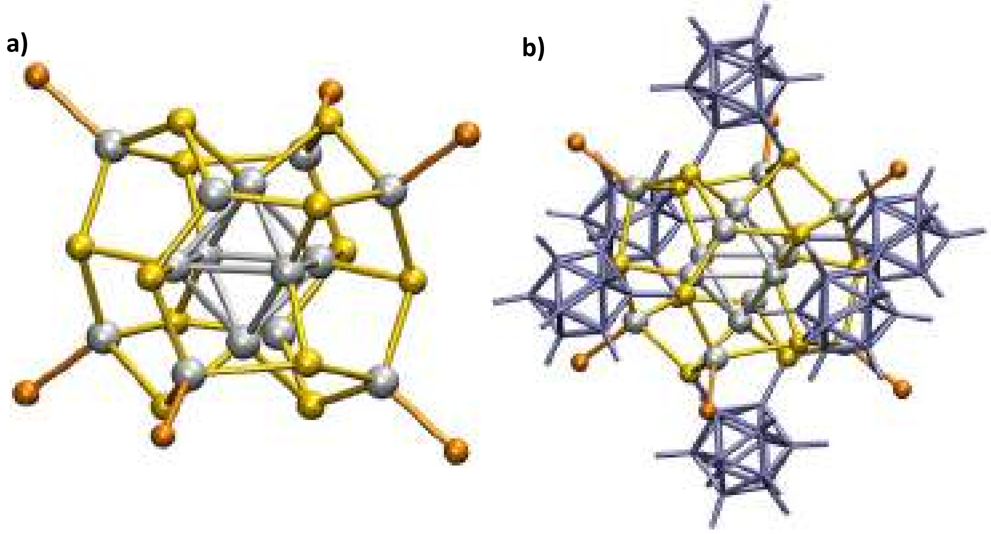

Figure S42. The DFT optimized relaxed structure of Ag_{14} a) without CBDT ligands b) with CBDT ligands. (Color code of the atoms, grey: silver, yellow: sulphur, orange: TPP, blue: carborane).

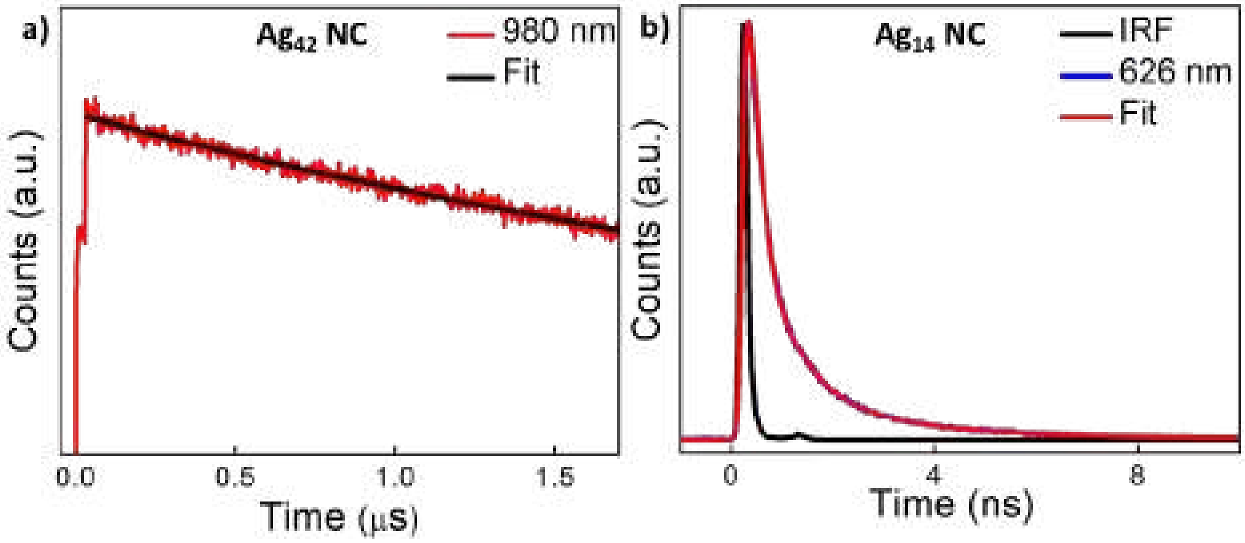

Figure S43. TCSPC data of a) lifetime decay of >1.5 μs for NIR emissive peak (980 nm) of Ag$_{42}$ and b) lifetime decay of 550 ps corresponding to the red emissive peak (626 nm) of Ag$_{14}$.

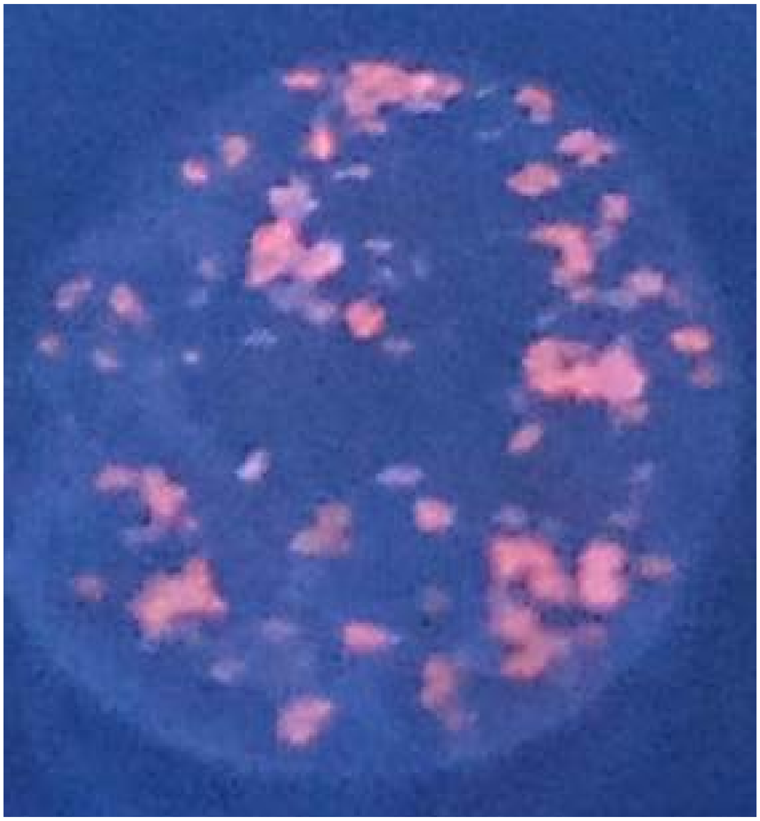

Figure S44. Photograph of the crystals of Ag$_{14}$ under 365 nm UV-light illumination. Red luminescence was observed from the crystals.

Table S1. Crystal data, and structure refinement for Ag_{14} NC

Identification code	Arijit Ag_{14} NC	
Empirical formula	$C_{228}H_{240}Ag_{14}Ag_{2}B_{60}P_{12}S_{13}$	
Formula weight	6143.13	
Temperature	293(2) K	
Wavelength	0.71073 Å	
Crystal system	Triclinic	
Space group	P -1	
Unit cell dimensions	a = 19.18(5) Å	a= 68.50(12)°.
	b = 19.19(4) Å	b= 82.39(19)°.
	c = 24.08(9) Å	g = 60.44(7)°.
Volume	7160(36) $Å^3$	
Z	1	
Density (calculated)	1.425 Mg/m^3	
Absorption coefficient	1.273 mm^{-1}	
F(000)	3048	
Crystal size	0.150 x 0.100 x 0.050 mm^3	
Theta range for data collection	2.926 to 18.000°.	
Index ranges	-16<=h<=16, -16<=k<=16, -20<=l<=20	
Reflections collected	67889	
Independent reflections	9814 [R(int) = 0.2609]	
Completeness to theta = 18.000°	99.5 %	
Absorption correction	Semi-empirical from equivalents	
Max. and min. transmission	0.7230 and 0.5910	
Refinement method	Full-matrix least-squares on F^2	
Data / restraints / parameters	9814 / 1854 / 1483	
Goodness-of-fit on F^2	1.613	
Final R indices [I>2sigma(I)]	R1 = 0.1869, wR2 = 0.4247	
R indices (all data)	R1 = 0.2756, wR2 = 0.4815	
Extinction coefficient	n/a	
Largest diff. peak and hole	1.783 and -2.024 $e.Å^{-3}$	

Table S2. Atomic coordinates (x 10^4) and equivalent isotropic displacement parameters ($Å^2$x 10^3) for Ag_{14}. U(eq) is defined as one third of the trace of the orthogonalized U^{ij} tensor.

	x	y	z	U(eq)
Ag(1)	5001(3)	3917(2)	5473(2)	134(2)
Ag(2)	3826(3)	5609(2)	4925(3)	134(2)
Ag(3)	4994(3)	5228(3)	5727(3)	136(2)
Ag(4)	6632(3)	5670(4)	5568(2)	141(2)
Ag(5)	3381(3)	7096(3)	3325(2)	133(2)
Ag(6)	6359(3)	2512(3)	4743(3)	143(2)
Ag(7)	3842(4)	4752(4)	6110(3)	188(2)
Ag(8)	1088(2)	4138(2)	9333(2)	81(1)
C(7)	7620(20)	6930(20)	4940(20)	95(8)
C(8)	7747(19)	6730(30)	4419(19)	99(9)
C(9)	7950(20)	7110(30)	3850(20)	110(10)
C(10)	8060(30)	7780(30)	3830(20)	116(10)
C(11)	7910(30)	8070(30)	4317(19)	111(10)
C(12)	7720(30)	7640(20)	4870(20)	102(9)
C(13)	8480(30)	5470(30)	5932(19)	100(9)
C(14)	9190(20)	5460(30)	5687(19)	90(10)
C(15)	9960(30)	4780(30)	5940(20)	108(11)
C(16)	9970(30)	4130(30)	6460(20)	110(12)
C(17)	9280(20)	4090(30)	6720(20)	111(12)
C(18)	8550(30)	4780(30)	6452(19)	101(11)
C(19)	7110(30)	6970(30)	6050(20)	131(10)
C(20)	7590(30)	6890(30)	6480(20)	138(11)
C(21)	7320(30)	7430(30)	6820(20)	144(12)
C(22)	6560(30)	8120(30)	6800(20)	159(13)
C(23)	6130(30)	8140(30)	6360(20)	160(13)
C(24)	6330(30)	7640(30)	6000(20)	150(12)
C(25)	8290(20)	1240(20)	4220(20)	100(9)
C(26)	9060(20)	540(30)	4330(20)	105(11)
C(27)	9740(30)	560(30)	4050(20)	116(12)

C(28)	9580(20)	1310(20)	3580(20)	93(10)
C(29)	8830(20)	2020(20)	3450(20)	88(10)
C(30)	8160(20)	1980(20)	3738(18)	80(9)
C(31)	7770(30)	270(30)	5290(20)	117(10)
C(32)	7810(30)	390(30)	5810(20)	118(11)
C(33)	8080(30)	-370(30)	6300(20)	136(12)
C(34)	8260(30)	-1210(30)	6420(20)	137(13)
C(35)	8240(30)	-1200(30)	5850(20)	132(12)
C(36)	8050(30)	-560(30)	5290(20)	122(11)
C(37)	6960(30)	860(30)	4080(30)	154(11)
C(38)	6290(30)	740(30)	4280(20)	164(11)
C(39)	5940(30)	500(30)	3970(20)	169(12)
C(40)	6370(30)	410(30)	3450(30)	161(12)
C(41)	7030(30)	510(30)	3250(20)	152(11)
C(42)	7360(30)	770(30)	3570(20)	147(11)
C(43)	3440(40)	8170(30)	1710(30)	135(11)
C(44)	4190(40)	7430(40)	1860(30)	166(14)
C(45)	4600(40)	7470(40)	1330(30)	174(15)
C(46)	4470(40)	8160(40)	820(30)	175(16)
C(47)	3760(40)	8910(40)	790(30)	182(16)
C(48)	3290(40)	8960(40)	1280(30)	163(14)
C(49)	2230(40)	7710(40)	2020(30)	173(11)
C(50)	2100(40)	7030(40)	2380(30)	167(12)
C(51)	1750(40)	6790(40)	2070(30)	171(12)
C(52)	1510(40)	7070(40)	1470(20)	169(12)
C(53)	1580(40)	7790(40)	1130(30)	172(12)
C(54)	2020(40)	8010(40)	1410(30)	171(12)
C(55)	1970(30)	9130(20)	2330(30)	189(13)
C(56)	1170(30)	9470(30)	2470(20)	211(15)
C(57)	620(20)	10300(40)	2430(20)	220(17)
C(58)	780(30)	11010(30)	2230(30)	221(17)
C(59)	1610(30)	10760(30)	2050(30)	209(15)
C(60)	2060(20)	9850(30)	2150(30)	195(14)
C(61)	-810(30)	4660(30)	8557(18)	97(9)
C(62)	-1090(30)	4570(30)	9130(20)	109(11)
C(63)	-1880(20)	4780(40)	9270(20)	120(12)

C(64)	-2330(30)	5000(40)	8763(19)	119(12)
C(65)	-2170(20)	5200(30)	8160(20)	114(11)
C(66)	-1340(20)	4920(30)	8090(20)	111(10)
C(67)	680(30)	3630(30)	8150(20)	103(11)
C(68)	390(40)	3100(30)	8220(30)	160(20)
C(69)	780(40)	2400(40)	8000(30)	180(30)
C(70)	1610(40)	2290(40)	7830(30)	150(20)
C(71)	2020(40)	2800(30)	7740(40)	190(40)
C(72)	1500(30)	3410(40)	7880(20)	113(17)
C(73)	30(20)	5510(30)	7785(18)	76(8)
C(74)	90(20)	5530(30)	7191(17)	84(9)
C(75)	-70(30)	6260(30)	6690(20)	91(10)
C(76)	-120(30)	6860(30)	6900(20)	95(10)
C(77)	-120(30)	6860(30)	7479(18)	92(9)
C(78)	-10(20)	6130(20)	7970(19)	83(8)
C(79)	2510(20)	4550(30)	8270(20)	94(9)
C(80)	2110(30)	5120(30)	7714(18)	109(12)
C(81)	2410(30)	4990(30)	7170(20)	110(12)
C(82)	3080(30)	4250(30)	7160(20)	118(13)
C(83)	3460(30)	3730(30)	7730(19)	126(13)
C(84)	3210(30)	3810(30)	8280(20)	121(13)
C(85)	1680(30)	5900(30)	8770(30)	126(10)
C(86)	2070(30)	6370(30)	8350(30)	133(12)
C(87)	1760(40)	7190(40)	8290(30)	134(12)
C(88)	1050(30)	7630(40)	8500(30)	138(13)
C(89)	640(30)	7180(30)	8890(30)	138(13)
C(90)	990(30)	6270(30)	9090(30)	127(12)
C(91)	2920(30)	4290(40)	9430(20)	137(11)
C(92)	3520(30)	4520(40)	9320(20)	150(12)
C(93)	4170(30)	4170(40)	9730(20)	156(13)
C(94)	4210(30)	3490(40)	10240(20)	154(13)
C(95)	3610(30)	3270(40)	10420(20)	152(13)
C(96)	2960(30)	3720(40)	10000(20)	138(12)
C(97)	2010(30)	2340(30)	10710(20)	133(9)
C(98)	1730(20)	3030(30)	10910(20)	137(10)
C(99)	1890(20)	2730(30)	11520(20)	142(10)

C(100)	2250(30)	1920(30)	11970(20)	156(11)
C(101)	2510(30)	1280(40)	11720(20)	157(10)
C(102)	2400(30)	1490(30)	11100(20)	151(10)
C(103)	1160(40)	2050(30)	10000(30)	247(16)
C(104)	1520(40)	1160(30)	10160(30)	256(17)
C(105)	1180(40)	670(40)	10170(30)	259(17)
C(106)	370(40)	1050(30)	10010(30)	257(17)
C(107)	100(40)	1910(30)	9870(30)	256(17)
C(108)	350(40)	2500(30)	9830(30)	249(17)
C(109)	2770(20)	2010(30)	9690(20)	210(14)
C(110)	3490(30)	1660(30)	10030(20)	217(16)
C(111)	4250(20)	1230(30)	9790(20)	226(17)
C(112)	4220(20)	1180(40)	9210(20)	229(18)
C(113)	3480(30)	1570(40)	8890(20)	222(17)
C(114)	2740(20)	1970(30)	9130(20)	214(16)
C(1)	1980(30)	6120(30)	4990(30)	106(5)
C(2)	2020(30)	7090(30)	4530(30)	98(5)
B(2)	1100(30)	8060(40)	4740(30)	101(6)
B(4)	1230(30)	7710(40)	4040(30)	96(6)
B(1)	1680(30)	6660(30)	4200(30)	98(5)
B(3)	1720(40)	6960(40)	5210(30)	106(5)
B(5)	1120(40)	6470(40)	5380(30)	112(6)
B(6)	1100(30)	6210(40)	4730(30)	106(6)
B(7)	580(30)	7610(40)	5320(30)	108(7)
B(8)	210(40)	7100(40)	4900(30)	108(7)
B(9)	560(30)	7270(40)	4100(30)	100(6)
B(10)	310(40)	8060(40)	4500(30)	103(7)
C(3)	4430(30)	5970(30)	6850(20)	109(6)
C(4)	5580(30)	5240(30)	6940(20)	97(6)
B(17)	5000(30)	6600(40)	7330(30)	109(6)
B(18)	5890(30)	5710(40)	7210(30)	100(6)
B(11)	4860(30)	5200(40)	8010(30)	114(7)
B(12)	4360(40)	6340(40)	7820(30)	119(7)
B(13)	5500(40)	5570(40)	7870(30)	110(7)
B(14)	5880(40)	4730(40)	7650(30)	104(7)
B(15)	4930(30)	4980(40)	7350(30)	107(6)

B(16)	4060(40)	5870(40)	7500(30)	120(7)
B(19)	5100(30)	6370(40)	6720(30)	100(6)
B(20)	4120(40)	6830(50)	7070(30)	114(7)
C(5)	5150(30)	2220(30)	6560(20)	93(5)
C(6)	5010(20)	2080(30)	5920(20)	85(5)
B(21)	5980(30)	1480(30)	6350(30)	91(5)
B(22)	5950(30)	540(40)	6810(30)	95(6)
B(23)	5630(30)	970(30)	6090(30)	89(6)
B(24)	4490(30)	1590(30)	6050(30)	87(6)
B(25)	4270(30)	2330(40)	6320(30)	90(5)
B(26)	4670(30)	1820(40)	7070(30)	96(6)
B(27)	4330(30)	1340(40)	6780(30)	93(6)
B(28)	5130(30)	740(40)	7300(30)	98(7)
B(29)	5050(30)	590(40)	6620(30)	93(6)
B(30)	5680(30)	1290(40)	7100(30)	97(6)
P(1)	7456(7)	6306(8)	5631(6)	75(4)
P(2)	7394(7)	1200(8)	4579(7)	87(4)
P(3)	2722(9)	8048(9)	2313(8)	116(5)
P(4)	2065(7)	4721(8)	8972(6)	74(3)
P(5)	218(7)	4463(8)	8445(6)	74(3)
P(6)	1738(8)	2545(9)	9942(7)	94(4)
S(1)	2813(8)	5124(8)	5234(7)	99(4)
S(2)	2897(7)	7116(7)	4375(7)	90(3)
S(3)	3890(8)	6082(8)	6220(7)	111(4)
S(4)	4987(7)	2822(8)	5195(7)	93(3)
S(5)	5123(8)	3172(9)	6579(7)	104(3)
S(6)	6096(7)	4801(9)	6413(6)	91(3)
S(7)	0	5000	10000	71(5)

REFERENCES

1. Baše, T.; Holub, J.; Fanfrlík, J.; Hnyk, D.; Lane, P. D.; Wann, D. A.; Vishnevskiy, Y. V.; Tikhonov, D.; Reuter, C. G.; Mitzel, N. W. Icosahedral Carbaboranes with Peripheral Hydrogen–Chalcogenide Groups: Structures from Gas Electron Diffraction and Chemical Shielding in Solution. *Chem. - A Eur. J.* **2019**, *25*, 2313–2321.

2. Baše, T.; Bastl, Z.; Plzák, Z.; Grygar, T.; Plešek, J.; Carr, M. J.; Malina, V.; Šubrt, J.; Boháček, J.; Večerníková, E.; Kříž, O. Carboranethiol-Modified Gold Surfaces. A Study and Comparison of Modified Cluster and Flat Surfaces. *Langmuir* **2005**, *21* (17), 7776–7785.

3. Bootharaju, M. S.; Dey, R.; Gevers, L. E.; Hedhili, M. N.; Basset, J. M.; Bakr, O. M. A New Class of Atomically Precise, Hydride-Rich Silver Nanoclusters Co-Protected by Phosphines. *J. Am. Chem. Soc.* **2016**, *138*, 13770–13773.

4. Ghosh, A.; Bodiuzzaman, M.; Nag, A.; Jash, M.; Baksi, A.; Pradeep, T. Sequential Dihydrogen Desorption from Hydride-Protected Atomically Precise Silver Clusters and the Formation of Naked Clusters in the Gas Phase. *ACS Nano* **2017**, *11*, 11145–11151.

5. Li, J. R.; Zhou, H. C. Bridging-Ligand-Substitution Strategy for the Preparation of Metal-Organic Polyhedra. *Nat. Chem.* **2010**, *2*, 893–898.

6. Mallick, A.; Garai, B.; Díaz, D. D.; Banerjee, R. Hydrolytic Conversion of a Metal-Organic Polyhedron into a Metal-Organic Framework. *Angew. Chemie - Int. Ed.* **2013**, *52*, 13755–13759.

7. Suzuki, K.; Tominaga, M.; Kawano, M.; Fujita, M. Self-Assembly of an M_6L_{12} Coordination Cube. *Chem. Commun.* **2009**, 1638–1640.

8. Enkovaara, J.; Rostgaard, C.; Mortensen, J. J.; Chen, J.; Dułak, M.; Ferrighi, L.; Gavnholt, J.; Glinsvad, C.; Haikola, V.; Hansen, H. A.; Kristoffersen, H. H.; Kuisma, M.; Larsen, A. H.; Lehtovaara, L.; Ljungberg, M.; Lopez-Acevedo, O.; Moses, P. G.; Ojanen, J.; Olsen, T.; Petzold, V *et. al*. Electronic Structure Calculations with GPAW: A Real-Space Implementation of the Projector Augmented-Wave Method. *J. Phys. Condens. Matter* **2010**, *22* (253202), 1–24.

9. Mortensen, J. J.; Hansen, L. B.; Jacobsen, K. W. Real-Space Grid Implementation of the Projector Augmented Wave Method. *Phys. Rev. B - Condens. Matter Mater. Phys.* **2005**, *71* (035109), 1–11.

10. Perdew, J. P.; Burke, K.; Ernzerhof, M. Generalized Gradient Approximation Made Simple. *Phys. Rev. Lett.* **1996**, *77* (18), 3865–3868.

11. Gavnholt, J.; Olsen, T.; Engelund, M.; Schiøtz, J. δ Self-Consistent Field Method to Obtain Potential Energy Surfaces of Excited Molecules on Surfaces. *Phys. Rev. B - Condens. Matter Mater. Phys.* **2008**, *78* (075441), 1–10.

12. Valiev, M.; Bylaska, E. J.; Govind, N.; Kowalski, K.; Straatsma, T. P.; Van Dam, H. J. J.; Wang, D.; Nieplocha, J.; Apra, E.; Windus, T. L.; De Jong, W. A. NWChem: A Comprehensive and Scalable Open-Source Solution for Large Scale Molecular Simulations.

Comput. Phys. Commun. **2010**, *181*, 1477–1489.

13. Johnson, B. G.; Fisch, M. J. An Implementation of Analytic Second Derivatives of the Gradient-Corrected Density Functional Energy. *J. Chem. Phys.* **1994**, *100*, 7429–7442.

14. Adamo, C.; Barone, V. Toward Reliable Density Functional Methods without Adjustable Parameters: The PBE0 Model. *J. Chem. Phys.* **1999**, *110*, 6158–6170.

15. Adamo, C.; Barone, V. Physically Motivated Density Functionals with Improved Performances: The Modified Perdew-Burke-Ernzerhof Model. *J. Chem. Phys.* **2002**, *116* (14), 5933–5940.

16. Jensen, F. Unifying General and Segmented Contracted Basis Sets. Segmented Polarization Consistent Basis Sets. *J. Chem. Theory Comput.* **2014**, *10* (3), 1074–1085.

17. Liang, T.; Ren, L. U. Some Studies Concerning Rotating Axes and Polyatomic Molecules. *Phys. Rev.* **1935**, *47*, 1659–1661.

18. Allouche, A. Gabedit — A Graphical User Interface for Computational Chemistry Softwares. *J. Comput. Chem.* **2011**, *32*, 174–182.

THE JOURNAL OF PHYSICAL CHEMISTRY C
A JOURNAL OF THE AMERICAN CHEMICAL SOCIETY

pubs.acs.org/JPCC

Article

Interference of Phosphate in Adsorption of Arsenate and Arsenite over Confined Metastable Two-Line Ferrihydrite and Magnetite

Chennu Sudhakar, Sritama Mukherjee, Avula Anil Kumar, Ganesan Paramasivam, P. Karthigai Meena, Nonappa, and Thalappil Pradeep*

Cite This: *J. Phys. Chem. C* 2021, 125, 22502−22512

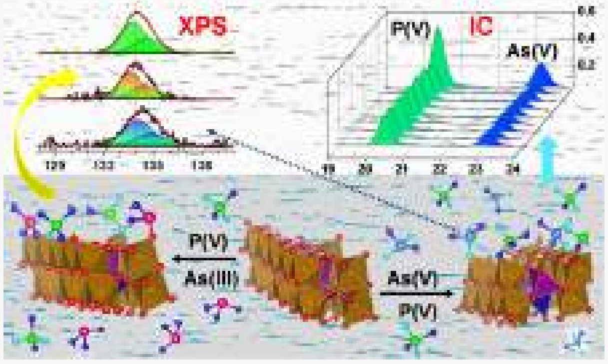

ABSTRACT: Contamination of groundwater by arsenic (As(III/V)) is a serious global issue, and phosphate (P(V)) is known to be the biggest interference in adsorption-based remediation methods. The present study is focused on understanding the interaction between phosphate and iron oxides/oxy-hydroxides with two well-known classes of potential adsorbents in the important pH range of 5−9 and the effect of such interactions on the uptake of arsenite and arsenate. Spectroscopic studies such as X-ray photoelectron spectroscopy (XPS) and Fourier transform infrared (FTIR) spectroscopy were used to understand the binding of various oxyanions of phosphorous and arsenic with the iron oxides/oxy-hydroxides, exploring the core levels of P 2p and Fe 2p. Materials used for adsorption experiments were magnetite (MAG) and a nanocomposite, confined metastable two-line ferrihydrite (CM2LF); CM2LF is used for arsenic remediation in the affected states in India. Further, we studied the interference of P(V) in As(III/V) adsorption. The kinetics of adsorption was quantified using ion chromatography (IC), where P(V) alone followed a pseudo-second-order model. In the case of mixed solutions, namely, AP_{mix1} (P(V) + As(III)) and AP_{mix2} (P(V) + As(V)), kinetics data suggested that P(V) or As(III/V) oxyanions partially follow the pseudo-second-order model. Results also confirmed that CM2LF performed better than magnetite (MAG) for As(III/V) uptake in the presence of P(V). As(III) and As(V) species are more competitive than P(V) at neutral pH. A model for the adsorption of P(V) species in water on ferrihydrite particles was developed using density functional theory (DFT). This accounted for phosphate complexation at various pH values. The study is highly useful in developing an affordable solution for sustainable arsenic remediation. Various aspects of sustainability are discussed.

■ INTRODUCTION

Phosphorus (P) is the 11th most common element and is essential for all known life forms on earth.[1,2] It exists in different inorganic and organic forms having various oxidation states (+V, +III, +I, 0, and −III). The dominant biological forms of P are $H_2PO_4^{1-}$, HPO_4^{2-}, and PO_4^{3-} at biologically relevant pH (7−9).[3] There are similarities between P and arsenic (As). Arsenic is a metalloid that sits just below P in the periodic table with larger atomic radii, the same number of valence electrons, and nearly identical electronegativity. Arsenic exists preferentially in +V, +III, and 0 oxidation states. The similarity between phosphorus and arsenic translates to the various species that they form, importantly phosphate (PO_4^{3-}) and arsenate (AsO_4^{3-}). The dissociation constants for P(V) in H_3PO_4 are close to those of As(V) in H_3AsO_4 over a range of physiological conditions. Also, As(V) can retain a negative charge even when it bonds with two other species, similar to P(V). Due to these similarities, As(V) and P(V) are not easily distinguishable by most life forms.[3] As(V) is taken up by cells via phosphate transporters and can substitute for P(V) in the early steps of many phosphate-based metabolic pathways.[3]

Interaction of arsenic with metal oxides or metal oxy-hydroxides is mainly influenced by pH (H^+/OH^- ions) and competing ions (phosphates, silicate, iron, manganese, calcium, magnesium, nitrate, chloride, and sulfate) generally present in groundwater.[4] The mobility of these oxyanions (P(V), As(III/V)) in the environment is influenced by redox potential, pH conditions, organic matter, and other competing oxyanions.[5] Phosphate can interact with iron oxide surfaces through Fe−O−P bonds. These are relevant processes in bacterial adhesion as in the case of organisms such as *Bacillus subtilis* and *Pseudomonas aeruginosa*.[6] Phosphate and arsenate are consid-

Received: May 18, 2021
Revised: September 19, 2021
Published: September 30, 2021

https://doi.org/10.1021/acs.jpcc.1c04317
J. Phys. Chem. C 2021, 125, 22502−22512

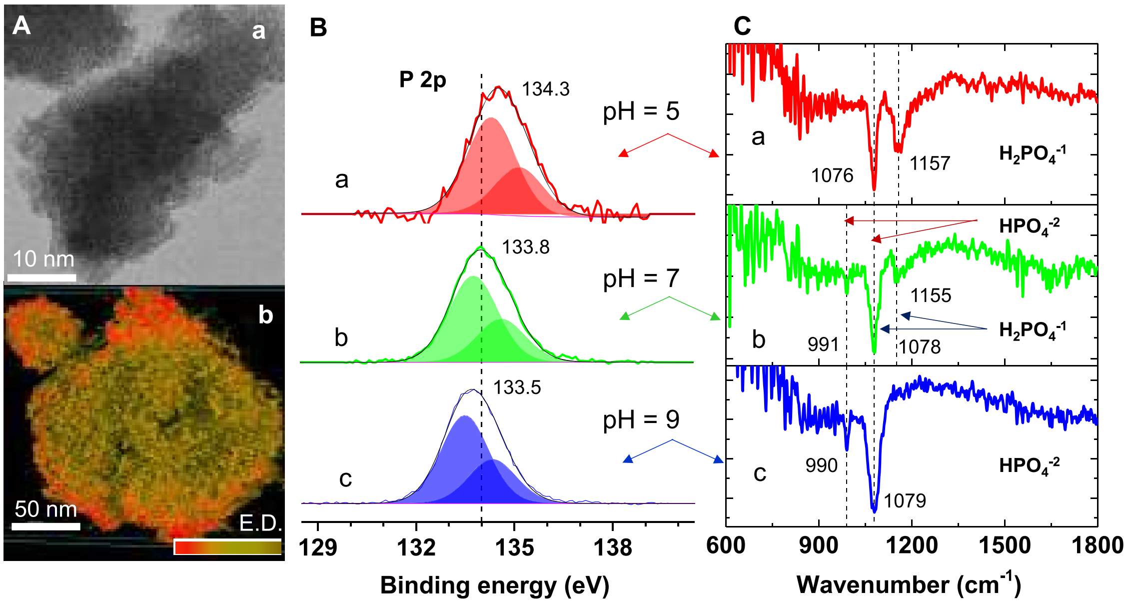

Figure 1. (A) (a) TEM image and (b) 3D reconstructed tomographic image of the two-line ferrihydrite composite (CM2LF); ED, electron density. (B) XPS P 2p spectra of aqueous phosphate solutions at various pH values of (a) 5, (b) 7, and (c) 9 after drying. The XPS samples were prepared by dropcasting the phosphate solutions onto an ITO plate and drying at room temperature for 2 days. (C) ATR-FTIR spectra of 100 mM phosphate at various pH values of (a) 5, (b) 7, and (c) 9 in the region of interest. All IR spectra shown here were subtracted from those of water.

ered to have similar adsorption characteristics because they have very similar protonation tendencies in aqueous medium.[7−10] Due to their structural similarities, PO_4^{3-} competes with AsO_4^{3-} during sorption and coprecipitation on iron oxy-hydroxides.[11−14] The presence and mobility of contaminants (in the context of arsenic and other heavy metal ions) in groundwater systems are strongly dependent on the interaction with iron and aluminum-based materials present in soils and waterways.[15] Studies on the desorption of arsenic compounds were reported in the presence of PO_4^{3-} and Cl^- and other constituents.[16]

While numerous PO_4^{3-} adsorption studies have been performed in view of its importance to soil,[17] in water, it is treated as a pollutant depending on its concentration levels.[18] For its removal, the adsorbents used are mainly iron oxides (hematite[19] and magnetite[20,21]) and iron oxy-hydroxides (ferrihydrite,[22] goethite,[23] and maghaemite[24]). Adsorption of phosphate onto iron oxides/oxy-hydroxides (commonly present in soils) plays a significant role in soil fertility as it influences the surface charge responsible for the attachment of organic matter to the soils.[23] The effect of pH on various complexation mechanisms, such as inner-sphere and outer-sphere adsorption on the hematite surface, was reported.[25] The molecular-scale structure of surface complexes depends on the mineral surfaces, and there is a brief discussion on models of surface complexation in a study by Wang et al.[26] Sodium phosphate interaction with iron oxide (Fe_2O_3) was understood using density functional theory (DFT) calculations.[27] Adsorption of phosphate on ferrihydrite[15]/magnetite[28] has been studied using X-ray photoelectron spectroscopy (XPS). Earlier, attenuated total reflectance-Fourier transform infrared (ATR-FTIR) spectroscopy was also used to study the influence of phosphate on the adsorption of As(V) on goethite and ferrihydrite.[29] Binary oxy-hydroxide such as Fe and Mn-based mixed oxy-hydroxide were used to study the competitive adsorption of arsenate and phosphate.[30] This suggests that the adsorption of arsenate (6−80 μM) on binary oxy-hydroxide decreased by approximately 7−20% in the presence of P(V) (120−300 μM). Even after considerable research, phosphate interference during arsenic adsorption is not well understood and needs a more comprehensive effort.

The present work focuses on elucidation of phosphate adsorption and its interference in the arsenic uptake on MAG and CM2LF substrates in a qualitative and quantitative manner. Experiments were conducted with different ionic forms of P and As. CM2LF is a nanoscale material that has been developed in our laboratory and is being used to supply arsenic-free water to over 1.2 million people every day. All adsorption experiments were conducted in the environmentally relevant pH range of 5−9. While XPS and IR spectroscopy were performed to obtain a detailed understanding of the surface complexation phenomenon during adsorption, all uptake experiments were quantified using ion chromatography (IC) and inductively coupled plasma-mass spectrometry (ICP-MS). Finally, DFT calculations were performed on various phosphate complexes at model surfaces, such as bidentate binuclear (^{2}C) [$>(FeO)_2(OH)PO$ or $>(FeO)_2(OH)_2P$], bidentate mononuclear (^{2}E) [$>FeO_2(OH)PO$ or $>FeO_2(OH)_2P$], monodentate mononuclear (^{1}V) [$>FeO—PO_2(OH)$ or $>FeO—PO(OH)_2$], and physically adsorbed species (T) [$>FeOH...O-PO_2(OH)$ or $>FeO...HO-PO_2(OH)$], to support the XPS results. ^{2}C, ^{2}E, and ^{1}V are referred to as inner-sphere complexes, and T is referred to as an outer-sphere complex. Also, a brief discussion is given on the sustainability aspects of both materials.

■ EXPERIMENTAL SECTION

Stock solutions of 100 mM P(V), As(III), and As(V) were prepared using KH_2PO_4, $NaAsO_2$, and $Na_2HAsO_4\cdot 7H_2O$ salts, respectively. P(III) was not examined as it is not a dominant form in the environment. A combination of P(V) and As(III) is referred to as AP_{mix1} and a mixture of P(V) and As(V) is referred to as AP_{mix2}. A 100 mM AP_{mix1} stock solution was prepared by mixing equimolar amounts of $NaAsO_2$ and

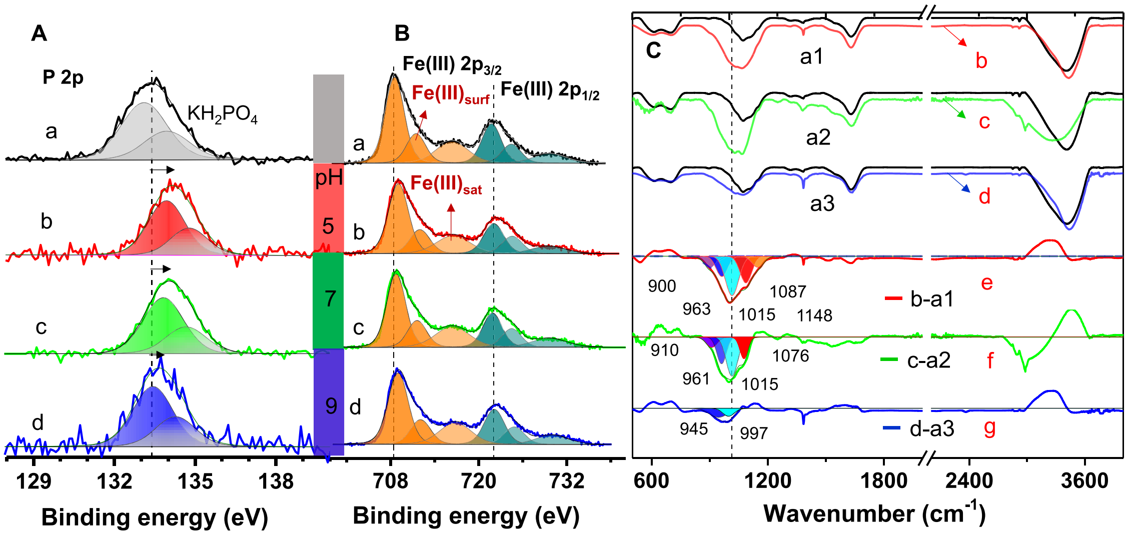

Figure 2. XPS spectra of the (A) P 2p region of (a) KH_2PO_4 solid, adsorbed phosphate on CM2LF at various pH values of (b) 5, (c) 7, and (d) 9. (B) Fe 2p region showing $2p_{3/2}$ and $2p_{1/2}$ features of (a) CM2LF before adsorption and (b−d) Fe 2p after phosphate adsorption at various pH values of 5, 7, and 9. (C) FTIR spectra of CM2LF before adsorption; it was treated with distilled water and adjusted to various pH values of (a1) 5, (a2) 7, and (a3) 9. FTIR spectra of CM2LF measured after phosphate adsorption at pH values of (b) 5, (c) 7, and (d) 9. The difference between the FTIR features before and after phosphate adsorption at various pH values of 5, 7, and 9 is represented by curves (e), (f), and (g), respectively. Various component features observed in the difference spectra are also shown.

KH_2PO_4. The mixture AP_{mix2} was made with equimolar quantities of $Na_2HAsO_4 \cdot 7H_2O$ and KH_2PO_4. The pH of the stock solutions was adjusted to 7 by adding dil. HCl or dil. NaOH whenever necessary. Further, 150 mg of CM2LF was added to 100 mL of 40 mM solutions of P(V), AP_{mix1}, and AP_{mix2}, each in 250 mL polypropylene conical flasks. The same process was followed for the MAG material. The flask was held on an orbital shaker for 24 h until an adsorption equilibrium was reached. The solution was centrifuged, and the residue (adsorbent) was washed several times with deionized water to remove the unreacted species (P or As) from the surface of the material. Thereafter, about 2−3 mg of the cleaned residue was suspended in 300 μL of distilled water for sample preparation for XPS, and similar sample preparation was carried out for IR spectroscopy. The suspension was dropcast on a 1 cm × 1 cm indium tin oxide (ITO) plate (nonconducting surface) that was kept in a vacuum desiccator for 48 h for complete drying and to prevent contamination. For a clear understanding of the kinetics of phosphate uptake and its interference in arsenic adsorption kinetics, IC and ICP-MS measurements were performed. For this, 100−150 mg of CM2LF was added to 5−20 ppm of 100 mL of P(V), AP_{mix1}, and AP_{mix2} solutions, each in a 250 mL polypropylene conical flask. The same process was followed for MAG. The solution was held on an orbital shaker, and 1 mL of the solution was collected at various time intervals of 3, 5, 10, 15, 20, 40, 60, and 90 min. The solutions were subjected to centrifugation immediately after collecting them. The material, if any, separated as residue, was discarded, the supernatant was filtered using a 0.2 μm membrane filter, and the filtrate was diluted to 5 mL using Millipore water of 18 MΩ resistance. Details of materials, instrumentation, and computational aspects are provided in the Supporting Information (SI).

■ RESULTS AND DISCUSSION

Figure 1A-a shows a transmission electron microscopy (TEM) image of CM2LF. The image suggests that the material is composed of amorphous particles, in agreement with the literature.[31] To further investigate the morphology of the CM2LF aggregates, transmission electron tomographic reconstruction was performed for CM2LF and its composites with As(III) and As(V). Accordingly, a series of two-dimensional (2D) projections were collected between ±69° with a 3° increase (see Supporting Information 2 for details). Three-dimensional (3D) reconstruction of CM2LF suggests that the material has a porous structure with random aggregation but with no well-defined packing patterns (Figures 1A-b and S1A-i,ii). Such random aggregation and porous structure are beneficial for the uptake of various species such as As(III/V) and P(V). Further, the tomographic reconstruction of As(III/V)-bound CM2LF nanoparticles shows no change in the morphological features (Figure S1B-i,ii for As(III)-adsorbed CM2LF and Figure S1C-i,ii for As(V)-adsorbed CM2LF). This suggests that the structures are intact even after As(III/V) binding. XPS and FTIR spectra of phosphate species were measured at pH 5, 7, and 9 to understand the degree of protonation and phosphate speciation at room temperature. P 2p energy levels of phosphate species are shifted to lower binding energies (134.3 > 133.8 > 133.5 eV) with increase in pH (Figure 1B). Note that the XPS spectra were measured in the dry state of materials. The materials, magnetite,[28,32,33] and two-line ferrhydrite[12,34] nanoparticles embedded into organic matter (chitosan and cellulose) are stable in the pH range of 5−9. Previous spectroscopic (XPS and Mossbauer) studies suggest that phosphate-adsorbed wet magnetite nanoparticles remain as magnetite after drying.[28,32,33] Kumar et al. studied arsenic-adsorbed CM2LF (in the dry state) using X-ray powder diffraction and electron energy-loss spectroscopy.[31] These studies demonstrated that there is no phase change in two-line ferrihydrite. These materials are converted from one phase to another, taking months or years under natural circumstances. However, the current study does not target studying dehydration,[35] surface reactivity,[36] and aggregation[36,37] of the bare two-line ferrihydrite nanoparticles. We dried the wet (after adsorption) samples at room temperature

(24−30 °C) for measurements. These experimental conditions cannot affect the chemical state of the elements (P, Fe, and As). Magnetite and CM2LF materials are stable even above 80 °C. Considering the previous reports, XPS data are valuable for identifying chemical states and for quantifying the elements, although the samples were dried prior to measurements. XPS data of each peak before and after the interaction of P(V)/AP_{mix1}/AP_{mix2} with CM2LF and MAG used in this work are shown in Supporting Information, Table S1. Deprotonation of hydroxyl groups attached to P causes an increase in the electron density (ED) on O atoms (P−OH to $P-O^-$), which results in an increase in the electron density on the P atom. This change leads to a fall in the binding energy (BE) of P 2p. These results are supported by theoretical calculations (Table S2). P(V) in solution at pH 5 has two vibrational features at 1076 and 1157 cm^{-1} (Figure 1C-a). These correspond to the symmetric stretching frequencies of −P−OH and −P = O of $H_2PO_4^{1-}$, with C_{2v} structure.[22,38] At pH 9, it shows two features at 990 and 1079 cm^{-1} (Figure 1C-c) corresponding to the bending of $-PO_2$ and the symmetric stretching of −P−OH groups of HPO_4^{2-}, with C_{3v} structure.[22,38] However, at pH 7, P(V) shows three characteristic peaks at 1155 and 1078 and 991 cm^{-1} (Figure 1C-b) due to $H_2PO_4^{1-}$ and HPO_4^{2-}, respectively.

Adsorption on CM2LF. The XPS analysis of phosphate standard in the solid form (KH_2PO_4) is shown in Figure 2A-a. The P 2p peak appears at 133.4 eV. The P 2p peak was deconvoluted into $2p_{3/2}$ and $2p_{1/2}$. The P 2p peak was shifted from 133.4 (KH_2PO_4) to 134.2, 134.1, and 133.9 eV upon its adsorption on CM2LF at pH values 5, 7, and 9, respectively. Throughout this paper, a blue shift indicates that the selected peak shifted to higher binding energy from a reference peak, and a red shift indicates the opposite. A large blue shift was observed at pH values 5 (0.8 eV) and 7 (0.7 eV) (Figure 2A-b,c). This suggests that P(V) forms more stable inner-sphere complexes (^2C) at pH values 5 and 7. On the other hand, a small blue shift was observed for pH 9 (Figure 2A-d), indicating that there is some amount of outer-sphere complexes (T) along with inner-sphere complexes. In contrast, P(V) may form more number of less stable inner-sphere complexes (^2E and ^1V). However, there is more chance of forming outer-sphere complexes at pH 9 due to the increase of the $Fe-O^-$ groups. A minor change observed in the position of the P 2p peak while comparing with pH values 5 and 7 arises due to the variation in the extent of protonation of surface complexes. Figure 2B-a shows Fe 2p fitted with three pairs of peaks of CM2LF.[39] The lowest binding energy corresponds to −Fe−O−Fe− groups, the next refers to the surface >Fe−OH groups (Fe(III)surf), followed by a satellite peak (Fe(III)sat). A significant blue shift was observed in Fe 2p due to adsorption of P(V) at various pH values, as shown in Supporting Information, Table S1. The shifted peaks did not match with Fe 2p of Fe(II) and Fe(IV) ions. Thus, the Fe 2p data suggest that there was no reduction or oxidation of iron (Fe(III)) upon P(V) uptake (Figure 2B). The observed blue shift in Fe 2p is due to the formation of inner-sphere complexes (−Fe−O−P−), which are discussed in Figure 7. FTIR spectroscopic studies were used to identify the inner-sphere complexes of P(V) with CM2LF. At first, we studied the pH influence on CM2LF in the range of 4−9 using FTIR spectroscopy. The results suggest that CM2LF functional groups are not affected by varying pH (Supporting Information, Figure S2). The IR spectrum at pH 5 (Figure 2C-e) was fitted with five peaks: 900, 963, 1015, 1087, and 1148 cm^{-1}. The 1015 cm^{-1} was assigned to −Fe−O−P−, 1148 cm^{-1} to P═O stretching, 1087 cm^{-1} to the PO_2 group, while 900 and 963 cm^{-1} corresponded to P−OH symmetric bending vibrations. These features refer to bidentate binuclear (^2C) species [$>(FeO)_2(OH)PO$ or $>(FeO)_2(OH)_2P$].[22,38,40] These features also correspond to C_1 symmetry complexes. In previous reports, at pH 4.5, the formation of less stable inner-sphere complexes (^2E and ^1V) were observed[41] when P(V) loadings were increased from 1.25 to 10 $\mu mol/m^2$ ($\mu mol/m^2 \approx$ ppb), i.e., a higher P(V) loading increases the chance of formation of less stable complexes (^2E and ^1V). Here, the P(V) loadings used were higher than 10 $\mu mol/m^2$. Thus, there may be some amount of ^2E and ^1V complexes. The spectrum observed at pH 7 (Figure 2C-f) shows four features at 910, 961, 1015, and 1076 cm^{-1} that refer to bidentate binuclear species [$>(FeO)_2(OH)PO$].[22,34] The pH 9 spectrum (Figure 2C-g) shows only two features at 945 and 997 cm^{-1}. These features are similar to 961 and 1015 cm^{-1} features (at pH 5) with a shift (16 cm^{-1}) that may correspond to deprotonated bidentate binuclear species [$>(FeO)_2PO_2$]. However, from these data, it is difficult to understand the exact surface complexes. XPS data confirm that the CM2LF surface is covered with more outer-sphere complexes than inner-sphere complexes at pH 9 (Figure 2A-d).

Adsorption on MAG. In the case of MAG, Fe $2p_{3/2}$ was deconvoluted into four peaks that corresponded to Fe(II), Fe(III), and two separate shake-up peaks for Fe(II) (Fe(II)sat) and Fe(III) (Fe(III)sat).[39,42] Similarly, deconvolution was performed for Fe $2p_{1/2}$. The Fe $2p_{3/2}$ (for Fe(II) and Fe(III)) feature of MAG appears at 707.9 eV before phosphate adsorption (Figure 3B-a), and after adsorption, it is blue-shifted by 0.6 and 0.4 eV at pH values 5 and 7, respectively, and no shift was observed in the case of pH 9 (Figure 3B-d). The shifts are shown in Supporting Information, Table S1. Upon P(V) interaction with MAG at various pH values, a considerable change was observed in P 2p. The P 2p was shifted from 133.4 (KH_2PO_4) to 134.5, 134.0, and 132.8 eV at pH values 5, 7, and 9, respectively, when P(V) interacted with

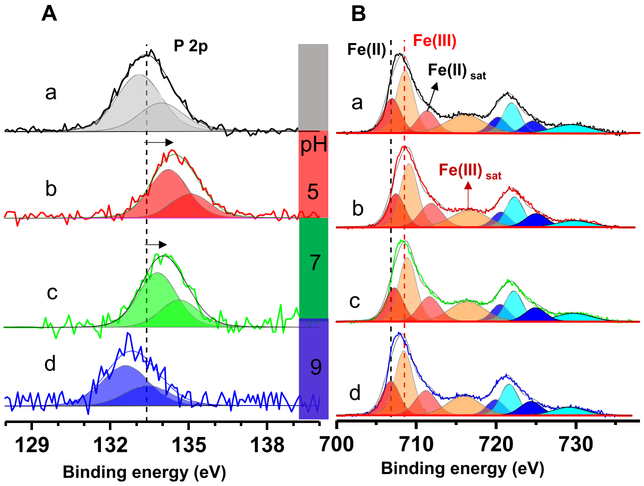

Figure 3. XPS spectra of the (A) P 2p region of (a) KH_2PO_4 solid, adsorbed phosphate on MAG at various pH values of (b) 5, (c) 7, and (d) 9. (B) Fe 2p region showing $2p_{3/2}$ and $2p_{1/2}$ features of MAG (a) before and (b−d) after adsorption at pH values of 5, 7, and 9, respectively.

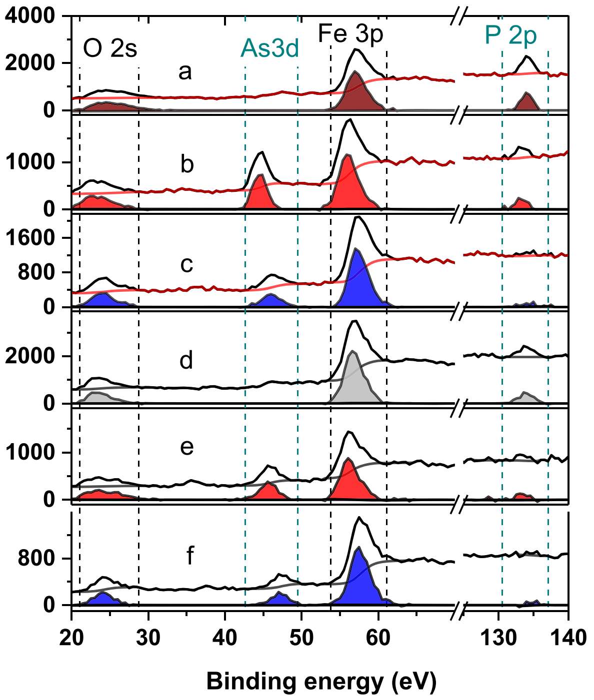

Atomic percentage(%)

sample	O	Fe	P	As
a: CM2LF+P(V)	55.9	13.5	3.6	---
b: CM2LF+ P(V)+As(III)	54.6	14.9	1.9	4.4
c: CM2LF+ P(V)+As(V)	52.9	14.6	1.2	4.8
d: MAG+P(V)	58.5	20.1	2.9	--
e: MAG+ P(V)+As(III)	56.3	20.0	1.1	2.7
f: MAG+ P(V)+As(V)	58.5	21.6	0.5	2.5

Figure 4. XPS spectra of CM2LF treated with (a) P(V), (b) AP_{mix1}, and (c) AP_{mix2} and MAG treated with (d) P(V), (e) AP_{mix1}, and (f) AP_{mix2}. The spectra show the regions corresponding to O 2s (20−28 eV), As 3d (40−50 eV), Fe 3p (52−60 eV), and P 2p (130−136 eV). The atomic compositions of O, As, Fe, and P in the materials were calculated after adsorption from the corresponding XPS spectrum; the values are presented in the table on the right-hand side.

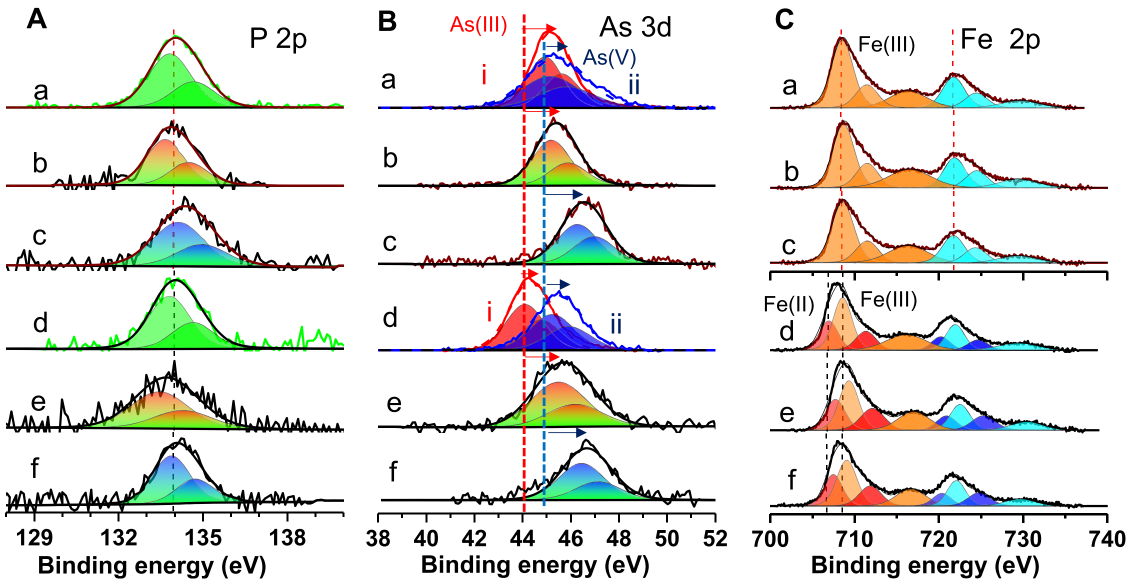

Figure 5. XPS spectra of (A) P 2p, (B) As 3d, and (C) Fe 2p. In the (A) P 2p region, CM2LF treated with (a) P(V), (b) AP_{mix1}, and (c) AP_{mix2} and MAG treated with (d) P(V), (e) AP_{mix1}, and (f) AP_{mix2}, respectively, are presented. In the As 3d region (B), the red and blue traces correspond to $NaAsO_2$ and $Na_2HAsO_4 \cdot 7H_2O$. Only As(III)-adsorbed materials are (a-i) CM2LF and (d-i) MAG and, on the other hand, As(V)-adsorbed materials are (a-ii) CM2LF and (d-ii) MAG. Traces (b) and (c), (e), and (f) are after adsorption of ions while using mixed solutions (AP_{mix1} and AP_{mix2}) as indicated above. In the (C) Fe 2p region, (a) CM2LF and (d) MAG are before adsorption and the remaining (b and c, e, and f) are after adsorption of ions while using mixed solutions, as above.

MAG (Figure 3A). The P 2p is more blue-shifted at pH 5 and less at pH 7 (Figure 3A-b,c). These results are similar to those of CM2LF, which suggest that phosphate forms monoprotonated bidentate binuclear (^{2}C) species at pH values 5 and 7.[28] According to the literature, the P 2p binding energy for adsorbed phosphate on magnetite is 133.6 eV when the P(V) uptake is in the range of 2−5 mg/g.[28] Previous FTIR and Mossbauer spectroscopic studies reflected that phosphate is attached to Fe(III) at the octahedral sites as monoprotonated bidentate binuclear complexes.[28] At pH 9, P 2p of the adsorbed phosphate shows a shift toward lower binding energy as compared to the KH_2PO_4 (Figure 3A-a,d). No shift was observed in the Fe $2p_{3/2}$ peak upon P(V) uptake as discussed before. The results at pH 9 suggest that most of the species are

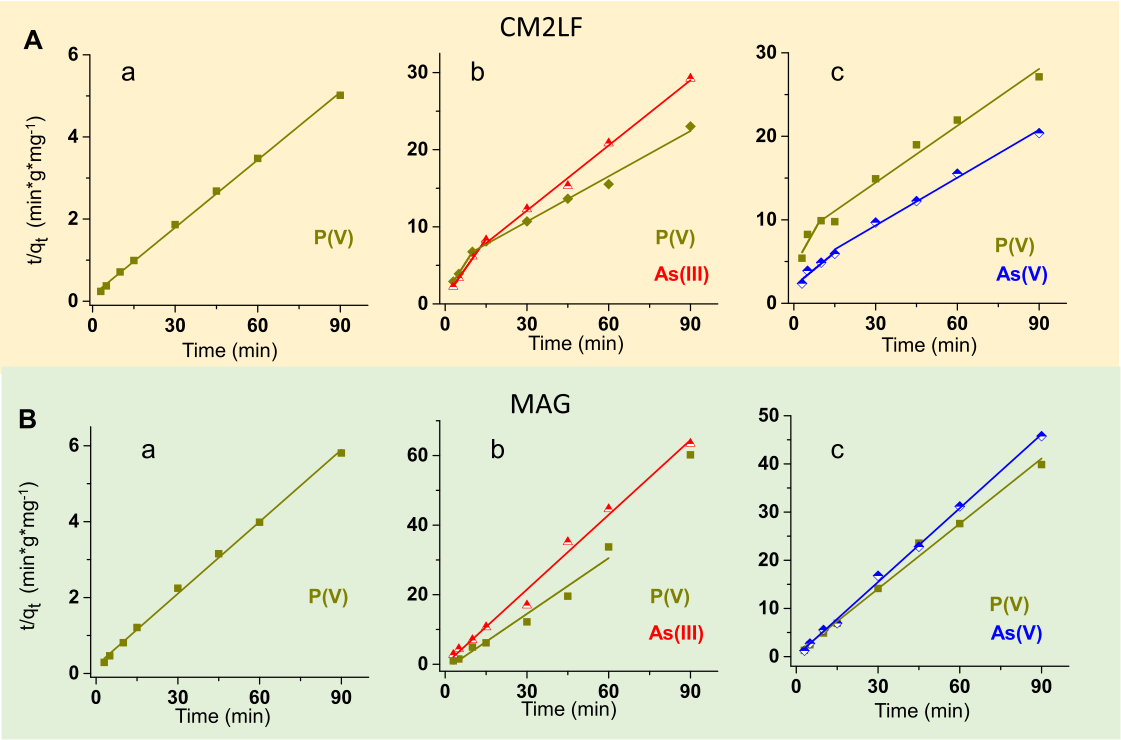

Figure 6. Pseudo-second-order kinetics plot for adsorption of (a), (b), and (c) indicating phosphate, AP_{mix1}, and AP_{mix2}, respectively, on (A) CM2LF and (B) MAG. The q_t of each data point was evaluated using the linear form of the pseudo-second-order equation where the unit of q_t is mg/g. In the case of CM2LF treated with AP_{mix1} and AP_{mix2}, the adsorption kinetics data showed two slopes from 0 to 10 and 15 to 90 min indicating varying rates of adsorption.

adsorbed through hydrogen bonding (outer-sphere complexes or physically bonded species). The physically bonded (T) species have lower P 2p binding energy compared to inner-sphere complexes. The binding energy of P 2p of various phosphate complexes (^{2}C, ^{2}E, ^{1}V, and T) was calculated from theoretical studies (see Figure 7).

The atomic percentage (Figure 4) shows the interference of P(V) in the adsorption of arsenic (As(III/V)) while each had a concentration of 20 mM. The P(V) uptake is higher for CM2LF (3.6%) than for magnetite (2.9%) (Figure 4a,d, respectively). In the case of mixtures (AP_{mix1} and AP_{mix2}), CM2LF (Figure 4b,c) shows better As(III/V) uptake capacity than magnetite (Figure 4e,f). This can be attributed to a lower number of adsorption sites (Fe−OH$_2^+$, Fe−OH) available in magnetite than CM2LF. The porous structure of CM2LF provides additional adsorption sites, as shown in Figure 1A-b. At pH 7, in the case of AP_{mix1}, the component As(III) and in the case of AP_{mix2}, the component As(V) were more adsorbed on CM2LF/MAG than P(V) (Figure 4b,c,e,f). The complexation of phosphate in the presence of As(III/V) was further evaluated by studying the energy levels of P 2p, As 3d, and Fe 2p (Figure 5).

In the case of CM2LF, there is no considerable shift observed in the P 2p peak between P(V) and AP_{mix1} (P(V) = 134.0, AP_{mix1} = 134.1 eV (Figure 5A-a,b)), and while looking at the corresponding As 3d region for AP_{mix1}, which showed a peak at 45.4 eV (Figure 5B-b), this is slightly blue-shifted from the As(III)-treated sample (45.1 eV (Figure 5B-a(i))). This blue shift indicates that the ratio of inner-sphere and outer-sphere complexes of As(III) is more in the case of AP_{mix1} than As(III) alone. The corresponding IR spectrum (Supporting Information, Figure S3d) shows features at 790, 830, 886, 970, 1010, and 1075 cm^{-1}, where the features at 790 cm^{-1} belong to the As−OH stretching, 830 cm^{-1} due to Fe−O−As bonds, 1075 cm^{-1} due to the PO$_2$ group, 970 cm^{-1} due to P−OH, and 1010 cm^{-1} to −Fe−O−P. IR data suggest that P(V) and As(III/V) are chemisorbed when they are co-adsorbed. Hence, XPS data suggest P(V) interference in As(III) complexation.

A slight red shift was observed in the P 2p peak in the case of AP_{mix1} adsorption (AP_{mix1} = 133.7 eV, Figure 5A-e) as compared to P(V) adsorption (P(V) = 134.1 eV, Figure 5A-d) on the MAG surface. This shift refers to physically adsorbed species. Thus, there are some amount of physically adsorbed phosphate species on the surface of MAG along with the chemically adsorbed species at pH 7. The AP_{mix1}-treated MAG shows the As 3d peak at 45.7 eV, and it is more blue-shifted as compared to As(III) alone (44.3 eV) (Figure 5B-d(i),e). The observed shift is high (1.4 eV), which suggests that there is a greater fraction of chemically adsorbed species in the case of AP_{mix1} compared to As(III) alone (in overall surface complexes). Thus, there is a positive effect on As(III) complexation in the presence of P(V), but vice versa is not true.

While comparing AP_{mix2}-treated CM2LF and P(V)-treated CM2LF, there is a noticeable shift (0.3 eV) observed in P 2p; the P 2p peaks are at 134.4 and 134.1 eV, respectively (Figure 5A-a,c). This may be due to the increased ratio of the inner- and outer-sphere complexes or a plausible conversion of less stable inner-sphere complexes (^{1}V) to more stable inner-sphere complexes (^{2}C) of P(V) in the presence of As(V). For the As 3d region of AP_{mix2}- (Figure 5B-c) and As(V) (Figure 5B-a(ii))-treated CM2LF, the peaks are at 46.5 and 45.3 eV, respectively. The shift between them is 1.2 eV, which suggests increased chemisorption of As(V) in the presence of P(V) than

Table 1. Adsorption Data in Terms of Initial Rates, Rate Constants, and Uptake of As at Equilibrium

adsorbate 100 mL	adsorbent (mg)	species pH 7	q_e (mg/g) ± 1%	k (min(mg/g))$^{-1}$ ± 2%	initial rate $h = kq_e^2$ ± 5%	R^2
20 ppm P(V)	CM2LF: 100	$H_xPO_4^{y-}$	18.26	0.02	6.67	0.99
	MAG: 100	$H_xPO_4^{y-}$	15.83	0.02	5.01	0.99
5 ppm P(V)+	CM2LF: 100	$H_xPO_4^{y-}$	3.39 (avg)	0.13 (avg)	1.49 (avg)	0.99
		H_3AsO_3	2.67 (avg)	0.29 (avg)	2.07 (avg)	0.99
5 ppm As(III)	MAG: 100	$H_xPO_4^{y-}$	3.30	0.51	5.55	0.96
		H_3AsO_3	2.28	0.28	1.45	0.99
5 ppm P(V)+	CM2LF: 100	$H_xPO_4^{y-}$	3.06 (avg)	0.04 (avg)	0.37 (avg)	0.74
		$H_xAsO_4^{y-}$	4.16 (avg)	0.05 (avg)	0.87 (avg)	0.99
5 ppm As(V)	MAG: 100	$H_xPO_4^{y-}$	2.30	1.64	8.67	0.99
		$H_xAsO_4^{y-}$	2.40	1.89	10.89	0.99

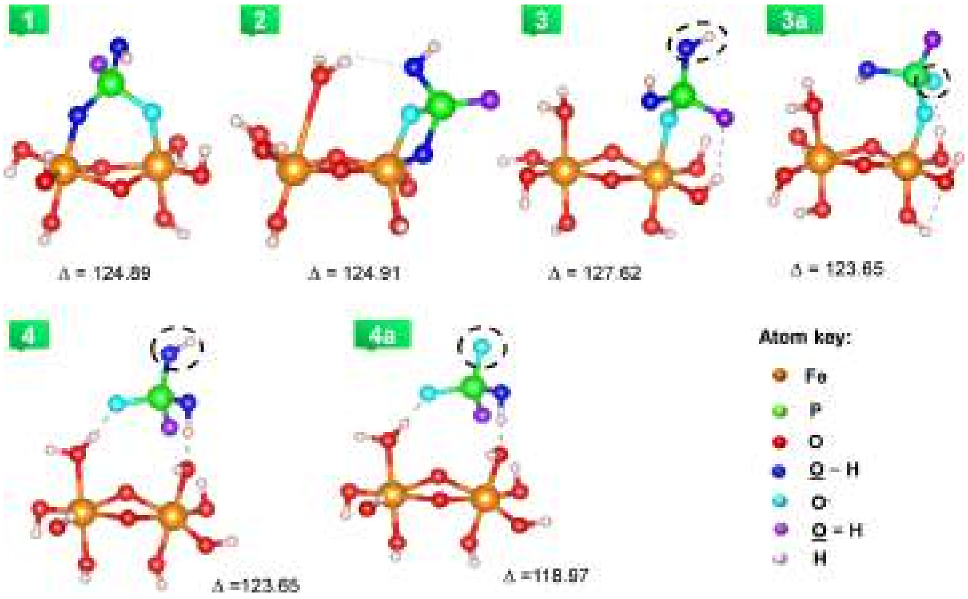

Figure 7. Various phosphate complexes with a small ferrihydrite cluster: (1) bidentate binuclear complex (^{2}C), (2) bidentate mononuclear complex (^{2}E), (3) monodentate mononuclear complex (^{1}V), (3a) deprotonated monodentate mononuclear complex (^{1}V-H), (4) outer-sphere complex (T), and (4a) deprotonated outer-sphere complex (T-H). Here, theoretical binding energies ($\Delta = T_{BE2}$) of P 2p in phosphate complexes are reported in eV.

As(V) alone. The corresponding IR spectrum (Supporting Information, Figure S3e) shows two features at 820 and 871 cm^{-1}; 820 cm^{-1} is assigned to the Fe−As−O−bond stretching and 871 cm^{-1} is due to As═O; these features correspond to stable inner-sphere complexes (^{2}C).

However, in the case of AP$_{mix2}$-treated MAG, no shift was observed in P 2p as compared to AP$_{mix2}$-treated MAG and P(V)-treated MAG at pH 7 (AP$_{mix2}$ = 134.1 eV, P(V) = 134.1 eV (Figure 5A-d,f)). As(V) shows a 3d peak at 46.6 eV (Figure 5B-f). The results are the same as in the case of CM2LF. Hence, similar complexes (^{2}C or ^{3}C (tridentate trinuclear complex)) can be expected here. These results suggest that the ratio of inner- and outer-sphere complexation of As(III/V) increases in the presence of P(V). On the other hand, these results may be obtained due to strong hydrogen bonding with the surrounding ferric hydroxyl groups (−Fe−OH) or arsenic hydroxyl groups (−As−OH). The consolidated results are presented in Table S3 in the Supporting Information.

The adsorption kinetics of oxyanions like P(V) with iron oxides/oxy-hydroxides was reported to follow pseudo-second-order kinetics that correlates with our experimental data as well (Figure 6A-a,B-a).[43−45] Initially, phosphate adsorption with CM2LF and MAG occurs rapidly, but 5 min onward, it becomes slower (Supporting Information, Figures S4A-a and S5A-a). In our earlier studies,[46] Raman spectroscopy measurements suggested pseudo-second-order kinetics for the adsorption of As(III/V) on CM2LF and MAG (Supporting Information, Figure S8). However, in the case of AP$_{mix1}$, P(V) and As(III) ions were competitive up to the initial 15 min for CM2LF (Supporting Information, Figure S4B-b), but at a later stage, As(III) reached an equilibrium state earlier than P(V), both following the pseudo-second-order kinetics with two slopes and variable adsorption rates (Figure 6A-b). In the case of AP$_{mix2}$, As(V) clearly showed a faster rate than P(V) on the CM2LF surface (Supporting Information, Figure S4B-c), showing similar kinetics behavior as the former (Figure 6A-c). These results confirm the interference (or competition) between P(V) and As(III/V) species during adsorption on CM2LF.

In the case of magnetite, while P(V) adsorption was faster than As(III) initially (Supporting Information, Figure S5B-b), and after 10 min, desorption of P(V) was observed for AP$_{mix1}$. However, in the case of AP$_{mix2}$, both P(V) and As(V) showed comparable rates of adsorption throughout with higher As(V) uptake (Supporting Information, Figure S5B-c). Thus, As(III/V) shows different adsorption kinetics for CM2LF and

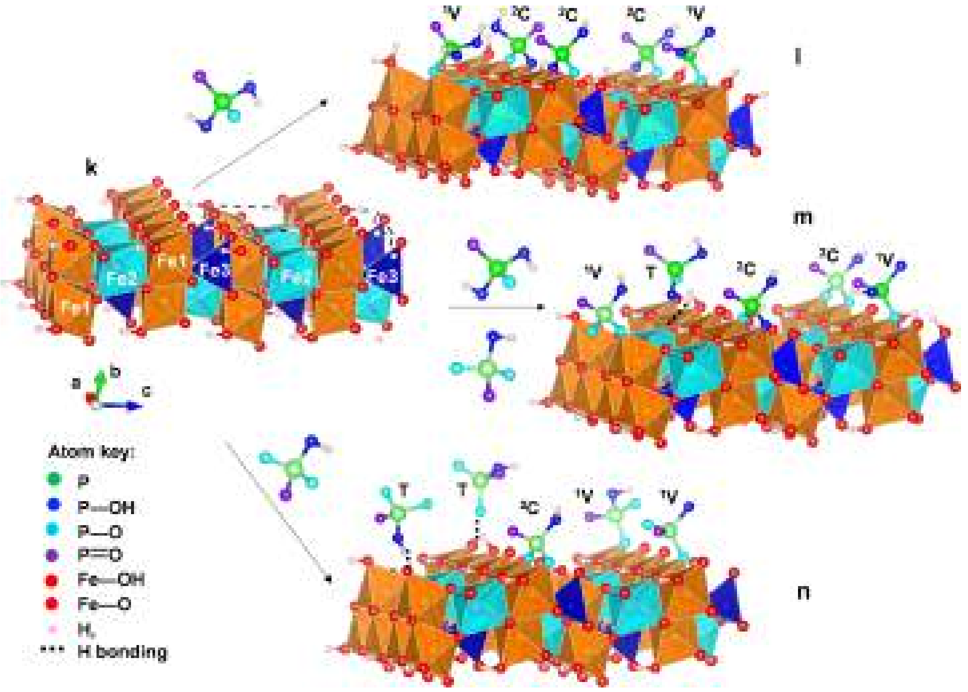

Figure 8. Schematic of a (010) plane of ferrihydrite (*k*) before adsorption, (l), (m), and (n) after phosphate adsorption at pH values of 5, 7, and 9, respectively.

magnetite. Kinetics data are given in Table 1. These results are presented as a schematic diagram (Supporting Information, Figure S7).

To understand the mechanism of adsorption of various phosphate species on CM2LF, theoretical studies were performed as discussed in the Supporting Information. In Figure 7, to find the theoretical binding energy (T_{BE}) of P 2p in various complexes, equation $T_{BE2} = -E + R = \Delta$ was used,[47] where E is the orbital energy, R is the relaxation energy, and Δ is computed using the ΔSCF method. Based on Δ, the binding energy of P 2p for the complexes given above follows the order ^{1}V > ^{2}E > ^{2}C > ^{1}V-H > T > T-H (Figure 7; Supporting Information, Table S2). Theoretical calculations of binding energy have been extended to As(III/V) complexes. Based on K, the binding energy of As 3d for the As(III) complexes follows the order ^{2}C > ^{1}V > ^{2}E > T (Supporting Information, Figure S6). In the case of As(V) complexes, it follows the order ^{2}E > ^{2}C > ^{1}V > T (Supporting Information, Figure S6). The binding energies of As 3d for As(V) complexes are higher than those of As(III) complexes.

To show phosphate adsorption on two-line ferrihydrite schematically at various pH values 5, 7, and 9, we used the unit cell parameters of two-line ferrihydrite as reported in Michel et al.[48,49] A rectangular slab was made with four unit cells and surfaces parallel to the (010) plane of FeOOH (Figure 8). In general, the ferrihydrite structure has three symmetry-distinct Fe atoms. Here, we represented them as octahedral Fe1 center (orange), octahedral Fe2 center (sky blue), and tetrahedral Fe3 center (blue) as reported by Pinney et al.[49] The CM2LF $-O^-/-OH$ groups are shown in red, while phosphorous-attached $-O^-$, $-OH$, and $=O$ groups are marked in sky blue, blue, and indigo, respectively. XPS and FTIR spectroscopy results suggest that phosphate species bind the surface Fe atoms through a ligand-exchange mechanism, at pH values 5 and 7. The results are supported by the literature.[28,50,51] In the ligand-exchange mechanism, $-P-\underline{(O^-/OH^-)}$ groups replace the $Fe-\underline{(O^-/-OH^-)}$ groups. Moreover, the formation of possible stable complexes of phosphate with two-line ferrihydrite is shown in Figure 8. Herein, P(V) forms ^{2}C (major) and ^{1}V (minor) complexes at pH 5 and 7 due to the presence of more labile groups $Fe-\underline{(OH/OH_2^+)}$; on the other hand, at pH 9, P(V) forms T (major), ^{2}C(minor), and (^{1}V) (minor) complexes as a result of an increase of less labile groups $Fe-\underline{O}^-$.

Sustainability Aspects of CM2LF and Magnetite Materials. To study the sustainability of CM2LF and magnetite systems, the following factors can be considered: (1) green synthesis, (2) material efficiency, (3) material stability, and (4) cost of production. Upon carefully observing these factors for both the materials, CM2LF was found to be a greener option than magnetite, owing to its ease and waterborne synthesis, higher arsenic uptake capacity, mechanical robustness, and cost-effective production process. Each aspect is discussed in quantitative detail in the SI.

■ CONCLUSIONS

Of the phosphate ions, $H_2PO_4^{1-}$ is dominant at pH 5 and HPO_4^{2-} is dominant at pH 9. Both species exist in water at pH 7 as confirmed by ATR-FTIR studies. The P 2p binding energy of adsorbed phosphate decreased gradually on CM2LF and MAG surfaces upon increasing pH from 5 to 9. The changes in P 2p energy levels suggest that surface complexes vary with changes in pH. The XPS and IR studies suggested that phosphate complexation with iron oxides/oxy-hydroxides was driven by the ligand-exchange mechanism, leading to the formation of Fe−O−P bonds at pH 5−7. The adsorbed materials showed P 2p binding energy in the order AP_{mix2} > AP_{mix1} > phosphate-only samples. Time-dependent ion chromatography measurements allowed us to understand the adsorption kinetics of As(III)/As(V) on CM2LF and MAG in the presence of P(V) at neutral pH. The As(III)/As(V) adsorption kinetics was affected by phosphate. Phosphate desorbs from magnetite in the presence of As(III). At higher concentrations (i.e., 20 mM P(V) and 20 mM As(III/V)), XPS data suggest that phosphate uptake by iron oxides/oxy-hydroxides is affected by As(III) and As(V). These studies confirm that As(III/V) is more competitive than P(V) toward iron oxides/oxy-hydroxides. However, P(V) levels in natural water are 100−1000 times higher than that of As(III/V), and, therefore, P(V) is an obvious interfering ion during arsenic adsorption. DFT calculations suggest that P 2p and As 3d binding energies vary with the type of complexation (^{2}C, ^{2}E, ^{1}V, and T). The degree of protonation of P(V) in phosphate surface complexes affects the P 2p binding energy. The binding energies of As 3d for As(V) complexes are higher than those of As(III) complexes.

■ ASSOCIATED CONTENT

Supporting Information

The Supporting Information is available free of charge at https://pubs.acs.org/doi/10.1021/acs.jpcc.1c04317.

> Materials and instrumentation; 3D reconstructed tomographic images of the two-line ferrihydrite composite (CM2LF) before and after arsenic adsorption; IR spectra of CM2LF treated in distilled water at various pH values; IR spectra of CM2LF after arsenic adsorption in the presence of P(V); time-dependent chromatograms of the interaction of CM2LF/magnetite with P(V)/AP$_{mix1}$/AP$_{mix2}$; equations for the pseudo-second-order model; theoretical binding energy of As 3d in various As(III/V) complexes with a small ferrihydrite cluster; schematic illustration of P(V) interference in As(III/V) adsorption based on time-dependent ion chromatography and XPS studies; pseudo-second-order adsorption kinetic plots for the adsorption of As(III) and As(V) on ferrihydrite; XPS data of materials before and after treatment with P(V), AP$_{mix1}$, and AP$_{mix2}$; and sustainability aspects of CM2LF and magnetite materials (PDF)

■ AUTHOR INFORMATION

Corresponding Author

Thalappil Pradeep − *DST Unit of Nanoscience (DST UNS) and Thematic Unit of Excellence (TUE), Department of Chemistry, Indian Institute of Technology Madras, Chennai 600036, India;* orcid.org/0000-0003-3174-534X; Phone: +91-44 2257 4208; Email: pradeep@iitm.ac.in; Fax: +91-44 2257 0545/0509

Authors

Chennu Sudhakar − *DST Unit of Nanoscience (DST UNS) and Thematic Unit of Excellence (TUE), Department of Chemistry, Indian Institute of Technology Madras, Chennai 600036, India*

Sritama Mukherjee − *DST Unit of Nanoscience (DST UNS) and Thematic Unit of Excellence (TUE), Department of Chemistry, Indian Institute of Technology Madras, Chennai 600036, India*

Avula Anil Kumar − *DST Unit of Nanoscience (DST UNS) and Thematic Unit of Excellence (TUE), Department of Chemistry, Indian Institute of Technology Madras, Chennai 600036, India;* orcid.org/0000-0001-6878-8736

Ganesan Paramasivam − *DST Unit of Nanoscience (DST UNS) and Thematic Unit of Excellence (TUE), Department of Chemistry, Indian Institute of Technology Madras, Chennai 600036, India*

P. Karthigai Meena − *DST Unit of Nanoscience (DST UNS) and Thematic Unit of Excellence (TUE), Department of Chemistry, Indian Institute of Technology Madras, Chennai 600036, India*

Nonappa − *Faculty of Engineering and Natural Sciences, Tampere University, Tampere FI-33101, Finland*

Complete contact information is available at: https://pubs.acs.org/10.1021/acs.jpcc.1c04317

Notes

The authors declare no competing financial interest.

■ ACKNOWLEDGMENTS

The authors thank IIT Madras and the Department of Science and Technology, Government of India, for constantly supporting their research program on nanomaterials.

■ REFERENCES

(1) Han, C.; Geng, J.; Ren, H.; Gao, S.; Xie, X.; Wang, X. Phosphite in Sedimentary Interstitial Water of Lake Taihu, a Large Eutrophic Shallow Lake in China. *Environ. Sci. Technol.* **2013**, *47*, 5679−5685.

(2) Park, S. W.; Kim, C. W.; Lee, J. H.; Shim, G.; Kim, K. S. Comparison of Arsenic Acid with Phosphoric Acid in the Interaction with a Water Molecule and an Alkali/Alkaline-Earth Metal Cation. *J. Phys. Chem. A* **2011**, *115*, 11355−11361.

(3) Wolfe-Simon, F.; Davies, P. C. W.; Anbar, A. D. Did Nature Also Choose Arsenic? *Int. J. Astrobiol.* **2009**, *8*, 69−74.

(4) Nguyen, V. L.; Chen, W.-H.; Young, T.; Darby, J. Effect of Interferences on the Breakthrough of Arsenic: Rapid Small Scale Column Tests. *Water Res.* **2011**, *45*, 4069−4080.

(5) Neupane, G.; Donahoe, R. J.; Arai, Y. Kinetics of Competitive Adsorption/Desorption of Arsenate and Phosphate at the Ferrihydrite−Water Interface. *Chem. Geol.* **2014**, *368*, 31−38.

(6) Cagnasso, M.; Boero, V.; Franchini, M. A.; Chorover, J. Atr-Ftir Studies of Phospholipid Vesicle Interactions with A-Feooh and A-Fe2o3 Surfaces. *Colloids Surf., B* **2010**, *76*, 456−467.

(7) Waychunas, G. A.; Rea, B. A.; Fuller, C. C.; Davis, J. A. Surface Chemistry of Ferrihydrite: Part 1. Exafs Studies of the Geometry of Coprecipitated and Adsorbed Arsenate. *Geochim. Cosmochim. Acta* **1993**, *57*, 2251−2269.

(8) Hiemstra, T.; Van Riemsdijk, W. H. Surface Structural Ion Adsorption Modeling of Competitive Binding of Oxyanions by Metal (Hydr)Oxides. *J. Colloid Interface Sci.* **1999**, *210*, 182−193.

(9) Goldberg, S.; Johnston, C. T. Mechanisms of Arsenic Adsorption on Amorphous Oxides Evaluated Using Macroscopic Measurements, Vibrational Spectroscopy, and Surface Complexation Modeling. *J. Colloid Interface Sci.* **2001**, *234*, 204−216.

(10) Fukushi, K.; Sverjensky, D. A. A Predictive Model (Etlm) for Arsenate Adsorption and Surface Speciation on Oxides Consistent with Spectroscopic and Theoretical Molecular Evidence. *Geochim. Cosmochim. Acta* **2007**, *71*, 3717−3745.

(11) Neil, C. W.; Lee, B.; Jun, Y.-S. Different Arsenate and Phosphate Incorporation Effects on the Nucleation and Growth of Iron(Iii) (Hydr)Oxides on Quartz. *Environ. Sci. Technol.* **2014**, *48*, 11883−11891.

(12) Tuutijärvi, T.; Repo, E.; Vahala, R.; Sillanpää, M.; Chen, G. Effect of Competing Anions on Arsenate Adsorption onto Maghemite Nanoparticles. *Chin. J. Chem. Eng.* **2012**, *20*, 505−514.

(13) Su, C.; Puls, R. W. Arsenate and Arsenite Removal by Zerovalent Iron: Effects of Phosphate, Silicate, Carbonate, Borate, Sulfate, Chromate, Molybdate, and Nitrate, Relative to Chloride. *Environ. Sci. Technol.* **2001**, *35*, 4562−4568.

(14) Roberts, L. C.; Hug, S. J.; Ruettimann, T.; Billah, M. M.; Khan, A. W.; Rahman, M. T. Arsenic Removal with Iron(Ii) and Iron(Iii) in

Waters with High Silicate and Phosphate Concentrations. *Environ. Sci. Technol.* **2004**, *38*, 307−315.

(15) Mallet, M.; Barthélémy, K.; Ruby, C.; Renard, A.; Naille, S. Investigation of Phosphate Adsorption onto Ferrihydrite by X-Ray Photoelectron Spectroscopy. *J. Colloid Interface Sci.* **2013**, *407*, 95−101.

(16) Tofan-Lazar, J.; Al-Abadleh, H. A. Kinetic Atr-Ftir Studies on Phosphate Adsorption on Iron (Oxyhydr)Oxides in the Absence and Presence of Surface Arsenic: Molecular-Level Insights into the Ligand Exchange Mechanism. *J. Phys. Chem. A* **2012**, *116*, 10143−10149.

(17) Kwon, K. D.; Kubicki, J. D. Molecular Orbital Theory Study on Surface Complex Structures of Phosphates to Iron Hydroxides: Calculation of Vibrational Frequencies and Adsorption Energies. *Langmuir* **2004**, *20*, 9249−9254.

(18) Kim, J.; Li, W.; Philips, B. L.; Grey, C. P. Phosphate Adsorption on the Iron Oxyhydroxides Goethite (A-Feooh), Akaganeite (B-Feooh), and Lepidocrocite (Γ-Feooh): A 31p Nmr Study. *Energy Environ. Sci.* **2011**, *4*, 4298−4305.

(19) Almasri, D. A.; Saleh, N. B.; Atieh, M. A.; McKay, G.; Ahzi, S. Adsorption of Phosphate on Iron Oxide Doped Halloysite Nanotubes. *Sci. Rep.* **2019**, *9*, No. 3232.

(20) Karunanayake, A. G.; Navarathna, C. M.; Gunatilake, S. R.; Crowley, M.; Anderson, R.; Mohan, D.; Perez, F.; Pittman, C. U.; Mlsna, T. Fe3o4 Nanoparticles Dispersed on Douglas Fir Biochar for Phosphate Sorption. *ACS Appl. Nano Mater.* **2019**, *2*, 3467−3479.

(21) Wang, T.; Xu, X.; Ren, Z.; Gao, B.; Wang, H. Adsorption of Phosphate on Surface of Magnetic Reed: Characteristics, Kinetic, Isotherm, Desorption, Competitive and Mechanistic Studies. *RSC Adv.* **2016**, *6*, 5089−5099.

(22) Arai, Y.; Sparks, D. L. Atr−Ftir Spectroscopic Investigation on Phosphate Adsorption Mechanisms at the Ferrihydrite−Water Interface. *J. Colloid Interface Sci.* **2001**, *241*, 317−326.

(23) Kubicki, J. D.; Paul, K. W.; Kabalan, L.; Zhu, Q.; Mrozik, M. K.; Aryanpour, M.; Pierre-Louis, A.-M.; Strongin, D. R. Atr−Ftir and Density Functional Theory Study of the Structures, Energetics, and Vibrational Spectra of Phosphate Adsorbed onto Goethite. *Langmuir* **2012**, *28*, 14573−14587.

(24) Han, J.; Ro, H.-M. Characterizing Preferential Adsorption of Phosphate on Binary Sorbents of Goethite and Maghaemite Using in Situ Atr-Ftir and 2d Correlation Spectroscopy. *Sci. Rep.* **2019**, *9*, No. 6130.

(25) Elzinga, E. J.; Sparks, D. L. Phosphate Adsorption onto Hematite: An in Situ Atr-Ftir Investigation of the Effects of Ph and Loading Level on the Mode of Phosphate Surface Complexation. *J. Colloid Interface Sci.* **2007**, *308*, 53−70.

(26) Wang, Z.; Giammar, D. E. Mass Action Expressions for Bidentate Adsorption in Surface Complexation Modeling: Theory and Practice. *Environ. Sci. Technol.* **2013**, *47*, 3982−3996.

(27) Ta, H. T. T.; Tieu, A. K.; Zhu, H.; Yu, H.; Ta, T. D.; Wan, S.; Tran, N. V.; Le, H. M. Chemical Origin of Sodium Phosphate Interactions on Iron and Iron Oxide Surfaces by First Principle Calculations. *J. Phys. Chem. C* **2018**, *122*, 635−647.

(28) Daou, T. J.; Begin-Colin, S.; Grenèche, J. M.; Thomas, F.; Derory, A.; Bernhardt, P.; Legaré, P.; Pourroy, G. Phosphate Adsorption Properties of Magnetite-Based Nanoparticles. *Chem. Mater.* **2007**, *19*, 4494−4505.

(29) Carabante, I.; Grahn, M.; Holmgren, A.; Hedlund, J. In Situ Atr−Ftir Studies on the Competitive Adsorption of Arsenate and Phosphate on Ferrihydrite. *J. Colloid Interface Sci.* **2010**, *351*, 523−531.

(30) Zeng, H.; Fisher, B.; Giammar, D. E. Individual and Competitive Adsorption of Arsenate and Phosphate to a High-Surface-Area Iron Oxide-Based Sorbent. *Environ. Sci. Technol.* **2008**, *42*, 147−152.

(31) Kumar, A. A.; Som, A.; Longo, P.; Sudhakar, C.; Bhuin, R. G.; Gupta, S. S.; Anshup; Sankar, M. U.; Chaudhary, A.; Kumar, R.; et al. Confined Metastable 2-Line Ferrihydrite for Affordable Point-of-Use Arsenic-Free Drinking Water. *Adv. Mater.* **2017**, *29*, No. 1604260.

(32) Worden, R. H. Analytical Methods|Geochemical Analysis (Including X-ray). In *Encyclopedia of Geology*; Selley, R. C.; Cocks, L. R. M.; Plimer, I. R., Eds.; Elsevier: Oxford, 2005; pp 54−76.

(33) Hou, L.; Liang, Q.; Wang, F. Mechanisms That Control the Adsorption−Desorption Behavior of Phosphate on Magnetite Nanoparticles: The Role of Particle Size and Surface Chemistry Characteristics. *RSC Adv.* **2020**, *10*, 2378−2388.

(34) Tejedor-Tejedor, M. I.; Anderson, M. A. The Protonation of Phosphate on the Surface of Goethite as Studied by Cir-Ftir and Electrophoretic Mobility. *Langmuir* **1990**, *6*, 602−611.

(35) Sassi, M.; Rosso, K. M. Roles of Hydration and Magnetism on the Structure of Ferrihydrite from First Principles. *ACS Earth Space Chem.* **2019**, *3*, 70−78.

(36) Erbs, J. J.; Gilbert, B.; Penn, R. L. Influence of Size on Reductive Dissolution of Six-Line Ferrihydrite. *J. Phys. Chem. C* **2008**, *112*, 12127−12133.

(37) Dzombak, D. A.; Morel, F. M. *Surface Complexation Modeling: Hydrous Ferric Oxide*; John Wiley & Sons: New York, 1990.

(38) Persson, P.; Nilsson, N.; Sjöberg, S. Structure and Bonding of Orthophosphate Ions at the Iron Oxide−Aqueous Interface. *J. Colloid Interface Sci.* **1996**, *177*, 263−275.

(39) Grosvenor, A. P.; Kobe, B. A.; Biesinger, M. C.; McIntyre, N. S. Investigation of Multiplet Splitting of Fe 2p Xps Spectra and Bonding in Iron Compounds. *Surf. Interface Anal.* **2004**, *36*, 1564−1574.

(40) Wang, X.; Hu, Y.; Tang, Y.; Yang, P.; Feng, X.; Xu, W.; Zhu, M. Phosphate and Phytate Adsorption and Precipitation on Ferrihydrite Surfaces. *Environ. Sci.: Nano* **2017**, *4*, 2193−2204.

(41) Abdala, D. B.; Northrup, P. A.; Arai, Y.; Sparks, D. L. Surface Loading Effects on Orthophosphate Surface Complexation at the Goethite/Water Interface as Examined by Extended X-Ray Absorption Fine Structure (Exafs) Spectroscopy. *J. Colloid Interface Sci.* **2015**, *437*, 297−303.

(42) Beji, Z.; Sun, M.; Smiri, L. S.; Herbst, F.; Mangeney, C.; Ammar, S. Polyol Synthesis of Non-Stoichiometric Mn−Zn Ferrite Nanocrystals: Structural/Microstructural Characterization and Catalytic Application. *RSC Adv.* **2015**, *5*, 65010−65022.

(43) Chandra, V.; Park, J.; Chun, Y.; Lee, J. W.; Hwang, I.-C.; Kim, K. S. Water-Dispersible Magnetite-Reduced Graphene Oxide Composites for Arsenic Removal. *ACS Nano* **2010**, *4*, 3979−3986.

(44) Kumar, S.; Nair, R. R.; Pillai, P. B.; Gupta, S. N.; Iyengar, M. A. R.; Sood, A. K. Graphene Oxide−Mnfe2o4 Magnetic Nanohybrids for Efficient Removal of Lead and Arsenic from Water. *ACS Appl. Mater. Interfaces* **2014**, *6*, 17426−17436.

(45) Yang, J.-C.; Yin, X.-B. Cofe2o4@Mil-100(Fe) Hybrid Magnetic Nanoparticles Exhibit Fast and Selective Adsorption of Arsenic with High Adsorption Capacity. *Sci. Rep.* **2017**, *7*, No. 40955.

(46) Sudhakar, C.; Anil Kumar, A.; Bhuin, R. G.; Sen Gupta, S.; Natarajan, G.; Pradeep, T. Species-Specific Uptake of Arsenic on Confined Metastable 2-Line Ferrihydrite: A Combined Raman-X-Ray Photoelectron Spectroscopy Investigation of the Adsorption Mechanism. *ACS Sustainable Chem. Eng.* **2018**, *6*, 9990−10000.

(47) Tardio, S.; Cumpson, P. J. Practical Estimation of Xps Binding Energies Using Widely Available Quantum Chemistry Software. *Surf. Interface Anal.* **2018**, *50*, 5−12.

(48) Michel, F. M.; Ehm, L.; Antao, S. M.; Lee, P. L.; Chupas, P. J.; Liu, G.; Strongin, D. R.; Schoonen, M. A. A.; Phillips, B. L.; Parise, J. B. The Structure of Ferrihydrite, a Nanocrystalline Material. *Science* **2007**, *316*, 1726−1729.

(49) Pinney, N.; Kubicki, J. D.; Middlemiss, D. S.; Grey, C. P.; Morgan, D. Density Functional Theory Study of Ferrihydrite and Related Fe-Oxyhydroxides. *Chem. Mater.* **2009**, *21*, 5727−5742.

(50) Antelo, J.; Avena, M.; Fiol, S.; López, R.; Arce, F. Effects of Ph and Ionic Strength on the Adsorption of Phosphate and Arsenate at the Goethite−Water Interface. *J. Colloid Interface Sci.* **2005**, *285*, 476−486.

(51) Antelo, J.; Fiol, S.; Pérez, C.; Mariño, S.; Arce, F.; Gondar, D.; López, R. Analysis of Phosphate Adsorption onto Ferrihydrite Using the Cd-Music Model. *J. Colloid Interface Sci.* **2010**, *347*, 112−119.

NOTE ADDED AFTER ASAP PUBLICATION

This paper was published on September 30, 2021, with a word misspelled in the title. The corrected version was reposted on October 4, 2021.

Supporting Information

Interference of Phosphate in Adsorption of Arsenate and Arsenite over Confined Metastable Two-Line Ferrihydrite and Magnetite

Chennu Sudhakar,[†] *Sritama Mukherjee,*[†] *Avula Anil Kumar,*[†] *Ganesan Paramasivam,*[†] *P. Karthigai Meena,*[†] *Nonappa,*[‡] *and Thalappil Pradeep*[*,†]

[†] DST Unit of Nanoscience (DST UNS) and Thematic Unit of Excellence (TUE), Department of Chemistry, Indian Institute of Technology Madras, Chennai 600036, India.

[‡]Faculty of Engineering and Natural Sciences, Tampere University, FI-33101, Tampere, Finland.

* Corresponding author

Thalappil Pradeep: pradeep@iitm.ac.in

Thalappil Pradeep, DST Unit of Nanoscience (DST UNS) and Thematic Unit of Excellence (TUE), Department of Chemistry, Indian Institute of Technology Madras, Chennai 600036, India.

Tel.: +91-44 2257 4208; Fax: +91-44 2257 0545/0509

SUPPORTING INFORMATION CONTENT

Total number of pages: 20

Total number of figures: 8

Total number of tables: 3

TABLE OF CONTENTS

MATERIALS

Potassium dihydrogen ortho phosphate (KH_2PO_4), Sodium arsenite ($NaAsO_2$), and disodium hydrogen arsenate ($Na_2HAsO_4 \cdot 7H_2O$) were purchased from SD Fine Chemicals Limited. Magnetite (Fe_3O_4) was purchased from Alfa Aesar. The syntheis of confined metastable 2-line ferrihydrite (CM2LF) was reported earlier.[1] Sodium hydroxide (NaOH) was purchased from Rankem Glasswares and Chemicals Pvt. Ltd., India. Hydrochloric acid (HCl) was purchased from Merck Life Science Pvt. Ltd., India. All chemicals were of analytical grade and were used without further purification. Deionized (DI) water was used throughout the experiments.

INSTRUMENTATION

X-ray Photoelectron Spectroscopy (XPS): measurements were done using an ESCA Probe TPD spectrometer of Omicron Nanotechnology. Polychromatic Al Kα was used as the X-ray source (hν = 1486.6 eV). Binding energy was calibrated with respect to C 1s at 284.8 eV. All the XPS spectra were deconvoluted using Casa XPS software. A PerkinElmer FTIR spectrometer was used to measure the infrared spectra. The spectrometer resolution was kept at 4 cm^{-1}. All the IR spectra were deconvoluted using Origin Pro 9.0 software. Various model building software were used to build the structures. The rectangular slab was built by using VESTA and Avogadro 1.2.0 software.

Transmission Electron Microscopy (TEM): TEM images were collected using JEM 3200FSC field emission microscope (JEOL) operated at 300 kV in bright field mode with Omega-type Zero-loss energy filter. The images were acquired with GATAN DIGITAL MICROGRAPH software while the specimen temperature was maintained at -187 °C.

Sample Preparation: The TEM samples were prepared by placing 5 µL aqueous dispersion (~5 mg/ mL) 300 hexagonal mesh Ni grid with ultrathin carbon support film. The grids were plasma cleaned for 30 s before use. After placing the aqueous dispersion, the grids were subjected to cleaning by dipping them in double-distilled water for 2 x15 s. The specimen was then dried under ambient conditions for 24 h before imaging.

SerialEM and Electron Tomographic Reconstruction: The tilt series were acquired with the SerialEM-software package.[2] Samples were tilted between ±69° angles with 3° increment steps.[3] Prealignment of tilt image series was, and the fine alignment and cropping were executed with IMOD.[4] The images were binned twice to reduce noise and computation time. Maximum entropy method (MEM) reconstruction scheme was carried out with a custom-made program on Mac or Linux cluster with a regularization parameter value of λ=1.0e^{3}.[4-5]

THEORETICAL CALCULATIONS

To find binding energy (BE) of P 2p in various phosphorous complexes used equation is $T_{BE2} = -E + R = \Delta$ [Tardio *et al.*, 2018], E equals to orbital energy of ejected electron from its orbit according to Koopman theorem ($-E = T_{BE1} = K$) and R is orbital relaxation after ionization. The electron correlation function is needed to add to the given equation ($T_{BE3} = -E + R + \Delta C$) to get more accurate results. Two calculations are needed to find the binding energy of a particular atom in a molecule using ΔSCF method. The first calculation involves optimizing the geometry of the molecule(or ion) and the chance to spot and find the locations of the orbitals of concern. The second calculation (which involves finding the energy of the core ionized molecule) requires two steps while executed with GAUSSIAN 09. The first step requires the interchange of the core orbital of interest with the highest occupied molecular orbital (HOMO). The second step involves ionization of a given molecule or ion that means an electron will be taken from the exchanged core orbital (2p) which is switched from core level to HOMO. The steps followed for binding energy calculation of the core electron are explained in detail in Tardio *et al.*, 2018.

DFT CALCULATIONS ON POSSIBLE PHOSPHATE COMPLEXES WITH $Fe_2O_{10}H_Y$

To support the XPS results, as a first step, DFT calculations were performed on two phosphate species, which exist in natural waters at pH 7. To determine the P 2p binding energy of $H_2PO_4^{1-}$ / HPO_4^{2-}species theoretically, two methods were used such as Hartree Fock (HF) and B3LYP (Becke, 3-parameter, Lee–Yang–Parr) method with (or without) solvent effect. The B3LYP method with solvent effect gave the best results for $H_2PO_4^{1-}$/ HPO_4^{2-} among other methods, using a basis set of 6-31G. These results are shown in Table S2. Therefore, the B3LYP method was chosen to find the T_{BE} of P 2p in various complexes. Finally, the B3LYP method was chosen without including the solvent effect for additional calculations in order to reduce the computational cost. Further theoretical calculations of binding energy have been extended to As(III/V) complexes.

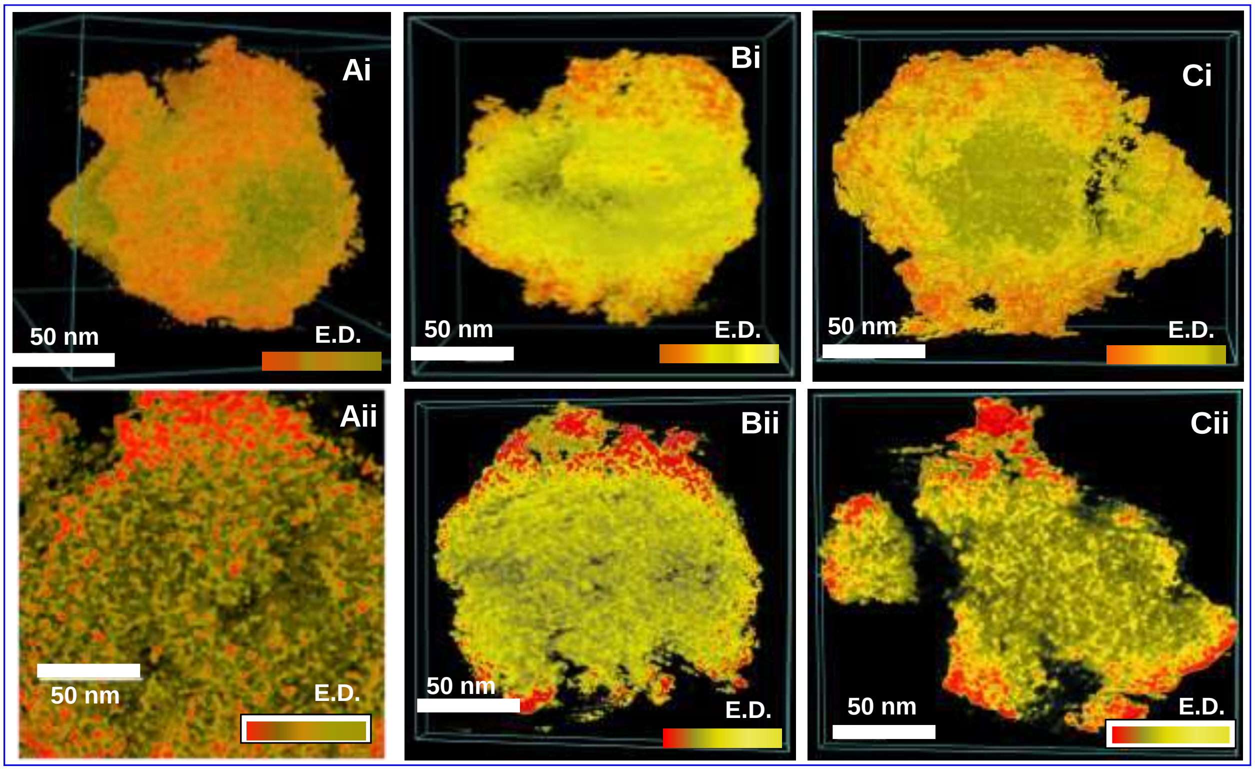

Figure S1. 3D reconstructed images of 2-line ferrihydrite composite (CM2LF) before and after arsenic treatment. Ai and Aii) CM2LF and its cross-sectional view before arsenic treatment. Bi and Bii) As (III) adsorbed CM2LF with and its cross-sectional view. Ci and Cii) As (V) adsorbed CM2LF and its cross-sectional view. E.D. refers to electron density.

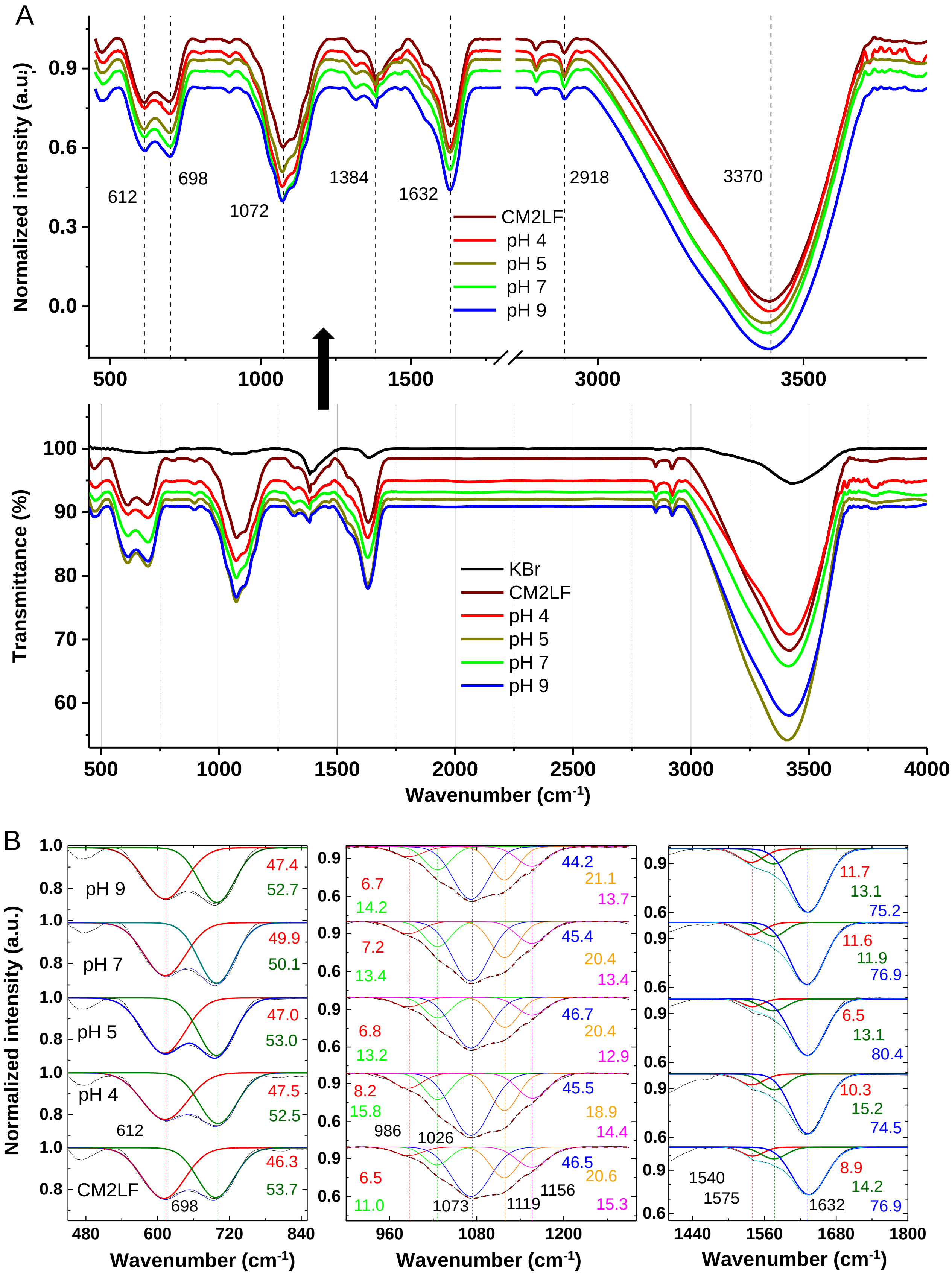
A
Normalized intensity (a.u.)
0.9
0.6
0.3
0.0
612
698
1072
1384
1632
2918
3370
CM2LF
pH 4
pH 5
pH 7
pH 9
500
1000
1500
3000
3500
Transmittance (%)
100
90
80
70
60
KBr
CM2LF
pH 4
pH 5
pH 7
pH 9
500
1000
1500
2000
2500
3000
3500
4000
Wavenumber (cm-1)
B
Normalized intensity (a.u.)
pH 9
47.4
52.7
pH 7
49.9
50.1
pH 5
47.0
53.0
pH 4
47.5
52.5
612
CM2LF
46.3
53.7
698
480
600
720
840
Wavenumber (cm-1)
6.7
14.2
44.2
21.1
13.7
7.2
13.4
45.4
20.4
13.4
6.8
13.2
46.7
20.4
12.9
8.2
15.8
45.5
18.9
14.4
986
1026
6.5
11.0
46.5
20.6
15.3
1073
1119
1156
960
1080
1200
Wavenumber (cm-1)
11.7
13.1
75.2
11.6
11.9
76.9
6.5
13.1
80.4
10.3
15.2
74.5
1540
1575
1632
8.9
14.2
76.9
1440
1560
1680
1800
Wavenumber (cm-1)

Figure S2. (A) FTIR spectra of CM2LF and CM2LF in distilled water at various pH: 4, 5, 7, and 9, also included only KBr. (B) zoomed spectra of (A) in three different regions 450 to 850, 900 to1300, and 1400 to 1800 cm^{-1}.

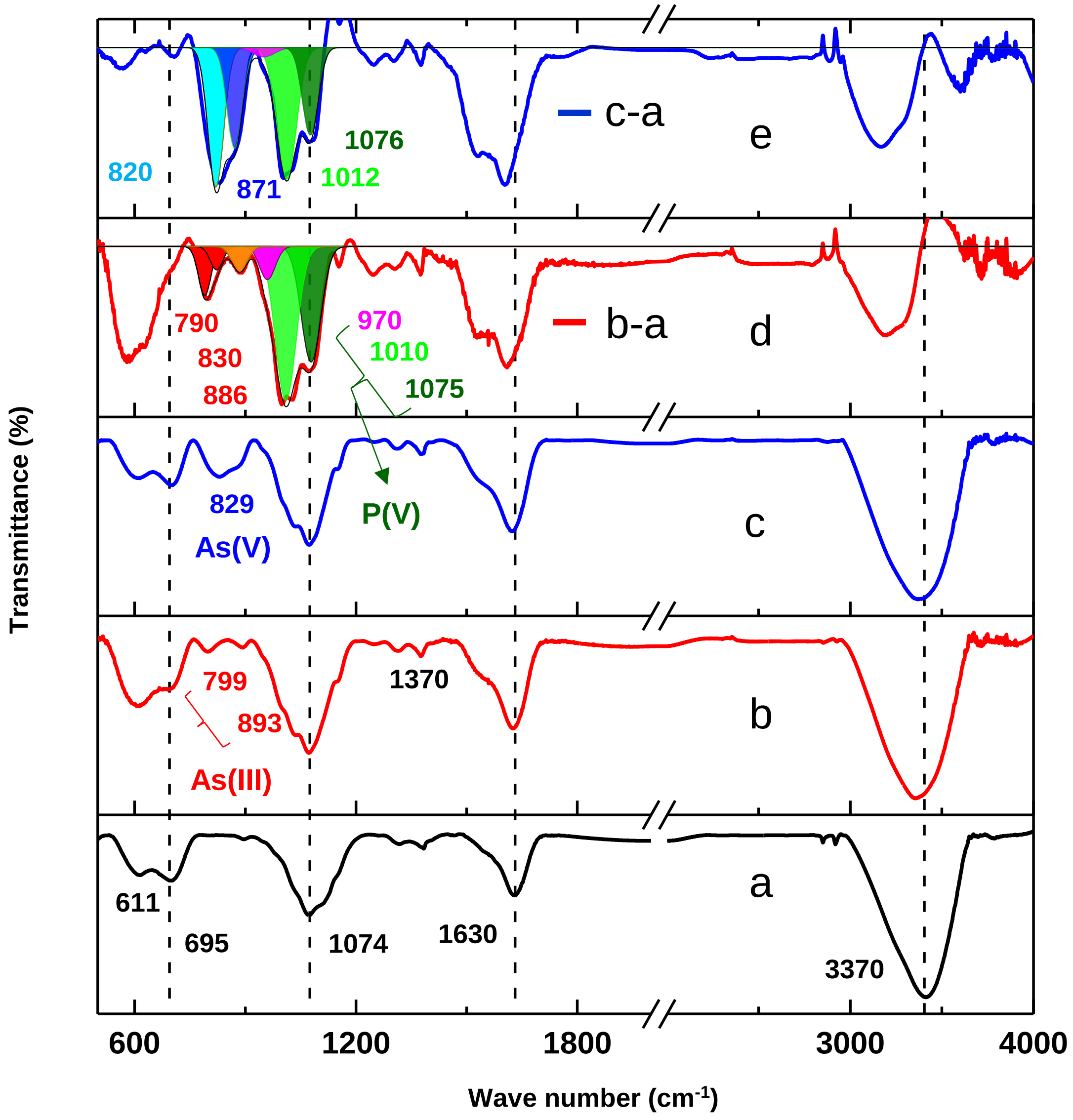

Figure S3. FTIR spectra of CM2LF (a) before adsorption, (b) AP$_{mix1}$ and (c) AP$_{mix2}$ adsorption. (d) Spectrum after subtraction (curve b-a). (e) Spectrum after subtraction (curve c-a).

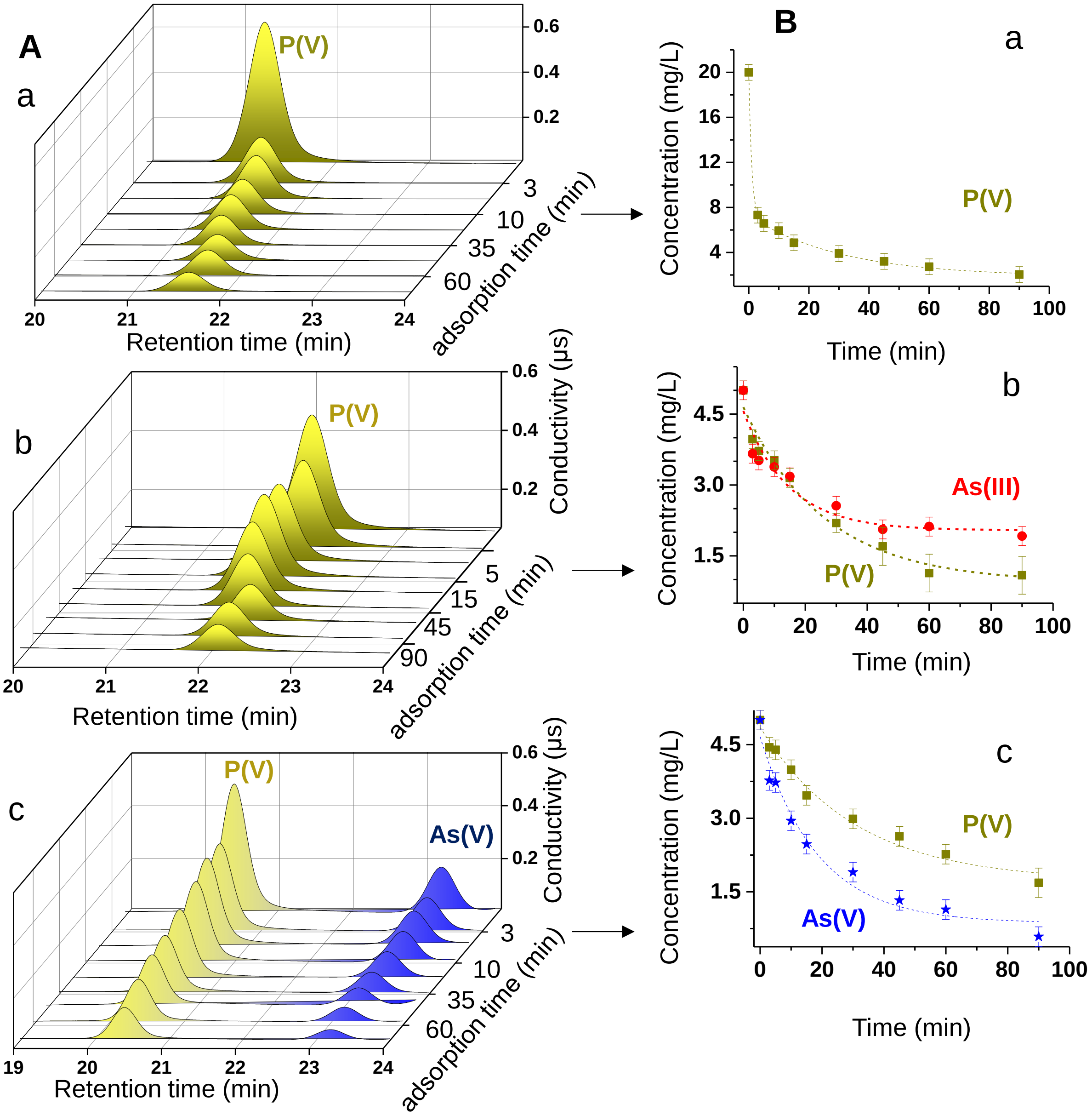

Figure S4. Time-dependent ion chromatograms showing the interaction of CM2LF with A) a) P(V), b) AP$_{mix1}$ and c) AP$_{mix2}$. Their concentration versus time plots are shown in B). For As(III) analysis ICP-MS is used.

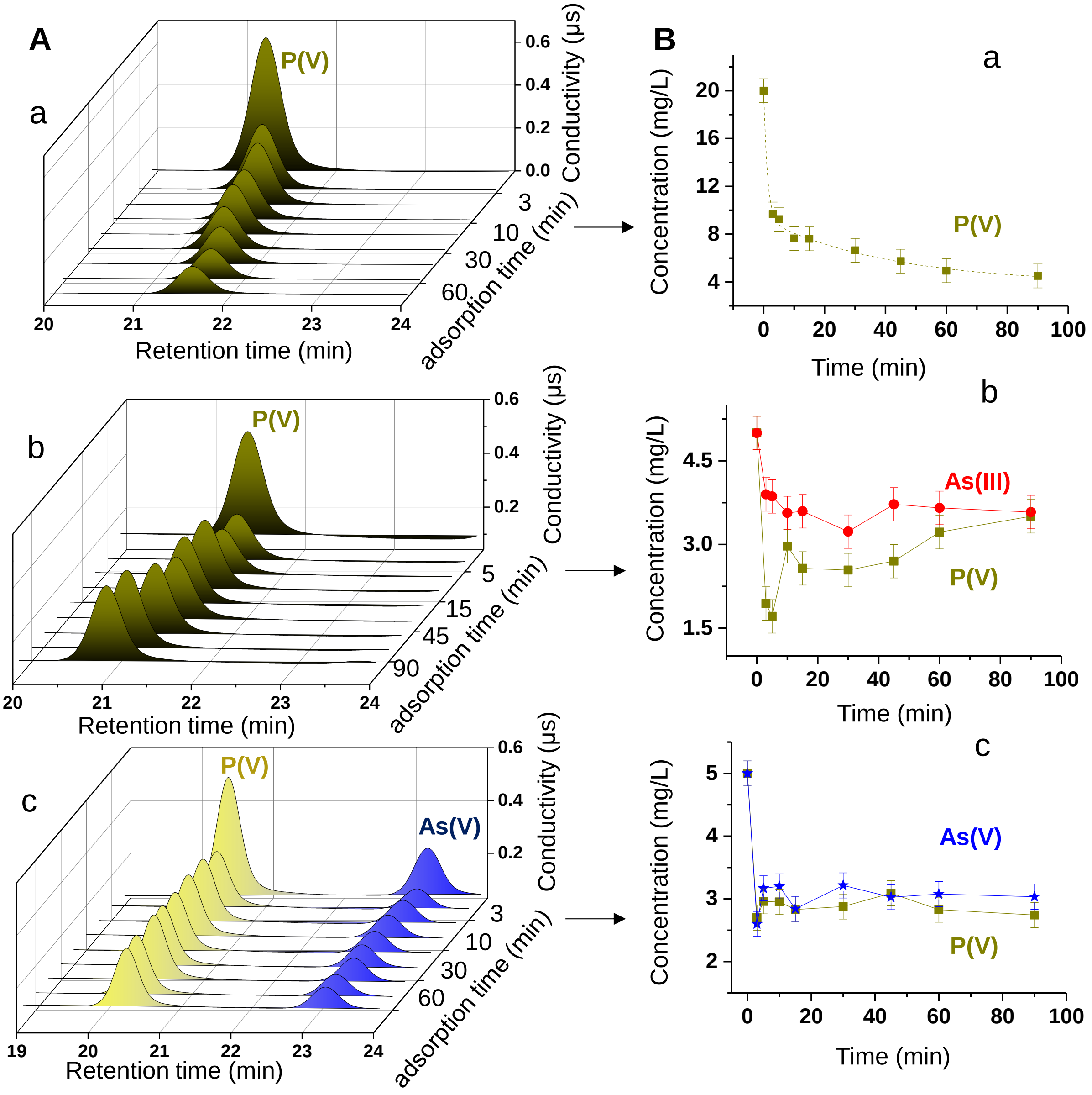

Figure S5. Time-dependent ion chromatograms showing the interaction of magnetite with A) a) P(V), b) AP_{mix1}, and c) AP_{mix2}. Their concentration versus time plots are shown in B). For As(III) analysis ICP-MS is used.

Adsorption kinetics can be expressed by using pseudo-second-order equation:

$$\frac{dq_t}{dt} = k(q_e - q_t)^2 \qquad \text{Equation (1)}$$

Where, q_t is the adsorption capacity of given material at time t, q_e is the adsorption capacity of the material at equilibrium and k is the pseudo-second-order rate constant, where initial rate is h = k${q_e}^2$. Integration of equation (1) with limits t = 0 to t and applying boundary conditions q_t = 0 at t = 0 gives,

$$\frac{t}{q_t} = (\frac{1}{q_e})t + \frac{1}{k{q_e}^2} \qquad \text{Equation (2)}$$

The values of k and q_e can be calculated by plotting t/q_t versus t.

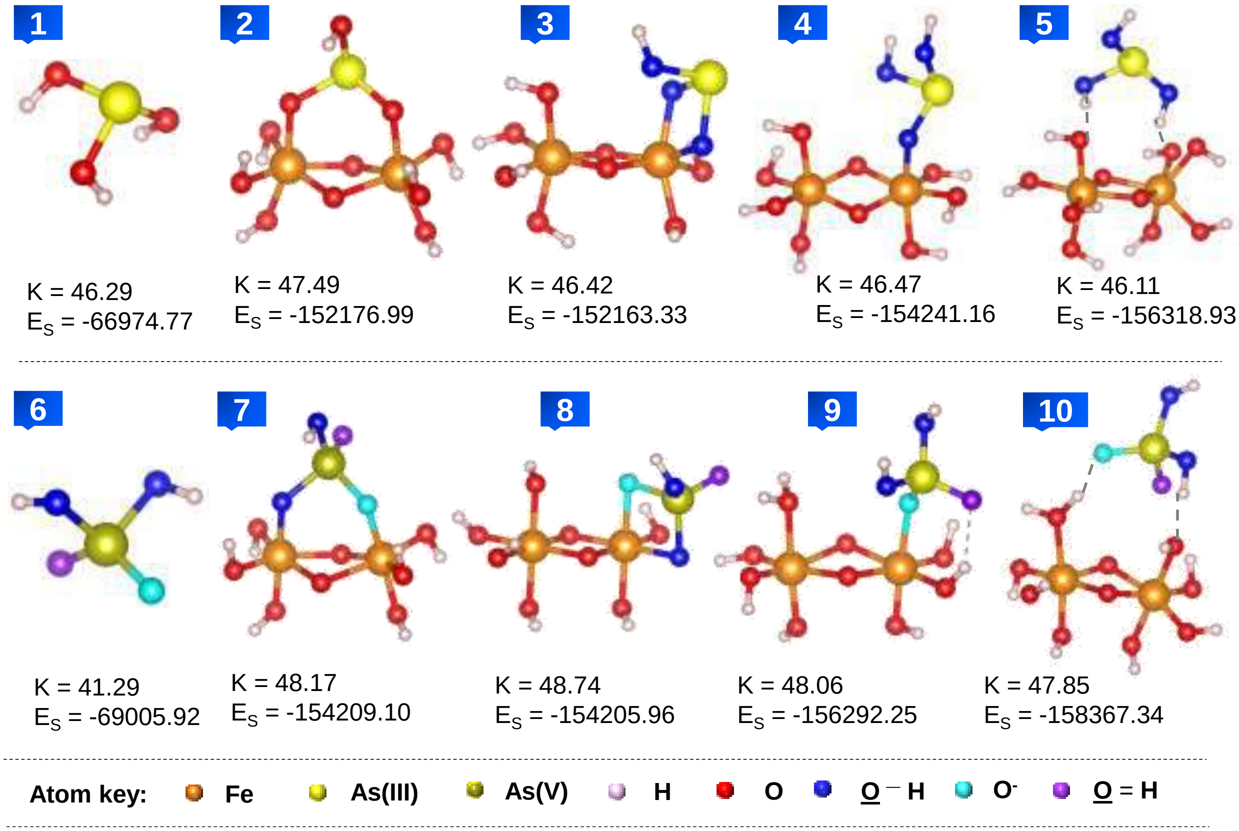

Figure S6. Theoretical binding energies (T$_{BE1}$) of As 3d in standard species 1) H$_3$AsO$_3$ and 6) H$_2$AsO$_4^{1-}$. As(III/V) species can form complex with a small ferrihydrite cluster in various ways: As(III) can bind as 2) bidentate binuclear complex (^{2}C), 3) bidentate mononuclear complex (^{2}E), 4) monodentate mononuclear complex (^{1}V) and 5) outer-sphere complex (T). Similarly, the corresponding As(V) ferrihydrite complexes are shown as 7), 8), 9) and 10). Here, theoretical binding energies (K = −E = T$_{BE1}$) of As 3d in arsenic complexes and their energies (E$_s$) are reported in eV.

Supporting Table 1

Table S1. XPS data of CM2LF and MAG before and after treated with P(V), AP$_{mix1}$, and AP$_{mix2}$.

Adsorbate	pH	Adsorbent	P 2p eV	Shift eV	As 3d eV	Shift eV	Fe $2p_{3/2}$ eV	Shift eV	Studies
		KH_2PO_4	133.4	---					current
		$NaAsO_2$			44.2				previous[6]
		$Na_2HAsO_4 \cdot 7H_2O$			44.8				
CM2LF							Fe(III): 708.5		current
CM2lF	5	P(V)	134.2	0.8			Fe(III): 708.9	0.4	
	9	P(V)	133.6	0.2			Fe(III): 709.1	0.6	
	7	P(V)	134.1	0.7			Fe(III): 708.8	0.3	
		As(III)			45.1	0.9			previous[6]
		As(III) + P(V)	134	0.5	45.4	1.2	Fe(III): 708.7	0.2	current
		As(V)			45.3	0.5			previous[6]
		As(V) + P(V)	134.4	1.0	46.5	1.7	Fe(III): 708.6	0.1	current
MAG							Main peak: 707.9 Fe(II): 706.9 Fe(III): 708.6		
MAG	5	P(V)	134.5	1.1			Main peak: 708.5 Fe(II): 707.4 Fe(III): 709.1	0.6 0.5 0.5	
	9	P(V)	132.8	-0.6			Main peak: 707.9 Fe(II): 706.8 Fe(III): 708.5	0.0 -0.1 -0.1	
	7	P(V)	134.0	0.6			Main peak: 708.3 Fe(II): 707.2 Fe(III): 708.9	0.4 0.3 0.3	
		As(III)			44.3	0.1			previous[6]
		As(III) + P(V)	133.7	0.1	45.7	1.5	Main peak: 708.5 Fe(II): 707.8 Fe(III): 709.3	0.6 0.7 0.7	current
		As(V)			45.5	0.7			previous[6]
		As(V) + P(V)	134.1	0.5	46.6	1.8	Main peak: 708.4 Fe(II):707.5 Fe(III): 709.1	0.5 0.6 0.6	current

Supporting Table 2

Table S2. DFT calculations for the P 2p binding energy of two phosphate species and each type of phosphate surface complex.

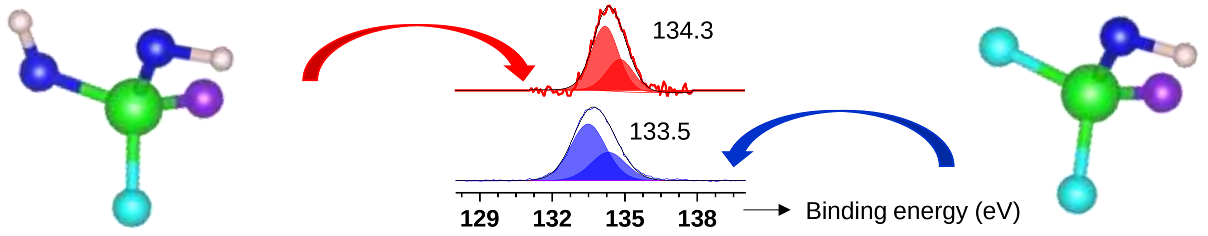

Species & Complexes	Optimized structure (A.U.)	After excitation (A.U.)	K (A.U.)	R (A.U.)	Δ (A.U.)	Δ = T_{BE2} (eV)	Method	Solvent effect
$H_2PO_4^{1-}$	-643.5993	-643.4714	4.6035	0.1279	4.7314	128.7501	B3LYP	
HPO_4^{2-}	-642.8234	-642.9396	4.3536	-0.1162	4.2374	115.3056	B3LYP	
$H_2PO_4^{1-}$	-643.7020	-643.4810	4.7808	0.2209	5.0018	136.1076	B3LYP	water
HPO_4^{2-}	-643.1887	-643.0357	4.7082	0.1530	4.8611	132.2788	B3LYP	water
$H_2PO_4^{1-}$	-641.4873	-641.3325	5.2826	0.1548	5.4374	147.9595	HF	
HPO_4^{2-}	-640.7106	-640.8178	5.0302	-0.1072	4.9230	133.9621	HF	
$H_2PO_4^{1-}$	-641.5943	-641.3859	5.4615	0.2084	5.6699	154.2869	HF	water
HPO_4^{2-}	-641.0802	-640.9102	5.3863	0.1700	5.5563	151.1968	HF	water
^{2}C	-3776.6787	-3776.4137	4.8545	0.2649	4.5895	124.8878	B3LYP	
^{2}E	-3775.6640	-3775.2396	5.0147	0.4245	4.5902	124.9057	B3LYP	
^{1}V	-3851.9797	-3851.6604	5.0094	0.3193	4.6901	127.6232	B3LYP	
^{1}V-H	-3851.8156	-3851.5166	4.8741	0.2989	4.5752	124.4970	B3LYP	
T	-3928.2736	3927.9462	4.8715	0.3274	4.5441	123.6504	B3LYP	
^{1}T-H	-3928.1196	3928.7922	4.6995	0.3274	4.3721	118.9698	B3LYP	

***** Complexes: ^{2}C = bidentate binuclear, ^{2}E = bidentate mononuclear, ^{1}V = monodentate mononuclear, ^{1}V-H = deprotonated monodentate mononuclear, T = outer-sphere, and T = deprotonated outer-sphere.

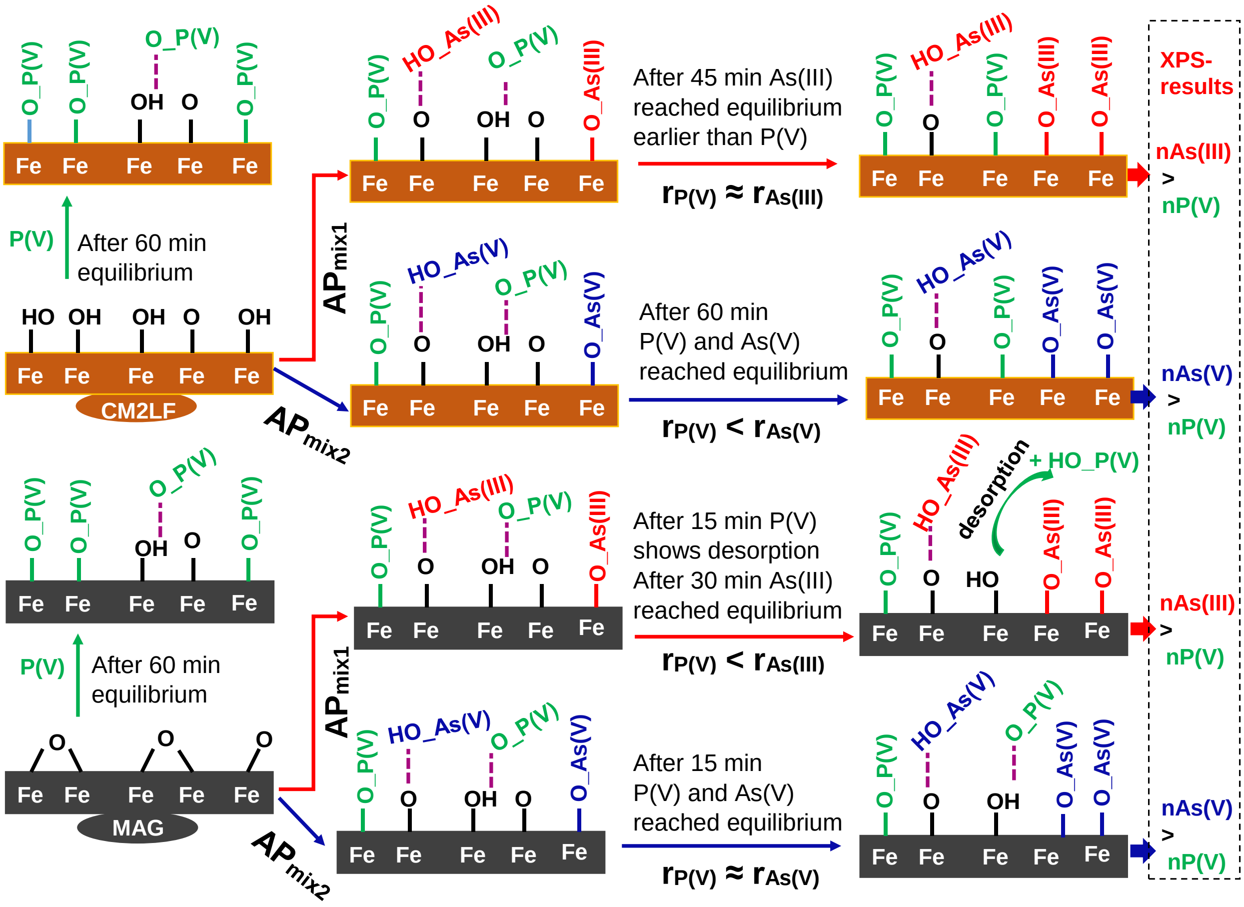

Figure S7. Schematic illustration of P(V) interference in the As(III/V) adsorption based on time dependent ion chromatography and XPS studies. The term r_x means rate of ions adsorption (X= P(V)/As(III)/As(V)). nAs(III/V) means no of adsorbed arsenic species, nP(V) no of adsorbed phosphate species.

Table S3. Interference of P(V) on the As(III/V) adsorption (experimental results).

Adsorbent	Species pH 7	Type of experiment	P 2p (eV)	Shift	As 3d (eV)	Shift	Electrostatic effects on P 2p/As 3d levels	Adsorption kinetics (PSO)
CM2LF	$H_xPO_4^{y-}$	Reference for P(V)	134.1					Solely follows PSO
	H_3AsO_3	Reference for As(III)			45.1			Solely follows PSO
	$H_xPO_4^{y-}$ + H_3AsO_3	AP_{mix1}	134.0	no	45.4	blue	no effect on P 2p effect on As 3d	P(V) and As(III) partially follows PSO
	$H_xAsO_4^{y-}$	Reference for As(V)			45.3			Solely follows PSO
	$H_xPO_4^{y-}$ + $H_xAsO_4^{y-}$	AP_{mix2}	134.4	blue	46.5	blue	effect on P 2p effect on As 3d	P(V) and As(V) partially follows PSO
MAG	$H_xPO_4^{y-}$	Reference for P(V)	134.1					Solely follows PSO
	H_3AsO_3	Reference for As(III)			44.3			Solely follows PSO
	$H_xPO_4^{y-}$ + H_3AsO_3	AP_{mix1}	133. 7	red	45.7	blue	effect on P 2p effect on As 3d	P(V) shows desorption As(III) equilibrium shifted
	$H_xAsO_4^{y-}$	Reference for As(V)			45.5			
	$H_xPO_4^{y-}$ + $H_xAsO_4^{y-}$	AP_{mix2}	134. 1	no	46.6	blue	no effect on P 2p effect on As 3d	P(V) and As(V) reached early equilibrium

***** PSO: pseudo-second-order

As 3d peak got blue-shifted for As(III) in case of AP_{mix1} as compared to only As(III) adsorbed materials (Table S3 and Figure 5). Similar results were observed in the case of AP_{mix2}. These results suggest that the speciation of adsorbed As(III) (ratio of chemisorbed and physisorbed species) on CM2LF and MAG gets affected due to the presence of P(V). We can conclude that P(V) ions are affecting the As(III/V) speciation on CM2LF and MAG. As far as adsorption kinetics is concerned, As(III/V) ions follow pseudo-second-order kinetics when alone and follow pseudo-second-order kinetics partially in presence of P(V) in case of AP_{mix1} and AP_{mix2} adsoprtion. Thus kinetics and adsorption equilibrium for As(III/V) get affected by presence of P(V) ions (Figure S7).

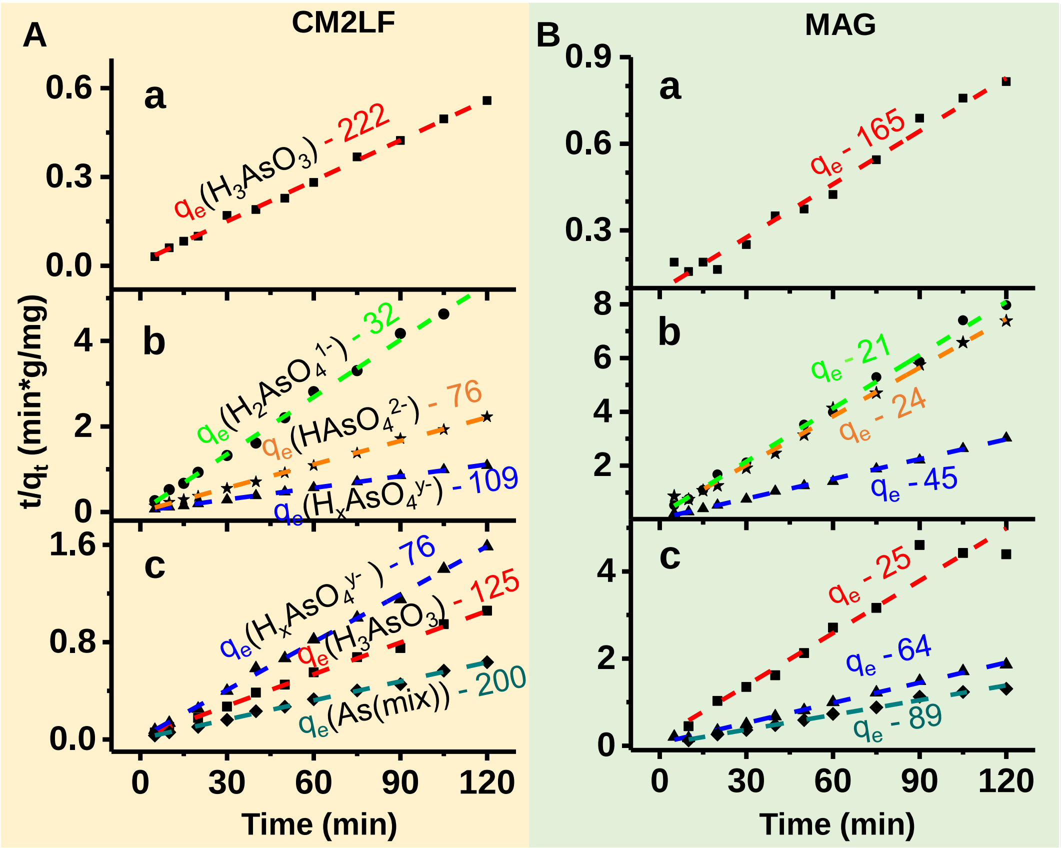

Figure S8. Pseudo-second-order kinetics for A) CM2LF and B) MAG, where a, b and c represent As(III), As(V) and As(mix) removal, respectively. The unit of q_e and q_t is mg/g. Kinetics data taken from Sudhakar et al., 2017[6].

Sustainability aspects of CM2LF and magnetite materials

CM2LF has a composite structure where the metastable 2-line ferrihydrite phase ($Fe_2O_3.0.5H_2O$) is confined in biopolymeric cages of chitosan. Particles used here are of 72 µm in size.[1] It is synthesized by the hydrolysis of a metal precursor (Fe^{3+})–chitosan complex using an alkaline medium followed by washing and drying it at ambient conditions. On the other hand, commercial grade magnetite nanoparticles used in this work are iron oxide (Fe_3O_4) grains of about 40 nm size that exhibit superparamagnetic properties at ambient temperature and can be prepared by various methods. Some reports follow refluxing of FeOOH and oleic acid in 1-octadecene[7], while others have reported alkali precipitation of solution with a molar ratio of Fe(II)/Fe(III) = 0.5 in deoxygenated water resulting in a black precipitate.[8]

1. Material efficiency: The removal effiency of a material can be considered based on its selectivity and uptake capacity for the contaminant. Results from the present study confirm that CM2LF performed better than magnetite (MAG) for As(III/V) uptake in presence of P(V) and shows higher affinity for As(III) and As(V) species than P(V) at neutral pH. On the other hand, our previous study has shown that the maximum adsorption capacity of CM2LF determined by Langmuir isotherm is 100 mg/g for AsIII/AsV and it has been tested in real time conditions[1]. For magnetite, it is 40 mg/g determined through time-dependent aqueous Raman measurements, but using Langmuir isotherm, it is 12.7 mg/g[9], while activated alumina shows a capacity of 15.9 mg/g[1]. Loading or dosage required is lower for materials exhibiting higher uptake capacity, leading to lesser waste generation and thus serves as a more sustainable option for purification processes.
2. Material stability: Although nanomaterials have been widely studied for their application in water purification, it is known that using loose nanoparticles for the same purpose may lead nanoparticle aggregation, conversion or dissolution/leaching, leading to secondary water pollution. These factors have led to the importance of using nanocomposites like CM2LF where nanoparticles are trapped inside templates making the system robust and stable, thus providing a more beneficial option. For example, there are reports where oxidation of magnetite takes place in aerated aqueous media[10] to form more stable iron oxide form (hematite: α-Fe_2O_3) or dissolution of magnetite by thermal or microbial reduction.[11-12] proving

that it is a less stable option to use for water purification. While, CM2LF has been tested for metals (Fe, As) and carbon leaching into water after its use in purification cartridges for long time by TCLP (Toxicity Characteristic Leaching Protocol) and TOC (Total Organic Carbon) procedures, it has shown negligible leaching, confirming its mechanical stability and thus making it more environment friendly.

3. Cost of production: Affordability is another factor to determine sustainability of materials. While, commercial magnetite (Fe II/III oxide, 97%, Alfa Aesar) costs \$51/kg[13] and has come down from an initial cost of production like \$2600/kg[7], bulk scale CM2LF is less than \$15/kg and the process requires no electrical power and no organic solvents. Hence, CM2LF can sustainably cater to larger strata of people, including economically weaker sections.

REFERENCES

1. Kumar, A. A.; Som, A.; Longo, P.; Sudhakar, C.; Bhuin, R. G.; Gupta, S. S.; Anshup; Sankar, M. U.; Chaudhary, A.; Kumar, R.. et al., Confined Metastable 2-Line Ferrihydrite for Affordable Point-of-Use Arsenic-Free Drinking Water. *Advanced Materials* **2017**, *29*, 1604260.
2. Mastronarde, D. N., Serialem. A Program for Automated Tilt Series Acquisition on Tecnai Microscopes Using Prediction of Specimen Position. *Microscopy and Microanalysis* **2003**, *9*, 1182.
3. Nonappa, N. E., Peter. Electron Tomography of Whole Mounts. *In: Imaging & Microscopy.* **2019**, *21*.
4. Kremer, J. R.; Mastronarde, D. N.; McIntosh, J. R. Computer Visualization of Three-Dimensional Image Data Using Imod. *Journal of Structural Biology* **1996**, *116*, 71-76.
5. Engelhardt, P. In Electron Microscopy: Methods and Protocols, Ed. J. Kuo, Humana Press, Totowa, Nj, **2007**.
6. Sudhakar, C.; Anil Kumar, A.; Bhuin, R. G.; Sen Gupta, S.; Natarajan, G.; Pradeep, T. Species-Specific Uptake of Arsenic on Confined Metastable 2-Line Ferrihydrite: A Combined Raman-X-Ray Photoelectron Spectroscopy Investigation of the Adsorption Mechanism. *ACS Sustainable Chemistry & Engineering* **2018**, *6*, 9990-10000.
7. Yavuz, C. T.; Mayo, J. T.; Carmen, Suchecki; Jennifer, Wang; Adam, Z. Ellsworth; Helen, D'Couto; Elizabeth, Quevedo; Laura, Gonzalez; Christina, Nguyen; Vicki, L. Colvin. Pollution Magnet: Nano-Magnetite for Arsenic Removal from Drinking Water. *Environmental Geochemistry and Health* **2010**, *32*, 327-334.
8. Kang, Y. S.; Risbud, S.; Rabolt, J. F.; Stroeve, P. Synthesis and Characterization of Nanometer-Size Fe3o4 and Γ-Fe2o3 Particles. *Chemistry of Materials* **1996**, *8*, 2209-2211.
9. Shahid, M. K.; Phearom, S.; Choi, Y.-G. Adsorption of Arsenic (V) on Magnetite-Enriched Particles Separated from the Mill Scale. *Environmental Earth Sciences* **2019**, *78*, 65.

10. Taylor, P., and Owen, D G. Oxidation of Magnetite in Aerated Aqueous Media. Technical Report: Canada, **1993**.

11. Dinov, K.; Ishigure, K.; Matsuura, C.; Hiroishi, D. Solubility of Magnetite in High Temperature Water and an Approach to Generalized Solubility Computations. *Journal of Nuclear Materials* **1993**, *207*, 266-273.

12. Kostka, J. E.; Nealson, K. H. Dissolution and Reduction of Magnetite by Bacteria. *Environmental Science & Technology* **1995**, *29*, 2535-2540.

13. Alfa Aesar, https://www.Fishersci.Com/Shop/Products/Iron-Ii-Iii-Oxide-97-Metals-Basis-Alfa-Aesar-3/Aa12374a1 (accessed Mar16, 2021).

RESEARCH ARTICLE

ADVANCED MATERIALS INTERFACES
www.advmatinterfaces.de

Aminoclay-Graphene Oxide Composite for Thin-Film Composite Reverse Osmosis Membranes with Unprecedented Water Flux and Fouling Resistance

Md Rabiul Islam, Pratishtha Khurana, Pillalamarri Srikrishnarka, Ankit Nagar, Madhuri Jash, Shantha Kumar Jenifer, Mohd Azhardin Ganayee, Mathava Kumar, and Thalappil Pradeep**

Present work attempts to incorporate aminoclay-graphene oxide composites into thin-film composite (TFC)-reverse osmosis membranes to improve the desalination efficiency of brackish water. The composite is coated on a polysulfone substrate as a result of interfacial polymerization of m-phenylene diamine and trimesoyl chloride, at different time durations. The prepared membranes are analyzed for their water permeation and salt rejection efficiencies using brackish feed water. The results indicated that the membrane loaded with 0.015 wt% of the composite delivered maximum flux at 20 bar pressure for 2000 ppm feed. Moreover, the water flow rate increased by ≈3.27 times (from 15.62 ± 0.36 to 50.28 ± 1.69 Lm^{-2} h^{-1}), compared to the unmodified TFC membrane. An enhancement in the salt rejection from 97.03 ± 1.07 to 99.51 ± 0.10% is also observed for the same feed water at 20 bar as compared to the unmodified membrane. Furthermore, antifouling tests with model bio-foulant humic acid revealed better stability and antifouling performance of the prepared membranes than the unmodified membranes under identical operating conditions. The membrane, therefore, assures high performance and lifetime owing to its mechanical and chemical stability, and hence suggests energy-efficient desalination.

1. Introduction

Water is the world's most precious resource, essential for the functioning of all life forms. Desalination using reverse osmosis (RO) has emerged as a promising method to eradicate the drinking water crisis.[1–7] An RO membrane generally consists of a polyester non-woven fabric upon which a polysulfone layer is casted. These two layers are porous, highly permeable, and provide mechanical support to the topmost layer. The polysulfone side of the membrane is coated with a cross-linked aromatic polyamide thin film by interfacial polymerization between the organic molecules (e.g., trimesoyl chloride, TMC) and aqueous (e.g., m-phenylene diamine, MPD) phases.[8–11] The presence of the active layer of polyamide improves the salt rejection, and antifouling properties of the membrane.[11,12] Additives including camphor sulfonic acid (CSA), triethylamine (TEA), and sodium lauryl sulfate (SLS) are also frequently used to enhance the membrane preparation by aiding the absorption of MPD on the polysulphone support.[12]

Despite copious advantages of membrane filtration systems, such as easy operation and high flexibility in technologies, they present some limitations, including chlorine sensitivity, and susceptibility to fouling, which impedes their large-scale applications.[13–15] In some cases, deposition of extra-cellular polymeric substances (EPS), soluble microbial products (SMP), and microbial cells in the pores resulting in a drop in flux and salt rejection capacity. The amide groups in the polyamide skin layer are also vulnerable to chlorine attack, even at a low chlorine dosage in the feed water.[16]

The polyamide chains allegedly undergo ring chlorination in the presence of chlorine, which disrupts hydrogen bonding between the chains and degrades the polymer matrix.[17] The disruption leads to a dramatic decline in the permeation flux, membrane life, and selectivity, which increases the required pressure for operation. Modification of the thin-film composite (TFC) membranes by adding different hydrophilic nanomaterials like carbon, alumina, silica zeolites, 2D materials, and their derivatives is common in order to combat these problems and improve water permeation characteristics.[8,18–28] Recently, several nanocomposites-based RO membranes have been explored extensively, as synergy of components enhances the physicochemical properties and increases thermal and

---

M. R. Islam, P. Khurana, P. Srikrishnarka, A. Nagar, M. Jash, S. K. Jenifer, M. A. Ganayee, M. Kumar, T. Pradeep
DST Unit of Nanoscience (DST UNS), and Thematic Unit of Excellence (TUE)
Department of Chemistry
Indian Institute of Technology Madras
Chennai 600 036, India
E-mail: pradeep@iitm.ac.in

M. Kumar
Environmental and Water Resources Engineering Division
Department of Civil Engineering
Indian Institute of Technology Madras
Chennai 600 036, India
E-mail: madhav@iitm.ac.in

The ORCID identification number(s) for the author(s) of this article can be found under https://doi.org/10.1002/admi.202100533.

DOI: 10.1002/admi.202100533

chemical stability of the resulting materials.[29] Besides, they can be readily incorporated onto the membrane by mixing them in the aqueous or organic phase before the fabrication reaction of the polyamide layer, or they can be bonded chemically to the surface of TFC via bonding agents.[19]

Among the most common additives used for TFC-RO membranes are graphene oxide (GO) and its derivatives, owing to their higher permeability, improved selectivity, and better chlorine tolerance than polyamide. GO is highly hydrophilic due to the presence of various oxygen-containing functional groups on its surfaces and edges, allowing better dispersion in water and enhancing the compatibility with polysulfone substrate via different covalent and non-covalent interactions.[30] GO forms hydrogen bonds with primary and secondary amines, in addition to covalent bonds with terminal free carboxyl groups of TMC in the linear portion of the polyamide layer.[31,32]

In the present work, we have investigated the effect of incorporating aminoclay-graphene oxide (AC-GO) composite on water flux, salt removal efficiency, and the antifouling tendency of the RO membranes. Aminoclay (AC) is an aminopropyl-functionalized magnesium phyllosilicate ($R_8Si_8Mg_6O_{16}(OH)_4$, where R is $CH_2CH_2NH_2$). It consists of octahedrally coordinated MgO/OH chains and an aminopropyl-functionalized silicate network on both sides.[33] The protonation of amine moiety makes it highly dispersible in water, enabling it to interact electrostatically with anions like $HAsO_4^{2-}$, CrO_4^{2-}, Fe $(CN)_6^{3-}$, F^-, NO^{3-}, and PO_4^{3-}, thereby facilitating their removal.[34,35] AC is also known to possess anti-algicidal properties, which encourages its application for real-time complex water treatment and desalination. Thus, combining the properties of GO and AC and utilizing the composite for water treatment appears rewarding.[36]

The present work reports the preparation and application of AC-GO composites in RO membranes. Optimization of various factors, such as the contact time of MPD and composite loading, followed by an effect on water permeability, salt rejection, and antifouling properties of the prepared TFC membranes, was conducted. The preparation procedures are simple, standard, and feasible, making the overall process scalable and sufficient for brackish water desalination in realistic applications.

2. Result and Discussion

2.1. Characterization of the Starting Materials: Graphene Oxide, Aminoclay, and Aminoclay-Graphene Oxide Composite

Here, we discuss the composite membrane and its characteristics. In view of the detailed studies that are available on them, only essential details are presented, that too in the Experimental Section. Synthesized GO, AC, and AC-GO composites were characterized by UV–vis spectroscopy, Raman spectroscopy, X-ray powder diffraction (XRD), field-emission scanning electron microscopy (FESEM), transmission electron microscopy (TEM), Fourier-transform infrared spectroscopy (FT-IR), and zeta potential measurements (Figures S2–S5, Supporting Information). Figure S2A, Supporting Information shows the UV–vis spectrum of aqueous GO with a characteristic peak at 232 nm and a shoulder at ≈310 nm, which correspond to π–π* and n–π* electronic transitions of C=C aromatic bonds and C=O bonds, respectively.[37–39] Figure S2B, Supporting Information represents the Raman spectrum of GO, which showed D- and G-bands at 1339 and 1599 cm^{-1}, respectively. D-band is observed due to structural imperfections created by the attachment of hydroxyl and epoxide groups on GO's carbon basal plane. The G-band is attributed to the metallicity of carbon in graphene, that is, in-plane vibrations.[38,40] The experimental XRD pattern of GO, shown in Figure S2C, Supporting Information, showed a peak at $2\theta = 10°$. It is attributed to the GO lattice's (002) plane, which corresponds to the interlayer spacing of 0.84 nm (expanded greatly from 0.34 nm in graphite).[41,42] TEM images showed a layered structure of nearly-transparent, wrinkled GO sheets (Figure S2D, Supporting Information).

The FESEM images of AC show micron-sized clay sheets (Figure S3A,B, Supporting Information). However, the well-defined layered structure and individual sheets of the clay could not be identified, presumably due to vigorous stirring during their preparation. A schematic of the layered structure of AC and the corresponding TEM image is shown in Figure S4, Supporting Information. Figures S5A,B, Supporting Information display the FESEM images of the AC-GO composite. The EDAX of AC-GO showed the presence of Mg, Si, and Cl, which confirmed the formation of amino-functionalized clay in the composite (Figure S5C, Supporting Information).

XRD patterns recorded for AC and AC-GO composite are shown in **Figure 1**A. AC showed a low angle reflection with a d_{001} interlayer spacing of ≈1.6 nm, which corresponded to the bilayer arrangement of propyl amino groups.[33,43] The broad in-plane reflections at higher angles ($d_{020,110}$ = 0.41 nm, $d_{130,200}$ = 0.238 nm) and the characteristic (060) reflection at $2\theta = 59°$ confirmed the formation of 2:1 tri-octahedral Mg-phyllosilicate clay with a talc-like structure.[33,43] The XRD pattern obtained for the AC-GO composite retained the features obtained for AC and GO individually, with slight shifts in the peak positions, which arose due to the amine's electrostatic interaction with the oxygen-containing groups of GO.[44] Thus, the observed pattern confirmed the formation of the composite with the retention of their chemical integrity. To determine the vibrational features of the AC-GO composite, we performed Raman measurements on AC, GO, and AC-GO composites. Raman spectrum of AC is shown in Figure 1B, which shows multiple peaks. Raman spectrum of GO showed its signature peaks at 1339 (D-band) and 1599 cm^{-1} (G-band). However, we could not observe the spectral feature of aminoclay in the AC-GO composite (Figure 1B), although IR features were observed. A significant Raman feature (both D-and G-band) of GO was observed in AC-GO with a blue shift (≈8 cm^{-1}). The composite exhibited characteristic D- and G-bands of GO at 1331 and 1597 cm^{-1}, respectively. This blue shift is attributed to the hydrogen bonding or electrostatic interaction between the amine of AC with the acid functional group of GO.

FT-IR spectra of GO, AC, and AC-GO composite are shown in Figure 1C. For GO, the broad peak between 3200–3400 cm^{-1} is due to O-H stretching. The peaks at 2975 and 2900 cm^{-1} correspond to asymmetric and symmetric stretching vibrations, respectively, of the CH_2 groups. The IR signals at 1710, 1554, 1410, 1170, and 1045 cm^{-1} are due to C=O stretching, C=C stretching, -OH bending, C-O stretching of epoxy, and C-O stretching vibration of alkoxy functionalities, respectively. For AC, the peaks at ≈3377, ≈2900, ≈2040, 1613, 1126, 1022, and 555 cm^{-1} are due to

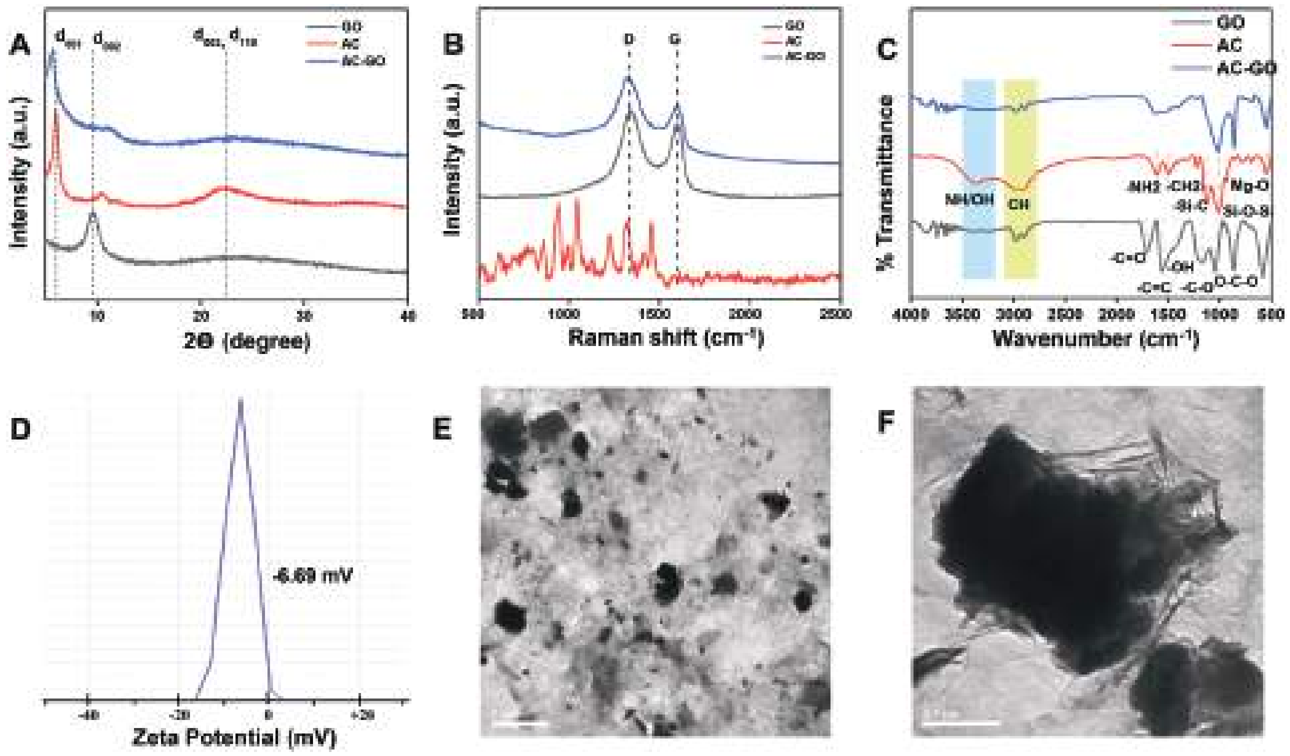

Figure 1. A) XRD pattern, B) Raman spectra, and C) FT-IR Spectra of GO, AC, and AC-GO composite; D) Zeta potential of AC-GO composite; E,F) TEM images of AC-GO composite at different magnifications (scale bars: 5 and 0.5 µm, respectively).

the stretching vibrations of OH, CH_2, NH_3^+, NH_2, Si-C, Si-O-Si, and Mg-O, respectively.[45,46] Also, the signal at ≈1500 cm^{-1} is due to -OH bending. The FT-IR spectrum of the AC-GO composite confirmed the presence of both AC and GO.[39,45,46] Zeta potential measurement of 10:1 (w/w%) AC-GO composite revealed a low negative potential of −6.69 ± 2.95 mV (Figure 1D), which could prove effective in removing water contaminants. This might be due to the presence of oxygen-containing functional groups on the GO sheet in excess of the positively charged moieties on the AC, as the latter has a positive zeta potential.[47] The morphology of the prepared AC-GO composite at different magnifications displayed a stacked lamellar structure having lateral dimensions extending to the micron regime, as explicated from TEM images (Figure 1E,F). Furthermore, the composite showed the presence of clay nanoparticles, viewed as dark features, on the surface of the GO sheet. The negatively-charged GO can form hydrogen bonds or covalent bonds with the terminal primary amine pendant group of the AC, and therefore, might serve as nucleation centers for the clay particles. The negatively charged carbonyl functional groups of GO can also plausibly have electrostatic interactions with the protonated amine moiety.[44] Additionally, Figure S6, Supporting Information showed three types of interactions between AC and GO in AC-GO composites, that is, AC-AC (green shade), GO-GO (red shade), and AC-GO (yellow shade).

2.2. Characterization of Modified TFC Membranes

Desalination takes place by permeation of water molecules diffusing through the membrane, secured in these cells, as presented in **Figure 2**A. Figure 2B further shows the motion of water molecules through the inter-lamellar spacing of the composite. The top surfaces and cross-sections of the AC-GO -modified TFC membranes were characterized using FESEM, and the data were compared with the polysulfone (PSf) substrate and unmodified membranes (TFC), as shown in Figure 2C–E. As shown in Figure 2E, the AC-GO modified (TFC/AC-GO/M30) membranes exhibited unique morphologies and possessed rougher surfaces compared to the PSf support and the other pristine membranes. The TFC/AC-GO membrane showed a typical "ridge and valley" morphology with nodule-like structures, while the PSf and TFC depicted smooth and porous surfaces, respectively. The presence of elements like Mg, Si, and Cl in TFC/AC-GO (Figure 2F) confirmed the coating of AC onto the surface of the membrane.

The FESEM images of the membranes incorporated with varying concentrations of the composite, ranging from 0.005 to 0.100 wt% AC-GO, unveiled diverse morphologies (Figures S7 and S8, Supporting Information). Evidently, the surface morphology of the membranes depends on the percentage of the incorporated composite material. Higher concentrations of AC-GO composite resulted in agglomeration. Similarly, increasing the MPD-substrate contact time resulted in the aggregation of the composite particles (Figure S9, Supporting Information). Excessive loading and extended reaction time are the reasons for such aggregation. Cross-sectional FESEM images revealed the presence of asymmetric, "finger-like" porous structures on the PSf support and the fabric underneath (Figure S10, Supporting Information). However, the polyamide layer was extremely thin and could not be resolved in imaging.

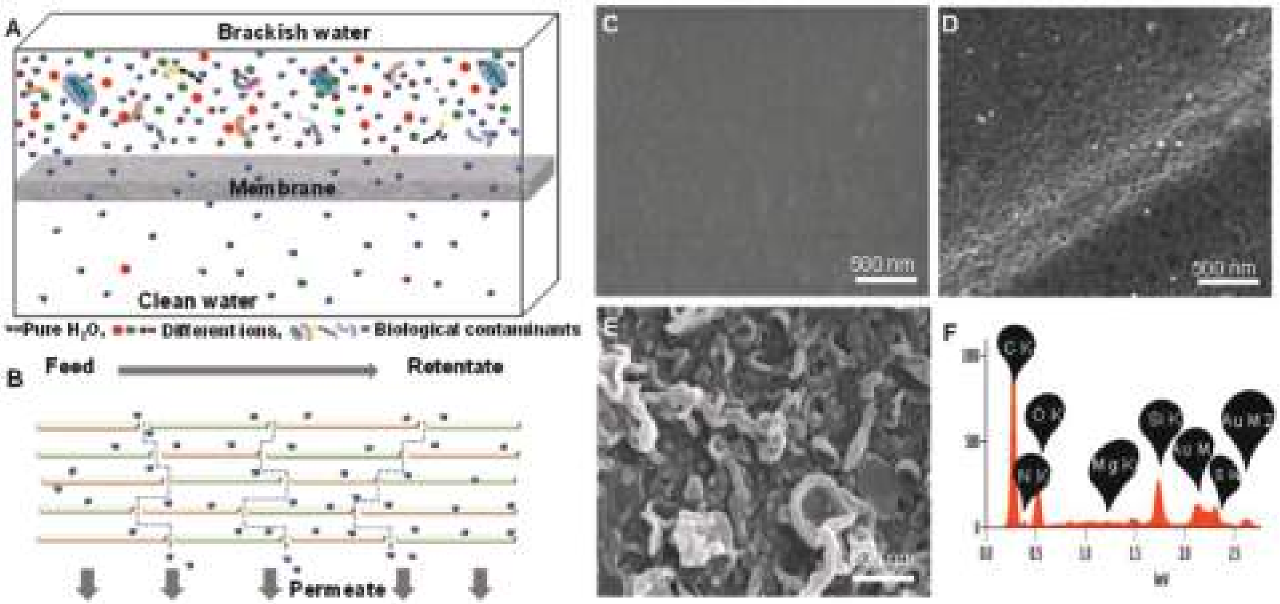

Figure 2. A) Schematic representation of water transport and ions removal across the membrane. B) Detailed mechanism of water transport pathways through the aminoclay-GO sheets. Green and orange bars are representations of aminoclay and GO sheets, respectively. FESEM images of C) Fabric, D) PSf, E) Optimized modified membrane (M30), and F) SEM EDS of the M30 membrane (top view).

Figure S11, Supporting Information shows the FT-IR spectrum of PSf, unmodified TFC, and AC-GO modified membranes. The broad hump centered at 3345 cm^{-1} matched the stretching vibrational frequencies of O-H and N-H groups. Enlarged view of the shaded spectrum showed peaks at 1665, 1583, 1485, 1240, 1150, and 1102 cm^{-1} that correspond to C=O stretching vibration of the amide functional group of the active polyamide layer, N-H, and C-N stretching vibrations of the amide group, C-C stretching, C-O stretching, S=O stretching and =C-H stretching vibrations, respectively, and these are common across all the membranes. However, in membranes other than PSf, two peaks were present at 1546 and 1607 cm^{-1}, which were assigned to N-H bending of the unreacted amine and amide groups, respectively. Conclusively, amide bond formation was observed from the spectra of unmodified TFC and AC-GO modified TFC membranes (M30).

2.3. Permeation Studies of Prepared Membranes

The performance of the prepared membranes was measured in terms of the permeation characteristics like water flux and % of salt rejection efficiency for brackish feed water samples. The data in **Figure 3** represents the outcome of these studies. Figure 3A shows a comparison of the cross-flow permeation results of flux and rejection for the PSf substrate, unmodified TFC (or the PA), and AC (0.015 wt%, TFC/AC), GO (0.015 wt%, TFC/GO), and AC-GO (0.015 wt%, TFC/AC-GO) modified M30 membranes, at 2000 ppm salt and 20 bar pressure. From Figure 3A, it is clear that modified membranes displayed higher water permeation, with improved salt rejection as compared to unmodified PSf membranes. The presence of lamellar nanostructures (TFC/AC and TFC/GO) favored water flow through the membrane matrix. The randomly-positioned nano-sheets (both AC and GO) created channels for water molecules to pass through. Further, the protonated amine moiety of AC and hydrophilic surface functional groups of GO facilitate electrostatic interactions, leading to higher flux than unmodified membranes. The incorporation of AC-GO composite further increased the water flux by 57% (≈1.57×), compared to TFC/AC and TFC/GO, while maintaining a high percentage of salt rejection (>99.5%).

The active layer in modified TFC-RO membranes was the dense polyamide layer, formed by the interfacial polymerization of MPD and TMC. The thickness of this polyamide layer and the amount of material incorporated were a function of contact time between the aqueous diamine solution and the membrane surface. Therefore, to study the effect of contact time of MPD, a set of six membranes, represented as M10 to M60, were prepared by increasing the reaction time of MPD solution with the PSf support (10–60 s), keeping the contact time of TMC solution (50 s) and concentration of AC-GO composite (0.015 wt%) constant.

Figure 3B–D depict an initial increase in water flux from M10 to M30 for all three feed salt concentrations (2000, 5000, and 10 000 ppm), followed by a steady decrease from M30 to M50, and similar for M50 and M60. For feed concentration of 2000 ppm of salt (Figure 3B), M30 exhibited a water flux of 50.28 ± 1.69 L (m^2 h)$^{-1}$, that is, ≈3.27× higher compared to the unmodified TFC membrane (PA), with 99.51 ± 0.10% salt rejection. For higher salt concentrations of 5000 and 10 000 ppm, water permeation for M30 was 39.23 ± 1.16 and 25.39 ± 0.80 L (m^2 h)$^{-1}$, with salt rejection efficiencies of 99.41 ± 0.07% and 99.21 ± 0.06%, respectively.

The unprecedented water permeation of the AC-GO modified polyamide matrix membranes was presumably due to the lamellar nanostructures of AC-GO. The stacking of AC on the GO sheets could create transport channels for water

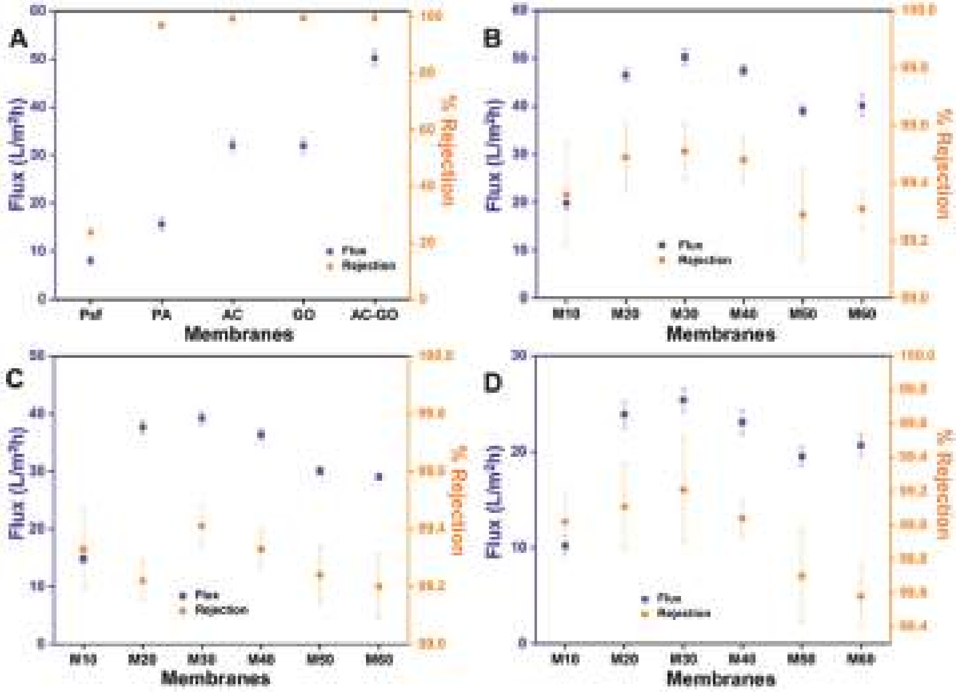

Figure 3. A) Water flux and % salt rejection for PSf support layer, unmodified M30 and modified M30 (0.015 wt% of AC, GO, and AC-GO) at 2000 ppm salt and 20 bar pressure, the average performance of membranes M10-M60 at B) 2000, C) 5000, and D) 10 000 ppm input concentration (feed water), under 20 bar pressure.

molecules and enhance adsorption of water molecules onto the membrane surface and within the inter-lamellar spaces of these stacked structures.[45] In addition, the increase of water permeance might be due to sorption capability in terms of solution-diffusion mechanism due to the presence of hydrophilic functional groups. However, on the contrary, the inclusion of denser nanostructures or higher concentrations of nanomaterials might cause agglomeration of nanosheets, posing resistance to the flow of water molecules, causing a reduction in water flux even at high operating pressures.[48] This agglomeration of 2D materials in the selective membrane layer geometrically leads to reduction in permeance due to the increase in path length. Because of these two opposing effects, an optimum water flux was obtained for TFC/AC-GO (0.015 wt%) M30 among the membranes studied here.

Figure 4A summarizes the study and compares the performance of the membranes at varying input salt concentrations. As observed from Figure 4A, with increasing salt concentration in the feed water sample, the flux declined gradually because of the lower net driving pressure due to the increased osmotic pressure of the feed at higher salt concentration. As the net driving pressure decreased, the relative amount of water passing through the membrane, compared to salt, decreased, resulting in lower salt rejection.

For M30, the water flux observed a continuous increase from 36.12 ± 0.99 to 85.60 ± 1.29 L $(m^2\ h)^{-1}$, corresponding to a pressure variation from 15 to 40 bar (Figure 4B). This direct relationship suggests an increase in the net driving pressure. Higher pressures, in excess of the osmotic pressure, forced the feed water through the membrane, leading to higher permeation and greater flux.[49] Permeation parameters (flux and percentage salt rejection) were plotted as a function of applied pressure to evaluate the membrane's performance. A sharp increase in % salt rejection was observed (98.53 ± 0.17% at 15 bar, to 99.51 ± 0.10% at 20 bar) initially. Further increase in pressure resulted in an insignificant change in % salt rejection, till a pressure of 35 bar. An additional increase of pressure to 40 bar resulted in a slight increase in the % salt rejection (Figure 4B).[50]

Contact angle studies were performed to observe the influence of contact time of the composite and the PSf support on the wettability of the membrane (Figure 4C); and loading of the AC-GO composite on the membranes keeping the contact time constant (Figure 4D). For M10, since the contact time of MPD and the PSf support was too short for nano-composite inclusion into the polymer matrix of the membrane, surface hydrophilicity was only slightly improved when compared to the unmodified membrane (Figure 4C), which was evident from the contact angles for M0 and M10. This slight improvement in surface hydrophilicity was reflected as the rise in flux from 15.62 ± 0.36 to 19.79 ± 1.22 L $(m^2\ h)^{-1}$. When contact time was increased to 50 s, the surface became highly hydrophilic compared to the unmodified membrane. The inclusion of a higher amount of clay composite resulted in the stacking of layers, posing resistance to water flow, thereby decreasing the flux.

Figure 4D shows the effect of incorporating AC-GO composite on the surface hydrophilicity of the thin-film composite membranes, and with an increase in the AC-GO composite concentration from 0 to 0.1 wt% (0–1000 ppm), the variation in water contact angle $(59\text{–}55^0)$, exhibiting improved hydrophilicity.

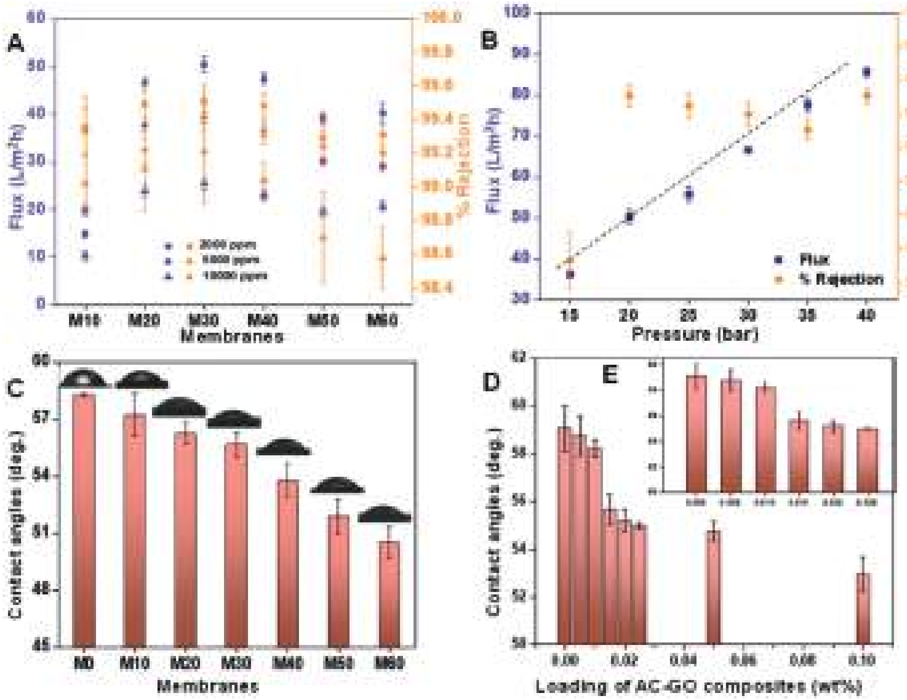

Figure 4. A) Variation in water flux at different feed water concentrations (2000, 5000, and 10 000 ppm), B) Permeation characteristics of M30 with varying pressure at 2000 ppm salt concentration, C) Contact angle of membranes (M0 to M60) with 0.015 wt% AC-GO and D) Contact angle of M30 at different AC-GO loadings and E) expanded view of D. M0 refers to the unmodified TFC.

2.4. Biofouling and Anti-Bacterial Study

To study the resistance of prepared membranes against surface biofouling, model foulant, humic acid was used, and the performance was evaluated in terms of normalized flux, J_n,

$$J_n = J/J_0 \tag{1}$$

where J is the instantaneous flux, and J_0 is the flux after compaction.

A comparative investigation of the antifouling performance of a commercial RO membrane (Vontron: model number: VM-TFC-80), an unmodified M30, and an AC-GO modified M30 was performed by treating them under identical experimental procedures (with 2000 ppm NaCl, 500 ppm humic acid, and 2 mM $CaCl_2$ under 20 bar pressure). **Figure 5**A shows the variation of the normalized flux of membranes with time under testing conditions: 2000 ppm NaCl, 500 ppm humic acid, and 2 mM $CaCl_2$. Before adding foulants to the feed water, compaction was done for 3 h with distilled water to maintain constant flux. During the initial hours of study, a significant reduction in water flux was observed for the commercial membrane, while unmodified and modified M30 showed only a slight decrease in water flux. This indicated that for the commercial membrane, fouling occurred within the first hour of the addition of foulants, perhaps because of high surface roughness and high affinity for humic acid in the feed water. After 3 h of examination, a sharp decline was observed for the unmodified membrane, indicating the deposition of humic acid on its surface. Even after 10 h of the experiment, the AC-GO modified membrane showed only a moderate decrease in water permeation. It implies less bio-fouling of the prepared membrane, plausibly due to the electrostatic repulsions between negatively charged humic acid at brackish water pH and negative zeta potential of the AC-GO composite. This repulsive force was effective in preventing the fouling of membranes incorporated with the clay composite. Since humic acid is hydrophobic, the extent of foulant deposition on the membrane was analyzed by measuring the contact angle on fresh and bio-fouled membranes (Figure 5A).

For the commercial membrane, maximum fouling was observed, and the contact angle changed from 40.7^0 to 60.2^0 in 10 h. For unmodified and modified composite membranes, the angle was observed to increase from 59.1^0 and 55.6^0 to 62.7^0 and 57.4^0, respectively, for the same period (Figure 5B). The difference in the contact angles indicated that scaling had occurred due to the added foulants. For AC-GO modified membrane, the change in angle was found to be the minimum, which suggested improved resistance to such foulants. A larger amount of humic acid was deposited onto the commercial membrane compared to the M30 membrane. The observed result could be attributed to repulsive forces existing between the composite and the foulant.

Figure 5C,D show that the M30 membrane exhibited good bacterial (*Escherichia coli* and *Bacillus subtilis*) growth inhibition, compared to the unmodified and commercial membranes. The M30 membrane showed 90% and 44% anti-bacterial effect on *E. coli* and *B. subtilis*, respectively. This agrees with the known anti-bacterial activity of GO against gram-positive and gram-negative bacteria. The commercial membrane failed to show such anti-bacterial effects, while the M30 membrane showed high stability in resisting bacteria and foulants (Figure 5).

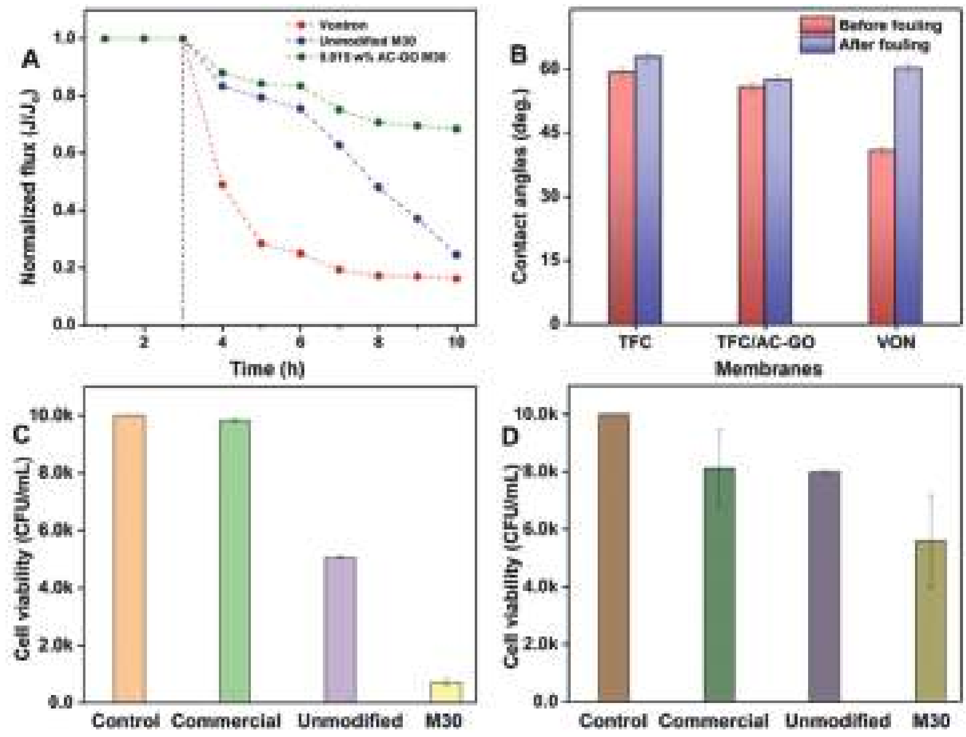

Figure 5. A) Normalized water flux for Von-VM-TFC-80, unmodified M30, and 0.015 wt% AC-GO modified membranes during the antifouling test with 2000 ppm NaCl, 500 ppm humic acid, and 2 mм $CaCl_2$ under 20 bar pressure, B) contact angle for fresh and humic acid-fouled membranes and cell viability test on the membrane with control, commercial, unmodified-TFC and M30 membranes with C) *E. Coli* and D) *B. Subtilis* bacteria after 8 h of incubation.

3. Conclusion

The potential use of TFC-RO membranes, modified with aminoclay-graphene oxide composite, was investigated. The membranes showed improved water flux due to increased surface area and enhanced hydrophilicity, along with enhanced salt rejection. For a feed concentration of 2000 ppm of salt, the membrane M30 modified with 0.015 wt% of composite exhibited a flux of ≈50.28 ± 1.69 L $(m^2\ h)^{-1}$ with $99.51 \pm 0.10\%$ salt rejection at 20 bar and 25 °C. The incorporation of AC-GO further increased the water permeation and showed a 57% (≈1.57×) enhancement compared to TFC/AC and TFC/GO membranes while maintaining high salt rejection (>99.5%). Overall, modified M30 membrane flux increased ≈3.27× compared to the unmodified TFC membrane (PA membrane) at 20 bar pressure in 2000 ppm feed NaCl solution. The membranes displayed a reduction in contact angle with an increase in contact time of PSf substrate and MPD, suggesting greater inclusion of composite into the substrate with time. Similar measurements were done for membranes with different composite loadings. The negative zeta potential of the composite was responsible for significantly improving fouling resistance to humic acid. These modified membranes were prepared by employing the standard procedure for interfacial polymerization. Therefore, the approach is simple and scalable to develop membranes for brackish water desalination.

4. Experimental Section

Materials: Natural graphite flakes (95% of carbon) were obtained from Active Carbon. Sulfuric acid (H_2SO_4, 95–98%) and hydrochloric acid (HCl, 36%) were purchased from Rankem Chemicals. Phosphorus pentoxide (P_2O_5, 95%) and hydrogen peroxide (H_2O_2, 98%) were purchased from SD Fine Chemicals. Potassium permanganate ($KMnO_4$, 98.5%) and potassium peroxydisulfate ($K_2S_2O_8$, 98%) were procured from Sisco Research Laboratories. Nitric acid (HNO_3) (65–68%), magnesium chloride ($MgCl_2.6H_2O$), (3-Aminopropyl) triethoxysilane (APTES), and sodium hydroxide (NaOH) were purchased from Merck. Acetone, ethanol, and sodium chloride (NaCl) from Loba Chemie. Polysulfone (PSf, MW 35 000 g mol^{-1}) and trimesoyl chloride (TMC, 99% purity) were procured from Sigma Aldrich. Calcium chloride ($CaCl_2$), oxalic acid, hexane (HPLC grade), dimethylsulfoxide (DMSO), *N*,*N*-dimethylformamide (DMF), and *N*-methyl-2-pyrrolidone (NMP) were purchased from Merck. D(+)– 10-camphor sulfonic acid (CSA) and sodium lauryl sulphate (SLS) were obtained from Spectrochem. m-Phenylenediamine (MPD, 98%) was procured from Alfa Aesar. Sodium lauryl sulfate (SLS), sodium chloride (NaCl), and sodium hypochlorite (NaClO, 6% available free chlorine) were purchased from Rankem. The sodium salt of humic acid (HA) containing 50–60% of HA was procured from Acros Organics. Luria Bertani (LB) Broth and Nutrient agar were purchased from HiMedia. Escherichia coli MTCC 443 and Bacillus subtilis ATCC 21 331 were procured from MTCC and ATCC, respectively. All chemicals were of analytical grade and used as received without further purification. Glassware was cleaned thoroughly with aqua regia (HCl:HNO3, 3:1 vol%), rinsed with deionized water (DI) water, and dried in an oven before use.

Characterization: The UV–vis spectroscopy measurements, in the range 200 to 1100 nm, were performed using PerkinElmer Lambda 25 spectrophotometer. IR spectra of the materials were measured using PerkinElmer Spectrum-One spectrometer, fit with a diamond crystal (for stronger signals due to greater penetration). However, germanium crystal was used for dark samples because of its high-refractive-index. Raman spectra of materials were obtained using WITec GmbH CRM200 confocal Raman spectroscope with 532 and 633 nm laser excitation. Morphological studies of the prepared composite and the membranes, elemental analysis, and elemental mapping were carried out using a scanning electron microscope equipped with energy dispersive analysis of X-rays (EDAX or EDS) (FEI Quanta 200) and HRTEM (JEOL 3010, 300 kV). Also, HRSEM images of the electrode materials were obtained through Thermo Scientific Verios G4 UC SEM. The experimental XRD patterns were obtained by Bruker D8 Advance X-ray diffractometer with Cu Kα radiation ($\lambda = 1.54$ Å). The hydrophilicity of the membranes was obtained by contact angle measurements using a Holmarc contact angle meter.

Preparation of Graphene Oxide: Graphene oxide (GO) was synthesized from graphite powder using a modified Hummer's method.[51,52] Graphite powder was oxidized using concentrated sulphuric acid (H_2SO_4), potassium persulphate ($K_2S_2O_8$), and phosphorus pentoxide (P_2O_5) as oxidizing agents. The resulting dark blue mixture was cooled to room temperature. It was then diluted, filtered with a membrane of 0.22 µm, and dried. The obtained powder was then added to cold H_2SO_4, to which potassium permanganate ($KMnO_4$) was slowly added with continuous stirring in an ice bath. After 15 min, sodium nitrate ($NaNO_3$) was added to the mixture. The solution was further stirred for 2 h at 35 °C and 200 mL distilled water was added slowly to complete the reaction. It was then further diluted with distilled water (≈500 mL), and 15 mL of hydrogen peroxide (H_2O_2) was added for further oxidation. The color of the mixture turned brown-yellow, which indicated the formation of GO. The product was first washed with hydrochloric acid (HCl) (1:10), then with water, and finally suspended in distilled water. The brown dispersion was dialyzed for 7–10 days to remove residual metal ions and acids. GO was then exfoliated via sonication for 1.5 h.

Preparation of Aminoclay: Aminopropyl functionalized aminoclay was prepared by using magnesium chloride ($MgCl_2.6H_2O$) and (3-Aminopropyl) triethoxysilane (APTES) as precursors.[33,53,54] Briefly, 8 g of $MgCl_2.6H_2O$ was added to 150 mL of ethanol in a 250 mL conical flask. To it, 12 mL of APTES was added drop-wise, and the solution was magnetically stirred for 24 h at room temperature to obtain a milky white suspension. The suspension was then aged at 40 °C, followed by centrifugation and washing with ethanol to get the white product, which was then grinded and sieved to produce the powdered material.

Preparation of Aminoclay-Graphene Oxide Composite: Prepared GO and AC were added in 1:10 (w/w%) ratio and left for stirring for 24 h at room temperature to obtain a brown-black slurry. The slurry was dried at 100 °C, followed by redispersion in water, centrifugation, and repeated washing with ethanol. The composite was dried at 60 °C, which was then ground into excellent powder by ball milling for 4 h.

Membrane Casting: The polysulfone (PSf) porous substrate was prepared by the phase inversion process, wherein the non-woven polyester fabric was cast with the polymer-doped solution using a flat RO membrane casting unit. First, the polymer solution (19 wt%) was prepared by dissolving 19 g of polysulfone pellets (Mol. Wt. ≈ 35 kDa) in 78.64 mL of *N*-methyl-2-pyrrolidone (NMP, density: 1.03 g cm^{-3}). The mixture was stirred continuously at 60 °C for 24 h to obtain a homogenous solution, which was subsequently degassed in a desiccator to remove air bubbles. Second, the fabric was placed on a flat glass sheet, and the polymer solution was uniformly spread on it, keeping a thickness of 0.2 mm by an adjustable casting knife. The prepared membranes were placed in DI water and preserved in Milli-Q water at ≈4 °C until further use.[31]

Preparation of Thin-Film Composite (TFC) Membranes: Both unmodified and modified TFC-RO membranes were prepared by interfacial polymerization on a PSf substrate. Detailed experimental conditions for synthesizing GO, AC, and AC-GO composite are provided in the Section 4. Briefly, an aqueous solution containing of m-phenylene diamine (MPD) (2.0 wt%), camphor sulphonic acid (CSA) (1.0 wt%), sodium lauryl sulphate (SLS) (0.2 wt%), and AC-GO composite (0.015 wt% for modified membranes), after probe sonication of 10 min, was allowed to come into contact with the PSf substrate for different time intervals (10, 20, 30, 40, 50, and 60 s, denoted as M10 to M60). The excess solution was drained-off, followed by the reaction with TMC (0.1 wt%) in hexane for 50 s, to induce polymerization between the diamine moiety of MPD and the acid chloride moiety of TMC. The membranes were then cured at 60 °C for 5 min. After thoroughly washing with water, the membranes were stored in Milli-Q water at ≈4 °C until further use.

Performance Studies of Membranes: The modified TFC membranes were analyzed for their performance, based on water flux and salt rejection rates of total dissolved solids (TDS), using a cross-flow permeation apparatus (Figure S1, Supporting Information). Cross-flow refers to the tangential flow of feed water with respect to the membrane. The set-up consisted of three membrane chambers, and each had an effective surface area of 32.3 cm^2. This arrangement allowed the analysis and comparison of the performance of three membranes simultaneously, under identical operating conditions. Unless stated otherwise, the running conditions were 20 bar pressure, room temperature (25 °C), neutral pH, and 3.75 L min^{-1} (225 L h^{-1}) flow rate with a 2000 ppm concentration of NaCl in feed water. However, before adding NaCl to the feed w, the membranes were compacted using distilled water for 3 h to achieve a constant flux. Also, throughout the RO test runs, both permeate and reject water were re-circulated to the feed inlet tank to maintain constant salt concentration during the study. Membrane's resistivity to chloride ions was tested at different NaCl concentrations (2000, 5000, and 10 000 ppm).

The salt rejection (*R*) and permeation flux (*J*) for the studies were determined using the following two equations,

$$R = \left(1 - \frac{C_p}{C_f}\right) \times 100\% \tag{2}$$

$$J = \frac{V}{A \cdot t} \tag{3}$$

where C_f and C_p are the salt concentrations in the feed and permeate, respectively, V is the volume of permeate collected over a time interval t for a membrane cross-sectional area, A.

Also, relation between flux (LMH) and permeance (LMH/bar) has been given below,

$$\text{Permeance} = \frac{\text{Flux}}{\text{bar}} \tag{4}$$

where LMH is liter per meter square per hour (L m^{-2} h^{-1}).

Anti-Bacterial Test of Membranes: *E. coli* and *B. subtilis* bacterial stock cultures were revived by inoculation in LB broth and were grown overnight at 37 °C and 120 rpm shaking for 4 h. The culture was used for inoculation into fresh LB broth and allowed to grow till the culture reached the log phase. The bacterial cells were washed twice in saline by centrifugation at 3000 rpm for 5 min to remove the nutrients in the medium. Membranes (commercial, unmodified and modified M30) uniformly cut in the dimensions of 0.5 cm × 0.5 cm were sterilized by spraying 70% ethanol on them and allowed to dry in a laminar flow chamber. These membranes were introduced into 1 mL of 104 CFU mL^{-1} of bacterial cells suspended in saline. The cells were shaken at 80 rpm for 8 h to avoid the settling of bacterial cells and to keep the cells in continuous contact with the membrane. The number of viable cells after incubation with the membranes was determined through the colony counting method by inoculating the cells interacted with the membrane on nutrient agar plates for 24 h at 37 °C. All the experiments were done in triplicates.

Supporting Information

Supporting Information is available from the Wiley Online Library or from the author.

Acknowledgements

MD. R.I., and P.K. contributed equally to this work. The authors thank the Department of Science and Technology (DST) and Nano Mission of India's Government for constantly supporting the research program on nanomaterials. MD.R.I. thanks the Council of Scientific and Industrial

Research (CSIR) for his SRF fellowships. M.J. and M.A.G. thank the University Grants Commission (U. G. C.) for their doctoral fellowship. P.K., P.S., A.N., and S.K.J. thank IIT Madras for their research fellowships.

Conflict of Interest

The authors declare no conflict of interest.

Data Availability Statement

Research data are not shared.

Keywords

aminoclay, desalination, graphene oxide, reverse osmosis, water purification

Received: April 3, 2021
Revised: July 12, 2021

---

[1] V. Albergamo, B. Blankert, E. R. Cornelissen, B. Hofs, W.-J. Knibbe, W. van der Meer, P. de Voogt, *Water Res.* **2019**, *148*, 535.
[2] G. Amy, N. Ghaffour, Z. Li, L. Francis, R. V. Linares, T. Missimer, S. Lattemann, *Desalination* **2017**, *401*, 16.
[3] X. Cheng, W. Zhou, P. Li, Z. Ren, D. Wu, C. Luo, X. Tang, J. Wang, H. Liang, *Chemosphere* **2019**, *234*, 545.
[4] M. Kumar, S. RaoT, A. M. Isloor, G. P. S. Ibrahim, Inamuddin, N. I. , A. F. Ismail, A. M. Asiri, *Int. J. Biol. Macromol.* **2019**, *129*, 715.
[5] A. Tabriz, M. A. Ur Rehman Alvi, M. B. Khan Niazi, M. Batool, M. F. Bhatti, A. L. Khan, A. U. Khan, T. Jamil, N. M. Ahmad, *Carbohydr. Polym.* **2019**, *207*, 17.
[6] X. Wang, H. Ma, B. Chu, B. S. Hsiao, *Desalination* **2017**, *420*, 91.
[7] Z. Yang, Y. Zhou, Z. Feng, X. Rui, T. Zhang, Z. Zhang, *Polymers* **2019**, *11*, 1252.
[8] I. H. Aljundi, *Desalination* **2017**, *420*, 12.
[9] J. E. Cadotte, *Mater. Sci. Synth. Membr.* **1985**, *269*, 273.
[10] M. Elimelech, W. A. Phillip, *Science* **2011**, *333*, 712.
[11] J. E. Cadotte, R. J. Petersen, R. E. Larson, E. E. Erickson, *Desalination* **1980**, *32*, 25.
[12] A. Ismail, M. Padaki, N. Hilal, T. Matsuura, W. J. Lau, *Desalination* **2015**, *356*, 140.
[13] H.-R. Chae, J. Lee, C.-H. Lee, I.-C. Kim, P.-K. Park, *J. Membr. Sci.* **2015**, *483*, 128.
[14] B. Mi, M. Elimelech, *Desalination* **2013**, *312*, 75.
[15] F. Shao, L. Dong, H. Dong, Q. Zhang, M. Zhao, L. Yu, B. Pang, Y. Chen, *J. Membr. Sci.* **2017**, *525*, 9.
[16] D. Manish, P. R. Buch, P. Rao, J. J. Trivedi, A. V. R. Reddy, *IJND* **2008**, *3*, 175.
[17] S. Avlonitis, W. T. Hanbury, T. Hodgkiess, *Desalination* **1992**, *85*, 321.
[18] A. S. Al-Hobaib, K. M. Al-Sheetan, M. R. Shaik, N. M. Al-Andis, M. S. Al-Suhybani, *Nanoscale Res. Lett.* **2015**, *10*, 379.
[19] S. Al Aani, A. Haroutounian, C. J. Wright, N. Hilal, *Desalination* **2018**, *427*, 60.
[20] S. Balta, A. Sotto, P. Luis, L. Benea, B. Van der Bruggen, J. Kim, *J. Membr. Sci.* **2012**, *389*, 155.
[21] M. Elma, C. Yacou, D. Wang, S. Smart, J. Costa, *Water* **2012**, *4*, 629.
[22] K. M. AL-Sheetan, M. R. Shaik, A. S. AL-Hobaib, N. M. Alandis, *J. Nanomater.* **2015**, *2015*, 363175.
[23] H. Huang, X. Qu, H. Dong, L. Zhang, H. Chen, *RSC Adv.* **2013**, *3*, 8203.
[24] M. Kadhom, W. Hu, B. Deng, *Membranes (Basel)* **2017**, *7*, 31.
[25] S. R. Lakhotia, M. Mukhopadhyay, P. Kumari, *Sci. Rep.* **2018**, *8*, 4976.
[26] C. X. C. Lin, L. P. Ding, S. Smart, J. C. D. da Costa, *J. Colloid Interface Sci.* **2012**, *368*, 70.
[27] L. Y. Ng, A. W. Mohammad, C. P. Leo, N. Hilal, *Desalination* **2013**, *308*, 15.
[28] C. Van Goethem, R. Verbeke, M. Pfanmöller, T. Koschine, M. Dickmann, T. Timpel-Lindner, W. Egger, S. Bals, I. F. J. Vankelecom, *J. Membr. Sci.* **2018**, *563*, 938.
[29] G. Xu, J.-N. Wang, C.-J. Li, *Desalination* **2013**, *328*, 83.
[30] Z. Komeily-Nia, L.-T. Qu, J.-L. Li, *Small Sci.* **2021**, *1*, 2000026.
[31] M. Ali, L. Wang, X. Wang, X. Feng, *Desalination* **2016**, *386*, 67;
[32] S. Xia, L. Yao, Y. Zhao, N. Li, Y. Zheng, *Chem. Eng. J.* **2015**, *280*, 720.
[33] K. K. R. Datta, A. Achari, M. Eswaramoorthy, *J. Mater. Chem. A* **2013**, *1*, 6707.
[34] Y.-C. Lee, E. J. Kim, H.-J. Shin, M. Choi, J.-W. Yang, *J. Ind. Eng. Chem.* **2012**, *18*, 871.
[35] Y.-C. Lee, W.-K. Park, J.-W. Yang, *J. Hazard. Mater.* **2011**, *190*, 652.
[36] Y.-C. Lee, E. Jin, S. W. Jung, Y.-M. Kim, K. Chang, J.-W. Yang, S.-W. Kim, Y.-O. Kim, H.-J. Shin, *Sci. Rep.* **2013**, *3*, 1292.
[37] D. C. Marcano, D. V. Kosynkin, J. M. Berlin, A. Sinitskii, Z. Sun, A. Slesarev, L. B. Alemany, W. Lu, J. M. Tour, *ACS Nano* **2010**, *4*, 4806.
[38] L. Peng, Z. Xu, Z. Liu, Y. Wei, H. Sun, Z. Li, X. Zhao, C. Gao, *Nat. Commun.* **2015**, *6*, 5716.
[39] H. Yu, B. Zhang, C. Bulin, R. Li, R. Xing, *Sci. Rep.* **2016**, *6*, 36143.
[40] K. Krishnamoorthy, M. Veerapandian, K. Yun, S.-J. Kim, *Carbon* **2013**, *53*, 38.
[41] K. Garg, R. Shanmugam, P. C. Ramamurthy, *Carbon* **2017**, *122*, 307.
[42] P. Ramesh, S. Bhagyalakshmi, S. Sampath, *J. Colloid Interface Sci.* **2004**, *274*, 95.
[43] K. K. R. Datta, M. Eswaramoorthy, C. N. R. Rao, *J. Mater. Chem.* **2007**, *17*, 613.
[44] A. Achari, K. K. R. Datta, M. De, V. P. Dravid, M. Eswaramoorthy, *Nanoscale* **2013**, *5*, 5316.
[45] Y.-C. Lee, B. Kim, W. Farooq, J. Chung, J.-I. Han, H.-J. Shin, S. H. Jeong, J.-Y. Park, J.-S. Lee, Y.-K. Oh, *Bioresour. Technol.* **2013**, *132*, 440.
[46] V. K. H. Bui, D. Park, Y.-C. Lee, *Chem. Eng. J.* **2018**, *336*, 757.
[47] Y.-X. An, W.-J. Qu, P.-Z. Yu, J.-G. Lü, *Pet. Sci.* **2018**, *15*, 366.
[48] H. Dong, *J. Membr. Sci.* **2015**, *494*, 92.
[49] M. Kadhom, B. Deng, *Microporous Mesoporous Mater.* **2019**, *279*, 82.
[50] W. Zhou, L. Song, *Environ. Sci. Technol.* **2005**, *39*, 3382.
[51] N. I. Zaaba, K. L. Foo, U. Hashim, S. J. Tan, W.-W. Liu, C. H. Voon, *Procedia Eng.* **2017**, *184*, 469.
[52] M. R. Islam, S. S. Gupta, S. K. Jana, P. Srikrishnarka, B. Mondal, S. Chennu, T. Ahuja, A. Chakraborty, T. Pradeep, *Adv. Mater. Interfaces* **2021**, *8*, 2001998.
[53] Y. Fukushima, M. Tani, *J. Chem. Soc., Chem. Commun.* **1995**, *1995*, 241.
[54] R. B. Ferreira, C. R. da Silva, H. O. Pastore, *Langmuir* **2008**, *24*, 14215.

Supporting Information

for *Adv. Mater. Interfaces,* DOI: 10.1002/admi.202100533

Aminoclay-Graphene Oxide Composite for Thin-Film Composite Reverse Osmosis Membranes with Unprecedented Water Flux and Fouling Resistance

Md Rabiul Islam, Pratishtha Khurana, Pillalamarri Srikrishnarka, Ankit Nagar, Madhuri Jash, Shantha Kumar Jenifer, Mohd Azhardin Ganayee, Mathava Kumar, and Thalappil Pradeep**

Supporting Information

Aminoclay-Graphene Oxide Composite for Thin-Film Composite Reverse Osmosis Membranes with Unprecedented Water Flux and Fouling Resistance

Md Rabiul Islam,[1#] Pratishtha Khurana,[1#] Pillalamarri Srikrishnarka,[1] Ankit Nagar,[1] Madhuri Jash,[1] Shantha Kumar Jenifer,[1] Mohd Azhardin Ganayee,[1] Mathava Kumar[2] and Thalappil Pradeep[1*]*

[1]DST Unit of Nanoscience and Thematic Unit of Excellence, Department of Chemistry, Indian Institute of Technology Madras, Chennai-600036, India

[2]Environmental and Water Resources Engineering, Division Department of Civil Engineering, Indian Institute of Technology Madras, Chennai-600036, India

[#] These authors are contributed equally to this work

Corresponding Author

**E-mail: pradeep@iitm.ac.in*

Table of Contents

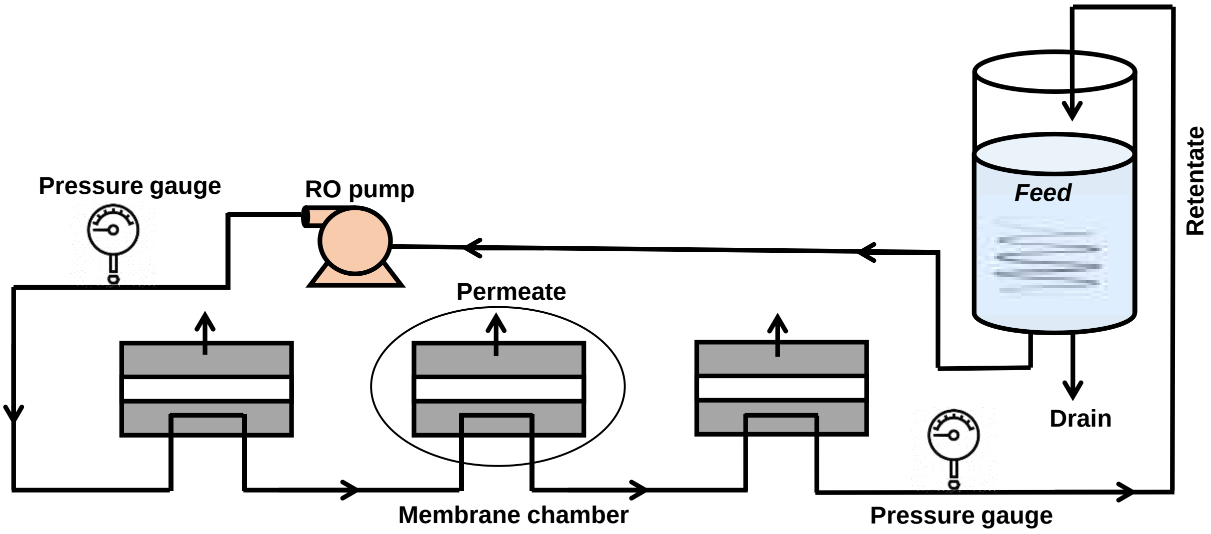

Figure S1. Experimental set-up of the RO skid.

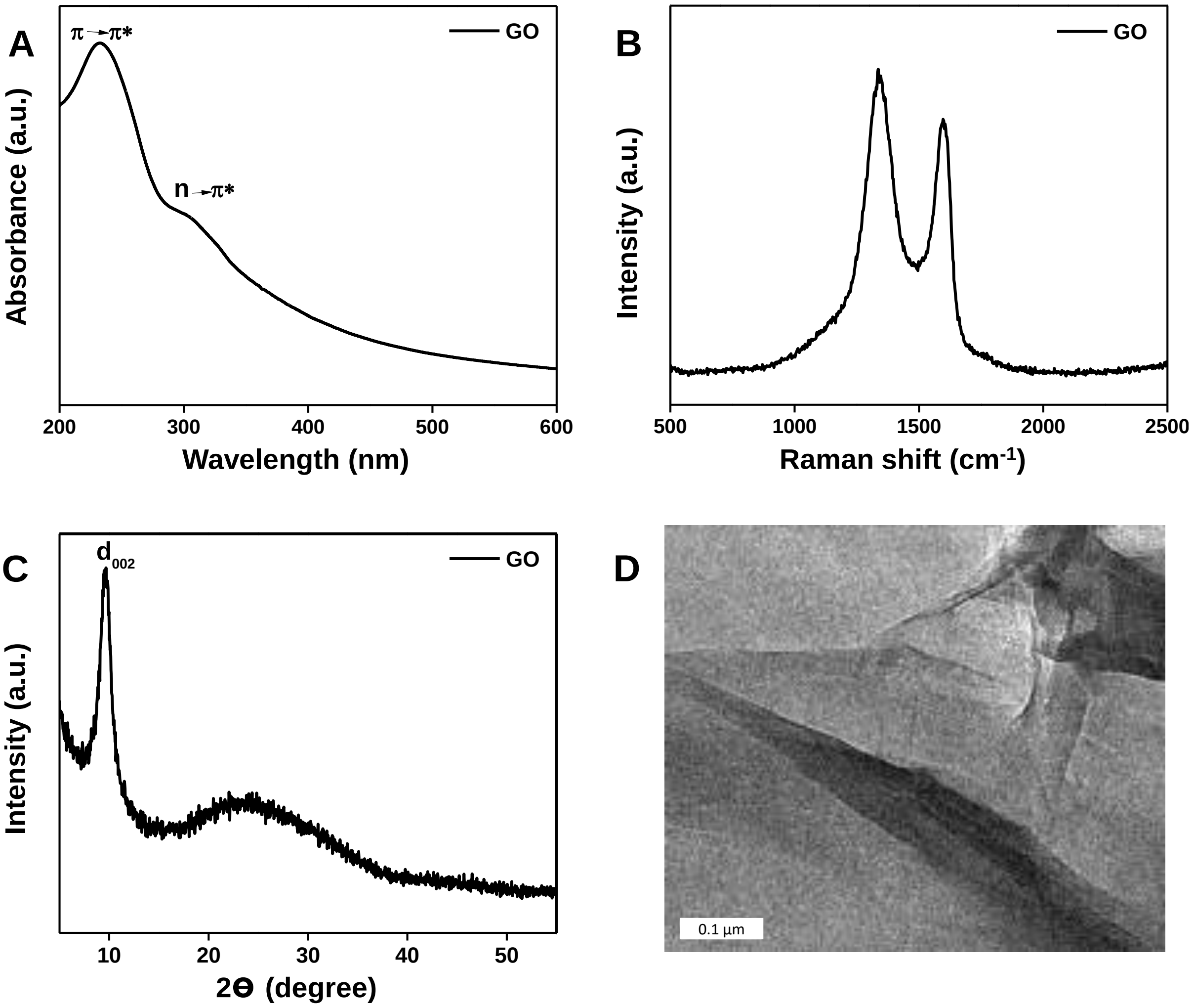

Figure S2. A) UV-Vis spectrum, B) Raman spectrum, C) XRD pattern, and D) TEM image of GO.

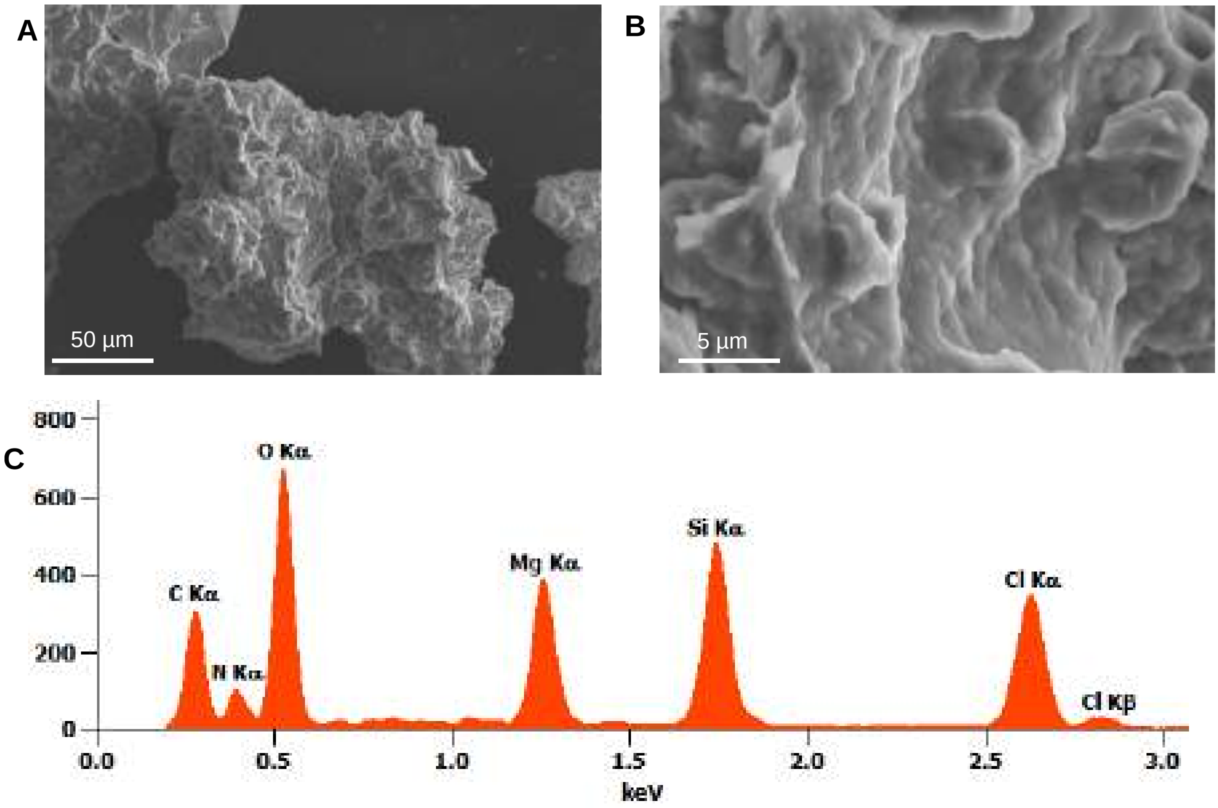

Figure S3. (A, B) FESEM images of AC at different magnifications. C) SEM EDS of AC.

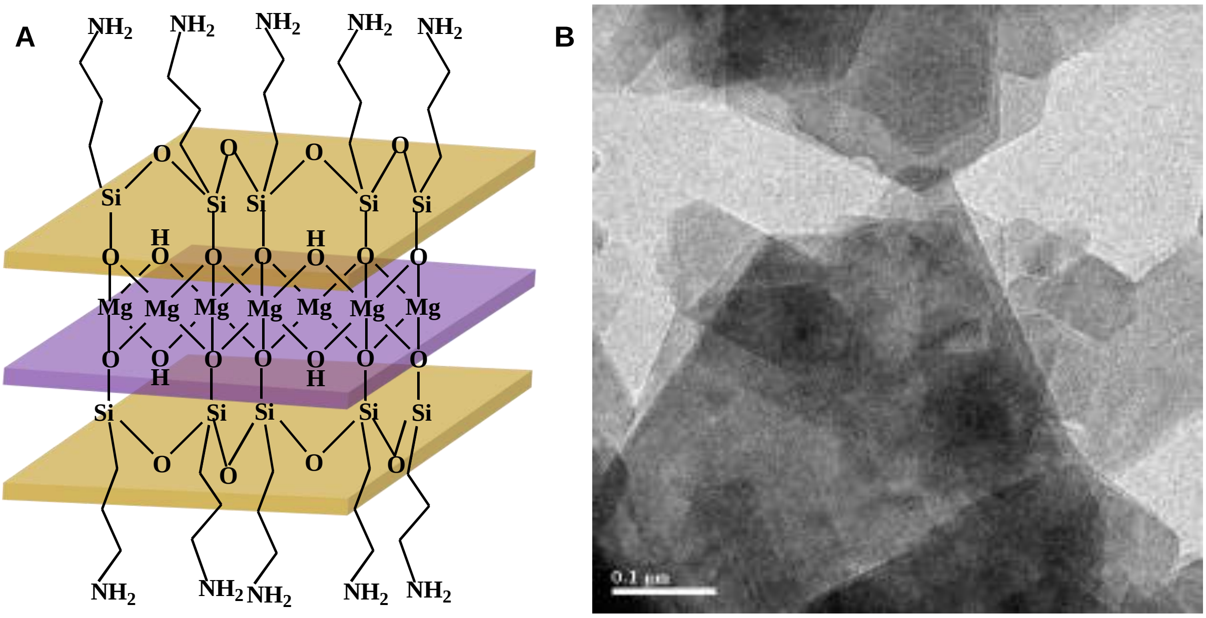

Figure S4. A) Schematic and B) corresponding TEM image of AC showing the layered structure.

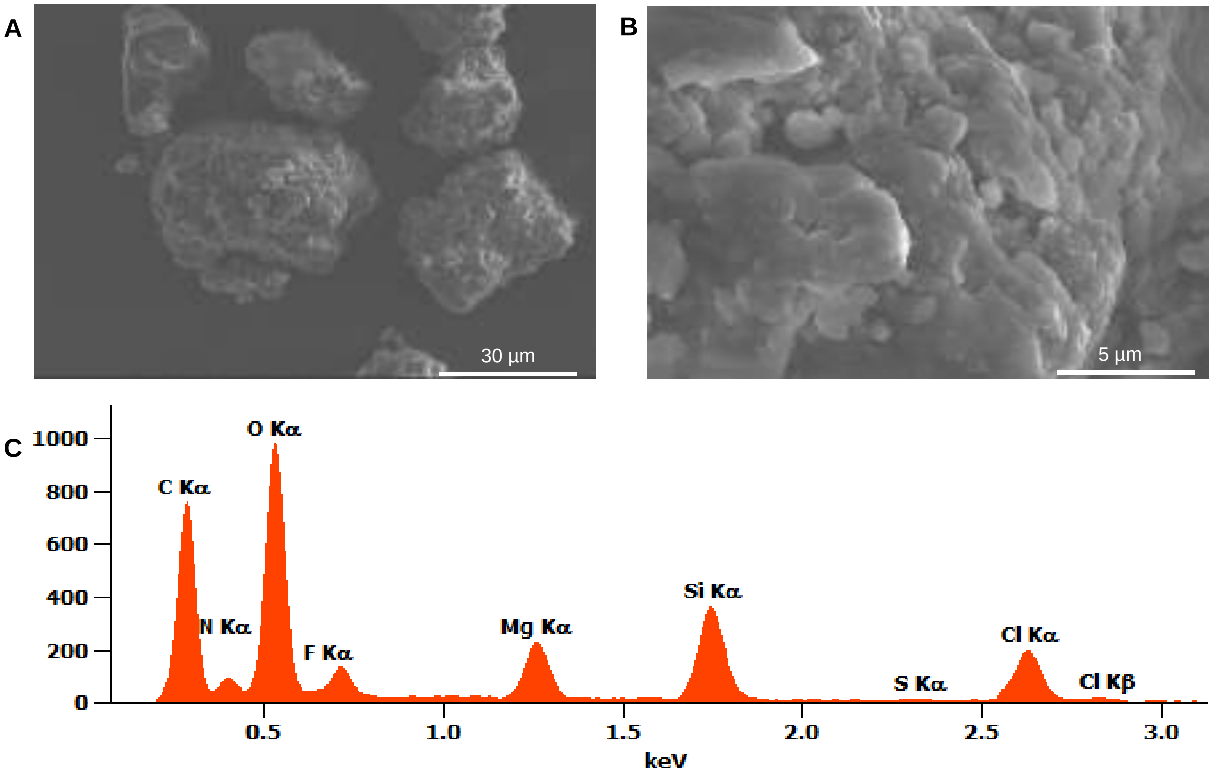

Figure S5. (A, B) FESEM images of AC-GO at different magnifications. C) SEM EDS of AC-GO.

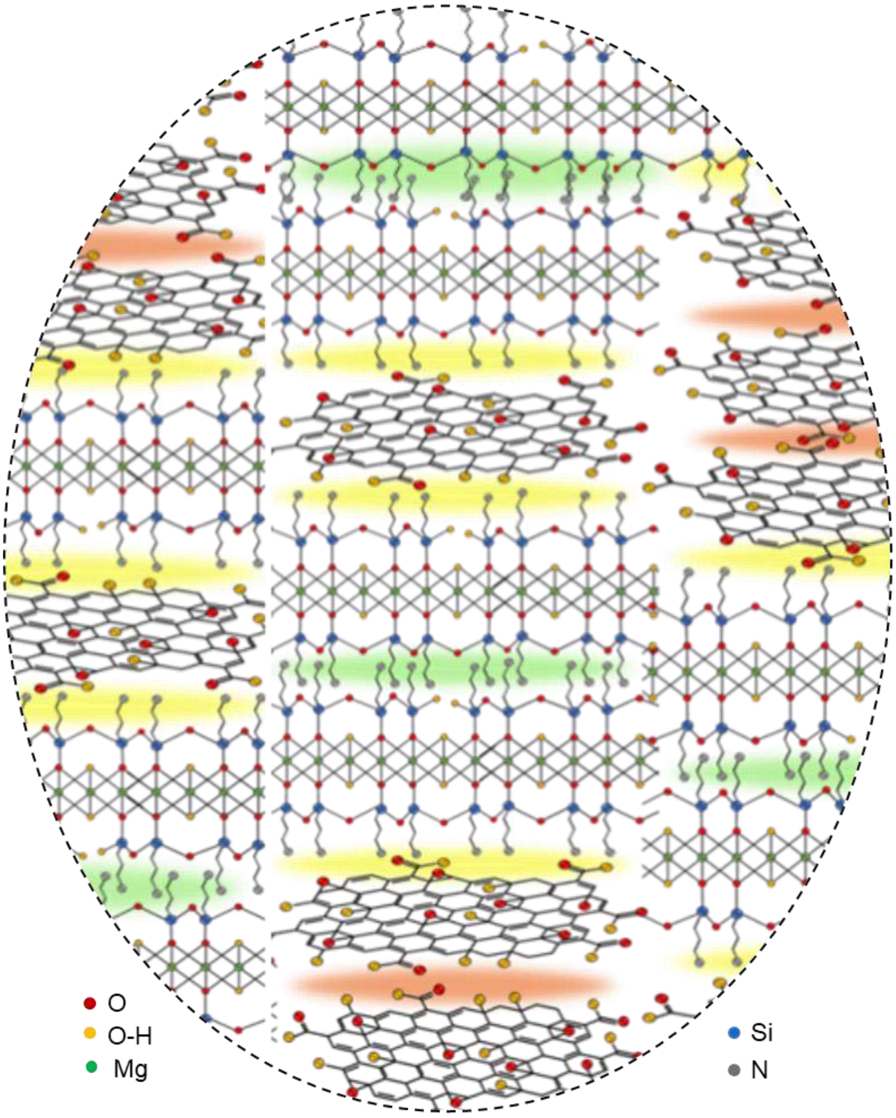

Figure S6. Possible bond formation between AC and GO in AC-GO composites (yellow shade shows AC and GO interaction, green shade for AC and AC interaction, and red shade for GO and GO sheets interaction).

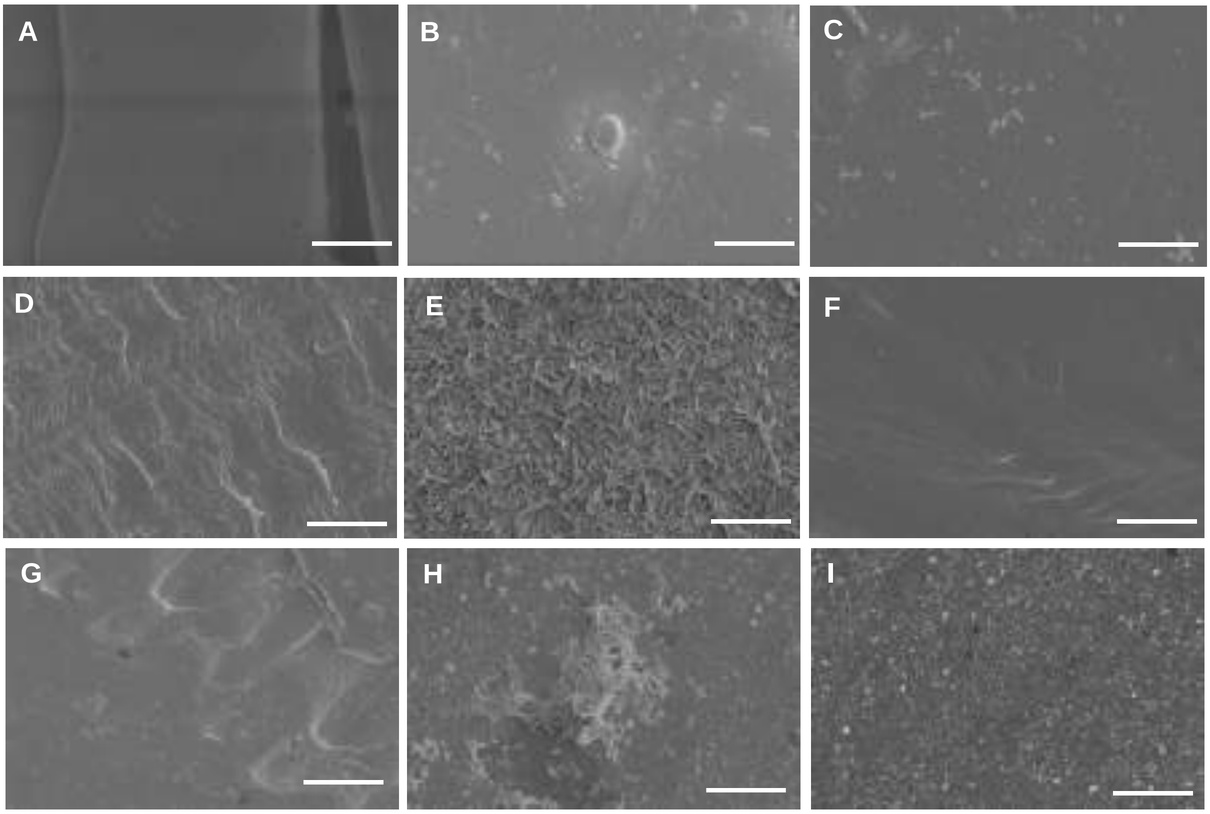

Figure S7. FESEM images of A) fabric, B) blank PSf and, loading dependent C) 0.005, D) 0.01, E). 0.015, F) 0.02, G) 0.025, H) 0.05 and I) 0.1 wt% of TFC/AC-GO membranes (scale bar for all images 5 µm).

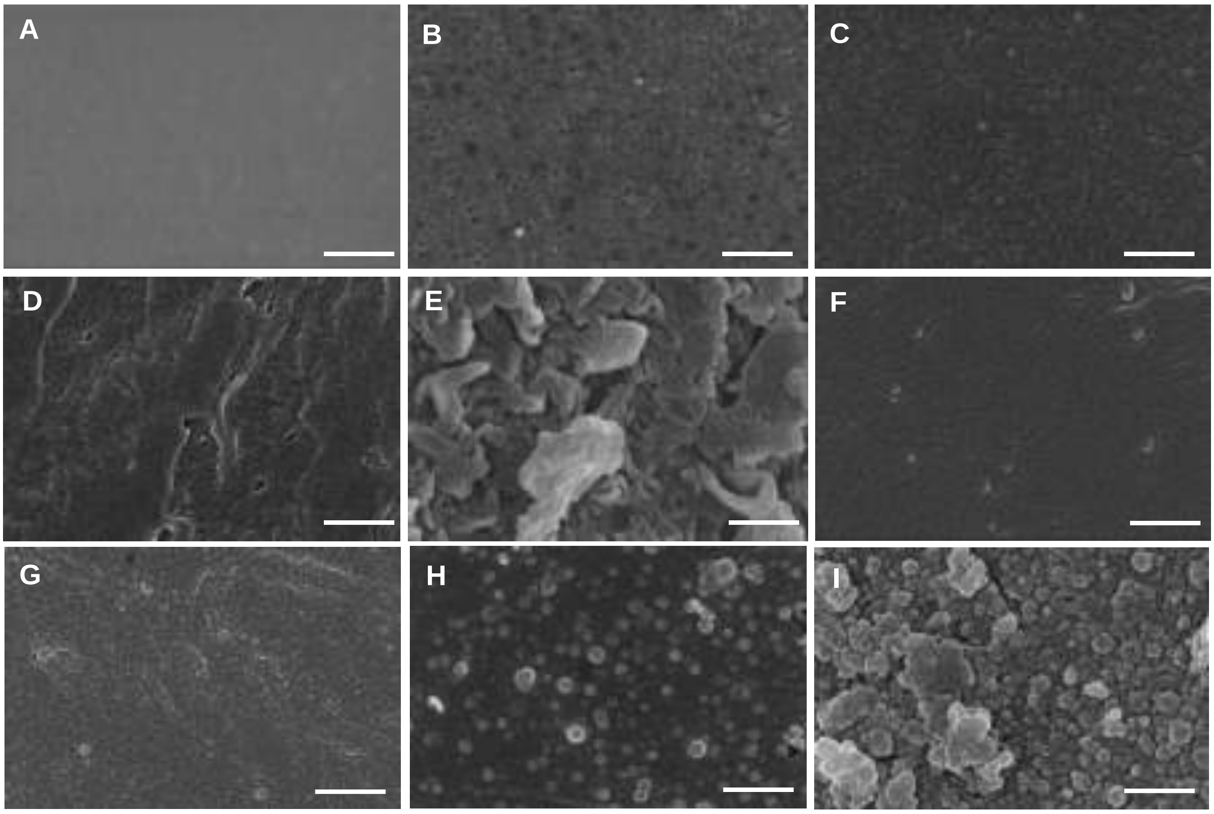

Figure S8. FESEM images of A) fabric, B) blank PSf and, loading dependent C) 0.005, D) 0.01, E). 0.015, F) 0.02, G) 0.025, H) 0.05 and I) 0.1 wt% of TFC/AC-GO membranes (scale bar for all images 500 nm).

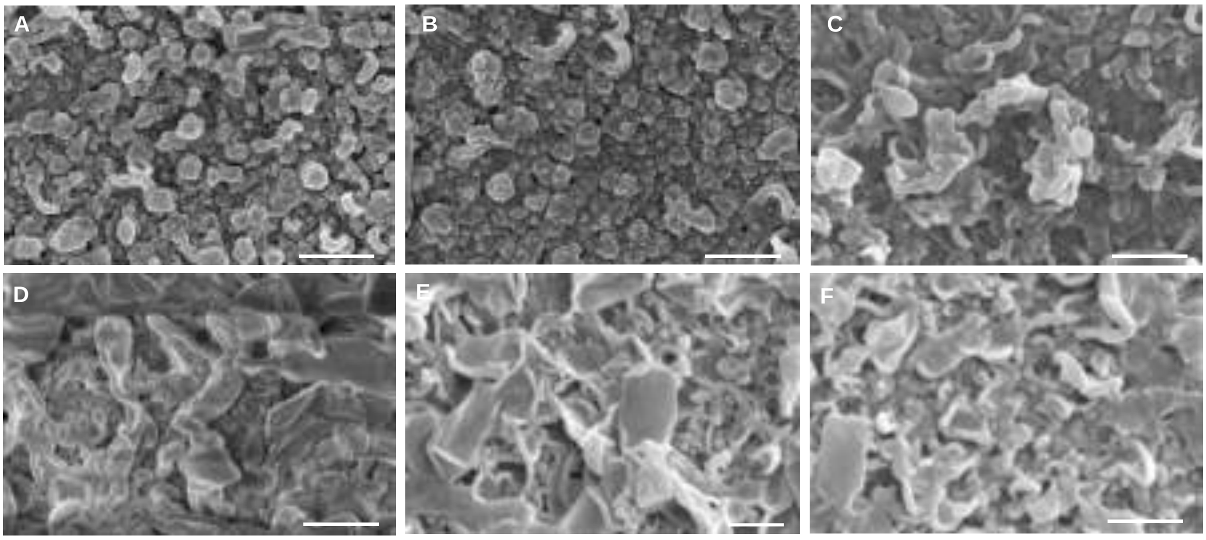

Figure 9. FESEM images of membrane: A) M10, B) M20, C) M30, D) M40, E) M50 and F) M60 (scale bar for all images 500 nm).

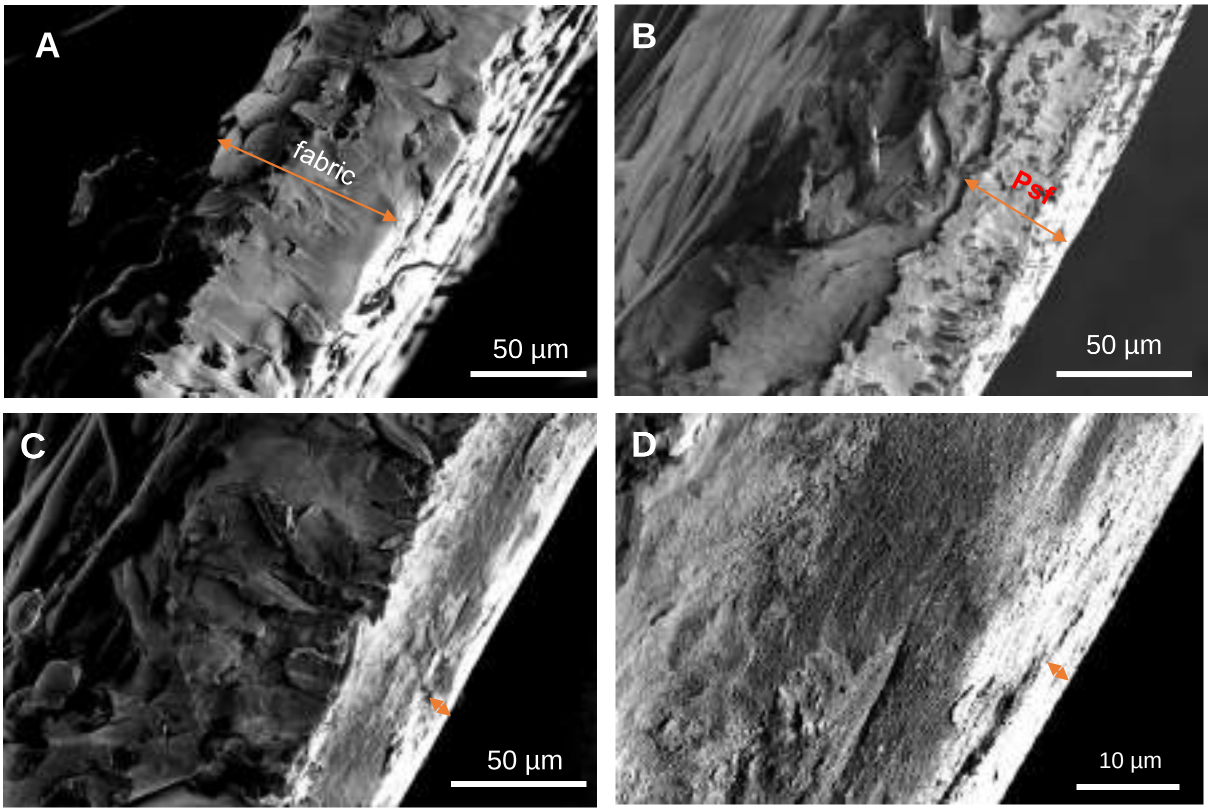

Figure 10. The cross-sectional view of A) fabric (scale bar 50 µm), B) fabric+PSf (scale bar 50 µm), C) M30 (scale bar 50 µm) and D) M30 membrane at higher magnification (scale bar: 10 µm).

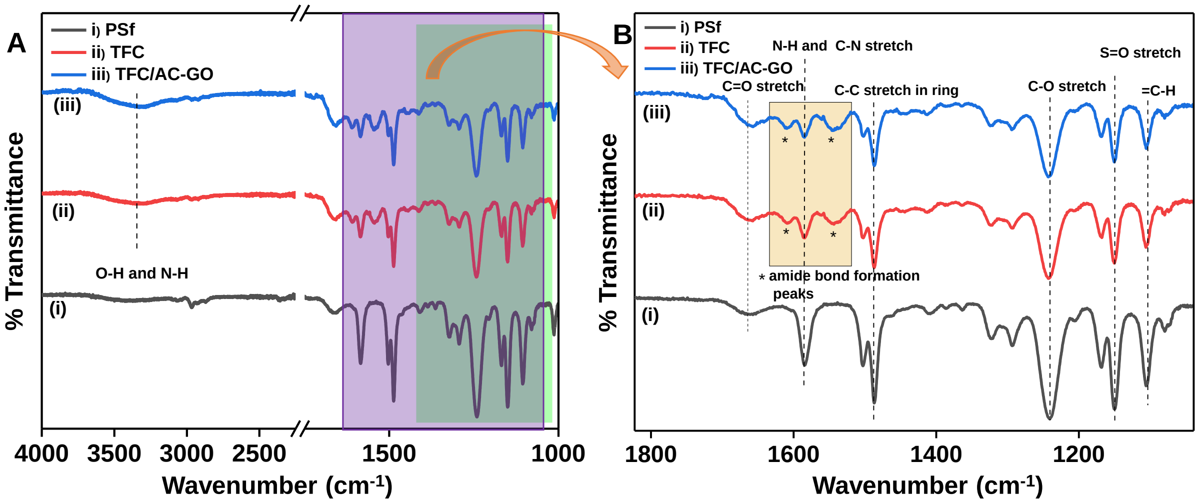

Figure S11. FTIR analysis of i) PSf, ii) unmodified TFC, and iii) AC-GO modified TFC membrane (M30).

Table S1. Water flux, % salt rejection and permeance for PSf support layer, unmodified M30, and modified M30 membranes (0.015 w% of AC, GO, and AC-GO) at 2000 ppm salt concentration and 20 bar pressure.

Membrane	**Flux (L/m^{2}h)**	**Permeance (Lm^{-2}h^{-1}bar^{-1})**	**% salt rejection**
PSf	8.04 ± 0.20	~ 0.402 ± 0.01	23.67 ± 1.58
PA	15.62 ± 0.36	~ 0.781 ± 0.02	97.03 ± 1.07
AC	32.02± 1.42	~ 1.601 ± 0.07	99.30 ± 0.36
GO	31.96 ± 1.55	~ 1.598 ± 0.08	99.51 ± 0.09
AC-GO	50.28 ± 1.69	~ 2.514 ± 0.08	99.51 ± 0.10

Table S2. Water flux and salt rejection studies of AC-GO modified M30 membrane at 20 bar pressure and different salt concentrations (2000, 5000, and 10,000 ppm).

	Salt concentration (ppm)					
Membrane	**2000 ppm**		**5000 ppm**		**10,000 ppm**	
	Flux (L/m^{2}h)	**% salt rejection**	**Flux (L/m^{2}h)**	**% salt rejection**	**Flux (L/m^{2}h)**	**% salt rejection**
M10	19.79 ± 1.22	99.36± 0.18	14.80 ± 0.58	99.33 ± 0.14	10.21 ± 0.44	99.02 ± 0.08
M20	46.47 ± 1.38	99.49 ± 0.12	37.68 ± 1.18	99.22 ± 0.07	23.91 ± 0.88	99.11 ± 0.05
M30	50.28 ± 1.69	99.51± 0.10	39.23 ± 1.16	99.41 ± 0.07	25.39 ± 0.80	99.21 ± 0.06
M40	47.42 ± 1.28	99.48 ± 0.08	36.32 ± 0.99	99.33 ± 0.07	23.07 ± 0.67	99.04 ± 0 11
M50	39.05 ± 1.08	99.29 ± 0.16	30.11 ± 0.69	99.24 ± 0.10	19.52 ± 0.40	98.70 ± 0.27
M60	40.13 ± 2.21	99.31 ± 0.07	29.04 ± 0.58	99.20 ± 0.11	20.69 ± 0.41	98.58 ± 0.05

Table S3. Pressure-dependent permeation studies of M30 membrane for feed water salt concentration of 2000 ppm.

Pressure (bar)	15	20	25	30	35	40
Flux (L/m^{2}h)	36.12 ± 0.99	50.28 ± 1.69	55.68 ± 1.94	66.63 ± 0.78	77.63 ± 1.73	85.60 ± 1.29

ACS Sustainable Chemistry & Engineering

pubs.acs.org/journal/ascecg Research Article

Cellulosic Ternary Nanocomposite for Affordable and Sustainable Fluoride Removal

Moses Egor,[‖] Avula Anil Kumar,[‖] Tripti Ahuja, Sritama Mukherjee, Amrita Chakraborty, Chennu Sudhakar, Pillalamarri Srikrishnarka, Sandeep Bose, Swathy Jakka Ravindran, and Thalappil Pradeep*

Cite This: *ACS Sustainable Chem. Eng.* 2021, 9, 12788−12799 Read Online

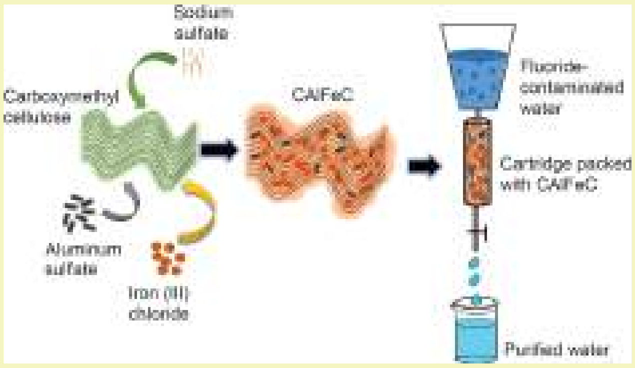

ABSTRACT: Adsorption is shown to be an extremely affordable and sustainable way of producing clean water, particularly in resource-limited settings. In this paper, we sought to synthesize an effective cellulose-based composite adsorbent from eco-friendly, earth-abundant, and consequently affordable ingredients at room temperature for fluoride removal from drinking water. We utilized the synergistic effect of various renewable materials and active sites of metal oxyhydroxides in developing an effective adsorbent, which is physically stable under the conditions of use. Nanoscale oxyhydroxides of aluminum and iron were scaffolded into a matrix of carboxymethyl cellulose (CMC) to form a nanocomposite adsorbent, which was prepared in water, eventually making a water-stable porous solid. This was used in batch and cartridge adsorption experiments for fluoride removal. The adsorbent surface before (*in situ*) and after fluoride uptake was characterized using various analytical techniques. The *in situ* composite exhibited a surface area of 134.3 m^2/g with an amorphous solid structure with Al and Fe uniformly distributed in the cellulose matrix. From the batch adsorption experiments, we observed 80% fluoride removal within the first 3 min of contact, with a maximum uptake capacity of 75.2 mg/g as modeled by the Langmuir adsorption isotherm, better than most reported materials. The adsorbent effectively reduced F^- levels in field water from 10 to 0.3 mg/L, less than 1.5 mg/L the World Health Organization upper limit for drinking water. Optimum F^- removal was achieved between the pH of 4−9; however, the effectiveness of the adsorbent was reduced in the presence of competing ions in the order $PO_4^{3-} > SiO_3^{2-} > CO_3^{2-} > HCO_3^- > SO_4^{2-}$. A cartridge experiment demonstrated the applicability of the adsorbent in a domestic point-of-use water purifier for defluoridation. Sustainability metrics of the material were evaluated. Defluoridation using the material is estimated to cost \$3.3 per 1000 L of treated water at the scale of community implementation projects.

KEYWORDS: *fluoride, defluoridation, carboxymethyl cellulose, iron oxyhydroxide, aluminum oxyhydroxide, composite adsorbent*

INTRODUCTION

Adsorption is widely used in environmental remediation applications, including air and water purification, targeting a wide range of organic and inorganic pollutants. Many water purification technologies utilize a variety of inorganic adsorbents such as oxides of Al, Fe, Ca, and Mn, silicates, and carbon-based adsorbents.[1−4] Biosorbents synthesized from alginates, chitosan, cellulose, and their derivatives with various functionalities have also been successfully applied in water purification.[5,6] On their own, these materials may not be very effective adsorbents and are often unstable and hence disintegrate in water, causing further contamination.[7] Efforts have been made to scaffold metal oxides in polymer frameworks for synergistic enhancement of adsorption capacity, along with stability.[8−10] Composite adsorbents consisting of metal oxyhydroxides embedded in organic polymer matrices have gained the attention of researchers due to their high adsorption efficiency and stability in aqueous media.[11−13] Such adsorbents utilizing organic matrices of chitosan, alginate, and cellulose, in which nanoparticles of metal oxides and hydroxides are confined, have been widely used to remove arsenic, Cr^{6+}, dyes, and fluoride from water.[5,11,14,15] Wang, Lin, Luo, and Long loaded Zr^{4+} onto carboxymethyl cellulose and reported impressive fluoride removal capacity of up to 47 mg/g. These and other studies[15−17] highlight the effectiveness of composite adsorbent

Received: May 15, 2021
Published: September 14, 2021

https://doi.org/10.1021/acssuschemeng.1c03272

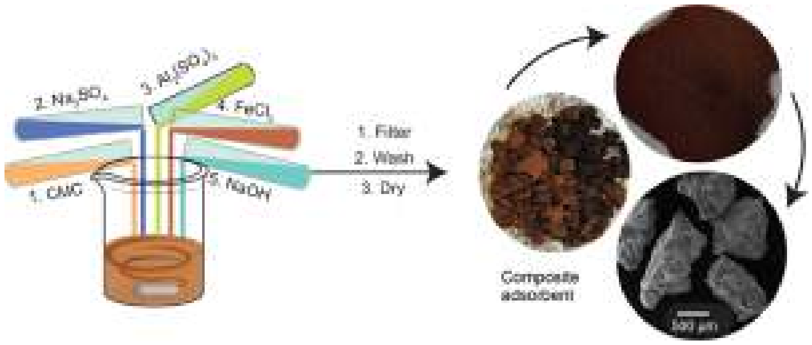

Figure 1. Schematic diagram illustrating the synthesis of CAlFeC.

materials used in the sequestration of both cationic and anionic water pollutants.

Over 30 countries are grappling with the health problems related to the ingestion of excess F^- (>1.5 mg/L) in surface and groundwater sources.[18] Fluorosis is prevalent in China, India, South America, North Africa, and countries along the East African rift valley. Fluoride pollution, therefore, is a global problem spanning nearly all geographical locations.[19] It is therefore evident that the need to develop affordable, effective, environmentally friendly, and sustainable defluoridation technologies can only increase, given the current and projected global demand for clean water. A key aspect of providing new solutions is affordability, implying the use of earth-abundant materials and simple processing.

In this paper, we present the facile synthesis, characterization, and application of a cellulose-based adsorbent referred to as a cellulose-Al-Fe nanocomposite (abbreviated as CAlFeC) by incorporating AlOOH and FeOOH into a carboxymethyl cellulose (CMC) matrix, which was used as an effective adsorbent to remove excess fluoride from water to bring it down to below the permissible guideline (<1.5 mg/L) of WHO. These metal oxyhydroxides have been shown to bear high adsorption potential owing to their metastable state, higher surface area due to their porous structures, nanoscale confinement in the polymer cages, and exposure of active surfaces for adsorption. CMC provides a rigid cellulose backbone onto which the metal oxyhydroxides are embedded, providing strength and rigidity even after prolonged exposure to water. Aluminum compounds have been shown to have very good F^- uptake capacity in several studies,[4,19] while iron(III) oxides provide structural rigidity and strength when embedded in polymer cages. Another similar study suggests that the synergistic action of these three main components is known to offer a rigid material with good adsorption capacity.[13] CAlFeC was used in batch and cartridge adsorption experiments to investigate adsorption kinetics in simulated field applications. The adsorbent was characterized before and after fluoride uptake using standard analytical techniques and a possible mechanism of F^- adsorption was developed.

From our evaluation, CAlFeC is a stable and effective adsorbent for fluoride, applicable under a wide range of environmental water conditions. At the adsorbent dose of 1 g/L, CAlFeC can be used to effectively reduce fluoride levels from 20 to <1.5 mg/L. From Table 2, even at elevated fluoride levels >20 mg/L, the amount of fluoride removed (q_e) increased, and increasing the adsorbent dose can achieve the desired 1.5 mg/L limit in the treated water. The material is easily synthesized from readily available nontoxic reagents and water as the only solvent used. All reactions were conducted at room temperature and under ordinary laboratory conditions without the need for sophisticated equipment or specialized skills. The ease and greenness of synthesis and the properties highlighted make CAlFeC suitable for use in low-income settings.

■ EXPERIMENTAL SECTION

Materials. Carboxymethyl cellulose (CMC) was purchased from Avantor Performance Materials India Ltd. Aluminum sulfate octadecahydrate ($Al_2(SO_4)_3 \cdot 18H_2O$) was purchased from Loba Chemie Pvt. Ltd., India. Ferric chloride hexahydrate ($FeCl_3 \cdot 6H_2O$) and NaOH were purchased from RANKEM Glassware and Chemicals Pvt. Ltd., India. Sodium sulfate anhydrous (Na_2SO_4) and sodium fluoride (NaF) were purchased from Merck India Ltd. All chemicals were of high-purity analytical grade and were used without further purification. Distilled water (DW) was used in all synthetic processes. Ultrapure water (QW) of electrical conductivity ~0.05 μS/cm and tap water (TW) of about 800 μS/cm were used in some batch adsorption experiments as described. Fluoride was determined by the ion-selective electrode (ISE) method (Thermo Scientific, Orion BNWP 96009). All reactions were carried out in polypropylene labware.

Methods: Synthesis of CAlFeC. About 132 mg of CMC, a cellulose precursor, was dissolved in 10 mL of DW and ultrasonicated for 5 min, followed by the addition of 1.4 g of sodium sulfate anhydrous with constant stirring for 1 h until the salt was dissolved. To this, 0.5 M aluminum sulfate solution (4 mL) was added, and the mixture was incubated for 3 h, followed by the addition of 1 M ferric chloride hexahydrate solution (4 mL), and was further incubated for 1 h. Sodium hydroxide solution (2 M) was added (about 15 mL) dropwise to adjust the pH of the mixture to 7. The resultant brown gel was further incubated for 12 h with vigorous stirring at room temperature, after which it was filtered and washed thoroughly with distilled water until the conductivity of the washed water was ≤200 μS/cm. The composite material formed was oven-dried at 60 °C for 12 h, after which it was ground, sieved to desired particle sizes, and used in fluoride adsorption studies. Figure 1 below shows a summary of the procedure used to synthesize CAlFeC.

The optimized synthetic protocol of CAlFeC above was arrived at after several separate reactions in which different parameters were optimized. The effect of polyvalent cations (Ca^{2+}, Mg^{2+}, Mn^{2+}, Zn^{2+}, Ce^{3+}, La^{3+}, Zr^{3+}, Ti^{4+}) and anions (SO_4^{2-}, SiO_3^{2-}, PO_4^{3-}, CO_3^{2-}, HCO_3^-) on the adsorbent structure was investigated. Each time, dry lumps of the solid adsorbent were shaken at 200 rpm with distilled water to evaluate the stability under wet conditions. The experimental conditions that yielded the adsorbent with the best balance of fluoride uptake and physical hardness (tested both in dry and wet conditions) were chosen for bulk synthesis and batch adsorption experiments. The adsorbent was ground and sieved to obtain particle sizes of 300, 212, and <150 μm (referred to as powder).

Adsorption Experiments. Effects of particle size, adsorbent dose, contact time, pH, initial adsorbate (fluoride) concentration, co-ions usually present in water, and the number of reusable cycles were evaluated in batch experiments. The aforementioned variables were

Table 1. Synergistic Effect of Components on the Strength and Effectiveness of CAlFeC

	composition				strength of material			
sample ID	CMC	Na_2SO_4	$Al_2(SO_4)_3$	$FeCl_3$	dry	wet	color of treated water	fluoride uptake (%)
CAlFeC1	√	√	√	—	very poor	very poor	turbid	95
CAlFeC2	√	√	—	√	excellent	excellent	very clear	24
CAlFeC3	√	—	√	√	poor	very poor	brown	96
CAlFeC4	—	√	√	√	poor	very poor	turbid	94
CAlFeC5	√	√	√	√	very good	very good	very clear	97

optimized to obtain the best conditions for the subsequent batch experiments. Typically, 100 mg of CAlFeC was placed in contact with 100 mL of 10 mg/L fluoride solution separately in DW and TW in a 250 mL polypropylene Erlenmeyer flask and shaken at 200 rpm in an orbital shaker for 2 h. The adsorption capacity of the material at particle sizes of 300 and 212 μm and powder was tested separately. After shaking, the mixture was decanted, and residual fluoride in the supernatant was determined by the ISE method (US-EPA method 9214). Fluoride-spiked laboratory TW was used to mimic environmental water. The choice of particle sizes of 300 and 212 μm was due to their applicability in cartridge packing in realistic applications.

The regeneration ability of CAlFeC was investigated using 0.1, 1, and 2 mol/L NaOH solutions as eluents. For the first cycle, a freshly prepared 10.3 mg/L fluoride-spiked water was placed in contact with CAlFeC for approximately 12 h. For the next cycle, the used adsorbent was filtered off and washed several times with NaOH solution and rinsed with DW, and then oven-dried at 60 °C.

Characterization of the Adsorbent. Fourier transform infrared spectroscopy (FTIR), Raman spectroscopy, X-ray diffractometry (XRD), scanning electron microscopy-energy-dispersive X-ray spectrometry (SEM-EDS), high-resolution transmission electron microscopy-energy-dispersive X-ray spectrometry (HRTEM-EDS), and Brunauer−Emmett−Teller (BET) surface area analysis techniques were used to characterize the adsorbent before and after fluoride uptake. SEM imaging was done with an FEI Quanta 200 coupled to the EDS system. Powdered samples of CAlFeC and fluoride-loaded CAlFeC (CAlFeC-F) were spread on carbon strips, sputter-coated with gold, and mounted. Powder XRD patterns of CAlFeC and CAlFeC-F were determined using a Bruker D8 Advance spectrometer at the Department of Chemistry, Indian Institute of Technology Madras, India. Raman spectra of CMC, CAlFeC, and CAlFeC-F were recorded using a confocal Raman spectrometer with 633 nm as the excitation source. BET surface area was measured by nitrogen adsorption−desorption experiments using a BET surface area analyzer (Micromeritics ASAP 2020). XPS analyses of elemental compositions of CAlFeC before and after its interaction with fluoride were performed using an ESCA Probe TPD spectrometer, Omicron Nanotechnology. Direct shear stress measurements were performed to determine the physical strength of the material in dry and wet conditions. The leaching of metals (Al and Fe) and total organic carbon (TOC) into the treated water was evaluated using the US-EPA method 1311. PerkinElmer NexION 300X inductively coupled plasma mass spectrometry (ICPMS) with appropriate standards and a TOC analyzer, Shimadzu TOC-V_{CPH}, were used to determine metal concentrations and TOC, respectively.

RESULTS AND DISCUSSION

Effect of Incorporating Other Polyatomic Anions as Binders. A crucial aspect of the material is its stability in water. We observed that sodium sulfate is essential for the stability and physical hardness of the material. Without it, the solid formed was easily crushed into powder, which would not be desirable in a water filtration column or cartridge as this would cause a pressure drop and possible leaching of its constituents into the treated water. Sulfate ions provide a stable linkage between cellulose fibers and the metal oxyhydroxides. In Figure 5, we have suggested a possible mechanism of binding of sulfate to facilitate crosslinking between cellulose chains, utilizing the OH groups.[21] The presence or absence of sodium sulfate, however, did not affect the fluoride uptake capacity of the adsorbent. It is known that carbonate and bicarbonate ions in solution interfere most with fluoride adsorption.[22] However, when carbonate and bicarbonate, instead of sulfate, were incorporated as binders into the adsorbent solid structure, there was a slight improvement in fluoride adsorption. The resulting adsorbent was, however, too soft to make a good filter cartridge or column packing. When sulfate was substituted with phosphate and silicate anions as stabilizers, there was a drastic reduction in the fluoride removal efficiency of the adsorbent (Figure S1B). The composite in which phosphate anion was incorporated as a binder formed a thick gel that could not be filtered or washed, and therefore its bulk synthesis was not viable. The addition of sodium sulfate, therefore, gave the best balance between fluoride removal, physical hardness of the solid adsorbent, and ease of gel separation. Poor fluoride uptake observed due to phosphate and silicate is attributed to their interference with adsorption sites and low porosity of the resultant adsorbent. This is consistent with a report of Kumar et al.[11]

Effect of Incorporating Other Polyvalent Cations. We investigated the effect of adding different polyvalent cations (Ca^{2+}, Mg^{2+}, Mn^{2+}, Zn^{2+}, Ce^{3+}, La^{3+}, Zr^{3+}, and Ti^{4+}) on the strength and fluoride uptake capacity of CAlFeC. The addition of other polyvalent cations gave mixed results, with some cations (Mg^{2+}, Mn^{2+}, and Zn^{2+}) resulting in better strength of the material but with very low fluoride uptake (Figure S1A), while others (Ca^{2+}, Ce^{3+}, La^{3+}, Zr^{3+}, and Ti^{4+}) resulted in a slight improvement in fluoride uptake performance with poor strength. However, the improvement was not significant enough to justify the additional cost of incorporating these extra components. It was observed that excluding Al^{3+} from the composition of the adsorbent drastically reduced its ability to remove fluoride, while the elimination of CMC, sodium sulfate, and ferric chloride yielded a very soft solid that completely disintegrated in water. The optimized composition described, therefore, yielded just the correct ratio of CMC/Al/Fe for the best balance of green strength, fluoride removal, and ease of gel separation. Fluoride removal capacity was lower in TW compared to DW due to the presence of competing ions. Figure S1A,B in the Supporting Information (SI) shows an increase in fluoride uptake capacity as the adsorbent particle size was reduced (from 300 μm to powder). A high surface area of powdered solid exposed more adsorption sites and hence improved the efficiency. However, granular solids (micron particles) are preferred for cartridge packing than powder to enhance hydraulic conductivity.

Synergistic Effect of the Components of CAlFeC. From the experiments done to investigate the effect of adding or removing the different components of CAlFeC, we found a cooperative interaction of the components to enhance the

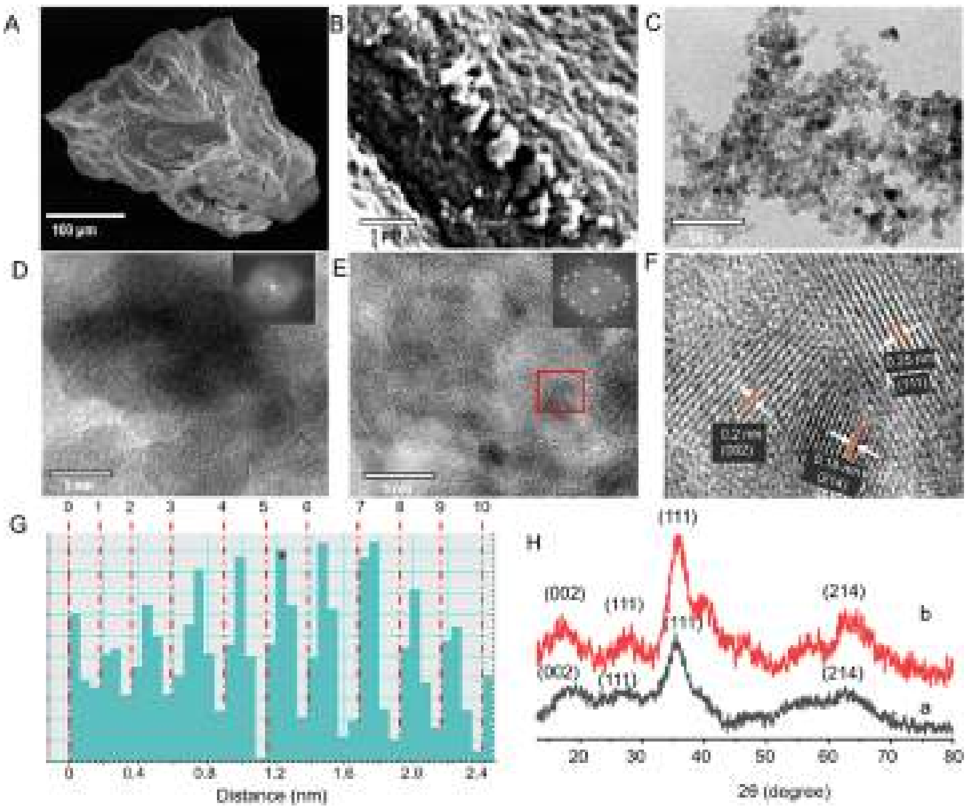

Figure 2. Micrographs and crystallographic features of CAlFeC showing SEM images (A, B; at a micron scale). HRTEM images (C−E) before beam irradiation (D) and after beam irradiation (E) with insets of corresponding FFT images. (F) Enlarged section of (E) showing lattice-resolved planes. (G) Lattice distance profile of FeOOH nanoparticles for the (111) crystal plane. It is a profile of 10 consecutive lattice planes, an average of which was considered as the lattice distance between the planes. (H) Powder X-ray diffraction patterns of CAlFeC before (a) and after (b) fluoride uptake.

properties of the adsorbent, i.e., its strength and effectiveness. As can be seen in Table 1, removing one or more of the components negatively affected the adsorption effectiveness and physical strength of the material. The increase in strength is attributed to entropic stabilization as more components are added, a phenomenon encountered in high entropy alloys. Fe^{3+} and Al^{3+}, upon interaction with other components of CAlFeC, and during coprecipitation with NaOH, resulted in the formation of a stable multicomponent system of different oxides, oxyhydroxides, and hydroxides, as confirmed by PXRD analysis. We determined that Al^{3+}, being a harder acid than Fe^{3+}, accounts for most of the fluoride removal capacity, while CMC, sulfate, and Fe^{3+} are mainly responsible for the structural rigidity of CAlFeC.

SEM images revealed a layered structure after the saturation of the composite surface with fluoride ions (Figure 2B). Elemental maps and EDS spectra show a fluoride signal only after fluoride adsorption (Figure S3). This confirms that fluoride is adsorbed and uniformly distributed on the adsorbent surface, as can be confirmed from mapping images in Figure S3A compared to S3B. HRTEM-EDS imaging of the adsorbent was carried out using a JEM 3010 (JEOL, Japan) coupled to the Oxford Semistem EDS system. The samples for HRTEM were prepared as drop-casts of the dispersion on carbon films supported on a copper grid and dried. Figure 2C−F shows the high-resolution transmission electron microscopic (HRTEM) images of CAlFeC at different magnifications. Figure 2D,E shows the time-dependent images of the same frame with insets of respective fast Fourier transform (FFT) images. The electron beam irradiation induced crystallization of the adsorbent structure. This is attributed to the crystallization of iron oxide/oxyhydroxide/hydroxide, which usually changes to more crystalline phases by electron irradiation.[23] Figure S4 presents the HRTEM elemental maps and atomic percentages of CAlFeC and CAlFeC-F, confirming fluoride uptake.

Lattice-resolved HRTEM image of CAlFeC (Figure 2F) reveals clear crystal planes (002), (111), and (214) with interplanar distances of 0.2, 0.245, and 0.18 nm of FeOOH, respectively. Semicrystalline nanoparticles of goethite and pseudoboehmite are responsible for the crystalline phases embedded in a largely amorphous cellulose matrix. The observed crystallization is due to the electron beam irradiation of the material. This results in more stable oxides/oxyhydroxides of Fe and Al such as hematite, goethite, and gibbsite by electron beam-induced crystallization.[13] This is corroborated by powder X-ray diffraction (PXRD) patterns of CAlFeC and CAlFeC-F.

In Figure 2H, the PXRD patterns reveal a largely amorphous solid structure with a few broad and less-intense peaks at 36 and 63° corresponding goethite (α-FeOOH) JCPDS no. 29-713. Other less-intense peaks that appeared at 27 and 57° matched with boehmite (γ-AlOOH), based on JCPDS no. 21-1307.[8] These crystalline phases also matched with the inorganic crystal structure database (ICSD) of goethite (α-FeOOH), gibbsite, hematite, hydrohematite, and a mixed Fe/Al oxyhydroxide with ICSD reference codes 03-0251, 33-0018, 89-8103, 33-664, and 13-157, respectively, from the ICSD

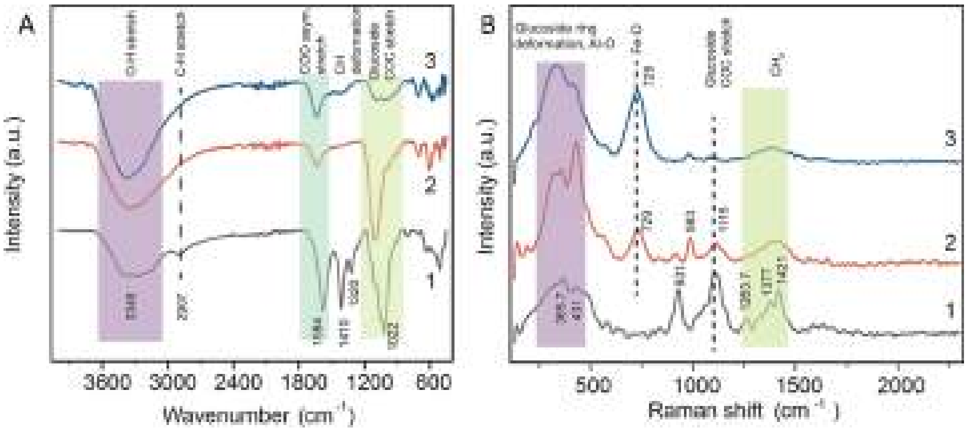

Figure 3. Vibrational spectroscopic features of the materials. (A) FTIR spectra of CMC (1), CAlFeC (2), and CAlFeC-F (3). (B) Raman spectra of CMC (1), CAlFeC (2), and CAlFeC-F (3). Note that FTIR data are presented in the transmission mode, and Raman data are in terms of scattering intensity.

database.[24,25] This confirms the presence of a mixture of metastable oxyhydroxides and oxides of iron and aluminum in the adsorbent structure. The high surface energies of these phases are responsible for the high adsorption capacity. Other previous studies[25,26] have shown that the FeOOH and AlOOH can be transformed to more crystalline phases by electron beam irradiation in TEM.

FTIR spectra of CMC, CAlFeC, and CAlFeC-F are presented in Figure 3A. The broad peak between 3200 and 3400 cm^{-1} is attributed to the stretching modes of O−H vibrations. This peak is more intense in CAlFeC and CAlFeC-F, which is due to the additional OH groups from metal oxyhydroxides and interstitial water molecules. Displacement of sodium ions and subsequent protonation of the carboxylate groups of CMC is another plausible explanation for the amplification of this feature. The peak at 2907 cm^{-1} corresponds to the −C−H stretching vibrations. This peak disappeared in CAlFeC and CAlFeC-F. The disappearance of $-CH_2-$ features is also seen at 1410 and 1320 cm^{-1}, an indication of strong binding of cellulose chains with metal oxyhydroxides during synthesis.

From Figure 3A, the peak at 1584 cm^{-1} is attributed to the asymmetric stretching of COO^- groups,[27] which diminished in CAlFeC and CAlFeC-F and shifted to 1640 cm^{-1}. This is due to the direct coordination of the carboxylate group to metal ions in a bidentate fashion, as indicated below.[28]

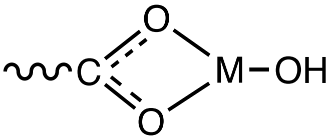

This confirms the participation of the COO^- group in strong metal binding during the formation of the nanocomposite. The prominent peak at 1022 cm^{-1} is assigned to the C−O−C of the β-1,4 glycosidic linkages between the sugar units of CMC. There is a reduction in the intensity of this peak in CAlFeC, and a much bigger reduction in CAlFeC-F, possibly due to surface coverage and also due to masking by fluoride. However, it has been shown that when the C−O−C links are vibrationally excited, all other atoms in the rings attached by that linkage are affected; hence, this peak cannot be assigned to the glycosidic link alone.[29] In the presence of an acidic solution of ferric chloride, some cellulose chains undergo hydrolysis and oxidation, leading to shorter oligosaccharide chains and gluconic acid.[30] This reaction is probably responsible for the cleavage of some C−O−C linkages in the cellulose chains and hence the lowering of intensity.

Raman spectra (Figure 3B) revealed the characteristic CMC features with few additional peaks due to the iron and aluminum oxyhydroxides in the composite. The broad peak between 300 and 500 cm^{-1} is due to the C−C−C, C−O−C, and C−C−O ring deformation of the glucopyranose rings. This peak became more prominent in CAlFeC and CAlFeC-F as it overlaps with the −OH vibration peaks of metal oxyhydroxides.[31] The Al−O characteristic peaks also appear in this region.[31] The peak at 729 cm^{-1} that appears in the nanocomposite is attributed to Fe−O stretching[23] but could be in combination with the γ vibration of OH groups of boehmite that also occurs at 730 cm^{-1}. The peak at 931 cm^{-1}, redshifted to 983 cm^{-1} in the composite, is assigned to COO^- deformation, whose intensity reduced in CAlFeC and CAlFeC-F as a result of strong metal−carboxylate group interaction highlighted in earlier IR data. The peak at 1115 cm^{-1} is attributed to C−O−C glycosidic stretch, with reduced intensities in CAlFeC and CAlFeC-F, possibly caused by restrictions to the vibrations of these groups as a result of confinement and masking in the composite matrix. The $-CH_2-$ twisting, wagging, and deformation peaks between 1200 and 1500 cm^{-1} become less prominent in the composite, which gives further evidence of a strong and complex interaction between CMC and other components of CAlFeC and adsorption of fluoride. Adsorption of fluoride did not significantly change the CAlFeC structure, implying physical adsorption rather than chemical transformation.

BET surface area for the as-prepared nanocomposite (before fluoride uptake) was obtained as 134.3 m^2/g. This high surface area is responsible for the excellent fluoride uptake capacity of CAlFeC. The average pore diameter of 74.259 Å was recorded, higher than what has been reported from similar materials.[13] This reveals the existence of mesopores in the material, which can be penetrated by free fluoride ions with an ionic radius of 1.47 Å. One may note that the surface area of best-performing materials is generally in this range and not very large.[11,13] The adsorbent recorded a pore volume of 0.298620 cm^3/g.

The XPS survey spectra of CAlFeC and CAlFeC-F are shown in Figure 4Aa,Ab, respectively. Deconvoluted peaks due to S 2p, Al 2p, Fe 2p, O 1s, C 1s, and F 1s are represented in Figure 4B−G, before (a) and after (b) adsorption of fluoride.

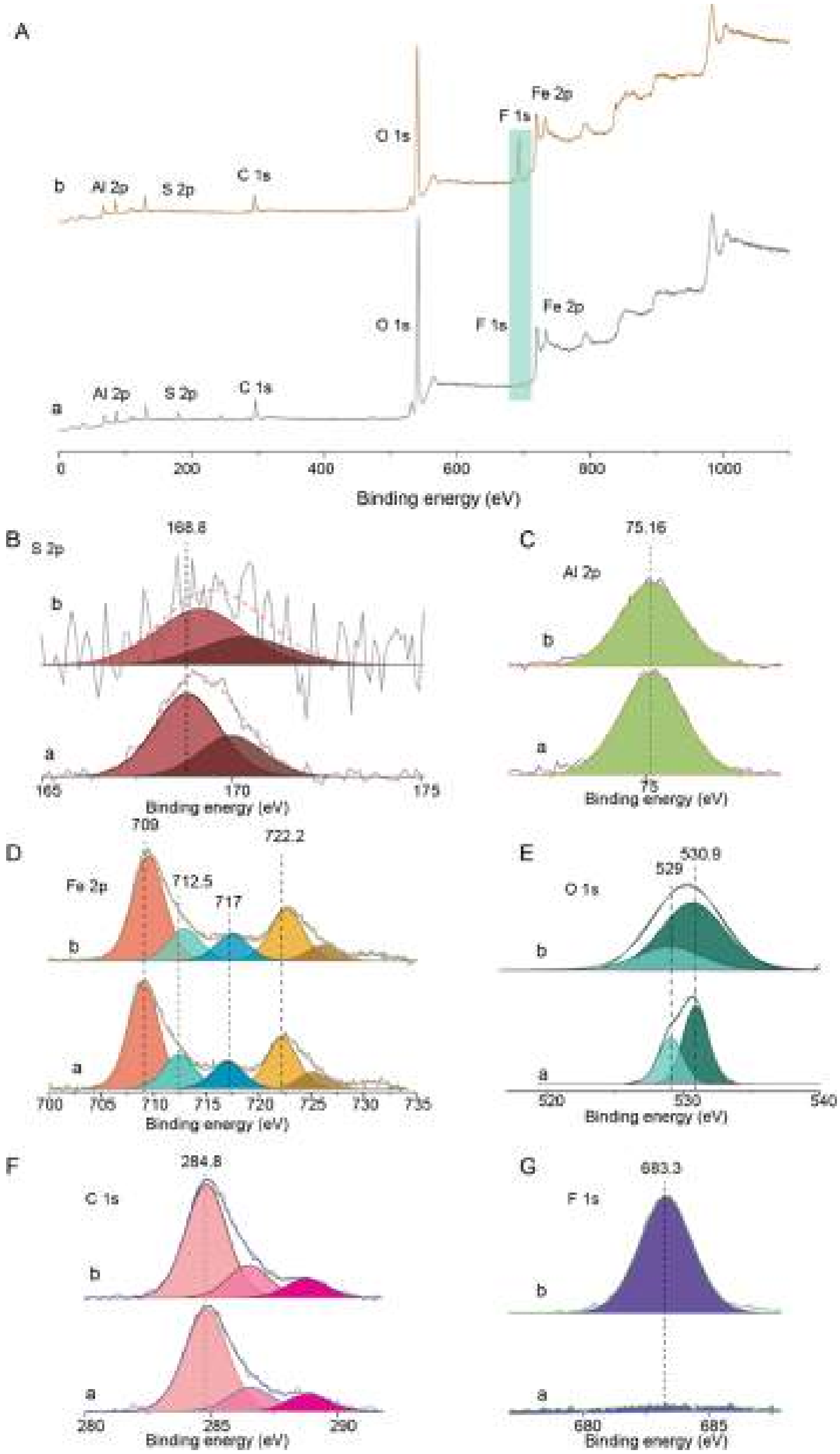

Figure 4. XPS features of CAlFeC: (A) survey spectra before (a) and after (b) fluoride adsorption; (B−G) XPS characteristics of the different elemental constituents of CAlFeC before (a) and after (b) fluoride uptake in each case.

The XPS spectrum of C 1s shows a characteristic peak at 284.8 eV for CAlFeC, which did not change after its interaction with fluoride. This is consistent with the observation by Mukherjee et al.[32] The peaks at 286.5 and 288.7 eV denote the presence of hydroxyl C−OH and carboxyl (C═O) bonds in the composite, which originate from

CMC.[32] The XPS peaks corresponding to F 1s appeared at 683.3 eV in CAlFeC-F but were absent in CAlFeC. This confirms the fluoride adsorption onto CAlFeC. The peak due to Al 2p appeared at its characteristic position at 75.2 eV and did not show any significant shift upon fluoride adsorption. The O 1s peak was very prominent at 530.9 eV, which did not show a change in its position after adsorption (Figure 4E). The peak due to Fe 2p appeared at 709.0 eV in CAlFeC but redshifted to 709.5 eV in CAlFeC-F. This points to the change in the bonding environment of Fe, possibly the exchange of −OH for F^- at the iron centers, leading to their increased stabilization owing to the chemisorption of fluoride. The S 2p peak is also significantly shifted from 168.8 to 169.2 eV. Although the bonding nature of sulfate in the nanocomposite is not fully understood, this result suggests its participation in fluoride binding. Figure 4 shows that except for Fe 2p and S 2p, most peak positions remained largely unchanged after fluoride adsorption, suggesting that a combination of physisorption and chemisorption contribute to fluoride binding, in addition to ion exchange and electrostatic surface interactions.[33]

Direct shear stress measurement was essential to evaluate the strength of the adsorbent. Dry and wet samples of the material were separately mounted in a shear box, and normal stress of 50, 100, and 150 kPa were applied, respectively, and the horizontal shear displacement was measured, as shown in Figure S2A. Figure S2B shows the Mohr−Coulomb failure envelopes for the dry and wet materials. The calculated internal angle of friction (φ) shown were 58.7 and 54.3° for the dry and wet materials, respectively, depicting a hard material comparable to dense gravel sand, a feature that is highly desirable for adsorbent-based water purifiers.[34]

Effect of Adsorbent Dose, pH, Counterion, and Cycle Study. The extent of fluoride removal increased with an increase in the sorbent dose to a saturation point at about 1 g/L (Figure S6A). This was taken as the sorbent dose for further experiments. At this adsorbent dose and initial fluoride concentrations <20 mg/L, the number of adsorption sites available was sufficient to lower fluoride concentrations to the permissible limit.

Change in pH of the medium affects not only the speciation of fluoride in solution but also the protonation state and thus the surface charge density of the adsorbent. At a relatively low pH, the adsorbent surface acquires a net positive charge as a result of the protonation of surface groups, as shown in eq 1.

$$\equiv \text{MOH} + \text{H}^+ \rightarrow \equiv \overset{+}{\text{M}}\text{OH}_2 \qquad (1)$$

This favors fluoride adsorption owing to electrostatic attraction and displacement of H_2O from the sites. However, when the pH is lower than 4, fluoride exists in a protonated form as HF, and the loss of negative charge lowers its uptake by the adsorbent.[22] From Figure S6B, we see that CAlFeC effectively adsorbs fluoride within a relatively wide pH range (4−9), consistent with other studies on similar materials.[32] Increase in pH beyond 9 lowered its fluoride uptake capacity. This is due to a negative charge imparted on the adsorbent surface at a pH higher than the pH_{pzc}, thereby repelling fluoride ions, consistent with other reports on similar materials.[3] Reduced fluoride adsorption at higher pH can also be attributed to competition for the adsorption sites with excess hydroxide ions.[22]

The effect of counterions, commonly present in environmental water, on the defluoridation capacity of CAlFeC was tested. It was observed that Cl^-, NO_3^-, SO_4^{2-}, Mg^{2+}, Ca^{2+}, Na^+, and K^+ did not significantly affect the fluoride uptake capacity of the adsorbent. However, the presence of CO_3^{2-}, HCO_3^-, PO_4^{3-}, and SiO_3^{2-} in contaminated water reduced the effectiveness of the adsorbent in the order $PO_4^{3-} > SiO_3^{2-} > CO_3^{2-} > HCO_3^- > SO_4^{2-}$ (Figure S6C). Fortunately, the levels of phosphate in environmental water are usually low. The bulky and highly charged orthophosphate anion is thought to be preferentially adsorbed to the cationic surface groups or blocks them, excluding fluoride. This is consistent with the research findings of another study, which found a similar trend of interference by coexisting ions.[35]

To regenerate an adsorbent sustainably, the eluent should have a quick desorbing ability, be affordable, and should not damage the adsorbent surface.[17] We, therefore, used NaOH and avoided acidic eluents that could easily react with metallic oxides in CAlFeC. The regeneration efficiency of the materials is shown in Figure S6D. When the spent adsorbent from the first cycle was washed with 2 mol/L NaOH, it retained 64% effective capacity even after the 4th cycle. The adsorbent can be regenerated and reused up to four times, hence reducing the cost of treated water. A higher concentration of NaOH was found to be a more effective regenerant.

Adsorption Isotherms. To gain an insight into the mechanism of adsorption, 100 mg of the adsorbent was contacted with 100 mL of varied initial fluoride concentrations (ranging from 3.2 to 202 mg/L) and stirred at 200 rpm in an orbital shaker for 24 h. The equilibrium adsorption capacity is usually expressed as the extent of adsorption in milligram of adsorbate loaded per gram of adsorbent (q_e), and the adsorption efficiency is calculated from eqs S1 and S2. The data obtained, presented in Table 2, were fitted into the Langmuir, Freundlich, Temkin, and Dubinin-Radushkevich adsorption isotherm models.

Table 2. Effect of the Initial Fluoride Concentration on the Adsorption Capacity of CAlFeC

C_o (mg/L)	C_e (mg/L)	q_e (mg/L)	fluoride removal (%)
3.2	0.09	3.11	97.2
6.2	0.2	6	96.8
10.5	0.46	10.04	95.6
17.3	0.89	16.41	94.9
27.2	2.6	24.6	90.4
52.7	14.5	38.2	72.5
78.9	32	46.9	59.4
105	48.5	56.5	53.8
157	91	66	42
202	125	77	38.1

From Table 2, we see that at the adsorbent dose of 1 g/L used, water containing up to 20 mg/L of fluoride can be effectively treated to the acceptable level of 1.5 mg/L. When the fluoride concentration is higher than 20 mg/L, a higher dose of CAlFeC can be used to achieve the required fluoride concentration in treated water. The amount of fluoride adsorbed (q_e) generally increased when higher initial fluoride concentrations were used, indicating the abundance of adsorption sites.

The Freundlich isotherm describes nonideal and reversible adsorption, usually physisorption, on heterogeneous adsorbent

Table 3. Comparison of CAlFeC with Other Similar Adsorbents

adsorbent	solvent(s) used in synthesis	maximum synthesis temperature (°C)	optimum pH of use	adsorption capacity, q_{max} (mg/g)	ref
Al_2O_3-Fe_3O_4-expanded graphite	acetic acid, vitriol	450	2−10	2.19	35
chitosan-based Ti−Al binary metal oxide	acetic acid, hydrochloric acid	425	3−10	2.22	37
magnesium-iron-aluminum trimetal composite	water	600	3−9	92.85	38
cellulose nanofiber-polyaniline-templated ferrihydrite nanocomposite	aniline	room temperature	3−4	50.8	13
La-doped Li−Al-layered double hydroxides supported by a polymeric anion exchanger	water, ethanol	70	4−9	75.7	8
Fe_3O_4/Al_2O_3 nanoparticle-coated polyurethane foams	methanol, petroleum ether	100	2−6	43.47	16
chitosan-reinforced Zr_xAl_{1-x} OOH nanocomposites			3−10.5	9.44	17
cellulosic FeOOH/AlOOH composite	water	room temperature	4−9	75.2	this study

surfaces. This empirical model can be applied to multilayer adsorption, with a nonuniform distribution of heat of adsorption and affinities over the heterogeneous surface.[36] The linear form of Freundlich isotherm is given in eq S3 in the SI. Fitting our data to this model (Figure S7B) gave linear regression, $R^2 = 0.9603$. The slope ranging between 0 and 1 is a measure of adsorption intensity or surface heterogeneity, becoming more heterogeneous as its value reaches closer to zero. A value below 1 indicates chemisorption, while $1/n > 1$ depicts cooperative adsorption.[36] We obtained a slope of 0.4 and $n = 2.5$, implying a fairly heterogeneous adsorbent surface and favorable adsorption.[6] The linear form of Langmuir isotherm is given in eq S4 in the SI. This model assumes equivalent adsorption sites on a uniform sorbent surface and no interaction or transmigration of adsorbed particles in a monolayer surface coverage.[36] Our adsorption data fitted best to the Langmuir isotherm (Figure S7A), with $R^2 = 0.9729$, and with an impressive maximum adsorption capacity, $q_{max} = 75.2$ mg/g. Such a high value of q_{max} has hardly been attained by other reports of fluoride adsorption.

Many similar adsorbents reported in other studies are only effective at low pH, or are less effective at neutral pH, or are difficult to separate from treated water. Besides, many of the reported synthetic protocols utilize aggressive chemicals, solvents, and temperatures. These problems are effectively solved in the present study. From Table 3, CAlFeC compares favorably with other related adsorbents in ease of synthesis, performance, and optimum pH range.

This, however, is not surprising, given the high porosity and surface area of CAlFeC, and hence the availability of adsorption sites. This implied that fluoride was largely chemisorbed in a monolayer on equivalent sites on the sorbent surface. This is consistent with the proposed mechanism of fluoride interaction with a similar adsorbent studied by Barathi et al.[33] in which a combination of ion exchange, Coulombic attraction, and hydrogen bonding is believed to be responsible for fluoride adsorption. An essential feature of the Langmuir isotherm is the separation factor R_L, which is calculated from eq S5 in the SI. The R_L value indicates the adsorption to be either unfavorable ($R_L > 1$), favorable ($0 < R_L < 1$), or irreversible ($R_L = 0$). In this work, $0 < R_L < 1$, indicates favorable adsorption. The Temkin isotherm model is presented in eq S6. It was initially used to describe the adsorption of hydrogen onto platinum electrodes within acidic solutions.[36] Its derivation assumes a uniform distribution of binding energies of the adsorbate. This model assumes that the heat of adsorption of all molecules in the layer would decrease linearly rather than logarithmically with coverage. Our data agreed fairly with this model, with $R^2 = 0.9537$ (Figure S7C).

The Dubinin-Radushkevich isotherm model is usually used to describe the adsorption mechanisms involving heterogeneous surfaces with Gaussian energy distribution. It is represented as eq S7 in which the parameter ε is obtained from eq S8 in the SI. The Dubinin-Radushkevich isotherm model is temperature-dependent, and when adsorption data at different temperatures are fitted, all suitable data lie on a characteristic curve. The model has often successfully fitted high and intermediate adsorbate concentrations; however, our data did not fit very well ($R^2 = 0.79$), as shown in Figure S7D.

Adsorption Kinetics. To investigate adsorption kinetics, the effect of contact time on fluoride uptake was studied. Fluoride solution (100 mL, 10.4 mg/L) was shaken with 100 mg of the sorbent. About 5 mL of the solution was withdrawn at different time intervals and tested for residual fluoride. Figure S8A shows that up to 80% of the fluoride was removed within the first 3 min, and equilibrium was attained within the 30 min of contact, indicating fast adsorption kinetics. This is essential as clean water can be obtained within a few min of treatment with the adsorbent. In all other experiments, a contact time of 120 min was used to ensure reaching the equilibrium concentration. Kinetic data were fitted into pseudo-first-order, pseudo-second-order, and intraparticle diffusion models.

The Lagergren pseudo-first-order model is given by the eq S9 in the SI.[39,40] CAlFeC adsorption data did not fit very well into this model, with $R^2 = 0.917$ (Figure S8C). Ho and McKay[41] developed the pseudo-second-order kinetic model based on the assumption that the rate-limiting step is chemical adsorption involving valence forces through sharing or exchange of electrons between sorbent and sorbate. The pseudo-second-order model is given by the eq S10 in the SI. Fluoride adsorption onto CAlFeC fitted best into this model with linear regression, $R^2 = 0.9999$ (Figure S8B). This is also in agreement with the fact that fluoride adsorption onto CAlFeC also obeys the Langmuir isotherm, hence giving evidence for the predominance of chemisorption. In this case, we suggest that the exchange of fluoride ions for surface hydroxide of AlOOH and FeOOH is as shown in the proposed mechanism illustrated in eq 2 and Figure 5.

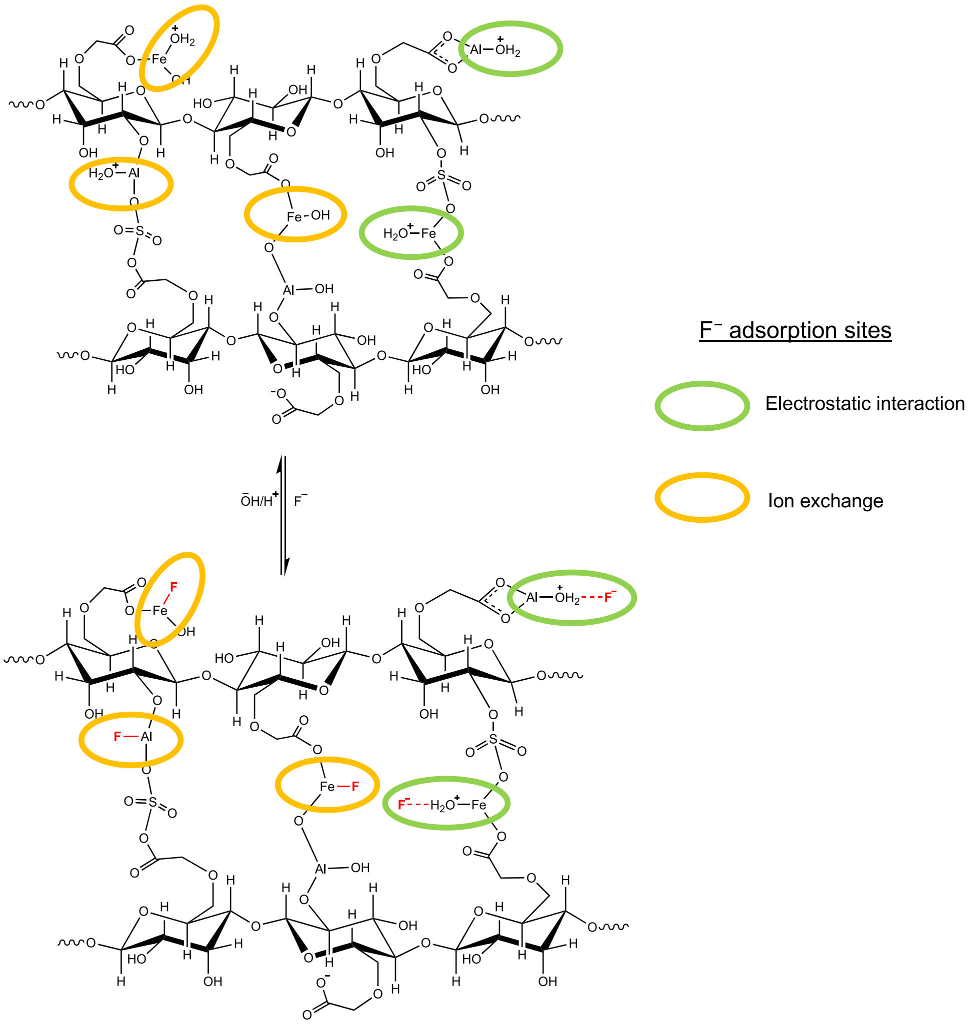

Figure 5. Proposed structure of CAlFeC and the suggested mechanism of fluoride adsorption. The metal centers shown here represent the oxyhydroxides.

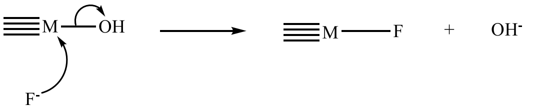

$$\equiv M-OH + F^- \longrightarrow \equiv M-F + OH^- \qquad (2)$$

Other related studies have proposed a similar mechanism of fluoride adsorption.[20,33]

Ionic interaction with protonated surface groups such as $\equiv M-\overset{+}{O}H_2 - - - - - - - - {}^{-}F$ is believed to be the other mechanisms of fluoride adsorption onto CAlFeC; moreover, protonated OH groups are good leaving groups that can be easily replaced by F^-. According to the Weber-Morris intraparticle diffusion kinetic model, in many adsorption cases, solute uptake varies almost proportionally with $t^{1/2}$ instead of t (where t is the contact time), as shown in eq S11[42] in the SI. The contribution of intraparticle diffusion in the transfer of adsorbate from the bulk of the solution into the porous solid structure cannot be ignored. This is often the rate-determining step when adsorption occurs in a rapidly stirred batch reactor.[43] Despite its contribution to the overall fluoride uptake, our experimental data fitted fairly to this model, with $R^2 = 0.9067$ (Figure S8D).

Leaching Experiment for TOC, Fe, and Al. The extent of leaching of total organic carbon (TOC), aluminum, and iron from the adsorbent into the treated water was evaluated. TOC was measured in the water before and after contact with CAlFeC using a TOC analyzer (Shimadzu TOC-V_{CPH}). The values of TOC were below the US-EPA permissible limit of 4 mg/L (Figure S5C); hence, there was no significant risk of formation of toxic organics even if chlorine disinfection was applied to the treated water. Leaching of iron and aluminum was determined using ICPMS (PerkinElmer NexION 300X). Ultrapure water before and after contact with the adsorbent was prepared in 5% nitric acid, and iron and aluminum were measured in a precalibrated ICPMS. The leaching protocol followed the US-EPA method 1311. The amount of iron was found to be below the US-EPA and WHO limits for drinking water, in the range of 64−140 μg/L, within the acceptable limit of 300 μg/L. Aluminum levels in purified water ranged from 26 to 120 μg/L in the experiments done with different particle sizes. All samples contained aluminum levels lower than the guideline value of 200 μg/L. These results indicate the inorganic components (metal oxyhydroxides) are mostly confined in the polymer cages, not easily leached, yet accessible to provide safe and clean drinking water upon removing fluoride.

Cartridge Experiment. A cartridge setup illustrated in Figure S5A was used to test the field applicability of CAlFeC to remove fluoride from water. Field water, with characteristics given in Table S1, was spiked with fluoride to 10.4 mg/L and passed through a cartridge packed with 21.7 g of CAlFeC of particle size 212 μm with the flow rate maintained at 10 mL/min. Figure S5B shows the changes in fluoride levels and pH of purified water after passing through the CAlFeC cartridge. It was found that about 20 liters of water contaminated with 10 mg/L of fluoride can be treated to less than 1.5 mg/L (WHO limit). Upon passing through CAlFeC, the pH of the water was slightly lowered from 8.0 to about 6.8, initially (Figure S5B), still within the normal pH range of 6.5−8.5 for potable water. This slight reduction in pH can be corrected by passing it through a second cartridge in series packed with a calculated amount of lime.

Sustainability Metrics. The sustainability of synthesis and utilization of CAlFeC was evaluated using sustainability indices and greenness parameters. These are the indicators of environment-conscious approaches to chemical reactions and manufacturing processes.[44−46] These indices were calculated using standard equations given in the SI, eqs S12−S16, and a summary of the results is shown in Table 4.

Table 4. Sustainability Metrics for the Synthesis and Use of CAlFeC

sl. no.	parameter	value
1	mass intensity (kg/kg)	5.68
2	water intensity (kg/kg)	36.67
3	reaction mass efficiency (%)	17.6
4	energy intensity (kW·h/kg)	2.0
5	*E* factor	0.124

Raw Materials. The major raw materials used were CMC, which was obtained from renewable plant materials, and the aluminum and iron salts used were nontoxic. The alkali used was neutralized during coprecipitation of an acidic solution of Al^{3+} and Fe^{3+}. The only solvent used was water, which is mostly reused and is easily recyclable. All raw materials are readily available and affordable.

Mass Intensity. Mass intensity is a measure of the total mass of materials used to produce a specified mass of product. Materials include reactants, reagents, and catalysts. Ideally, Mass intensity equals unity when no waste is produced and all materials are incorporated into the product. Mass intensity was determined from eq S12 and was found to be 5.68 kg/kg. This value could be improved by minimizing the loss of product during the filtration and washing process. Water intensity was estimated from eq S13 in the SI and was found to be 36.67 kg/kg, a relatively high figure, but comparable to the findings from other similar studies.[13,32] The water (over 95%) was used for washing the material, and this can be recycled and reused. A significantly large amount of water was used to wash the material before drying, and this spent water can be stored and used in the next several rounds of preliminary washing before it is recycled.

Reaction Mass Efficiency. Reaction mass efficiency was determined from eq S14, and a value of 17.6% was obtained. From our calculations, about 5 L of water (used mainly to wash the composite) is required to form 300 g of adsorbent, which can give about 300 L of purified water. The whole process is, therefore, water positive. Regeneration and reuse of adsorbent can significantly improve these figures.

Energy Intensity. Using eq S15, it was found that about 2 kW·h/kg of electricity was required for stirring, suction filtration, and oven-drying. Electricity cost could be reduced by scaling up the quantity of material synthesized and by utilizing sunshine to dry the material.

Resulting Emissions. The synthesis of CAlFeC does not produce any harmful solvents, fumes, or byproducts. Spent water used in washing has high TDS but can be recycled and reused. The *E* factor (environmental factor) was estimated from eq S16 and was found to be 0.124, an indication of a negligible amount of waste products during synthesis. An *E* factor close to the ideal value of zero signifies the optimal utilization of reagents and minimization of waste products.

Toxicity Potential. CMC is a nontoxic food-grade substance. $Al_2(SO_4)_3$ and $FeCl_3$ have low acute toxicity, and NaOH is corrosive.[47] They are nonflammable and stable at room temperature. Simple precautionary safety measures have to be taken during the synthesis of CAlFeC.

Disposal of Waste. The fluoride-loaded adsorbent can be regenerated and reused 3−4 times by treatment with a strong alkali. The spent adsorbent can be safely disposed of in leach-free landfills.

Affordability. This fluoride removal technology can provide fluoride-free water at a cost of about \$3.3/kL of safe drinking water. This is comparable to the cost of an adsorbent synthesized in a related study[13] but reasonably more affordable compared to membrane technologies such as reverse osmosis.

CONCLUSIONS

The synthesis of an environmentally friendly, highly effective adsorbent for the removal of fluoride from water is presented in this report. Readily available and low-cost reagents were used to synthesize the adsorbent in an aqueous medium at room temperature. The synthesis protocol was optimized to ensure reduced cost, robustness, effectiveness, and ease of use. From several studies, the adsorbent was found to be a hard, porous, and largely amorphous solid but became semicrystalline upon electron beam irradiation. The adsorbent was applicable in a pH range of 4−9. Regeneration is possible by treatment with sodium hydroxide, and this would give up to four reusable cycles. It is effective for fluoride removal even in the presence of other ions commonly present in environmental waters, although PO_4^{3-} and SiO_3^{2-} ions significantly reduced its effectiveness. It was observed that no significant leaching of the adsorbent components (Al, Fe, and TOC) into treated water took place and the adsorbate-laden material met the leaching characteristics prescribed by the US-EPA. The material exhibited fast adsorption kinetics, following the pseudo-second-order model, with over 80% of fluoride removal happening within 3 min of contact. The approach presented confirms the possibility of creating sustainable absorbent materials with enhanced capacity by nanostructuring, using multiple components.

Isotherm studies showed that adsorption of fluoride follows the Langmuir adsorption model, largely as chemisorption through ion exchange and Coulombic attraction on charged groups. About 22 g of the adsorbent could effectively treat up to 20 L of water contaminated with 10 mg/L F^-. On evaluation of the sustainability and greenness of synthesis and use, the process was found to be water, energy, and atom efficient, with the only toxic waste being the spent adsorbent that can be safely disposed of in landfills. From estimation, the cost per liter of purified water is expected to be low, enabling its applicability in poor rural communities affected by excess fluoride in drinking water.

■ ASSOCIATED CONTENT

Supporting Information

The Supporting Information is available free of charge at https://pubs.acs.org/doi/10.1021/acssuschemeng.1c03272.

> Equations used in the main text; graphs showing the effect of incorporating different cations and anions into CAlFeC structure on its F^- uptake capacity; images showing stable and unstable adsorbent in contact with water; mechanical stability (hardness) of the adsorbent in dry and wet conditions; TEM-EDS and SEM-EDS elemental maps of CAlFeC before and after F^- adsorption; cartridge setup and results of leaching experiment; and adsorption isotherms and kinetics graphs (PDF)

■ AUTHOR INFORMATION

Corresponding Author

Thalappil Pradeep − *DST Unit of Nanoscience (DST UNS) and Thematic Unit of Excellence (TUE), Department of Chemistry, Indian Institute of Technology Madras, Chennai 600 036, India;* orcid.org/0000-0003-3174-534X; Email: pradeep@iitm.ac.in

Authors

Moses Egor − *Busitema University, 236 Tororo, Uganda; Mbarara University of Science and Technology, 1410 Mbarara, Uganda; DST Unit of Nanoscience (DST UNS) and Thematic Unit of Excellence (TUE), Department of Chemistry, Indian Institute of Technology Madras, Chennai 600 036, India*

Avula Anil Kumar − *DST Unit of Nanoscience (DST UNS) and Thematic Unit of Excellence (TUE), Department of Chemistry, Indian Institute of Technology Madras, Chennai 600 036, India;* orcid.org/0000-0001-6878-8736

Tripti Ahuja − *DST Unit of Nanoscience (DST UNS) and Thematic Unit of Excellence (TUE), Department of Chemistry, Indian Institute of Technology Madras, Chennai 600 036, India*

Sritama Mukherjee − *DST Unit of Nanoscience (DST UNS) and Thematic Unit of Excellence (TUE), Department of Chemistry, Indian Institute of Technology Madras, Chennai 600 036, India*

Amrita Chakraborty − *DST Unit of Nanoscience (DST UNS) and Thematic Unit of Excellence (TUE), Department of Chemistry, Indian Institute of Technology Madras, Chennai 600 036, India*

Chennu Sudhakar − *DST Unit of Nanoscience (DST UNS) and Thematic Unit of Excellence (TUE), Department of Chemistry, Indian Institute of Technology Madras, Chennai 600 036, India*

Pillalamarri Srikrishnarka − *DST Unit of Nanoscience (DST UNS) and Thematic Unit of Excellence (TUE), Department of Chemistry, Indian Institute of Technology Madras, Chennai 600 036, India;* orcid.org/0000-0001-5187-6879

Sandeep Bose − *DST Unit of Nanoscience (DST UNS) and Thematic Unit of Excellence (TUE), Department of Chemistry, Indian Institute of Technology Madras, Chennai 600 036, India*

Swathy Jakka Ravindran − *DST Unit of Nanoscience (DST UNS) and Thematic Unit of Excellence (TUE), Department of Chemistry, Indian Institute of Technology Madras, Chennai 600 036, India;* orcid.org/0000-0002-7882-7871

Complete contact information is available at: https://pubs.acs.org/10.1021/acssuschemeng.1c03272

Author Contributions

[‖]M.E. and A.A.K. contributed equally to this work.

Notes

The authors declare no competing financial interest.

■ ACKNOWLEDGMENTS

The authors thank Sugi Shivan for making FTIR measurements, Biswajit Modal for HRTEM-EDS, and Manu Santhanam for his help in conducting direct shear stress analysis. The authors are grateful to the technicians of the Department of Chemistry, IIT Madras, for helping to carry out PXRD and BET analyses. The authors thank Ramesh Kumar for his help in setting up the cartridge experiment. For their help in TOC measurements, the authors wish to thank Ligy Philip and Narasamma of the Department of Civil Engineering, IIT Madras. Finally, M.E. is grateful to all members of the Pradeep Research Group for their help with experimental work and interpretation. The authors thank IIT Madras and the Department of Science and Technology, Government of India, for supporting our research program on nanomaterials. M.E. is a student of Mbarara University of Science and Technology and was a research fellow at IIT Madras during this work.

■ REFERENCES

(1) Nagar, A.; Pradeep, T. Clean Water through Nanotechnology: Needs, Gaps, and Fulfillment. *ACS Nano* **2020**, *14*, 6420−6435.

(2) Raghav, S.; Kumar, D. Adsorption Equilibrium, Kinetics, and Thermodynamic Studies of Fluoride Adsorbed by Tetrametallic Oxide Adsorbent. *J. Chem. Eng. Data* **2018**, *63*, 1682−1697.

(3) Wan, Z.; Chen, W.; Liu, C.; Liu, Y.; Dong, C. Preparation and Characterization of Gamma-AlOOH @CS Magnetic Nanoparticle as a Novel Adsorbent for Removing Fluoride from Drinking Water. *J. Colloid Interface Sci.* **2015**, *443*, 115−124.

(4) Gai, W.-Z.; Zhang, S.-H.; Yang, Y.; Zhang, X.; Deng, Z.-Y. Separation of Excess Fluoride from Water Using Amorphous and Crystalline AlOOH Adsorbents. *ACS Omega* **2021**, *6*, 16488−16497.

(5) Carpenter, A. W.; deLannoy, C.-F.; Wiesner, M. R. Cellulose Nanomaterials in Water Treatment Technologies. *Environ. Sci. Technol.* **2015**, *49*, 5277−5287.

(6) Viswanathan, N.; Sundaram, C. S.; Meenakshi, S. Sorption Behaviour of Fluoride on Carboxylated Cross-Linked Chitosan Beads. *Colloids Surf., B* **2009**, *68*, 48−54.

(7) Gericke, M.; Trygg, J.; Fardim, P. Functional Cellulose Beads: Preparation, Characterization, and Applications. *Chem. Rev.* **2013**, *113*, 4812−4836.

(8) Cai, J.; Zhang, Y.; Qian, Y.; Shan, C.; Pan, B. Enhanced Defluoridation Using Novel Millisphere Nanocomposite of La-Doped Li-Al Layered Double Hydroxides Supported by Polymeric Anion Exchanger. *Sci. Rep.* **2018**, *8*, No. 11741.

(9) Jing, C.; Cui, J.; Huang, Y.; Li, A. Fabrication, Characterization, and Application of a Composite Adsorbent for Simultaneous Removal of Arsenic and Fluoride. *ACS Appl. Mater. Interfaces* **2012**, *4*, 714−720.

(10) Zhang, J.; Kong, Y.; Yang, Y.; Chen, N.; Feng, C.; Huang, X.; Yu, C. Fast Capture of Fluoride by Anion-Exchange Zirconium−Graphene Hybrid Adsorbent. *Langmuir* **2019**, *35*, 6861−6869.

(11) Kumar, A. A.; Som, A.; Longo, P.; Sudhakar, C.; Bhuin, R. G.; Gupta, S. Sen.; Anshup; Sankar, M. U.; Chaudhary, A.; Kumar, R.; Pradeep, T. Confined Metastable 2-Line Ferrihydrite for Affordable

Point-of-Use Arsenic-Free Drinking Water. *Adv. Mater.* **2017**, *29*, No. 1604260.
(12) Sankar, M. U.; Aigal, S.; Maliyekkal, S. M.; Chaudhary, A.; Anshup; Kumar, A. A.; Chaudhari, K.; Pradeep, T. Biopolymer-Reinforced Synthetic Granular Nanocomposites for Affordable Point-of-Use Water Purification. *Proc. Natl. Acad. Sci. USA* **2013**, *110*, 8459−8464.
(13) Mukherjee, S.; Ramireddy, H.; Baidya, A.; Amala, A. K.; Sudhakar, C.; Mondal, B.; Philip, L.; Pradeep, T. Nanocellulose-Reinforced Organo-Inorganic Nanocomposite for Synergistic and Affordable Defluoridation of Water and an Evaluation of Its Sustainability Metrics. *ACS Sustainable Chem. Eng.* **2020**, *8*, 139−147.
(14) Abouzeid, R. E.; Khiari, R.; El-Wakil, N.; Dufresne, A. Current State and New Trends in the Use of Cellulose Nanomaterials for Wastewater Treatment. *Biomacromolecules* **2019**, *20*, 573−597.
(15) Hussain, Z.; Daosheng, L.; Xi, L.; Jianxiong, K. Defluoridation by a Mg−Al−La Triple-Metal Hydrous Oxide: Synthesis, Sorption, Characterization and Emphasis on the Neutral pH of Treated Water. *RSC Adv.* **2015**, *5*, 43906−43916.
(16) Kumari, S.; Khan, S. Defluoridation Technology for Drinking Water and Tea by Green Synthesized Fe_3O_4/Al_2O_3 Nanoparticles Coated Polyurethane Foams for Rural Communities. *Sci. Rep.* **2017**, *7*, No. 8070.
(17) Prabhu, S. M.; Sasaki, K. Fabrication of Chitosan-Reinforced ZrxAl1-XOOH Nanocomposites and Their Arsenite and Fluoride Depollution Densities from Single/Binary Systems. *ChemistrySelect* **2017**, *2*, 6375−6387.
(18) WHO. *Fluorides and Oral Health*; WHO: Geneva, 1994; Vol. *846*.
(19) Chen, H.; Yan, M.; Yang, X.; Chen, Z.; Wang, G.; Schmidt-Vogt, D.; Xu, Y.; Xu, J. Spatial Distribution and Temporal Variation of High Fluoride Contents in Groundwater and Prevalence of Fluorosis in Humans in Yuanmou County, Southwest China. *J. Hazard. Mater.* **2012**, *235*−*236*, 201−209.
(20) Rathore, V. K.; Mondal, P. Competitive Adsorption of Arsenic and Fluoride onto Economically Prepared Aluminum Oxide/Hydroxide Nanoparticles: Multicomponent Isotherms and Spent Adsorbent Management. *Ind. Eng. Chem. Res.* **2017**, *56*, 8081−8094.
(21) Klemm, D.; Philipp, B.; Heinze, T.; Heinze, U.; Wagenknecht, W. *Comprehensive Cellulose Chemistry: Functionalization of Cellulose*; Wiley-VCH Verlag GmbH: Weinheim, 1998; *Vol. 2*.
(22) Chen, Y.; Zhang, Q.; Chen, L.; Bai, H.; Li, L. Basic Aluminum Sulfate@graphene Hydrogel Composites: Preparation and Application for Removal of Fluoride. *J. Mater. Chem. A* **2013**, *1*, No. 13101.
(23) Hanesch, M. Raman Spectroscopy of Iron Oxides and (Oxy)Hydroxides at Low Laser Power and Possible Applications in Environmental Magnetic Studies. *Geophys. J. Int.* **2009**, *177*, 941−948.
(24) Saalfeld, H.; Wedde, M. Refinement of the Crystal Structure of Gibbsite, $Al(OH)_3$. *Z. Krist.* **1974**, *139*, 129−135.
(25) Wolska, E. The Structure of Hydrohematite. *Z. Krist.: Cryst. Mater.* **1981**, *154*, 69−76.
(26) Arami, H.; Mazloumi, M.; Khalifehzadeh, R.; Sadrnezhaad, S. K. Electron Beam-Induced "Nanocalcination" of Boehmite Nanostrips to Mesoporous α-Alumina Phase. *J. Am. Ceram. Soc.* **2007**, *90*, 3311−3313.
(27) Colthup, N. B.; Daly, L. H.; Wiberley, S. E. *Introduction to Infrared and Raman Spectroscopy*, 3rd ed.; Academic Press, Inc.: Sandiego, 1990.
(28) Dudev, T.; Lim, C. Monodentate versus Bidentate Carboxylate Binding in Magnesium and Calcium Proteins: What Are the Basic Principles? *J. Phys. Chem. B* **2004**, *108*, 4546−4557.
(29) Makarem, M.; Lee, C. M.; Kafle, K.; Huang, S.; Chae, I.; Yang, H.; Kubicki, J. D.; Kim, S. H. Probing Cellulose Structures with Vibrational Spectroscopy. *Cellulose* **2019**, *26*, 35−79.
(30) Zhang, H.; Li, N.; Pan, X.; Wu, S.; Xie, J. Direct Transformation of Cellulose to Gluconic Acid in a Concentrated Iron(III) Chloride Solution under Mild Conditions. ACS Sustain. *Chem. Eng.* **2017**, *5*, 4066−4072.
(31) Ruan, H. D.; Frost, R. L.; Kloprogge, J. T. Comparison of Raman Spectra in Characterizing Gibbsite, Bayerite, Diaspore and Boehmite. *J. Raman Spectrosc.* **2001**, *32*, 745−750.
(32) Mukherjee, S.; Kumar, A. A.; Sudhakar, C.; Kumar, R.; Ahuja, T.; Mondal, B.; Srikrishnarka, P.; Philip, L.; Pradeep, T. Sustainable and Affordable Composites Built Using Microstructures Performing Better than Nanostructures for Arsenic Removal. *ACS Sustainable Chem. Eng.* **2019**, *7*, 3222−3233.
(33) Barathi, M.; Krishna Kumar, A. S.; Kumar, C. U.; Rajesh, N. Graphene Oxide−Aluminium Oxyhydroxide Interaction and Its Application for the Effective Adsorption of Fluoride. *RSC Adv.* **2014**, *4*, 53711−53721.
(34) David, E. Mechanical Strength and Reliability of the Porous Materials Used as Adsorbents/ Catalysts and the New Development Trends. *Arch. Mater. Sci. Eng.* **2015**, *73*, 5−17.
(35) Xu, C.; Li, J.; He, F.; Cui, Y.; Huang, C.; Jin, H.; Hou, S. $Al_2O_3-Fe_3O_4$−Expanded Graphite Nano-Sandwich Structure for Fluoride Removal from Aqueous Solution. *RSC Adv.* **2016**, *6*, 97376−97384.
(36) Foo, K. Y. Y.; Hameed, B. H. H. Insights into the Modeling of Adsorption Isotherm Systems. *Chem. Eng. J.* **2010**, *156*, 2−10.
(37) Thakre, D.; Jagtap, S.; Sakhare, N.; Labhsetwar, N.; Meshram, S.; Rayalu, S. Chitosan Based Mesoporous Ti-Al Binary Metal Oxide Supported Beads for Defluoridation of Water. *Chem. Eng. J.* **2010**, *158*, 315−324.
(38) Zhao, W.; Chen, Y.; Zhang, W.; Wang, J.; Hu, C.; He, W. Synthesis, Performance, and Mechanism of Magnesium-Iron-Aluminum Trimetal Composite as an Adsorbent for Fluoride Removal in Water Treatment. *Can. J. Chem. Eng.* **2016**, *94*, 2289−2297.
(39) Qiu, H.; Lv, L.; Pan, B.; Zhang, Q.; Zhang, W.; Zhang, Q. Critical Review in Adsorption Kinetic Models. *J. Zhejiang Univ., Sci., A* **2009**, *10*, 716−724.
(40) Yuh-Shan, H. Citation Review of Lagergren Kinetic Rate Equation on Adsorption Reactions. *Scientometrics* **2004**, *59*, 171−177.
(41) Ho, Y. S.; McKay, G. The Kinetics of Sorption of Divalent Metal Ions onto Sphagnum Moss Peat. *Water Res.* **2000**, *34*, 735−742.
(42) Alkan, M.; Demirbaş, Ö.; Doğan, M. Adsorption Kinetics and Thermodynamics of an Anionic Dye onto Sepiolite. *Microporous Mesoporous Mater.* **2007**, *101*, 388−396.
(43) Kannan, N.; Sundaram, M. M. Kinetics and Mechanism of Removal of Methylene Blue by Adsorption on Various Carbons—a Comparative Study. *Dyes Pigments* **2001**, *51*, 25.
(44) Sheldon, R. A. Metrics of Green Chemistry and Sustainability: Past, Present, and Future. *ACS Sustainable Chem. Eng.* **2018**, *6*, 32−48.
(45) Makeower, J. The Tenth Annual State of Green Business, *Phoenix*, 2017.
(46) Cohen, S.; Bose, S.; Guo, D.; Miller, A.; Berger, O.; DeFrancia, K.; Filiatraut, B.; Qiu, W.; Loman, M.; Zhang, C. *The Growth of Sustainability Metrics; Sustainability Metrics White Paper Series,*1 of 3, 2014.
(47) NCBI. Aluminum Sulfate, CID=24850 https://pubchem.ncbi.nlm.nih.gov/compound/Aluminum-sulfate (accessedJuly 4, 2020).

Supporting Information

A Cellulosic Ternary Nanocomposite for Affordable and Sustainable Fluoride Removal

Moses Egor,[§,‡,†,#] Avula Anil Kumar,[†,#] Tripti Ahuja,[†] Sritama Mukherjee,[†] Amrita Chakraborty,[†] Chennu Sudhakar,[†] Pillalamarri Srikrishnarka,[†] Sandeep Bose,[†] Swathy Jakka Ravindran,[†] Thalappil Pradeep*,[†]

[§] Busitema University, P.O. Box 236, Tororo, Uganda

[‡] Mbarara University of Science and Technology, P.O. Box 1410, Mbarara, Uganda

[†] DST Unit of Nanoscience (DST UNS) and Thematic Unit of Excellence (TUE), Department of Chemistry, Indian Institute of Technology Madras, Chennai 600 036, India

[#] These authors contributed equally to this work

* Corresponding author
E-mail: pradeep@iitm.ac.in
Tel.: +91-44 2257 4208; Fax: +91-44 2257 0545/0509

Supporting Information Content

Total number of pages: 14

Total number of figures: 8

Total number of equations: 16

Total number of tables: 1

Table of contents

FIGURES:

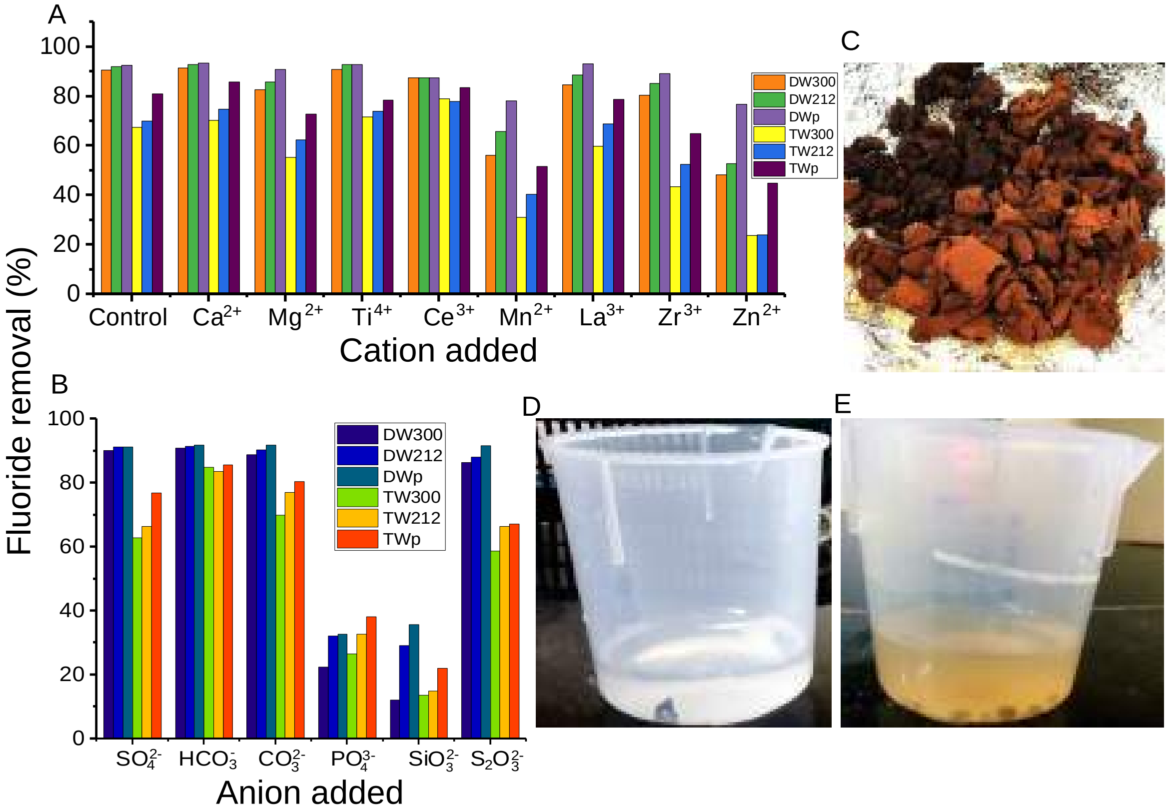

Figure S1. Effect of addition of other polyvalent cations (A) and other polyatomic anions (B) on the fluoride removal capacity of CAlFeC, tested with fluoride solution in distilled water (DW) and tap water (TW) and with particle sizes of 300 µm, 212 µm and powder, respectively. (C) Physical appearance of dried CAlFeC. (D and E) Show the stable and unstable composite, respectively, when shaken with water.

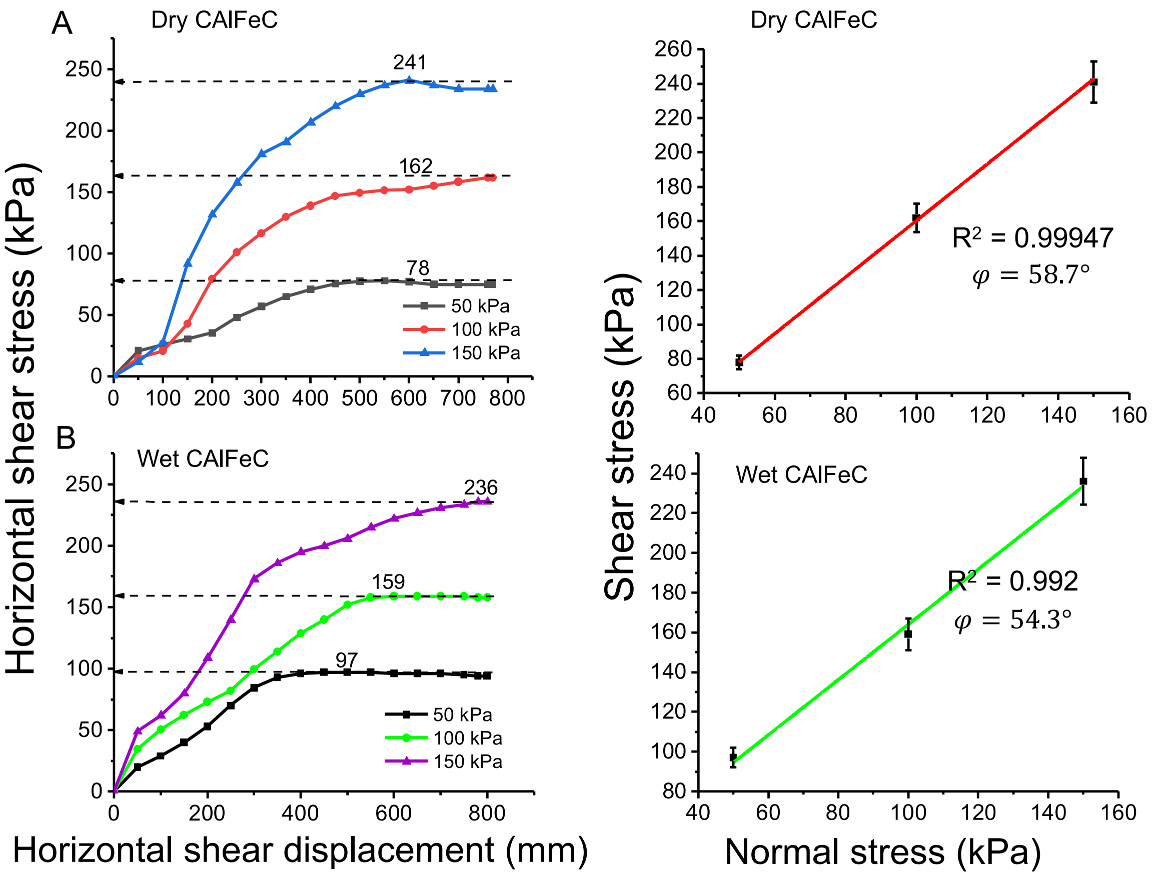

Figure S2. Direct shear stress test results of dry CAlFeC (A) and wet CAlFeC (B) and their corresponding Mohr-Coulomb failure patterns.

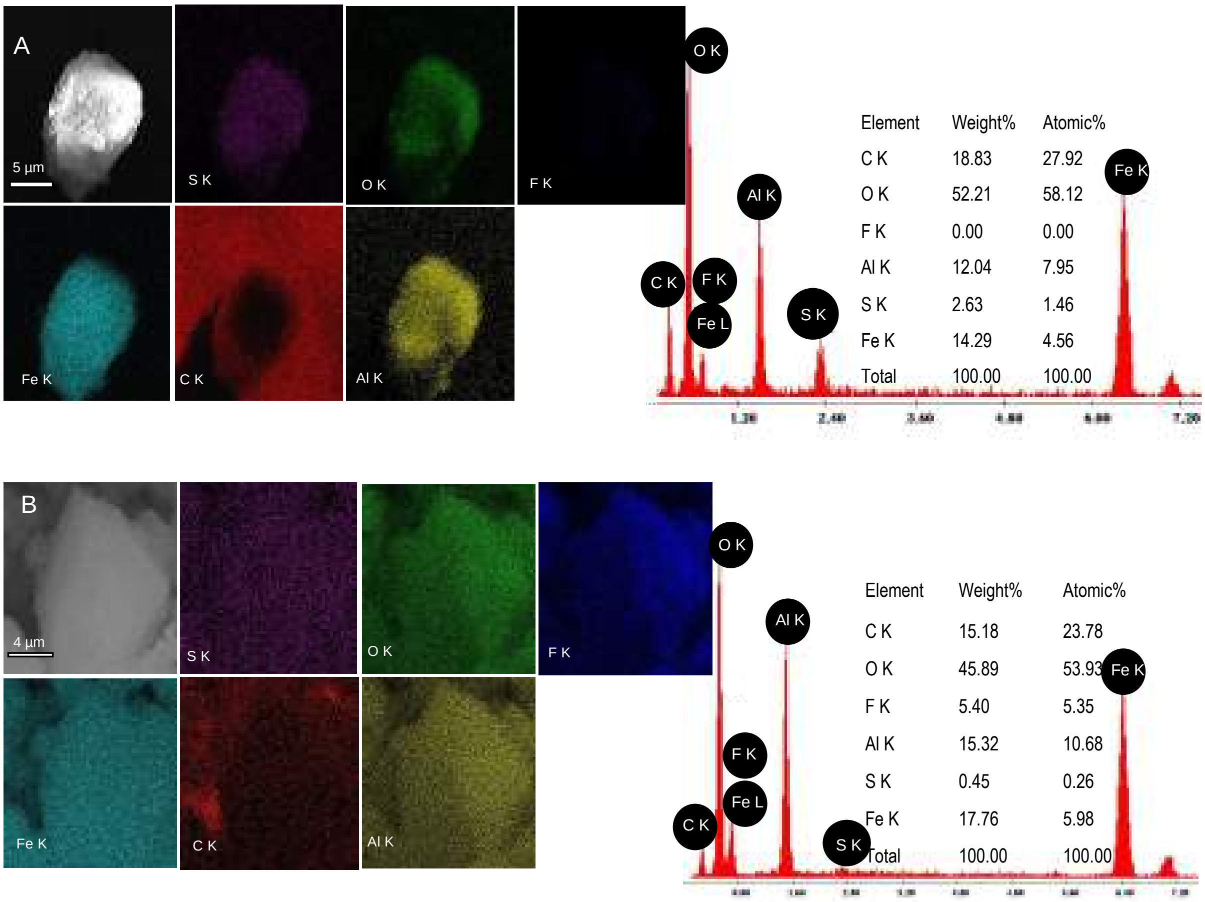

Element	Weight%	Atomic%
C K	18.83	27.92
O K	52.21	58.12
F K	0.00	0.00
Al K	12.04	7.95
S K	2.63	1.46
Fe K	14.29	4.56
Total	100.00	100.00

Element	Weight%	Atomic%
C K	15.18	23.78
O K	45.89	53.93
F K	5.40	5.35
Al K	15.32	10.68
S K	0.45	0.26
Fe K	17.76	5.98
Total	100.00	100.00

Figure S3. SEM-EDS elemental maps and spectra of CAlFeC (A) and CAlFeC-F (B).

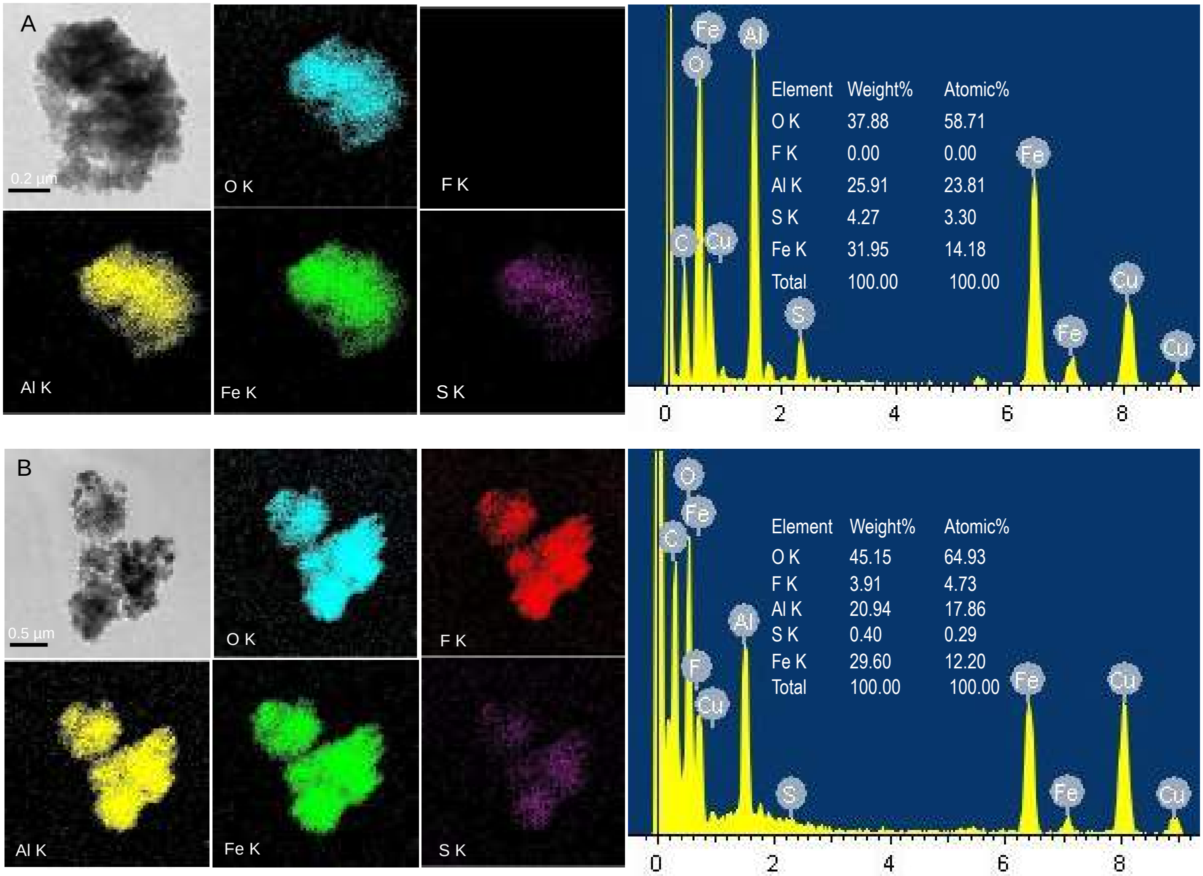

Element	Weight%	Atomic%
O K	37.88	58.71
F K	0.00	0.00
Al K	25.91	23.81
S K	4.27	3.30
Fe K	31.95	14.18
Total	100.00	100.00

Element	Weight%	Atomic%
O K	45.15	64.93
F K	3.91	4.73
Al K	20.94	17.86
S K	0.40	0.29
Fe K	29.60	12.20
Total	100.00	100.00

Figure S4. HRTEM-EDS element maps and spectra of CAlFeC (A) and CAlFeC-F (B).

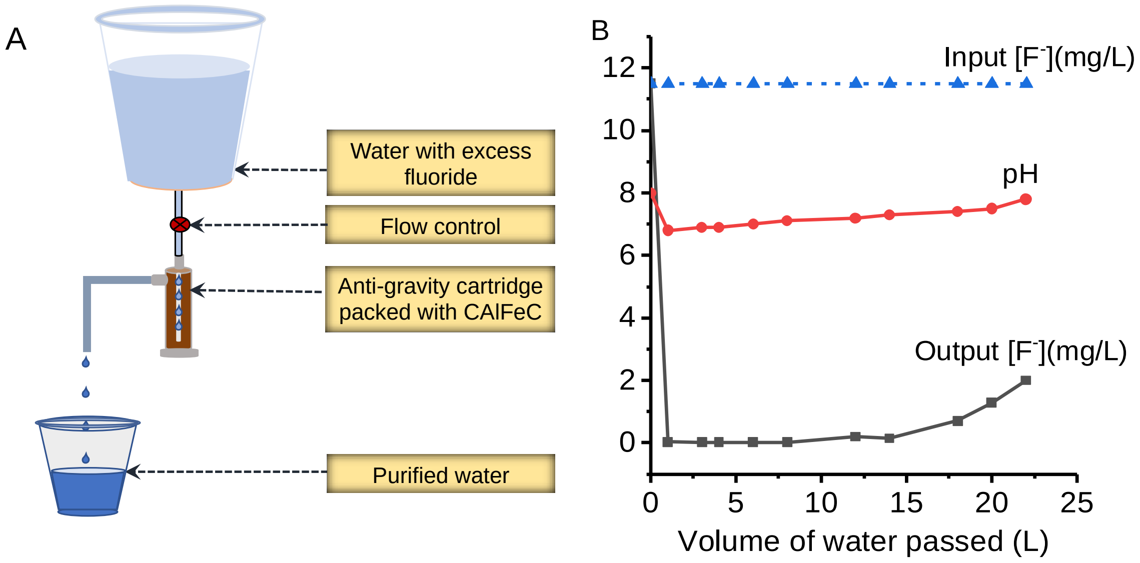

C

	TOC/mg/L	TC/mg/L	IC/mg/L
Ultrapure water	-0.208	0.000	0.208
Ultrapure water + CAlFeC	0.258	0.341	0.83
10 mg/L F^- in ultrapure water + CAlFeC	2.725	3.054	0.3289

Figure S5. Cartridge experiment setup (A), changes in pH and fluoride levels during cartridge run (B) and the results of TOC leaching measurements (C).

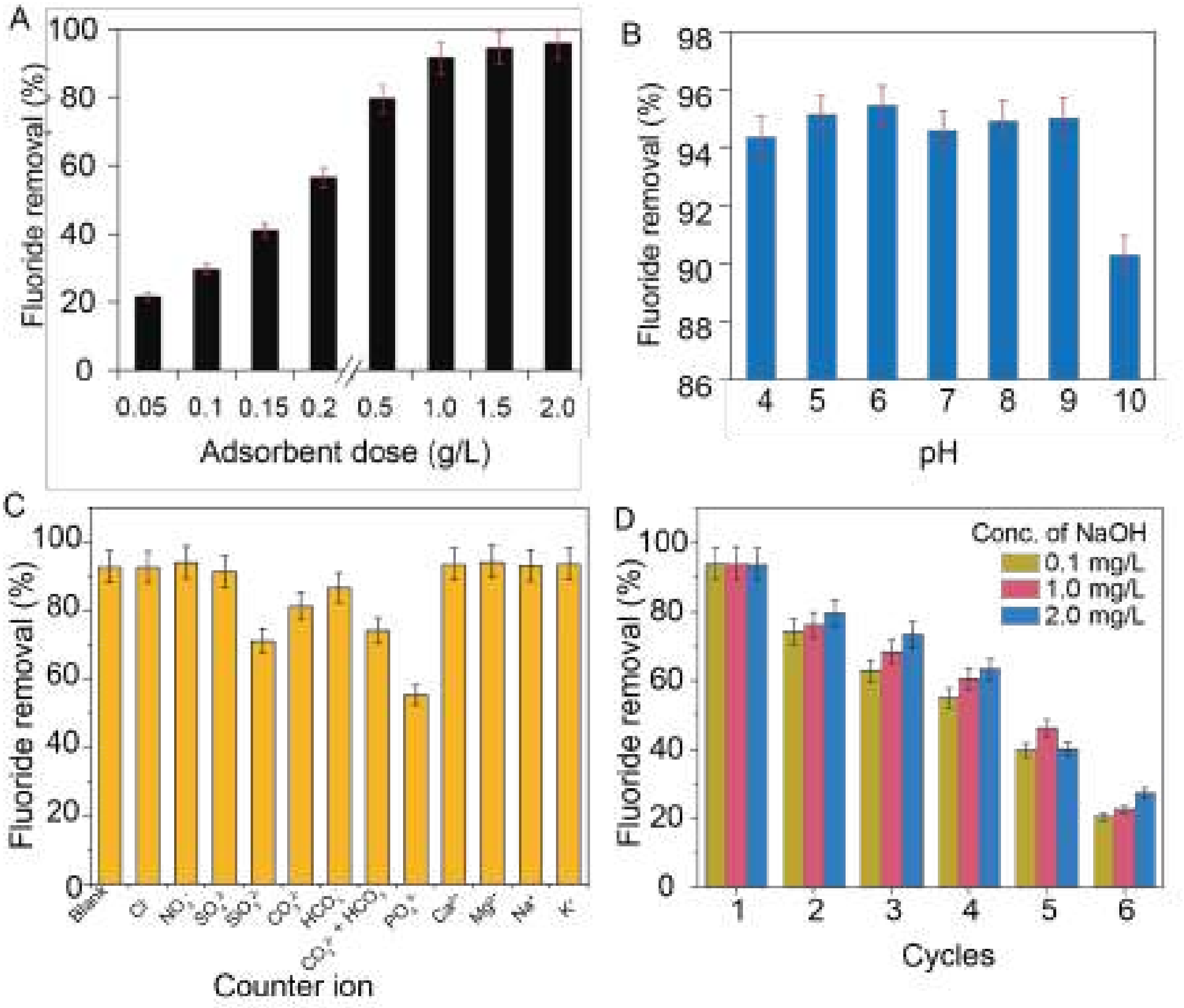

Figure S6. Fluoride adsorption characteristics of CAlFeC showing the effect of adsorbent dose (A), pH of the medium (B), counter-ions (C), and the effect of regeneration (D).

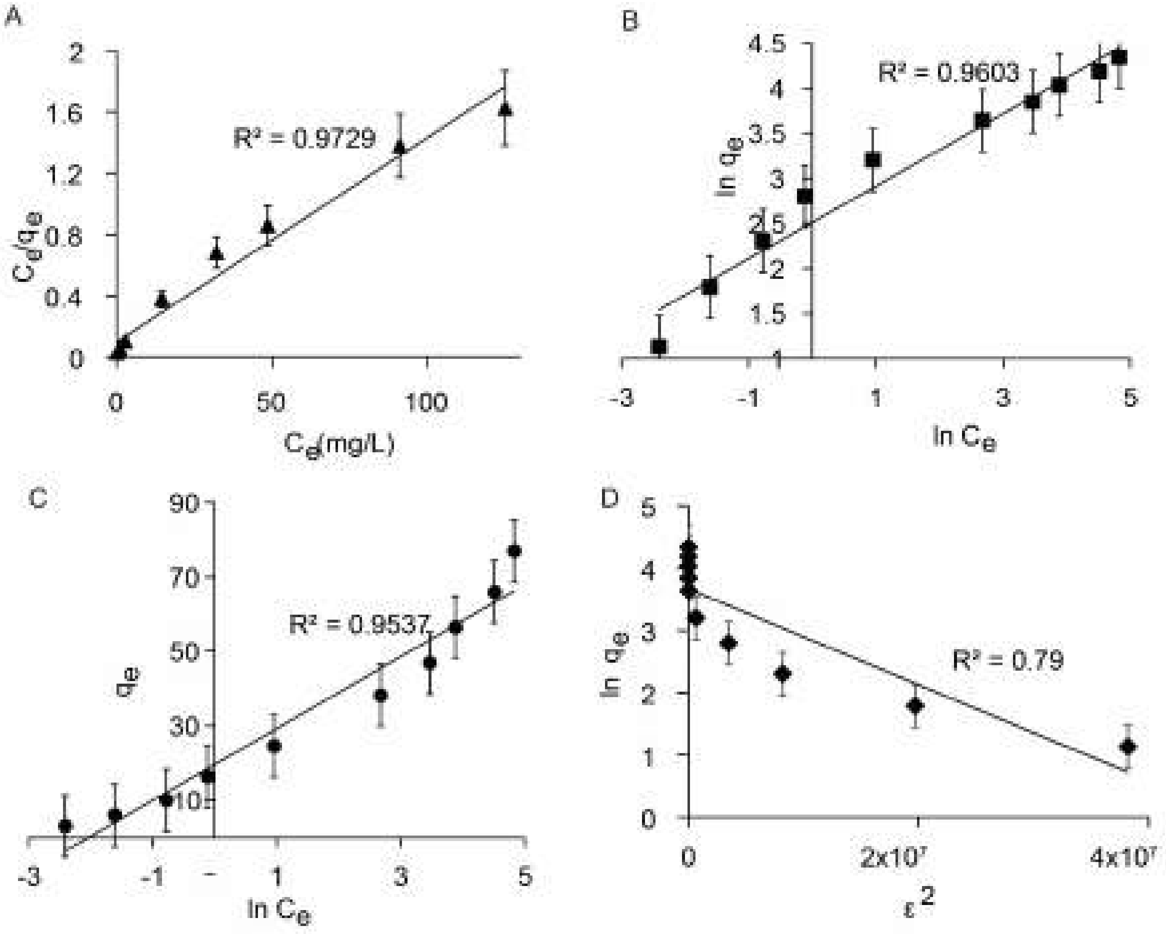

Figure S7. Adsorption isotherms of CAlFeC for fluoride showing Langmuir (A), Freundlich (B), Temkin (C) and Dubinin-Radushkevich (D) isotherm fittings.

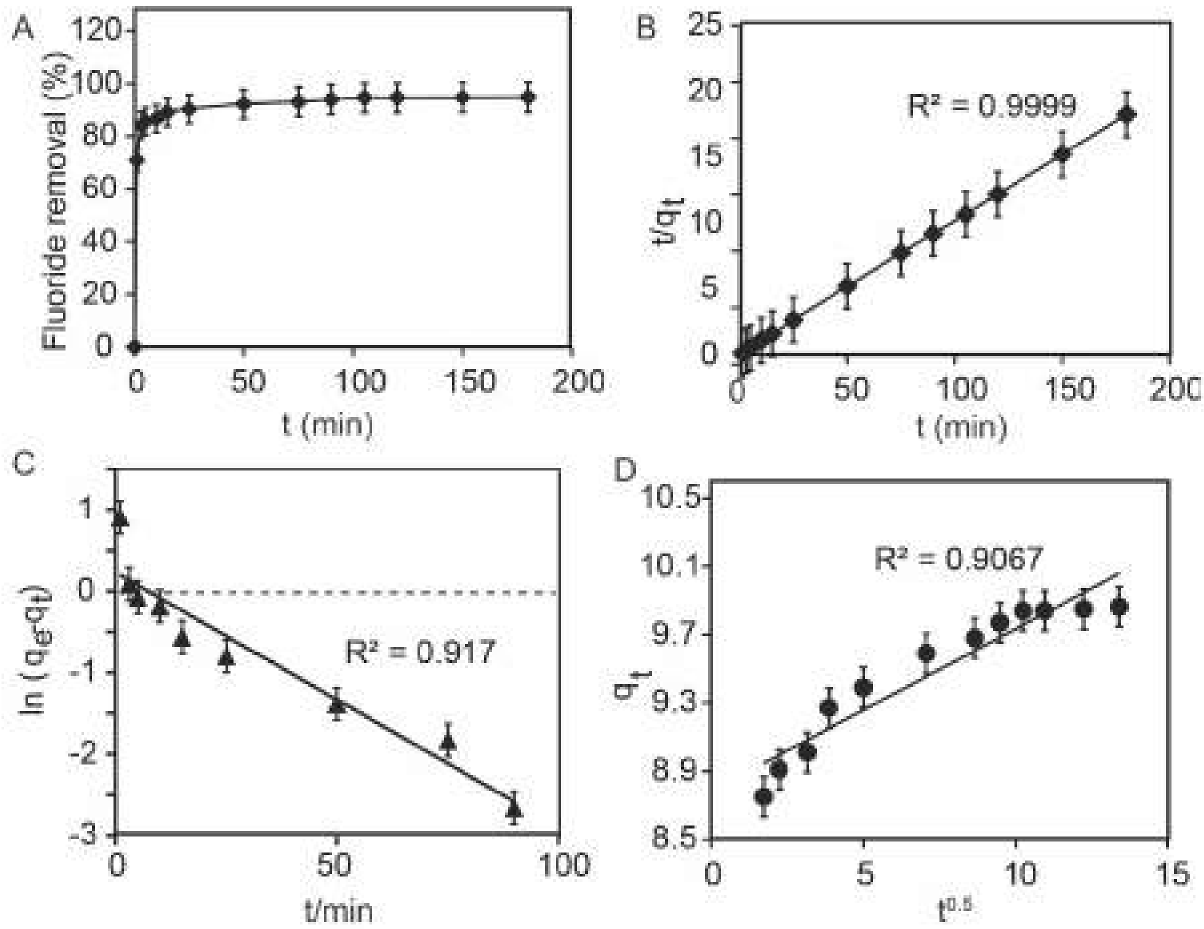

Figure S8. Adsorption kinetics data showing the effect of contact time (A) and adsorption kinetics models: pseudo-second order (B), pseudo-first order (C) and intraparticle diffusion (D).

EQUATIONS:

Equation S1. The maximum uptake of F^- (q_e) was calculated using the equation given by:

$$q_e = \frac{(C_0 - C_e)V}{w}$$

where q_e is the amount of F^- ions adsorbed per gram of the adsorbent (mg/g) at equilibrium, C_e is the equilibrium concentration of fluoride in the bulk solution (mg/L), C_0 is the initial fluoride concentration (mg/L), V is the volume of solution (L) and w is the mass of the adsorbent (g).

Equation S2. Percentage of fluoride removal:

$$\%\ Removal = \left(\frac{C_0 - C_e}{C_0}\right)100\%$$

Equation S3. The linear form of Freundlich adsorption isotherm is given as

$$ln\ q_e = ln\ k + \frac{1}{n}\ ln\ C_e$$

where k is the adsorption capacity and n is the adsorption intensity

Equation S4. The linear form of Langmuir adsorption isotherm is given by equation

$$\frac{C_e}{q_e} = \frac{1}{bq_{max}} + \frac{C_e}{q_{max}}$$

where q_{max} is the maximum surface density at monolayer coverage and b is the Langmuir adsorption constant (L/mg) related to the free energy of adsorption and $1/q_{max}$ and $1/bq_{max}$ are the Langmuir constants.

Equation S5. Separation factor R_L, which is calculated from the following equation:

$$R_L = \frac{1}{1 + bC_o}$$

Equation S6. The Temkin isotherm model is represented in the form:

$$q_e = \frac{RT}{k} ln\, A + \left(\frac{RT}{b}\right) ln\, C_e$$

where k, A and b are Temkin constants.

Equation S7. Dubinin-Radushkevich isotherm model is given by the equation:

$$ln\, q_e = ln\, q_o - k\varepsilon^2$$

Equation S8. The parameter ε in Equation S7 is obtained from the formula:

$$\varepsilon = RT\, ln\left(1 + \frac{1}{C_e}\right)$$

where R and T are the gas constant and absolute temperature, respectively.

Equation S9. Lagergren pseudo-first order model is given by the equation below:

$$ln\, (q_e - q_t) = ln\, q_e - k_1 t$$

where k_1 is the rate constant and q_t is the adsorption capacity at any given time, t.

Equation S10. Ho & Mckay pseudo-second order model is given by the equation below:

$$\frac{t}{q_t} = \frac{1}{K_2 q_e^2} + \frac{t}{q_e}$$

where k_2 is the pseudo-second order rate constant.

Equation S11. Weber-Morris intraparticle diffusion kinetic model

$$q_t = k_i \sqrt{t}$$

where k_i is the rate constant.

Equation S12. $$\text{Mass intensity} = \frac{\text{Mass of all materials used excluding water}}{\text{Mass of product}}\ \text{kg/kg product}$$

Equation S13. $$\text{Water intensity} = \frac{\text{Mass of all water used}}{\text{Mass of product}}\ \text{kg/kg product}$$

Equation S14. $$\text{Reaction mass efficiency} = \frac{\text{Mass of product}}{\text{Mass of all reactants}} \times 100\%$$

Equation S15. $$\text{Energy intensity} = \frac{\text{Amount of non renewable energy uses}}{\text{Mass of product}} \text{ kW.h/kg}$$

Equation S16. $$\text{E factor} = \frac{[\text{kg (raw materials)} - \text{kg (desired product)}]}{\text{kg (total product including water)}}$$

TABLES:

Table S1. Characteristics of TW before and after spiking with F$^-$, and after contact with CAlFeC.

Property of TW	**Before spiking with F$^-$**	**After spiking with F$^-$**	**After contact with CAlFeC**
Electrical conductivity (µS/cm)	760.3	810	620.5
pH	7.2	8.1	6.7
Fluoride (mg/L)	0.03	10.4	0.6

THE JOURNAL OF PHYSICAL CHEMISTRY C
A JOURNAL OF THE AMERICAN CHEMICAL SOCIETY

pubs.acs.org/JPCC Article

Isotopic Exchange of Atomically Precise Nanoclusters with Materials of Varying Dimensions: From Nanoscale to Bulk

Papri Chakraborty, Paulami Bose, Jayoti Roy, Abhijit Nag, Biswajit Mondal, Amrita Chakraborty, and Thalappil Pradeep*

Cite This: *J. Phys. Chem. C* 2021, 125, 16110−16117 Read Online

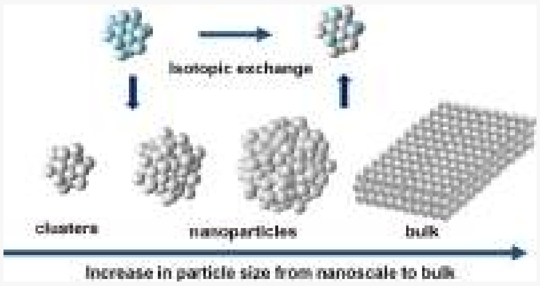

ABSTRACT: We present isotopic exchange reactions of atomically precise silver nanoclusters (NCs) with materials of different dimensions, namely, NCs, plasmonic nanoparticles (NPs), and bulk metals, all made of silver. Isotopically pure $^{109}Ag_{25}(DMBT)_{18}^{-}$ and $^{107}Ag_{25}(DMBT)_{18}^{-}$ (DMBT is 2,4-dimethyl benzene thiol) were reacted with Ag NPs of different sizes in the range of ∼2−11 nm, protected with the same ligand. The exchange of $^{107}Ag/^{109}Ag$ atoms in the NC was monitored using electrospray ionization mass spectrometry. The reaction kinetics was analyzed by fitting the temporal evolution of the reactant concentration to a kinetic model. The reaction timescales of NC−NP reactions were significantly longer compared to those of the NC−NC exchange process under similar conditions. Differences between NC−NC exchange and NC−NP exchange highlighted the importance of the structure in controlling the reaction. Moreover, isotopic exchanges of the NC were also studied with the bulk metal to obtain a complete understanding of how the kinetics of atom transfer varies upon changing the size of the reacting partner from nanoscale to bulk.

1. INTRODUCTION

Atomically precise nanoclusters (NCs) are a class of nanomaterials that are gaining importance due to their precise structures and unique properties.[1−12] These NCs are composed of a metal core capped by ligand monolayers. One of the growing areas of research is exploring the chemical reactions of these NCs.[13] Ligand exchange[14−18] and metal exchange[17,19−21] reactions of NCs have been explored by various research groups. Intercluster reactions have established that NCs can react just as molecules.[13,22,23] $Au_{25}(SR)_{18}^{-}$ and $Ag_{44}(SR)_{30}^{4-}$ (SR is a thiolate ligand) react spontaneously to form alloy NCs as the product.[22] Similar reactions were also observed between $Au_{25}(SR)_{18}^{-}$ and $Ag_{25}(SR)_{18}^{-}$.[23,24] Intercluster reactions were also used to create bimetallic[22,23,25] and trimetallic NCs.[26] Literature studies suggest that a possible route of such reactions is through the exchange of metal or metal−ligand fragments.[22] Monolayers of ligands, protecting the surface of the NCs, are dynamic,[27] and the metal−ligand interface plays a decisive role in controlling such reactions of NCs.[28] Zhang et al. further showed that collisions between NCs are essential for such reactions to occur.[29] Li et al. also demonstrated intramolecular metal-exchange pathways in NCs.[30] However, a complete understanding of the mechanism of reactions of NCs is still elusive.

Recent studies revealed that there can also be specific interactions between NCs and nanoparticles (NPs). $Ag_{44}(SR)_{30}^{4-}$ NCs interact with gold nanorods and form shells of NCs surrounding the nanorods.[31] However, the possibilities of atomic exchange have remained unexplored in this case. In another report, Bose et al. reported the formation of superlattices by the reaction of $Au_{25}(SR)_{18}^{-}$ with AgNPs due to the formation of uniformly sized alloy NPs by atom transfer between NCs and NPs.[32] Kazan et al. showed that doping in NCs can occur by a reaction with metal surfaces.[33] From such studies, it is clear that NCs behave differently in the case of NC−NC, NC−NP, or NC−bulk surface reactions, and in each case, the reactions are guided by specific driving forces. However, further research in this area is required to address how the mechanism, kinetics, and dynamics are affected during reactions of NCs with particles of different size regimes.

Isotopic exchange reactions have been widely used to understand dynamics in the structures of proteins and polymers.[34−37] Similarly, isotopic exchange in NCs also resolved their structural dynamics.[38,39] Two $Ag_{25}(DMBT)_{18}^{-}$ NCs, prepared with isotopically pure ^{107}Ag and ^{109}Ag, respectively, reacted to produce isotopically mixed $Ag_{25}(DMBT)_{18}^{-}$.[40] The isotopic exchange was similar to the exchanges observed in H_2O and D_2O, which revealed that NCs indeed behave as simple molecules. Such isotopic exchanges in

Received: March 13, 2021
Revised: July 8, 2021
Published: July 19, 2021

https://doi.org/10.1021/acs.jpcc.1c02264

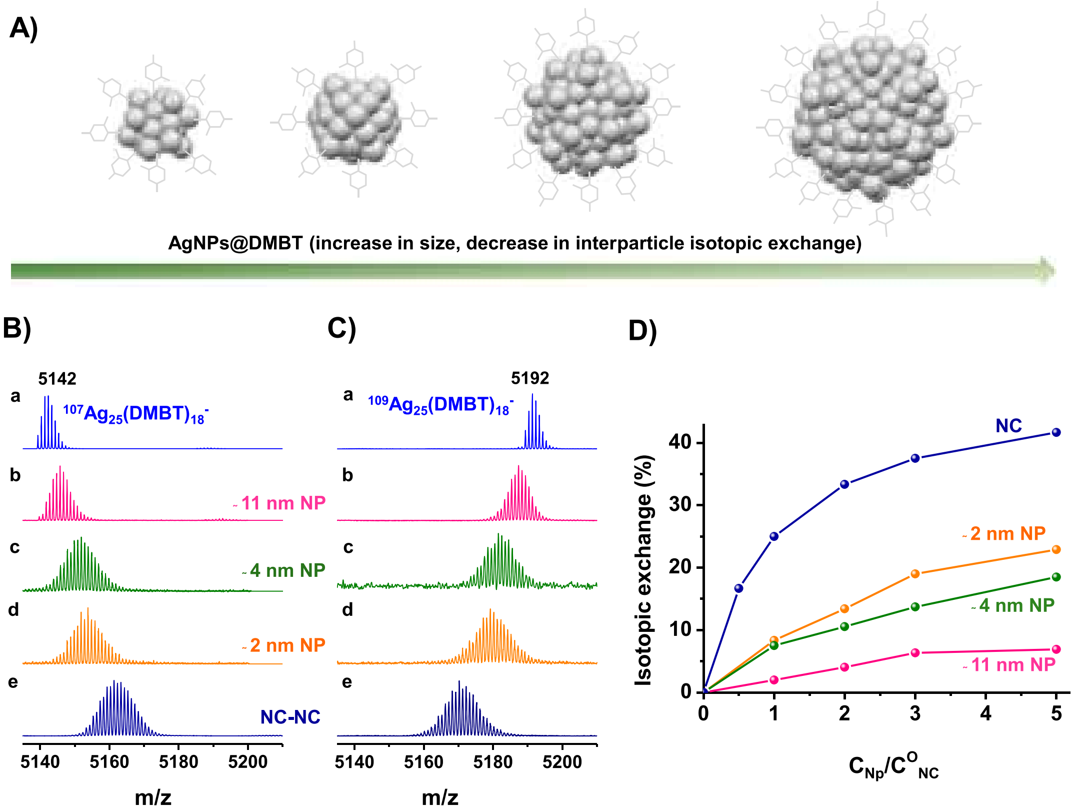

Figure 1. (A) Schematic showing NPs of increasing sizes, (B,C) ESI MS of (a) parent isotopic NCs, $^{107}Ag_{25}(DMBT)_{18}^{-}$ and $^{109}Ag_{25}(DMBT)_{18}^{-}$, respectively, and products formed by the reaction of the isotopic NCs with (b) ~11, (c) ~4, (d) ~2 nm AgNPs, and (e) NC (made from naturally abundant Ag) at 1:5 molar ratio in each case. (D) Plot showing the extent of isotopic exchange (%) as a function of the ratio of the concentration of NPs (C_{NP}) and concentration of isotopic NCs (C^{o}_{NC}) used in the NC−NP and NC−NC reactions.

NCs were driven by their entropy of mixing and were distinctly different compared to bimetallic intercluster atomic exchanges of different metals, which are mainly driven by enthalpy.[22] However, the isotopic exchange in NCs upon reaction with classical NPs and bulk metals was not explored earlier. NPs exhibit different sizes, facets, stability, and surface area. Similarly, bulk metals also offer different interfaces for the reaction. The isotopic exchange in each of these cases is expected to show different behaviors. A complete study of the isotopic exchange of NCs with materials of different sizes will provide further insights into how the spontaneous atom exchange of NCs varies with the size of the reacting material.

In this work, we studied the isotopic metal atom exchange kinetics of NCs upon reaction with NPs of different sizes and demonstrated how the kinetics of reactions change with an increase in the size of the reacting particles. We used isotopically pure $^{107}Ag_{25}(DMBT)_{18}^{-}$ or $^{109}Ag_{25}(DMBT)_{18}^{-}$ (DMBT is 2,4-dimethyl benzene thiol) and Ag NPs protected by DMBT (AgNPs@DMBT) in the size range of ~2−11 nm, made from isotopically mixed (natural) Ag, for our reaction. The isotopic exchange was studied using high-resolution electrospray ionization mass spectrometry (ESI MS). We further explored the isotopic exchange in NCs by the reaction with Ag foil and Ag powder to understand how the exchange kinetics is affected upon reaction with bulk materials as well. The exchange was also studied after forming a self-assembled monolayer of DMBT ligands on the Ag foil, which also highlighted the role of the protecting ligands or the ligand−metal interface in controlling the atom transfer process.

2. EXPERIMENTAL METHODS

2.1. Materials. Silver nitrate (made of naturally abundant Ag) was purchased from RANKEM, India. 2,4-DMBT, tetraphenyl phosphonium bromide (PPh_4Br), and sodium borohydride ($NaBH_4$) were purchased from Sigma-Aldrich. Ag foils (>98% purity) were obtained from the local market and Ag powder of size ~2−3.5 μm was obtained from Sigma-Aldrich. The solvents used were of high-performance liquid chromatography grade. Isotopically pure ^{107}Ag (98%) and ^{109}Ag (98%) foils were purchased from Cambridge Isotope Laboratories, Inc.

2.2. Synthesis of $^{107}Ag_{25}(DMBT)_{18}^{-}$ and $^{109}Ag_{25}(DMBT)_{18}^{-}$. Isotopically pure $^{107}Ag_{25}(DMBT)_{18}^{-}$ and $^{109}Ag_{25}(DMBT)_{18}^{-}$ NCs were synthesized using isotopically pure $^{107}AgNO_3$ and $^{109}AgNO_3$ salts and following the previously established synthetic protocols.[40,41] Details of synthesis are mentioned in the Supporting Information, and ESI MS of the NCs is presented in Figure S1.

2.3. Synthesis of AgNPs. DMBT-protected AgNPs (referred to as AgNPs@DMBT) were synthesized by modifying the conventional protocols known for the synthesis of AgNPs.[42,43] In a typical synthesis, 25 mg of $AgNO_3$ (commercially available, made from naturally abundant Ag) was dissolved in 0.5 mL of water, and 58 μL of 2,4-DMBT in 10 mL of MeOH was added to it. Subsequently, Ag was reduced to its zero-valent state by slowly adding a freshly prepared $NaBH_4$ solution in 8 mL of ice-cold water. Two sets of syntheses were carried out by using different quantities of $NaBH_4$ (35 and 25 mg) to alter the size of the resulting NPs.

The reaction mixture was stirred for about 12 h at room temperature. The as-synthesized particles were first precipitated and then repeatedly washed with methanol. Finally, the AgNPs@DMBT were obtained as dark brown precipitates. These NPs were soluble in dichloromethane (DCM) and further characterized by using UV−vis and high-resolution transmission electron microscopy (HRTEM) (Figure S2A,B). The plasmonic nature of the particles was reflected in their UV−vis spectra. A particle size distribution of 1.8 ± 0.5 and 3.9 ± 1.2 nm was observed in the HRTEM images of the NPs synthesized using 35 and 25 mg of $NaBH_4$, respectively. Another synthesis was performed by slightly altering the precursor quantities with 50 mg of $AgNO_3$, 10 μL of 2,4-DMBT, and 25 mg of $NaBH_4$. AgNPs@DMBT of slightly larger size were formed in this case, which showed a reduced solubility in DCM. Therefore, they were dispersed in DCM and subsequently characterized using UV−vis and HRTEM (Figure S2C). These AgNPs showed a particle size distribution of 11.2 ± 3.1 nm. The AgNPs@DMBT were stable for weeks when stored in a refrigerator under dark conditions. The sizes of the particles refer to the metal core diameter observed in HRTEM images. The binding of the DMBT ligands on the surface of the AgNPs was confirmed from Raman spectroscopic studies, as shown in Figure S3. Upon functionalization of the AgNPs, the S−H bond of DMBT was replaced by an Ag−S bond, which was proved by the absence of the S−H stretching peak.

2.4. Reaction between NCs and AgNPs. For carrying out the reactions of the NCs with AgNPs, first, stock solutions of 1 mg/mL were prepared for all the particles. Then, 20 μL of the stock NC solution was mixed with 20, 40, 60, and 100 μL of the stock NP solution, and the reaction mixture was appropriately diluted with DCM, keeping the total volume as 5 mL. This allowed reactions to occur at different NC/NP concentrations (i.e., 1:1, 1:2, 1:3, and 1:5, respectively in w/v). A similar procedure was followed for the reaction with AgNPs of the three different sizes.

2.5. Preparation of Monolayer-Protected Foils. Ag foils were first washed with soap water and then cleaned with methanol to remove the surface contaminants. The Ag surface was further cleaned with acetic acid and again with methanol. The cleaned Ag foils were then dried by purging with N_2 gas. Ag foils of size 1 cm × 1 cm were used in our experiments. For preparing the monolayers on the foils, the cleaned Ag foils were soaked in a methanolic solution of the thiol (1 mM). It was kept undisturbed overnight, and then, the excess thiol was washed using methanol. The cleaned monolayer-protected foils were then dried under N_2 gas.

2.6. Reaction with Bare and Monolayer-Protected Foils. 20 μL of the stock (1 mg/mL) NC solution was diluted with DCM to a final volume of 5 mL. Bare and monolayer-protected foils were then immersed in this NC solution, and the reaction was monitored with time.

2.7. Reaction with Ag Powder. From the stock NC solution (1 mg/mL), 20 μL of the sample was taken out and diluted in DCM to a total volume of 5 mL. To this solution, Ag powder of desired mass was added, and the reaction was monitored with time.

3. RESULTS AND DISCUSSION

3.1. Reaction of Isotopic NCs with Plasmonic NPs. To investigate the interparticle isotopic exchange between sub-nanometer-sized NCs and classical plasmonic nanomaterials, we chose $Ag_{25}(DMBT)_{18}^-$ and AgNPs@DMBT with increasing size as our systems of study (Figure 1A). Metallic NPs show different facets and distribution of capping ligands on the NP surface compared to NCs. Moreover, as conventional NPs are larger compared to atomically precise NCs, they are expected to exhibit more stability due to their reduced surface area. All such factors may significantly alter the dynamics and kinetics of exchange compared to intercluster isotopic exchanges.

We present the essential characterization data of the materials used, although briefly and that too in the Supporting Information. We prepared isotopically pure $^{107}Ag_{25}(DMBT)_{18}^-$ and $^{109}Ag_{25}(DMBT)_{18}^-$. The ESI MS data of the samples confirm the purity of $^{107}Ag_{25}(DMBT)_{18}^-$ (Figure 1Ba) and $^{109}Ag_{25}(DMBT)_{18}^-$ (Figure 1Ca), which show peaks centered at m/z 5142 and m/z 5192, respectively. Full-range mass spectra of the systems are presented in the Supporting Information (Figure S1). The AgNPs@DMBT were made from naturally abundant Ag, which contained ^{107}Ag and ^{109}Ag in the ratio 51.8:48.2. Three AgNPs@DMBT systems of average sizes, 1.8 ± 0.5, 3.9 ± 1.2, and 11.2 ± 3.1 nm, were used in our study. TEM images of the AgNPs and particle size distribution from TEM are presented in Figure S2. These are referred to as ∼2, ∼4, and ∼11 nm AgNPs, respectively, in the subsequent text. The optical absorption spectra of the AgNPs are also presented in Figure S2, which showed that the particles are plasmonic in nature. The synthetic protocol and characterization of the NCs and the NPs were discussed in the Experimental Methods. Note that Ag NPs of lower sizes exhibiting plasmonic behavior have also been reported earlier.[44−46] The surface plasmonic nature of the ∼2 nm AgNPs also supported that the sample did not contain any significant contribution from NCs. Isotopically pure NCs [$^{107}Ag_{25}(DMBT)_{18}^-$/$^{109}Ag_{25}(DMBT)_{18}^-$] were mixed with AgNPs@DMBT at varying NC: NP concentrations (w/v). We monitored the isotopic exchange in the NC by using ESI MS. Time-dependent ESI MS was performed on the reaction of $^{107}Ag_{25}(DMBT)_{18}^-$/$^{109}Ag_{25}(DMBT)_{18}^-$ with different AgNPs@DMBT NPs: ∼2 (Figure S4), ∼4 (Figure S5), and ∼11 nm (Figure S6) at NC/NP mixing ratios of 1:1, 1:2, 1:3, and 1:5, respectively, in each case. Mixing ratios are given in terms of w/v concentration of the particles. Upon mixing the solutions of $^{107}Ag_{25}(DMBT)_{18}^-$ and AgNPs@DMBT, isotopic exchange of ^{107}Ag with ^{109}Ag occurred in the NCs. Due to the exchange of ^{107}Ag with ^{109}Ag, the parent peak distribution of $^{107}Ag_{25}(DMBT)_{18}^-$ (m/z 5142) broadened gradually and shifted to a higher mass with the progress of the reaction and finally attained an equilibrium state after about 1 h (Figures S4−S6, panel a in each case). Similar results were also obtained when $^{109}Ag_{25}(DMBT)_{18}^-$ was reacted with AgNPs@DMBT of different sizes (Figures S4−S6, panel b in each case). In this case, the parent peak for $^{109}Ag_{25}(DMBT)_{18}^-$ (m/z 5192) broadened and shifted to lower mass, with the progress of the reaction due to the exchange of ^{109}Ag with ^{107}Ag atoms.

We attempted to quantify the effect of size of AgNPs on the extent of interparticle isotopic exchange. A schematic showing AgNPs@DMBT of increasing size is presented in Figure 1A. We found that the extent of isotopic exchange (%) increased with an increase in the concentration of AgNPs (NC/NP concentration from 1:1 to 1:5) in the solution for each size of the NPs (Figure S7). Corresponding UV−vis spectra of the NC−NP mixtures, equilibrated after ∼1 h of reaction, are presented in Figure S8. For the reaction with ∼2 and ∼4 nm

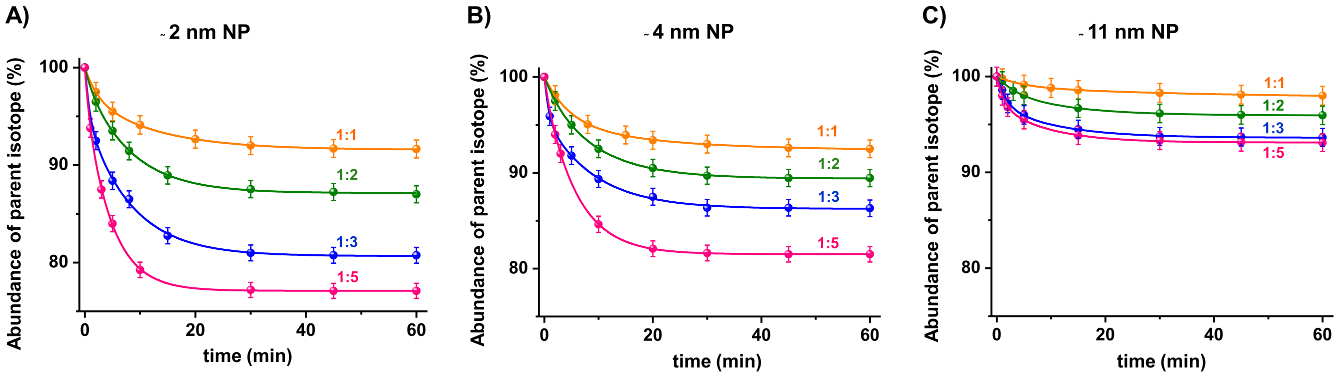

Figure 2. Abundance of the parent isotope (%) in NC as a function of reaction time (min) during the reaction with (A) ~2, (B) ~4, and (C) ~11 nm AgNPs at different NC/NP concentrations. The curves are fitted with a biexponential function. The average of three kinetic measurements is plotted, and the uncertainty is indicated by error bars at each point.

AgNPs at lower concentrations, that is, a NC/NP ratio of 1:1 or 1:2, the UV−vis spectra of the mixture resembled those of the NC with slight changes in the peak position, suggesting interaction between the particles. At higher NP concentrations, that is, a NC/NP ratio of 1:3 or 1:5, the plasmonic peaks of the NPs became prominent, which also showed minor shifts in peak positions and width, indicating slight changes in the size distribution of the plasmonic particles due to isotopic exchanges. In the reaction of the NC with ~11 nm AgNPs, the spectra resembled a mixture of NC and NP with dominant NC features at all NC/NP concentrations due to the lesser extent of isotopic exchange.

For comparison with the isotopic exchange in sub-nanometer-sized NCs under identical conditions, we also carried out reactions of $^{107}Ag_{25}(DMBT)_{18}^{-}$/$^{109}Ag_{25}(DMBT)_{18}^{-}$ with $Ag_{25}(DMBT)_{18}^{-}$ synthesized from naturally abundant Ag (NC−NC reaction). The isotopic exchange in this case was rapid and stoichiometric in nature, and the system equilibrated instantaneously (Figure S9), as observed earlier.[40] Though the size of the NC (1.9 ± 0.5 nm) (Figure S10) was comparable to the size of the ~2 nm plasmonic NPs and both were protected by the same monolayer of ligands, the drastic difference in their reactivity highlighted how the precision in the structure of the particles controlled the reaction. Isotopic exchange in the case of the NC−NC reaction was highly facile, in comparison to the reaction of the NC with plasmonic NPs of similar size. This suggests that the exchange between identical metal−ligand fragments that constitutes the aspicule structure[47] of the NCs is a major reason behind the fast reaction in the case of the NC−NC reaction. The final exchanged states (after ~1 h of reaction) for 1:5 molar ratio in the case of all the NC−NP (~2, ~4, and ~11 nm) and NC−NC reactions are presented in Figure 1B,C. This revealed that the isotopic exchange in the NCs increased with a decrease in the size of the reacting particles and the extent of exchange was maximum in the case of the NC−NC reaction. This was true for all molar ratios of mixing, as evident from Figure 1D, which showed isotopic exchange (%) in the final product NC as a function of the NP/NC concentrations (w/v) for all the reactions. However, it is to be noted that the number of particles per milliliter (details are presented in the Supporting Information) will be significantly different in identical w/v concentrations of NCs and NPs. The number of particles per milliliter is higher for NCs compared to the larger NPs with equivalent amounts of Ag in them. Therefore, the higher probability of interaction in the case of the NC−NC reaction also contributes to the higher extent of exchange. Here, the isotopic exchange (%) was calculated from the m/z values and isotopic distribution of the peaks of the NCs after completion of the reaction. Further details of this calculation are presented in the Supporting Information. It is to be noted that the AgNPs were made from naturally abundant Ag, where both ^{107}Ag and ^{109}Ag atoms were present. Although only exchanges of the type 107−109 were detectable in ESI MS, it is obvious that there were also exchanges between similar isotopes (107−107) and (109−109) as well. Also, as the ratio of $^{107}Ag/^{109}Ag$ in the parent AgNPs was nearly 1, both the isotopic atoms had an equal probability of exchange at least in the initial stages of the reaction. However, using only one of the reactants as isotopically pure [$Ag_{25}(DMBT)_{18}^{-}$ in this case] was sufficient to understand the kinetics of the reaction. Moreover, by analyzing the final reaction products using TEM, we confirmed that both NCs and NPs were present in the mixture after attaining the thermodynamic equilibrium (Figure S11).

To obtain further insights into the kinetics of this isotopic exchange, that is, the timescales and rates of isotopic atom transfer during NC−NP reactions, we monitored the decrease in the abundance (%) of the parent isotope in the NCs as a function of time of reaction. Here, the abundance (%) of the parent isotope in the NCs refers to the abundance of ^{107}Ag or ^{109}Ag when the reaction was performed with $^{107}Ag_{25}(DMBT)_{18}^{-}$ or $^{109}Ag_{25}(DMBT)_{18}^{-}$, respectively. As both cases gave similar results, we considered an average of these two cases in calculating the abundances in Figure 2. The abundance of the parent isotope in the NCs (%) versus the time (min) of reaction is shown in Figure 2A−C, for ~2, ~4, and ~11 nm AgNPs, respectively. In each of these cases, the kinetics was monitored for four different NC/NP mixing ratios, that is, 1:1, 1:2, 1:3, and 1:5, respectively. The abundance of the parent isotope was assumed to be 100% at zero reaction time, and this theoretical data point was included in all cases. In each case, the abundance of the parent isotope (%) [$Y(t)$] was fitted to a biexponential function of the form, $Y(t) = A_0 + A_1 e^{-t/\tau_1} + A_2 e^{-t/\tau_2}$. Here, τ_1 and τ_2 are the two timescales of the reaction and A_1 and A_2 are proportionality factors to the contribution of each timescale. A_0 denotes the value of $Y(t)$ when the reaction attains equilibrium. The average reaction time, τ, was determined by integrating $Y(t)$ over time. Further details of the fitting are presented in the Supporting Information. The values of τ_1 and τ_2 and the calculation of τ are presented in Table S1. The two timescales differed by approximately 1 order of magnitude. The faster

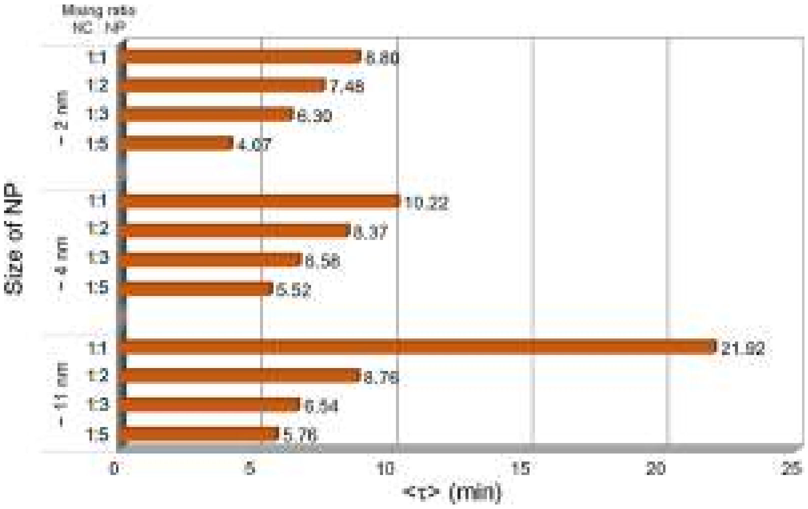

Figure 3. Average timescales (τ) of the isotopic exchange reaction of the NC with AgNPs of different sizes and at different NC/NP mixing ratios.

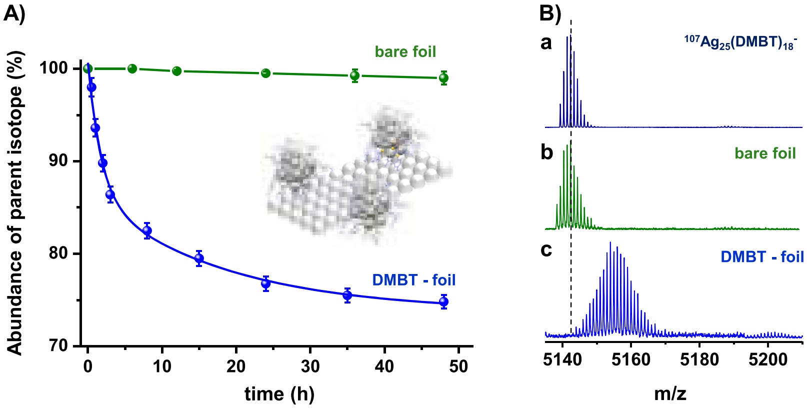

Figure 4. (A) Abundance of the parent isotope (%) in the NC as a function of reaction time (h) during the reaction with bare and monolayer-protected Ag foils. A schematic showing the reaction of the NCs with a foil is presented as an inset. (B) ESI MS of (a) $^{107}Ag_{25}(DMBT)_{18}^-$ and product taken after 48 h of the reaction of $^{107}Ag_{25}(DMBT)_{18}^-$ with (b) bare and (c) DMBT-protected Ag foils.

reaction component, that is, the shorter timescale of the reaction, possibly corresponds to the exchange of the surface atoms, whereas the slower reaction component, that is, of the longer timescale, corresponds to the diffusion of exchanged atoms into the core to attain an equilibrium state, as observed earlier in the case of intercluster isotopic exchanges.[38] The variation in τ with different NC/NP mixing ratios for the three different sizes of AgNPs@DMBT is presented in Figure 3. For a particular size of AgNP, τ decreased, that is, the rate increased with the increase in the concentration of the AgNPs in the solution, that is, from the NC/NP mixing ratio of 1:1 to 1:5. Thus, a higher concentration of AgNPs favored higher exchange rates and transferred more atoms to the NCs, resulting in a greater isotopic exchange (%), as observed in Figure 1D. Also, the reaction timescale or rate showed a dependence on the size of the AgNPs, as presented in Figure 3. Generally, τ increased or rate decreased as we increased the particle size. However, this correlation decreased with an increase in the concentration of the NPs (NP/NC ratio) in the solution. This might be attributed to the fact that at a higher NP concentration, a higher number of collisions occurred between the NCs and the NPs, which dominated over other factors such as size or surface area of the NPs in controlling the timescales of the reactions.

3.2. Reaction of Isotopic NCs with Bulk Silver Foils.

From the above experiments, it was clear how the isotopic exchange of NCs with NPs differed compared to an intercluster isotopic exchange. We further attempted to understand how bulk metal also transfers atoms to the NCs. We investigated the isotopic exchange in the NCs upon reaction with bare and monolayer-protected Ag foils. Here also, the NC used was isotopically pure [$^{107}Ag_{25}(DMBT)_{18}^-$/$^{109}Ag_{25}(DMBT)_{18}^-$] and the Ag foils were composed of naturally abundant Ag. The methods used for cleaning the metal surface and preparation of the monolayers on the foils were discussed in the Experimental Methods. The NC concentration was kept the same as that used in the case of reactions with AgNPs. An Ag foil (1 cm × 1 cm) was immersed in the NC solution, and the reaction was monitored for about 48 h. ESI MS was performed by taking out small fractions of the solution at different time intervals. No external stirring was applied to avoid the effect of any mechanical perturbations on the isotopic exchange process. Time-dependent ESI MS revealed that exchange in the NCs was drastically less when reacted with bare Ag foil (Figure S12). The peaks for the parent NC ions were almost unshifted and exhibited only slight broadening in the isotopic distribution with time. In contrast, when the Ag foil was protected by a monolayer of 2,4-DMBT ligands (Ag foil@

DMBT), significant exchange was observed (Figure S13). Similar behavior was observed using both $^{107}Ag_{25}(DMBT)_{18}^-$ and $^{109}Ag_{25}(DMBT)_{18}^-$ as the isotopically labeled NCs. The abundance of parent isotope (%) is presented as a function of reaction time in Figure 4A. This revealed that there was negligible change in the abundance of the parent NCs upon reaction with the bare Ag foil. However, upon reaction with Ag foil@DMBT, the abundance of the parent isotope of the NCs decreased significantly with the reaction time. The exchange was initially fast, and hence, the abundance decreased sharply in the initial 3 h of the reaction. The reaction then slowed down, and the abundance of the parent NCs decreased gradually to about 75% after 48 h. The isotopic exchange kinetics in the case of the reaction with Ag foil@DMBT also followed a biexponential fitting with two timescales of 1.78 and 18.17 h for the shorter and longer reaction component, respectively. ESI MS showing product NCs after 48 h when $^{107}Ag_{25}(DMBT)_{18}^-$ was used for the reaction with bare and monolayer-protected foils is presented in Figure 4B. A similar exchange was also observed during the reaction with $^{109}Ag_{25}(DMBT)_{18}^-$ (Figures S12 and S13). From our study, it is clear that the preadsorbed thiols on the Ag foils accelerated the reaction. A similar observation was also reported by Bürgi and co-workers where doping of Au NCs was observed by the reaction with Ag foils.[33]

3.3. Reaction of Isotopic NCs with Bulk Ag Powder.

We further investigated the reaction of the NCs with bulk Ag powder. From the previous experiments, we know that the bare Ag foil exhibited negligible reactivity. However, we know that the reactivity increases with an increase in the surface area. To explore the role of the surface area of the bulk metal on the isotopic exchange process, we performed a reaction of the NCs $[^{107}Ag_{25}(DMBT)_{18}^-/^{109}Ag_{25}(DMBT)_{18}^-]$ with bare Ag powder. First, we performed a reaction with about 80 mg of Ag powder, which was almost equivalent to the mass of 1 cm × 1 cm bare Ag foil of ~0.1 mm thickness. Time-dependent ESI MS (Figure S14A) revealed that the reaction of the NCs with Ag powder was somewhat favored. While in the case of the bare Ag foil, the exchange was negligible even after 48 h, whereas a significant extent of exchange was observed within 2 h of the reaction with the Ag powder. Upon reducing the quantity of the Ag powder to 40 and 20 mg, the isotopic exchange decreased (Figure S14B,C). The decrease in the abundance of the parent isotope in the NCs (%) was studied similarly as a function of reaction time to obtain greater insights into the kinetics of the reaction. This is presented in Figure 5. The reaction was not monitored beyond 2 h as the intensity of the NCs in ESI MS started to decrease, which might be attributed to a certain extent of degradation of the NCs in the presence of Ag powder. It can be seen from Figure 5 that for the first 5 min, there was no change in the abundance of the isotope, suggesting a very slow initial reaction rate, and then, the reaction progressed gradually. Thus, it is clear that initially, a certain period of time was required for the activation of the bare surface of the Ag powder, and this activation might have occurred due to the adsorption of NCs on the surface or the deposition of Ag-thiolates, resulting from the decomposition of the NCs. We also monitored the reaction using UV−vis studies (Figure S15), which also showed that there was a certain extent of degradation of the NCs in the presence of the Ag powder and this degradation also increased with an increase in the amount of Ag powder. However, the kinetics of reactions could not be fitted with mono-, bi-, or triexponential functions, suggesting even complex steps involved in the case of the isotopic exchange reaction of NC with bulk Ag powder, which might arise due to the degradation of the NCs or the possibility of oxygen adsorption on the surface of the Ag powder.

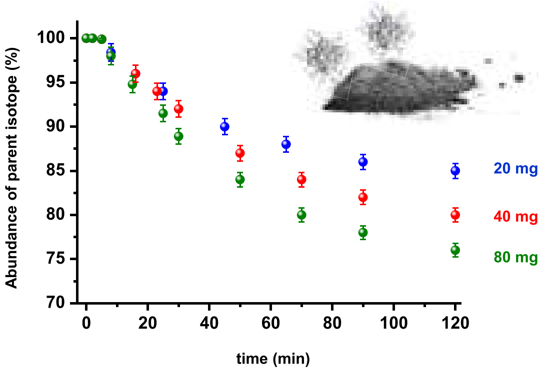

Figure 5. Abundance of parent isotope (%) of the isotopic NC as a function of time (min) during the reaction with various quantities of Ag powder, with a fixed quantity of the NC. A scheme of this reaction is presented as an inset. The average of three kinetic measurements is plotted, and the uncertainty is indicated by error bars at each point.

It is evident that in the case of the above reactions with AgNPs, bulk foil, or powder, there will be changes in their isotopic composition as well, as atoms from the NCs will also be transferred to them. These changes may occur through the deposition of isotopically enriched metal or metal thiolates coming from the NCs. Although isotopic exchanges are mainly driven by the entropy of mixing, in these reactions, there could also be some enthalpy effects depending on the exchanges occurring on the AgNPs or bulk Ag counterparts. The enthalpy effects could arise from possible ligand exchanges, slight changes in the size and morphology of the AgNPs, or possible changes in the surface of the Ag foil or Ag powder upon reaction with the NCs. However, this aspect could not be investigated in the current study as AgNPs are beyond the mass range of the present instrument. MS in the megadalton range with adequate resolution should be able to detect this.[48−50] Moreover, using isotopically enriched DMBT ligands will also help to resolve the extent of ligand exchanges in these reactions, which are areas for future study. Future investigations will also involve studying the effect of shape of the materials on such exchange reactions. The state of the surface of the reacted foil and Ag powder might also be of potential interest for further studies. The isotopic composition of the surface of the bulk Ag foil or Ag powder might also get altered upon reaction with the NCs.

4. CONCLUSIONS

By using isotopic exchange reactions, we presented a complete study on how the dynamics of the spontaneous atom transfer process in atomically precise NCs vary upon reaction with materials of different sizes. Isotopically pure NCs, $^{107}Ag_{25}(DMBT)_{18}^-$ and $^{109}Ag_{25}(DMBT)_{18}^-$, were used in our study. Upon increasing the size of the reacting partner from the NC to the NP regime, protected with the same ligand, the exchange process was found to slow down. The exchange rates further decreased upon reacting with materials in the bulk such as a metal foil and micron-scale metal powder. By monitoring the time-dependent changes of the isotopic abundance of the reacting NCs, we analyzed the kinetics of the process and determined the different timescales involved in such reactions. The isotopic exchanges are mainly brought about by the entropy of mixing. Our studies demonstrate the spontaneity of atom transfer when NCs are brought in contact with NPs and bulk metals. This method may emerge as a simple procedure to alter the isotopic composition of metal surfaces.

■ ASSOCIATED CONTENT

Supporting Information

The Supporting Information is available free of charge at https://pubs.acs.org/doi/10.1021/acs.jpcc.1c02264.

> Instrumentation; experimental methods of the synthesis of NCs; biexponential fitting of the reaction kinetics; ESI MS of pure $^{107}Ag_{25}(DMBT)_{18}$ and $^{109}Ag_{25}(DMBT)_{18}$ NCs; time-dependent and concentration-dependent ESI MS of reaction of isotopic NCs with Ag NPs of different sizes, bare and monolayer-protected Ag foils, and bulk Ag powder; and TEM and optical absorption spectra for the characterization of the parent NCs and NPs as well as their reaction products (PDF)

■ AUTHOR INFORMATION

Corresponding Author

Thalappil Pradeep − *DST Unit of Nanoscience (DST UNS) and Thematic Unit of Excellence (TUE), Department of Chemistry, Indian Institute of Technology Madras, Chennai 600 036, India;* orcid.org/0000-0003-3174-534X; Email: pradeep@iitm.ac.in

Authors

Papri Chakraborty − *DST Unit of Nanoscience (DST UNS) and Thematic Unit of Excellence (TUE), Department of Chemistry, Indian Institute of Technology Madras, Chennai 600 036, India;* Present Address: Institute of Nanotechnology, Karlsruhe Institute of Technology, 76344 Eggenstein-Leopoldshafen and Institute of Physical Chemistry, Karlsruhe Institute of Technology, 76131 Karlsruhe, Germany

Paulami Bose − *DST Unit of Nanoscience (DST UNS) and Thematic Unit of Excellence (TUE), Department of Chemistry, Indian Institute of Technology Madras, Chennai 600 036, India*

Jayoti Roy − *DST Unit of Nanoscience (DST UNS) and Thematic Unit of Excellence (TUE), Department of Chemistry, Indian Institute of Technology Madras, Chennai 600 036, India*

Abhijit Nag − *DST Unit of Nanoscience (DST UNS) and Thematic Unit of Excellence (TUE), Department of Chemistry, Indian Institute of Technology Madras, Chennai 600 036, India*

Biswajit Mondal − *DST Unit of Nanoscience (DST UNS) and Thematic Unit of Excellence (TUE), Department of Chemistry, Indian Institute of Technology Madras, Chennai 600 036, India*

Amrita Chakraborty − *DST Unit of Nanoscience (DST UNS) and Thematic Unit of Excellence (TUE), Department of Chemistry, Indian Institute of Technology Madras, Chennai 600 036, India*

Complete contact information is available at: https://pubs.acs.org/10.1021/acs.jpcc.1c02264

Notes

The authors declare no competing financial interest.

■ ACKNOWLEDGMENTS

P.C. and A.N. thank IIT Madras for providing their postdoctoral fellowships. P.B., J.R., and B.M. thank IIT Madras for their doctoral research fellowships. A.C. thanks CSIR for her doctoral research fellowship. We thank the Department of Science and Technology, Government of India, for supporting our research programme.

■ REFERENCES

(1) Du, Y.; Sheng, H.; Astruc, D.; Zhu, M. Atomically Precise Noble Metal Nanoclusters as Efficient Catalysts: A Bridge between Structure and Properties. *Chem. Rev.* **2020**, *120*, 526−622.

(2) Jin, R.; Zeng, C.; Zhou, M.; Chen, Y. Atomically Precise Colloidal Metal Nanoclusters and Nanoparticles: Fundamentals and Opportunities. *Chem. Rev.* **2016**, *116*, 10346−10413.

(3) Kang, X.; Zhu, M. Tailoring the Photoluminescence of Atomically Precise Nanoclusters. *Chem. Soc. Rev.* **2019**, *48*, 2422−2457.

(4) Jin, R. Atomically Precise Metal Nanoclusters: Stable Sizes and Optical Properties. *Nanoscale* **2015**, *7*, 1549−1565.

(5) Maity, P.; Xie, S.; Yamauchi, M.; Tsukuda, T. Stabilized Gold Clusters: From Isolation toward Controlled Synthesis. *Nanoscale* **2012**, *4*, 4027−4037.

(6) Yao, Q.; Wu, Z.; Liu, Z.; Lin, Y.; Yuan, X.; Xie, J. Molecular Reactivity of Thiolate-Protected Noble Metal Nanoclusters: Synthesis, Self-Assembly, and Applications. *Chem. Sci.* **2021**, *12*, 99−127.

(7) Ghosh, A.; Mohammed, O. F.; Bakr, O. M. Atomic-Level Doping of Metal Clusters. *Acc. Chem. Res.* **2018**, *51*, 3094−3103.

(8) Song, X.-R.; Goswami, N.; Yang, H.-H.; Xie, J. Functionalization of Metal Nanoclusters for Biomedical Applications. *Analyst* **2016**, *141*, 3126−3140.

(9) Agrachev, M.; Ruzzi, M.; Venzo, A.; Maran, F. Nuclear and Electron Magnetic Resonance Spectroscopies of Atomically Precise Gold Nanoclusters. *Acc. Chem. Res.* **2019**, *52*, 44−52.

(10) Yamazoe, S.; Koyasu, K.; Tsukuda, T. Nonscalable Oxidation Catalysis of Gold Clusters. *Acc. Chem. Res.* **2014**, *47*, 816−824.

(11) Matus, M. F.; Häkkinen, H. Atomically Precise Gold Nanoclusters: Towards an Optimal Biocompatible System from a Theoretical-Experimental Strategy. *Small* **2021**, *17*, 2005499.

(12) Xia, N.; Wu, Z. Controlling Ultrasmall Gold Nanoparticles with Atomic Precision. *Chem. Sci.* **2021**, *12*, 2368−2380.

(13) Krishnadas, K. R.; Baksi, A.; Ghosh, A.; Natarajan, G.; Som, A.; Pradeep, T. Interparticle Reactions: An Emerging Direction in Nanomaterials Chemistry. *Acc. Chem. Res.* **2017**, *50*, 1988−1996.

(14) Knoppe, S.; Bürgi, T. The Fate of $Au_{25}(SR)_{18}$ Clusters Upon Ligand Exchange with Binaphthyl-Dithiol: Interstaple Binding Vs. Decomposition. *Phys. Chem. Chem. Phys.* **2013**, *15*, 15816−15820.

(15) Huang, Z.; Ishida, Y.; Narita, K.; Yonezawa, T. Kinetics of Cationic-Ligand-Exchange Reactions in Au_{25} Nanoclusters. *J. Phys. Chem. C* **2018**, *122*, 18142−18150.

(16) Knoppe, S.; Dharmaratne, A. C.; Schreiner, E.; Dass, A.; Bürgi, T. Ligand Exchange Reactions on Au_{38} and Au_{40} Clusters: A Combined Circular Dichroism and Mass Spectrometry Study. *J. Am. Chem. Soc.* **2010**, *132*, 16783−16789.

(17) Niihori, Y.; Hossain, S.; Kumar, B.; Nair, L. V.; Kurashige, W.; Negishi, Y. Perspective: Exchange Reactions in Thiolate-Protected Metal Clusters. *APL Mater.* **2017**, *5*, 053201.

(18) Niihori, Y.; Kikuchi, Y.; Kato, A.; Matsuzaki, M.; Negishi, Y. Understanding Ligand-Exchange Reactions on Thiolate-Protected Gold Clusters by Probing Isomer Distributions Using Reversed-Phase High-Performance Liquid Chromatography. *ACS Nano* **2015**, *9*, 9347−9356.

(19) Wang, S.; Song, Y.; Jin, S.; Liu, X.; Zhang, J.; Pei, Y.; Meng, X.; Chen, M.; Li, P.; Zhu, M. Metal Exchange Method Using Au_{25}

Nanoclusters as Templates for Alloy Nanoclusters with Atomic Precision. *J. Am. Chem. Soc.* **2015**, *137*, 4018−4021.

(20) Wang, S.; Xiong, L.; Sun, G.; Tang, L.; Zhang, J.; Pei, Y.; Zhu, M. The Mechanism of Metal Exchange in Non-Metallic Nanoclusters. *Nanoscale Adv.* **2020**, *2*, 664−668.

(21) Zhang, B.; Safonova, O. V.; Pollitt, S.; Salassa, G.; Sels, A.; Kazan, R.; Wang, Y.; Rupprechter, G.; Barrabés, N.; Bürgi, T. On the Mechanism of Rapid Metal Exchange between Thiolate-Protected Gold and Gold/Silver Clusters: A Time-Resolved in Situ XAFS Study. *Phys. Chem. Chem. Phys.* **2018**, *20*, 5312−5318.

(22) Krishnadas, K. R.; Ghosh, A.; Baksi, A.; Chakraborty, I.; Natarajan, G.; Pradeep, T. Intercluster Reactions between $Au_{25}(SR)_{18}$ and $Ag_{44}(SR)_{30}$. *J. Am. Chem. Soc.* **2016**, *138*, 140−148.

(23) Krishnadas, K. R.; Baksi, A.; Ghosh, A.; Natarajan, G.; Pradeep, T. Structure-Conserving Spontaneous Transformations between Nanoparticles. *Nat. Commun.* **2016**, *7*, 13447.

(24) Huang, B.; Pei, Y. On the Mechanism of Inter-Cluster Alloying Reactions: Two-Stage Metal Exchange of $[Au_{25}(PET)_{18}]^-$ and $[Ag_{25}(DMBT)_{18}]^-$ Clusters. *J. Mater. Chem. A* **2020**, *8*, 10242−10251.

(25) Baksi, A.; Schneider, E. K.; Weis, P.; Chakraborty, I.; Fuhr, O.; Lebedkin, S.; Parak, W. J.; Kappes, M. M. Linear Size Contraction of Ligand Protected Ag_{29} Clusters by Substituting Ag with Cu. *ACS Nano* **2020**, *14*, 15064−15070.

(26) Khatun, E.; Chakraborty, P.; Jacob, B. R.; Paramasivam, G.; Bodiuzzaman, M.; Dar, W. A.; Pradeep, T. Intercluster Reactions Resulting in Silver-Rich Trimetallic Nanoclusters. *Chem. Mater.* **2020**, *32*, 611−619.

(27) Salassa, G.; Sels, A.; Mancin, F.; Bürgi, T. Dynamic Nature of Thiolate Monolayer in $Au_{25}(SR)_{18}$ Nanoclusters. *ACS Nano* **2017**, *11*, 12609−12614.

(28) Krishnadas, K. R.; Natarajan, G.; Baksi, A.; Ghosh, A.; Khatun, E.; Pradeep, T. Metal−Ligand Interface in the Chemical Reactions of Ligand-Protected Noble Metal Clusters. *Langmuir* **2019**, *35*, 11243−11254.

(29) Zhang, B.; Salassa, G.; Bürgi, T. Silver Migration between $Au_{38}(SC_2H_4Ph)_{24}$ and Doped $Ag_xAu_{38-x}(SC_2H_4Ph)_{24}$ Nanoclusters. *Chem. Commun.* **2016**, *52*, 9205−9207.

(30) Li, Y.; Chen, M.; Wang, S.; Zhu, M. Intramolecular Metal Exchange Reaction Promoted by Thiol Ligands. *Nanomaterials* **2018**, *8*, 1070.

(31) Chakraborty, A.; Fernandez, A. C.; Som, A.; Mondal, B.; Natarajan, G.; Paramasivam, G.; Lahtinen, T.; Häkkinen, H.; Nonappa; Pradeep, T. Atomically Precise Nanocluster Assemblies Encapsulating Plasmonic Gold Nanorods. *Angew. Chem., Int. Ed.* **2018**, *57*, 6522−6526.

(32) Bose, P.; Chakraborty, P.; Mohanty, J. S.; Nonappa; Ray Chowdhuri, A.; Khatun, E.; Ahuja, T.; Mahendranath, A.; Pradeep, T. Atom Transfer between Precision Nanoclusters and Polydispersed Nanoparticles: A Facile Route for Monodisperse Alloy Nanoparticles and Their Superstructures. *Nanoscale* **2020**, *12*, 22116−22128.

(33) Kazan, R.; Müller, U.; Bürgi, T. Doping of Thiolate Protected Gold Clusters through Reaction with Metal Surfaces. *Nanoscale* **2019**, *11*, 2938−2945.

(34) Kaltashov, I. A.; Bobst, C. E.; Abzalimov, R. R. H/D Exchange and Mass Spectrometry in the Studies of Protein Conformation and Dynamics: Is There a Need for a Top-Down Approach? *Anal. Chem.* **2009**, *81*, 7892−7899.

(35) Maier, C. S.; Deinzer, M. L. Protein Conformations, Interactions, and H/D Exchange. *Methods in Enzymol*; Academic Press, 2005; Vol. *402*; pp 312−360.

(36) Nishimura, C.; Dyson, H. J.; Wright, P. E. Enhanced Picture of Protein-Folding Intermediates Using Organic Solvents in H/D Exchange and Quench-Flow Experiments. *Proc. Nat. Acad. Sci. U.S.A.* **2005**, *102*, 4765−4770.

(37) Lou, X.; Lafleur, R. P. M.; Leenders, C. M. A.; Schoenmakers, S. M. C.; Matsumoto, N. M.; Baker, M. B.; van Dongen, J. L. J.; Palmans, A. R. A.; Meijer, E. W. Dynamic Diversity of Synthetic Supramolecular Polymers in Water as Revealed by Hydrogen/Deuterium Exchange. *Nat. Commun.* **2017**, *8*, 15420.

(38) Chakraborty, P.; Nag, A.; Natarajan, G.; Bandyopadhyay, N.; Paramasivam, G.; Panwar, M. K.; Chakrabarti, J.; Pradeep, T. Rapid Isotopic Exchange in Nanoparticles. *Sci. Adv.* **2019**, *5*, No. eaau7555.

(39) Tang, L.; Kang, X.; Wang, X.; Zhang, X.; Yuan, X.; Wang, S. Dynamic Metal Exchange between a Metalloid Silver Cluster and Silver(I) Thiolate. *Inorg. Chem.* **2021**, *60*, 3037−3045.

(40) Chakraborty, P.; Nag, A.; Natarajan, G.; Bandyopadhyay, N.; Paramasivam, G.; Panwar, M. K.; Chakrabarti, J.; Pradeep, T. Rapid Isotopic Exchange in Nanoparticles. *Sci. Adv.* **2019**, *5*, No. eaau7555.

(41) Joshi, C. P.; Bootharaju, M. S.; Alhilaly, M. J.; Bakr, O. M. $[Ag_{25}(SR)_{18}]^-$: The "Golden" Silver Nanoparticle. *J. Am. Chem. Soc.* **2015**, *137*, 11578−11581.

(42) Diantoro, M.; Fitriangingsih, R.; Mufti, N.; Fuad, A. Synthesis of Silver Nanoparticles by Chemical Reduction at Various Fraction of Msa and Their Structure Characterization. *AIP Conf. Proc.* **2014**, *1589*, 257−261.

(43) Banne, S. V.; Patil, M. S.; Kulkarni, R. M.; Patil, S. J. Synthesis and Characterization of Silver Nano Particles for Edm Applications. *Mater. Today: Proc.* **2017**, *4*, 12054−12060.

(44) Scholl, J. A.; Koh, A. L.; Dionne, J. A. Quantum Plasmon Resonances of Individual Metallic Nanoparticles. *Nature* **2012**, *483*, 421−427.

(45) Campos, A.; Troc, N.; Cottancin, E.; Pellarin, M.; Weissker, H.-C.; Lermé, J.; Kociak, M.; Hillenkamp, M. Plasmonic Quantum Size Effects in Silver Nanoparticles Are Dominated by Interfaces and Local Environments. *Nat. Phys.* **2019**, *15*, 275−280.

(46) Park, J.; Kwon, S. G.; Jun, S. W.; Kim, B. H.; Hyeon, T. Large-Scale Synthesis of Ultra-Small-Sized Silver Nanoparticles. *Chem. Phys. Chem.* **2012**, *13*, 2540−2543.

(47) Natarajan, G.; Mathew, A.; Negishi, Y.; Whetten, R. L.; Pradeep, T. A Unified Framework for Understanding the Structure and Modifications of Atomically Precise Monolayer Protected Gold Clusters. *J. Phys. Chem. C* **2015**, *119*, 27768−27785.

(48) Sipe, D. M.; Plath, L. D.; Aksenov, A. A.; Feldman, J. S.; Bier, M. E. Characterization of Mega-Dalton-Sized Nanoparticles by Superconducting Tunnel Junction Cryodetection Mass Spectrometry. *ACS Nano* **2018**, *12*, 2591−2602.

(49) Doussineau, T.; Désert, A.; Lambert, O.; Taveau, J.-C.; Lansalot, M.; Dugourd, P.; Bourgeat-Lami, E.; Ravaine, S.; Duguet, E.; Antoine, R. Charge Detection Mass Spectrometry for the Characterization of Mass and Surface Area of Composite Nanoparticles. *J. Phys. Chem. C* **2015**, *119*, 10844−10849.

(50) Howder, C. R.; Bell, D. M.; Anderson, S. L. Optically Detected, Single Nanoparticle Mass Spectrometer with Pre-Filtered Electrospray Nanoparticle Source. *Rev. Sci. Instrum.* **2014**, *85*, 014104.

Supporting Information

Isotopic Exchange of Atomically Precise Nanoclusters with Materials of Varying Dimensions: From Nanoscale to Bulk

Papri Chakraborty, Paulami Bose, Jayoti Roy, Abhijit Nag, Biswajit Mondal, Amrita Chakraborty and Thalappil Pradeep[*]

DST Unit of Nanoscience (DST UNS) and Thematic Unit of Excellence (TUE), Department of Chemistry, Indian Institute of Technology Madras, Chennai 600 036, India.

Table of contents

Experimental methods

Instrumentation. UV-vis studies were performed using a PerkinElmer Lambda 25 UV-vis spectrometer. ESI MS measurements were performed using a Waters Synapt G2Si high resolution mass spectrometer. Capillary voltage of 3 KV, cone voltage 20, source offset 20, source temperature 100 °C, desolvation temperature 150 °C and desolvation gas flow of 400 L/h was used for ESI MS studies. Transmission electron microscopy experiments were performed in a JEOL 3010 instrument. Raman measurements were carried out using a WITec GmbH alpha300S confocal Raman equipped with a 532 nm laser as the excitation source.

Synthesis of $^{107}Ag_{25}(DMBT)_{18}^-$ and $^{109}Ag_{25}(DMBT)_{18}^-$. First, $^{107}AgNO_3$ and $^{109}AgNO_3$ salts were synthesized starting from isotopically pure ^{107}Ag and ^{109}Ag foils. Next, isotopically pure $^{107}Ag_{25}(DMBT)_{18}^-$ and $^{109}Ag_{25}(DMBT)_{18}^-$ clusters were synthesized using the reported protocol for synthesis of $Ag_{25}(DMBT)_{18}^-$ clusters.[1-2] About 38 mg of $AgNO_3$ was dissolved in 2 mL methanol and 90 µL of 2,4-DMBT thiol was added to it. Further, about 17 mL of DCM was added to it and the reaction mixture was kept for stirring at 0 °C. After about 15 mins, 6 mg of PPh_4Br in 1 mL methanol was added to it. About 5 mins later, 15 mg of $NaBH_4$ in 0.5 mL water was added. The reaction was continued for 8 h and then stored in the refrigerator for about 2 days. The sample was then centrifuged and insoluble materials were removed. The solvents were then evaporated using a rotary evaporator and the as-obtained crude cluster was repeatedly washed with methanol. The purified clusters were then extracted in DCM.

Calculation of theoretical isotope patterns with varying composition of ^{107}Ag/^{109}Ag: We calculated the isotopic patterns of $[Ag_{25}(DMBT)_{18}]^-$ with varying ^{107}Ag/^{109}Ag ratio by following our previous report.[2] The abundance of each isotope (^{107}Ag and ^{109}Ag) in $[Ag_{25}(DMBT)_{18}]^-$ cluster was varied such that the isotopic composition is (x,y) i.e., {(100,0), (99,1), (98,2).......(0,100)} where x and y are the abundance of ^{107}Ag and ^{109}Ag, respectively. The experimental spectra were compared with the calculated spectra to find the best match and hence confirm the abundances of each isotope in the clusters.

Biexponential fitting of the reaction kinetics.

Equation used for fitting the kinetic plots of NC-NP reactions is:

$$Y(t) = A_0 + A_1 e^{-t/\tau_1} + A_2 e^{-t/\tau_2} \qquad (1)$$

where $Y(t)$ is the time-dependent property, i.e. abundance of the parent isotope (%) in this case, τ_1 and τ_2 are the timescales and A_0, A_1 and A_2 are the fitting parameters. A_0 corresponds to the value of *Y(t)* when reaction reaches an equilibrium state.

The contribution, a_1 and a_2, of the timescales τ_1 and τ_2, respectively, to the overall process was evaluated using the following formula:

$$a_1 = \frac{A_1}{A_1 + A_2}, \; a_2 = \frac{A_2}{A_1 + A_2}, \qquad (2)$$

The average timescale of the reaction, $\langle\tau\rangle$, was calculated as follows:

$$\langle\tau\rangle = a_1\tau_1 + a_2\tau_2 \qquad (3)$$

Calculation of no of particles/mL for:

a) $Ag_{25}(DMBT)_{18}$ cluster

Molecular weight = 5167

Mass of 1 Ag NC (m) = $\frac{5167 \times 10^{3}}{6.023 \times 10^{23}}$ mg = 8.58×10^{-18} mg

Mass of Ag_{25} NCs in 1 mL of the stock solution considered in the experiments (W) = 1 mg

No. of particles per mL of the stock solution = $\frac{W}{m} = 1.17 \times 10^{17}$

Size of the metal core of the NC (2R, from single crystal XRD) ~ 1 nm; this diameter is smaller than the core size from TEM (1.9 nm), which is slightly overestimated.

Surface area = $4\pi R^2$ = 3.14 nm^2

The surface of the NC is covered by 18 DMBT ligands.

So, 1 DMBT ligand is assumed to occupy a surface area of ~0.17 nm^2.

The ligand coverage for the ~2 nm, ~4 nm and ~11 nm plasmonic NPs are not known exactly. So, the approximation that 1 DMBT ligand covers 0.17 nm^2 of the surface area of the particles is used to calculate the ligand coverage even for the other NPs, although the ligand packing is likely to be different.

Mass of 1 DMBT ligand (C_8H_9S) = $\frac{137 \times 10^{3}}{6.023 \times 10^{23}}$ mg = 22.75×10^{-20} mg

b) ~ 2 nm AgNP

Average size of metal core of the Ag NP (HRTEM), 2R = 1.8 nm

Volume of 1 Ag NP metal core (sphere), V = $\frac{4}{3}\pi R^3$ = 3.05 nm^3

Density of Ag NPs, $\rho = 10.5\ \frac{g}{cm^3} = 1.05 \times 10^{-17}\ \frac{mg}{nm^3}$

Mass of metal core of 1 Ag NP = $V\rho = 3.2 \times 10^{-17}$ mg

Surface area of 1 AgNP = $4\pi R^2$ = 10.17 nm^2

No. of DMBT ligands covering the surface ~ 60

As mentioned before, this number is based on the TEM core size, which is likely to slightly overestimate the metal core dimension.

Mass of the ligands = $60 \times 22.75 \times 10^{-20}$ mg = 1.36×10^{-17} mg

Total mass of 1 Ag NP (m) = mass of metal core + mass of ligands = 4.56×10^{-17} mg

Mass of AgNPs in 1 mL of the stock solution considered in the experiments (W) = 1 mg

No. of particles per mL of the stock solution = $\frac{W}{m}$ = 2.19×10^{16}

c) ~ 4 nm AgNP

Average size of metal core of the Ag NP (HRTEM), 2R = 3.9 nm

Volume of 1 Ag NP metal core (sphere), V = $\frac{4}{3}\pi R^3$ = 31.04 nm^3

Density of Ag NPs, ρ = 10.5 $\frac{\text{g}}{\text{cm}^3}$ = 1.05×10^{-17} $\frac{\text{mg}}{\text{nm}^3}$

Mass of metal core of 1 Ag NP = Vρ = 3.2×10^{-16} mg

Surface area of 1 AgNP = $4\pi R^2$ = 47.76 nm^2

No. of DMBT ligands covering the surface ~ 281

Mass of the ligands = 281 × 22.75 × 10^{-20} mg = 0.64×10^{-16} mg

Total mass of 1 Ag NP (m) = mass of core + mass of ligands = m = 3.84×10^{-16} mg

Mass of AgNPs in 1 mL of the stock solution considered in the experiments (W) = 1 mg

No. of particles per mL of the stock solution = $\frac{W}{m}$ = 2.60×10^{15}

d) ~ 11 nm AgNP

Average size of metal core of Ag NP (HRTEM), 2R = 11.2 nm

Volume of 1 Ag NP metal core (sphere), V = $\frac{4}{3}\pi R^3$ = 735.2 nm^3

Density of Ag NPs, ρ = 10.5 $\frac{\text{g}}{\text{cm}^3}$ = 1.05×10^{-17} $\frac{\text{mg}}{\text{nm}^3}$

Mass of metal core of 1 Ag NPs, m = Vρ = 7.72×10^{-15} mg

Surface area of 1 AgNP = $4\pi R^2$ = 393.88 nm^2

No. of DMBT ligands covering the surface ~ 2317

Mass of the ligands = 2317 × 22.75 × 10^{-20} mg = 0.53×10^{-15} mg

Total mass of 1 Ag NP (m) = mass of core + mass of ligands = m = 8.25×10^{-15} mg

Mass of AgNPs in 1 mL of the stock solution considered in the experiments (W) = 1 mg

No. of particles per mL of the stock solution = $\frac{W}{m}$ = 1.21×10^{14}

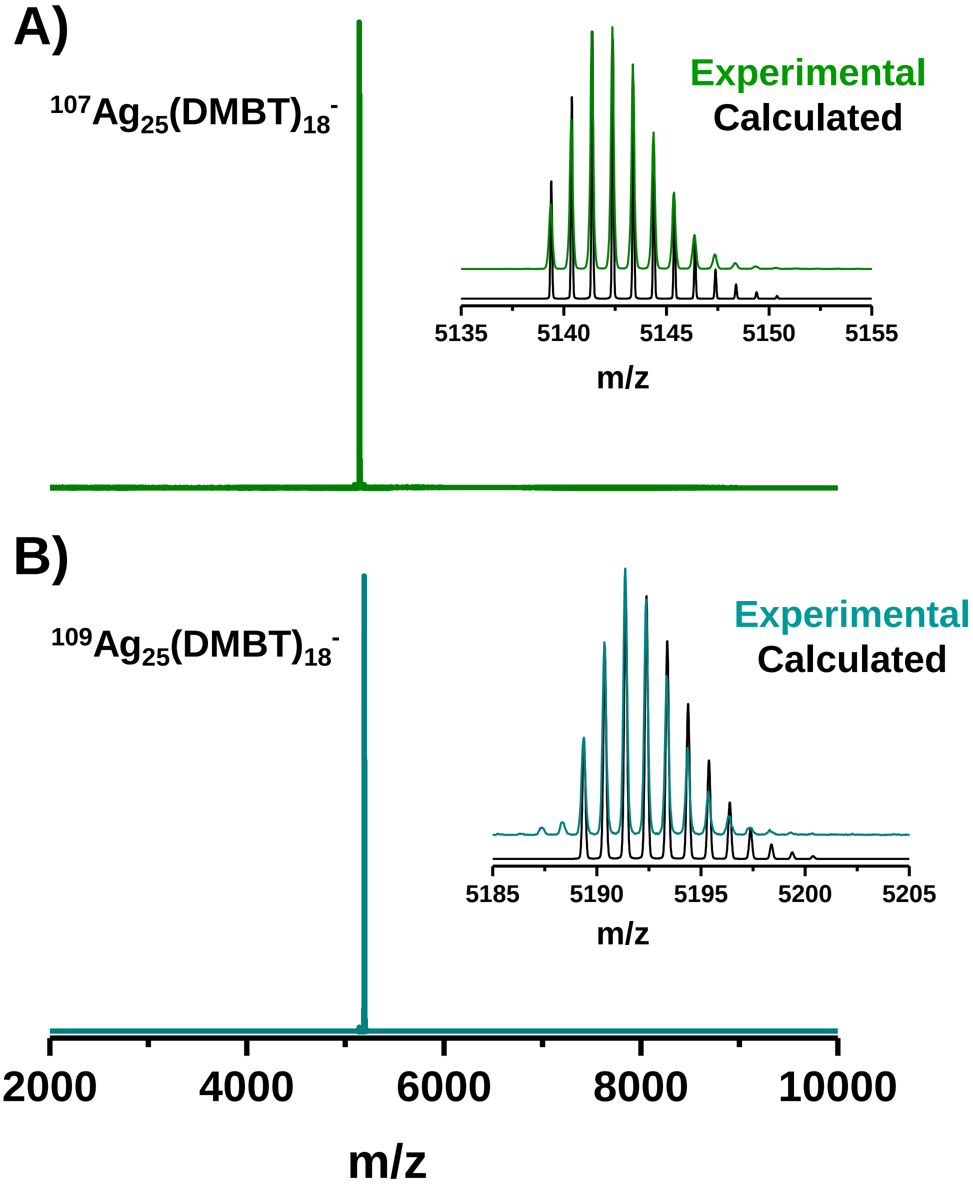

Figure S1. ESI MS of A) $^{107}Ag_{25}(DMBT)_{18}^-$ and B) $^{109}Ag_{25}(DMBT)_{18}^-$. Insets show the comparison of the experimental and theoretical isotopic patterns. The slight mismatches in the patterns may be attributed to some impurity present in the sample from the other isotope as the isotopic enrichment was 98%. However, this small discrepancy in the patterns may be neglected for further interpretation of the results.

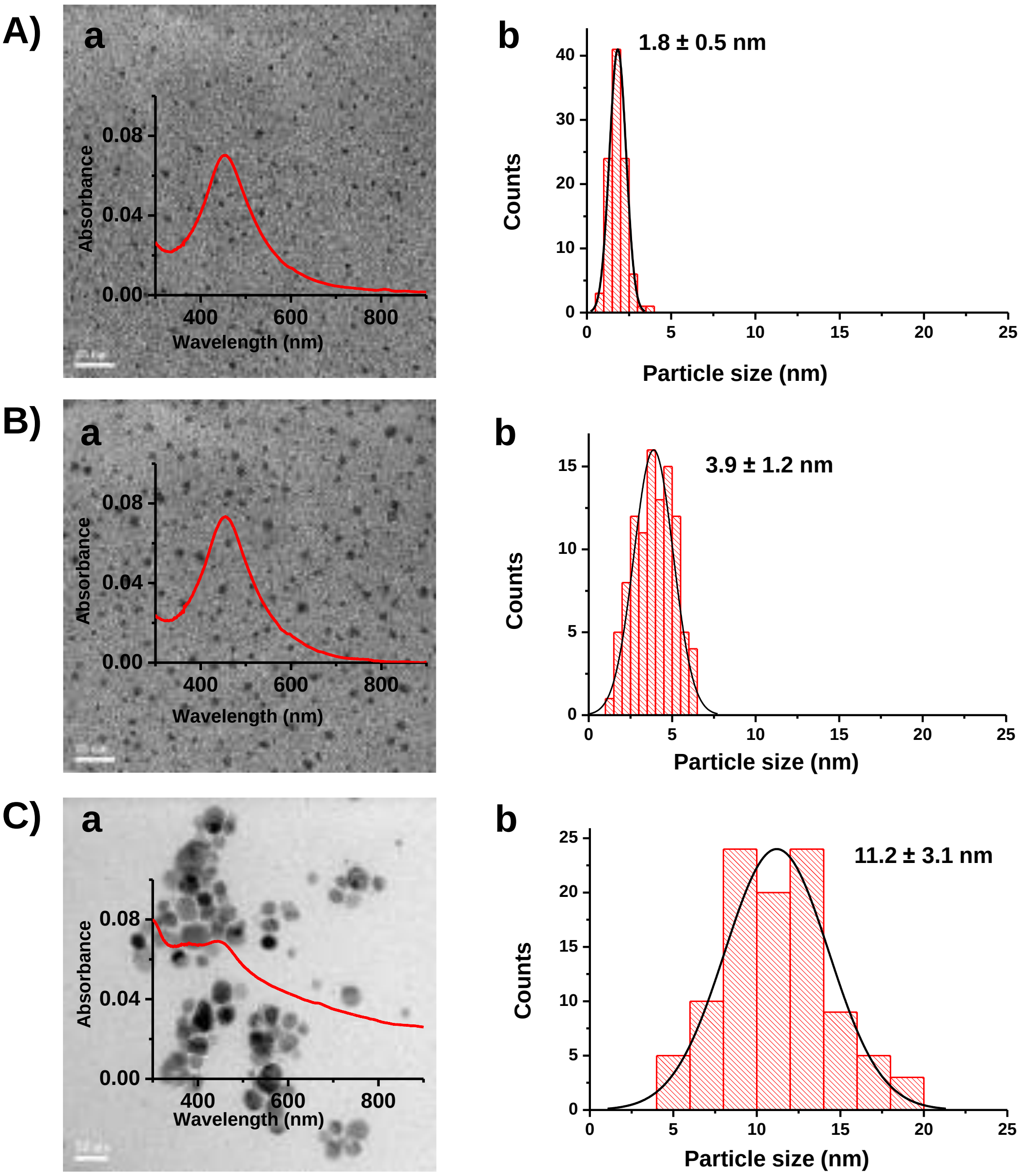

Figure S2. Characterization of AgNPs@DMBT of size A) ~2 nm, B) ~4 nm and C) ~11 nm, respectively. TEM images are shown in (a) and particle size distribution of the NPs are shown in (b). UV-vis spectra of the respective NPs are presented in the insets of (a) for each set.

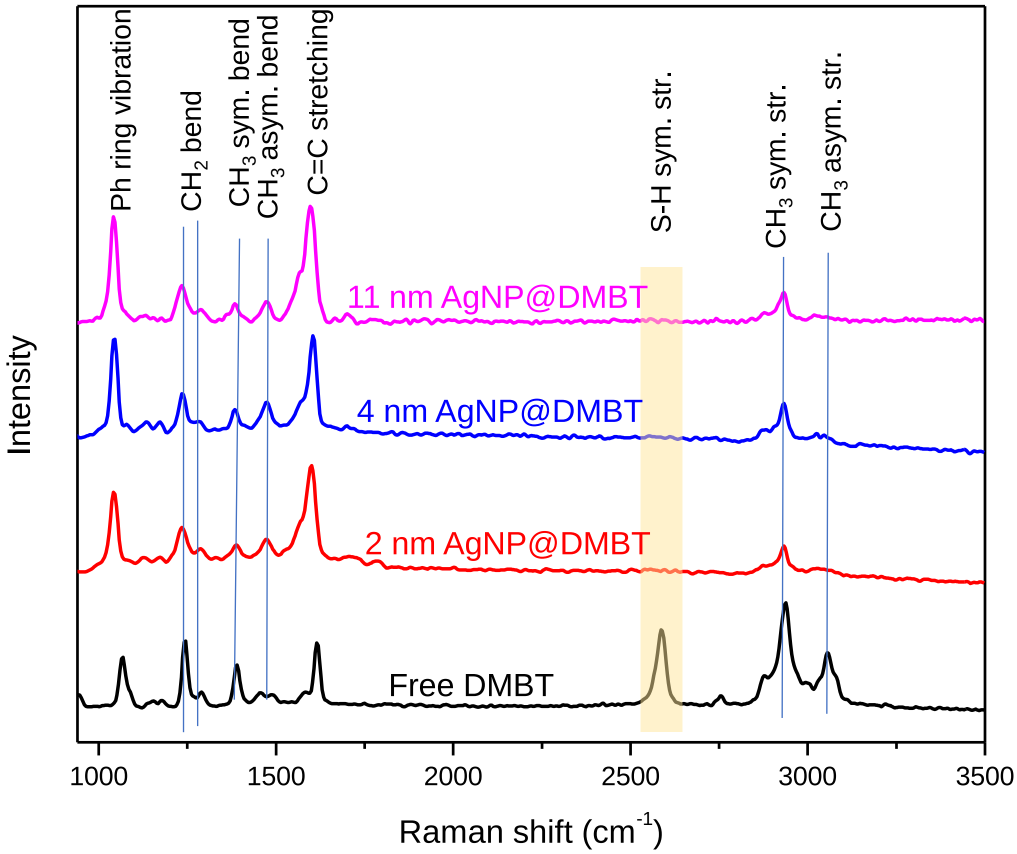

Figure S3. Raman spectra of 11 nm AgNP, 4 nm AgNP, 2 nm AgNP protected with DMBT and pure DMBT ligand.

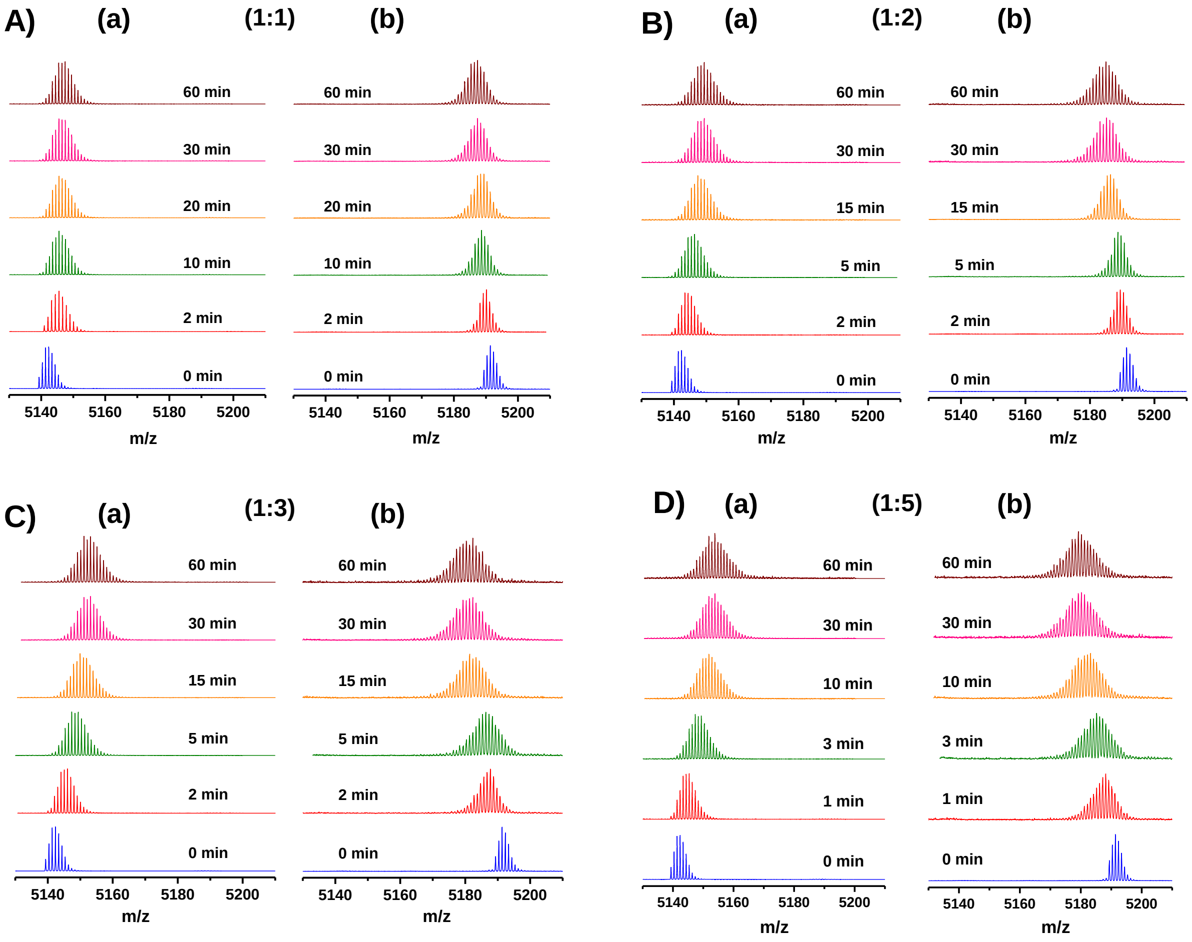

Figure S4. Time-dependent ESI MS showing the isotopic exchange in the cluster when reacted with ~ 2 nm AgNP@DMBT at NC:NP mixing ratios of A) 1:1, B) 1:2, C) 1:3 and D) 1:5, respectively. In each of A), B), C) and D), (a) denotes the case where $^{107}Ag_{25}(DMBT)_{18}^{-}$ was used and (b) denotes the case where $^{109}Ag_{25}(DMBT)_{18}^{-}$ was used as the isotopically labelled cluster for reaction with AgNP@DMBT, respectively.

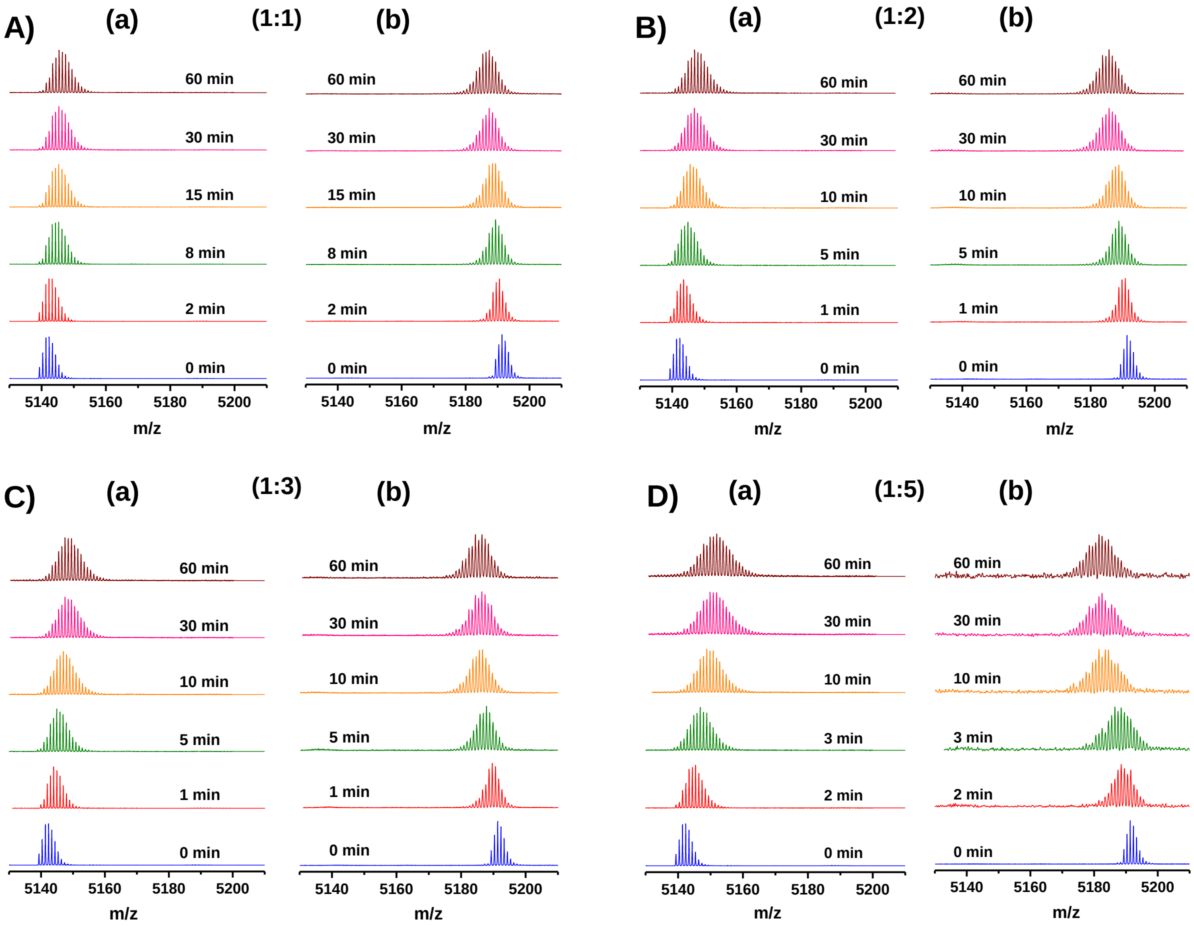

Figure S5. Time-dependent ESI MS showing the isotopic exchange in the cluster when reacted with ~ 4 nm AgNP@DMBT at NC:NP mixing ratios of A) 1:1, B) 1:2, C) 1:3 and D) 1:5, respectively. In each of A), B), C) and D), (a) denotes the case where $^{107}Ag_{25}(DMBT)_{18}^-$ was used and (b) denotes the case where $^{109}Ag_{25}(DMBT)_{18}^-$ was used as the isotopically labelled cluster for reaction with AgNP@DMBT, respectively.

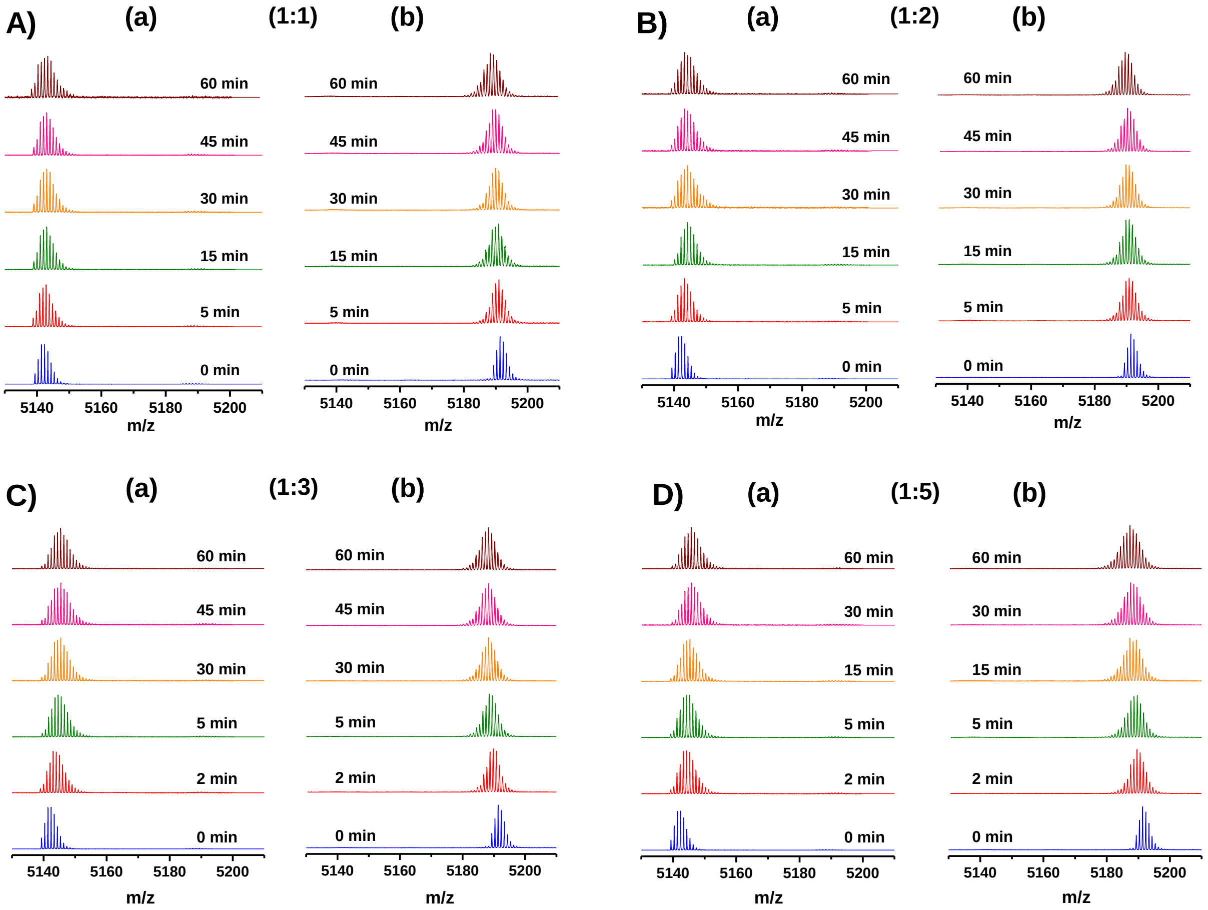

Figure S6. Time-dependent ESI MS showing the isotopic exchange in the cluster when reacted with ~ 11 nm AgNP@DMBT at NC:NP mixing ratios of A) 1:1, B) 1:2, C) 1:3 and D) 1:5, respectively. In each of A), B), C) and D), (a) denotes the case where ^{107}Ag$_{25}$(DMBT)$_{18}^{-}$ was used and (b) denotes the case where ^{109}Ag$_{25}$(DMBT)$_{18}^{-}$ was used as the isotopically labelled cluster for reaction with AgNP@DMBT, respectively.

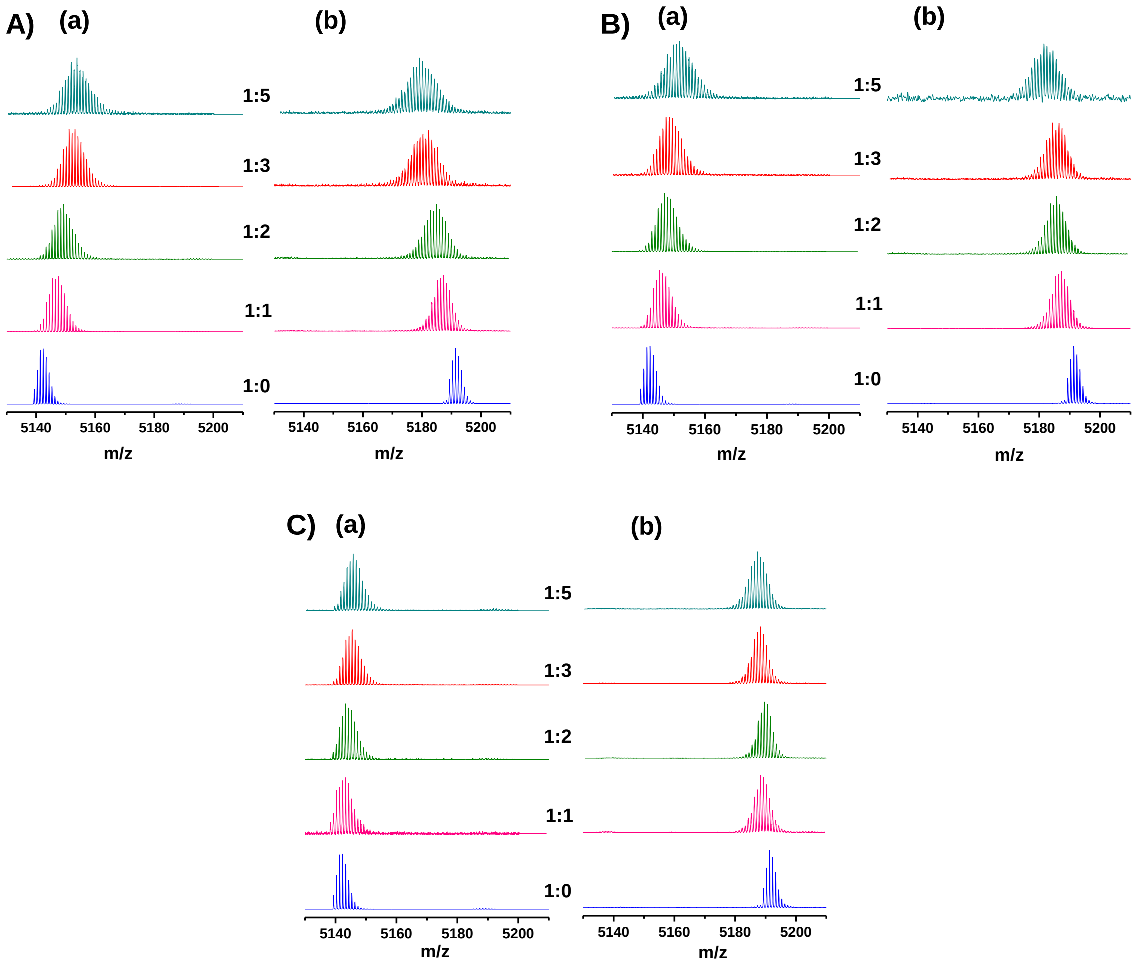

Figure S7. ESI MS showing the final equilibrated state of the clusters, after completion of the exchange reaction with A) ~ 2 nm, B) ~ 4 nm and C) ~ 11 nm AgNP@DMBT, respectively, at various NC : NP mixing ratios. Panel (a) refers to the reaction with $^{107}Ag_{25}(DMBT)_{18}^{-}$ and panel (b) refers to the reaction with $^{109}Ag_{25}(DMBT)_{18}^{-}$. The NC:NP mixing ratio is indicated beside each spectrum. The mass spectrum of the final equilibrated state shown here are actually the data at 60 min of reaction of the respective cases, presented in Figures S4-S6. Those data are recombined in this figure to increase the clarity in understanding the extent of exchange with NC:NP mixing ratios, for a given size of AgNP.

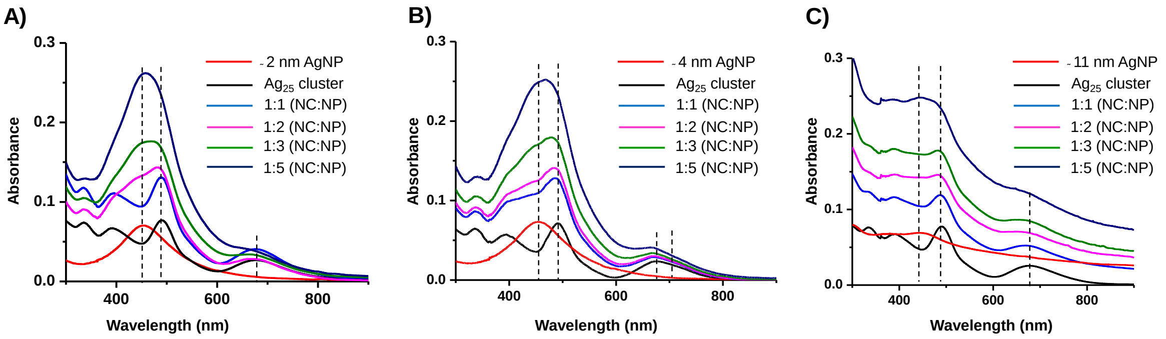

Figure S8. UV-vis spectra for the products of reaction of NC with AgNPs of sizes A) ~2 nm, B) ~4 nm and C) ~11 nm, at different NC:NP mixing ratios.

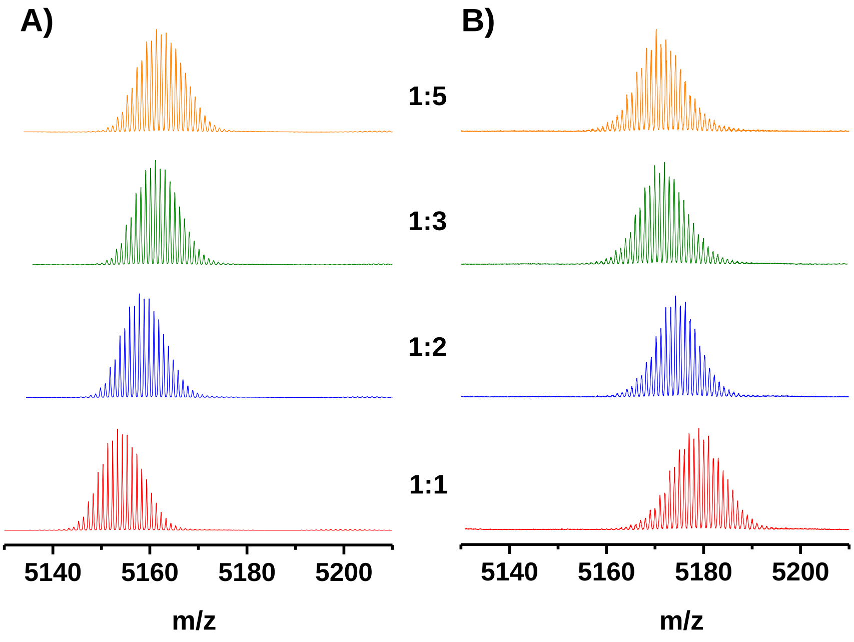

Figure S9. ESI MS of the product formed by reaction of A) $^{107}Ag_{25}(DMBT)_{18}^{-}$ and B) $^{109}Ag_{25}(DMBT)_{18}^{-}$ with normal $Ag_{25}(DMBT)_{18}^{-}$ (made from naturally abundant Ag). The reaction was rapid, so the ESI MS was measured within 1 min of mixing the reactants. The NC ($^{107/109}Ag_{25}(DMBT)_{18}^{-}$) : NC (normal $Ag_{25}(DMBT)_{18}^{-}$) mixing ratio is indicated for each of the spectra.

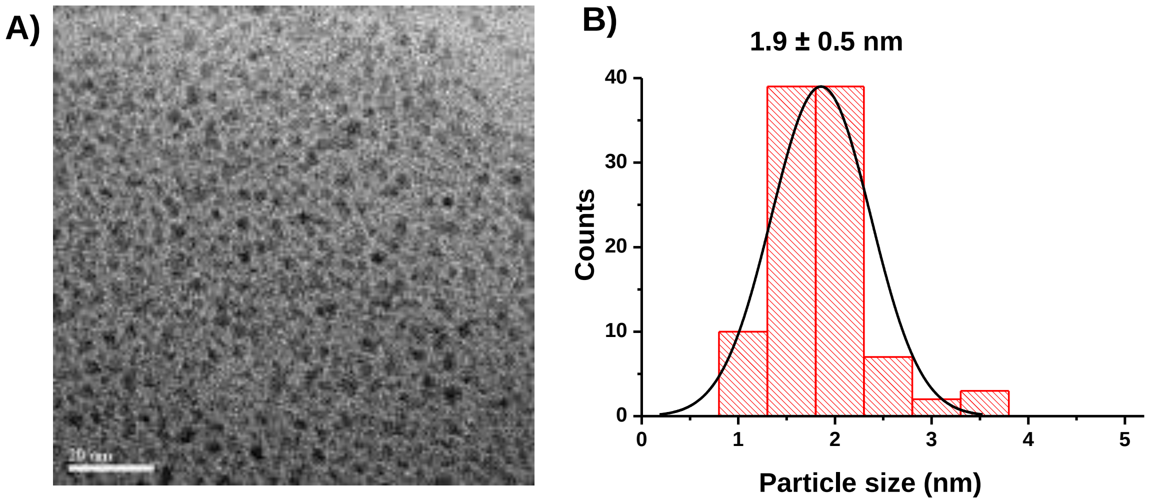

Figure S10. A) TEM image of $Ag_{25}(DMBT)_{18}^-$ cluster and B) particle size distribution of the clusters.

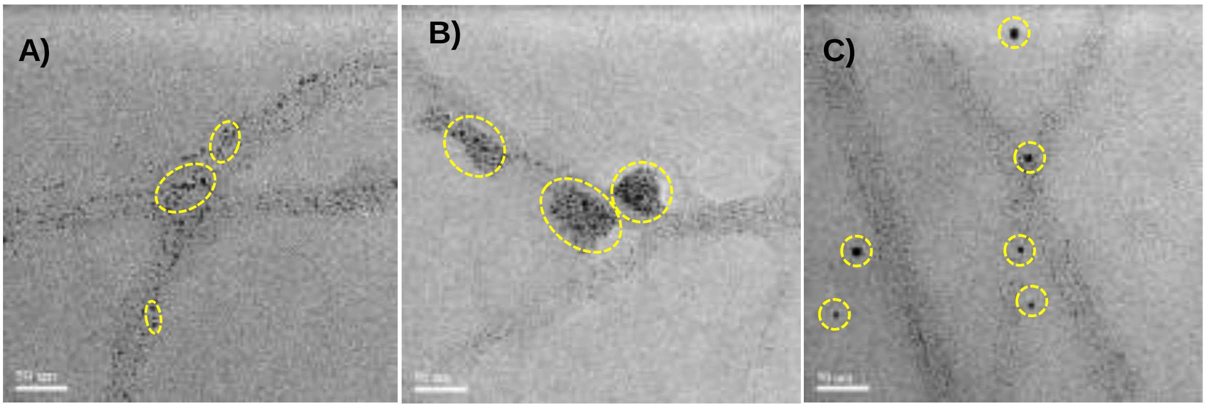

Figure S11. TEM image of the final product of reaction of $Ag_{25}(DMBT)_{18}^-$ with A) ~2 nm, B) ~4 nm and C) ~11 nm AgNPs@DMBT, respectively. The areas containing the larger sized NPs are marked and the smaller particles represent the NCs.

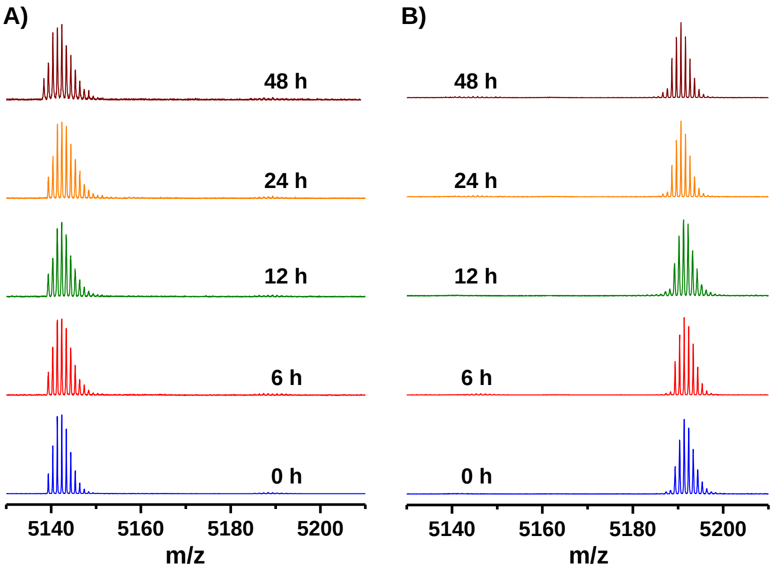

Figure S12. Time dependent ESI MS showing reaction of A) $^{107}Ag_{25}(DMBT)_{18}^{-}$ and B) $^{109}Ag_{25}(DMBT)_{18}^{-}$ with bare Ag foil.

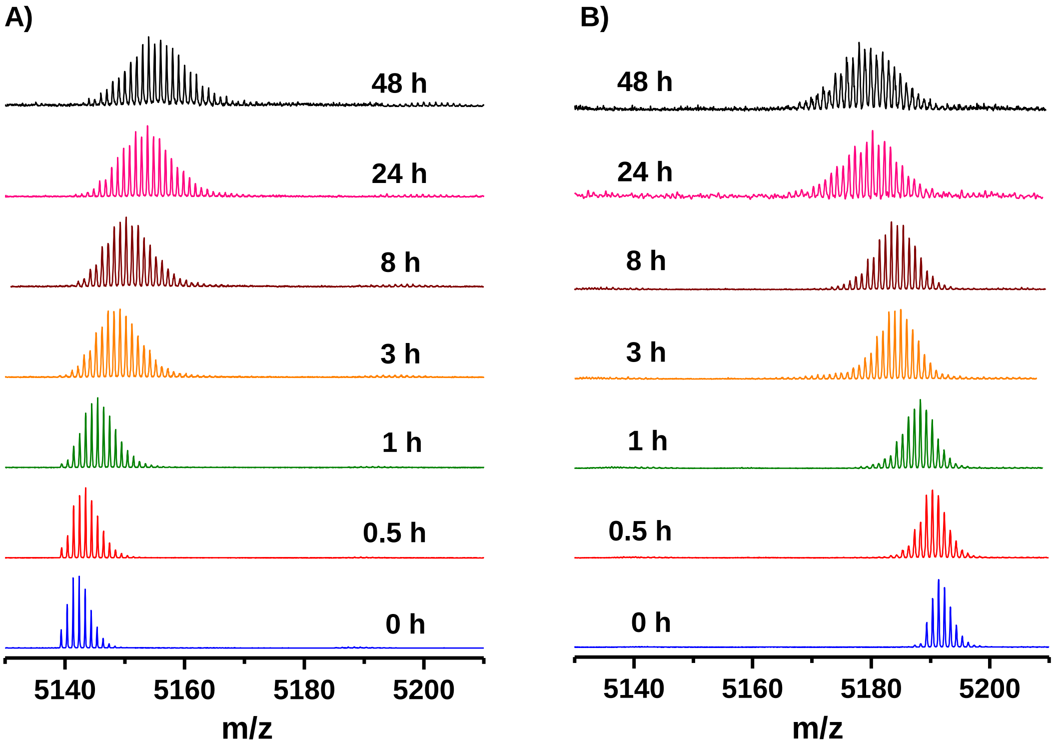

Figure S13. Time dependent ESI MS showing reaction of A) $^{107}Ag_{25}(DMBT)_{18}^{-}$ and B) $^{109}Ag_{25}(DMBT)_{18}^{-}$ with 2,4- DMBT protected Ag foil.

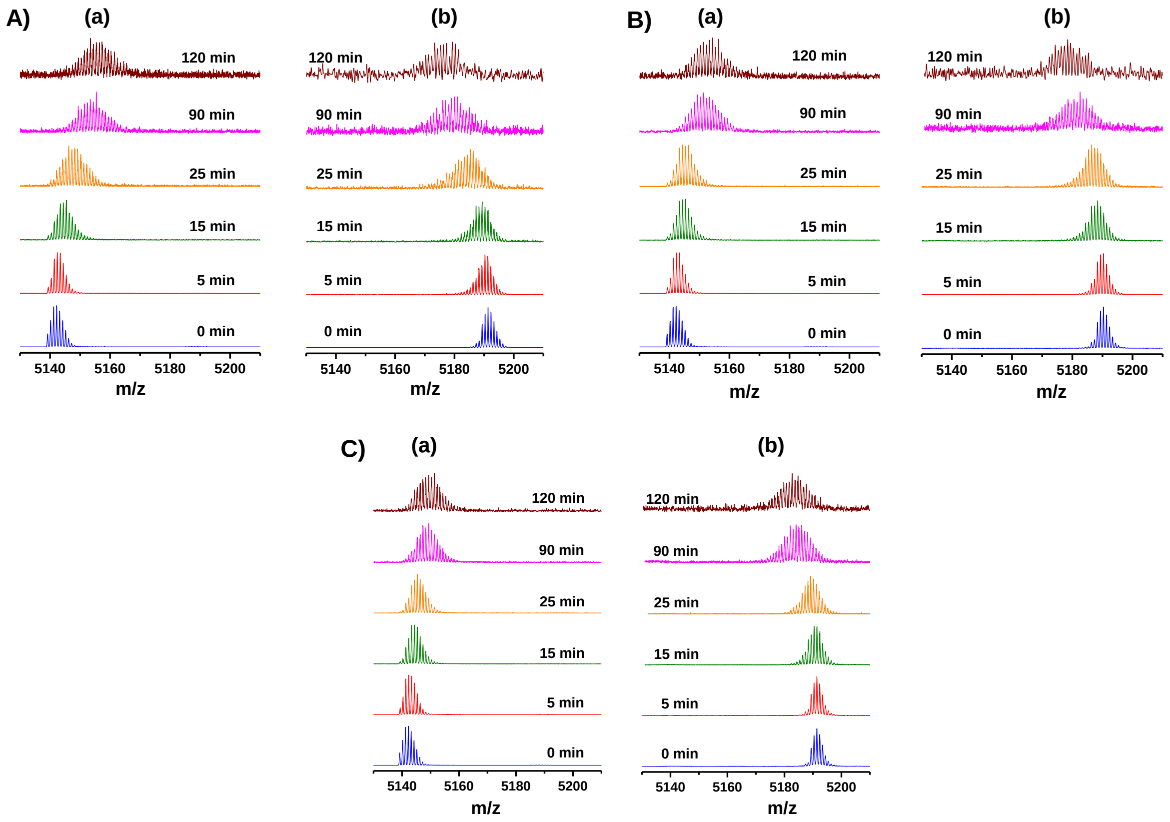

Figure S14. Time dependent ESI MS showing reaction of the cluster with A) ~80 mg, B) ~40 mg and C) ~20 mg bulk Ag powder. In each of A), B) and C), (a) denotes the case where $^{107}Ag_{25}(DMBT)_{18}^{-}$ was used and (b) denotes the case where $^{109}Ag_{25}(DMBT)_{18}^{-}$ was used as the isotopically labelled cluster for reaction with Ag powder, respectively.

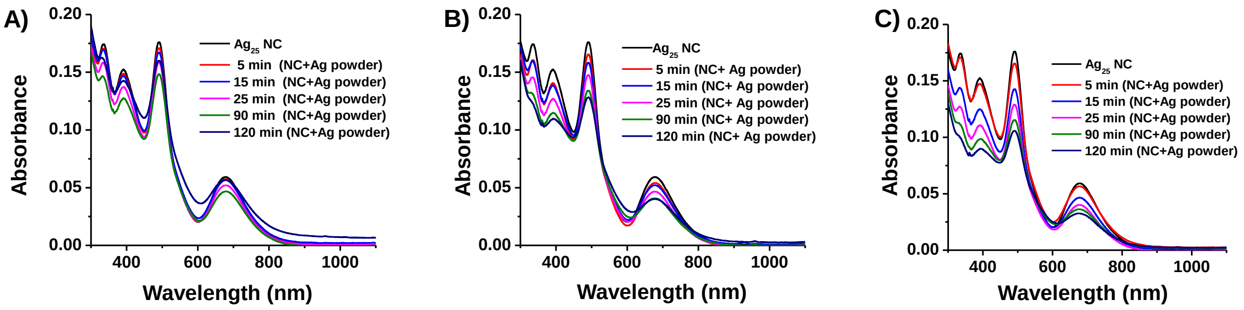

Figure S15. Time dependent UV-vis study of the reaction of $Ag_{25}(DMBT)_{18}^{-}$ NCs with A) 20 mg, B) 40 mg and C) 80 mg of bulk Ag powder.

Table S1. Timescales of reaction of NCs with NPs of different sizes and at different mixing ratios

Size of AgNPs	NC:NP mixing ratio	a_1	τ_1 (min)	a_2	τ_2 (min)	$\langle\tau\rangle$ (min)
~2 nm	1:1	0.34	2.20	0.66	12.20	8.80
	1:2	0.09	1.22	0.91	8.10	7.48
	1:3	0.24	0.75	0.76	8.06	6.30
	1:5	0.12	0.56	0.88	4.55	4.07
~4 nm	1:1	0.63	4.64	0.37	19.72	10.22
	1:2	0.15	3.19	0.85	9.28	8.37
	1:3	0.30	0.73	0.70	9.09	6.58
	1:5	0.05	0.59	0.95	5.78	5.52
~11 nm	1:1	0.48	4.82	0.52	37.71	21.92
	1:2	0.34	3.28	0.66	11.58	8.76
	1:3	0.46	1.67	0.54	10.70	6.54
	1:5	0.42	1.20	0.58	9.07	5.76

References

1. Joshi, C. P.; Bootharaju, M. S.; Alhilaly, M. J.; Bakr, O. M. $[Ag_{25}(Sr)_{18}]^-$: The “Golden” Silver Nanoparticle. *J. Am. Chem. Soc.* **2015**, *137*, 11578-11581.

2. Chakraborty, P.; Nag, A.; Natarajan, G.; Bandyopadhyay, N.; Paramasivam, G.; Panwar, M. K.; Chakrabarti, J.; Pradeep, T. Rapid Isotopic Exchange in Nanoparticles. *Sci. Adv.* **2019**, *5*, eaau7555.

ACS Sustainable Chemistry & Engineering

pubs.acs.org/journal/ascecg

Letter

Triboelectric Generators for Sustainable Reduction Leading to Nanoparticles and Nanoclusters

Vishal Kumar, Pillalamarri Srikrishnarka, Jyoti Sarita Mohanty, Murugesan Paulthangam Kannan, Ramamurthy Nagarajan, and Thalappil Pradeep*

Cite This: https://doi.org/10.1021/acssuschemeng.1c01586

Read Online

ABSTRACT: In this letter, we demonstrate a sustainable, fast, and facile room temperature synthesis of plasmonic nanoparticles and luminescent nanoclusters of gold. The synthesis was performed using an affordable, easy to build, and robust triboelectric generator (TG). The electricity generated by the TG was transferred to the solution continuously to synthesize gold nanoclusters (AuNCs). The obtained AuNCs had extremely narrow size distributions with mean particle sizes of ∼2 nm and showed bright pink luminescence under UV light. The approach was also extended to synthesize plasmonic gold nanoparticles (AuNPs). With this method, the synthesis time could be reduced from hours to several minutes without requiring any reducing agents. Tunability in size by simple variation of synthetic conditions and the consequent change in properties make this method usable for diverse applications.

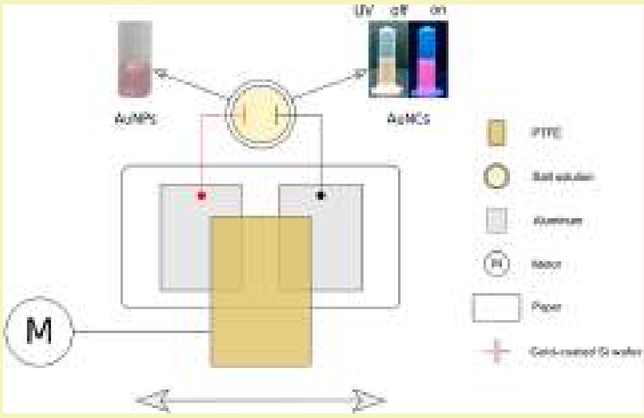

KEYWORDS: *Triboelectric generator, Gold nanoparticles, Gold nanoclusters*

INTRODUCTION

Electrostatic charging or tribocharging plays an important role in a wide variety of fields.[1−3] It has applications in areas such as photocopying,[4] energy harvesting and power generation,[5] synthesis of materials,[6] sensors,[7] air filtration,[8,9] X-ray generation (triboluminescence) and imaging,[10] and so forth.[11,12] The history of triboelectricity dates backs 300 BC to ancient Greek philosophers like Plato.[13] The word "triboelectricity" was coined from two Greek words "tribo" meaning to rub and "elektron" (latter electricity) meaning amber.[14,15] Tribocharging occurs when two materials are rubbed against each other and separated. A triboelectric series puts these materials based on the polarity and magnitude of charge generated. The farther materials are in the triboelectric series, the greater the amount of charge they acquire upon contact. The one high up in the series gets positively charged, while the other gets negatively charged. A triboelectric generator (TG)[5] or paper generator[16] uses triboelectric charging between materials and combines it with electrostatic induction to generate electricity. An increase in current from ∼0.6 μA[5] to ∼1.22 mA[17] was recorded for TG, in less than a decade, which is an increase of more than 3 orders of magnitude. However, with these advancements, the complexity has also increased which could limit its broader applicability.

As bulk material reduces to the nanometer scale, its physical and chemical properties change drastically. These changes are primarily a result of higher surface-to-volume ratios and changes in the electronic structure. One of the characteristic features of metal NPs is surface plasmon resonance (SPR), which is the collective oscillation of their conduction band electrons by the impinging light. This oscillation is responsible for the intense color of noble metal nanoparticles (NPs). NPs of this kind have sizes typically above 3 nm.[18] Their physical and chemical properties make them ideal for labeling and detection of biomolecules,[19] photodynamic therapy,[20] colorimetric sensing,[21] surface-enhanced Raman spectroscopy (SERS),[22,23] carriers for drug delivery,[24] catalysis,[25] and many more.[26]

Upon further scaling down the size to the subnanometer regime, the particle size approaches the Fermi wavelength of electrons, and the quantum size effect becomes predominant. The quasi-continuous band transitions into molecule-like discrete energy states exhibiting drastically different optical and electronic properties compared to NPs and corresponding bulk materials.[27,28] At this scale, the electronic properties are

Received: March 8, 2021
Revised: May 20, 2021

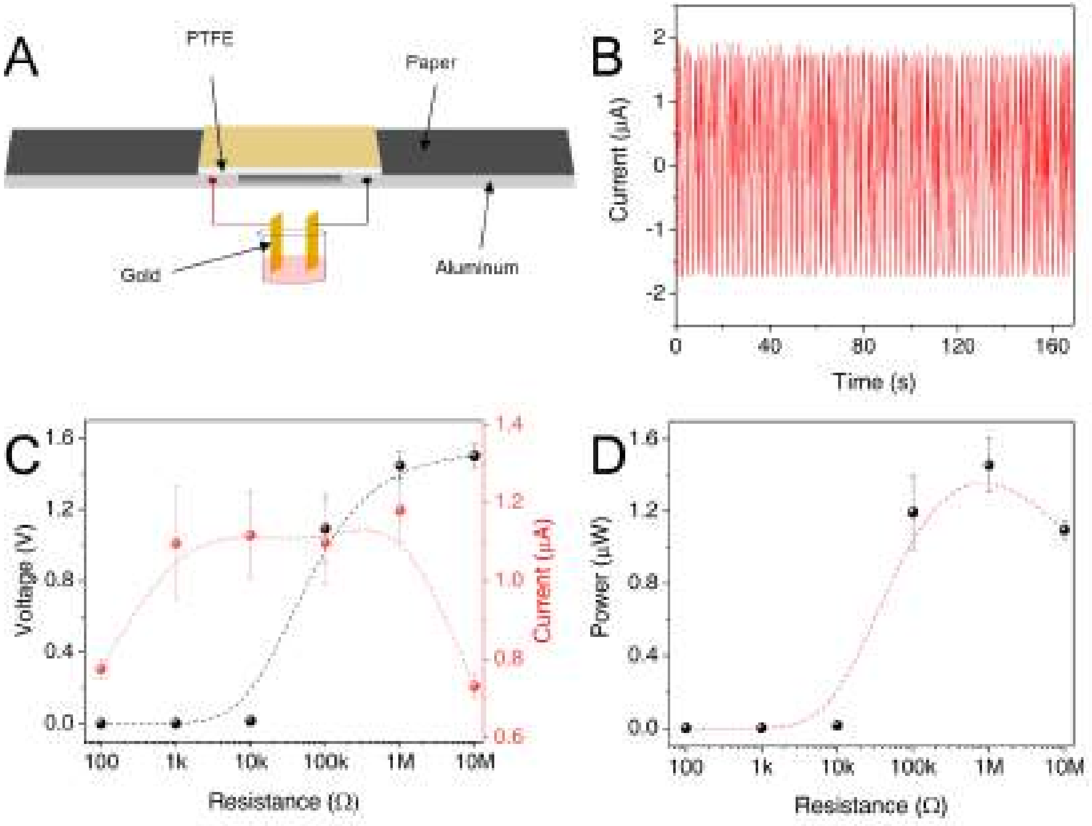

Figure 1. (A) Schematic of triboelectric generator setup for synthesis of NPs and NCs. (B) Short circuit current for the TG as a function of cycle of operations. (C) Output peak voltage and peak current. (D) Dependence of peak power with increasing resistance.

susceptible to the size and shape of the metal, and every atom counts in deciding the properties of such materials. This regime of the matter is called nanoclusters (NCs).[29] Properties vary significantly in the NPs and NCs regimes. For example, in the case of gold and silver, many NCs are visibly luminescent, while NPs have no observable luminescence. The fluorescence lifetimes and two-photon cross sections differ vastly for NCs and NPs. Moreover, the fluorescent emission of metal NCs can be tuned from infrared to UV regions by varying the core sizes.[27] These and several other unique properties have made metal NCs useful in areas such as bioimaging,[30] catalysis,[31,32] chemical sensing,[33] and so forth.[28,34,35] With time, several techniques to synthesize NPs and NCs have been developed.[26,28,36] However, for NCs, the diversity possible makes it challenging to synthesize specific NCs.

In this letter, we demonstrated a simple and affordable means to synthesize AuNPs and AuNCs at room temperature using TG. Some early reports on the reduction of metal ions to NPs and bulk metal using triboelectric charging[37−39] are available. Besides, one study demonstrated the synthesis of platinum NCs (PtNCs) using a triboelectric nanogenerator (TENG).[40] However, we did not find any reports concerning the synthesis of AuNCs using TG. Further, in a previous study,[40] the synthesis of PtNCs was performed on a catalytic surface which was also acting as an electrode. Moreover, the work exploits[40] the high surface activity of nanostructures like nanosheets. On the other hand, in our work, neither did we use any catalytic surface as an electrode nor exploit the high surface activity of nanostructures like nanosheets. The current TG requires a fewer number of components making it cost effective to assemble. The design is simple and easy to use. With several simple modifications to the existing design,[16,41] we significantly improved the robustness and longevity, enabling continuous synthesis of materials. The synthesis of NPs and NCs does not require any reducing agent, and capping agents were used to confine the size in the nanoscale regime. Typically, in wet chemical synthesis of NCs, sodium borohydride ($NaBH_4$) is used as a reducing agent, which is toxic and a health hazard. Since our synthesis procedure does not require any reducing agent, the synthesis process is green and sustainable. Moreover, the capping agent, 11-mercaptoundecanoic acid, used is nontoxic.

We discuss the synthesis of AuNPs, first followed by that of AuNCs. Initial results showed reduction, which was further established by spectroscopy and other techniques.

■ MATERIALS AND METHODS

Materials. Tetrachloroauric acid trihydrate ($HAuCl_4 \cdot 3H_2O$) was prepared starting from pure gold. The ligand, 11-mercaptoundecanoic acid (11-MUA), was purchased from Sigma-Aldrich. Glutathione reduced (GSH) was purchased from SRL. Mercaptosuccinic acid (MSA) was purchased from Aldrich. Sodium hydroxide (NaOH) pellets were purchased from Rankem. All the chemicals were used as received without further purification.

Instrumentation. UV−vis spectra were recorded using a PerkinElmer Lambda 25 instrument. High-resolution transmission electron microscopy (HRTEM) images were collected using a JEOL JEM 3010 (JEOL Japan) microscope. X-ray photoelectron spectroscopy (XPS) was carried out using an Omicron ESCA probe spectrometer with polychromatic Mg Kα X-rays ($h\nu$ = 1253.6 eV). Photoluminescence spectra were collected using a Jobin Yvon NanoLog instrument. The current and voltage measurements were performed using a Keithley 6514 system electrometer.

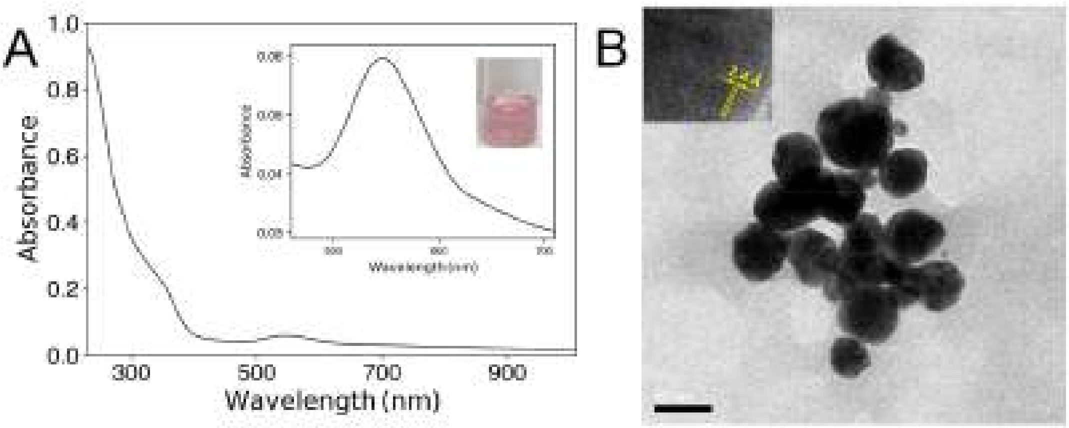

Figure 2. (A) UV−vis spectrum of triboelectrically synthesized MUA-AuNPs. Inset shows an expanded view showing the plasmonic peak at ∼540 nm. (B) Photograph of the MUA-AuNPs (scale bar 50 nm). Inset shows lattice fringes.

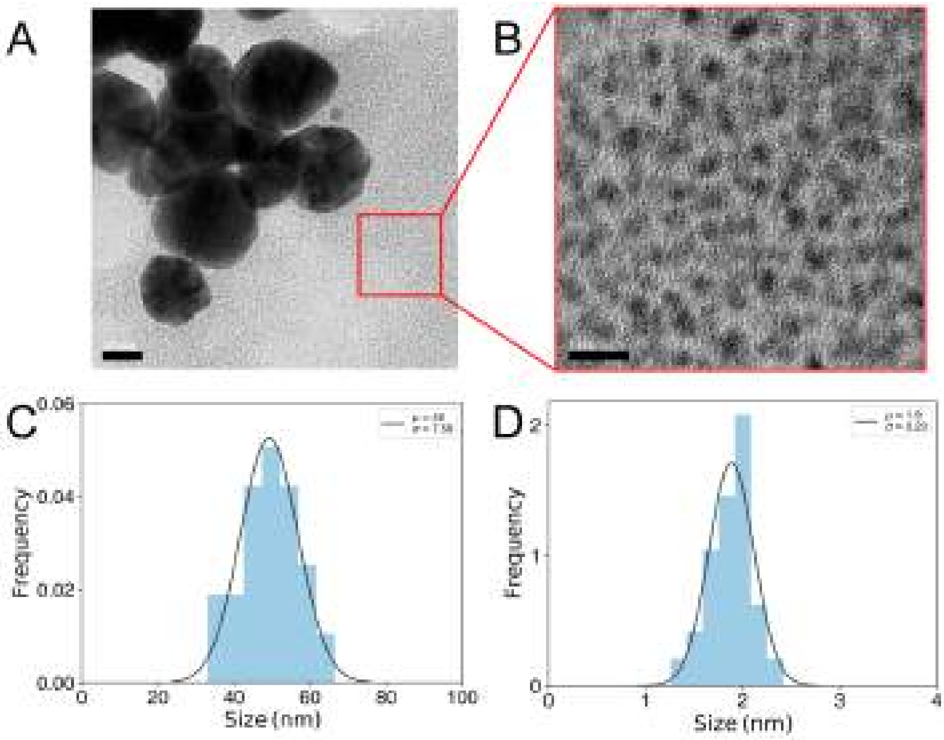

Figure 3. Two types of particles were observed in HRTEM: (A) bigger (scale bar 20 nm) and (B) smaller (scale bar 5 nm). (C, D) Size distributions for bigger and smaller MUA-AuNPs, respectively.

Design of TG. We chose the freestanding triboelectric layer mode[42] to operate the TG in view of its ease of operation. Two aluminum (Al) tapes (thickness, t = ∼0.05 mm; area, A = 13 cm × 7 cm) acting as electrodes were pasted on office paper (t = ∼0.08 mm) separated by 6 cm. In initial experiments, a PTFE (t = 0.5 mm; A = 11 cm × 6 cm) sheet was driven over these electrodes gently with the help of a motor. The continuous rubbing of the PTFE on to the paper keeps it negatively charged. The charged PTFE, when moved over the electrodes, generates an electric current that could be transferred to a load. However, the continuous rubbing by the PTFE also causes scuffing of the Al, which significantly limits its long-term usability. To address this issue, we attached a paper on top of the electrodes and checked for the output current, as shown in Figure 1A. We did not observe any loss in current, and with this addition, we were able to increase the robustness and longevity of the system. The voltage and current of the TG were measured at various resistances, as shown in Figure 1C. The peak current stays almost the same up to 1 MΩ and then began to drop as resistance increases. The peak voltage first rises and then started to saturate at ∼1.6 V beyond 1 MΩ. The peak power for the TG was calculated from the peak voltage and peak current. The power rises with an increase in resistance, reaching a maximum at ∼1 MΩ and then starts to fall off. We found that the TG works best when the distance between electrodes is of the order of the width of the electret (PTFE) (Figure S1) used for rubbing.[42] To transfer the current into the solution, gold-coated silicon wafers were connected to the TG and dipped into the solution as shown in Figure 1A. Table S1 provides a brief comparison of the reported TENGs with our TG.

■ RESULTS AND DISCUSSION

Synthesis of AuNPs. For the synthesis of AuNPs, we used 11-MUA as a capping agent with $HAuCl_4$ as a precursor. The reaction volume was kept fixed to 2000 μL for all the experiments. For this experiment, 750 μL of 1 mM 11-MUA in

https://doi.org/10.1021/acssuschemeng.1c01586
ACS Sustainable Chem. Eng. XXXX, XXX, XXX−XXX

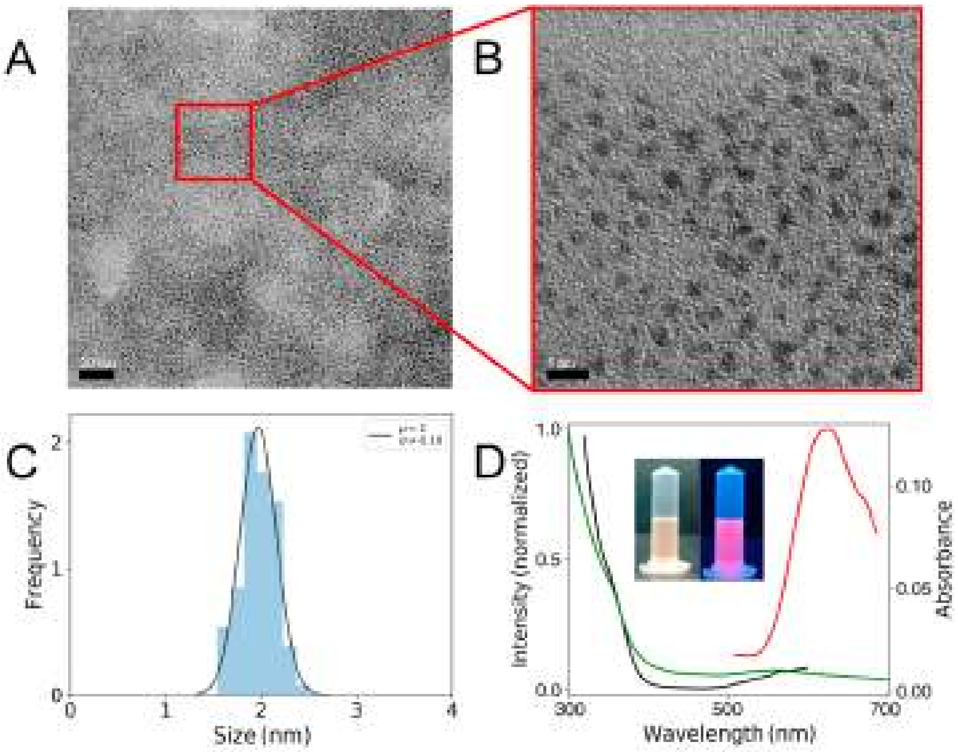

Figure 4. (A) HRTEM image of MUA-AuNCs (scale bar 20 nm). (B) Magnified TEM images (scale bar 5 nm). (C) MUA-AuNPs size distribution. (D) UV−vis absorption (green), fluorescence excitation (black, λ_{em} = 623 nm), and emission (red, λ_{ex} = 355 nm) spectra of MUA-AuNCs. The inset shows a photograph of MUA-AuNCs solution with UV light off (right) and on (left).

ethanol and 1250 μL of 10 mM of $HAuCl_4$ in distilled water were mixed. The solution was connected to the TG at room temperature with mild stirring, and electricity was applied for 30 min. During the synthesis, the current drawn by the solution does not show a significant decrease from the short circuit current, and the peak voltage of ∼5.5 mV was recorded as shown in Figure S2. The solution was then centrifuged at 9000 rpm, and the precipitate was collected. The precipitate was washed five times in ethanol to remove any excess Au(I)−thiolate complexes and reactants present.[43] Finally, the precipitate was resuspended in water by adding a small amount of NaOH.[44−46] NaOH was added because the basic pH allows the carboxyl groups to deprotonate and stabilize the NP dispersion through electrostatic repulsion.[44]

A wine-red colored solution was obtained which showed an absorption peak at ∼540 nm, indicating the presence of AuNPs. The spectrum also showed a broad shoulder peak centered near ∼350 nm, as shown in Figure 2A. There is a slight shoulder in the red region, likely due to variations in particle morphologies. Nearly spherical particles of ∼50 nm are seen in the TEM. The inset of Figure 2B shows a *d* spacing of ∼0.24 nm, corresponding to the (111) plane of face-centered cubic Au. From the HRTEM, we observed particles with two kinds of distributions. The larger particles have average particle sizes of ∼50 nm (Figure 3A,C), and smaller particles have average sizes of ∼2 nm (Figure 3B,D).

Synthesis of AuNCs. The synthesis of AuNCs was carried out similarly to that of the AuNPs, except for the change in the reaction medium. The ligand, 11-MUA, is sparingly soluble in water but highly soluble in ethanol. So, to reduce turbidity, we chose ethanol as the reaction medium. We prepared 10 mM of $HAuCl_4$ in ethanol starting from a 330 mM aqueous solution of $HAuCl_4$. About 1 mM 11-MUA was prepared in ethanol. The solution was prepared by mixing reactants in the same volume as for the synthesis of AuNPs. After applying a current for 30 min, the solution was centrifuged at 9000 rpm. The obtained precipitate was washed several times in ethanol to remove any excess of Au(I)−thiolate complexes and reactants present. Finally, the precipitate was dispersed in water with NaOH or NH_4OH, to enhance solubility.[43] The solution showed bright luminescence under UV light. The HRTEM images (Figure 4A, B) showed uniform MUA-AuNCs of ∼2 nm diameters. Figure 4D shows the UV−vis spectrum and fluorescence spectrum of the synthesized particles. The UV−vis spectrum showed an absorption at ∼560 nm and a shoulder band at ∼360 nm. A bright pink luminescence was obtained upon exposure to UV light. The fluorescence spectrum showed a strong emission peak at 623 nm upon excitation at 355 nm, which complies with the UV−vis spectrum. The characteristic feature of thiolate-protected gold clusters appears around 610 nm.[47] From the HRTEM images, we obtained a mean particle size of ∼2 nm with a standard deviation, σ, of ∼0.19 nm (Figure 4C). The XPS spectrum (Figure S4) showed a binding energy of 84.3 eV, corresponding to Au $4f_{7/2}$, taking the C 1s line of adventitious hydrocarbon at 284.8 eV as the reference. The binding energy is between 84.0 eV for Au(0) and 85.0 eV for Au(I), which indicates the presence of both Au(0) and Au(I) species in NC. AuNCs with thiolate protection is known to show the Au $4f_{7/2}$ feature around 84.45 eV.[33] The S $2p_{3/2}$ feature appears at 163.3 eV, as expected in the case of thiolate-protected clusters (Figure S5).

To further explore this process, we conducted experiments with water-soluble ligands, GSH and MSA. They were chosen as NPs made can form stable dispersions in water without the

https://doi.org/10.1021/acssuschemeng.1c01586

use of a base. The gold solution with both GSH and MSA gave NPs upon applying triboelectricity. The formations of GSH-AuNPs and MSA-AuNPs were confirmed with UV−vis spectroscopy with plasmonic peaks at ∼550 and ∼560 nm, respectively (Figure S6).

■ CONCLUSION

We demonstrated a facile and fast technique for the synthesis of NPs and NCs using TG. The approach we devised is easy to perform and does not require any conventional reducing agent. Further, the TG used to carry out the synthesis requires a fewer number of components which makes it affordable and easy to build. With this technique, differently sized nanomaterials can be synthesized at room temperature. Several factors could affect the size of the synthesized particles. These include varying the voltage and current. One way to increase both the current and voltage is by using materials with high surface areas like electrospun fibers, which could significantly enhance the triboelectric charging. Other parameters of equal importance include the effect of the synthesis medium (its dielectric constant and dipole moment) and frequency of rubbing. Further, increasing the frequency of rubbing and/or enhancing surface area with micro- or nanostructuring results in an enhanced rate of charge transfer, thus increasing the yield of NPs and NCs. Using nanostructured surfaces for triboelectric charging typically increases the voltage by several folds (Table S1), which may affect particle synthesis, and it needs to be taken into account. Extending the method for the preparation of nanoparticles of other metals and alloys may be possible. The methodology developed is sustainable and simple.

■ ASSOCIATED CONTENT

Supporting Information

The Supporting Information is available free of charge at https://pubs.acs.org/doi/10.1021/acssuschemeng.1c01586.

> Peak current at varying electrode distance, brief comparison of performance of published TENGs with our TG, XPS spectrum of MUA-AuNCs in Au 4f region, XPS spectrum of MUA-AuNCs in S 2p region current and voltage measurements for aqueous gold solution during synthesis of MUA-AuNPs, size distribution of MUA-AuNCs, current and voltage measurement for gold solution in ethanol during synthesis of MUA-AuNCs, and UV−vis spectra of aqueous GSH-AuNPs and MSA-AuNPs suspensions (PDF)

■ AUTHOR INFORMATION

Corresponding Author

Thalappil Pradeep − *Department of Chemistry, DST Unit of Nanoscience (DST UNS) and Thematic Unit of Excellence (TUE), Indian Institute of Technology Madras, Chennai 600036, India;* orcid.org/0000-0003-3174-534X; Email: pradeep@iitm.ac.in

Authors

Vishal Kumar − *Department of Chemistry, DST Unit of Nanoscience (DST UNS) and Thematic Unit of Excellence (TUE) and Department of Chemical Engineering, Indian Institute of Technology Madras, Chennai 600036, India;* orcid.org/0000-0002-2374-0568

Pillalamarri Srikrishnarka − *Department of Chemistry, DST Unit of Nanoscience (DST UNS) and Thematic Unit of Excellence (TUE) and Department of Chemical Engineering, Indian Institute of Technology Madras, Chennai 600036, India;* orcid.org/0000-0001-5187-6879

Jyoti Sarita Mohanty − *Department of Chemistry, DST Unit of Nanoscience (DST UNS) and Thematic Unit of Excellence (TUE), Indian Institute of Technology Madras, Chennai 600036, India*

Murugesan Paulthangam Kannan − *Department of Chemistry, DST Unit of Nanoscience (DST UNS) and Thematic Unit of Excellence (TUE), Indian Institute of Technology Madras, Chennai 600036, India*

Ramamurthy Nagarajan − *Department of Chemical Engineering, Indian Institute of Technology Madras, Chennai 600036, India*

Complete contact information is available at: https://pubs.acs.org/10.1021/acssuschemeng.1c01586

Notes

The authors declare no competing financial interest.

■ ACKNOWLEDGMENTS

We thank the Department of Science and Technology, Government of India, for continuously supporting our research program. V.K. and P.S. acknowledge institute graduate fellowships.

■ REFERENCES

(1) Kok, J. F.; Renno, N. O. Electrostatics in Wind-Blown Sand. *Phys. Rev. Lett.* **2008**, *100* (1), 014501.

(2) Steinpilz, T.; Joeris, K.; Jungmann, F.; Wolf, D.; Brendel, L.; Teiser, J.; Shinbrot, T.; Wurm, G. Electrical Charging Overcomes the Bouncing Barrier in Planet Formation. *Nat. Phys.* **2020**, *16* (2), 225−229.

(3) Sayfidinov, K.; Cezan, S. D.; Baytekin, B.; Baytekin, H. T. Minimizing Friction, Wear, and Energy Losses by Eliminating Contact Charging. *Science Advances* **2018**, *4* (11), No. eaau3808.

(4) Pai, D. M.; Springett, B. E. Physics of Electrophotography. *Rev. Mod. Phys.* **1993**, *65* (1), 163−211.

(5) Fan, F. R.; Tian, Z. Q.; Lin Wang, Z. Flexible Triboelectric Generator. *Nano Energy* **2012**, *1* (2), 328−334.

(6) Li, A.; Luo, Q.; Park, S.-J.; Cooks, R. G. Synthesis and Catalytic Reactions of Nanoparticles Formed by Electrospray Ionization of Coinage Metals. *Angew. Chem., Int. Ed.* **2014**, *53* (12), 3147−3150.

(7) Yang, Y.; Zhu, G.; Zhang, H.; Chen, J.; Zhong, X.; Lin, Z.-H.; Su, Y.; Bai, P.; Wen, X.; Wang, Z. L. Triboelectric Nanogenerator for Harvesting Wind Energy and as Self-Powered Wind Vector Sensor System. *ACS Nano* **2013**, *7* (10), 9461−9468.

(8) Liu, J.; Jiang, T.; Li, X.; Wang, Z. L. Triboelectric Filtering for Air Purification. *Nanotechnology* **2019**, *30* (29), 292001.

(9) Srikrishnarka, P.; Kumar, V.; Ahuja, T.; Subramanian, V.; Selvam, A. K.; Bose, P.; Jenifer, S. K.; Mahendranath, A.; Ganayee, M. A.; Nagarajan, R.; Pradeep, T. Enhanced Capture of Particulate Matter by Molecularly Charged Electrospun Nanofibers. *ACS Sustainable Chem. Eng.* **2020**, *8* (21), 7762−7773.

(10) Camara, C. G.; Escobar, J. V.; Hird, J. R.; Putterman, S. J. Correlation between Nanosecond X-Ray Flashes and Stick-Slip Friction in Peeling Tape. *Nature* **2008**, *455* (7216), 1089−1092.

(11) Galembeck, F.; Burgo, T. A. L.; Balestrin, L. B. S.; Gouveia, R. F.; Silva, C. A.; Galembeck, A. Friction, Tribochemistry and Triboelectricity: Recent Progress and Perspectives. *RSC Adv.* **2014**, *4* (109), 64280−64298.

(12) Nag, A.; Baksi, A.; Ghosh, J.; Kumar, V.; Bag, S.; Mondal, B.; Ahuja, T.; Pradeep, T. Tribochemical Degradation of Polytetrafluoro-

ethylene in Water and Generation of Nanoplastics. *ACS Sustainable Chem. Eng.* **2019**, 7 (21), 17554−17558.

(13) Lacks, D. J.; Shinbrot, T. Long-Standing and Unresolved Issues in Triboelectric Charging. *Nature Reviews Chemistry* **2019**, *3* (8), 465−476.

(14) Hummel, R. E. Electrical Conduction in Metals and Alloys. In *Electronic Properties of Materials*; Springer: New York, 2011; pp 79−114. .

(15) Lacks, D. J.; Mohan Sankaran, R. Contact Electrification of Insulating Materials. *J. Phys. D: Appl. Phys.* **2011**, *44* (45), 453001.

(16) Karagozler, M. E.; Poupyrev, I.; Fedder, G. K.; Suzuki, Y. Paper Generators. In *Proceedings of the 26th Annual ACM Symposium on User Interface Software and Technology - UIST '13*; ACM Press: New York, 2013; pp 23−30. .

(17) Chun, J.; Ye, B. U.; Lee, J. W.; Choi, D.; Kang, C. Y.; Kim, S. W.; Wang, Z. L.; Baik, J. M. Boosted Output Performance of Triboelectric Nanogenerator via Electric Double Layer Effect. *Nat. Commun.* **2016**, 7 (May), 1−9.

(18) Jin, R.; Zeng, C.; Zhou, M.; Chen, Y. Atomically Precise Colloidal Metal Nanoclusters and Nanoparticles: Fundamentals and Opportunities. *Chem. Rev.* **2016**, *116* (18), 10346−10413.

(19) Wilson, R. The Use of Gold Nanoparticles in Diagnostics and Detection. *Chem. Soc. Rev.* **2008**, *37* (9), 2028.

(20) Cheng, Y.; Samia, A. C.; Meyers, J. D.; Panagopoulos, I.; Fei, B.; Burda, C. Highly Efficient Drug Delivery with Gold Nanoparticle Vectors for in Vivo Photodynamic Therapy of Cancer. *J. Am. Chem. Soc.* **2008**, *130* (32), 10643−10647.

(21) Kim, Y.; Johnson, R. C.; Hupp, J. T. Gold Nanoparticle-Based Sensing of "Spectroscopically Silent" Heavy Metal Ions. *Nano Lett.* **2001**, *1* (4), 165−167.

(22) Kneipp, K.; Haka, A. S.; Kneipp, H.; Badizadegan, K.; Yoshizawa, N.; Boone, C.; Shafer-Peltier, K. E.; Motz, J. T.; Dasari, R. R.; Feld, M. S. Surface-Enhanced Raman Spectroscopy in Single Living Cells Using Gold Nanoparticles. *Appl. Spectrosc.* **2002**, *56* (2), 150−154.

(23) Xie, J.; Zhang, Q.; Lee, J. Y.; Wang, D. I. C. The Synthesis of SERS-Active Gold Nanoflower Tags for In Vivo Applications. *ACS Nano* **2008**, *2* (12), 2473−2480.

(24) Song, J.; Zhou, J.; Duan, H. Self-Assembled Plasmonic Vesicles of SERS-Encoded Amphiphilic Gold Nanoparticles for Cancer Cell Targeting and Traceable Intracellular Drug Delivery. *J. Am. Chem. Soc.* **2012**, *134* (32), 13458−13469.

(25) Grisel, R.; Weststrate, K. J.; Gluhoi, A.; Nieuwenhuys, B. E. Catalysis by Gold Nanoparticles. *Gold Bulletin* **2002**, *35* (2), 39−45.

(26) Daniel, M.-C.; Astruc, D. Gold Nanoparticles: Assembly, Supramolecular Chemistry, Quantum-Size-Related Properties, and Applications toward Biology, Catalysis, and Nanotechnology. *Chem. Rev.* **2004**, *104* (1), 293−346.

(27) Lu, Y.; Chen, W. Sub-Nanometre Sized Metal Clusters: From Synthetic Challenges to the Unique Property Discoveries. *Chem. Soc. Rev.* **2012**, *41* (9), 3594.

(28) Chakraborty, I.; Pradeep, T. Atomically Precise Clusters of Noble Metals: Emerging Link between Atoms and Nanoparticles. *Chem. Rev.* **2017**, *117* (12), 8208−8271.

(29) Yau, S. H.; Varnavski, O.; Goodson, T. An Ultrafast Look at Au Nanoclusters. *Acc. Chem. Res.* **2013**, *46* (7), 1506−1516.

(30) Wu, X.; He, X.; Wang, K.; Xie, C.; Zhou, B.; Qing, Z. Ultrasmall Near-Infrared Gold Nanoclusters for Tumor Fluorescence Imaging in Vivo. *Nanoscale* **2010**, *2* (10), 2244.

(31) Herzing, A. A.; Kiely, C. J.; Carley, A. F.; Landon, P.; Hutchings, G. J. Identification of Active Gold Nanoclusters on Iron Oxide Supports for CO Oxidation. *Science* **2008**, *321* (5894), 1331−1335.

(32) Du, X.; Jin, R. Atomically Precise Metal Nanoclusters for Catalysis. *ACS Nano* **2019**, *13* (7), 7383−7387.

(33) Sun, J.; Zhang, J.; Jin, Y. 11-Mercaptoundecanoic Acid Directed One-Pot Synthesis of Water-Soluble Fluorescent Gold Nanoclusters and Their Use as Probes for Sensitive and Selective Detection of Cr 3+ and Cr 6+. *J. Mater. Chem. C* **2013**, *1* (1), 138−143.

(34) Jeseentharani, V.; Pugazhenthiran, N.; Mathew, A.; Chakraborty, I.; Baksi, A.; Ghosh, J.; Jash, M.; Anjusree, G. S.; Deepak, T. G.; Nair, A. S.; Pradeep, T. Atomically Precise Noble Metal Clusters Harvest Visible Light to Produce Energy. *Chemistry Select* **2017**, *2* (4), 1454−1463.

(35) Chang, T.-K.; Cheng, T.-M.; Chu, H.-L.; Tan, S.-H.; Kuo, J.-C.; Hsu, P.-H.; Su, C.-Y.; Chen, H.-M.; Lee, C.-M.; Kuo, T.-R. Metabolic Mechanism Investigation of Antibacterial Active Cysteine-Conjugated Gold Nanoclusters in Escherichia Coli. *ACS Sustainable Chem. Eng.* **2019**, 7 (18), 15479−15486.

(36) Kurashige, W.; Niihori, Y.; Sharma, S.; Negishi, Y. Precise Synthesis, Functionalization and Application of Thiolate-Protected Gold Clusters. *Coord. Chem. Rev.* **2016**, *320−321*, 238−250.

(37) Chen, C.-H.; Lee, P.-W.; Tsao, Y.-H.; Lin, Z.-H. Utilization of Self-Powered Electrochemical Systems: Metallic Nanoparticle Synthesis and Lactate Detection. *Nano Energy* **2017**, *42*, 241−248.

(38) Liu, C.; Bard, A. J. Electrostatic Electrochemistry at Insulators. *Nat. Mater.* **2008**, *7* (6), 505−509.

(39) Baytekin, B.; Baytekin, H. T.; Grzybowski, B. A. What Really Drives Chemical Reactions on Contact Charged Surfaces? *J. Am. Chem. Soc.* **2012**, *134* (17), 7223−7226.

(40) Han, J.; Meng, X.; Lu, L.; Wang, Z. L.; Sun, C. Triboelectric Nanogenerators Powered Electrodepositing Tri-Functional Electrocatalysts for Water Splitting and Rechargeable Zinc-Air Battery: A Case of Pt Nanoclusters on NiFe-LDH Nanosheets. *Nano Energy* **2020**, 72, 104669.

(41) Ceceri, K. *Make: Paper Inventions: Machines That Move, Drawings That Light Up, and Wearables and Structures You Can. Cut, Fold, and Roll*; Maker Media, Inc., 2015.

(42) Wang, Z. L.; Lin, L.; Chen, J.; Niu, S.; Zi, Y. Triboelectric Nanogenerator: Freestanding Triboelectric-Layer Mode. In *Triboelectric Nanogenerators*; Springer, 2016; pp 109−153. .

(43) Qian, H.; Zhu, Y.; Jin, R. Size-Focusing Synthesis, Optical and Electrochemical Properties of Monodisperse Au38 (SC2H4Ph)24 Nanoclusters. *ACS Nano* **2009**, *3* (11), 3795−3803.

(44) Laaksonen, T.; Ahonen, P.; Johans, C.; Kontturi, K. Stability and Electrostatics of Mercaptoundecanoic Acid-Capped Gold Nanoparticles with Varying Counterion Size. *ChemPhysChem* **2006**, *7* (10), 2143−2149.

(45) Shivhare, A.; Wang, L.; Scott, R. W. J. Isolation of Carboxylic Acid-Protected Au 25 Clusters Using a Borohydride Purification Strategy. *Langmuir* **2015**, *31* (5), 1835−1841.

(46) Su, C. H.; Wu, P. L.; Yeh, C. S. PH Dependence of Interparticle Coupling for Gold Nanoparticle Assemblies Formation: Electrostatic Attraction and Hydrogen Bonding. *Bull. Chem. Soc. Jpn.* **2004**, *77* (1), 189−193.

(47) Chang, H.-C.; Chang, Y.-F.; Fan, N.-C.; Ho, J. A. Facile Preparation of High-Quantum-Yield Gold Nanoclusters: Application to Probing Mercuric Ions and Biothiols. *ACS Appl. Mater. Interfaces* **2014**, *6* (21), 18824−18831.

Triboelectric Generators for Sustainable Reduction Leading to Nanoparticles and Nanoclusters

Vishal Kumar,[†‡] Pillalamarri Srikrishnarka,[†‡] Jyoti Sarita Mohanty,[†] Murugesan Paulthangam Kannan,[†] Ramamurthy Nagarajan,[‡] Thalappil Pradeep[†*]

†Department of Chemistry, DST Unit of Nanoscience (DST UNS) and Thematic Unit of Excellence (TUE), Indian Institute of Technology Madras, Chennai 600036, India

‡Department of chemical Engineering, Indian Institute of Technology Madras, Chennai 600036, India

Number of pages: 10

Number of figures: 6

Number of tables: 1

***Corresponding author:** Thalappil Pradeep, Department of Chemistry, DST Unit of Nanoscience (DST UNS) and Thematic Unit of Excellence (TUE), Indian Institute of Technology Madras, Chennai 600036, India

E-mail: pradeep@iitm.ac.in

Table of Contents

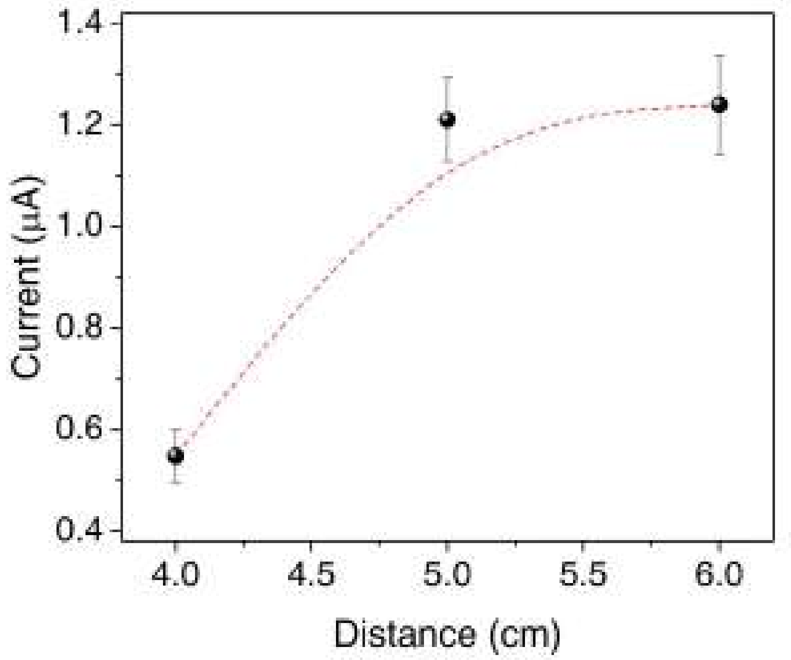

Figure S1. Peak current at different separation between Al electrodes.

Typically, in TENG, nanostructured materials are used to increase the effective contact area, which significantly amplifies the electrostatic charging compared to normal surface. The effect of this increased charging is reflected mainly as a high-voltage output, but the increase in current in not as substantial. Since power (P = I×V), the power values are much higher in such systems. But high voltage (> 100 V) in such systems might have a negative effect on the synthesis of NPs and NCs.

Table S1. A brief comparison of performance of published TENGs with our TG.

	Voltage	**Current**	**Power**	**Mode**	**Materials**
This work	1.4 V	1.2 µA	1.45 µW (~ 1 MΩ)	sliding	1. Teflon sheet 2. paper
Nano Energy **2013**, 2 (4), 491–497[1]	265 V	0.9 µA	0.23 mW (~ 300 MΩ)s	tapping	1. PVA electrospun nanofibers on PET film 2. Teflon film
Nanoscale Research Letters **2018**, 13 (1), 365[2]	8.5 V	0.6 µA	4.8 µW (~16 MΩ)	tapping	1. starch film 2. hand
Nanoscale **2014**, 6 (14), 7842–7846[3]	138 V	65 µA	38 mW (~ 9 MΩ)	tapping	1. electrospun pvdf fibers 2. electrospun nylon fibers

*The values of voltage and current represent the value at peak power.

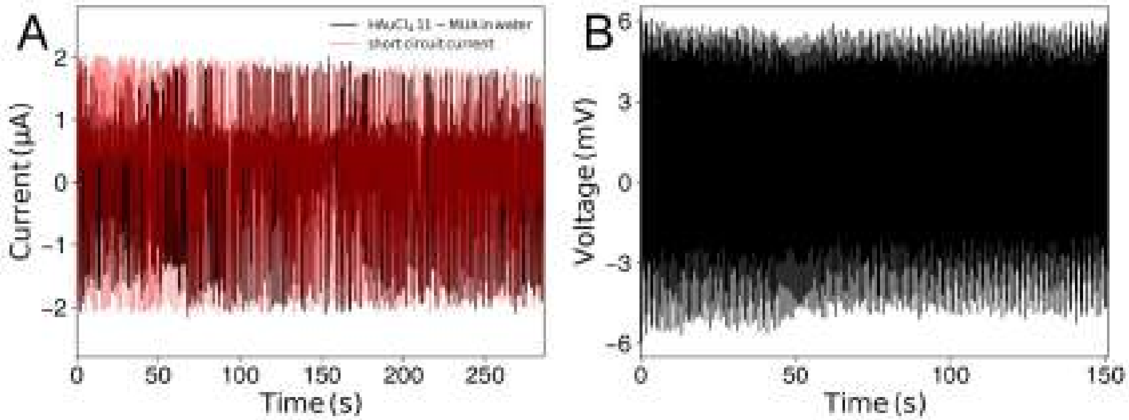

Figure S2. (A) Short circuit current for TG (red), and the current (black) drawn and (B) voltage for the aqueous gold solution during synthesis of MUA-AuNPs.

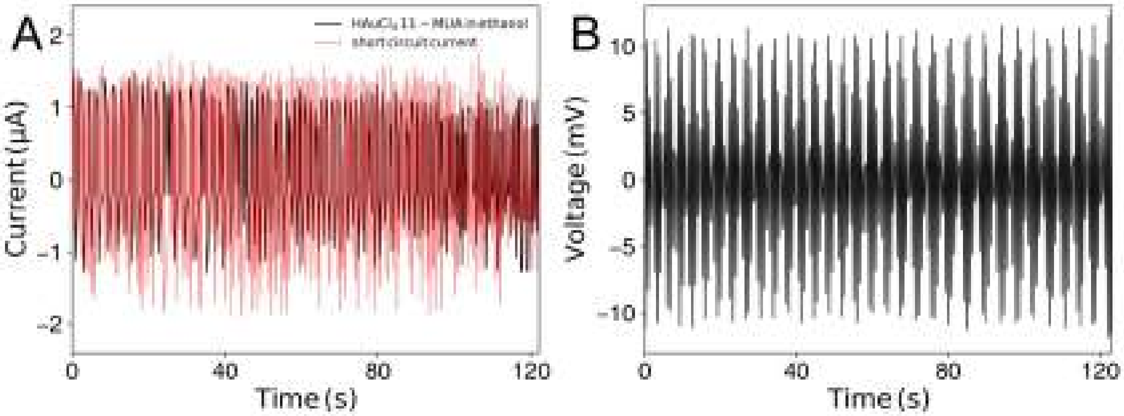

Figure S3. (A) Short circuit current for TG (red) and the current (black) drawn, and (B) voltage for the gold solution in ethanol, during synthesis of MUA-AuNCs.

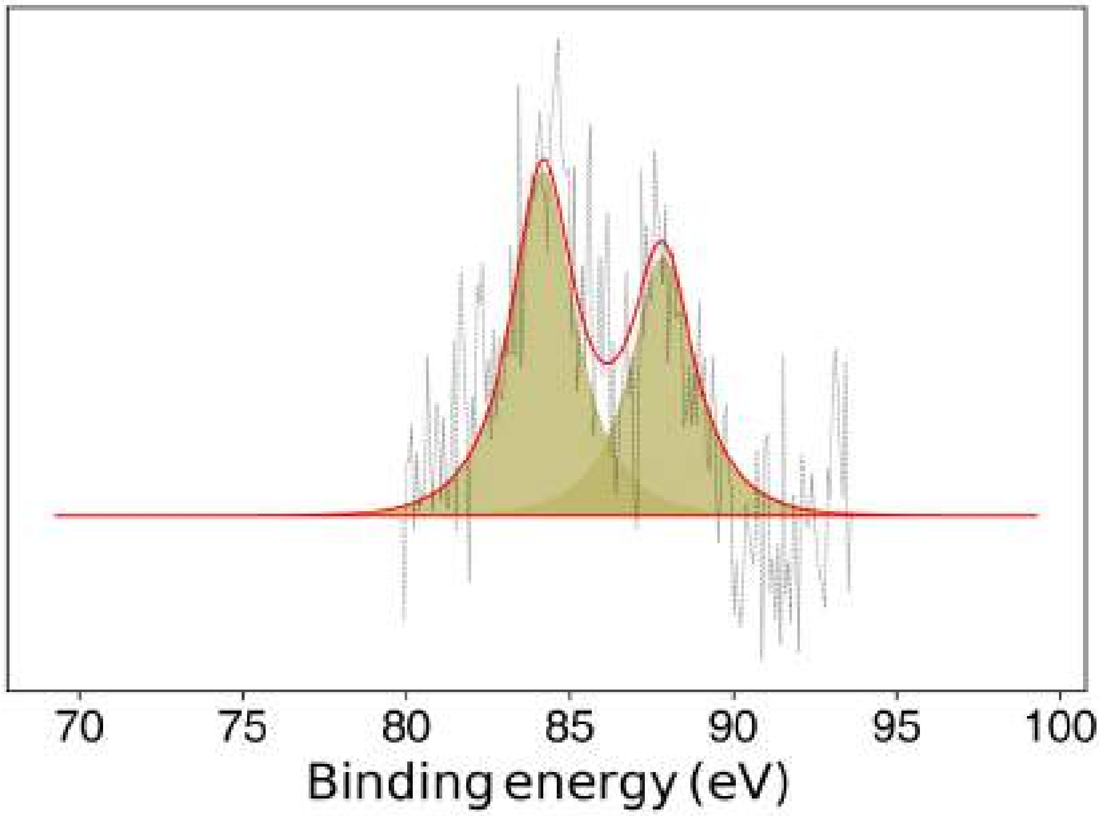

Figure S4. XPS spectrum of MUA-AuNCs in the Au 4f region.

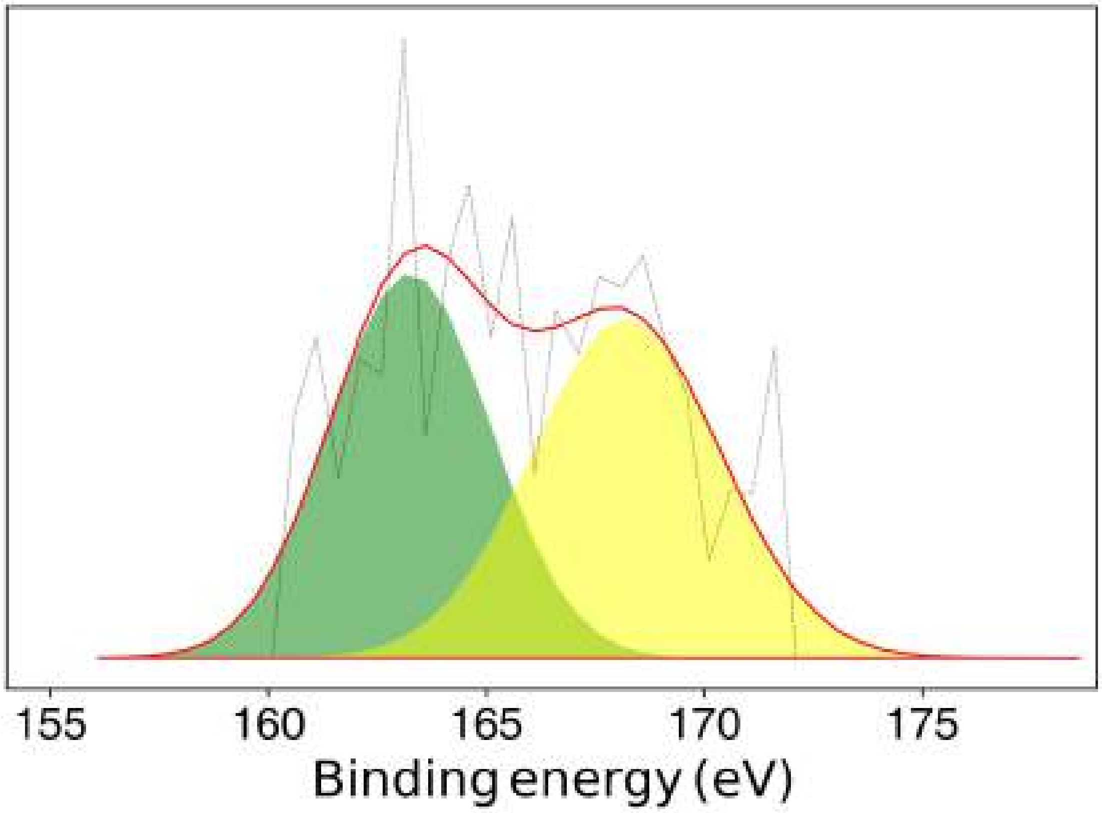

Figure S5. XPS spectrum of MUA-AuNCs (fitted using the survey spectra) in the S 2p region.

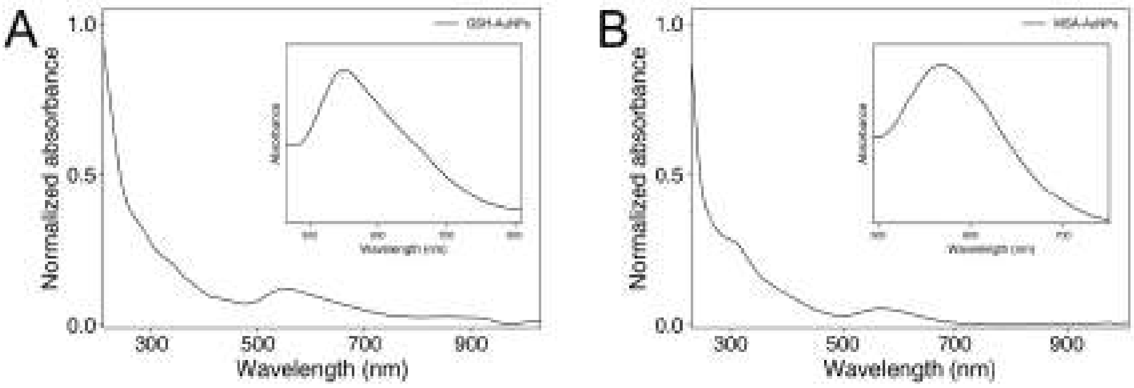

Figure S6. UV-Vis spectra for (A) GSH-AuNPs, and (B) MSA-AuNPs and inset showing the plasmonic peak at 550 nm and 560 nm, respectively.

REFERENCES

(1) Zhong, J.; Zhong, Q.; Fan, F.; Zhang, Y.; Wang, S.; Hu, B.; Wang, Z. L.; Zhou, J. Finger Typing Driven Triboelectric Nanogenerator and Its Use for Instantaneously Lighting up LEDs. *Nano Energy* **2013**, *2* (4), 491–497, DOI 10.1016/j.nanoen.2012.11.015.

(2) Zhu, Z.; Xia, K.; Xu, Z.; Lou, H.; Zhang, H. Starch Paper-Based Triboelectric Nanogenerator for Human Perspiration Sensing. *Nanoscale Research Letters* **2018**, *13* (1), 365, DOI 10.1186/s11671-018-2786-9.

(3) Zheng, Y.; Cheng, L.; Yuan, M.; Wang, Z.; Zhang, L.; Qin, Y.; Jing, T. An Electrospun Nanowire-Based Triboelectric Nanogenerator and Its Application in a Fully Self-Powered UV Detector. *Nanoscale* **2014**, *6* (14), 7842–7846, DOI 10.1039/C4NR01934B.

Nanoscale

ROYAL SOCIETY OF CHEMISTRY

PAPER

View Article Online
View Journal

Cite this: DOI: 10.1039/d1nr00619c

Gold cluster-loaded dendritic nanosilica: single particle luminescence and catalytic properties in the bulk†

Jyoti Sarita Mohanty,[a] Ayan Maity,[b] Tripti Ahuja,[a] Kamalesh Chaudhari,[a] Pillalamarri Srikrishnarka,[a] Vivek Polshettiwar[b] and Thalappil Pradeep*[a]

Received 29th January 2021,
Accepted 6th May 2021

DOI: 10.1039/d1nr00619c

rsc.li/nanoscale

We report a hybrid material in which surface anchoring-induced enhanced luminescence of Au_{QC}@BSA clusters on high surface area dendritic fibrous nanosilica of 800 nm diameter enabled their luminescence imaging at a single particle level. The photophysical and structural properties of the hybrid material were characterized by various spectroscopic and microscopic techniques. Concomitant imaging using scattering and luminescence of such mesostructures and their response to analytes have been used to develop a chemical sensor. The hybrid material was found to be catalytically active in silane to silanol conversion, and 100% conversion was observed in 4 h when the reaction was carried out at 30 °C in the presence of light. Such materials at submicron dimensions with enhanced surface area, emission in the solid state along with a high quantum yield of 12% in water along with enhanced scattering, and surface functionalities present numerous benefits for the creation of multifunctional materials.

Introduction

Atomically precise noble metal nanoclusters owing to their fascinating physical and chemical properties have been studied extensively.[1–5] Different ligands such as thiols,[6] DNA,[7,8] dendrimers,[9] and proteins[3] have been used for synthesizing such sub-nanometer-sized clusters. Among them, use of proteins as ligands is emerging as a result of the simple synthetic procedure employed in cluster synthesis and due to their biocompatible nature and promising applications. Bovine serum albumin (BSA),[10,11] Lactoferrin (Lf),[12] Lysozyme (Lyz),[13,14] *etc.*, are the commonly used proteins for synthesizing noble metal nanoclusters. Intense photoluminescence, high quantum yield, and stability over a wide range of pH make them suitable candidates in the field of sensors.[15]

Protein protected clusters (PPCs) are sensitive to specific metal ions. Xie *et al.* reported the sensing of Hg^{2+} using BSA-protected gold clusters (Au_{QC}@BSA) for the first time.[16] The subscript, QC is used to indicate a quantum cluster, to ensure that these are distinctly different from BSA protected plasmonic nanoparticles. Subsequently, several other groups have demonstrated sensing of heavy metal ions like Cu^{2+}, Hg^{2+}, and Pb^{2+} using PPCs.[3,5,17,18] Mercury is one of the most hazardous environmental contaminants among other heavy metal ions. It is toxic both in the inorganic and organic forms.[19] Different methods have been developed to determine trace levels of Hg^{2+}. Luminescent PPCs are suitable candidates for approaching such problems.

Anchoring such cluster systems on suitable substrates can extend their applications in the field. A few attempts have also been made in this direction using a variety of hybrid materials. Binding of Au_{QC}@BSA to nanofibers was demonstrated by Ghosh *et al.* and they have used it for the detection of Hg^{2+}.[20] A CdTe@SiO_2 hybrid sphere was synthesized by Wang *et al.*, where Au_{QC}@BSA was covalently linked to the hybrid sphere through EDC chemistry and used it as a ratiometric fluorescent probe for the determination of Cu^{2+}.[21] Mohammed *et al.* have shown simultaneous sensing and scavenging of heavy metal ions using an Au_{QC}@BSA-cellulose nanocrystal (CNC) composite.[22] Adsorption of heavy metal ions by the composite showed a visible change in the color. Recently, Upadhyay *et al.* synthesized porous, pH responsive Au_{QC}@BSA hydrogel beads which were used for the removal of heavy metal cations from contaminated water.[23]

Silane to silanol chemistry has been used in organic synthesis for industrial applications to prepare silicon based pre-

---

[a] *DST Unit of Nanoscience (DST UNS), and Thematic Unit of Excellence (TUE), Department of Chemistry, Indian Institute of Technology Madras, Chennai-600 036, India. E-mail: pradeep@iitm.ac.in*

[b] *Department of Chemical Sciences, Tata Institute of Fundamental Research (TIFR), Mumbai-400 005, India*

† Electronic supplementary information (ESI) available: Zeta potential and UV-Vis absorption spectra of DFNS@Au_{QC}BSA, HRTEM images showing the structural evolution during the formation of DFNS@Au_{QC}BSA, XRD pattern, time dependent PL spectra of DFNS@Au_{QC}BSA, AFM phase imaging of DFNS and DFNS@Au_{QC}BSA, optical and fluorescence images of DFNS, the effect of light in the catalytic reaction at 45 °C and UV-Vis absorption spectra of DFNS@Au_{QC}BSA after catalytic reaction. See DOI: 10.1039/d1nr00619c

cursors.[24] The traditional way for synthesizing these silanol molecules is *via* hydrolysis of halosilanes, by reacting siloxanes with alkali substrates or by controlled oxidation of organosilanes.[25] Among them, the stoichiometric oxidation of silane with water is environmentally friendly. The reaction not only produces silanols with improved selectivity but also releases hydrogen which is also a useful by-product, although conducting this reaction at lower temperature is always a synthetic challenge.[26] Dendritic fibrous nanosilica (DFNS)[27] is a mesosphere with thin sheet-like fibers of 3.5 to 5.2 nm thickness. It possesses radially oriented fibrous channels with variable pore sizes ranging from 3 nm to 25 nm. Such dendritic fibrous morphology with a high surface area and better chemical and thermal stability made them distinctive from the conventional mesoporous silica materials. Until now, there have been no reports on DFNS-based luminescent materials using protein protected clusters. Herein, for the first time, we have synthesized a hybrid material, DFNS@ Au_{QC}BSA by anchoring luminescent Au_{QC}@BSA on the DFNS substrate. It has been shown before that adhesion on substrates increases luminescence of protein protected clusters.[20,22] The hybrid material was capable of sensing Hg^{2+} and was found to be catalytically active for silane to silanol conversion.

Experimental

Materials

Bovine serum albumin (BSA) at pH 6–7 was purchased from SRL Chemical Co. Ltd, India. Tetrachloroauric acid trihydrate ($HAuCl_4·3H_2O$) was purchased from CDH, India. Tetraethyl orthosilicate, 3-aminopropyl triethoxysilane and sinapic acid were purchased from Sigma Aldrich, India. Urea, *p*-xylene, and sodium hydroxide (NaOH) were purchased from Rankem, India. Sodium borohydride ($NaBH_4$) was purchased from Spectrochem, India. Cetyl trimethyl ammonium bromide (CTAB) was purchased from Fluka, India. All the chemicals were used without further purification.

Instrumentation

UV-Vis spectra were collected using a PerkinElmer Lambda 25 instrument in the range of 200–1100 nm. Luminescence measurements were carried out on a Jobin Yvon NanoLog instrument. The band pass for excitation and emission was set as 3 nm. X-ray photoelectron spectroscopy (XPS) studies were conducted with an Omicron ESCA probe spectrometer with polychromatic Mg Kα X-rays ($h\nu$ = 1253.6 eV). The samples were spotted as drop-cast films on a sample stub. A constant analyser energy of 20 eV was used for the measurements. High resolution transmission electron microscopy (HRTEM) was performed with a JEOL 3010 instrument working at 300 kV, equipped with an ultra high resolution (UHR) pole piece. Energy dispersive X-ray analysis (EDS) was carried out with an Oxford EDAX housed in the TEM. A sample for HRTEM was prepared by dropping the dispersion on a carbon coated copper grid and drying under ambient conditions. High resolution scanning electron microscopy (HRSEM) images were collected using a Quanta 200 FEG SEM. Depending upon the compatibility of the sample, the instrument can work on three different operating modes namely, the high vacuum mode, low vacuum mode and environmental scanning electron microscope mode. For imaging purpose, samples were spotted on an indium tin oxide (ITO) conducting glass substrate and dried under ambient conditions. Atomic force microscopy (AFM) images were obtained using the asylum research Cypher ES AFM. Tapping mode (AC mode) was used for the measurement. X-ray diffraction (XRD) data were collected with a Bruker AXS, D8 discover diffractometer using Cu-Kα (λ = 1.54 Å) radiation. The diffractogram was collected from 5–100 degree 2θ range. Dark-field imaging of the hybrid material was performed using an Olympus BX-51 microscope and a 100 W quartz halogen light source on a Cyto Viva microscope setup. A broadband white light was used for the imaging purpose *via* a dark field condenser and a 100× oil immersion objective was used for collecting the scattered/emitted light from the particle. Imaging was performed using a true-color charge-coupled device (CCD). Hyperspectral image analysis software was used for spectral analysis and a mercury lamp was used for fluorescence images. GC-MS study was carried out using an Agilent 7890B instrument. For the light induced catalysis reaction, a Xe lamp of range 385–740 nm (Power 250 mW cm^{-2}) wavelength was used.

Synthesis

Synthesis of DFNS. Dendritic fibrous nanosilica (DFNS) was synthesized following a previously reported method.[28] The reaction was carried out using a 2 L four-neck round-bottom (RB) flask under refluxing conditions with a water condenser. In a typical synthesis, CTAB (10 g, 0.027 mol) and urea (12 g, 0.2 mol) were dissolved in 500 mL of water and mixed at 700 rpm using a magnetic stirrer for 30 minutes at room temperature. To the above solution, TEOS (50 mL, 0.24 mol) in 500 mL of *p*-xylene was added dropwise over 30 minutes under stirring. This reaction mixture was further stirred for 30 minutes. Then, 1-pentanol (30 mL) was added slowly into the reaction mixture and stirred for 30 minutes. The reaction mixture was heated to 130 °C (oil bath temperature) during 30 minutes ramp up and refluxed for 6 h under stirring at 700 rpm. After cooling, the solid product was isolated *via* centrifugation and washed several times with water and ethanol. After drying for 12 h at 80 °C, CTAB was removed by calcination at 550 °C for 6 h in air.

Synthesis of APTS functionalized DFNS. Functionalization of DFNS was performed following the reported method.[29] In brief, grafting of APTS was carried out by refluxing 2 g of calcined DFNS with 3-aminopropyl triethoxysilane (2 mL, 8.5 mM) in 250 mL of toluene at 80 °C for 24 h. The resulting material was washed repeatedly with toluene and ethanol followed by drying under vacuum at 60 °C for 12 h. The obtained material was APTS functionalized DFNS.

Synthesis of the hybrid material, DFNS@ Au_{QC}BSA. In a typical synthesis, 20 mg of BSA in 0.5 mL DI H_2O was added into 8 mg of APTS functionalized DFNS in 0.5 mL DI H_2O under vigorous stirring. After 5 minutes, 6 mM $HAuCl_4$ was added to the above mixture followed by the addition of 150 μL 1 M NaOH. The reaction mixture was stirred vigorously until the solution turned golden brown in color. The change in color indicated the formation of clusters. The reaction was carried out for 10 h at room temperature. The sample was centrifuged, and the residue was washed with DI H_2O and this process was followed repeatedly to ensure the removal of unbound clusters from the solution. Then the final residue was used for various characterization studies.

Oxidation of silanes by DFNS@Au_{QC}BSA

About 5 mg DFNS@Au_{QC}BSA was placed in a 10 mL round bottom test-tube. To the reaction tube, a mixture of tetrahydrofuran (1 mL), water (30 μL) and silane [dimethylphenylsilane (230 μL, 1.5 mM), triisopropylsilane (307 μL, 1.5 mM), tributylsilane (385 μL, 1.5 mM) and triphenylsilane (391 mg, 1.5 mM)] was added and the reaction mixture was vigorously stirred at required temperature. The reaction was monitored by taking aliquots at different intervals of time and the products were determined by GC-MS analysis.

Results and discussion

Synthesis and characterization of the hybrid material, DFNS@Au_{QC}BSA

The hybrid material, DFNS@Au_{QC}BSA, made of Au_{QC}BSA and DFNS was synthesized by a two-step procedure. In the first step, BSA was covalently linked to the amine functionalized DFNS in an aqueous medium to form a DFNS-BSA complex and in the next step, $HAuCl_4$ was added to the above complex at alkaline pH (Fig. 1A). BSA acted as both reducing and stabilizing agents during the synthesis of Au_{QC}@BSA.[10] Basically, when $HAuCl_4$ is added to BSA, it forms a complex through its various functional groups and reduces Au^{3+} to Au^{+} and further reduction of Au^{+} to its metallic state is achieved at alkaline pH. The DFNS-BSA-$HAuCl_4$ complex at pH ~ 12 was allowed to stir at room temperature. After 4 h, the turbid reaction mixture started changing its color from yellowish to light brown and finally turned to golden brown after 10 h of reaction. Change in color indicated the formation of the cluster on DFNS. The nanosized pores and fibrous morphology of DFNS provided an efficient template for the encapsulation of sub-nanometer sized Au_{QC}@BSA. To observe the structural changes, FESEM and HRTEM studies were performed for both parent DFNS and the hybrid material. Fig. 1(B, C) and (F, G) represent the FESEM and HRTEM images of the parent DFNS, respectively. DFNS is dendritic mesospheres of diameter ~800 nm with increasing fibrous morphology towards the outer surface and is of uniform size. After 10 h of reaction, FESEM and HRTEM studies of the hybrid material were carried out and are shown in Fig. 1(D, E) and (H, I), respectively.

Incorporation of clusters on DFNS gave rise to a well-defined structure, where the clusters were uniformly dispersed towards the outer surface of the DFNS and appeared as a ring-like pattern. Distinct morphological changes were observed in DFNS@Au_{QC}BSA compared to the parent DFNS but no significant change in their size could be observed from both FESEM and HRTEM studies. It suggested that incorporation of the clusters on the DFNS did not bring any change in the overall

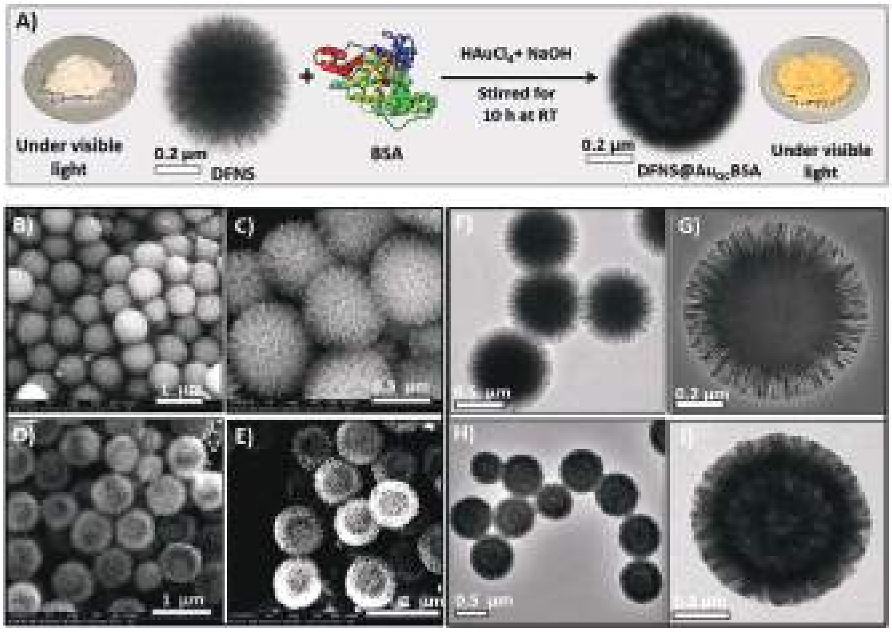

Fig. 1 (A) Schematic illustration showing the synthetic process leading to the hybrid material, DFNS@Au_{QC}BSA. (B and C) and (D and E) are the FESEM images of DFNS and DFNS@Au_{QC}BSA, respectively. (F and G) and (H and I) are the HRTEM images of DFNS and DFNS@Au_{QC}BSA, respectively. A well-defined morphological change was observed in DFNS@Au_{QC}BSA.

size or shape of the material. As the sizes of the clusters were less than 2 nm, they were difficult to be observed from the HRTEM images of the hybrid material. Isolated Au_{QC}BSA clusters were not prepared in solution, but they were investigated before.[3,10] The core size of such clusters was found to be less than 2 nm.[30,31]

UV-Vis and zeta potential study of DFNS@Au_{QC}BSA

Surface modification of DFNS helped to conjugate BSA onto it effectively and this was achieved through APTS functionalization, by replacing the hydroxyl groups (–OH) of DFNS with the amine (–NH_2) groups. This was monitored by measuring zeta potential of DFNS which was changed from −16.9 mV to +19.3 mV after functionalization. The binding of BSA to the amine functionalized DFNS was confirmed from the surface charge of −26.1 mV and it reached −34.7 mV after 10 h, which confirmed the binding and encapsulation of the cluster on DFNS (Fig. S1A†). To evaluate the changes in the optical properties during the formation of the hybrid material, UV-Vis spectra were collected (Fig. S1B†). BSA has a sharp absorption feature at 280 nm due to the presence of aromatic amino acid residues while DFNS did not show any absorption feature in the 300–800 nm range. A slight decrease in the absorption peak along with a gradual increase in absorbance from 800 nm was found in the DFNS-BSA complex, which suggested the conjugation of the protein onto DFNS. After 10 h of the reaction, the absorption feature at 280 nm decreased significantly along with a slope around 375 nm which confirmed the formation of clusters inside the protein template and proved successful incorporation of the cluster on DFNS.

Evolution of DFNS@Au_{QC}BSA

To understand the evolution of the hybrid material, time dependent HRTEM studies were conducted. Control experiments were also performed to know the effect of NaOH on DFNS during the synthesis (Fig. S2†). Addition of NaOH into the solution of DFNS induced a drastic morphological change due to etching of the surface (Fig. S2B†). But when NaOH was added into the DFNS-BSA complex, similar morphological changes were not observed; it was due to the conjugation of BSA on the fibrous channels of DFNS which prevented the etching of the DFNS surface (Fig. S2C†). During *in situ* synthesis of the cluster, $HAuCl_4$ was added to the DFNS-BSA complex followed by the addition of NaOH into the mixture. Although formation of the cluster started after 4 h of the reaction (started to show luminescence under UV light), visible morphological changes were not observed compared to the parent DFNS (Fig. S2D†). But after 6 h, the structure of the hybrid material started to emerge (Fig. S2E†) and a well-defined pattern with uniform arrangement of clusters towards the periphery of DFNS was observed post 10 h of the reaction (Fig. S2F†). During the reaction, a slight etching from the surface of the material was seen. We have already mentioned that the formation of clusters occurs only at alkaline pH. Therefore, here NaOH played a major role in reducing the gold ions in the cluster synthesis rather than only interacting with the surface of DFNS and this could be the reason for minimal surface etching seen in the hybrid material as compared to the parent DFNS. According to our earlier report, sizes of BSA and the cluster (including the protein shell) were found to be around 7.3 and 9 nm, respectively.[32] As the pore sizes of the DFNS decrease from the outer surface towards the center, BSA could easily enter into the compatible pore of the DFNS. A probable mechanism for the formation of DFNS@Au_{QC}BSA could be explained on the basis of dendritic fibrous morphology with varying pore sizes of DFNS which made it accessible for the conjugation of BSA (through its various functional groups) on DFNS from all the directions followed by the formation of the cluster with the addition of $HAuCl_4$ into alkaline medium. The reduced pore sizes towards the center of the DFNS restricted the entry of BSA as well as the growth of the cluster around the center which resulted in the formation of ring patterns near the edges of DFNS.

HRTEM EDS analysis of DFNS@Au_{QC}BSA

The incorporation of clusters on DFNS was confirmed further using HRTEM EDS elemental mapping (Fig. 2). The EDS map of Au L clearly showed a uniform dispersion of the cluster only at the edge while Si was nearly absent on that specific region as shown in the Si K map. The presence of silica was observed at the center of the hybrid material, where Au was nearly absent. Distribution of oxygen in O K was found similar to that of the Si K map and dispersion of S in the S K map matched well with the Au L map as the source of sulphur was from the protein. These data confirmed the presence of clusters as well as their uniform distribution at the edges of the hybrid material as speculated in the earlier section. Fig. 2F provides the quantification data of the hybrid material.

The powder X-ray diffraction (PXRD) pattern of DFNS showed a diffraction peak at $2\theta = 22.5°$ and BSA showed two diffraction peaks at $2\theta = 9°$ and $2\theta = 20.5°$ related to its crystalline nature (Cu Kα). The obtained values matched with the values reported.[29,33] For the hybrid material, very weak and broad peaks around $2\theta = 38°$ and 64° along with the one at $2\theta = 22.5°$ were observed, due to Au (111), Au (220) and amorphous SiO_2, respectively (Fig. S3†).

Photoluminescence properties of DFNS@Au_{QC}BSA

DFNS@Au_{QC}BSA showed strong red emission both in the solution and solid state indicating effective incorporation of clusters on DFNS, which were responsible for the strong luminescence exhibited by the hybrid material. DFNS@Au_{QC}BSA showed an emission maximum of ~640 nm with two excitation maxima around 365 and 500 nm (Fig. 3A). The photographs of the hybrid material in the aqueous solution under visible and UV light are shown in the inset of Fig. 3A. The material was freeze dried into a powder form and the powders also showed bright luminescence under UV light (Fig. 3B). A similar excitation maximum was observed for both solid and solution states. But a red shift from 640 to 645 nm was observed in the emission maximum of the solid material. This shift was attributed to the confinement of the cluster in the solid form.

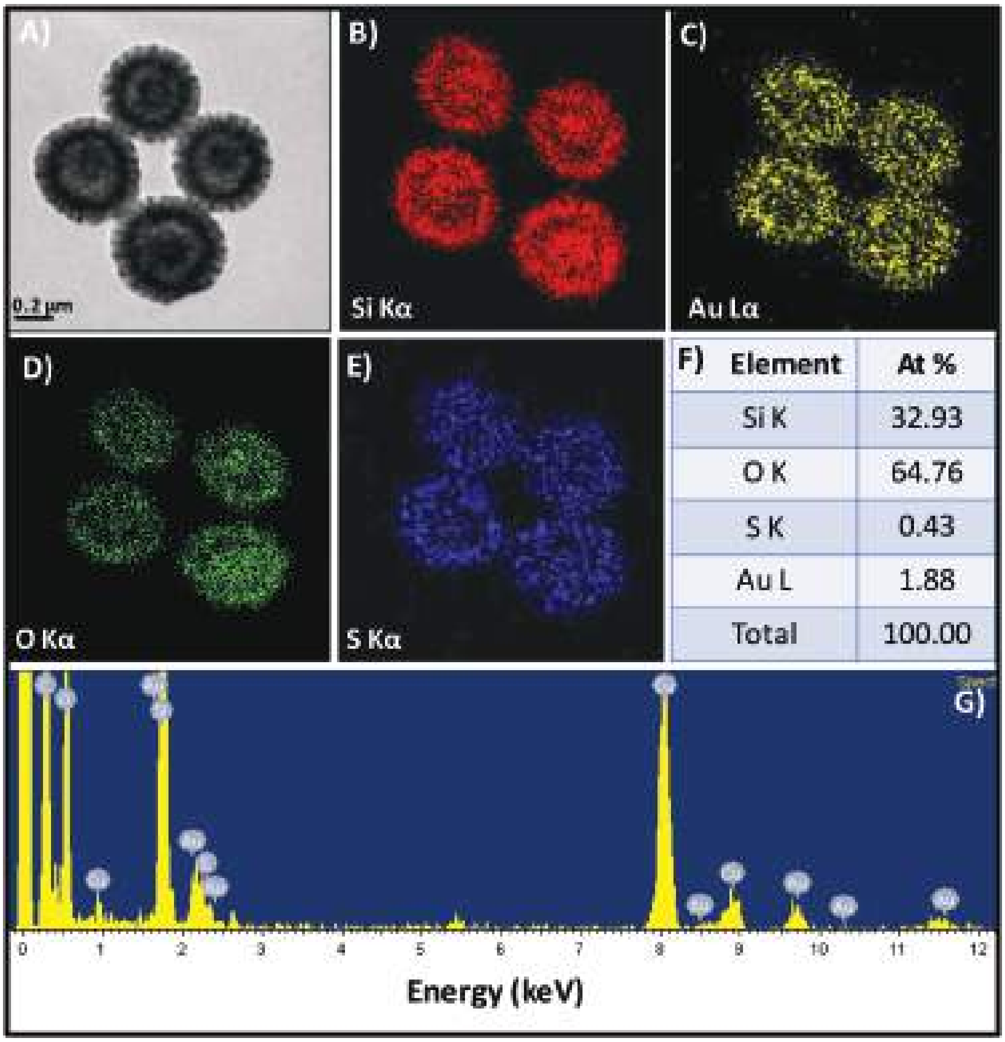

Element	At %
Si K	32.93
O K	64.76
S K	0.43
Au L	1.88
Total	100.00

Fig. 2 EDS analysis to confirm the presence of clusters in the DFNS@Au$_{QC}$BSA. (A) TEM image of the hybrid material and the corresponding Si Kα, Au Lα, O Kα, and S Kα maps are shown in B, C, D and E, respectively. Au Lα mapping shows the presence of gold only at the edges of the sphere while the absence of silica from those regions is clearly seen from the Si Kα map. Quantification data and EDS spectrum showing the presence of expected elements in DFNS@Au$_{QC}$BSA are presented in F and G, respectively.

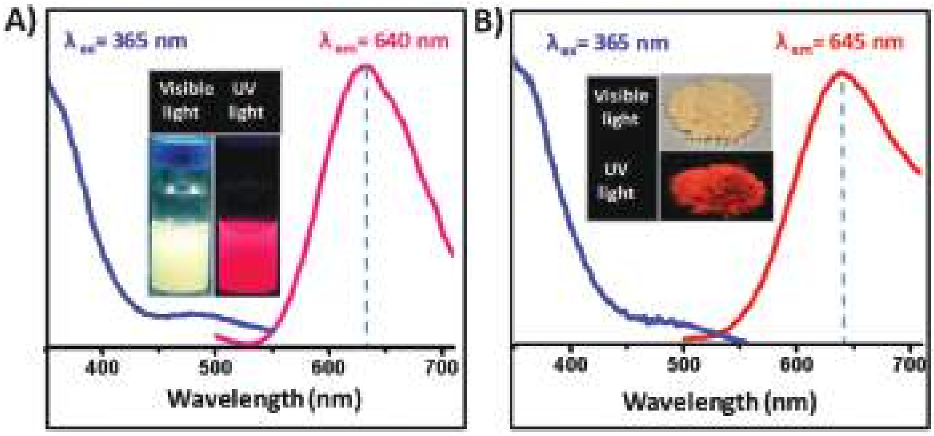

Fig. 3 Luminescence profile of DFNS@Au$_{QC}$BSA in the (A) solution and (B) solid states. Photographs of DFNS@Au$_{QC}$BSA in the solution and powder form under UV and visible light are shown in the respective insets. Both the samples were excited at 365 nm. The emission was found around 640 nm for the solution and around 645 nm for the solid state.

Resemblance of the luminescence spectrum with that of Au_{QC}BSA in solution suggested that the clusters formed on the DFNS surface were essentially similar to that in the free state.[10]

The evolution of luminescence during the formation of the hybrid material was studied by measuring the time dependent PL spectra (Fig. S4†). After 4 h of synthesis, the mixture started to show faint luminescence and the color of the mixture also changed from slightly yellowish to light brown. This was an indication of the formation of the cluster. With time, a gradual increase in the luminescence intensity was observed along with a change in the color of the mixture. Maximum emission intensity was observed after 10 h of the reaction and the color of the reaction mixture turned golden brown. All the samples were excited at 365 nm and emission maxima were found to be around 640 nm. Luminescence of the hybrid material was stable and PL spectra up to 5 days are shown in Fig. S4.† The luminescence profile of the DFNS@Au_{QC}BSA at various stages of the reaction did not show any shift in its emission wavelength which suggested the formation of a stable species on DFNS.

Investigation of structural morphology of DFNS@Au_{QC}BSA using AFM

The formation of a hybrid material was further studied using atomic force microscopy (AFM). The 3D topographical images of DFNS and the hybrid material are presented in Fig. 4A and C, respectively. It clearly showed the significant changes in the morphology of the hybrid material as compared to their parent analogues. The height profile of a single DFNS particle was found to be 650 nm (Fig. 4B) while in the case of a single particle of the hybrid material, the height decreased to 320 nm (Fig. 4D).

We have mentioned in section 3.1 that during the growth of clusters on DFNS, the fibrous morphology of the latter was decreased due to etching of the surface. Although the exact reason is not apparent in this study, the reduced fibrous morphology could be the probable reason for the significant change in the height of the hybrid material.

Phase imaging provides complementary information on the topography and reveals the variations in the surface properties including the composition of the material. A large area phase image of the parent DFNS is shown in Fig. S5A† and the high resolution image of the edge of a DFNS is presented in Fig. S5B.† A thin sheet-like surface was observed in the parent DFNS which could be compared to the fibrous morphology as seen in the HRTEM image. But the hybrid material appeared to be completely different from the parent structure (Fig. S5C†). The thickness of the edge was increased, and it exhibited a brighter contrast which was absent in the case of parent DFNS (Fig. S5D†). The enhanced contrast was due to the presence of clusters at the edge of the hybrid material which was supported by the observation made by TEM EDS mapping.

XPS studies of DFNS@Au_{QC}BSA

X-ray photoelectron spectroscopy (XPS) helps to determine the oxidation state and binding properties of the protein stabilized gold clusters. XPS analysis of DFNS@Au_{QC}BSA confirmed the existence of the metallic state of gold. Au $4f_{7/2}$ appeared at 84.5 eV close to its Au^0 binding energy. The observed slightly higher binding energy (BE) could be contributed to its bonding environment. The S $2p_{3/2}$ and $2p_{1/2}$ BEs of 164.0 and 165.5 eV, respectively, are characteristic of thiolate.[12,34] This suggested that the cluster core is stabilized by the thiol groups

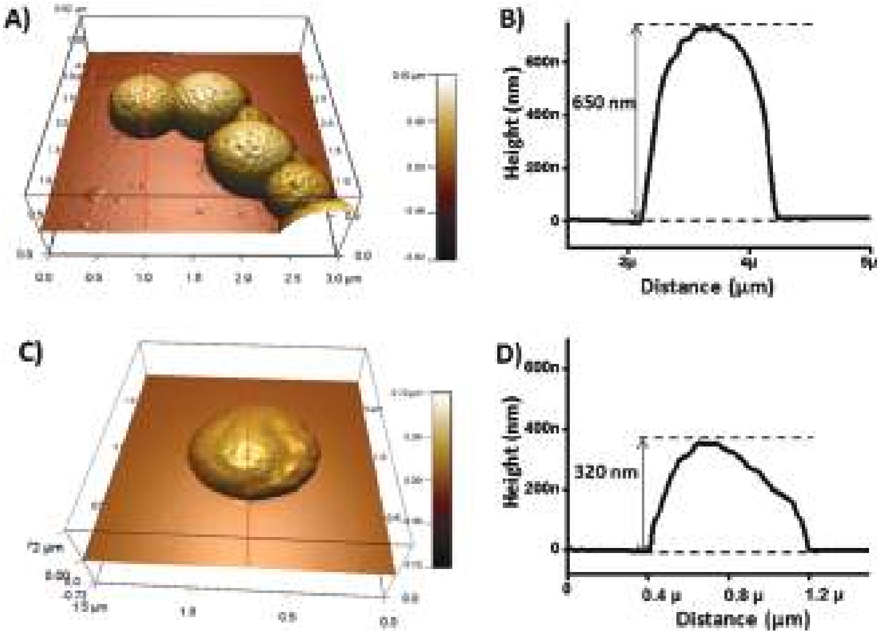

Fig. 4 The 3D topographical images of DFNS and the hybrid material are presented in (A) and (C), respectively. (B) and (D) Height profiles of DFNS and the hybrid material based on the line scans (labelled in red) in the AFM images, respectively.

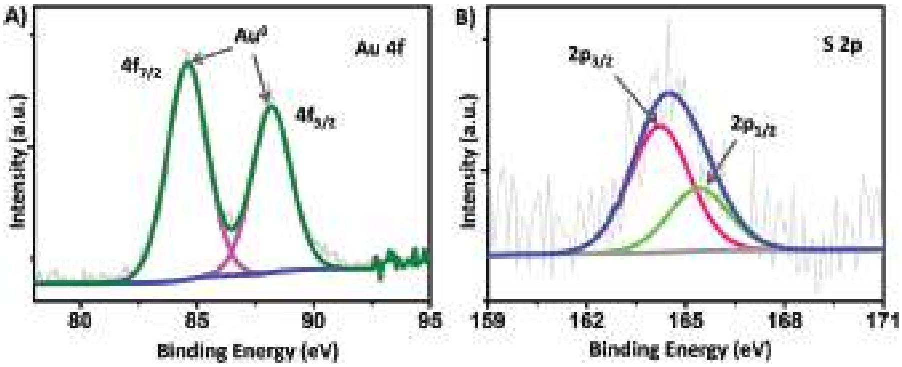

Fig. 5 XPS analysis of DFNS@Au_{QC}BSA showing metallic (A) Au 4f and thiolate (B) S 2p regions.

of the protein (mostly through the cysteine residues and are highly reactive, BSA has 35 cysteines). Slightly higher binding energy could be attributed to the oxidized state of sulphur, which is observed in the case of thiolate protected clusters upon X-ray exposure, thus leading to sulphite, sulphonate and sulphate species.[35,36] The cluster remained intact on DFNS as no Au^+ was observed. This is in agreement with the luminescence data also (Fig. 5).

Darkfield microscopy and metal ion sensing using DFNS@Au_{QC}BSA

The hybrid material, DFNS@Au_{QC}BSA, with distinct structural properties was observable under an optical microscope. For this analysis, a diluted solution of the sample was dropcast and dried on a glass slide. Dark field optical microscopy images of the parent DFNS appeared as spherical particles and a large area optical image of them is shown in Fig. 6A. The particles were subjected to hyperspectral imaging (HSI) analysis and the scattering spectrum of a single DFNS was collected (Fig. 6B). The corresponding single DFNS is provided in the inset of B in which the specific positions from where the spectra were collected are marked as 1 and 2. The scattering intensity was higher at the center than the edges and was due to the fibrous morphology, with decreasing density from the center towards the edge of the DFNS. Interestingly, the dark field image of the hybrid material was entirely different from

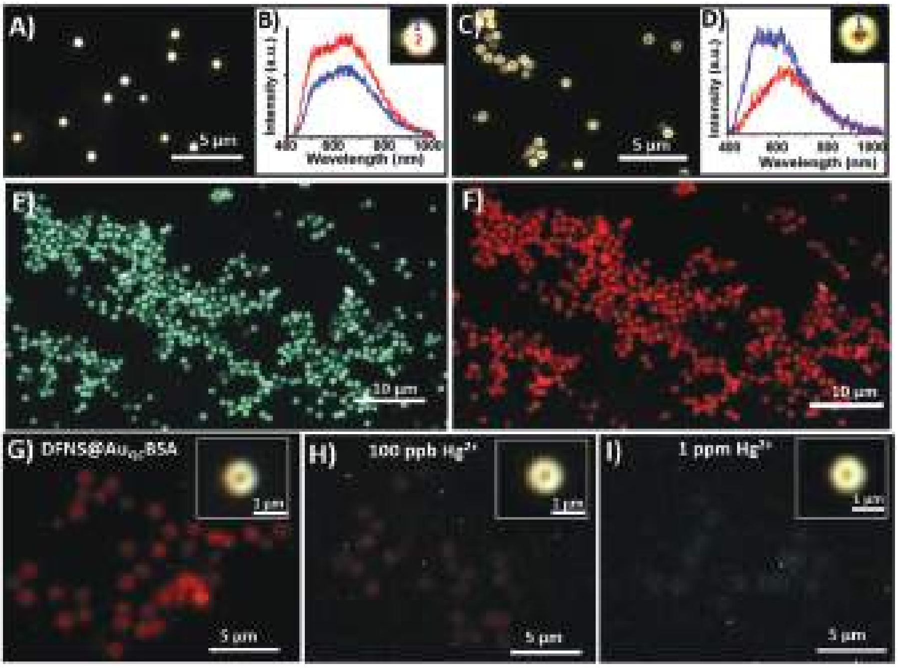

Fig. 6 Large area optical images of (A) DFNS and (C) DFNS@Au_{QC}BSA. The corresponding scattering spectra collected from the surface of DFNS and DFNS@Au_{QC}BSA are presented in (B) and (D), respectively. The positions in the single particle from where the spectra are collected are marked in the insets. (E) The white light and the corresponding (F) fluorescence image of DFNS@Au_{QC}BSA. (G–I) Fluorescence images of DFNS@Au_{QC}BSA, (G) before and after exposure to Hg^{2+} at concentrations of (H) 100 ppb and (I) 1 ppm, respectively. The corresponding optical images are shown in the insets.

that of the parent DFNS and appeared like hollow spheres or donuts (Fig. 6C).

Scattering spectra of the hybrid material were collected from similar positions as in the parent DFNS (Fig. 6D) and the corresponding single hybrid material particle is given in the inset. The results obtained were opposite to that of parent DFNS, where a higher scattering intensity was observed from the edge of the hybrid material compared to the center. The presence of clusters at the edges of the hybrid material results in such unique structure under an optical microscope which was strengthened by EDS mapping as well as AFM phase imaging. The increased electron density at the edges due to the clusters contributed to this enhanced scattering intensity. Fig. 6E shows a large area optical light image of the hybrid material and the corresponding fluorescence image is depicted in Fig. 6F. The fluorescence image exhibits red emission due to the clusters anchored on the surface of DFNS and similar hollow sphere structures were also observed in fluorescence images. Hg^{2+} is known to quench the luminescence of Au_{QC}@BSA and the interaction of Hg^{2+} with the core of the cluster has been suggested as the plausible reason for this quenching effect. In order to study the effect of Hg^{2+} on the luminescence of the hybrid material, different concentrations of Hg^{2+} were introduced to the former. Gradual disappearance of the luminescence intensity from the hybrid material upon addition of varying concentrations (100 ppb, 1 ppm) is shown in Fig. 6G–I. Though a significant decrease in the luminescence of the hybrid material was observable at 100 ppb of Hg^{2+}, a complete quenching of the luminescence occurred upon exposure to 1 ppm concentration of the Hg^{2+}. In both the cases, the optical images of the hybrid material remained unaffected as shown in the inset of Fig. 6H and I as scattering intensity was nearly the same. It suggested that even at higher concentration of Hg^{2+}, the structure of the material was not affected. Parent DFNS was not luminescent and a large area optical image and the corresponding fluorescence image of DFNS are shown in Fig. S6A and S6B,† respectively. Different concentrations of Hg^{2+} were introduced to the parent DFNS and optical images were captured. No structural changes were observed. Thus, it can be confirmed that the quenching effect was due to the clusters alone. This approach is advantageous over the solution phase method as single particle level investigations are possible.

Conversion of silane to silanol by DFNS@Au_{QC}BSA

DFNS acts as an excellent material to support metal nanoparticles and organometallic complexes to design nanocatalysts.[27] This prompted us to use the hybrid material (DFNS@Au_{QC}BSA) for the oxidation of organosilanes to silanols. The silane to silanol reaction was performed in a tetrahydrofuran THF–water mixture at 45 °C using 5 mg of the hybrid material as the catalyst as shown in scheme Fig. 7A. The result showed that these clusters were catalytically active (Fig. 7B). The catalyst showed higher kinetics for dimethylphenylsilane as compared to other silanes with 77% of silane to silanol conversion in 10 h. For other silanes, kinetics as well as conversion dropped as a function of neighbouring functional group of the silane molecule. For both triisopropylsilane and tributylsilane, 42% silane was converted to silanol while for triphenylsilane, only 19% conversion was observed and such reduced conversion rate could be attributed to the steric hindrance caused due to the presence of the bulky phenyl group. To study the catalytic effect of the hybrid material, the conversion of dimethylphenylsilane to dimethylphenylsilanol reaction was performed at 45 °C in the presence and absence of light (>385 to 740 nm) but no significant improvement was observed as compared to the conventional reaction without light (Fig. S7†). To maximize the effect of light on the catalysis reaction, temperature was reduced to 30 °C and in this case, it was possible to differentiate the effect of light on the catalysis

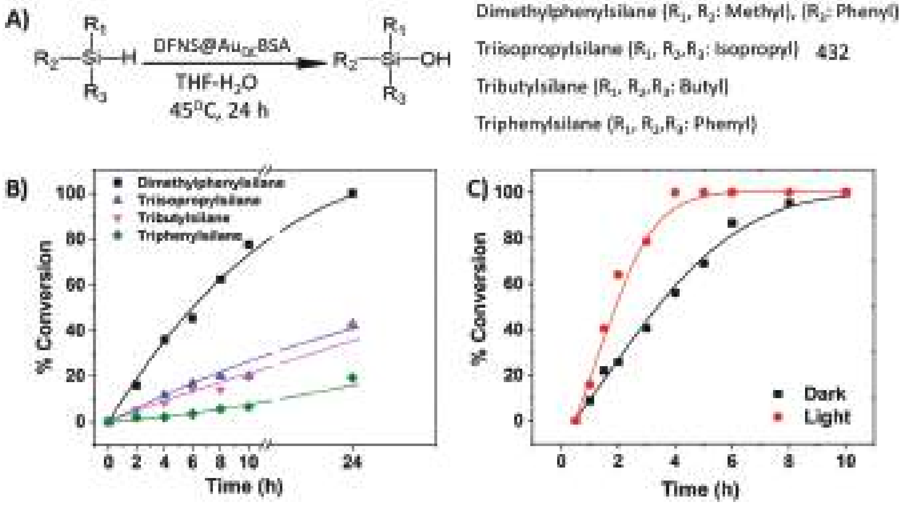

Fig. 7 (A) The reaction scheme showing the conversion of silane to silanol. (B) The conversion of various silanes to silanol at 45 °C during different time intervals. (C) The effect of light for the dimethylphenylsilane to dimethylphenylsilanol conversion reaction, at 30 °C (error in the catalytic measurements is ±5%).

as compared to the reaction conducted in the dark at 30 °C (Fig. 7C). In the presence of light, the reaction occurred much faster (100% conversion in 4 h) while only 56% conversion was observed without light at 4 h. There was no role of the enzyme in the silane hydrolysis reaction which was confirmed by controlled catalytic experiments using DFNS and BSA complex, in which no catalytic activity was found under similar experimental conditions. Thus, the enhancement could be directly attributed to the presence of clusters.

UV-Vis absorption spectra of DFNS@Au$_{QC}$BSA were measured in the presence and absence of light, after the catalytic reaction (Fig. S8†). In both the cases, a plasmonic peak around 532 nm was found which was absent before the catalytic activity (Fig. S1B†). This clearly suggested the change in the size of the cluster after catalysis. It showed that the catalytic conditions made gold clusters to aggregate.

Conclusions

In conclusion, we have developed a luminescent hybrid material (DFNS@Au$_{QC}$BSA) using Au$_{QC}$@BSA loaded on DFNS which can act both as a chemical sensor and a catalyst. Utilizing the scattering and luminescence properties, imaging of such mesostructures was performed and they were used for sensing Hg^{2+}. This approach enabled a single particle luminescence imaging with a unique donut like mesostructure. The hybrid material was demonstrated as the catalyst in the oxidation of organosilanes to silanols, with higher kinetics of 77% conversion for dimethylphenylsilane to dimethylphenylsilanol. The efficiency of the catalyst was found to increase in the presence of light when the reaction was performed at 30 °C and 100% conversion was achieved only in 4 h. The hybrid material has great potential in numerous applications in various fields using combined properties of the luminescent clusters and DFNS. Additional experiments are required to understand the system in more detail and to improve the sensitivity of detection as well as the catalytic efficiency of the material.

Conflicts of interest

There are no conflicts to declare.

Acknowledgements

We thank the Department of Science and Technology, Govt. of India for their continuous support on our research program on nanomaterials. V. P. thanks the Department of Atomic Energy, Govt. of India for funding. J. S. M. thanks Council of Scientific and Industrial Research (CSIR) for her research fellowship. T. A. and P.S. thank IIT Madras for their research fellowship.

Notes and references

1 R. Jin, *Nanoscale*, 2010, **2**, 343–362.
2 A. Mathew and T. Pradeep, *Part. Part. Syst. Charact.*, 2014, **31**, 1017–1053.
3 P. L. Xavier, K. Chaudhari, A. Baksi and T. Pradeep, *Nano Rev.*, 2012, **3**, 14767–14782.
4 D. M. Chevrier, A. Chatt and P. Zhang, *J. Nanophotonics*, 2012, **6**, 064504-1–064504-16.
5 Q. Yao, Z. Wu, Z. Liu, Y. Lin, X. Yuan and J. Xie, *Chem. Sci.*, 2021, **12**, 99–127.
6 I. Chakraborty and T. Pradeep, *Chem. Rev.*, 2017, **117**, 8208–8271.
7 J. T. Petty, J. Zheng, N. V. Hud and R. M. Dickson, *J. Am. Chem. Soc.*, 2004, **126**, 5207–5212.
8 C. He, P. M. Goodwin, A. I. Yunus, R. M. Dickson and J. T. Petty, *J. Phys. Chem. C*, 2019, **123**, 17588–17597.
9 J. Zheng, J. T. Petty and R. M. Dickson, *J. Am. Chem. Soc.*, 2003, **125**, 7780–7781.
10 J. Xie, Y. Zheng and J. Y. Ying, *J. Am. Chem. Soc.*, 2009, **131**, 888–889.
11 A. Mathew, P. R. Sajanlal and T. Pradeep, *J. Mater. Chem.*, 2011, **21**, 11205–11212.
12 P. L. Xavier, K. Chaudhari, P. K. Verma, S. K. Pal and T. Pradeep, *Nanoscale*, 2010, **2**, 2769–2776.
13 A. Baksi, P. L. Xavier, K. Chaudhari, N. Goswami, S. K. Pal and T. Pradeep, *Nanoscale*, 2013, **5**, 2009–2016.
14 A. Baksi and T. Pradeep, *Nanoscale*, 2013, **5**, 12245–12254.
15 H. Li, W. Zhu, A. Wan and L. Liu, *Analyst*, 2017, **142**, 567–581.
16 J. Xie, Y. Zheng and J. Y. Ying, *Chem. Commun.*, 2010, **46**, 961–963.
17 N. Goswami, A. Giri, M. S. Bootharaju, P. L. Xavier, T. Pradeep and S. K. Pal, *Anal. Chem.*, 2011, **83**, 9676–9680.
18 M. A. Habeeb Muhammed, P. K. Verma, S. K. Pal, A. Retnakumari, M. Koyakutty, S. Nair and T. Pradeep, *Chem. – Eur. J.*, 2010, **16**, 10103–10112.
19 L. Trasande, P. J. Landrigan and C. Schechter, *Environ. Health Perspect.*, 2005, **113**, 590–596.
20 A. Ghosh, V. Jeseentharani, M. A. Ganayee, R. G. Hemalatha, K. Chaudhari, C. Vijayan and T. Pradeep, *Anal. Chem.*, 2014, **86**, 10996–11001.
21 Y.-Q. Wang, T. Zhao, X.-W. He, W.-Y. Li and Y.-K. Zhang, *Biosens. Bioelectron.*, 2014, **51**, 40–46.
22 N. Mohammed, A. Baidya, V. Murugesan, A. A. Kumar, M. A. Ganayee, J. S. Mohanty, K. C. Tam and T. Pradeep, *ACS Sustainable Chem. Eng.*, 2016, **4**, 6167–6176.
23 A. Upadhyay and C. P. Rao, *ACS Appl. Mater. Interfaces*, 2019, **11**, 7965–7973.
24 Y. Okada, M. Oba, A. Arai, K. Tanaka, K. Nishiyama and W. Ando, *Inorg. Chem.*, 2010, **49**, 383–385.
25 W. Li, A. Wang, X. Yang, Y. Huang and T. Zhang, *Chem. Commun.*, 2012, **48**, 9183–9185.
26 K. B. Sharpless, *Angew. Chem., Int. Ed.*, 2002, **41**, 2024–2032.

27 A. Maity and V. Polshettiwar, *ChemSusChem*, 2017, **10**, 3866–3913.

28 A. Maity, A. Das, D. Sen, S. Mazumder and V. Polshettiwar, *Langmuir*, 2017, **33**, 13774–13782.

29 R. Singh, R. Belgamwar, M. Dhiman and V. Polshettiwar, *J. Mater. Chem. B*, 2018, **6**, 1600–1604.

30 J. S. Mohanty, K. Chaudhari, S. Chennu and T. Pradeep, *J. Phys. Chem. C*, 2019, **123**, 28969–28976.

31 H. W. Li, Y. Yue, T. Y. Liu, D. Li and Y. Wu, *J. Phys. Chem. C*, 2013, **117**, 16159–16165.

32 A. Baksi, A. Mitra, J. S. Mohanty, H. Lee, G. De and T. Pradeep, *J. Phys. Chem. C*, 2015, **119**, 2148–2157.

33 M. W. Sabaa, D. H. Hanna, M. H. Abu Elella and R. R. Mohamed, *Mater. Sci. Eng., C*, 2019, **94**, 1044–1055.

34 G. J. Ashwell, B. U. Wojcik and L. J. Phillips, *Angew. Chem., Int. Ed.*, 2010, **49**, 3508–3512.

35 T. Laihoa, J. A. Leiroa and J. Lukkarib, *Appl. Surf. Sci.*, 2003, **212–213**, 525–529.

36 X. L. Guével, B. Hötzer, G. Jung, K. Hollemeyer, V. Trouillet and M. Schneider, *J. Phys. Chem. C*, 2011, **115**, 10955–10963.

ELECTRONIC SUPPLEMENTARY INFORMATION

Gold Clusters-Loaded Dendritic Nanosilica: Single Particle Luminescence and Catalytic Properties in the Bulk

Jyoti Sarita Mohanty, [a] Ayan Maity,[b] Tripti Ahuja, [a] Kamalesh Chaudhari,[a] Pillalamarri Srikrishnarka,[a] Vivek Polshettiwar[b] and Thalappil Pradeep*[a]

[a]DST Unit of Nanoscience (DST UNS), and Thematic Unit of Excellence (TUE), Department of Chemistry, Indian Institute of Technology Madras, Chennai- 600 036, India.
*E-mail: pradeep@iitm.ac.in
[b]Department of Chemical Sciences, Tata Institute of Fundamental Research (TIFR), Mumbai- 400 005, India.

*Email: pradeep@iitm.ac.in

TABLE OF CONTENT

A)

Sample	Zeta potential (mV)
DFNS	-16.9
Amine Funct. DFNS	+19.3
BSA	-28.4
Amine funct. DFNS+BSA	-26.1
DFNS@Au$_{QC}$BSA (10 h)	-34.7

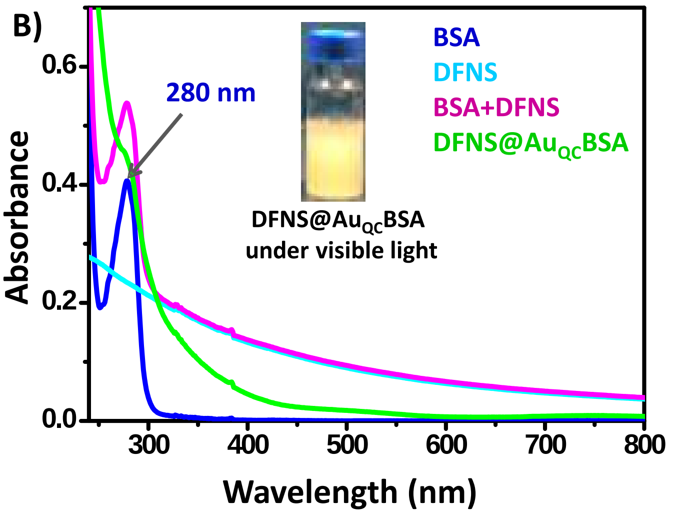

Fig. S1 (A) Comparative Zeta potential values of DFNS@Au$_{QC}$BSA and its related systems. (B) UV-Vis absorption spectra of DFNS@Au$_{QC}$BSA showing the synthesis of cluster on DFNS surface. The spectra were collected using water as the solvent. Inset shows the photograph of DFNS@Au$_{QC}$BSA under visible light.

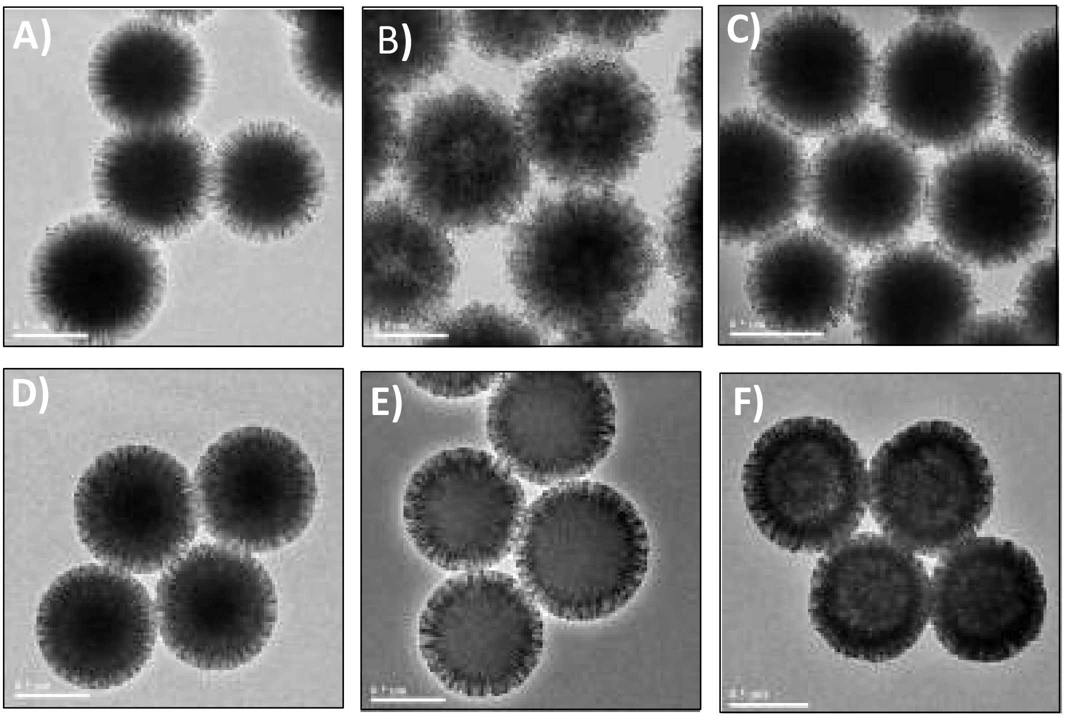

Fig. S2 HRTEM images showing the evolution of DFNS@Au$_{QC}$BSA structure. A) DFNS, (B) DFNS, and (C) DFNS+BSA at alkaline pH. HRTEM images of DFNS+BSA+HAuCl$_4$ at alkaline pH after (D) 4 h, (E) 6 h, and (F) 10 h of the reaction. The hybrid structure was obtained after 10 h of the reaction.

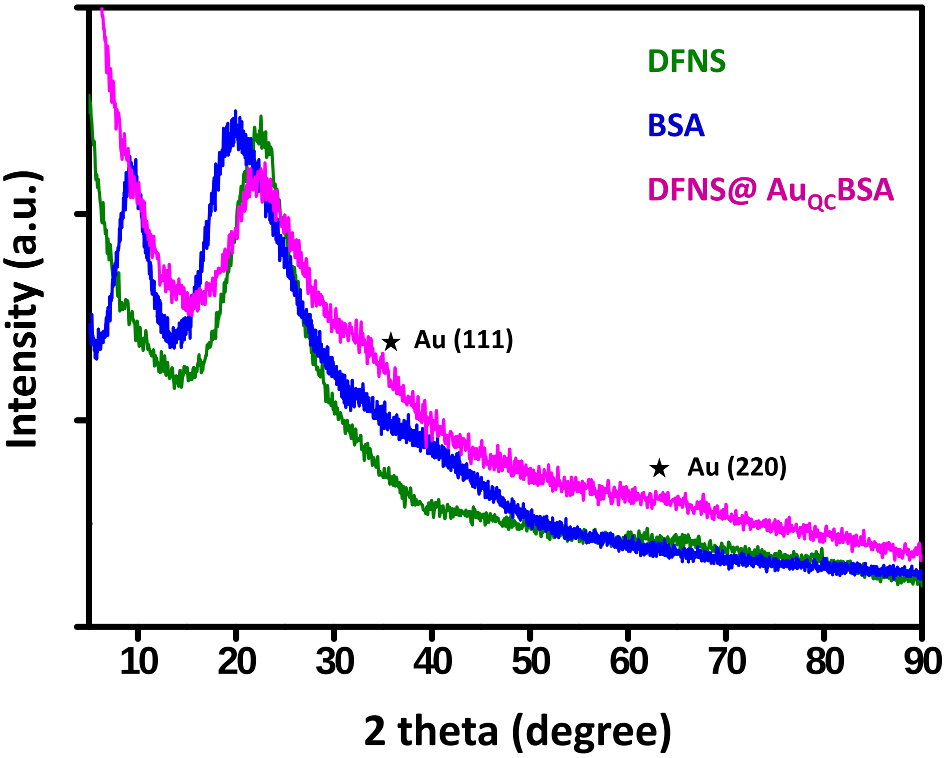

Fig. S3 Powder X-ray diffraction patterns of DFNS, BSA and DFNS@Au$_{QC}$BSA.

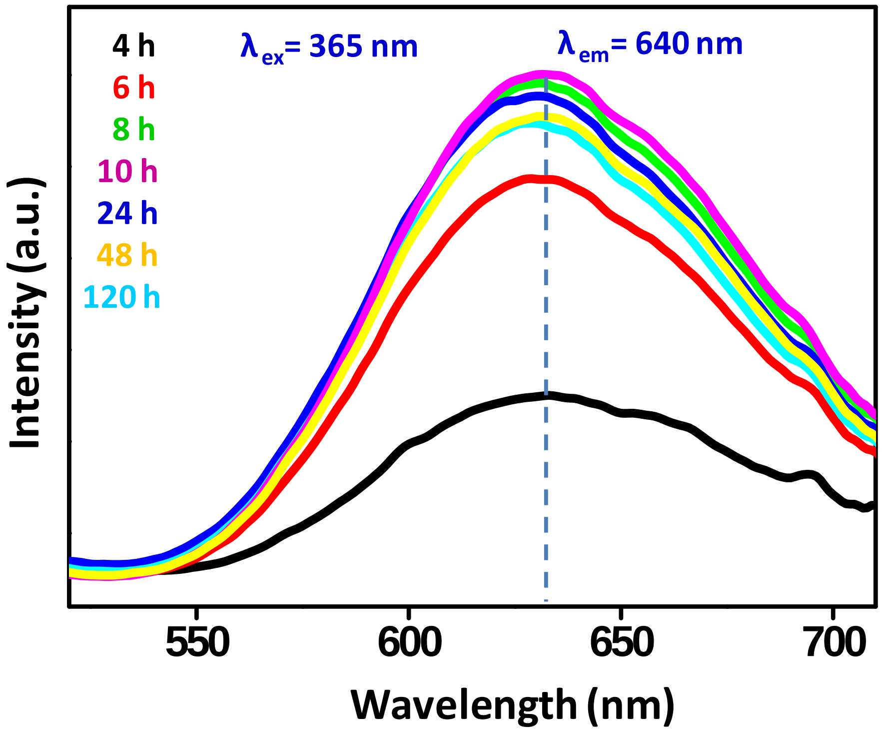

Fig. S4 Time dependent PL spectra during the synthesis of DFNS@Au$_{QC}$BSA. Luminescence started to appear after 4 h of the reaction and PL spectrum has taken up to 5 days. The emission maximum was found ~640 nm when excited at 365 nm.

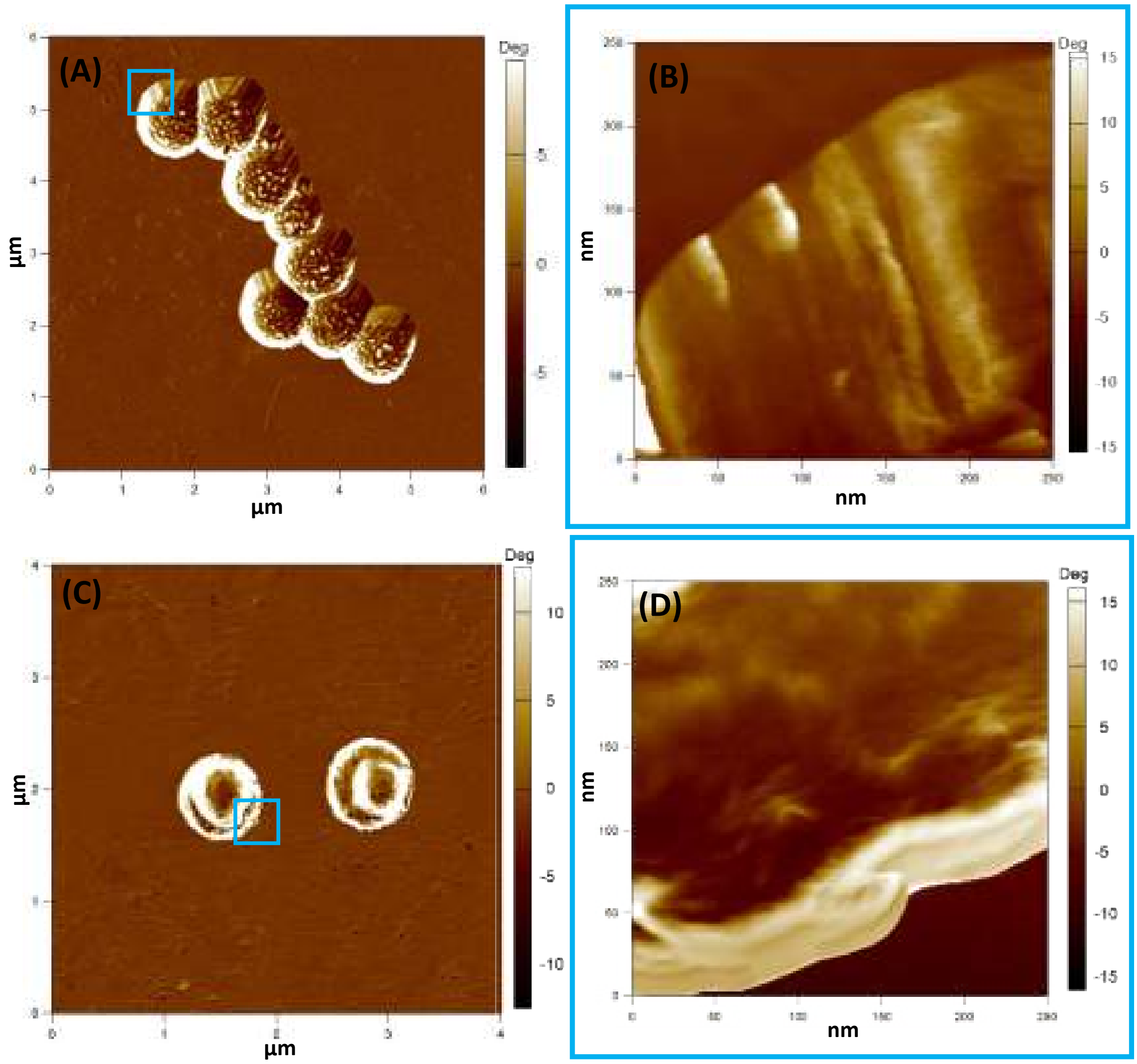

Fig. S5 AFM large area phase imaging of (A) DFNS and (C) DFNS@Au$_{QC}$BSA. The regions marked in the A and C are shown in image B and D, respectively. The high resolution image D (DFNS@Au$_{QC}$BSA), showing the clear contrast and morphological difference than the DFNS.

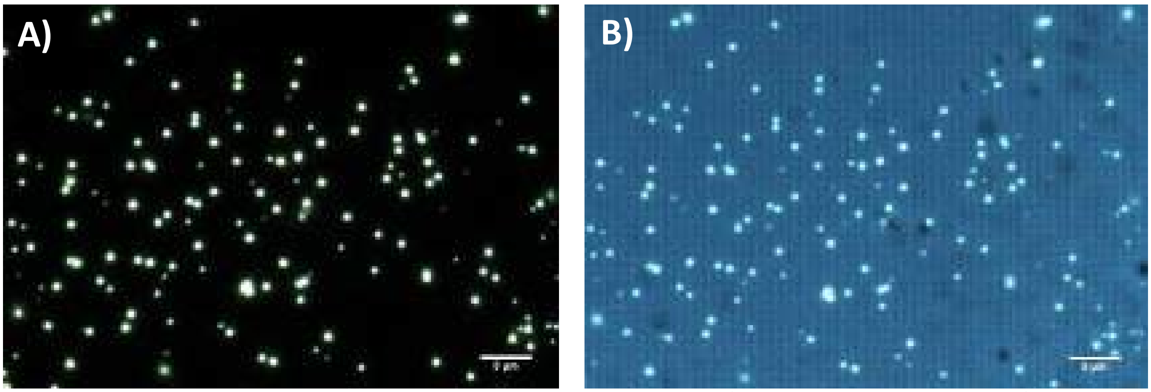

Fig. S6 A large area optical (A) and the corresponding fluorescence images of the parent DFNS (B). Scale bars in A and B are 5 μm.

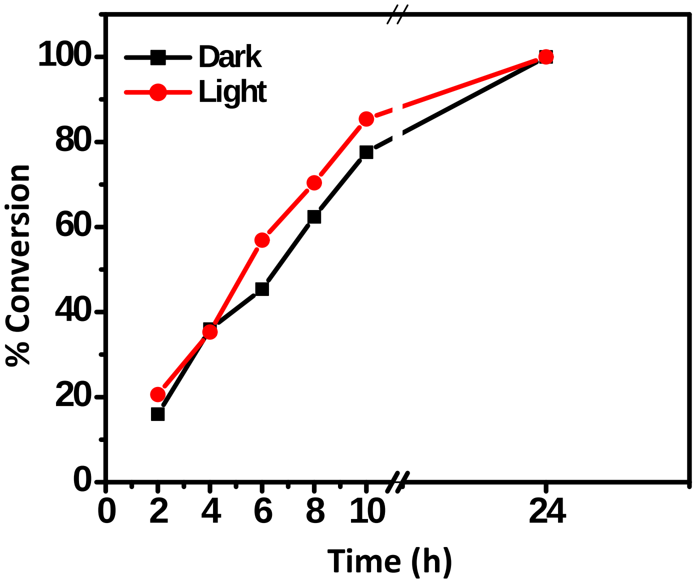

Fig. S7 The effect of light on the conversion of dimethylphenylsilane to dimethylphenylsilanol at 45 °C. (Error in the catalytic measurements is ± 5%).

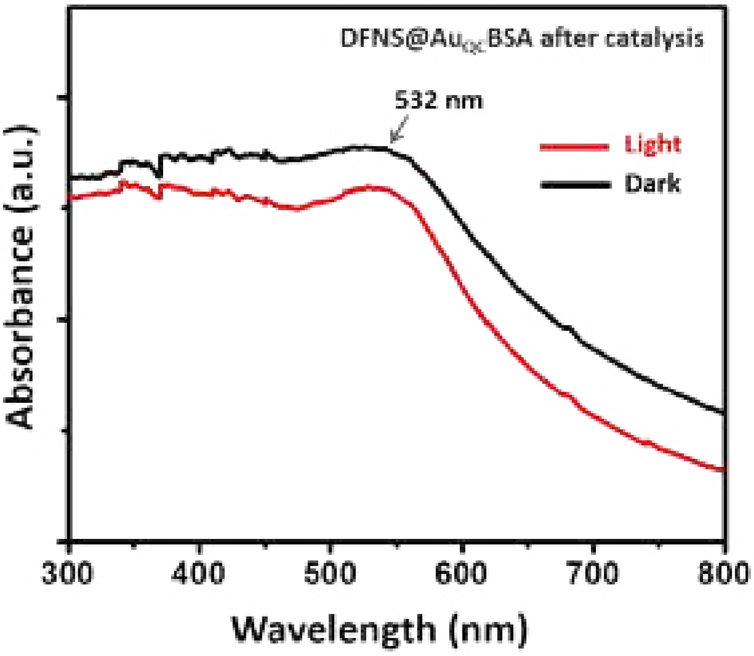

Fig. S8 UV-Vis absorption spectra of DFNS@Au$_{QC}$BSA in presence (red trace) and absence (black trace) of light, after catalytic reaction showing the presence of plasmonic peak around 532 nm.

THE JOURNAL OF PHYSICAL CHEMISTRY C
A JOURNAL OF THE AMERICAN CHEMICAL SOCIETY

pubs.acs.org/JPCC Article

Transformation of Nanodiamonds to Onion-like Carbons by Ambient Electrospray Deposition

Deeksha Satyabola,[†] Tripti Ahuja,[†] Sandeep Bose, Biswajit Mondal, Pillalamarri Srikrishnarka, M. P. Kannan, B. K. Spoorthi, and Thalappil Pradeep*

Cite This: *J. Phys. Chem. C* 2021, 125, 10998−11006

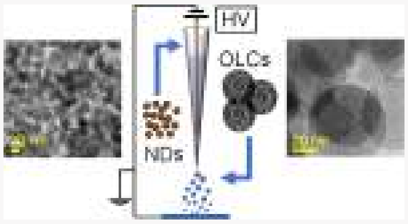

ABSTRACT: Onion-like carbons (OLCs) are a class of fullerene-like circular nanoallotropes of carbon, typically synthesized from nanodiamond (ND) *via* thermal annealing, plasma spraying, and laser ablation. These methods require high temperature, high vacuum, or inert gas. Here, we report an ambient electrospray deposition (AESD) process to transform NDs (11 ± 1 nm in size) into OLCs (50 ± 13 nm in size) in water. Transmission electron microscopy (TEM), field emission scanning electron microscopy (FESEM), Raman spectroscopy, and X-ray photoelectron spectroscopy (XPS) were used for the characterization of NDs and OLCs. High-resolution TEM images showed an increased interplanar spacing from ND (0.23 nm) to OLC (0.39 nm). Raman spectra showed a shift in the ND peak from 1336 cm^{-1} to D-band at 1349 cm^{-1}, and XPS quantitatively estimated an increase in the graphitization ratio (sp^2/sp^3) from 0.95 to 3.16 after AESD. Comparison of electrospray with sonic spray confirmed that such a transformation required an external voltage as well. AESD was also performed for NDs dispersed in ethanol and acetonitrile, which showed a solvent-dependent transformation.

1. INTRODUCTION

Carbon has always amazed scientists with its unique ability to form bonds of various kinds, and this property is distinctly different from other elements in the periodic table.[1,2] Due to this, several nanoallotropes of carbon have been identified since the discovery of fullerenes.[3−6] These nanoallotropes can be converted to each other accompanied by a change in their hybridization.[1,2] One such allotrope of carbon is nanodiamond (ND), also known as ultradispersed diamond (UDD). It has a core−shell-like architecture[2] with an sp^3 (diamond) core and sp^2 (graphitic) shells, surrounded by dangling bonds on the surface. NDs are transformed into sp^2-hybridized carbon called onion-like carbons (OLCs) by the process of graphitization. OLCs are multilayered fullerene-like carbon shells, also called carbon nano-onions (CNOs), or carbon onions (COs).[7,8] They have demonstrated their applicability in electrical double-layer capacitors[9] and high-performance supercapacitor electrodes[10] for energy storage due to high charge−discharge rates[9] and possess capacitance similar to carbon nanotubes. High conductivity and compatibility to form composites with other inorganic materials have made them ideal candidates for solar cell applications.[11] They have also been studied for biomedical imaging,[12] biochemical sensing,[13] and therapeutic nanocarriers[14] due to nontoxicity, suitability, and covalent functionalization with most naturally occurring biomolecules. Nitrogen-doped CNOs with gold[15] and copper[16] nanoparticles have enabled the formation of nanocomposite electrochemical sensors and efficient oxygen reduction electrocatalysts, respectively. COs have also been utilized for water treatment[17] because of their ability to absorb heavy metal ions.

Besides the applications of OLCs in capacitors, sensors, water treatment, and so forth, there have also been efforts to discover new methods for the synthesis of OLCs. The OLCs were synthesized initially using carbonaceous materials or amorphous carbon soot *via* heat treatment above 2500 K[18] and high-energy electron beam irradiation.[19] Both the precursors and methods used for the synthesis of OLCs have been modified over time.[20−28] ND, methane, propane, and aromatic compounds have been utilized to obtain various structures of OLCs ranging from spherical and polyhedral to hollow or those containing metal cores, through annealing,[20,21] chemical vapor deposition (CVD),[22] carbon ion implantation,[23] arc-discharge,[24] pyrolysis,[25,26] and so forth. Among all these methods and precursors, large quantities of OLCs have been synthesized from ND due to the ease of synthesis and availability.[7] The annealing of ND to OLCs introduced by Kuznetsov *et al.* requires a high temperature of 1273−1773 K and high vacuum.[20] Later, Gubarevich *et al.* introduced a plasma-spray method for the synthesis of OLCs from NDs, which required a current of 100 kA and arc discharge at ∼10

Received: January 8, 2021
Revised: April 27, 2021
Published: May 13, 2021

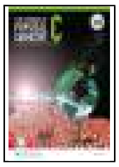

https://doi.org/10.1021/acs.jpcc.1c00166

kPa of argon.[27] The conversion of ND to a new diamond, through CO as the intermediate, accompanied by a high-temperature laser-induced transformation has also been reported.[28]

In this paper, we have introduced a simple technique called ambient electrospray deposition (AESD) for the transformation of ND to OLC at room temperature and atmospheric pressure. AESD is a subset of electrospray ionization (ESI) that has immense applications in mass spectrometry (MS).[29] AESD has been proved to be a promising technique for the synthesis of functional nanomaterials as well.[30−32] Li *et al.* have used ESI for the synthesis of silver and gold nanoparticles[30] and showed an improved catalytic activity by their use in the reduction of *p*-nitrophenol. Our group has also reported the formation of metallic nanobrushes of silver[31] and distinct phases of Cu_2S[32] using AESD.

Our method of transformation of ND to OLC involves two steps: (1) ES of ND suspension and (2) soft-landing/deposition of the product on a conducting surface. ND before ES and the transformed product (OLC) after ES were thoroughly characterized by transmission electron microscopy (TEM), field emission scanning electron microscopy (FESEM), Raman spectroscopy, and X-ray photoelectron spectroscopy (XPS). To understand the mechanism of transformation of NDs to OLCs, a comparative study of ES and sonic spray (SS) was performed. While SS leads to graphitization of ND as in ES, the final nanoallotrope obtained using SS differed from OLCs. This proved that an external voltage is necessary and is essential to produce OLCs at ambient temperature and atmospheric pressure. Additional parameters that distinguish ES from SS such as the presence of charge and electric field at the spray tip and Laplace pressure on the droplet were also evaluated. Furthermore, we changed the solvent from water to acetonitrile (MeCN) and ethanol (EtOH) to understand the effect of the solvent on graphitization. Transformation of ND to OLCs was facile in water as compared to MeCN and EtOH. Factors such as dielectric constant and surface tension vary in different solvents, which affect ES and play a significant role in the transformation.[33−36] Additionally, understanding the interactions between ND and solvent molecules is also required. Such an interaction has been studied in detail by Holt *et al.*[37] between ND and EtOH vapors. They have mentioned a possibility of hydrogen bonding between the polar functionalities on ND and EtOH molecules, which may stabilize the surface of ND. Other attempts to understand the interaction and solubility of ND are also known by dissolving it in various polar and nonpolar solvents.[38] All of them are known to stabilize the ND particles and form dispersions, ascertaining that the interactions between adjacent ND particles[39] and with the solvent[38] molecules are pertinent to understand the transformation.

2. MATERIALS AND EXPERIMENTAL METHODS

2.1. Materials. ND powder, ≥97% purity, was purchased from Sigma-Aldrich. Borosilicate glass capillaries (outer and inner diameters of 1.5 and 0.86 mm, respectively) were prepared with a tip diameter of 30−45 μm (determined using an optical microscope) to form a nanospray emitter using a micropipette puller (P-97), Sutter instrument, USA. Indium tin oxide (ITO) glass slides were purchased from Zhuhai Kaivo Electronic Optoelectronics Technology Co., Ltd. Other reagents such as MeCN and EtOH were of analytical grade and used without further purification. Deionized (DI) water (~18.2 MΩ) obtained from Milli-Q was used throughout the experiments.

2.2. Preparation of ND Suspension and Substrates for Characterization. ND (1.5 mg) was dissolved in DI water (1 mL) to obtain a 125 mM stock suspension. Concentration was evaluated in terms of the C content present. It was mixed thoroughly on a SPINIX vortex shaker for 3 min and successively diluted to prepare a 1.25 mM ND suspension. The diluted suspension (1.25 mM) of ND was used for ES and SS because low concentrations are most suitable in nanoESI.[36] Similarly, ND suspension (1.25 mM) was prepared in MeCN and EtOH to examine the effect of solvents on the transformation of ND. The suspension was electrosprayed on the carbon-coated copper grid by placing it on top of an ITO glass slide (22 mm × 22 mm × 1.1 mm) for HRTEM analysis. The same copper grid was fixed on a conducting carbon tape and used for FESEM analysis. The electrosprayed ITO glass slide was used directly for Raman and XPS characterization.

2.3. Instrumentation. TEM and HRTEM measurements of ND, before and after ES, were performed using a JEOL3010 at an accelerating voltage of 200 kV. FESEM measurements were performed using a Thermo scientific Verios G4 UC having a retractable detector. Confocal Raman imaging of ND, before and after ES, was performed on a WITec alpha300 S with a frequency-doubled Nd:YAG laser at 532 nm with 10 mW laser power, 2 s acquisition time, and 20 accumulations. To identify the chemical oxidation states and for quantitative estimation of ND and OLC, XPS was performed with an electron spectroscopy for chemical analysis (ESCA) probe temperature-programmed desorption (TPD) spectrometer of Omicron Nanotechnology with a polychromatic Al Kα ($h\nu$ = 1486.6 eV) source having a step size of 0.08 eV. The binding energies (BEs) of all the elements were calibrated with respect to C 1s at 284.8 eV. The percentage of peak area was calculated by taking the relative sensitivity factor (RSF) of carbon as unity.

2.4. Ambient Electrospray Deposition (AESD) Setup. The AESD setup (Figure 1) used for ES was composed of an

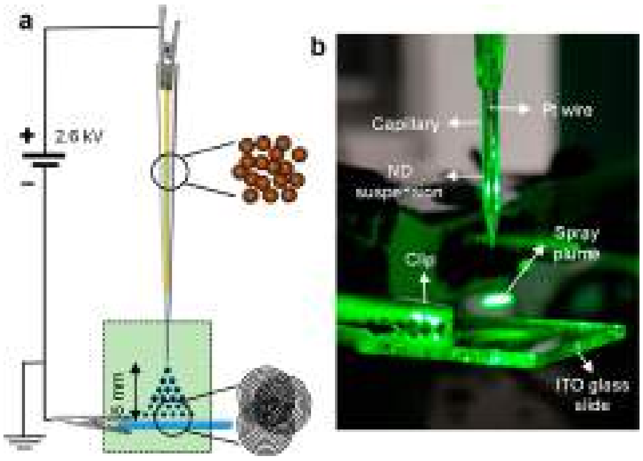

Figure 1. (a) Schematic representation of the AESD setup. (b) Magnified optical image of the rectangular area in (a) shows the spray plume soft-landing on the ITO glass slide. The spray plume in (b) was visualized with a laser.

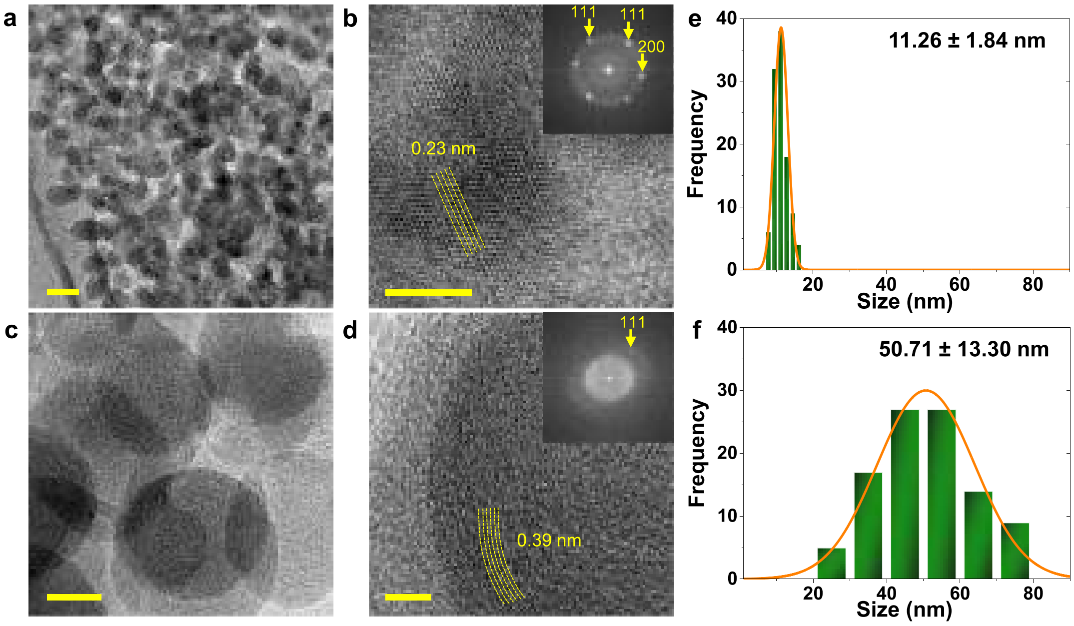

Figure 2. TEM and HRTEM images of NDs (a,b) depicting a lattice spacing of 0.23 nm, and OLCs (c,d) obtained after ES with a lattice spacing of 0.39 nm. Insets of (b,d) show the corresponding FFT images. Particle size distribution gives a mean size of (e) 11.26 ± 1.84 nm for ND and (f) 50.71 ± 13.30 nm for OLC. The scale bars in (a,c) are 20 nm and (b,d) are 5 nm.

external voltage source supplied by a variable DC power supply and a nanospray assembly. The nanospray assembly was made of a nanoESI capillary, platinum (Pt) wire (0.2 mm in diameter), and ITO glass slide. The Pt wire was inserted in a borosilicate capillary already filled with the ND suspension using a microinjector pipette tip. The distance between the capillary tip to the ITO glass slide was 8 mm. The assembly was supported by a clamp and stand to keep it stable and firm. The positive terminal of the voltage source was connected to the Pt wire, and the negative terminal was connected to the ITO glass slide, which was grounded. It was found that ES was possible only in the positive mode. Therefore, the same was followed throughout all the experiments. The applied voltage and time required to collect 20 μL of the sample in the spray plume were 2.6 kV and 1 h, respectively. The potential and tip to capillary distance were optimized as described by Jana *et al.*[32]

2.5. Sonic Spray (SS) Setup. The SS setup (Figure S5) was composed of a N_2 gas cylinder connected sideways to a T-connector, a fused silica capillary (inner and outer diameters were 150 and 300 μm, respectively) connected from the top of the T-connector, and a vial (1.5 mL) that collects the SS. ND suspension (1.25 mM) was loaded in a 500 μL Hamilton syringe connected with the silica capillary using a union connector and placed on the syringe pump. The syringe pump continuously infused the ND suspension at a constant flow rate of 5 μL min^{-1}, which generated uncharged microdroplets on contact with high-pressure N_2. These microdroplets were collected for 3 h in the vial and later diluted with 50 μL of DI water for TEM and Raman. Subsequently, the SS was performed at different pressures (5, 10, and 15 psi) to optimize the pressure-induced graphitization.

3. RESULTS AND DISCUSSION

3.1. Transformation of NDs to OLCs Using AESD. In AESD, a nanoESI capillary containing ND suspension (1.25 mM) was connected to the positive terminal of an external voltage source (2.6 kV) (Figure 1a). As a result, a positive charge was accumulated on the ES plume of ND, which was soft-landed on a negatively charged counterelectrode, an ITO glass slide. This region is marked by a rectangle in Figure 1a. This is shown as an optical image in Figure 1b.

3.2. Characterization of ND before and after ES. TEM images of NDs before and after ES are shown in Figure 2a−d. The ND particles are spherical and highly aggregated (Figure 2a). The aggregation of NDs was attributed to the Coulombic interaction among the surface functionalities of adjacent particles.[39] NDs showed the characteristic diamond lattice (Figure 2b) with a lattice spacing of 0.23 nm due to the (111) plane, comparable to that of diamond (0.21 nm). The product of ES shown in Figure 2c,d was characterized as unique onion-like concentric circular structures called OLCs. Unlike ND, the OLCs are large and composed of concentric circular rings. The increase in the size of OLCs is evident by the respective particle size distribution of ND and OLCs shown in Figure 2e,f. The average particle size of ND was 11.26 ± 1.84 nm, which increased to 50.71 ± 13.30 nm in OLCs (Figure 2e,f). The HRTEM image of OLCs (Figure 2d) showed a lattice spacing of 0.39 nm. This lattice spacing of OLCs varied from 0.33 to 0.35 nm.[20,27,28] Such a variation is attributed to the different synthetic protocols followed for this work compared to the other conventional routes. The majority of OLCs obtained by ES are overlapped with others or are deformed slightly along the periphery on account of their soft-landing process on the ITO surface (Figure 2c). It was difficult to discern individual rings inside the OLCs most of the time; however, the concentric circular nature was noticeable in the HRTEM image (Figure 2d). The FFT images of NDs and OLCs are shown as insets in Figure 2b,d, indicating the prominent planes in each. The FFT of ND shows three pairs of bright spots indicating its crystalline nature, and OLCs show a concentric ring pattern that represents the multilayered fullerene-like carbon shells as described by Isabel *et al.*[40] Moreover, some of the FFT images of OLCs had two intense

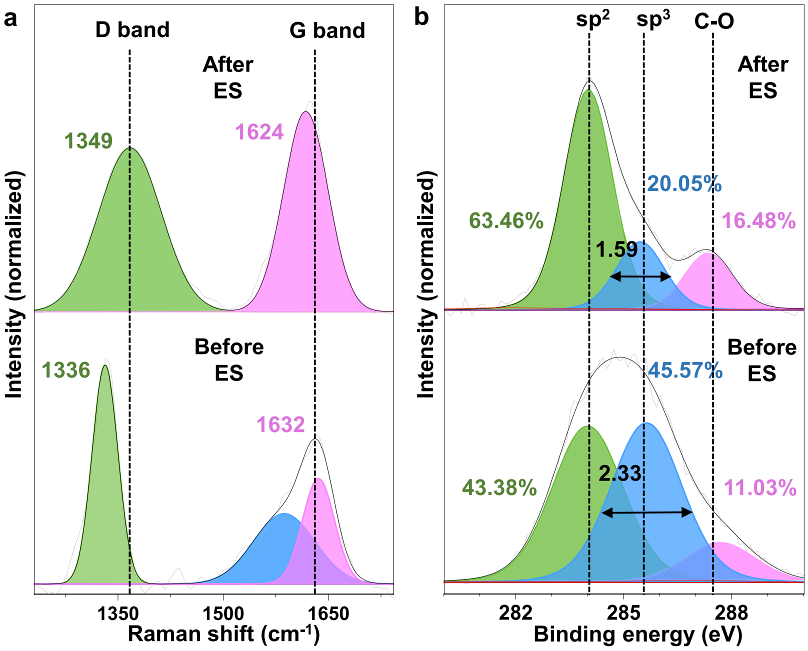

Figure 3. Stacked Raman spectra (a) showcasing shift in the ND peak at 1336 cm^{-1} (before ES) to a broad D-band (green) at 1349 cm^{-1} (after ES), graphitic sp^2-C peak at 1632 cm^{-1} also got shifted to the G-band (pink) at 1624 cm^{-1}. Stacked C 1s core-level XPS spectra (b) of drop-casted ND (before ES) and OLCs (after ES) provide the percentages of sp^2-C (green), sp^3-C (blue), and C−O bound C (pink). The as-obtained and fitted spectra are represented by gray and black curves, respectively.

spots (not shown here), which correspond to parallel layers characteristic of graphitic structures. Such a discrepancy was attributed to the presence of sp^2-graphitic cover over ND. This was because the spray conditions were not adequate to convert all NDs into OLCs.

The transformation of ND to OLC took place over a considerable region. It is evident by the large-area TEM images of ND and OLC shown in Figure S1a,b.

We chose FESEM to see the morphological variations in ND before and after ES. The distinct morphology and surface structure of ND and OLCs were difficult to perceive; nonetheless, the transformation from highly agglomerated ND particles (Figure S2a) to overlapping OLCs (Figure S2b) was seemingly evident. OLCs were observed distinctly due to their large size in contrast to ND particles; the average size of OLCs was 33−46 nm (Figure S2b).

The applicability of AESD to form OLCs at higher concentrations (5 mM of ND suspension) was also tested. Figure S3a−d shows the TEM and FESEM images of the product obtained upon ES of 5 mM aqueous suspension of ND, which also resembled OLCs. Close inspection of the TEM images revealed the concentric nature of the OLCs, similar to other concentrations (Figure S3a,b). The size of OLCs varied in a wide range from 31 to 50 nm as evident by the FESEM images (Figure S3c,d).

Besides monitoring the effect of concentration on the transformation, it is equally important to know the formation of the same product on different substrates after ES. To show that ES on the ITO glass slide and carbon-coated copper grid resulted in the same product, the deposited product on the ITO glass slide was removed by scratching; then, the resulting product was dissolved in 50 μL of DI water and drop-casted on a TEM grid. Respective TEM and HRTEM images of the product obtained upon direct ES on an ITO glass slide are shown in Figure S4a,b, respectively. These images also showed the formation of concentric circular rings, but they were slightly distorted which may be due to the scratching of the thin-layered product from the ITO surface. Thus, the transformation was substrate-independent, to a significant extent.

XRD measurements of ND and OLC are important for easy visualization of the change in the lattice structure of ND upon transformation to OLC. The OLCs were deposited as a thin film after ES on the ITO glass slide, and the signals obtained were weak with intense background due to ITO. Therefore, we moved to alternative techniques such as Raman spectroscopy and XPS.

ND is a suitable Raman analyte that possesses distinct vibrational features. However, its photoluminescence nature creates a huge rise in the background of the Raman spectrum. The background associated with the vibrational features of ND can be reduced by decreasing the wavelength of the excitation laser employed because the lower wavelength such as 230 nm matches with the band gap (5.4 eV) of ND.[41] As the excitation laser (532 nm) has a wavelength higher than 230 nm, the background in the Raman spectrum was corrected using suitable baseline correction. The spectra were normalized, and peaks were fitted thereafter. Figure 3a shows the stacked Raman spectra of ND before and after ES. In Raman spectra, peak position and full width at half-maximum (fwhm) (Figure 3a) provide useful information pertaining to the change in the hybridization of ND (sp^3) to OLCs (sp^2). Before ES, ND shows an intense and sharp peak at 1336 cm^{-1} with 43 cm^{-1} fwhm value due to the presence of a cubic lattice of sp^3-diamond in the ND core. It also showed a broad peak in the region of 1580−1650 cm^{-1}, which was fitted with a combination of two peaks (103 and 54 cm^{-1} fwhm) and corresponds to the G-band of the graphitic shell surrounding the ND core, specifically the in-plane stretching vibration of the sp^2 C−C bonds. The broadness of the G-band is also

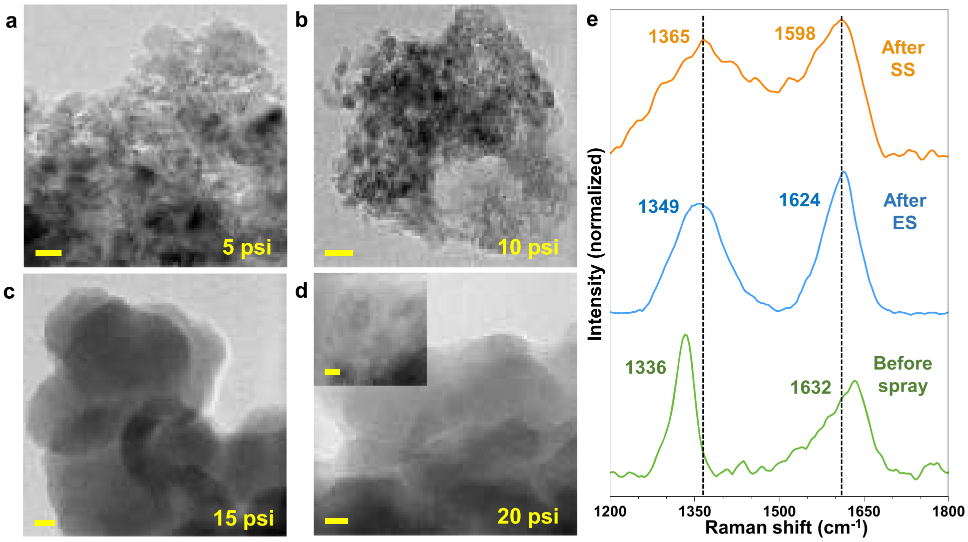

Figure 4. TEM images (a−d) of the product obtained after SS at 5, 10, 15, and 20 psi. The inset of (d) shows its HRTEM image. Comparative Raman spectra (e) showing shifts in the peak positions before spray (green), after ES at 2.6 kV (blue), and after SS at 20 psi (orange). The scale bar in (a−d) is 20 nm each [inset of (d) is 5 nm].

attributed to the presence of several other functionalities[42] on the surface, such as ν(C═C), δ(O−H), mixed sp^2−sp^3 carbon, and some defects appearing on its surface. After ES, the sharp ND peak at 1336 cm^{-1} (43 cm^{-1} fwhm) is blue-shifted to a broader peak at 1349 cm^{-1} (105 cm^{-1} fwhm). The latter was assigned to the D-band of disordered sp^2-C over ND. Another sp^2-C peak appears at 1632 cm^{-1} (before ES), which was fitted with two peaks at 1586 cm^{-1} (103 cm^{-1} fwhm) and 1636 cm^{-1} (54 cm^{-1} fwhm), showed a red shift to a relatively sharp and single G-band around 1624 cm^{-1} (75 cm^{-1} fwhm) after ES, corroborated with the literature.[42−44] In conventional annealing methods, fwhm values of the diamond feature and that of the G-band increase up to 600 °C and decrease subsequently with a further increase in temperature.[43] In ES, the fwhm of the diamond peak increased and that of the G-band decreased after ES. Compared to detonated (~40 cm^{-1}) or annealed ND, electrosprayed ND (105 cm^{-1}) showed a large increase in fwhm. The physical reason behind the variation of fwhm values in detonation and annealed ND is due to the phonon confinement effect as explained by Mermoux *et al.*[42] The detailed reason behind the large increase in fwhm after ES is yet to be understood. A table showing a comparison of observed Raman peaks with the authentic OLCs from the literature[7] is mentioned in Supporting Information, Table S1.

It was difficult to convert all the ND suspension into OLCs because the spray conditions governed the overall transformation. Therefore, a better approach to estimate the amount of ND transformed to OLC was using XPS. It can evaluate the amount of OLCs formed based on the percentage of C transformed from sp^3 to sp^2. Quantification of sp^2-C was achieved by performing high-resolution XPS of ND before and after ES. High-resolution spectra were fitted using Shirley background with an equal fwhm for all peaks. Figure 3b shows the C 1s core-level XPS spectra of the NDs (before ES) and OLCs (after ES). The sp^2- and sp^3-hybridized C appear at binding energies of 284 and 285.5 eV, respectively. The surface of ND also contains oxygen-bound functionalities that are represented by the C−O peak at 287.5 eV. The fwhm of the C 1s peak was 2.33 eV in ND and 1.59 eV in OLC. The peaks were in good agreement with the existing literature and showed a decrease in the fwhm values from ND to OLC, and such a difference is attributed to intrinsic charge discrepancy.[45] The area under each deconvoluted C1s peaks yields the percentage of sp^2-C, sp^3-C, and C−O. In the transformation of NDs to OLCs, the proportion of sp^2-C has increased by 20% with a simultaneous decrease in sp^3-C. The sp^2/sp^3 ratio has increased from 0.95 in ND to 3.16 in OLCs (calculation S1, sp^2/sp^3 ratio), confirming the formation of OLCs.

3.3. Comparison between ES and SS of ND.

To understand the mechanism and the parameters essential for the transformation, we performed an SS experiment, which was devoid of an external voltage. The schematic of the sonic spray setup is shown in Figure S5. A Hamilton syringe containing ND suspension (1.25 mM) was discharged *via* a silica capillary at a flow rate of 5 μL min^{-1} using a syringe pump. N$_2$ gas was maintained at 20 psi, which generated microdroplets of ND suspension, a phenomenon similar[46] to that of ES.

Figure 4a−d shows the TEM images of the product of SS obtained at varied pressures from 5 to 20 psi. Fine aerosol droplets were obtained in the spray in this range. Most of the ND particles remain unmodified at 5 and 10 psi (Figure 4a,b), but with an increase in pressure to 15 and 20 psi (Figure 4c,d), transformation resulted in mild graphitization in ND. The nanostructures obtained using SS were different in morphology from the OLCs obtained by ES. The structure, shape, and size of the product of SS were highly distorted and imperfect, compared to the symmetrical and circular OLCs obtained through ES.

To confirm the graphitization in SS, Raman spectral analysis was performed. Figure 4e shows stacked Raman spectra of ND, before spray, after ES, and after SS. The ND peak before spray at 1336 cm^{-1} was broadened and shifted to 1365 cm^{-1} upon SS by 29 cm^{-1}, compared to a shift of 16 cm^{-1} on ES. This shift was attributed to the D-band of graphite in both ES and SS. Similarly, the peak at 1632 cm^{-1} was blue-shifted to 1598 cm^{-1}, which corresponds to the G-band of C after SS. The fwhm of the diamond peak in SS also increased to 184.94 cm^{-1}, compared to 105.05 cm^{-1} in ES. These shifts confirmed the pressure-induced graphitization of ND in the SS. This comparison revealed that high pressure facilitates the process of graphitization. However, SS could not produce the OLCs of defined shape and morphology as obtained *via* AESD.

AESD and SS also differ in terms of the radius of the capillary tip used, which is crucial to consider as it decides the size of the droplet. The droplet size is smaller in AESD that employs the nano-ESI mechanism than SS that is based on ES, which may favor the transformation to OLCs in the former. To check that we electrosprayed the ND suspension with a fused-silica capillary (tip radius: 75 μm, three times larger than the borosilicate capillary used in nano-ESI). It was observed that concentric OLCs were formed, but most of them had irregular shapes which were fused to each other along the edges compared to separate OLCs produced using AESD (Figure S6). Thus, the transformation was weakly dependent on the droplet size. Therefore, we concluded that an SS experiment with voltage can also form OLCs.

It is difficult to study the mechanism of the transformation of the sp^3-hybridized diamond core in ND to sp^2-hybridised OLC, due to the inherently small size and high speed of the microdroplets formed during ES, which demands sophisticated high-speed cameras coupled with microscopy to capture the ultrafast plume in ES.[47] A comparison of ES with SS aided in accounting for the external factors responsible for the transformation of NDs to OLCs *via* AESD. The optimized parameters used in ES and SS are listed in Table 1.

Table 1. Parameters Used in ES and SS

parameter	ES	SS
voltage applied (kV)	2.6	N/A
charge on the droplet[29] (C)	$\sim 10-^{14}$	N/A
electric field (V m^{-1})	1.45×10^7	N/A
radius of the capillary tip (μm)	25	75
Laplace pressure (kPa)	5.8	2

Considering the importance of these parameters at 2.6 kV, the electric field[33] at the tip of the capillary was calculated as 1.45×10^7 V m^{-1} (calculation S2a, electric field at the capillary tip). Such a high electric field at the capillary tip is responsible for the generation of droplets by ES, with a charge[29] of $\sim 10^{-14}$ C. Furthermore, the droplet present on the curved surface of the capillary tip possesses an interfacial tension, which can be related to the pressure inside the droplets and radius of curvature of the capillary used. This pressure is termed as Laplace pressure and can be calculated at the capillary tip interface for ES and SS, using the relation mentioned by Lee *et al.*[48] (calculation S2b, Laplace pressure at the capillary tip). The Laplace pressure in the capillary was higher in ES compared to SS by 3.8 kPa, attributed to the smaller radius of curvature of the capillary used in ES. An increase of 3.8 kPa in ES was insignificant for rupturing the ND lattice. Thus, additional parameters such as the electric field also should play an important role. ES uses external voltage, which generates a high electric field, and charge on the droplet, unlike SS. This reaffirmed that the transformation to OLCs is highly dependent on the presence of charge and high electric field on the droplet at the capillary tip.

Besides the role of the Laplace pressure and electric field, several rearrangements in the bond can happen as the droplet is discharged from the capillary tip. The process of spray takes microseconds. Various other phase transformations are known[49−51] to happen at ultrafast and femtosecond time scales such as the nonthermal melting in Ge semiconductors,[49] superheating, and melting of bulk ice.[51] Since these phase transformations involve rearrangements in bonds; we suggest that the transformation of ND to OLC is facile on a short-time scale. However, the actual mechanism of such a transformation is still elusive. We may conclude that high Laplace pressure combined with the electric field and charge on the droplets facilitates the conversion in ES.

3.4. Effect of Solvents on the Formation of OLCs *via* AESD.

ES is highly dependent on the physical and chemical properties of the solvent such as polarity, dielectric constant (ε), and surface tension (γ).[29,36] To understand the effect of these properties of the solvent on the conversion of ND to OLCs, we performed the ES in MeCN and EtOH in addition to DI water. The parameters of ES, namely, capillary-tip to ITO distance, the concentration of ND suspension, and duration of spray, were kept constant throughout the ES performed with various solvents. MeCN and EtOH showed a liquid jet spray at 2.6 kV due to which the external voltage was reduced to 1.4 kV to get a proper spray plume. This is because MeCN and EtOH have low surface tension, which allowed the formation of a Taylor cone at a lower voltage compared to DI water.[34] The properties which affect the ES in solvents are presented in Table 2.

Table 2. Factors Affecting ES in DI Water, MeCN, and EtOH

solvent	polarity	ε (F/m)	γ (dyne/cm)	V (kV)	conversion
DI water	1	78.54	72.00	2.6	high
MeCN	0.46	36.64	28.40	1.4	low
EtOH	0.65	24.60	22.10	1.4	low

The transformation was found to be most favorable with DI water in the regime of parameters used. The high dielectric constant and polarity of water are known to stabilize the high charge states and multiply charged species more efficiently.[29] On the other hand, high surface tension of water makes it difficult to release the spray in the form of a stable, gentle spray plume at a lower voltage.[34] Since external voltage is an important criterion for the formation of OLCs as inferred by the comparison of ES and SS, a high voltage must have facilitated the conversion to OLCs better in water compared to MeCN and EtOH. Thus, the overall effect led to the transformation of ND particles in DI water more efficiently than in the other two solvents.

Figure 5a,b shows the TEM images of ND before and after ES, respectively, in MeCN. Similar to DI water, the extremely aggregated nature of ND particles was retained in MeCN. The average size of ND particles in MeCN also stayed the same, which is apparent from Figure 5a. After ES, mild graphitization was seen, but no OLCs were observed (Figure 5b) and large amounts of ND particles stayed unmodified. Corresponding Raman spectra corroborated the TEM results (Figure 5e). The sharp peak at 1335 cm^{-1} before ES in MeCN was shifted slightly to a higher wavenumber at 1339 cm^{-1} after ES. As the change was within the instrumental resolution (4 cm^{-1}), it was concluded that the ND was affected negligibly after ES in MeCN. The G-band of ND in MeCN at 1642 cm^{-1} on the other hand was slightly red-shifted at 1639 cm^{-1} after ES, but it lies in the same 1580−1650 cm^{-1} region.

Figure 5c,d shows the TEM images of ND dissolved in EtOH before and after ES. In this case also, graphitization was observed after ES (Figure 5d), but most of the ND particles

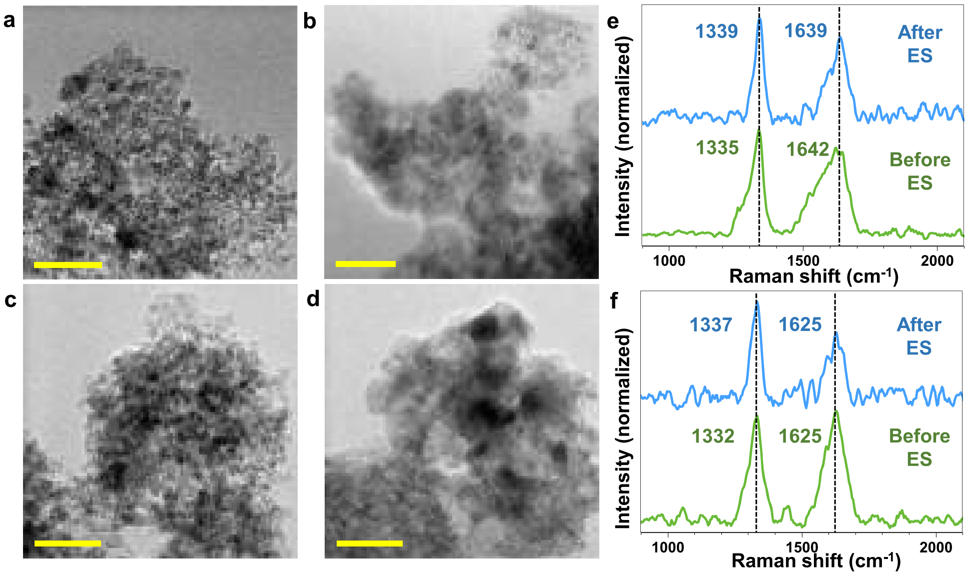

Figure 5. TEM images of ND dissolved in MeCN (a,b) and EtOH (c,d) before and after ES, respectively. Stacked Raman spectra of ND dissolved in MeCN (e) and EtOH (f) before (green) and after (blue) ES. The scale bars in (a−d) are 50 nm.

remain untransformed. Raman spectra of ND in EtOH before and after ES are shown in Figure 5f. The ND sp^3-C peak at 1332 cm^{-1} before ES got shifted to 1337 cm^{-1}, whereas the broad G-band at 1625 cm^{-1} stayed at the same position after ES. As mentioned earlier, the G-band is a contribution of several functionalities present on the ND surface. A major contribution to the G-band can arise due to hydrogen bonding of the polar surface functionalities on the ND surface with solvent molecules, due to which the Raman spectra of ND in MeCN and EtOH are significantly different.

The transformation of ND to OLCs in ES involves a complex mechanism as evident by the large increase in the size of OLCs in comparison to NDs. Such a complex mechanism may include transport reactions, which are stated as reactions in which a substance goes to a vapor state and comes back to the parent state in a pure form.[52] ND suspension can undergo a similar process by application of external voltage during AESD, which evaporates some of its particles to a gaseous state that can settle on the surface as OLCs. Although an in-depth computational study may reveal the exact mechanism behind the transformation, so far, a complete understanding of the mechanism is elusive.

We propose that the reaction mechanism for graphitization from sp^3-hybridized C can be triggered on the surface and proceed inward, resulting in OLCs. Understanding the interaction of ND with charged solvent species at the nanoscale can be a vital step in determining the pathway of transformation in ES. For instance, in the case of water as a solvent, it is possible that the positively charged suspension in the nanoESI capillary can provide an impetus for protonation of the surface functionalities, followed by their elimination.[53] This leads to the formation of a positive charge on the surface of ND. To compensate for the positive charge on the surface of ND, either a rearrangement or C═C bond formation from the neighboring carbon atoms may take place. A similar process happens at other locations on the surface of ND, which triggers graphitization on the surface, and this may proceed inward. A series of such events could lead to OLC formation.

4. CONCLUSIONS

In conclusion, we devised a methodology for the transformation of NDs to OLCs using AESD. TEM, FESEM, Raman, and XPS were used to characterize NDs and the ES-produced material. An increase in size and lattice spacing was observed in the TEM and HRTEM micrographs. Raman and XPS spectra showed the conversion of sp^3- to sp^2-hybridized carbon. The characteristic vibrational peak of the sp^3 core in ND was shifted from 1336 to the D-band at 1349 cm^{-1} with a decrease in intensity in the Raman spectra which showed that the transformation to OLCs occurred after ES. Although a complete mechanism behind the transformation of NDs to OLCs during AESD is difficult to comprehend at this stage, a comparison between ES and SS confirmed that high voltage is an essential condition for the generation of charged microdroplets to form OLCs. The application of high-pressure gas on SS led to graphitization; however, OLCs were not obtained. In addition, due to the dependency of ES on the type of solvent used, AESD was performed in three solvents, namely, DI water, MeCN, and EtOH. The high polarity and dielectric constant of DI water tend to easily stabilize various charged species formed during ES, but its high surface tension compared to the other two made the formation of the Taylor cone difficult. Consequently, the transformation of ND in DI water occurred more efficiently than MeCN and EtOH. In this way, AESD in its simple form has served as an efficient technique for the transformation of NDs to OLCs under ambient conditions, compared to the conventional methods that require high temperature and pressure. The current sp^2/sp^3 conversion ratio of NDs to OLCs (0.95−3.16) can be scaled up using a multispray technique. AESD also avoids the use of subsidiary gas spray such as ESI and can be used for the direct synthesis of electrode materials. This approach of transformation at ambient temperature and pressure will open new areas for creating novel functional nanomaterials.

■ ASSOCIATED CONTENT

Supporting Information

The Supporting Information is available free of charge at https://pubs.acs.org/doi/10.1021/acs.jpcc.1c00166.

> Large-area TEM and FESEM images of NDs and OLCs, TEM and FESEM images of OLCs from ES of 5 mM ND suspension, TEM images of the product obtained after ES on the ITO glass slide, schematic of SS setup, TEM images of OLCs obtained after ES using fused silica capillary, tabular comparison of Raman peaks of ND and OLC with the literature, calculation of the sp^2/sp^3 ratio, evaluation of the electric field, and Laplace pressure at the tip of the capillary (PDF)

■ AUTHOR INFORMATION

Corresponding Author

Thalappil Pradeep − *DST Unit on Nanoscience, Thematic Unit of Excellence, Department of Chemistry, Indian Institute of Technology Madras, 600 036 Chennai, India;* orcid.org/0000-0003-3174-534X; Phone: +91-044-2257-4208; Email: pradeep@iitm.ac.in

Authors

Deeksha Satyabola − *DST Unit on Nanoscience, Thematic Unit of Excellence, Department of Chemistry, Indian Institute of Technology Madras, 600 036 Chennai, India*

Tripti Ahuja − *DST Unit on Nanoscience, Thematic Unit of Excellence, Department of Chemistry, Indian Institute of Technology Madras, 600 036 Chennai, India*

Sandeep Bose − *DST Unit on Nanoscience, Thematic Unit of Excellence, Department of Chemistry, Indian Institute of Technology Madras, 600 036 Chennai, India*

Biswajit Mondal − *DST Unit on Nanoscience, Thematic Unit of Excellence, Department of Chemistry, Indian Institute of Technology Madras, 600 036 Chennai, India*

Pillalamarri Srikrishnarka − *DST Unit on Nanoscience, Thematic Unit of Excellence, Department of Chemistry, Indian Institute of Technology Madras, 600 036 Chennai, India;* orcid.org/0000-0001-5187-6879

M. P. Kannan − *DST Unit on Nanoscience, Thematic Unit of Excellence, Department of Chemistry, Indian Institute of Technology Madras, 600 036 Chennai, India*

B. K. Spoorthi − *DST Unit on Nanoscience, Thematic Unit of Excellence, Department of Chemistry, Indian Institute of Technology Madras, 600 036 Chennai, India*

Complete contact information is available at: https://pubs.acs.org/10.1021/acs.jpcc.1c00166

Author Contributions

†Equal contribution. D.S. and T.A. contributed equally to this work. T.P., D.S., and T.A. conceived the idea and designed the experiments. D.S., T.A., and B.K.S. performed the experiments and analyzed the data. S.B. offered advice on the SS experiment. B.M., P.S., and M.P.K. performed imaging. The manuscript was written with the contribution of all authors. All authors have approved the final version of the manuscript.

Notes

The authors declare no competing financial interest.

■ ACKNOWLEDGMENTS

We thank the Department of Science and Technology (DST), Government of India, for constantly supporting our research activities. D.S. acknowledges the Department of Chemistry, IIT Madras. T.A., S.B., B.M., and P.S. acknowledge the institute graduate fellowship. M.P.K. acknowledges MRF Ltd. B.K.S. acknowledges University Grants Commission (UGC) for her research fellowship.

■ REFERENCES

(1) Shenderova, O. A.; Zhirnov, V. V.; Brenner, D. W. Carbon Nanostructures. *Crit. Rev. Solid State Mater. Sci.* **2002**, *27*, 227−356.

(2) Georgakilas, V.; Perman, J. A.; Tucek, J.; Zboril, R. Broad Family of Carbon Nanoallotropes: Classification, Chemistry, and Applications of Fullerenes, Carbon Dots, Nanotubes, Graphene, Nanodiamonds, and Combined Superstructures. *Chem. Rev.* **2015**, *115*, 4744−4822.

(3) Kroto, H. W.; Heath, J. R.; O'Brien, S. C.; Curl, R. F.; Smalley, R. E. C60: Buckminsterfullerene. *Nature* **1985**, *318*, 162−163.

(4) Iijima, S. Helical Microtubules of Graphitic Carbon. *Nature* **1991**, *354*, 56−58.

(5) Novoselov, K. S.; Geim, A. K.; Morozov, S. V.; Jiang, D.; Zhang, Y.; Dubonos, S. V.; Grigorieva, I. V.; Firsov, A. A. Electric Field Effect in Atomically Thin Carbon Films. *Science* **2004**, *306*, 666−669.

(6) Ajayan, P. M. Nanotubes from Carbon. *Chem. Rev.* **1999**, *99*, 1787−1800.

(7) Zeiger, M.; Jäckel, N.; Mochalin, V. N.; Presser, V. Review: Carbon Onions for Electrochemical Energy Storage. *J. Mater. Chem. A* **2016**, *4*, 3172−3196.

(8) Mykhailiv, O.; Zubyk, H.; Plonska-Brzezinska, M. E. Carbon Nano-Onions: Unique Carbon Nanostructures with Fascinating Properties and Their Potential Applications. *Inorg. Chim. Acta.* **2017**, *468*, 49−66.

(9) Portet, C.; Yushin, G.; Gogotsi, Y. Electrochemical Performance of Carbon Onions, Nanodiamonds, Carbon Black and Multiwalled Nanotubes in Electrical Double Layer Capacitors. *Carbon* **2007**, *45*, 2511−2518.

(10) Borgohain, R.; Li, J.; Selegue, J. P.; Cheng, Y.-T. Electrochemical Study of Functionalized Carbon Nano-Onions for High-Performance Supercapacitor Electrodes. *J. Phys. Chem. C* **2012**, *116*, 15068−15075.

(11) Zheng, D.; Yang, G.; Zheng, Y.; Fan, P.; Ji, R.; Huang, J.; Zhang, W.; Yu, J. Carbon Nano-Onions as a Functional Dopant to Modify Hole Transporting Layers for Improving Stability and Performance of Planar Perovskite Solar Cells. *Electrochim. Acta* **2017**, *247*, 548−557.

(12) Ghosh, M.; Sonkar, S. K.; Saxena, M.; Sarkar, S. Carbon Nano-Onions for Imaging the Life Cycle of Drosophila Melanogaster. *Small* **2011**, *7*, 3170−3177.

(13) Sun, W.; Zhang, X.; Jia, H.-R.; Zhu, Y.-X.; Guo, Y.; Gao, G.; Li, Y.-H.; Wu, F.-G. Water-Dispersible Candle Soot−Derived Carbon Nano-Onion Clusters for Imaging-Guided Photothermal Cancer Therapy. *Small* **2019**, *15*, 1804575.

(14) Trusel, M.; Baldrighi, M.; Marotta, R.; Gatto, F.; Pesce, M.; Frasconi, M.; Catelani, T.; Papaleo, F.; Pompa, P. P.; Tonini, R.; et al. Internalization of Carbon Nano-Onions by Hippocampal Cells Preserves Neuronal Circuit Function and Recognition Memory. *ACS Appl. Mater. Interfaces* **2018**, *10*, 16952−16963.

(15) Sohouli, E.; Shahdost-Fard, F.; Rahimi-Nasrabadi, M.; Plonska-Brzezinska, M. E.; Ahmadi, F. Introducing a Novel Nanocomposite Consisting of Nitrogen-Doped Carbon Nano-Onions and Gold Nanoparticles for the Electrochemical Sensor to Measure Acetaminophen. *J. Electroanal. Chem.* **2020**, *871*, 114309.

(16) Shao, H.; Zhang, X.; Huang, H.; Zhang, K.; Wang, M.; Zhang, C.; Yang, Y.; Wen, M.; Zheng, W. Magnetron Sputtering Deposition Cu@Onion-like N-C as High-Performance Electrocatalysts for Oxygen Reduction Reaction. *ACS Appl. Mater. Interfaces* **2017**, *9*, 41945−41954.

(17) Porada, S.; Borchardt, L.; Oschatz, M.; Bryjak, M.; Atchison, J. S.; Keesman, K. J.; Kaskel, S.; Biesheuvel, P. M.; Presser, V. Direct Prediction of the Desalination Performance of Porous Carbon

Electrodes for Capacitive Deionization. *Energy Environ. Sci.* **2013**, *6*, 3700−3712.

(18) de Heer, W. A.; Ugarte, D. Carbon Onions Produced by Heat Treatment of Carbon Soot and Their Relation to the 217.5 Nm Interstellar Absorption Feature. *Chem. Phys. Lett.* **1993**, *207*, 480−486.

(19) Ugarte, D. Curling and Closure of Graphitic Networks under Electron-Beam Irradiation. *Nature* **1992**, *359*, 707−709.

(20) Kuznetsov, V. L.; Chuvilin, A. L.; Butenko, Y. V.; Mal'kov, I. Y.; Titov, V. M. Onion-like Carbon from Ultra-Disperse Diamond. *Chem. Phys. Lett.* **1994**, *222*, 343−348.

(21) Tomita, S.; Sakurai, T.; Ohta, H.; Fujii, M.; Hayashi, S. Structure and Electronic Properties of Carbon Onions. *J. Chem. Phys.* **2001**, *114*, 7477−7482.

(22) Chen, X. H.; Deng, F. M.; Wang, J. X.; Yang, H. S.; Wu, G. T.; Zhang, X. B.; Peng, J. C.; Li, W. Z. New Method of Carbon Onion Growth by Radio-Frequency Plasma-Enhanced Chemical Vapor Deposition. *Chem. Phys. Lett.* **2001**, *336*, 201−204.

(23) Cabioc'h, T.; Jaouen, M.; Thune, E.; Guérin, P.; Fayoux, C.; Denanot, M. F. Carbon Onions Formation by High-Dose Carbon Ion Implantation into Copper and Silver. *Surf. Coating. Technol.* **2000**, *128−129*, 43−50.

(24) Alexandrou, I.; Wang, H.; Sano, N.; Amaratunga, G. A. J. Structure of Carbon Onions and Nanotubes Formed by Arc in Liquids. *J. Chem. Phys.* **2004**, *120*, 1055−1058.

(25) Garcia-Martin, T.; Rincon-Arevalo, P.; Campos-Martin, G. Method to Obtain Carbon Nano-Onions by Pyrolisys of Propane. *Cent. Eur. J. Phys.* **2013**, *11*, 1548−1558.

(26) Choucair, M.; Stride, J. A. The Gram-Scale Synthesis of Carbon Onions. *Carbon* **2012**, *50*, 1109−1115.

(27) Gubarevich, A. V.; Kitamura, J.; Usuba, S.; Yokoi, H.; Kakudate, Y.; Odawara, O. Onion-like Carbon Deposition by Plasma Spraying of Nanodiamonds. *Carbon* **2003**, *41*, 2601−2606.

(28) Xiao, J.; Li, J. L.; Liu, P.; Yang, G. W. A New Phase Transformation Path from Nanodiamond to New-Diamond via an Intermediate Carbon Onion. *Nanoscale* **2014**, *6*, 15098−15106.

(29) Banerjee, S.; Mazumdar, S. Electrospray Ionization Mass Spectrometry: A Technique to Access the Information beyond the Molecular Weight of the Analyte. *Int. J. Anal. Chem.* **2012**, *2012*, 1−40.

(30) Li, A.; Luo, Q.; Park, S.-J.; Cooks, R. G. Synthesis and Catalytic Reactions of Nanoparticles Formed by Electrospray Ionization of Coinage Metals. *Angew. Chem., Int. Ed.* **2014**, *53*, 3147−3150.

(31) Sarkar, D.; Mahitha, M. K.; Som, A.; Li, A.; Wleklinski, M.; Cooks, R. G.; Pradeep, T. Metallic Nanobrushes Made Using Ambient Droplet Sprays. *Adv. Mater.* **2016**, *28*, 2223−2228.

(32) Jana, A.; Jana, S. K.; Sarkar, D.; Ahuja, T.; Basuri, P.; Mondal, B.; Bose, S.; Ghosh, J.; Pradeep, T. Electrospray Deposition-Induced Ambient Phase Transition in Copper Sulphide Nanostructures. *J. Mater. Chem. A* **2019**, *7*, 6387−6394.

(33) Kebarle, P.; Tang, L. From Ions in Solution to Ions in the Gas Phase - the Mechanism of Electrospray Mass Spectrometry. *Anal. Chem.* **1993**, *65*, 972A−986A.

(34) Chowdhury, S. K.; Chait, B. T. Method for the Electrospray Ionization of Highly Conductive Aqueous Solutions. *Anal. Chem.* **1991**, *63*, 1660−1664.

(35) Karas, M.; Bahr, U.; Dülcks, T. Nano-Electrospray Ionization Mass Spectrometry: Addressing Analytical Problems beyond Routine. *Fresenius. J. Anal. Chem.* **2000**, *366*, 669−676.

(36) Iavarone, A. T.; Jurchen, J. C.; Williams, E. R. Effects of Solvent on the Maximum Charge State and Charge State Distribution of Protein Ions Produced by Electrospray Ionization. *J. Am. Soc. Mass Spectrom.* **2000**, *11*, 976−985.

(37) Inel, G. A.; Ungureau, E.-M.; Varley, T. S.; Hirani, M.; Holt, K. B. Solvent-Surface Interactions between Nanodiamond and Ethanol Studied with in Situ Infrared Spectroscopy. *Diam. Relat. Mater.* **2016**, *61*, 7−13.

(38) Nunn, N.; Torelli, M.; McGuire, G.; Shenderova, O. Nanodiamond: A High Impact Nanomaterial. *Curr. Opin. Solid State Mater. Sci.* **2017**, *21*, 1−9.

(39) Pentecost, A.; Gour, S.; Mochalin, V.; Knoke, I.; Gogotsi, Y. Deaggregation of Nanodiamond Powders Using Salt- and Sugar-Assisted Milling. *ACS Appl. Mater. Interfaces* **2010**, *2*, 3289−3294.

(40) Israde-Alcántara, I.; Bischoff, J. L.; Domínguez-Vázquez, G.; Li, H. C.; DeCarli, P. S.; Bunch, T. E.; Wittke, J. H.; Weaver, J. C.; Firestone, R. B.; West, A.; et al. Evidence from Central Mexico Supporting the Younger Dryas Extraterrestrial Impact Hypothesis. *Proc. Natl. Acad. Sci. U. S. A.* **2012**, *109*, E738−E747.

(41) Mermoux, M.; Crisci, A.; Petit, T.; Girard, H. A.; Arnault, J.-C. Surface Modifications of Detonation Nanodiamonds Probed by Multiwavelength Raman Spectroscopy. *J. Phys. Chem. C* **2014**, *118*, 23415−23425.

(42) Mermoux, M.; Chang, S.; Girard, H. A.; Arnault, J.-C. Raman Spectroscopy Study of Detonation Nanodiamond. *Diam. Relat. Mater.* **2018**, *87*, 248−260.

(43) Cebik, J.; McDonough, J. K.; Peerally, F.; Medrano, R.; Neitzel, I.; Gogotsi, Y.; Osswald, S. Raman Spectroscopy Study of the Nanodiamond-to-Carbon Onion Transformation. *Nanotechnology* **2013**, *24*, 205703.

(44) Mykhaylyk, O. O.; Solonin, Y. M.; Batchelder, D. N.; Brydson, R. Transformation of Nanodiamond into Carbon Onions: A Comparative Study by High-Resolution Transmission Electron Microscopy, Electron Energy-Loss Spectroscopy, X-Ray Diffraction, Small-Angle x-Ray Scattering, and Ultraviolet Raman Spectroscopy. *J. Appl. Phys.* **2005**, *97*, 074302.

(45) Xie, F. Y.; Xie, W. G.; Gong, L.; Zhang, W. H.; Chen, S. H.; Zhang, Q. Z.; Chen, J. Surface Characterization on Graphitization of Nanodiamond Powder Annealed in Nitrogen Ambient. *Surf. Interface Anal.* **2010**, *42*, 1514−1518.

(46) Lee, J. K.; Samanta, D.; Nam, H. G.; Zare, R. N. Spontaneous Formation of Gold Nanostructures in Aqueous Microdroplets. *Nat. Commun.* **2018**, *9*, 1562.

(47) Kim, H.-H.; Kim, J.-H.; Ogata, A. Time-Resolved High-Speed Camera Observation of Electrospray. *J. Aerosol Sci.* **2011**, *42*, 249−263.

(48) Lee, S.; Kim, D. H.; Needham, D. Equilibrium and Dynamic Interfacial Tension Measurements at Microscopic Interfaces Using a Micropipet Technique. 1. A New Method for Determination of Interfacial Tension. *Langmuir* **2001**, *17*, 5537−5543.

(49) Siders, C. W.; Cavalleri, A.; Sokolowski-Tinten, K.; Tóth, C.; Guo, T.; Kammler, M.; von Hoegen, M. H.; Wilson, K. R.; von der Linde, D.; Barty, C. P. J. Detection of Nonthermal Melting by Ultrafast X-Ray Diffraction. *Science* **1999**, *286*, 1340−1342.

(50) Rousse, A.; Rischel, C.; Fourmaux, S.; Uschmann, I.; Sebban, S.; Grillon, G.; Balcou, P.; Förster, E.; Geindre, J. P.; Audebert, P.; et al. Non-Thermal Melting in Semiconductors Measured at Femtosecond Resolution. *Nature* **2001**, *410*, 65−68.

(51) Iglev, H.; Schmeisser, M.; Simeonidis, K.; Thaller, A.; Laubereau, A. Ultrafast Superheating and Melting of Bulk Ice. *Nature* **2006**, *439*, 183−186.

(52) Schäfer, H. Introduction and Historical Review. *Chem. Transp. React.* **1964**, *3*, 1−3.

(53) Banerjee, S.; Zare, R. N. Syntheses of Isoquinoline and Substituted Quinolines in Charged Microdroplets. *Angew. Chem.* **2015**, *127*, 15008−15012.

Supporting Information

Transformation of Nanodiamonds to Onion-like Carbons by Ambient Electrospray Deposition

Deeksha Satyabola,[#] *Tripti Ahuja,*[#] *Sandeep Bose, Biswajit Mondal, Pillalamarri Srikrishnarka, M. P. Kannan, B. K. Spoorthi, and Thalappil Pradeep**

DST Unit on Nanoscience, Thematic Unit of Excellence, Department of Chemistry, Indian Institute of Technology Madras, 600 036, Chennai, India

Phone: +91-044-2257-4208, Email: pradeep@iitm.ac.in

[#]Equal contribution

*Corresponding author

KEYWORDS: nanodiamond, onion-like carbon, ambient electrospray deposition, graphitization, sonic spray

Table of Contents

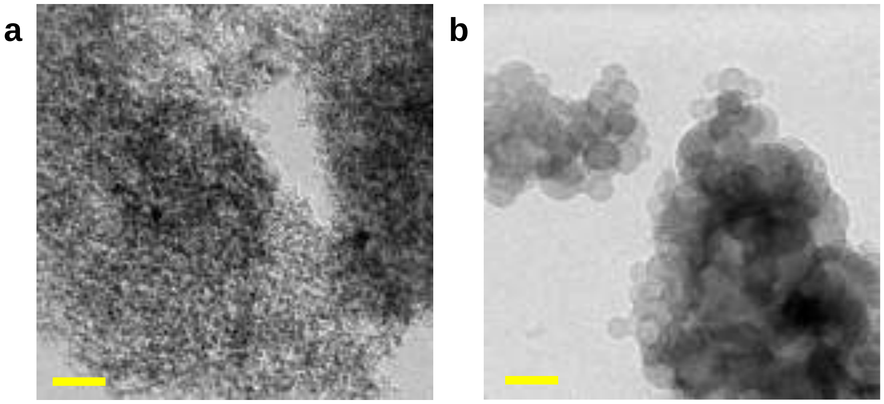

Figure S1. Large area TEM images of ND (1.25 mM aqueous suspension) (a) and OLCs (b) showing an increment in the size of ND upon transformation to OLCs after AESD at 2.6 kV. The scale bars in (a, b) are 100 nm.

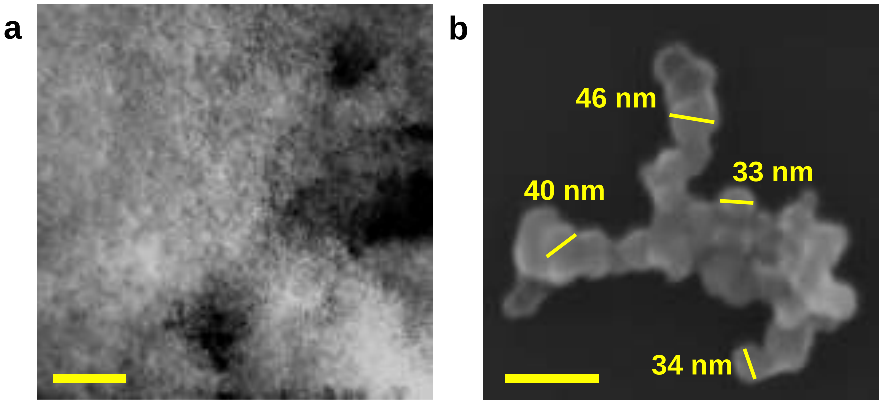

Figure S2. FESEM images of ND (1.25 mM aqueous suspension) (a) and OLCs (b). Size of OLCs varied from 33–46 nm. The scale bars in (a, b) are 100 nm.

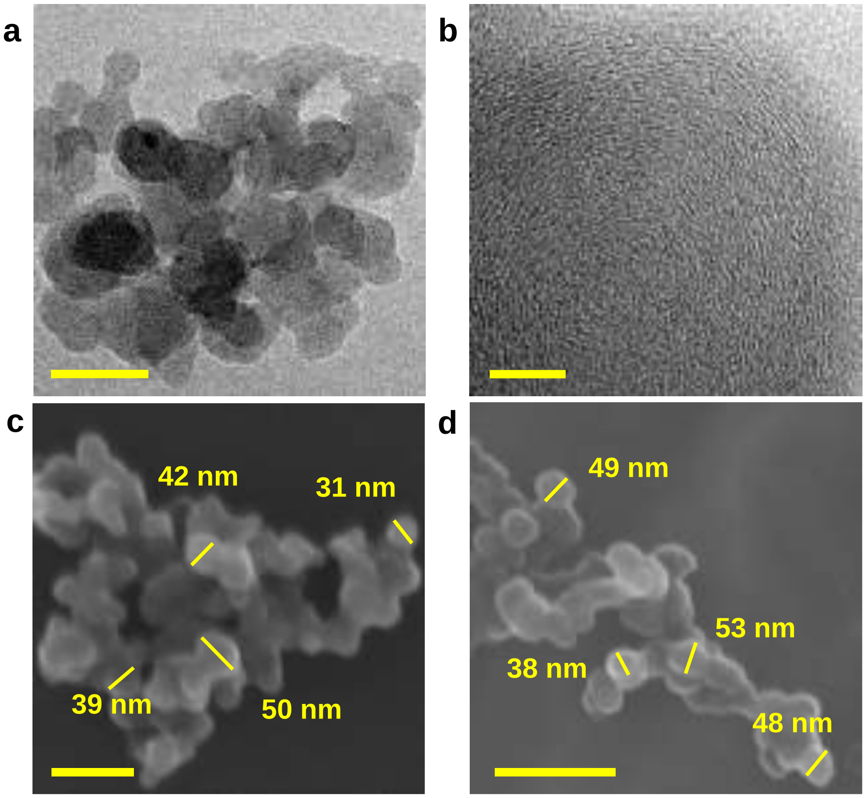

Figure S3. TEM images (a) HRTEM image (b), and FESEM images (c, d) of OLCs obtained after ES of 5 mM ND suspension in water. The scale bars in a, b, c, and d are 50, 5, 100, and 200 nm.

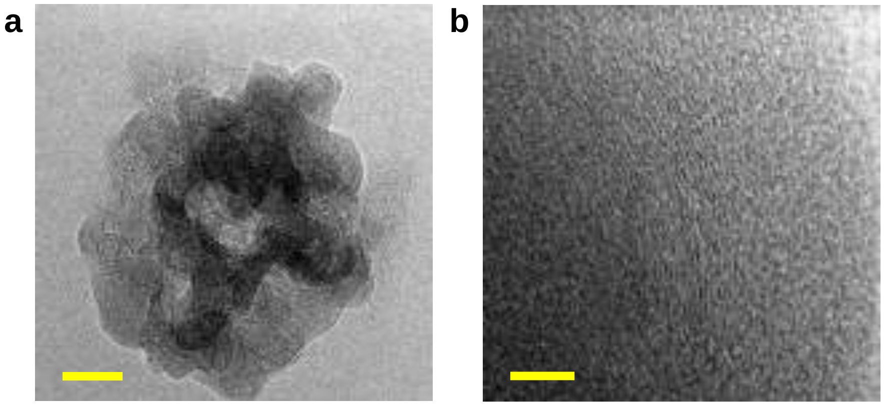

Figure S4. TEM images (a, b) of the product obtained after direct ES on ITO glass slide. The product was scratched from ITO, dissolved in DI water, and drop-casted on a TEM grid. The scale bars in (a) and (b) are 20 and 5 nm, respectively.

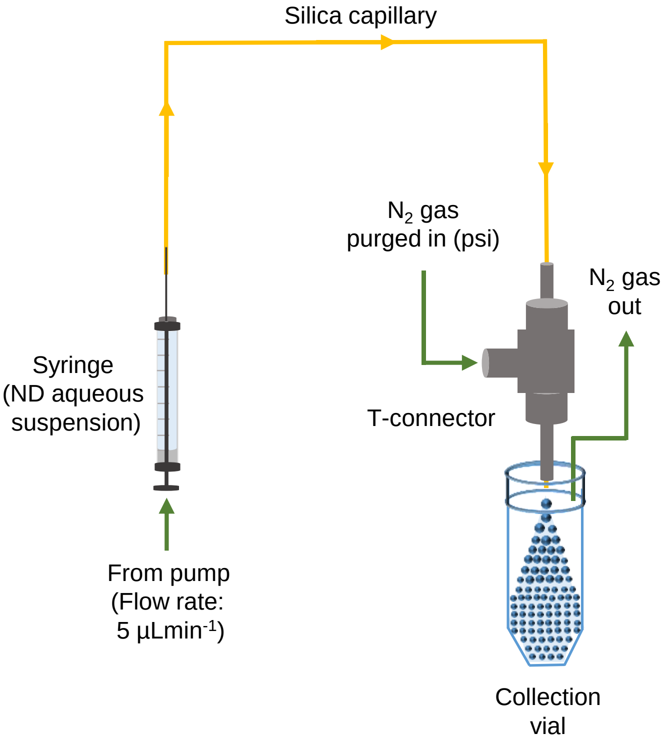

Figure S5. Schematic of the SS set-up.

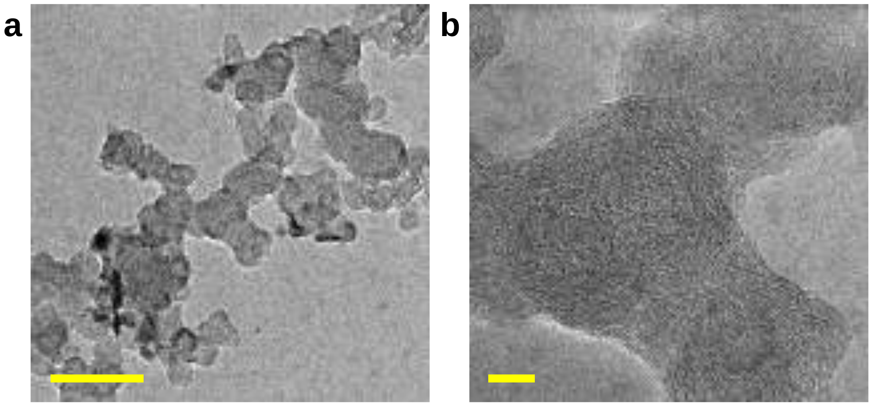

Figure S6. TEM images of OLCs obtained after ES using fused silica capillary. The scale bars in (a) and (b) are 100 and 10 nm.

Table S1. Comparison of the observed Raman peaks with literature[1]

Characteristic feature	Before ES (ND)		After ES (OLC)	
	Observed/ cm^{-1}	Literature/ cm^{-1}	Observed/ cm^{-1}	Literature/ cm^{-1}
D-band	1336	~1326	1349	~1343
G-band	1632	~1647	1624	~1585

Calculation S1. Calculation of increase in sp^2/sp^3 ratio in XPS after AESD

Description	Percentage of sp^2 and sp^3 content	
	Before ES (ND)	After ES (OLC)
sp^2	43.38	63.46
sp^3	45.57	20.05
sp^2/sp^3	0.95	3.16

Calculation S2.

S2a. Evaluation of electric field at the capillary-tip

The electric field at the tip of the capillary with inner radius, r_c (25 μm) placed at a distance, d (8 mm) from the ITO glass slide can be calculated using the relation described below, provided the applied voltage, V_c (2.6 kV) is known.[2]

$$E_c = \frac{V_c}{r_c \ln(4d/r_c)}$$

$$E_c = \frac{2.6 \times 10^3\ V}{25 \times 10^{-6}\ m\ ln\left(\frac{4 \times 8 \times 10^{-3}\ m}{25 \times 10^{-6}\ m}\right)}$$

$$E_c = \frac{2.6 \times 10^3\ V}{25 \times 10^{-6}\ m\ \times 7.15} = 1.45 \times 10^7\ Vm^{-1}$$

S2b. Evaluation of Laplace pressure on the microdroplet in ES and SS

Laplace pressure, ΔP is related to the interfacial tension, γ across the capillary tip with a radius of curvature, r_c using this relation[3]

$$\Delta P = \frac{2\gamma}{r_c}$$

The inner radius of curvature is 25 and 75 µm for borosilicate and silica capillary used in ES and SS, respectively. The interfacial tension or surface tension of water is 75 mN/m, which gave approximate Laplace pressure as 5.8 kPa and 2 kPa.

For ES,

$$\Delta P = \frac{2 \times (72 \times 10^{-3}\ Nm^{-1})}{25 \times 10^{-6}\ m};\ \Delta P \approx\ 5.8\ kPa$$

For SS,

$$\Delta P = \frac{2 \times (72 \times 10^{-3}\ Nm^{-1})}{75 \times 10^{-6}\ m};\ \Delta P \approx 2\ kPa$$

References

(1) Zeiger, M.; Jäckel, N.; Mochalin, V. N.; Presser, V. Review: Carbon Onions for Electrochemical Energy Storage. *J. Mater. Chem. A* **2016**, *4*, 3172–3196.

(2) Kebarle, P.; Tang, L. From Ions in Solution to Ions in the Gas Phase - the Mechanism of Electrospray Mass Spectrometry. *Anal. Chem.* **1993**, *65*, 972–986.

(3) Lee, S.; Kim, D. H.; Needham, D. Equilibrium and Dynamic Interfacial Tension Measurements at Microscopic Interfaces Using a Micropipet Technique. 1. A New Method for Determination of Interfacial Tension. *Langmuir* **2001**, *17*, 5537–5543.

Chemical Science

ROYAL SOCIETY OF CHEMISTRY

EDGE ARTICLE

View Article Online
View Journal | View Issue

Check for updates

Cite this: *Chem. Sci.*, 2021, **12**, 6370

All publication charges for this article have been paid for by the Royal Society of Chemistry

Received 8th January 2021
Accepted 24th March 2021

DOI: 10.1039/d1sc00112d

rsc.li/chemical-science

Ambient microdroplet annealing of nanoparticles†

Angshuman Ray Chowdhuri,‡ B. K. Spoorthi,‡ Biswajit Mondal, Paulami Bose, Sandeep Bose and Thalappil Pradeep *

Conversion of polydisperse nanoparticles to their monodisperse analogues and formation of organized superstructures using them involve post synthetic modifications, and the process is generally slow. We show that ambient electrospray of preformed polydisperse nanoparticles makes them monodisperse and the product nanoparticles self-assemble spontaneously to form organized films, all within seconds. This phenomenon has been demonstrated with thiol-protected polydisperse silver nanoparticles of 15 ± 10 nm diameter. Uniform silver nanoparticles of 4.0 ± 0.5 nm diameter were formed after microdroplet spray, and this occurred without added chemicals, templates, and temperature, and within the time needed for electrospray, which was of the order of seconds. Well organized nanoparticle assemblies were obtained from such uniform particles. A home-made and simple nanoelectrospray set-up produced charged microdroplets for the generation of such nanostructures, forming cm^2 areas of uniform nanoparticles. A free-standing thin film of monodisperse silver nanoparticles was also made on a liquid surface by controlling the electrospray conditions. This unique method may be extended for the creation of advanced materials of many kinds.

Introduction

Chemical processes in microdroplets are a rapidly evolving subject. Examples include synthesis of molecules[1,2] and pharmaceutical products[3] as well as conformational changes in proteins.[4,5] Such synthesis can also produce nanoparticles (NPs) without reducing agents starting from metal ions in solutions.[6–8] This synthetic method can be tuned with the application of an electrical potential and can lead to assemblies of nanomaterials, and a viable method for forming 1D structures with potential applications was demonstrated.[7] Materials science with charged microdroplets can produce nanoholes on 2D materials[9] and metallic thin films on liquid surfaces.[10]

The science of nanomaterials, especially noble metal nanomaterials, has expanded into almost every area of materials science.[11–14] The properties of these materials are heavily dependent on their size, shape, and distribution. These aspects are especially important for their electronic structure and consequently applications involving chemistry, physics, and biology.[14] As a result, several methods have been developed to control the size dispersity of such materials. Digestive ripening is one of the most commonly used methods in this regard for noble metal NPs.[15–17] The method typically involves high-temperature annealing involving refluxing of NP suspensions for extended periods to achieve monodispersity.[15,18,19] However, extremely precise conditions for a long time, of the order of days, are required to obtain uniform particles. Therefore, it is important to develop a facile and fast method for making monodisperse nanostructures.

Ultrafast acceleration of chemical reactions and synthesis of NPs starting from metal precursors in droplets suggest that new chemical bonds of diverse kinds can be formed and broken under such synthetic conditions.[1,2,6–8] This prompted us to explore the possibility of spontaneous dissociation and reassembly of preformed NPs in microdroplets. To our surprise, such droplet-induced dissociation and reassembly of polydisperse silver NPs protected with thiols resulted in highly monodisperse NPs in the microsecond time scale. The deposition of such monodisperse particles produced a film of uniform NPs, and this process is millions of times faster than digestive ripening. Exploring the science through a series of control experiments showed that metal thiolates are transient precursor species formed in this process. We have also optimized conditions under which such a process is feasible to make cm^2 area films of uniform particles. As this method is similar to high-temperature annealing, leading to monodispersity, we term it microdroplet annealing.

Results and discussion

Observation of microdroplet annealing

In the present experiment, we have utilized a home-built nanoelectrospray source to deliver charged microdroplets

---

DST Unit of Nanoscience (DST UNS), Thematic Unit of Excellence (TUE), Department of Chemistry, Indian Institute of Technology Madras, Chennai 600 036, India. E-mail: pradeep@iitm.ac.in

† Electronic Supplementary Information (ESI) available: Characterization of polydisperse silver nanoparticles; HRTEM, UV-vis, FTIR, and EDS; optimization of a range of parameters to obtain monodisperse nanoparticles and supplementary figures; schematic representation of a probable mechanism of such a process. See DOI: 10.1039/d1sc00112d

‡ These two authors contributed equally to this work.

containing polydisperse 2-phenylethanethiol (PET)-protected silver NPs (Ag@PET NPs) in dichloromethane (DCM) onto a transmission electron microscopy (TEM) grid placed on an indium tin oxide (ITO)-coated collector plate. The collector was grounded through a picoammeter to monitor the deposition current, and a potential in the range of 4.5–5.0 kV was applied to the solution held within a glass spray tip through a platinum (Pt) wire electrode. The spray plume was ejected from the nanoelectrospray tip, which can be visualized with a laser torch. Further details are available in the experimental section and ESI.† Various other substrates could be used in place of the TEM grid (see below).

In the present work, an organized assembly of uniform NPs was formed on the TEM grid, starting from the corresponding polydisperse NPs. The as-synthesized Ag@PET NPs have a broad size distribution, as shown schematically in Fig. 1a. The particle size distribution covers a broad range, from 2–25 nm, as determined by TEM (Fig. 1b(i)). This distribution is typical of such NPs. Further details of the characterization of the starting material are presented in the ESI (Fig. S1†). A *d*-spacing of 0.23 nm is due to Ag(111) and it suggested the growth of pure metallic NPs.[20] The characteristic Fourier-transform infrared spectroscopy (FTIR) features of the as-synthesized Ag@PET NPs confirm the attachment of PET on the AgNPs (Fig. S1c, ESI†). The as-synthesized Ag@PET NPs exhibit prominent surface plasmon resonance at 451 nm (Fig. S1d, ESI†). Details of synthesis and characterization are also presented in the experimental section and ESI.†

Ag@PET NPs in DCM were transferred to a home-built borosilicate spray capillary of 50 μm inner diameter (ID) for microdroplet-induced reaction. A schematic representation of the home-built electrospray set-up is shown in Fig. 1. In the course of electrospray deposition of Ag@PET NPs, a dark circular spot of 0.5 cm diameter due to the impinging plume appeared on the substrate kept at a distance *d* from the spray tip, shown in the bottom panel of Fig. 1. The drastic change observed in the course of the reaction is shown in Fig. 1b. Positively charged microdroplets convert polydisperse Ag@PET NPs to an ordered 2D superlattice structure of uniform NPs.[21–28] A superlattice in the current context refers to a localized periodic assembly of uniform NPs which possess inherent periodicity of the element. Such structures are possible only with uniform particles, and the Ag@PET NPs formed have a particle size distribution of 4.00 ± 0.50 nm, which is evident from the expanded portion of the TEM image (inset of Fig. 1b(ii)). From separate experiments it is known that droplet formation and deposition occurs in hundreds of microseconds to milliseconds.[3,29–31] Surprisingly, microdroplet chemistry *via* ambient electrospray converts irregular particles into a superstructure of uniform particles within a fraction of a second.[6–10]

Optimizing microdroplet annealing

In the process of optimization, a series of trials were made to achieve ordered NP assemblies. Finally, ordered structures of Ag@PET NPs were obtained at an applied voltage of 5 kV, *d* of 1.5 cm and flow rate of 1.0 mL h^{-1}, and the data are shown in

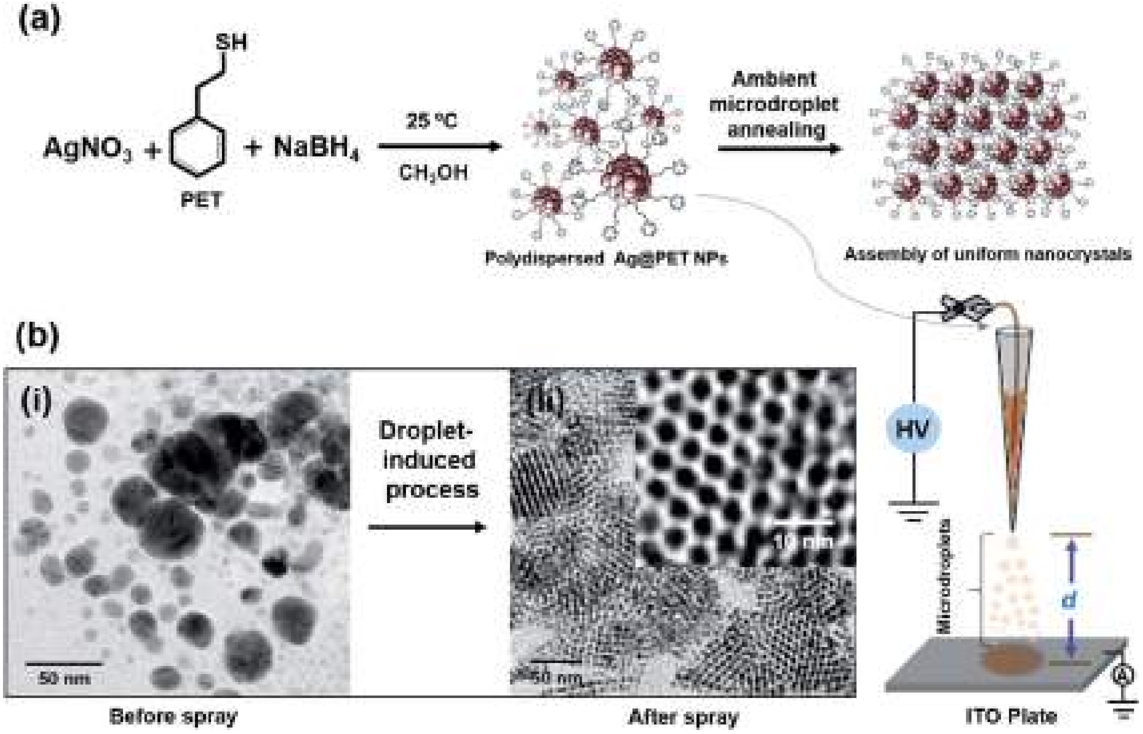

Fig. 1 Schematic representation of (a) the synthetic route of polydisperse Ag@PET NPs and the experimental process leading to the conversion of polydisperse NPs to monodisperse analogues by ambient microdroplet annealing. The experimental set-up for ambient microdroplet annealing is presented schematically in the bottom panel. (b) TEM images of Ag@PET NPs before and after electrospray, respectively (inset of b(ii) shows a corresponding expanded view of the TEM image). Electrospray tip-to-collector distance (*d*) was kept at 1.5 cm.

Fig. 2. A large-area view of monodisperse Ag@PET NPs is shown in Fig. 2a, which form a nearly continuous uniform 2D structure. The corresponding magnified images are shown in Fig. 2b–f, which portray the orientation of the superlattice domains. The inter-particle gap in the superlattice structure was ~1.2 nm (Fig. 2e), slightly less than the length of two PET ligands (the distance between S and Ph–C4 in the PET ligand is ~0.7 nm (ref. 32)), suggesting ligand interactions driving the assembly. Ligands usually form interdigitated structures in these types of assemblies.[33] The Ag(111) lattice spacing of 0.23 nm (Fig. 2f) and the TEM-energy dispersive spectroscopy (TEM-EDS) data (Fig. S2†) confirm the formation of crystalline AgNPs. The FTIR spectrum (Fig. S2b†) shows that PET protection remains intact after such ambient solution-state conversion. The reduced width of the optical absorption spectrum confirms the narrowness of particle sizes after electrospray (Fig. S2a†). This abrupt change in particle distribution post-electrospray suggests a digestive ripening-type of phenomenon through microdroplet chemistry. Inside the microdroplets, polydisperse Ag@PET NPs of size between 2 and 25 nm get reorganized and become uniform particles of 4.00 ± 0.50 nm size (inset of Fig. 2a). Images at different magnifications (Fig. 2b–d) suggest that there is scope for the formation of a 3D superlattice assembly due to overlayer deposition. Negatively charged microdroplets did not produce such superlattice assemblies.

Events within microdroplets can be modified by altering *d*, under a particular electric field. Monodispersity was achieved at $d = 1–2.5$ cm at a spray voltage of 5 kV (Fig. S3b–d, ESI†). At shorter and longer *d*, polydispersity was seen, as shown in Fig. S3a and e–h, ESI†. This observation suggests that at $d < 1$ cm there was not enough time for the reorganization of the NPs in the microdroplets. At $d > 2.5$ cm, droplets were not producing NP assembly owing to the destabilization of microdroplets, due to evaporation of solvents. It could be demonstrated that when *d* was 1.5 cm, Ag@PET NPs achieved the perfect condition for self-assembly leading to superlattices. An optimum structure was obtained at 1.5 cm, and hence this *d* was maintained for other experiments. After fixing *d*, the electrospray voltage was optimized between 0.5 and 7.0 kV. In this process, the electric field and deposition current of microdroplets were adjusted accordingly. The monodisperse assembly of Ag@PET NPs was obtained at 5.0 kV (Fig. S4e, ESI†). The rate of flow of Ag@PET NPs from the spray emitter was also an essential parameter. The size of microdroplets depended on the flow rate. For the given condition, microdroplets produced ordered structures at a flow rate of 1.0 mL h^{-1}, as shown in Fig. S5b, ESI.†

Solvent plays a vital role in the generation of a suitable environment within the microdroplets. The generation of the spray-plume and materials formed in microdroplets are highly dependent on the polarity of the solvent. The dielectric constant

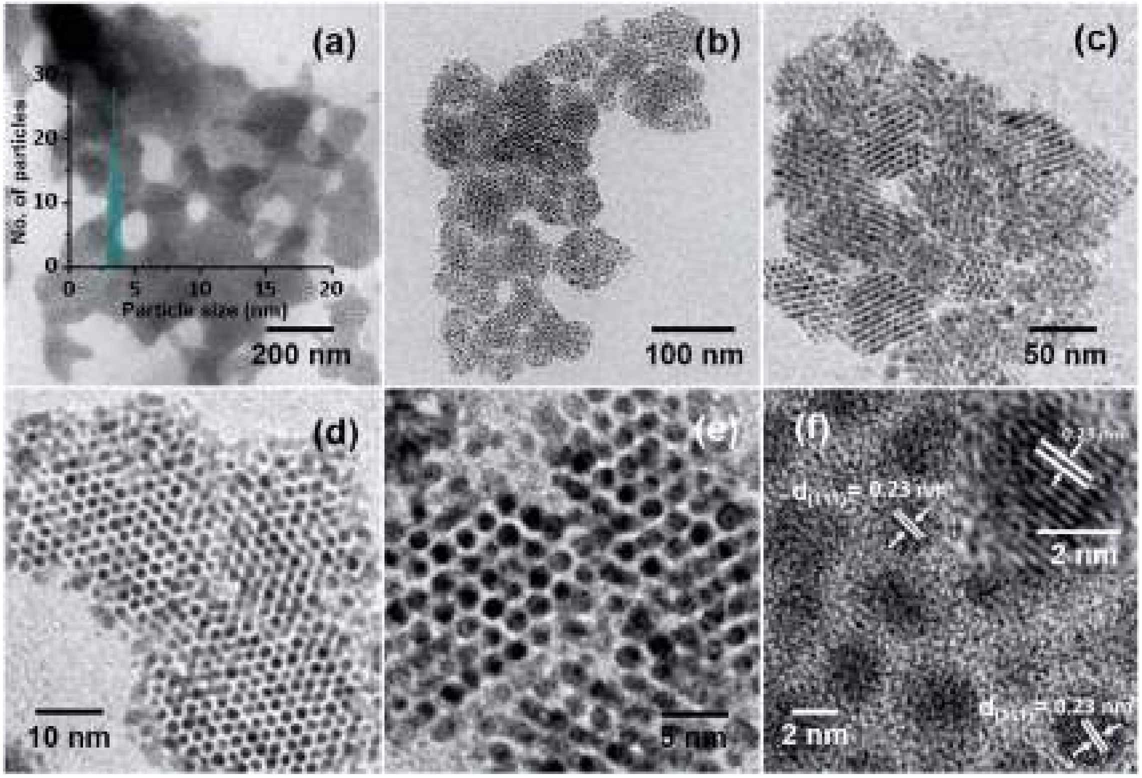

Fig. 2 HRTEM images (at different magnifications) of Ag@PET NPs after electrospray under optimized conditions. (a) Large-area TEM image, showing a 2D sheet-like morphology, the particle size distribution obtained is shown in the inset. Expanded images: (b and c) assembly leading to superlattices, (d and e) TEM images showing uniform inter-particle distance, and (f) the (111) lattice plane of Ag@PET NPs; the HRTEM image of a particle is expanded in the inset.

(ε), pH, and pressure of the droplet environment are important electrospray parameters.[31,34] In this regard, solvents with different ε were studied under the above-optimized conditions to check the effect of solvents on the formation of such structures within microdroplets. Monodispersity was achieved for a few solvents having a particular range of ε under optimized conditions in the case of PET-protected silver NPs, as shown in Fig. S6c–g.† Organized assembly was observed when such a process was continued with DCM having an ε of 8.93. Other solutions, with solvents such as carbon tetrachloride, $\varepsilon = 2.24$, diethyl ether, $\varepsilon = 4.33$, chloroform, $\varepsilon = 4.81$, tetrahydrofuran, $\varepsilon = 7.82$, pyridine, $\varepsilon = 12.40$, acetone, $\varepsilon = 20.70$, dimethylformamide, $\varepsilon = 37.50$, and acetonitrile, $\varepsilon = 38.25$ were unable to produce such monodisperse assembly. This study was continued with four different capillaries with IDs in the range 30–60 μm under the optimized conditions. An ID of 50 μm was most appropriate under these conditions.

Extension to other ligands

It is clear that an unusual phenomenon in microdroplets was observed with PET protected AgNPs under a particular condition. In order to check the possibility of such transformations with other protecting ligands, trials were made with different ligands, especially thiols with different denticities and chain lengths under the optimized conditions achieved for Ag@PET NPs. Different polydisperse AgNPs were synthesized with 2,4-dimethylbenzenethiol (DMBT) and water-soluble sodium citrate (Cit), and their TEM images are shown in Fig. S7a and c, ESI.† Previously optimized conditions did not produce monodispersity in these cases (Fig. S7b and d, ESI†). Polydisperse dithiol-protected AgNPs were synthesized with 1,4-benzenedithiol (BDT) and 1,6-hexanedithiol (HDT), and spray experiments were performed subsequently. In the case of Ag@BDT NPs, monodispersity without such assembly was seen (Fig. S8a and b, ESI†). However, spray of Ag@HDT NPs was inefficient even to produce a significant change in the particle size, as presented in Fig. S8c and d.† These experiments were extended to comparatively long-chain thiols like octadecanethiol (ODT)- and dodecanethiol (DDT)-protected AgNPs. A broad size distribution was observed after the spray of ODT and DDT-protected AgNPs (Ag@ODT NPs & Ag@DDT NPs), which may be due to the difficulty in reorganization of long carbon chain thiols within microdroplets (Fig. S9, ESI†). Optimization of spray conditions is necessary to get monodisperse assemblies for these NP systems. However, ambient microdroplet annealing produced monodisperse assembly of Ag@DMBT NPs at 8.5 kV and $d = 1.5$ cm, as shown in Fig. S10.† The method was also successful in creating uniform NPs of ethanethiol (ET)-protected Ag NPs from polydisperse NPs at an applied voltage of 4.0 kV and $d = 1.0$ cm (Fig. S11†). Therefore, it is clear that this process is general and is applicable for different NP systems under specific electrospray conditions. Optimization of spray conditions is essential for a particular NP system. The concentration of polydisperse Ag@PET NPs taken for the spray experiments is also important. Fig. S12 of the ESI† shows the TEM images of Ag@PET NPs after spraying at different concentrations. These experiments demonstrate that uniformity is dependent on the starting concentration of the polydisperse Ag NPs. In summary, monodispersity needs optimization of a range of parameters.

Nebulization spray

The aerosol spray can also be produced by nebulization.[31,34] This process does not require an applied electric potential. Ag@PET NPs (Fig. 3a) were sprayed using dry N_2 gas with four different pressures, using a microcapillary of 50 μm diameter. A schematic of this spray set-up is presented in Fig. 3b. Microdroplets produced in the spray can create uniform particles with an average particle size of 4 nm, as shown in Fig. 3c. Thus, monodispersity can be achieved by voltage-free spray as well. However, the spray does not produce uniform ordered superstructures, which may be due to the high-pressure of N_2 gas from the emitter. This may require additional optimization of the pressure needed. Fig. S13† shows the TEM images of Ag@PET NPs after spray at different N_2 nebulization pressures. For all these cases, a nearly similar particle size distribution was observed.

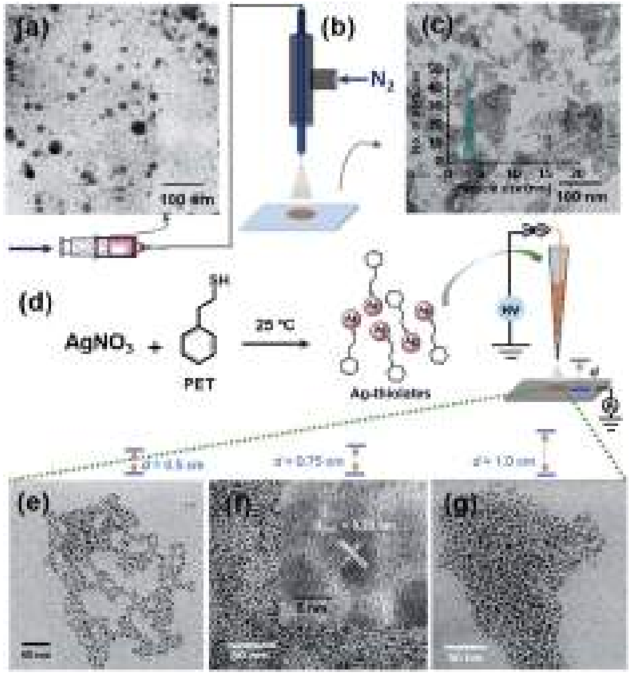

Fig. 3 Generation of monodisperse Ag@PET NPs from polydisperse Ag@PET NPs using microdroplets. (a) TEM of the as-synthesized Ag@PET NPs, (b) schematic representation of the spray of polydisperse Ag@PET NPs using dry N_2 gas without an electric field; the ID of the silica microcapillary was 50 μm, the same as the spray tip used in the electrospray. (c) TEM image of monodisperse Ag@PET NPs after spray (size distribution is in the inset), (d) schematic of the formation of soluble Ag–PET thiolates and their electrospray at three different *d* values, (e–g) TEM images of Ag@PET NPs obtained at a *d* of 0.50 cm, 0.75 cm, and 1.00 cm, respectively. Nearly ordered assemblies are formed from thiolates at $d = 0.75$. An expanded view of the same image is shown in the inset of f, showing the Ag(111) lattice.

Thiolate intermediates

A probable mechanism for the formation of such organized structures was hypothesized with inputs from control experiments. We know that Ag^+ and thiols in solution form thiolates during the formation of NPs[35,36] and clusters.[37,38] Silver thiolates are formed when clusters decompose.[39,40] Therefore, we propose that silver thiolates are formed in droplets as intermediates during the formation of uniform NPs. To prove this, we conducted a spray experiment by taking Ag–PET thiolates as precursors (see the experimental section for their synthesis), instead of polydisperse NPs. Thiolates were sprayed at three different d values (Fig. 3e–g). All the experiments produced silver NPs, but the organized structures with silver lattice planes were seen at $d = 0.75$ cm (Fig. 3f). This suggests that microdroplet spray of solvated polydisperse particles resulted in highly ordered assemblies, most likely through a transient thiolate species, as presented in Fig. S14.†

Large-area films

This ambient ion-based methodology has been introduced for the creation of free-standing metallic monodisperse nanoparticles–nanosheets (NPs–NSs). In an earlier study, we electrodeposited metal salts on a liquid surface and got self-organized films of the particles under the influence of electrohydrodynamic flow.[10] A similar approach was used here. The set-up, schematically represented in Fig. 4a is the same as that shown in Fig. 1, except that multiple nozzles and a liquid substrate were used. The multi-nozzle electrospray enlarges the magnitude of the NPs–NSs on the liquid substrate. In this objective, a series of trials were performed using different solvents. It was observed that among the solvents studied, the ordered NP structure was formed on the water surface. These uniform NPs-NSs, composed of superlattice structures of silver NPs, can be used for diverse applications. The large-area TEM image in Fig. 4b confirms the compactness of the assembly. The particle size distribution was in the range of 4.5 ± 0.5 nm. The formation of a brown colored thin film of NPs–NSs was observed and is shown in the inset of Fig. 4b. Fig. 4c shows the corresponding magnified image. The lattice spacing of these NPs–NSs matches with the (111) plane of AgNPs, proving the metallic nature of AgNPs. Similarly, polydisperse NPs were deposited on an ITO surface under optimized spray conditions and were redispersed in DCM. A uniform film of monodisperse NPs was observed using a TEM, as shown in Fig. S16 (ESI†).

Polydisperse silver NPs can also form 3D assemblies on a metal substrate as shown in Fig. 5a. If we look closely at the structures, a layer-upon-layer assembly of nanoparticles is observed, which is indicated by arrows in Fig. 5b. During spray for an extended period, the incoming microdroplets with the transient metal-thiolates are continuously reduced to NPs and get deposited on preexisting nanoparticle layers.[7] The 3D crystal structures formed this way could generate exceptional properties.[41,42] Fig. S17 in the ESI† shows the growth of a multilayer assembly with respect to time. The developed superlattice structures can be used as an ink for electrospray-based printing of a range of crystalline materials. This ambient approach can also print bulk composites and porous architectures. The simplicity of

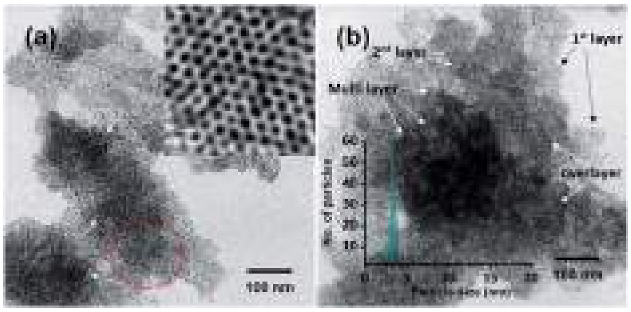

Fig. 5 Formation of 3D ordered monodisperse assemblies of AgNPs by electrospray for an extended period. (a) TEM image of Ag@PET NPs after 10 min of electrospray, which shows the deposition of layers of NPs (an expanded view of the TEM image is shown in the inset). Genesis of a second layer of superlattices is shown by the arrows. (b) TEM image of Ag@PET NPs after 15 min of electrospray (inset: particle size distribution). More layers are seen. Arrows indicate the formation of multiple layers to create 3D superlattices.

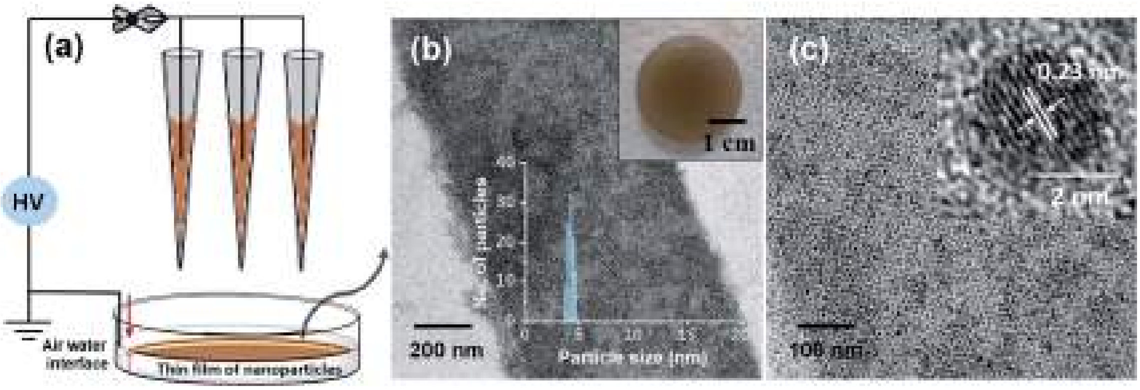

Fig. 4 (a) Schematic illustration of the electrospray deposition of Ag@PET NPs on a water surface. The formation of a thin film of Ag@PET NPs on a liquid surface is also shown, (b) a large-area TEM image of monolayer Ag@PET NPs from the deposited film (inset: photograph of the free standing film deposited on water after spray and its particle size distribution), (c) HRTEM image of NPs which confirms the ordered structure and formation of metallic Ag particles. The well-defined Ag(111) lattice is shown in the inset of c.

this ambient process is expected to create interest for the development of such 3D structures directly from polydisperse NPs.

A series of control experiments were performed to optimize the ordered structure by varying different parameters, especially, spray distance (*d*), voltage and flow rate. The experiment was repeated under the optimized conditions. It was confirmed that an electric field and a deposition current of ~35 nA were also vital for the creation of such nanostructures. This methodology may provide an opportunity to produce large scale monodisperse silver NP assemblies *via* such ambient microdroplet annealing. Moreover, this ambient technique could certainly be used as a facile synthetic approach for the development of unique nanomaterials of other materials with emerging properties for a broad range of applications. The possibility of assembly over large areas along with uniform synthesis offers new possibilities.

Conclusions

In summary, we developed a fast method of making monodisperse silver NPs by electrospraying highly polydisperse NPs synthesized in solution, under ambient conditions. Microdroplets from the spray formed a uniform assembly of nanostructures composed of ordered AgNPs upon deposition on a substrate. Control experiments proved that the electric field, the tip-to-collector distance, and the flow rate are the key factors for the oriented growth of such superlattices. This process does not require any sophisticated instrumentation, and it transforms polydisperse NPs to superlattices composed of monodisperse NPs within seconds. This process may be considered green as no solvents or additional processing is involved, unlike solution state post-processing methods. Microdroplet spray on a water surface makes a thin film of monodisperse metallic sheets of uniform NPs assisted by electrohydrodynamic flow. The method described in this work may be utilized for the development of multimetallic superlattice structures or high entropy alloys by efficient control of the composition of metals, leading to new properties.

Experimental

Materials and chemicals used

Silver nitrate ($AgNO_3$) was purchased from RANKEM. Sodium borohydride ($NaBH_4$), 2-phenylethanethiol (PET), 1,4-benzenedithiol (BDT), 2,4-dimethylbenzenethiol (DMBT), sodium citrate (Cit), ethanethiol (ET), 1-octadecanethiol (ODT), and dodecanethiol (DDT) were purchased from Sigma Aldrich Chemicals. Pure ethanol, methanol, dichloromethane, pyridine, carbon tetrachloride, acetone, diethyl ether, chloroform, acetonitrile, and *N*,*N*-dimethylformamide were sourced from Merck India and used as solvents for the electrospray deposition experiments.

Synthesis of PET protected silver NPs (Ag@PET NPs)

Polydisperse Ag@PET NPs were synthesized by our previously described method with slight modifications.[33] Briefly, PET (0.58 μL) was added to pure methanol (30 mL) at 25 °C. Subsequently, $AgNO_3$ (50 mg) in Millipore water (0.5 mL) was added to the above solution. The mixture was gently stirred for 15 min to form silver thiolates. After that, $NaBH_4$ (25 mg) was dissolved in 8 mL ice-cold water and was subsequently added slowly into the flask and stirred for another 12 h to allow the complete growth of Ag@PET NPs. The as-synthesized Ag@PET NPs were washed with methanol and extracted in different solvents for further experiments.

Synthesis of other ligand protected silver NPs

Different ligand protected AgNPs were synthesized for comparative experiments. BDT, DMBT, ET, HDT, Cit, ODT, and DDT were used separately during the synthesis of AgNPs in individual trials. For every case, the experimental procedure was similar, except for the addition of a particular thiol in methanol at the beginning of the synthesis. After synthesis, the products were washed with methanol and extracted in DCM for electrospray experiments.

Electrospray deposition experiments

A home-made electrospray set-up was used for the generation of microdroplets (Fig. 1a).[7] A micropipette puller (P-97, Sutter Instruments, U.S.A.) was used for pulling a borosilicate glass capillary of 1.5 mm outer diameter (OD) and 0.86 mm ID. It was cut into two pieces having tips of 50 μm ID and 150 μm OD. Each tip of the capillary was checked using an optical microscope to ensure the size and quality of the cut. Polydisperse Ag@PET NPs (100 μg mL^{-1}) in DCM were filled in the nanoelectrospray tips using a microinjector pipette tip, and Pt wire (0.5 mm diameter) was inserted into the solution, making an electrode for high voltage connection. A multi-nozzle spray setup was used for scaling up the method. A syringe pump controlled the flow rate of the microdroplets to achieve the best structures. The syringe needle was connected to a high voltage power source through a copper clip. The experiments were carried out in different solvents and solvent mixtures having different ε and at varying potentials. Among the solvents used, spray with DCM showed the best result. More control experiments were carried out with silver thiolates in DCM. ITO-coated glass slides were procured from Aldrich. Millipore water was used in all the experiments.

Microdroplet generation through nebulizer gas

For nebulization spray, a home-built set-up was used as presented in the schematic (Fig. 3b). A Hamilton syringe was connected to a silica capillary (50 μm ID) through a union connector. Microdroplets were generated by spraying solvents through a fused silica capillary of 50 μm ID with 10, 20, 30, and 40 pounds per square inch (psi) N_2 gas for nebulization.

Characterization of the nanostructures

TEM and HRTEM were performed at an accelerating voltage of 200 kV on a JEOL 3010, 300 kV instrument equipped with a UHR polepiece. A Gatan 794 multiscan CCD camera was used for image acquisition. Energy-dispersive X-ray spectroscopy (EDS) spectra were collected on an Oxford Semistem system housed on the TEM. The formation of NPs during microdroplet deposition was examined directly using 300-mesh carbon-coated copper grids (spi Supplies, 3530C-MB) under different experimental conditions. Silver NPs were deposited directly on the TEM grids under different experimental conditions. Particle size distributions were obtained from TEM images using ImageJ.

Author contributions

The idea was suggested by TP. ARC and SB performed most of the experiments. The manuscript was written through contributions of all authors. All the authors approved the final version of the manuscript.

Conflicts of interest

There are no conflicts to declare.

Acknowledgements

The authors thank the Department of Science and Technology, Govt. Of India, for continuously supporting our research program on nanomaterials. SB thanks UGC for a research fellowship. PB and SB thank IIT Madras for their research fellowships. We thank Vishal Kumar for help with charge measurements.

References

1 T. Muller, A. Badu-Tawiah and R. G. Cooks, *Angew. Chem., Int. Ed.*, 2012, **51**, 11832–11835.

2 X. Yan, R. M. Bain and R. G. Cooks, *Angew. Chem., Int. Ed.*, 2016, **55**, 12960–12972.

3 S. Banerjee and R. N. Zare, *Angew. Chem., Int. Ed.*, 2015, **54**, 14795–14799.

4 S. Banerjee, *J. Mass Spectrom.*, 2013, **48**, 193–204.

5 D. N. Mortensen and E. R. Williams, *Anal. Chem.*, 2015, **87**, 1281–1287.

6 A. Li, Q. Luo, S.-J. Park and R. G. Cooks, *Angew. Chem., Int. Ed.*, 2014, **53**, 3147–3150.

7 D. Sarkar, M. K. Mahitha, A. Som, A. Li, M. Wleklinski, R. G. Cooks and T. Pradeep, *Adv. Mater.*, 2016, **28**, 2223–2228.

8 A. Li, Z. Baird, S. Bag, D. Sarkar, A. Prabhath, T. Pradeep and R. G. Cooks, *Angew. Chem., Int. Ed.*, 2014, **53**, 12528–12531.

9 D. Sarkar, B. Mondal, A. Som, S. J. Ravindran, S. K. Jana, C. K. Manju and T. Pradeep, *Global Challenges*, 2018, **2**, 1800052–1800059.

10 D. Sarkar, R. Singh, A. Som, C. K. Manju, M. A. Ganayee, R. Adhikari and T. Pradeep, *J. Phys. Chem. C*, 2018, **122**, 17777–17783.

11 P. K. Jain, X. Huang, I. H. El-Sayed and M. A. El-Sayed, *Acc. Chem. Res.*, 2008, **41**, 1578–1586.

12 R. Jin, C. Zeng, M. Zhou and Y. Chen, *Chem. Rev.*, 2016, **116**, 10346–10413.

13 X. Chen and S. S. Mao, *Chem. Rev.*, 2007, **107**, 2891–2959.

14 I. Chakraborty and T. Pradeep, *Chem. Rev.*, 2017, **117**, 8208–8271.

15 J. R. Shimpi, D. S Sidhaye and B. L. V. Prasad, *Langmuir*, 2017, **33**, 9491–9507.

16 B. L. V. Prasad, S. I. Stoeva, C. M. Sorensen and K. J. Klabunde, *Langmuir*, 2002, **18**, 7515–7520.

17 S. Stoeva, K. J. Klabunde, C. M. Sorensen and I. Dragieva, *J. Am. Chem. Soc.*, 2002, **124**, 2305–2311.

18 P. Sahu and B. L. V. Prasad, *Langmuir*, 2014, **30**, 10143–10150.

19 P. Sahu and B. L. V. Prasad, *Nanoscale*, 2013, **5**, 1768–1771.

20 A. Mayoral, A. Vazquez-Duran, D. Ferrer, J. M. Montejano-Carrizales and M. Jose-Yacaman, *CrystEngComm*, 2010, **12**, 1090–1095.

21 K. Vijaya Sarathy, G. U. Kulkarni and C. N. R. Rao, *Chem. Commun.*, 1997, 537–538.

22 B. L. V. Prasad, C. M. Sorensen and K. J. Klabunde, *Chem. Soc. Rev.*, 2008, **37**, 1871–1883.

23 C. N. R. Rao, K. Pramoda and R. Kumar, *Chem. Commun.*, 2017, **53**, 10093–10107.

24 P. Chen, Z. Zhang, X. Duan and X. Duan, *Chem. Soc. Rev.*, 2018, **47**, 3129–3151.

25 K. J. Si, Y. Chen, Q. Shi and W. Cheng, *Adv. Sci.*, 2018, **5**, 1700179–1700200.

26 N. R. Glavin, R. Rao, V. Varshney, E. Bianco, A. Apte, A. Roy, E. Ringe and P. M. Ajayan, *Adv. Mater.*, 2019, **32**, 1904302–1904323.

27 F. Schulz, O. Pavelka, F. Lehmkühler, F. Westermeier, Y. Okamura, N. S. Mueller, S. Reich and H. Lange, *Nat. Commun.*, 2020, **11**, 3821–3829.

28 P. Xiong, B. Sun, N. Sakai, R. Ma, T. Sasaki, S. Wang, J. Zhang and G. Wang, *Adv. Mater.*, 2020, **32**, 1902654–1902665.

29 P. Kebarle and L. Tang, *Anal. Chem.*, 1993, **65**, 972A–986A.

30 S. Banerjee and S. Mazumdar, *Int. J. Anal. Chem.*, 2012, **8**, 282574–282613.

31 J. K. Lee, D. Samanta, H. G. Nam and R. N. Zare, *Nat. Commun.*, 2018, **9**, 1562–1570.

32 K. Salorinne, T. Lahtinen, J. Koivisto, E. Kalenius, M. Nissinen, M. Pettersson and H. Hakkinen, *Anal. Chem.*, 2013, **85**, 3489–3492.

33 P. Bose, P. Chakraborty, J. S. Mohanty, Nonappa, A. Ray Chowdhuri, E. Khatun, T. Ahuja, A. Mahendranath and T. Pradeep, *Nanoscale*, 2020, **12**, 22116–22128.

34 J. K. Lee, K. L. Walker, H. S. Han, J. Kang, F. B. Prinz, R. M. Waymouth, H. G. Nam and R. N. Zare, *PNAS*, 2019, **116**, 19294–19298.

35 C. P. Joshi, M. S. Bootharaju, M. J. Alhilaly and O. M. Bakr, *J. Am. Chem. Soc.*, 2015, **137**, 11578–11581.

36 C. Liu, T. Li, H. Abroshan, Z. Li, C. Zhang, H. J. Kim, G. Li and R. Jin, *Nat. Commun.*, 2018, **9**, 744–749.

37 M. J. Rosemary and T. Pradeep, *J. Colloid Interface Sci.*, 2003, **268**, 81–84.

38 I. Chakraborty, A. Govindarajan, J. Erusappan, A. Ghosh, T. Pradeep, B. Yoon, R. L. Whetten and U. Landman, *Nano Lett.*, 2012, **12**, 5861–5866.

39 E. Khatun, A. Ghosh, D. Ghosh, P. Chakraborty, A. Nag, B. Mondal, S. Chennu and T. Pradeep, *Nanoscale*, 2017, **9**, 8240–8248.

40 K. Zheng, X. Yuan, N. Goswami, Q. Zhang and J. Xie, *RSC Adv.*, 2014, **4**, 60581–60596.

41 B. Li, X. Wen, R. Li, Z. Wang, P. G. Clem and H. Fan, *Nat. Commun.*, 2014, **5**, 4179–4185.

42 C. Yan and T. Wang, *Chem. Soc. Rev.*, 2017, **46**, 1483–1509.

Electronic Supplementary Information

Ambient Microdroplet Annealing of Nanoparticles

*Angshuman Ray Chowdhuri, B. K. Spoorthi, Biswajit Mondal, Paulami Bose, Sandeep Bose, Thalappil Pradeep**

DST Unit of Nanoscience (DST UNS) and Thematic Unit of Excellence (TUE), Department of Chemistry, Indian Institute of Technology Madras, Chennai - 600036, India
*Email: pradeep@iitm.ac.in

Table of contents

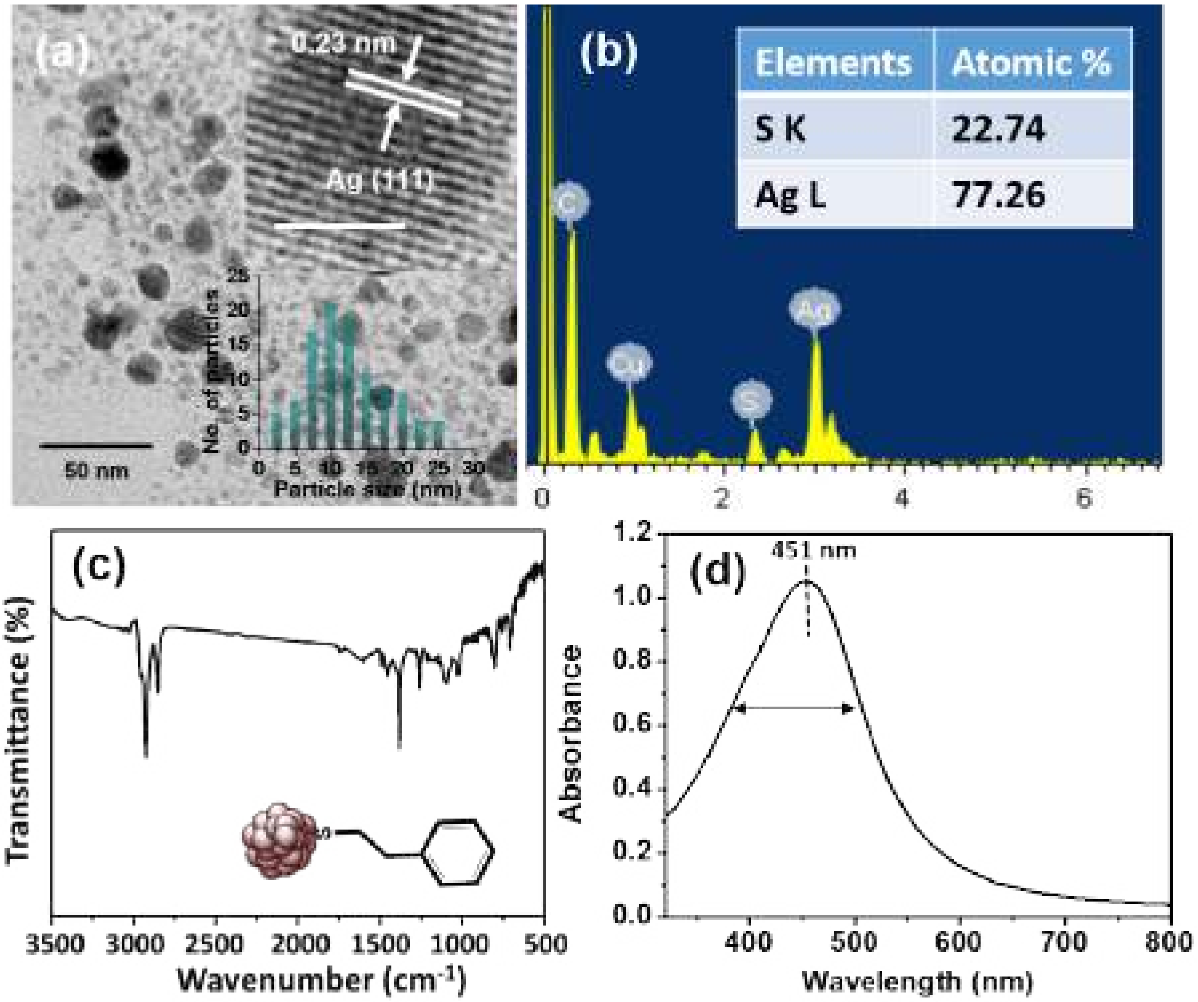

Fig. S1 Characterization of as-synthesized polydispersed Ag@PET NPs. (a) TEM image of the as synthesized polydispersed Ag@PET NPs (insets: HRTEM of a particle showing Ag(111), scale bar is 2 nm, and the observed particle size distribution), (b) TEM-EDS spectrum, (c) FTIR spectrum exhibits the attachment of PET with the AgNPs. The absence of S-H stretch at 2560 cm^{-1} is due to the binding of the thiol on the silver surface. Result indicated the loss of thiolate proton and RS-Ag bond formation in the NPs. (d) UV-Vis spectrum of Ag@PET NPs shows the plasmonic feature at 451 nm.

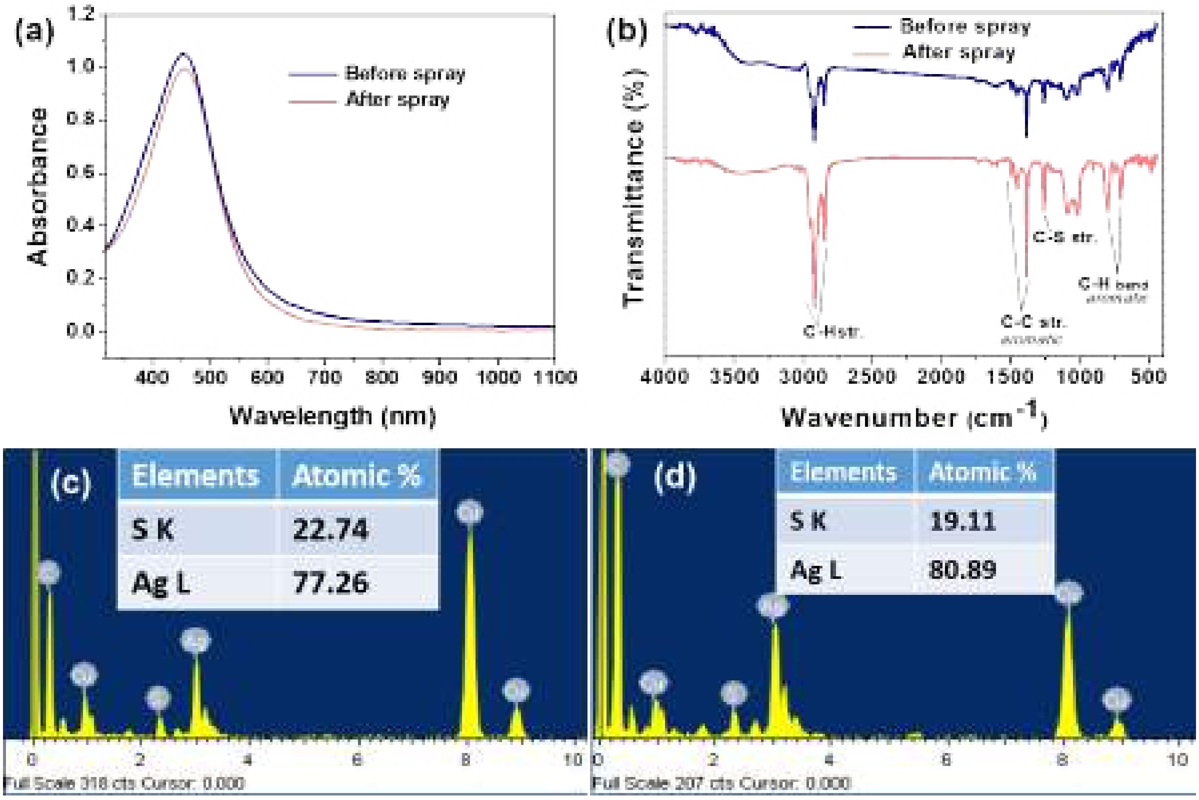

Elements	Atomic %
S K	22.74
Ag L	77.26

Elements	Atomic %
S K	19.11
Ag L	80.89

Fig. S2 (a) UV-Vis, (b) FTIR spectra of Ag@PET NPs before and after electrospray. After spray, the NPs were collected from ITO and dissolved in DCM for UV-Vis study. The FITR spectrum after electrospray suggests that PET remains intact on the silver assemblies after the spray. The characteristic peaks in the EDS of Ag@PET NPs (c) before and (d) after electrospray.

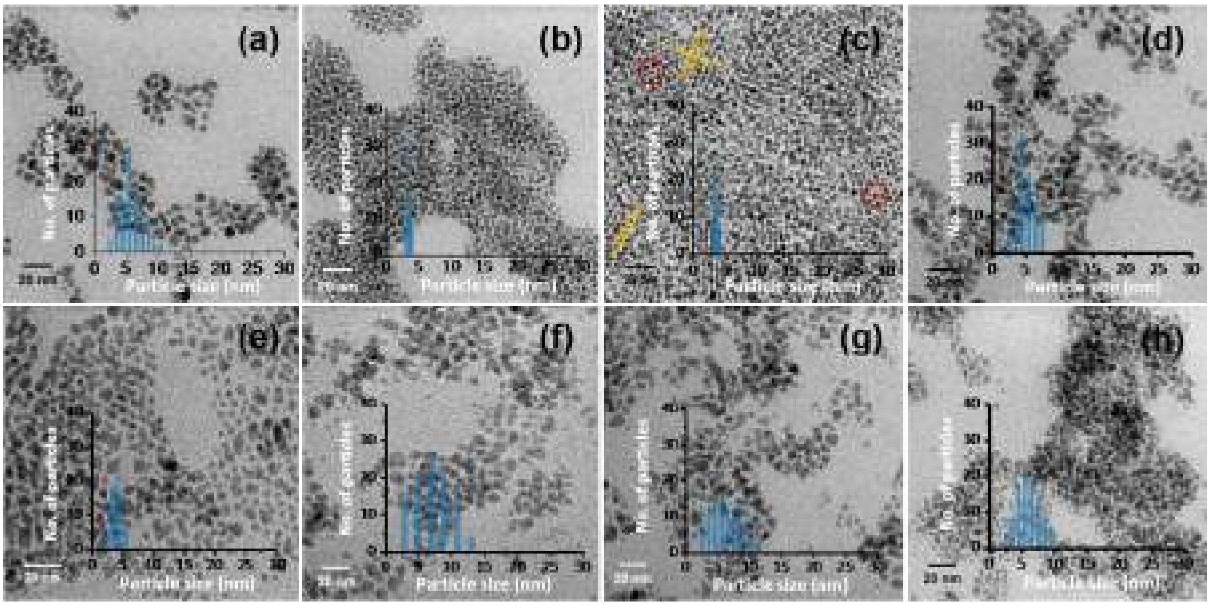

Fig. S3 Optimization of *d* for the formation of monodispersed assemblies of Ag@PET NPs. TEM images of the NPs while *d* was kept at (a) 0.5, (b) 1.0, (c) 1.5, (d) 2.0, (e) 2.5, (f) 3.0, (g) 3.5, and (h) 4.0 cm, during electrospray.

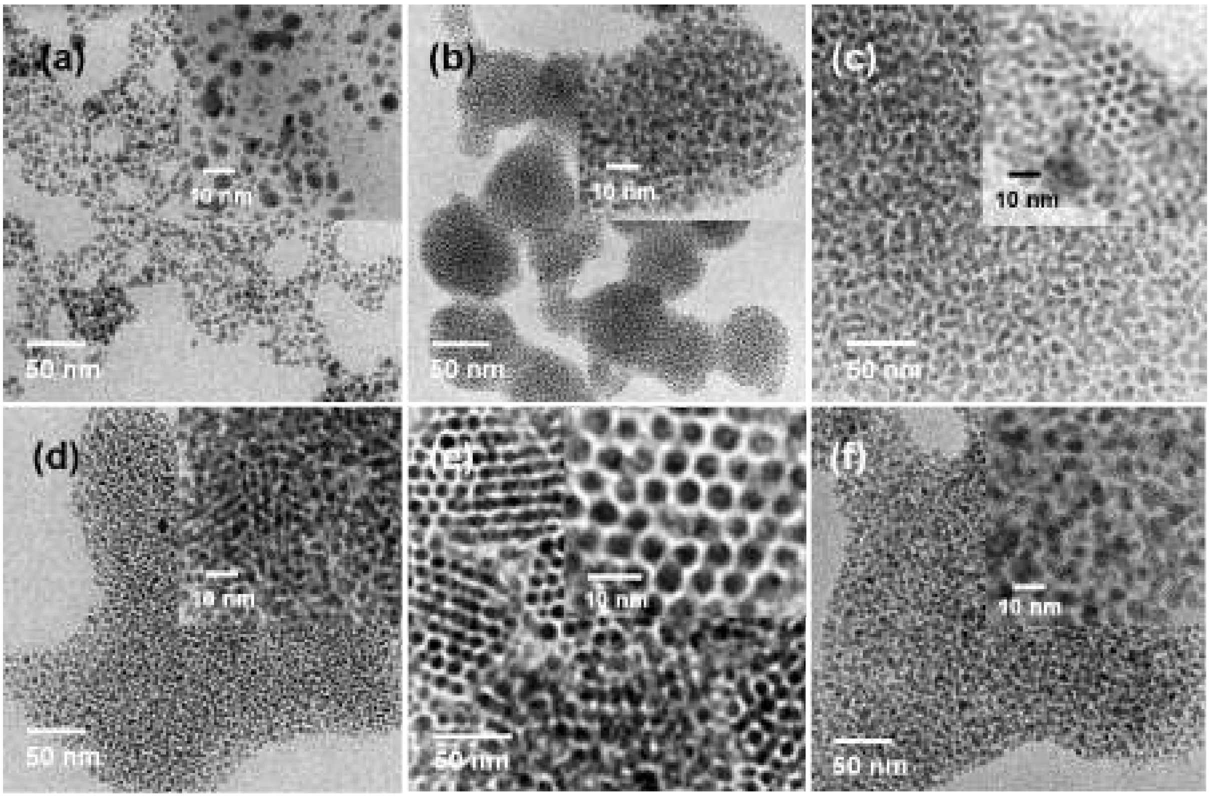

Fig. S4 Optimization of the applied voltage for the process. TEM images of NPs at applied voltages of (a) 0.5, (b) 1.0, (c) 2.0, (d) 3.0, (e) 5.0, and (f) 7.0 kV.

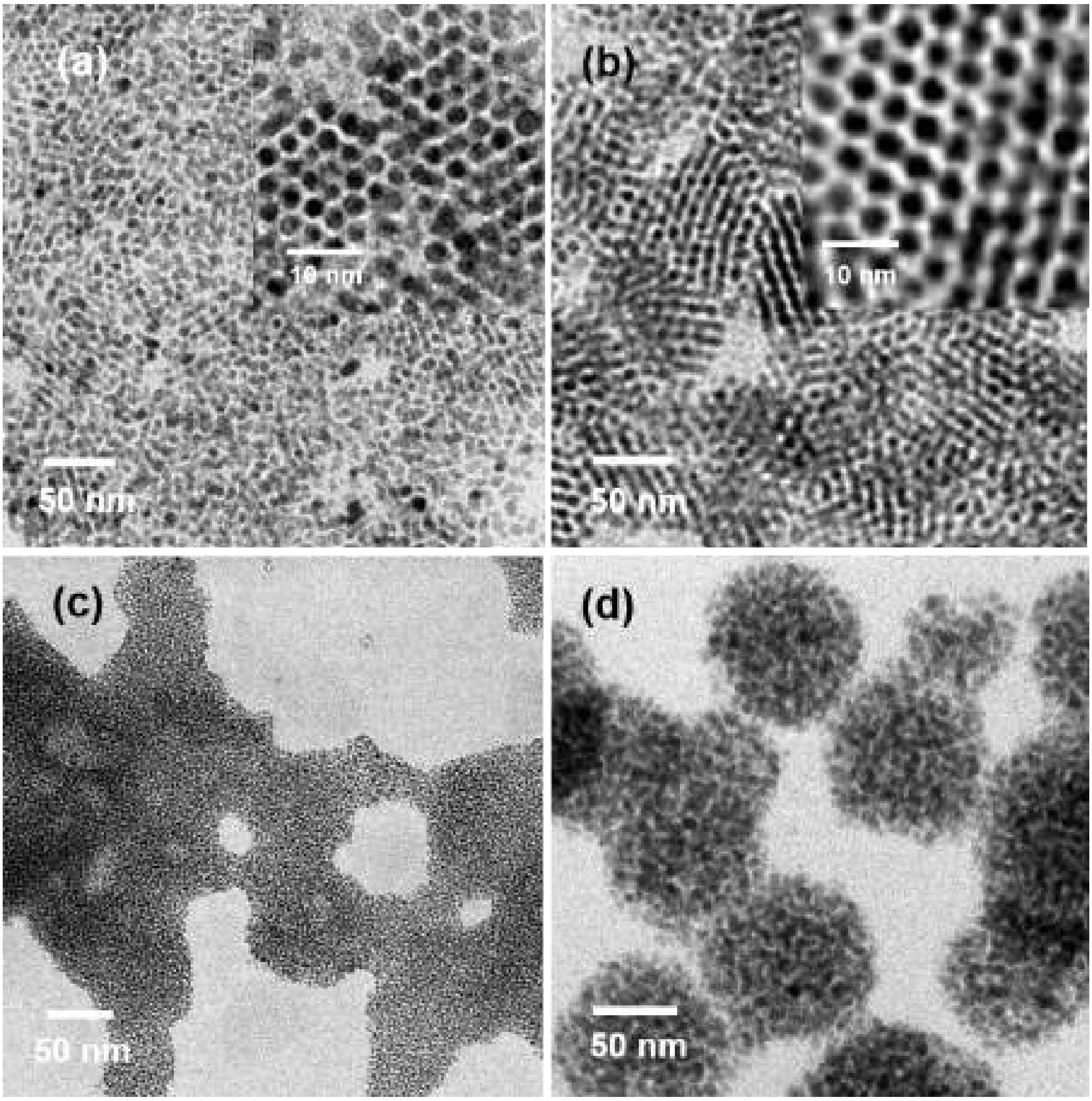

Fig. S5 TEM images of Ag@PET NPs after electrospray with the flow rates of (a) 0.50, (b) 1.00 (optimized conditions, presented in Figure 1b), (c) 1.25, and (d) 1.50 mL/h.

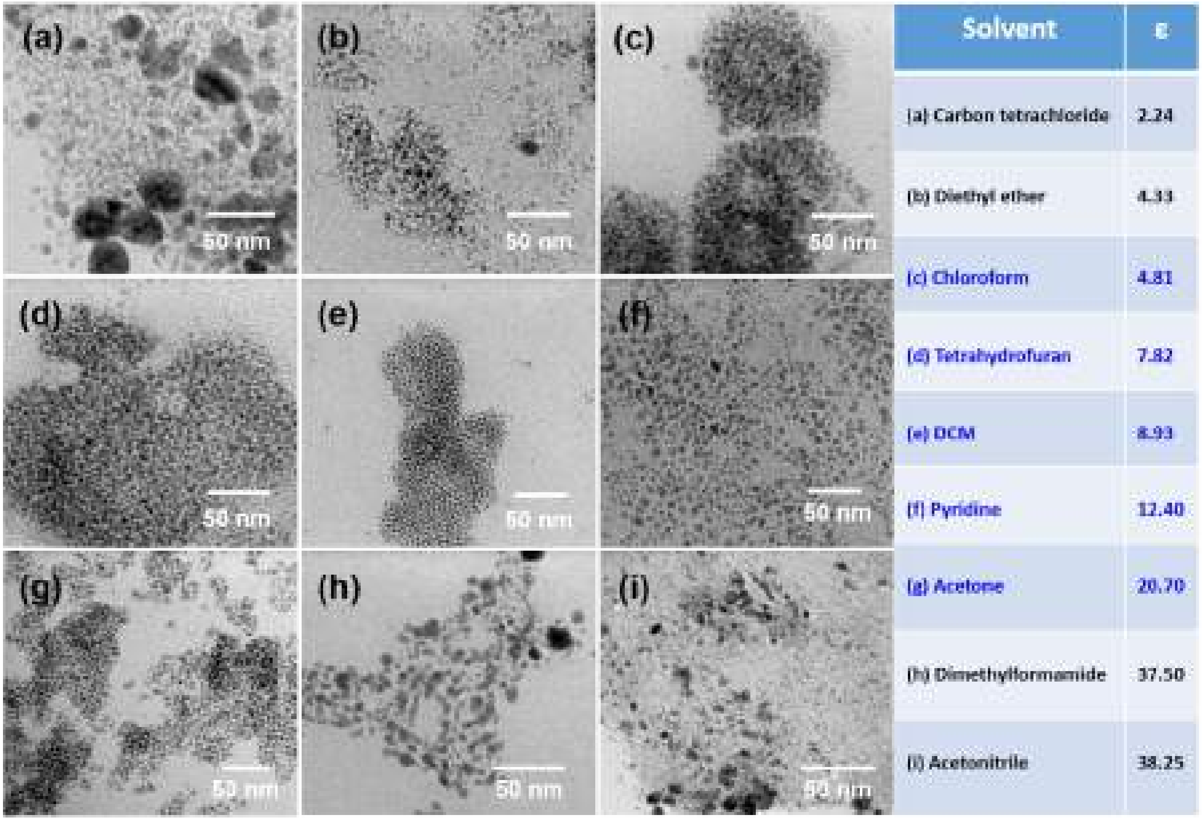

Solvent	ε
(a) Carbon tetrachloride	2.24
(b) Diethyl ether	4.33
(c) Chloroform	4.81
(d) Tetrahydrofuran	7.82
(e) DCM	8.93
(f) Pyridine	12.40
(g) Acetone	20.70
(h) Dimethylformamide	37.50
(i) Acetonitrile	38.25

Fig. S6 Electrospray of Ag@PET NPs in different solvents having lower to higher dielectric constant (ε) is studied. The environment (pH, pressure, charge) inside the microdroplet is changing with the physical and chemical properties (polarity, surface tension, viscosity) of the solvents used for electrospray. TEM images of Ag@PET NPs after electrospray in (a) carbon tetrachloride, (b) diethyl ether, (c) chloroform, (d) tetrahydrofuran, (e) DCM, (f) pyridine, (g) acetone, (h) dimethylformamide, and (i) acetonitrile. The ε values of solvents are presented in the table. Monodispersed NPs were achieved between ε = 4.81–20.70, as shown in Figure c-g.

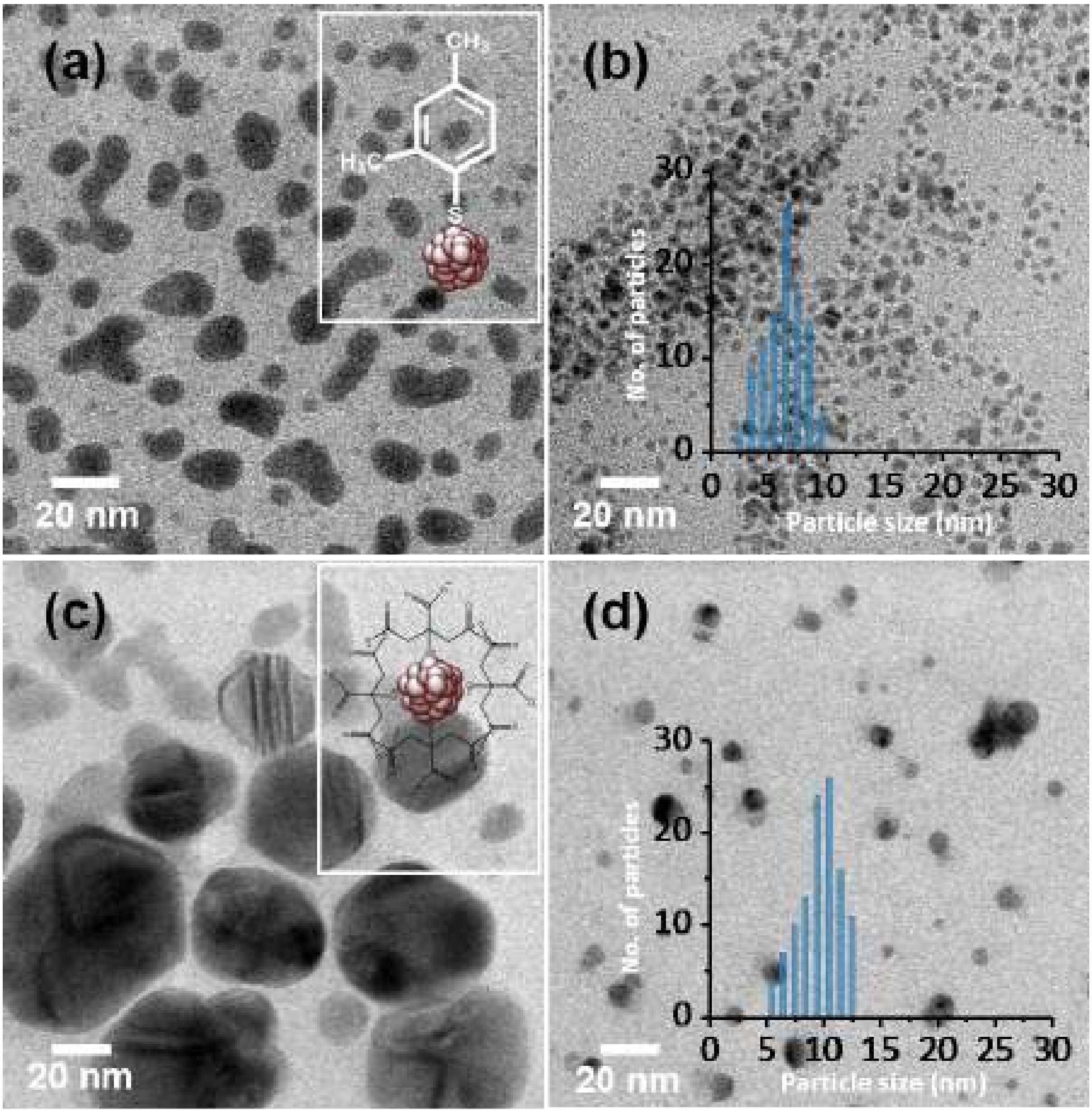

Fig. S7 TEM images of as-synthesized (a) Ag@DMBT NPs and (c) Ag@Cit NPs. Images of the corresponding product NPs after electrospray are in (b) and (d), respectively, at optimized condition used for Ag@PET NPs. The particle size distribution after spray is presented in the inset. Monodispersity was not achieved.

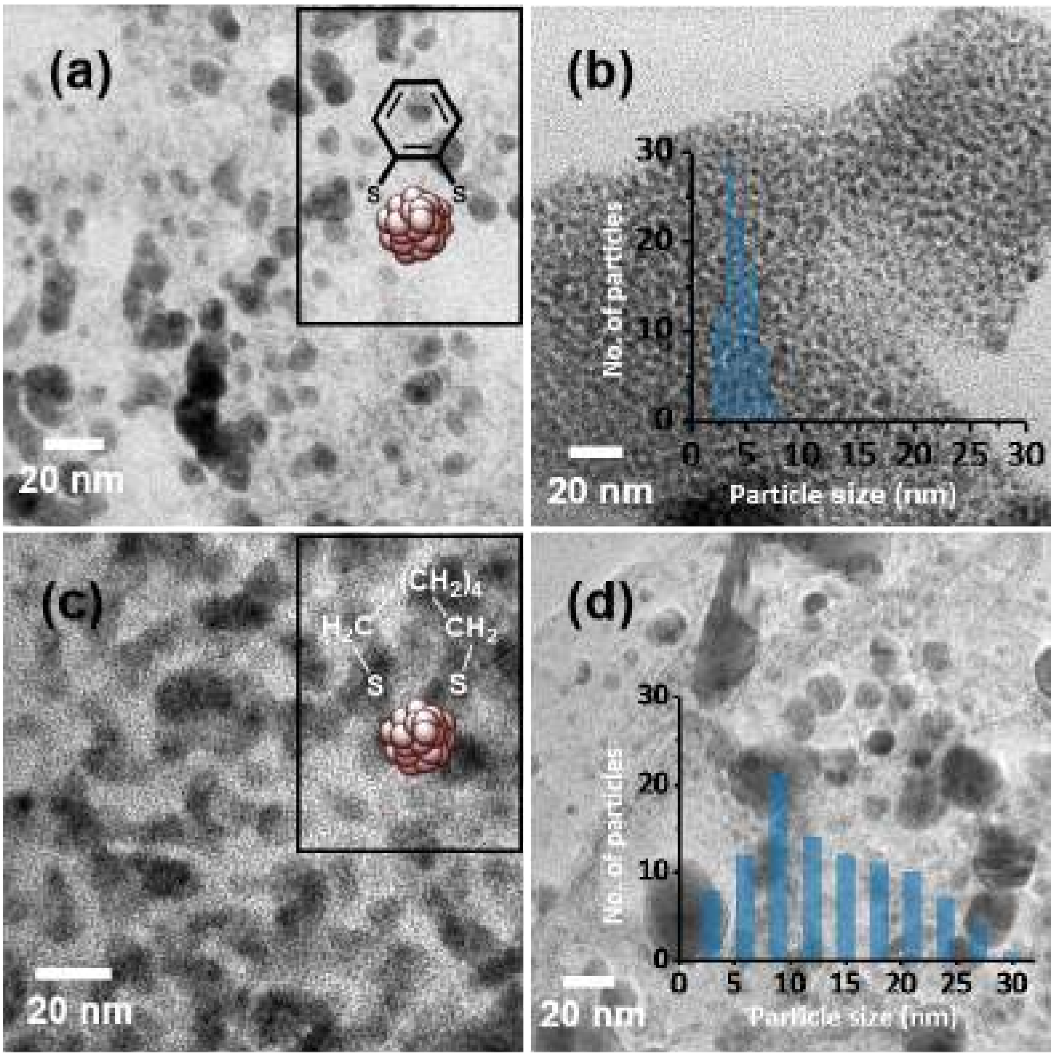

Fig. S8 TEM images of as-synthesized (a) Ag@BDT NPs and (c) Ag@HDT NPs. Images of the corresponding product NPs after electrospray are in (b) and (d), respectively, at optimized condition used for Ag@PET NPs. Particle size distribution in inset b suggests the particles tend to achieve monodispersity without forming superlattices.

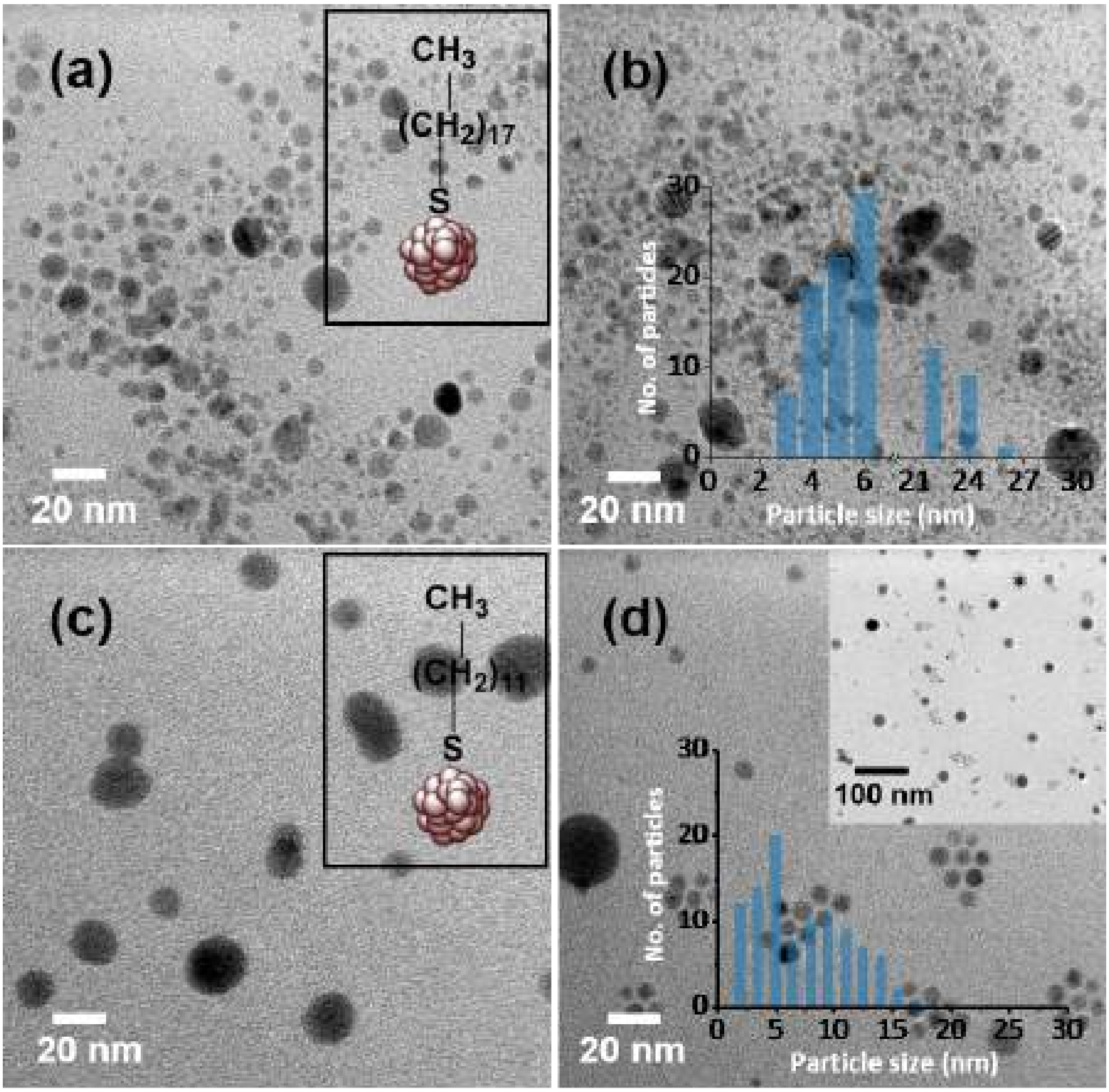

Fig. S9 TEM images of as-synthesized (a) Ag@ODT NPs and (c) Ag@DDT NPs. Images of the corresponding product NPs after electrospray are in (b) and (d), respectively, at optimized condition used for Ag@PET NPs.

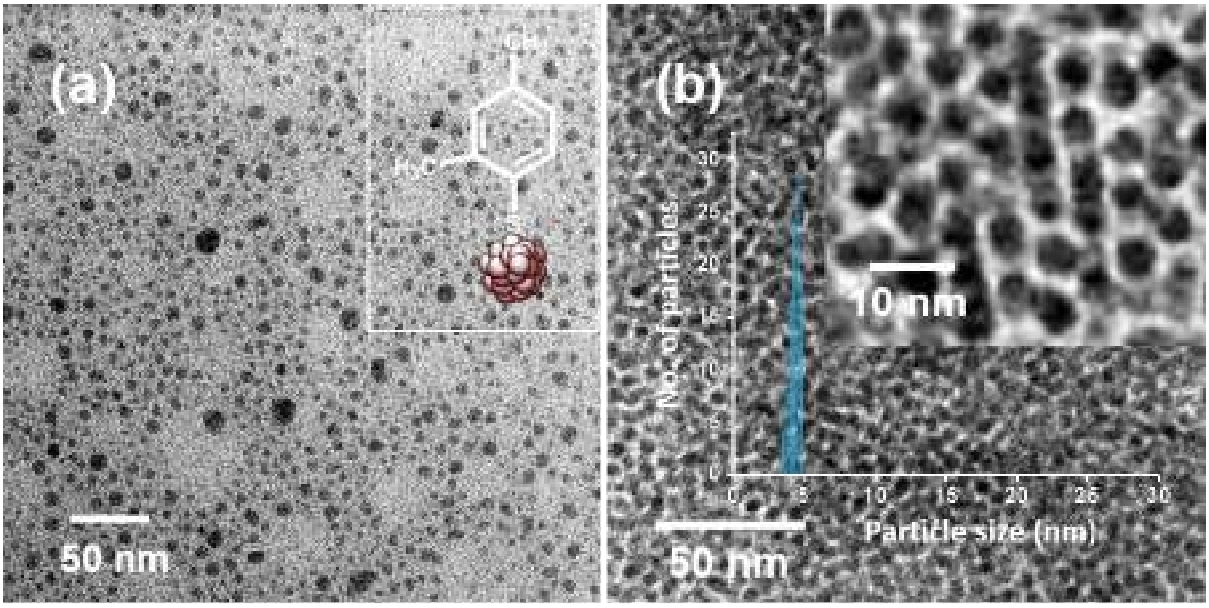

Fig. S10 TEM images of as-synthesized (a) Ag@DMBT NPs. (b) Corresponding monodispersed NPs after electrospray at applied voltage of 8.5 kV, *d* = 1.5 cm. Expanded view of the TEM image and particle size distribution are presentated in the inset. Uniform assembly of NPs of 4.25 ± 0.50 nm was observed after the spray. The ambient microdroplet annealing process was capable of producing such ordered assembly of uniform Ag@DMBT NPs at optimized spray conditions.

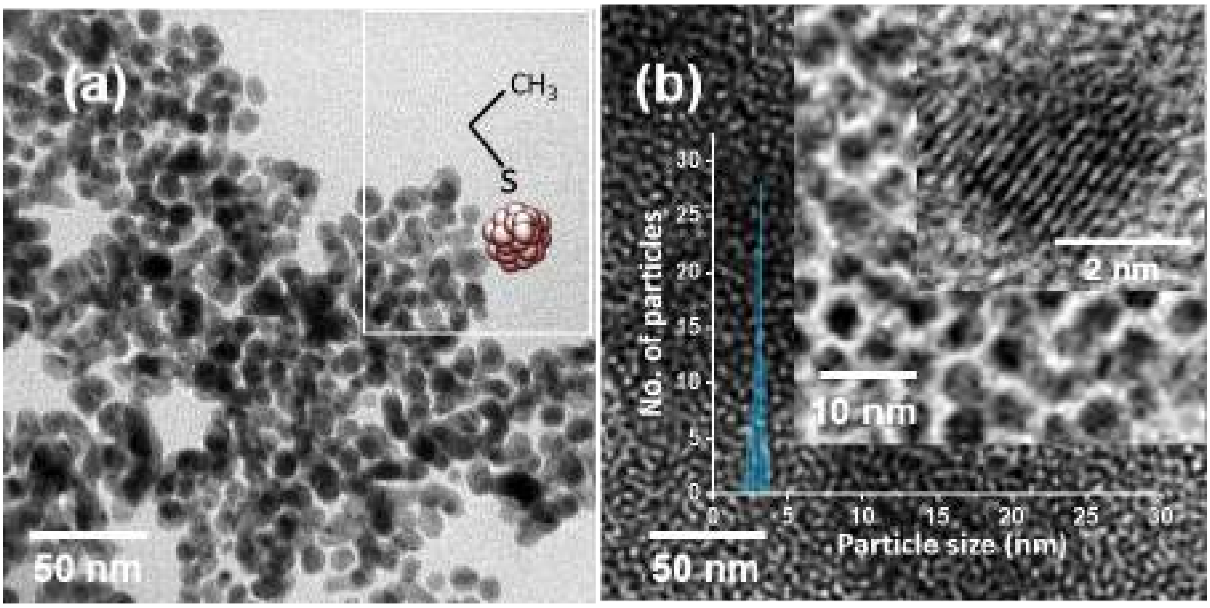

Fig. S11 TEM images of as-synthesized (a) Ag@ET NPs. (b) Corresponding monodispersed NPs after electrospray at applied voltage of 4 kV, d = 1.0 cm. Expanded view of the TEM images and particle size distribution are presentated in the inset. Monodispersed NPs of 3.0 ± 1.0 nm were obtained after the spray. Uniform assembly of NPs was achieved by the ambient microdroplet annealing.

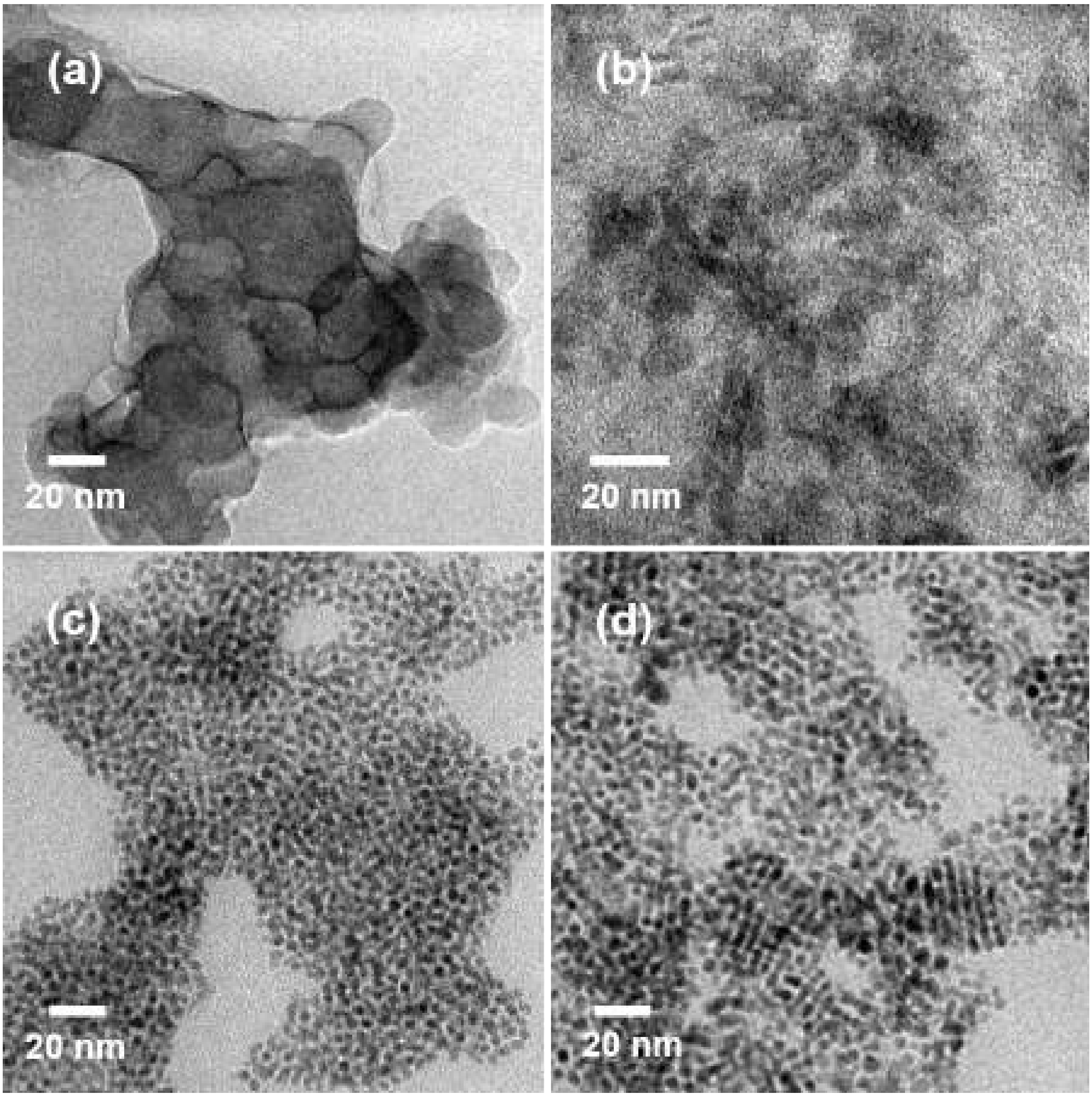

Fig. S12 Variation of concentration of as-synthesized Ag@PET NPs for the creation of organized assemblies. TEM images of the species obtained from (a) 25, (b) 50, (c) 75, and (d) 125 µg/mL concentration of polydispersed Ag@PET NPs. About 100 µg/mL of NPs produced best result as presented in Figure 2. Result revealed that this process is dependent on the concentration of Ag@PET NPs.

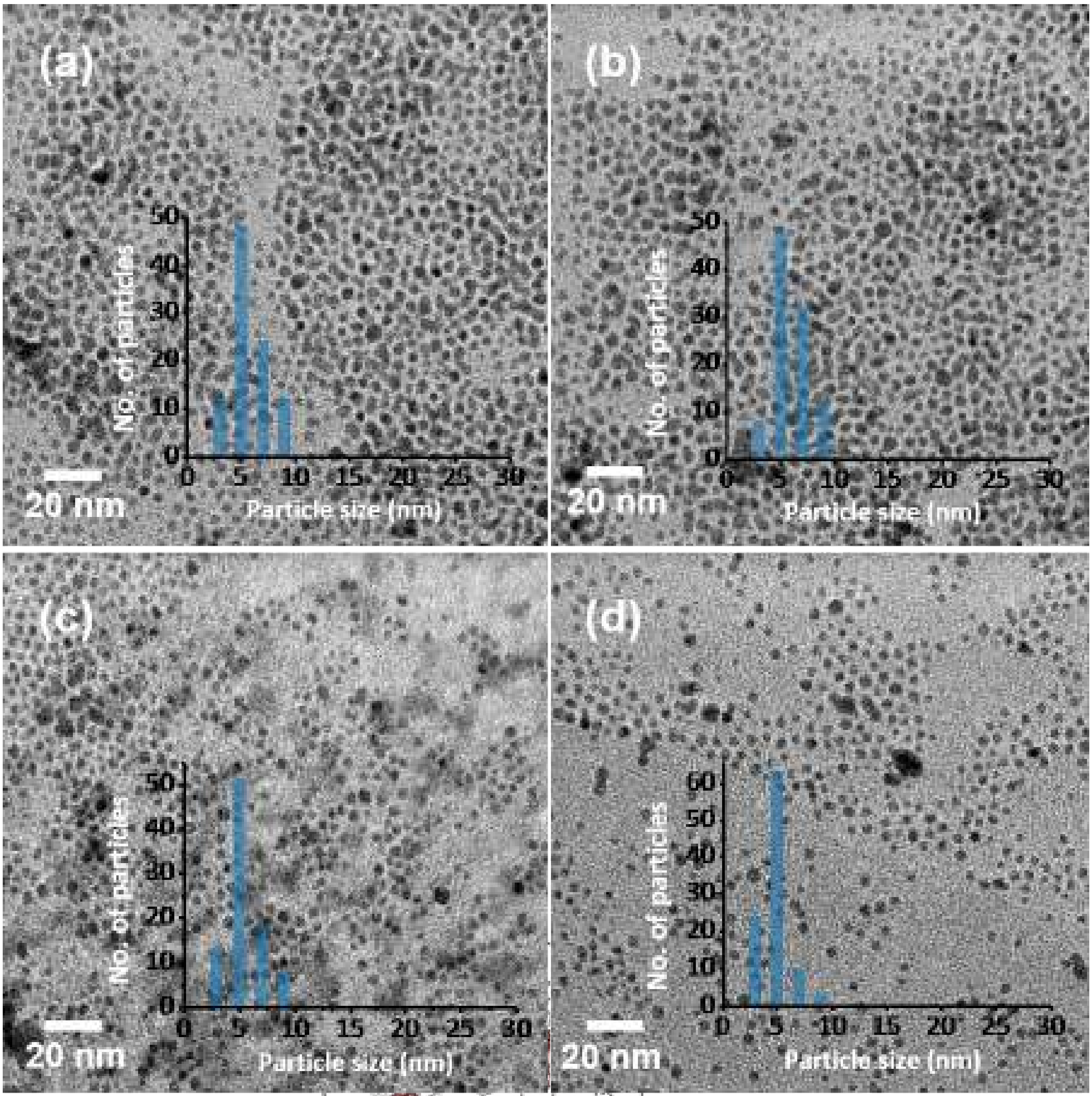

Fig. S13 Spray of polydispersed Ag@PET NPs by using dry N_2 gas. TEM images of monodispersed Ag@PET NPs after spray at different pressures of N_2 gas: (a) 10, (b) 20, (c) 30, and (d) 40 psi.

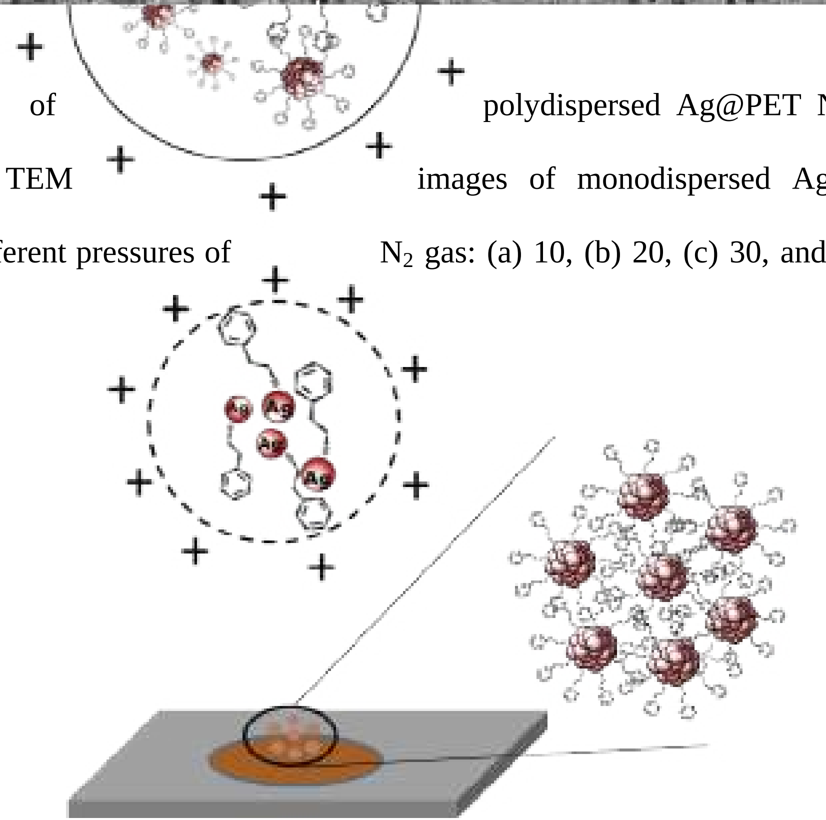

Fig. S14 Schematic representation of a probable mechanism for the formation of monodispersed Ag@PET NPs and their well-defined assemblies via droplets. Our nebulization experiments show that charge on the droplet was not essential.

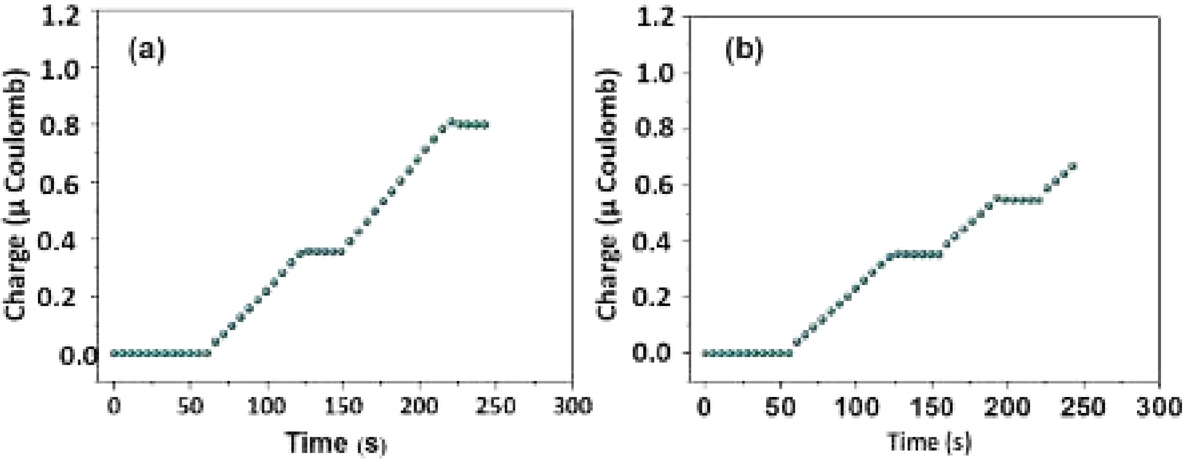

Fig. S15 Measurement of charge of microdroplets loaded with Ag@PET NPs during electrospray deposition with respect to time at *d* of (a) 1.0 cm and (b) 1.5 cm. During the course of electrospray, the charge of the ITO plate (substrate) was measured continuously with respect to time using an electrometer. The charge was increasing upon deposition of positively charged microdroplets on the ITO plate. This experiment was carried out to test the charge of the droplet. It was important to mention that there was no charge accumulation on the substrate during spray. Similar experiments were carried out for *d* of (a) 1.0 cm and (b) 1.5 cm. When the charge was constant, there was no spray, as spray happened in short intervals.

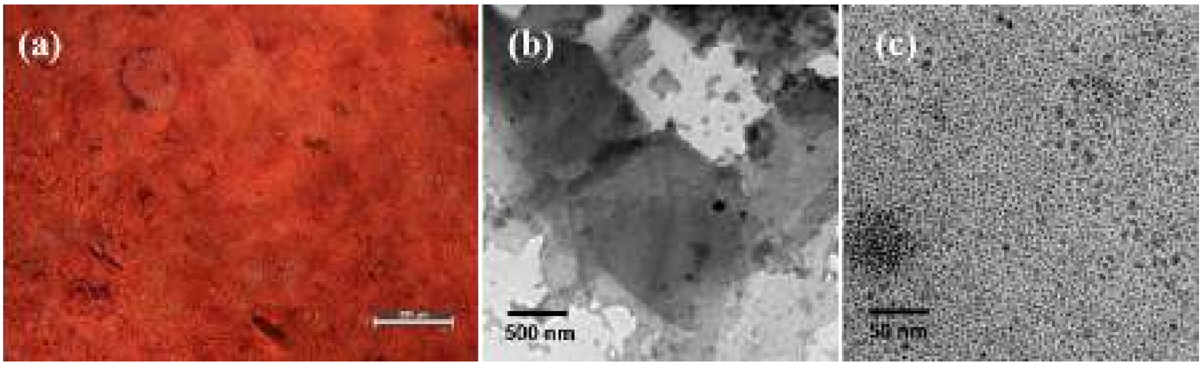

Fig. S16 (a) Optical microscope image of deposited film on ITO surface. Deposited NPs on ITO surface is redispersed in DCM and placed on carbon-coated copper grids. (b) TEM image of NPs film deposited on ITO surface and (c) corresponding high magnification image.

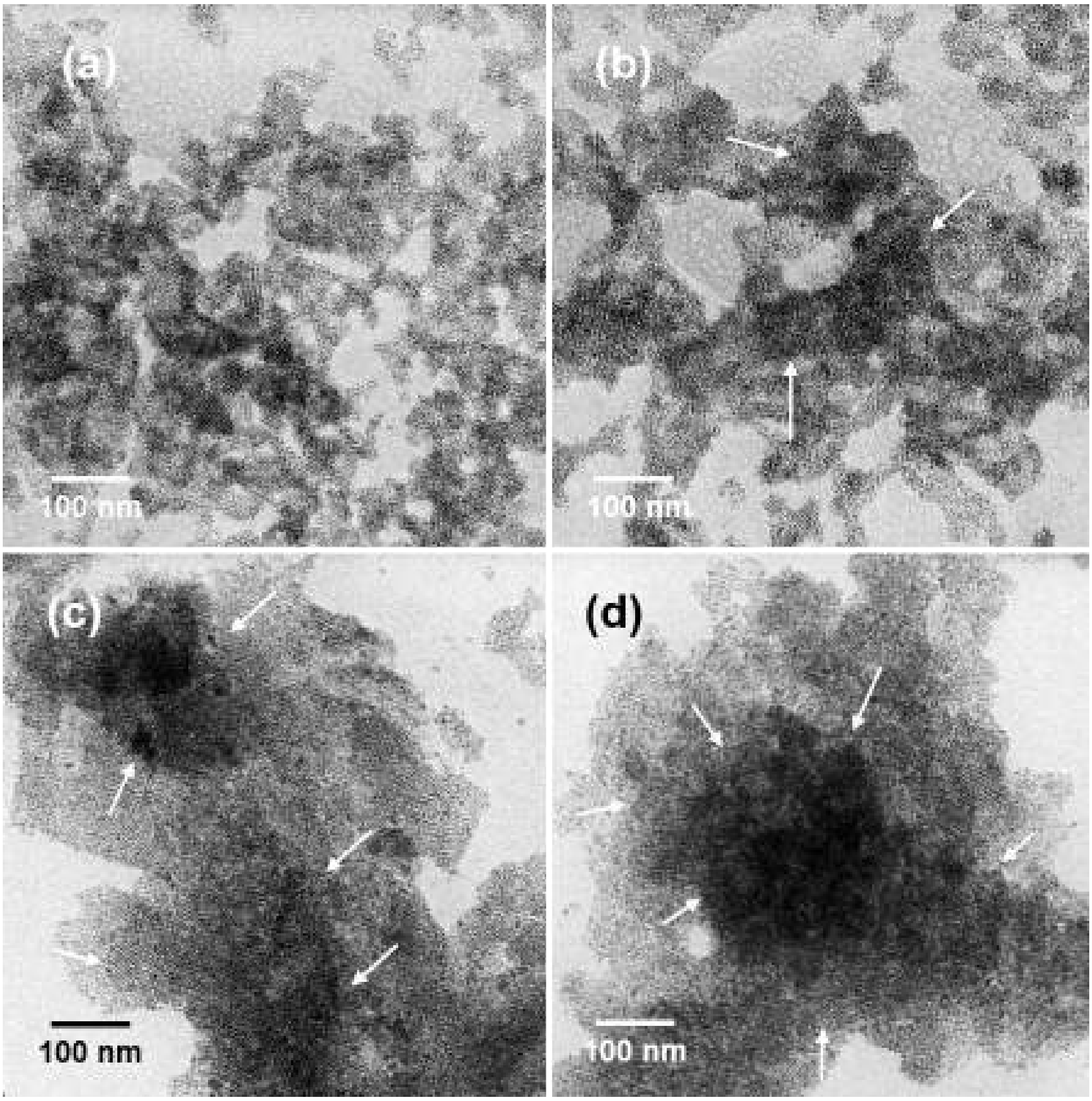

Fig. S17 Formation of 3D assemblies during different times of spray; (a) 4, (b) 6, (c) 8, and (d) 15 min. More layers were generated with respect to time. White arrows indicate the formation of overlayer structures.

ACS Sustainable Chemistry & Engineering

pubs.acs.org/journal/ascecg Research Article

Molecular Materials through Microdroplets: Synthesis of Protein-Protected Luminescent Clusters of Noble Metals

Sandeep Bose, Amit Chatterjee, Shantha Kumar Jenifer, Biswajit Mondal, Pillalamarri Srikrishnarka, Debasmita Ghosh, Angshuman Ray Chowdhuri, M. P. Kannan, Sailaja V. Elchuri, and Thalappil Pradeep*

Cite This: *ACS Sustainable Chem. Eng.* 2021, 9, 4554−4563 Read Online

ACCESS | Metrics & More | Article Recommendations | SI Supporting Information

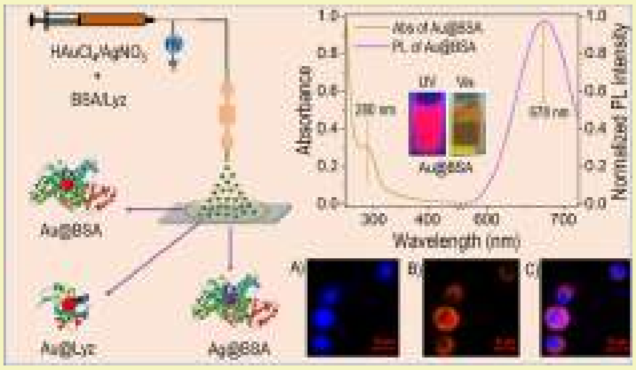

ABSTRACT: Atomically precise noble metal nanoclusters protected with proteins have emerged as a new research frontier in nanoscience due to their unique optical and chemical properties as well as promising applications. In the present work, we have employed an ambient electrospray technique to synthesize protein-protected luminescent clusters of gold and silver within the time scale of a few microseconds, which typically takes hours. In the absence of an electric field, the spray results in nanoparticles and no cluster formation was noticed. Synthesis of these clusters in microdroplets leads to severalfold enhancement in the rate of cluster formation. Spectroscopic investigations such as optical absorption, transmission electron microscopy, and matrix-assisted laser desorption ionization mass spectrometry confirm the molecular nature of the particles formed. Luminescence of electrospray-synthesized clusters shows multifold enhancement as compared to the clusters synthesized in the solution phase. Luminescence of the clusters synthesized in microdroplets increases with the distance traveled by the spray. The formation of clusters via electrospray affects the secondary structure of the protein, and its conformation is different from that of the parent protein. The Au@BSA cluster is utilized for in vitro imaging of retinoblastoma NCC-RbC-51 cells demonstrating a biological application of the resultant material. The absence of solvents and additional reagents enhances the sustainability of the method.

KEYWORDS: *nanoclusters, electrospray, microdroplets, conformation, retinoblastoma*

1. INTRODUCTION

Atomically precise luminescent clusters of noble metals are fascinating materials of immense promise.[1−8] Protein-protected clusters (PPCs) belong to a subclass of atomically precise noble metal clusters.[9−11] They possess many interesting properties, one of which is photoluminescence. Because of their unusual stability at ambient conditions, high quantum yield, and biocompatibility, these clusters are used in diverse areas,[12,13] such as sensing,[14−16] targeted drug delivery,[17,18] biolabeling,[19,20] multimodal imaging,[21−23] therapeutic applications,[24] and so forth. Bovine serum albumin (BSA), lysozyme (Lyz), human serum albumin, lactoferrin, and so forth are a few commonly used proteins to synthesize silver- and gold-based molecular clusters.[25−34]

Electrospray ionization (ESI) is a well-known technique for molecular ionization in mass spectrometry. In the recent past, the electrospray (ES) method has been used for chemical synthesis, which refers to the synthesis of molecules and materials in microdroplets formed in ES. This synthetic tool has been used previously for the generation of nanoparticles and nanostructures.[35−40] Synthesis of such materials in microdroplets leading to new properties such as luminescence in the visible region is yet to be explored. Luminescent materials, especially of biological importance such as PPCs prepared by this technique, will result in new and effective ways of processing such materials, for example, in the development of luminescent thin films. Reports of PPCs in solution suggest that reaction between noble metal ions and macromolecules is a multistep process.[32,41] These involve several complicated processes,[32] such as conformational changes in the protein, formation of metal ion−protein complex, reduction of metal ions, for example, Au^{3+} ions to Au^{0} via Au^{+}, the gradual evolution of clusters by sequential and slow addition of Au atoms to the core, and the formation of

Received: December 17, 2020
Revised: February 26, 2021
Published: March 16, 2021

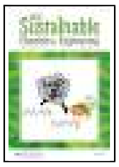

Au−S bonds with cysteine as well as methionine residues of the protein, for protecting the metal core in the solution phase. All of these processes finally result in molecular clusters with intense luminescence. Such synthesis in the solution phase is a slow process and takes several hours to complete.

The fascinating thing about microdroplet reactions is that such processes occur in the timescale of microseconds[42,43] during which the droplets are produced and products are deposited on a collecting surface. Conformational changes of macromolecules and the formation of nanoparticles also occur in microdroplets under similar time scales.[35,39,44,45]

One of the interesting applications of these clusters is their use in bioimaging, especially for cancer cells. Retinoblastoma is a rare form of cancer that rapidly develops from the immature cells of the retina. It is the most common primary malignant intraocular cancer in children and almost exclusively found in young children. Retinoblastoma (Rb) arises due to mutation in the Rb gene leading to inactivated retinoblastoma protein.[46] It is a tumor suppressor protein, and its mutation leads to pediatric intraocular cancer. Rb could be caused either by germline mutation of the Rb1 gene or sporadic external factors and mutagens[47] and viruses like HP.[48] The Rb1 gene was the first tumor suppressor gene to be cloned.[49] Additionally, MYCN amplification could lead to Rb in 3% of tumors.[50,51] Rb tumors could originate from neuronal cells, glial cells, or stem cells of the retina. Besides, a Rb tumor is known to originate from the neuroectodermal cells.[52] The diagnosis of retinoblastoma is usually performed by fundoscopy. Imaging Rb tumors plays an important role in determining the therapeutic interventions as well as in detecting associated brain abnormalities, that is, intracranial tumor extension,[53,54] possible midline intracranial primitive neuroectodermal tumor,[55,56] and brain malformations in patients with 13q deletion syndrome.[57,58] Imaging Rb presents several challenges in front of clinicians due to its superficial position and the presence of fluids in the eye. Second, calcification of the vitreous bodies makes the tumor highly reflective, making imaging challenging.[59] Therefore, new molecules need to be synthesized, which can reach the posterior section of the eye and can image the Rb cells.

All of these together propose the possibility of making luminescent PPCs through microdroplets. In the present work, we have prepared ES-synthesized luminescent Au@BSA clusters, referred to as ES Au@BSA. Similar clusters, ES Au@Lyz and ES Ag@BSA, have also been prepared. We have utilized ES Au@BSA for in vitro imaging of Rb cells. The properties were compared with standard solution-processed samples, referred to as SP Au@BSA, SP Au@Lyz, and SP Ag@BSA. We have also observed that clusters formed by the spray show enhancement of luminescence when compared to those made through conventional SP methods.[28,29,31]

2. EXPERIMENTAL SECTION

2.1. Materials Required. Tetrachloroauric acid trihydrate ($HAuCl_4{\cdot}3H_2O$) was prepared in-house, starting from elemental gold. Silver nitrate ($AgNO_3$) and sodium hydroxide (NaOH) were purchased from Rankem, India. BSA was purchased from Sisco Research Laboratory. Lysozyme (Lyz) and Sodium borohydride ($NaBH_4$, 98%) were purchased from Sigma-Aldrich. Milli-Q water with 18.2 MΩ cm resistivity was used for all these experiments. Sinapic acid (99% purity) was used as the matrix for matrix-assisted laser desorption ionization mass spectrometry (MALDI MS) was purchased from Sigma-Aldrich. All chemicals for the experiment were used without further purification.

2.2. Solution Phase Synthesis of Au@BSA and Au@Lyz Cluster. Au@BSA was synthesized by mixing solutions of BSA and $HAuCl_4$ to get the final concentrations of 169 μM and 1.69 mM, respectively. At the optimized condition, the molar ratio of protein to Au^{3+} was 1:10. The total volume of the solution was 1 mL. To this, 100 μL of 1 M NaOH was added. The resulting mixture was stirred vigorously for 24 h until the solution became golden brown. Similarly, for Au@Lyz, similar concentration ratios of Au^{3+} and Lyz were used and the solution was stirred for 12 h. Both the solutions were freeze-dried and stored at 4 °C for later use. Microdroplets-based synthesis of PPCs will be presented in a later section.

2.3. Solution Phase Synthesis of Ag@BSA Cluster. For Ag@BSA synthesis, an aqueous solution of $AgNO_3$ and BSA having concentrations of 169 μM and 1.69 mM, respectively, were mixed. To this, 100 μL of 1 M NaOH was added. About 1 μL of 0.05 M $NaBH_4$ was added to the resulting mixture and stirred for 30 min until the solution turned golden brown. The sample was freeze-dried and stored at 4 °C for later use.

2.4. MALDI MS of the ES Au@BSA Cluster. MALDI MS of the ES Au@BSA cluster was carried out using a Voyager-DE PRO Biospectrometry Workstation from Applied Biosystems. A pulsed N_2 laser of 337 nm wavelength was used for ionizing the sample. Sinapic acid was chosen as the matrix. Matrix solution was prepared by using a mixture of acetonitrile and 0.1% trifluoroacetic acid in the ratio 1:3 in milli-Q water. About 5 μL of the analyte was mixed thoroughly with 50 μL of the matrix solution in a microcentrifuge tube. About 10 μL of the resulting mixture was spotted on the sample plate and air-dried before the measurement.

2.5. Quantum Yield Measurement of the Solution-Processed (SP) and ES Sample. For the red luminescent Au@BSA, Ag@BSA, and Au@Lyz, the PL quantum yield (QY) was calculated using Rhodamine 6G as a standard (QY = 95%, λ_{exc} = 488 nm). A freshly prepared solution was used to avoid errors. At this excitation wavelength, the absorbance values of both the dye and the clusters were adjusted to be the same. Photoluminescence (PL) spectra were recorded for the solutions with the same absorbance, and areas of the PL curves were calculated. Integrated PL intensities versus the corresponding absorbance values were plotted and fitted with a straight line to obtain two slopes which were utilized for determining the QY, using the established equation

$$\phi_{cluster} = \phi_{dye}(K_{cluster}/K_{dye}) \times (\mathrm{R.\ I.})_{cluster}{}^{2}/(\mathrm{R.\ I.})_{dye}{}^{2}$$

where $K_{cluster}$ and K_{dye} are the straight-line slopes and $(\mathrm{R.I.})_{cluster}$, $(\mathrm{R.I.})_{dye}$, and $\Phi_{cluster}$, Φ_{dye} are the refractive indices of the solvents and quantum yields of the clusters and the dye, respectively.

2.6. Effect of pH Change and Time-dependent Stability of Clusters. The pH of the cluster was adjusted by the addition of aq. NaOH or HCl dropwise. The change in the pH of the solution was measured by a digital pH meter. PL intensities of the samples were measured using a fluorimeter. Time-dependent luminescence intensity measurements were performed for 6 months at an interval of 30 days to check the stability of the clusters.

2.7. Cellular Uptake Studies by Fluorescence Microscopy. NCC-RbC-51 cell lines were procured from Riken cell bank, Japan. The cells were maintained in RPMI 1640 medium with 10% fetal bovine serum at 37 °C in a 5% CO_2 humidified incubator. These cells were incubated with ES Au@BSA clusters, and the uptake studies were performed for a period of 1 and 24 h. After incubation, the cell lines in the medium were centrifuged and the suspension cells were taken for analysis. The cells were mounted on a mounting medium containing Hoechst 33342 to stain the nuclei. These cells were covered with a coverslip and kept for further imaging. An optimized concentration of 1 mg/mL ES Au@BSA was used for uptake studies.

3. RESULTS AND DISCUSSION

3.1. Microdroplets-Based Synthesis. A schematic of the experimental setup is shown in Figure 1. In the present experiment, an aqueous solution of 169 μM $HAuCl_4$ was mixed with 1.69 mM proteins (BSA/Lyz) at 1:1 (v/v) ratio.

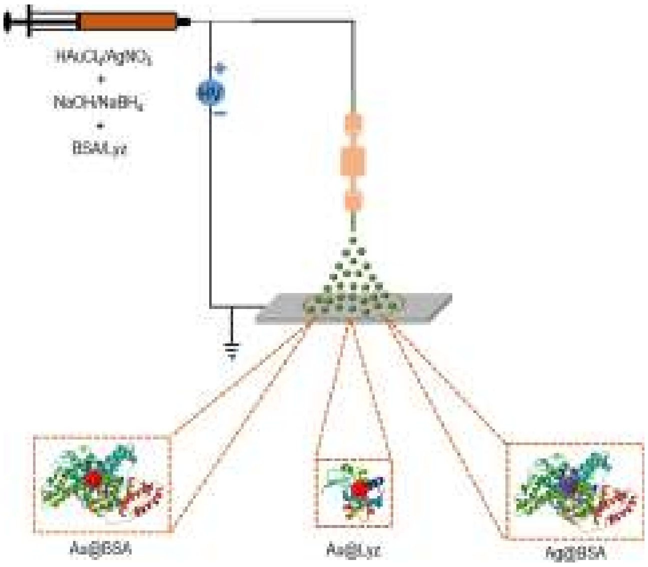

Figure 1. Schematic of the experimental setup utilized to synthesize the clusters by electrospray deposition.

About 100 μL of 1 M NaOH was added to the resulting mixture, and the solution was electrosprayed. A home-built nano-electrospray ionization source was used to direct the charged microdroplets of the resulting mixture. The spray was performed using a Hamilton syringe (1 mL) connected to a capillary delivering liquid at a constant flow rate of 5 μL/min. The potential applied to the tip of the needle was in the range of 4.5−5.0 kV. About 1% methanol was used for better ionization of the charged droplets. During electrospray, the reaction between the precursors takes place in the microdroplets resulting in the formation of luminescent PPCs. This is because during electrospray, solvent evaporation occurs and the electrospray product get deposited on the substrate as a solid. Once it is converted to the solid phase from the aerosol, it is not likely to react with the ligands. Thus, the reaction can only occur during its travel from the tip to the substrate. The reaction product was collected on a conducting glass slide, washed with water, and used for further experiments. The spectroscopic characterizations were performed immediately after synthesis within a time span of 5−10 min. We have varied the applied electric field to observe the change in the luminescence properties of the cluster. Beyond the threshold potential (4.5−5 kV) necessary for electrospray under the present conditions, further increase did not lead to a change in luminescence (Figure S1). Two clusters, namely, ES Au@BSA and ES Au@Lyz, were prepared by this method.

We have selected the proteins BSA and Lyz for electrospray synthesis because these are widely used as model proteins for cluster synthesis. These clusters are biocompatible which enables them to be used in applications such as sensing, biolabeling, multimodal imaging, targeted drug delivery, and so forth unlike thiol-protected noble metal clusters which are toxic to cells, limiting their use in biological mediums for sensing, imaging, and therapeutic purposes. These are also stable in solution as well as in the solid state. These materials can also be used in different physiological conditions. This is why we have selected PPC over other thiol-protected noble metal clusters.

We have selected ES Au@BSA, ES Ag@BSA, and ES Au@Lyz for comparison in our experiments because all of these materials are equally useful for applications in biological mediums. We also want to show that the method is not selective to a particular protein or a particular metal and can be applied universally for the synthesis of different PPCs. Moreover, we want to show that different molecular weights of the proteins (BSA and Lyz) do not affect the cluster formation in charged microdroplets.

For the synthesis of ES Ag@BSA, $AgNO_3$ was used as the starting material. The silver cluster was prepared by keeping Ag and protein concentrations the same as those used for the gold cluster. For the silver cluster, $NaBH_4$ was used as an external reducing agent.[29] For comparison of the ES product with the SP sample, similar concentrations of the gold/silver and proteins were used. To clarify that the reaction occurred in droplets and not in bulk, a mixture of $HAuCl_4$ and BSA (protein in aq. NaOH) was kept without spraying and the product was compared with the ES sample. For comparison of luminescence, the mixture was kept without spraying for 1 h which was similar to the total time duration to complete the electrospray process and process the reaction product to get it into solution. An equal volume of the mixture was taken for electrospray as well as for bulk reaction. While the ES sample shows luminescence, the bulk mixture did not show it (Figure S2). Both the samples had equal time for interaction. Therefore, we concluded that the reaction occurred in the charged droplets, and there was no formation of Au@BSA cluster before the mixture was sprayed. In all of our experiments, we have used the single nozzle spray where the reactants were mixed and sprayed immediately after mixing. A control experiment was performed to check the effect of electrospray on the formation of clusters. In the absence of an applied field, when high-pressure nebulizing gas (N_2) was employed for the reaction, no cluster formation was noticed. The reaction leads to the formation of nanoparticles (Figure S3) that show characteristic plasmonic features for Au and Ag (Figure S4). Figure 2A shows the optical absorption feature of ES Au@BSA along with its luminescence feature. UV−Vis spectra show characteristic absorption of a PPC. Usually, in PPCs, the plasmonic feature of Au/Ag disappears, and there are no distinct absorption features. However, a slight hump appears at 280 nm, which corresponds to the features of aromatic amino acids in the protein. The UV−vis spectra of PPCs are dominated by protein features and features of the cluster core on the other hand are not clearly visible in these spectra as reported in the literature.[27] For this reason, UV−vis spectra of PPCs have not been correlated to the atomicity of the cluster, unlike that of monolayer protected clusters, where these features are more pronounced. A comparison of the UV−Vis spectra of Au_{30}@BSA synthesized by both the SP and ES methods shows similarities in them (Figure S5).

PL features of these ES clusters show emission in the range of 670−685 nm. ES Ag@BSA and ES Au@Lyz show emission maxima at 678 and 684 nm, respectively (Figure S6), whereas ES Au@BSA shows a maximum at 678 nm (Figure 2A). Multiple peak maxima are attributed to the different cluster size distributions or the presence of different chemical environments of the metal core. The excitation wavelength for all these clusters is 365 nm. The inset in Figure 2A displays the photographic image of intense red luminescent ES Au@BSA. The presence of a cluster was further strengthened by XPS analysis, which indicates the presence of a metallic core and proves the absence of metal complexes. In XPS, features at 84.2 and 87.9 eV correspond to $4f_{7/2}$ and $4f_{5/2}$ of a Au (0) core

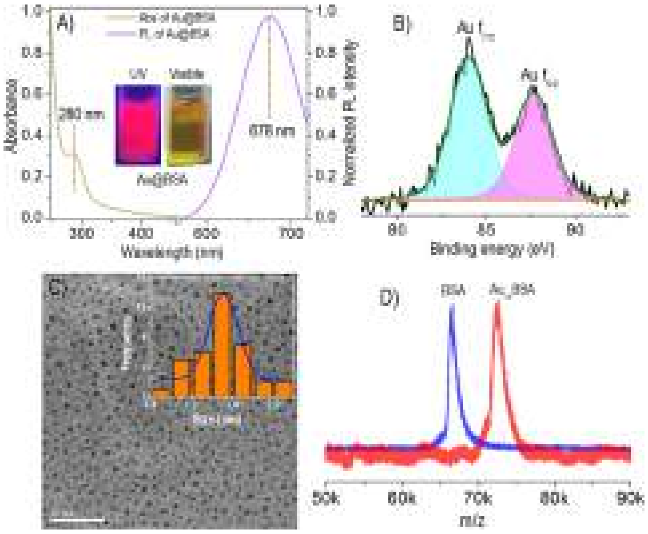

Figure 2. (A) UV−Vis spectrum (left) and PL spectrum (right) of ES Au@BSA. (B) X-ray photoelectron spectrum of ES Au@BSA in the Au 4f region, showing Au (0) oxidation state in the clusters. (C) TEM image of ES Au@BSA cluster with the inset showing the size distribution of these clusters. An average size of 1.5 nm is shown. Clusters show beam-induced damage, and the core size shown is not a true reflection of the cluster size. (D) MALDI MS of BSA and ES Au_{30}BSA. BSA shows a peak at 66,463 Da, and the cluster exhibits a feature at 72,375 Da. The difference between protein and cluster peak is equivalent to 30 Au atoms.

(Figure 2B). There is a slight shift in the binding energy toward a higher value possibly due to the reduced size of the core. Similarly, the Ag (0) core of the cluster was confirmed by peaks at 368.2 and 373.5 eV due to $3d_{5/2}$ and $3d_{3/2}$ of Ag (0), respectively (Figure S7). The spectrum for Ag (0) has a higher binding energy component, which may be assigned to the positively charged silver atoms chemically bonded to the sulfur atoms of the thiol groups present in the protein.[60]

The spectrum for Ag (0) has a higher binding energy component, which may be assigned to the smaller clusters or surface atoms of a cluster. The XPS feature around 163 eV is attributed to $2p_{3/2}$ of sulfur, which is characteristic of thiolate binding to the Au/Ag core (Figure S8). Therefore, it is clear that the core of the cluster is stabilized by the thiol groups of proteins. The TEM image has shown (Figure 2C) the presence of nanometer-sized clusters. Protein-protected Au or Ag nanoclusters with a small core size are ultrasmall nanoparticles and are typically below 2 nm in diameter. However, the size distribution of the cluster from the TEM image presents an average size of 1.5 nm. This is because these clusters are sensitive toward the high-energy electron beam, and nanoparticles were formed due to the aggregation of clusters caused by continuous irradiation of the beam. This has been studied in detail in the past.[61] TEM images of ES Ag@BSA and ES Au@Lyz are shown in Figure S9. Molecular nature of the ES Au@BSA cluster was confirmed by the MALDI mass spectrum. Figure 2D displays the mass spectrum of the protein, BSA, along with that of the gold cluster. The spectra were collected in the positive mode. The mass spectrum of BSA shows a distinct peak at m/z of 66,463 Da due to a mono-cation. We have observed another distinct feature for our ES Au@BSA cluster at m/z of 72,375 Da. The difference between the cluster peak and parent protein peak is equivalent to the mass of 30 Au atoms, and hence, we have assigned this peak to a Au_{30} core encapsulated with BSA. There are 35 cysteine and 5 methionine residues in 1 BSA. This favors the formation of a Au_{30} core inside a BSA molecule. This cluster was previously reported and studied with different techniques.[27,62,63] We followed the same ratio of metal ion/protein concentration during electrospray synthesis. As a result, the Au_{30} core was formed. No other cluster core was seen, and no parent protein was observed. Optical absorption features and TEM images of SP clusters were used as a reference to confirm the molecular nature of ES Ag@BSA and ES Au@Lyz (Figure S10).

Stability of the ES clusters was measured over a period of about 6 months. No significant change was noticed in stability when measured at an interval of 30 days. After 6 months, almost 90% of the luminescence intensity was intact in these clusters (Figure S11A). The retention of PL properties for such a long time enables its utility for bioimaging and sensing. Biocompatibility of the clusters made them useful to work effectively in the biological medium for which understanding the stability of these clusters over varying pH ranges is essential. As these clusters are encapsulated in proteins, the effect of pH on the capping is more prominent than the cluster core. Figure S11B shows the change in luminescence intensity at varying pH. When the solution was changed from acidic to alkaline medium, there was an increase in the luminescence intensity of the clusters. This is because tyrosine (Tyr) residues in the protein can reduce Au (III) ions through their phenolic groups, and their reduction capability can be greatly improved by adjusting the pH of the reaction above the pK_a of Tyr (~10).[9] We observed an increase in luminescence intensity

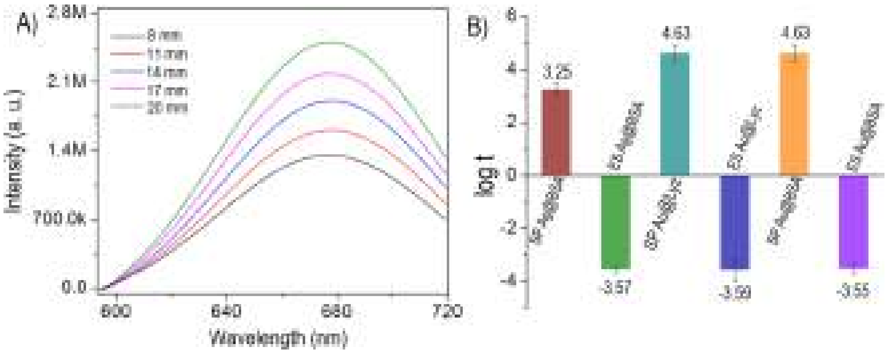

Figure 3. (A) Distance-dependent luminescence measurement to show the formation and origin of luminescence of ES Au@BSA clusters in microdroplets. (B) Comparison of the total time required for the synthesis of clusters (in terms of log scale) in the solution phase as well as by electrospray.

https://doi.org/10.1021/acssuschemeng.0c09145
ACS Sustainable Chem. Eng. 2021, 9, 4554−4563

while changing the pH from acidic to alkaline as evident from Figure S11B.

3.2. Origin of Luminescence and Enhanced Rate of the Reaction.

To prove the origin of luminescence in droplets, distance-dependent luminescence measurements were performed. Solutions of the same concentrations were electrosprayed for the same time at different distances (d), and luminescence was measured. With an increase in distance, d, enhancement in luminescence was noticed (Figure 3A). The reason for such an enhancement could be the enhanced reactivity in the droplets as the reactants get more time to react when the distance goes on increasing. We have further increased the tip to substrate distance (up to 32 mm) to check its effect on luminescence (Figure S12). From the experiment, we have observed that up to a certain distance, luminescence is increasing but the increase is not linear. This may be due to the fact that during the electrospray process, solvent evaporation occurs and the droplet concentrates with an increase in distance. This may lead to self-quenching of the luminescent material in the droplets or it may be quenched due to the presence of water (solvent), which is a well-known quencher. Increasing the distance beyond a certain point shows that luminescence is almost constant. This may be due to the fact that after a certain distance, the reaction comes to an end as a result of the complete evaporation of the droplet.

We have compared the time required for the solution-phase synthesis of clusters with that of ES clusters. The reaction time for the formation of ES clusters is the same as the time of travel of the droplets from the nozzle tip to the solid substrate. The reaction time for the traveling droplets was adjusted by varying the distance between the tip to the substrate. The movements of the droplets were recorded using a high-speed camera at 400,000 frames per second (fps) (Figure S13). The time gap between two images is 2.5 μs. The velocity distribution of the microdroplets was determined by tracking 20 individual droplets. The velocity distribution of the microdroplets was fitted with a straight line which shows a constant velocity of the droplets during the reaction (Figure S14). The detail of the velocity calculation is discussed in the Supporting Information. The estimated reaction time was calculated by integrating the speed of the microdroplets over the travelling distance. The travelling time, that is, the time of product formation for ES Au@Lyz, ES Ag@BSA, and ES Au@BSA, were calculated as 260.9, 267.5, and 282.0 μs, respectively, whereas in the solution phase, the time required for the formation of these clusters was 12 h, 30 min, 12 h, respectively. These SP clusters are termed as SP Au@Lyz, SP Ag@BSA, and SP Au@BSA, respectively. Figure 3B shows the plot of the comparison of time required for the synthesis of clusters in the solution phase as well as by electrospray, plotted on a logarithmic scale. For SP clusters, the time required was several hours and hence shows a value in the positive axis. However, the ES clusters require very little time, of the order of microseconds and show a value in the negative axis, which is evident from the graph. The rate of enhancement of reactions can be calculated by taking an antilog of the difference between the values for both processes. The values of the rate of enhancement of the reaction in droplets for ES Ag@BSA, ES Au@Lyz, and ES Au@BSA, respectively, were 6.72×10^6, 1.65×10^8, and 1.53×10^8 times faster than that of SP synthesis. Synthesis of protein-protected clusters at such a fast rate is an exciting phenomenon because during this small time scale, several processes, such as reduction of Au^{3+} to Au, conformational changes in proteins, the formation of metal−protein complex, aggregation of the gold atoms to form clusters, and any other event involved in forming a stable cluster, occurs. As the process is extremely fast, it is difficult to perform spectroscopy on the droplets and understand the phenomena happening in single droplets. Hence, the complete mechanism of the reaction is uncertain.

3.3. Enhancement of Luminescence Using Droplets.

For a given concentration of the reactants, when luminescence of clusters prepared by both the methods were compared, we observed an enhancement in luminescence for the ES cluster. ES Au@BSA shows 2-fold enhancement in luminescence, whereas ES Ag@BSA and ES Au@Lyz show 1.2- and 1.6-fold enhancement, respectively (Figure 4). In order to make this comparison, the amount of clusters used and all other parameters such as volume, temperature, pH, excitation wavelength, age of the samples, and spectrometer parameters were held the same.

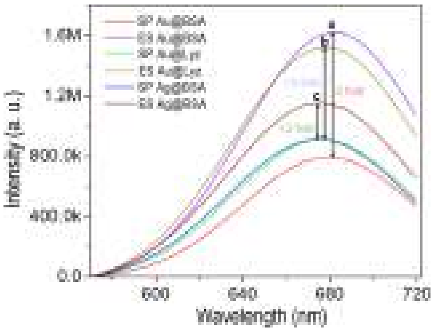

Figure 4. Comparison of luminescence of ES clusters with the SP clusters for a given concentration. ES clusters show 2-fold, 1.6-fold, and 1.2-fold enhancement in luminescence for ES Au@BSA, ES Au@Lyz, and ES Ag@BSA, respectively, compared to SP clusters.

In the solution phase, the reactant gets enough time to react and form luminescent clusters, but in droplets, the interaction time between the reactants is less. Such a small interaction time leading to luminescence enhancement is intriguing. Luminescence from these clusters is strongly dependent on their physicochemical environment. There are several factors that could possibly affect luminescence; one is the unfolding of proteins in microdroplets. Some of the important factors that affect the molecular environment of the protein around the cluster core are solvents, external salts, buffers, pH, ionic strength, oxygen content, and temperature. Lee et al. have shown that cytochrome *c* in a slightly acidic environment can lead to conformational changes in the protein.[45] However, reports also exist on the base-induced unfolding of proteins where an increase in pH leads to the breaking of disulfide bonds.[32] During electrospray, the use of a base such as NaOH can result in the unfolding of proteins. The presence of an electric field could also break the hydrogen bonds and electrostatic interactions that result in additional unfolding. This leads to an enhancement in the metal (Au/Ag)−ligand (S) interaction responsible for charge transfer. With all these, there is an enhancement in luminescence. From the MALDI MS, we obtain a Au_{30} cluster core with the number of gold atoms higher than the previously reported Au_{25} cluster core.[9] This could also result in the enhancement of metal−ligand interaction. Another factor that possibly contributes to the enhanced luminescence is the evaporation of the solvent during the process. As the solvent evaporates, the droplets concentrate, and the reactants are in close vicinity of each other and are forced to react under the field. This results in the enhancement of luminescence in comparison to the SP method, where the reactants are in random motion and get distributed over a large volume.

Generally, noncovalent interactions make the clusters more rigid and energetically stable. Such interactions restrict the intramolecular vibrational/rotational motions, which help in increasing the radiative processes and reduce the nonradiative processes. During electrospray, protein unfolding happens that enhances the internal motions of the protein and increases the nonradiative processes leading to a reduction in luminescence of the clusters. There are two factors that enhance luminescence, whereas the other quenches luminescence. Thus, the overall enhancement is less pronounced as luminescence is a result of all these factors. Spectroscopic investigations on these fast-moving charged droplets may shed light on the possible mechanism of luminescence enhancement in these ES clusters. Figure S15 shows the comparison of QY between the ES clusters and SP clusters. It is to be noted that the measured QYs of ES Au@BSA, ES Au@Lyz, and ES Ag@BSA are 9.8, 7.2, and 4.9%, respectively, which is higher than that of SP clusters (5.2, 4.8, and 3.9%, respectively). QY values are a reflection of the enhanced luminescence in ES clusters.

3.4. Understanding the Conformational Changes of the Protein in ES Au@BSA. For understanding the secondary structure of protein during electrospray, a double derivative of FTIR was studied. We have employed the technique to understand conformational changes in the protein before and after the formation of the cluster. We have utilized only BSA, SP Au@BSA, and ES Au@BSA for the study. In FTIR studies, change in the secondary structure of the protein is reflected in the characteristic stretching and bending vibrations arising in the amide region, namely amide I ($1600-1690$ cm^{-1}), amide II ($1480-1575$ cm^{-1}), amide III ($1229-1301$ cm^{-1}), and amide A (3300 cm^{-1}). The band close to 1650 cm^{-1} is due to the C=O stretching vibration and out of plane C−N stretching, a signature of amide I region. Amide II region is attributed to the N−H bending vibration. A broad feature around $3000-3300$ cm^{-1} corresponds to the amide A region and is attributed to the N−H or O−H stretching vibration. Figure S16 shows the FTIR spectra of BSA and ES Au@BSA. As the amide I region is more sensitive to the secondary structure of the protein, we have performed the second derivative of IR ($1600-1690$ cm^{-1}). The bands in the regions of 1648−1660, 1612−1642, 1662−1688, and 1648 ± 2 are assigned to α-helix, β-sheets, β-turns, and random coils, respectively. Therefore, in the second derivative IR of BSA, the peak at 1651 cm^{-1} was assigned to α-helix and bands from $1615-1639$ cm^{-1} were assigned to β-sheets. A new band appearing in the 1648 cm^{-1} range of ES Au@BSA is assigned to the random coil or unordered structure (Figure 5). On the other hand, the band at 1651 cm^{-1} is becoming featureless as we move from BSA to ES Au@BSA as the protein structure became relaxed due to the perturbation in the α-helical region. This indicates a large change in the protein structure. When compared with the FTIR of BSA, there is a change in the protein structure for the SP Au@BSA also. But no noticeable change is there in the FTIR spectra of SP Au@BSA and ES Au@BSA.

3.5. Bioimaging of Retinoblastoma Cells. Rb is an intraocular tumor that is curable if diagnosed early. The mode of treatment for Rb has changed from systemic chemotherapy to direct ophthalmic artery chemotherapy and intravitreous injection.[64,65] Success has been achieved in ocular survival, but treating the tumors that grow from the retina to the vitreous humor, namely vitreous seeds, has been more difficult to cure and may relapse. On the basis of the appearance in fundoscopy, these vitreous seeds were classified as dusts, spheres, and clouds.[66] Dusts are loose tumor cells in the vitreous, clouds are dense tumor fragments formed by translocation of the primary tumor content to the vitreous, and spheres are translucent solid tumors formed by further clonal growth of the dust or the cloud or by sprouting of the primary retinal tumor.[67] Each class of seeds required a different dose and number of intravitreal injections. Thus, imaging the Rb tumor to identify the type of seeds so that the right concentration and dose of chemotherapy can be selected is an unmet need for the treatment of Rb.

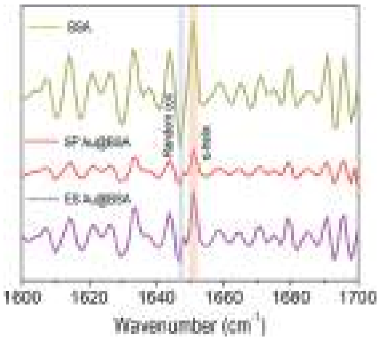

Figure 5. Second derivative FTIR spectra of BSA and ES Au@BSA. Decrease in the intensity of α-helix and the evolution of random coil nature in ES Au@BSA confirm the conformational changes in the protein after cluster formation.

Previous studies have used topotecan, a fluorescent drug for the visualization of tumors and seeds.[68] Corson et al. have used bioluminescence imaging of luciferase-expressing human retinoblastoma cells injected into the vitreous of newborn rat eyes, but spatial and temporal development of tumors in this model has not been studied.[69] In the present study, we have used a red luminescent ES Au@BSA cluster for imaging Rb cells. Several previous studies have demonstrated the performance of SP clusters for bioimaging purposes.[70,71] Research is still evolving for improving the quantum efficiency of nanoclusters and several methods such as aggregation of nanoclusters are employed for increasing the quantum yield.[72] We made ES clusters that exhibited enhanced quantum yields compared to SP clusters. Therefore, we tested these clusters for bioimaging purposes. We have used commercial retinoblastoma cell lines NCC-RbC-51 (metastatic cell lines), which grow as loose aggregates, resembling vitreous seeds, classified as dust.[73] Before the experiment, the stability of ES Au@BSA cluster in the RPMI 1640 medium was measured. The cluster shows good stability for 40 h and no degradation was noticed (Figure S17A). Excitation at 480 nm was used for the fluorescence imaging of Rb cells (Figure S17B). Our results showed that with as low a concentration as 1 mg/ml and within 1 h of treatment, there was uptake of the nanocluster (Figure S18). This suggests that the cluster shows good penetration into the Rb cells and could be used for rapid fluorescence imaging of the cells. Rapid imaging techniques are needed in RB tumor imaging as usually patients are children below 5 years of age and longer time interval modalities are difficult to administer. This could be used as an alternative to

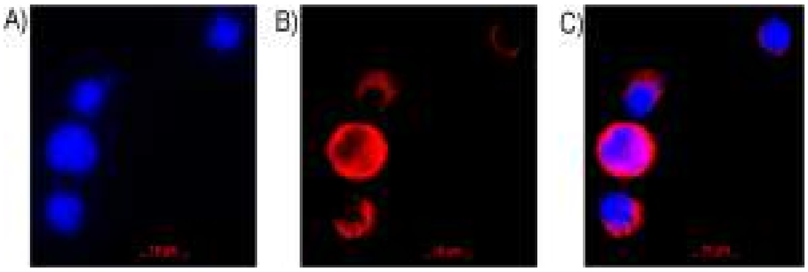

Figure 6. Fluorescence microscopic image of ES Au@BSA cluster in retinoblastoma NCC-RbC-51 cells after 24 h incubation. 1 mg/mL of cluster concentration was used for imaging. (A) Cell nucleus stained with DAPI. (B) Fluorescent image of ES Au@BSA cluster showing red luminescence inside the cells. (C) Overlay of the images, A and B showing the selective diffusion of ES Au@BSA cluster into the cytosol of the cells.

other luminescent materials which take more time for uptake and cause cell toxicity. Cellular uptake of the particles was increased up to 24 h (Figure 6). These particles are expected to be nontoxic to Rb cells as the BSA-protected noble metal clusters are known to be nontoxic to cancer cells.[41] Ag_{18}@BSA clusters synthesized previously by our group exhibited no toxicity to HeLa cells for a period of 24 h at varying concentrations from 2 to 10 μM.[41] The newly synthesized cluster diffused gradually into the cytosol and localized in it, in agreement with an earlier study which showed that atomically precise metal clusters localize in cytosol after 24 h.[41] The nucleus was stained with DAPI in these experiments. The results indicate that the molecular cluster can be used as an excellent probe for in vitro imaging of NCC-RbC-51 cell lines. Thus, in a clinical scenario, the synthesized clusters could be used to image the dust of vitreous seeds in Rb patients. It could also be used to identify the type of vitreous seeds present in Rb patients.

The fluorescence intensity from these clusters is generally lower than that from organic dyes. Although the luminescence intensity is less compared to that of organic dyes, these clusters show stable luminescence in cells, unlike organic dyes that undergo photobleaching. We have performed a photobleaching experiment under UV irradiation for both the cluster and a dye (rhodamine 6G) using UV irradiation (300 W, for 5 min). We have observed a slight change in the luminescence of the cluster, whereas the luminescence of the dye was significantly reduced. When the UV light was turned off, reversible photobleaching leads to a complete recovery of luminescence after 30 min for the cluster, which was not observed in the case of the dye (Figure S19). Similar reversible photobleaching for clusters was observed by Hemmateenejad et al.[74] Hence, these clusters can be used effectively for diagnosis and imaging purposes. The tumor-specific targeting of gold clusters was achieved in earlier studies by targeting specific molecules on cancer cells such as integrins and folate receptors using RGD peptides and folate-conjugated gold clusters, respectively.[75,76] Cancer cells specifically overexpress Nucleolin proteins on the cell surface. An aptamer targeting this protein, AS1411, was conjugated to the gold clusters to achieve tumor-specific targeting.[77] In future studies, we will conjugate ES clusters to EpCAM aptamer that would specifically target cancer cells.[78]

3.6. Sustainability of the Electrospray Method. Electrospray is a simple, direct, and one-step method for the synthesis of these luminescent clusters in charged microdroplets. The synthetic method is one-pot and does not require harsh experimental conditions such as high temperature or pressure. We have employed water as a solvent and avoided the use of organic solvents. The method also uses a reduced quantity of solvents for the production of materials as compared to the solution phase. Major advantage of this method is that it minimizes the amount of reagents needed for the synthesis and hazardous reducing agents such as N_2H_4, formaldehyde, ethylene glycol, and so forth are not used. The single-step process ensures no wastage of materials during the synthesis as compared to a multistep process where processing involves loss of solvents and other chemicals. Ambient processing, use of water as the solvent, absence of hazardous reducing agents, reduced time, reduced waste of materials, and direct deposition on substrates of choice make this method a more sustainable and greener alternative to traditional methods.

The other advantage of using electrospray is that it requires only a few microseconds for the actual process of synthesis. Hence, we can synthesize larger quantities of materials in less time using the spray method as compared to the solution phase. A multinozzle spray can be used for scaling up the production of materials if required. Moreover, the synthesis of these materials can also be performed using an electrospinning machine where a larger volume of solution can be used just like the solution-phase synthesis. Hence, in terms of yield, quality of the product, and total time needed for materials production, we believe that the electrospray method is better.

4. CONCLUSIONS

In summary, we have successfully synthesized red luminescent protein-protected clusters using charged microdroplets. The molecular nature of the cluster was confirmed by MALDI MS, which revealed that ES Au@BSA has an Au_{30} core. Synthesis of the clusters in microdroplets leads to severalfold enhancement in the rate of the reaction. ES clusters show severalfold enhancement in luminescence when compared to the same clusters prepared by the conventional solution-phase method. The origin of luminescence in microdroplets was proven by measuring distance-dependent luminescence. The ES Au@BSA cluster was utilized for in vitro imaging of retinoblastoma NCC-RbC-51 cells, which will be useful for diagnosis and for detecting associated brain abnormalities.

■ ASSOCIATED CONTENT

Supporting Information

The Supporting Information is available free of charge at https://pubs.acs.org/doi/10.1021/acssuschemeng.0c09145.

Detailed description of instrumentation, spectroscopic data, and other results (PDF)

AUTHOR INFORMATION

Corresponding Author

Thalappil Pradeep − *DST Unit of Nanoscience (DST UNS) and Thematic Unit of Excellence (TUE), Department of Chemistry, Indian Institute of Technology Madras, Chennai 600 036, India*; orcid.org/0000-0003-3174-534X; Phone: 91-44-22574208; Email: pradeep@iitm.ac.in; Fax: 91-44-2257 0545/0509

Authors

Sandeep Bose − *DST Unit of Nanoscience (DST UNS) and Thematic Unit of Excellence (TUE), Department of Chemistry, Indian Institute of Technology Madras, Chennai 600 036, India*

Amit Chatterjee − *Department of Nanobiotechnology, Vision Research Foundation, Sankara Nethralaya, Chennai 600006, India*

Shantha Kumar Jenifer − *DST Unit of Nanoscience (DST UNS) and Thematic Unit of Excellence (TUE), Department of Chemistry, Indian Institute of Technology Madras, Chennai 600 036, India*

Biswajit Mondal − *DST Unit of Nanoscience (DST UNS) and Thematic Unit of Excellence (TUE), Department of Chemistry, Indian Institute of Technology Madras, Chennai 600 036, India*

Pillalamarri Srikrishnarka − *DST Unit of Nanoscience (DST UNS) and Thematic Unit of Excellence (TUE), Department of Chemistry, Indian Institute of Technology Madras, Chennai 600 036, India*; orcid.org/0000-0001-5187-6879

Debasmita Ghosh − *DST Unit of Nanoscience (DST UNS) and Thematic Unit of Excellence (TUE), Department of Chemistry, Indian Institute of Technology Madras, Chennai 600 036, India*

Angshuman Ray Chowdhuri − *DST Unit of Nanoscience (DST UNS) and Thematic Unit of Excellence (TUE), Department of Chemistry, Indian Institute of Technology Madras, Chennai 600 036, India*

M. P. Kannan − *DST Unit of Nanoscience (DST UNS) and Thematic Unit of Excellence (TUE), Department of Chemistry, Indian Institute of Technology Madras, Chennai 600 036, India*

Sailaja V. Elchuri − *Department of Nanobiotechnology, Vision Research Foundation, Sankara Nethralaya, Chennai 600006, India*; orcid.org/0000-0002-9780-2717

Complete contact information is available at:
https://pubs.acs.org/10.1021/acssuschemeng.0c09145

Notes

The authors declare no competing financial interest.

ACKNOWLEDGMENTS

We would like to thank the Department of Science and Technology, Government of India for constantly supporting our research program of nanomaterials. S.B., B.M., S.K.J., D.G., P.S., and A.R.C. thank IIT Madras for their research fellowships. A.C. thanks SERB/DST (Grant no- EMR/2015/000607) for a research fellowship. M.P.K. thanks MRF for a fellowship. T.P. acknowledges funding for the Centre of Excellence on Molecular Materials and Functions by IIT Madras.

REFERENCES

(1) Mathew, A.; Pradeep, T. Noble Metal Clusters: Applications in Energy, Environment, and Biology. *Part. Part. Syst. Char.* **2014**, *31*, 1017−1053.

(2) Udayabhaskararao, T.; Pradeep, T. New Protocols for the Synthesis of Stable Ag and Au Nanocluster Molecules. *J. Phys. Chem. Lett.* **2013**, *4*, 1553−1564.

(3) Jin, R.; Zeng, C.; Zhou, M.; Chen, Y. Atomically Precise Colloidal Metal Nanoclusters and Nanoparticles: Fundamentals and Opportunities. *Chem. Rev.* **2016**, *116*, 10346−10413.

(4) Jin, R. Atomically Precise Metal Nanoclusters: Stable Sizes and Optical Properties. *Nanoscale* **2015**, *7*, 1549−1565.

(5) Zheng, J.; Nicovich, P. R.; Dickson, R. M. Highly Fluorescent Noble-Metal Quantum Dots. *Annu. Rev. Phys. Chem.* **2007**, *58*, 409−431.

(6) Hassinen, J.; Pulkkinen, P.; Kalenius, E.; Pradeep, T.; Tenhu, H.; Häkkinen, H.; Ras, R. H. A. Mixed-Monolayer-Protected Au25Clusters with Bulky Calix[4]arene Functionalities. *J. Phys. Chem. Lett.* **2014**, *5*, 585−589.

(7) Chakraborty, I.; Pradeep, T. Atomically Precise Clusters of Noble Metals: Emerging Link between Atoms and Nanoparticles. *Chem. Rev.* **2017**, *117*, 8208−8271.

(8) Krishnadas, K. R.; Natarajan, G.; Baksi, A.; Ghosh, A.; Khatun, E.; Pradeep, T. Metal-Ligand Interface in the Chemical Reactions of Ligand-Protected Noble Metal Clusters. *Langmuir* **2019**, *35*, 11243−11254.

(9) Xie, J.; Zheng, Y.; Ying, J. Y. Protein-Directed Synthesis of Highly Fluorescent Gold Nanoclusters. *J. Am. Chem. Soc.* **2009**, *131*, 888−889.

(10) Xavier, P. L.; Chaudhari, K.; Baksi, A.; Pradeep, T. Protein-Protected Luminescent Noble Metal Quantum Clusters: An Emerging Trend in Atomic Cluster Nanoscience. *Nano Rev.* **2012**, *3*, 14767.

(11) Chevrier, D. M.; Thanthirige, V. D.; Luo, Z.; Driscoll, S.; Cho, P.; MacDonald, M. A.; Yao, Q.; Guda, R.; Xie, J.; Johnson, E. R.; et al. Structure and Formation of Highly Luminescent Protein-Stabilized Gold Clusters. *Chem. Sci.* **2018**, *9*, 2782−2790.

(12) Goswami, N.; Zheng, K.; Xie, J. Bio-NCs - the marriage of ultrasmall metal nanoclusters with biomolecules. *Nanoscale* **2014**, *6*, 13328−13347.

(13) Sun, C.; Yang, H.; Yuan, Y.; Tian, X.; Wang, L.; Guo, Y.; Xu, L.; Lei, J.; Gao, N.; Anderson, G. J.; et al. Controlling Assembly of Paired Gold Clusters within Apoferritin Nanoreactor for in Vivo Kidney Targeting and Biomedical Imaging. *J. Am. Chem. Soc.* **2011**, *133*, 8617−8624.

(14) Mathew, A.; Sajanlal, P. R.; Pradeep, T. Selective Visual Detection of TNT at the Sub-Zeptomole Level. *Angew. Chem., Int. Ed.* **2012**, *51*, 9596−9600.

(15) Hu, D.; Sheng, Z.; Gong, P.; Zhang, P.; Cai, L. Highly Selective Fluorescent Sensors for Hg2+ Based on Bovine Serum Albumin-Capped Gold Nanoclusters. *Analyst* **2010**, *135*, 1411−1416.

(16) Chen, T.-H.; Tseng, W.-L. (Lysozyme Type VI)-Stabilized Au8 Clusters: Synthesis Mechanism and Application for Sensing of Glutathione in a Single Drop of Blood. *Small* **2012**, *8*, 1912−1919.

(17) Wang, Y.; Chen, J.; Irudayaraj, J. Nuclear Targeting Dynamics of Gold Nanoclusters for Enhanced Therapy of HER2+ Breast Cancer. *ACS Nano* **2011**, *5*, 9718−9725.

(18) Yu, Y.; New, S. Y.; Xie, J.; Su, X.; Tan, Y. N. Protein-Based Fluorescent Metal Nanoclusters for Small Molecular Drug Screening. *Chem. Commun.* **2014**, *50*, 13805−13808.

(19) Habeeb Muhammed, M. A.; Verma, P. K.; Pal, S. K.; Retnakumari, A.; Koyakutty, M.; Nair, S.; Pradeep, T. Luminescent Quantum Clusters of Gold in Bulk by Albumin-Induced Core Etching of Nanoparticles: Metal Ion Sensing, Metal-Enhanced Luminescence, and Biolabeling. *Chem.—Eur. J.* **2010**, *16*, 10103−10112.

(20) Lin, C.-A. J.; Yang, T.-Y.; Lee, C.-H.; Huang, S. H.; Sperling, R. A.; Zanella, M.; Li, J. K.; Shen, J.-L.; Wang, H.-H.; Yeh, H.-I.; et al. Synthesis, Characterization, and Bioconjugation of Fluorescent Gold Nanoclusters toward Biological Labeling Applications. *ACS Nano* **2009**, *3*, 395−401.

(21) Zhang, A.; Tu, Y.; Qin, S.; Li, Y.; Zhou, J.; Chen, N.; Lu, Q.; Zhang, B. Gold Nanoclusters as Contrast Agents for Fluorescent and X-Ray Dual-Modality Imaging. *J. Colloid Interface Sci.* **2012**, *372*, 239−244.

(22) Zhou, W.; Cao, Y.; Sui, D.; Guan, W.; Lu, C.; Xie, J. Ultrastable BSA-Capped Gold Nanoclusters with a Polymer-like Shielding Layer against Reactive Oxygen Species in Living Cells. *Nanoscale* **2016**, *8*, 9614−9620.

(23) Wu, X.; He, X.; Wang, K.; Xie, C.; Zhou, B.; Qing, Z. Ultrasmall Near-Infrared Gold Nanoclusters for Tumor Fluorescence Imaging in Vivo. *Nanoscale* **2010**, *2*, 2244−2249.

(24) Zhang, X.-D.; Chen, J.; Luo, Z.; Wu, D.; Shen, X.; Song, S.-S.; Sun, Y.-M.; Liu, P.-X.; Zhao, J.; Huo, S.; et al. Enhanced Tumor Accumulation of Sub-2 Nm Gold Nanoclusters for Cancer Radiation Therapy. *Adv. Healthcare Mater.* **2014**, *3*, 133−141.

(25) Fernández-Iglesias, N.; Bettmer, J. Synthesis, purification and mass spectrometric characterisation of a fluorescent Au9@BSA nanocluster and its enzymatic digestion by trypsin. *Nanoscale* **2014**, *6*, 716−721.

(26) Yue, Y.; Liu, T.-Y.; Li, H.-W.; Liu, Z.; Wu, Y. Microwave-Assisted Synthesis of BSA-Protected Small Gold Nanoclusters and Their Fluorescence-Enhanced Sensing of Silver(I) Ions. *Nanoscale* **2012**, *4*, 2251−2254.

(27) Mohanty, J. S.; Baksi, A.; Lee, H.; Pradeep, T. Noble Metal Clusters Protected with Mixed Proteins Exhibit Intense Photoluminescence. *RSC Adv.* **2015**, *5*, 48039−48045.

(28) Le Guével, X.; Hötzer, B.; Jung, G.; Hollemeyer, K.; Trouillet, V.; Schneider, M. Formation of Fluorescent Metal (Au, Ag) Nanoclusters Capped in Bovine Serum Albumin Followed by Fluorescence and Spectroscopy. *J. Phys. Chem. C* **2011**, *115*, 10955−10963.

(29) Mathew, A.; Sajanlal, P. R.; Pradeep, T. A Fifteen Atom Silver Cluster Confined in Bovine Serum Albumin. *J. Mater. Chem.* **2011**, *21*, 11205−11212.

(30) Mohanty, J. S.; Xavier, P. L.; Chaudhari, K.; Bootharaju, M. S.; Goswami, N.; Pal, S. K.; Pradeep, T. Luminescent, Bimetallic AuAg Alloy Quantum Clusters in Protein Templates. *Nanoscale* **2012**, *4*, 4255−4262.

(31) Xavier, P. L.; Chaudhari, K.; Verma, P. K.; Pal, S. K.; Pradeep, T. Luminescent Quantum Clusters of Gold in Transferrin Family Protein, Lactoferrin Exhibiting FRET. *Nanoscale* **2010**, *2*, 2769−2776.

(32) Chaudhari, K.; Xavier, P. L.; Pradeep, T. Understanding the Evolution of Luminescent Gold Quantum Clusters in Protein Templates. *ACS Nano* **2011**, *5*, 8816−8827.

(33) Chan, P.-H.; Chen, Y.-C. Human Serum Albumin Stabilized Gold Nanoclusters as Selective Luminescent Probes forStaphylococcus aureusand Methicillin-ResistantStaphylococcus aureus. *Anal. Chem.* **2012**, *84*, 8952−8956.

(34) Baksi, A.; Xavier, P. L.; Chaudhari, K.; Goswami, N.; Pal, S. K.; Pradeep, T. Protein-Encapsulated Gold Cluster Aggregates: The Case of Lysozyme. *Nanoscale* **2013**, *5*, 2009−2016.

(35) Sarkar, D.; Mahitha, M. K.; Som, A.; Li, A.; Wleklinski, M.; Cooks, R. G.; Pradeep, T. Metallic Nanobrushes Made Using Ambient Droplet Sprays. *Adv. Mater.* **2016**, *28*, 2223−2228.

(36) Sarkar, D.; Mahapatra, A.; Som, A.; Kumar, R.; Nagar, A.; Baidya, A.; Pradeep, T. Patterned Nanobrush Nature Mimics with Unprecedented Water-Harvesting Efficiency. *Adv. Mater. Interfaces* **2018**, *5*, 1800667.

(37) Sarkar, D.; Singh, R.; Som, A.; Manju, C. K.; Ganayee, M. A.; Adhikari, R.; Pradeep, T. Electrohydrodynamic Assembly of Ambient Ion-Derived Nanoparticles to Nanosheets at Liquid Surfaces. *J. Phys. Chem. C* **2018**, *122*, 17777−17783.

(38) Sarkar, D.; Mondal, B.; Som, A.; Ravindran, S. J.; Jana, S. K.; Manju, C. K.; Pradeep, T. Holey MoS2 Nanosheets with Photocatalytic Metal Rich Edges by Ambient Electrospray Deposition for Solar Water Disinfection. *Glob. Chall.* **2018**, *2*, 1800052.

(39) Jana, A.; Jana, S. K.; Sarkar, D.; Ahuja, T.; Basuri, P.; Mondal, B.; Bose, S.; Ghosh, J.; Pradeep, T. Electrospray Deposition-Induced Ambient Phase Transition in Copper Sulphide Nanostructures. *J. Mater. Chem. A* **2019**, *7*, 6387.

(40) Lee, J. K.; Samanta, D.; Nam, H. G.; Zare, R. N. Spontaneous Formation of Gold Nanostructures in Aqueous Microdroplets. *Nat. Commun.* **2018**, *9*, 1562.

(41) Ghosh, D.; Bodiuzzaman, M.; Som, A.; Raja, S.; Baksi, A.; Ghosh, A.; Ghosh, J.; Ganesh, A.; Samji, P.; Mahalingam, S.; Karunagaran, D.; Pradeep, T. Internalization of a Preformed Atomically Precise Silver Cluster in Proteins by Multistep Events and Emergence of Luminescent Counterparts Retaining Bioactivity. *J. Phys. Chem. C* **2019**, *123*, 29408−29417.

(42) Müller, T.; Badu-Tawiah, A.; Cooks, R. G. Accelerated Carbon−Carbon Bond-Forming Reactions in Preparative Electrospray. *Angew. Chem., Int. Ed.* **2012**, *51*, 11832−11835.

(43) Banerjee, S.; Zare, R. N. Syntheses of Isoquinoline and Substituted Quinolines in Charged Microdroplets. *Angew. Chem., Int. Ed.* **2015**, *54*, 14795−14799.

(44) Li, A.; Luo, Q.; Park, S.-J.; Cooks, R. G. Synthesis and Catalytic Reactions of Nanoparticles Formed by Electrospray Ionization of Coinage Metals. *Angew. Chem., Int. Ed.* **2014**, *53*, 3147−3150.

(45) Lee, J. K.; Kim, S.; Nam, H. G.; Zare, R. N. Microdroplet Fusion Mass Spectrometry for Fast Reaction Kinetics. *Proc. Natl. Acad. Sci. U.S.A.* **2015**, *112*, 3898−3903.

(46) Dimaras, H.; Corson, T. W. Retinoblastoma, the Visible CNS Tumor: A Review. *J. Neurosci. Res.* **2019**, *97*, 29−44.

(47) Moll, A. C.; Koten, J. W.; Lindenmayer, D. A.; Everse, L. A.; Tan, K. E.; Hamburg, A.; Faber, J. A.; Den Otter, W. Three Histopathological Types of Retinoblastoma and Their Relation to Heredity and Age of Enucleation. *J. Med. Genet.* **1996**, *33*, 923−927.

(48) Orjuela, M.; Castaneda, V. P.; Ridaura, C.; Lecona, E.; Leal, C.; Abramson, D. H.; Orlow, I.; Gerald, W.; Cordon-Cardo, C. Presence of Human Papilloma Virus in Tumor Tissue from Children with Retinoblastoma: An Alternative Mechanism for Tumor Development. *Clin. Cancer Res.* **2000**, *6*, 4010−4016.

(49) Knudson, A. Retinoblastoma: Teacher of Cancer Biology and Medicine. *PLoS Med.* **2005**, *2*, No. e349.

(50) Bowles, E.; Corson, T. W.; Bayani, J.; Squire, J. A.; Wong, N.; Lai, P. B.-S.; Gallie, B. L. Profiling genomic copy number changes in retinoblastoma beyond loss ofRB1. *Gene Chromosome Canc.* **2007**, *46*, 118−129.

(51) AACR. MYCN Drives RB-Null Retinoblastoma Initiation. *Canc. Discov.* **2017**, *7*, OF13.

(52) Kyritsis, A. P.; Tsokos, M.; Triche, T. J.; Chader, G. J. Retinoblastoma-origin from a primitive neuroectodermal cell? *Nature* **1984**, *307*, 471−473.

(53) Jackson, C. G.; Glasscock, M. E., 3rd; McKennan, K. X.; Koopmann, C. F.; Levine, S. C.; Hays, J. W.; Smith, H. P. The Surgical Treatment of Skull-Base Tumors with Intracranial Extension. *Otolaryngol. Head Neck Surg.* **1987**, *96*, 175−185.

(54) Hu, Y.-C.; Chang, C.-H.; Chen, C.-H.; Ger, L.-P.; Liu, W.-S.; Lin, L.-C.; Leung, C.-M.; Chang, K.-C. Impact of Intracranial Extension on Survival in Stage IV Nasopharyngeal Carcinoma: Identification of a Subset of Patients with Better Prognosis. *Jpn. J. Clin. Oncol.* **2011**, *41*, 95−102.

(55) Abuzayed, B.; Khreisat, W.; Maaiah, W.; Agailat, S. Supratentorial Primitive Neuroectodermal Tumor Presenting with Intracranial Hemorrhage in Adult. *J. Neurosci. Rural Pract.* **2014**, *5*, 176−179.

(56) Hader, W. J.; Drovini-Zis, K.; Maguire, J. A. Primitive Neuroectodermal Tumors in the Central Nervous System Following Cranial Irradiation. *Cancer* **2003**, *97*, 1072−1076.

(57) Wang, Y.-P.; Wang, D.-J.; Niu, Z.-B.; Cui, W.-T. Chromosome 13q Deletion Syndrome Involving 13q31-qter: A Case Report. *Mol. Med. Rep.* **2017**, *15*, 3658−3664.

(58) Dryja, T. P.; Rapaport, J. M.; Joyce, J. M.; Petersen, R. A. Molecular Detection of Deletions Involving Band Q14 of Chromosome 13 in Retinoblastomas. *Proc. Natl. Acad. Sci. U.S.A.* **1986**, *83*, 7391−7394.

(59) de Graaf, P.; Göricke, S.; Göricke, S.; Rodjan, F.; Galluzzi, P.; Maeder, P.; Castelijns, J. A.; Brisse, H. J. Guidelines for imaging retinoblastoma: imaging principles and MRI standardization. *Pediatr. Radiol.* **2012**, *42*, 2−14.

(60) Porcaro, F.; Carlini, L.; Ugolini, A.; Visaggio, D.; Visca, P.; Fratoddi, I.; Venditti, I.; Meneghini, C.; Simonelli, L.; Marini, C.; et al. Synthesis and Structural Characterization of Silver Nanoparticles Stabilized with 3-Mercapto-1-Propansulfonate and 1-Thioglucose Mixed Thiols for Antibacterial Applications. *Materials* **2016**, *9*, 1028.

(61) Ramasamy, P.; Guha, S.; Shibu, E. S.; Sreeprasad, T. S.; Bag, S.; Banerjee, A.; Pradeep, T. Size Tuning of Au Nanoparticles Formed by Electron Beam Irradiation of Au25 Quantum Clusters Anchored within and Outside of Dipeptide Nanotubes. *J. Mater. Chem.* **2009**, *19*, 8456−8462.

(62) Subramanian, V.; Jena, S.; Ghosh, D.; Jash, M.; Baksi, A.; Ray, D.; Pradeep, T. Dual Probe Sensors Using Atomically Precise Noble Metal Clusters. *ACS Omega* **2017**, *2*, 7576−7583.

(63) Ghosh, D.; Ganayee, M. A.; Som, A.; Srikrishnarka, P.; Murali, N.; Bose, S.; Chakraborty, A.; Mondal, B.; Ghosh, P.; Pradeep, T. Hierarchical Assembly of Atomically Precise Metal Clusters as a Luminescent Strain Sensor. *ACS Appl. Mater. Interfaces* **2021**, *13*, 6496.

(64) Chantada, G.; Schaiquevich, P. Management of Retinoblastoma in Children: Current Status. *Pediatr. Drugs* **2015**, *17*, 185−198.

(65) Francis, J. H.; Levin, A. M.; Zabor, E. C.; Gobin, Y. P.; Abramson, D. H. Ten-Year Experience with Ophthalmic Artery Chemosurgery: Ocular and Recurrence-Free Survival. *PLoS One* **2018**, *13*, No. e0197081.

(66) Munier, F. L.; Gaillard, M.-C.; Balmer, A.; Soliman, S.; Podilsky, G.; Moulin, A. P.; Beck-Popovic, M. Intravitreal Chemotherapy for Vitreous Disease in Retinoblastoma Revisited: From Prohibition to Conditional Indications. *Br. J. Ophthalmol.* **2012**, *96*, 1078−1083.

(67) Munier, F. L. Classification and Management of Seeds in RetinoblastomaEllsworth Lecture Ghent August 24th 2013. *Ophthalmic Genet.* **2014**, *35*, 193−207.

(68) Francis, J. H.; Marr, B. P.; Schaiquevich, P.; Kellick, M. G.; Abramson, D. H. Properties and Clinical Utility of Topotecan Fluorescence: Uses for Retinoblastoma. *Br. J. Ophthalmol.* **2015**, *99*, 1320−1322.

(69) Corson, T. W.; Samuels, B. C.; Wenzel, A. A.; Geary, A. J.; Riley, A. A.; McCarthy, B. P.; Hanenberg, H.; Bailey, B. J.; Rogers, P. I.; Pollok, K. E.; et al. Multimodality Imaging Methods for Assessing Retinoblastoma Orthotopic Xenograft Growth and Development. *PLoS One* **2014**, *9*, No. e99036.

(70) Zhang, L.; Wang, E. Metal Nanoclusters: New Fluorescent Probes for Sensors and Bioimaging. *Nano Today* **2014**, *9*, 132−157.

(71) Bai, Y.; Shu, T.; Su, L.; Zhang, X. Fluorescent Gold Nanoclusters for Biosensor and Bioimaging Application. *Crystals* **2020**, *10*, 357−368.

(72) Krishna Kumar, A. S.; Tseng, W.-L. Perspective on Recent Developments of near Infrared-Emitting Gold Nanoclusters: Applications in Sensing and Bio-Imaging. *Anal. Methods* **2020**, *12*, 1809−1826.

(73) Winter, U.; Aschero, R.; Fuentes, F.; Buontempo, F.; Zugbi, S.; Sgroi, M.; Sampor, C.; Abramson, D.; Carcaboso, A.; Schaiquevich, P. Tridimensional Retinoblastoma Cultures as Vitreous Seeds Models for Live-Cell Imaging of Chemotherapy Penetration. *Int. J. Mol. Sci.* **2019**, *20*, 1077−1090.

(74) Hemmateenejad, B.; Shahrivar-Kevishahi, A.; Shakerizadeh-Shirazi, F. Reversible Photobleaching of Gold Nanoclusters: A Mechanistic Investigation. *J. Phys. Chem. C* **2016**, *120*, 28215−28223.

(75) Link, S.; Beeby, A.; FitzGerald, S.; El-Sayed, M. A.; Schaaff, T. G.; Whetten, R. L. Visible to Infrared Luminescence from a 28-Atom Gold Cluster. *J. Phys. Chem. B* **2002**, *106*, 3410−3415.

(76) Li, H.; Li, H.; Wan, A. Luminescent Gold Nanoclusters for in Vivo Tumor Imaging. *Analyst* **2020**, *145*, 348−363.

(77) Chen, D.; Li, B.; Cai, S.; Wang, P.; Peng, S.; Sheng, Y.; He, Y.; Gu, Y.; Chen, H. Dual Targeting Luminescent Gold Nanoclusters for Tumor Imaging and Deep Tissue Therapy. *Biomaterials* **2016**, *100*, 1−16.

(78) Jayashree, B.; Srimany, A.; Jayaraman, S.; Bhutra, A.; Janakiraman, N.; Chitipothu, S.; Krishnakumar, S.; Baddireddi, L. S.; Elchuri, S.; Pradeep, T. Monitoring of Changes in Lipid Profiles during PLK1 Knockdown in Cancer Cells Using DESI MS. *Anal. Bioanal. Chem.* **2016**, *408*, 5623−5632.

Supporting information

Molecular Materials through Microdroplets: Synthesis of Protein-Protected Luminescent Clusters of Noble Metals

Sandeep Bose,[1] Amit Chatterjee,[2] Shantha Kumar Jenifer,[1] Biswajit Mondal,[1] Pillalamarri Srikrishnarka,[1] Debasmita Ghosh,[1] Angshuman Ray Chowdhuri,[1] M. P. Kannan,[1] Sailaja V. Elchuri,[2] Thalappil Pradeep[1,]*

[1]DST Unit of Nanoscience (DST UNS) and Thematic Unit of Excellence (TUE), Department of Chemistry, Indian Institute of Technology Madras, Chennai - 600 036, India

[2]Department of Nanobiotechnology, Vision Research Foundation, Sankara Nethralaya, Chennai-600006, India

*Email: pradeep@iitm.ac.in

SUPPORTING INFORMATION CONTENT

Total number of pages – 16

Total number of figures – 19

Total number of tables – 0

Instrumentation

Droplet synthesized clusters were characterized high-resolution transmission electron microscopy (HRTEM), X-ray photoelectron spectroscopy (XPS), photoluminescence (PL) spectroscopy, UV-Vis spectroscopy, fluorescence microscopy, circular dichroism (CD), Fourier-transform infrared spectroscopy (FTIR) and matrix-assisted laser desorption ionization mass spectrometry (MALDI MS). UV-Vis absorption spectra were recorded using a Perkin Elmer Lambda 25 spectrophotometer. Optical absorption spectra were typically measured in the range of 200-1100 nm with a band-pass filter of 1 nm. MALDI MS of the cluster was measured using Voyager-DE Pro Biospectrometry Workstation from Applied Biosystems. TEM measurements were performed using JEOL3010 (JEOL Japan) operating at 200 kV. Photoluminescence measurements were carried out in a HORIBA, Jobin Yvon Nanolog fluorescence spectrometer. Band-pass of 3 nm was used for all the excitation and emission spectra. XPS measurements were conducted with an Omicron ESCA probe spectrometer with polychromatic Mg Kα X-rays ($h\nu$ = 1253.6 eV). A high-speed camera (Phantom v1212) coupled with Keyence VH-Z100R, zoom lens was used for the measurement of the travel time of droplets. To visualize the electrospray 700 x magnification was set. FTIR was carried out with PerkinElmer spectrum 2 with universal attenuated total reflectance (UATR) with a diamond crystal. Photographic images were taken with a Nikon D5100 DSLR camera. The cells were imaged using a fluorescence microscope (Carl Zeiss, Germany) and image acquisition was performed using a high-NA oil immersion objective of 100X magnification. The sample was excited at 405 and 488 nm. For 405 nm excitation, emission was collected from 410 to 550 nm, and for 488 nm excitation, emission was collected from 520 to 690 nm. For electrospray, the aqueous solution was pushed through a NE-300 infusion syringe pump.

Calculation of the time of travel of the Si QDs at different distances

For calculating the time required to travel from tip of the nozzle to the substrate, the average velocity of about 20 microdroplets coming out of nozzle at different distances were calculated.

For the calculation of time of travel between the tip to substrate the following formula was used:

Time (t) = Total number of frames/frame rate

Once the distance and time were known, the speed of each droplet was calculated by plotting it as a function of the individual droplets. This was fitted with a straight line. After the velocity was calculated, other parameters were fixed and the distance between the tip to substrate was fixed at 5 mm for each of the cluster. The time required to travel was calculated by the formula, t = s/v, where,

t = Average time required by the droplets to reach the substrate.

S = Distance between the tip and substrate

v = Average velocity of the droplet

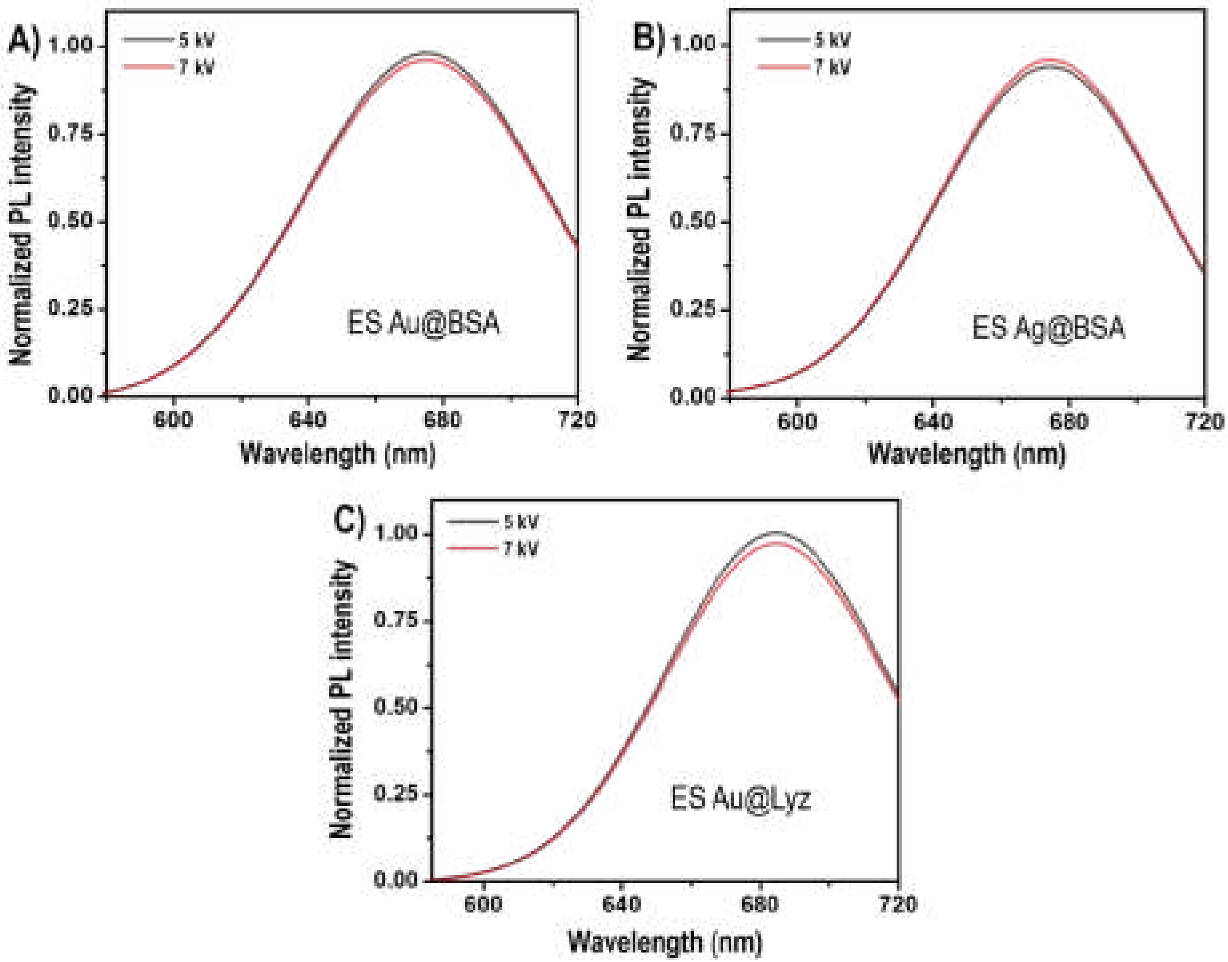

Figure S1. A comparison of the luminescence of clusters synthesized at two different electrospray potentials.

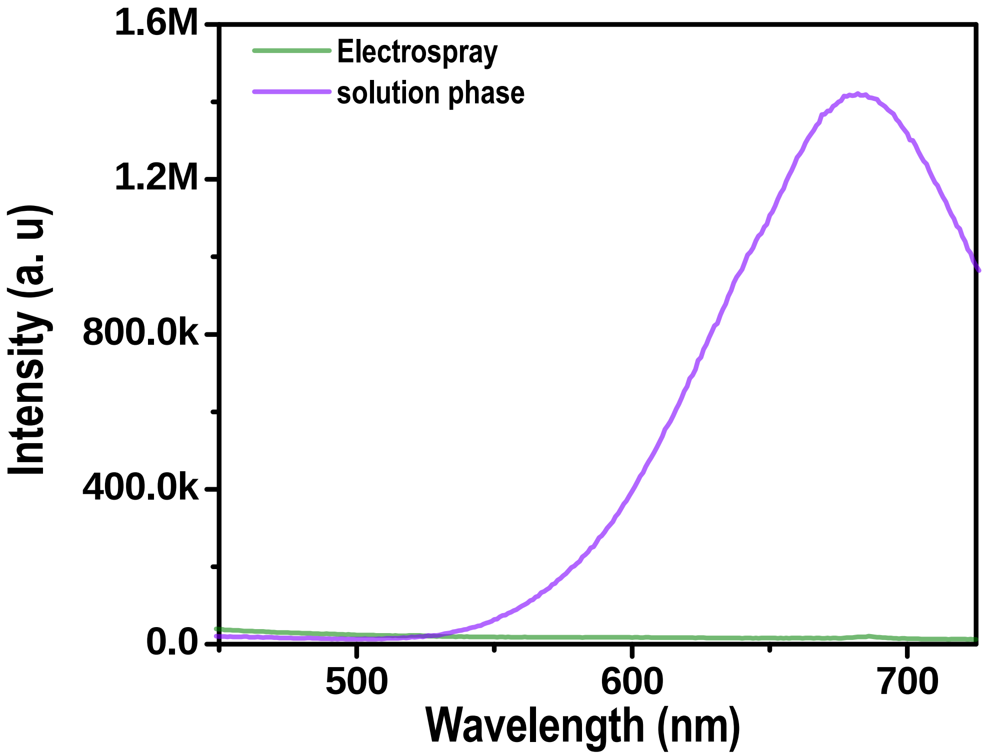

Figure S2. Comparison of PL spectra of the ES and SP sample after 1 h of reaction. After 1 h of electrospray, PL spectrum shows luminescence which suggests that Au@BSA cluster was formed. In order to prove that there was no reaction within 1 h in the solution phase, a mixture of precursors was kept for 1 h and the PL spectrum was measured. No luminescence was observed in the solution phase during this time scale.

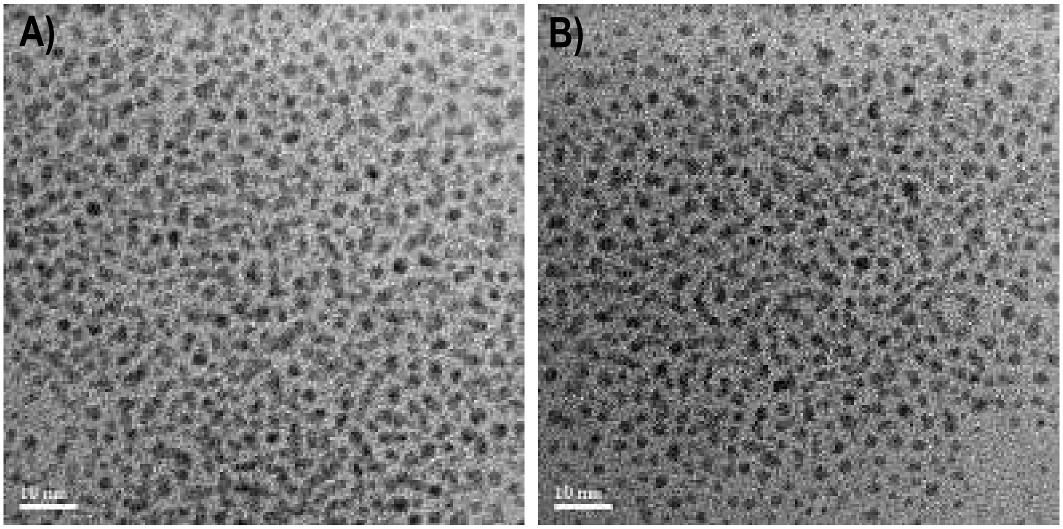

Figure S3. A) TEM image of the Au nanoparticles obtained when the spray was performed using nebulizing gas in the absence of an electric field. **B)** TEM image of the Ag nanoparticles obtained under similar conditions. See also Figure S3. It produced non-luminescent nanoparticles.

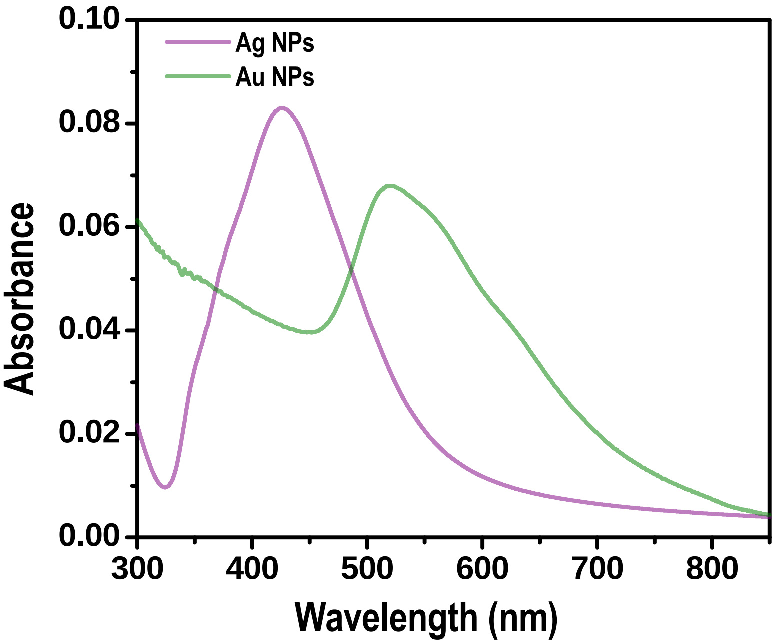

Figure S4. UV-Vis spectra of Ag and Au nanoparticles obtained after spray in the absence of electric field.

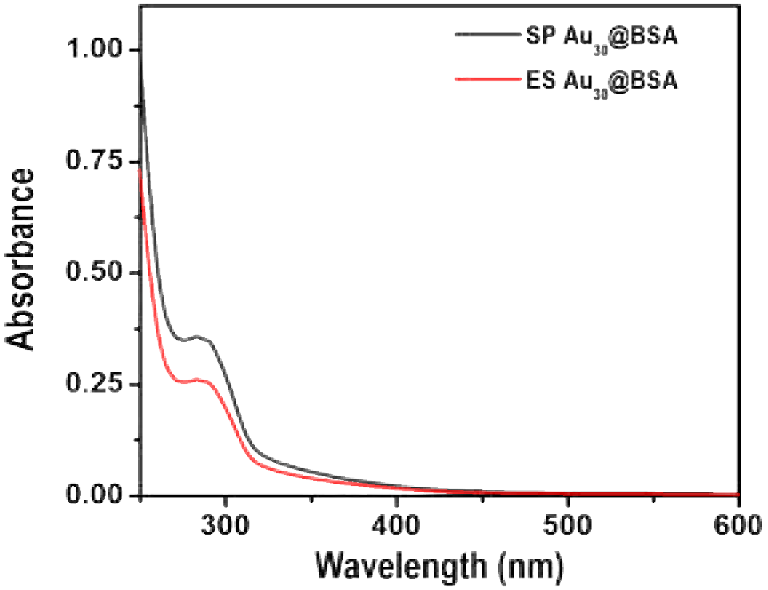

Figure S5. A comparison of UV-Vis spectra of Au_{30}@BSA synthesized by the SP and ES methods. Au_{30}@BSA synthesized by both these methods show similarities in the UV-Vis spectra.

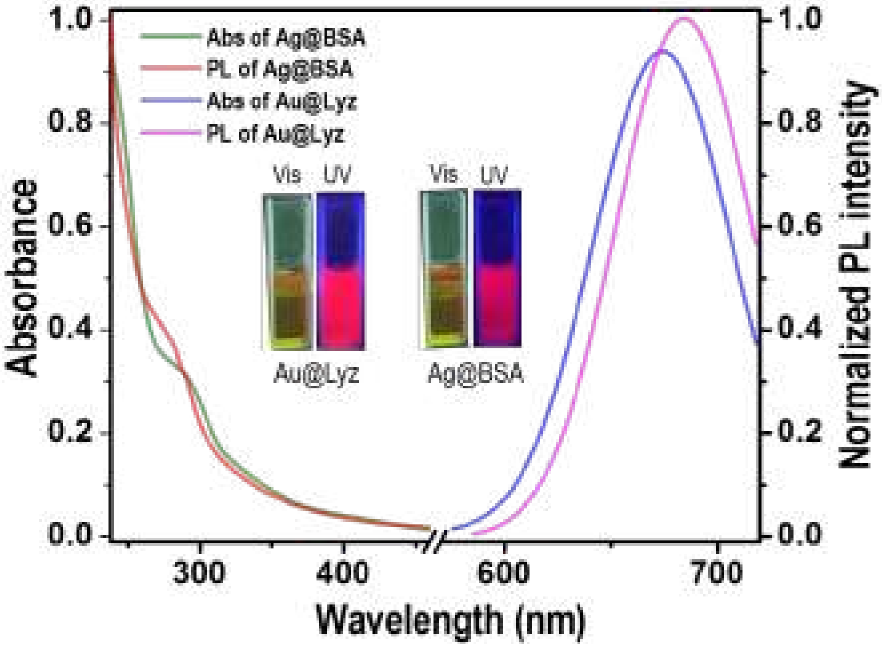

Figure S6. Absorbance (Abs) and photoluminescence (PL) spectra of ES Au@Lyz and ES Ag@BSA obtained as a result electrospray. Inset shows the photographs of ES Au@Lyz and ES

Ag@BSA under UV and visible light. Under UV light, both of these clusters show red luminescence.

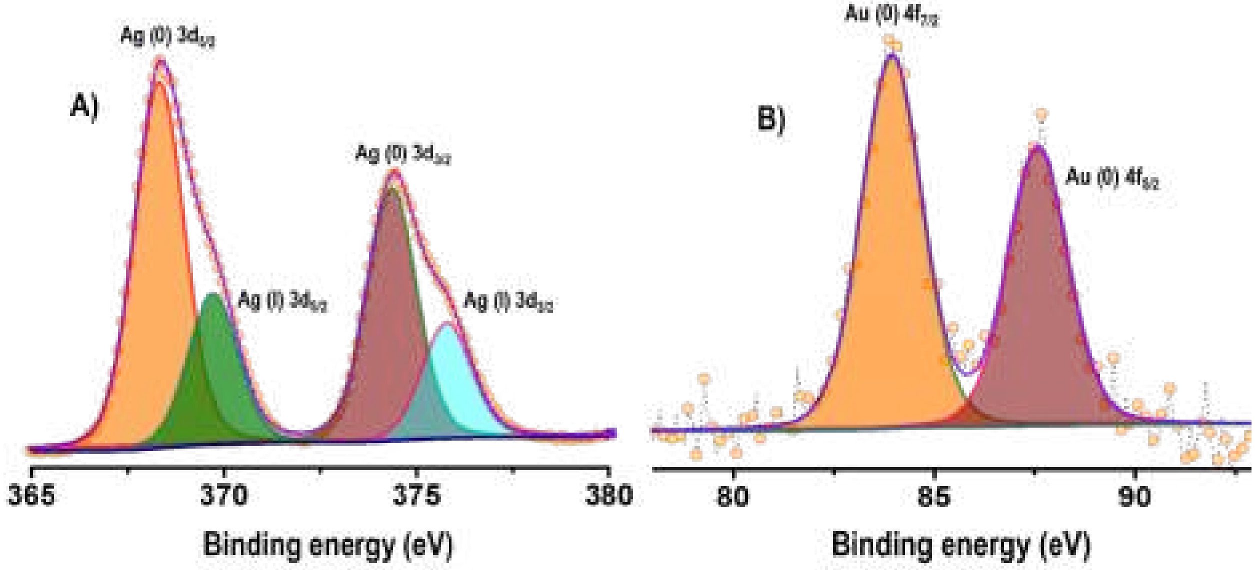

Figure S7. A) and **B)** are the X-ray photoelectron spectra of ES Ag@BSA and ES Au@Lyz, in the Ag 3d and Au 4f regions, respectively, showing Ag (0) and Au (0) oxidation states in the clusters. The spectrum for Ag (0) shows a higher binding energy component, which is assigned to the positively charged silver atoms bonded to the sulphur atoms of the thiol groups of the protein.

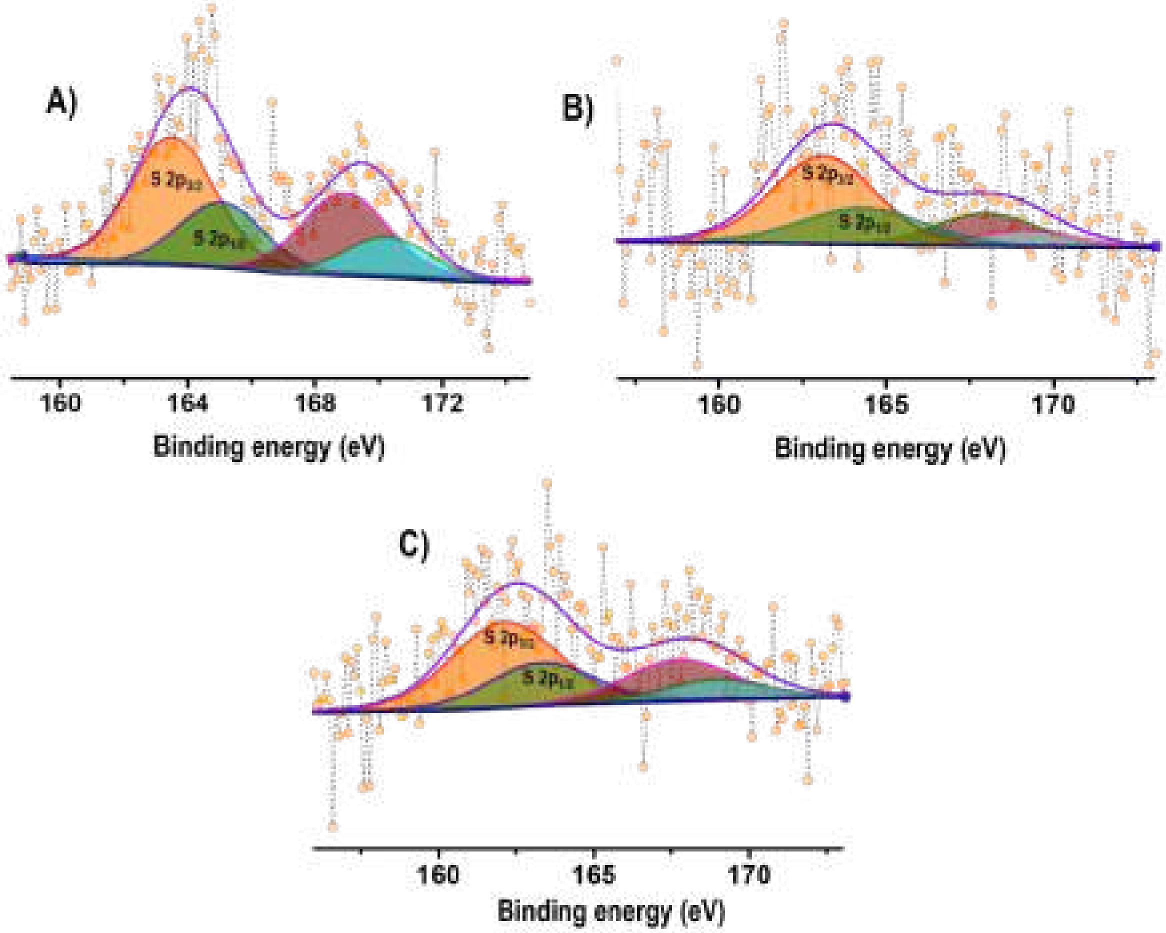

Figure S8. XPS spectra of **A)** ES Au@BSA, **B)** ES Ag@BSA and **C)** ES Au@Lyz, in the S 2p region, showing the oxidized state of sulfur in the clusters. The S $2p_{3/2}$ feature around 163 eV supports the thiolate binding on the Au/Ag core. Oxidation, contributing to the higher energy features is a characteristic feature in such materials upon X-ray irradiation.

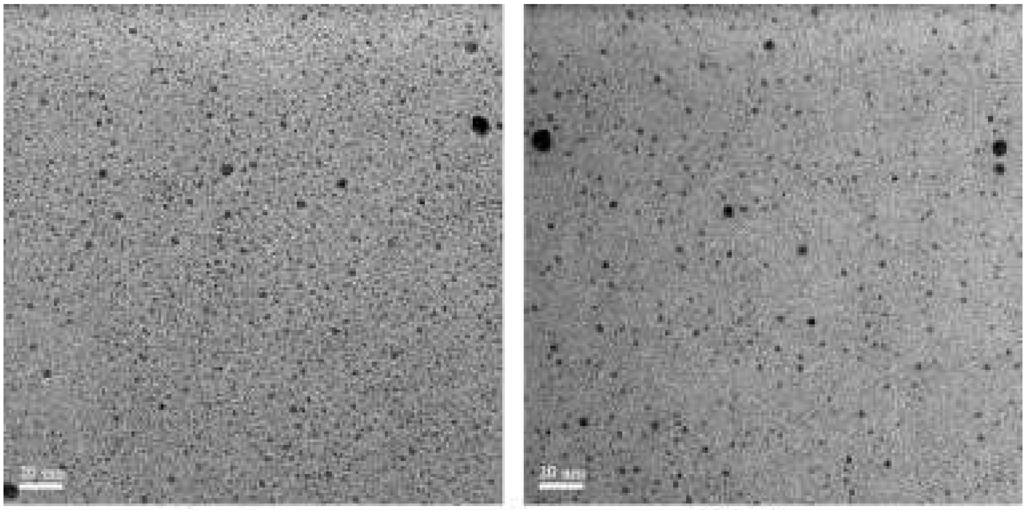
ES Ag@BSA   ES Au@Lyz

Figure S9. TEM images of ES Ag@BSA and ES Au@Lyz. Electron beam-induced aggregation of clusters is visible.

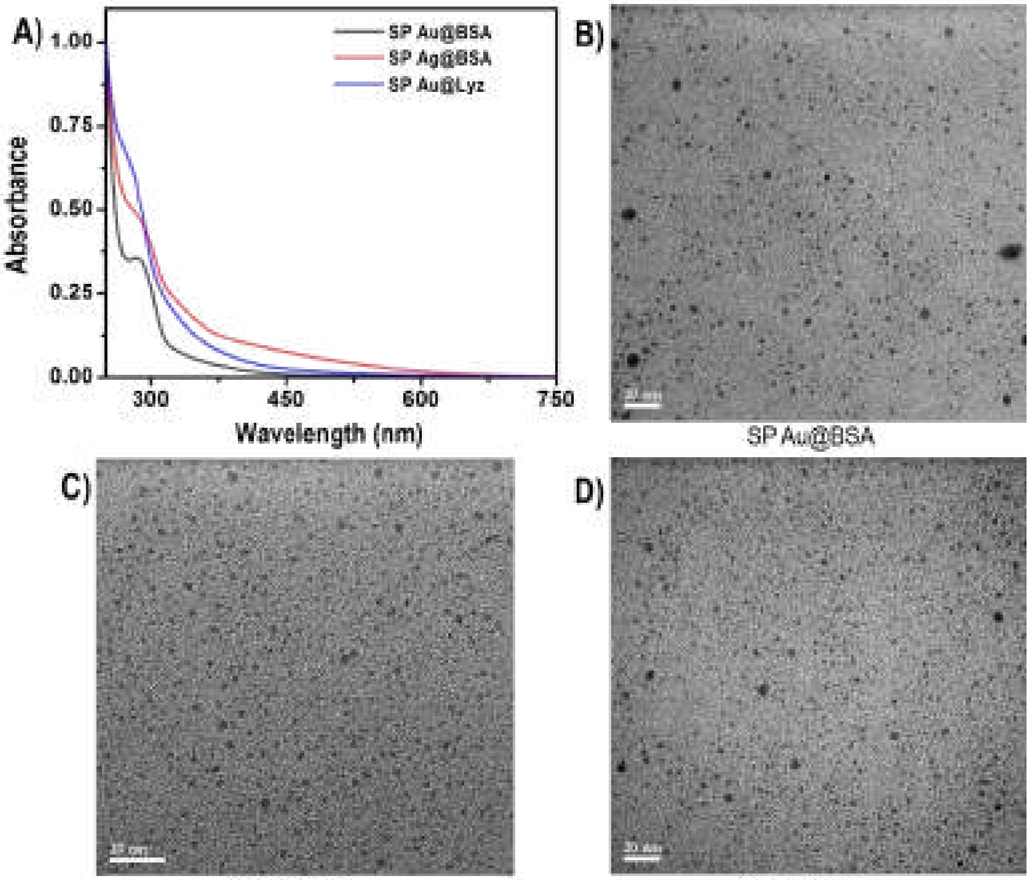

SP Au@BSA

SP Ag@BSA   SP Au@Lyz

Figure S10. A) UV-Vis feature of all the solution-processed clusters, i.e. SP Au@BSA, SP Ag@BSA and SP Au@Lyz. B), C) and D) are the TEM image of the SP Au@BSA, SP Ag@BSA and SP Au@Lyz, respectively.

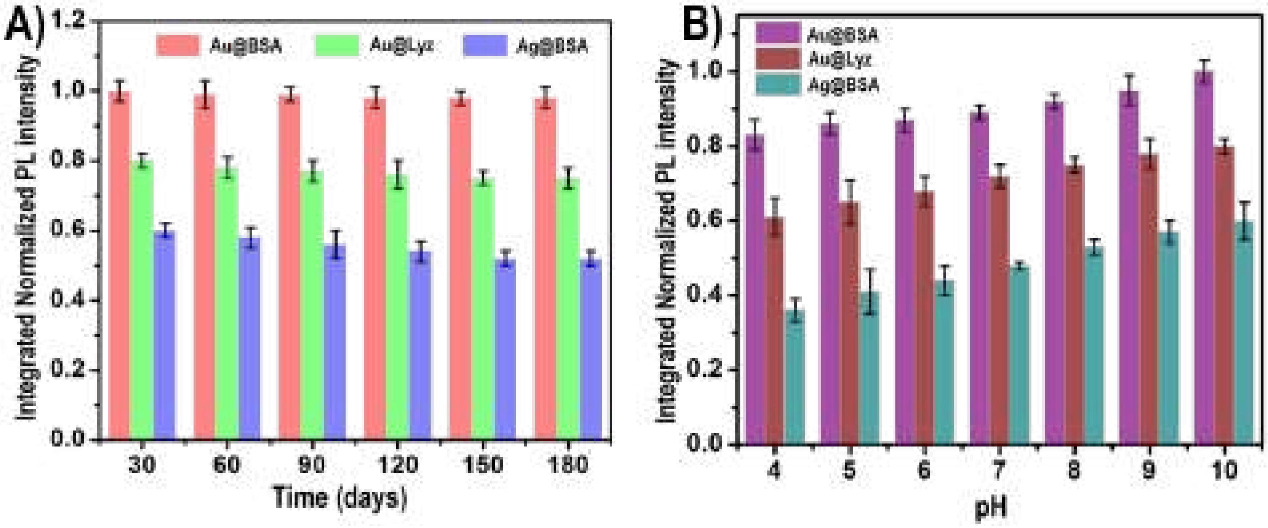

Figure S11. A) Time-dependent stability of the electrosprayed clusters measured over a period of six months at an interval of 30 days. Almost no change in the stability was noticed. **B)** Effect of pH on the luminescence of the electrosprayed clusters measured in the range of 4-10. An increase in pH results in the increase in the luminescence. This suggests that unfolding occurs in the alkaline medium due to breakage of disulfide bonds that favors the formation of these luminescent clusters.

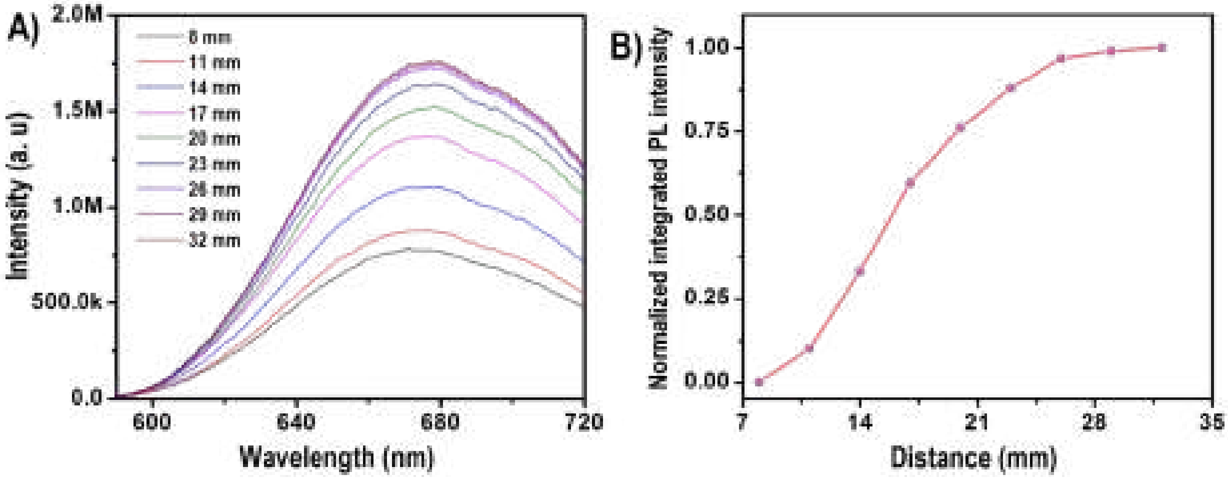

Figure S12. A) Distance-dependent changes in the luminescence intensity of ES Au@BSA measured up to a distance of 32 mm between the tip to the substrate. B) Distance-dependent luminescence of the ES Au@BSA cluster, which show a non-linear increase and indicates the self-quenching of the luminescence in droplets upon increasing the distance.

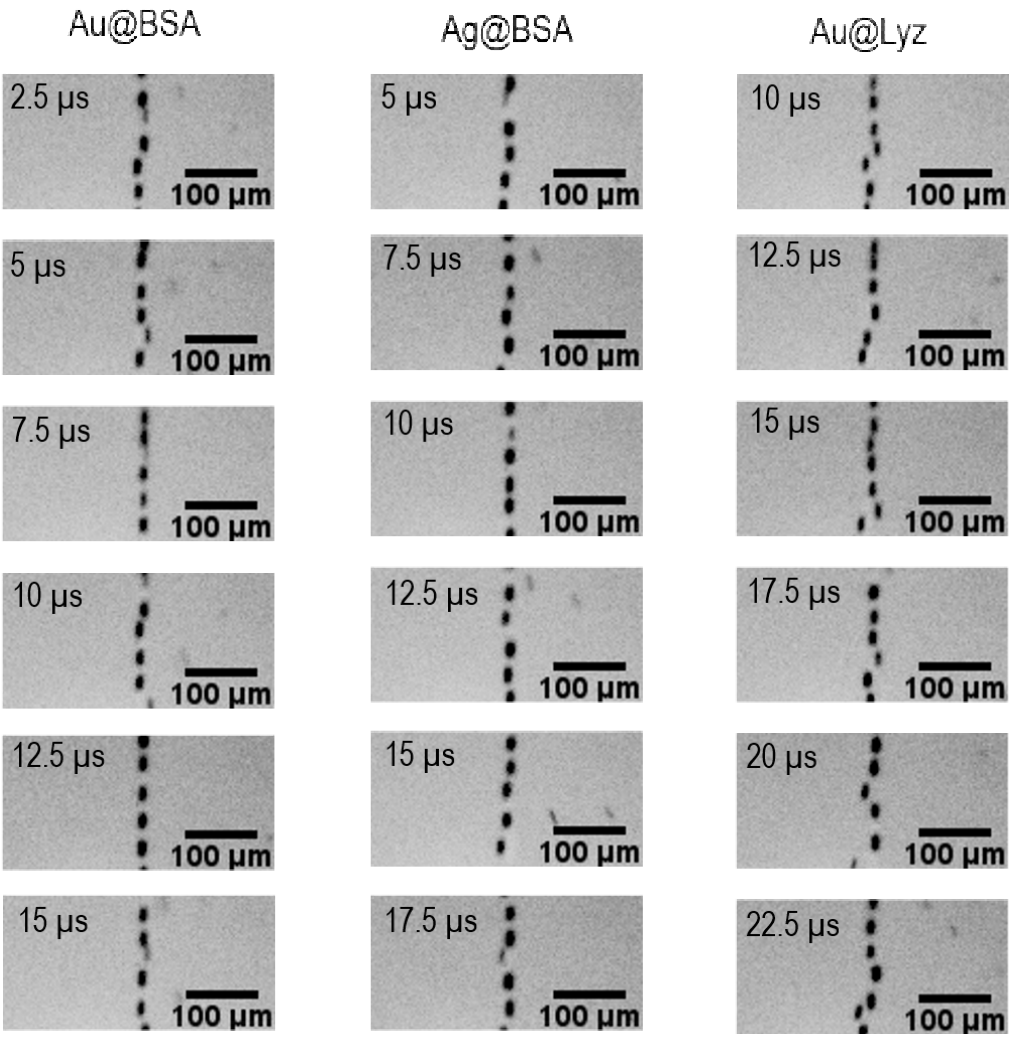

Figure S13. High speed camera images of the individual charged microdroplets (recorded at 400,000 fps) formed as a result of electrospray during the synthesis of Au@BSA, Ag@BSA and Au@Lyz. Movement of these droplets were monitored to calculate the velocity of the droplets.

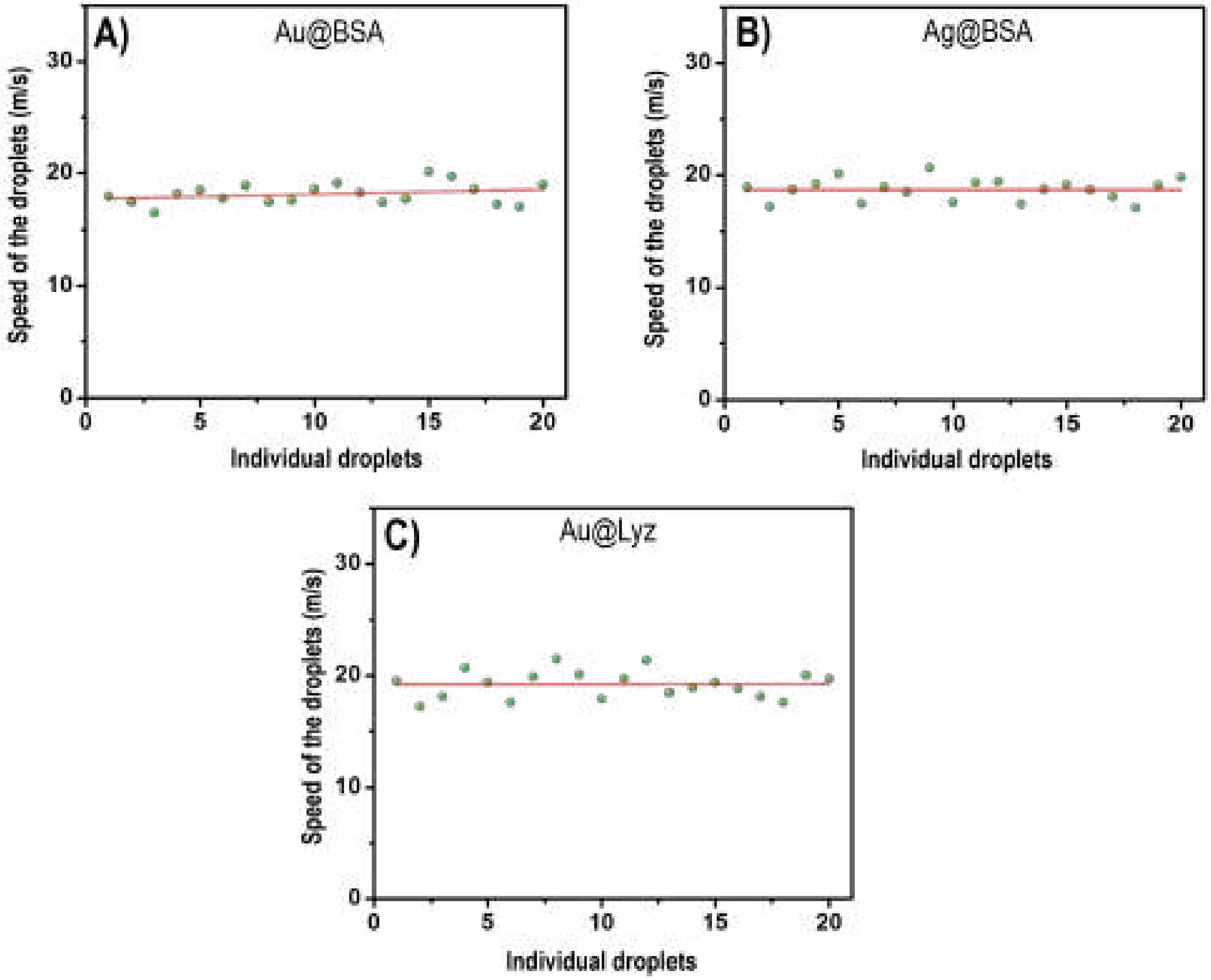

Figure S14. Speed of 20 individual droplets is plotted against droplet number. The velocity distribution is fitted with a straight line and the fitting shows a constant velocity. The calculated speed for A) Au@BSA, B) Ag@BSA and C) Au@Lyz is 17.73±0.41, 18.69±0.45 and 19.26±0.59 m/s, respectively.

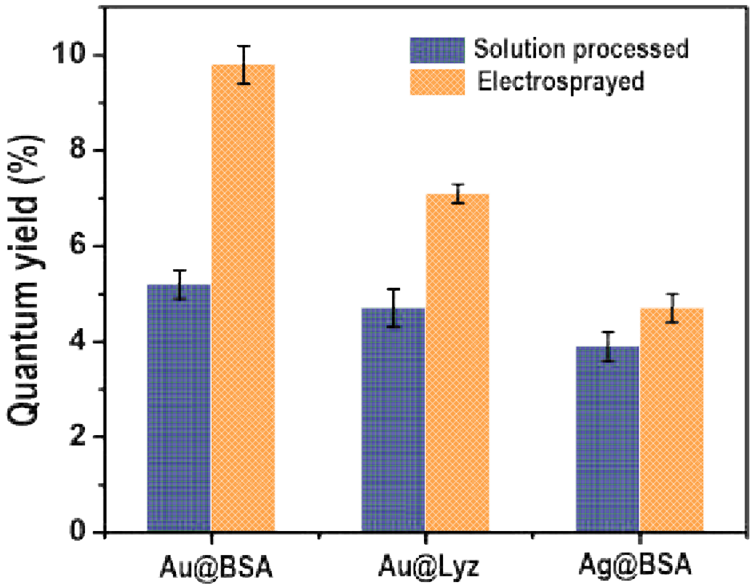

Figure S15. Comparison of the quantum yields of the solution-processed clusters and electrosprayed clusters that are prepared under similar concentrations of precursors. Electrosprayed clusters have higher QYs than solution-processed clusters which supports luminescence enhancement upon electrospray.

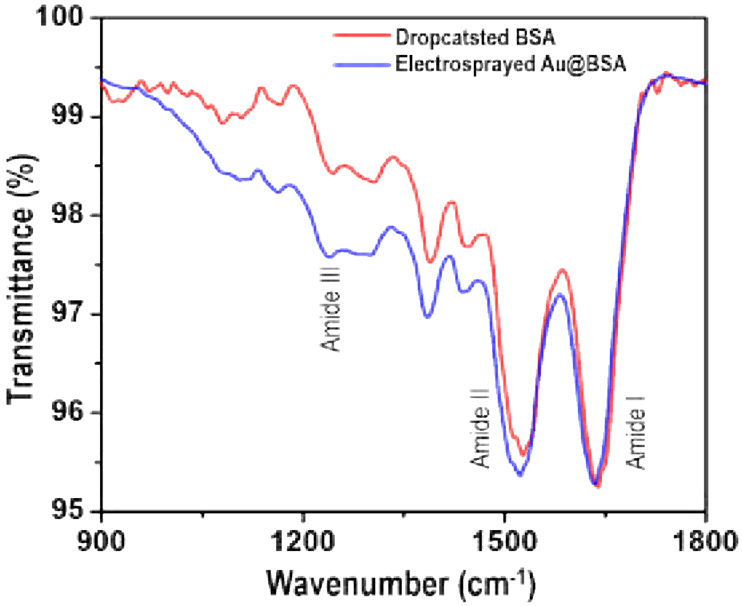

Figure S16. Comparison of the infrared spectra of BSA and ES Au@BSA cluster.

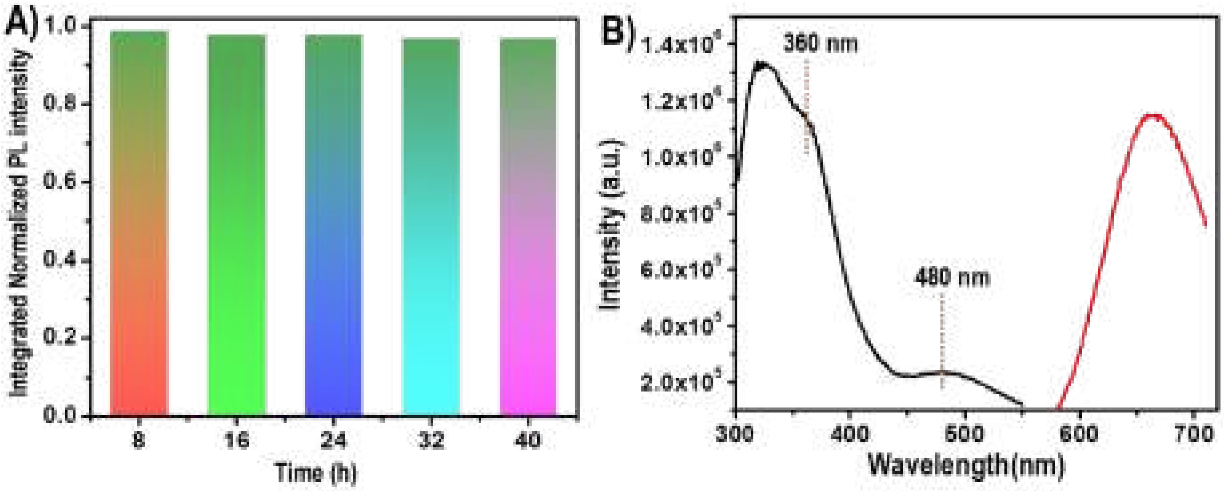

Figure S17. A) Stability of ES Au@BSA in the biological medium, RPMI 1640, was measured. It shows good stability over a period of 40 h and no degradation of the cluster in the medium was noticed. **B)** Excitation and emission spectra of ES Au@BSA cluster. Excitation spectrum features two peaks at 360 nm and 480 nm. Both the excitations give red luminescence. Excitation at 480 nm was used for the fluorescence imaging of Rb cells.

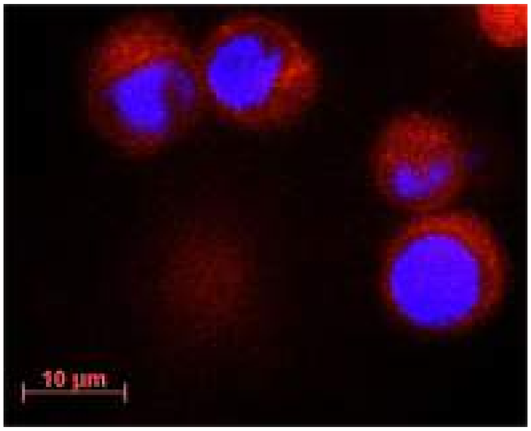

Figure S18. Cellular uptake studies performed on the Rb cells using ES Au@BSA cluster for 1 h. The fluorescence image of the Rb cells show good penetration depth of the clusters into the cell. This suggests that ES Au@BSA could be used for rapid fluorescence imaging of the Rb cells. This could be used as an alternative to the other luminescent materials which take more time for uptake and causes cell toxicity.

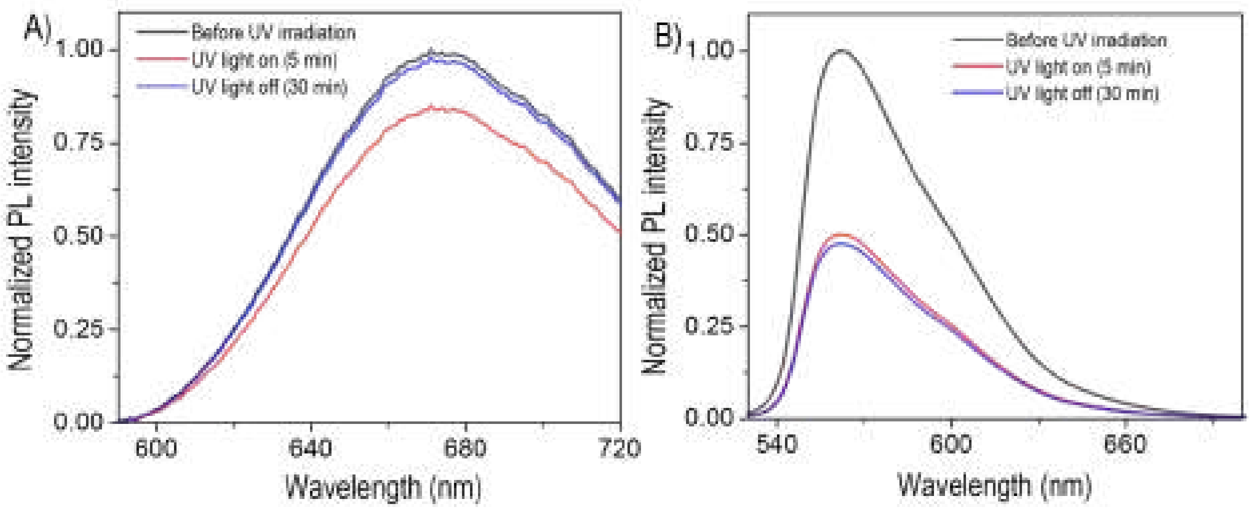

Figure S19. Photo-bleaching experiment performed A) on the ES Au@BSA cluster and B) on the dye (Rhodamine-6G). The dye shows significant degradation as compared to the cluster. Also reversible photo-bleaching was noticed for the cluster which was absent in case of dye (after 30 min in absence of UV light).

THE JOURNAL OF PHYSICAL CHEMISTRY C
A JOURNAL OF THE AMERICAN CHEMICAL SOCIETY

pubs.acs.org/JPCC Article

Facile Crystallization of Ice I_h via Formaldehyde Hydrate in Ultrahigh Vacuum under Cryogenic Conditions

Jyotirmoy Ghosh,[‡] Gaurav Vishwakarma,[‡] Subhadip Das, and Thalappil Pradeep*

Cite This: J. Phys. Chem. C 2021, 125, 4532−4539 Read Online

ACCESS | Metrics & More | Article Recommendations | SI Supporting Information

ABSTRACT: Although hexagonal ice (ice I_h) is the most common and highly studied crystalline form of ice, its nucleation from clathrate hydrates is poorly understood. Here, we report the formation of ice I_h through the dissociation of formaldehyde hydrate, prepared under ultrahigh vacuum (UHV) in the temperature window of 130−135 K. This unique route for crystallization is highly facile, and it occurs below the usual crystallization temperature of ice I_h of 155 K in UHV; the associated activation energy is also lower. Time-dependent reflection absorption infrared spectroscopy was used to detect the formaldehyde hydrate and to determine the crystallization kinetics of ice I_h. The dissociation of formaldehyde hydrate is found to be a diffusion-controlled process, which reduces the activation barrier of crystallization. This study provides evidence that formaldehyde hydrate can exist in extremely low (P, T) conditions without forming the geminal diol or its polymer in the presence of water. This new and facile route of crystallization in the context of interstellar environments may have implications for cometary and prebiotic science.

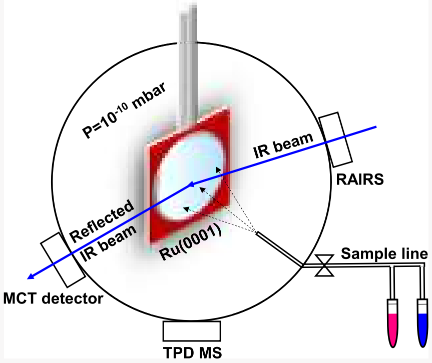

INTRODUCTION

Ice is one of the most abundant solids found in comets,[1] interstellar medium (ISM),[2,3] and the universe.[4] The structure of ice is crucial to an understanding of its physical and chemical properties, which have significant importance in planetary science, astrochemistry, and physical chemistry. There are several amorphous and crystalline forms of ice at different conditions of pressure and temperature, leading to the rich polymorphism of water.[5,6] Among these various forms, hexagonal ice (ice I_h) is the most abundant, and it occurs naturally on the surface of Earth. In the astrophysical or interstellar environment, in vacuum, ice is commonly found in an amorphous form as a result of the extremely low-temperature conditions present there.[7] This amorphous ice, upon annealing, first crystallizes into metastable cubic ice (ice I_c) and further converts into more stable ice I_h at ∼155 K.[7]

Several studies[8−15] have been carried out to determine the kinetics and mechanisms associated with ice crystallization. In addition, the effect of guest molecules on ice crystallization has also been studied. Strong acids like HNO_3[16] and HCl[17] are known to promote crystallization of amorphous solid water (ASW) to ice I_h. Here, excess protons (H^+) provided by the acids facilitated crystallization. However, NaCl[17] shows the opposite effect and hinders crystallization. In another study,[18] the effect of methanol and butane on the crystallization of ASW was investigated. Methanol reduces the ASW crystallization temperature to 152 K by enhancing the crystallization, whereas butane[18] and propane[19] do not show such an effect.

The presence of guest molecules has various effects on ice, and the formation of clathrate hydrates (CHs) is one such example.[20−22] CHs are solid, crystalline host−guest complexes, where different gases (guests) are trapped inside the hydrate network made of water molecules (host).[23,24] Previous reports[25−28] suggest that CHs act as precursors for the formation of ice I_c. Neon hydrate is known to transform into a crystalline ice XVI when it is kept under a prolonged vacuum.[6] Moreover, we have shown recently that ice I_c can be formed by the dissociation of acetone hydrate in ultrahigh vacuum (UHV) at 130−135 K.[29] In our previous study, the existence of CHs in the interstellar environment was also confirmed experimentally.[22] Therefore, CHs can be an ideal precursor, which can transform into ice I_h under extremely low pressures and temperatures, conditions relevant to the interstellar medium (ISM).

Herein, we have formed formaldehyde hydrate, which acts as the precursor for ice I_h under UHV at 130−135 K. Formaldehyde is prone to undergo polymerization when it comes in contact with water, and this polymerization can be prevented only when it forms formaldehyde hydrate.[30] In addition, formaldehyde also likes to form geminal diol in the presence of water at ambient conditions.[30] Therefore, the normal terrestrial condition is not suitable for the formation of

Received: November 17, 2020
Revised: January 22, 2021
Published: February 22, 2021

https://dx.doi.org/10.1021/acs.jpcc.0c10367
J. Phys. Chem. C 2021, 125, 4532−4539

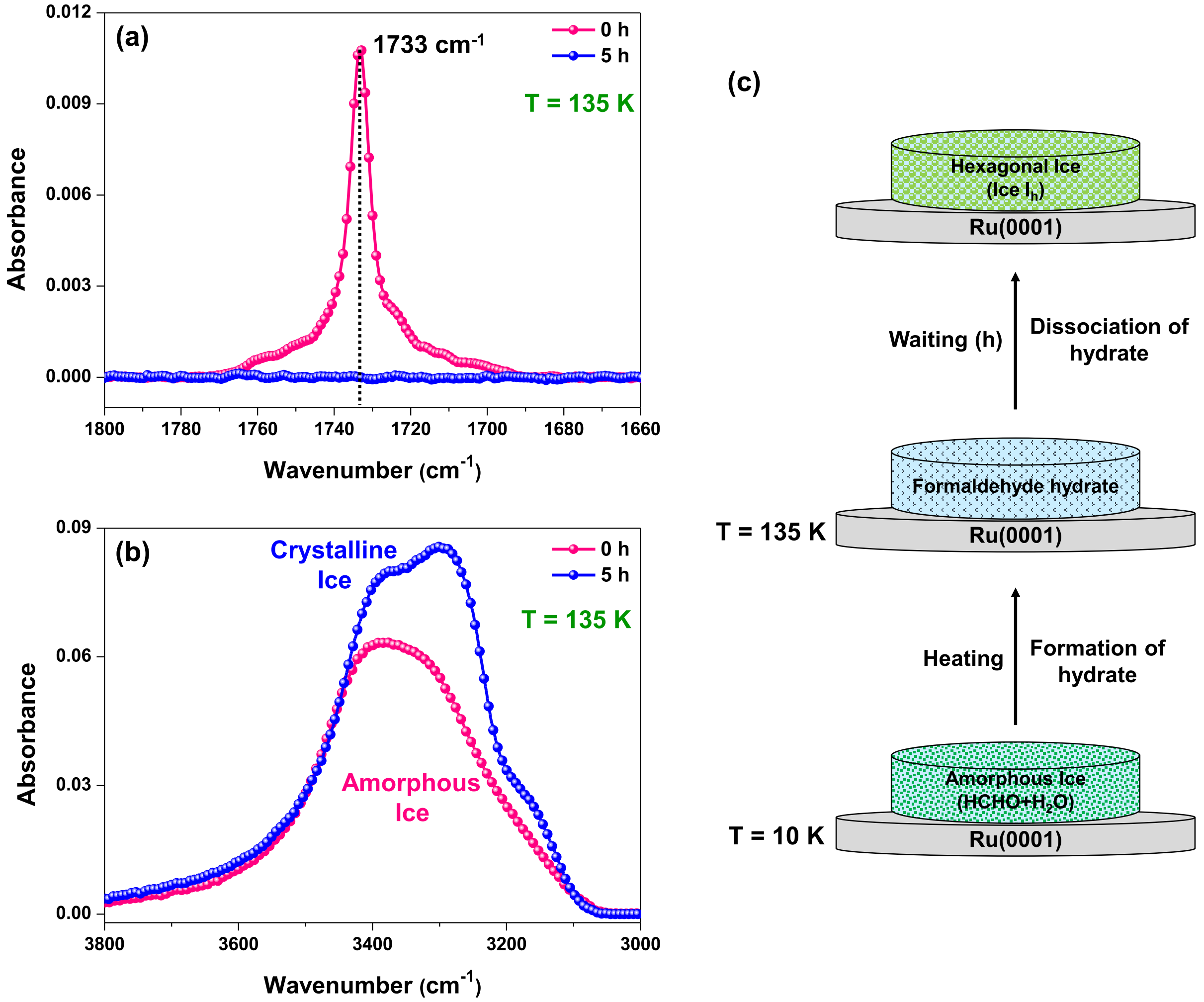

Figure 1. Time-dependent RAIR spectra of 300 MLs of formaldehyde:H_2O (1:1) at 135 K in the (a) C═O and (b) O−H stretching regions. The mixture was codeposited on Ru(0001) substrate at 10 K and annealed at a rate of 2 K·min^{-1} to 135 K. The O−H band changed due to the dissociation of formaldehyde hydrate which resulted in ice crystallization. The schematic illustration in (c) shows the formation of formaldehyde hydrate and its dissociation, stepwise. Dissociation of formaldehyde hydrate leads to the formation of hexagonal ice (ice I$_h$).

formaldehyde hydrate. It was suggested that it could only be formed at low-temperature conditions present in space or ISM.[30] This study provides direct evidence of the earlier claim that it is indeed possible to create formaldehyde hydrate in astrophysical environments without undergoing polymerization or formation of geminal diol in the presence of water. Moreover, formaldehyde is known to exist in ISM,[31−34] cometary ice,[32,35,36] and extraterrestrial environment,[37] and its linear polymer was the first polymeric compound found in space.[38] The high abundance of formaldehyde and the inherent temperature of comets (120−140 K) suggest that the presented transformation route may occur in comets in regular intervals. Moreover, this unique process of ice crystallization is facile with respect to the conventional process as it occurs at a lower temperature. Here, the high mobility of water molecules during the dissociation of hydrate acts as the driving force. Hama et al.[39] have reported the formation of crystalline ice by subliming a water/neon matrix (1/1000 ratio) at 11−12 K under UHV, where matrix sublimation makes water molecules highly mobile.[39] It helps to overcome the kinetic barrier for rearrangement of the H-bonding network, which makes crystallization possible even at a lower temperature. In a nutshell, we have found a unique and facile mechanistic route for ice crystallization, which links the existence of ice I$_h$ and CH in comets. This study does give some directions to the ice composition and structure possible in many astrophysical bodies like comets, which may have further implications from the cometary and prebiotic science perspective.

■ EXPERIMENTAL METHODS

All the experiments were performed in a custom-built ultrahigh vacuum (UHV) instrument (base pressure of ~5 × 10^{-10} mbar). The instrument was discussed in detail elsewhere.[40] Briefly, it has three UHV chambers (namely ionization chamber, octupole chamber, and scattering chamber) made of stainless steel, equipped with reflection absorption infrared (RAIR) spectroscopy and temperature-programmed desorption (TPD) mass spectrometry. Each vacuum chamber was pumped by turbomolecular pumps (TMPs), which were backed by oil-free diaphragm pumps (Pfeiffer Vacuum). The pressure of the experimental chamber was measured by a Bayard−Alpert (B−A) gauge (Pfeiffer Vacuum) controlled by the "MaxiGauge" vacuum gauge controller (Pfeiffer, Model TPG 256 A).

Here, a ruthenium single crystal, Ru(0001), with 1.5 cm diameter and 1 mm thickness was used as the substrate. A thin film of ice was grown layer by layer on this substrate at a low temperature (10 K). The substrate was mounted on a copper holder, which in turn was connected at the tip of a closed-cycle helium cryostat (Coldedge Technologies). The temperature of the substrate was monitored with the help of a K-type thermocouple sensor and a platinum sensor attached to the copper holder near the substrate. The substrate temperature could be varied in a wide temperature window of 8−1000 K. Before the sample deposition, the substrate was heated to 400 K multiple times to ensure surface cleanliness. Temperature ramping was controlled and monitored by a temperature controller (Lakeshore 336).

For the current study, formaldehyde vapor was obtained by thermolysis of solid paraformaldehyde (95% pure) purchased from Sigma-Aldrich. Here, paraformaldehyde was used as a precursor for the formation of formaldehyde vapor.[41] The solid paraformaldehyde was taken in a vacuum-sealed test tube, and it was connected to the sample line of the instrument through a glass-to-metal seal. The test tube was heated at ~120 °C in a silicone oil bath to generate the formaldehyde vapor upon thermolysis.[41] The generated vapor of formaldehyde was then introduced into the UHV chamber through a high-precision all-metal leak valve. Millipore water (H_2O of 18.2 M Ω resistivity) was taken in a separate test tube connected to the sample line through a glass-to-metal seal. The water was further purified through several freeze−pump−thaw cycles before introduction into the UHV chamber. Here, it must be noted that out of the two sample inlet lines, one was exclusively used for formaldehyde while the other line was used for water deposition. During the exposure of these samples to the substrate, mass spectra were recorded to check the purity as well as to measure the ratio of the mixtures with the help of a residual gas analyzer, attached near the sample inlet line. The substrate was kept at a perpendicular position near the sample inlet tubes for consistent growth of ice. The deposition of molecular solids was controlled through leak valves and represented in terms of monolayers (MLs), assuming that 1.33×10^{-6} mbar·s = 1 ML, which was estimated to contain $\sim 1.1 \times 10^{15}$ molecules·cm^{-2}. The inlet pressures for sample deposition were decided based on the coverage required at the time of the experiment. Importantly, the substrate does not play any significant role during the experiment as these experiments were carried out under multilayer conditions.

Here, 300 MLs of formaldehyde:H_2O (1:1) were prepared by backfilling the UHV chamber at a total pressure of $\sim 5 \times 10^{-7}$ mbar (where formaldehyde inlet pressure = 2.5×10^{-7} mbar and water inlet pressure = 2.5×10^{-7} mbar), and the mixture was exposed to the surface for 10 min. After deposition, the mixed ice was heated at a rate of 2 K·min^{-1} to the experimental temperatures. The ice sample was monitored by RAIR spectroscopy at different temperatures. The experimental conditions were kept the same such as the position of the substrate and external IR detector during the time-dependent study.

RAIR spectra were recorded using a Bruker FT-IR spectrometer, Vertex 70. The external IR beam was focused onto the substrate using gold-plated mirrors through ZnSe windows (transparent to the IR beam) attached to the vacuum chamber. The reflected IR beam from the substrate was refocused using another gold-plated mirror to a liquid N_2 cooled external IR detector (mercury cadmium telluride; MCT). The spectra were collected in the 4000−550 cm^{-1} range with a 2 cm^{-1} resolution. Each spectrum was an average of 512 scans to get a better signal-to-noise ratio. The IR beam path outside the UHV chamber was purged with dry N_2.

RESULTS AND DISCUSSION

Here, we report a unique and facile transformation route for the formation of hexagonal ice (ice I_h) via formaldehyde hydrate, relevant to astrophysical environments. The interstellar-like environment was mimicked in an UHV chamber, and more details of this chamber are discussed in the Experimental Methods section. Three hundred monolayers of formaldehyde:H_2O (1:1) were codeposited on Ru(0001) substrate at 10 K and heated at a rate of 2 K·min^{-1} to 135 K. The mixture was kept at 135 K for 5 h under UHV. Figure 1a and 1b show the RAIR spectra obtained immediately after the codeposited film was annealed at 135 K (0 h trace) and after 5 h (5 h trace) in the C═O and O−H stretching regions, respectively. In Figure 1a, the C═O stretching peak at 1733 cm^{-1} is due to the formaldehyde hydrate, which was obtained by heating the formaldehyde:H_2O mixture. To understand the origin of this peak, which is assigned to formaldehyde hydrate, temperature-dependent RAIRS measurement of the formaldehyde:H_2O mixture was carried out separately, as shown in Figure S1. The C═O stretching region in Figure S1a suggests that formaldehyde hydrate starts to form at 110 K during continuous heating. Here, the other features (1731, 1722, and 1716 cm^{-1}) come from the irregular crystallite formation of formaldehyde in the amorphous ice pores. These IR features of the formaldehyde crystallites are assigned based on the temperature-dependent RAIR study of pure formaldehyde, which undergoes crystallization at ~90 K (Figure S2). It is clear that the IR feature of formaldehyde hydrate (1733 cm^{-1}) is entirely new as compared to the other features of formaldehyde. Moreover, previous reports[20−22] suggest that the vibrational signature of the guest molecules trapped in hydrate cages usually falls in between their vapor (1746 cm^{-1})[41] and condensed (1723 cm^{-1})[41] phase frequencies. This clearly suggests that the 1733 cm^{-1} peak is due to hydrate since it also falls between the IR peak positions of vapor and condensed phases of formaldehyde. Moreover, a full-range IR spectrum of the formaldehyde:water mixture is shown in Figure S3 along with the assignments.

On the other hand, the O−H stretching region in Figure S1a shows a profound change due to heating. At low temperature (<90 K), the O−H stretching band has three broad shoulders, positioned at 3510, 3422, and 3275 cm^{-1}. These features are due to the formation of H-bonding interaction between water and formaldehyde. These shoulders gradually disappeared as the ice mixture was heated beyond 90 K, eventually becoming a broad peak, which is the characteristic feature of ASW. Similar H-bonded features and their disappearance with heating were also observed with the acetonitrile and water mixture.[42] Here, the breaking of H-bonds occurs due to heating, and they are completely broken at 90 K, the crystallization temperature of formaldehyde. At this point, most of the formaldehyde gets phase-separated and desorbed as the system is heated further. However, a small amount of formaldehyde, which was buried into the ASW pores, could not escape, leading to the formation of formaldehyde hydrate. It must be noted that although clathrate hydrates are crystalline in nature, the unit cells of hydrates are complex, and the water molecules reside in several inequivalent sites; therefore, the O−H stretching band of the host ice network is broadened.[20,43,44] Moreover, we have confirmed the structure of the resultant ice system left after the dissociation of formaldehyde hydrate. In this regard, we have compared the characteristic O−H stretching bands of pure crystalline ice I_h film and the resultant ice system left after the dissociation of formaldehyde hydrate at 135 K, as shown in Figure S4. Both of these experiments were carried out separately, and they produced similar O−H stretching bands, which again proved that the dissociation of formaldehyde produces nothing but ice I_h. Moreover, time-dependent studies of pure 150 MLs of H_2O were carried out at 120 and 130 K (Figure S5), and self-crystallization of ice was not observed. In addition, the time-dependent RAIR spectra of pure water at 135 K (Figure S6) clearly suggest that the crystallization is only due to the dissociation of formaldehyde hydrate at this condition. It is clear that the dissociation of formaldehyde hydrate alone produced ice I_h, even at a lower temperature.

To present more clear evidence for the 1733 cm^{-1} peak, being the characteristic feature of formaldehyde hydrate, we have done an isothermal time-dependent RAIR study of 150 MLs of pure formaldehyde at 95 K, as shown in Figure 2. This particular temperature (95 K) is chosen as formaldehyde undergoes crystallization above this temperature. Figure 2 shows multiple C═O stretching features, which are attributed to the crystalline phase of formaldehyde. The intensity of these IR features gradually reduced with time, which accounts for the desorption of formaldehyde. Moreover, the temperature desorption-mass spectrum (TPD-MS) of pure formaldehyde also shows a desorption peak at ∼97 K, as shown in Figure S7. It must be noted that these multiple features do not match with the 1733 cm^{-1} peak. It is entirely a new feature, which further supports our earlier claim that it arises only because of formaldehyde hydrate and not because of bulk formaldehyde or its aggregates. Moreover, it was observed that ice I_h crystallization via formaldehyde hydrate was associated with time-dependent kinetics. This was confirmed by conducting isothermal time-dependent RAIRS measurements at 130, 132, 135, and 137 K, where gradual changes of both C═O and O−H stretching bands are displayed (Figure S8−S11).

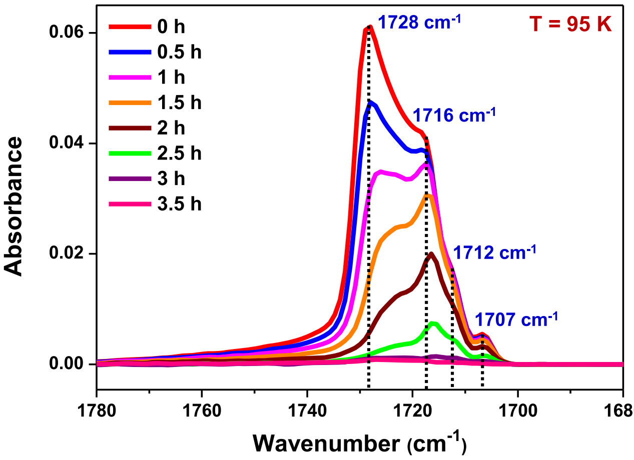

Figure 2. Isothermal time-dependent RAIR spectra of 150 MLs of pure formaldehyde film at 95 K in the C═O stretching region. Formaldehyde vapor was deposited on Ru(0001) substrate at 10 K, and then it was heated from 10 to 95 K at a rate of 2 K·min^{-1}.

CRYSTALLIZATION KINETICS

The crystallization kinetics and associated thermodynamic properties of ice are of paramount importance not only in basic science but also in planetary science, astrochemistry, and physical chemistry. In this regard, RAIRS was found to be a useful tool to determine the crystallization kinetics of ice by monitoring the change in O−H stretching[13,14,17] and decoupled O−D stretching bands[15,45] of H_2O during crystallization. In this study, both these spectral bands were used to evaluate the kinetics of ice I_h crystallization.

Time-dependent RAIRS studies of formaldehyde:HDO (5% D_2O in H_2O) were conducted for the evaluation of the crystallization kinetics and its parameters (rate constants, Avrami exponent values) at 130, 132, 135, and 137 K (Figures S12−S15). In Figure S14a at 135 K, the 0 and 5 h spectra show pure ASW behavior and complete crystallization, respectively. The fraction crystallized with time t was calculated by subtracting the spectrum obtained at time zero from the spectrum at time t at a fixed wavenumber (3302 cm^{-1} in Figure S14b indicated by the vertical dashed line) for each temperature. Similarly, in Figure S14a, the crystallization fraction ($x(t)$) was calculated at a fixed wavenumber, 2427 cm^{-1} (indicated by the vertical dashed line), where a broad, amorphous spectrum (t = 0) changed into a relatively sharp crystalline spectrum (t = 5 h). Here, differences in the integrated peak area between the completely ASW and (partly) crystalline films at each time interval were considered. However, changes in the absorbance (ΔA) at a fixed wavenumber (∼2427 cm^{-1} in Figure S14b, indicated by a vertical line) produced almost the same result for $x(t)$ as that obtained from the integrated peak area. A similar approach was adopted in several previous reports.[13,14,17,29] The crystallization fraction, $x(t)$, was calculated by eq 1

$$x(t) = \frac{\Delta A(1)}{\Delta A(2)} \tag{1}$$

where $\Delta A(1)$ is the difference in the absorbance at a particular time t and that at time zero, and $\Delta A(2)$ is the difference in the absorbance of a completely crystallized film and that at time zero.

Figure 3a and 3b demonstrate the change in crystallization fraction at different temperatures with time as obtained from the O−H and decoupled O−D stretching bands at a fixed wavenumber. The change of the shape of the curve from sigmoidal to exponential with temperature shows that the rate of crystallization increases with increasing temperature. Now, the nucleation and growth mechanism of ASW crystallization was predicted by fitting the crystallization fraction $x(t)$ to the Avrami equation at different temperatures.

$$x(t) = 1 - \exp[-k(T)\cdot t]^n \tag{2}$$

Here $k(T)$ is the rate constant, t is time, and n is the Avrami exponent. For all temperatures, n held an integer value between 1 and 4, which reflected the nature of the transformation, whether it is diffusion or interface-controlled, and dictated the geometry of the growing particles.[7,46] Thus, the Avrami exponent, n, can be used to predict the nature of the transformation process. After rearrangement and simplification, eq 2 becomes

$$\ln(-\ln[1 - x(t)]) = n\ln(t) + n\ln k(T) \tag{3}$$

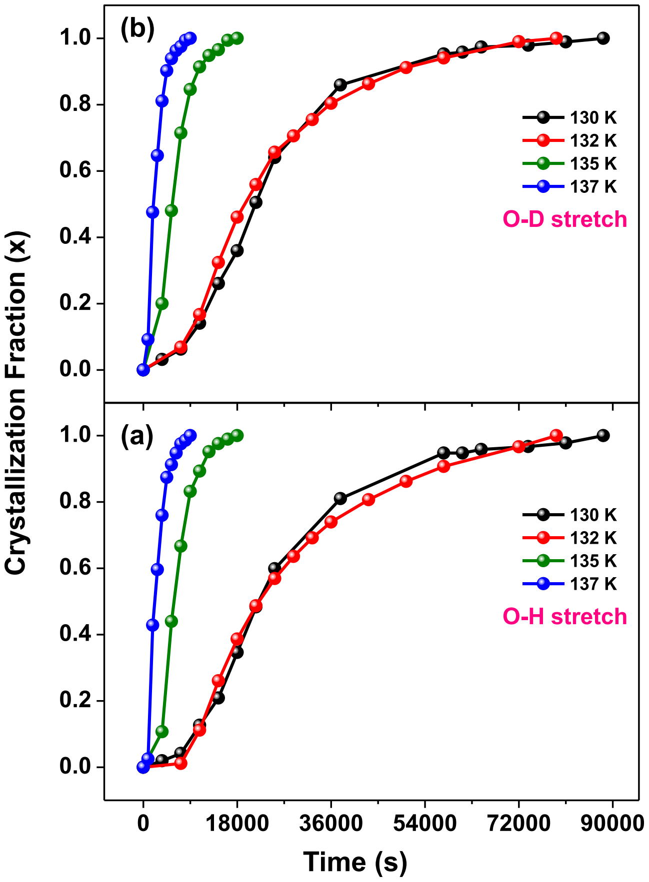

Figure 3. Crystallization fraction of 300 MLs of formaldehyde:HDO (5% D_2O in H_2O) obtained from isothermal RAIRS measurements at 130, 132, 135, and 137 K. The crystallization fraction was estimated from (a) the 3302 cm^{-1} peak in the O−H stretching region and (b) the 2427 cm^{-1} peak in the decoupled O−D stretching region.

Figure 4a and 4b demonstrate a plot between $\ln(-\ln[1 - x(t)])$ vs $\ln(t)$ using eq 3. The slope and intercept of the linearly fitted lines were used to determine the values of n and $k(T)$ for different temperatures. Values of n and $k(T)$ obtained from the analysis of O−H and decoupled O−D stretching bands for different temperatures are listed in Table S1.

The evaluated value of n (1.65−1.34, in Table S1) reflects that crystallization kinetics is diffusion-controlled with particles growing into a predominantly spherical geometry[46−48] as the theory of phase transformation by nucleation and growth also suggests that the crystallization kinetics is diffusion-controlled with particles growing into a predominantly spherical geometry for n having fractional values.[13,14,29] Here we propose that the dissociation of formaldehyde hydrate can enhance the diffusion or mobility of H_2O molecules which in turn prompt the crystallization of ice.[29] Moreover, for the ASW films thicker than 20 MLs, n is about 4, and the crystallization proceeds via homogeneous nucleation followed by three-dimensional growth as reported in previous studies.[9,10,13] All these reports involve pure solid water film, and the only driving force for crystallization is annealing to higher temperatures. However, our study involves mixed film of formaldehyde and H_2O in a 1:1 ratio, where formaldehyde is desorbing from bulk as well as from the interface simultaneously. So, there is random generation of crystalline domains throughout the ice mixture which grow and soon reach the surface/interface of the films and would inhibit the three-dimensional growth, and therefore the decrease in the value of n is reasonable.[49−52] Figure 5a and 5b demonstrate that all of the crystallization rates at different temperatures were fitted in an Arrhenius plot obtained from the O−H and decoupled O−D stretching regions, respectively. The activation energy (E_a) was evaluated from the slope of the linearly fitted lines. Activation energy obtained in this study was ~53.65 and ~56.70 kJ mol^{-1}, and it is comparable with the previously reported values for the crystallization of pure ASW evaluated by different experimental techniques.[10,11,13,15,17] Here, crystallization occurred at a lower temperature than the usual crystallization temperature, which can be attributed to the high mobility of water molecules after hydrate dissociation.

■ CONCLUSIONS

In this study, we have observed experimentally the formation of hexagonal ice (ice I_h) at 130−135 K, which is lower than its usual crystallization temperature in UHV. This facile

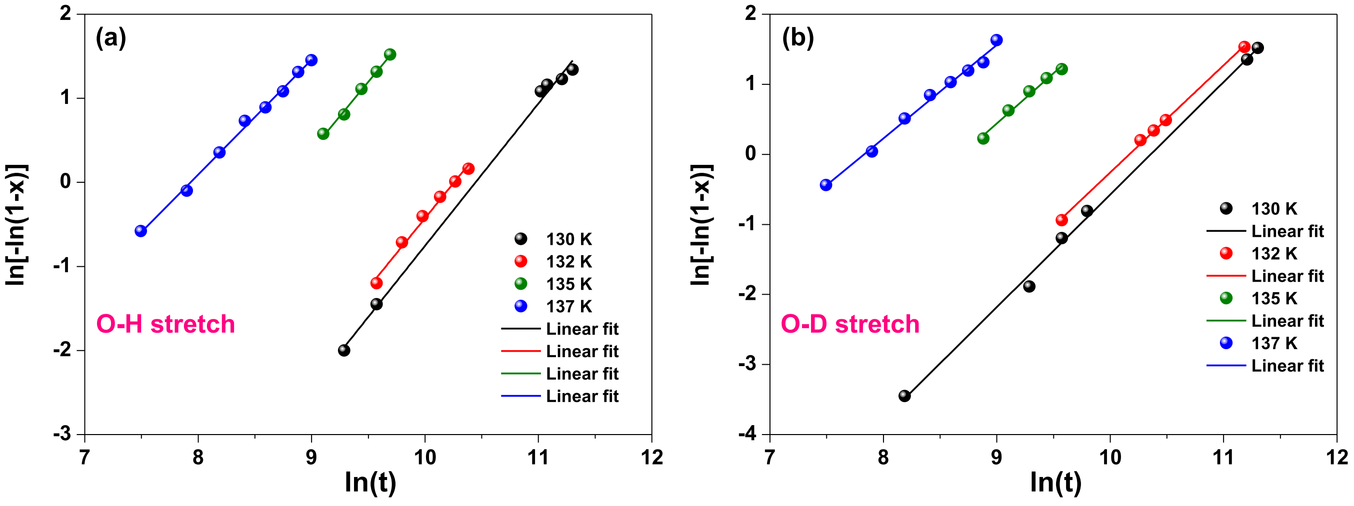

Figure 4. Plot of $\ln(-\ln[1-x(t)])$ vs $\ln(t)$ at different temperatures of 130, 132, 135, and 137 K. These data points are obtained from the analysis of (a) the O−H and (b) the O−D stretching regions and fitted using the Avrami equation.

https://dx.doi.org/10.1021/acs.jpcc.0c10367
J. Phys. Chem. C 2021, 125, 4532−4539

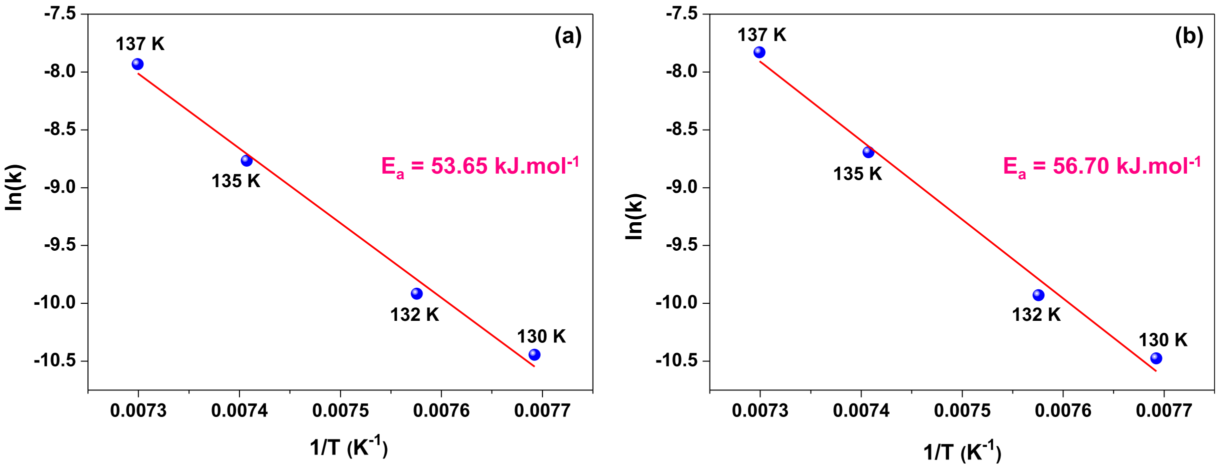

Figure 5. Plot of ln k(T) vs inverse temperature ($1/T$), obtained from the analysis of (a) the O−H and (b) the O−D stretching regions, respectively. The data points were fitted to obtain a straight line. Activation energy (E_a) can be calculated from the slope of the straight line.

crystallization happens due to the dissociation of formaldehyde hydrate, which acts as a precursor. The experiments were carried out in UHV and cryogenic temperatures and have direct relevance to the astrophysical environments or ISM. Formaldehyde is known to form geminal diol or undergo polymerization by reacting with water under ambient conditions. However, formaldehyde in its clathrate hydrate form does not show such an effect. This study shows that formaldehyde hydrate can exist in the extremely low-pressure conditions present in astrophysical environments or ISM without undergoing polymerization or reaction leading to geminal diol. Moreover, formaldehyde hydrate dissociated to form ice I_h after keeping for extended periods under UHV. Since formaldehyde and water are present in space, it is likely that a hydrate of it is formed. We believe that we have found a mechanistic route for the formation of ice I_h, which links the existence of ice I_h and formaldehyde hydrate in astrophysical environments/ISM.

■ ASSOCIATED CONTENT

Supporting Information

The Supporting Information is available free of charge at https://pubs.acs.org/doi/10.1021/acs.jpcc.0c10367.

> Isothermal time-dependent RAIR spectra of pure formaldehyde, formaldehyde:H_2O, and formaldehyde:HDO at different temperatures, crystallization fractions, and different crystallization parameters of formaldehyde:HDO at different temperatures (PDF)

■ AUTHOR INFORMATION

Corresponding Author

Thalappil Pradeep − *DST Unit of Nanoscience (DST UNS) and Thematic Unit of Excellence (TUE), Department of Chemistry, Indian Institute of Technology Madras, Chennai 600036, India;* orcid.org/0000-0003-3174-534X; Email: pradeep@iitm.ac.in

Authors

Jyotirmoy Ghosh − *DST Unit of Nanoscience (DST UNS) and Thematic Unit of Excellence (TUE), Department of Chemistry, Indian Institute of Technology Madras, Chennai 600036, India*

Gaurav Vishwakarma − *DST Unit of Nanoscience (DST UNS) and Thematic Unit of Excellence (TUE), Department of Chemistry, Indian Institute of Technology Madras, Chennai 600036, India*

Subhadip Das − *DST Unit of Nanoscience (DST UNS) and Thematic Unit of Excellence (TUE), Department of Chemistry, Indian Institute of Technology Madras, Chennai 600036, India*

Complete contact information is available at: https://pubs.acs.org/10.1021/acs.jpcc.0c10367

Author Contributions

J.G., G.V., and S.D. designed and performed the experiments. J.G. and G.V. analyzed the results. T.P. proposed the project and supervised the progress. The manuscript was written through contributions of all authors.

Author Contributions

‡J.G. and G.V. contributed equally.

Notes

The authors declare no competing financial interest.

■ ACKNOWLEDGMENTS

We thank the Department of Science and Technology (DST), Government of India, for supporting our research. J.G. thanks the University Grants Commission (UGC) for his research fellowship. G.V. thanks IITM for his research fellowship.

■ REFERENCES

(1) Jenniskens, P.; Blake, D. F. Structural transitions in amorphous water ice and astrophysical implications. *Science* **1994**, *265* (5173), 753.

(2) Allamandola, L.; Bernstein, M.; Sandford, S.; Walker, R. Evolution of interstellar ices. *Space Sci. Rev.* **1999**, *90* (1−2), 219−232.

(3) Burke, D. J.; Brown, W. A. Ice in space: Surface science investigations of the thermal desorption of model interstellar ices on dust grain analogue surfaces. *Phys. Chem. Chem. Phys.* **2010**, *12* (23), 5947−5969.

(4) Boogert, A. C. A.; Gerakines, P. A.; Whittet, D. C. B. Observations of the Icy Universe. *Annu. Rev. Astron. Astrophys.* **2015**, *53* (1), 541−581.

(5) Salzmann, C. G.; Radaelli, P. G.; Slater, B.; Finney, J. L. The polymorphism of ice: five unresolved questions. *Phys. Chem. Chem. Phys.* **2011**, *13* (41), 18468−18480.

(6) Falenty, A.; Hansen, T. C.; Kuhs, W. F. Formation and properties of ice XVI obtained by emptying a type sII clathrate hydrate. *Nature* **2014**, *516*, 231−233.

(7) Jenniskens, P.; Blake, D. F. Crystallization of amorphous water ice in the solar system. *Astrophys. J.* **1996**, *473* (2), 1104−1113.

(8) Backus, E. H. G.; Grecea, M. L.; Kleyn, A. W.; Bonn, M. Surface crystallization of amorphous solid water. *Phys. Rev. Lett.* **2004**, *92* (23), 236101.

(9) Dohnálek, Z.; Kimmel, G. A.; Ciolli, R. L.; Stevenson, K. P.; Smith, R. S.; Kay, B. D. The effect of the underlying substrate on the crystallization kinetics of dense amorphous solid water films. *J. Chem. Phys.* **2000**, *112* (13), 5932−5941.

(10) Kondo, T.; Kato, H. S.; Bonn, M.; Kawai, M. Deposition and crystallization studies of thin amorphous solid water films on Ru(0001) and on CO-precovered Ru(0001). *J. Chem. Phys.* **2007**, *127* (9), 094703.

(11) Safarik, D. J.; Mullins, C. B. The nucleation rate of crystalline ice in amorphous solid water. *J. Chem. Phys.* **2004**, *121* (12), 6003−6010.

(12) Smith, R. S.; Huang, C.; Wong, E. K. L.; Kay, B. D. Desorption and crystallization kinetics in nanoscale thin films of amorphous water ice. *Surf. Sci.* **1996**, *367* (1), L13−L18.

(13) Smith, R. S.; Matthiesen, J.; Knox, J.; Kay, B. D. Crystallization Kinetics and Excess Free Energy of H_2O and D_2O Nanoscale Films of Amorphous Solid Water. *J. Phys. Chem. A* **2011**, *115* (23), 5908−5917.

(14) Smith, R. S.; Petrik, N. G.; Kimmel, G. A.; Kay, B. D. Thermal and Nonthermal Physiochemical Processes in Nanoscale Films of Amorphous Solid Water. *Acc. Chem. Res.* **2012**, *45* (1), 33−42.

(15) Yuan, C.; Smith, R. S.; Kay, B. D. Communication: Distinguishing between Bulk and Interface-Enhanced Crystallization in Nanoscale Films of Amorphous Solid Water. *J. Chem. Phys.* **2017**, *146* (3), 031102.

(16) McClure, S. M.; Barlow, E. T.; Akin, M. C.; Tanaka, P. L.; Safarik, D. J.; Truskett, T. M.; Mullins, C. B. Effect of Dilute Nitric Acid on Crystallization and Fracture of Amorphous Solid Water Films. *J. Phys. Chem. C* **2007**, *111* (28), 10438−10447.

(17) Lee, D. H.; Kang, H. Acid-Promoted Crystallization of Amorphous Solid Water. *J. Phys. Chem. C* **2018**, *122* (42), 24164−24170.

(18) Souda, R. Effects of methanol on crystallization of water in the deeply supercooled region. *Phys. Rev. B: Condens. Matter Mater. Phys.* **2007**, *75* (18), 184116.

(19) Ghosh, J.; Hariharan, A. K.; Bhuin, R. G.; Methikkalam, R. R. J.; Pradeep, T. Propane and propane-water interactions: A study at cryogenic temperatures. *Phys. Chem. Chem. Phys.* **2018**, *20* (3), 1838−1847.

(20) Buch, V.; Devlin, J. P.; Monreal, I. A.; Jagoda-Cwiklik, B.; Uras-Aytemiz, N.; Cwiklik, L. Clathrate hydrates with hydrogen-bonding guests. *Phys. Chem. Chem. Phys.* **2009**, *11* (44), 10245−10265.

(21) Ghosh, J.; Bhuin, R. G.; Ragupathy, G.; Pradeep, T. Spontaneous formation of tetrahydrofuran hydrate in ultrahigh vacuum. *J. Phys. Chem. C* **2019**, *123* (26), 16300−16307.

(22) Ghosh, J.; Methikkalam, R. R. J.; Bhuin, R. G.; Ragupathy, G.; Choudhary, N.; Kumar, R.; Pradeep, T. Clathrate Hydrates in Interstellar Environment. *Proc. Natl. Acad. Sci. U. S. A.* **2019**, *116* (5), 1526−1531.

(23) Sloan, E. D.; Koh, C. A. *Clathrate Hydrates of Natural Gases*, 3rd ed.; CRC Press: Boca Raton, FL, 2007; p 752.

(24) Sloan, E. D., Jr Fundamental principles and applications of natural gas hydrates. *Nature* **2003**, *426*, 353−363.

(25) Falenty, A.; Hansen, T. C.; Kuhs, W. F. Cubic Ice Formation and Annealing During CO_2 Clathrate Hydrate Decomposition at Low Temperatures. *Physics and Chemistry of Ice 2010*; Hokkaido University Press: Sapporo, Japan, 2011; p 411.

(26) Falenty, A.; Kuhs, W. F. Self-Preservation" of CO_2 Gas Hydrates-Surface Microstructure and Ice Perfection. *J. Phys. Chem. B* **2009**, *113* (49), 15975−15988.

(27) Kuhs, W. F.; Genov, G.; Staykova, D. K.; Hansen, T. Ice Perfection and Onset of Anomalous Preservation of Gas Hydrates. *Phys. Chem. Chem. Phys.* **2004**, *6* (21), 4917−4920.

(28) Takeya, S.; Uchida, T.; Nagao, J.; Ohmura, R.; Shimada, W.; Kamata, Y.; Ebinuma, T.; Narita, H. Particle Size Effect of CH_4 Hydrate for Self-Preservation. *Chem. Eng. Sci.* **2005**, *60* (5), 1383−1387.

(29) Ghosh, J.; Bhuin, R. G.; Vishwakarma, G.; Pradeep, T. Formation of Cubic Ice via Clathrate Hydrate, Prepared in Ultrahigh Vacuum under Cryogenic Conditions. *J. Phys. Chem. Lett.* **2020**, *11* (1), 26−32.

(30) Ripmeester, J. A.; Ding, L.; Klug, D. D. A Clathrate Hydrate of Formaldehyde. *J. Phys. Chem.* **1996**, *100* (32), 13330−13332.

(31) Allamandola, L. J.; Sandford, S. A.; Valero, G. J. Photochemical and thermal evolution of interstellar/precometary ice analogs. *Icarus* **1988**, *76* (2), 225−252.

(32) Schutte, W. A.; Allamandola, L. J.; Sandford, S. A. Formaldehyde and organic molecule production in astrophysical ices at cryogenic temperatures. *Science* **1993**, *259* (5098), 1143−1145.

(33) Snyder, L. E.; Buhl, D.; Zuckerman, B.; Palmer, P. Microwave Detection of Interstellar Formaldehyde. *Phys. Rev. Lett.* **1969**, *22* (13), 679−681.

(34) Tielens, A.; Hagen, W. Model calculations of the molecular composition of interstellar grain mantles. *Astron. Astrophys.* **1982**, *114*, 245.

(35) Schutte, W. A. Production of organic molecules in interstellar ices. *Adv. Space Res.* **2002**, *30* (6), 1409−1417.

(36) Schutte, W. A.; Allamandola, L. J.; Sandford, S. A. Very low temperature formaldehyde reactions and the build-up of organic molecules in comets and interstellar ices. *Adv. Space Res.* **1995**, *15* (3), 401−406.

(37) Wickramasinghe, N. C. Polyoxymethylene Polymers as Interstellar Grains. *Mon. Not. R. Astron. Soc.* **1975**, *170* (1), 11P−16P.

(38) Huebner, W. F. First Polymer in Space Identified in Comet Halley. *Science* **1987**, *237* (4815), 628−630.

(39) Hama, T.; Ishizuka, S.; Yamazaki, T.; Kimura, Y.; Kouchi, A.; Watanabe, N.; Sugimoto, T.; Pirronello, V. Fast crystalline ice formation at extremely low temperature through water/neon matrix sublimation. *Phys. Chem. Chem. Phys.* **2017**, *19* (27), 17677−17684.

(40) Bag, S.; Bhuin, R. G.; Methikkalam, R. R. J.; Pradeep, T.; Kephart, L.; Walker, J.; Kuchta, K.; Martin, D.; Wei, J. Development of Ultralow Energy (1 - 10 eV) Ion Scattering Spectrometry Coupled with Reflection Absorption Infrared Spectroscopy and Temperature Programmed Desorption for the Investigation of Molecular Solids. *Rev. Sci. Instrum.* **2014**, *85* (1), 014103.

(41) Schutte, W. A.; Allamandola, L. J.; Sandford, S. A. An Experimental Study of the Organic Molecules Produced in Cometary and Interstellar Ice Analogs by Thermal Formaldehyde Reactions. *Icarus* **1993**, *104* (1), 118−137.

(42) Bhuin, R. G.; Methikkalam, R. R. J.; Sivaraman, B.; Pradeep, T. Interaction of acetonitrile with water-ice: An infrared spectroscopic study. *J. Phys. Chem. C* **2015**, *119* (21), 11524−11532.

(43) Ghosh, J.; Methikkalam, R. R. J.; Bhuin, R. G.; Ragupathy, G.; Choudhary, N.; Kumar, R.; Pradeep, T. Reply to Choukroun et al.: IR and TPD data suggest the formation of clathrate hydrates in laboratory experiments simulating ISM. *Proc. Natl. Acad. Sci. U. S. A.* **2019**, *116* (29), 14409.

(44) Devlin, J. P.; Wooldridge, P. J.; Ritzhaupt, G. Decoupled isotopomer vibrational frequencies in cubic ice: A simple unified view of the Fermi diads of decoupled H2O, HOD, and D2O. *J. Chem. Phys.* **1986**, *84* (11), 6095−6100.

(45) Xu, Y.; Petrik, N. G.; Smith, R. S.; Kay, B. D.; Kimmel, G. A. Growth Rate of Crystalline Ice and the Diffusivity of Supercooled Water from 126 to 262 K. *Proc. Natl. Acad. Sci. U. S. A.* **2016**, *113* (52), 14921.

(46) Hage, W.; Hallbrucker, A.; Mayer, E.; Johari, G. P. Crystallization Kinetics of Water below 150 K. *J. Chem. Phys.* **1994**, *100* (4), 2743−2747.

(47) Doremus, R. H. *Rates of Phase Transformations*; Academic Press, Inc.: Orlando, FL, 1985.

(48) Rao, C. N. R.; Rao, K. J. In *Phase Transitions in Solids: An Approach to the Study of the Chemistry and Physics of Solids*; McGraw-Hill: New York, 1978; pp 81−173.

(49) Moghadam, M. M.; Pang, E. L.; Philippe, T.; Voorhees, P. W. Simulation of phase transformation kinetics in thin films under a constant nucleation rate. *Thin Solid Films* **2016**, *612*, 437−444.

(50) Očenášek, J.; Novák, P.; Agbo, S. Finite-thickness effect on crystallization kinetics in thin films and its adaptation in the Johnson−Mehl−Avrami−Kolmogorov model. *J. Appl. Phys.* **2014**, *115* (4), 043505.

(51) Pang, E. L.; Vo, N. Q.; Philippe, T.; Voorhees, P. W. Modeling interface-controlled phase transformation kinetics in thin films. *J. Appl. Phys.* **2015**, *117* (17), 175304.

(52) Schultz, J. M. Effect of Specimen Thickness on Crystallization Rate. *Macromolecules* **1996**, *29* (8), 3022−3024.

Facile Crystallization of Ice I_h via Formaldehyde Hydrate in Ultrahigh Vacuum under Cryogenic Conditions

Jyotirmoy Ghosh,[†] *Gaurav Vishwakarma,*[†] *Subhadip Das,*[†] *and Thalappil Pradeep*[†,*]

[†]DST Unit of Nanoscience (DST UNS) and Thematic Unit of Excellence (TUE), Department of Chemistry, Indian Institute of Technology Madras, Chennai 600036, India

AUTHOR INFORMATION

Corresponding Author

Corresponding author: *E-mail: pradeep@iitm.ac.in

Table of contents

Supporting Information 1:

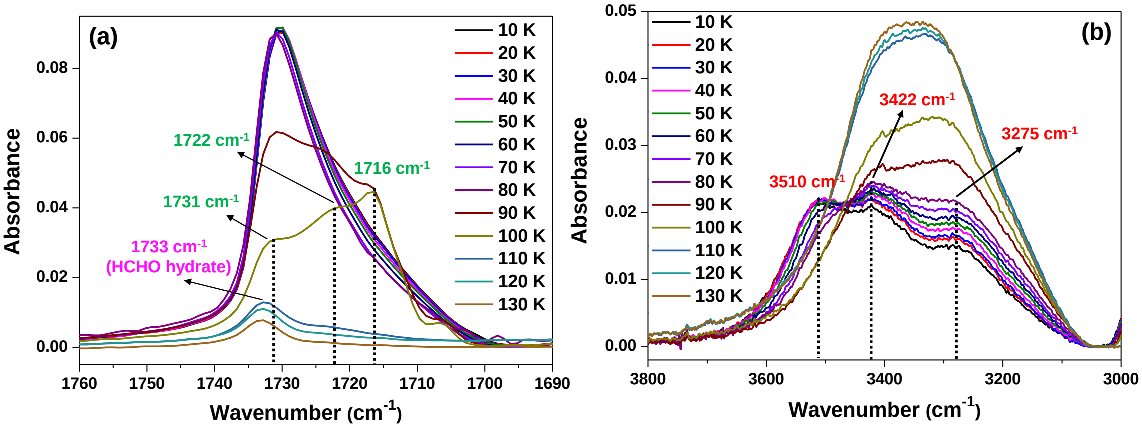

Figure S1. Temperature-dependent RAIR spectra of 300 MLs of formaldehyde:H_2O (1:1) in the (a) C=O and (b) O-H stretching regions. The mixture was co-deposited on Ru(0001) substrate at 10 K, and annealed at a rate of 2 K.min^{-1}.

Supporting Information 2:

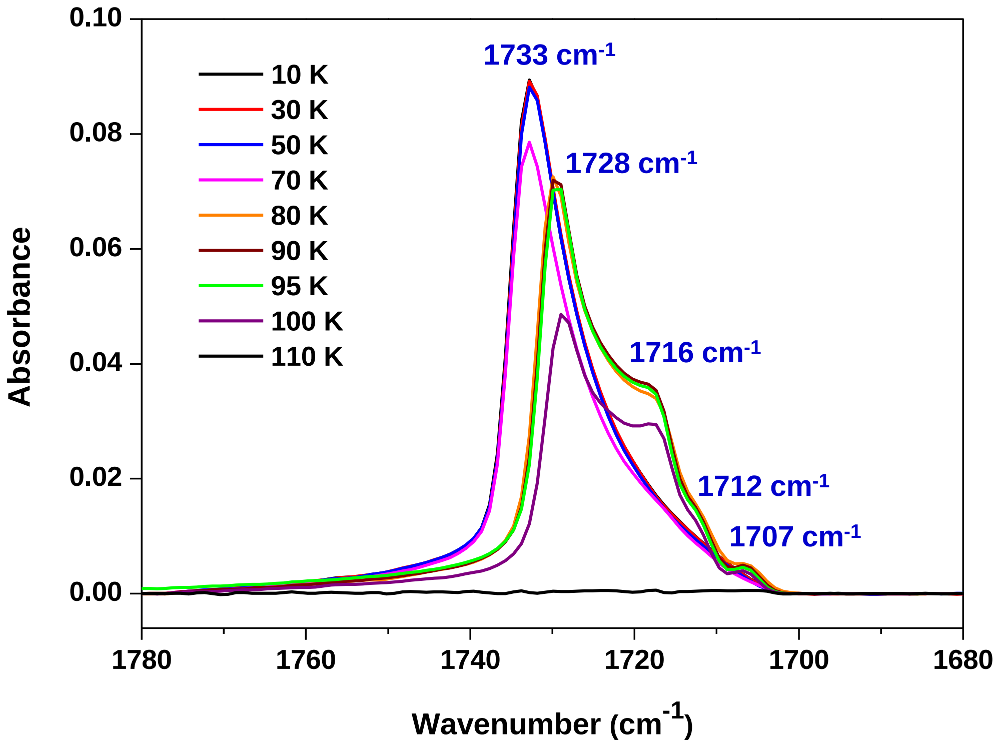

Figure S2. Temperature-dependent RAIR spectra of 150 MLs of pure formaldehyde in the C=O stretching region. The formaldehyde vapor was deposited on Ru(0001) substrate at 10 K, and annealed at a rate of 2 K.min^{-1}.

Supporting Information 3:

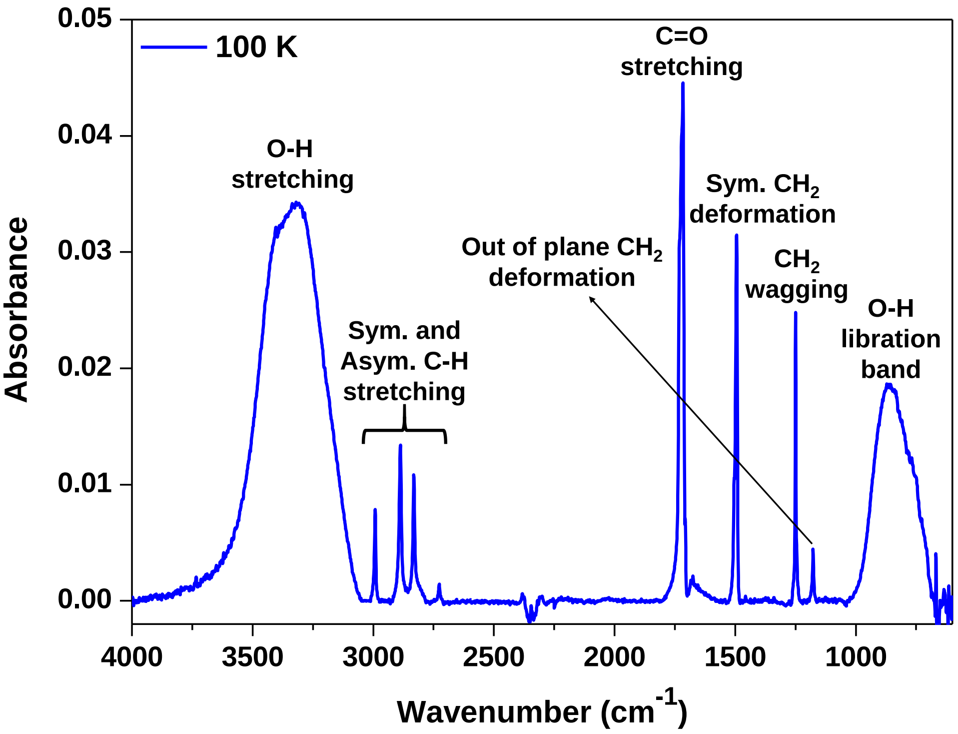

Figure S3. Full scale RAIR spectrum of 300 MLs of formaldehyde:H_2O (1:1) at 100 K.

Supporting Information 4:

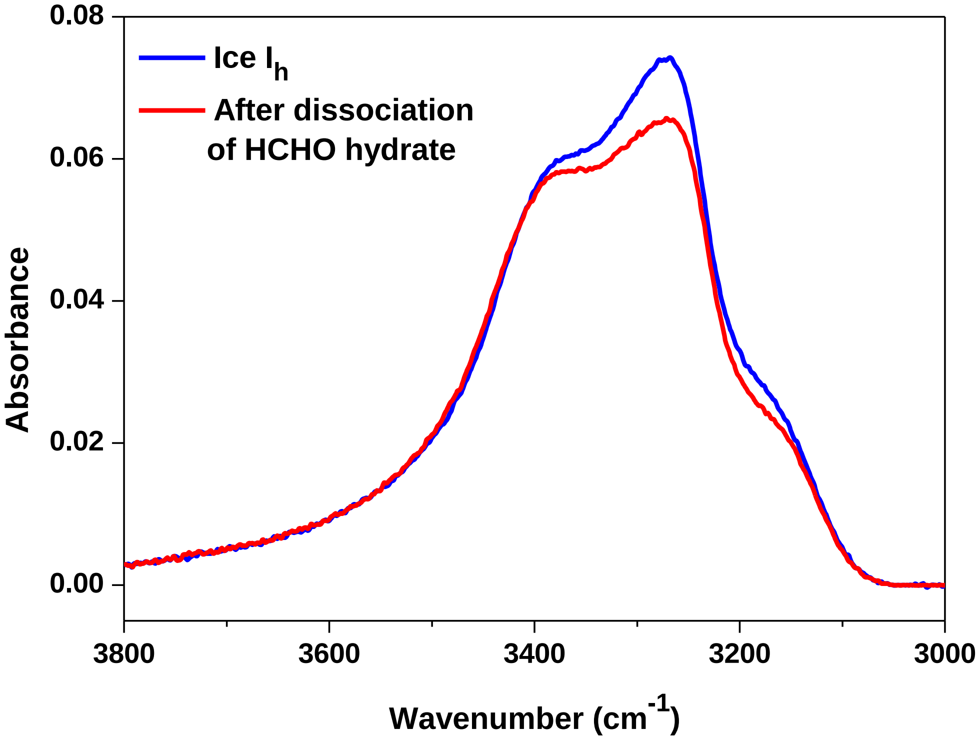

Figure S4. Comparison of O-H stretching bands of 150 MLs of solid crystalline H_2O film, which was heated to 155 K to produce ice I_h (blue trace) and the resultant ice system left after the dissociation of formaldehyde hydrate at 135 K (red trace). Both of these experiments were carried out separately. Here, the similarity of the O-H stretching bands of these two systems suggest that dissociation of formaldehyde produces nothing but ice I_h.

Supporting Information 5:

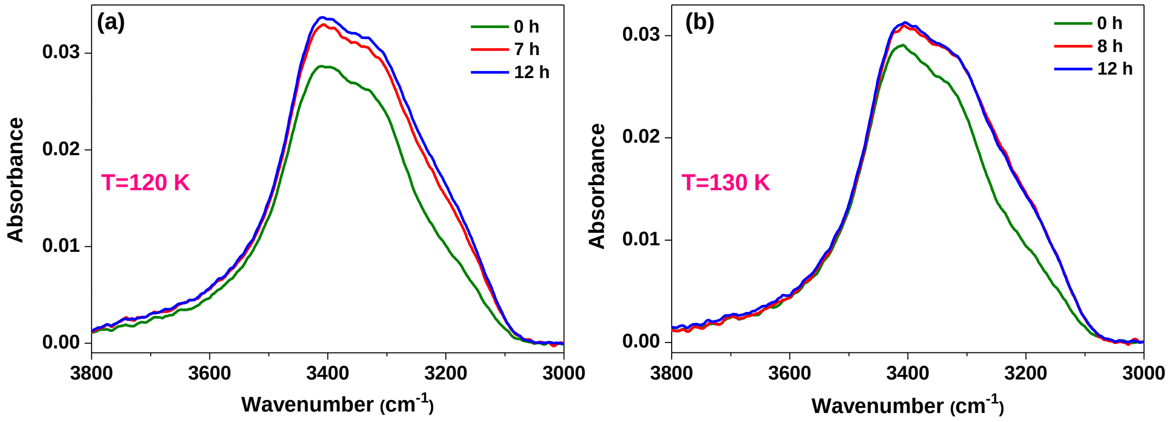

Figure S5. Time-dependent RAIR spectra of 150 MLs of solid H_2O film at (a) 120 K, and (b) at 130 K in the O-H stretching region. The water vapor was deposited at 10 K on Ru(0001) substrate. The ice films were annealed at 2 K.min^{-1} rate to the respective temperatures.

Supporting Information 6:

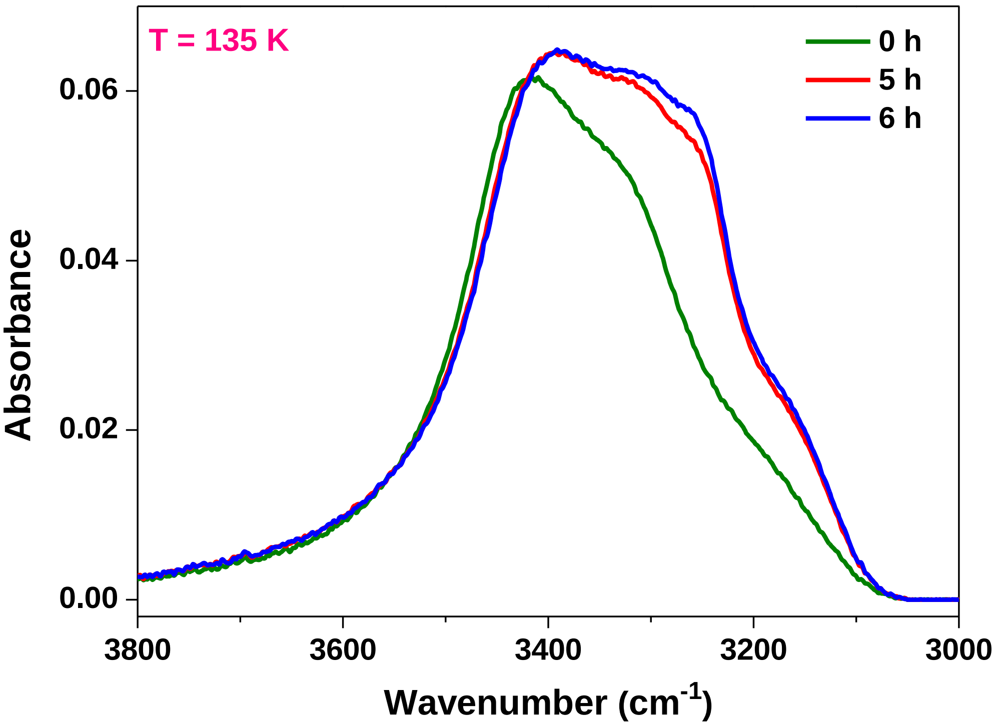

Figure S6. Time-dependent RAIR spectra of 150 MLs of solid H_2O film at 135 K in the O-H stretching region. The water vapor was deposited at 10 K on Ru(0001) substrate. The ice films were annealed at 2 K.min^{-1} rate to the respective temperatures.

Supporting Information 7:

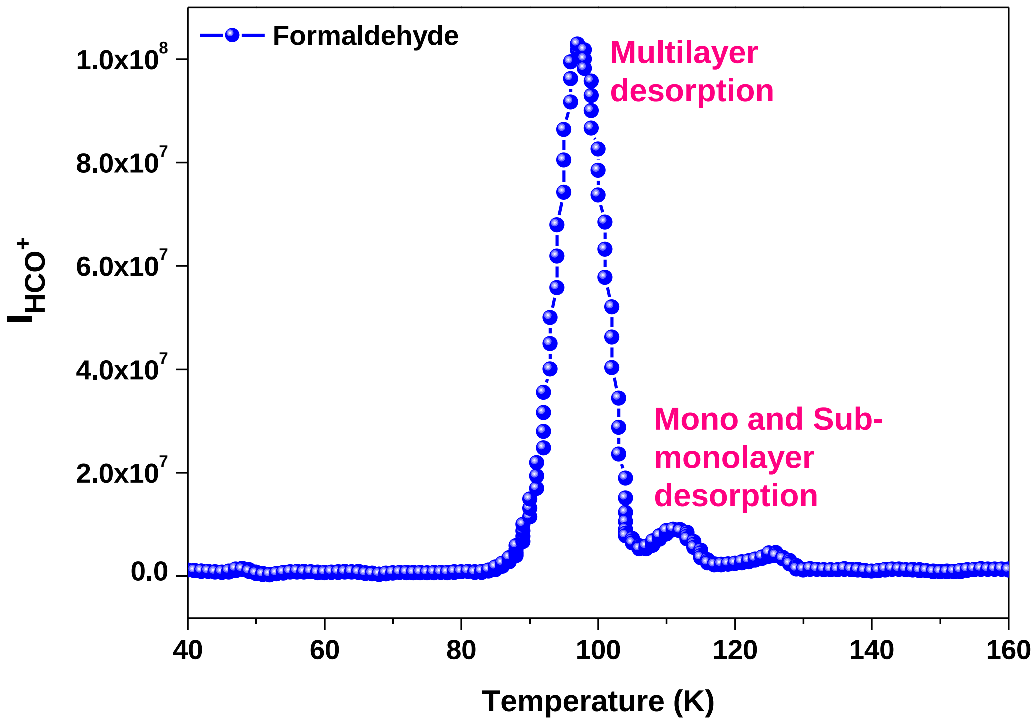

Figure S7. TPD-MS spectra of 150 MLs of pure formaldehyde. Ramping rate = 30 K.min^{-1}. Here, the intensities of HCO$^+$ (m/z = 29) under these conditions are plotted.

Supporting Information 8:

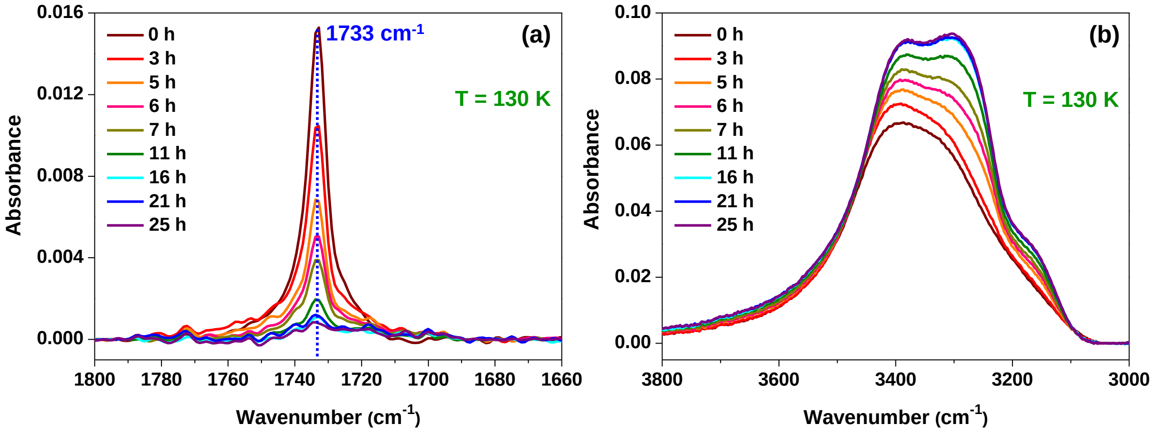

Figure S8. Time-dependent RAIR spectra of 300 MLs of formaldehyde:H_2O (1:1) at 130 K in the (a) C=O stretching region, and (b) O-H stretching region. The mixture was co-deposited on Ru(0001) substrate at 10 K, and annealed at a rate of 2 K.min^{-1} to 130 K.

Supporting Information 9:

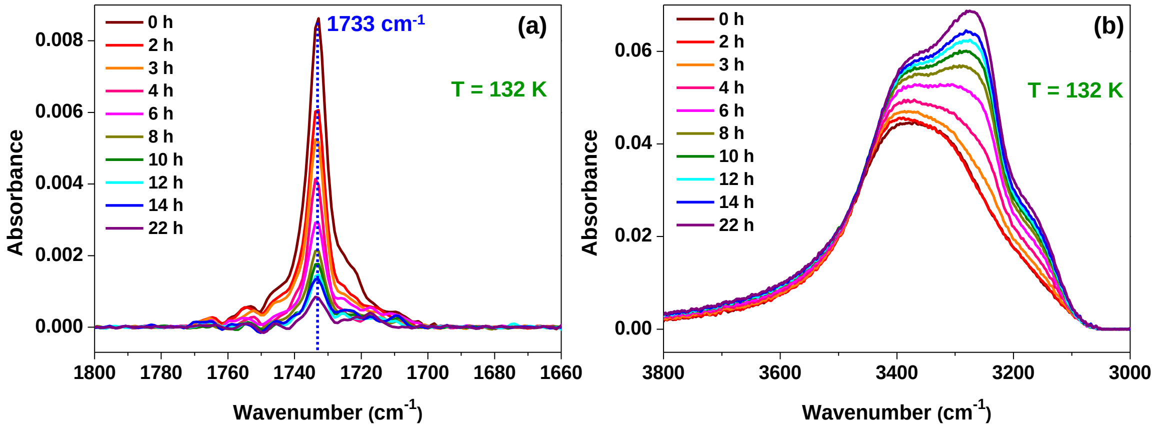

Figure S9. Time-dependent RAIR spectra of 300 MLs of formaldehyde:H_2O (1:1) at 132 K in the (a) C=O stretching region, and (b) O-H stretching region. The mixture was co-deposited on Ru(0001) substrate at 10 K, and annealed at a rate of 2 K.min^{-1} to 132 K.

Supporting Information 10:

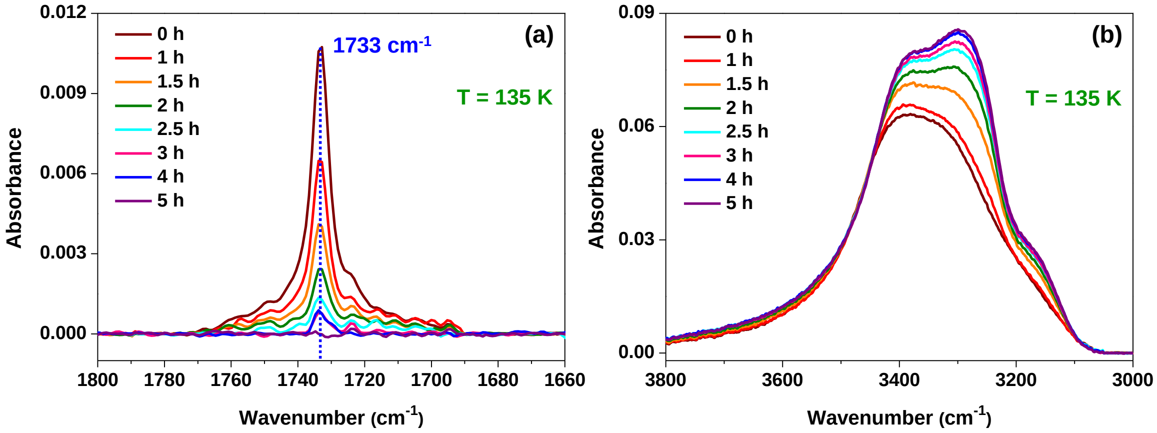

Figure S10. Time-dependent RAIR spectra of 300 MLs of formaldehyde:H_2O (1:1) at 135 K in the (a) C=O stretching region, and (b) O-H stretching region. The mixture was co-deposited on Ru(0001) substrate at 10 K, and annealed at a rate of 2 K.min^{-1} to 135 K.

Supporting Information 11:

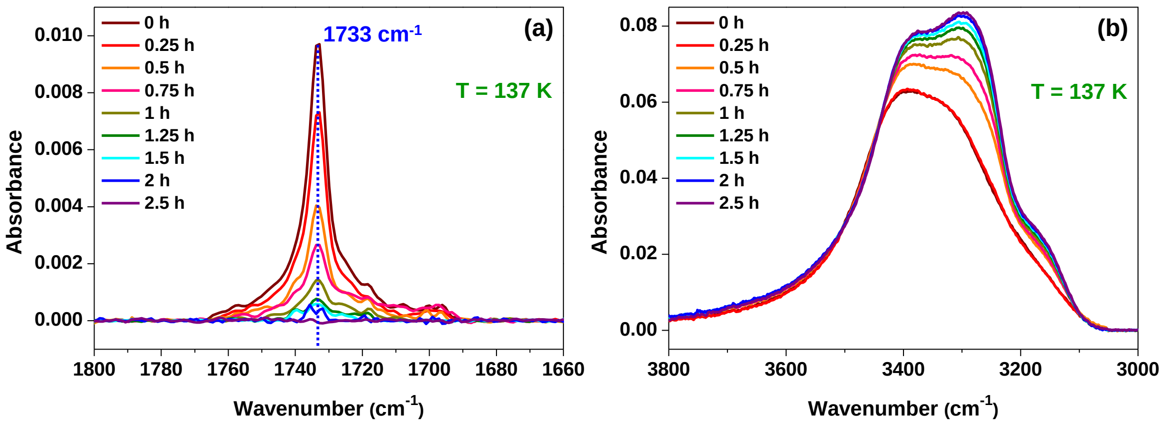

Figure S11. Time-dependent RAIR spectra of 300 MLs of formaldehyde:H_2O (1:1) at 137 K in the (a) C=O stretching region, and (b) O-H stretching region. The mixture was co-deposited on Ru(0001) substrate at 10 K, and annealed at a rate of 2 K.min^{-1} to 137 K.

Supporting Information 12:

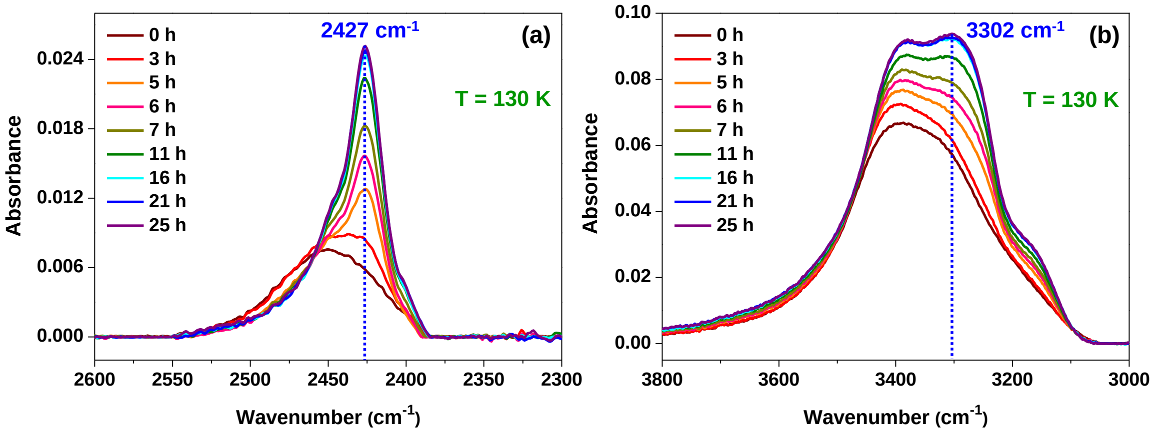

Figure S12. Time-dependent RAIR spectra of 300 MLs of formaldehyde:HDO (5% D_2O in H_2O) at 130 K in the (a) decoupled O-D stretching region, and (b) O-H stretching region. The mixture was co-deposited on Ru(0001) substrate at 10 K, and annealed at a rate of 2 K.min^{-1} to 130 K. The vertical lines at a fixed wavenumber are used to measure the absorbance changes with time, which was further utilized for calculation of crystallization fraction.

Supporting Information 13:

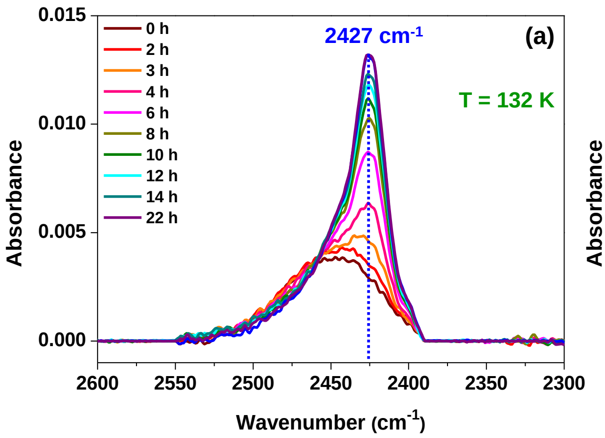

Figure S13. Time-dependent RAIR spectra of 300 MLs of formaldehyde:HDO (5% D_2O in H_2O) at 132 K in the (a) decoupled O-D stretching region, and (b) O-H stretching region.

Supporting Information 14:

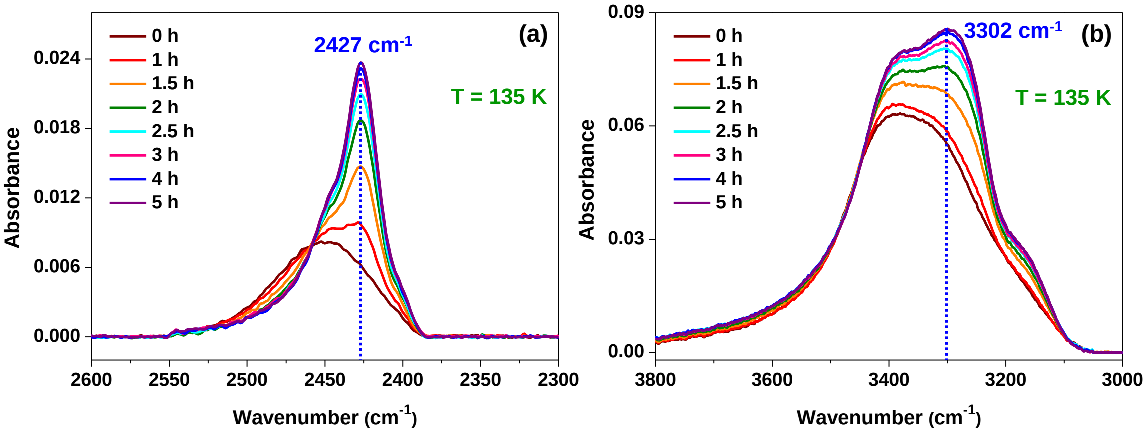

Figure S14. Time-dependent RAIR spectra of 300 MLs of formaldehyde:HDO (5% D_2O in H_2O) at 135 K in the (a) decoupled O-D stretching region, and (b) O-H stretching region.

Supporting Information 15:

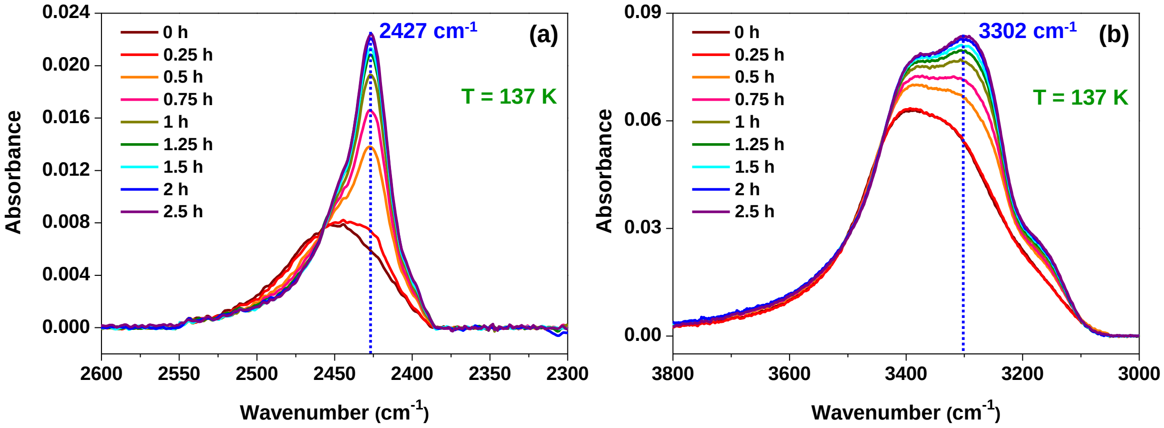

Figure S15. Time-dependent RAIR spectra of 300 MLs of formaldehyde:HDO (5% D_2O in H_2O) at 137 K in the (a) decoupled O-D stretching region, and (b) O-H stretching region.

Table S1: The parameters for crystallization of ice I_h during the dissociation of formaldehyde hydrate at different temperatures.

	Temperature (K)	*n*	Rate constant; *k* (s^{-1})
O-H stretching	130	1.65	3.07×10^{-5}
	132	1.60	3.47×10^{-5}
	135	1.59	1.52×10^{-4}
	137	1.39	3.58×10^{-4}
O-D stretching	130	1.64	3.38×10^{-5}
	132	1.52	3.94×10^{-5}
	135	1.50	1.65×10^{-4}
	137	1.34	4.01×10^{-4}

ACSNANO

www.acsnano.org

2D-Molybdenum Disulfide-Derived Ion Source for Mass Spectrometry

Pallab Basuri, Sourav Kanti Jana, Biswajit Mondal, Tripti Ahuja, Keerthana Unni, Md Rabiul Islam, Subhashree Das, Jaydeb Chakrabarti, and Thalappil Pradeep*

Cite This: https://dx.doi.org/10.1021/acsnano.0c09985 **Read Online**

ACCESS | Metrics & More | Article Recommendations | Supporting Information

ABSTRACT: **Generation of current or potential at nanostructures using appropriate stimuli is one of the futuristic methods of energy generation. We developed an ambient soft ionization method for mass spectrometry using 2D-MoS$_2$, termed streaming ionization, which eliminates the use of traditional energy sources needed for ion formation. The ionic dissociation-induced electrokinetic effect at the liquid−solid interface is the reason for energy generation. We report the highest figure of merit of current generation of 1.3 A/m^2 by flowing protic solvents at 22 μL/min over a 1 × 1 mm^2 surface coated with 2D-MoS$_2$, which is adequate to produce continuous ionization of an array of analytes, making mass spectrometry possible. Weakly bound ion clusters and uric acid in urine have been detected. Further, the methodology was used as a self-energized breath alcohol sensor capable of detecting 3% alcohol in the breath.**

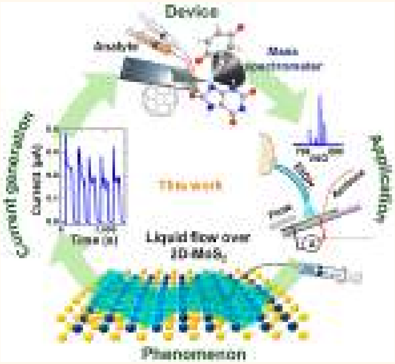

KEYWORDS: *ambient soft ionization, mass spectrometry, 2D-MoS$_2$, dissociation-induced electrokinetic effect, ion clustering, self-energized breath alcohol sensor*

Mass spectrometry has been used for a century as an analytical technique to study materials. Ionization is the primary step in mass spectrometric analysis. Several path-breaking discoveries of ionization such as electrospray ionization (ESI) and matrix-assisted laser desorption ionization (MALDI) have revolutionized mass spectrometry in the past two decades. Yet, demand for ambient ion sources is increasingly high. Although the impact of mass spectrometry in materials has been increasing,[1] use of advanced materials for mass spectrometry is recent. Several attempts have been made to use advanced materials for easy sampling and ionization. For example, carbon nanotubes and other 1D nanostructures have made ionization possible for common analytes at an applied potential of a few volts.[2] Thermospray, a voltage-free ion source, was developed in the 1980s, whereby spray-based ionization was assisted by thermal energy.[3] A sonic spray ionization source was developed later whereby high-speed gas flow broke up the bulk liquid to droplets, which underwent dehydration to release ionic species into the gas phase.[4] Zero-volt paper spray was developed in 2015 whereby chromatographic paper surfaces were used to generate droplets with the help of the pneumatic force of the vacuum of the mass spectrometer.[5] Triboelectric nanogenerators (TNGs) were also used as an alternative energy source for ionization.[6] However, nanotechnology-enabled molecular ionization without the application of external energy is unknown in mass spectrometry.

Deriving alternate energy on a material platform can be revolutionary.[7−9] Sliding an aqueous electrolyte over electrically charged surfaces resulting in electrical power is such an example of energy harvesting. A considerable number of investigations on this subject have established the underlying mechanisms of current generation. For instance, generation of an electrical potential over carbon nanomaterials was discussed in a variety of pathways;[10−18] among them, the electrokinetic effect is a celebrated mechanism.[19,20] A macroscopic understanding of this phenomenon suggests selective ion adsorption at the liquid/solid interface resulting in the formation of an electrical double layer (EDL), composed of a diffusive layer of counterions that is separated by an electroneutral liquid layer called a Stern layer.[21] The thickness of the diffusive layer is considered as the Debye length (λ_D). A pressure difference (ΔP) at the two ends of the stream, which is responsible for the electrokinetic effect, results in a charge separation in the

Received: November 28, 2020
Accepted: February 9, 2021

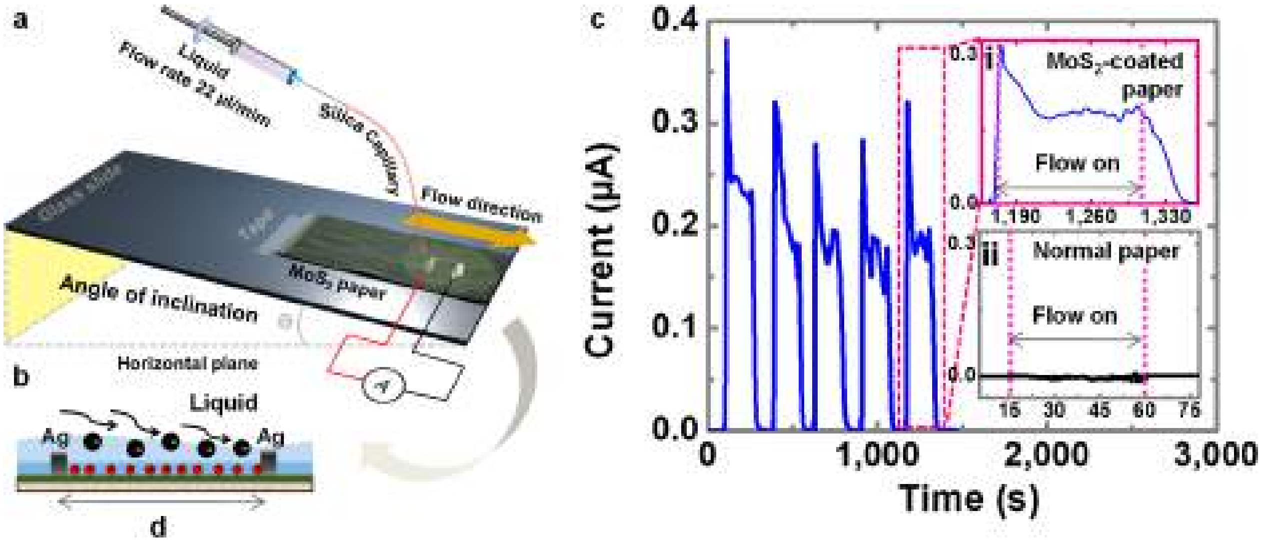

Figure 1. Liquid flow over MoS$_2$-coated paper in the device. (a) Schematic representation of the device fabricated for the flow-induced current or potential generation. The dark green sheet attached to the glass slide and connected to the picoammeter (A) is the 2D-MoS$_2$-coated paper. The device was kept inclined with an angle θ. The liquid was pushed through a syringe connected to a syringe pump (flow rate of 22 μL/min). (b) Side view of the electrode area. "*d*" is the contact distance. Positive and negative ions are shown as spheres. (c) Time-dependent current profile (5 repetitive on/off cycles) with methanol flow on a MoS$_2$ surface. Insets: (i) Zoomed-in view of one such cycle of generated current over MoS$_2$ and (ii) data of current generation over normal filter paper.

diffused layer, leading to a rise of the streaming potential (U_s). Pressure-induced relative motion of charged species with respect to its counterionic part in a stream is termed as streaming current (I_s). Several of the critical parameters that manipulate the magnitude and the polarity of current such as flow direction,[22] surface roughness,[23] slip velocity,[24] charge holding, and separation capacity[25] have been controlled using micro- and nanostructured functional materials.

For example, hydrophobic surfaces were used to increase ion velocity. But these surfaces have large air gaps on them. Trapped air cannot hold the charge. Reduced charge-holding capacity leads to poor potential generation.[26,27] An engineered micropatterned surface filled with oil showed enhanced voltage production.[28] More recently, polymer-coated carbon-based low-dimensional materials such as graphene, graphene oxide, and graphene foam drew attention for enhanced energy harvesting due to their higher ion adsorption capacity, and they generated a potential in the range of 0.4 to 30 mV.[14,29,30] However, generated current can be shunted through such low-resistance carbon-based 2D materials due to their semimetallic characteristics.[31] Semiconducting transition metal chalcogenides could be a better choice in this regard. Ohno *et al.* showed an output potential of over 5 V by flowing highly concentrated NaCl (1 M) droplets over single-layer MoS$_2$ created over a polymer substrate.[31] Generation of current has also been observed under a potential bias; for example, 3D graphene foam over a porous nickel surface produced a 25 μA current at a bias voltage of 80 μV, having an 80 cm/s fluid velocity.[32] In the past, Subramanian *et al.* reported a transverse electrokinetic effect by flowing polar liquids across an assembly of gold nanoparticles.[33,34] However, lack of suitable materials restricts us from utilizing an electrokinetic effect for applications of societal relevance. Therefore, it is indeed necessary to study advanced materials to generate stable, repeatable, and larger currents, which can result in a cost-effective technology.

In this article, we report the flow of organic liquids over 2D-MoS$_2$ coated on a filter paper, and the flow of dissociated ions was utilized to generate a DC current or potential. We fabricated a small device to control the magnitude and polarity of the current. Using this technology, we report an electrokinetic current/potential-driven ambient ion source for mass spectrometry, termed "streaming ionization mass spectrometry (SI-MS)". which is capable of imparting soft ionization of analytes without an external power supply. We demonstrated molecular ionization of fullerenes, benzoquinone, iodine, glucose, *etc.*, and mass spectra of some of their loosely bound ionic clusters were detected. To demonstrate a socially relevant application using this method, we detected uric acid by flowing raw urine over the nanostructured surface. We have also presented the experimental results, and a mechanism was proposed for power generation and confirmed by control experiments. We observed that the flow of pure methanol generated a record-high current of 1.3 μA for the prepared device in comparison to other organic solvents such as ethanol, propanol, acetonitrile, and acetone. Detailed insights on the generation of current and its dependence on the physicochemical properties of different solvents have also been obtained. Additionally, we utilized the magnitude of streaming current as a probe to detect ethanol in the breath, for which we have fabricated a paper-based disposable sensor. This cost-effective device allowed us to detect down to 3% of alcohol in the breath.

RESULTS AND DISCUSSION

Design and Characterization of the Device. The construction of our flow device is schematically illustrated in Figure 1a. A detailed description of the device with the optical images and the measurement procedure are discussed in the Methods section and Figure S1. Briefly, a Whatman 42 filter paper (pore size of 2.5 μm) was used as a support material, and 2D-MoS$_2$ was coated on it. On top of this coated paper, two silver contacts were made at a distance of 1 mm between them, which were finally connected to a picoammeter (Keithley, model 6485). The synthesis procedure and characterization using various spectroscopic and microscopic techniques of a few-layer MoS_2 are presented in the Methods section and in Figure S2, respectively. Similarly, a schematic illustration of the detailed fabrication procedure of the MoS_2-coated paper and its characterization are also discussed in the Methods section and in Figure S3, respectively. One important point to be noted is that deposition of the MoS_2 dispersion over the paper results in a few-layer stacking of sheets, which was characterized by Raman spectroscopy (Figure S3e).

We allowed the flow of different alcohols (methanol, ethanol, propanol, *etc.*) across the two silver contacts over the fabricated surface, at a given flow rate (U_L) of 22 μL/min, and the current (I_f) was measured as a function of flow time. The data are shown in Figure 1c. The flow on and off periods were within 2−3 min. Figure 1c quantifies the magnitude and the polarity of the current produced after switching on and off methanol flow for multiple cycles. A zoomed-in view of one such cycle is shown in the inset (Figure 1ci), in which methanol was allowed to flow for 144 s (1169 to 1313 s). We have repeated the same measurement multiple times up to 126 min, as shown in Figure S4a. To prove that the current generation is solely due to methanol flow over 2D-MoS_2, one control experiment with normal filter paper was performed, and it showed negligible current (Figure 1cii). The fibrous nature of the paper generates an additional capillary pressure (P_c) along with pump pressure (ΔP), which controls the magnitude of the streaming current. Upon careful inspection of Figure S4b, we note that the response time of the device in which the current increases to a maximum value (I_{fmax}) is 1.4 s. In this time interval, the liquid velocity (V_L) over the surface reached a maximum due to the resultant pressure (ΔP_r) of both P_c and ΔP. Thus, there is a proportional relation between ΔP_r and I_f across the electrode. It is likely that the response time of such a flow-based device would primarily depend upon the flow rate and the properties of the liquid such as viscosity and surface tension. After reaching the maximum current (I_{fmax}), the current falls to 60% of the maximum value and subsequently gets stabilized until the flow was switched off (Figure S4c). This is due to the fact that the capillarity force at the wet surface comes to an equilibrium condition, and as a consequence, the current becomes stable. It is also noticed that the time taken for the current to fall to the background level is much longer than the rise time (Figure S4d). The liquid−paper interface makes a microfluidic system, in which the initial fast rise in current is due to the additional effect of capillarity force along with ΔP_r. To validate this conjecture, we have conducted an experiment where we have reduced the “flow-off” period in which the paper is left to dry from 2 min to 10 s, and as a consequence, the capillary-driven surge current (I_{fmax}) in each on/off cycle was restricted. Figure S5a shows that I_f goes to I_{fmax} in the first cycle, and in the remaining two cycles, the current does not jump to I_{fmax} again; instead a steady behavior was seen. In the first cycle, there is an unrestricted motion of liquid due to the capillary action in the fibrous paper, but after the first cycle, the fibrous structure is filled with liquid, and thus there is no role of capillary action in the second and third cycle (Figure S5a). In Figure S5b, the capillary action was retained by shortening the liquid “flow off” time, and therefore, the substrate got dried completely in between cycles and a stable current was observed. We have also flowed methanol over MoS_2-coated glass and a plastic film, as shown in Figure S6, where we have not observed such a surge current. Capillarity-driven surge current can therefore be expressed in the form

$$\Delta P_r = \Delta P + P_c \tag{1}$$

and

$$I_f \alpha \Delta P_r \tag{2}$$

Also, in a control experiment we observed that addition of a suction pump in front of the device generates a steady current with higher magnitude (Figure S7b) in comparison to a device with no pump (Figure S7a). The inset of Figure S7b schematically presents the experimental arrangement. We have also noticed that there is no current in the absence of net flow of liquid. This was checked by dipping the device in bulk methanol. In this case, rapid rise and fall of the current was observed due to immediate wetting of the surface (Figure S8). The inset of the figure shows the experimental procedure schematically.

As the liquid flow is responsible for current generation, it is important to understand whether the direction of the current is toward the flow direction (U_f) or not. This was understood by changing the flow direction, which results in the generation of current with opposite polarity. Figure S9 represents the correlation of the flow direction and the polarity of the current. The inset of each figure illustrates the flow direction responsible for the current. We find a parallel relation between I_f and U_f. This indicates that the anion is flowing along the flow direction, and current flows opposite to it.

In addition to I_f, potential differences across the two contacts (V_f) were also recorded in an open-circuit potential (OCP) measurement, performed with a CH600A electrochemical workstation. A detailed OCP circuit diagram is illustrated schematically in Figure S10a,b. Potential generation follows the same trend, as shown in the I_f−t trace. From the V_f−t trace, we observed a capillarity-driven voltage surge (V_{fmax}) in the first few seconds, which gets stabilized subsequently to a lower value after a certain time interval, as shown in Figure S10c. Potential generation decreases with decreasing polarity (Figure S10d). It should be noted that experiments were performed repeatedly on the same paper, over a period of months, which suggests long-term durability of our device.

Understanding Current Generation. For a theoretical understanding of the underlying mechanism of flow-induced current generation, we considered three essential thermodynamic factors of the liquids such as (a) dissociation constant (K_a), (b) dielectric constant (ε), and (c) viscosity (η). The magnitudes of these factors for different solvents were plotted against the magnitude of current generated by them under similar conditions. To do so, an experiment was performed where methanol, ethanol, and propanol were passed one after another under identical conditions and corresponding I_f values were measured. The data presented in Figure S11 show that the values are 250, 100, and 20 nA for methanol, ethanol, and propanol, respectively. Figure S12 represents the variation of the current with all the aforementioned factors. The I_f−pK_a trace shows that the current falls linearly with the pK_a value of the liquids. We find that the higher the dissociation of molecules, the higher the I_f. If we consider the first step of the mechanism to be dissociation of the molecule, we may suggest that polar protic molecules got dissociated by experiencing a dipolar interaction over the MoS_2 surface. This dipole−dipole

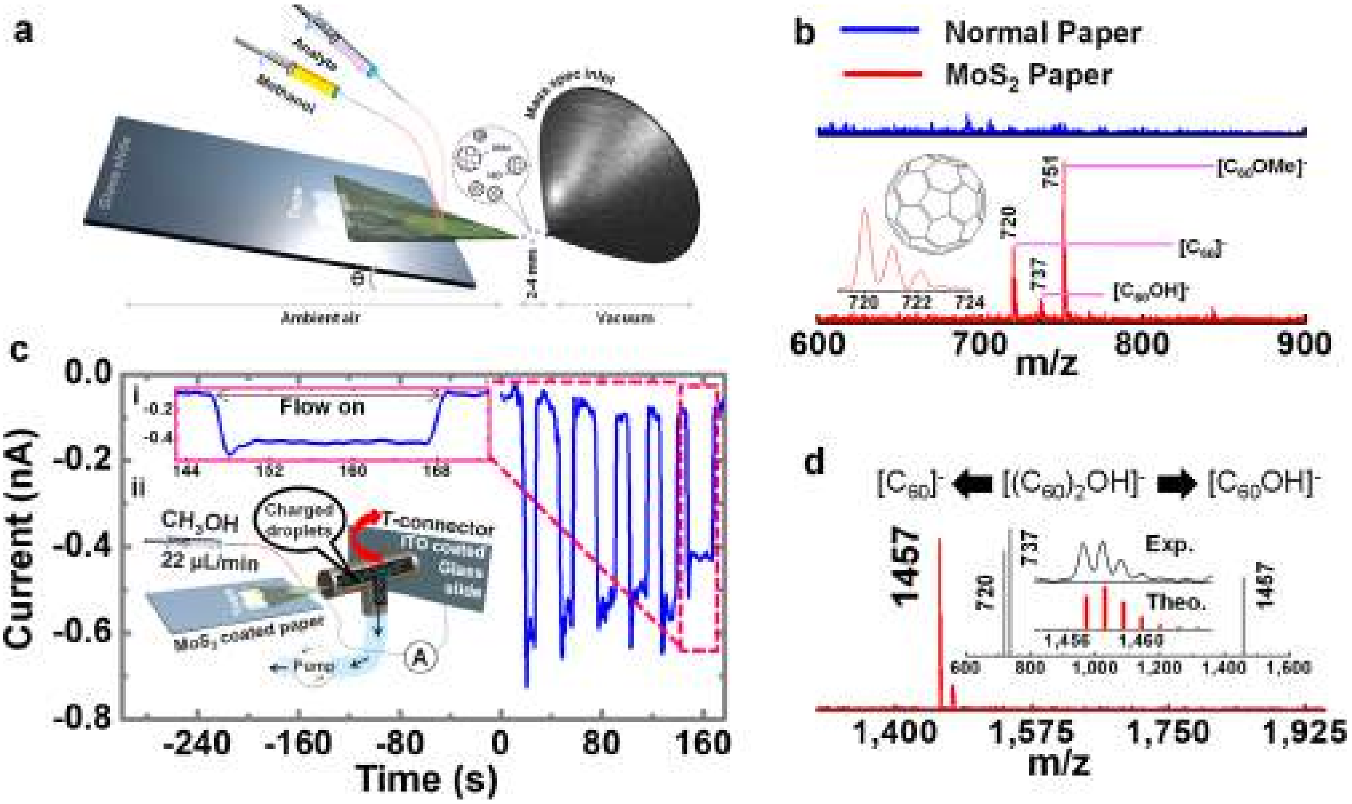

Figure 2. Streaming ionization mass spectrometry (SI-MS). (a) Schematic representation of the ion source. A MoS$_2$-coated triangular paper attached to a glass slide is held in front of the mass spectrometer inlet. The ion source was kept inclined with an angle of θ. The liquids are pushed through two syringes connected to separate pumps. The optimized flow rates of the solvent and the analyte pumps were 22 and 11 μL/min, respectively. The average dimensions of the triangular-shaped paper are 10 mm in width at the base and 10 mm in length. (b) Comparative SI-MS of C_{60} using uncoated and coated MoS$_2$ paper. Inset shows the molecular structure of C_{60} and the zoomed-in peak of *m*/*z* 720. (c) Current−time profile of the generated spray due to the formation of charged microdroplets. Insets: (i) Zoomed-in view of the first spray cycle and (ii) schematic view of the experimental setup. (d) Mass spectrum of the C_{60} dimer in the selected mass range. Inset of d shows the fragmentation pattern of the peak at *m*/*z* 1457. The isotopic distribution of the peak (Exp.) at *m*/*z* 1457 is compared with the theoretical pattern (Theo.).

interaction energy (E_{dd}), in addition to the kinetic energy (E_k) of the molecule, drives the acid dissociation reaction. Thus, the Gibbs free energy of dissociation (ΔG^0) can be correlated with both E_{dd} and E_k of the molecules,

$$\Delta G^o = E_k + E_{dd} \tag{3}$$

At equilibrium, ΔG^0 equals $-RT \ln K_a$ for the liquid. Due to less terminal velocity of the liquid (2.45 mm/s, the experimental procedure is discussed in the Methods section) over the substrate, the kinetic energy term becomes negligible in comparison to the dipole−dipole interaction energy, and hence, the above equation can be represented as $\Delta G^o \sim E_{dd}$. Here, E_{dd} is assumed to be static and can be expressed over a distance, r, as[35]

$$E_{dd} = l/\varepsilon_0(\rho \times P_{MeOH} \times P_{MoS} \times \int_0^1 r_1 dr_1/(z^2 + r_1^2)^{3/2}) \tag{4}$$

Here, ε_0, ρ, P_{MeOH}, and P_{MoS} are the permittivity through free space, approximated number density of MoS$_2$ over the surface, and dipole moment of methanol and MoS$_2$, respectively. The parameters l and z are the distance between two silver contacts and the sum of the dipolar radii of methanol and MoS$_2$, respectively. Appendix 1 gives a detailed calculation of ρ. In Appendix 2, we calculated the ΔG^0 and E_{dd} quantitatively. We found that the left-hand side and the right-hand side of eq 3 are both on the order of 10^{-20} J/molecule. This validates that the dipole−dipole interaction is the driving force for the dissociation of the liquid molecules in the initial step of current generation. The other factor that governs the current generation upon the liquid flow over the MoS$_2$ surface is the dielectric constant of the liquid, with which we observed a linear relation with I_f. The I_f−ε trace (Figure S12a) shows that methanol produces higher current than propanol, linear to ε. On the other hand, the viscosity of the liquid shows a reciprocal relationship with I_f, as presented in Figure S12b. In Figure S13a we have also shown that the current falls linearly with increasing pK_a of the liquid.

Considering all the above observations, here, we propose a possible mechanism, which has been represented schematically in Figure S14. It consists of two essential steps: first, dipole−dipole interaction leading to the dissociation of liquid molecules and, second, flow of anions leading to an electrokinetic current. The dissociation-induced electrokinetic effect, which resulted in a large current, can be better viewed by the Helmholtz−Smoluchowski model,[36]

$$I_f = -\varepsilon\varepsilon_0\zeta A_c \Delta P_r/\eta l \tag{5}$$

,and the potential gradient can be expressed as

$$V_f = \varepsilon\varepsilon_0\zeta\Delta P_r/\eta K \tag{6}$$

https://dx.doi.org/10.1021/acsnano.0c09985

where ζ is the zeta potential of MoS_2, which is on the order of −41.2 mV (Figure S15) and A_c is the approximate area of the MoS_2 sheets. We observed a reciprocal relation between the contact distance (l) and I_f, as presented in Figure S12d. There is also a linear relationship between the flow rate and the current produced (Figure S12e). The flow rate is related to the syringe pump pressure (ΔP), as shown in Appendix 4.

We have demonstrated flow-induced current using reduced graphene oxide (rGO), which produced an order of magnitude reduced current, as shown in Figure S16a. The Raman spectrum of the sample is presented in the insets of Figure S16a. Figure S16b shows the UV−vis spectrum, and the inset shows the transmission electron microscopic (TEM) image of rGO used for the experiment. The device was also tested with other liquids such as water, acetic acid, dimethylformamide, acetone, acetonitrile, dichloromethane, chloroform, toluene, and hexane (Figure S17). We observed significant current for the first three liquids.

Besides the production of current, we have found that the current is depleting in the presence of foreign molecules having very high electron affinity such as C_{60}. We have drop casted 10 μL of C_{60} (in toluene) during the I_f−t measurement, and we observed a sudden decrease of I_f, which again gets back to its stable value after C_{60} gets washed off (Figure S18). This provides an indication that C_{60} may be disturbing the EDL and gets ionized at the same time, as it has high electron affinity. To prove the fact that the current depletion is not due to the effect of solvent or mechanical iteration, we performed a control experiment in which only toluene was passed along with methanol. We observed that addition of toluene does not affect the current generation, as presented in Figure S19.

Design and Characterization of the Ion Source. Having established that flow induces a current (I_f) and the fact that addition of analyte affects I_f, we developed an ambient ion source for mass spectrometry in which in-flow molecular ionization was observed in the negative ion mode. Ambient ionization such as electrospray ionization (ESI),[37] paper spray ionization (PSI),[38,39] low-temperature plasma ionization (LTP),[40] and atmospheric pressure photoionization (APPI)[41] are techniques that require either a large electrical potential or a laser field to ionize molecules in solution. Although soft, they do provide some residual energy to the ion, leading to fragmentation. This limits their use in characterizing weakly bound molecular or ionic aggregates due to possible dissociation. Figure 2a schematically represents our ion source, which is a modified paper. The only difference made here compared to Figure 1 is in the shape of the paper. We changed the geometry of the paper from rectangular (in Figure 1) to an equilateral triangle to use the tip of the triangle for the generation of changed microdroplets.

Analytes of interest such as C_{70}, C_{60}, iodine, and benzoquinone were examined initially to characterize the system due to their high electron affinity in the range of 2.7 to 1.85 eV, which enables us to analyze them easily in negative ion mode.[42−45] However, ionization of a few other analytes including amino acids, aliphatic amines, and biomolecules are also shown later in this article to demonstrate the applicability of our ion source in diverse situations. Examining the mass spectra presented in Figure 2b, it is seen that the "streaming ion source" provides soft ionization in which weak noncovalent interactions such as ion clustering through electrostatic or van der Waals interaction can also be observed. Flow of C_{60} results in three major ion products, $[C_{60}]^-$, $[C_{60}OH]^-$, and $[C_{60}MeO]^-$, where the latter two ions are due to the clustering of C_{60} with OH^- and MeO^-. These are absent in the standard mass spectrum of C_{60} by conventional soft ionization techniques such as ESI or PSI (Figure S20). Flow of C_{60} (as a toluene/methanol solution) on a bare filter paper shows negligible current, and therefore, we did not observe its ions (Figure 2b). To prove that the generated droplets contain high charges due to the presence of ions in it, we measured the current carried by the droplets in Figure 2c, using a setup presented in its inset.

Clustering of other species was also achieved with flow of other alcohols such as ethanol and propanol (Figure S21). All the mass assignments are based on the fragmentation pattern in the MS/MS spectra, as shown in Figures S22 and S23. We performed similar experiments with other solvents as well. Solvents such as acetone, acetonitrile, and other nonpolar solvents, which do not produce current as discussed earlier, did not cause ionization as expected (Figure S24a−e). Interestingly, DMF also shows a current and results in ionization of C_{60}. Figure S24f displays the mass spectrum of C_{60} in DMF, where we observed a peak at m/z 764 along with m/z 720 due to the formation of $[C_{60}N(CH_3)_2]^-$. We have also added glucose during the ionization of C_{60} in methanol and we observed a glucose-bound C_{60} peak in the mass spectrum (Figure S25). This was done to see whether the −OH group of glucose shows similar behavior to that shown by other alcohols. Looking at the ion chronogram of C_{60} in Figure S26a, we can conclude that the shape of the chronogram follows a similar trend to that of the I_f−t profile (Figure 1c).

We have also performed an *in situ* measurement, in which both current due to the solvent flow over MoS_2-coated paper and the ion current of the mass spectrometer were measured simultaneously. In Figure S27a (top), we have demonstrated a flow-induced current of 0.5 μA upon methanol flow on the MoS_2-coated paper. After a while, as the C_{60} flow was switched on, the flow current comes to the background level; however, at the same time, ion current (Figure S27a (bottom)) in the chronogram increases to the maximum. This is due to the fact that C_{60} gets ionized immediately when it comes in contact with the methanol stream on the MoS_2 paper. This leads to a decrease in flow current on the paper and simultaneously increases the ion current intensity in the mass spectrum. There is a time delay between decrease of flow current and corresponding increase of ion current as shown in Figure S27a (i and ii), and this is probably due to the travel time of ionized species on the electrode in solution and subsequently into the mass spectrometer. The mass spectra corresponding to C_{60} flow, off and on, are given in Figure S27b (i and ii). Inset of the mass spectrum in Figure S27b is a schematic illustration of the experimental setup.

In addition to ion clustering of C_{60} with different alcohols (methanol, ethanol, propanol, and glucose (methanol)), we have also observed two peaks at m/z 1457 and 1473 in the mass spectrum. Fragmentation patterns (Figure 2b) of the ions reveal that the peaks correspond to $[(C_{60})_2OH]^-$ and $[O(C_{60})_2OH]^-$, respectively. C_{70} also ionizes similar to C_{60} (Figure S28). The mass spectrum of benzoquinone in Figure S29a shows a molecular ion peak at m/z 108. Flowing iodine solution in methanol gives two major peaks at m/z 127 and 381, corresponding to I^- and I_3^-, respectively (Figure S29b). Ion clustering data of a few other analytes such as tryptophan, histidine, and methylamine chloride are shown in Figure S30. Uric acid levels in body fluids are tested to diagnose gout. We

https://dx.doi.org/10.1021/acsnano.0c09985

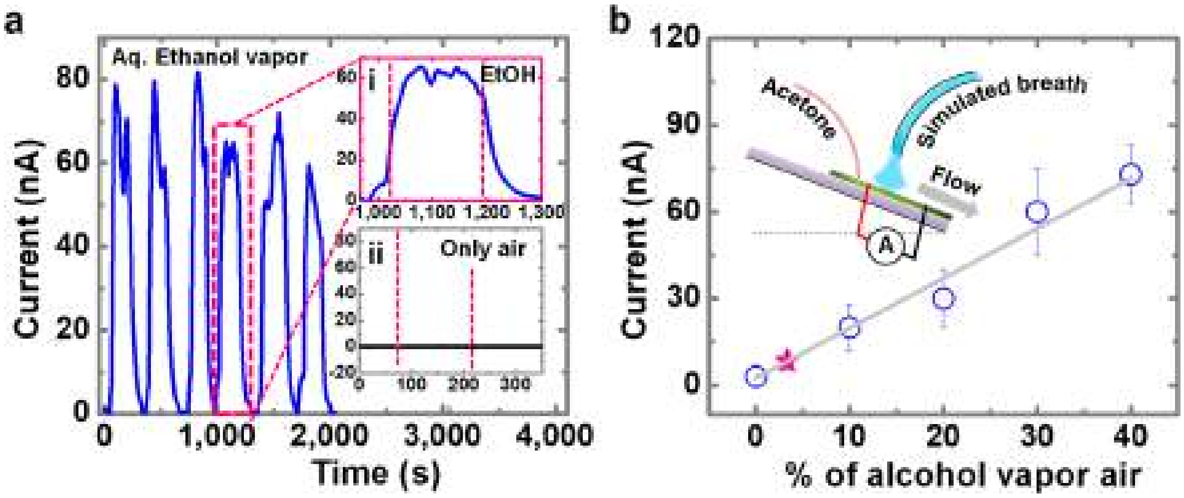

Figure 3. Flow device for the detection of alcohol in breath. (a) Current−time trace during alcohol vapor (40% aq.) exposure. Inset shows (i) zoomed-in data of one such current cycle and (ii) current generated in the absence of ethanol vapor. (b) Fitted calibration curve (gray line). The data point shown as a pink star is taken from the breath of a volunteer who had consumed alcohol. Inset of the figure schematically illustrates the device detecting simulated breath. Each experiment was repeated three times independently. Data are presented as mean, and error bar shows ± SD. The gray line is a linear fit of the generated current *vs* % of alcohol vapor exposed to the device. Data points were taken using standard water−ethanol solution in a glass trap and evaporating it with a nitrogen stream, and the red star corresponds to the measured alcohol concentration.

performed SI-MS of a raw urine sample (5 μL) of a healthy individual in which we detected deprotonated uric acid at m/z 167 (Figure S31). The assignment was supported by the fragmentation data. In Figure S32, we observed mass spectra corresponding to the deprotonated peaks of propanol, benzyl alcohol, and glucose, respectively. However, by the same process we did not observe peaks in the positive ion mode (Figure S33). Generation of such deprotonated negative ions further validates our proposed mechanism, termed *dissociation-induced electrokinetic effect*. This gives strong support to the fact that the anions of the dissociated alcohol molecules move with the flow, resulting in charge separation. Movement of these negatively charged ions generates current.

We have observed that the vapors of alcohols also affect the ionization process. This phenomenon was observed in an experiment where we saw ethoxide added a C_{60} peak at m/z 765 along with the peaks at m/z 720, 737, and 751 during SI-MS of C_{60} upon exposure to ethanol vapors (Figure S34b). Here we flow C_{60} (in toluene) along with methanol prior to the exposure of ethanol vapor. The experimental setup is presented schematically in Figure S34a. The chronograms shown in Figure S34c and d prove that the interaction time of ethanol vapor is less than a few seconds. This clearly demonstrates that ethanol molecules in the vapor phase dissolve in the solution phase and undergo dissociation.

Fabrication of a Breath Alcohol Sensor. To demonstrate a potential sensing application of the device, we have used the MoS_2-coated paper as a disposable sensor for breath alcohol detection. The device was modified in such a way that the breath of a drunken person can interact directly with the flowing liquid on the MoS_2-coated surface. We used acetone as a flowing liquid because it does not produce current by itself (Figure S17). In Figure 3a, a simulated alcoholic breath containing 40% aqueous ethanol was blown over the device. The inset of Figure 3b shows a schematic diagram of the breath alcohol sensing device, in which simulated alcoholic breath was passed by blowing air through a liquid trap containing aqueous ethanol. A detailed description of the device is discussed in the Methods section. We observed that the magnitude of the current varies upon the concentration of alcohol present in the vapor. For this, we changed the ethanol concentration in the vapor during the air blowing, by changing the concentration of ethanol in the liquid trap. A plot of current with concentration of ethanol is shown in Figure 3b. Table S1 shows the current measured in each repeatable experiment with different concentrations of alcohol in the mixture. Finally, the actual breath of a volunteer after 10 min of consuming 650 mL of beer containing 9% (v/v) alcohol was blown on the same paper, and the corresponding current was measured. The breath alcohol concentration was found to be less than 3% from the extrapolation of the calibration graph.

CONCLUSION

In conclusion, we have introduced a 2D-MoS_2-coated paper-based device that generates current on the order of microamperes by flowing polar organic liquids over it. We demonstrated that the phenomenon of current generation is by a dissociation-induced electrokinetic effect in which the dissociation is driven by dipolar interactions over the MoS_2 surface. Applying the same strategy, we developed an ambient ionization source termed SI-MS, which in contrast to the conventional ion sources is power supply free, allowing soft ionization of analytes in flow. We demonstrated that SI-MS is capable of detecting loosely bound ion clusters such as $[(C_{60})_2OH]^-$, $[O(C_{60})_2OH]^-$, $[C_{60}MeO]^-$, $[C_{60}OH]^-$, I_3^-, di-, tri- and tetramers of tryptophan, dimer of histidine, and mono-, di-, and trimers of methylamine ions. The ion source is not limited by the type of liquid that is flowing. Mixed solvents such as methanol and toluene, as demonstrated for the detection of C_{60} in toluene, show the ionization of an analyte soluble in a nonpolar solvent. To demonstrate the use of the ion source in real analytical situations, we detected uric acid in raw urine during flow. It can also be utilized to characterize noncovalent interactions, such as van der Waals, electrostatic, and hydrogen bonding interactions in molecular systems of relevance to chemistry and biology. Fabrication of such an ion

https://dx.doi.org/10.1021/acsnano.0c09985

source, sampling procedure, and ionization are simple, cost-effective, and eliminate safety issues during work. A potent sensing application is demonstrated for alcohol detection in the breath. The science introduced presents a method for harnessing the power of advanced materials. Our work may be utilized in the fields of sensors and microfluidics, for example, flow-based detection of specific molecules in biofluids. On the other hand, the device presented as a breath alcohol sensor can alternatively be used as a gas sensor for the detection of volatile organic compounds in ambient air.

METHODS

Synthesis of MoS_2. The 2D-MoS_2 nanostructures were synthesized from bulk MoS_2 using a chemical exfoliation method. Required chemicals for the synthesis and other experiments and a brief synthetic procedure are discussed in Supporting Information S1a and b.

Fabrication of the Current Generation Device. The current generation device was built by sticking a rectangular-shaped MoS_2-coated paper on a glass slide using cellophane tape. Two silver contacts, using commercially available silver conducting paint made of polymer-coated micron-scale silver particles, were made on the paper and connected to a picoammeter (Keithley 6485). These micron-thick silver contacts were stable upon the flow of liquids and generated current for several hours. The silver paint is nonoxidizable under the conditions used due to the polymeric medium. The entire device was mounted on an *xyz* moving stage. A syringe pump was used to push the liquids through a silica capillary to the modified paper surface with a preferred flow rate. Fabrication of MoS_2-coated paper and design of the flow current device are presented in Supporting Information S 1d and S2a.

Characterization. The optical properties of as-synthesized MoS_2 were characterized by a PerkinElmer Lambda 25 UV−vis spectrometer and a CRM-Alpha300 S (WITec GmnH) Raman spectrometer. Structural features of 2D-MoS_2 were studied using high-resolution transmission electron microscopy (JEOL 3010).

The MoS_2-coated paper was characterized using Raman spectroscopy. The morphology of the bare filter paper and MoS_2-coated filter paper was observed by scanning electron microscopy (FEI Quanta 200 scanning electron microscope). Detailed characterization is briefly discussed in Supporting Information S1c and e.

Fabrication of the Ion Source. The ion source is similar to the current generation device. A triangularly cut MoS_2-coated paper was fixed on a glass slide, and the tip was held facing the mass spectrometer inlet. The solutions were pushed through a capillary using a syringe pump.

Mass Spectrometric Measurements. All the mass spectrometric measurements were performed using a linear ion trap Thermo LTQ-XL mass spectrometer. Sheath gas flow rate, tube lens, and capillary voltages were set to zero. Supporting Information S3c discusses mass spectrometric details in brief.

Fabrication of the Breath Analyzer. An opened end of a silicone tube was held right above our device, while the other end of the tube was connected to a liquid trap. The aqueous ethanol solution kept inside the liquid trap was then vaporized with air flow. The generated current was measured using a picoammeter.

ASSOCIATED CONTENT

Supporting Information

The Supporting Information is available free of charge at https://pubs.acs.org/doi/10.1021/acsnano.0c09985.

> Additional information on experimental details, materials characterization, control experimental results, table for alcoholic breath analysis, and calculations on electrokinetic energy (PDF)

AUTHOR INFORMATION

Corresponding Author

Thalappil Pradeep − *DST Unit of Nanoscience (DST UNS) and Thematic Unit of Excellence (TUE), Department of Chemistry, Indian Institute of Technology Madras, Chennai 600 036, India;* orcid.org/0000-0003-3174-534X; Email: pradeep@iitm.ac.in

Authors

Pallab Basuri − *DST Unit of Nanoscience (DST UNS) and Thematic Unit of Excellence (TUE), Department of Chemistry, Indian Institute of Technology Madras, Chennai 600 036, India*

Sourav Kanti Jana − *DST Unit of Nanoscience (DST UNS) and Thematic Unit of Excellence (TUE), Department of Chemistry, Indian Institute of Technology Madras, Chennai 600 036, India;* orcid.org/0000-0001-5772-7022

Biswajit Mondal − *DST Unit of Nanoscience (DST UNS) and Thematic Unit of Excellence (TUE), Department of Chemistry, Indian Institute of Technology Madras, Chennai 600 036, India*

Tripti Ahuja − *DST Unit of Nanoscience (DST UNS) and Thematic Unit of Excellence (TUE), Department of Chemistry, Indian Institute of Technology Madras, Chennai 600 036, India*

Keerthana Unni − *DST Unit of Nanoscience (DST UNS) and Thematic Unit of Excellence (TUE), Department of Chemistry, Indian Institute of Technology Madras, Chennai 600 036, India*

Md Rabiul Islam − *DST Unit of Nanoscience (DST UNS) and Thematic Unit of Excellence (TUE), Department of Chemistry, Indian Institute of Technology Madras, Chennai 600 036, India*

Subhashree Das − *DST Unit of Nanoscience (DST UNS) and Thematic Unit of Excellence (TUE), Department of Chemistry, Indian Institute of Technology Madras, Chennai 600 036, India*

Jaydeb Chakrabarti − *Department of Chemical, Biological and Macromolecular Sciences, S. N. Bose National Centre for Basic Sciences, Kolkata 700098, India*

Complete contact information is available at: https://pubs.acs.org/10.1021/acsnano.0c09985

Author Contributions

P.B. designed and performed the electrical current generation experiments with the help of S.K.J., T.A., K.U., and S.D. The material was synthesized by B.M. and R.I. J.C. helped with the calculations leading to an understanding of current generation. P.B. wrote the initial draft of the paper with input from all the authors. The project was conceived under the supervision of T.P.

Notes

The authors declare no competing financial interest.

ACKNOWLEDGMENTS

P.B., B.M., and T.A. thank IIT Madras for their research fellowships. R.I. thanks CSIR for his fellowship.

REFERENCES

(1) Chakraborty, P.; Pradeep, T. The Emerging Interface of Mass Spectrometry with Materials. *NPG Asia Mater.* **2019**, *11*, 48.

(2) Narayanan, R.; Sarkar, D.; Cooks, R. G.; Pradeep, T. Molecular Ionization from Carbon Nanotube Paper. *Angew. Chem., Int. Ed.* **2014**, *53*, 5936−5940.

(3) Blakley, C. R.; Carmody, J. J.; Vestal, M. L. Liquid Chromatograph-Mass Spectrometer for Analysis of Nonvolatile Samples. *Anal. Chem.* **1980**, *52*, 1636−1641.

(4) Hirabayashi, A.; Sakairi, M.; Koizumi, H. Sonic Spray Ionization Method for Atmospheric Pressure Ionization Mass Spectrometry. *Anal. Chem.* **1994**, *66*, 4557−4559.

(5) Wleklinski, M.; Li, Y.; Bag, S.; Sarkar, D.; Narayanan, R.; Pradeep, T.; Cooks, R. G. Zero Volt Paper Spray Ionization and Its Mechanism. *Anal. Chem.* **2015**, *87*, 6786−6793.

(6) Li, A.; Zi, Y.; Guo, H.; Wang, Z. L.; Fernández, F. M. Triboelectric Nanogenerators for Sensitive Nano-Coulomb Molecular Mass Spectrometry. *Nat. Nanotechnol.* **2017**, *12*, 481−487.

(7) Liu, J.; Goswami, A.; Jiang, K.; Khan, F.; Kim, S.; McGee, R.; Li, Z.; Hu, Z.; Lee, J.; Thundat, T. Direct-Current Triboelectricity Generation by a Sliding Schottky Nanocontact on MoS_2 Multilayers. *Nat. Nanotechnol.* **2018**, *13*, 112−116.

(8) Yuan, Q.; Zhao, Y.-P. Hydroelectric Voltage Generation Based on Water-Filled Single-Walled Carbon Nanotubes. *J. Am. Chem. Soc.* **2009**, *131*, 6374−6376.

(9) Lee, J.-H.; Lee, J. H.; Xiao, J.; Desai, M. S.; Zhang, X.; Lee, S.-W. Vertical Self-Assembly of Polarized Phage Nanostructure for Energy Harvesting. *Nano Lett.* **2019**, *19*, 2661−2667.

(10) Pei, J.; Huang, J.; Huang, Z.; Liu, K. Liquid Flow-Induced Electricity in Carbon Nanomaterials. *Sustainable Energy & Fuels* **2019**, *3*, 599−610.

(11) Kim, S. H.; Haines, C. S.; Li, N.; Kim, K. J.; Mun, T. J.; Choi, C.; Di, J.; Oh, Y. J.; Oviedo, J. P.; Bykova, J.; Fang, S.; Jiang, N.; Liu, Z.; Wang, R.; Kumar, P.; Qiao, R.; Priya, S.; Cho, K.; Kim, M.; Lucas, M. S.; et al. Harvesting Electrical Energy from Carbon Nanotube Yarn Twist. *Science* **2017**, *357*, 773.

(12) Ghosh, S.; Sood, A. K.; Kumar, N. Carbon Nanotube Flow Sensors. *Science* **2003**, *299*, 1042.

(13) Ghosh, S.; Sood, A. K.; Ramaswamy, S.; Kumar, N. Flow-Induced Voltage and Current Generation in Carbon Nanotubes. *Phys. Rev. B: Condens. Matter Mater. Phys.* **2004**, *70*, 205423.

(14) Yang, S.; Su, Y.; Xu, Y.; Wu, Q.; Zhang, Y.; Raschke, M. B.; Ren, M.; Chen, Y.; Wang, J.; Guo, W.; Ron Shen, Y.; Tian, C. Mechanism of Electric Power Generation from Ionic Droplet Motion on Polymer Supported Graphene. *J. Am. Chem. Soc.* **2018**, *140*, 13746−13752.

(15) Arun, R. K.; Singh, P.; Biswas, G.; Chanda, N.; Chakraborty, S. Energy Generation from Water Flow over a Reduced Graphene Oxide Surface in a Paper−Pencil Device. *Lab Chip* **2016**, *16*, 3589−3596.

(16) Yin, J.; Zhang, Z.; Li, X.; Zhou, J.; Guo, W. Harvesting Energy from Water Flow over Graphene? *Nano Lett.* **2012**, *12*, 1736−1741.

(17) Dhiman, P.; Yavari, F.; Mi, X.; Gullapalli, H.; Shi, Y.; Ajayan, P. M.; Koratkar, N. Harvesting Energy from Water Flow over Graphene. *Nano Lett.* **2011**, *11*, 3123−3127.

(18) Liu, J.; Dai, L.; Baur, J. W. Multiwalled Carbon Nanotubes for Flow-Induced Voltage Generation. *J. Appl. Phys.* **2007**, *101*, 064312.

(19) Allnatt, A. R. Theory of Phenomenological Coefficients in Solid-State Diffusion. I. General Expressions. *J. Chem. Phys.* **1965**, *43*, 1855−1863.

(20) Dukhin, S. S. Development of Notions as to the Mechanism of Electrokinetic Phenomena and the Structure of the Colloid Micelle. *Surf. Colloid Sci.* **1974**, *7*, 1−47.

(21) Werkhoven, B. L.; Everts, J. C.; Samin, S.; van Roij, R. Flow-Induced Surface Charge Heterogeneity in Electrokinetics Due to Stern-Layer Conductance Coupled to Reaction Kinetics. *Phys. Rev. Lett.* **2018**, *120*, 264502.

(22) Oatley-Radcliffe, D. L.; Aljohani, N.; Williams, P. M.; Hilal, N. Electrokinetic Phenomena for Membrane Charge. In *Membrane Characterization*; Elsevier: Amsterdam, 2017; Vol. *1*, pp 405−422.

(23) Schnitzer, C.; Ripperger, S. Influence of Surface Roughness on Streaming Potential Method. *Chem. Eng. Technol.* **2008**, *31*, 1696−1700.

(24) Zhao, H. Streaming Potential Generated by a Pressure-Driven Flow over Superhydrophobic Stripes. *Phys. Fluids* **2011**, *23*, 022003.

(25) Revil, A.; Schwaeger, H.; Cathles, L. M., Iii; Manhardt, P. D. Streaming Potential in Porous Media: 2. Theory and Application to Geothermal Systems. *Journal of Geophysical Research: Solid Earth* **1999**, *104*, 20033−20048.

(26) Rothstein, J. P. Slip on Superhydrophobic Surfaces. *Annu. Rev. Fluid Mech.* **2010**, *42*, 89−109.

(27) Fouché, F.; Dargent, T.; Coffinier, Y.; Treizebré, A.; Vlandas, A.; Senez, V. Superhydrophobic Surfaces' Influence on Streaming Current Based Energy Harvester. *J. Phys.: Conf. Ser.* **2016**, *773*, 012022.

(28) Fan, B.; Bhattacharya, A.; Bandaru, P. R. Enhanced Voltage Generation through Electrolyte Flow on Liquid-Filled Surfaces. *Nat. Commun.* **2018**, *9*, 4050.

(29) Yin, J.; Zhang, Z.; Li, X.; Yu, J.; Zhou, J.; Chen, Y.; Guo, W. Waving Potential in Graphene. *Nat. Commun.* **2014**, *5*, 3582.

(30) Yin, J.; Li, X.; Yu, J.; Zhang, Z.; Zhou, J.; Guo, W. Generating Electricity by Moving a Droplet of Ionic Liquid along Graphene. *Nat. Nanotechnol.* **2014**, *9*, 378−383.

(31) Aji, A. S.; Nishi, R.; Ago, H.; Ohno, Y. High Output Voltage Generation of over 5 V from Liquid Motion on Single-Layer MoS_2. *Nano Energy* **2020**, *68*, 104370.

(32) Huang, W.; Zhao, Y.; Wang, G.; Qiao, Z.; Gao, F.; Wang, X.; Wang, G.; Deng, Y.; Fan, X.; Zhang, J.; Duan, R.; Qiu, X.; Sun, L. Generating Electricity Using Graphene Nanodrums. *RSC Adv.* **2015**, *5*, 34065−34069.

(33) Subramaniam, C.; Pradeep, T.; Chakrabarti, J. Flow-Induced Transverse Electrical Potential across an Assembly of Gold Nanoparticles. *Phys. Rev. Lett.* **2005**, *95*, 164501.

(34) Subramaniam, C.; Pradeep, T.; Chakrabarti, J. Transverse Electrokinetic Effect: Experiments and Theory. *J. Phys. Chem. C* **2007**, *111*, 19103−19110.

(35) Griffiths, D. J. *Introduction to Electrodynamics*, 4th ed.; PearsonPrentice Hall: Upper Saddle River, NJ, 1999; p 33.

(36) Darnet, M.; Marquis, G. Modelling Streaming Potential (SP) Signals Induced by Water Movement in the Vadose Zone. *J. Hydrol.* **2004**, *285*, 114−124.

(37) Yamashita, M.; Fenn, J. B. Electrospray Ion Source. Another Variation on the Free-Jet Theme. *J. Phys. Chem.* **1984**, *88*, 4451−4459.

(38) Wang, H.; Liu, J.; Cooks, R. G.; Ouyang, Z. Paper Spray for Direct Analysis of Complex Mixtures Using Mass Spectrometry. *Angew. Chem., Int. Ed.* **2010**, *49*, 877−880.

(39) Basuri, P.; Sarkar, D.; Paramasivam, G.; Pradeep, T. Detection of Hydrocarbons by Laser Assisted Paper Spray Ionization Mass Spectrometry (LAPSI MS). *Anal. Chem.* **2018**, *90*, 4663−4668.

(40) Harper, J. D.; Charipar, N. A.; Mulligan, C. C.; Zhang, X.; Cooks, R. G.; Ouyang, Z. Low-Temperature Plasma Probe for Ambient Desorption Ionization. *Anal. Chem. (Washington, DC, U. S.)* **2008**, *80*, 9097−9104.

(41) Robb, D. B.; Covey, T. R.; Bruins, A. P. Atmospheric Pressure Photoionization: An Ionization Method for Liquid Chromatography−Mass Spectrometry. *Anal. Chem.* **2000**, *72*, 3653−3659.

(42) Wang, X. B.; Woo, H. K.; Huang, X.; Kappes, M. M.; Wang, L. S. Direct Experimental Probe of the On-Site Coulomb Repulsion in the Doubly Charged Fullerene Anion $C_{70}{}^{2-}$. *Phys. Rev. Lett.* **2006**, *96*, 1−4.

(43) Huang, D. L.; Dau, P. D.; Liu, H. T.; Wang, L. S. High-Resolution Photoelectron Imaging of Cold $C_{60}{}^{-}$ Anions and Accurate Determination of the Electron Affinity of C_{60}. *J. Chem. Phys.* **2014**, *140*, 224315.

(44) Fu, Q.; Yang, J.; Wang, X.-B. On the Electronic Structures and Electron Affinities of the *m*-Benzoquinone (BQ) Diradical and the *o*-, *p*-BQ Molecules: A Synergetic Photoelectron Spectroscopic and Theoretical Study. *J. Phys. Chem. A* **2011**, *115*, 3201−3207.

(45) Zanni, M. T.; Taylor, T. R.; Greenblatt, B. J.; Soep, B.; Neumark, D. M. Characterization of the $I_2{}^{-}$ Anion Ground State

Using Conventional and Femtosecond Photoelectron Spectroscopy. *J. Chem. Phys.* **1997**, *107*, 7613−7619.

https://dx.doi.org/10.1021/acsnano.0c09985

Supporting information:

2D-Molybdenum Disulfide-Derived Ion Source for Mass Spectrometry

Pallab Basuri[¶], Sourav Kanti Jana[¶], Biswajit Mondal[¶], Tripti Ahuja[¶], Keerthana Unni[¶], Md Rabiul Islam[¶], Subhashree Das[¶], Jaydeb Chakrabarti[ζ] and Thalappil Pradeep[¶]*

¶ DST Unit of Nanoscience (DST UNS) and Thematic Unit of Excellence (TUE), Department of Chemistry, Indian Institute of Technology Madras, Chennai 600 036, India

ζ Department of Chemical, Biological and Macromolecular Sciences, S. N. Bose National Centre for Basic Sciences, Sector III, Block JD, Salt Lake, Kolkata 700098, India

Correspondence to: pradeep@iitm.ac.in

S1. Materials, synthesis, and characterization

a. Chemicals:

All the chemicals were purchased commercially and used directly without further purification. Bulk MoS_2 powder and 1.6 M n-butyllithium (hexane), C_{60}, C_{70}, and glucose were purchased from Sigma Aldrich. Benzoquinone, iodine (I_2), benzoic acid, and acetic acid were purchased from Rankem. All the HPLC grade solvents were purchased either from Sigma Aldrich or Rankem. Water used was Milli-Q water, having conductivity of 0.05 μScm^{-1} and total organic carbon content was below 2 ppb.

b. Synthesis of MoS_2:

MoS_2 NSs were synthesized using chemical exfoliation method from bulk MoS_2 powder.[1] In a round bottom flask, 300 mg of bulk MoS_2 powder was taken in argon atmosphere as a precursor material to which 3 mL of 1.6 M n-butyllithium was added. It was then stirred for two days under the same condition at room temperature (23 ^{o}C). The product was then washed with hexane, followed by 100 mL of distilled water. This was done to remove excess reactant form the solution mixture. The final solution was agitated in a bath sonicator for 1 h. Thereafter, the aqueous dispersion was centrifuged at 18000 rpm to remove un-exfoliated MoS_2 from the mixture. As-prepared 2D-MoS_2 was further characterized with UV- Vis, Raman spectroscopy, and transmission electron microscopy.

c. Characterization of the as-synthesized 2D-MoS_2:

As-synthesized 2D-MoS_2 was first characterized using UV-vis spectroscopy. The UV-vis spectra presented at **Figure S2c** show one major peak at 415 nm and two small humps at 618 and 671 nm. TEM image confirms that the exfoliated MoS_2 are of few layers (**Figure S2a**). The lattice spacing (d_{100} = 0.27 nm) of (100) plane of MoS_2 is shown in **Figure S2b** and the inset of the Figure shows the FFT pattern of the same. Major characterization was done using Raman spectroscopy. **Figure S2d** shows two different Raman spectra. Bottom spectrum is for bulk MoS_2 powder, while the Raman spectrum of as-prepared MoS_2 is presented at the top. We see a large gap of 27 cm^{-1} between E^1_{2g} and A_{1g} in the bulk spectrum, which got shrunk in exfoliated MoS_2. The gap in the top spectrum is almost 18 cm^{-1} and this is matched with he reported literature.[2]

d. Fabrication of 2D-MoS_2-Coated paper:

Figure S3a schematically illustrates the overall fabrication procedure of MoS_2-coated paper. Typically, the dispersed MoS_2 solution of 10 ml was drop casted on a Whatman 42 filter paper kept on a glass petri-dish. The filter paper was folded in such a way that during drop casting, the solution should not spill out from the paper. Subsequently, the paper was dried at 35-40 ^{0}C in a hot air oven overnight. This dried paper was used directly for further experiments. Finally, the dried paper was characterized through Raman spectroscopy and Scanning electron microscopy (SEM).

e. Characterization of the fabricated paper:

The MoS_2-coated paper was first characterized using SEM. **Figure S3b** and **c** show the difference between uncoated and coated paper. In coated paper, we observed that MoS_2 layers got stacked during deposition and drying. This was further confirmed by the Raman spectrum of the coated paper. The Raman spectrum presented at **Figure S3e** shows that the E^1_{2g}-A_{1g} gap got further increased from 18 cm^{-1} to 22-23 cm^{-1}.[3] In **Figure S3d**, we have shown a Raman map of the MoS_2-coated paper. This confirms uniform coating of MoS_2 over the paper.

This paper was used for multidimensional applications such as fabrication of flow-induced energy harvesting, ion generation and alcohol sensing.

S2. Experimental setup

a. Design of the flow current device:

A custom-built setup was used for measuring flow-induced current. To build the setup, a rectangular shaped paper of 1×2 cm^2 area was stuck on a glass slide at its edge using a cellophane tape. Two silver contacts were made with silver paste to connect the copper wires with a picoammeter (Keithley 6485). **Figure S1d** shows the optical image of the device and inset of the Figure shows a zoomed in image of the same. Optimum contact distance was maintained by measuring the flow-induced current by varying the distance between two silver contacts (1-7 mm). We held the glass slide by a clamp which was mounted on a xyz micro positioning stage. Then we placed a fused silica capillary over the rectangular paper. The capillary was used to flow the fluids with a preferred flow rate. Flow direction and velocity were also controlled by placing an inlet of a vacuum pump in front of the paper. The pressure was controlled by a regulator and set to $\sim 10^{-2}$ bar. Flow rate of the solvents was maintained through a syringe pump (NE-300). The background current of the picoammeter was recorded without flowing any liquid over the surface. We show the background current of the picoammeter with (**Figure S1b**) and without (**Figure S1a**) connecting to the device but before flowing any liquid. In **Figure S1e** we show a photograph of the entire setup, in which the picoammeter shows a reading of 0.24 µA.

We have also measured the resistance across the electrode during methanol flow. The resistance comes in the range of 50 to 100 kΩ (~0.1 MΩ). This is similar to the resistance of bulk methanol. This large resistance hints that the current generation must be due to the charged species generated in the flow.

S3. Experimental details

a. Measurement of the terminal velocity of the liquid flowing over MoS_2-coated paper:

We captured a video clip during the liquid flow over MoS_2-coated paper. Parameters of the device were fixed at a constant value, such as $U_L = 22$ µl/min, $\Theta = 45^0$, and methanol was used as a solvent. Here Θ corresponds to the angle of inclination of the MoS_2-coated paper with respect to the horizontal plane. We measured the travel time of liquid flow through the filter paper and it was measured within 1 cm, starting from a point at one end (where the opening outlet of the fused silica capillary was placed on the paper) to the other end of the paper. Average of three consecutive measurements yields the terminal velocity of the fluid moving over MoS_2-coated paper surface and it was 2.45 mm/s.

b. Open circuit potential measurements:

The open circuit potential was measured through an electrochemical analyzer and the data are shown in **Figure S10b**. The flow rate of methanol was set at 22µl/min. **Figure S10d** shows the change in the potential with the viscosity of the flowing solvent.

c. Mass spectrometric measurements:

All the mass spectrometric experiments were performed in a LTQ XL mass spectrometer from Thermo Scientific. In the streaming ion source, we used methanol with a flow rate of 22 µl/min. and flow rate for the analyte was 11 µl/min. The ion source was held on a xyz micro positioning stage and the glass slide was fixed at an angle of 45° with horizontal plane using a clamp. The angle was measured through a protractor. We also held a USB digital camera to adjust the distance between the paper tip and the inlet of the mass spectrometer. The average size of the paper used was 50 mm^2. The tube lens and the capillary voltages of the mass spectrometer were set to zero to avoid ionization within the inlet region. Sheath gas flow was kept at zero psi. Data acquisition was done in a continuous mode. All the data were recorded in negative ion mode, as during the flow we always ended up with the anions flowing with the liquid. The positive mode spectra had no signal. We have compared both positive and negative mode mass spectra of C_{60} as shown in **Figure S33**; however, we could not observe any such background signal as shown in the negative ion mode mass spectrum.

S4. Control experiments for current generation

a. Drying time-dependent experiment:

An experiment was conducted to monitor the effect of capillarity in the filter paper on current generation. We have initially run the experiment by flowing methanol with a flow rate of 22 µl/min and waited for 40 s to stabilize the current. After that, we have switched off the syringe pump and waited for 10 sec. This was repeated two more times. We observed that if we allow a continuous flow of liquid on a wet paper, an instantaneous increment of current can be avoided. We infer that the capillary force of the paper results in generating $I_{f_{max}}$.

b. Current measurement on MoS_2-coated glass and plastic slides:

We prepared MoS_2-coated glass and polystyrene slides in a similar way. We made two silver contacts over these two surfaces. Flowing of methanol over these MoS_2-coated substrates also generates the current as shown in the I_f-t trace in **Figure S6**.

c. Effect of vacuum pump on the stability of current:

We observed that placing the inlet of a vacuum pump at the end of the MoS_2-coated paper makes the flow-induced current stable. This pump increases the force, experienced by the liquid resulting in a unidirectional flow with sufficient kinetic energy to overcome the zigzag flow of liquid. **Figure S7a** shows that the current fluctuation caused by the non-uniform capillary flow of liquid inside the paper in the absence of pumping. A stable current reading was monitored with pumping (**Figure S7b**). The inset of this Figure shows the schematic diagram of the setup with a pump. Pump pressure was controlled using a regulator and an optimum distance was maintained between the edge of the paper and the inlet of the pump to avoid surface drying caused by rapid suction.

d. Paper dipped experiment:

We have conducted an experiment to show that the liquid flow over the MoS_2-coated surface is an essential factor to generate the current. To verify this conjecture, MoS_2-coated paper was directly dipped into a plastic vial containing methanol and simultaneous current was measured. We observed an initial rise of the current caused by methanol filling into the fiber network of the paper through capillary action and current reached zero as the paper became fully wetted with methanol (**Figure S8**).

e. Flow direction dependency:

To check the relation between the polarity of the current and flow direction, we have conducted an experiment where we allowed to flow methanol in a direction shown in the inset of **Figure S9a**. Current was recorded through a picoammeter as shown in **Figure S9a**. To check the current flow direction, polarity of the picoammeter was reversed as schematically illustrated in the inset of **Figure S9b** and we observed that the polarity of the current also got reversed.

f. Simultaneous flow of alcohols:

We conducted an experiment in which methanol, ethanol, and propanol were flown on a single paper and flow-induced current corresponding to each alcohol was recorded simultaneously. This experiment was done using three separate syringe pumps. We used three separate capillaries for each pump. During the measurement of flow-induced current, we first switched on/ off the methanol pump and consecutively other pumps were switched on/off. We observed the highest and lowest current due to the flow of methanol and propanol, respectively.

g. Flow of water-methanol mixture:

Water-methanol mixture shows different physical properties in terms of viscosity, surface tension, *etc.* than the individual liquids. From a plot of viscosity *vs.* percentage of methanol, we can understand that 50 % methanol-water mixture has the highest viscosity. We have also checked the influence of viscosity of the liquid on the current generation. For that, we have flown a mixture of methanol and water with different volume ratios ranging from 0 to 100 %. We see exactly opposite curvature for both the viscosity *vs.* current profile (**Figure S13b**). We observed that at 50% methanol-water, the current is lowest. This also proves the linear relation between viscosity and current.

h. Zeta potential measurement of MoS_2:

Zeta potential of MoS_2 was measured in solution phase with a Malvern Zetasizer Nano ZSP. As-synthesized MoS_2 in water shows a zeta potential of -41.2 mV, as shown in **Figure S15**.

i. Current generation over reduced graphene oxide (rGO)-coated paper:

To demonstrate that the dissociation-induced electrokinetic effect on other 2D surfaces, we used rGO-coated paper and allowed to flow methanol over it. We observed that rGO generates a much lower current than MoS_2. This is because the polar Mo-S bond helps in methanol dissociation and at the same time the sulfur groups help to hold the positive charge over the surface. But such dissociation and charge holding capacity are very less in case of rGO which leads to less current production. Hence, we observed approximately 250 nA on MoS_2 whereas rGO generates only 50-60 nA (**Figure S16a**).

j. C_{60} drop-cast experiment:

We have also studied how C_{60} ionization was affected by the methanol flow-induced current. For this experiment, we drop-casted 10 µl of C_{60} in toluene on the paper when the methanol flow current reached a stable value. We observed a sudden fall of the current (**Figure S18**). **Figure S18a** shows a schematic diagram of the setup.

k. Mixed solvent flow experiment:

To demonstrate that current depletion during drop-cast of C_{60} solution is not due to the use of nonpolar toluene, we made toluene flow along with methanol and recorded the current simultaneously. Flow of these two solvents was controlled in two different paths. In the first case, the flow of methanol was followed by flowing toluene along with methanol. In the second case, we did the flow in the reverse order, where the flow of toluene was followed by that of the toluene-methanol mixture. In both the cases, the current generation due to the flow of methanol was unrelated to the flow of toluene.

S5: Mass spectrometric experiments

a. Paper spray and electrospray ionization of C_{60}:

For paper spray ionization, a triangular shaped filter paper was connected with a high voltage power supply. During mass spectrometry measurements, we have drop-casted C_{60} in toluene-methanol mixture and applied -4 kV to the paper to generate electrospray plume from the tip of the paper. We observed a peak corresponding to the molecular ion peak of C_{60}. The paper spray ionization setup is schematically illustrated in **Figure S20c**. In electrospray ionization, we have observed very little intensity of the molecular ion peak of C_{60}.

b. *In-situ* current and mass spectrometric measurement:

For this experiment, we fabricated the electrodes on the triangularly cut MoS_2-coated paper and a picoammeter was connected through a copper wire. Finally, we held the paper in front of the mass spectrometer inlet. Upon methanol flow, we observed a current reading in the picoammeter, whereas, upon drop-casting of C_{60}, the picoammeter reading comes back to the background level. However, at the same time, ion current in the chronogram of the mass spectrometer appeared and the corresponding mass spectrum for C_{60} ionization was observed simultaneously.

c. Tip to inlet distance dependency and the inlet temperature dependency on ionization:

We had attached the ion source over an xyz micropositioning stage. This was to see the effect of increasing distance on the peak intensity of C_{60}. In an experiment, we observed that the maximum operating distance to detect the peak at *m/z* 720 was up to 5 mm, from the mass spec inlet (**Figure S35a**). We had also checked the effect of the inlet temperature. We observed exponential growth of ion intensity with increasing temperature (**Figure S35b**). We kept it at 275 ^{0}C for all our mass spectrometric measurements.

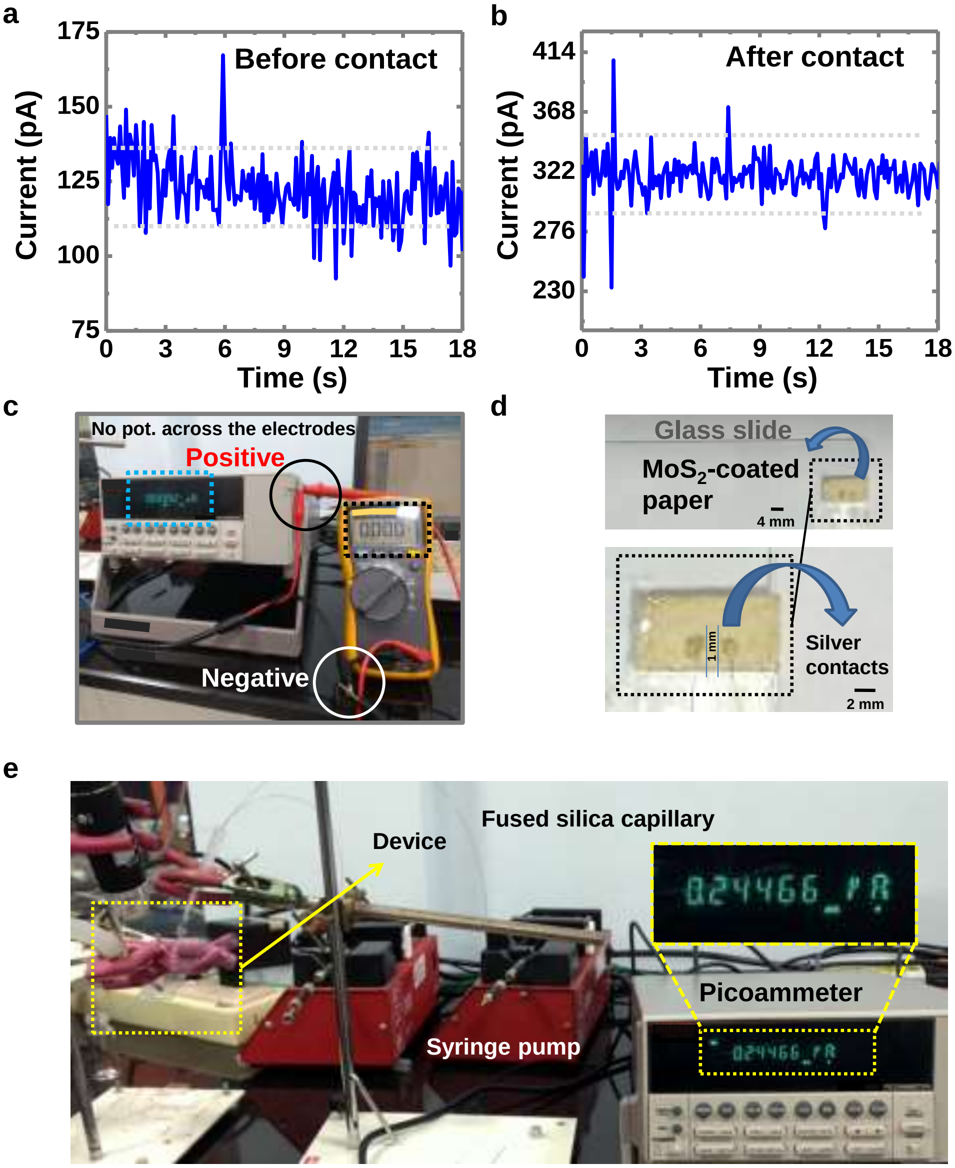

Figure S1. Background current and optical image of the overall setup. a) Background current before connecting the picoammeter to the MoS_2-coated paper. b) After making contacts and connecting the picoammeter to the MoS_2-coated paper. These data were recorded before flowing any liquid over the surface. c) Optical image in which the two electrodes of the picoammeter were connected to a multimeter to show that there was no external potential applied. d) Optical image of the device. Inset shows the zoomed in area of the silver contacts. e) Optical image of the entire setup during current generation. Picoammeter displayed a reading of 0.24466 µA in one of our experiments.

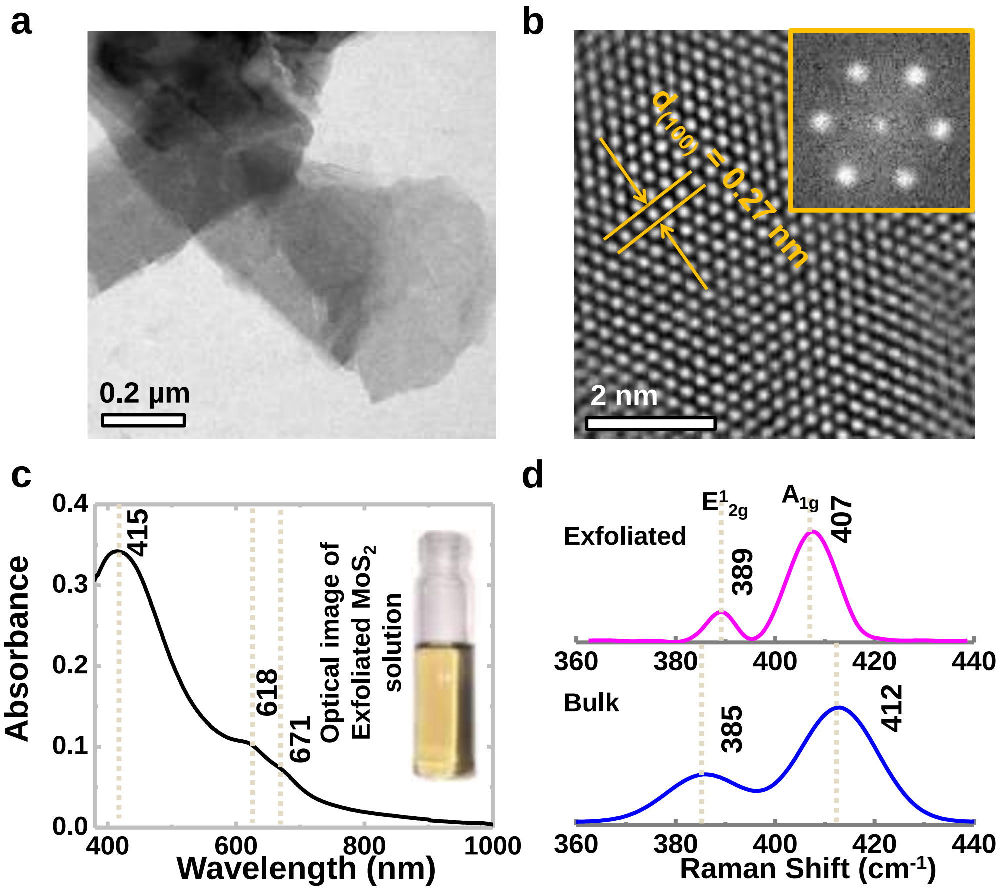

Figure S2. Characterization of exfoliated MoS_2 NSs. a) Representative TEM image of as-synthesized MoS_2 nanosheets. b) HRTEM image of the MoS_2 nanosheets showing a lattice spacing of 0.27 nm. Inset shows the corresponding FFT pattern. c) UV-vis absorption spectrum of the solution. Inset shows an optical image of the solution. d) Comparative Raman spectra of bulk and nano MoS_2. Peaks are labeled. Shift in the modes indicate the extent of exfoliation.

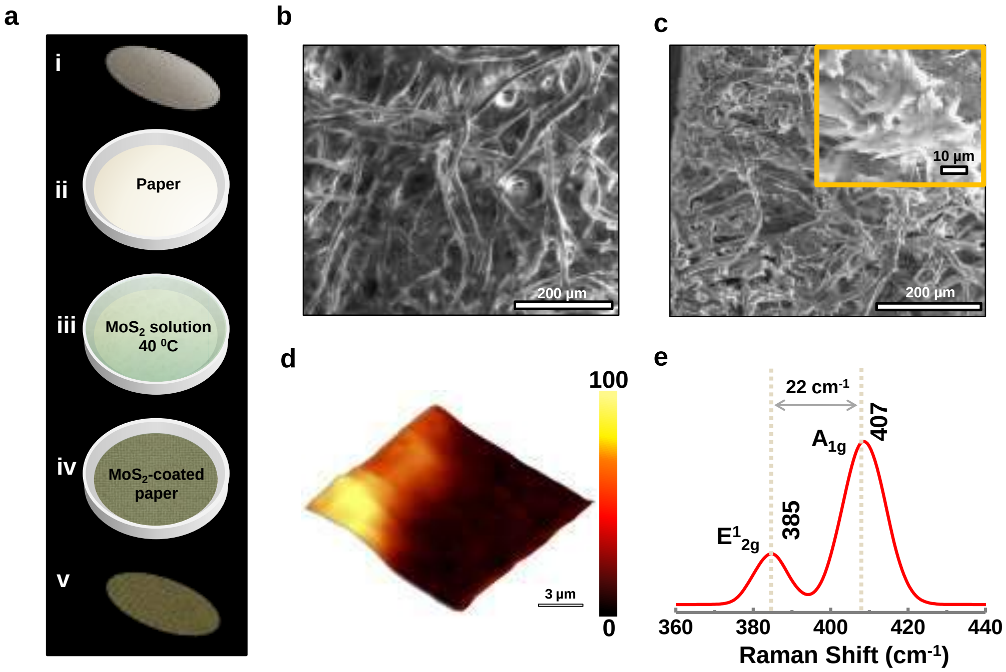

Figure S3. Fabrication and characterization of the MoS_2-coated paper. a) The process of fabricating MoS_2-coated paper, schematically. i-v are different stages during the process. b) SEM image of the Whatman 42 filter paper. c) SEM image of the MoS_2-coated Whatman 42 filter paper. Inset shows a zoomed in image of the stacked MoS_2 nanosheets. d) Raman mapping of the coated paper. Total Raman intensity was used for imaging. e) Raman spectrum of the coated paper.

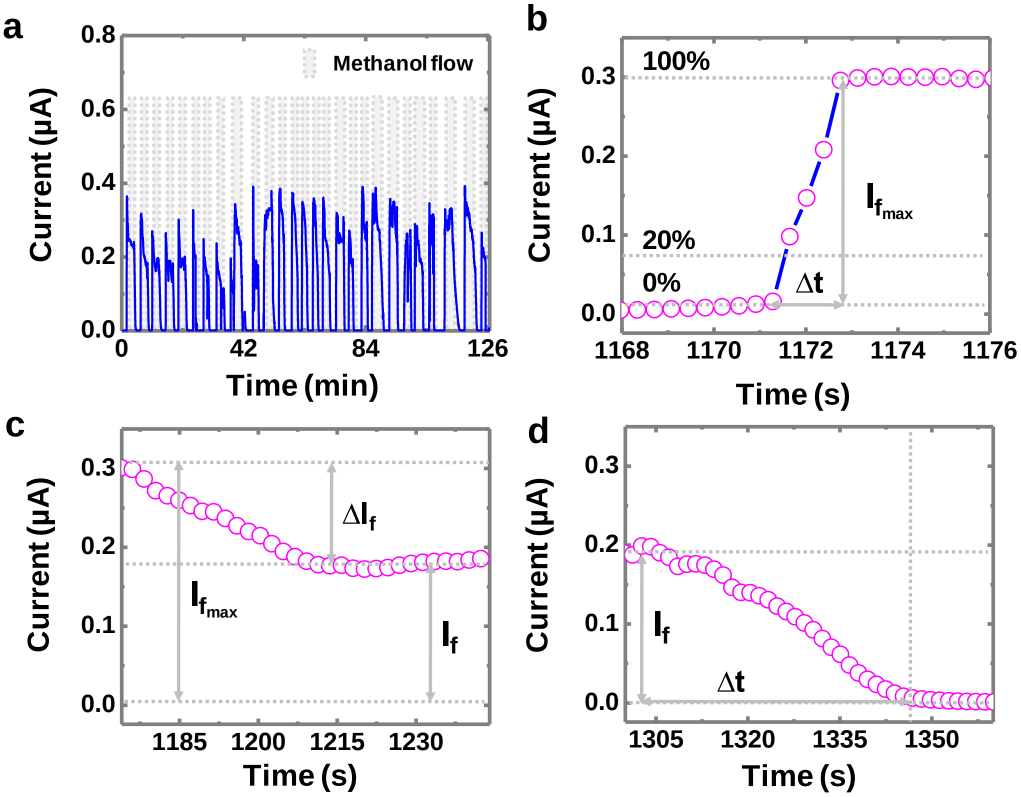

Figure S4. I_f-t traces. a) Multiple cycles of flow on/off for 126 min. b) Zoomed in view of initial rise of current to I_{fmax}, c) stabilization at a value of 60% of I_{fmax}, and d) fall of current to the background level.

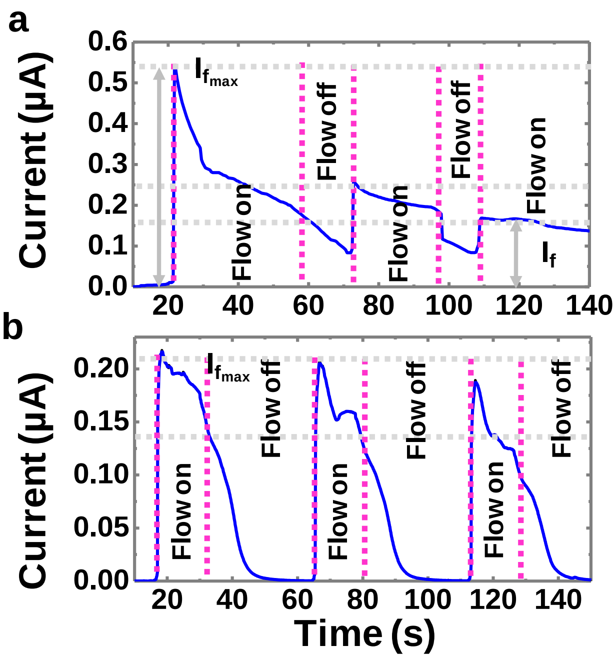

Figure S5. Difference in the I_f-t profile in different drying time scales. a) drying time of 10 sec and b) 30-35 sec.

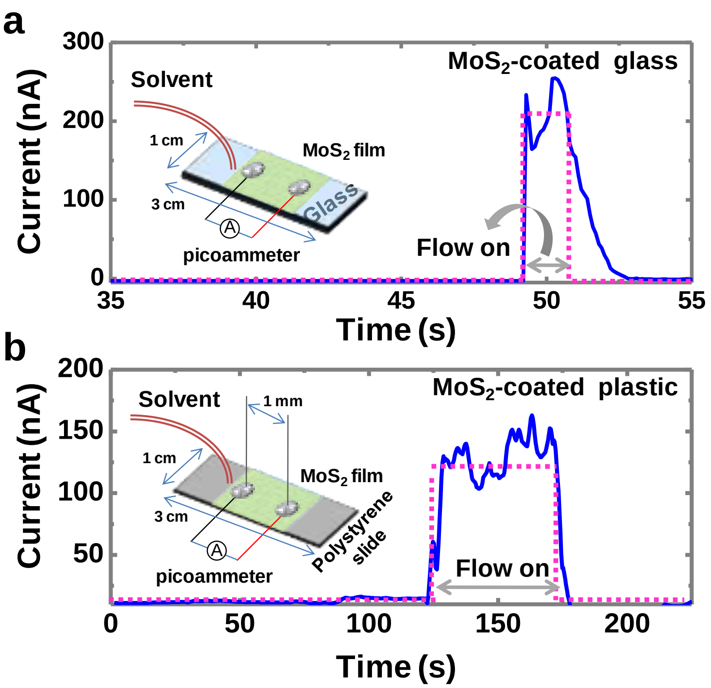

Figure S6. Effect of support material on current generation. Current-time trace on a) a MoS$_2$-coated glass surface, and b) MoS$_2$-coated plastic surface. Insets of both the Figures schematically show the device arrangements. Standard biological glass slides were cut into proper dimension and coated with MoS$_2$ films. The plastic used was polystyrene slides and the MoS$_2$ film was prepared in the same way (as illustrated in Figure S3a).

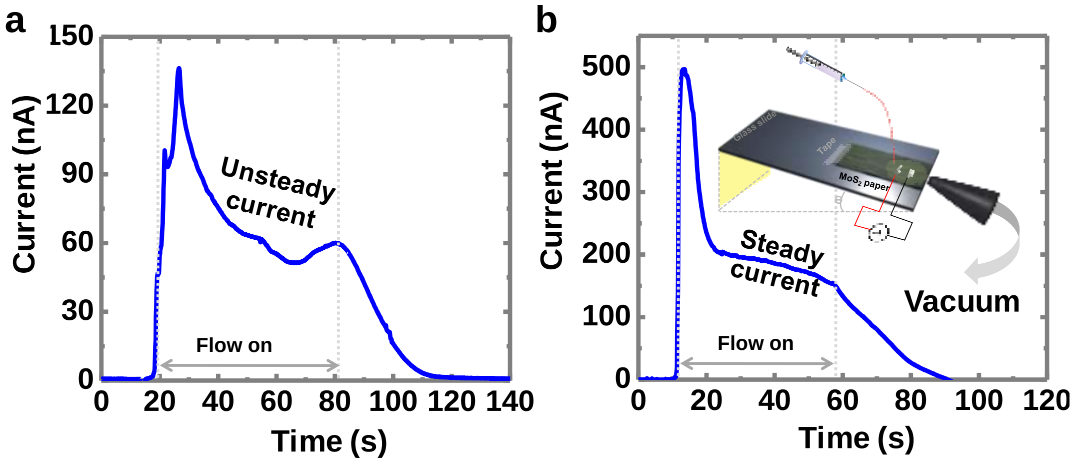

Figure S7. Effect of vacuum during current generation. a) Current generation without applying vacuum. b) Current-time profile after applying vacuum in front of the device, as shown schematically in the inset.

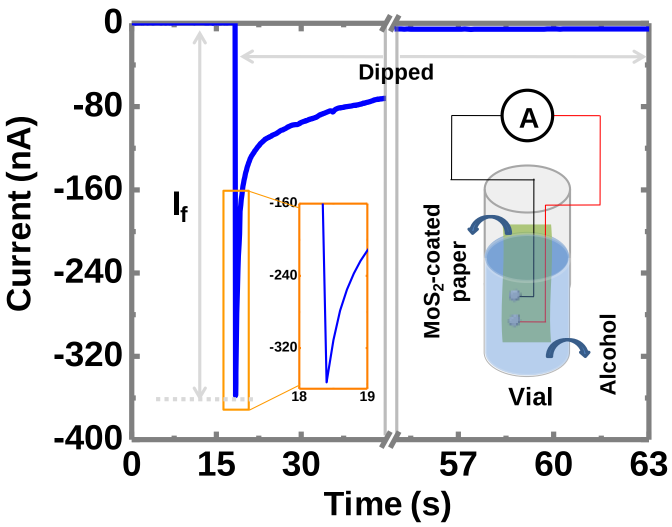

Figure S8. MoS_2-coated paper dipping experiment. We dipped the MoS_2-coated paper inside a vial containing methanol and current was recorded with time. We observed a sudden increase and subsequent fall in current. The inset schematically represents the experimental setup.

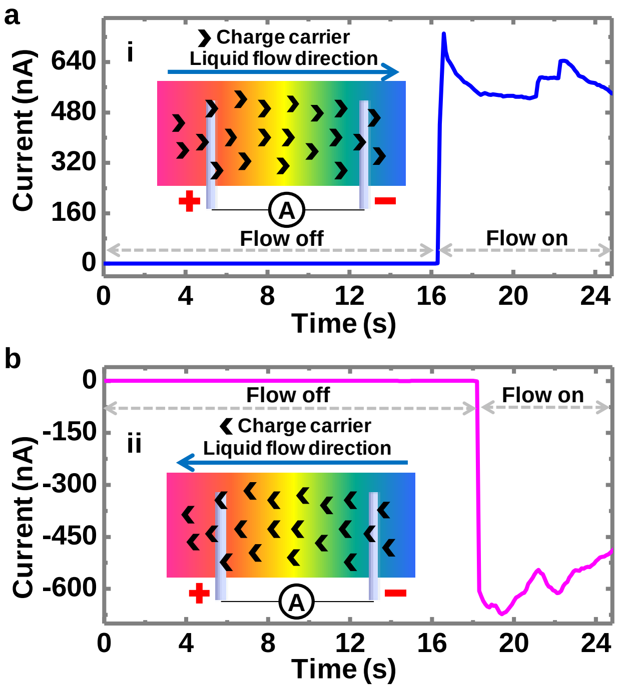

Figure S9. Flow direction and the polarity of the current. a) Current-time trace while direction of the flow is from the positive electrode to the negative electrode. Inset represents a schematic diagram of the corresponding flow direction. b) Current-time trace while the flow direction was changed in the same setup. Inset shows the schematic diagram of the corresponding flow direction; the flow direction of the liquid and the charge carrier are indicated.

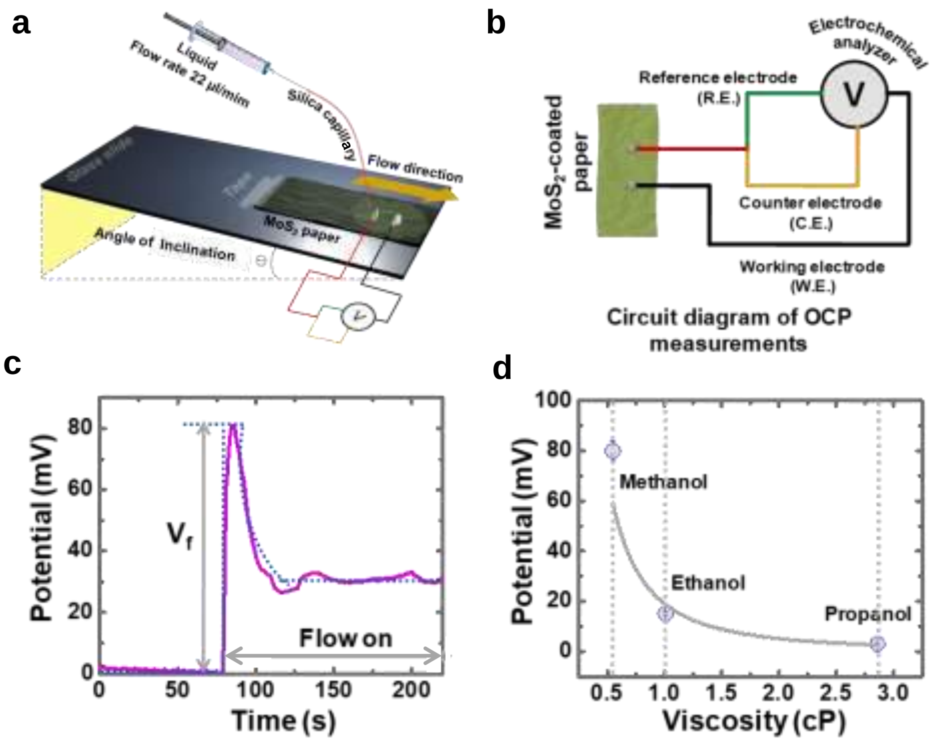

Figure S10. Open circuit potential (OCP) measurement over MoS_2-coated paper. a) schematic diagram of the device. b) The circuit diagram of the OCP measurements. c) The potential-time trace of the OCP using methanol as a flowing liquid. d) Potential-viscosity trace representing comparative potential generation using methanol, ethanol, and propanol. Each experiment was repeated thrice independently. Data are presented as mean, and error bar shows ±SD.

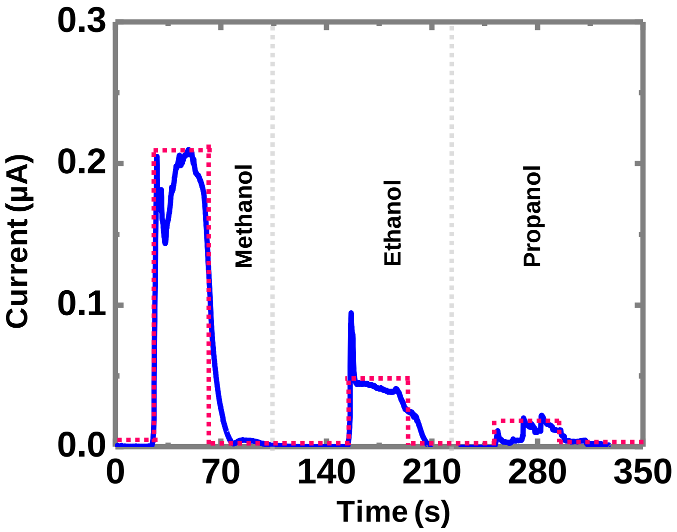

Figure S11. Comparative current generation profile using methanol, ethanol and propanol. The unsteady fall and rise of current in the first and third cycles are due to omnidirectional flow of liquid in the absence of a vacuum pump (as shown earlier in Figure S7).

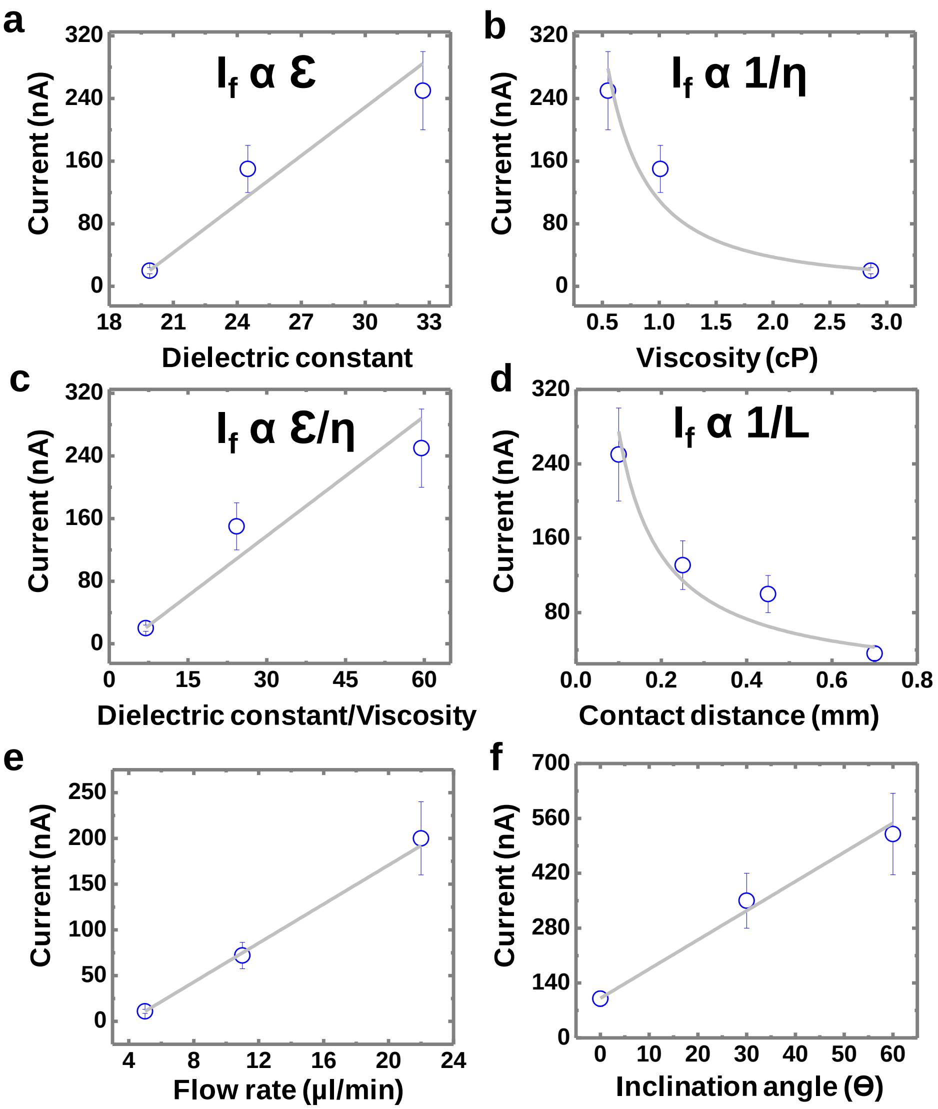

Figure S12. Experimental validation of the electrokinetic effect. a) Current *vs.* dielectric constant of the liquid. b) Current *vs.* viscosity of the liquid. c) Current *vs.* the ratio of dielectric constant and viscosity of the liquid. d) current *vs.* contact distance. e) Current *vs.* flow rate. f) Current *vs.* inclination angle. Appropriate fits are used. Each experiment was repeated thrice independently. Data are presented as mean, and error bar shows ±SD.

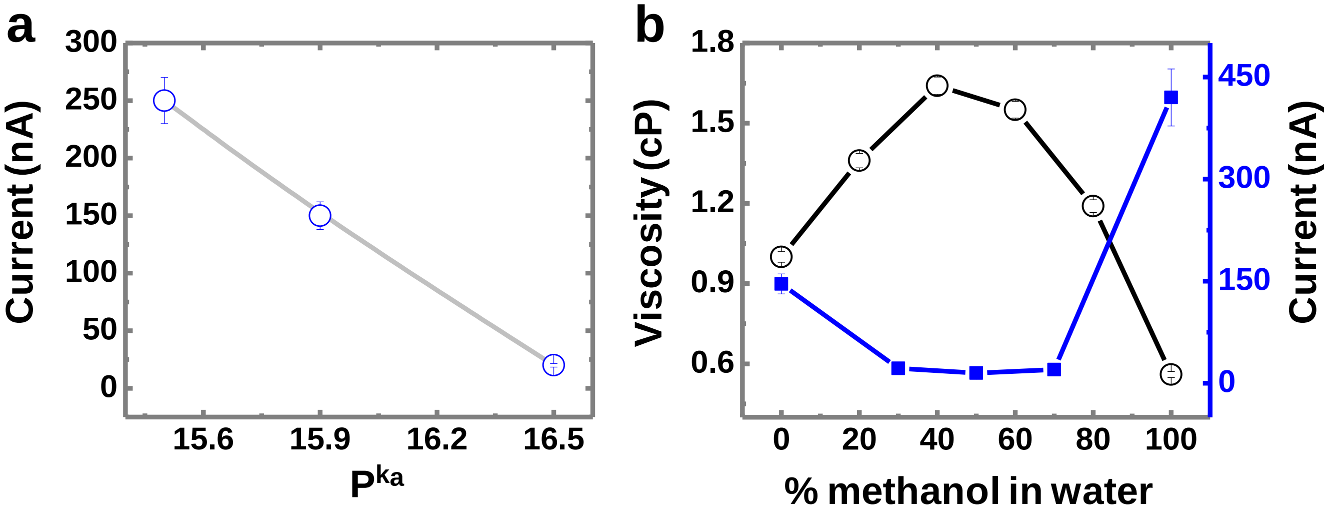

Figure S13. Magnitude of current with dissociation constant and viscosity. a) Current-pK_a trace of all the alcohols. Each experiment was repeated thrice independently. Data are presented as mean, and error bar shows ±SD. b) Viscosity[4] and current profile in different concentration of methanol in water flow.

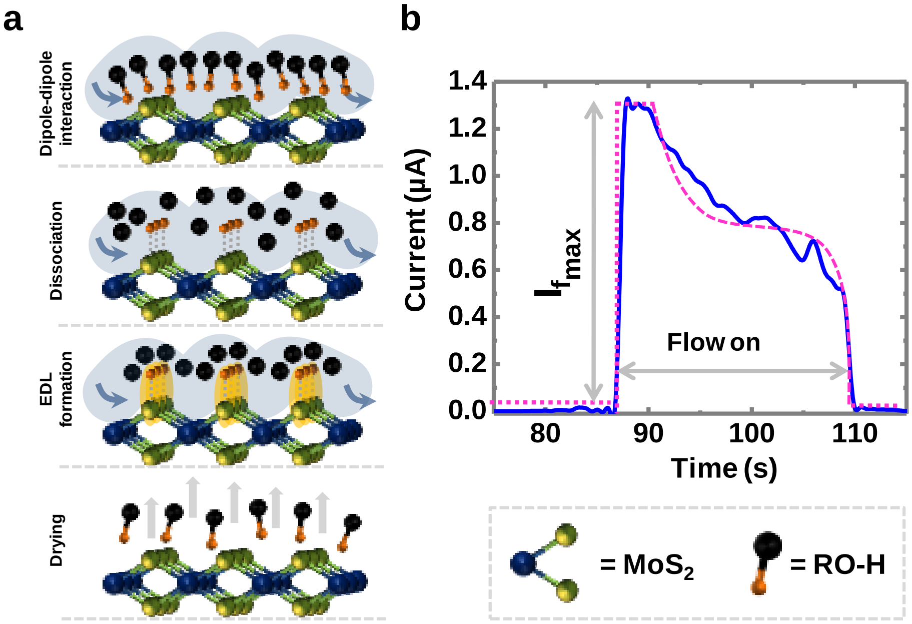

Figure S14. Mechanistic understanding of the current generation. a) Schematic representation of the speculated phenomenon, dissociation-induced electrokinetic effect. b) Different stages of the current-time trace leading to correlation of the mechanism.

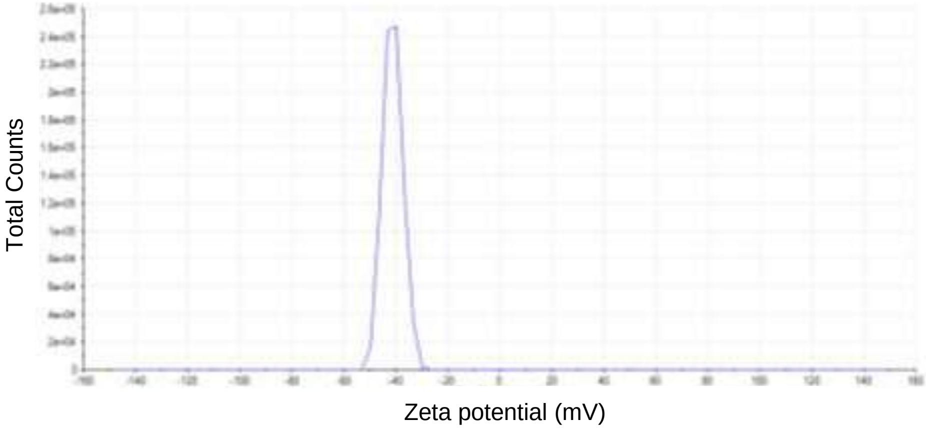

Figure S15. Zeta potential (ς) analysis of MoS_2 in solution. Zeta potential distribution shows that the maximum zeta potential of MoS_2 solution is -41.2 mV.

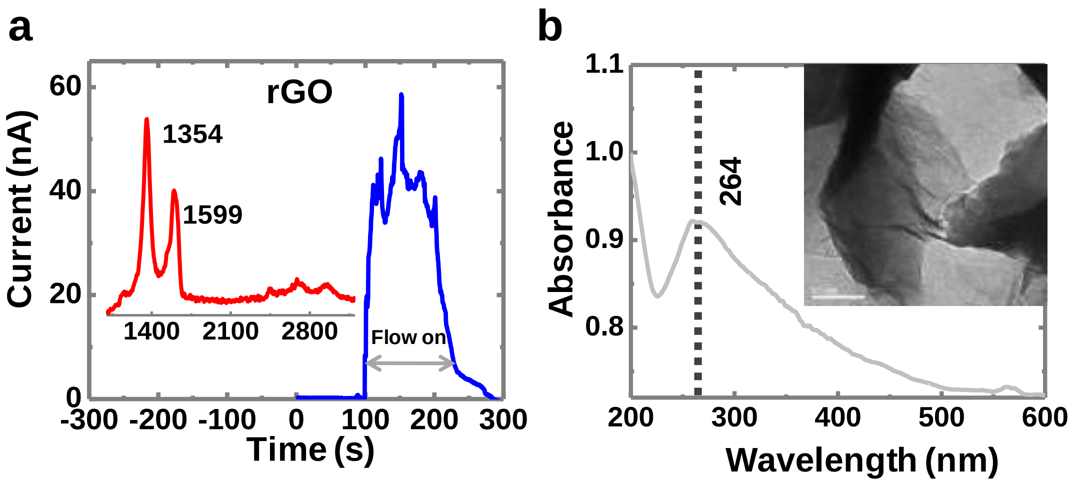

Figure S16. Current generation on rGO. a) Current generation on reduced graphene oxide. Inset shows the characteristic Raman features of the rGO-coated paper. b) UV-vis spectrum of rGO used for current generation. Inset presents a TEM image of the same.

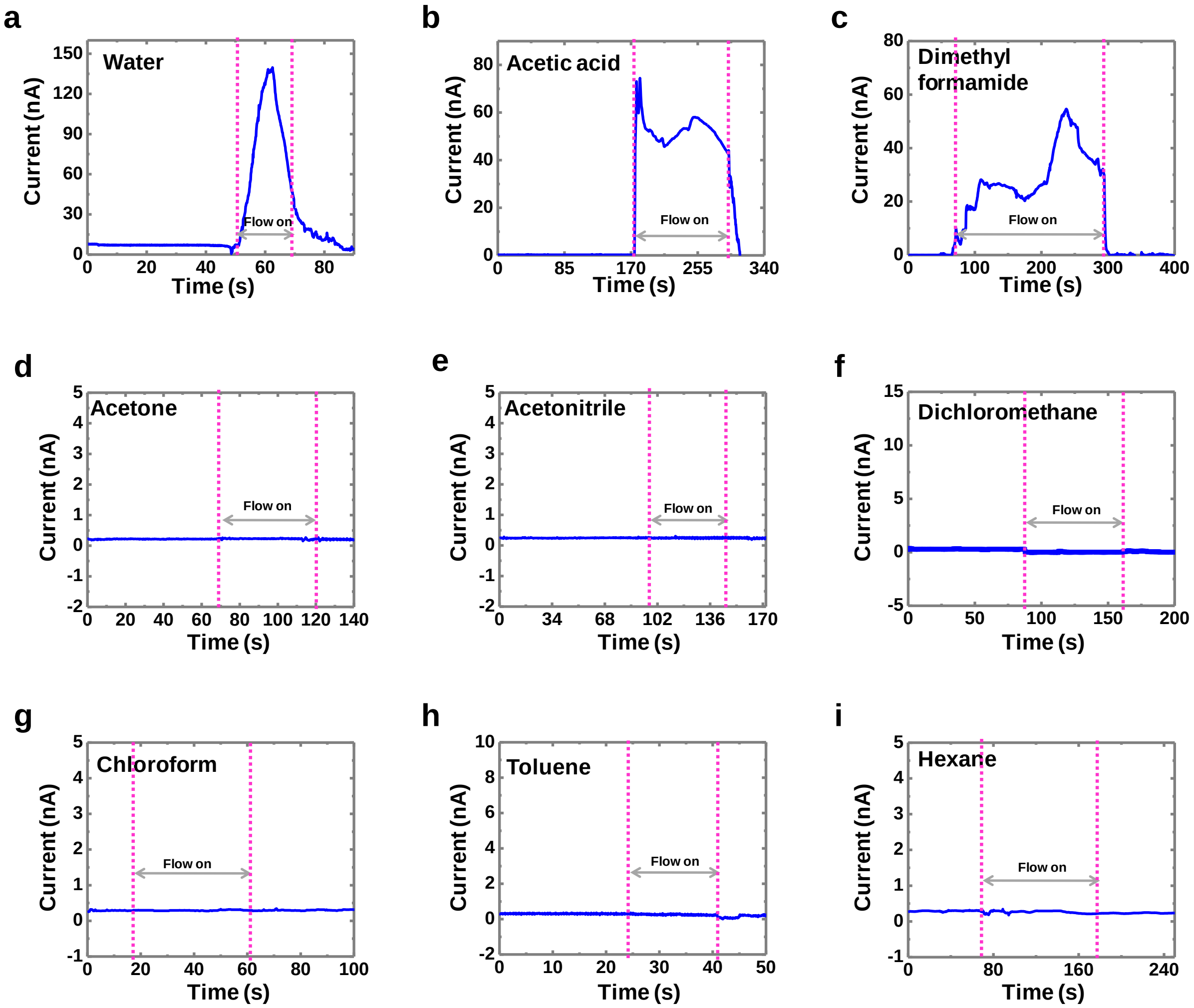

Figure S17. Current-time trace of other solvents. Current generation using a) water, b) acetic acid, c) dimethyl formamide, d) acetone, e) acetonitrile, f) dichloromethane, g) chloroform, h) toluene and i) hexane. The unsteady fall and rise of current in b and c are due to omnidirectional flow of liquid in the absence of a vacuum pump (as shown earlier in Figure S7).

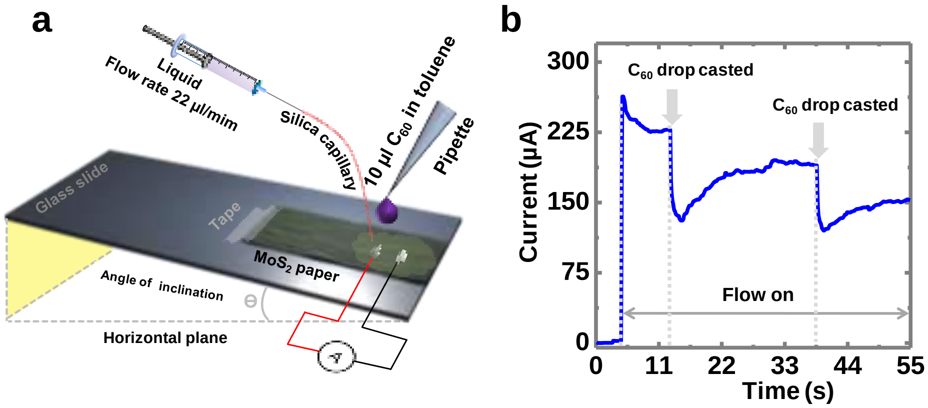

Figure S18. Effect of electron scavenging molecule during current generation. a) Schematic diagram of the experimental setup. b) The current-time trace during drop-casting of 10 µl of C_{60} while the flow is on. The flowing liquid is methanol here with 22 µl/min flow rate.

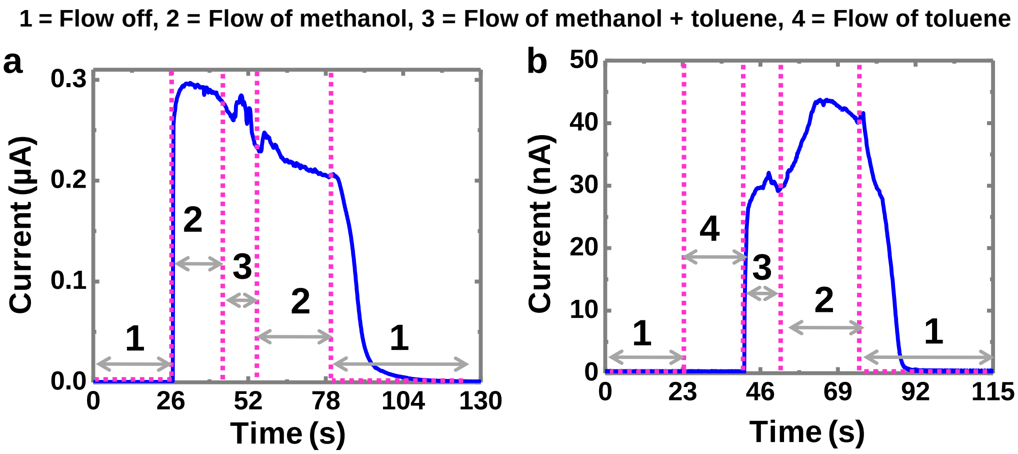

Figure S19. Current time trace in mixed solvent flow. a) Flow of methanol first then mixture of toluene and methanol. b) Flow of toluene first then mixture of methanol and toluene.

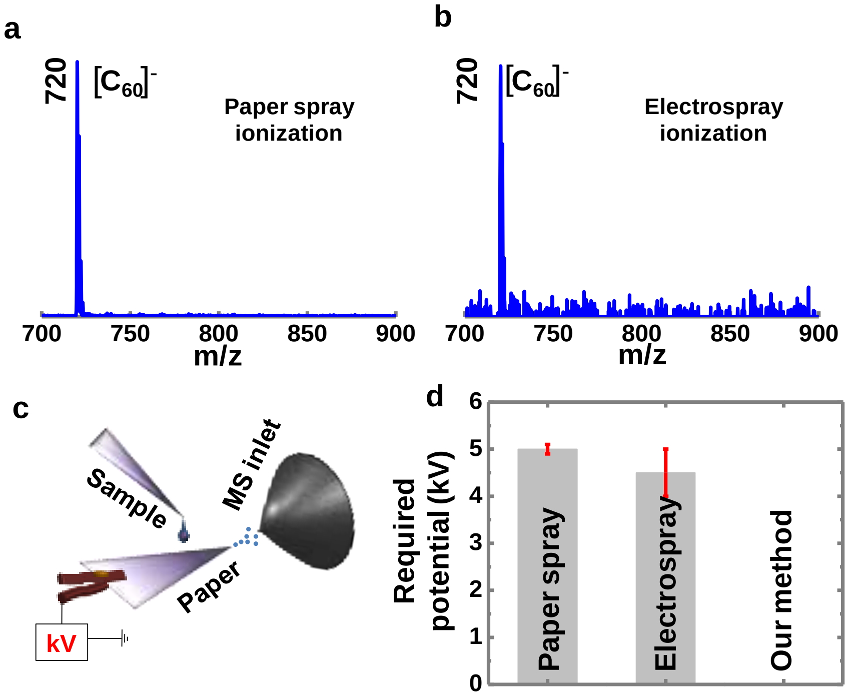

Figure S20. Comparison of our method of ionization with standard paper spray ionization and electrospray ionization methods. a) PSI mass spectrum of C_{60}. b) ESI mass spectrum of C_{60}. We observed a very low intense peak for C_{60}. However, peaks corresponding to C_{60} dimer, methoxide, and hydroxide added C_{60} were not observed. Both the PSI and ESI MS were done in toluene-methanol mixture. c) Schematic representation of paper spray ionization in which potentials of the order of kilovolts are applied for ionization. Similar is the case for electrospray ionization. d) Comparative study between these conventional methods with our method to obtain C_{60} peak at *m/z* 720.

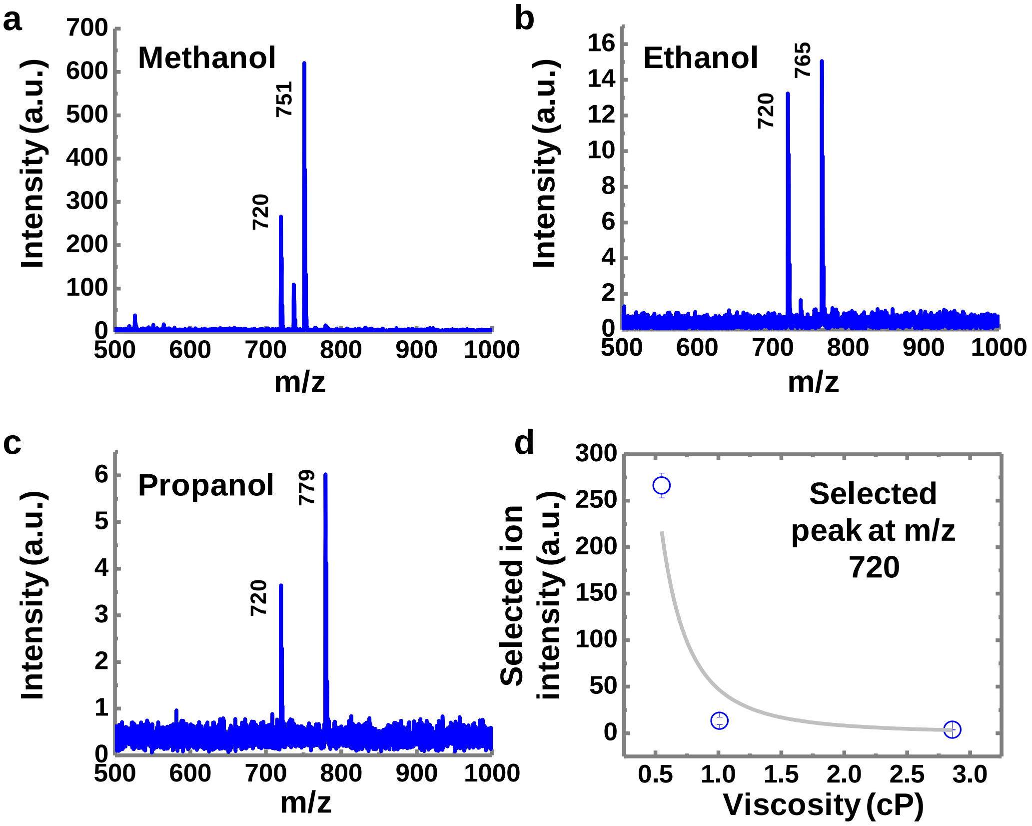

Figure S21. Comparative mass spectra of C_{60} flowing with three different alcohols. a) Methanol, b) ethanol, and c) propanol. Actual intensities of individual spectra are presented in the Y axis. d) Actual intensities of the peak *m/z* 720 are plotted against the viscosity of alcohols.

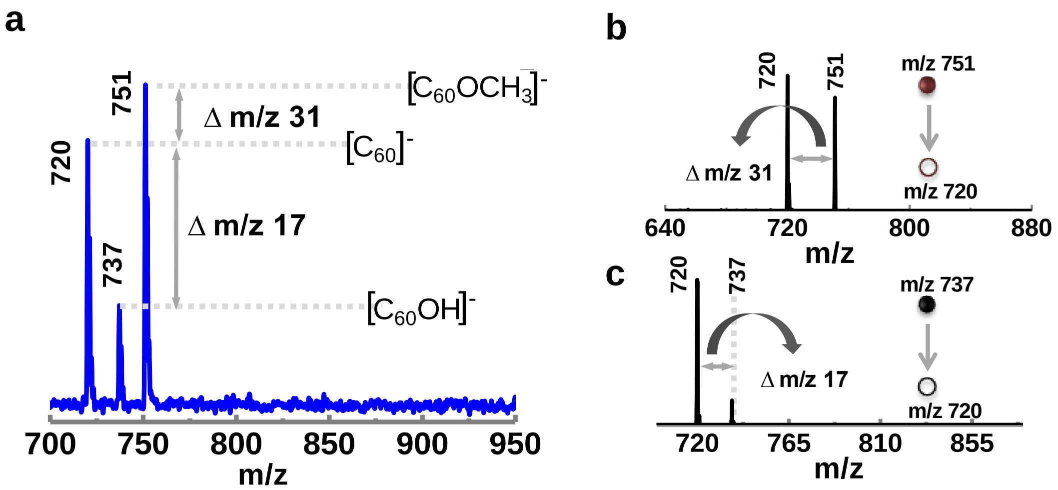

Figure S22. Fragmentation pattern of hydroxide and methoxide added peak of C_{60}. a) MS^1 spectrum recorded during the flow of C_{60} along with methanol. b) MS^2 spectrum of *m/z* 751. It shows the loss of *m/z* 31 corresponding to methoxide ion. c) MS^2 spectrum of *m/z* 737. It shows the loss of *m/z* 17 corresponding to the hydroxide ion.

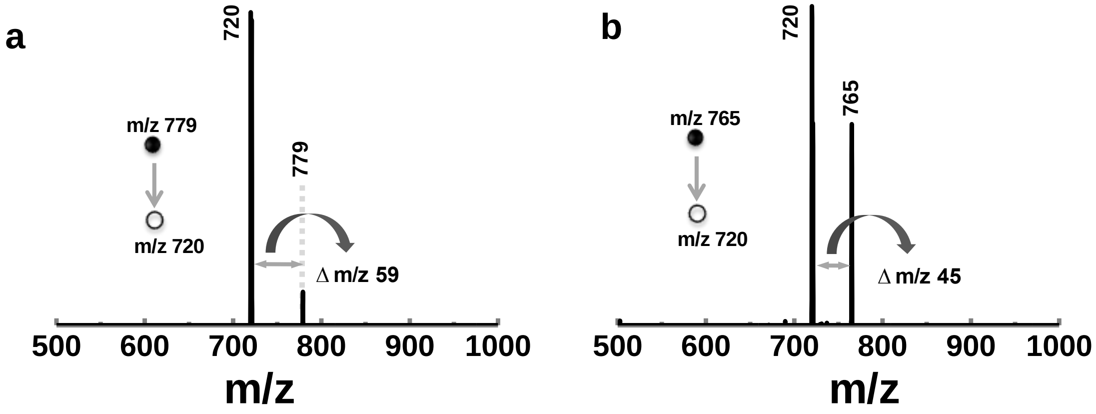

Figure S23. Fragmentation pattern of ethoxide and propoxide added peak of C_{60}. a) MS^2 spectrum of *m/z* 779. It shows the loss of *m/z* 59 corresponding to propoxide ion. b) MS^2 spectrum of *m/z* 765. It shows the loss of *m/z* 65 corresponding to ethoxide ion.

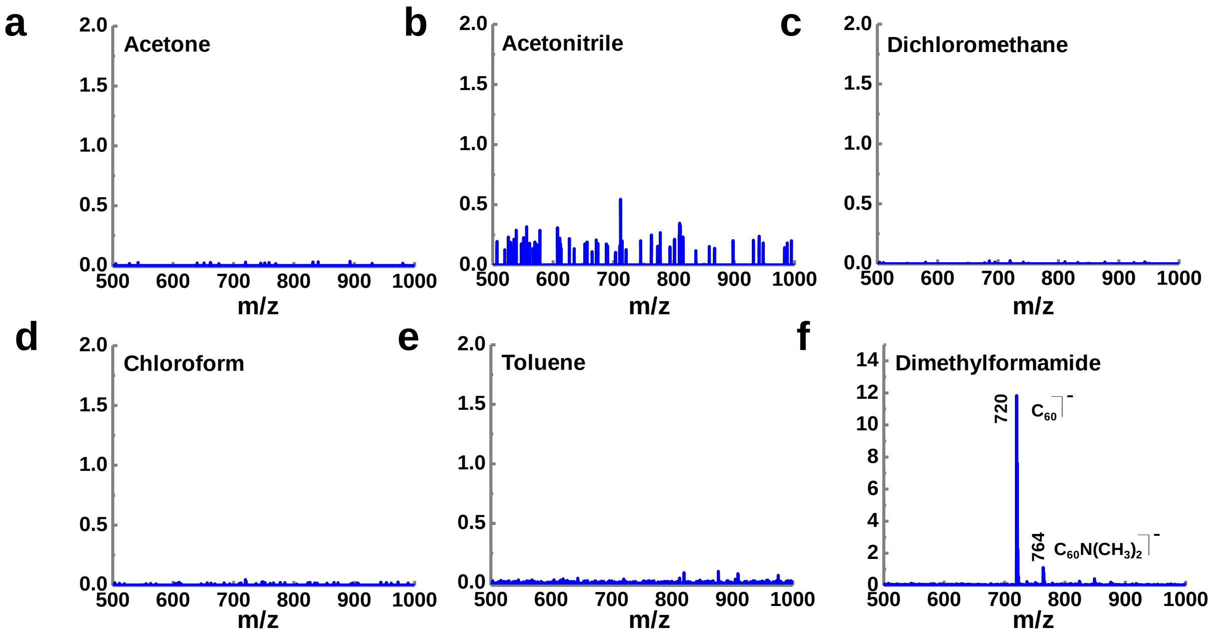

Figure S24. Mass spectra of C_{60} in different solvents with varying polarity. a) Acetone, b) acetonitrile, c) dichloromethane, d) chloroform, e) toluene, and f) Dimethylformamide. A peak at *m/z* 764 is observed in DMF along with *m/z* 720 ($[C_{60}]^-$) which could be due to the species $[C_{60}N(CH_3)_2]^-$.

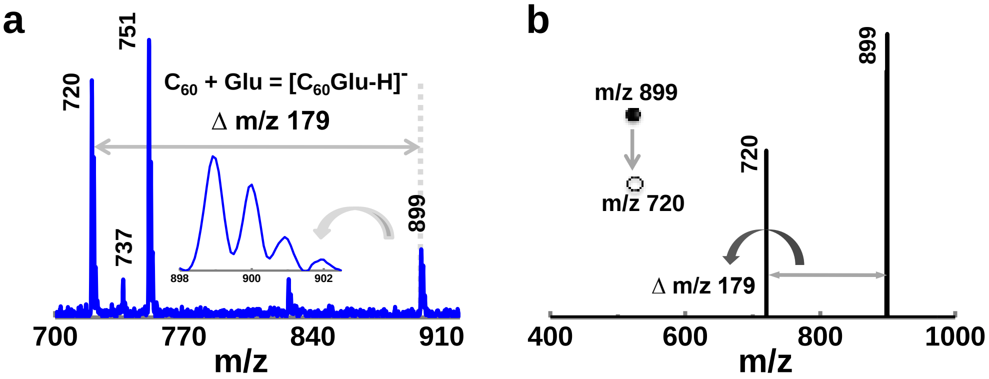

Figure S25. Glucose addition of C_{60}. a) MS^1 spectrum recorded during the flow of methanolic solution of C_{60} and glucose. We observed a peak at *m/z* 899 at *m/z* 179 higher than the molecular ion peak of C_{60}. Inset shows the isotopic distribution of the peak. b) MS^2 spectrum of the peak at m/z 899 leads to the loss of *m/z* 179 corresponding to deprotonated glucose.

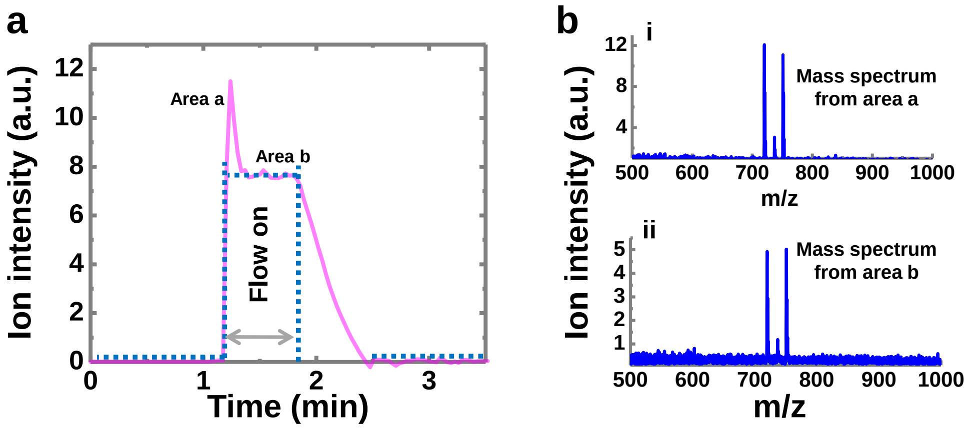

Figure S26. Extent of ionization of C_{60}. a) Total ion chronogram (TIC). b) Mass spectrum at maximum ion intensity and mass spectrum after reaching equilibrium.

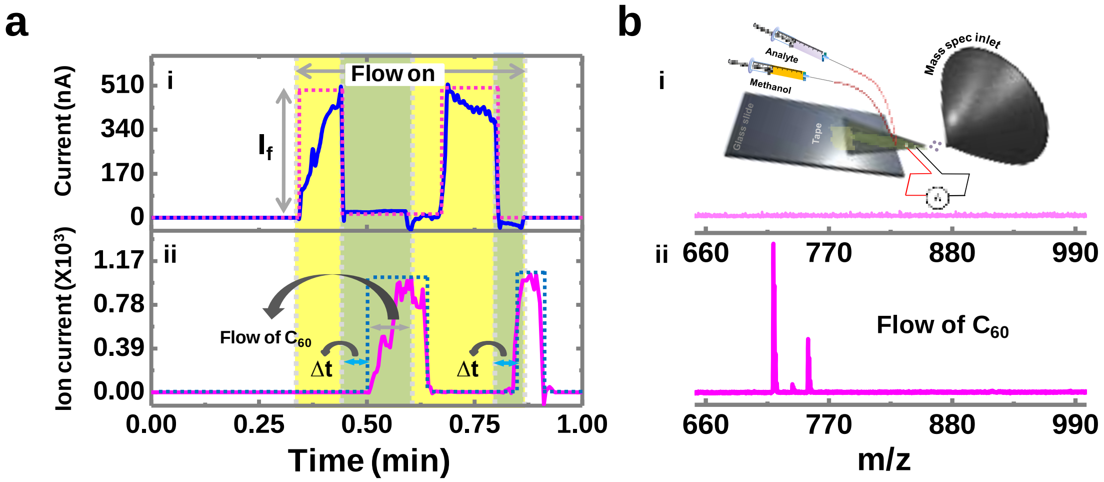

Figure S27. *In-situ* current measurement and mass spectrometry. a) (i) Current-time trace measured using picoammeter and (ii) simultaneous ion current-time trace in the total ion chronogram. The yellow traces in both the spectra indicate flow of methanol over the paper and the green traces indicate the flow of methanol and C_{60} (in toluene) together. The label, Δt represents the time delay between the start of the C_{60} pump and observing peak in the mass spectrum. The delay is travel time of C_{60} over the surface. b) (i) Mass spectrum in the absence of C_{60} and (ii) mass spectrum during the flow of C_{60} along with methanol flow. The reduced current generation in the first cycle is due to the mechanical instability of the flow in front of the mass spectrometer inlet due to high vacuum. Once the paper gets sufficiently wet and the tip to inlet distance is optimized, it produces continuous and stable flow to give proper signal in picoammeter (second cycle) as well as in the mass spectrometer. We choose optimal tip to inlet distance after achieving a background signal as shown in b(i).

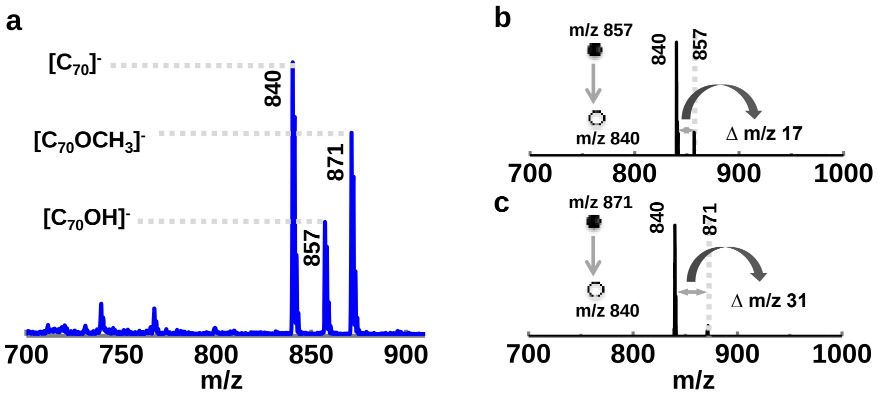

Figure S28. Mass spectra of C_{70}. a) MS^1 mass spectrum of C_{70} during the flow of methanol. b) and c) MS^2 spectra of peaks at *m/z* 857 and *m/z* 871. We observed similar loss of *m/z* 17 and 31 corresponding to hydroxide and methoxide species.

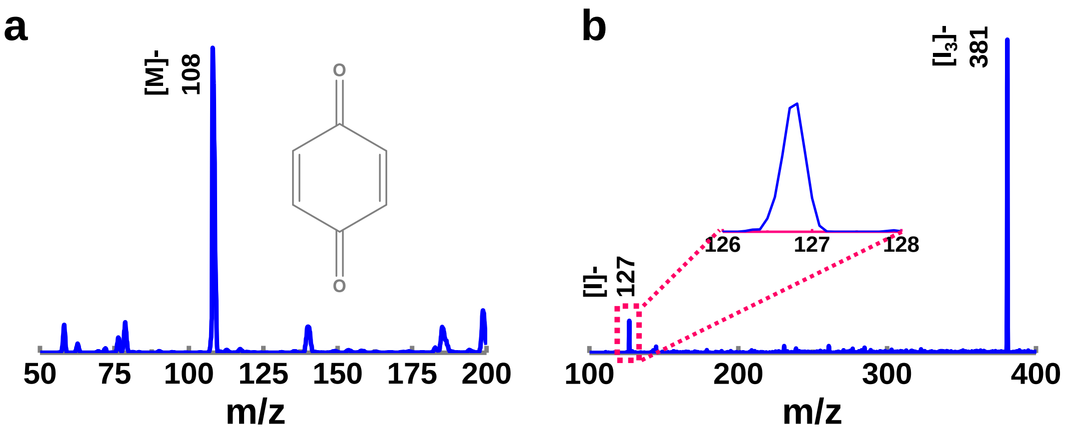

Figure S29. Molecular ionization of benzoquinone and iodine. a) MS^1 spectrum of benzoquinone. The peak at *m/z* 108 corresponds to the molecular ion peak of benzoquinone. b) MS^1 spectrum of iodine. Any of these peaks was not present during the experiment with normal paper.

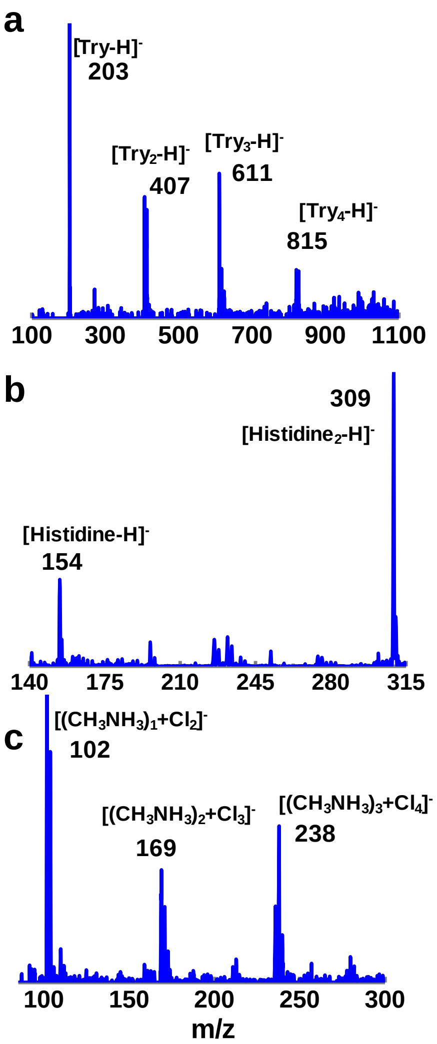

Figure S30. Detection of ion clusters. SI-MS spectra of a) tryptophan, b) hystidine and c) methylamine chloride. Deprotonated mono-, di-, tri-, and tetramer of tryptophan, mono- and dimer of histidine and di- and trimer of methylamine were observed in the mass spectrum. The experiments were done by dissolving each component in methanol at a concentration of 3 mM.

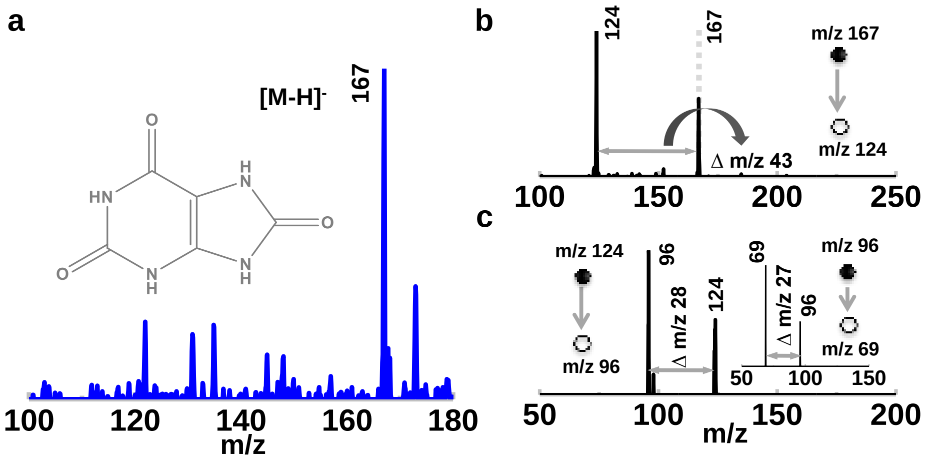

Figure S31. SI-MS of urine samples. a) MS^1 mass spectrum of uric acid during the flow of 5 µL raw urine with methanol. b) and c) MS^2 MS^3 spectra of peaks at *m/z* 167 and 124. We observed a characteristic loss of *m/z* 43 and 28 corresponding to loss of HCNO and CO. The inset of the Figure 32C is the MS^4 spectrum of the peak at *m/z* 96 which shows characteristic loss of 27 corresponding to neutral loss of HCN.

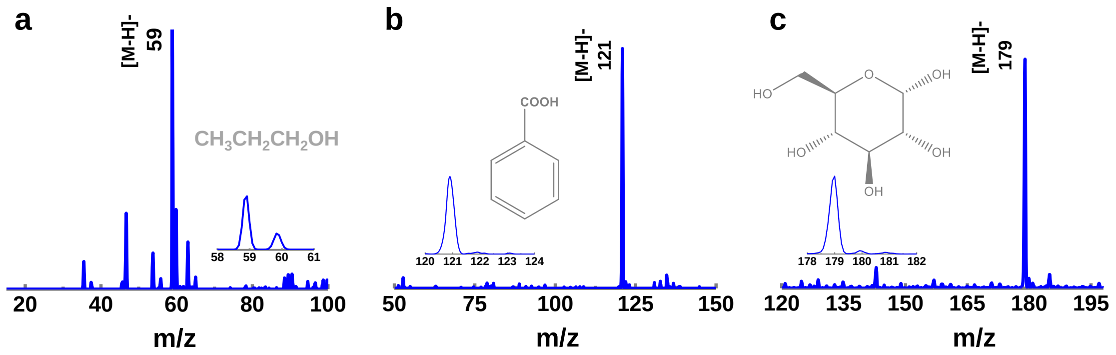

Figure S32. SI-MS of other small molecules during methanol flow. Mass spectra of a) Propanol, b) benzoic acid in acetone and c) glucose in water during the flow. Insets shows the isotopic distributions of the corresponding peaks. We have observed simultaneous current generation for propanol.

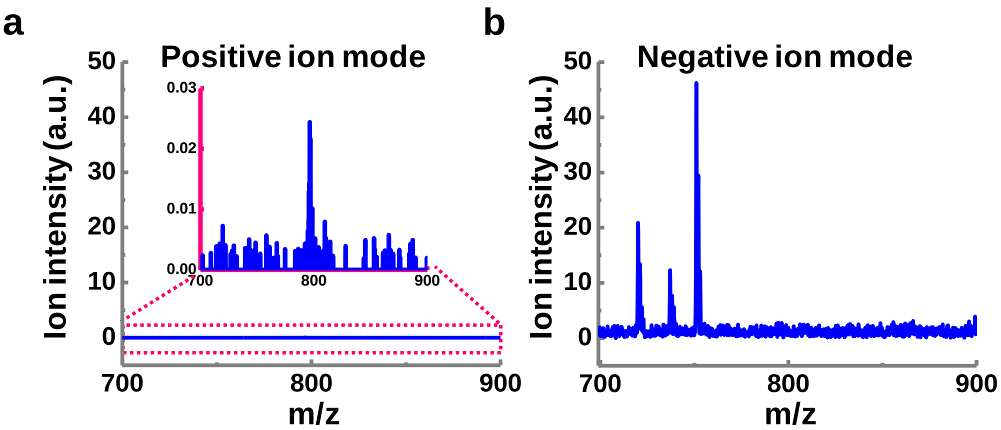

Figure S33. Mass spectra in the positive and negative ion modes. a) Positive ion mode mass spectrum of C_{60} which shows no peak. Zoomed in peaks with an absolute intensity of 0.02 are due to electronic or chemical noise in the mass spectrometer. b) Negative ion mode mass spectrum of C_{60}.

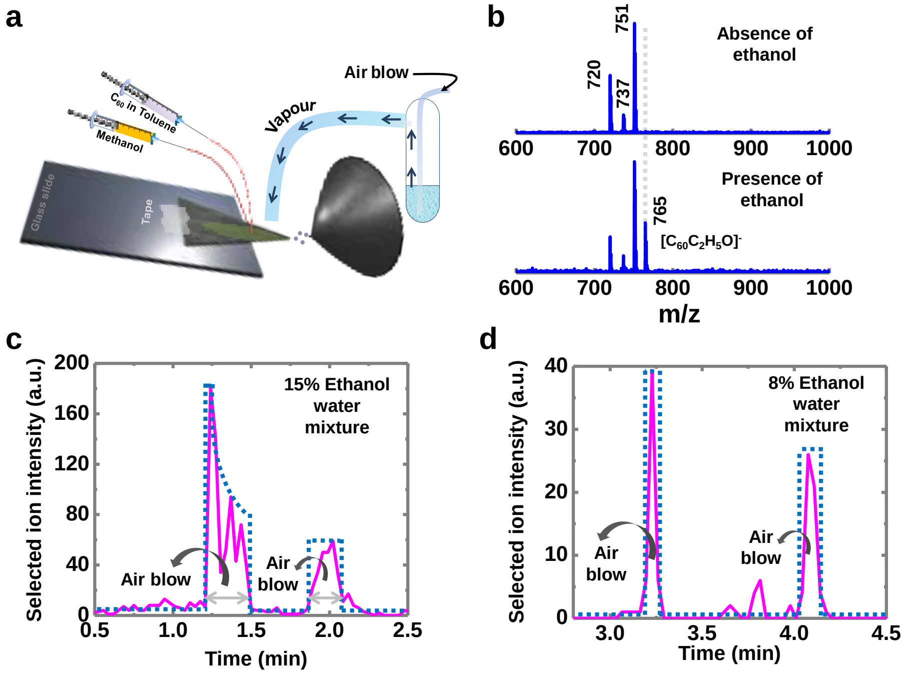

Figure S34. Interaction of ethanol vapor with the liquid flow during the course of ionization. a) Schematic representation of the setup shows the flow of C_{60} solution (in toluene) along with methanol, and the vapors of ethanol exposed to the system through a tube. b) mass spectra of C_{60} in the absence (top) and presence (bottom) of ethanol vapor. Peak indicated as m/z 765 corresponding to ethoxide added C_{60} was observed immediately upon exposure of ethanol vapor. Extracted ion chronograms of the mass selected peak at *m/z* 765 are plotted while the device is exposed to c) 16%, and d) 8% aqueous ethanol vapor. The rise of the chronogram indicates the presence of the ethoxide added C_{60} signal in the time window.

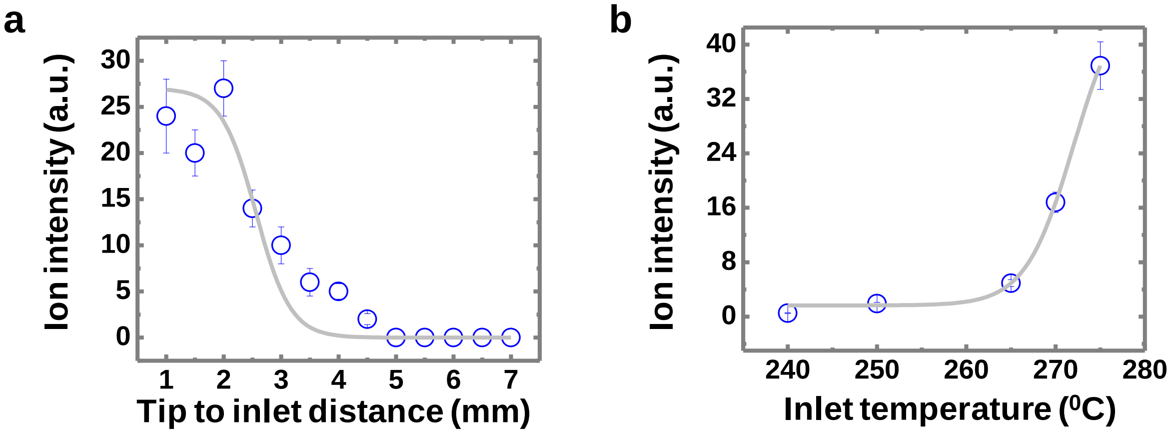

Figure S35. Effect of vacuum and temperature at the inlet on ionization. a) Plot of ion intensity *vs.* tip to inlet distance plot which shows that the increasing the distance leads to decreasing suction. b) Plot of ion intensity *vs.* inlet temperature. Each experiment was repeated thrice independently. Data are presented as mean, and error bar shows ±SD.

Table S1.
A summary of various experiments using simulated breath

Exp. No.	**Exp details**	**Used sample**	**Flowing solvent**	**Magnitude of current (nA)**
1	Only air	Only air	Acetone	0
2	Blow air through 0% ethanol in water	Water	Acetone	2-5
3	Blow air through 10% ethanol in water	Ethanol (aq)	Acetone	12-25
4	Blow air through 20% ethanol in water	Ethanol (aq)	Acetone	20-40
5	Blow air through 30% ethanol in water	Ethanol (aq)	Acetone	50-75
6	Normal breath	Direct breath	Acetone	0-2
7	Breath after drinking beer	Direct breath	Acetone	6-12

Appendix i

Calculation of number density (ρ):

We calculated an approximate number density of MoS_2 over the paper surface. To simplify our calculations, following things are assumed,

i) MoS_2 was taken as an individual molecule instead of an extended 2D layer.

ii) Only MoS_2 exist in solution

iii) During drop-casting the MoS_2 molecules distributed homogeneously all over the surface.

iv) The drop-casted MoS_2 forms a monolayer of molecules.

v) There is no loss during the drop-casting process.

Weight calculation was done by measuring the mass of MoS_2 taken before drop-casting over the paper. To measure the amount of MoS_2 drop-casted over the surface in grams, we took a similar volume of water and MoS_2 solution and then measured the weight of both. Subtracting the weight of water gives the weight of MoS_2 in the solution. For instance, we may say that the weight of MoS_2 will be in the range of µg or 10^{-6} g in 20 ml solution. This would be $(10^{-6}/160)\times 6.023\times10^{23}$ molecules = 0.037×10^{17} molecules

$N = 0.037\times10^{17}$

This many number of molecules are distributed all over the surface.

The surface area (A) of the Whatman 42 filter having a radius of 21 mm is $\prod R^2$ (1.1)

$A = 3.14\times (21\times10^{-3})^2 = 1323\times10^{-6}\ m^2 = 1.3\times10^{-3}\ m^2$

Hence, Number density $\rho = N/A$ (1.2)

$= (0.037\times10^{17})/(1.3\times10^{-3})\ m^{-2}$

$= 0.028\times10^{20}\ m^{-2} = 2.8\times10^{18}\ m^{-2}$

Appendix ii

Dipole-dipole interaction energy and the dissociation of molecules:

For our calculation flow of methanol was taken as a model system

$$\Delta G^o = E_k + E_{dd} \qquad (2.1)$$

$$E_{dd} = 1/\mathcal{E}o\ (\rho \times P_{\mathrm{MeOH}} \times P_{\mathrm{MoS}} \times \int_0^l r_1 dr_1/(z^2 + r_1{}^2)^{3/2}) \qquad (2.2)$$

For this, following are the assumptions to simplify the problem:

i) The alcohol molecules undergo dissociation at equilibrium condition

ii) P_{Methanol} and P_{MoS} are approximated to 1D

iii) The dipolar radius of MoS_2 is approximated to the bond distance of Mo-S bond, which is ~5.896 A^o.[5]

iv) The dipolar radius of R-OH molecule is approximated to the bond distance of OH bond which is ~0.956 A^o.[6]

v) We used free space permittivity for the calculation which is 8.8×10^{-12} $N^{-1}C^2m^{-2}$.

So, from the left-hand side of the equation,

$$\Delta G^0 = -RT\ln K_a \qquad (2.3)$$

$$= 8.314\ JK^{-1}Mol^{-1}\times298.15\ K\times(\ pK_a) = 8.314\times298.15\times15.5\ JMol^{-1}$$

$$= 38.42\times10^3\ JMol^{-1}$$

Now ΔG^0/molecule = 38.42×10^3 J/(6.023×10^{23})

$= 6.4\times10^{-20}$ J/molecule

Now, from the right-hand side of the equation,

$$E_k = 1/2\ mv^2 \qquad (2.4)$$

$$= 1/2\ 32\times10^{-3}\times (2.45\times10^{-3})^2\ J/mol = 96.04\times10^{-9}\ J/mol$$

$$= 96.04\times10^{-9}/(6.023\ X\ 10^{23})\ J/molecule$$

$$= 15.94\times10^{-32}\ J/molecule$$

$$E_{dd} = 1/\mathcal{E}o\ (\rho \times P_{\mathrm{MeOH}} \times P_{\mathrm{MoS}} \times \int_0^l r_1 dr_1/(z^2 + r_1{}^2)^{3/2}) \qquad (2.2)$$

$$= -1/\mathcal{E}o\ (\rho \times P_{\mathrm{MeOH}} \times P_{\mathrm{MoS}} \times \left|1/(z^2 + l^2)^{\frac{1}{2}} - 1/z\right|$$

$$= \{1/(8.8\times10^{-12}\ N^{-1}C^2m^{-2})\}\{2.8\times10^{18}m^{-2}\times(1\times3.3\times10^{-30}\ Cm)^2\times10^{10}m^{-1}\}$$

$= 3.4\times10^{-20}$ Nm $= 3.4\times10^{-20}$ J

This is the dipole-dipole interaction energy experienced by one methanol molecule

So overall right-hand side,

$= (15.94\times10^{-32} + 3.4\times10^{-20})$ J/molecule (As the kinetic energy term is very less)

Hence, by neglecting the kinetic energy we can write,

The right-hand side of the equation 1.1 results in the value of 3.4×10^{-20} J/molecule

It is thus concluded that the energy required for heterolytic bond dissociation of alcohol is comparable with the dipole-dipole interaction energy between methanol and the MoS_2 dipole.

Appendix iii

Calculation of number of ions passing across the electrode area:

For the calculation purpose we use methanol as a liquid to flow

For this calculation we assume that,

i) The number of molecules get ejected are passing through the electrodes.

ii) 100% dissociation of methanol occurs

We measured the velocity of the liquid as 2.45×10^{-3} m/s

The electrodes are separated at 1×10^{-3} m distance

Time taken for the molecules to pass the electrodes is 0.408 s.

At 0.408 s, volume of liquid ejected from the fused silica capillary is $(22\times10^{-6}/60)\times0.408$ l = 0.15×10^{-3} ml.

The density of methanol is 0.791 g/ml

So, the mass of the corresponding volume = $0.791\times0.15\times10^{-3}$ g = 0.12×10^{-3} g = $0.12\times10^{-3}/32$ mol

= 3.6×10^{-6} mol = $3.6\times10^{-6}\times6.023\times10^{23}$ molecules

= 22.26×10^{17} molecule

= 22.26×10^{17} ions (as per the assumption)

Appendix iv

Flow rate to pump pressure conversion.

We used NE-300 syringe pump from New Era Pump Systems, Inc.

The esteemed linear force (lbf-s) can be calculated from the following equation,[7] [8]

$F=F_m(R/R_m)$ (4.1)

Here, F_m, R, and R_m are maximum linear force (lbf-s), rate, and maximum rate, respectively.

Now, for NE-300 model, F_m= 35 lbs. at minimum speed, 18 lbs. at maximum speed

R= 22 µl/min

R_m= 38 lbf-s

The pump pressure (ΔP) in psi can be calculated as below,[8]

$\Delta P = F\times E/\{\pi D^2/400)/2.45^2\}$ (4.2)

Here, E and D are the pump efficiency and the diameter of the syringe (in mm)

For a Hamilton 500 µl gas tight syringe, D=3.11 mm.

Hence, at 90% efficiency, the pump pressure would be 2910.92 psi.

Appendix v

Mathematical validation of Helmholtz–Smoluchowski model in our system:

In Helmholtz-Smoluchowski model,

$$I_f = -\mathcal{E}\mathcal{E}_0 \zeta A_c \Delta P_r / \eta l \tag{5.1}$$

This equation is used for the streaming current across two point separated by l distance in a A_c diameter capillary.

$\mathcal{E}$ = Dielectric const of methanol = 32 unit less

$\mathcal{E}_0$ = Free space permittivity = 8.8×10^{-12} $N^{-1}C^2m^{-2}$

ζ = zeta potential of MoS_2 = -41.2×10^{-3} V

η= Viscosity = 0.5×10^{-3} Nsm^{-2}

ΔP= 2911 psi at 22 µl/min flow rate.

= 2911X6894 Nm^{-2}

Here we took that methanol flowing over 10 nM length MoS_2 sheets So $A_c = 10\times10^{-9}$ m

Now,

RHS,

$\mathcal{E}\mathcal{E}_0 \zeta A_c \Delta P_r / \eta l$ = $32X8.8X10^{-12}\times(-41.2X10^{-3})\times10\times10^{-9}\times2911\times6894/(0.5X10^{-3}\times1\times10^{-3})$

= 4656 nA.

= 4.656 µA

The maximum amount of current we achieved is 1.3 µA, which is quite matching with the amount of current calculated from Helmholtz-Smoluchowski model within a factor of 0.25. This loss is possibly due to the contact resistance or loss of charges by other factors.

Reference:

1. Mondal, B.; Mahendranath, A.; Som, A.; Bose, S.; Ahuja, T.; Kumar, A. A.; Ghosh, J.; Pradeep, T., Rapid Reaction of MoS_2 Nanosheets with Pb^{2+} and Pb^{4+} Ions in Solution. *Nanoscale* **2018**, *10*, 1807-1814.
2. Kioseoglou, G.; Hanbicki, A. T.; Currie, M.; Friedman, A. L.; Jonker, B. T., Optical Polarization and Intervalley Scattering in Single Layers of MoS_2 and $MoSe_2$. *Scientific Reports* **2016**, *6*, 25041.
3. Robinson, B. J.; Giusca, C. E.; Gonzalez, Y. T.; Kay, N. D.; Kazakova, O.; Kolosov, O. V., Structural, Optical and Electrostatic Properties of Single and Few-Layers MoS_2: Effect of Substrate. *2D Materials* **2015**, *2*, 015005.
4. Mikhail, S. Z.; Kimel, W. R., Densities and Viscosities of Methanol-Water Mixtures. *Journal of Chemical & Engineering Data* **1961**, *6*, 533-537.
5. Fitri, D. A.; Purqon, A., Calculation Study of Electric Properties on Molybdenum Disulfide by Using Density Functional Theory. *J. Phys.: Conf. Ser.* **2017**, 877 (International Conference on Energy Sciences, 2016), 012071/1-012071/5.
6. Venkateswarlu, P.; Gordy, W., Methyl Alcohol. II. Molecular Structure. *The Journal of Chemical Physics* **1955**, *23*, 1200-1202.
7. Syringe Pump Linear Force. https://www.chemyx.com/support/knowledge-base/applications/syringe-pump-linear-force/ (accessed November 16, 2020).
8. Precision Syringe Pumps Peristaltic Pumps Syringe Heaters Accessories. http://www.syringepump.com/download/NE-300Brochure.pdf (accessed November 16, 2020).

ACS APPLIED NANO MATERIALS

www.acsanm.org Article

Scalable Drop-to-Film Condensation on a Nanostructured Hierarchical Surface for Enhanced Humidity Harvesting

Ankit Nagar, Ramesh Kumar, Pillalamarri Srikrishnarka, Tiju Thomas,* and Thalappil Pradeep*

Cite This: *ACS Appl. Nano Mater.* 2021, 4, 1540−1550 Read Online

ACCESS | Metrics & More | Article Recommendations | Supporting Information

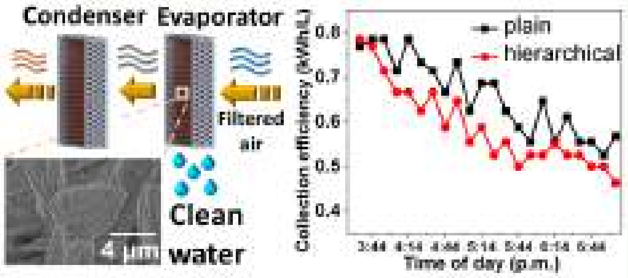

ABSTRACT: Active cooling-based atmospheric water generators, despite their growing demand, continue to be energy intensive and offer poor collection efficiencies (energy consumption per liter of water production). Despite progress in micro-/ nanofabrication techniques and functional coatings, advanced surfaces have not been successfully scaled onto such harvesters to accelerate condensation and improve their efficiencies. Here, we present a scalable dual-nanostructured hierarchical surface that comprises sporadically distributed bundles of randomly oriented faceted microcones having facets composed of nanostructures, which are either bumps or ridges. Condensate removal on this surface occurs via drop-to-film coalescence, followed by film shedding in the form of macrodrops. Compared to a conventional plain metal surface used for condensation, the improvement in latent heat transfer coefficient using a hierarchically textured surface ranged from 19.9% at a subcooling of ~8 °C to 1048.4% at a subcooling of ~1 °C in laboratory scale experiments, subcooling being defined with respect to the dew point. To demonstrate utility at industrial scale and to ensure scalability of the modified surfaces, we create a prototype assembly comprising a tube-fin heat exchanger with hierarchically textured fins, cooled using a standard refrigeration cycle, producing ~25 L of water per day. The prototype containing hierarchically textured fins provides ~10.8% enhanced water collection at ~10.4% improved average collection efficiency compared to the traditional water generator when tested in outdoor conditions.

KEYWORDS: *condensation, heat transfer, hierarchical nanostructures, water harvesting, drinking water*

INTRODUCTION

Atmospheric water generators (AWGs) have gained significant scientific and commercial attention in the past decade because of their ability to provide clean water in regions of extreme water scarcity.[1] Most of the commercial AWGs are based on a refrigeration cycle, where a coolant undergoes a reverse Carnot cycle to exchange heat with the surrounding air and enable its condensation.

The collection efficiency of such an AWG system can be defined as energy consumption per unit volume of product water. It depends on ambient temperature and humidity. Although efficiencies of current AWGs are improved by implementing varied configurations of heat exchangers to extend the air−surface contact time,[2] hydrophobizing the copper tubes to promote jumping-droplet condensation,[3] or preconcentrating moisture in the input air to increase the dew point temperature,[4] the fin surfaces of heat exchangers have rarely been modified to enhance the overall performance.[5] In this work, we present rationally designed hierarchical structures created on aluminum fins of heat exchangers, prepared using a one-step, top-down process, in which condensed droplets drain by combining with the liquid film present on the surface. Subsequently, the film sheds itself under gravity, in the form of macrodrops. Such a mechanism of shedding is then compared with the already existing mechanisms of dropwise (DwC),[6−10] filmwise (FwC),[11−13] and state-of-the-art hierarchical condensation, by choosing the appropriate test surfaces that are known to demonstrate these mechanisms.[14,15] We perform lab-scale water collection experiments across the entire possible range of subcooling (~0−8 °C, below the dewpoint), on chosen test surfaces to compare their water harvesting abilities. As a final step, we build a prototype atmospheric water generator (AWG) comprising of hierarchically textured surface for condensation and compare it against an identical counterpart (representative of a conventional AWG) having plain metal surface for condensation. The results show an ~10.4% improvement in the collection efficiency, and an ~10.8% improvement in the overall water collection.

Received: November 12, 2020
Accepted: February 5, 2021
Published: February 18, 2021

https://dx.doi.org/10.1021/acsanm.0c03032
ACS Appl. Nano Mater. 2021, 4, 1540−1550

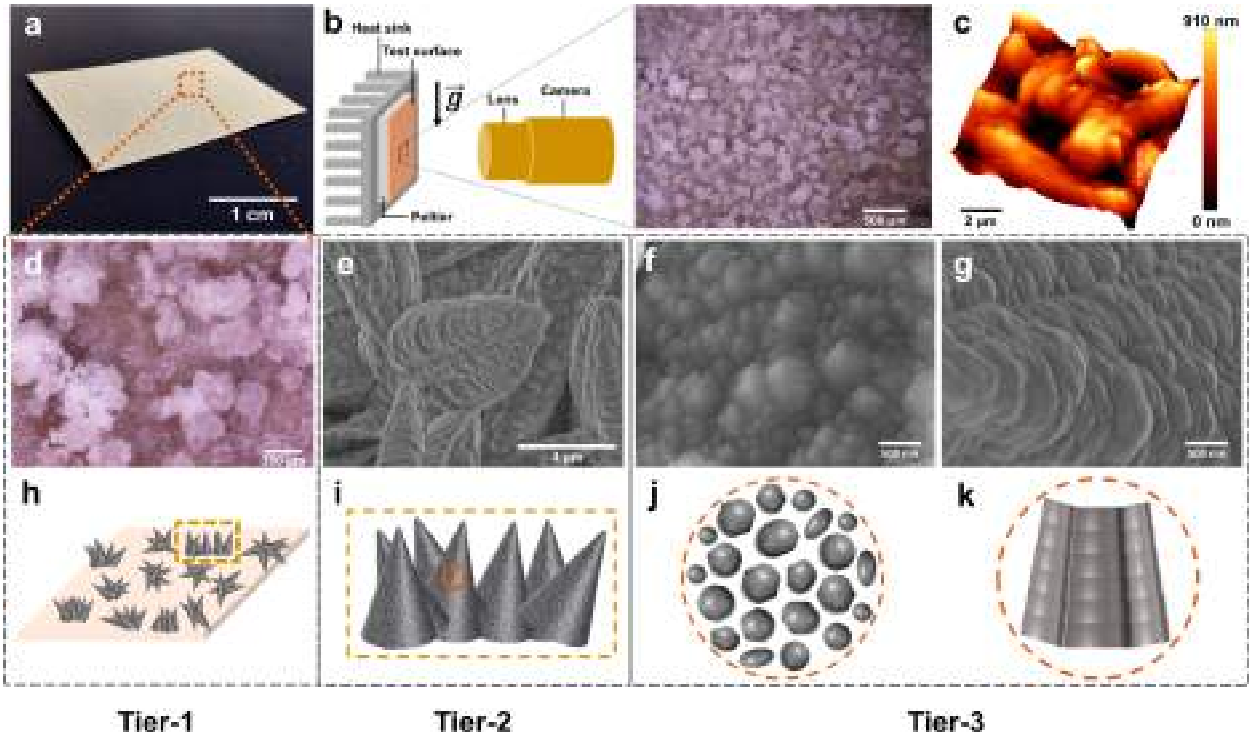

Figure 1. Hierarchical surface. (a) Photograph of the hierarchical surface. (b) Setup for optical microscopy (not to scale). (c) AFM topography image of the surface showing height variation, and dashed white line indicating chosen linear path for measuring average nanoscale (tier-3) roughness. (d) Optical image of the surface showing bundles. (e) FESEM image of a few faceted microcones of a bundle in random orientation. (f) FESEM image showing facet of a cone with presence of irregularly shaped nanobumps, and nanochannels dividing the bumps. (g) FESEM image of another conical facet possessing parallel ridges divided by nanochannels. (h−k) Respective schematics of the surface showing bundles as tier-1 of the hierarchy, faceted microcones as tier-2, and the dual nanostructures as tier-3.

Scheme 1. Plain Aluminum Surface (p) Functionalized with 1H, 1H, 2H, 2H-Perfluorodecyltriethoxysilane (PDES) to Achieve a Plain Hydrophobic Surface (p-hp) and Plain Surface Etched to Create a Hierarchical Surface (h), Which was Silanized by PDES to Result in a Hierarchical Hydrophobic Surface (h-hp)[a]

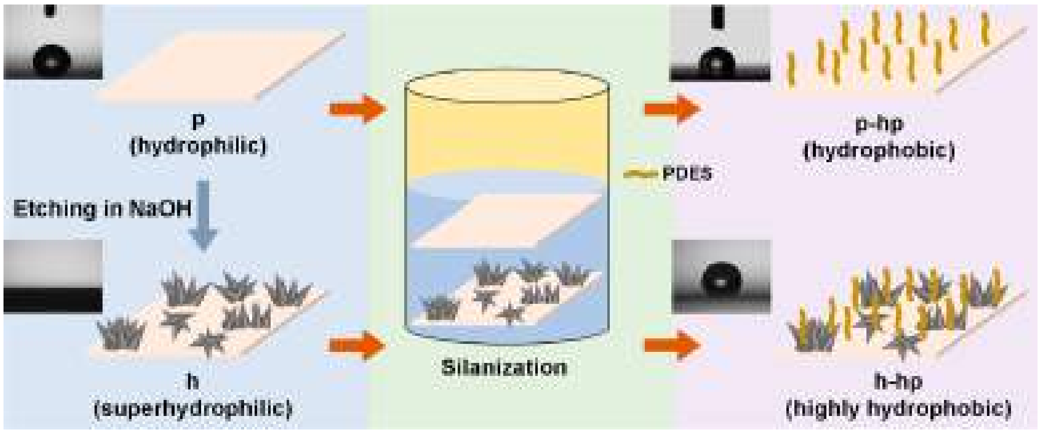

[a] The respective static contact angle measurements are shown in the insets and contact angle data are shown in Table 1.

RESULTS AND DISCUSSION

Dual-Nanostructured Hierarchical Surface. A lower radius of curvature of a nucleation site results in a faster rate of vapor diffusion.[16] Thus, quicker droplet growth occurs selectively on “pointed” sites. Therefore, we propose a surface design comprising sharp micrometer-sized structures and additional nanostructures on top of these microstructures to promote nucleation more effectively.

Sophisticated techniques like photolithography[10,17] and deep reactive-ion etching[18] are multistep and expensive. In addition, prospects for scalability are a concern. In contrast, we use a simple, one-step chemical etching approach to create the hierarchical surface.

In Figure 1, we present the hierarchical structures created on an aluminum sheet via the etching process. A photograph of the sheet postetching is shown in Figure 1a. The top level of hierarchy (tier-1) was observed through optical microscopy (setup shown in Figure 1b) and comprises bundles in the range of 100 μm, as shown in Figure 1d. Other than the regions covered with bundles, the surface also has white regions at the base, as visible in Figure 1d. As observed in FESEM, all bundles as well as white regions at the base comprise randomly oriented faceted microcones (tier-2), as shown in Figure 1e. The facets of these cones comprise two types of morphologies, nanobumps and parallel nanoridges, all of which vary in size and shape, as shown in Figure 1g and h, respectively. These together constitute tier-3 of the hierarchy. Pictorial representations of the surface are shown in Figures 1h−-k. Average surface roughness constituted by the entire hierarchy was measured as 212.9 nm, obtained using atomic force microscopy (Figure 1c). Average nanoscale roughness comprising the tier-3 nanostructures present on the surface of microcones was linearly measured on one of the conical surfaces and was obtained as 19.3 nm (dashed white line in Figure 1c). More details are discussed in the Methods section.

Choice of Test Surfaces and Contact Angle Measurements. Four test surfaces were prepared using aluminum substrates. They were composed of: First, a plain surface (abbreviated as p), commonly used in fins, as part of fin-tube heat exchangers; second, a plain hydrophobic surface (p-hp), prepared by functionalization of the r surface with 1H, 1H, 2H, 2H-perfluorodecyltriethoxysilane (PDES); third, a superhydrophilic aluminum surface (h), comprising the hierarchy discussed in the previous section and fourth, a hydrophobic aluminum surface comprising the hierarchical structures (h-hp), prepared by functionalization of the h surface with PDES (Scheme 1). Table 1 presents the static, advancing and receding contact angles, and contact angle hysteresis (CAH) of the test surfaces.

Table 1. Contact Angle Data of the Test Surfaces

surface	static contact angle θ (deg)	advancing contact angle θ_A (deg)	receding contact angle θ_R (deg)	CAH = $\theta_A - \theta_R$ (deg)
plain (p)	71.1 ± 1.7	98.9 ± 1.5	67.7 ± 1.6	31.2
plain-hydrophobic (p-hp)	97.2 ± 1 0.0	113.2 ± 1.0	95.2 ± 0.9	18
hierarchical (h)	<5	<5		
hierarchical-hydrophobic (h-hp)	148.8 ± 2.2	157.8 ± 0.8	134.5 ± 6.5	6.6

Table 1 shows that p is moderately hydrophilic ($\theta = 71.1°$). Silane functionalization of p renders the surface slightly hydrophobic, which is presented as p-hp ($\theta = 97.2°$). The hierarchically structured surface, h, shows a superhydrophilic nature ($\theta < 5°$), whereas upon functionalization, h-hp shows hydrophobic character ($\theta = 143.7°$). The h surface was superhydrophilic and absorbed droplets through capillary action as soon as they came into contact with the surface. Therefore, receding angle and CAH could not be measured for this surface. The CAH values of the surfaces and their relation to the latent heat transfer coefficient and water harvesting behavior will be discussed in the later sections.

Shedding Mechanisms vs Subcooling. To observe and compare the shedding mechanisms of droplets on the test surfaces as a function of subcooling, we recorded droplet dynamics during condensation using the same configuration as shown in Figure 1e.

Representing a conventional heat exchanger fin surface, p exhibited irregularly shaped droplets of the order of 1 mm on its surface, across the entire range of subcooling (Figure 2a). These millimeter-sized droplets continue to coalesce with the freshly nucleating smaller droplets in their vicinity and grow bigger in size (Figure S5). However, they only shed from the surface after reaching a size on the order of 1 mm. Surface coverage by such droplets reduces the available area for fresh condensate to appear, thereby inhibiting heat exchange with the surroundings.

Droplets on the p-hp surface remain spherical to a greater extent than p surface, because of the lower surface energy (Figures S5 and S6). However, the droplets on the p-hp surface only shed at higher subcooling via rolling, that too upon reaching a size on the order of 1 mm. Surface h shows the presence of droplets of sizes ranging from tens to hundreds of micrometers across the entire range of subcooling. The white regions are indicative of reflectance occurring from wet spots. Figure 2c-i shows encircled wet bundles and a droplet on the order of 100 μm resting on one such bundle. The wet bundles are also shown in Video S3. Figure 2c-ii shows multiple droplets of the order of 10 μm on a single bundle, indicated by arrows. An identical droplet behavior is observed at high subcooling, with representative droplets on the order of 100 μm, shown in Figure 2c-iii. The growth and nature of shedding for droplets on the h surface are discussed in the next section.

Shedding on Hierarchical Structures. To observe the mechanism for droplets on the order of 100 μm, we recorded a video with multiple such droplets in a frame, at 30 frames per second, under full-ring illumination (Video S1). The droplets reside on top of the bundles, whereas the base of the bundles is covered with water film (Figure 3a). The droplets can therefore only reside in a Cassie−Bexter or Wenzel state, with air gaps between themselves and the basal film. They grow intermittently and undergo slight movement (for example, at t = 02:41.70 min), until the base area of the droplet grows beyond that of the bundle, resulting in toppling of the droplet down the bundle to merge with the basal film (Figure 3a and Figure S10, t = 05:17.67). The merged droplet extends itself across the base of the bundle and the surrounding film, as suggested by the distorted reflection of the illuminated ring within the droplet (Figure 3a, t = 05:17.67). This toppling-assisted coalescence, or Mode 1, is shown schematically in Figure 4a.

Another mechanism of drop-to-film coalescence for ∼100 μm droplets is observed when a drop receded into the surrounding bundle upon coming into its contact, via capillary action (Figure 3a, Mode 2, t = 3:39.75 min). This is represented as Mode 2 in the schematic shown in Figure 4a. Time-lapsed images are shown in Figure 3b.

To observe the dynamics of droplets on the order of 10 μm, we focus on a single bundle and record the dynamics at 30 frames per second (Video S2). The large droplet observed initially was pinned to the bundle and kept growing in a partial wetting (PW) state (Figure 3b, $t \leq$ 5:50.34 min), until it came in contact with the basal film at the bundle. After coalescence with the basal film, fresh droplets were seen growing and coalescing on the bundle (t = 5:50.37−06:29.12 min), which eventually combined to form a large droplet of size comparable to that of the bundle (t = 13:39.91 min). The large droplet continues to grow in the PW state until coalescence with the basal film occurs again (t = 13:39.94 min). This cycle repeats itself. Schematic representation of this cycle is shown in Figure 4b, divided into six stages.

https://dx.doi.org/10.1021/acsanm.0c03032
ACS Appl. Nano Mater. 2021, 4, 1540−1550

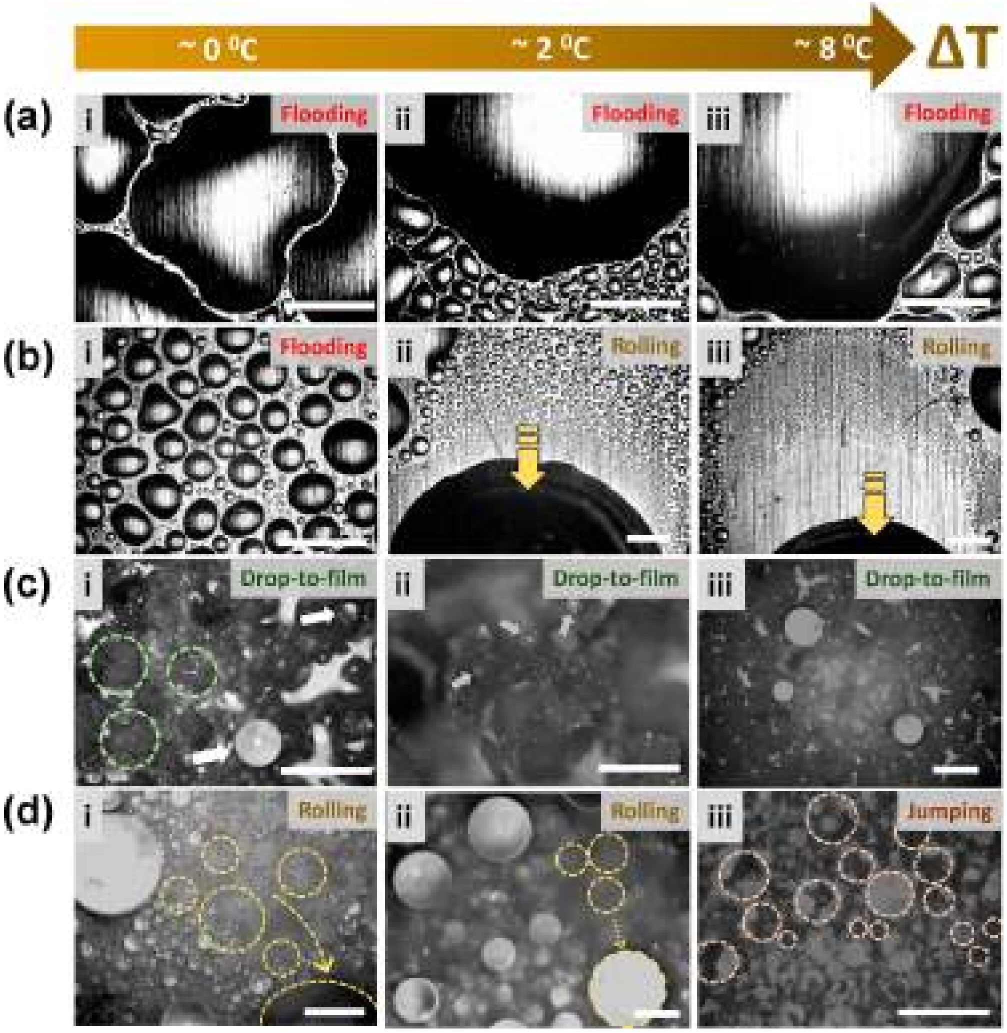

Figure 2. Optical images showing shedding mechanisms on test surfaces at varying degrees of subcooling. The observations were begun only after 30 min of condensation had already happened and condensation dynamics had stabilized. (a) Pain aluminum surface, p. Scale bar: 1 mm. (b) Plain-hydrophobic surface, p-hp. Scale bar: 1 mm. (c) Hierarchically structured surface, h. Dashed circles in i indicate reminiscent wet bundles, after the respective droplets have undergone coalescence with the film (Figure S7). The white arrows in i and ii indicate droplets on different bundles and on the same bundle, respectively. Scale bar: 500 μm. (d) Hierarchically structured hydrophobic surface, h-hp. The dashed yellow circles in i and ii represent regions where droplets were present a few milliseconds (ms) ago and are removed now, after coalescence and subsequent rolling (Figure S8). The dashed pink circles in iii represent regions where previously present droplets combined and jumped-off the surface, resulting in the present image. Scale bar: 500 μm.

Given the presence of basal film across the entire surface, parts of the surface has completely submerged bundles (Figure 4c), which become visible only upon drying using a hot air blower (Video S3). Therefore, observed droplets could nucleate only on bundles with heights more than the thickness of the basal film.

Because the lowering of surface energy promotes DwC on a surface and improves droplet mobility and rate of surface renewal, it becomes crucial to perform low-surface-energy functionalization of the h surface to promote DwC and understand the difference in shedding mechanisms between the h and h-hp surfaces. Moreover, although the h-hp surface has microstructures to retain Cassie–Baxter (CB) state of droplets, it also possesses nanostructures on top of these microstructures, to allow smaller droplets to nucleate beneath the CB droplet and eventually merge with it, leading to hierarchical condensation. To verify this claim, we performed dynamic optical imaging during condensation on the surface (Figure 5). Droplets on a single bundle are monitored (bundle lying within the dashed square box in Figure 4a). Initially (t = 0 min), several droplets on the order of 100 μm are found on the bundle that coalesce with time and become larger in size (t = 8 s), also moving slightly over the bundle by releasing free energy after coalescence. This renews the surface for fresh droplets to nucleate (t = 8 min 18 s), whereas the bigger droplet continues to grow through condensation as well as coalescence. Upon reaching a certain size, greater than 500 μm (t = 9 min 24 s), the bigger droplet rolls off the bundle. Thereafter, fresh droplets nucleate and grow (t = 14 min 26 s), repeating the cycle. Coalescence of droplets happening on the tip of the bundle is also assisted by the coalescence of shaded droplets, present beneath the bigger droplet (Figure 5b-i). This is proved by performing focal plane shift imaging (FPSI) on another substantially big droplet (>500 μm) on the surface (Figure 5b). Upon shifting the focal plane at an intermediate position, between the droplet base and the base of the surface, numerous smaller droplets of the order of 10 μm are seen undergoing movement and coalescence on the conical surfaces.

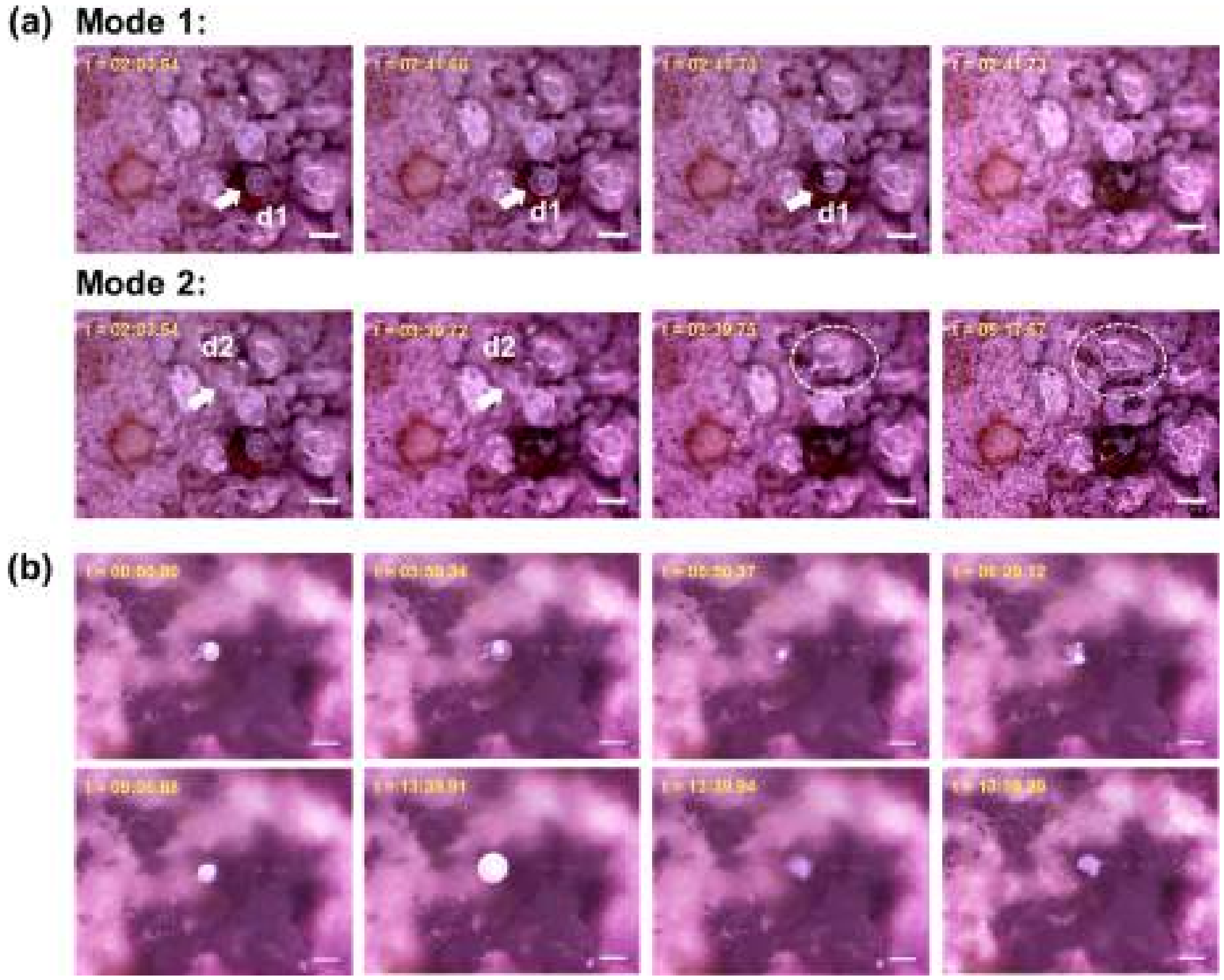

Figure 3. Drop-to-film condensation. (a) Mode 1 and Mode 2 are shown using select droplets of the order of 100 μm, undergoing drop-to-film condensation. Mode 1 shows toppling-induced coalescence occurring at *t* = 2:41.73 min, where a droplet topples from the bundle upon reaching a critical size. Mode 2 shows capillary-induced coalescence where droplet d2 recedes into the film via a neighboring bundle that acts as a capillary. Scale bar: 100 μm. (b) Dynamics of droplets on the order of 10 μm on a single bundle. A droplet grows on the bundle and coalesces at *t* = 5:50.37 min, followed by nucleation of new droplets that combine to form a larger droplet on the bundle, which grows until it encounters the film underneath and coalesces with the film. Scale bar: 50 μm.

As an illustration, Figure 4b-ii, iii shows shaded droplets 1 and 2 undergoing coalescence and resulting in 1′, whereas droplet 3 lost its sphericity and hung between the cones as 3′. The presence of shaded droplets like 1, 2, 3, 1′, and 3′ beneath the larger droplet shown in Figure 5b-i confirms hierarchical condensation, also reported previously by Yan et al.[14] In combination with hierarchical condensation, cross-sectional imaging of the surface at high subcooling (~8 °C) also reveals the jumping-droplet mode of shedding (see Figure S9). However, the jumping mode is not observed at lower subcooling.

Heat Transfer Performance. After developing an understanding of the shedding phenomena for the test surfaces, we further test the surfaces for their water harvesting performances and the corresponding latent (or condensation) heat transfer coefficients, by exposing them to a constant ambient air flux at varying amounts of subcooling (see Methods). Figure 6a represents a schematic of the setup wherein a test surface is placed on a Peltier-heat sink assembly and cooled down to the required temperature by supplying DC power to the Peltier. A constant ambient air flux is maintained over the surface using a DC fan (see Methods). Each collection experiment is performed for 3 h. It is noteworthy that unlike a majority of the previous studies,[19−22] in which condensation is performed by exposing the surface to saturated humidity in a closed chamber, we perform all lab-scale experiments in the presence of noncondensable gases. The water collection flux, as plotted in Figure 6b, shows substantially better performance of the h surface, compared to the other surfaces, particularly in the subcooling regime of ~1−6 °C. Regardless of the degree of subcooling, the h surface begins to collect water 30−50 min after the beginning of the experiment, whereas others followed a sharp increase in the collection onset with a decrease in subcooling (Figure 6c). We further evaluate the latent heat transfer coefficient, HTC, using the following equation:

$$\mathrm{HTC} = \frac{\dot{m} h_{\mathrm{fg}}}{\Delta T} \tag{1}$$

where $\dot{m}$ is the mass transfer flux, or the rate of water collection.[23] The HTCs for different subcooling were plotted separately, to highlight the differences at each subcooling.

Postnucleation, when a droplet reaches a critical size during its growth after multiple coalescence events, the gravitational force exerted by the droplet balances the retention force,

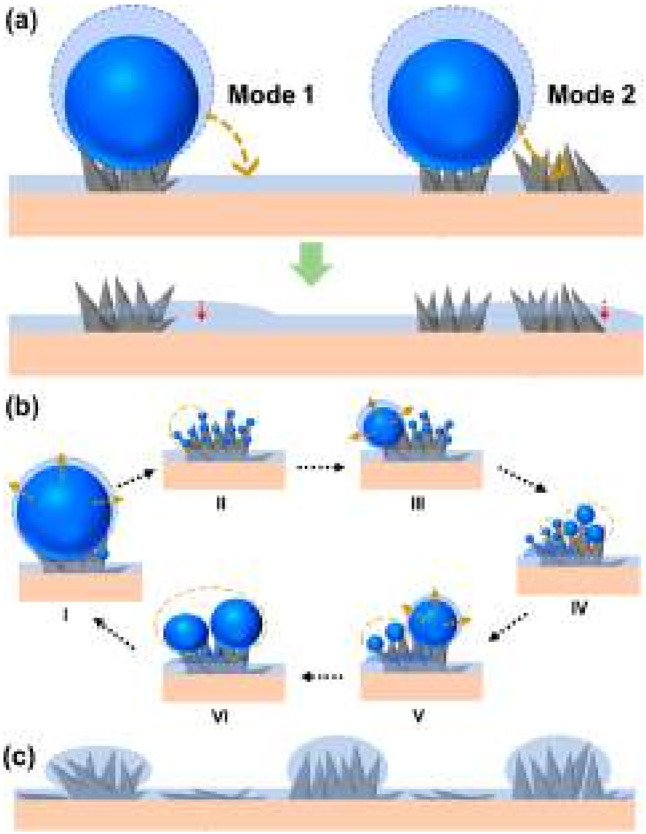

Figure 4. Configurations of water present on the h surface. (a) Droplet on the order of 100 μm rolls down the bundle upon crossing the bundle size at its base (Mode 1). Another droplet (Mode 2) on the same order recedes into the basal film through a neighboring bundle upon coming into its contact, via capillary action. (b) Large droplet, a few tens of micrometers in size, undergoes coalescence with the film beneath it (Stage I). This is followed by the growth of fresh droplets on multiple cones (Stage II), which coalesce with each other, and the bigger droplet continues to grow in a partial wetting state (Stage III) until it comes into contact with the basal film to subsequently get drained. This allows fresh nucleation (Stage IV) and subsequent coalescence (Stage V and VI), and the process continues in a cycle (Video S2). (c) Bundles completely covered with water (Video S3).

causing it to roll down the surface. The critical size can be obtained from the following equation:

$$mg\sin\alpha = \gamma_{\text{water}}(\cos\theta_a - \cos\theta_r)W \qquad (2)$$

where expression on the left side of the equation represents the gravitational force exerted by the droplet of mass m, parallel to the surface with tilt angle α, γ_{water} is the surface tension of water, θ_a and θ_r are the advancing and receding angles, respectively, and W is the width of the droplet.[24] Therefore, lower CAH ($\theta_a - \theta_r$) implies lower droplet critical size, which should contribute to a faster rate of surface renewal and therefore lead to better water collection or mass transfer. Figure 6c shows that droplets begin to roll earlier on a surface with lower CAH as the collection on r-hp begins earlier compared to p, at all degrees of subcooling. When cumulative water collection for 3 h is plotted against subcooling, it is observed that at low and intermediate subcooling (<3 °C), r-hp is a better collector compared to r. Lower CAH in the case of p-hp leads to higher mobility of the droplets, allowing them to roll down easily. At high subcooling (>6 °C), p provides better collection flux than p-hp, indicating that affinity for water vapor, or rate of nucleation, dominates over CAH in this regime. Surface functionalization for planar surfaces, therefore, limits the collection flux and HTC at high subcooling but improves both at low subcooling.

The h surface showed the highest HTC across the entire subcooling range. When compared to the p surface, the h surface demonstrated as high as a 10-fold improvement (~1048.4%) in HTC at $\Delta T \approx 1$ °C. The superior performance of h is attributed to the presence of a large number of nucleation sites, the dual nature of nanochannels that allows effective drop-to-film coalescence, and the presence of faceted microcones all across the base, which greatly reduces the basal area occupied by the film, thus preventing domination of the film mode of condensation. Given the complex morphology of h and h-hp, wetting states of the droplets, and their coalescence mechanisms, functionalization does not provide a clear overall advantage in terms of collection flux (or HTC). Although h always shows better overall performance compared to h-hp, the difference is more significant at low subcooling. The poor performance of h-hp at low subcooling can be attributed to its lower affinity toward water vapor, resulting in a lower rate of nucleation. This factor becomes insignificant at high subcooling and the difference between h and h-hp is reduced with an increase in subcooling, mainly due to hierarchical condensation occurring on the h-hp surface, which eliminates the possibility of flooding at high subcooling. Also, hierarchical condensation is supported by the jumping-droplet mode on h-hp, which occurs only at high subcooling. Therefore, nanochannel-assisted drop-to-film coalescence proves to be the most efficient mode of condensation, among other existing modes, such as jumping-droplet condensation,[3,25−27] FwC, DwC,[6,28,29] hierarchical condensation,[14] and a combination of jumping-droplet and hierarchical condensation mechanisms. However, the observed enhancement in HTC obtained in the case of the h surface, at lab-scale, should be retained while performing large-scale condensation as well, such as on tube-fin heat exchangers, where practical challenges like local water logging between the fins or complex surface−air interaction due to compact arrangement of fins may reduce the heat transfer and, rather, bring down the collection efficiency. Therefore, two refrigeration-based AWG prototypes are assembled in which the evaporators comprise p and h surfaces to verify whether improved HTC at lab-scale, in the case of h surface, translates to enhanced collection efficiency of its corresponding prototype at an industry scale. The following section discusses the details about assembled prototypes, their testing, and results.

Feasibility of h-Surface after Scale-up. A home-build AWG prototype of 25 L/day capacity (Figure 7a and Figure S11) is assembled, which comprises a standard refrigeration cycle to cool the h surface below the dew point. Two identical prototypes are created, where the evaporator in one comprises fins made of the conventional p surface (the p prototype), and the other comprises fins made of the h surface (the h prototype). Therefore, the only difference between the two prototypes is the surface morphology of the evaporator fins. The collected water is filtered and mineralized to render it drinkable. However, the aspect of quality of the collected water is deliberately not discussed, to avoid deviation from the focus of this article.

The prototypes were kept in the open and run for ~4 h in the evening (3:24−7:24 p.m.) on March 6, 2020, in Chennai,

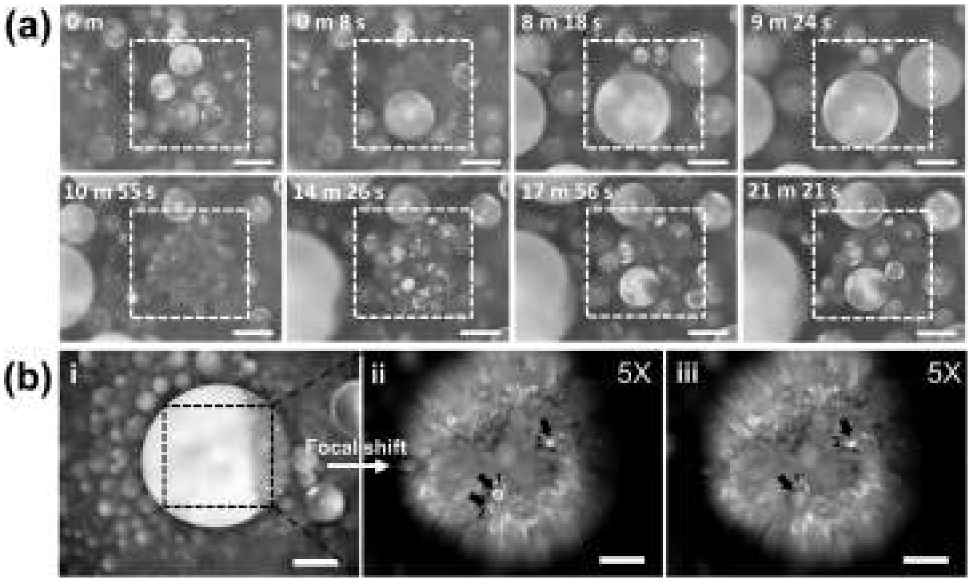

Figure 5. Dynamic optical imaging of h-hp surface during condensation. (a) Top view of the surface, showing droplet dynamics on a single bundle confined within the dashed white box. Scale bar: 200 μm. (b) (i) Larger sink droplet. Scale bar: 500 μm. (ii) Upon shifting the focal plane beneath the droplet, in the dashed black box region, shaded droplets are observed that undergo coalescence (1 + 2 = 1′) and distortion in shape (from 3 to 3′) during movement across microcones, as shown in (iii). Scale bar: 500 μm.

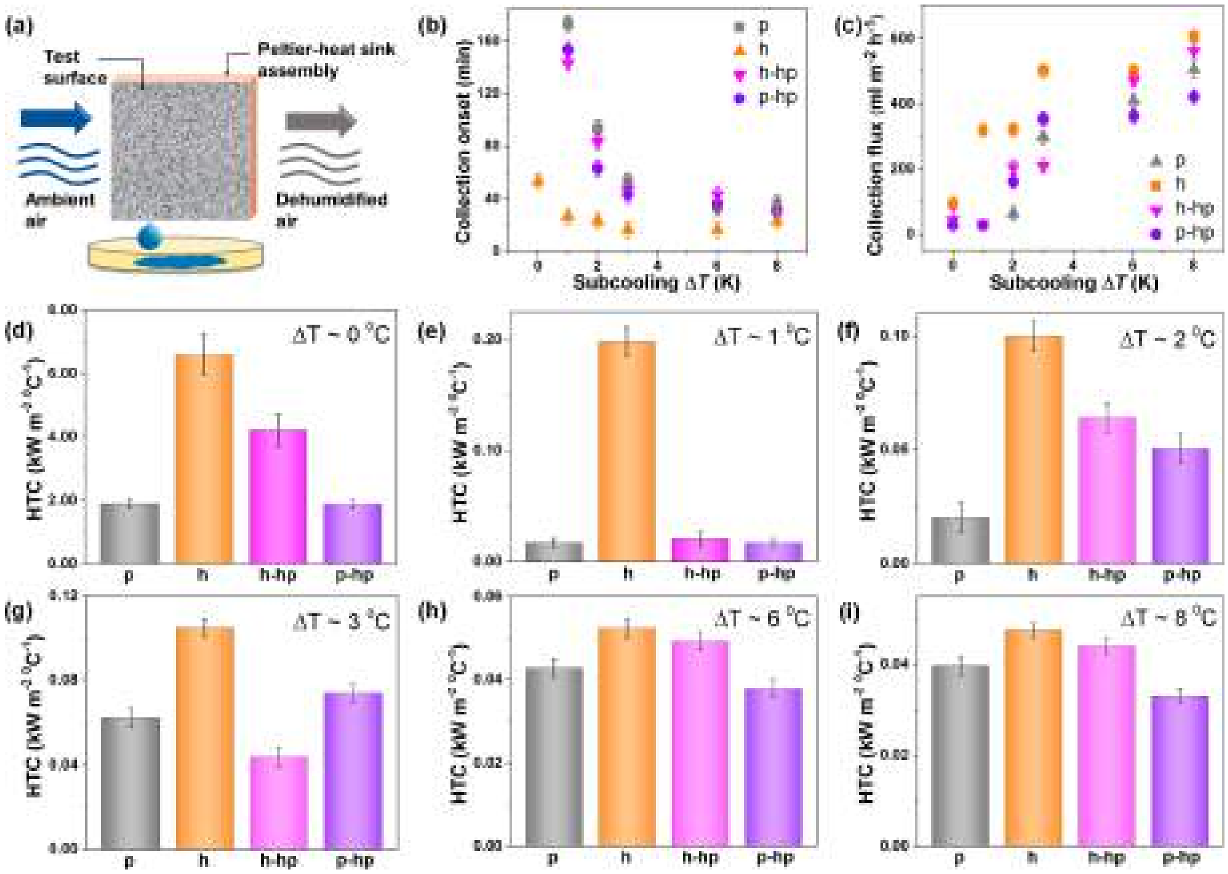

Figure 6. (a) Schematic of the setup for testing water collection performance of the test surfaces. (b) Plot of onset of water collection against subcooling. (c) Cumulative water collected plotted as water collection flux against subcooling. (d−i) Latent heat transfer coefficients for all test surfaces corresponding to water collection experiments performed on the test surfaces across the subcooling range of ∼0−8 °C.

India. Five trial runs are performed (Figure 7 and Figures S12−S16). The temperature during the test run dropped from 38.7 to 30 °C, whereas RH increased from 44 to 67% (Figure 7b). As a result, the dew point dropped from 27.5 to 23.4 °C (Figure S8b). During the course of the test run, the h surface showed an ∼10.8% enhancement in the overall water collection, and an ∼10.4% improvement in the average collection efficiency, compared to the p surface (Figure S8a

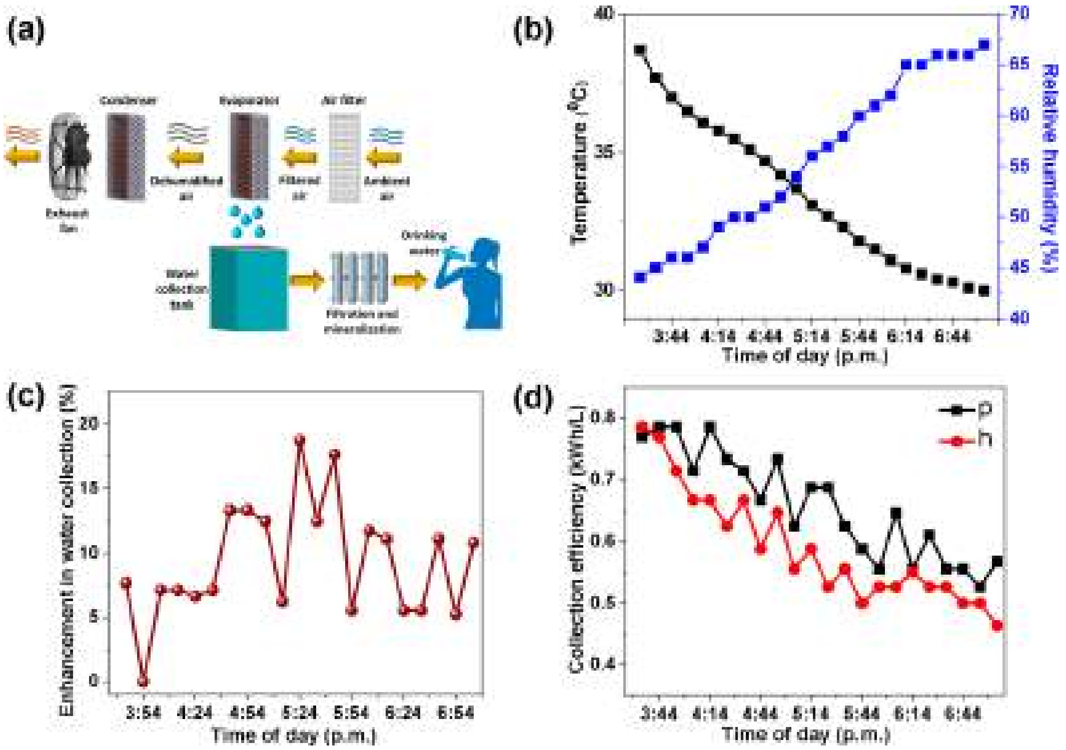

Figure 7. Prototype testing corresponding to h and p surfaces. (a) Schematic of the AWG prototype of 25 L/day capacity, where evaporator fins were the only difference between the two prototypes. (b) Ambient conditions (temperature and RH) during the course of testing. (c) Percentage enhancement in water collection of the h prototype compared to the p prototype as a function of time. (d) Collection efficiency of the prototypes as a function of time.

Table 2. Commercial Refrigeration Cycle-Based Water Generators Worldwide

			Ambient conditions		
organization	power consumption (W)	rRate of water production (L day^{-1})	T (°C)	relative humidity (%)	collection efficiency (kWh/L)
H2O machine (USA)[30]	1700	68			0.60
GENAQ Technologies (Spain)[31]	700	50			0.34
Atlantis Solar and Wind (USA)[31]	1200	100			0.29
Atmos H2O (USA)[32]	500	23			0.52
Airowater (India)[33]	500	25		70	0.48
Nu Image Solutions (USA)[34]	830	30	30	80	0.66
Ray Agua (Spain)[35]	2450	200	30	80	0.35
WAE (India)[36]	400	50			0.91
Hendrx Water (China)[37]	900	15	30	80	1.44
this work (h prototype)	656	25	33	56	0.63

and Figure 7d). The percentage enhancement in the collection performance of the h prototype, compared to the r prototype, ranged from 0 to 17.6% across the duration of the experiment (Figure 7c). The collection efficiency of the prototypes is compared by plotting the amount of energy consumed per liter of water produced. Considering all the energy-consuming parts (except postcollection processes) of the prototypes, the h prototype was consistently more energy efficient than the p prototype during the course of testing (Figure 7d). Such behavior is observed across almost all trial runs (Figures S12–S16). The advantage of energy savings due to a drop-to-film-wise shedding mechanism could be further leveraged by periodically turning the power off briefly before the replenishment is about to occur and turning it on immediately after the it is complete. This will lead to energy-efficient shedding and eliminate the local maxima in the h-curve (Figure 7d). Adopting such a strategy for the r surface will not offer a significant advantage because of absence of any "sharp-curvature" nucleation sites for quick nucleation of fresh droplets, postshedding, when the power is turned on again. Faster drop-to-filmwise shedding may be another way forward by mechanical agitation once the droplets have been nucleated.

Several commercial water generators based on refrigeration cycle-based active cooling are available. The performance of these systems depends on the ambient temperature, relative humidity, absolute humidity, air flux across the condensing surface, amount of refrigerant, and system design. Given these dependencies, an exact comparison is not possible. Nevertheless, we list out nine water generators across the globe alongside our prototype to provide a fair idea of the value of this work (Table 2).

■ CONCLUSIONS

For efficient and scalable heterogeneous condensation, we propose a hierarchically textured surface, fabricated by a one-step process, exhibiting drop-to-film condensation. The surface exhibits a higher heat transfer coefficient compared to its functionalized counterpart, and the conventional plain metal surfaces used as references, which show dropwise, film-wise, jumping-droplet, or hierarchical condensation. The drop-to-film coalescence on the hierarchical surface occurs via nanochannels. Following are the primary reasons for the enhanced heat transfer obtained in case of hierarchical surface: (1) the large number of nucleation sites offered by the faceted microcones and the nanostructures present on their surfaces; (2) high affinity for water vapor; and (3) capillary-action assisted, or toppling-induced coalescence of droplets on the order of 100 μm with the basal film. These advantages have led us to a significant 10.8% improvement in the overall water collection of the prototype composed of hierarchical condensing surface, compared to a prototype containing a plain metal condensing surface, whereas the instantaneous improvement (over a 10 min period) in collection ranged from 0 to 17.6%, depending on the atmospheric conditions during field testing. The above-mentioned reasons together with the strategy of further enhancing energy efficiency by ways such as periodic supply of power, better heat exchanger design, induction of mechanical vibrations for faster shedding, etc., will further render the surface fit for scalable use in applications ranging from water generation to heat management.

■ METHODS

Fabrication of the Test Surfaces. The dual-nanostructured hierarchical surface (h) was fabricated by dipping the plain surface in NaOH solution (30 mM) prepared in deionized (di) water for a period of 15 h at a temperature of 60 °C. The surface was subsequently rinsed in di water and dried with a hot air gun.

The functionalized surfaces, r-hp and h-hp, were prepared by dipping the p and h surfaces in 1% ethanol solution of PDES for a period of 2 h. The surfaces were subsequently taken out, rinsed in deionized water, and dried using an air gun.

Contact Angle Measurements. Contact angle measurements were performed using drops of volume ~3 μL using a Holmarc contact angle meter.

Surface Characterization. Morphology of the hierarchical surface was observed using scanning electron microscope (Verios G4 UC, FEI) and optical microscope (VH-Z100R, Keyence).

For powder X-ray Diffraction (XRD), the h surface was scraped and powder was collected. The measurement was performed on Bruker D8 Advance X-ray powder diffractometer. The plot of diffraction intensity vs 2θ revealed presence of $Al_2O_3{\cdot}3H_2O$ and $Al(OH)_3$ phases, belonging to hexagonal and monoclinic crystal systems, respectively (Figure S1).

Topography and roughness were obtained by performing atomic force microscopy on the as-prepared surface using a Witec GmbH confocal Raman microscope (CRM-Alpha300 S) in a region of 10 μm × 10 μm.

The uniform functionalization of the h-hp and p-hp surfaces is evident from the EDS mapping performed on both surfaces and distribution of fluorine in them (Figure S2, S3).

Observation of Shedding Mechanisms. We chose low (~0 °C), intermediate (~4 °C), and high (~8 °C) subcooling conditions for this study. All laboratory experiments were performed at ambient conditions at a temperature of 23.6 ± 0.5 °C and relative humidity of 50 ± 1% in still air. The test surface (4 cm × 4 cm) was adhered to the cold side of a Peltier using silver paste. The Peltier was then anchored on a heat sink DC fan assembly using the same silver paste. The Peltier was then connected to a DC power supply to calibrate input power as a function of surface temperature. The video recording was begun only after ~30 min of condensation had already taken place and the dynamics had reached an equilibrium. Videos were recorded for each surface and each selected subcooling value, and key frames represented in Figure 2 were selected from the videos. During each recording, the magnification was varied from 100× to 1000×, and droplets across the entire surface were observed to identify their variety. We have made a reasonable assumption that wetting states of droplets, the nature of coalescence events, and shedding modes are independent of air flux across the surface. Therefore, all imaging experiments were performed in still air to avoid noise because of air flow and concerned regions were kept under focus.

Shedding on Hierarchical Structures. The droplet dynamics were investigated under an optical microscope in the same configuration as shown in Figure 1b. The hierarchical surface temperature was kept at the dew point (12.6 °C; under ambient conditions of 23.6 °C, 50% RH).

FPSI on h-hp Surface. To verify the hierarchical mode of condensation and capture droplet dynamics on a single bundle, we kept a single bundle under focus and recorded a video. Imaging was begun only after 30 min of condensation had occurred (at $\Delta T \approx 0$ °C) and the droplet dynamics had stabilized. For FPSI, a bigger droplet was focused and the focal plane was gradually shifted from the top surface of the droplet to beneath it. This brought the smaller droplets into focus, that existed beneath this large droplet.

Heat Transfer Experiments. A square duct with the duct size of 4 cm × 4 cm was created and the Peltier-heat sink assembly was fitted inside the duct in a way that only the surface protruded on the inside wall of the duct, parallel to it (Figure S4). A DC fan flowing ambient air at a constant speed on 2.5 m/s (or a flux of 8.65 cubic feet per minute) across the duct was put at one end, leaving the other end open for dehumidified air to exit. Along with the hierarchical surface, we select test surfaces such that all modes of condensation could be observed, either individually, or in combination with one another, for comparison of their performance under identical conditions.

Fabrication of the Prototypes. For the h prototype, the rolled sheet of aluminum (0.1 mm in thickness) was kept for etching in a 30 mM NaOH solution, prepared in di water. Fins of the size 10 in. × 14 in. were prepared out of the etched sheet and a punching die was used to create holes for fitting the copper tubes. The fins were packed in the traditional fin-tube heat exchanger configuration with a density of 12 fins per inch, resulting in a combined surface area of 4.07 m^2. This assembly was used as the evaporator. Further, another identical heat exchanger was prepared, but with the unetched sheet, to be used as condenser. An AC fan (22A230HBAC) was used to provide an air flux of 360 cubic feet per minute across the system.

The p prototype was identical to the h prototype, except that the evaporator and condenser both comprised unetched fins in the case of p prototype.

Test Runs of the Prototypes. Five test runs with variable time intervals were performed on the two prototypes during day time in Chennai, India. During each test run, ambient conditions (temperature and RH), surface temperature of the fins, and water collected were measured in intervals of 10 min.

■ ASSOCIATED CONTENT

Supporting Information

The Supporting Information is available free of charge at https://pubs.acs.org/doi/10.1021/acsanm.0c03032.

Powder XRD and SEM-EDS, lab-scale prototype, optical images of jumping-droplet condensation on the hierarchical superhydrophobic surface, images of the scaled prototype, and results of test runs of prototypes (PDF)

Video S1, video of multiple 100 μm droplets in a frame, at 30 frames per second, under full-ring illumination (MP4)

Video S2, dynamics of droplets of the order of 10 μm on a single bundle at 30 frames per second (MP4)

Video S3, drying of wet bundles using hot air flow (MP4)

AUTHOR INFORMATION

Corresponding Authors

Tiju Thomas − *Department of Metallurgical and Materials Engineering, Indian Institute of Technology Madras, Chennai 600036, India;* orcid.org/0000-0001-8322-6387; Email: tijuthomas@iitm.ac.in

Thalappil Pradeep − *DST Unit of Nanoscience, Thematic Unit of Excellence, Department of Chemistry, Indian Institute of Technology Madras, Chennai 600036, India;* orcid.org/0000-0003-3174-534X; Email: pradeep@iitm.ac.in

Authors

Ankit Nagar − *DST Unit of Nanoscience, Thematic Unit of Excellence, Department of Chemistry and Department of Metallurgical and Materials Engineering, Indian Institute of Technology Madras, Chennai 600036, India*

Ramesh Kumar − *Department of Metallurgical and Materials Engineering, Indian Institute of Technology Madras, Chennai 600036, India*

Pillalamarri Srikrishnarka − *DST Unit of Nanoscience, Thematic Unit of Excellence, Department of Chemistry, Indian Institute of Technology Madras, Chennai 600036, India;* orcid.org/0000-0001-5187-6879

Complete contact information is available at:
https://pubs.acs.org/10.1021/acsanm.0c03032

Notes

The authors declare no competing financial interest.

ACKNOWLEDGMENTS

We gratefully acknowledge the Department of Science and Technology (DST) for supporting our research program. A.N., P.S., and C.S. thank IIT Madras for their doctoral student fellowships. We also acknowledge the help offered by Sagar Patil, Sudeep Patel, Guthi Raja, Swathi Choudhary, and Arpan Soren during prototype assembly and testing.

REFERENCES

(1) Nagar, A.; Pradeep, T. Clean Water through Nanotechnology: Needs, Gaps, and Fulfillment. *ACS Nano* **2020**, *14* (6), 6420−6435.

(2) Dulberg, S.; Kohavi, A. System and Method for High-Efficiency Atmospheric Water Generator and Dehumidification Apparatus. U.S. Patent 20180266708, 2018.

(3) Miljkovic, N.; Enright, R.; Nam, Y.; Lopez, K.; Dou, N.; Sack, J.; Wang, E. N. Jumping-Droplet-Enhanced Condensation on Scalable Superhydrophobic Nanostructured Surfaces. *Nano Lett.* **2013**, *13* (1), 179−187.

(4) Tu, R.; Hwang, Y. Reviews of Atmospheric Water Harvesting Technologies. *Energy* **2020**, *201*, 117630.

(5) Tu, Y.; Wang, R.; Zhang, Y.; Wang, J. Progress and Expectation of Atmospheric Water Harvesting. *Joule* **2018**, *2* (8), 1452−1475.

(6) Parin, R.; Martucci, A.; Sturaro, M.; Bortolin, S.; Bersani, M.; Carraro, F.; Del Col, D. Nano-Structured Aluminum Surfaces for Dropwise Condensation. *Surf. Coat. Technol.* **2018**, *348*, 1−12.

(7) Maa, J. R. Drop Size Distribution and Heat Flux of Dropwise Condensation. *Chem. Eng. J.* **1978**, *16* (3), 171−176.

(8) Orejon, D.; Askounis, A.; Takata, Y.; Attinger, D. Dropwise Condensation on Multiscale Bioinspired Metallic Surfaces with Nanofeatures. *ACS Appl. Mater. Interfaces* **2019**, *11* (27), 24735−24750.

(9) Rose, J. W. Dropwise Condensation Theory and Experiment: A Review. *Proc. Inst. Mech. Eng., Part A* **2002**, *216* (2), 115−128.

(10) Chen, X.; Wu, J.; Ma, R.; Hua, M.; Koratkar, N.; Yao, S.; Wang, Z. Nanograssed Micropyramidal Architectures for Continuous Dropwise Condensation. *Adv. Funct. Mater.* **2011**, *21* (24), 4617−4623.

(11) Oh, J.; Zhang, R.; Shetty, P. P.; Krogstad, J. A.; Braun, P. V.; Miljkovic, N. Thin Film Condensation on Nanostructured Surfaces. *Adv. Funct. Mater.* **2018**, *28* (16), 1707000.

(12) Edalatpour, M.; Liu, L.; Jacobi, A. M.; Eid, K. F.; Sommers, A. D. Managing Water on Heat Transfer Surfaces: A Critical Review of Techniques to Modify Surface Wettability for Applications with Condensation or Evaporation. *Appl. Energy* **2018**, *222*, 967−992.

(13) Hou, Y.; Yu, M.; Chen, X.; Wang, Z.; Yao, S. Recurrent Filmwise and Dropwise Condensation on a Beetle Mimetic Surface. *ACS Nano* **2015**, *9* (1), 71−81.

(14) Yan, X.; Chen, F.; Sett, S.; Chavan, S.; Li, H.; Feng, L.; Li, L.; Zhao, F.; Zhao, C.; Huang, Z.; Miljkovic, N. Hierarchical Condensation. *ACS Nano* **2019**, *13* (7), 8169−8184.

(15) Yang, K.-S.; Lin, K.-H.; Tu, C.-W.; He, Y.-Z.; Wang, C.-C. Experimental Investigation of Moist Air Condensation on Hydrophilic, Hydrophobic, Superhydrophilic, and Hybrid Hydrophobic-Hydrophilic Surfaces. *Int. J. Heat Mass Transfer* **2017**, *115*, 1032−1041.

(16) Park, K.-C.; Kim, P.; Grinthal, A.; He, N.; Fox, D.; Weaver, J. C.; Aizenberg, J. Condensation on Slippery Asymmetric Bumps. *Nature* **2016**, *531* (7592), 78−82.

(17) Moazzam, P.; Tavassoli, H.; Razmjou, A.; Warkiani, M. E.; Asadnia, M. Mist Harvesting Using Bioinspired Polydopamine Coating and Microfabrication Technology. *Desalination* **2018**, *429*, 111−118.

(18) Wang, X.; Zeng, J.; Li, J.; Yu, X.; Wang, Z.; Zhang, Y. Beetle and Cactus-Inspired Surface Endows Continuous and Directional Droplet Jumping for Efficient Water Harvesting. *J. Mater. Chem. A* **2021**, *9*, 1507−1516.

(19) Cho, H. J.; Preston, D. J.; Zhu, Y.; Wang, E. N. Nanoengineered Materials for Liquid−Vapour Phase-Change Heat Transfer. *Nat. Rev. Mater.* **2017**, *2* (2), 1−17.

(20) Tsuchiya, H.; Tenjimbayashi, M.; Moriya, T.; Yoshikawa, R.; Sasaki, K.; Togasawa, R.; Yamazaki, T.; Manabe, K.; Shiratori, S. Liquid-Infused Smooth Surface for Improved Condensation Heat Transfer. *Langmuir* **2017**, *33* (36), 8950−8960.

(21) Azimi, G.; Dhiman, R.; Kwon, H.-M.; Paxson, A. T.; Varanasi, K. K. Hydrophobicity of Rare-Earth Oxide Ceramics. *Nat. Mater.* **2013**, *12* (4), 315−320.

(22) Preston, D. J.; Mafra, D. L.; Miljkovic, N.; Kong, J.; Wang, E. N. Scalable Graphene Coatings for Enhanced Condensation Heat Transfer. *Nano Lett.* **2015**, *15* (5), 2902−2909.

(23) Bergman, T. L.; Incropera, F. P.; DeWitt, D. P.; Lavine, A. S. *Fundamentals of Heat and Mass Transfer*; John Wiley & Sons, 2011.

(24) Furmidge, C. G. L. Studies at Phase Interfaces. I. The Sliding of Liquid Drops on Solid Surfaces and a Theory for Spray Retention. *J. Colloid Sci.* **1962**, *17* (4), 309−324.

(25) Mulroe, M. D.; Srijanto, B. R.; Ahmadi, S. F.; Collier, C. P.; Boreyko, J. B. Tuning Superhydrophobic Nanostructures to Enhance Jumping-Droplet Condensation. *ACS Nano* **2017**, *11* (8), 8499−8510.

(26) Kim, M.-K.; Cha, H.; Birbarah, P.; Chavan, S.; Zhong, C.; Xu, Y.; Miljkovic, N. Enhanced Jumping-Droplet Departure. *Langmuir* **2015**, *31* (49), 13452−13466.

(27) Boreyko, J. B.; Chen, C.-H. Self-Propelled Dropwise Condensate on Superhydrophobic Surfaces. *Phys. Rev. Lett.* **2009**, *103* (18), 184501.

(28) Zamuruyev, K. O.; Bardaweel, H. K.; Carron, C. J.; Kenyon, N. J.; Brand, O.; Delplanque, J.-P.; Davis, C. E. Continuous Droplet Removal upon Dropwise Condensation of Humid Air on a

Hydrophobic Micropatterned Surface. *Langmuir* **2014**, *30* (33), 10133−10142.

(29) Chen, C.-H.; Cai, Q.; Tsai, C.; Chen, C.-L.; Xiong, G.; Yu, Y.; Ren, Z. Dropwise Condensation on Superhydrophobic Surfaces with Two-Tier Roughness. *Appl. Phys. Lett.* **2007**, *90* (17), 173108.

(30) H2O Machine https://h2omachine.com/wp-content/uploads/2020/02/large-h20-spec-sheet3.pdf (accessed 2020-12-27).

(31) GENAQ Cumulus http://www.genaq.com/cumulus-tech-specs/ (accessed 2020-12-20).

(32) Atmos H2O Hawaii http://atmosh2ohawaii.com/technical-information/ (accessed 2020-12-20).

(33) AirOWater https://www.airowater.com/products/product/dewpoint/ (accessed 2020-12-20).

(34) Nu Image Solutions https://nuimagesolution.com/awg/nu-water-30.pdf (accessed 2020-12-20).

(35) Ray Agua https://www.rayagua.com/brouchers/1.CORPORATE_BROCHURE.pdfhttps://www.rayagua.com/brouchers/1.CORPORATE_BROCHURE.pdfhttps://www.rayagua.com/brouchers/1.CORPORATE_BROCHURE.pdf (accessed 2020-12-20).

(36) WAE Atmospheric Water Generator https://www.waecorp.com/emergency-equipment/36https://www.waecorp.com/emergency-equipment/36 (accessed 2020-12-20).

(37) ZL9510D Household Air Water Generator http://1909115108.pool201-site.make.yun300.cn/product/15.html (accessed 2020-12-20).

Supporting Information

Scalable Drop-To-Film Condensation on a Nanostructured Hierarchical Surface for Enhanced Humidity Harvesting

Ankit Nagar[†,‡], *Ramesh Kumar*[‡], *Pillalamarri Srikrishnarka*[†], *Tiju Thomas*[*,‡] *and Thalappil Pradeep*[*,†]

[†]DST Unit of Nanoscience, Thematic Unit of Excellence, Department of Chemistry, Indian Institute of Technology Madras, Chennai 600036, India.

[‡]Department of Metallurgical and Materials Engineering, Indian Institute of Technology Madras, Chennai 600036, India.

Email: tijuthomas@iitm.ac.in, [*,‡] pradeep@iitm.ac.in [*,†]

S1. Characterization of the h surface

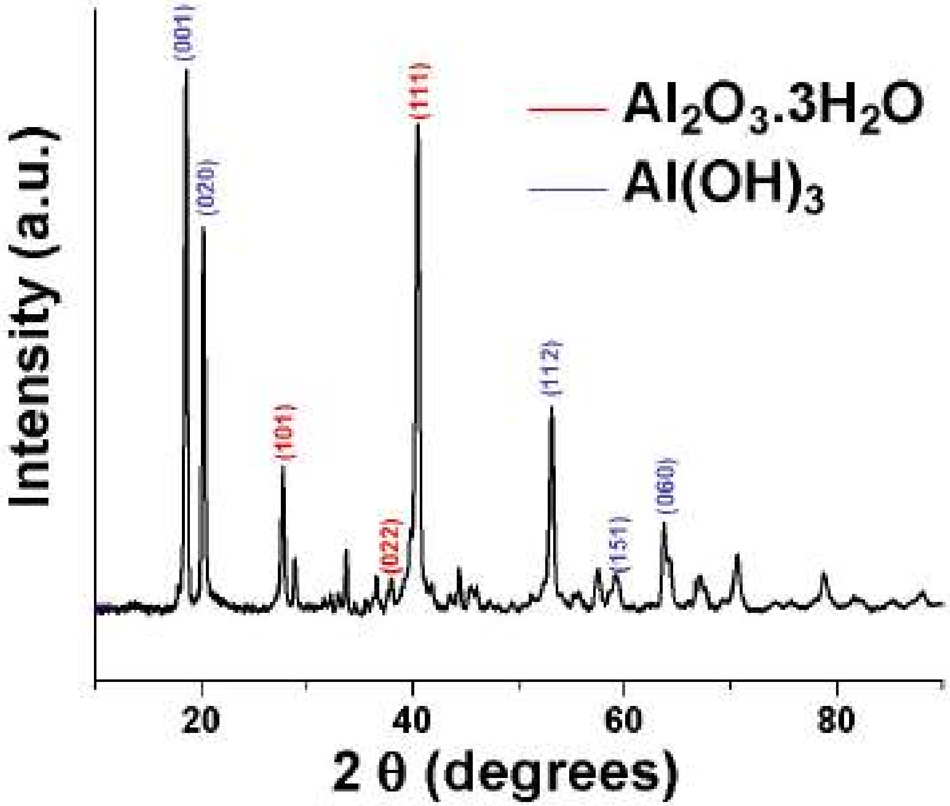

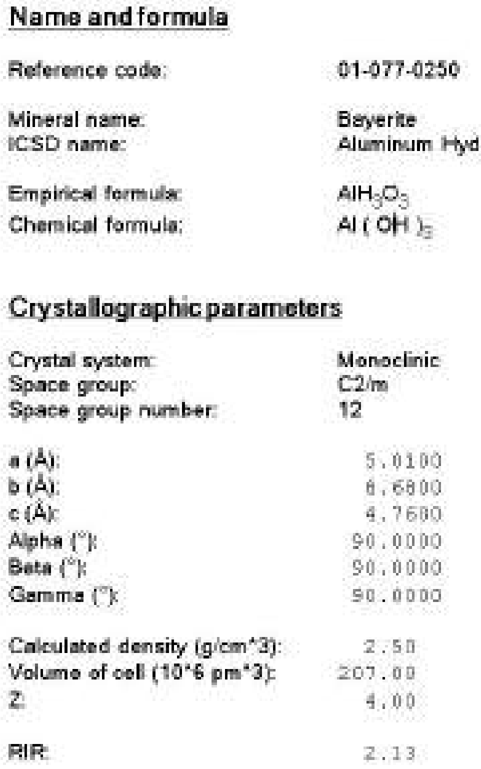

Name and formula

Reference code:	01-077-0250
Mineral name:	Bayerite
ICSD name:	Aluminum Hydroxide
Empirical formula:	AlH_3O_3
Chemical formula:	$Al (OH)_3$

Crystallographic parameters

Crystal system:	Monoclinic
Space group:	C2/m
Space group number:	12
a (Å):	5.0100
b (Å):	8.6800
c (Å):	4.7600
Alpha (°):	90.0000
Beta (°):	90.0000
Gamma (°):	90.0000
Calculated density (g/cm^3):	2.50
Volume of cell (10^6 pm^3):	207.00
Z:	4.00
RIR:	2.13

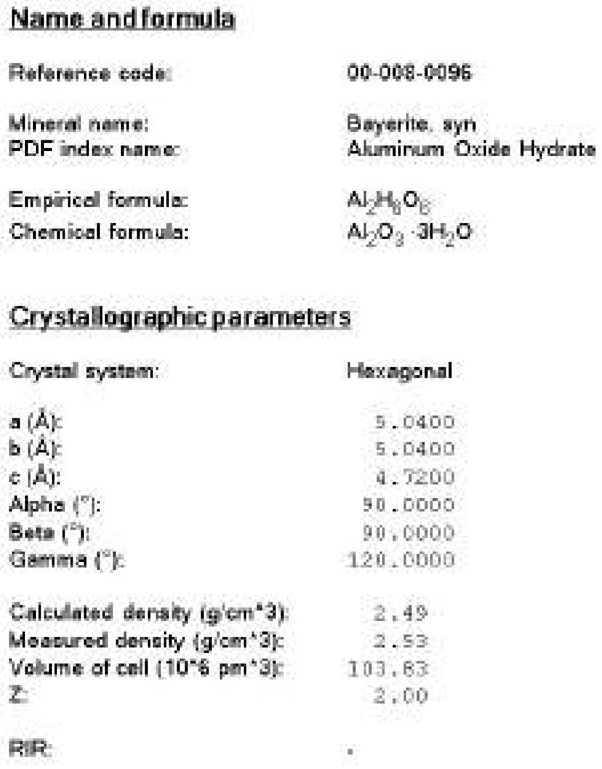

Name and formula

Reference code:	00-008-0096
Mineral name:	Bayerite, syn
PDF index name:	Aluminum Oxide Hydrate
Empirical formula:	$Al_2H_6O_6$
Chemical formula:	$Al_2O_3 \cdot 3H_2O$

Crystallographic parameters

Crystal system:	Hexagonal
a (Å):	5.0400
b (Å):	5.0400
c (Å):	4.7200
Alpha (°):	90.0000
Beta (°):	90.0000
Gamma (°):	120.0000
Calculated density (g/cm^3):	2.49
Measured density (g/cm^3):	2.53
Volume of cell (10^6 pm^3):	103.83
Z:	2.00
RIR:	-

Figure S1. Powder XRD of the particulates obtained after scraping the hierarchically structured surface (h).

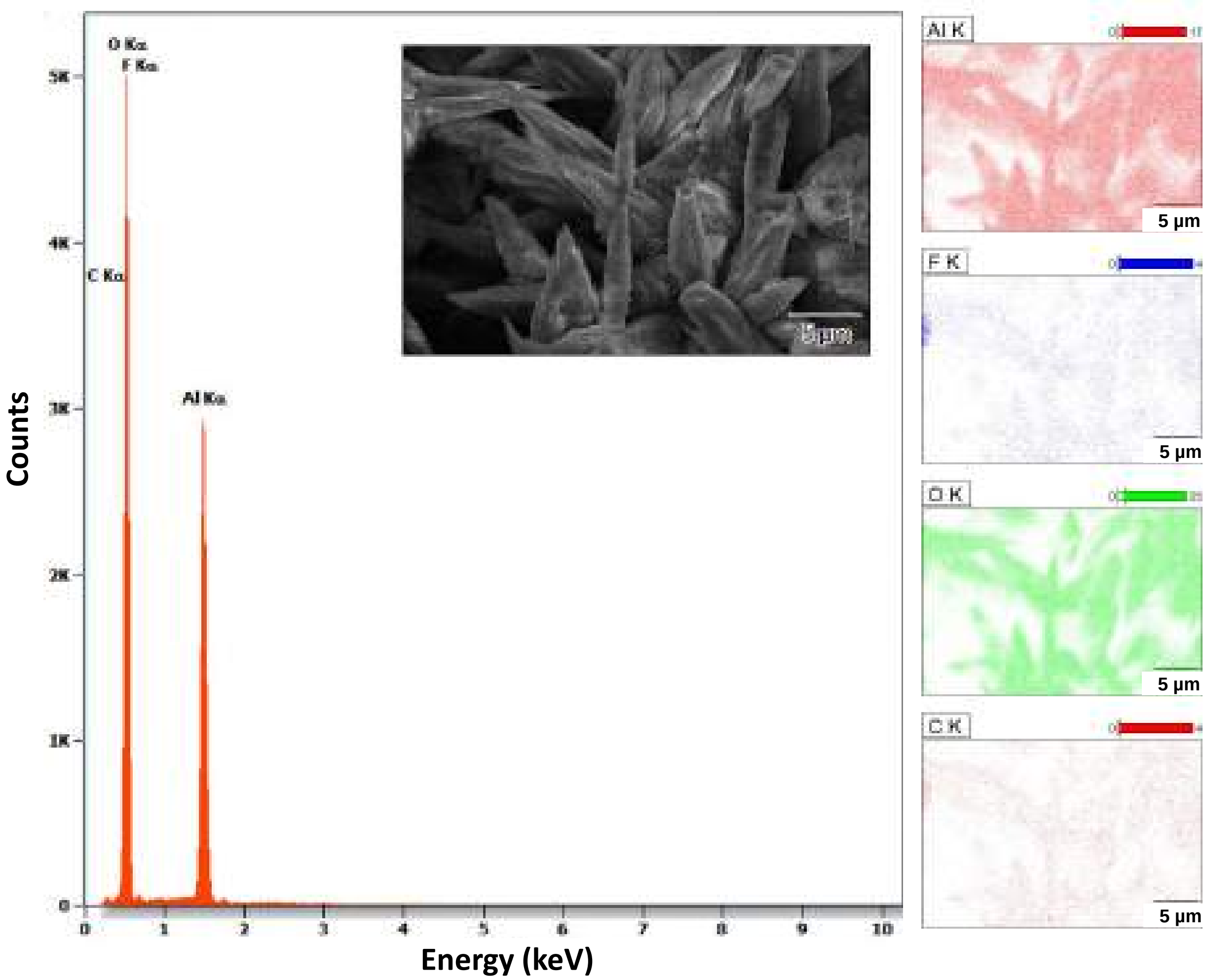

Figure S2. EDS spectrum and mapping of the h-hp surface to verify silane functionalization through fluorine distribution over the surface.

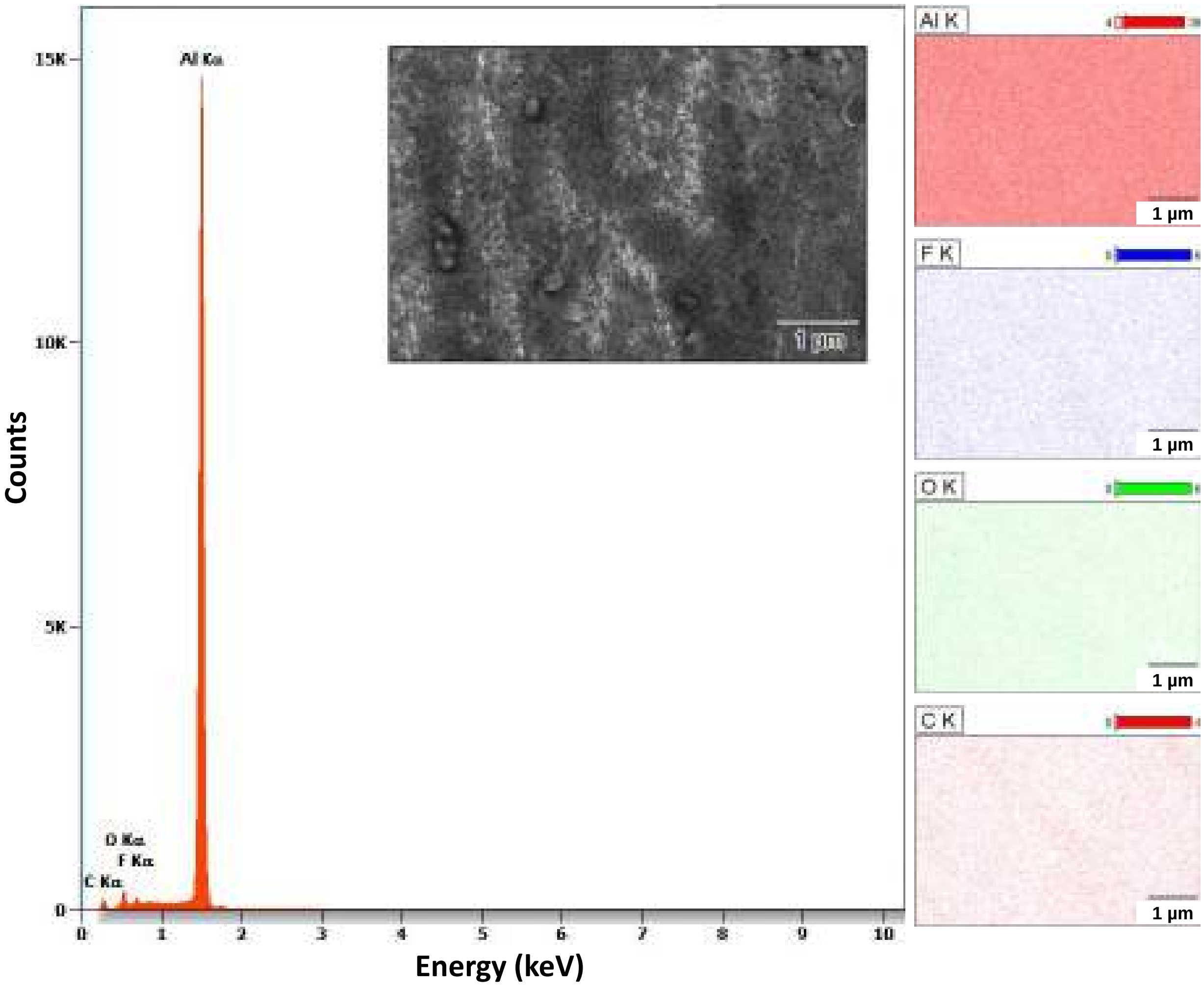

Figure S3. EDS spectrum and mapping of silane-coated plain aluminium surface (p-hp) to verify silane functionalization through fluorine distribution over the surface.

S2. Lab-scale setup to perform water collection experiments

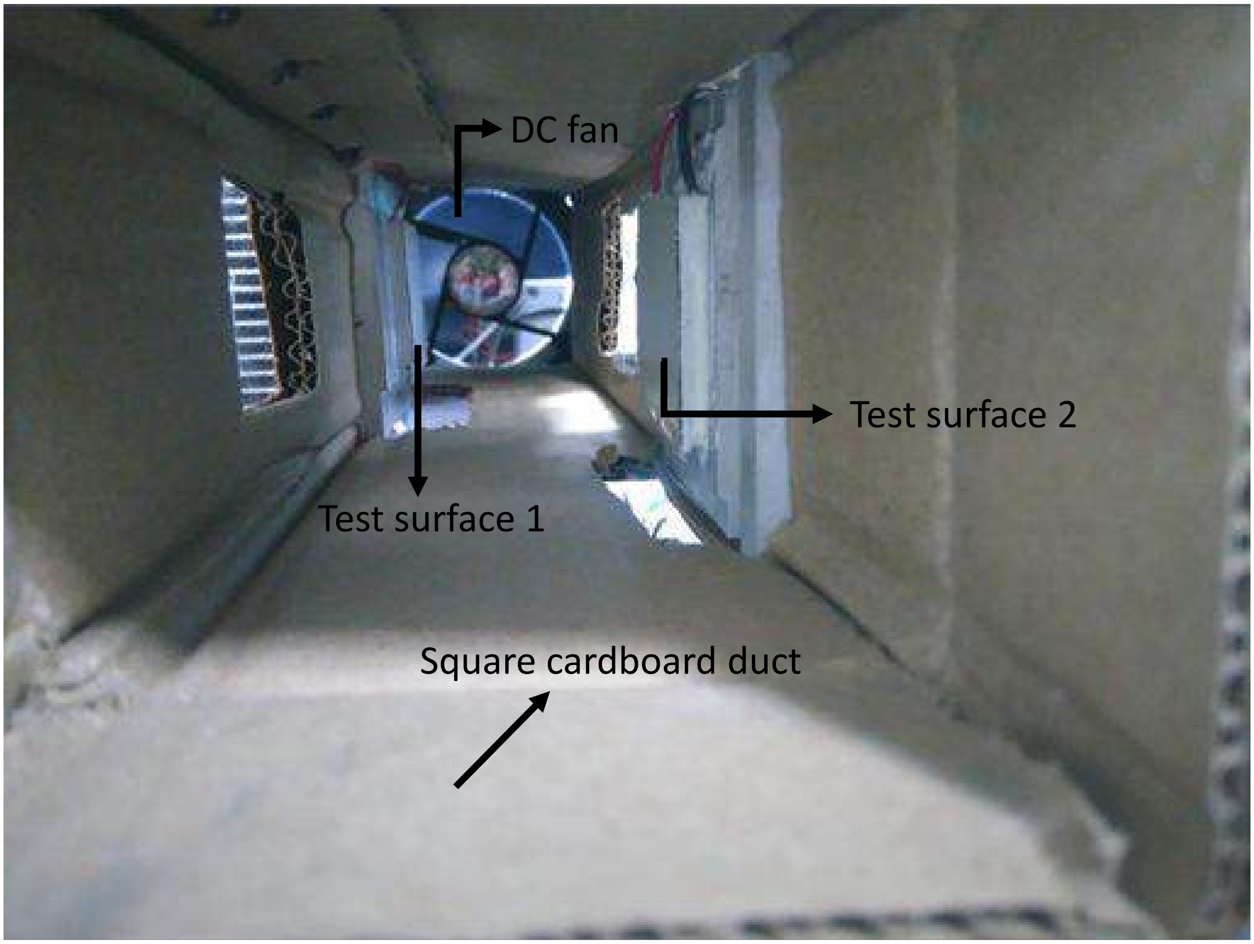

Figure S4. Inside view of a square duct made out of cardboard for restricted flow of ambient air. The test surfaces put on the peltier-heat sink assembly were exposed to the ambient air flowing inside the duct by means of a dc fan. Two surfaces were tested at the same time, placed on opposite walls of the box, with few cms distance apart.

S3. Gravity-assisted rolling on p surface

Droplets of the order of 1 mm roll down the p surface and, in the process, collect smaller droplets along with them, as shown in the figure below. The size and shape of rolling droplet being similar across the entire subcooling, it has only been shown as an illustration at ΔT~ 2 ^{0}C.

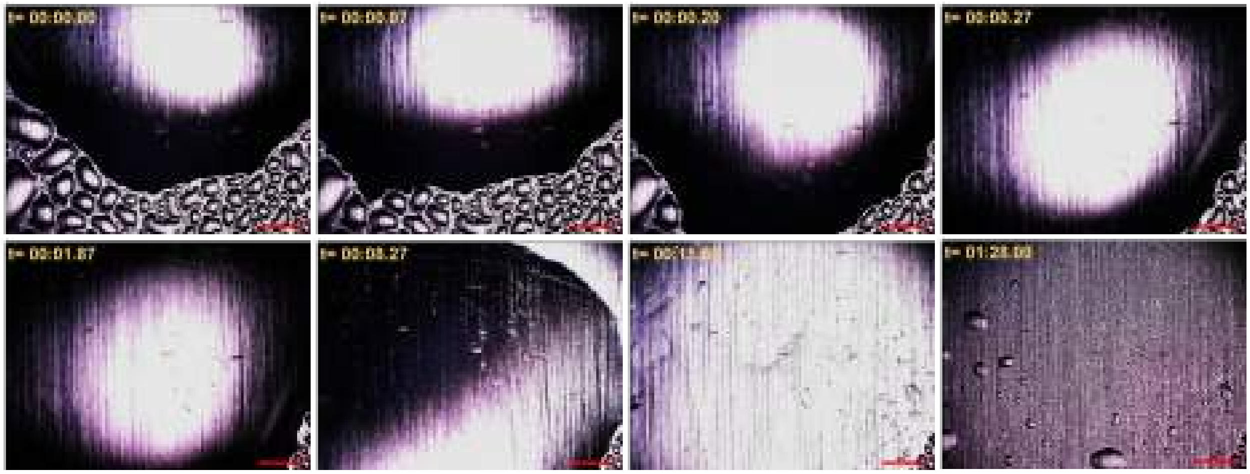

Figure S5. Rolling droplet of the order of 1 mm on the p surface, shown by time-resolved optical images (time in minutes). The event was recorded at 15 frames per second, and at a subcooling of ~2 ^{0}C. Scale bar: 500 μm.

S4. Gravity-assisted rolling on p-hp surface

Droplets of the order of 1 mm roll down the p-hp surface and, in the process, collect smaller droplets along with them, as shown in the figure below. The size and shape of rolling droplet being similar across the entire subcooling, it has only been shown as an illustration at ΔT~ 8 ^{0}C.

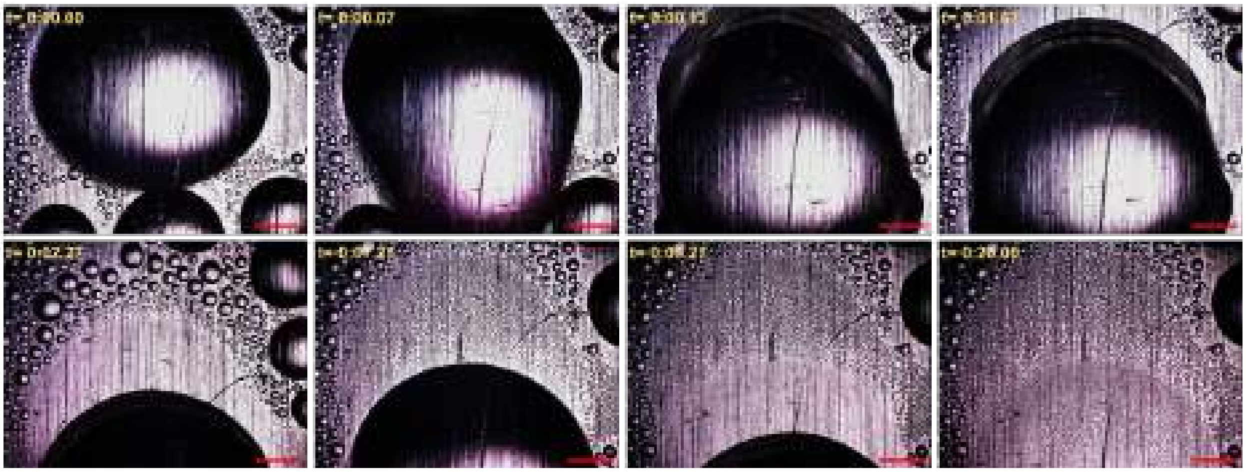

Figure S6. Rolling droplet of the order of 1 mm on the p-hp surface, shown by time-resolved optical images (time in minutes). The event was recorded at 15 frames per second, and at a subcooling of ~8 ^{0}C. Scale bar: 500 μm.

S5. Drop-to-film coalescence on h surface

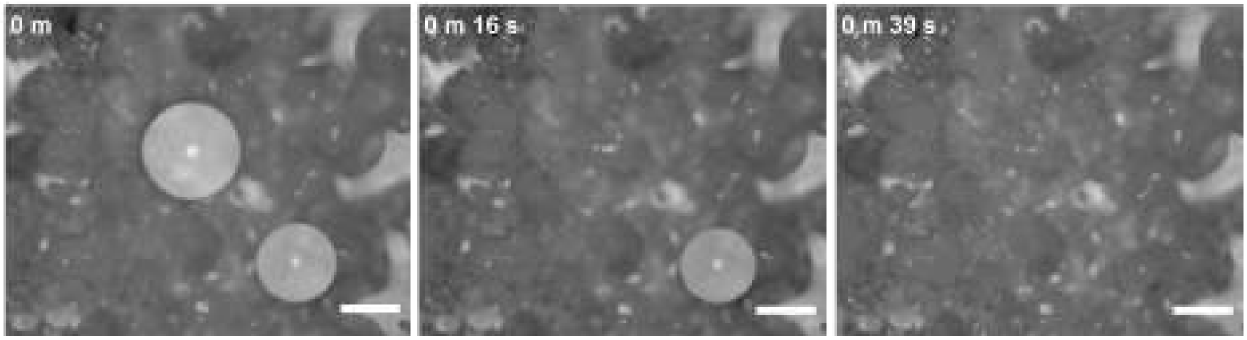

Figure S7. Droplets of the order of 100 μm leave behind a wet bundle after undergoing coalescence with the film. The coalescence mechanism has been discussed through Figures 3 and 4 in the article.

S5. Gravity-assisted rolling on h-hp surface

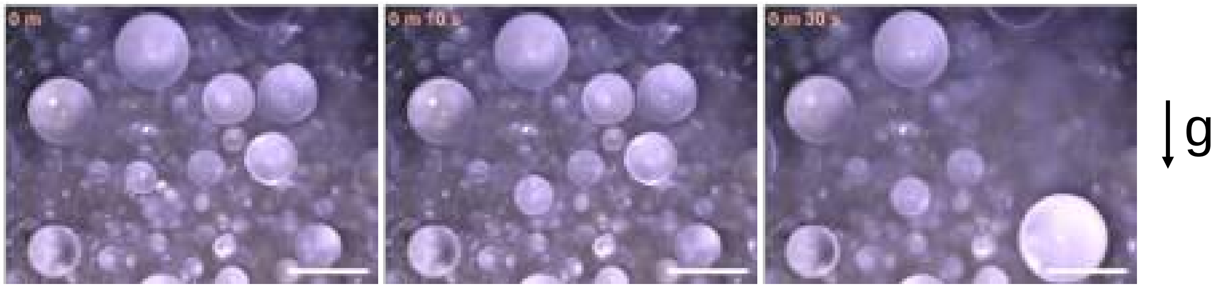

Figure S8. Coalescence of multiple droplets forms a larger droplet of the order of 100 μm which rolls down under the effect of gravity.

S6. Jumping-droplet condensation on h-hp surface

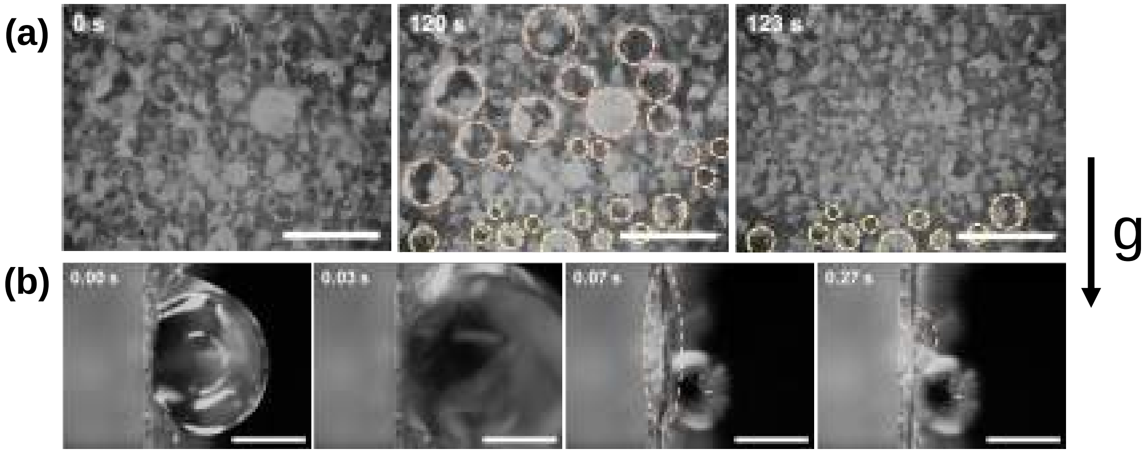

Figure S9. Representative examples of jumping mode of condensation on h-hp surface at ΔT~ 8 ^{0}C.(a)Time-resolved optical imaging of the h-hp surface from the front side (gravity acting downwards). The droplets grow and reach the top of the surface as time passes. Upon reaching a certain size, a set of droplets suddenly jump off the surface (indicated by pink dashed circles).

The jumping is evident from the yellow circled droplets beneath them, which stay as is, after the jumping event has occurred. All scale bars: 1 mm. (b) Side-view time-resolved imaging revealed jumping of an O (1 mm) droplet from the surface (t= 0 s), leaving behind a reminiscent water film (t= 0.07 s). Another droplet begins to grow at the same location (t=0.27 s) and the cycle continues to repeat itself. All scale bars: 1 mm.

S7. Toppling droplet on h surface

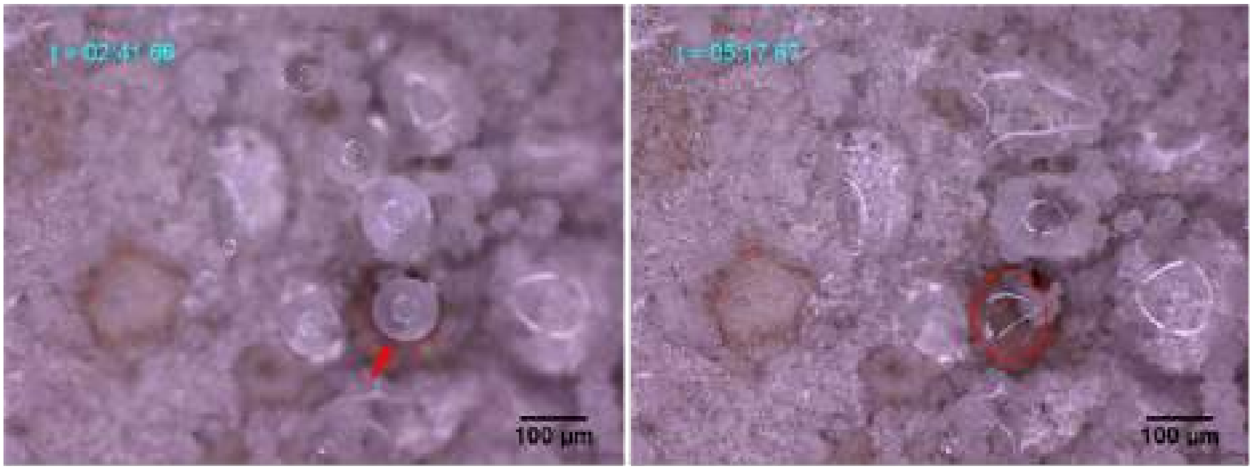

Figure S10. At t=2:41.73 mins, the droplet (indicated by red arrow) topples down the bundle, as evident from the distorted reflection of the toppled droplet later at t= 05:17.67 mins (within the dashed circle in red). The reflection extends from the bundle to the surrounding basal water film indicative of the toppling.

S8. Test runs of the p and h prototypes

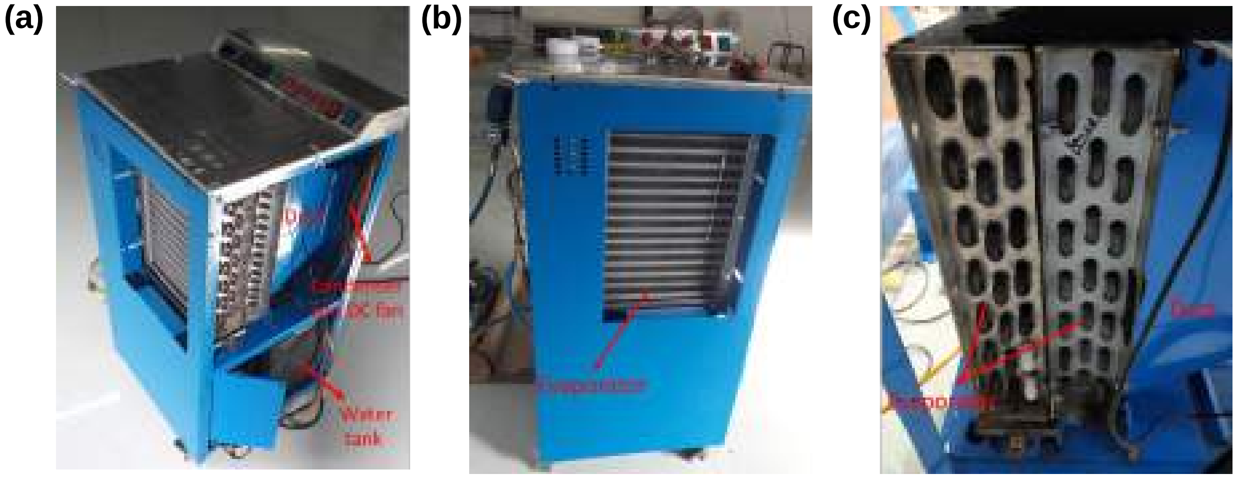

Figure S11. Images of one of the home-built prototype assembly showing various parts: (a) Perspective view, (b) front view (without air filter), and (c) side view.

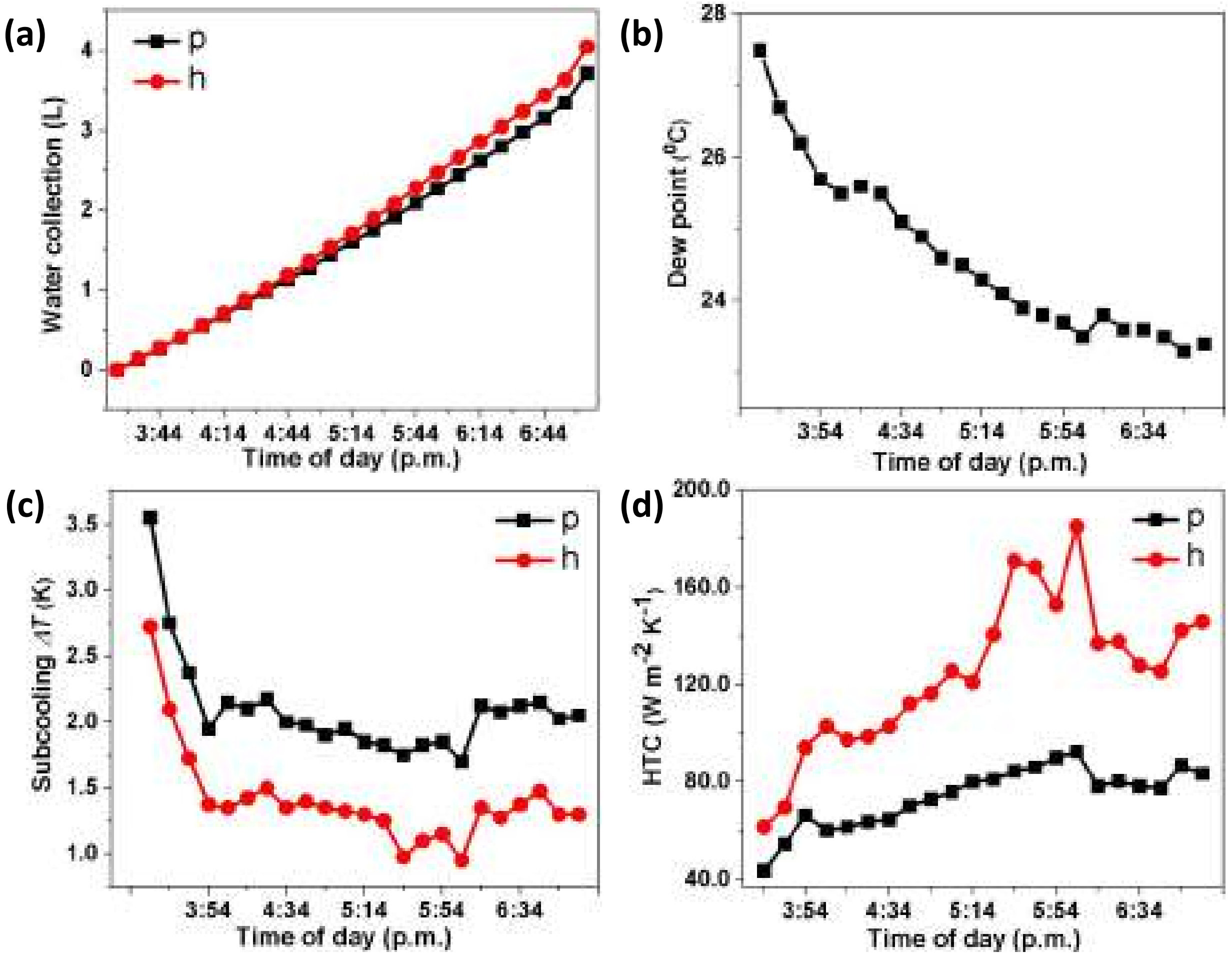

Figure S12. (a) Cumulative water collection, (b) Dew point, (c) Subcooling, and (d) HTC for the first test run (corresponding to Figure 7 in the main text).

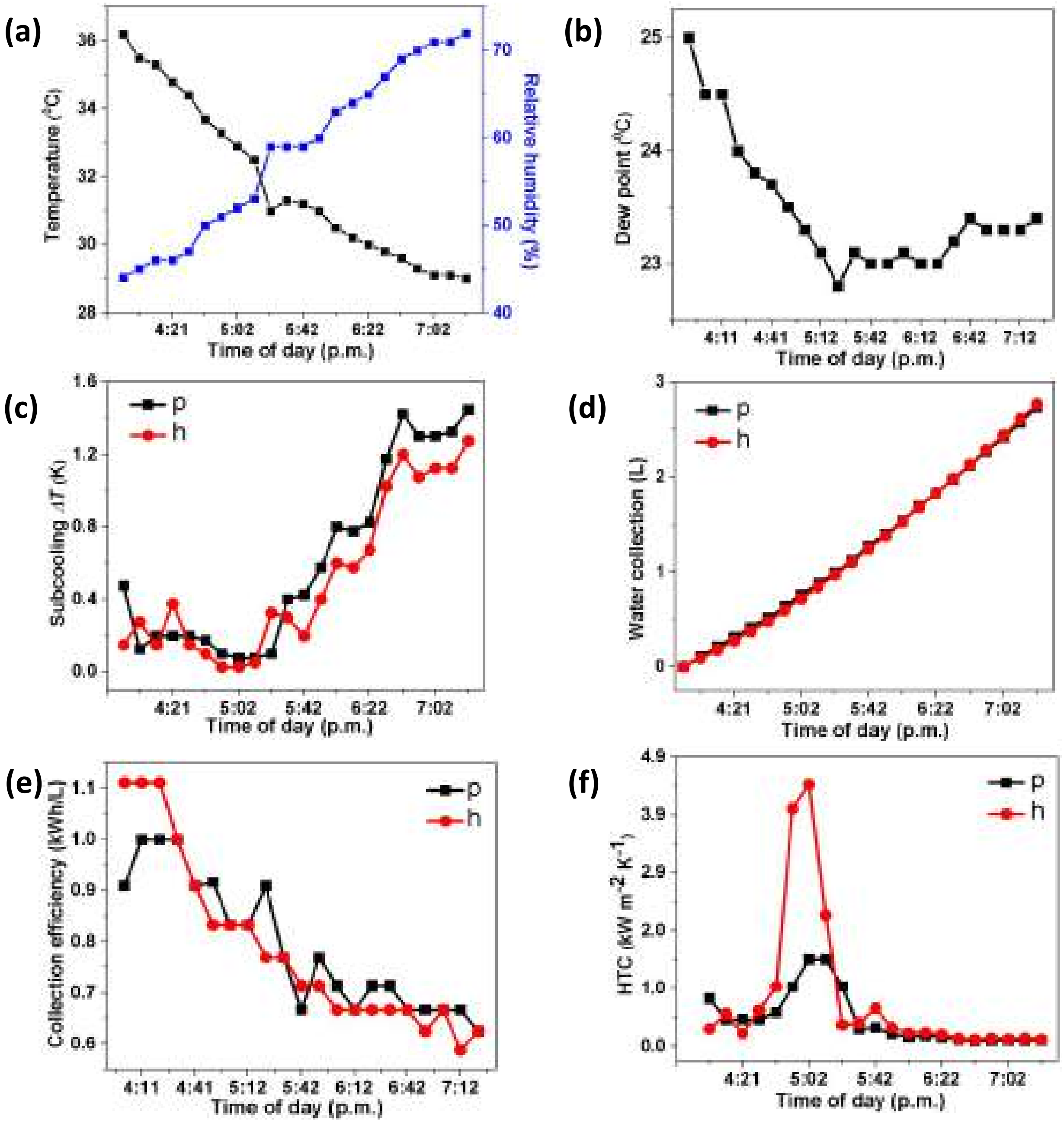

Figure S13. Second test run of the prototypes, showing variation in (a) ambient conditions, (b) dew point temperature, (c) degree of subcooling, (d) cumulative water collected, (e) collection efficiency, and (f) HTC, for the duration of the test run.

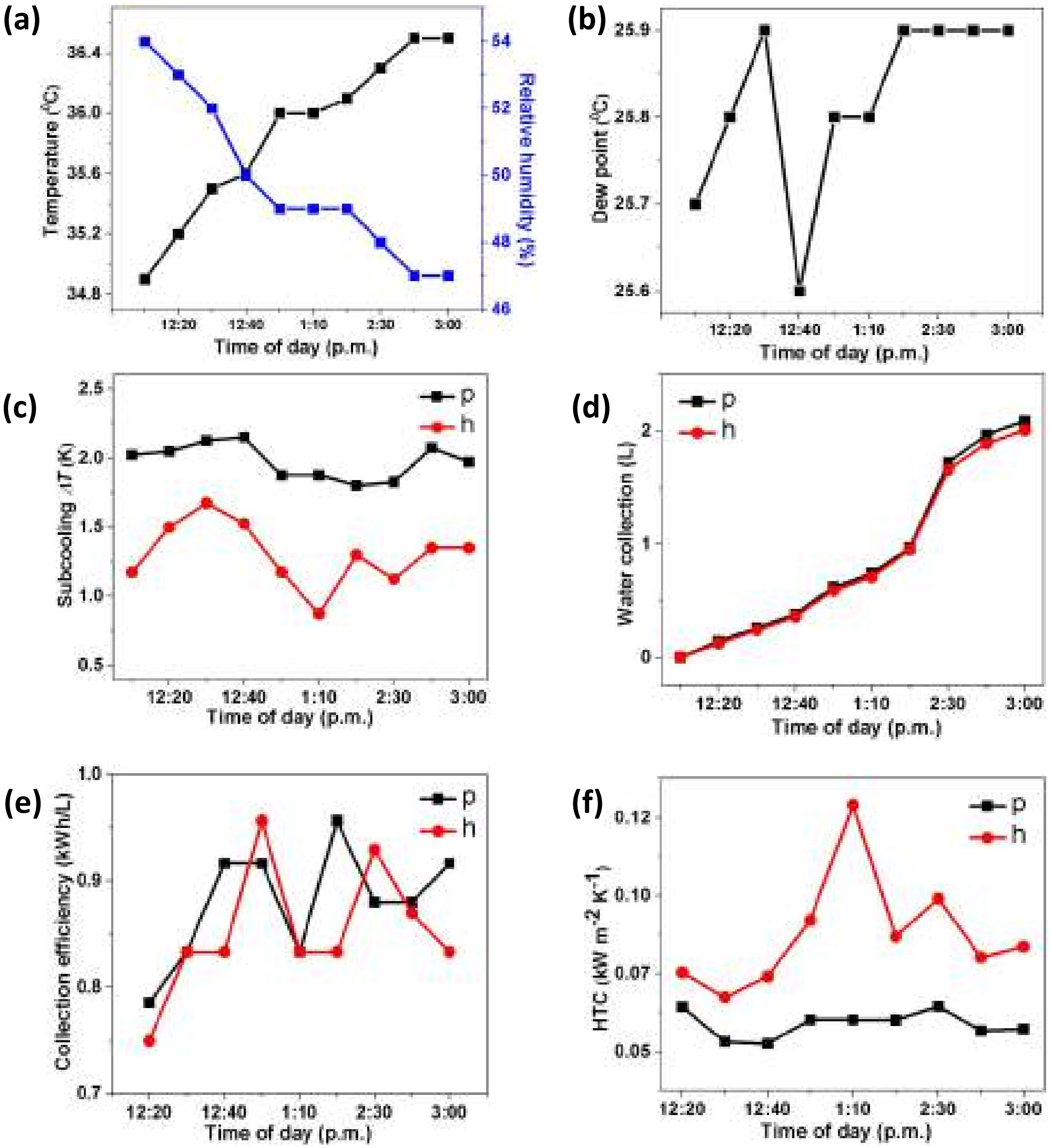

Figure S14. Third test run of the prototypes, showing variation in (a) ambient conditions, (b) dew point temperature, (c) degree of subcooling, (d) cumulative water collected, (e) collection efficiency, and (f) HTC, for the duration of the test run.

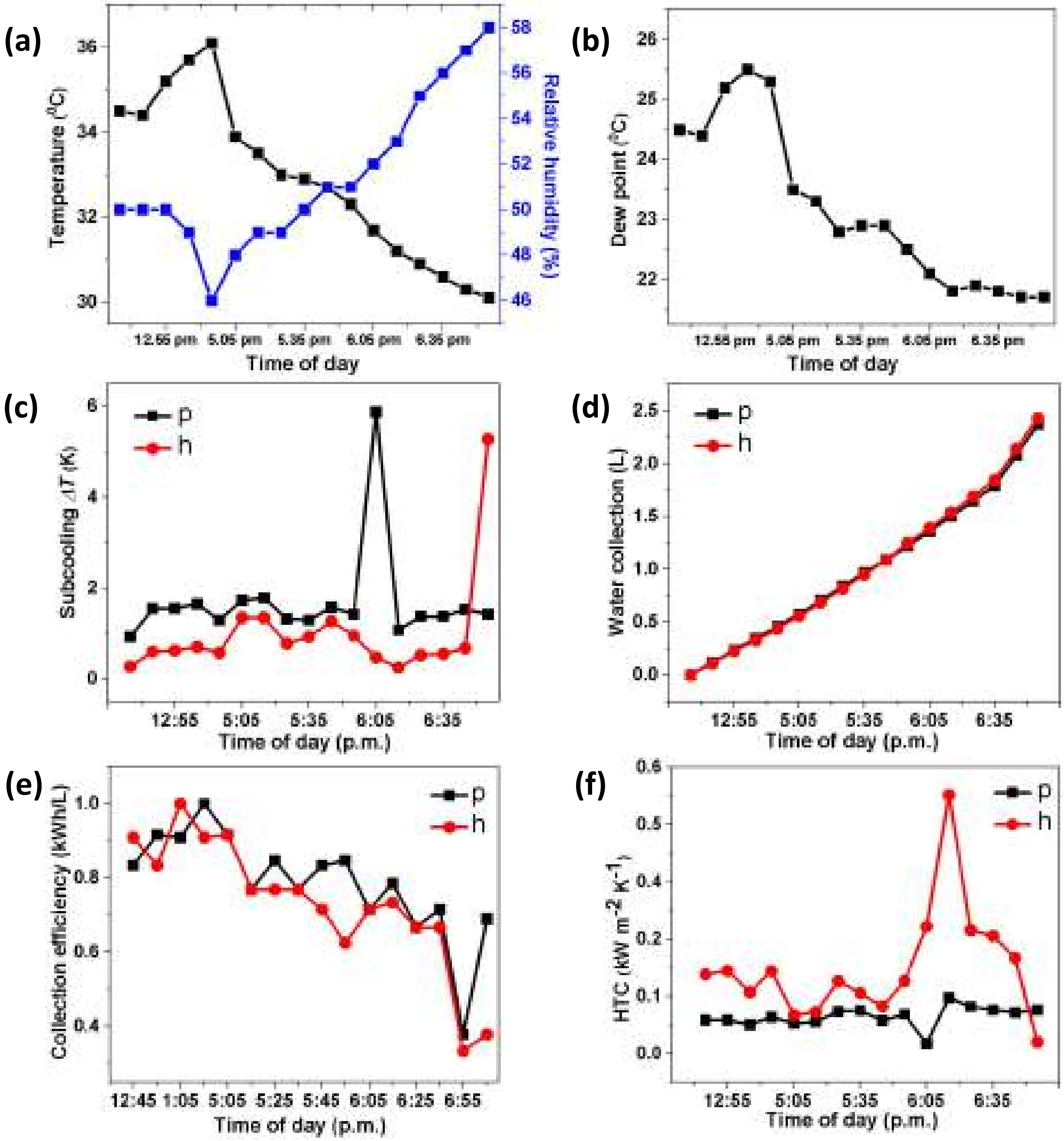

Figure S15. Fourth test run of the prototypes, showing variation in (a) ambient conditions, (b) dew point temperature, (c) degree of subcooling, (d) cumulative water collected, (e) collection efficiency, and (f) HTC, for the duration of the test run.

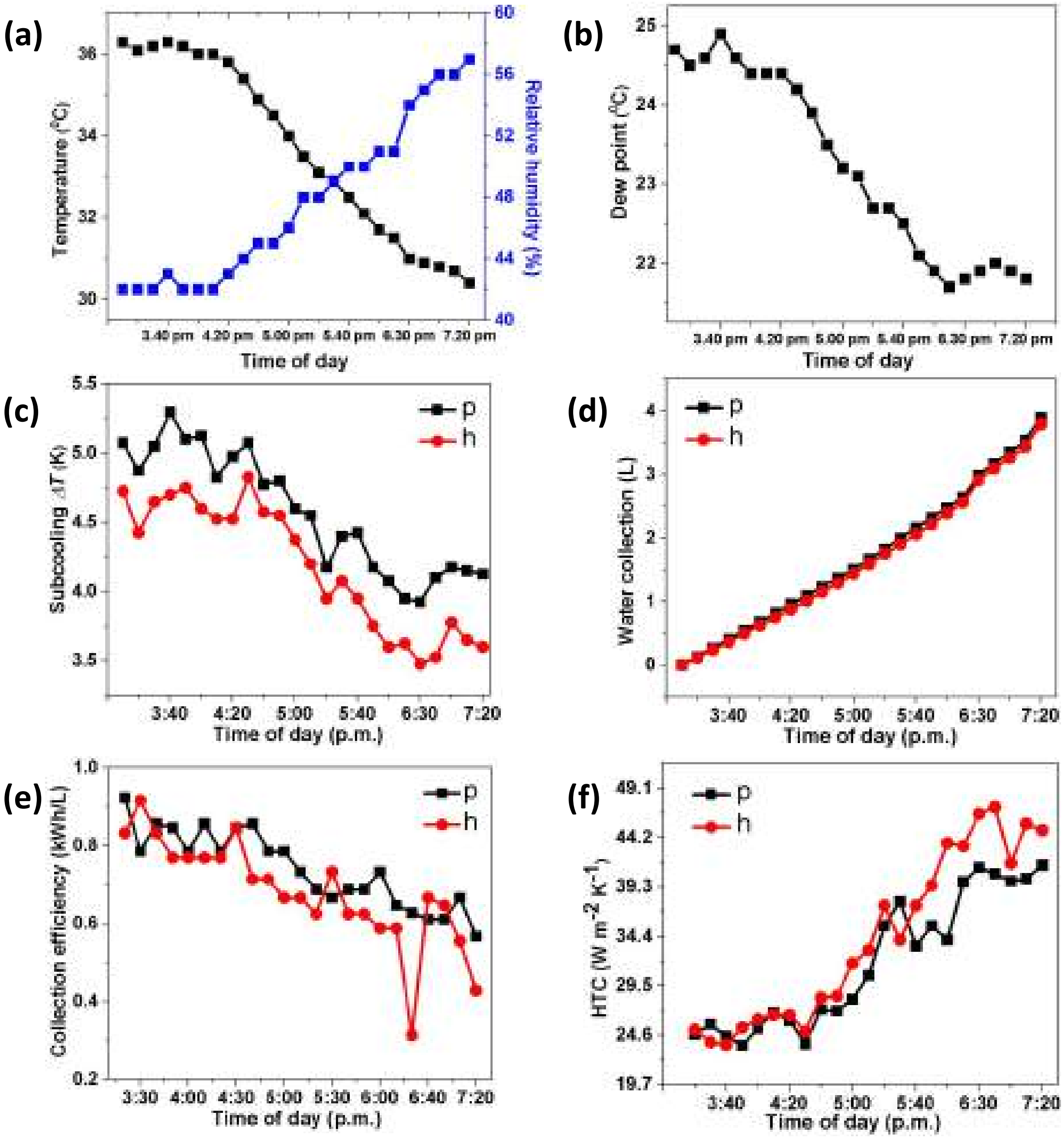

Figure S16. Fifth test run of the prototypes, showing variation in (a) ambient conditions, (b) dew point temperature, (c) degree of subcooling, (d) cumulative water collected, (e) collection efficiency, and (f) HTC, for the duration of the test run.

THE JOURNAL OF PHYSICAL CHEMISTRY C
A JOURNAL OF THE AMERICAN CHEMICAL SOCIETY

pubs.acs.org/JPCC

Article

Toward Vibrational Tomography of Citrate on Dynamically Changing Individual Silver Nanoparticles

Tripti Ahuja,[†] Kamalesh Chaudhari,[†] Ganesan Paramasivam, Gopi Ragupathy, Jyoti Sarita Mohanty, and Thalappil Pradeep*

Cite This: *J. Phys. Chem. C* 2021, 125, 3553−3566

Read Online

ACCESS | Metrics & More | Article Recommendations | Supporting Information

ABSTRACT: This study explored changes in binding modes of the most common ligand, citrate on silver nanoparticles (AgNPs) using single-particle surface-enhanced Raman scattering (SP-SERS). Single AgNPs of 50 ± 10 nm diameter anchored on clean glass slides were monitored using time-dependent SP-SERS with 632.8 nm excitation at 1.3 μW incident (0.5 μW absorbed) power per nanoparticle. We observed several distinct spectra of citrate during time-dependent SP-SERS. Analysis of 1400 spectra showed the existence of two major groups termed as favorable (F) and probable (P) spectra based on their likelihood of appearance and intensities. These distinct spectra corresponded to a multitude of binding modes, structures, and variants of photocatalyzed products of citrate on the surface of dynamically changing AgNPs. Density functional theory (DFT) simulations were performed to model the structures and binding modes of citrate on an Ag(111) surface, and corresponding Raman spectra were computed and compared with distinct spectral types. Experiments performed with deuterated (2,2,4,4-d_4) citrate-capped AgNPs provided additional evidence to understand the shifts in vibrational features obtained in SP-SERS of citrate-capped AgNPs. These systematic analyses of time-dependent SP-SERS spectra may be used for the reconstruction and vibrational tomography (VT) of ligands at the single-particle level. The proposed VT approach is similar to sectioning an object through a multitude of orientations and reconstructing its three-dimensional structure, although the structures reconstructed here are molecular orientations.

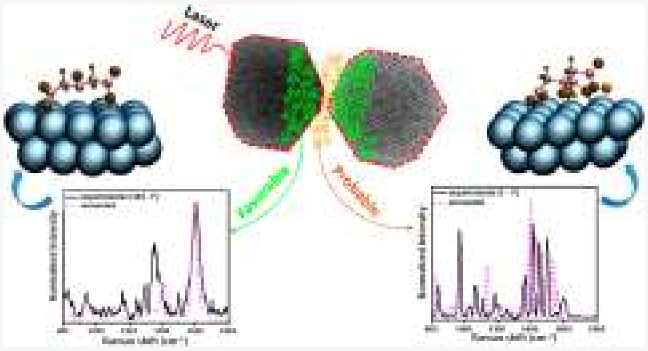

INTRODUCTION

Trisodium citrate (TSC) has been used in the synthesis of colloidal nanoparticles (NPs) and has probably become the most common reducing and stabilizing agent in the history of noble metal nanomaterials.[1−7] This ligand is shown to be important in particle aggregation,[8] ligand exchange reactions,[9] particle growth mechanism,[10] enzyme catalysis reactions,[11] and others. Due to its large implications, it is indeed necessary to explore its structure on the surface of NPs meticulously. TSC, a complex molecule with three carboxylate (COO^-) groups and one α-hydroxyl (α-OH) group, can adopt a variety of structures with different binding modes.[12] Enormous efforts have been made by the scientific community to understand its molecular structure on the surface of NP using various methods.[7,12−19] Munro et al.have performed in-depth studies to understand the formation of TSC-reduced colloids and their surface properties by UV−vis absorption spectroscopy, nuclear magnetic resonance (NMR), and surface-enhanced Raman scattering (SERS).[17] Among all the techniques, SERS serves as a powerful analytical tool for sensitive, qualitative, and semiquantitative analyses. Authors proposed that COO^- of adsorbed citrate (termed as citrate in the discussion below) bind nonequivalently on the Ag surface, where one of the terminal and the central COO^- groups bind to the Ag surface, and the other terminal COO^- remains unbound.[17] Other recent studies[7,12,14,17,19] have also proposed various binding modes of citrate. X-ray photoelectron spectroscopy (XPS) has been used to determine the surface composition and suggested that citrate anions are adsorbed on the surface of AuNPs through the central COO^- group.[16,19] Attenuated total reflectance infrared (ATR-IR) spectroscopy was used to study intermolecular interactions between the adsorbed and dangling citrate anions. Further, dimer and trimer structures of citrate on the AuNPs surface were proposed.[19] Such studies helped to understand the stabilizing nature of ligands used in the preparation of NPs. Other techniques, like atomic force microscopy (AFM),[20] scanning tunneling microscopy (STM),[21] Fourier transform infrared

Received: November 5, 2020
Revised: January 20, 2021
Published: February 4, 2021

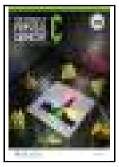

ACS Publications

https://dx.doi.org/10.1021/acs.jpcc.0c09981
J. Phys. Chem. C 2021, 125, 3553−3566

spectroscopy (FTIR),[19,22] and solid-state nuclear magnetic resonance (SS-NMR),[15] have also been used to explore the stabilizing nature of citrate. Density functional theory (DFT) and molecular dynamics have been applied to understand the surface coordination of the COO^- of citrate with the NP surface.[12,15] Such studies imparted valuable information on the hydrogen bonding networks between citrate ions,[19] their binding schemes,[13,17] and the effect of aging.[7,16]

In the past decade, single-particle and single-molecule SERS gained large interest in various fields of applications such as catalysis, sensing, live cell imaging, and so on. A study at the single-particle level provides newer and deeper insights about the system under study.[23−27] Despite the large number of investigations[12,15,17,18,21,28] on understanding the nature of citrate on the NP surface, structural details of the species at the surface are still unknown, as such studies are challenging. All the studies mentioned above have been performed on an ensemble of NPs. Although citrate-capped Au and Ag NPs have been used extensively in single-particle and single-molecule SERS studies,[29−31] understanding the binding modes and existence of photocatalyzed products of citrate at a single-particle level are still elusive.

Herein we introduce a technique that couples confocal Raman microspectroscopy (CRM) with dark field microscopy (DFM) to visualize dynamically changing AgNPs under laser irradiation and perform temporal SERS at the single-particle level. Time-dependent single-particle SERS (SP-SERS) measurements were performed on specific AgNPs (showing surface plasmon resonance (SPR), between 640−670 nm and appearing red in DFM). A large set of distinct SERS spectra (1400 spectra) of citrate were observed in time-dependent SP-SERS measurements. Each spectrum took about 2 s for measurement, which includes spectrum accumulation, data storage, and a dwell time (1 s) before collecting the next spectrum. Due to the large number of distinct spectra, a cluster analysis (CA) algorithm was used to group the spectra. Two types of groups were observed from the CA, which were termed as favorable (F) and probable (P) spectra based on their likelihood of appearance and intensities. F-spectra appeared frequently (number of spectra > 5) in temporal SERS, whereas P-spectra appeared less than five times. Theoretical simulations were performed to model binding modes of citrate on the Ag(111) surface, and the Raman spectra were computed, which were compared with the experimental spectral groups. Additional investigations on understanding the changes in the vibrational frequencies were performed using isotopically labeled (2,2,4,4-d_4-deuterated) citrate-protected AgNPs. Each of the distinct spectra of citrate gave complementary pieces of information about its structure and variants. This systematic analysis of distinct spectra of ligands using SP-SERS and DFM in conjunction with computations may lead to a vibrational tomography (VT) of ligands and understand details of one of the most ubiquitous NPs, including their ligand shell with their details of adsorbate structure. We note that the term VT is used here to indicate the approach that resembles slicing of an object (ligand) through several orientations and reconstructing its three-dimensional structure. However, the structure reconstructed is that of the ligands and their orientations using VT, and a detailed picture of the core of the nanoparticle can be obtained only via electron microscopy. Combined inputs from electron microscopy and VT may be used to reconstruct the complete 3D picture of the NPs.

MATERIALS AND METHODS

Materials. TSC dihydrate (>99%) was purchased from Merck Life Science Private Limited. Silver nitrate (99.9%) was purchased from RANKEM, India. 3-(Mercaptopropyl)-trimethoxysilane was purchased from Sigma-Aldrich. Deuterated citric acid was purchased from Cambridge Isotopes Laboratories, Inc. Other reagents were of analytical grade and used without further purification. Deionized water (DI; ∼18.2 MΩ) obtained from Milli-Q was used throughout the experiments.

Synthesis of Citrate-Capped Silver Nanoparticles. AgNP sols were synthesized using the modified Turkevich method.[32,33] Briefly, $AgNO_3$ (17 mg in 100 mL of DI water) solution was heated to boil, and then trisodium citrate (40 mg in 2 mL of DI water) was added. Once the color of the solution changed to pale yellow, it was quenched under tap water. The formation of AgNPs was confirmed by UV−vis spectroscopy, transmission electron microscopy (TEM), and DFM. Synthesized AgNPs were polydispersed in size, and their shape was confirmed by imaging techniques.

Immobilization of Nanoparticles. The immobilization of AgNPs on the glass slide was done by the pinpoint immobilization method. Briefly, an ultrasonically cleaned 1 mm thick glass slide (SCHOTT) was flushed with 5 mL of a solution of (3-mercaptopropyl)trimethoxysilane (2 μM in ethanol). Then it was washed extensively with ethanol twice to remove excess MPTMS, followed by DI water. About a 10 μL dispersion of NPs was drop-casted and covered with a clean glass coverslip for 30 min of incubation. After incubation, the coverslip was removed and the glass slide was washed extensively with DI water to remove the unbound NPs. Then, 2 μL of DI water was dropped on the immobilized region and covered with a 0.145 mm thick Nexterion cleanroom cleaned coverslip. It was sealed with nail paint on the sides to avoid drying of samples. In the overall procedure, care was taken to expose only one side of the slide to chemicals.

Instrumentation. UV−visible spectroscopic measurements were performed using a PerkinElmer Lambda 25 spectrophotometer in the range of 200−1100 nm. TEM measurements were performed using a JEOL 3010, 300 kV instrument. Samples were spotted on carbon-coated copper grids by drop-casting followed by drying in ambient air. Field emission scanning electron microscopy (FESEM) measurements were performed using a Thermo Scientific Verios G4 UC SEM having a retractable detector.

Single-Particle Imaging and Confocal Raman Microspectroscopy Setup for SP-SERS. Home-built dark-field assisted confocal Raman microspectroscopy (DF CRMS) setup was used for single-particle measurements. Immobilized NPs were first focused with Dage Excel M cooled CCD camera with the help of a Cytoviva high-resolution dark-field condenser and Olympus 100× oil immersion objective. Time-dependent SP-SERS spectra were collected with a WITec GmbH confocal Raman microscope equipped with 632.8 nm (He−Ne gas) laser having an output power of 650 μW on the sample for monitoring red-colored AgNPs. This instrument was equipped with an Olympus BX41 optical microscope and a thermoelectrically cooled charge-coupled detector (ANDOR CCD Detection System) with a 1024 × 1024 pixel format, operating at −80 °C. The initial signals were calibrated using the 520 cm^{-1} vibrational mode of silicon with 100× air objective. A total of 150 grooves/mm grating was used for collecting plasmonic scattering spectra

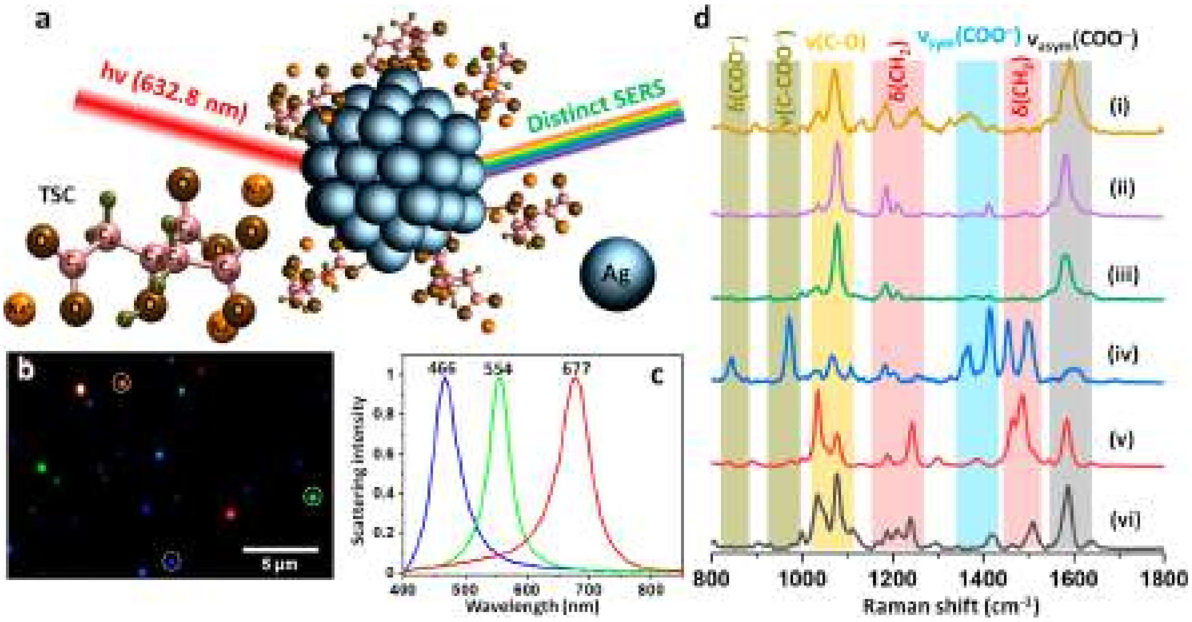

Figure 1. (a) Schematic representation of the interaction of citrate-capped AgNP with an excitation laser leading to the appearance of distinct SP-SERS spectra, (b) plasmonic hyperspectral image, (c) plasmonic scattering spectra (normalized) of immobilized citrate-capped AgNPs, spectra of encircled individual nanoparticles (b) are shown in (c), and (d) distinct SP-SERS spectra of citrate (i–vi) obtained during time-dependent measurements (colored bands correspond to vibrational modes of adsorbed species, and each distinct spectrum belongs to various binding modes and structures of citrate). An individual TSC and a silver atom are also shown in (a).

of AgNPs and 600 grooves/mm was used for SERS measurements. Acquisition time was 1 s throughout the time-dependent experiments.

SP-SERS Spectral Collection. For the SP-SERS spectral collection, the following steps were undertaken:

- At first, an individual red particle was focused using the dark-field camera with a white light source. Then, its plasmonic scattering spectrum was collected.
- Then a white light was switched off, followed by the irradiation of the laser on the same particle, and time-dependent SERS spectra were collected with the measurement time of 2 s.
- Time-dependent spectra were collected for 200–400 s per particle.
- The laser was then turned off, and finally, the plasmonic scattering spectrum of the same particle was collected.
- The above-mentioned sequence was repeated for all the red particles that were monitored for SP-SERS.

Peak Fitting of SP-SERS Spectra. Peak fitting of SP-SERS spectra were performed by using the OriginPro 2020b (Learning Edition, OriginLab Corporation, Northampton, MA, U.S.A.) software. In a nonlinear fitting, under the category of peak functions, the Gaussian function was chosen for peak fitting. The best fit was adapted by selecting parameters (base, center, fwhm, and area of peaks) in such a way that minimized the deviations of the experimental spectra, compared to fitted plots. Multiple iterations of χ-square were performed to converge the fit.

Data Processing and Cluster Analysis. Data processing and analysis were performed using Matlab 2016 (Mathworks) and IJ toolkit plugins of ImageJ.[34] Baseline correction and peak fitting of spectra were done in the origin. The spectra were vector normalized for better comparison and band assignments.

Theoretical Calculations. The structures and interactions of a citrate molecule on the surface of a AgNP were studied computationally by considering a few simplified model systems such as a small piece of the surface that was cut out from a bulk Ag crystal along the (111) plane to largely mimic the facets of Ag NPs. The geometry optimizations were performed in the real space density functional theory (DFT) with the projector augmented wave method (PAW), as implemented in GPAW,[35,36] using the PBE functional.[37] The PAW setup was used as Ag ($4d^{10}5s^1$), O ($2s^22p^4$), C ($2s^22p^2$), H ($1s^1$), and Na ($3s^1$), with scalar-relativistic effects included for Ag. The geometry optimizations of the Ag nanocluster and surface were kept fixed and carried out with a grid spacing of 0.2 Å and minimizing the residual forces without any symmetry constraints by 0.05 eV/Å.

Further, DFT calculations were performed using the B3LYP/6-31+G(d) functional/basis set, as implemented in the Gaussian 09 package.[35,37] The structures of global and local minima (stable and transition structures) were optimized with the B3LYP density functional. The 6-31+G(d) basis set was adopted for C, H, O, and Na, whereas the Ag atom was described by the LANL2DZ basis set and the associated effective core potential, which was demonstrated to be a suitable choice to describe the reactivity of the metal centers. The calculated vibrational spectra of the citrate molecule were compared with the experimental spectra, and the main peaks were identified. The calculated harmonic vibrational frequencies were typically larger than the fundamental frequencies observed experimentally and therefore have to be scaled according to the method and basis set used. The determination of appropriate scale factors for estimating fundamental experimental frequencies from theoretical harmonic frequencies has received considerable attention in the literature.[38] The scaling factor for B3LYP/6-31+G(d), as obtained from the literature, was 0.95.[39]

■ RESULTS AND DISCUSSION

Distinct Spectra of Citrate Obtained During SP-SERS. Visualizing NPs at the single-particle level and understanding the nature of ligands on the particle surface are important in the development of ligand-stabilized NPs.[15] Laser-induced plasmon tuning and the subsequent appearance of SERS in single AgNPs were demonstrated in our recent work, where a simultaneous study of plasmonic spectroscopy and Raman scattering was performed using a custom-built DFM-coupled confocal Raman microspectrometer.[32] To conduct the present work, a similar setup with modifications in the excitation source and dark field condenser was used. A schematic and a photograph of the experimental setup are presented in Figure S1, which is capable of measuring the plasmonic scattering spectra of single NPs and time-dependent SERS spectra of the capped ligands on them, sequentially. Citrate-capped AgNPs used for SP-SERS were characterized by UV−visible absorption spectroscopy and TEM (Figure S2). Out of all the immobilized AgNPs, red-colored AgNPs, as seen under DFM, were monitored selectively with an excitation source (632.8 nm) at 1.3 μW incident (0.5 μW absorbed) power per NP. Laser power calculations incident/absorbed per NP are explained in the Supporting Information (SI). AgNPs were selected such that their plasmonic scattering band (640−670 nm) was at slightly higher wavelength with respect to the Raman excitation wavelength. This was done to overlap the high energy shoulder of the plasmon with the Raman excitation and downward molecular vibronic transitions, which results in better SERS activity.[40] This is one of the conditions for the on-resonance state of SERS.[32,40] The LSPR spectrum in the range of 640−670 nm in the plasmonic hyperspectral imaging corresponds to the scattering property of selected individual NPs, whereas the LSPR band centered around 419 nm in the UV−visible spectrum corresponds to the absorption property of the bulk colloid. To understand the distribution of immobilized individual AgNPs and their interparticle spacing, we have performed FESEM of immobilized AgNPs on conducting glass slide (ITO-coated transparent glass slide with dimensions, 76 × 26 × 1.1 mm, similar to HSI glass slide). Single NPs and small aggregates of 2−3 particles were observed in such FESEM images, and these were considered as individual NPs (Figure S3). For the immobilized AgNPs used for SP-SERS, the particle density and interparticle distance calculations derived from them were performed using DFM images shown in Figure S4. Further verification of such individual particles was performed using plasmonic scattering spectroscopy.

In the past, various aggregating agents like mineral acids and salts have been used to enhance SERS signals of citrate, using citrate-capped AgNPs.[17,41] Unlike previous reports, we have successfully acquired time-dependent SP-SERS spectra of citrate in the absence of aggregating agents. This was possible due to the particle dynamics-induced plasmon-enhanced Raman scattering (PDI-PERS) phenomenon.[32] A schematic shown in Figure 1a shows the appearance of distinct spectra from an individual citrate-capped AgNP due to PDI-PERS. Immobilized individual AgNPs were characterized by plasmonic hyperspectral imaging and spectroscopy (Figure 1b,c). Distinctly different spectra (Figure 1d) were obtained during time-dependent SERS. To understand these distinct spectra of citrate (Figure 1d), we investigated the vibrational bands of TSC experimentally and theoretically. DFT optimized structure of TSC and simulated Raman spectrum of the same are presented in comparison to the experimental spectrum (Figure S5). A good match between the simulated and experimental spectra of TSC was observed (Figure S5a). Five major bands in the range of 750−2000 cm^{-1} were present in the Raman spectrum of TSC. Band assignments and the various modes of vibrations are displayed in Figure S5a and S5b, respectively. Assignments (Table S1) of distinct SERS spectra of citrate (Figure 1d) were made with the help of the simulated Raman spectrum of TSC (Figure S5a) and existing literature on the SERS of citrate.[14,17,19,42] Each contrasting color band in Figure 1d corresponds to a specific vibrational mode of citrate. Vibrational markers of the carboxylate group of citrate corresponding to $\upsilon_{\text{asym}}(\text{COO}^-)$ and $\upsilon_{\text{sym}}(\text{COO}^-)$ were present in the regions of 1560−1640 and 1350−1420 cm^{-1}, respectively, depicted in gray and blue bands. Dominant intensities of $\upsilon_{\text{asym}}(\text{COO}^-)$ and $\upsilon_{\text{sym}}(\text{COO}^-)$ vibrations in the spectra showed the binding between the COO$^-$ group and the Ag surface. The third important band lies in the region of 1050−1100 cm^{-1}, which corresponds to υ(C−O). Bending vibrations of $\delta(\text{COO}^-)$ appeared at 820−870 cm^{-1}, while stretching vibrations of (C−COO) appeared at 930−980 cm^{-1}. These were weak or absent in the SP-SERS spectra, although they were intense in a typical Raman spectrum. This was attributed to the tilting of COO$^-$ group with respect to the Ag surface in the adsorbed state.[17] Bands at 1130−1170 and 1440−1480 cm^{-1} were assigned to CH$_2$ vibrations.

Distinct SP-SERS spectra (Figure 1d, i−vi) displayed variations in their peak positions and intensities that have been correlated to the different binding modes and intermediates of citrate. To ensure that these distinct features were only from citrate or its derived species but not from the immobilizing agent, that is, (3-mercaptopropyl)-trimethoxysilane (MPTMS), we performed a control experiment where AgNPs were drop-casted without MPTMS and used for SP-SERS. Similar vibrational features (Figure S6) were observed in the absence of MPTMS, which confirmed that the peaks arose from citrate. Additional data were obtained using deuterated citrate (to be presented later). Plasmonic scattering spectra and DFM images of AgNPs monitored before and after laser exposure are shown in Figure S7. Changes in the color of AgNPs are attributed to laser-induced particle reshaping and reorientation of NPs, as reported previously.[32] To avoid significant heating effects on NPs, we have performed experiments at a low laser power of ∼1.3 μW per NP (particle size was 50 ± 10 nm). Insights obtained from the distinct SP-SERS spectra of citrate are discussed in the sections below.

CA of Time-Dependent SP-SERS Spectra. We monitored 25 individual red-colored particles, as seen in DFM images (Figure S7) for time-dependent SP-SERS. Some were SERS active (20%), and others were inactive (80%). A total of 1400 spectra, each with a measurement time of 2 s were collected from SERS active NPs (five particles). Although we have monitored as many as 25 particles for SP-SERS, only 20% of all NPs were SERS active since SERS is highly specific, and citrate is a nonresonant molecule. Also, monitoring SP-SERS of AgNPs with similar plasmonic scattering spectra from heterogeneous sample is challenging and tricky. We have done statistical analysis of SERS spectra obtained from SERS-active NPs and not on all the NPs. We obtained 1400 SERS spectra on which cluster analysis was performed to understand the variability in spectra corresponding to the orientations of the ligand. Since we have monitored a large set of time-dependent SERS spectra, the issue of statistical reliability arising from a small set of SERS-active NPs is not important for the conclusions drawn. To gain insights into the molecular information from a large set of spectra, a CA algorithm[34,43] was applied for statistical grouping. The algorithm groups or classifies the random SP-SERS spectra into clusters or groups of similar spectra. A cluster is a set of

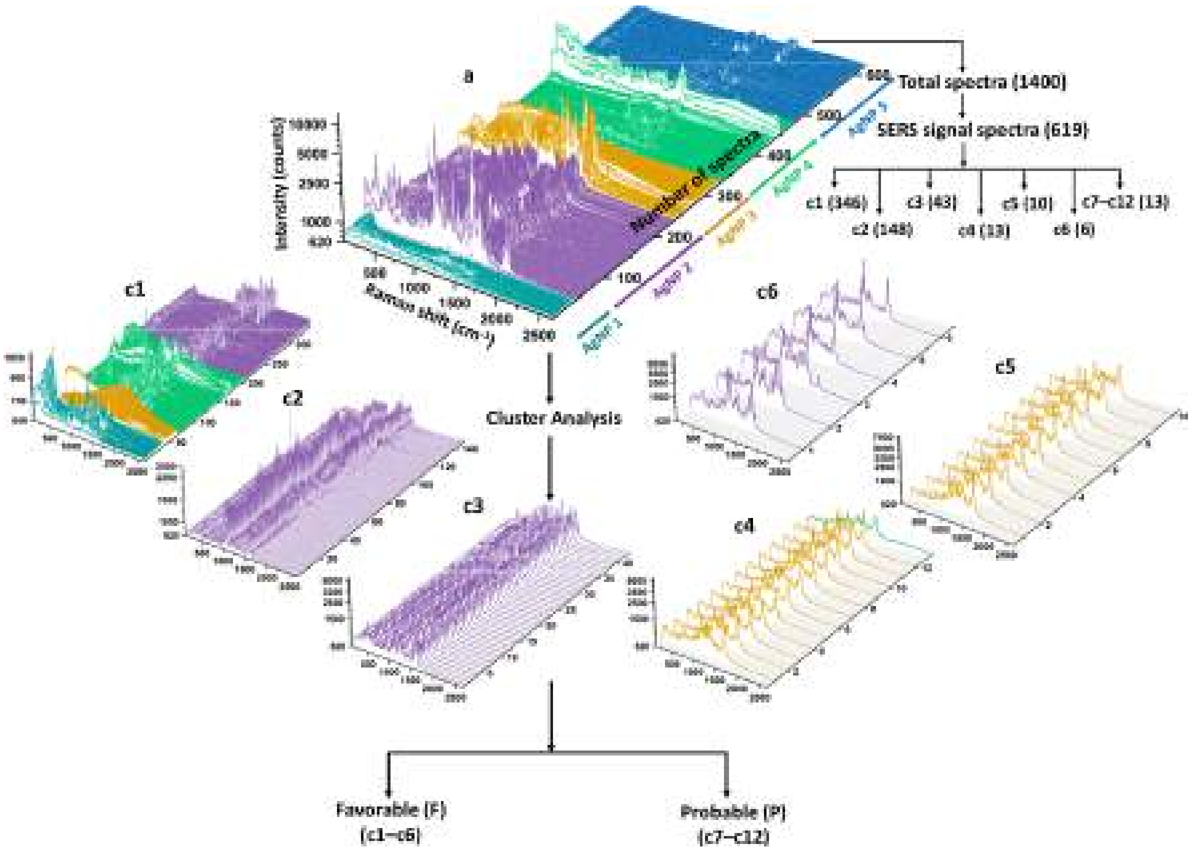

Figure 2. CA of time-dependent SP-SERS spectra leading to multiple spectral collections. (a) Waterfall stack of 619 spectra obtained from five individual AgNPs, where the *z*-axis indicates the number of spectra that are color coded for each AgNP under observation. c1−c6 and c7−c12 represent various clusters that consist of spectra based on their similarity after CA of (a). Finally, two subgroups, termed as F and P spectra, were obtained from different clusters based on their likelihood of appearance and intensities (see text).

entities, which are alike, based on specific features.[44] These spectra were used for CA, and the algorithm was run with various parameters such as tolerance limit, randomization seed, and noise threshold.[34] These technical terms, CA code, and the sequence of steps followed for running the algorithm have been explained in the SI, clustering methods and algorithms. All the spectra (1400) were grouped to 15 clusters. When more than 15 clusters were chosen, it resulted in the generation of certain identical clusters. We observed that when fixed values of the cluster center tolerance limit, randomization seed, noise-threshold, and same set of spectra and number of clusters were taken while running CA, it resulted in the same pattern of clusters, indicating that such clustering is representative of the set.

Two major categories were observed in CA based on the value of noise-threshold. One category corresponded to those spectra, which were above a noise-threshold, and others were below the threshold. The intensity of the signals was measured in terms of counts. The category with the intensity of signals of more than 80 contained 619 spectra displayed in Figure 2a. Each colored spectral group (Figure 2a) originated from an individual particle. Various colors in Figure 2 indicate a set with spectra obtained from five individual AgNPs. It is important to have some idea about the morphology and nature of the SERS-yielding AgNPs. It is equally important to know which types of orientations are preferred for which individual NPs. Hence, to have information about AgNPs and the orientations of citrate arising from the former, we have grouped SP-SERS spectra with high S/N in different clusters with various colors.

The remaining 781 spectra (Figure S8) out of 1400 belonged to a second category with intensities below the noise-threshold. Some spectra composed of cosmic rays also appeared that possessed sharp spikes and spurious features having a line width typically narrower than Raman bands.[45] Such cosmic rays/spikes[45] were removed from the signal spectra. It was done to avoid interference from such peaks in the spectral assignment.

Distinct spectra observed were shown in the waterfall plot (Figure 2a). In the set of 15 clusters, 3 clusters with 781, 35, and 5 spectra belonged to blank, broad, and noisy spectra, respectively (Figure S8). From the remaining 12 clusters, 6 clusters possessed 346, 148, 43, 13, 10, and 6 spectra, as shown in Figure 2 (c1−c6), and the other 6 clusters (c7−c12) possessed 4, 4, 2, 1, 1, and 1 spectra, respectively, presented in Figure S9. These 12 clusters possess spectra with better S/N and were further classified into two subgroups as F and P spectra based on their likelihood of appearance and intensities. An overview of the CA process is outlined in Figure 2.

Analysis of Structural Models of Citrate: F and P Spectra. The first group (F-spectra) with six clusters contained spectra with the probability of appearance greater than 1% (i.e., number of spectra > 5 per cluster) and had intensities in the range of 100−2000 counts. The other group (P-spectra) also possessed six clusters, where each cluster contained less than five spectra and had intensities in the range of 2000−12000. When adsorbates are present on the more uniform surfaces of NPs, they may give SERS with lower intensities but when they are present at hotspots, such as vertices or grooves, higher intensities could occur.[46] Also, enhanced signal intensity in P-spectra

Table 1. Various Binding Modes of $-COO^-$ Group of Citrate[a]

S. No.	Type of bond vibration	Coordination	Schematic representation
(1)	$\nu_{asym}(COO^-) > \nu_{sym}(COO^-)$	Unidentate (η^1)	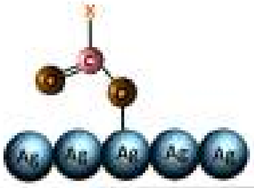
(2)	$\nu_{sym}(COO^-) > \nu_{asym}(COO^-)$	Bidentate (η^2)	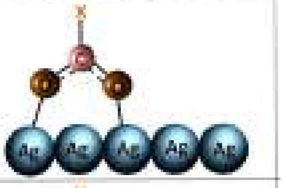
(3)	$\nu_{sym}(COO^-) > \nu_{asym}(COO^-)$	Bridging (μ)	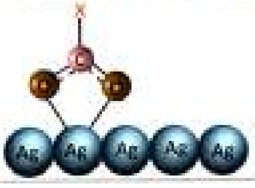

[a] X attached with $-COO^-$ indicates the remaining structure of citrate.

Scheme 1. Photodecarboxylation of Citrate to Acetonedicarboxylate in a Two-Step Process Due to the Presence of α-OH Group and Laser-Induced Plasmon Heating[a]

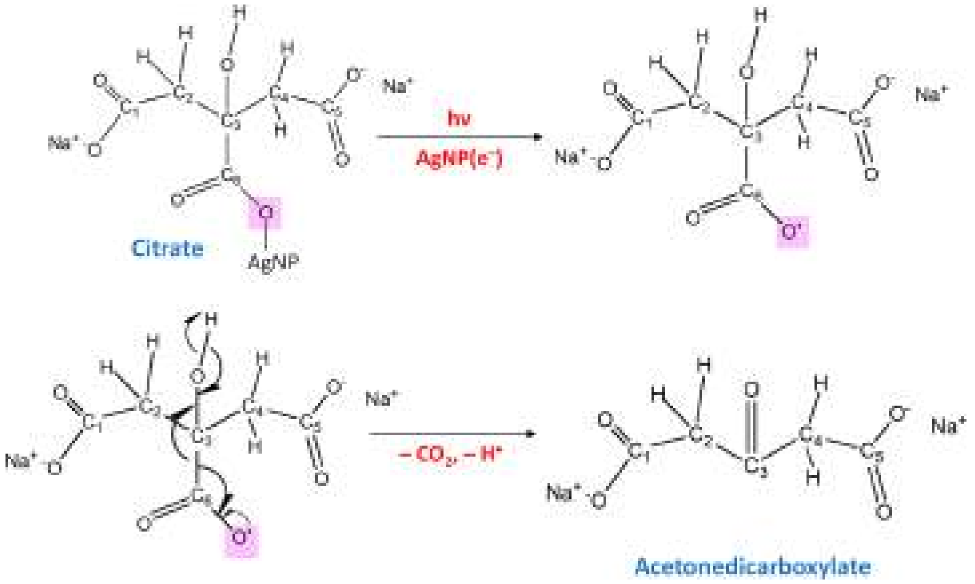

[a] Photolysis produces a free electron at both the C_6OO and the AgNP, which are shown. The product, acetonedicarboxylate, is bound to AgNPs.

compared to F-spectra is likely to be due to the laser-induced reshaping of AgNPs with time that leads to the preferential appearance of hotpots on the NP surface.[32] Chemical enhancement (CE) process that arises due to the formation of charge transfer complexes between the ligands and NPs are very likely to contribute to SERS intensity fluctuations. The contribution of CE may result in further enhancement of SERS intensities giving rise to the SERS-probable spectra. According to the literature, various binding modes of citrate such as unidentate (η^1),[11,19,41] bidentate (η^2),[7,11,19] bridging (μ),[11,15,19] combination (η^1, η^2, μ), and photodecomposed products[47,48] are reported. A list of all the η^1, η^2, and μ binding modes of one of the carboxylate (COO^-) of citrate is presented in Table 1.

An OH group in the α-position of carboxylic acid/carboxylate (Scheme 1) is known to enhance photodecarboxylation reaction, because this group can be transformed into an aldehyde or ketone group by two consecutive electron-transfer reactions.[49] Photodecarboxylation of citrate to acetonedicarboxylate has been described with the schematic shown below (Scheme 1). In such photodecarboxylation, along with the removal of CO_2, $H^\bullet$ is also produced. Understanding of the fate of $H^\bullet$ on the surface of AgNPs is elusive at present, and we have not attempted to study this.

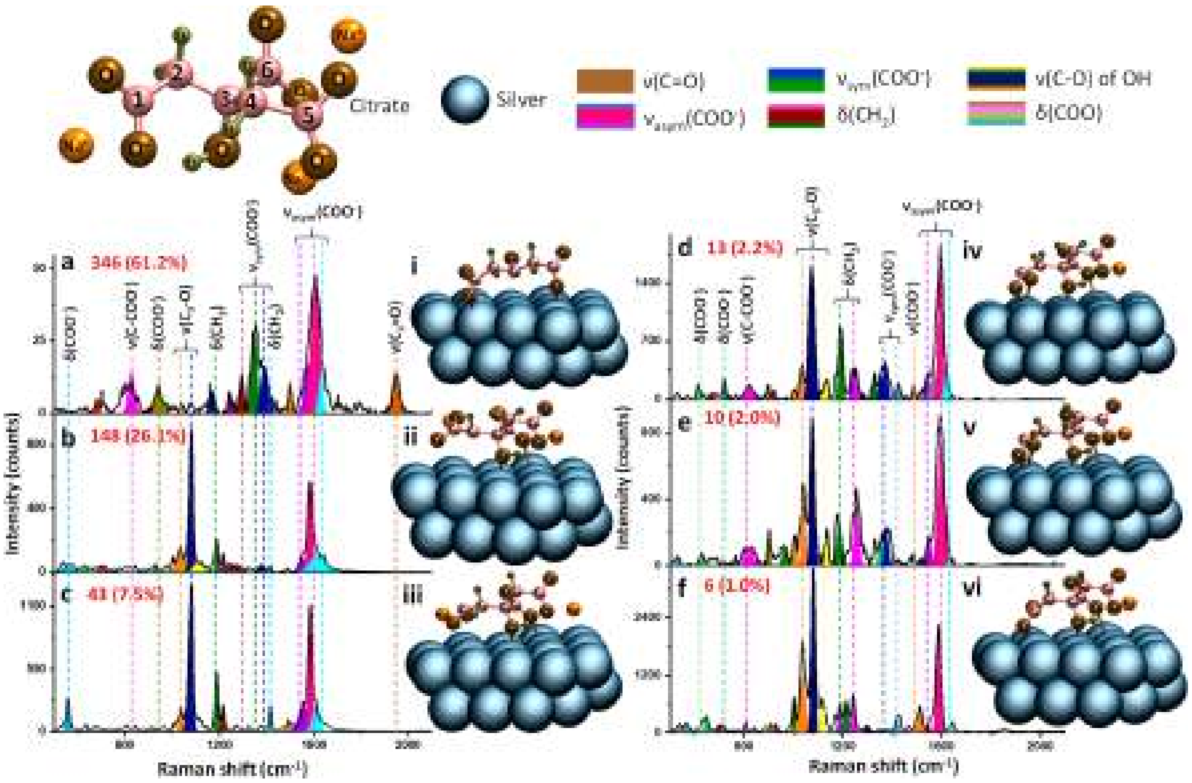

Figure 3. F-spectra with the percentage of spectral populations (a−f) and the corresponding structural models (i−vi) as insets. Specific features of relevance in each spectrum are indicated. TSC, silver atom, and vibrational bands are shown at the top. All six carbon atoms are numbered in TSC. Vibrational modes are color-coded.

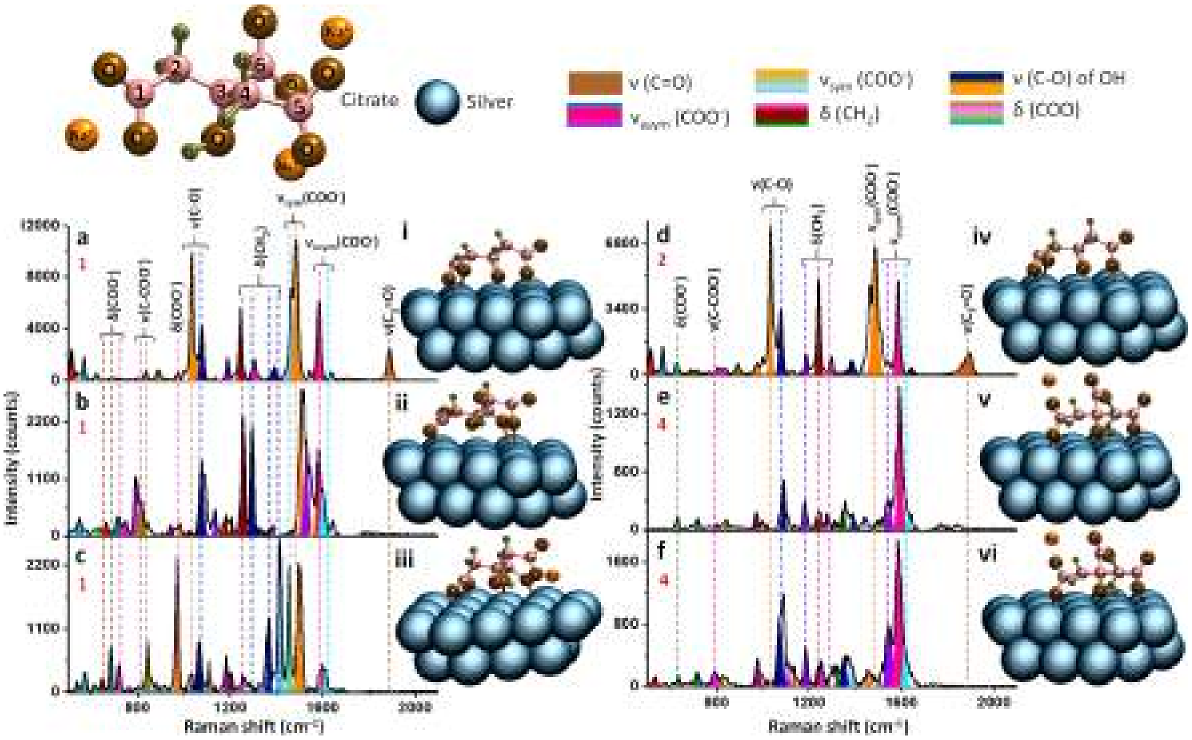

Figure 4. P-spectra and the number of their spectral populations (a−f), with the corresponding structural models (i−vi). Specific features of relevance in each spectrum are indicated. TSC, silver atom, and vibrational bands are shown at the top. All six carbon atoms are numbered in TSC. Vibrational modes are color-coded.

Citrate, a complex molecule possesses six carbon atoms with three COO^- and one α-OH group. Three COO^- groups are positioned as C_1 (terminal), C_5 (terminal), and C_6 (central), as shown in Scheme 1. The α-OH group is attached to C_3 as C_3−O.

Different adsorbate models were proposed based on the existing literature[11−16,18,19,47] and new DFT simulations. In the analysis sequence, at first, peak fitting of the F and P spectra (Figure 3 and Figure 4) was performed to evaluate the changes in the vibrational bands. Details about the peak fitting are discussed in the Materials and Methods section. Later, intensity differences of COO$^-$, C−O, and CH$_2$ peaks were considered to propose different binding modes and structures of citrate. In all the spectra, peak intensities of υ_{asym}(COO$^-$) vibrations were stronger than υ_{sym}(COO$^-$), suggesting that unidentate coordination of COO$^-$ (η^1) with Ag surface was largely preferred in SP-SERS.[14,41] In contrast, higher intensity of υ_{sym}(COO$^-$) indicates the bidentate or bridging (η^2 or μ) coordination. In the proposed models and DFT simulations of adsorbate structures, when COO$^-$ was bound with the Ag surface, Na$^+$ attached with the specific COO$^-$ was neglected that satisfies the coordination of COO$^-$ with Ag surface and charge balance. Proposed models corresponding to the spectra are discussed below.

F-Spectra. In the case of F-spectra, two types of spectra were observed dominantly. In the first type (Figure 3a), the peak corresponding to υ(C$_3$−O) was absent while in the other (Figure 3b−f) it was present. Peak intensity of υ(C$_3$−O) was higher than υ_{asym}(COO$^-$) in the spectra (Figure 3b,c,e,f), except in Figure 3d, where the intensity ratio was the reverse. Moreover, υ_{asym}(COO$^-$) vibrations were stronger than υ_{sym}(COO$^-$) in all spectra (Figure 3a−f).

In the first spectrum (Figure 3a) of the F category, υ_{asym}(COO$^-$) being dominant over υ_{sym}(COO$^-$), indicated the η^1 binding mode for C$_1$, C$_5$, and C$_6$ carboxylates.[41] However, a peak at 1946 cm^{-1} corresponding to υ(C$_3$═O) was observed that arises due to the photodecarboxylation of C$_6$OO$^-$, as shown in Scheme 1.[47] The third major peak at 1080−1120 cm^{-1} due to υ(C$_3$−O) of α-OH was absent, which indicated no direct interaction of C$_3$−O with the Ag surface.[19] Hence, the structural model in Figure 3a(i) with η^1 of C$_1$OO$^-$, C$_5$OO$^-$, and υ(C$_3$═O) was favored for the first spectrum (Figure 3a). This model contributes about 61.2% (346 spectra) of the total population (619 spectra) of SP-SERS. Spectra with photodecarboxylation is dominant. Due to localized plasmon heating, photodecarboxylated species can appear more even when the laser power is low.

In the spectrum of Figure 3b, the appearance of a peak at 1074−1080 cm^{-1} corresponds to direct interaction of υ(C$_3$−O) with the surface. The absence of the 1946 cm^{-1} peak indicates that this spectrum is devoid of decarboxylated species (Scheme 1). As υ_{asym}(COO$^-$) is stronger than υ_{sym}(COO$^-$), the η^1 mode is favored for C$_1$, C$_5$, and C$_6$. The absence of peaks in the region of 1345−1385 cm^{-1} suggests C$_1$OO$^-$ and C$_5$OO$^-$ away from the Ag surface. Thus, a model corresponding to η^1 of C$_6$OO$^-$ and υ(C$_3$−O) interacting with Ag surface is shown in Figure 3b(ii). This model contributes to 26.1% (148 spectra) of the total population.

The spectrum of Figure 3c is similar to Figure 3b, with the only differences in enhanced intensities of peaks at ∼1200 and ∼1400 cm^{-1}. These features are due to CH$_2$ vibrations and the enhanced intensity suggests that CH$_2$ groups vibrate perpendicular to the Ag surface. A new peak at 558 cm^{-1} is present, which is due to δ(COO$^-$).[17] Hence, the structural model of citrate for the spectrum in Figure 3c is similar to Figure 3b, with CH$_2$ groups perpendicular to the Ag surface and this model contributes 7.5% (43 spectra) to the total population.

In Figure 3d, four new peaks appear at 720, 820, 1324, and 1364 cm^{-1}, which are due to δ(COO$^-$) and υ_{sym}(COO$^-$). These vibrations arise when COO$^-$ is in the η^2 mode.[7,11,41] With the presence of δ(COO$^-$), we may suggest that either of the C$_1$OO$^-$ and C$_5$OO$^-$ remain away from the Ag surface. The higher intensity of υ_{asym}(COO$^-$) than υ_{sym}(COO$^-$) favors η^1 binding of C$_6$OO$^-$. Thus, we propose η^2 of C$_1$OO$^-$ and η^1 of C$_6$OO$^-$, along with υ(C$_3$−O) binding with the Ag surface, and the corresponding structural model is presented in Figure 3d(iv). This model contributes to 2.2% (13 spectra) of the total population.

Figure 3e is similar to Figure 3d with slight variations in δ(CH$_2$) vibrations. These variations do not cause much change in the COO$^-$ binding, rather the orientation of the CH$_2$ groups gets affected. The structural model is presented as Figure 3e(v), and it contributes 2.0% (10 spectra) to the total population.

The spectrum in Figure 3f has a new peak at 1508 cm^{-1}, which is due to the υ_{asym}(COO$^-$). This arises due to the η^1 binding of the terminal carboxylates (C$_1$OO$^-$ and C$_5$OO$^-$). Other peaks at ∼1080 cm^{-1} and the weak intensity of ∼1380 cm^{-1} are due to υ(C$_3$−O) and η^1 of C$_6$OO$^-$. With the presence of δ(COO$^-$), we suggest that either of the C$_1$OO$^-$ and C$_5$OO$^-$ remain away from the Ag surface. Hence, η^1 for both C$_1$OO$^-$ and C$_6$OO$^-$, and υ(C$_3$−O) are proposed for this spectrum, and a model is presented in Figure 3f(vi) that contributes to 1% of the total SP-SERS.

P-Spectra. In the P group (Figure 4) also, two types of spectra were observed. In the first type, the intensity of υ_{sym}(COO$^-$) was higher than υ_{asym}(COO$^-$) and υ(C$_3$−O), favoring η^2 and μ (Figure 4a,c,d) binding modes of COO$^-$, while in the second type, υ_{asym}(COO$^-$) vibrations were stronger than υ_{sym}(COO$^-$) and υ(C$_3$−O) (Figure 4b,e,f), favoring the η^1 binding mode.

In Figure 4a, the combination of υ_{sym}(COO$^-$) and δ(CH$_2$) vibrations that appear at 1388, 1462, and 1486 cm^{-1} were higher in intensity than υ_{asym}(COO$^-$) at 1584 cm^{-1}, indicating the η^2 mode of C$_1$OO$^-$, C$_5$OO$^-$, and C$_6$OO$^-$. However, the presence of 1890 cm^{-1} peak corresponds to υ(C$_3$═O) (Scheme 1). Also, two other peaks at 1033 and 1078 cm^{-1} due to υ(C−O) were present. The intense peak at 1033 cm^{-1} indicates the coupling of C−O with CH$_2$ vibrations. Thus, η^2 of C$_1$OO$^-$ with η^1 of C$_5$OO$^-$ and υ(C$_3$═O) are favored for this spectrum, and the corresponding adsorbate model is presented as Figure 4a(i). This spectrum appeared only once during the time-dependent spectra.

The spectrum in Figure 4b has υ_{asym}(COO$^-$) as a dominant feature with multiple peaks at 1512, 1530, 1585, and 1602 cm^{-1}, respectively, which indicate η^1 binding for all the three COO$^-$ groups. Peaks around ∼1380−1420 cm^{-1} due to υ_{sym}(COO$^-$) are absent. Enhanced δ(CH$_2$) features indicate that these vibrate perpendicular to the surface, and the peak intensity at ∼1077 cm^{-1} is weak, which supports weaker interaction of υ(C$_3$−O) with the surface. Thus, η^1 of C$_1$OO$^-$, C$_5$OO$^-$, and C$_6$OO$^-$ are favored for the spectrum, and the corresponding structure is shown in Figure 4b(ii). This spectrum also appeared once during SP-SERS.

In Figure 4c, υ_{sym}(COO$^-$) peaks are more dominant than υ_{asym}(COO$^-$), indicating the η^2 mode for C$_1$OO$^-$, C$_5$OO$^-$, and C$_6$OO$^-$. The presence of a strong peak at 970 cm^{-1} is due to δ(COO$^-$), leading to terminal carboxylates (C$_1$OO$^-$/C$_5$OO$^-$) away from the surface. The absence of the 1080 cm^{-1} peak depicts no binding of υ(C$_3$−O) with the surface. The structural model having a η^2 binding of C$_1$OO$^-$ and C$_6$OO$^-$ with C$_5$OO$^-$ remaining unbound is presented in Figure 4c(iii). This spectrum also appeared once in the set.

Table 2. Summary of Spectral Probability of Occurrence, Vibrational Features, Assignments, and Their Corresponding Binding Modes of Citrate Attributed to F and P Spectra

subgroup (type of cluster)	probability of occurrence/total SERS spectra (619)	major vibrational peaks (cm^{1}; intensity counts*)	vibrational assignments	binding modes	figures and structures
F(c1)	346	1605 > 1389, 1948	$\upsilon_{asym}(COO^-) > \upsilon_{sym}(COO^-)$, decarboxylated-$\upsilon(C_3{=}O)$	η^1 of C_1OO^- and C_5OO^-	Figure 3a,a(i)
F(c2)	148	1585, 1081, 1187 (227*), 1385 (absent)	$\upsilon_{asym}(COO^-$, $\upsilon(C_3-O)$, and $\delta(CH_2)$	η^1 of C_6OO^- and $\delta(CH_2)$	Figure 3b,b(ii)
F(c3)	43	1585, 1081, 1187 (553*), 1385 (absent)	$\upsilon_{asm}(COO^-)$, $\upsilon(C_3-O)$, and $\delta(CH_2)$	η^1 of C_6OO^- and $\delta(CH_2)$ ⊥ to Ag surface	Figure 3c,c(iii)
F(c4)	13	720, 820, 1324, 1586 > 1364, 1077, 1187 (885*)	$\upsilon_{asym}(COO^-) > \upsilon_{sym}(COO^-)$, $\delta(COO^-)$, $\upsilon(C_3-O)$, and $\delta(CH_2)$	η^1 of C_6OO^-, η^2 of C_1OO^- and $\delta(CH_2)$ ⊥ to Ag surface	Figure 3d,d(iv)
F(c5)	10	720, 820, 1324, 1586 > 1364, 1077, 1187 (250*)	$\delta(COO^-)$, $\upsilon_{asym}(COO^-) > \upsilon_{sym}(COO^-)$, $\upsilon(C_3O)$, and $\delta(CH_2)$	η^1 of C_6OO^-, η^2 of C_1OO^- and $\delta(CH_2)$	Figure 3e,e(v)
F(c6)	6	720, 820, 1508, 1586, 1077	$\delta(COO^-)$, $\upsilon_{asym}(COO^-) > \upsilon_{sym}(COO^-)$ and $\upsilon(C_3-O)$	η^1 of C_1OO^- and C_6OO^-	Figure 3f,f(vi)
P(c7)	4	1585 > 1364, 1077	$\upsilon_{asym}(COO^-) > \upsilon_{sym}(COO^-)$ and $\upsilon(C_3-O)$	η^1 of C_1OO and C_5OO^-	Figure 4f,4f(ui)
P(c8)	4	1586 > 1364, 1077	$\upsilon_{asym}(COO^-) > \upsilon_{sym}(COO^-)$ and $\upsilon(C_3-O)$	η^1 of C_1OO and C_5OO^-	Figure 4e,e(v)
P(c9)	2	1035 (10100*), (1388 and 1462 > 1486 and 1584), 1890	$\upsilon(C_3-O) + \delta(CH_2)$, $\upsilon_{sym}(COO) > \upsilon_{asym}(COO^-)$, $\delta(CH_2)$, and decarboxylated-$\upsilon(C_3{=}O)$	η^2 of C_1OO^- and η^1 of C_5OO^-	Figure 4d,d(iv)
P(c10)	1	(1365 and 1412 > (1586 and 1612), (1454, 1497), (720, 820, 970)	$\upsilon_{sym}(COO^-) > \upsilon_{asym}(COO^-)$, $\delta(CH_2]$, and $\delta(COO^-)$	η^3 of C_1OO^- and C_6OO^-	Figure 4c,c(iii)
P(c11)	1	1512, 1530, 1584, 1253, and 1293	$\upsilon_{asym}(COO^-) > \upsilon_{sym}(COO^-)$ and $\delta(CH_2)$	η^1 of C_1OO^-, C_5OO^-, C_6OO^-, and $\delta(CH_2)$ ⊥ to Ag surface	Figure 4b,b(ii)
P(c12)	1	1035 (7700*), (1388 and 1462 > 1486 and 1584), 1890	$\upsilon(C_3-O) + \delta(CH_2)$, $\upsilon_{sym}(COO^-) > \upsilon_{asym}(COO^-)$, $\delta(CH_2)$, and decarboxylated-$\upsilon(C_3{=}O)$	η^2 of C_1OO^- and η^1 of C_5OO^-	Figure 4a,a(i)

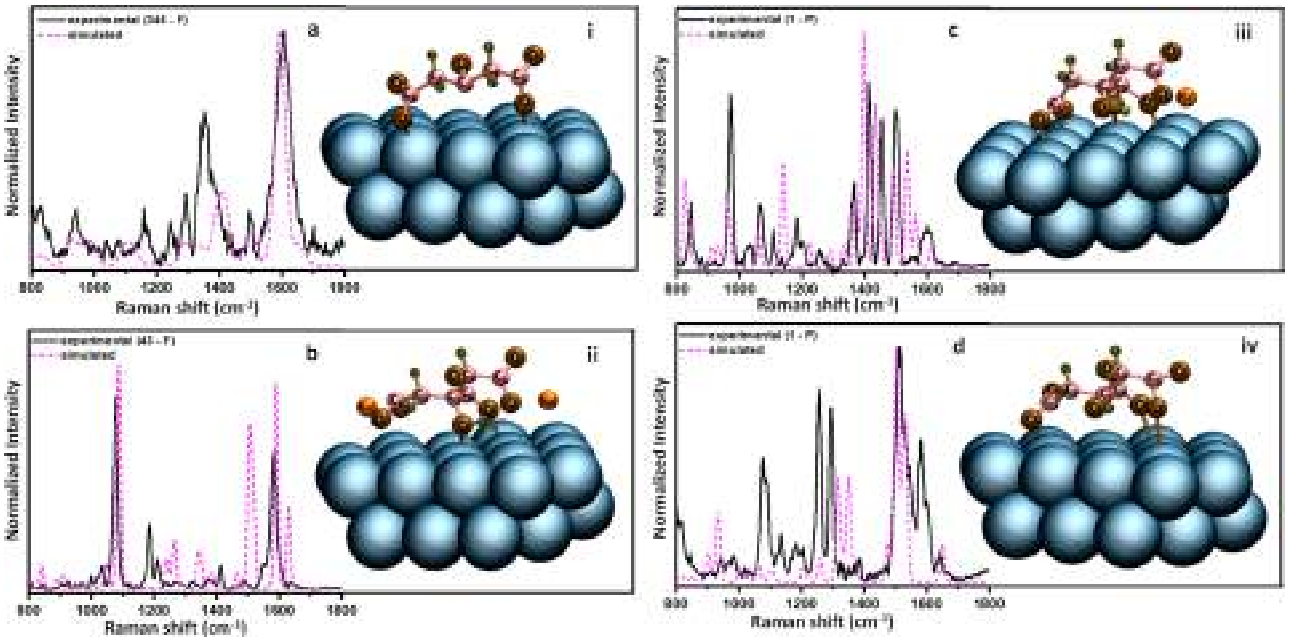

Figure 5. Comparison between simulated and experimental (F and P) spectra (a−d) and their corresponding optimized structures (i−iv) with various binding modes of COO^- and C−O. Simulated spectra of a, b, c, and d correspond to F-346 (Figure 3a), F-43 (Figure 3c), P-1 (Figure 4c), and P-1 (Figure 4b) spectra, respectively.

Figure 4d is similar to Figure 4a, with the only difference in intensities of 1585 and 1030 cm^{-1}. In the spectrum in Figure 4d, the 1030 cm^{-1} peak is more intense than that at 1585 cm^{-1}, while the spectrum in Figure 4a has the reverse. This indicates that $\upsilon(COO^-)$ and $\upsilon(C_3-O)$ are the same as shown in the structure shown in Figure 4a(i). However, slight variations are observed in the orientation with respect to the surface. This spectrum appeared twice in the set.

The spectra in Figure 4e,f have similar features with variations in peak intensities of ∼1580 and ∼1077 cm^{-1}. As the $\upsilon_{asym}(COO^-)$ peak is dominant over $\upsilon_{sym}(COO^-)$, we propose a structure with η^1 binding of C_1OO^- and C_5OO^-. The presence of the ∼1077 cm^{-1} peak confirms the binding of $\upsilon(C_3-O)$ with the surface. Hence, the structural model having η^1 of C_1OO^-, C_5OO^- with $\upsilon(C_3-O)$ is presented in the insets of Figure 4e(v) and f(vi). These spectra (Figure 4e,f) appeared four times in the set.

https://dx.doi.org/10.1021/acs.jpcc.0c09981
J. Phys. Chem. C 2021, 125, 3553−3566

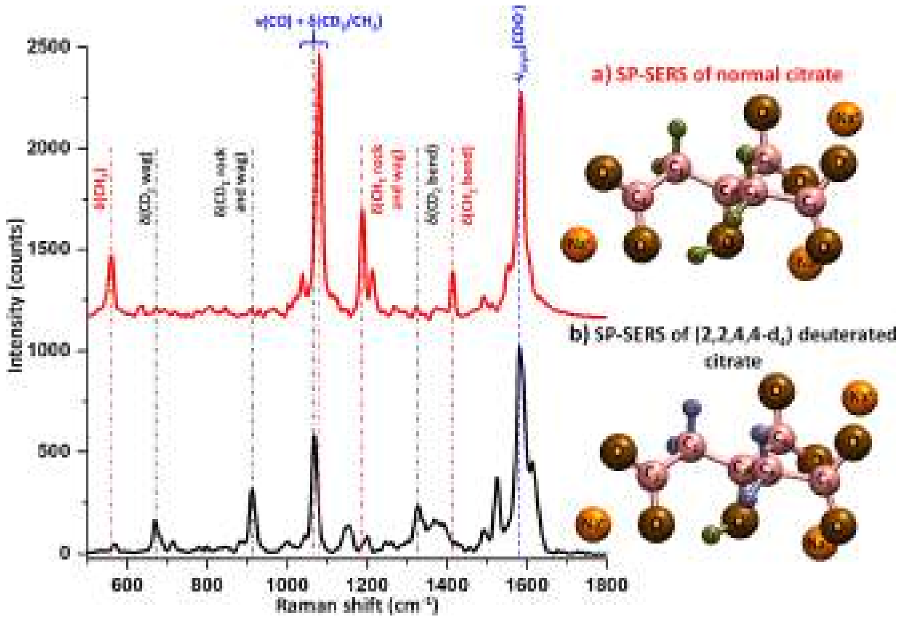

Figure 6. Comparison of SP-SERS spectra of normal citrate-capped AgNPs (a) and deuterated citrate-capped AgNPs (b). Structural models corresponding to normal citrate and deuterated citrate are shown next to the spectra. Spectral assignments are marked with dotted lines.

Scheme 2. Schematic Representation of Various Ligand Geometries of Citrate on the Crystallographic Planes of AgNPs, Shown in Two Tomographic Arrangements (I and II)[a]

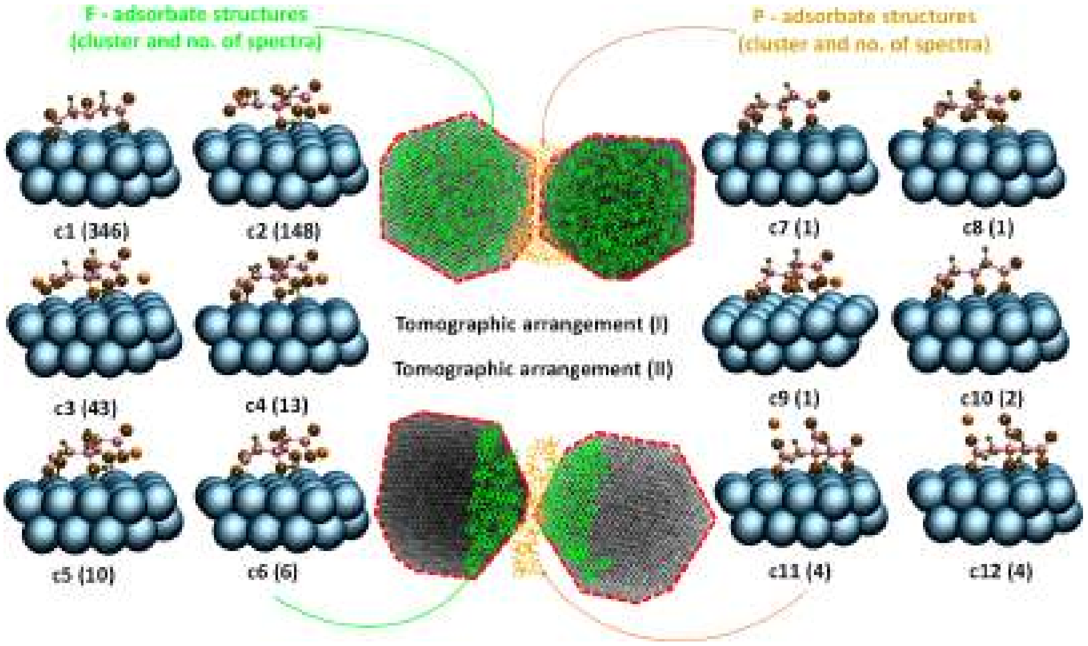

[a] A combination of all these structures lead to VT of citrate. The images of AgNPs shown are selected from HRTEM data and are used for illustrative purposes.

To make it easier for the reader to correlate the data, a summary of all the binding modes of citrate occurring in the two subgroups of F and P spectra are tabulated in Table 2.

Based on the proposed models, these structures were simulated according to the bonding interactions of the COO^- and α-OH groups to the NP surface, namely, η^1, η^2, and μ coordination or a combination of these. Interaction of citrate with the surface of AgNP was studied computationally by considering a few simplified model systems, such as a surface that was cut out from the bulk Ag crystal along the (111) plane, to largely mimic one of the facets of AgNPs. Frequency calculations were performed to assess the nature of $\upsilon(COO^-)$ and $\upsilon(C_3{-}O)$. The simplified model surface with 25 silver atoms provide sufficient space to accommodate all the possible interactions of citrate over the Ag surface. Although a larger model would have been considered, a lesser number of Ag atoms also made it feasible to conduct vibrational frequency calculations. Coordinates of the optimized structures of citrate, Ag_{55}, Ag_{25}, and Ag_{25}−citrate structures are mentioned in the Appendices of the SI. Four structures of citrate with different binding modes and a comparison between the experimental and simulated spectra, corresponding to F and P groups are presented in Figure 5a–d. The spectra displayed a positive correlation between the simulated and the experimental spectra with optimized structures of citrate as insets. It is evident that simulated spectra were sensitive toward the binding of COO^- with the Ag surface, through η^1, η^2, and μ coordination. The binding mode η^1 was favorable than η^2 and μ in most of the optimized structures (Figure 5).

However, some discrepancies were observed between the experimental and theoretical spectra, which are attributed to factors such as geometrical discrepancies between simulated models and experimentally accessible NPs, neglecting the influence of water present as a medium and larger surface coverage of citrate. The differences in experimental and simulated spectra could also be due to an admixture of binding modes of citrate for which there was no feasible way to perform simulations.

Insights about Citrate Binding Modes Using Isotopically Labeled Citrate-Capped AgNPs. In order to confirm that such modes of vibrations are due to citrate and variants of photocatalyzed products, time-dependent SP-SERS experiments were performed also with deuterated AgNPs. Deuterated citrate (2,2,4,4-d_4) was used for the synthesis of deuterium-labeled AgNPs using the modified Turkevich method.[33]

Synthesized deuterated AgNPs were characterized by UV–vis absorption spectroscopy, TEM, DFM, and plasmonic scattering spectroscopy (Figure S10). A comparative Raman plot was made between normal and deuterated TSC to understand the vibrational shifts appearing in the C and D vibrations (Figure S11). A similar CA was performed on the time-dependent SP-SERS of deuterated citrate-capped AgNPs, which resulted in two subgroups (F and P) according to their likelihood of spectral appearance and intensities (Figure S12). A comparative SP-SERS plot between deuterated and normal citrate is presented in Figure 6 to understand the changes in the vibrational bands described. Major features corresponding to $\upsilon_{\text{asym}}(COO^-)$ and $\upsilon(C-O)$ modes were present at similar peak positions in deuterated citrate-capped AgNPs as in normal AgNPs. However, variations were observed in CH_2 and CD_2 vibrations, marked with dotted lines in Figure 6.

A schematic below (Scheme 2) explains the various binding modes of citrate we have identified on dynamically changing individual AgNPs.

The center of the schematic has AgNPs capped with citrate molecules in two possible orientations (I and II) with varying hotspots and SERS favorable conditions. In one arrangement, adsorbates are present in-between the NPs (hotspot) and on the surface, while in the other arrangement, adsorbates are available at the hotspots and locations near the hotspots where strong plasmonic coupling takes place. Adsorbates present at the hotspot belong to the P-category, while adsorbates on the surface of NP or the places surrounding the hotspots belong to the F-category. A combination of all these multitude of orientations and binding modes help to reconstruct the three-dimensional structure of citrate on the surface of AgNPs, leading to VT of citrate-protected nanoparticles. Data collection and reconstruction of these orientations are similar to the steps used in tomographic reconstruction. Such a study can be used to probe the changing ligand geometry during changes in the particle, such as that which could occur during particle reconstruction upon laser-irradiation. Many of these binding modes and orientations of citrate may have been influenced by the change in temperature due to laser-induced heating. Most of the ligand structure information we have obtained corresponds to room temperature. However, some of the orientations may have arisen due to increased local plasmonic heating.[32] However, the incident laser power of 1.3 μW per NP is far less than the laser power (0.1–60 mW) used for other studies to evaluate local temperature (100–2000 K).[50−53] Richard-Lacroix and Deckert have reported that under SERS/TERS conditions, local temperature cannot be quantified exactly via the Boltzmann equation alone, and the antiStokes/Stokes ratio depends on more factors and not exclusively temperature.[50] Moreover, in the case of SP-SERS for polydisperse AgNPs, there are fluctuations caused in the SERS intensity with different locations of hotspots that makes it challenging to evaluate the localized temperature using the scattering ratio of antiStokes and Stokes lines. However, this is a way forward to evaluate the dependence of ligand orientations on the increase of temperature due to the localized plasmonic heating using coherent antiStokes Raman spectroscopy (CARS).[51] But, with fast spectral acquisition and enhanced computational capabilities and with improved models it will be possible to understand each one of the binding geometries existing on the nanoparticle surface. This knowledge will be useful in reconstructing the most of the ligand geometries possible on the nanoparticle, leading to VT of ligands at the single-particle level.

Limitations and Solutions of the Technique. Some of the limitations associated with the existing SP-SERS and VT techniques and their possible solutions are mentioned below.

1 The imaging of AgNPs by DFM-coupled confocal Raman microspectrometer lacks information about the morphology of AgNPs, but correlative FESEM with the above-mentioned integrated technique can be performed to precisely define the time-dependent morphology of NPs.
2 Several efficient software are available to match Raman spectrum of the unknown sample with the existing library of Raman spectra. Similarly, some library of orientations of a specific molecule can be developed to obtain an immediate 3D picture or reconstruct ligand on the surface of NPs.
3 Particle reshaping after performing time-dependent SERS leads to changes in NP but that gives mobility to ligands to adsorb at different facets for different orientations. However, better SERS-active and stable NPs with ligands having multitude of orientations can be utilized to work efficiently with the reconstruction and VT of ligands.

■ CONCLUSIONS

In this work, we have analyzed time-dependent SP-SERS spectra of citrate adsorbed on AgNPs. Studies were performed with 632.8 nm excitation at 1.3 μW incident power per NP. SP-SERS played an important role in capturing the rare adsorbate structures and intermediates of analytes on the NP surface. We performed CA on temporal SERS spectra to simplify and organize a set 1400 distinct spectra. This resulted in two subgroups of spectra based on their likelihood of appearance and intensities. The first group (F-spectra) where each cluster possessed spectral populations greater than 1% of the total and another (P-spectra) that contained below 1% of the spectra. These distinct spectra were correlated to the different binding modes, structures, and photocatalyzed variants of citrate adsorbed on the AgNP surface. Various binding modes were proposed, and DFT simulations were performed on them generating distinct spectra. The η^1 binding was more favorable than η^2 and μ binding of COO^- in most of the SP-SERS spectra. Sodium citrate (2,2,4,4-d_4) capped AgNPs were used to confirm the variations observed in the vibrational features. We demonstrated the general background and rationale for the development of VT of ligands protected nanoparticles with the necessary experimental and theoretical tools.

■ ASSOCIATED CONTENT

Supporting Information

The Supporting Information is available free of charge at https://pubs.acs.org/doi/10.1021/acs.jpcc.0c09981.

Figures S1−S12, Table S1, calculations SI−SII, Code I, references, and appendices (PDF)

■ AUTHOR INFORMATION

Corresponding Author

Thalappil Pradeep − *DST Unit on Nanoscience, Thematic Unit of Excellence, Department of Chemistry, Indian Institute of Technology Madras, Chennai 600036, India;* orcid.org/0000-0003-3174-534X; Phone: +91044-2257-4208; Email: pradeep@iitm.ac.in

Authors

Tripti Ahuja − *DST Unit on Nanoscience, Thematic Unit of Excellence, Department of Chemistry, Indian Institute of Technology Madras, Chennai 600036, India*

Kamalesh Chaudhari − *DST Unit on Nanoscience, Thematic Unit of Excellence, Department of Chemistry, Indian Institute of Technology Madras, Chennai 600036, India*

Ganesan Paramasivam − *DST Unit on Nanoscience, Thematic Unit of Excellence, Department of Chemistry, Indian Institute of Technology Madras, Chennai 600036, India*

Gopi Ragupathy − *DST Unit on Nanoscience, Thematic Unit of Excellence, Department of Chemistry, Indian Institute of Technology Madras, Chennai 600036, India*

Jyoti Sarita Mohanty − *DST Unit on Nanoscience, Thematic Unit of Excellence, Department of Chemistry, Indian Institute of Technology Madras, Chennai 600036, India*

Complete contact information is available at: https://pubs.acs.org/10.1021/acs.jpcc.0c09981

Author Contributions

[†]These authors contributed equally to this work. T.P. proposed the idea of VT of ligands. T.A., K.C., and T.P. conceived the experiments. T.A. performed all SP-SERS measurements. T.A. did data analysis. K.C. contributed in programming and coding. G.P. and G.R. performed DFT simulations. J.S.M. helped with TEM measurements.

Notes

The authors declare no competing financial interest.

■ ACKNOWLEDGMENTS

We thank the Department of Science and Technology, Government of India for constantly supporting our research activities. T.A. acknowledges an Institute Graduate Fellowship. G.P. is thankful for an Institute Postdoctoral Fellowship. We thank Mr. Amoghavarsha Kini, Mr. Gaurav Vishwakarma, and Mr. Pillalamarri Srikrishnarka for their valuable input in relation to this work.

■ ABBREVIATIONS

AgNPs, silver nanoparticles
SERS, surface-enhanced Raman scattering
SP-SERS, single-particle surface-enhanced Raman scattering
F, favorable
P, probable
DFT, density functional theory
DFM, dark-field microscopy
CRM, confocal Raman microspectroscopy
CA, cluster analysis

■ REFERENCES

(1) Henglein, A.; Giersig, M. Formation of Colloidal Silver Nanoparticles: Capping Action of Citrate. *J. Phys. Chem. B* **1999**, *103*, 9533−9539.

(2) Grzelczak, M.; Pérez-Juste, J.; Mulvaney, P.; Liz-Marzán, L. M. Shape Control in Gold Nanoparticle Synthesis. *Chem. Soc. Rev.* **2008**, *37*, 1783−1791.

(3) Ke, F.; Qiu, L.; Yuan, Y.; Jiang, X.; Zhu, J. Fe_3O_4 Nanoparticles Were Synthesized by a Solvothermal Method as Reported Previously. *J. Mater. Chem.* **2012**, *125*, 1−8.

(4) Wu, G.-W.; He, S.-B.; Peng, H.-P.; Deng, H.-H.; Liu, A.-L.; Lin, X.-H.; Xia, X.-H.; Chen, W. Citrate-Capped Platinum Nanoparticle as a Smart Probe for Ultrasensitive Mercury Sensing. *Anal. Chem.* **2014**, *86*, 10955−10960.

(5) Ojea-Jiménez, I.; López, X.; Arbiol, J.; Puntes, V. Citrate-Coated Gold Nanoparticles as Smart Scavengers for Mercury(II) Removal from Polluted Waters. *ACS Nano* **2012**, *6*, 2253−2260.

(6) Choi, C. K. K.; Chiu, Y. T. E.; Zhuo, X.; Liu, Y.; Pak, C. Y.; Liu, X.; Tse, Y. L. S.; Wang, J.; Choi, C. H. J. Dopamine-Mediated Assembly of Citrate-Capped Plasmonic Nanoparticles into Stable Core-Shell Nanoworms for Intracellular Applications. *ACS Nano* **2019**, *13*, 5864−5884.

(7) Grys, D.-B.; de Nijs, B.; Salmon, A. R.; Huang, J.; Wang, W.; Chen, W.-H.; Scherman, O. A.; Baumberg, J. J. Citrate Coordination and Bridging of Gold Nanoparticles: The Role of Gold Adatoms in AuNP Aging. *ACS Nano* **2020**, *14*, 8689−8696.

(8) Xie, H.; Tkachenko, A. G.; Glomm, W. R.; Ryan, J. A.; Brennaman, M. K.; Papanikolas, J. M.; Franzen, S.; Feldheim, D. L. Critical Flocculation Concentrations, Binding Isotherms, and Ligand Exchange Properties of Peptide-Modified Gold Nanoparticles Studied by UV - Visible, Fluorescence, and Time-Correlated Single Photon Counting Spectroscopies. *Anal. Chem.* **2003**, *75*, 5797−5805.

(9) Lin, S.-Y.; Tsai, Y.-T.; Chen, C.-C.; Lin, C.-M.; Chen, C.-h. Two-Step Functionalization of Neutral and Positively Charged Thiols onto Citrate-Stabilized Au Nanoparticles. *J. Phys. Chem. B* **2004**, *108*, 2134−2139.

(10) Polte, J.; Ahner, T. T.; Delissen, F.; Sokolov, S.; Emmerling, F.; Thunemann, A. F.; Kraehnert, R. Mechanism of Gold Nanoparticle Formation in the Classical Citrate Synthesis Method Derived from Coupled in Situ XANES and SAXS Evaluation. *J. Am. Chem. Soc.* **2010**, *132*, 1296−1301.

(11) Glusker, J. P. Citrate Conformation and Chelation: Enzymatic Implications. *Acc. Chem. Res.* **1980**, *13*, 345−352.

(12) Monti, S.; Barcaro, G.; Sementa, L.; Carravetta, V.; Ågren, H. Characterization of the Adsorption Dynamics of Trisodium Citrate on Gold in Water Solution. *RSC Adv.* **2017**, *7*, 49655−49663.

(13) Floate, S.; Hosseini, M.; Arshadi, M. R.; Ritson, D.; Young, K. L.; Nichols, R. J. An In-Situ Infrared Spectroscopic Study of the Adsorption of Citrate on Au(111) Electrodes. *J. Electroanal. Chem.* **2003**, *542*, 67−74.

(14) Li, M.; Xiao, Y.; Zhang, Z.; Yu, J. Bimodal Sintered Silver Nanoparticle Paste with Ultrahigh Thermal Conductivity and Shear Strength for High Temperature Thermal Interface Material Applications. *ACS Appl. Mater. Interfaces* **2015**, *7*, 9157−9168.

(15) Al-Johani, H.; Abou-Hamad, E.; Jedidi, A.; Widdifield, C. M.; Viger-Gravel, J.; Sangaru, S. S.; Gajan, D.; Anjum, D. H.; Ould-Chikh,

S.; Hedhili, M. N.; et al. The Structure and Binding Mode of Citrate in the Stabilization of Gold Nanoparticles. *Nat. Chem.* **2017**, *9*, 890−895.

(16) Mikhlin, Y. L.; Vorobyev, S. A.; Saikova, S. V.; Vishnyakova, E. A.; Romanchenko, A. S.; Zharkov, S. M.; Larichev, Y. V. On the Nature of Citrate-Derived Surface Species on Ag Nanoparticles: Insights from X-Ray Photoelectron Spectroscopy. *Appl. Surf. Sci.* **2018**, *427*, 687−694.

(17) Munro, C. H.; Smith, W. E.; Garner, M.; Clarkson, J.; White, P. C. Characterization of the Surface of a Citrate-Reduced Colloid Optimized for Use as a Substrate for Surface-Enhanced Resonance Raman-Scattering. *Langmuir* **1995**, *11*, 3712−3720.

(18) Wulandari, P.; Nagahiro, T.; Fukada, N.; Kimura, Y.; Niwano, M.; Tamada, K. Characterization of Citrates on Gold and Silver Nanoparticles. *J. Colloid Interface Sci.* **2015**, *438*, 244−248.

(19) Park, J. W.; Shumaker-Parry, J. S. Structural Study of Citrate Layers on Gold Nanoparticles: Role of Intermolecular Interactions in Stabilizing Nanoparticles. *J. Am. Chem. Soc.* **2014**, *136*, 1907−1921.

(20) Biggs, S.; Mulvaney, P.; Zukoski, C. F.; Grieser, F. Study of Anion Adsorption at the Gold-Aqueous Solution Interface by Atomic Force Microscopy. *J. Am. Chem. Soc.* **1994**, *116*, 9150−9157.

(21) Lin, Y.; Pan, G.-B.; Su, G.-J.; Fang, X.-H.; Wan, L.-J.; Bai, C.-L. Study of Citrate Adsorbed on the Au(111) Surface. *Langmuir* **2003**, *19*, 10000−10003.

(22) Wulandari, P.; Nagahiro, T.; Michioka, K.; Tamada, K.; Ishibashi, K.; Kimura, Y.; Niwano, M. Coordination of Carboxylate on Metal Nanoparticles Characterized by Fourier Transform Infrared Spectroscopy. *Chem. Lett.* **2008**, *37*, 888−889.

(23) Shi, X.; Li, H.-W.; Ying, Y.-L.; Liu, C.; Zhang, L.; Long, Y.-T. In Situ Monitoring of Catalytic Process Variations in a Single Nanowire by Dark-Field-Assisted Surface-Enhanced Raman Spectroscopy. *Chem. Commun.* **2016**, *52*, 1044−1047.

(24) Nie, S.; Emory, S. R. Probing Single Molecules and Single Nanoparticles by Surface-Enhanced Raman Scattering. *Science* **1997**, *275*, 1102−1106.

(25) Kang, B.; Austin, L. A.; El-Sayed, M. A. Real-Time Molecular Imaging throughout the Entire Cell Cycle by Targeted Plasmonic-Enhanced Rayleigh/Raman Spectroscopy. *Nano Lett.* **2012**, *12*, 5369−5375.

(26) Kang, B.; Austin, L. A.; El-Sayed, M. A. Observing Real-Time Molecular Event Dynamics of Apoptosis in Living Cancer Cells Using Nuclear-Targeted Plasmonically Enhanced Raman Nanoprobes. *ACS Nano* **2014**, *8*, 4883−4892.

(27) Perassi, E. M.; Hrelescu, C.; Wisnet, A.; Döblinger, M.; Scheu, C.; Jäckel, F.; Coronado, E. A.; Feldmann, J. Quantitative Understanding of the Optical Properties of a Single, Complex-Shaped Gold Nanoparticle from Experiment and Theory. *ACS Nano* **2014**, *8*, 4395−4402.

(28) Park, J. W.; Shumaker-Parry, J. S. Strong Resistance of Citrate Anions on Metal Nanoparticles to Desorption under Thiol Functionalization. *ACS Nano* **2015**, *9*, 1665−1682.

(29) Zhang, Z.; Bando, K.; Mochizuki, K.; Taguchi, A.; Fujita, K.; Kawata, S. Quantitative Evaluation of Surface-Enhanced Raman Scattering Nanoparticles for Intracellular PH Sensing at a Single Particle Level. *Anal. Chem.* **2019**, *91*, 3254−3262.

(30) Kleinman, S. L.; Ringe, E.; Valley, N.; Wustholz, K. L.; Phillips, E.; Scheidt, K. A.; Schatz, G. C.; Van Duyne, R. P. Single-Molecule Surface-Enhanced Raman Spectroscopy of Crystal Violet Isotopologues: Theory and Experiment. *J. Am. Chem. Soc.* **2011**, *133*, 4115−4122.

(31) Wilson, A. J.; Willets, K. A. Visualizing Site-Specific Redox Potentials on the Surface of Plasmonic Nanoparticle Aggregates with Superlocalization SERS Microscopy. *Nano Lett.* **2014**, *14*, 939−945.

(32) Chaudhari, K.; Ahuja, T.; Murugesan, V.; Subramanian, V.; Ganayee, M. A.; Thundat, T.; Pradeep, T. Appearance of SERS Activity in Single Silver Nanoparticles by Laser-Induced Reshaping. *Nanoscale* **2019**, *11*, 321−330.

(33) Kimling, J.; Maier, M.; Okenve, B.; Kotaidis, V.; Ballot, H.; Plech, A. Turkevich Method for Gold Nanoparticle Synthesis Revisited. *J. Phys. Chem. B* **2006**, *110*, 15700−15707.

(34) Rueden, C. T.; Schindelin, J.; Hiner, M. C.; DeZonia, B. E.; Walter, A. E.; Arena, E. T.; Eliceiri, K. W. ImageJ2: ImageJ for the next Generation of Scientific Image Data. *BMC Bioinf.* **2017**, *18*, 1−26.

(35) Frisch, M. J.; Trucks, G. W.; Schlegel, H. B.; Scuseria, G. E.; Robb, M. A.; Cheeseman, J. R.; Scalmani, G.; Barone, V.; Mennucci, B.; Petersson, G. A.;et al.*Gaussian*; Gaussian, Inc: Wallingford, CT, 2009.

(36) Yang, Y.; Weaver, M. N.; Merz, K. M. Assessment of the "6-31+Gt; + LANL2DZ" Mixed Basis Set Coupled with Density Functional Theory Methods and the Effective Core Potential: Prediction of Heats of Formation and Ionization Potentials for First-Row-Transition-Metal Complexes. *J. Phys. Chem. A* **2009**, *113*, 9843−9851.

(37) Hehre, W. J. Ab Initio Molecular Orbital Theory. *Acc. Chem. Res.* **1976**, *9*, 399−406.

(38) Sinha, P.; Boesch, S. E.; Gu, C.; Wheeler, R. A.; Wilson, A. K. Harmonic Vibrational Frequencies: Scaling Factors for HF, B3LYP, and MP2Methods in Combination with Correlation Consistent Basis Sets. *J. Phys. Chem. A* **2004**, *108*, 9213−9217.

(39) Merrick, J. P.; Moran, D.; Radom, L. An Evaluation of Harmonic Vibrational Frequency Scale Factors. *J. Phys. Chem. A* **2007**, *111*, 11683−11700.

(40) Zhang, R.; Zhang, Y.; Dong, Z. C.; Jiang, S.; Zhang, C.; Chen, L. G.; Zhang, L.; Liao, Y.; Aizpurua, J.; Luo, Y.; et al. Chemical Mapping of a Single Molecule by Plasmon-Enhanced Raman Scattering. *Nature* **2013**, *498*, 82−86.

(41) Deacon, G. B.; Phillips, R. J. Relationships between the Carbon-Oxygen Stretching Frequencies of Carboxylato Complexes and the Type of Carboxylate Coordination. *Coord. Chem. Rev.* **1980**, *33*, 227−250.

(42) Vinogradova, E.; Tlahuice-Flores, A.; Velazquez-Salazar, J. J.; Larios-Rodriguez, E.; Jose-Yacaman, M. Surface-Enhanced Raman Scattering of N-Acetylneuraminic Acid on Silver Nanoparticle Surface. *J. Raman Spectrosc.* **2014**, *45*, 730−735.

(43) Anil, K. J.; Dubes, R. C. *Algorithms for Clustering Data*; Prentice Hall: Englewood Cliffs, NJ, 1988.

(44) Hu, W.; Duan, S.; Luo, Y. Theoretical Modeling of Surface and Tip-Enhanced Raman Spectroscopies. *Wiley Interdiscip. Rev.: Comput. Mol. Sci.* **2017**, *7*, e1293.

(45) Gautam, R.; Vanga, S.; Ariese, F.; Umapathy, S. Review of Multidimensional Data Processing Approaches for Raman and Infrared Spectroscopy. *EPJ. Technol. Instrum.* **2015**, *2*, 1−38.

(46) Wei, H.; Xu, H. Hot Spots in Different Metal Nanostructures for Plasmon-Enhanced Raman Spectroscopy. *Nanoscale* **2013**, *5*, 10794−10805.

(47) Kumari, G.; Zhang, X.; Devasia, D.; Heo, J.; Jain, P. K. Watching Visible Light-Driven CO2 Reduction on a Plasmonic Nanoparticle Catalyst. *ACS Nano* **2018**, *12*, 8330−8340.

(48) Borer, P.; Hug, S. J.; Sulzberger, B.; Kraemer, S. M.; Kretzschmar, R. Photolysis of Citrate on the Surface of Lepidocrocite: An in Situ Attenuated Total Reflection Infrared Spectroscopy Study. *J. Phys. Chem. C* **2007**, *111*, 10560−10569.

(49) Abrahamson, H. B.; Rezvani, A. B.; Brushmiller, J. G. Photochemical and Spectroscopic Studies of Complexes, of Iron(III) with Citric Acid and Other Carboxylic Acids. *Inorg. Chim. Acta* **1994**, *226*, 117−127.

(50) Richard-Lacroix, M.; Deckert, V. Direct Molecular-Level near-Field Plasmon and Temperature Assessment in a Single Plasmonic Hotspot. *Light: Sci. Appl.* **2020**, *9*, 1−13.

(51) Zhang, C.; Wang, J.; Jasensky, J.; Chen, Z. Molecular Orientation Analysis of Alkyl Methylene Groups from Quantitative Coherent Anti-Stokes Raman Scattering Spectroscopy. *J. Phys. Chem. Lett.* **2015**, *6*, 1369−1374.

(52) Pozzi, E. A.; Zrimsek, A. B.; Lethiec, C. M.; Schatz, G. C.; Hersam, M. C.; Van Duyne, R. P. Evaluating Single-Molecule Stokes and Anti-Stokes SERS for Nanoscale Thermometry. *J. Phys. Chem. C* **2015**, *119*, 21116−21124.

(53) Sun, Y.; Yanagisawa, M.; Kunimoto, M.; Nakamura, M.; Homma, T. Estimated Phase Transition and Melting Temperature of APTES

Self-Assembled Monolayer Using Surface-Enhanced Anti-Stokes and Stokes Raman Scattering. *Appl. Surf. Sci.* **2016**, *363*, 572−577.

Supporting Information

Toward Vibrational Tomography of Citrate on Dynamically Changing Individual Silver Nanoparticles

Tripti Ahuja,[†] Kamalesh Chaudhari,[†] Ganesan Paramasivam, Gopi Ragupathy, Jyoti Sarita Mohanty, and Thalappil Pradeep*

DST Unit on Nanoscience, Thematic Unit of Excellence, Department of Chemistry, Indian Institute of Technology Madras, Chennai, India

Tel: +91044-2257-4208, E-mail: pradeep@iitm.ac.in

[†]Equal contribution

*corresponding author

Keywords: silver nanoparticles, surface-enhanced Raman scattering, citrate, single-particle spectroscopy, adsorbate structure, cluster analysis

Table of Contents

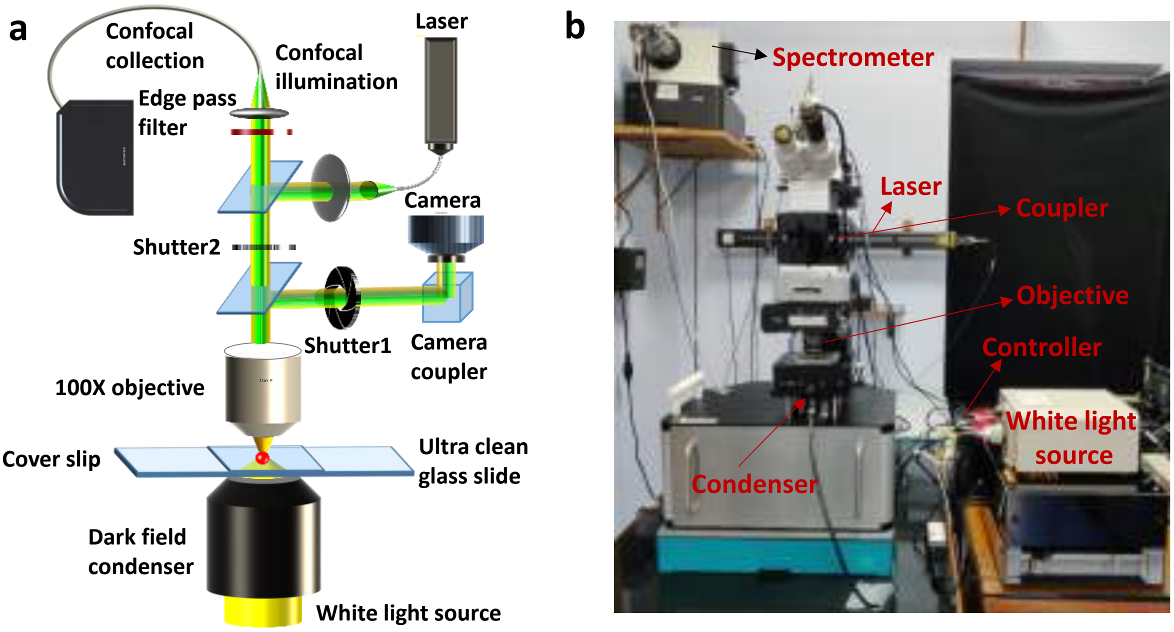

Figure S1. (a) Schematic representation of the set-up for dark field microscopy coupled with confocal Raman microspectrometer, and (b) optical photograph of the set-up presented in (a).

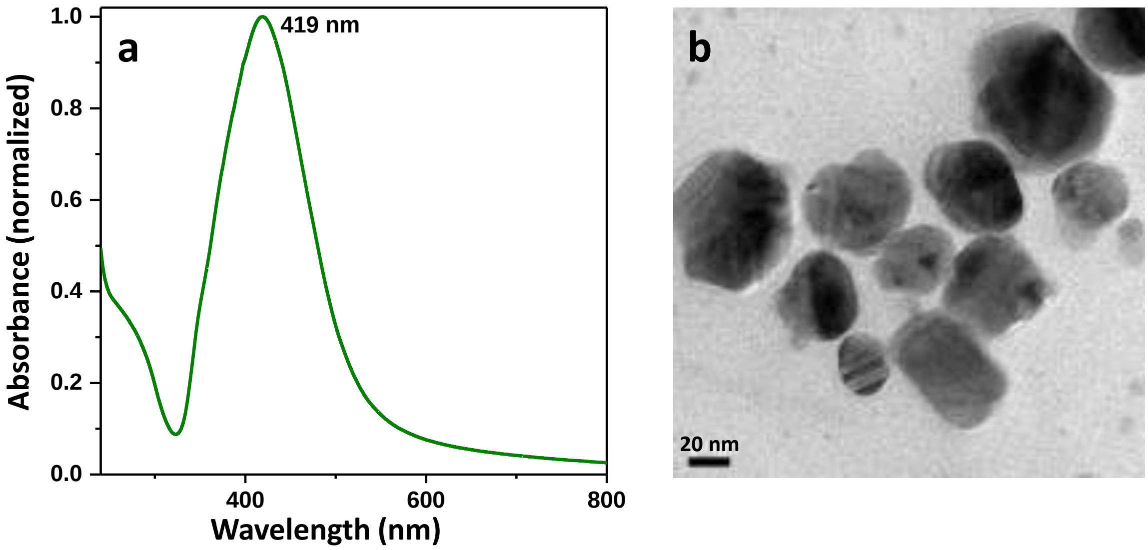

Figure S2. Characterization of citrate-capped AgNPs. (a) UV-visible absorption spectrum and (b) TEM image of as-synthesized AgNPs.

Calculation SI. Laser power incident per nanoparticle:

Average diameter (D) of AgNPs = 50 nm

Average radius (R) of AgNPs = 25 nm

Area for spherical NPs – ($A_1 = 4\pi R^2$) is 7850 nm^2

Spot size of laser beam – $A_2 = \pi r^2$ and radius of beam spot (r) = $(1.22 \times \lambda \times f/d)$, where λ is wavelength of incident laser light (632.8 nm), f is focal length of objective (1.8 mm for 100 X objective) and d is beam diameter (1.22 mm)

r = (1.22 x 632.8 nm x 1.8 mm)/1.22 mm = 1139.04 nm or 1.14 μm

$A_2 = 3.14 \times 1139.04 \times 1139.04 = 4.073\times10^6$ nm^2

Laser power at laser spot size (4.073×10^6 nm^2) was 650 μW

So, for 1 nm^2 size laser power is 159.6×10^{-6} μW

Laser power per NP (A_1 = 7850 nm^2) is 1.3 μW

Calculation SII. Laser power absorbed per nanoparticle:

Absorption/extinction efficiency (Q_{ext}) of NP, $Q_{ext} = \sigma_{eff}/\pi r^2$, where σ_{eff} is the extinction coefficient/cross-section, and r is the radius of the NP.

From UV-visible data of AgNPs, Absorbance (A) = ξcl, A = 0.532, c is concentration of NPs = 0.333×10^{-4} $molL^{-1}$, l is length of cuvette = 1 cm, thus, ξ (molar extinction coefficient) = 1.598×10^7.

$\sigma_{eff} = (\xi \times 1000 \times 2.303)/N_A = 0.611\times10^{-13}$, N_A is the Avogadro number.

$Q_{ext} = 7.787\times10^{-4}$
Laser power absorbed per NP = laser intensity x Q_{ext} = 650 μW x 7.787×10^{-4} = 0.5061 μW or ~506 nW.

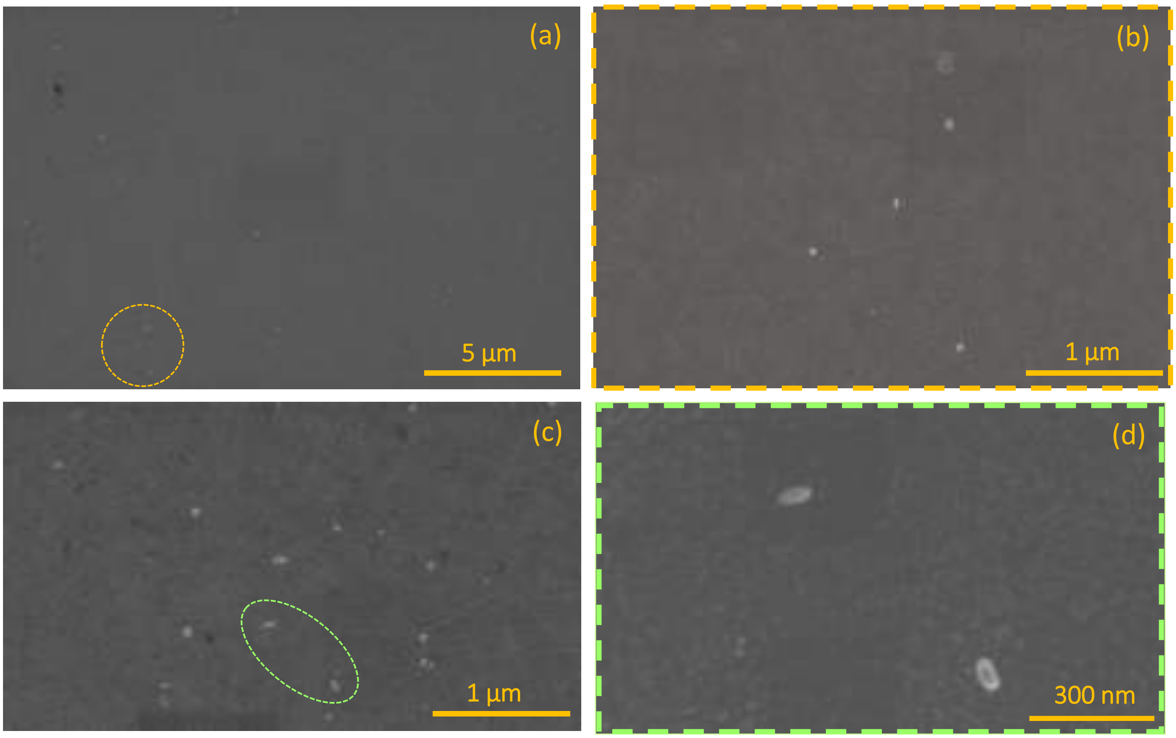

Figure S3. FESEM images of AgNPs immobilized on an ITO glass slide. (a) Large area FESEM image, (b) magnified image of the encircled area of (a), (c) another large area FESEM image with 5 times higher magnification, and (d) magnified image of the encircled area of (c).

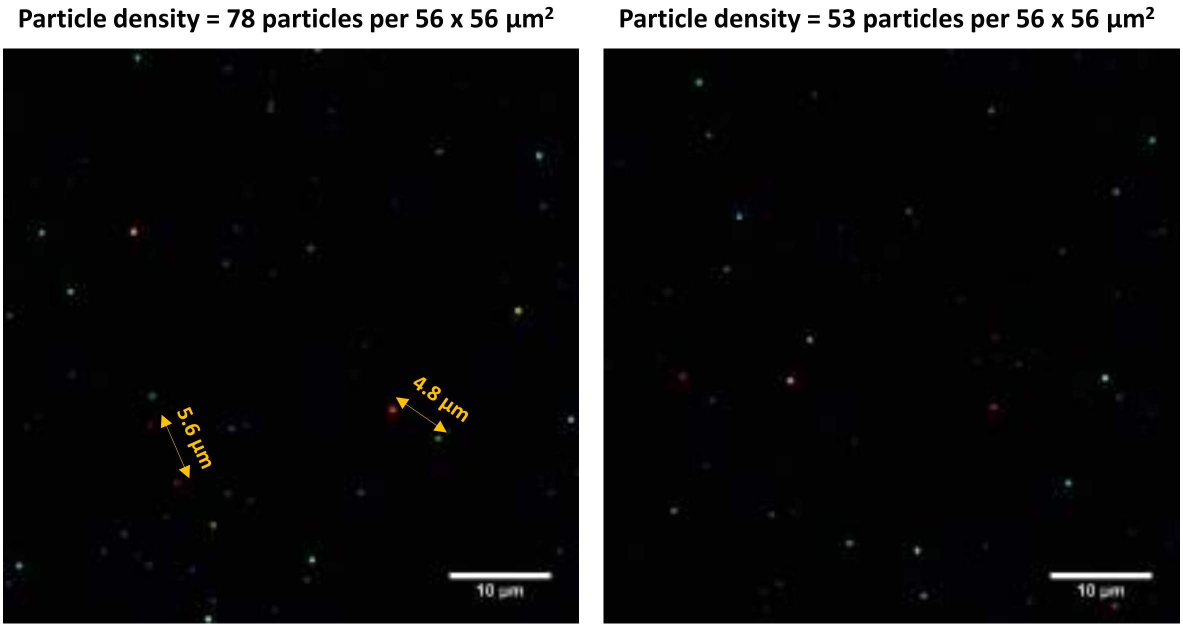
Particle density = 78 particles per 56 x 56 μm^2

Particle density = 53 particles per 56 x 56 μm^2

Figure S4. Particle density calculations for the immobilized AgNPs used for SP-SERS. The particle density calculations were performed using DFM images with Image J software. Inter-particle distances are also mentioned in the DFM images.

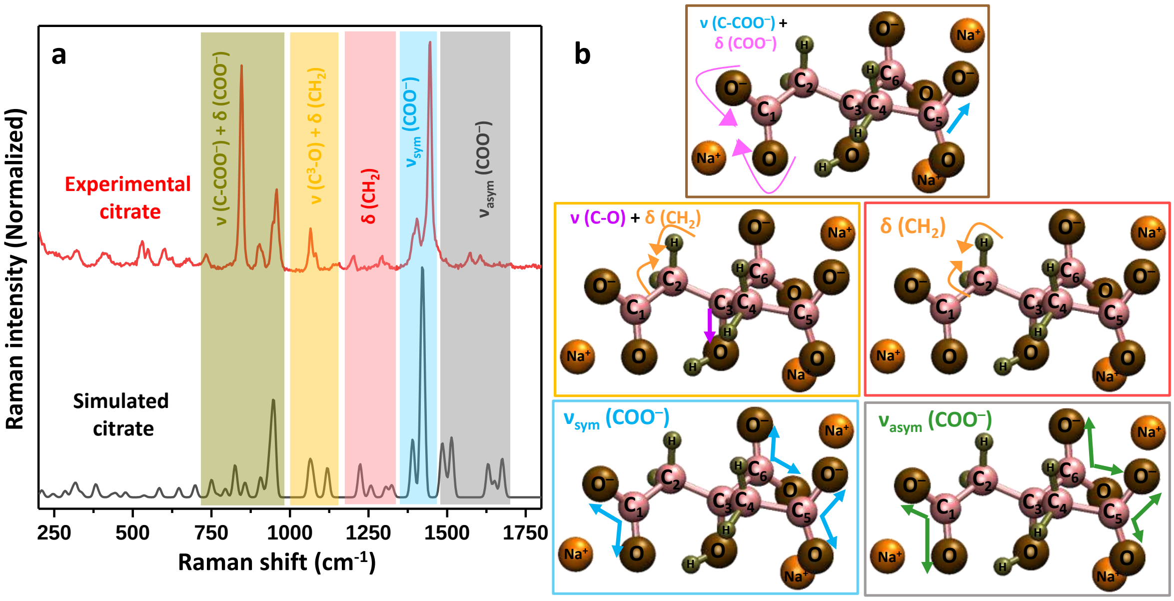

Figure S5. (a) Comparison between the experimental and DFT calculated Raman spectra of TSC (assignments of the vibrational bands are displayed vertically along with colored bands) and (b) DFT optimized structures of TSC, calculated at the B3LYP/6-31 + G(d) level. The vibrational modes of TSC are shown pictorially with arrows.

Table S1. Band assignments of SERS frequencies for distinct spectra of citrate (Figure 1b of manuscript) with the help of the simulated Raman spectrum of TSC (Figure S3a) and existing literature[1–2] on the SERS of citrate.

Frequency bands (SERS, Figure 1b) (cm^{-1})	Simulated Raman of TSC, Figure S3a (cm^{-1})	Literature[1–2] (SERS) of adsorbed citrate(cm^{-1})	Assignments
820–870	824	843	ν(C-COO⁻)+ δ(COO⁻)
930–980	948	956	ν(C-COO⁻)
1050–1100	1065, 1072	1057	ν(C-O)
1170–1330	1118, 1224, 1258	1212, 1267	δ(CH_2) + γ(CH_2) + δ(COO⁻)
1350–1420	1390	1417	ν_{sym}(COO⁻)
1440–1480	1422, 1483		δ(CH_2)
1560–1640	1629	1575	ν_{asym}(COO⁻)

Notes: ν indicates stretching, ν_{sym} is symmetric stretching, ν_{asym} is asymmetric stretching, δ is in-plane bending and rocking, γ is out-of-plane wagging and twisting.

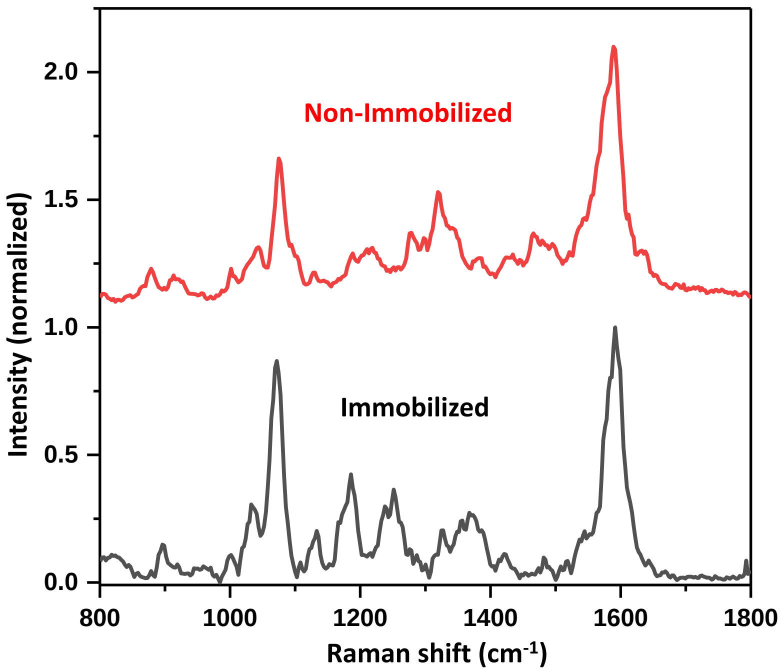

Figure S6. Comparison between SERS spectra obtained in immobilized and non-immobilized AgNPs. In both the cases, spectra were similar which indicated that spectra were due to citrate rather than MPTMS.

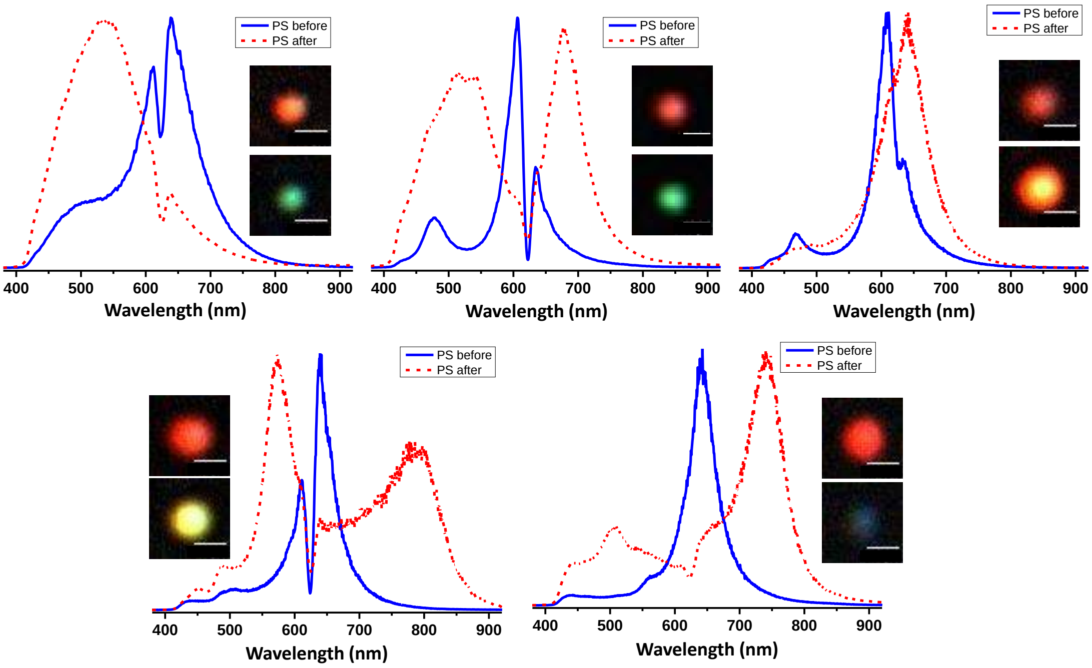

Figure S7. Plasmonic scattering spectra of single AgNPs before and after laser exposure. DFM images of the particles monitored before and after laser exposure are displayed along with their scattering spectra. Dip in peak in all spectra is due to presence of laser band pass filter in the optical path (scale bar in all DFM images is 0.5 µm).

II. Clustering methods and algorithms:

In the CA algorithm, a k-means++ algorithm[3-4] adapted from ImageJ was used to spread out the initial cluster centers (CCs). A CC is a point which is closest to the members of that cluster. In this approach, the first CC was chosen randomly among the spectral data points to be clustered. Then, remaining CCs were chosen such that the probability of the point to become a CC is dependent on its squared distance from the closest existing CC. Once the k-centers were chosen, k-means clustering algorithm was performed.

Technical terms (TT)	Brief explanation of TT	Limiting values for cluster analysis
Tolerance limit[4]	It stops the iterative process of CA when the distance between the successive points is $\leq 10^{-7}$ value.	10^{-7}
Randomization seed[4]	The seed is the initial value of the internal state of the pseudorandom number generator. It is enabled so that the cluster centers are initialized to the same values every time algorithm starts.	200
Noise threshold	It indicates S/N value and the spectra with maximum intensity ≤80 were considered as noise.	80

Step 1. All the data collected from time dependent SERS measurement was exported from Witec Raman spectrometer control software in a text format. These text files were used as input files to prepare files suitable for cluster analysis algorithm in ImageJ.[3-4] The customized MATLAB code named as *before cluster analysis* shown below (Code 1), was used to prepare data for cluster analysis. ImageJ cluster analysis algorithm was used to visualize clustering process.

Code 1: Before cluster analysis

```
clear all;
nos=1400; % number of spectra
nx=40;
ny=35;
nof=7; % number of files
start_fileno = 1;
noiselevel = 80;
noise_limit = 80; % noise limit to distinguish between noise and spectrum
x=importdata('x.txt');
raylb4=100; % Data point before which rayleigh appears <<
raylcorrect=1; % set to 1 if rayleigh needs to be corrected <<
speclen=1024; % length of spectrum <<
xzeroI=28; %array index where x is zero <<
smoothFlag = 0; %set to 1 if smoothing is required
RamanBadDataRm = 0; %set to 1 if bad data at specific points need to be removed
```

```
BadData8 = 292;
repeat_smooth = 2;
for i=start_fileno:1:(start_fileno + nof-1)
   y_temp = importdata(sprintf('y%i.txt',i));
   if i==1
      A=y_temp;
   else
      A=vertcat(A,y_temp);
   end
end
A=reshape(A,[],nos);
```

Step 2. Files generated by above program were used as input files for k-means++ and k-means algorithm in ImageJ. This step generated clustered datasets from input spectra.

Step 3. A second customized MATLAB code, named as *after cluster analysis* was used to prepare cluster analysed data for further plotting and analysis. Then these spectra were imported in Origin 2017 to plot as shown in Figure 2 and subsequent sections. The MATLAB code *after cluster analysis* code (Code 2) is given below.

Code 2: After cluster analysis

```
clear all;
nos=1400; % number of spectra
nx=40;
ny=35;
nof=7; % number of files
start_fileno = 1;
nocs=15; % number of clusters
clusters = dlmread('Clusters.txt');
centroid = dlmread('Centroid.txt');
cluster_average = zeros(1024,nocs);
cluster_frequency = zeros(nocs,1);
cluster_centroid = zeros(nocs,1);
x=importdata('x.txt');
normalized = 0; % set to 1 if spectra need to be normalized before cluster analysis

raylb4=100; % Data point before which rayleigh appears <<
raylcorrect=1; % set to 1 if rayleigh needs to be corrected <<
speclen=1024; % length of spectrum <<
xzeroI=28; %array index where x is zero <<
smoothFlag = 0; %set to 1 if smoothing is required
RamanBadDataRm = 0; %set to 1 if bad data at specific points need to be removed
BadData8 = 292;
noise_limit = 80; % noise limit to distinguish between noise and spectrum
repeat_smooth = 2;
noiselevel = 80;

x=importdata('x.txt');
for i=start_fileno:1:(start_fileno + nof-1)
   y_temp = importdata(sprintf('y%i.txt',i));
```

```
    if i==1
        A=y_temp;
    else
        A=vertcat(A,y_temp);
    end
end

A=reshape(A,[],nos);
yr=zeros(1024,1);
if raylcorrect == 1
    for i= 1:nos
        yr_temp = A(1:1024,i); % original spectrum

        y_max=max(yr_temp(raylb4:1024));
        y_min=min(yr_temp(raylb4:1024));

        [maxr,maxrI] = max(yr_temp(1:raylb4));   %to identify rayleigh and store its position to
maxrI
        %xr = x-x(maxrI);        %to change X-axis-so that the rayleigh is at zero

        if maxrI>xzeroI
            yr(1:(speclen-(maxrI-xzeroI))) = yr_temp((maxrI-xzeroI+1):speclen);
            yr((speclen-(maxrI-xzeroI)+1):speclen) = y_min;
        elseif maxrI<xzeroI
            yr(1:(xzeroI-maxrI)) = y_min;
            yr((xzeroI-maxrI+1):speclen) = yr_temp(1:(speclen-(xzeroI-maxrI)));
        end

        if RamanBadDataRm==1
            yr(BadData8) = (yr(BadData8-1)+yr(BadData8+1))/2;
        end

        for j= 1:repeat_smooth
            if smoothFlag==1
                yr = smooth(yr);          % to smoothen
            end
        end

        if (y_max-y_min)<noise_limit
            A(1:1024,i) = 0;
        else
            A(1:1024,i) = yr(1:1024); % normalized spectrum
        end

    end
end

C=zeros(nx,ny,1024);

Z=zeros(1024,1);
```

```
for i=1:1:nx
   for j=1:1:ny
   C(i,j,1:1024)=A(1:1024,(j+ny*(i-1)));
   if (max(C(i,j,200:1024))-min(C(i,j,200:1024)))<noiselevel
      C(i,j,1:1024) = Z(1:1024,1);
   end
   end
end
for i=1:1:nx
   for j=1:1:ny
   cluster_average(1:1024,(clusters(i,j)+1))                                          =
cluster_average(1:1024,(clusters(i,j)+1))+reshape(C(i,j,1:1024),1024,1);
   cluster_frequency((clusters(i,j)+1)) = cluster_frequency((clusters(i,j)+1)) + 1;
   cluster_centroid((clusters(i,j)+1)) = centroid((clusters(i,j)+1));
   dlmwrite(sprintf('%d.txt',11000000+(clusters(i,j)+1)*10000+((i-
1)*ny)+j),reshape(C(i,j,1:1024),1024,1),'delimiter','\t');
%         if(sum(reshape(C(i,j,1:1024),1024,1))~=0)
   if (max(C(i,j,200:1024))-min(C(i,j,200:1024)))>=noiselevel
      dlmwrite(sprintf('z%d.txt',11000000+((i-
1)*ny)+j),reshape(C(i,j,1:1024),1024,1),'delimiter','\t');
      end
   end
end

for i=1:1:nocs
   cluster_average(1:1024,i) = cluster_average(1:1024,i)/cluster_frequency(i);
end

dlmwrite('cluster_average.txt',cluster_average,'delimiter','\t');
dlmwrite('cluster_frequency.txt',cluster_frequency,'delimiter','\n');
dlmwrite('cluster_centroid.txt',cluster_centroid,'delimiter','\n');
clear all;
```

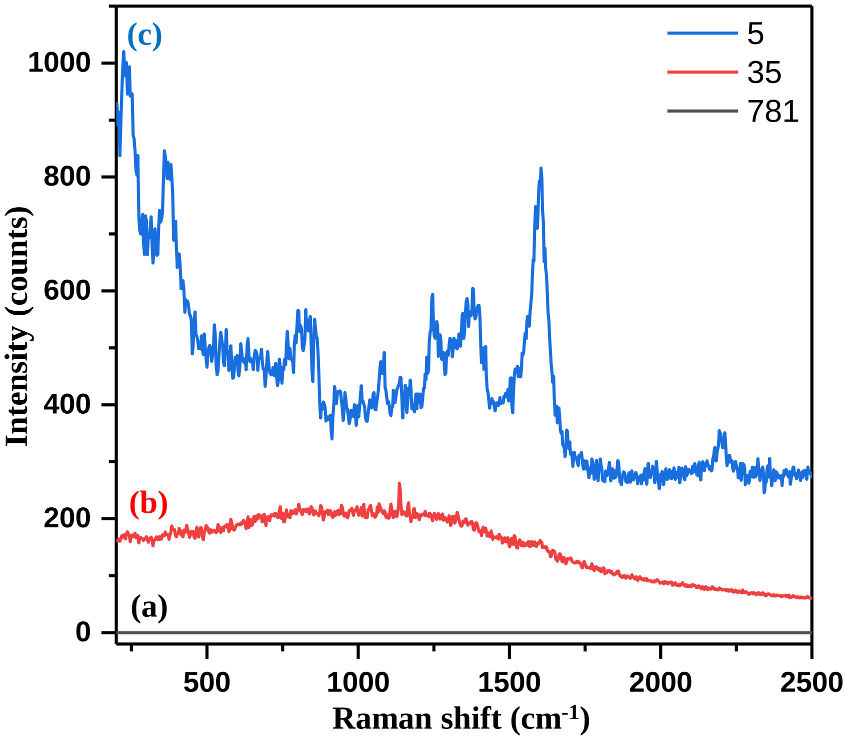

Figure S8. Set of three clusters out of 15 clusters which contain, (a) 781 spectra with no SERS features (blank spectrum), (b) 35 SERS spectra with broad background, and (c) 5 spectra with noisy SERS features.

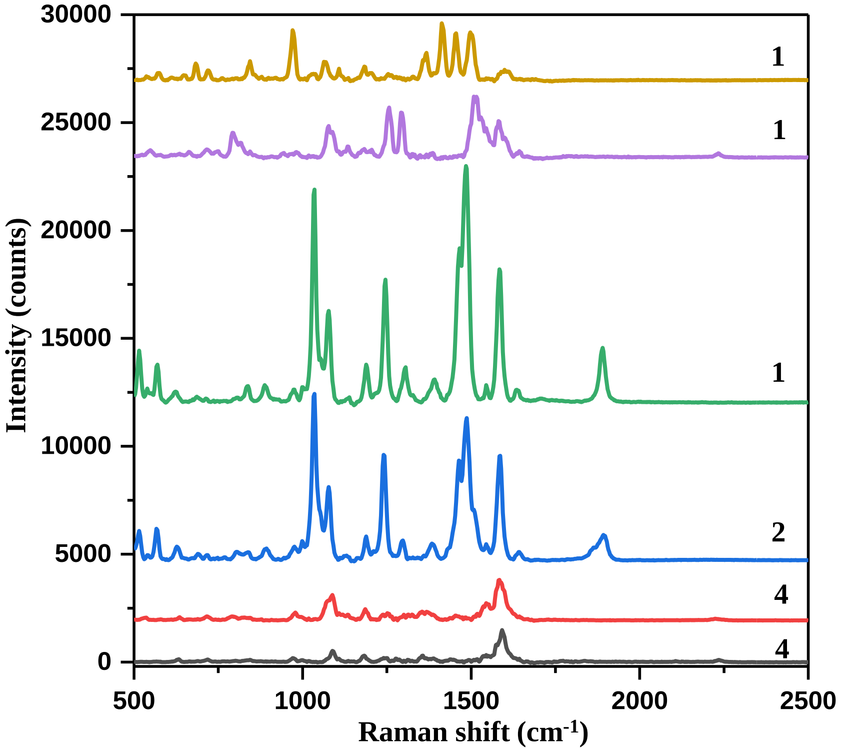

Figure S9. Set of 6 clusters as P-spectra out of 15 clusters which contain 4, 4, 2, 1, 1, and 1 spectra, respectively.

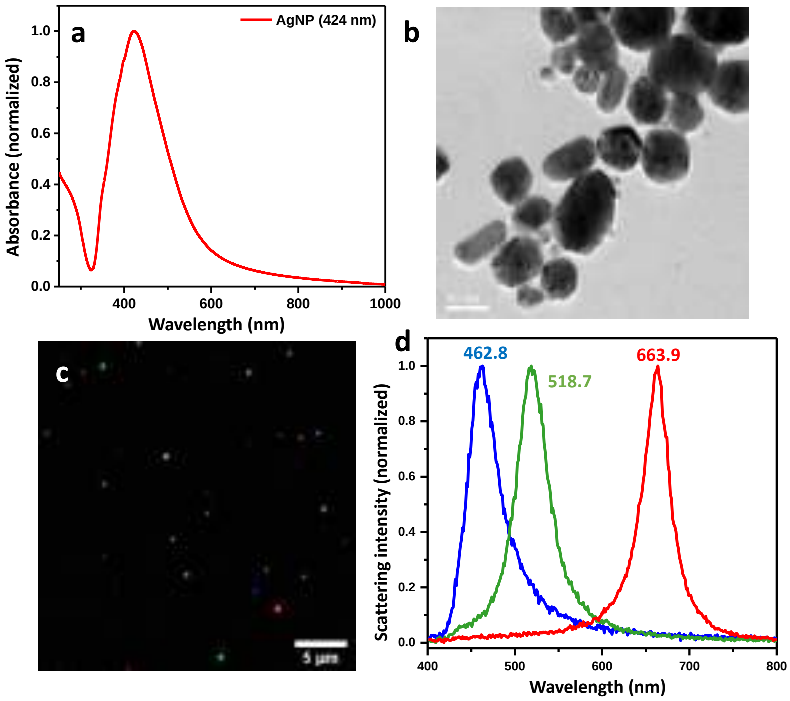

Figure S10. Spectroscopic and microscopic characterization of deuterated capped AgNPs, (a) UV-Vis absorption spectrum with maximum peak at 424 nm, (b) TEM image with polydispersed particles, (c) DF image, and (d) plasmonic scattering spectra of deuterated citrate-capped AgNPs.

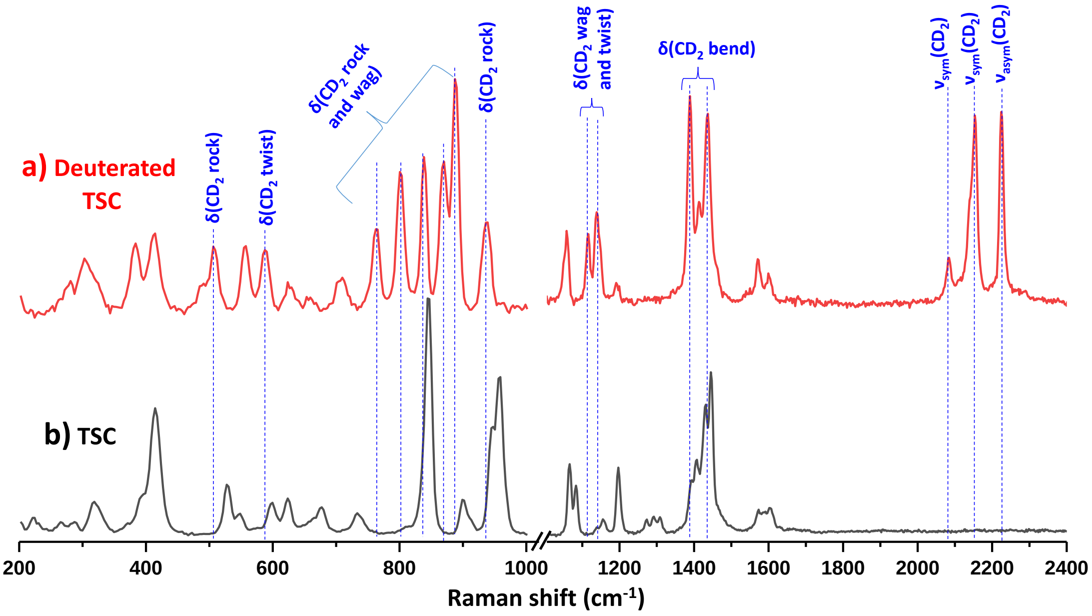

Figure S11. Comparison of Raman spectra of (a) deuterated TSC and (b) normal TSC, using bulk samples.

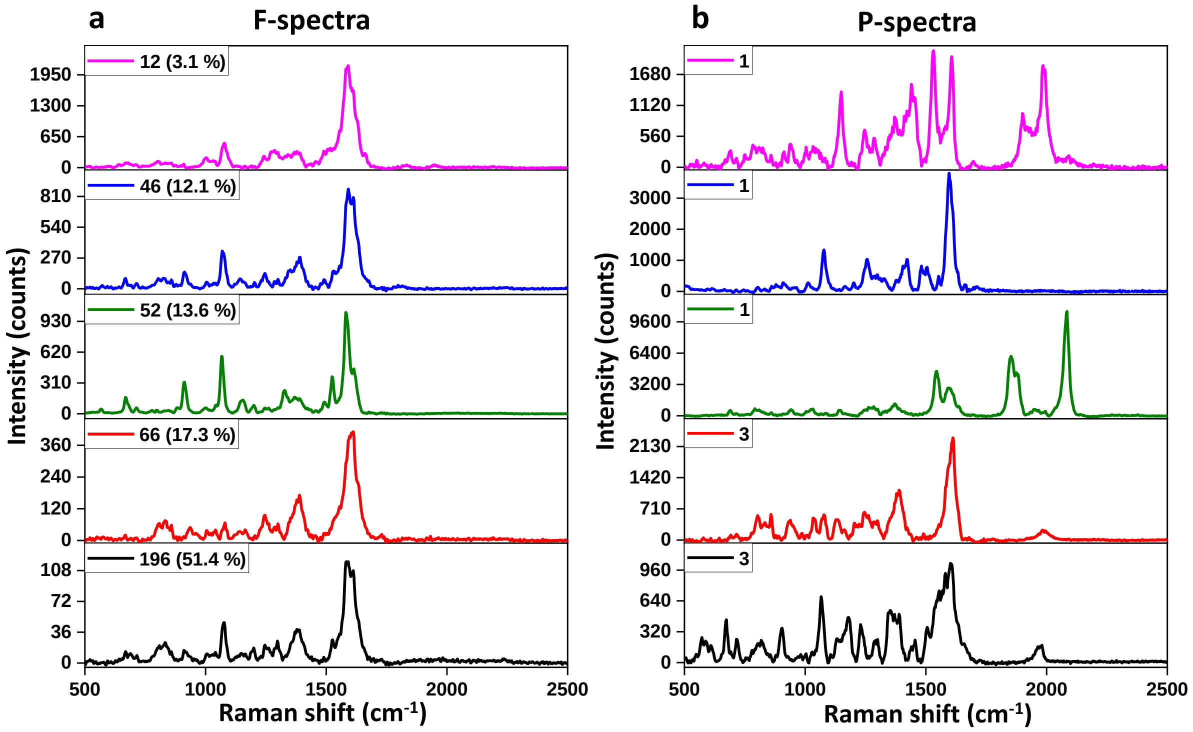

Figure S12. Cluster analysis of time-dependent SP-SERS spectra of deuterated citrate-capped AgNPs, (a) F-spectra and (b) P-spectra, with number of spectra observed.

References

(1) Li, M.; Xiao, Y.; Zhang, Z.; Yu, J., Bimodal Sintered Silver Nanoparticle Paste with Ultrahigh Thermal Conductivity and Shear Strength for High Temperature Thermal Interface Material Applications. *ACS applied materials & interfaces* **2015**, *7*, 9157-9168.

(2) Munro, C. H.; Smith, W. E.; Garner, M.; Clarkson, J.; White, P. C., Characterization of the Surface of a Citrate-Reduced Colloid Optimized for Use as a Substrate for Surface-Enhanced Resonance Raman Scattering. *Langmuir* **1995**, *11*, 3712-3720.

(3) Arthur, D.; Vassilvitskii, S. k-Means++: The Advantages of Careful Seeding. *Proc. eighteenth Annu. ACM-SIAM Symp. Discret. algorithms. Soc. Ind. Appl. Math. Philadelphia, PA, USA* **2007**, 1027–1035.

(4) Rueden, C. T.; Schindelin, J.; Hiner, M. C.; DeZonia, B. E.; Walter, A. E.; Arena, E. T.; Eliceiri, K. W., ImageJ2: ImageJ for the next generation of scientific image data. *BMC Bioinformatics* **2017**, *18*, 529.

III. APPENDICES

Appendix 1. Coordinates of sodium citrate, Ag_{55}, Ag_{25} and other Ag_{25}-citrate structures.

1. Sodium citrate ($Na_3C_6H_5O_7$)

O	-0.287728000	0.826372000	1.300655000
O	2.158453000	-0.299283000	1.331221000
O	1.390335000	-2.170024000	0.364647000
O	2.422009000	0.193671000	-1.816339000
O	-3.503193000	-1.237222000	-0.480474000
O	1.659781000	2.102369000	-0.890211000
O	-2.785993000	0.676975000	0.430821000
C	-0.075581000	-0.273624000	0.395296000
C	0.134736000	0.246952000	-1.074757000
C	-1.288466000	-1.221397000	0.471738000
C	1.236767000	-0.997866000	0.785593000
C	1.518058000	0.914131000	-1.298827000
C	-2.615813000	-0.559531000	0.104675000
H	-0.662549000	0.969092000	-1.280142000
H	0.036478000	-0.603240000	-1.755296000
H	-1.126982000	-2.094997000	-0.159341000
H	-1.378770000	-1.581702000	1.505820000
H	-1.220604000	1.099662000	1.115614000
Na	-4.744263000	0.568061000	-0.555540000
Na	1.666754000	1.895683000	1.279374000
Na	3.301592000	-1.298623000	-0.510336000

2. Silver 55 (Ag_{55})

Ag	15.345910000	13.509980000	15.901190000
Ag	16.057290000	12.267170000	13.652680000
Ag	17.686390000	12.061900000	16.084790000
Ag	17.490020000	14.576050000	14.633250000
Ag	15.088260000	10.770880000	15.951910000
Ag	14.773500000	14.853420000	13.648510000
Ag	13.275810000	12.487090000	14.478040000
Ag	17.396800000	14.548610000	17.532420000
Ag	15.896390000	12.168320000	18.353460000
Ag	15.570570000	16.267500000	16.054290000
Ag	13.150560000	12.488450000	17.384150000
Ag	12.964780000	14.976770000	15.949590000
Ag	14.611710000	14.772570000	18.369230000
Ag	16.797150000	11.011930000	11.343700000
Ag	20.015440000	10.617880000	16.129670000
Ag	19.630580000	15.625430000	13.280080000
Ag	14.856280000	8.046450000	15.890800000
Ag	14.220440000	16.164340000	11.308370000
Ag	11.245730000	11.458330000	12.957430000
Ag	19.447870000	15.567410000	19.039540000
Ag	15.835400000	18.982900000	16.093820000
Ag	11.061420000	11.369730000	18.742420000
Ag	10.662250000	16.464390000	15.829020000

Ag	13.963500000	15.997130000	20.725650000
Ag	18.481660000	10.775900000	13.663520000
Ag	18.283140000	13.325010000	12.170140000
Ag	15.806250000	9.417740000	13.547110000
Ag	15.496470000	13.587800000	11.166370000
Ag	13.988080000	11.222500000	12.004180000
Ag	19.982500000	13.168580000	14.759810000
Ag	17.486630000	9.202290000	16.115190000
Ag	19.856750000	13.057040000	17.672690000
Ag	18.360060000	10.663340000	18.498360000
Ag	16.963170000	15.998410000	12.184740000
Ag	19.661380000	15.673520000	16.174840000
Ag	17.783440000	17.404010000	14.623970000
Ag	12.931350000	9.641140000	14.425910000
Ag	15.635980000	9.316660000	18.369820000
Ag	12.891240000	9.625090000	17.345200000
Ag	12.617580000	13.862570000	12.064940000
Ag	15.056960000	17.698320000	13.604720000
Ag	12.321640000	16.342610000	13.499390000
Ag	11.024480000	11.384060000	15.841920000
Ag	10.821780000	13.970660000	14.376080000
Ag	18.052390000	13.154650000	19.941970000
Ag	17.769490000	17.391660000	17.547910000
Ag	16.733900000	15.769990000	20.026890000

Ag	13.719670000	10.996310000	19.785860000
Ag	15.216690000	13.420600000	20.833640000
Ag	13.202650000	17.833320000	15.831410000
Ag	14.948950000	17.595660000	18.488220000
Ag	10.490240000	13.944820000	17.139090000
Ag	12.427320000	13.676710000	19.902220000
Ag	12.280640000	16.307540000	18.403880000
Ag	16.462380000	10.825280000	20.679450000

3. Silver 25 (Ag_{25})

Ag	-0.526591000	4.548611000	0.471818000
Ag	-3.835957000	0.874027000	0.392892000
Ag	-1.148575000	1.792758000	0.619146000
Ag	1.616364000	2.736915000	0.830726000
Ag	-4.366444000	-1.924946000	0.522431000
Ag	-1.712819000	-0.977191000	0.891676000
Ag	1.011342000	-0.079974000	1.028763000
Ag	3.705683000	0.873098000	1.306293000
Ag	-2.286226000	-3.739358000	0.928996000
Ag	0.412379000	-2.860705000	1.219832000
Ag	3.145368000	-1.927431000	1.428854000
Ag	-4.036887000	2.170234000	-2.096629000
Ag	-1.331732000	3.091356000	-2.029127000
Ag	1.330521000	4.000458000	-1.825405000
Ag	-4.599037000	-0.588600000	-1.880428000

Ag	-1.905469000	0.299916000	-1.765493000
Ag	0.767176000	1.215954000	-1.563349000
Ag	3.441557000	2.125811000	-1.356325000
Ag	-2.520143000	-2.504653000	-1.545869000
Ag	0.187319000	-1.559923000	-1.374475000
Ag	2.883706000	-0.639169000	-1.168181000
Ag	5.598581000	0.267707000	-0.924594000
Ag	-0.362134000	-4.310377000	-1.033606000
Ag	2.290664000	-3.411458000	-0.823013000
Ag	4.940300000	-2.499723000	-0.627870000

4. $Ag_{25}C_5H_4O_5$ (SERS-F – 346 structure)

Ag	5.520465000	0.907704000	0.316855000
Ag	5.971178000	-1.761946000	-0.383074000
Ag	2.907973000	1.884224000	0.842834000
Ag	3.355290000	-0.890361000	0.194404000
Ag	3.837361000	-3.620691000	-0.600445000
Ag	0.274687000	2.824151000	1.277452000
Ag	0.733780000	0.099087000	0.584242000
Ag	1.205906000	-2.697449000	-0.148953000
Ag	-2.403508000	3.741646000	1.620845000
Ag	-1.916085000	0.995949000	1.073238000
Ag	-1.480586000	-1.730294000	0.284070000
Ag	-0.990844000	-4.484467000	-0.363638000
Ag	-4.547283000	1.977590000	1.343300000

Ag	-4.132137000	-0.772508000	0.707928000
Ag	-3.665436000	-3.536695000	-0.016903000
Ag	4.308579000	2.660354000	-1.450632000
Ag	1.685827000	3.615409000	-1.024903000
Ag	2.150798000	0.925782000	-1.873782000
Ag	-0.951144000	4.527045000	-0.589911000
Ag	-0.518348000	1.837986000	-1.389680000
Ag	-0.058537000	-0.864984000	-2.100695000
Ag	-3.191995000	2.804934000	-0.933292000
Ag	-2.708324000	0.074962000	-1.685327000
Ag	-2.247898000	-2.652225000	-2.400382000
Ag	-4.898316000	-1.752167000	-1.833280000
C	0.820034263	1.320037647	4.441468396
O	3.916001719	0.882275140	3.961329015
O	-2.141035803	0.028091868	5.556009558
O	3.458260994	2.916721939	3.119162173
O	-1.931426343	1.105601910	3.594223380
C	2.061305095	2.125424586	4.894728811
C	-0.400606402	1.701544548	5.332712191
C	3.241430806	1.968102698	3.933975732
C	-1.618814766	0.910610935	4.831893735
H	2.341230989	1.772666788	5.895277195
H	1.785746554	3.186195418	4.932803931
H	-0.571228731	2.781079491	5.212259890

H	-0.198296068	1.469397432	6.383789841
O	1.129787427	0.012181280	4.833341719

5. $Na_2Ag_{25}C_6H_5O_7$ (SERS-F – 43) structure

Ag	5.520465000	0.907704000	0.316855000
Ag	5.971178000	-1.761946000	-0.383074000
Ag	2.907973000	1.884224000	0.842834000
Ag	3.355290000	-0.890361000	0.194404000
Ag	3.837361000	-3.620691000	-0.600445000
Ag	0.274687000	2.824151000	1.277452000
Ag	0.733780000	0.099087000	0.584242000
Ag	1.205906000	-2.697449000	-0.148953000
Ag	-2.403508000	3.741646000	1.620845000
Ag	-1.916085000	0.995949000	1.073238000
Ag	-1.480586000	-1.730294000	0.284070000
Ag	-0.990844000	-4.484467000	-0.363638000
Ag	-4.547283000	1.977590000	1.343300000
Ag	-4.132137000	-0.772508000	0.707928000
Ag	-3.665436000	-3.536695000	-0.016903000
Ag	4.308579000	2.660354000	-1.450632000
Ag	1.685827000	3.615409000	-1.024903000
Ag	2.150798000	0.925782000	-1.873782000
Ag	-0.951144000	4.527045000	-0.589911000
Ag	-0.518348000	1.837986000	-1.389680000
Ag	-0.058537000	-0.864984000	-2.100695000

Ag	-3.191995000	2.804934000	-0.933292000
Ag	-2.708324000	0.074962000	-1.685327000
Ag	-2.247898000	-2.652225000	-2.400382000
Ag	-4.898316000	-1.752167000	-1.833280000
O	0.548763000	-0.126205000	2.608466000
H	-0.398563000	0.113621000	2.897185000
C	0.989926000	-1.011462000	3.635461000
O	-0.465435000	-2.699236000	2.630513000
O	1.219024000	-3.405418000	3.947542000
O	3.769708391	-2.950022451	3.643746733
O	-1.866029000	-1.546840000	5.434391000
O	4.753787596	-1.062855361	2.917156683
O	-1.702308000	0.013489000	3.824380000
C	2.525617000	-0.878251000	3.772406000
C	0.310154000	-0.582966000	4.971173000
C	0.550907000	-2.505084000	3.371353000
C	3.778940553	-1.688463100	3.435909329
C	-1.210931000	-0.694554000	4.786044000
H	2.862879000	-1.630545000	4.496425000
H	2.749967000	0.128945000	4.143677000
H	0.594986000	0.461209000	5.165049000
H	0.643987000	-1.221501000	5.796046000
Na	-2.598094000	-2.104913000	3.283721000
Na	4.297617388	-4.559615379	2.632164410

6. $NaAg_{25}C_6H_5O_7$ (SERS-T - 1) structure

Ag	2.496605000	3.098282000	-1.665644000
Ag	-0.365573000	2.728299000	-1.583074000
Ag	-3.207349000	2.348384000	-1.471175000
Ag	4.230888000	0.886525000	-1.931651000
Ag	1.384581000	0.446171000	-1.863032000
Ag	-1.477036000	0.085034000	-1.801691000
Ag	-4.280764000	-0.309596000	-1.729911000
Ag	3.118229000	-1.774673000	-2.115194000
Ag	0.307768000	-2.191538000	-2.053806000
Ag	-2.489366000	-2.563943000	-1.983306000
Ag	-0.549050000	4.136187000	0.974189000
Ag	-3.374752000	3.738309000	1.089532000
Ag	4.024894000	2.313972000	0.628912000
Ag	1.189164000	1.903657000	0.664823000
Ag	-1.627894000	1.483513000	0.744293000
Ag	-4.457279000	1.150946000	0.888501000
Ag	5.788924000	0.099405000	0.322923000
Ag	2.971875000	-0.322843000	0.470771000
Ag	0.149198000	-0.761766000	0.478106000
Ag	-2.695967000	-1.109572000	0.565216000
Ag	-5.483300000	-1.489795000	0.607721000
Ag	4.693459000	-2.530775000	0.138289000
Ag	1.913466000	-2.962630000	0.236633000

Ag	-0.916761000	-3.354716000	0.317915000
Ag	-3.693499000	-3.717346000	0.346520000
O	0.296192131	-1.817850222	3.249500827
H	1.127566786	-2.401094160	2.983144529
C	0.392978000	-1.040627000	4.128097000
O	2.505195198	0.050546815	3.041168770
O	1.189777578	1.229227172	2.750893918
O	-1.266028000	1.262706000	3.056655000
O	3.478139000	-1.986170000	5.215591000
O	-2.674679000	-0.533692000	2.881644000
O	2.442580000	-2.916165000	3.407776000
C	-1.003236000	-0.574535000	4.608968000
C	1.051844000	-2.010698000	5.158947000
C	1.503828320	0.236090182	3.714196880
C	-1.725008000	0.106219000	3.442145000
C	2.437014000	-2.372416000	4.601974000
H	-0.845569000	0.132215000	5.452798000
H	-1.604016000	-1.451103000	4.934083000
H	0.406094000	-2.914782000	5.248162000
H	1.161803000	-1.506669000	6.143791000
Na	4.052363000	-1.181211000	3.150619000

7. $Ag_{25}C_6H_5O_7$ (SERS-T - 1)

Ag	3.689200401	1.344305096	-1.177426490
Ag	4.606139649	-1.215548756	-1.830453751

Ag	1.065482529	1.773183811	-0.183682435
Ag	2.012904348	-0.884764732	-0.780823395
Ag	2.956245865	-3.505327242	-1.530248645
Ag	-1.586552017	2.153755017	0.726498345
Ag	-0.647583032	-0.457533333	0.080905058
Ag	0.312929101	-3.139056537	-0.603157229
Ag	-4.293181670	2.494555528	1.557434694
Ag	-3.295467553	-0.117527015	1.049598157
Ag	-2.396508769	-2.743724158	0.314881830
Ag	-1.413132949	-5.372550827	-0.290992854
Ag	-5.985555804	0.289230965	1.796410448
Ag	-5.072100886	-2.350731567	1.217376141
Ag	-4.122686475	-5.001238846	0.541104733
Ag	1.800399937	2.625420608	-2.744473345
Ag	-0.846704480	3.022184124	-1.845796424
Ag	0.060922486	0.432604894	-2.646533390
Ag	-3.495664493	3.374490808	-0.933214844
Ag	-2.609824989	0.782893422	-1.679467144
Ag	-1.678558512	-1.808367117	-2.343640974
Ag	-5.302624023	1.182918324	-0.741128099
Ag	-4.349920258	-1.433095099	-1.448991577
Ag	-3.413227310	-4.048123474	-2.116132947
Ag	-6.047935459	-3.698100944	-1.071038761
O	0.702747888	-0.125581656	2.292175192

H	-0.279630050	-0.038569798	2.686865347
C	0.417449049	-1.206658570	3.066434372
O	-0.769372897	-3.253744620	2.452048853
O	1.246207566	-3.455612133	3.435586057
O	3.092776035	-2.492591508	1.754637241
O	-2.556705888	-1.878933974	4.742869512
O	3.155528898	-0.459100841	0.943854564
O	-2.073434638	-0.381962864	3.352458348
C	1.879095832	-0.731210078	2.886480587
C	-0.083804062	-0.817646786	4.490246330
C	0.293741301	-2.777545092	2.964408274
C	2.775797643	-1.253932789	1.762567594
C	-1.573976170	-1.179340486	4.395436205
H	2.508681436	-1.323965658	3.561875449
H	1.929744158	0.329898200	3.158698940
H	-0.016707149	0.276577284	4.575041917
H	0.534913828	-1.291501312	5.259815655

ACS APPLIED MATERIALS & INTERFACES

www.acsami.org Research Article

Hierarchical Assembly of Atomically Precise Metal Clusters as a Luminescent Strain Sensor

Debasmita Ghosh, Mohd Azhardin Ganayee, Anirban Som, Pillalamarri Srikrishnarka, Nidhi Murali, Sandeep Bose, Amrita Chakraborty, Biswajit Mondal, Pijush Ghosh, and Thalappil Pradeep*

Cite This: https://dx.doi.org/10.1021/acsami.0c19239 Read Online

ABSTRACT: We demonstrate the formation of a versatile luminescent organo-inorganic layered hybrid material, composed of bovine serum albumin (BSA)-protected Au_{30} clusters and aminoclay sheets. X-ray diffraction revealed the intercalation of Au_{30}@BSA in the layered superstructure of aminoclay sheets. Coulombic attraction of the clusters and the clay initiates the interaction, and the appropriate size of the clusters allowed them to intercalate within the lamellar aminoclay galleries. Electron microscopy measurements confirmed the hierarchical structure of the material and also showed the cluster-attached clay sheets. Zeta potential measurement and dynamic light scattering probed the gradual formation of the ordered aggregates in solution. The hybrid material could be stretched up to 300% without fracture. The emergence of a new peak in the luminescence spectrum was observed during the course of mechanical stretching. This peak increased in intensity gradually with the degree of elongation or strain of the material. A mechanochromic luminescence response was further demonstrated with a writing experiment on a luminescent mat of the material, made by electrospinning.

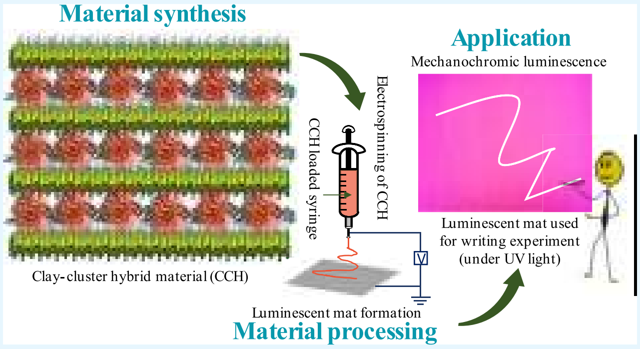

KEYWORDS: *protein-protected noble metal clusters, mechanochromic luminescence, hierarchical, bioinspired, aminoclay*

INTRODUCTION

Metal nanoclusters (NCs), especially of gold and silver, protected with ligands have drawn attention due to their unique molecular properties such as dye-like absorption, characteristic emission, chirality, reactivity, and so forth.[1] Among them, intense luminescence in the visible and NIR regions made these clusters very attractive in multiple areas of research. Protein-protected clusters (PPCs), a subclass of atomically precise clusters, have been grown within proteins.[2−4] They are water-soluble and exhibit intense luminescence. Besides, they are comparatively more stable than other classes of ligand-protected NCs. The highest quantum yield (QY) of noble metal cluster systems till date have been known for PPCs.[5] This has made PPCs to be used for a range of multidisciplinary applications, especially in sensing and biology.[6] Different topics such as sensing of hazardous analytes, targeting and bioimaging, drug delivery, and therapeutic applications have been researched upon for more than a decade. Recently, cluster-conjugated hybrid materials are being pursued for improved performance.

Clays have been used from antiquity.[7,8] In prehistoric times, clays were used to make bricks. They were used as bleaching materials and as soaps in ancient civilizations. Nowadays, they are used in our daily life in toothpastes, paints, pencils, different household ceramics, and so forth.[9] Considerable interest has been developed in clay materials due to their applications in catalysis,[10] functional nanocomposites,[11,12] separation,[13] biomedicine,[14] ferrofluids,[15] and so forth. Despite these widespread applications, poor solubilities of common clays such as kaolinite, smectite, bentonites, and so forth, in water, limit their utilization in specific applications. Mann and co-workers synthesized a tailormade clay, coined as aminoclay, which is an aminopropyl-functionalized magnesium phyllosilicate clay.[16−18] It has high water solubility and shows fascinating properties.[19−22]

Nacre, the gold standard for biomimicry, also known as the mother of pearl is an example of a bioinspired structural material.[23−26] Nacre mimics are nanocomposites made by assembling two-dimensional (2D) nanosheets to achieve a higher-order structure and high mechanical performance, similar to nacre.[27−29] The unique combination of strength and toughness in these biomimetic hybrid materials made them fascinating light-weight structural components for the

Received: October 27, 2020
Accepted: January 21, 2021

future.[30] Nacre mimics are obtained by intercalating a soft phase between the layers of a hard phase. Both the hard and soft phases contribute to the mechanical properties of the resultant hybrid material. Mimicking the characteristics of these natural materials is not an easy task.[31−33] Clay materials, due to their unique 2D structure, have often been utilized as the hard phase in nacre mimics. Polymers, biomolecules, and a combination of both have been used as the soft phase. Although the systematic integration of hard and soft phases in a hierarchical fashion is a recent development, confinement of guest molecules in layered 2D matrices to form an organo-inorganic hybrid is well established.[34] Multifunctional polymer−clay hydrogels were formed by "guest-molecule-directed self-assembly" of a nanocomposite.[35] Lipid templates helped to grow higher-order organoclay pipes by self-assembly.[36] Wrapping of biomolecules such as proteins, enzymes, DNAs, and so forth, by the aminoclay, was carried out to make functional hybrid materials for real-life use.[37,38] The secondary structure of the entrapped biomolecules was retained during bioimmobilization.[39] Thus, there is reduced probability for losing the biological function in these hybrid materials. Their structural and chemical properties could be integrated to enhance their applications, and their thermal and chemical stability enhanced their scope in biocatalysis, biosensing, and biomedical devices.

Herein, we have made an attempt to incorporate optically active biomolecules between the layers of functionalized clay sheets to create a unique nacre mimic. Highly luminescent, stable, and BSA-protected Au_{30} NC was used to intercalate in the aminoclay template. Water-soluble Au_{30}@BSA clusters attach to the aminoclay sheets through Coulombic interactions due to their opposite charges in solution and form a water-insoluble hierarchical organo-inorganic hybrid material. The layered structure of the hybrid material was observed through field emission scanning electron microscopy (FESEM). Intercalation of the cluster between the layers of aminoclay sheets was identified from powder X-ray diffraction (pXRD). Gradual formation of larger aggregates in solution during the synergistic interaction of both the cluster and the aminoclay sheets was seen in dynamic light scattering (DLS) measurements. These cluster-attached clay sheets were also identified by transmission electron microscopy (TEM). Luminescence of Au_{30}@BSA was retained in the hybrid material. The material was cast into different shapes after the addition of polyvinyl alcohol (PVA) into it. This PVA-added hybrid material was highly ductile in nature. The material, shaped as a dog bone, could be stretched to 300% of its original length without failure. Moreover, the change in the luminescence of the cluster was observed when the material was stretched, indicating its inherent strain sensitivity. This sensitivity was enhanced and was evident in the form of changing luminescence of an electrospun mat, when it was used for writing. Combination of interesting optical and mechanical properties in a cluster-based hybrid material makes it an exciting material.

EXPERIMENTAL METHODS

Materials. Magnesium chloride and BSA (about 96% purity) at pH 6−7 were purchased from Sisco Research Laboratory. Tetrachloroauric acid trihydrate ($HAuCl_4 \cdot 3H_2O$) was prepared in-house starting from elemental gold. Sodium hydroxide pellets were purchased from a local supplier (Rankem, India). Milli-Q water with a resistivity of 18.2 MΩ·cm was used for synthesis. 3-Aminopropyltriethoxysilane was purchased from Sigma-Aldrich. PVA (MW: 85,000−124,000) was purchased from S. D. Fine-Chem Limited. All the chemicals were used as received without further purification.

Synthesis of Au_{30}@BSA NC. About 25 mg of BSA was dissolved in 1 mL of Milli-Q water. Then, 1 mL of 6 mM $HAuCl_4$ aqueous solution was mixed with it and stirred vigorously for 5 min. Then, 100 μL of 1 M NaOH solution was added to it. The reaction was stirred for 12 h. A brown colored solution was formed, indicating the formation of Au_{30}@BSA, which showed bright red luminescence.

Synthesis of Aminoclay. The aminoclay was synthesized by a method reported earlier.[17,18] An organosilane precursor-like 3-aminopropyltriethoxysilane (1.3 mL, 5.85 mmol) was used at room temperature to prepare the amine-functionalized nanoclay. A solution of magnesium chloride (0.84 g, 3.62 mmol) in ethanol (20 g) was prepared. The precursor was added dropwise to the solution and kept for constant stirring at room temperature for 24 h. The white gel-type material was formed, which was recovered by centrifugation followed by washing with ethanol and distilled water and finally dried at 313 K.

Synthesis of a Clay-Cluster Hybrid (Will be Denoted as CCH Subsequently) and Its Casting in Different Forms. About 20 mL of aqueous solution of aminoclay (250 mg/mL) was prepared by sonication. This was mixed with 20 mL of Au_{30}@BSA solution (10:1 weight % of clay/cluster) under constant stirring. The reaction was continued for 12 h. Then, the resultant solution (I) was air-dried at room temperature. Finally, a luminescent solid clay-cluster hybrid (CCH) was formed.

PVA (6 weight %) was added to I to prepare precursor solutions for making various shapes. The solution was dried in a Petridish to form the film samples. Using plaster of paris, the dog bone-shaped die was made. Here, die is the molding device, which was used for shaping the CCH. The dog bone-shaped luminescent PVA-added CCH was made using this die.

Formation of Luminescent Mats by Electrospinning. Clay-cluster luminescent nanofibers were made using the ESPIN-NANO electrospinning machine. The same mixture, which was used to make the dog bone-shaped sample, was loaded into a 2 mL syringe for electrospinning. The luminescent spun mat was collected on top of the Al sheet. The parameters used for spinning were: flow rate, 0.15 mL/h; voltage, 18 kV, and working distance, 12 cm.

Stress−Strain Experiments. Tensile strength measurements of cluster-sandwiched aminoclay materials were conducted by Nano Plug and Play servo-hydraulic testing machine of 5 kN capacity, which comes with an application software capable of doing tension, compression, three-point bend, fatigue tests, and so forth. Materials were stretched in different percentages of elongation, for example, 80, 140, 250, and 300%. Experiments were carried out with both dog bone-shaped and rectangular film samples. In both cases, the trend of the luminescence with % of elongation was the same. Five positions were marked for each sample, shown in Figure 5A. Luminescence was measured before and immediately after the tensile strength experiments. The gauge length of the sample was 17 mm, the rate of elongation was 0.05 mm/s, and the test mode was stroke. The elongation of the specimen was calculated by [(final gauge length − initial gauge length)/initial gauge length × 100].

Writing Experiments. The luminescent membrane was placed inside a ziplock cover, and a pattern was drawn on it with the tip of a cotton swab. After this, we saw it under UV light. To show the uniform pressure sensitivity across the membrane, the grid pattern was drawn. In a similar way, the alphabet *a* was written on another membrane.

Characterization. UV−vis spectra were recorded using a PerkinElmer Lambda 25 UV−vis spectrometer. Photoluminescence measurement for Au_{30}@BSA was carried out in a HORIBA, Jobin Yvon NanoLog instrument. Solid-state luminescence of CCH was measured in a Witec GmbH, Alpha-SNOM alpha300 S confocal Raman instrument. For excitation, a 532 nm laser source was used, and the emission spectrum was recorded. Particle size and zeta potential measurements in solution were conducted using a Malvern Zetasizer Nano ZSP instrument. FESEM measurements were carried

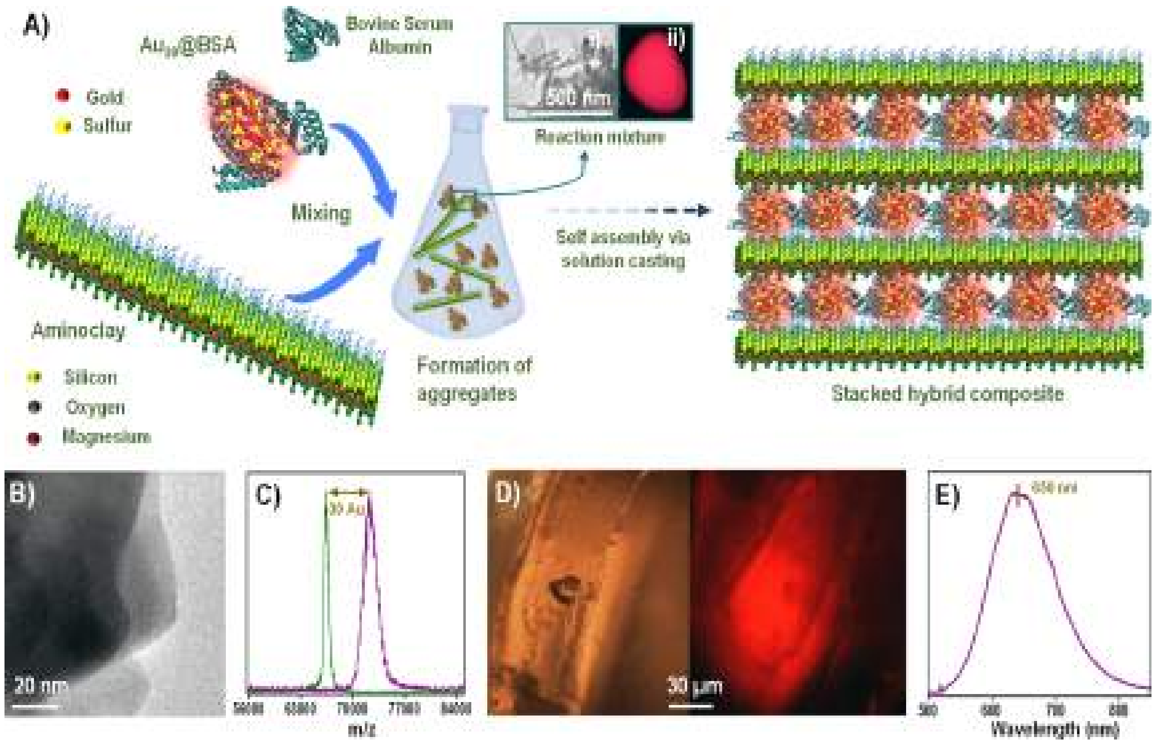

Figure 1. (A) Schematic representation of the formation of the organo-inorganic CCH material. The inset shows the TEM image (i) and photograph (ii) of the intense red luminescent aggregates formed during the reaction of the clay and cluster. The schematic of the aminoclay sheet is presented for representation purpose only. (B) TEM image of the aminoclay sheet. (C) MALDI MS of the Au_{30}@BSA. (D) Optical (left) and fluorescence (right) images of CCH. (E) Luminescence spectrum of CCH showed a maximum at 650 nm for 365 nm excitation.

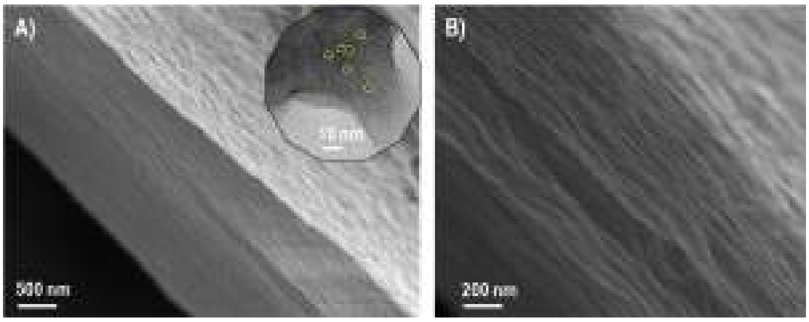

Figure 2. Electron microscopic characterization of the composite. (A) FESEM images of a cross-sectional view of CCH. The inset shows the TEM image of the cluster-attached clay sheets. (B) Layers of clay sheets are seen clearly in a zoomed-in image.

out using a Thermo Scientific Verios G4 UC instrument. High-resolution TEM (HRTEM) was carried out with a JEOL 3010 (JEOL Ltd.), a 300 kV instrument equipped with an ultrahigh-resolution pole piece. Dark field imaging was performed using an Olympus BX-51 microscope having a 100 W quartz halogen light source mounted on a CytoViva microscope setup. Matrix-assisted laser desorption ionization mass spectrometry (MALDI MS) measurements of proteins and clusters were conducted using an Applied Biosystems Voyager-DE PRO MALDI TOF spectrometer. A pulsed nitrogen laser of 337 nm was used for ionizing the proteins and the clusters, using the sinapic acid matrix. pXRD data were collected with a Bruker AXS, D8 Discover diffractometer using Cu Kα (λ = 1.54 υ) radiation.

■ RESULTS AND DISCUSSION

Preparation of the Luminescent Organo-Inorganic Hybrid Material. Aminoclay, a synthetic clay, is aminopropyl-functionalized 2D magnesium phyllosilicate. Dispersing the as-synthesized aminoclay in water results in the protonation of amine groups and leads to its exfoliation into individual 2D clay sheets. The parent cluster Au_{30}@BSA was characterized by (A) UV−vis and (B) luminescence spectra, shown in Figure S1. The cluster showed an emission at 650 nm. The light brown color of the cluster solution in visible light and its bright red color under UV light are shown in the inset of Figure S1B. The hydrodynamic diameter of the cluster solution was 6 nm, as shown in Figure S2. Mixing a clear solution of the exfoliated clay with an aqueous solution of Au_{30}@BSA NCs (10:1 weight %) resulted in the immediate formation of a slight turbid solution, indicating a reaction between the two. The turbidity of the reaction mixture increased with time and was left under stirring for 12 h at room temperature for completion of the reaction. Finally, the turbid solution was air-dried at room temperature to obtain a brown translucent film. Here, the oppositely charged clusters and clay sheets attach together through Coulombic interaction to create a hybrid material in the course of the reaction. The formation of the CCH is represented schematically in Figure 1A.

Randomly oriented clay sheets were observed in the course of the reaction (shown in inset a), which shows red luminescence under UV light due to the presence of the clusters (shown in inset b). The TEM image of the parent aminoclay is shown in Figure 1B. MALDI MS of pure BSA (green trace) and the Au_{30}@BSA cluster (purple trace) is shown in Figure 1C. BSA showed its molecular ion peak at m/z 66.42 kDa, and the cluster showed the peak at m/z 72.28 kDa. The difference in the m/z value in MALDI MS spectra of the cluster than the parent protein confirmed the atomicity of the Au_{30} core within BSA.[40] Bright red luminescence of CCH was seen by fluorescence microscopy, shown in Figure 1D (right side). The luminescence spectrum of CCH showed a maximum at 650 nm (Figure 1E), similar to the cluster, which confirmed that the cluster is intact in the hybrid. The oxidation state of Au remains unchanged after the formation of CCH. The lifetime of the hybrid material is similar to that of the cluster, 0.13 ns (62%), 1.23 ns (25%), and 33.0 ns (13%). The QYs of Au_{30}@BSA and the CCH are 29 and 40%, respectively. This hybrid material is very stable up to 200 °C and in the pH range of 1−14. The sample was characterized in detail to reveal the structure of the composite material.

Formation of the Nacre-like Layered Structure. Self-ordering of the hybrid material into multilayered structures is shown in Figure 2. Removal of water from the composite material led to self-ordering and stacking of layers, which is confirmed from the FESEM image, presented in Figure 2A. FESEM images were measured from using dried samples. Due to opposite electrostatic charges present on the cluster and the clay sheets, they attract each other, forming a single layer of CCH. These layers stack together to form a hierarchical layered structure, which can be seen from Figure 2B, although the clusters, due to their very small core size (∼1 nm), cannot be seen in the FESEM images. However, the red luminescence of CCH confirms their presence. The TEM image of CCH (shown in inset of Figure 2A) shows the clear presence of clusters attached to aminoclay sheets. The wavy nature of the surface showed the nanoscale roughness of CCH, which is clear from Figure S3.

Intercalation of Au_{30} Clusters into Layered Galleries. From the data presented, the layered structure of the biomimetic material, CCH, and the attachment of the NCs with aminoclay were confirmed. However, the position of the clusters in the composite was not clear from microscopic studies. To prove our hypothesis that clusters intercalate between the layers of aminoclay sheets in CCH, pXRD was performed. The parent aminoclay shows several peaks in its pXRD pattern corresponding to different crystallographic planes of the clay (Figure S4). The peak at $2\theta = 6.1°$ (shown in Figure 3A) corresponds to an interlayer spacing of 1.45 nm between the aminoclay sheets [(001) plane]. The peak shifts to $2\theta = 1.5°$ in CCH, corresponding to an interlayer spacing of 6.00 nm. The increase in interlayer spacing from the aminoclay to CCH points to intercalation of the Au_{30}@BSA cluster between the aminoclay sheets. Complete disappearance of the aminoclay peak in CCH suggests that CCH is a pure phase and excess aminoclay does not exist. Although the clusters intercalated between the clay sheets could not be clearly resolved in FESEM, a distance of 6 nm between the layers was confirmed (Figure 3B). A long-range ordered structure of CCH is shown in Figure 3C.

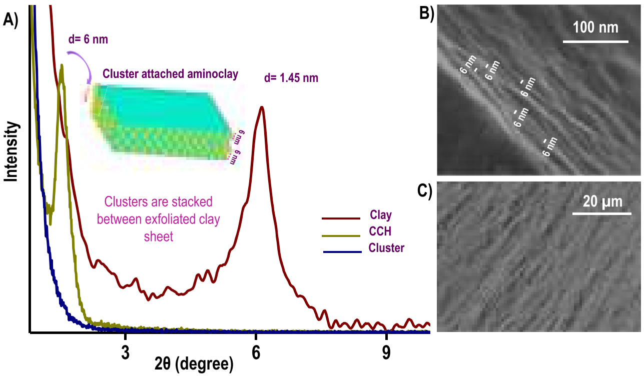

Figure 3. (A) Powder XRD data of the cluster, aminoclay, and CCH. Intercalation of the cluster is evident. (B) FESEM image showing a cross-sectional view of CCH. This shows the 6.00 nm spacing between the layers. (C) FESEM image showing the long-range ordered structure of CCH.

Probable Mechanism for the Interaction of Au_{30} Clusters and Aminoclay. The mechanism of formation of the intercalated hybrid structure was investigated by zeta potential measurements and DLS. Host−guest interaction of biomolecules and organoclay was studied earlier. Successful intercalation depends on two factors, electrostatic interaction between the host and the guest and the size of the guest molecules. In our case, Coulombic interactions between the positively charged aminoclay sheets and negatively charged NCs helped to form the coassembly of the clusters in between the delaminated sheets. The zeta potential value for aminoclay was +25.6 mV, and for NCs, it was −22.0 mV. The zeta potential value of the solution after the formation of CCH was +8.5 mV (shown in Figure 4B). Considerable reduction of the positive charge of aminoclay in presence of NCs confirmed that CCH was formed through electrostatic interactions between the positively charged aminopropyl moieties of the clay and the negatively charged carboxylate groups on the protein surface. The reduced zeta potential value of CCH also contributed to their aggregation, and the solution thus becomes turbid. Finally, a uniformly stacked hybrid organo-inorganic structure was formed from solution during drying.

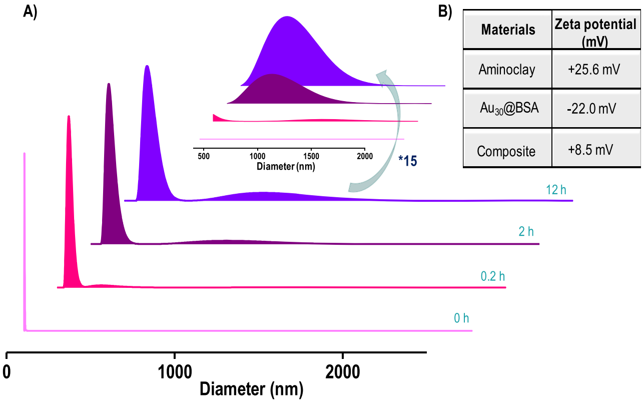

Materials	Zeta potential (mV)
Aminoclay	+25.6 mV
Au_{30}@BSA	-22.0 mV
Composite	+8.5 mV

Figure 4. (A) Time-dependent DLS data show the conversion of a nanometer-scale material into micron-scale particles. (B) Zeta potential values are shown in a tabular form.

Regular stacking of the hybrid material also depends on the size of the guest molecule. An earlier report[34] showed the formation of regular stacking between myoglobin (Mb) and aminoclay, while disordered stacking was observed for hemoglobin (Hb) (with aminoclay). The surface charge of

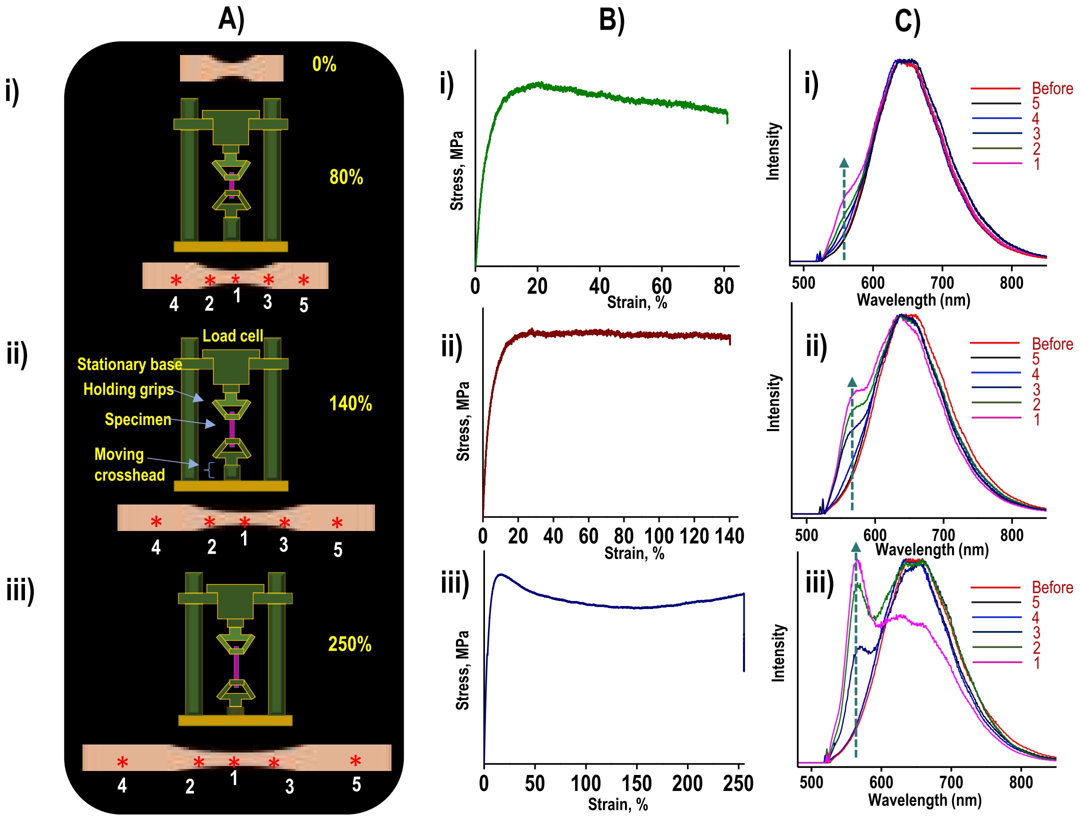

Figure 5. (A) Schematic representation of the tensile strength experiment. This experiment was carried out using dog bone-shaped luminescent PVA-added CCH samples. Samples were stretched up to 80, 140, and 250% of their original size. Each point, where the luminescence spectrum was collected, is marked by an asterisk (*) and labeled 1, 2, 3, 4, and 5 (corresponding to the different positions of the sample). (B) Stress−strain curve of the experiment. These three measurements correspond to three separate samples. (C) Corresponding changes in the luminescence profile. The spectra were collected from points (*) illustrated in (A).

both Hb and Mb is the same; however, the size of Hb is larger than that of Mb. Although this interaction is initiated through opposite charges, Hb failed to produce the regularly stacked structure due to larger size. In our case, the hydrodynamic size of Au_{30}@BSA is only 6 nm (shown in Figure S2). This size is small enough to be accommodated between the clay sheets, and thus, a regular hierarchical structure could be formed in this case.

The attachment of the clusters to aminoclay sheets and subsequent formation of larger ordered aggregates was probed by time-dependent DLS measurements. A systematic increase in the hydrodynamic diameter of the aggregates in the reaction mixture with time is shown in Figure 4A. This points to the fact that the cluster-attached aminoclay sheets stacked together to form larger structures in solution as the reaction progressed. These subsequently act as the nucleation sites for the new cluster-attached aminoclay sheets for deposition and micrometer-sized aggregates started to form (shown in the inset of Figure 4A), making the solution turbid. These ultimately come together during drying to form highly ordered hierarchical structures.

Stress−Strain Behavior of CCH. Cluster-sandwiched clay materials were cast in different shapes, such as film, dog bone, and so forth, to study their mechanical properties. During casting of the sample, PVA was added to the mixture. Since the clusters are already intercalated with CCH, the addition of PVA is not expected to alter the interlayer spacing. The layered structure of CCH was retained, as shown in Figure S5. Although the polymer and clay interaction is not new in the literature,[41,42] this composition is completely new, where PVA acts as a binder for our hybrid material. To study the stress−strain behavior, we have performed tensile strength measurements. This material showed highly ductile behavior after mixing with PVA (6 weight %). It could stretch up to 300% without failure (Figure S6).

For a systematic understanding of the mechanical property of the material, tensile strength experiments were conducted under the displacement control mode. This was performed in such a way that the final elongation of the sample was 80, 140, and 250% of the original sample length. A schematic representation of the experiment is shown in Figure 5A. The corresponding stress−strain curves are shown in Figure 5B, respectively. Interestingly, the change in the luminescence of the material was observed upon elongation, and a new luminescence peak at 575 nm emerged along with the peak of cluster luminescence at 650 nm. Here, the luminescence spectra were measured immediately after the tensile strength experiments, using 365 nm excitation. The intensity of the 575 nm peak (with respect to the 650 nm peak) was dependent on the degree of elongation of the sample. The luminescence spectra collected from different locations (1, 2, 3, 4, and 5) of the dog bone-shaped material after 80, 140, and 250% elongation are shown in Figure 5C. Intensity of the 575 nm peak increases with the degree of elongation of the sample. The change in the luminescence spectrum was not uniform throughout the length of the sample. The intensity of the 575 nm peak was maximum at the center, that is, at position 1, and minimum at the edges, that is, at positions 4 and 5. Positions 3

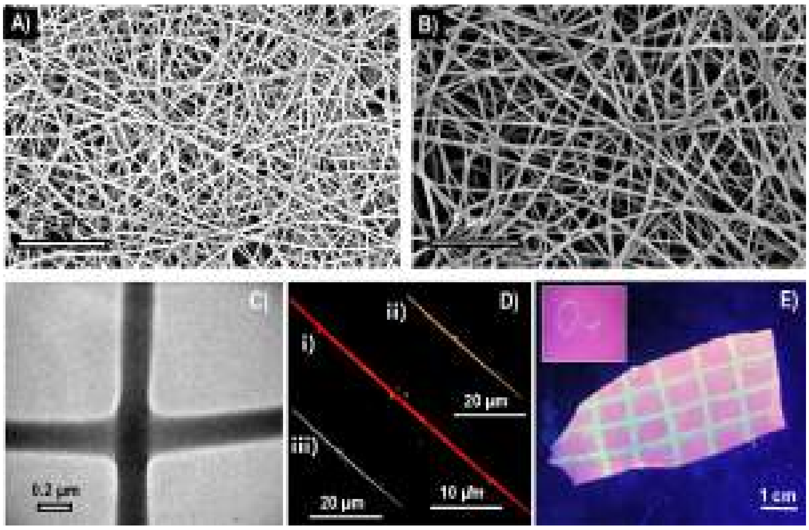

Figure 6. Characterization and application of nanofibers made from CCH. (A,B) FESEM image of an electrospun cluster-based clay material, in different magnifications. (C) TEM image of the fiber. (D) Dark field image of a single fiber showing the red luminescence (i). Inset shows bright field image of a single fiber (ii), and same image is shown in the gray scale (iii). (E) Writing experiment on the electrospun mat (see the inset) shows white light emission from the luminescent mat under UV light. Mechanochromic luminescence is shown by drawing the grid pattern on the luminescent mat with the tip of the cotton swab. The same effect is shown on another mat by writing “a” in a similar fashion (see the inset). White light emission was seen from the red luminescent mat under UV light in both cases. The UV light source of 365 nm excitation was used to visualize the luminescent pattern.

and 4 showed intermediate intensity. With regard to the intensity of the 575 nm peak for different degrees of elongation, only a small hump was observed for 80% elongation. The same peak became more prominent for the sample stretched to 140% and at 250%, the intensity surpassed that at 650 nm. It is important to mention that the spectra collected from different points across the length of the sample prior to elongation showed only the 650 nm peak at comparable intensity (Figure S7). Upon elongation at 250%, the peak at 650 nm got split and at 600 nm, a shoulder peak was observed. The spectra did not show significant change with time, in the course of 1 week, suggesting that irreversible changes have happened to the composite.

Luminescence in noble metal NCs is perceived to originate due to ligand to metal charge transfer (LMCT). In Au_{30}@BSA, the Au core is protected by cysteine residues of the protein through the formation of Au−S bonds. The presence of these Au−S bonds was confirmed by the extended X-ray absorption fine structure experiment in an earlier report.[43] In CCH, the cluster layer is sandwiched between two aminoclay layers. Stretching of the sample is likely to perturb the structure of the confined proteins. These, in turn, would affect the Au−S bonds. Thus, small changes in the bond length of Au−S bonds or their relative orientations around the Au core can happen, which would perturb the electronic states of the cluster. This can bring about changes in the luminescence of the cluster. This is proposed as one of the possible reasons for the emergence of the peak at 575 nm. Under high pressures, red shifts of the absorption and the emission onset of the $Au_{21}(SR)_{12}(dppm)_2$ (SR = cyclohexanethiolate; dppm = bisdiphenylphosphinemethane) and $Au_{28}(S\text{-}TBBT)_{20}$ (S-TBBT = *tert*-butyl-benzenethiolate) NCs were shown in a recent report.[44] This red shift is due to the narrowing of the energy levels of NCs because of the delocalization of the core electrons to the ligands under compression. These high-pressure experiments were carried out in a diamond anvil cell, and the effects of compression on clusters were monitored in situ using the changes in the optical properties. In our studies, a blue-shifted peak was observed under elongation. This new report supports our observation that the change in luminescence of CCH upon stretching originates from the alteration of the cluster structure, which cannot go back to a relaxed state due to its confinement within the aminoclay sheets. The change in the peak width in the newly originated peak was also observed. This may be due to the reason that all the clusters have not undergone the same amount of structural change at the same percentage of strain.

Application of Mechanochromic Luminescence. The change in the luminescence spectrum of the confined sandwiched cluster upon application of mechanical forces is the first of this kind in the literature of such clusters. Some gold complexes are known to show mechanoresponses.[45,46] Disruption of an ordered structure could lead to changes in photoluminescence. Organoboron materials showed solid-state mechanochromic luminescence.[47,48]

These clusters have long been utilized as chemical sensors to sense analytes such as toxic metal ions (such as Hg^{2+} and Pb^{2+}), explosives (such as 2,4,6-trinitrotoluene and 1,3,5-trinitroperhydro-1,3,5-triazine), and small molecules (such as dopamine, halocarbons, etc.).[49,50] In these cases, analytes interact with the cluster chemically and thus quench the luminescence. In order to utilize the newly found mechanochromic luminescence of the clusters in CCH, we proceeded to make large-area electrospun mats incorporating the composites. The reason for choosing the nanofiber mat was to have 1D geometry, which is known to have enhanced the performance due to their large surface-to-volume ratio.[51] Electrospun mats of luminescence cluster-coated polymers have been shown to enhance sensitivity toward analytes.[50,52]

Electrospun mats were created using the same composite material used for mechanical studies. This mat exhibited bright red luminescence, indicating intactness of the confined clusters (shown in Figure S8). After the electrospining process, the morphology of the fibers in the electrospun mat was studied in detail through microscopy. Uniform fibers were clearly seen in FESEM images (Figure 6A,B) at different magnifications, constituting the mat. Similar observations regarding the dimension of the fibers were also obtained from the TEM images (Figure 6C). The luminescence property of a single fiber was measured through fluorescence microscopy. The image showing a red luminescent fiber is shown in Figure 6D. The corresponding optical image is shown in the inset of Figure 6D. Pressure-sensitive nature of the incorporated fiber mat was examined by a writing experiment using a cotton swab. The areas where pressure was exerted during this writing experiment appeared white when exposed to UV light, while rest of the mat retained red luminescence (Figure 6E). Such a change in the luminescence in response to mechanical forces can be used as a security feature for devices.

SUMMARY AND CONCLUSIONS

In conclusion, protein-protected noble metal clusters were intercalated between the layers of aminoclay sheets to create a luminescent hierarchical organo-inorganic hybrid material. Coulombic interactions between these two species helped them to assemble and to create a higher order, insoluble structural material. FESEM studies proved the layered structure of CCH, and intercalation of the luminescent clusters between these clay layers was proven by pXRD measurements. DLS and zeta potential measurements shed light on the mechanistic pathway of the formation of CCH. High ductility of the material was shown by tensile strength measurements. Structural distortion in the cluster-sandwiched material led to the emergence of a new emission peak. This new property could be utilized to create a cluster-based pressure sensor. The mechanochromic luminescence response of the composite could also be utilized for monitoring physical damage in structures.

ASSOCIATED CONTENT

Supporting Information

The Supporting Information is available free of charge at https://pubs.acs.org/doi/10.1021/acsami.0c19239.

UV−vis spectrum, emission spectrum, DLS data of Au_{30}@BSA, pXRD data of aminoclay, stress−strain behavior of the dog bone sample, and luminescence spectra collected before the tensile strength experiment (PDF)

AUTHOR INFORMATION

Corresponding Author

Thalappil Pradeep − *DST Unit of Nanoscience (DST UNS) and Thematic Unit of Excellence, Department of Chemistry, Indian Institute of Technology Madras, Chennai 600036, India*; orcid.org/0000-0003-3174-534X;
Email: pradeep@iitm.ac.in

Authors

Debasmita Ghosh − *DST Unit of Nanoscience (DST UNS) and Thematic Unit of Excellence, Department of Chemistry, Indian Institute of Technology Madras, Chennai 600036, India*

Mohd Azhardin Ganayee − *DST Unit of Nanoscience (DST UNS) and Thematic Unit of Excellence, Department of Chemistry, Indian Institute of Technology Madras, Chennai 600036, India*

Anirban Som − *DST Unit of Nanoscience (DST UNS) and Thematic Unit of Excellence, Department of Chemistry, Indian Institute of Technology Madras, Chennai 600036, India*; orcid.org/0000-0002-6646-679X

Pillalamarri Srikrishnarka − *DST Unit of Nanoscience (DST UNS) and Thematic Unit of Excellence, Department of Chemistry, Indian Institute of Technology Madras, Chennai 600036, India*; orcid.org/0000-0001-5187-6879

Nidhi Murali − *Department of Applied Mechanics, Indian Institute of Technology Madras, Chennai 600036, India*

Sandeep Bose − *DST Unit of Nanoscience (DST UNS) and Thematic Unit of Excellence, Department of Chemistry, Indian Institute of Technology Madras, Chennai 600036, India*

Amrita Chakraborty − *DST Unit of Nanoscience (DST UNS) and Thematic Unit of Excellence, Department of Chemistry, Indian Institute of Technology Madras, Chennai 600036, India*

Biswajit Mondal − *DST Unit of Nanoscience (DST UNS) and Thematic Unit of Excellence, Department of Chemistry, Indian Institute of Technology Madras, Chennai 600036, India*

Pijush Ghosh − *Department of Applied Mechanics, Indian Institute of Technology Madras, Chennai 600036, India*; orcid.org/0000-0002-6077-6498

Complete contact information is available at:
https://pubs.acs.org/10.1021/acsami.0c19239

Author Contributions

D.G. synthesized the cluster and CCH and designed and conducted all laboratory experiments. D.G. conducted spectroscopic and mass spectrometric experiments and wrote the draft of the manuscript. M.A.G. synthesized the aminoclay. N.M. performed the tensile strength experiments. P.G. supervised the tensile strength experiments. P.S. helped with the electrospinning experiments for making nanofibers. Microscopic measurements were conducted by A.S., P.S., S.B., A.C., and B.M. The whole project was supervised by T.P. The manuscript was written with contributions of all authors.

Notes

The authors declare no competing financial interest.

ACKNOWLEDGMENTS

We thank the Department of Science and Technology, Government of India for continuous support of our research program on nanomaterials. D.G. thanks IIT Madras for a student fellowship.

REFERENCES

(1) Chakraborty, I.; Pradeep, T. Atomically Precise Clusters of Noble Metals: Emerging Link between Atoms and Nanoparticles. *Chem. Rev.* **2017**, *117*, 8208−8271.

(2) Xie, J.; Zheng, Y.; Ying, J. Y. Protein-Directed Synthesis of Highly Fluorescent Gold Nanoclusters. *J. Am. Chem. Soc.* **2009**, *131*, 888−889.

(3) Xavier, P. L.; Chaudhari, K.; Baksi, A.; Pradeep, T. Protein-Protected Luminescent Noble Metal Quantum Clusters: An Emerging Trend in Atomic Cluster Nanoscience. *Nano Rev.* **2012**, 3, 14767−14782.

(4) Ghosh, D.; Baksi, A.; Mudedla, S. K.; Nag, A.; Ganayee, M. A.; Subramanian, V.; Pradeep, T. Gold-Induced Unfolding of Lysozyme: Toward the Formation of Luminescent Clusters. *J. Phys. Chem. C* **2017**, *121*, 13335−13344.

(5) Kang, X.; Zhu, M. Tailoring the Photoluminescence of Atomically Precise Nanoclusters. *Chem. Soc. Rev.* **2019**, *48*, 2422−2457.

(6) Goswami, N.; Zheng, K.; Xie, J. Bio-NCs - The Marriage of Ultrasmall Metal Nanoclusters with Biomolecules. *Nanoscale* **2014**, *6*, 13328−13347.

(7) Weiss, A. Secret of Chinese Porcelains. *Angew. Chem.* **1963**, *75*, 755−762.

(8) Sposito, G.; Skipper, N. T.; Sutton, R.; Park, S.-H.; Soper, A. K.; Greathouse, J. A. Surface Geochemistry of the Clay Minerals. *Proc. Natl. Acad. Sci. U.S.A.* **1999**, *96*, 3358−3364.

(9) Sanchez, C.; Belleville, P.; Popall, M.; Nicole, L. Applications of Advanced Hybrid Organic-Inorganic Nanomaterials: From Laboratory to Market. *Chem. Soc. Rev.* **2011**, *40*, 696−753.

(10) Scheuermann, G. M.; Thomann, R.; Mülhaupt, R. Catalysts Based Upon Organoclay with Tunable Polarity and Dispersion Behavior: New Catalysts for Hydrogenation, C-C Coupling Reactions and Fluorous Biphase Catalysis. *Catal. Lett.* **2009**, *132*, 355−362.

(11) Balazs, A. C.; Emrick, T.; Russell, T. P. Nanoparticle Polymer Composites: Where Two Small Worlds Meet. *Science* **2006**, *314*, 1107−1110.

(12) Bonderer, L. J.; Studart, A. R.; Gauckler, L. J. Bioinspired Design and Assembly of Platelet Reinforced Polymer Films. *Science* **2008**, *319*, 1069−1073.

(13) Hsu, R.-S.; Chang, W.-H.; Lin, J.-J. Nanohybrids of Magnetic Iron-Oxide Particles in Hydrophobic Organoclays for Oil Recovery. *ACS Appl. Mater. Interfaces* **2010**, *2*, 1349−1354.

(14) Viseras, C.; Cerezo, P.; Sanchez, R.; Salcedo, I.; Aguzzi, C. Current Challenges in Clay Minerals for Drug Delivery. *Appl. Clay Sci.* **2010**, *48*, 291−295.

(15) Tzitzios, V.; Basina, G.; Bakandritsos, A.; Hadjipanayis, C. G.; Mao, H.; Niarchos, D.; Hadjipanayis, G. C.; Tucek, J.; Zboril, R. Immobilization of Magnetic Iron Oxide Nanoparticles on Laponite Discs -An Easy Way to Biocompatible Ferrofluids and Ferrogels. *J. Mater. Chem.* **2010**, *20*, 5418−5428.

(16) Whilton, N. T.; Burkett, S. L.; Mann, S. Hybrid Lamellar Nanocomposites Based on Organically Functionalized Magnesium Phyllosilicate Clays with Interlayer Reactivity. *J. Mater. Chem.* **1998**, *8*, 1927−1932.

(17) Mann, S.; Burkett, S. L.; Davis, S. A.; Fowler, C. E.; Mendelson, N. H.; Sims, S. D.; Walsh, D.; Whilton, N. T. Sol-Gel Synthesis of Organized Matter. *Chem. Mater.* **1997**, *9*, 2300−2310.

(18) Burkett, S. L.; Press, A.; Mann, S. Synthesis, Characterization, and Reactivity of Layered Inorganic-Organic Nanocomposites Based on 2:1 Trioctahedral Phyllosilicates. *Chem. Mater.* **1997**, *9*, 1071−1073.

(19) Bromley, K. M.; Patil, A. J.; Seddon, A. M.; Booth, P.; Mann, S. Bio-Functional Mesolamellar Nanocomposites Based on Inorganic/Polymer Intercalation in Purple Membrane (Bacteriorhodopsin) Films. *Adv. Mater.* **2007**, *19*, 2433−2438.

(20) Datta, K. K. R.; Achari, A.; Eswaramoorthy, M. Aminoclay: A Functional Layered Material with Multifaceted Applications. *J. Mater. Chem. A* **2013**, *1*, 6707−6718.

(21) Patil, A. J.; Li, M.; Dujardin, E.; Mann, S. Novel Bioinorganic Nanostructures Based on Mesolamellar Intercalation or Single-Molecule Wrapping of DNA Using Organoclay Building Blocks. *Nano Lett.* **2007**, *7*, 2660−2665.

(22) Mann, S. Self-assembly and Transformation of Hybrid Nano-Objects and Nanostructures under Equilibrium and Non-equilibrium Conditions. *Nat. Mater.* **2009**, *8*, 781−792.

(23) Wegst, U. G. K.; Bai, H.; Saiz, E.; Tomsia, A. P.; Ritchie, R. O. Bioinspired Structural Materials. *Nat. Mater.* **2015**, *14*, 23−36.

(24) Sellinger, A.; Weiss, P. M.; Nguyen, A.; Lu, Y.; Assink, R. A.; Gong, W.; Brinker, C. J. Continuous Self-Assembly of Organic-Inorganic Nanocomposite Coatings that Mimic Nacre. *Nature* **1998**, *394*, 256−260.

(25) Mayer, G. Rigid Biological Systems as Models for Synthetic Composites. *Science* **2005**, *310*, 1144−1147.

(26) Munch, E.; Launey, M. E.; Alsem, D. H.; Saiz, E.; Tomsia, A. P.; Ritchie, R. O. Tough, Bio-Inspired Hybrid Materials. *Science* **2008**, *322*, 1516−1520.

(27) Das, P.; Malho, J.-M.; Rahimi, K.; Schacher, F. H.; Wang, B.; Demco, D. E.; Walther, A. Nacre-Mimetics with Synthetic Nanoclays up to Ultrahigh Aspect Ratios. *Nat. Commun.* **2015**, *6*, 5967−5980.

(28) Luz, G. M.; Mano, J. F. Biomimetic Design of Materials and Biomaterials Inspired by the Structure of Nacre. *Philos. Trans. R. Soc., A* **2009**, *367*, 1587−1605.

(29) Liu, Y.; Yu, S.-H.; Bergström, L. Transparent and Flexible Nacre-Like Hybrid Films of Aminoclays and Carboxylated Cellulose Nanofibrils. *Adv. Funct. Mater.* **2018**, *28*, 1703277−1703285.

(30) Kakisawa, H.; Sumitomo, T. The Toughening Mechanism of Nacre and Structural Materials Inspired by Nacre. *Sci. Technol. Adv. Mater.* **2011**, *12*, 064710−064714.

(31) Gerhard, E. M.; Wang, W.; Li, C.; Guo, J.; Ozbolat, I. T.; Rahn, K. M.; Armstrong, A. D.; Xia, J.; Qian, G.; Yang, J. Design Strategies and Applications of Nacre-Based Biomaterials. *Acta Biomater.* **2017**, *54*, 21−34.

(32) Deville, S.; Saiz, E.; Nalla, R. K.; Tomsia, A. P. Freezing as a Path to Build Complex Composites. *Science* **2006**, *311*, 515−518.

(33) Mao, L.-B.; Gao, H.-L.; Yao, H.-B.; Liu, L.; Colfen, H.; Liu, G.; Chen, S.-M.; Li, S.-K.; Yan, Y.-X.; Liu, Y.-Y.; Yu, S.-H. Synthetic Nacre by Predesigned Matrix-Directed Mineralization. *Science* **2016**, *354*, 107−110.

(34) Patil, A. J.; Mann, S. Self-Assembly of Bio-Inorganic Nanohybrids using Organoclay Building Blocks. *J. Mater. Chem.* **2008**, *18*, 4605−4615.

(35) Martin, J. E.; Patil, A. J.; Butler, M. F.; Mann, S. Guest-Molecule-Directed Assembly of Mesostructured Nanocomposite Polymer/Organoclay Hydrogels. *Adv. Funct. Mater.* **2011**, *21*, 674−681.

(36) Patil, A. J.; Muthusamy, E.; Seddon, A. M.; Mann, S. Higher-Order Synthesis of Organoclay Pipes using Self-Assembled Lipid Templates. *Adv. Mater.* **2003**, *15*, 1816−1819.

(37) Lin, L.; Liu, M.; Chen, L.; Chen, P.; Ma, J.; Han, D.; Jiang, L. Bio-Inspired Hierarchical Macromolecule-Nanoclay Hydrogels for Robust Underwater Superoleophobicity. *Adv. Mater.* **2010**, *22*, 4826−4830.

(38) Patil, A. J.; Li, M.; Mann, S. Integrative Self-Assembly of Functional Hybrid Nanoconstructs by Inorganic Wrapping of Single Biomolecules, Biomolecule Arrays and Organic Supramolecular Assemblies. *Nanoscale* **2013**, *5*, 7161−7174.

(39) Patil, A. J.; Muthusamy, E.; Mann, S. Fabrication of Functional Protein-Organoclay Lamellar Nanocomposites by Biomolecule-Induced Assembly of Exfoliated Aminopropyl-Functionalized Magnesium Phyllosilicates. *J. Mater. Chem.* **2005**, *15*, 3838−3843.

(40) Ghosh, D.; Bodiuzzaman, M.; Som, A.; Raja, S.; Baksi, A.; Ghosh, A.; Ghosh, J.; Ganesh, A.; Samji, P.; Mahalingam, S.; Karunagaran, D.; Pradeep, T. Internalization of a Preformed Atomically Precise Silver Cluster in Proteins by Multistep Events and Emergence of Luminescent Counterparts Retaining Bioactivity. *J. Phys. Chem. C* **2019**, *123*, 29408−29417.

(41) Johnsy, G.; Datta, K. K. R.; Sajeevkumar, V. A.; Sabapathy, S. N.; Bawa, A. S.; Eswaramoorthy, M. Aminoclay: A Designer Filler for the Synthesis of Highly Ductile Polymer-Nanocomposite Film. *ACS Appl. Mater. Interfaces* **2009**, *1*, 2796−2803.

(42) Verho, T.; Karppinen, P.; Gröschel, A. H.; Ikkala, O. Imaging Inelastic Fracture Processes in Biomimetic Nanocomposites and Nacre by Laser Speckle for Better Toughness. *Adv. Sci.* **2018**, *5*, 1700635.

(43) Chevrier, D. M.; Thanthirige, V. D.; Luo, Z.; Driscoll, S.; Cho, P.; MacDonald, M. A.; Yao, Q.; Guda, R.; Xie, J.; Johnson, E. R.; Chatt, A.; Zheng, N.; Zhang, P. Structure and Formation of Highly Luminescent Protein-Stabilized Gold Clusters. *Chem. Sci.* **2018**, *9*, 2782−2790.

(44) Li, Q.; Mosquera, M. A.; Jones, L. O.; Parakh, A.; Chai, J.; Jin, R.; Schatz, G. C.; Gu, X. W. Pressure-Induced Optical Transitions in Metal Nanoclusters. *ACS Nano* **2020**, *14*, 11888−11896.

https://dx.doi.org/10.1021/acsami.0c19239
ACS Appl. Mater. Interfaces XXXX, XXX, XXX−XXX

(45) Lee, Y.-A.; Eisenberg, R. Luminescence Tribochromism and Bright Emission in Gold(I) Thiouracilate Complexes. *J. Am. Chem. Soc.* **2003**, *125*, 7778−7779.

(46) Assefa, Z.; Omary, M. A.; McBurnett, B. G.; Mohamed, A. A.; Patterson, H. H.; Staples, R. J.; Fackler, J. P., Jr. Syntheses, Structure, and Photoluminescence Properties of the 1-Dimensional Chain Compounds [(TPA)2Au][Au(CN)2] and (TPA)AuCl (TPA = 1,3,5-Triaza-7-phosphaadamantane). *Inorg. Chem.* **2002**, *41*, 6274−6280.

(47) Zhang, G.; Lu, J.; Sabat, M.; Fraser, C. L. Polymorphism and Reversible Mechanochromic Luminescence for Solid-State Difluoroboron Avobenzone. *J. Am. Chem. Soc.* **2010**, *132*, 2160−2162.

(48) Sun, X.; Zhang, X.; Li, X.; Liu, S.; Zhang, G. A Mechanistic Investigation of Mechanochromic Luminescent Organoboron Materials. *J. Mater. Chem.* **2012**, *22*, 17332−17339.

(49) Mathew, A.; Sajanlal, P. R.; Pradeep, T. Selective Visual Detection of TNT at the Sub-Zeptomole Level. *Angew. Chem., Int. Ed.* **2012**, *51*, 9596−9600.

(50) Ghosh, A.; Jeseentharani, V.; Ganayee, M. A.; Hemalatha, R. G.; Chaudhari, K.; Vijayan, C.; Pradeep, T. Approaching Sensitivity of Tens of Ions Using Atomically Precise Cluster-Nanofiber Composites. *Anal. Chem.* **2014**, *86*, 10996−11001.

(51) Ling, S.; Qin, Z.; Huang, W.; Cao, S.; Kaplan, D. L.; Buehler, M. J. Design and Function of Biomimetic Multilayer Water Purification Membranes. *Sci. Adv.* **2017**, *3*, No. e1601939.

(52) Subramanian, V.; Jena, S.; Ghosh, D.; Jash, M.; Baksi, A.; Ray, D.; Pradeep, T. Dual Probe Sensors Using Atomically Precise Noble Metal Clusters. *ACS Omega* **2017**, *2*, 7576−7583.

https://dx.doi.org/10.1021/acsami.0c19239

Supporting Information

Hierarchical Assembly of Atomically Precise Metal Clusters as a Luminescent Strain Sensor

Debasmita Ghosh,[1] *Mohd Azhardin Ganayee,*[1] *Anirban Som,*[1] *Pillalamarri Srikrishnarka,*[1] *Nidhi Murali,*[2] *Sandeep Bose,*[1] *Amrita Chakraborty,*[1] *Biswajit Mondal,*[1] *Pijush Ghosh,*[2] *Thalappil Pradeep*[1]**

[1]DST Unit of Nanoscience (DST UNS) and Thematic Unit of Excellence, Department of Chemistry, Indian Institute of Technology Madras, Chennai 600036, India.

[2]Department of Applied Mechanics, Indian Institute of Technology Madras, Chennai 600036, India.

Corresponding Author

*E-mail: pradeep@iitm.ac.in

Table of Contents

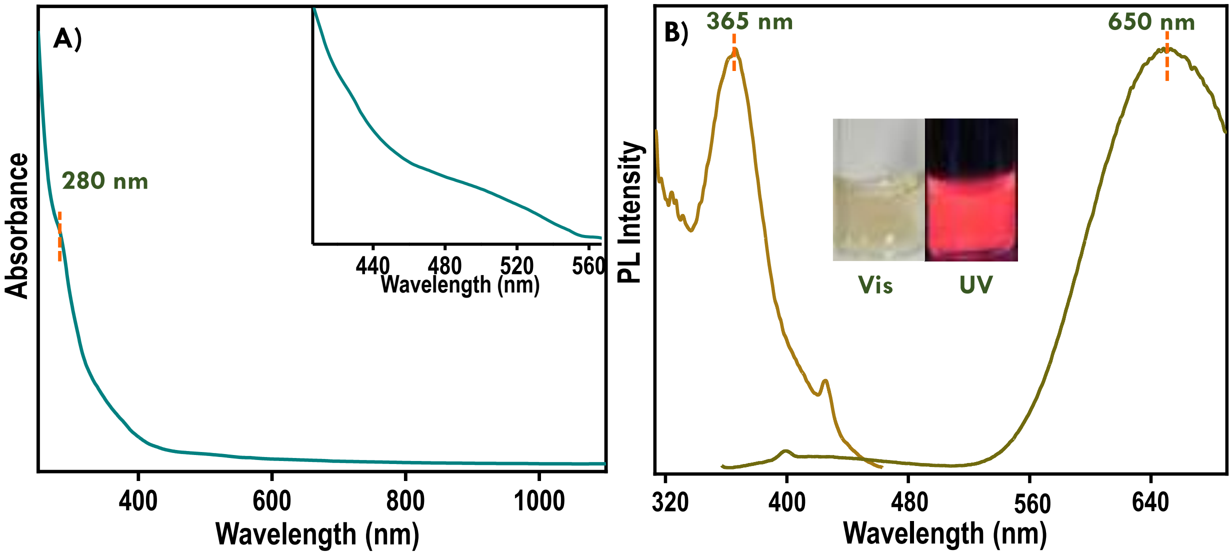

Figure S1. A) UV-vis spectrum of Au_{30}@BSA showing a peak around 280 nm and a broad peak from 450 to 550 nm (shown in the inset). B) Excitation and emission spectrum of Au_{30}@BSA. Emission spectrum shows the maxima at 650 nm for excitation at 365 nm. Inset shows the light brown color of the cluster solution under visible light and bright red color under UV light.

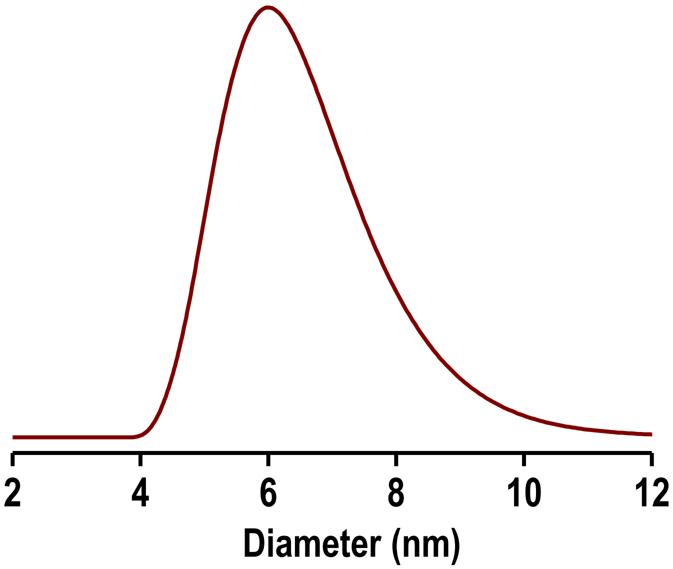

Figure S2. Particle size distribution of Au_{30}@BSA showing the cluster size to be 6 nm.

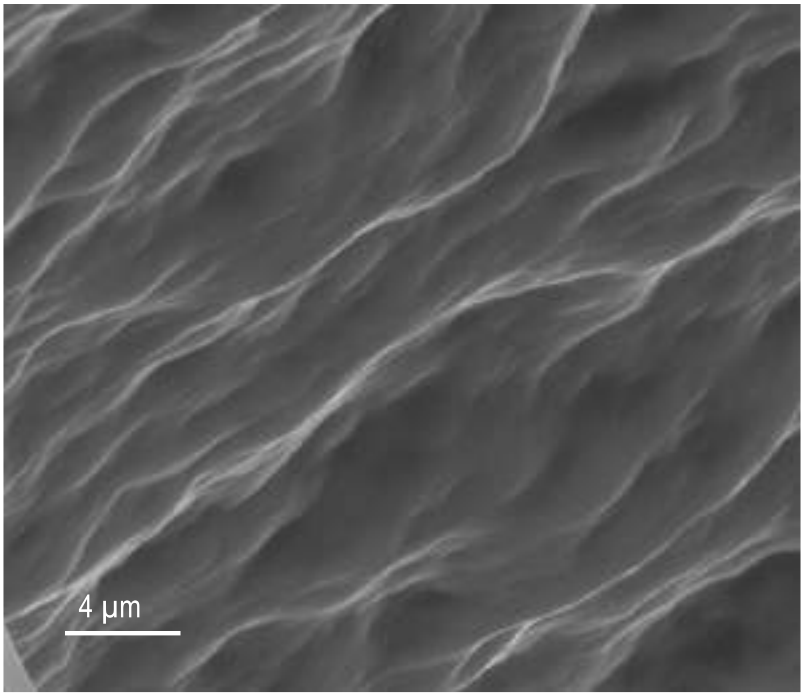

Figure S3. FESEM image shows the roughness of the surface of CCH.

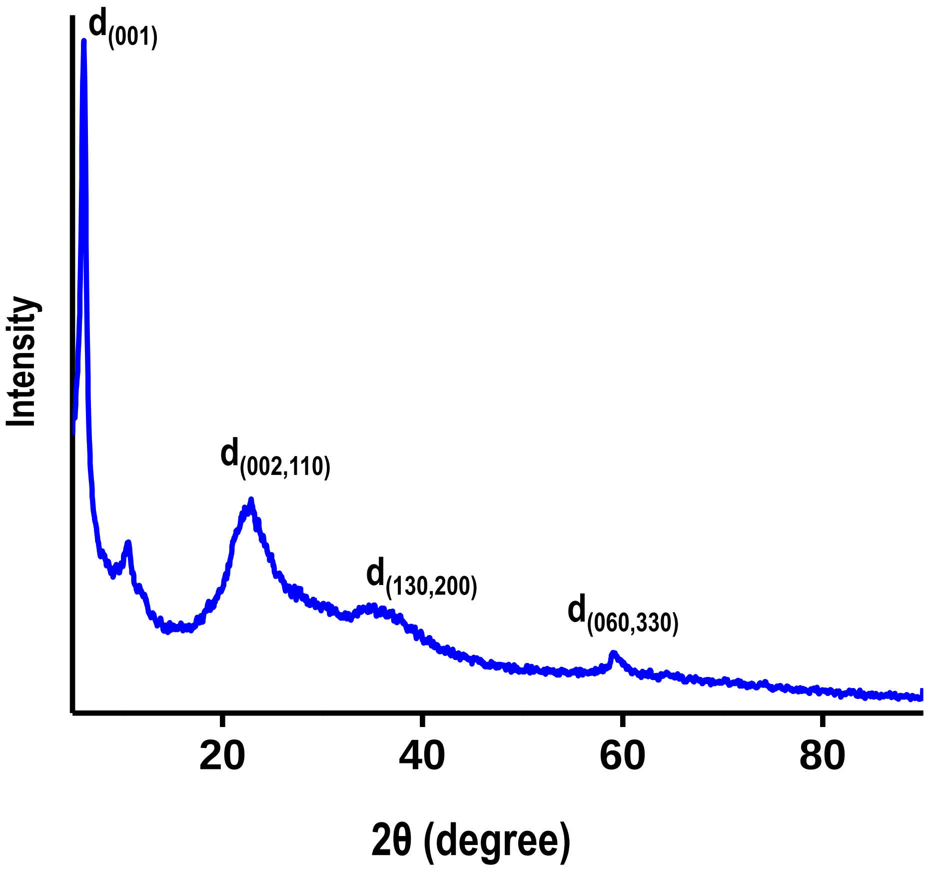

Figure S4. Powder XRD pattern of aminoclay shows several peaks corresponding to different crystallographic planes of the clay.

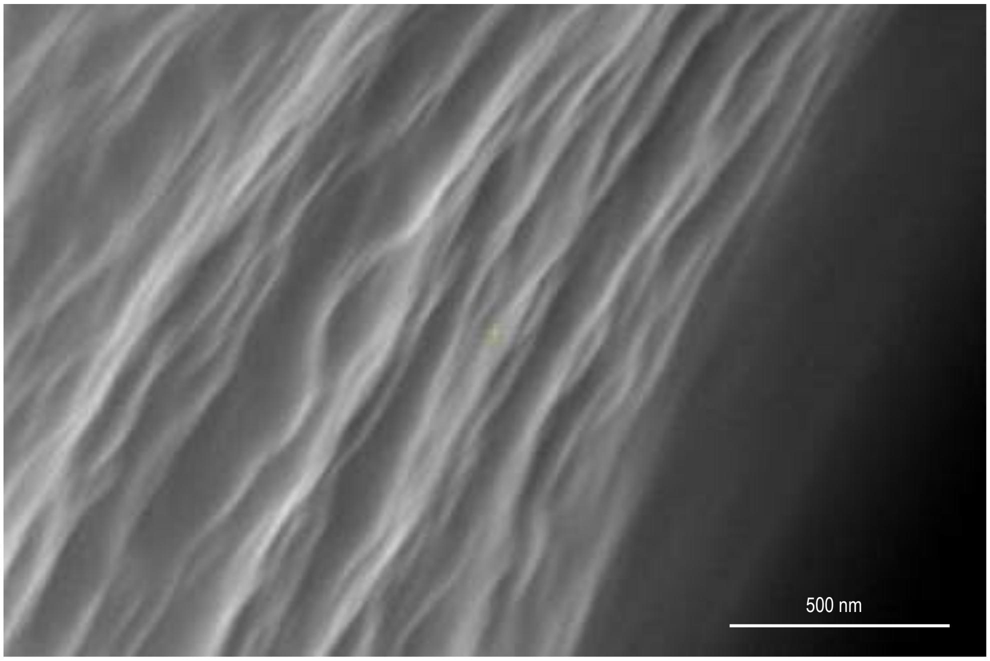

Figure S5. FESEM image of PVA added CCH showing the layered structure.

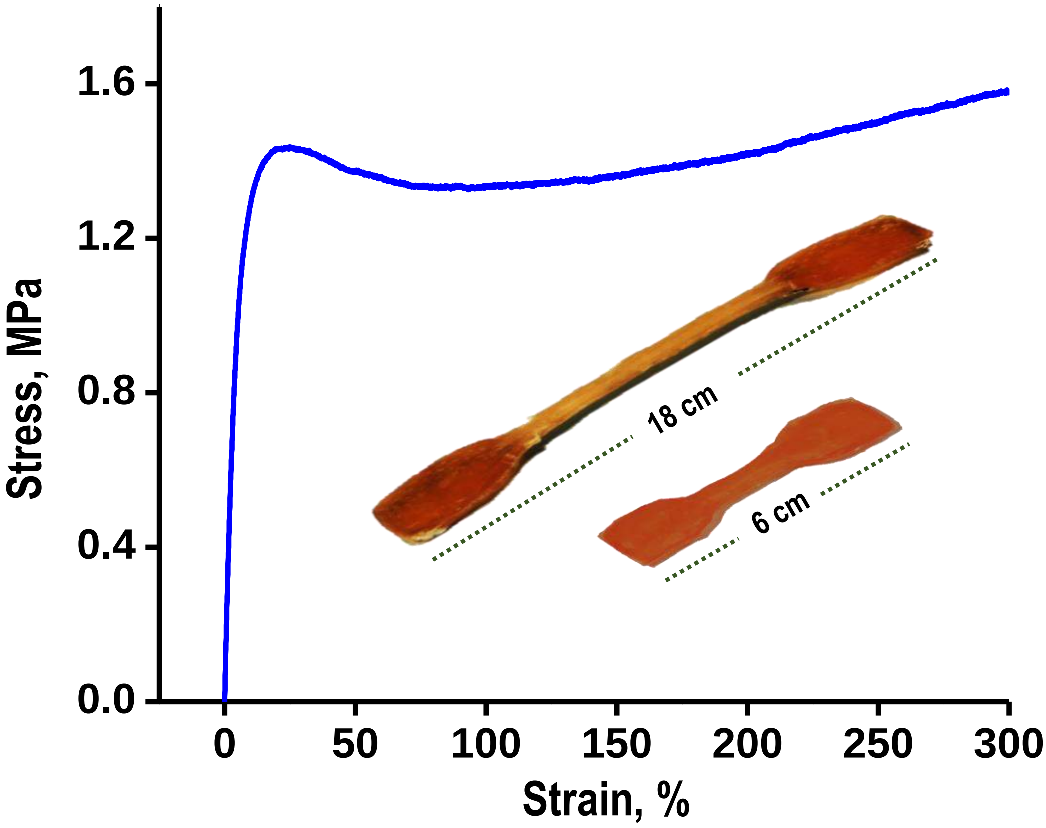

Figure S6. Stress-strain behavior of the dog bone sample showing high ductility of the material.

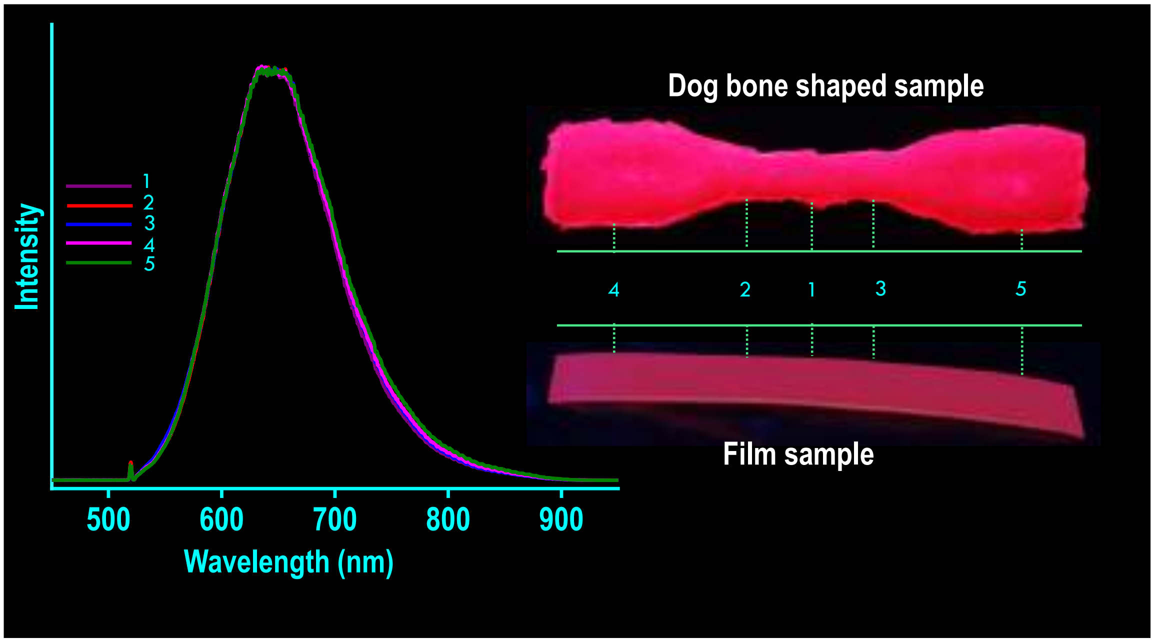

Figure S7. The luminescence spectrum collected from different positions (1, 2, 3, 4, and 5) of the dog bone and film samples before the tensile strength experiment. Inset shows the actual red luminescent dog bone and film samples used for experiment, different positions are marked.

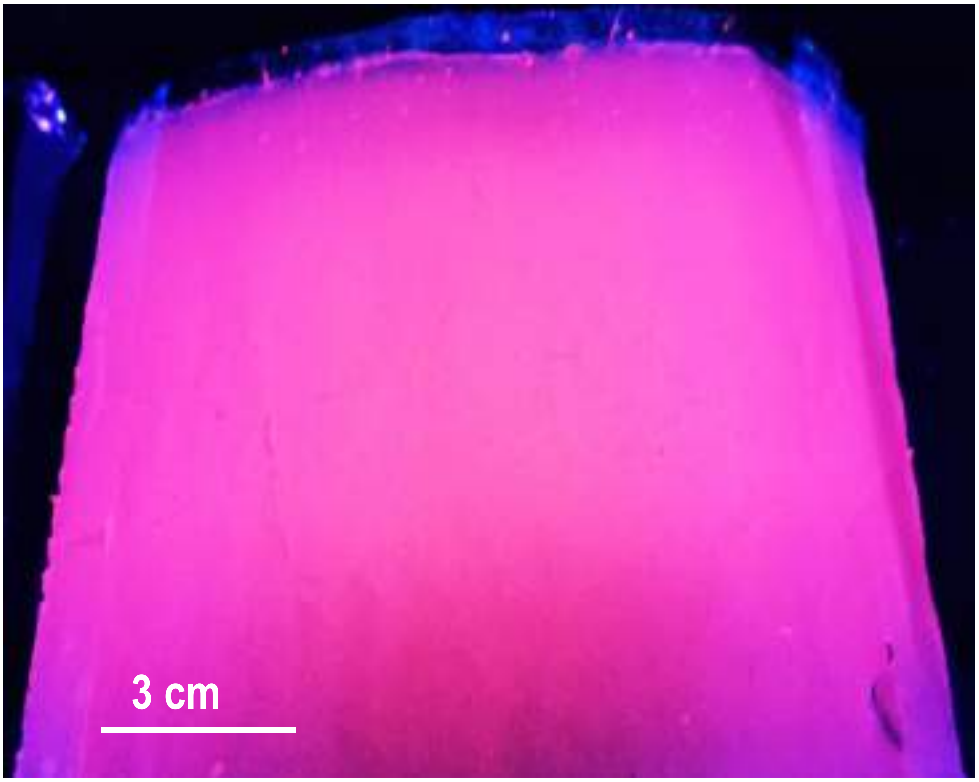

Figure S8. Image of electrospun CCH under UV light showing bright red luminescence.

THE JOURNAL OF
PHYSICAL
CHEMISTRY C
A JOURNAL OF THE AMERICAN CHEMICAL SOCIETY

pubs.acs.org/JPCC Article

Near-Infrared Chiral Plasmonic Microwires through Precision Assembly of Gold Nanorods on Soft Biotemplates

Amrita Chakraborty, Nonappa, Biswajit Mondal, Kamalesh Chaudhari, Heikki Rekola, Ville Hynninen, Mauri A. Kostiainen,* Robin H. A. Ras,* and Thalappil Pradeep*

Cite This: *J. Phys. Chem. C* 2021, 125, 3256−3267

Read Online

ABSTRACT: Directing the assembly of plasmonic nanoparticles into chiral superstructures has diverse applications including, chiroptical sensing, nonlinear optics, and biomedicine. Though soft template-mediated assemblies of both spherical and nonspherical gold nanoparticles have made significant progress, most approaches require sophisticated chemical synthesis or advanced methodologies. Besides, reports of structurally precise chiral plasmonic assemblies beyond nanoscale are limited. Here, we propose an efficient yet simple strategy to grow such precision assemblies up to mesoscale, which is beneficial for a broader community. Briefly, cationic gold nanorods (AuNRs) are allowed to systematically assemble along atomically precise, chiral, rodlike tobacco mosaic virus (TMV) particles via electrostatic attraction under ambient condition. This leads to spontaneous formation of helical hybrid microwires with high structural precision, as evidenced by cryogenic transmission electron microscopy and tomography. Resulting composite superstructures show a strong circular dichroism response at the plasmon wavelength of the AuNRs, which is supported by simulations using discrete dipole approximation. Further, chirality of the system is investigated at a single-microwire level using polarized dark-field scattering microscopy. An alternative chiral template, negatively charged colloidal cellulose nanocrystals, also arrange AuNRs into similar chiral microstructures. Thus, our report proposes a generic methodology to obtain chiral plasmonic response at the NIR region using inexpensive templates that will encourage the exploration of a wider range of nanoscale templates for creating hybrid mesostructures with emerging optoelectronic properties.

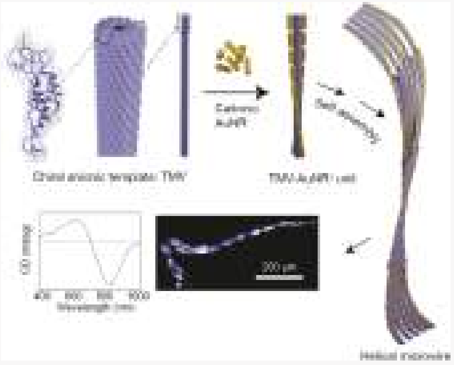

■ INTRODUCTION

Chirality is ubiquitous in nature and encountered at all length scales, from molecular-level to macroscopic objects. At molecular and macromolecular levels, biomolecules such as amino acids (except glycine), carbohydrates, proteins, and nucleic acids represent inherently chiral entities.[1] Further, at higher length scales, proteins (e.g., collagen and fibrin) and other biopolymers (e.g., agarose) undergo polymerization, resulting in helical fibrillar nanostructures.[2] Importantly, chiral entities absorb either right or left circularly polarized light preferentially (chiroptical properties). The differential absorption of right and left circularly polarized light leads to circular dichroism (CD).[3] CD spectroscopy is a powerful tool detecting molecular chirality,[4] protein folding−unfolding mechanisms, and conformational changes during chemical reactions.[5] However, most chiral organic molecules absorb in the ultraviolet (UV) region, and signals are weak in the visible region of the electromagnetic spectrum. Selective functionalization of dye molecules with chiral substituents allows CD signals in the visible range of the spectrum.[6] Beyond the molecular level, chirality can also be amplified using self-assemblies to achieve helices, twisted tapes, or twisted ribbon-like nanostructures.[7]

Unlike organic molecules, metal nanoparticles possess the capacity to confine light, enhancing light−matter interaction. Many theoretical[8,9] and experimental[10,11] studies have shown that incorporation of plasmonic nanoparticles dramatically enhances the chiroptical response of a chiral system, thereby lowering its detection limit. They also serve as building blocks for optical metamaterials. Moreover, these plasmon-enhanced CD signals shift to the position of the plasmon resonance frequency of the respective nanoparticles, i.e., the visible−near-infrared (NIR) region.[12,13] Thus, a broad wavelength range can be exploited simply by regulating the size and shapes of the nanoparticles. Such a phenomenon has application potential in circular polarizers,[14] detectors of circularly polarized light,[15] sensors of biomolecules,[16] and asymmetric catalysis.[17] Therefore, strategies to efficiently conjugate plasmonic property and chirality have become an active field of research. Nanostruc-

Received: December 27, 2020
Revised: January 8, 2021
Published: February 1, 2021

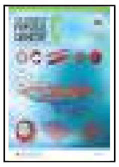

https://dx.doi.org/10.1021/acs.jpcc.0c11512

tures with right- or left-handedness in their intrinsic morphology give highly intense CD signals. But they are either fabricated by a top-down approach like nanolithography, which has limitations in producing genuinely three-dimensional morphologies, especially in large-scale production, or achieved through wet chemical syntheses that are laborious, complex, and suffer from nonuniformity and poor reproducibility.

Therefore, functionalization of commonly available spherical or anisotropic noble-metal nanoparticles (NMNPs) with chiral moieties such as cysteine,[18] peptides,[19] polyfluorenes,[10] or DNA,[20] has evolved as a rather straightforward approach to induce chirality. Due to the interaction between these chiral molecules and the plasmon of the achiral nanoparticle, such composites show a prominent CD signal, which is called surface plasmon-enhanced circular dichroism (SPECD). From the numerous theoretical[8,21,22] and experimental studies[18,19,23] we can conclude that SPECD produces the strongest signal when chiral molecules are placed at the plasmonic hotspots within a 3D nanoparticle assembly. However, placing a single molecule in the hotspot with precision is challenging. Govorov and co-workers have shown that spherical gold nanoparticles, arranged in an asymmetric, i.e., tetrahedral or helical geometry, produce a collective CD signal at their plasmonic resonance frequency.[21] Since then, a number of methodologies have been developed to arrange presynthesized NPs of desired size and shape along a soft helical backbone, e.g., peptides,[24,25] nematic liquid crystals,[26] fiber-like soft materials,[27] supramolecular backbones,[28] and DNA origami.[29,30] The success of this strategy lies in the extent of precision by which the template can regulate the nanoparticles' three-dimensional arrangement. DNA origami, being programmable, serves as one of the precise methods for arranging NMNPs in a desired geometry.[31] However, the cost-intensive nature and high level of expertise required for DNA nanotechnology prohibit it from being the most accessible strategy for materials scientists. Thus, although the field of template-assisted chiral plasmonic nanomaterials has made considerable progress, there is still room for a strategically simple way to assemble metallic nanoparticles on inexpensive soft templates with high structural precision. Bacterial cells[32] and viral capsids of well-defined structures[33] are recently being explored as alternative building blocks of higher-level assemblies, leading to functional nanomaterials. Simple electrostatic interactions can efficiently assemble protein cages within themselves,[34] as well as with plasmonic nanoparticles,[35] creating highly ordered superstructures. Keeping these in mind, we have chosen tobacco mosaic virus (TMV) as the chiral template. Native TMV is a biocolloidal substrate of rodlike morphology with known crystal structure, highly negative surface charge (ζ-potential, −25.4 mV in phosphate buffer of pH 7.8), and precise size and shape monodispersity. A viral RNA, helically wrapped by 2130 coat proteins, generates a right-handed chirality in its structure.[36] In the present work, we have allowed cationic AuNRs to arrange along the TMV surfaces through electrostatic self-assembly and observed a strong bisignate circular dichroism signal at the visible−NIR wavelength range. The generality of our strategy to create NIR chiral plasmonic microwires is established using cellulose nanocrystals (CNC) as another template. DNA origami and peptide production technologies, though result in assemblies of high structural precision, are not easily scalable. On the contrary, extraction and purification procedures of TMVs and CNCs are well established in plant biotechnology, allowing the production of these templates in kilograms. Moreover, for various device-based applications like telecommunication, significant effort has been made to make mesoscale helical superstructures.[37] The morphology and surface charge distribution of TMV and CNC guide a spontaneous translation of chirality from nanoscale to micron scale range, which is a clear advantage of the present strategy. Thus, our approach addresses some of the most important challenges of achieving precision assembly of nanoparticles up to micron scale toward creating SPECD in the NIR region.

■ EXPERIMENTAL METHODS

Preparation and Characterization of Tobacco Mosaic Virus Particles. The leaves of a month-old *Nicotiana tabacum* (var. Samson) plants were inoculated by rubbing them with wild-type TMV stock. The upper leaves that showed severe TMV symptoms were collected after 22 days to achieve 52 g of leaf biomass. TMV was purified following the procedure reported by Chapman.[38] Precisely, 0.5 M phosphate buffer of pH 7.2 along with 1% (v/v) 2-mercaptoethanol were used to homogenize the leaves. The leaf juice was filtered and extracted with butan-1-ol, centrifuged, and the aqueous phase was collected. PEG 8000 (4%) was used to precipitate the TMV. This pellet of virus was washed by phosphate buffer (10 mM, pH 7.2) mixed with 0.7 M NaCl and 4% PEG. It was then resuspended and further purified according to Liljeström et al.[39] The stock TMV was diluted using DI water just before the experiments.

Synthesis of AuNR. Highly monodisperse gold nanorods of aspect ratio ∼3.4 were prepared following a seedless synthetic procedure proposed by our group.[40] CTAB solution (20 mL, 100 mM) was taken in a 50 mL conical flask and kept in a water bath to maintain the temperature at 28 °C. To this, 1 mL of 10 mM $HAuCl_4 \cdot 3H_2O$, 130 μL of 10 mM freshly prepared $AgNO_3$, and 140 μL of 100 mM fresh ascorbic acid were added sequentially with mild stirring. As soon as the brownish-yellow solution (due to the complex formed by CTAB and $HAuCl_4$) became colorless due to the reduction of Au^{3+} to Au^+ by ascorbic acid, 200 μL of 1.67 mM $NaBH_4$ (freshly prepared in ice-cold water) was added at one shot. The stirring was stopped immediately after the addition of $NaBH_4$. Although the colorless solution slowly turned dark brown within 30 min, showing the high yield of nanorods, it was kept undisturbed for at least 4 h to ensure that the growth was complete.

Cationization of AuNRs. The excess CTAB-stabilized AuNRs were washed using distilled water for further use. For that, the as-synthesized AuNRs were taken in 2 mL plastic vials and centrifuged at 13 000 rpm for 20 min, the supernatant from each vial was discarded, and the precipitate was resuspended in 1.5 mL of DI water. This was again centrifuged in a similar way, but this time, the precipitate was not resuspended in water. Rather, 20 μL of 4 mM ethanolic solution of (11-mercaptoundecyl)-*N*,*N*,*N*-trimethylammonium bromide (MUTAB) was added to the pellet in each vial and shaken vigorously for 30 min. It was kept overnight without stirring and then washed with water. Precisely, the pellet was dispersed in 2 mL of DI water, centrifuged, and then 1.9 mL of water was decanted. Finally, it was dispersed in a suitable amount of water to attain an absorbance of 1.2 such that the MUTAB concentration in the solution was significantly less than 0.002 mM.

Synthesis of CNCs. As described by Hynninen et al.,[41] Whatman grade 1 filter papers were ground to form a homogeneous powder. To 15 g of this paper powder, 64% sulfuric acid solution was added in a round-bottom flask and mixed thoroughly by stirring. This was hydrolyzed at 45 °C for 45 min and then diluted 10 times using Milli-Q water to cease the reaction. This was kept still until complete sedimentation. The precipitate was collected after decanting the clear supernatant. The pellet was redispersed in Milli-Q water and centrifuged at 6000 rpm for 20 min first, and in the second round, at 2500 rpm for 45 min. Further purification was carried out by dialysis against Milli-Q water until the conductivity of the dialysate reduced below 5 μS/cm. Then, it was passed through a Whatman 541 filter paper and stored at +4 °C. The concentration of CNC was determined gravimetrically by slow evaporation of water and the stock solution was found to be 3.5 wt %.

TMV-AuNR$^+$ Assembly Formation. The MUTAB-functionalized AuNR$^+$ solution was diluted by adding DI water until the absorbance of the LSPR was ~1.2. The TMV stock solution was diluted using DI water to 0.21 mg/mL. The diluted TMV solution was added at 25 μL steps to a cuvette for UV−vis spectrometer, containing 2 mL of AuNR$^+$ solution and mixed gently using a pipette. After every addition, absorption spectra were measured to ensure systematic assembly from the slight gradual shift in the absorption peak maxima. There was no significant time gap needed between TMV addition and measurement of absorption spectra.

CNC-AuNR$^+$ Assembly Formation. This was the same as the assembly with TMV. CNC of 0.009 mg/mL concentration was added in 2 μL steps.

Instrumentation. All of the UV−vis absorption spectra were recorded using a PerkinElmer Lambda 25 UV−vis spectrometer.

The TEM measurements were performed using a JEOL 3010 (JEOL Japan) transmission electron microscope, using a 200 kV acceleration voltage.

SerialEM and 3D Reconstruction. For transmission electron tomographic reconstruction, tilt series of 2D projections were acquired with the SerialEM software package.[42,43] The specimen was tilted between ±69° angles with 2° increment steps under low-dose mode.[44] The acquired stack of images was first subjected to a series of preprocessing, coarse alignment, and final alignment, and further aligned using IMOD software package.[45] The final aligned file was then utilized for 3D reconstruction with custom-made maximum entropy method (MEM) program with a regularization parameter value of $\lambda = 1.0 \times 10^{-3}$ on MacPro.[46] The 3D isosurface and solid colored images were produced using UCSF Chimera.

Cryo-Transmission Electron Microscopy. The cryo-TEM images were collected using a JEM 3200FSC field emission microscope (JEOL) operated at 300 kV in bright-field mode with an Omega-type zero-loss energy filter. Prior to sample preparation, 200-mesh copper grids with a lacey carbon support film (Electron Microscopy Sciences) were plasma-cleaned using a Gatan Solarus (Model 950) plasma cleaner for 30 s. The samples for Cryo-TEM imaging were prepared by placing 3 μL of the sample on plasma-treated TEM grids and plunge-frozen into a −170 °C ethane−propane (1:1) mixture using a Leica automatic plunge freezer EM GP2 with 2 s blotting time under 100% humidity. The vitrified specimen was cryo-transferred to the microscope. The images were acquired with Gatan Digital Micrograph software, while the specimen temperature was maintained at −187 °C.

Circular Dichroism Study. The circular dichroism spectra of all of the samples were measured in a Jasco J-1500 spectrometer. A quartz cuvette of 10 mm path length was used for each measurement.

Modeling the Circular Dichroism. We used discrete dipole approximation (DDA)[47,48] to calculate the CD signal for a nanoparticle assembly. The nanoparticle coordinates were determined from TEM tomography measurement, and the model contained 293 nanoparticles. The exact orientation of the nanorods could not be extracted from the tomography data; instead, we had set the long axis of the nanorods along the main axis of the nanorod assembly with a normally distributed variance (sigma) of 20°. The length of the nanorod was set to 34 nm with a variance of 6.2 nm, and the diameter was set to 10 nm with a 2 nm variance. As the parameters had a randomly generated component, all of the results presented were average values obtained from 40 simulation runs.

In the simulations, each nanoparticle was represented by a point dipole. The polarizability of the point dipole was calculated using the modified long-wavelength approximation (MLWA),[49] assuming an ellipsoidal shape for the particle

$$\alpha_{\mathrm{MLWA},j} = \frac{\alpha_j}{1 - \frac{k^2}{j}\alpha_j - \frac{2}{3}ik^3\alpha_j}$$

where α_j is the quasistatic polarizability of the particle along its semiaxes $j = [a, b, c]$, given by

$$\alpha_j = 4\pi abc\frac{\varepsilon_1(\omega) - \varepsilon_2}{3\varepsilon_2 + 3L_j(\varepsilon_1(\omega) - \varepsilon_2)}$$

The term L_j is given by[50]

$$L_j = \frac{abc}{2}\int_0^\infty \frac{dq}{(q + j^2)\sqrt{(q + a^2)(q + b^2)(q + c^2)}}$$

Finally, the polarizability of the nth nanoparticle of the structure is represented by a matrix

$$\alpha_n = \begin{pmatrix} \alpha_{\mathrm{MLWA},a} & 0 & 0 \\ 0 & \alpha_{\mathrm{MLWA},b} & 0 \\ 0 & 0 & \alpha_{\mathrm{MLWA},c} \end{pmatrix}$$

This polarizability matrix was then rotated for each nanoparticle to account for the different orientations of the nanorods within the structure. Finally, we calculated the CD response of the self-assembled system using the discrete dipole approximation (DDA).[47,48] The induced dipole moments in the whole nanoparticle assembly were

$$\mathbf{P} = (1 - \hat{\boldsymbol{\alpha}}\,\mathbf{G}^0)^{-1}\hat{\boldsymbol{\alpha}}\,\mathbf{E}^{\mathrm{ext}}$$

We calculated the matrix inversion and used it to evaluate the dipole moments for different incident fields $\mathbf{E}_{\mathbf{ext}} = \mathbf{E}_k^{\mathrm{L/R}}\exp(i\mathbf{k}\cdot\mathbf{r})$. Here, the vector $\mathbf{k}$ was scanned over 100 different orientations on a unit sphere to obtain an average response of the structure to match the experiment done in solution, and $\mathbf{E}_k^{\mathrm{L/R}}$ defines the left- and right-handed polarizations for the corresponding $\mathbf{k}$-value. From the dipole moments, we calculated the extinction cross section as

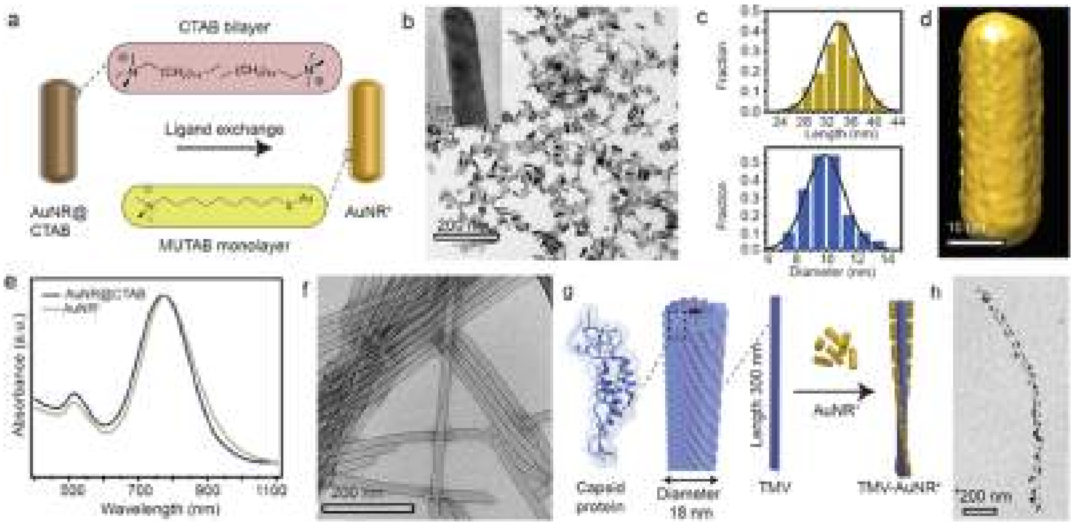

Figure 1. Starting materials and product of the electrostatic assembly. (a) Schematic of the functionalization of AuNR@CTAB with MUTAB via ligand exchange method, (b) TEM image of AuNR$^+$, (c) distribution of length and diameter of 200 AuNR$^+$s measured from the TEM images, and (d) TEM tomographic image of a single AuNR$^+$. (e) Comparative absorption spectra of AuNRs before and after MUTAB functionalization. (f) TEM image of negatively stained TMVs. (g) Cartoon representation of the TMV structure and the schematic presentation of the electrostatic interaction between TMV and AuNR$^+$. (h) TEM image of the resulting TMV-AuNR$^+$ composite.

$$\sigma_{\text{ext}} = 4\pi k \sum_{j=1}^{N} \frac{\text{Im}[\mathbf{E}^*_{\text{ext},j} \cdot \mathbf{p}_j]}{|E_{\text{ext},j}|^2}$$

and the absorption cross section as[47]

$$\sigma_{\text{abs}} = 4\pi k \sum_{j=1}^{N} \frac{1}{|\mathbf{E}_{\text{ext},j}|^2} \left\{ \text{Im}\left[\mathbf{P}_j (\alpha_j^{-1})^* \mathbf{P}_j^* - \frac{2}{3} k^3 |\mathbf{P}_j|^2 \right] \right\}$$

Finally, the circular dichroism signal was calculated from the cross sections as

$$\frac{\sqrt{\sigma_{\text{R}}} - \sqrt{\sigma_{\text{L}}}}{\sqrt{\sigma_{\text{R}}} + \sqrt{\sigma_{\text{L}}}}$$

Here, the subindices R and L corresponded to the two different circular polarizations.

■ RESULTS AND DISCUSSION

Cationization of AuNRs. Spherical nanoparticles of gold typically generate CD signals of moderate intensity over a narrow spectral range.[13,24] On the contrary, AuNRs are capable of generating a much stronger electronic field owing to the anisotropic distribution of their free electrons.[31] Besides, their longitudinal surface plasmon resonance (SPR) frequency is highly sensitive to their size, aspect ratio, and electronic environment, i.e., the presence and orientation of neighboring particles. Hence, AuNRs are promising building blocks for tunable and intense CD signal. In an aqueous medium, cetyl trimethylammonium bromide (CTAB) molecules form a bilayer that covers the AuNRs. Although the ζ-potential of CTAB-protected AuNR (AuNR@CTAB) is highly positive (+30 mV) due to the quaternary amine group of CTAB, there is no covalent bond between the gold atoms and the CTAB molecules, making the protective layer labile. Therefore, using a typical ligand exchange method, we functionalized the AuNRs with a thiol, containing positively charged end group and a chain length comparable to that of CTAB, namely, (11-mercaptoundecyl)-*N*,*N*,*N*-trimethylammonium bromide (MUTAB). The Au−S bond formation facilitated the replacement of CTAB bilayer by MUTAB molecules, producing MUTAB-protected AuNRs, which is abbreviated here as AuNR$^+$ (Figures 1a and S1). The TEM image of AuNR$^+$ (Figure 1b) and the distribution of their length and diameter (Figure 1c) suggest uniform shape and narrow size dispersity, with the mean length being 34 ± 4.5 nm and mean diameter being 10 ± 1.2 nm (aspect ratio, ∼3.4). The 3D reconstruction of a single AuNR$^+$ morphology using electron tomography is shown in Figure 1d and Video S1. Its comparison with that of AuNR@CTAB (Figure S2) further shows that the morphology was intact on ligand exchange. Comparing the absorption spectra of AuNR@CTAB and AuNR$^+$ (Figure 1e), it can be concluded that the ligand exchange did not alter the dispersity and electronic environment of the as-synthesized AuNRs. The resulting AuNR$^+$ retained its cationic nature, as suggested by its positive ζ-potential (+18 mV).

Assembly of AuNR$^+$ on TMV. TMV is an anisotropic biocolloidal substrate with a radius of 18 nm and a length of 300 nm (Figure 1f).[36] The virus is semiflexible, atomically precise, and therefore highly suitable as a soft template for drug delivery,[51] ordered assemblies of chromophores,[52] nanoparticles,[53] and deposition of metal ions.[54] The crystal structure of TMV reveals that there are 130 turns of the coat proteins along the length of a single TMV causing a spiral negative charge distribution on the surface.[55] Therefore, cationic AuNR$^+$ got adhered on the TMV guided by the strong electrostatic attraction. In case of such assemblies, the relative position of adjacent nanoparticles has great influence on the final structure and properties of composite materials. Moreover, nanorods being anisotropic in morphology, the relative angles between the longitudinal axes of AuNR$^+$s within themselves and between AuNR$^+$s and TMVs act as another crucial parameter while forming a binary assembly. Previously, it has been observed that AuNRs have a tendency to follow the orientation of anisotropic templates.[56] In this case also, directional synergy played an important role, which led the AuNR$^+$s to attach to the TMV particles keeping their longitudinal axis almost parallel to that of the TMV. This

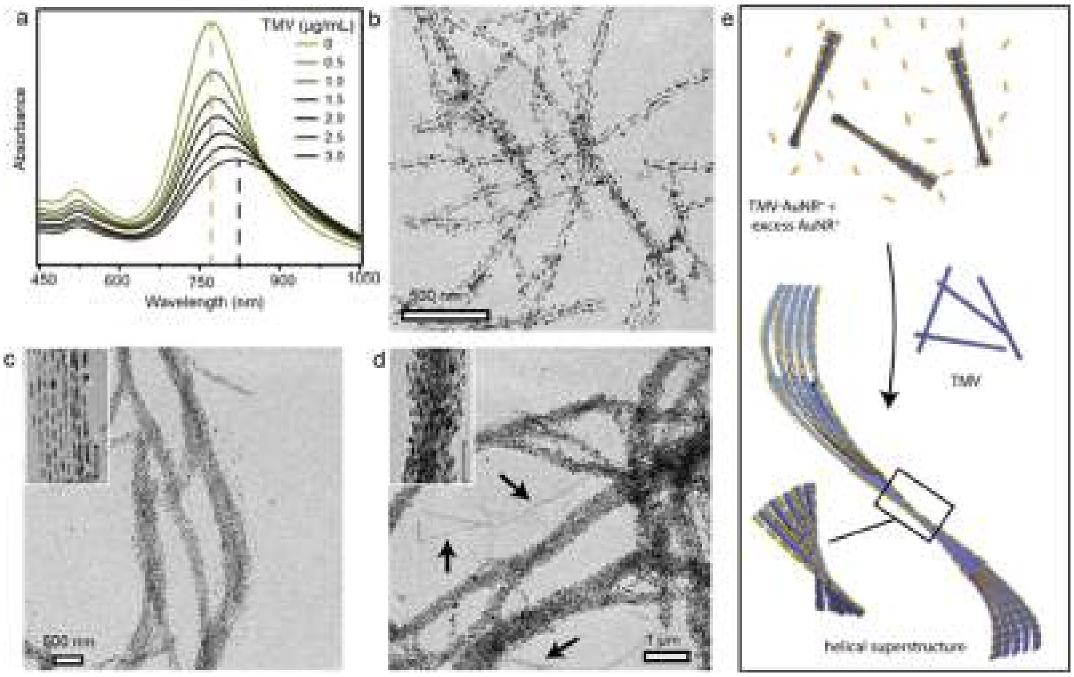

Figure 2. Long-range assembly of TMV-AuNR$^+$s. (a) Change in the absorption spectra of AuNR$^+$ (0.16 nM) with gradual TMV addition. (b) TEM image of the assembly at 2 μg/mL TMV. (c) TEM image of the assembly at 6 μg/mL TMV showing ribbon-like morphology; the magnified image in the inset reveals its 2D superlattice (scale bar, 50 nm). (d) TEM image of a bundle-like assembly at 10 μg/mL TMV; the magnified image in the inset shows 3D superlattice (scale bar, 500 nm), and the arrows point to the excess TMVs. (e) Schematic of the assembly formation.

structure was also favored by the maximum attraction between cationic AuNR$^+$ and anionic TMVs. Figure 1g represents the electrostatic assembly schematically, and Figure 1h shows a TEM image of the resulting TMV-AuNR$^+$ composite. Notably, the AuNR$^+$ aligned themselves in stripes on opposite sides of the cylindrical TMV rather than covering their entire surface evenly, as observed previously by Liz Marzan's group in the case of carbon nanotube template.[57] The perfectly cylindrical shape of TMV led to the end-to-end arrangement of AuNR$^+$s without any defect (misalignment of rods) enabling greater uniaxial plasmon coupling.

Long-Range Assembly of TMV-AuNR$^+$. TMVs are well dispersed in the aqueous medium, owing to their high negative surface charge. However, they are known to form 2D hexagonally close-packed bundles under certain conditions.[58,59] Stoichiometric ratio of the two constituents is crucial for a binary assembly. Hence, to study the assembly at different stoichiometric ratios of AuNR$^+$ and TMV, the latter was added stepwise to 0.16 nM AuNR$^+$ solution and analyzed after each addition. The volume of TMV solution was too small (final dilution was 5%) to significantly alter the AuNR$^+$ concentration in the medium. Figure 2a shows the change in the absorption spectrum of AuNR$^+$ during the process. The longitudinal surface plasmon resonance (LSPR) band of AuNR$^+$, i.e., the one appearing at the longer wavelength (here at ~770 nm), is known to be more sensitive to any change in the system compared to the transverse surface plasmon resonance (TSPR) band at 520 nm. In agreement, we observed a gradual redshift of the LSPR peak maximum with increasing concentration of TMV along with a decrease in the value of absorbance, peak broadening, and rise in the baseline. The redshift implies plasmonic coupling among the AuNR$^+$s in the longitudinal direction. As a control experiment, a comparable concentration of MUTAB was added to native TMV, and their TEM image revealed that it did not induce any specific interaction among TMVs (Figure S3a). At a low TMV concentration, we observed that some of the AuNR$^+$ assembled along the TMVs and excess AuNR$^+$ was found to remain dispersed in the medium (Figure S3b). With an increase in the TMV concentration, increasingly more AuNR$^+$ took part in the binary assembly. The resulting LSPR peak broadened as it was now having contributions from both free AuNR$^+$ (LSPR at ~770 nm) and AuNR$^+$s arranged onto the TMV surfaces (LSPR at >770 nm). These two factors, together with the rise in the baseline, indicate the abundance of TMV-templated assembly of AuNR$^+$ to higher-order structures in the medium. Figure 2b–d shows the TEM images of the resulting composite structures in the presence of 2, 6, and 10 μg/mL TMV, respectively. The electron microscopy images suggest that as the concentration of TMV increases, the discrete TMV-AuNR$^+$ units containing one TMV each, acted as the nucleating sites and excess TMV and AuNR$^+$ participated in further assembly, leading to a long-range structure. Owing to the complementary hydrophobic interactions between the dipolar ends of the helical structure, TMVs are known to take part in a head-to tail assembly.[60] In accordance, initially, the TMV-AuNR$^+$ structures grew longitudinally much more than in the transverse direction, as shown in Figure 2b. Unidirectional assembly of native TMVs is favored as this minimizes the repulsion between the carboxylic residues at the assembly interface. But upon AuNR$^+$ attachment, the negative surface charge of TMVs was neutralized. Therefore, growth of the assembly in the transverse direction also became feasible. This process maximized the attractive force between the two components with opposite surface charges and minimized the repulsive force between similar surface charges. As shown in Figure 2c, gradually, it took the shape of a ribbon, showing an ABAB... arrangement along the width, where A = TMV and B

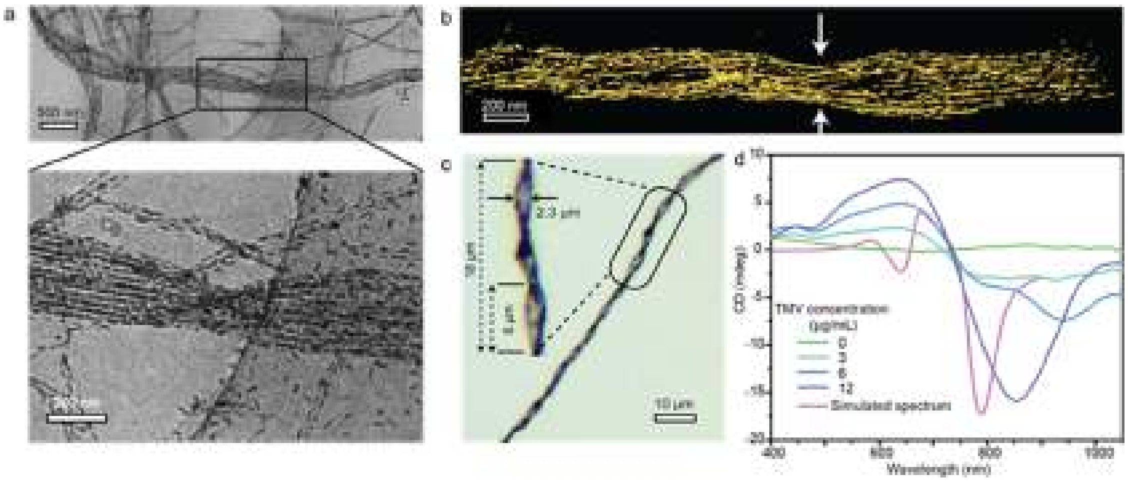

Figure 3. Plasmonic chirality of the TMV-AuNR$^+$ wires. (a) Cryo-TEM image of a ribbon-like TMV-AuNR$^+$ superstructure along with the magnified view of a twisted section and (b) the corresponding 3D reconstructed image with arrows pointing to the helical twist. (c) Optical image of a TMV-AuNR$^+$ microwire in the presence of 12 μg/mL TMV showing repetitive twists. Magnified view of the marked section shows the pitch length. (d) Experimental CD spectra showing stronger signals with gradually higher TMV concentration, along with the simulated CD spectrum calculated from the AuNR$^+$ coordinates obtained from (b).

= linear array of AuNR$^+$. The inset in Figure 2c presents a magnified view revealing the 2D superlattice domains of these superstructures. Figure 2e schematically presents the long-range assembly. With a further increase in the TMV concentration, due to overgrowth, this 2D ribbon-like superstructure attained thick wirelike morphology with 3D bundled superlattice structures (as shown in Figure 2d). Beyond this point, addition of TMV only made these wires thicker and longer without any significant morphological change. Finally, these wires with length of several microns started to precipitate and excess free TMV can be observed in the corresponding TEM images.

Origin of the Helical Structure Leading to Plasmonic Chirality. From Figure 2, it is evident that the long and thick TMV-AuNR$^+$ superstructures contain hints of structural twists in the long range. To eliminate any drying artifact, we characterized this binary superstructure under cryogenic conditions. Although the periodic array of TMVs and AuNR$^+$ appears parallel locally (inset in Figure 2c), the cryo-TEM image in Figure 3a shows that the ribbon-like TMV-AuNR$^+$ composite wires indeed show helicity in their structure. A magnified image displays that it is completely twisted at places. Using a tilt series of images, we reconstructed a 3D structure of this wire (Figure 3b, Video S2), which presents a clearer view. The origin of this helicity lies in the crystal structure of TMV, where a right-handed RNA helix is buried inside the capsomeres. These capsomeres show an axial repeat distance of 69 Å, which consists of 49 subunits, while the basic helix makes three turns. Previous studies have shown that chiral rod-shaped viruses align in a twisted manner with each other to minimize their interaction energy.[61] In this case, the net effect of a strong attraction between AuNR$^+$ and TMV and the helical distribution of negative charge along the TMV surface gave rise to the helicity in the superstructure. In a study by Liljeström et al.,[39] spherical cationic gold nanoparticles, in a high electrolyte concentration, were mixed with TMVs and the mixture was dialyzed. This way, instead of any kinetically driven random electrostatic assembly, the authors obtained a highly ordered ribbon-like superstructure through a zipper-like mechanism. Furthermore, the superstructure showed helicity, generating a CD signal around the plasmon wavelength of AuNPs. The success of this strategy lies in the colloidal stability of the AuNPs against the electrolyte. However, in some cases, the plasmonic nanoparticles tend to aggregate irreversibly even at a moderate salt concentration. The present study addresses this limitation. We show that fairly ordered helical superstructures can be achieved by a slow stepwise addition of the chiral template to the pool of AuNR$^+$, without the risk of electrolyte treatment. We also note that the helicity became more prominent with the growth of the superstructure. Figure 3c presents an optical microscopy image of a composite ribbon-like structure that is several hundreds of microns in length and up to 2.3 μm in width. Periodic structural twists can be seen along the entire microwire. The inset shows a magnified view of the marked portion, which reveals a pitch of 6 μm. The optical images of the system at various TMV concentrations in Figure S4 show that at a lower TMV concentration, the structures contained occasional twists. However, at TMV concentrations higher than 12 μg/mL, the pitch increased with the width of the microwires (Figure S4b,c). Thus, through the self-assembly process, the molecular-level chirality was transposed to the chiral structures of multiple orders of magnitude larger length scales. Notably, in the proposed mixing protocol, we hypothesize that each structural unit of the template got saturated by AuNR$^+$ before more templates entered the system. However, when we performed the reverse addition process, i.e., gradually added a small amount of AuNR$^+$ to an aqueous solution of TMV, the former chose random structural units of TMV to attach to. This continued, making the subsequent long-range assembly impossible. In the cryo-TEM images, we see that the assembly did not continue beyond a few TMV-AuNR$^+$ units (Figure S5).

Besides, the circular dichroism measurements reveal that the structural helicity of the microwires had a preferred handedness that gave rise to an overall chirality. In Figure 3d, we see that the system gives a bisignated CD signal of peak-dip feature with a zero-crossing point around the absorption maximum of the AuNR$^+$. This nature of the CD spectra is typical for helical plasmonic assemblies. Here, although the AuNR$^+$s arranged on

https://dx.doi.org/10.1021/acs.jpcc.0c11512
J. Phys. Chem. C 2021, 125, 3256−3267

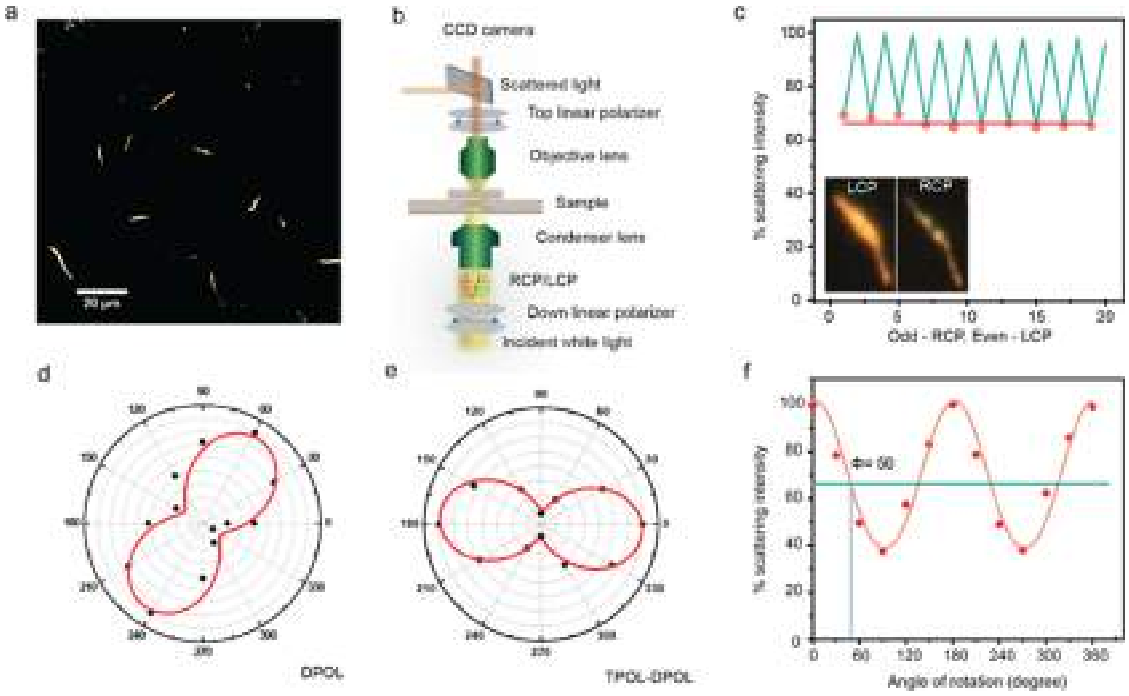

Figure 4. Chirality study of single microwires. (a) Dark-field optical image of the composite wires made of TMV-AuNR$^+$, (b) schematic representation of the PDFSMS setup, and (c) changes in the scattering intensity of a single microwire (the inset shows the images) when it was illuminated with RCP and LCP alternatively and observed through an analyzer. (d) Polar map of a single wire when it was illuminated with a linearly polarized light at different angles (0−360°) without analyzer and (e) with analyzer. (f) The polar plot in (e) presented as a 2D *XY* plot to find the angle of optical rotation of a microwire.

the surface of TMV in near-parallel 1D arrays, the right-handed distribution of surface charge on TMV guided the assembly to finally give the right-handed global twists. As explained in detail in the previous study with gold nanoparticles by Liljeström et al.,[39] if one observes from the transverse direction, the nanorods show a left-handed arrangement, which gives the peak-dip-type CD signal. In solution, the experimental CD spectra are the average of chiral signals coming from the axial as well as transverse directions of the TMV-AuNR$^+$ composite microwires. Now, considering the micron-scale length of the wires, any light propagating along their longitudinal axis would be heavily damped by the gold nanorods, decreasing the contribution of this orientation in the experimental CD. Therefore, the left-handed arrangement from the transverse direction predominates and the resulting signal follows the peak-dip nature. A similar CD signal was also reported by Nicholas A. Kotov's group for ribbon-like chiral plasmonic composite structures.[62]

As predicted from the electron microscopy and optical images, with a higher TMV concentration in the medium, the CD signal became stronger in both positive and negative sides while keeping the baseline and the zero-crossing position almost constant. Beyond a certain TMV concentration (12 μg/mL of TMV), as the wires became too heavy to stay dispersed in the aqueous medium, the bulk CD spectrum got flattened (Figure S6). To avoid dependency of chirality on concentration, asymmetry factor or *g*-factor of the system was calculated from these CD spectra and the corresponding absorbance spectra at different TMV concentrations following an established method.[63] As shown in Figure S6c, a prominent peak-dip trend of the spectrum was observed for 12 μg/mL TMV concentration that shows a standard value for this kind of systems.[62] Using the CD data and corresponding absorbance values from Liljeström et al.,[61] the *g*-factor of TMV-gold nanoparticle system at a 200 mM salt concentration is also plotted in Figure S6d. Both the systems show comparable negative peak intensity, but a much stronger (∼10 times higher) positive signal in the case of TMV-AuNR$^+$ suggests better chiral response in the case of AuNR$^+$. Taking the position of the AuNR$^+$s in the assembly from the coordinates of its cryo-TEM tomogram and using the discrete dipole approximation (DDA), we simulated the CD signal of the TMV-AuNR$^+$ microstructure shown in Figure 3b. The model contains 293 nanorods, each represented as a point dipole, with polarizability obtained from the modified long-wavelength approximation (MLWA). Taking the length of the nanorods as 34 ± 6 nm and the diameter as 10 ± 2 nm (for details, see the Experimental Methods section), we obtain the CD spectrum presented along with the experimental spectra in Figure 3d. The zero-crossing position of this simulated spectrum matches well with our experimental result, the signal intensity being comparable to the one when the TMV concentration was 12 μg/mL. The sharpness of the simulated CD spectrum can be attributed to the fact that the model takes coordinates from the cryo-tomographic image of a single structure. However, in solution (as shown in Figure 3a), the length and width of the microwires vary to some extent, which contribute to the broadening of bulk CD spectra. The experimental spectra are smoothened and the simulated spectrum is multiplied by a simple integer for ease of comparison.

Chirality Estimation at Single-Microwire Level. Owing to its ensemble-averaging nature, bulk CD measurements often mask the sensitivity of CD spectroscopy. Therefore, researchers are having a growing interest in detecting chirality at a single-particle level using far-field extinction microscopy[64]

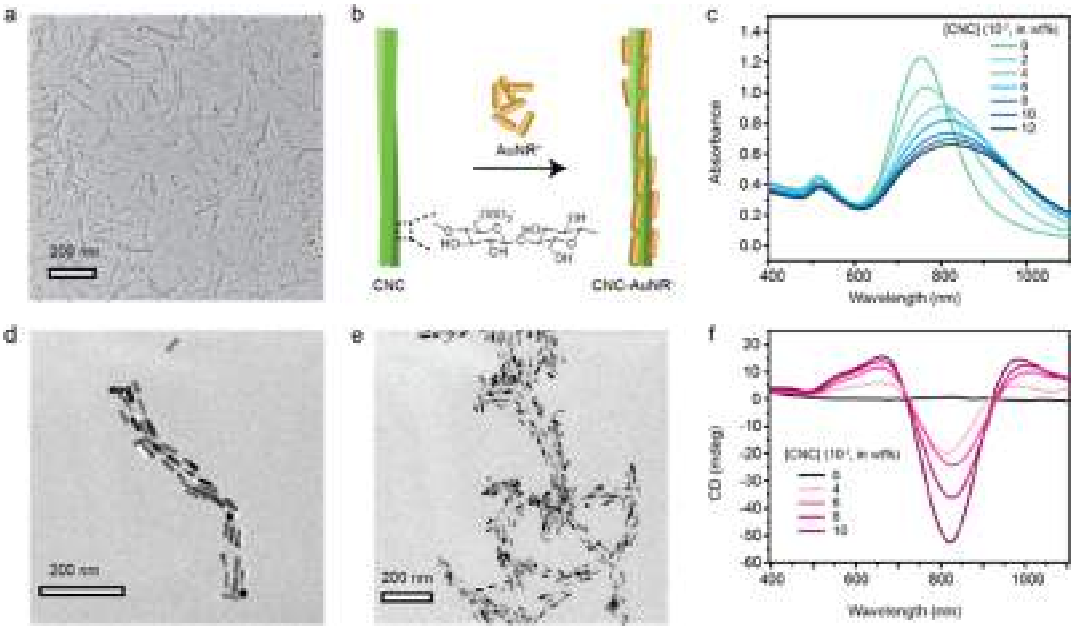

Figure 5. Long-range assembly of AuNR$^+$ with CNC. (a) Cryo-TEM image of negatively stained CNCs, (b) schematic of the arrangement of AuNR$^+$ on twisted CNC surface, (c) change in the absorption spectrum of AuNR$^+$ with gradual addition of CNC. TEM images of (d) short-range assembly at 0.02 wt % of CNC and (e) long-range assembly at high CNC concentration (~0.06 wt %). (f) CD spectra of the sample with increasing CNC concentrations.

and single-particle chiral scatterometry.[65] Using a much simpler technique, namely, polarized dark-field scattering microspectroscopy (PDFSMS), we have determined the chirality associated with individual composite TMV-AuNR$^+$ microwires. PDFSMS allows the detection of chirality associated with individual gold nanorod aggregates both qualitatively and quantitatively.[66] This is possible because of the optical rotation due to plasmonic circular dichroism of the anisotropic nanoparticle assemblies. Here, using the same principle and experimental setup, we studied chirality associated with individual TMV-AuNR$^+$ microwires. Precisely, we used an upright dark-field microscope to image the TMV-AuNR$^+$ sample placed between a glass slide and a glass coverslip. Depending on the TMV-to-AuNR$^+$ ratio, we observed dotlike, rodlike, and wirelike structures (Figure S7). Figure 4a shows the dark-field optical image of the sample containing 6 μg/mL TMV in the absence of any polarizer. Then, we modified the setup, as shown in Figure 4b, such that the sample could be illuminated with right- and left-handed circularly polarized light, and optical rotation in the light scattered by the microwires could be detected. For this, a linear analyzer was added in the path of scattered light. Figure 4c shows changes in the average grayscale intensity for one of the microwires (inset, Figure 4c) upon alternate illumination with RCP and LCP light. This plot shows repeatability of the measurements as well as reveals that upon changing the illumination from LCP to RCP, the scattering intensity passing through the analyzer is reduced to 65%. Such an alteration of intensity proves that the individual microwires are chiral, as expected from their twisted structures. Quantification of the chirality of microwires was based on the optical rotation of scattered light. Precisely, to illuminate the sample with linearly polarized light at different angles, we kept a linear polarizer at the bottom of the sample (down-side polarizer, i.e., DPOL). Then, dark-field images were collected without and with analyzer, i.e., another linear polarizer kept above the sample (top-side polarizer, i.e., TPOL). These data are shown in Figure 4d,e, respectively. Then, the percentage reduction in scattering intensity (65%) due to the optical rotation was correlated with the changes in the linearly polarized scattering intensity upon varying angle of linearly polarized illumination. It showed that when illumination is changed from LCP to RCP, the scattered light rotates by 50°, which is a measurement of the optical rotation exhibited by the corresponding microwire. Notably, in aqueous dispersion, differential absorption for RCP and LCP was observed, but not optical rotation, as the TMV-AuNR$^+$ wires were oriented in all possible directions. Hence, output could be only circular and unpolarized light, and thus, bulk circular dichroism spectra were not affected by linear dichroism components.

Generalization of the Strategy Using Cellulose Nanocrystals (CNC). To show the generic nature of this approach, we used anisotropic nanocellulose particles, viz., CNC. Cellulose is found in many skeletal systems of plants, mostly in a chiral nematic liquid crystal phase. Below a critical concentration, a form of cellulose exists as a whisker-like colloidal substance[67] with an average aspect ratio of 12, known as CNC, whose cryo-TEM images are shown in Figure 5a. These rodlike CNCs contain sulfate half-ester groups on their surface and have a right-handed twisted structure,[68] which results in a helical distribution of negative surface charge similar to that of TMVs. Though these are not atomically precise, they are highly crystalline, the surface contains negatively charged groups (ζ-potential, −64 mV), and most importantly, these are produced cost-effectively from renewable resources. Earlier, CNCs have shown the potential to serve as a chiral template both in its nematic phase[69] and as single crystals.[70] Here, we added 0.02 wt % of colloidal CNC at each step to 0.16 nM AuNR$^+$ solution following the same strategy. As depicted in Figure 5b, the AuNR$^+$s attached to the CNC surface keeping their longitudinal axis parallel to that of the CNCs.

Notably, in this case, they attached to the CNCs covering their entire surface. During the process, the positive ζ-potential of the system decreased continuously (Figure S8), suggesting surface charge neutralization through electrostatic assembly. Figure 5c shows that the absorption spectra gradually shift toward the right and get broadened, verifying a similar interaction as expected from the TMV case. Indeed, the TEM image of the sample at a low CNC concentration (Figure 5d) suggests that the AuNR$^+$s arranged themselves unidirectionally along the length of the CNC. At a higher concentration of CNC, a long-range assembly produced longer and thicker composite structures. In Figure 5e, we see such an assembled structure, where, although the CNCs are hardly visible due to low contrast, the pattern of AuNR$^+$ arrangement clearly indicates that they were longitudinally attached to an anisotropic soft template of higher aspect ratio. Circular dichroism study shows that CNC-AuNR$^+$ also produced a chiral signal at the position of the maximum absorption of AuNR$^+$. Similar to the case of TMV, with the increase in the concentration of CNC, as the microstructures grew, the system showed a stronger chiral signal keeping the zero-crossing position fixed. In the case of CNC, the template was not perfectly cylindrical like TMV, but they rather contained right-handed structural twist in their inherent geometry. Therefore, the CNC-AuNR$^+$ composite did not produce ribbon-like ordered structure with global twists. Instead, the nanorods evenly covered the CNC surfaces, guided by the grooves of CNCs. Several studies have shown that the dihedral angle between nanoparticles significantly alters their chiral response.[71] Although less ordered, the CNC-AuNR$^+$ assemblies contained higher relative angle between consecutive gold nanorods compared to their uniaxial end-to-end arrangement in the TMV-AuNR$^+$ system, which gave rise to a stronger CD signal in the case of CNC-AuNR$^+$.

The calculated *g*-factor of CNC-AuNR$^+$ implies that the chiral response of this system is comparable to that of TMV-AuNR$^+$ (Figure S9). Notably, the spectra fail to show a stronger signal intensity with an increase in CNC concentration beyond 0.06 wt % CNC. This can be attributed to the fact that CNC-templated assemblies of AuNR$^+$ show greater polydispersity, leading to a flattening of the absorbance spectra (as evident from Figure 5c). However, the strong CD spectra and standard *g*-factor values imply that our strategy works well for CNC too, which may be extended to any template of this kind.

■ CONCLUSIONS

In the field of template-assisted plasmonic chirality, we present a simple strategy to obtain a binary assembly with structural precision. Using surface chemistry as a key, by a slow stepwise addition of the rod-shaped chiral templates to a large pool of well-dispersed AuNRs, we observed systematic attachment of the AuNRs to the templates following their structural helicity. With a gradual increase in the template concentration in the system, these unit composite structures participate in a long-range assembly that gives longer, thicker wirelike structures with an overall structural chirality. Thus, by following the proper mixing protocol, without any sophisticated template or complex sample preparation technique or highly specialized and tedious chemical synthesis, we can create structures that show plasmonic chirality in the NIR wavelength region. Besides being simple and general in nature, this method is highly reproducible, easily scalable, and efficient for tuning the length of the structures (Figure 2c−e), thereby bridging between nanoscale and microscale structural chirality. Interestingly, although both TMV and CNC-templated assemblies of AuNR$^+$ give rise to plasmonic chirality around the same wavelength following the same strategy, they may be suitable for very different applications. If the radiative and nonradiative losses can be minimized, then the chiral plasmonic wires with length of several microns made of TMV-AuNR$^+$ might have potential utility in nonlinear optics and in telecommunication kind of devices. They can also be excellent waveguides to preferentially propagate one circularly polarized light over the other, due to their chirality. On the other hand, the CNC-AuNR$^+$ system does not give such long unidirectional structures, but at gradually higher concentration of CNC, they show increasingly stronger signal in CD spectra (Figure 5f). Hence, the CNC-AuNR$^+$ system would be more suitable for other applications where a strong chirality in the NIR region is crucial. Further, using PDFSMS, we could detect the chirality of a single TMV-AuNR$^+$ composite microwire. This method has the potential to detect TMV or similar chiral templates with an unprecedented detection limit. Thus, the chiral plasmonic materials proposed in this study hold importance to diverse fields of physics, chemistry, material science, and biology.

■ ASSOCIATED CONTENT

SI Supporting Information

The Supporting Information is available free of charge at https://pubs.acs.org/doi/10.1021/acs.jpcc.0c11512.

Additional characterization of AuNR before and after MUTAB functionalization; TEM images of TMV-AuNR$^+$ in the presence of low TMV concentration; scanning electron micrograph; polarized optical image and dark-field optical images of TMV-AuNR$^+$; cryo-TEM images of TMV-AuNR$^+$ resulting from reverse addition; raw circular dichroism spectra of TMV-AuNR$^+$ at various TMV concentrations; and change in ζ-potential of CNC-AuNR$^+$ system with increasing CNC concentration (PDF)

Tomographic reconstruction of AuNR$^+$ (AVI)

Tomographic reconstruction of TMV-AuNR$^+$ (AVI)

■ AUTHOR INFORMATION

Corresponding Authors

Mauri A. Kostiainen − *Department of Bioproducts and Biosystems, Aalto University, FI-00076 Aalto, Finland;* orcid.org/0000-0002-8282-2379; Email: mauri.kostiainen@aalto.fi

Robin H. A. Ras − *Department of Applied Physics and Department of Bioproducts and Biosystems, Aalto University, FI-00076 Aalto, Finland;* orcid.org/0000-0002-2076-242X; Email: robin.ras@aalto.fi

Thalappil Pradeep − *DST Unit of Nanoscience and Thematic Unit of Excellence, Department of Chemistry, Indian Institute of Technology Madras, Chennai 600036, India;* orcid.org/0000-0003-3174-534X; Email: pradeep@iitm.ac.in

Authors

Amrita Chakraborty − *DST Unit of Nanoscience and Thematic Unit of Excellence, Department of Chemistry,* *Indian Institute of Technology Madras, Chennai 600036, India*

Nonappa − *Faculty of Engineering and Natural Sciences, Tampere University, FI-33101 Tampere, Finland; Department of Applied Physics, Aalto University, FI-00076 Aalto, Finland;* orcid.org/0000-0002-6804-4128

Biswajit Mondal − *DST Unit of Nanoscience and Thematic Unit of Excellence, Department of Chemistry, Indian Institute of Technology Madras, Chennai 600036, India*

Kamalesh Chaudhari − *DST Unit of Nanoscience and Thematic Unit of Excellence, Department of Chemistry, Indian Institute of Technology Madras, Chennai 600036, India*

Heikki Rekola − *Institute of Photonics, University of Eastern Finland, FI-80101 Joensuu, Finland; Faculty of Engineering and Natural Sciences, Tampere University, FI-33101 Tampere, Finland;* orcid.org/0000-0003-3059-4535

Ville Hynninen − *Department of Applied Physics, Aalto University, FI-00076 Aalto, Finland*

Complete contact information is available at: https://pubs.acs.org/10.1021/acs.jpcc.0c11512

Author Contributions

A.C., T.P., M.A.K., and R.H.A.R. conceived the experimental design. A.C. prepared the samples and performed UV−vis studies and CD spectroscopy. N. performed cryo-TEM sample preparation and imaging, electron tomography reconstruction, and image analysis. B.M. collected TEM images. K.C. performed the PDFSMS study. H.R. carried out theoretical modeling of the CD spectrum. V.H. synthesized the CNCs. A.C. and N. wrote the first draft of the manuscript, and the final version of the manuscript was prepared through the contributions of all authors.

Notes

The authors declare no competing financial interest.

■ ACKNOWLEDGMENTS

The authors thank the Department of Science and Technology, Government of India, and the Academy of Finland (Project 308578), HYBER Centre of Excellence Programme (2014−2019), and Photonics Research and Innovation (PREIN, project no. 320166) flagship for supporting our research. A.C. and B.M. thank the Council of Scientific and Industrial Research and IIT Madras, respectively, for their research fellowships. The authors acknowledge the provision of facilities and technical support by Aalto University at OtaNano-Nanomicroscopy Center (Aalto-NMC). They also thank Prof. Anton Kuzyk and Ryssy Joonas for their support in circular dichroism measurements.

■ REFERENCES

(1) Blackmond, D. G. The origin of biological homochirality. *Cold Spring Harbor Perspect. Biol.* **2010**, *2*, No. a002147.

(2) Runnels, C. M.; Lanier, K. A.; Williams, J. K.; Bowman, J. C.; Petrov, A. S.; Hud, N. V.; Williams, L. D. Folding, Assembly, and Persistence: The Essential Nature and Origins of Biopolymers. *J. Mol. Evol.* **2018**, *86*, 598−610.

(3) Ranjbar, B.; Gill, P. Circular Dichroism Techniques: Biomolecular and Nanostructural Analyses- A Review. *Chem. Biol. Drug Des.* **2009**, *74*, 101−120.

(4) Nakanishi, K.; Berova, N.; Woody, R. *Circular Dichroism: Principles and Applications*; VCH: New York, 1994; p 230.

(5) Kelly, S. M.; Jess, T. J.; Price, N. C. How to study proteins by circular dichroism. *Biochim. Biophys. Acta, Proteins Proteomics* **2005**, *1751*, 119−139.

(6) Palmans, A. R. A.; Meijer, E. W. Amplification of Chirality in Dynamic Supramolecular Aggregates. *Angew. Chem., Int. Ed.* **2007**, *46*, 8948−8968.

(7) Liu, M.; Zhang, L.; Wang, T. Supramolecular Chirality in Self-Assembled Systems. *Chem. Rev.* **2015**, *115*, 7304−7397.

(8) Govorov, A. O. Plasmon-Induced Circular Dichroism of a Chiral Molecule in the Vicinity of Metal Nanocrystals. Application to Various Geometries. *J. Phys. Chem. C* **2011**, *115*, 7914−7923.

(9) Ben-Moshe, A.; Maoz, B. M.; Govorov, A. O.; Markovich, G. Chirality and chiroptical effects in inorganic nanocrystal systems with plasmon and exciton resonances. *Chem. Soc. Rev.* **2013**, *42*, 7028−7041.

(10) Oh, H. S.; Liu, S.; Jee, H.; Baev, A.; Swihart, M. T.; Prasad, P. N. Chiral Poly(fluorene-alt-benzothiadiazole) (PFBT) and Nanocomposites with Gold Nanoparticles: Plasmonically and Structurally Enhanced Chirality. *J. Am. Chem. Soc.* **2010**, *132*, 17346−17348.

(11) Hentschel, M.; Schaeferling, M.; Duan, X.; Giessen, H.; Liu, N. Chiral plasmonics. *Sci. Adv.* **2017**, *3*, No. e1602735.

(12) Lieberman, I.; Shemer, G.; Fried, T.; Kosower, E. M.; Markovich, G. Plasmon-Resonance-Enhanced Absorption and Circular Dichroism. *Angew. Chem., Int. Ed.* **2008**, *47*, 4855−4857.

(13) Wang, Y.; Xu, J.; Wang, Y.; Chen, H. Emerging chirality in nanoscience. *Chem. Soc. Rev.* **2013**, *42*, 2930−2962.

(14) Gansel, J. K.; Thiel, M.; Rill, M. S.; Decker, M.; Bade, K.; Saile, V.; von Freymann, G.; Linden, S.; Wegener, M. Gold Helix Photonic Metamaterial as Broadband Circular Polarizer. *Science* **2009**, *325*, 1513.

(15) Hodgkinson, I.; Wu, Q. H. Inorganic Chiral Optical Materials. *Adv. Mater.* **2001**, *13*, 889−897.

(16) Hendry, E.; Carpy, T.; Johnston, J.; Popland, M.; Mikhaylovskiy, R. V.; Lapthorn, A. J.; Kelly, S. M.; Barron, L. D.; Gadegaard, N.; Kadodwala, M. Ultrasensitive detection and characterization of biomolecules using superchiral fields. *Nat. Nanotechnol.* **2010**, *5*, 783−787.

(17) Tang, Y.; Cohen, A. E. Enhanced Enantioselectivity in Excitation of Chiral Molecules by Superchiral Light. *Science* **2011**, *332*, 333.

(18) Shukla, N.; Bartel, M. A.; Gellman, A. J. Enantioselective Separation on Chiral Au Nanoparticles. *J. Am. Chem. Soc.* **2010**, *132*, 8575−8580.

(19) Slocik, J. M.; Govorov, A. O.; Naik, R. R. Plasmonic Circular Dichroism of Peptide-Functionalized Gold Nanoparticles. *Nano Lett.* **2011**, *11*, 701−705.

(20) Shemer, G.; Krichevski, O.; Markovich, G.; Molotsky, T.; Lubitz, I.; Kotlyar, A. B. Chirality of Silver Nanoparticles Synthesized on DNA. *J. Am. Chem. Soc.* **2006**, *128*, 11006−11007.

(21) Govorov, A. O.; Gun'ko, Y. K.; Slocik, J. M.; Gérard, V. A.; Fan, Z.; Naik, R. R. Chiral nanoparticle assemblies: circular dichroism, plasmonic interactions, and exciton effects. *J. Mater. Chem.* **2011**, *21*, 16806−16818.

(22) García-Etxarri, A.; Dionne, J. A. Surface-enhanced circular dichroism spectroscopy mediated by nonchiral nanoantennas. *Phys. Rev. B* **2013**, *87*, No. 235409.

(23) Maoz, B. M.; Chaikin, Y.; Tesler, A. B.; Bar Elli, O.; Fan, Z.; Govorov, A. O.; Markovich, G. Amplification of Chiroptical Activity of Chiral Biomolecules by Surface Plasmons. *Nano Lett.* **2013**, *13*, 1203−1209.

(24) Merg, A. D.; Boatz, J. C.; Mandal, A.; Zhao, G.; Mokashi-Punekar, S.; Liu, C.; Wang, X.; Zhang, P.; van der Wel, P. C. A.; Rosi, N. L. Peptide-Directed Assembly of Single-Helical Gold Nanoparticle Superstructures Exhibiting Intense Chiroptical Activity. *J. Am. Chem. Soc.* **2016**, *138*, 13655−13663.

(25) Pigliacelli, C.; Sanjeeva, K. B.; Nonappa; Pizzi, A.; Gori, A.; Bombelli, F. B.; Metrangolo, P. In Situ Generation of Chiroptically-Active Gold-Peptide Superstructures Promoted by Iodination. *ACS Nano* **2019**, *13*, 2158−2166.

(26) Querejeta-Fernández, A.; Chauve, G.; Methot, M.; Bouchard, J.; Kumacheva, E. Chiral Plasmonic Films Formed by Gold Nanorods and Cellulose Nanocrystals. *J. Am. Chem. Soc.* **2014**, *136*, 4788−4793.

(27) Guerrero-Martínez, A.; Auguié, B.; Alonso-Gómez, J. L.; Džolić, Z.; Gómez-Graña, S.; Žinić, M.; Cid, M. M.; Liz-Marzán, L. M. Intense Optical Activity from Three-Dimensional Chiral Ordering of Plasmonic Nanoantennas. *Angew. Chem., Int. Ed.* **2011**, *50*, 5499−5503.

(28) Chen, L.; Zheng, J.; Feng, J.; Qian, Q.; Zhou, Y. Reversible modulation of plasmonic chiral signals of achiral gold nanorods using a chiral supramolecular template. *Chem. Commun.* **2019**, *55*, 11378−11381.

(29) Funck, T.; Nicoli, F.; Kuzyk, A.; Liedl, T. Sensing Picomolar Concentrations of RNA Using Switchable Plasmonic Chirality. *Angew. Chem., Int. Ed.* **2018**, *57*, 13495−13498.

(30) Kuzyk, A.; Schreiber, R.; Fan, Z.; Pardatscher, G.; Roller, E.-M.; Högele, A.; Simmel, F. C.; Govorov, A. O.; Liedl, T. DNA-based self-assembly of chiral plasmonic nanostructures with tailored optical response. *Nature* **2012**, *483*, 311−314.

(31) Zhou, C.; Duan, X.; Liu, N. DNA-Nanotechnology-Enabled Chiral Plasmonics: From Static to Dynamic. *Acc. Chem. Res.* **2017**, *50*, 2906−2914.

(32) Feng, W.; Kadiyala, U.; Yan, J.; Wang, Y.; DiRita, V. J.; VanEpps, J. S.; Kotov, N. A. Plasmonic nanoparticles assemblies templated by helical bacteria and resulting optical activity. *Chirality* **2020**, *32*, 899−906.

(33) Selivanovitch, E.; Douglas, T. Virus capsid assembly across different length scales inspire the development of virus-based biomaterials. *Curr. Opin. Virol.* **2019**, *36*, 38−46.

(34) Sasaki, E.; Hilvert, D. Self-Assembly of Proteinaceous Multishell Structures Mediated by a Supercharged Protein. *J. Phys. Chem. B* **2016**, *120*, 6089−6095.

(35) Kostiainen, M. A.; Hiekkataipale, P.; Laiho, A.; Lemieux, V.; Seitsonen, J.; Ruokolainen, J.; Ceci, P. Electrostatic assembly of binary nanoparticle superlattices using protein cages. *Nat. Nanotechnol.* **2013**, *8*, 52−56.

(36) Fraenkel-Conrat, H. Tobacco Mosaic Virus. In *The History of Tobacco Mosaic Virus and the evolution of Molecular Biology*; Plenum: New York, 1986; pp 5−17.

(37) Feng, W.; Kim, J.-Y.; Wang, X.; Calcaterra, H. A.; Qu, Z.; Meshi, L.; Kotov, N. A. Assembly of mesoscale helices with near-unity enantiomeric excess and light-matter interactions for chiral semiconductors. *Sci. Adv.* **2017**, *3*, No. e1601159.

(38) Chapman, S. N. *Plant Virology Protocols: From Viral Sequence to Protein Function*, 2nd ed.; Humana Press Inc.: NJ, 2008; p 677.

(39) Liljeström, V.; Ora, A.; Hassinen, J.; Rekola, H.; Nonappa; Heilala, M.; Hynninen, V.; Joensuu, J.; Ras, R.; Törmä, P.; Ikkala, O.; Kostiainen, M. Cooperative colloidal self-assembly of metal-protein superlattice wires. *Nat. Commun.* **2017**, *8*, No. 671.

(40) Samal, A.; Sreenivasan, S.; Thalappil, P. Investigation of the role of NaBH4 in the chemical synthesis of gold nanorods. *J. Nanopart. Res.* **2010**, *12*, 1777−1786.

(41) Hynninen, V.; Hietala, S.; McKee, J. R.; Murtomäki, L.; Rojas, O. J.; Ikkala, O.; Nonappa. Inverse Thermoreversible Mechanical Stiffening and Birefringence in a Methylcellulose/Cellulose Nanocrystal Hydrogel. *Biomacromolecules* **2018**, *19*, 2795−2804.

(42) Mastronarde, D. N. SerialEM: A Program for Automated Tilt Series Acquisition on Tecnai Microscopes Using Prediction of Specimen Position. *Microsc. Microanal.* **2003**, *9*, 1182−1183.

(43) Mastronarde, D. N. Automated electron microscope tomography using robust prediction of specimen movements. *J. Struct. Biol.* **2005**, *152*, 36−51.

(44) Nonappa, N.; Engelhardt, P. Electron Tomography of Whole Mounts. *Imaging Microsc.* **2019**, *21*, 22−24.

(45) Kremer, J. R.; Mastronarde, D. N.; McIntosh, J. R. Computer Visualization of Three-Dimensional Image Data Using IMOD. *J. Struct. Biol.* **1996**, *116*, 71−76.

(46) Engelhardt, P. Three-dimensional reconstruction of chromosomes using electron tomography. *Methods Mol. Biol.* **2007**, *369*, 365−385.

(47) Yang, W. H.; Schatz, G. C.; Van Duyne, R. P. Discrete dipole approximation for calculating extinction and Raman intensities for small particles with arbitrary shapes. *J. Chem. Phys.* **1995**, *103*, 869−875.

(48) García de Abajo, F. J. Colloquium: Light scattering by particle and hole arrays. *Rev. Mod. Phys.* **2007**, *79*, 1267−1290.

(49) Moroz, A. Depolarization field of spheroidal particles. *J. Opt. Soc. Am. B* **2009**, *26*, 517−527.

(50) Bohren, C. F.; Huffman, D. R. *Absorption and Scattering of Light by Small Particles*; John Wiley and Sons: NJ, 1983; p 530.

(51) Lin, R. D.; Steinmetz, N. F. Tobacco mosaic virus delivery of mitoxantrone for cancer therapy. *Nanoscale* **2018**, *10*, 16307−16313.

(52) Anaya-Plaza, E.; Aljarilla, A.; Beaune, G.; Nonappa; Timonen, J. V. I.; de la Escosura, A.; Torres, T.; Kostiainen, M. A. Phthalocyanine−Virus Nanofibers as Heterogeneous Catalysts for Continuous-Flow Photo-Oxidation Processes. *Adv. Mater.* **2019**, *31*, No. 1902582.

(53) Zhang, J.; Zhou, K.; Zhang, Y.; Du, M.; Wang, Q. Precise Self-Assembly of Nanoparticles into Ordered Nanoarchitectures Directed by Tobacco Mosaic Virus Coat Protein. *Adv. Mater.* **2019**, *31*, No. 1901485.

(54) Dujardin, E.; Peet, C.; Stubbs, G.; Culver, J.; Mann, S. Organization of Metallic Nanoparticles Using Tobacco Mosaic Virus Templates. *Nano Lett.* **2003**, *3*, 413−417.

(55) Czapar, A. E.; Zheng, Y.-R.; Riddell, I. A.; Shukla, S.; Awuah, S. G.; Lippard, S. J.; Steinmetz, N. F. Tobacco Mosaic Virus Delivery of Phenanthriplatin for Cancer therapy. *ACS Nano* **2016**, *10*, 4119−4126.

(56) Sánchez-Iglesias, A.; Grzelczak, M.; Pérez-Juste, J.; Liz-Marzán, L. M. Binary Self-Assembly of Gold Nanowires with Nanospheres and Nanorods. *Angew. Chem., Int. Ed.* **2010**, *49*, 9985−9989.

(57) Correa-Duarte, M. A.; Pérez-Juste, J.; Sánchez-Iglesias, A.; Giersig, M.; Liz-Marzán, L. M. Aligning Au Nanorods by Using Carbon Nanotubes as Templates. *Angew. Chem., Int. Ed.* **2005**, *44*, 4375−4378.

(58) Li, T.; Zan, X.; Winans, R. E.; Wang, Q.; Lee, B. Biomolecular Assembly of Thermoresponsive Superlattices of the Tobacco Mosaic Virus with Large Tunable Interparticle Distances. *Angew. Chem., Int. Ed.* **2013**, *52*, 6638−6642.

(59) Warmke, H. E.; Edwardson, J. R. Electron microscopy of crystalline inclusions of tobacco mosaic virus in leaf tissue. *Virology* **1966**, *30*, 45−57.

(60) Niu, Z.; Bruckman, M.; Kotakadi, V. S.; He, J.; Emrick, T.; Russell, T. P.; Yang, L.; Wang, Q. Study and characterization of tobacco mosaic virus head-to-tail assembly assisted by aniline polymerization. *Chem. Commun.* **2006**, 3019−3021.

(61) Gibaud, T.; Barry, E.; Zakhary, M. J.; Henglin, M.; Ward, A.; Yang, Y.; Berciu, C.; Oldenbourg, R.; Hagan, M. F.; Nicastro, D.; Meyer, R. B.; Dogic, Z. Reconfigurable self-assembly through chiral control of interfacial tension. *Nature* **2012**, *481*, 348−351.

(62) Yeom, J.; Yeom, B.; Chan, H.; Smith, K. W.; Dominguez-Medina, S.; Bahng, J. H.; Zhao, G.; Chang, W. S.; Chang, S. J.; Chuvilin, A.; Melnikau, D.; Rogach, A. L.; Zhang, P.; Link, S.; Král, P.; Kotov, N. A. Chiral templating of self-assembling nanostructures by circularly polarized light. *Nat. Mater.* **2015**, *14*, 66.

(63) Nguyen, L.; Dass, M.; Ober, M. F.; Besteiro, L. V.; Wang, Z. M.; Nickel, B.; Govorov, A. O.; Liedl, T.; Heuer-Jungemann, A. Chiral Assembly of Gold−Silver Core−Shell Plasmonic Nanorods on DNA Origami with Strong Optical Activity. *ACS Nano* **2020**, *14*, 7454−7461.

(64) Vinegrad, E.; Vestler, D.; Ben-Moshe, A.; Barnea, A. R.; Markovich, G.; Cheshnovsky, O. Circular Dichroism of Single Particles. *ACS Photonics* **2018**, *5*, 2151−2159.

(65) Karst, J.; Cho, N. H.; Kim, H.; Lee, H.-E.; Nam, K. T.; Giessen, H.; Hentschel, M. Chiral Scatterometry on Chemically Synthesized Single Plasmonic Nanoparticles. *ACS Nano* **2019**, *13*, 8659−8668.

(66) Chaudhari, K.; Pradeep, T. Optical rotation by plasmonic circular dichroism of isolated gold nanorod aggregates. *Appl. Phys. Lett.* **2014**, *105*, No. 203105.

(67) Kontturi, E.; Laaksonen, P.; Linder, M. B.; Nonappa; Gröschel, A. H.; Rojas, O. J.; Ikkala, O. Advanced Materials through Assembly of Nanocelluloses. *Adv. Mater.* **2018**, *30*, No. 1703779.

(68) Usov, I.; Nyström, G.; Adamcik, J.; Handschin, S.; Schütz, C.; Fall, A.; Bergström, L.; Mezzenga, R. Understanding nanocellulose chirality and structure−properties relationship at the single fibril level. *Nat. Commun.* **2015**, *6*, No. 7564.

(69) Cheng, Z.; Ma, Y.; Yang, L.; Cheng, F.; Huang, Z.; Natan, A.; Li, H.; Chen, Y.; Cao, D.; Huang, Z.; Wang, Y.; Liu, Y.; Yang, R.; Zhu, H. Plasmonic-Enhanced Cholesteric Films: Coassembling Anisotropic Gold Nanorods with Cellulose Nanocrystals. *Adv. Opt. Mater.* **2019**, *7*, No. 1801816.

(70) Majoinen, J.; Hassinen, J.; Haataja, J. S.; Rekola, H. T.; Kontturi, E.; Kostiainen, M. A.; Ras, R. H. A.; Törmä, P.; Ikkala, O. Chiral Plasmonics Using Twisting along Cellulose Nanocrystals as a Template for Gold Nanoparticles. *Adv. Mater.* **2016**, *28*, 5262−5267.

(71) Kuzyk, A.; Schreiber, R.; Zhang, H.; Govorov, A. O.; Liedl, T.; Liu, N. Reconfigurable 3D plasmonic metamolecules. *Nat. Mater.* **2014**, *13*, 862−866.

https://dx.doi.org/10.1021/acs.jpcc.0c11512
J. Phys. Chem. C 2021, 125, 3256−3267

Supporting Information

Near-Infrared Chiral Plasmonic Microwires Through Precision Assembly of Gold Nanorods On Soft Biotemplates

Amrita Chakraborty,[1] Nonappa,[2,3] Biswajit Mondal,[1] Kamalesh Chaudhari,[1] Heikki Rekola,[2,4] Ville Hynninen,[3] Mauri A. Kostiainen,[5] Robin H. A. Ras,[3,5*] and Thalappil Pradeep[1*]*

[1]DST Unit of Nanoscience and Thematic Unit of Excellence, Department of Chemistry, Indian Institute of Technology Madras, Chennai 600036 India. [2]Faculty of Engineering and Natural Sciences, Tampere University, FI-33101 Tampere, Finland. [3]Department of Applied Physics, Aalto University, FI-00076 Aalto, Finland. [4]Institute of Photonics, University of Eastern Finland, FI-80101 Joensuu, Finland. [5]Department of Bioproducts and Biosystems, Aalto University, FI-00076 Aalto, Finland.

Table of contents

Video S2	Tomographic reconstruction of TMV-AuNR$^+$	Attached

Supporting Figures

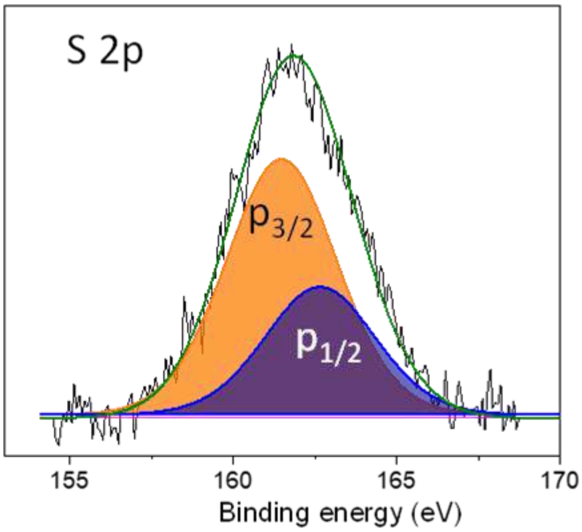

Figure S1. Confirmation of MUTAB functionalization of AuNR. XPS of AuNR$^+$ in the S 2p region shows two peaks at 161.5 eV and 162.7 eV, assigned to $2p_{3/2}$ and $2p_{1/2}$, respectively. These positions match well with thiolate (RS^-) bound to the surfaces of AuNRs.

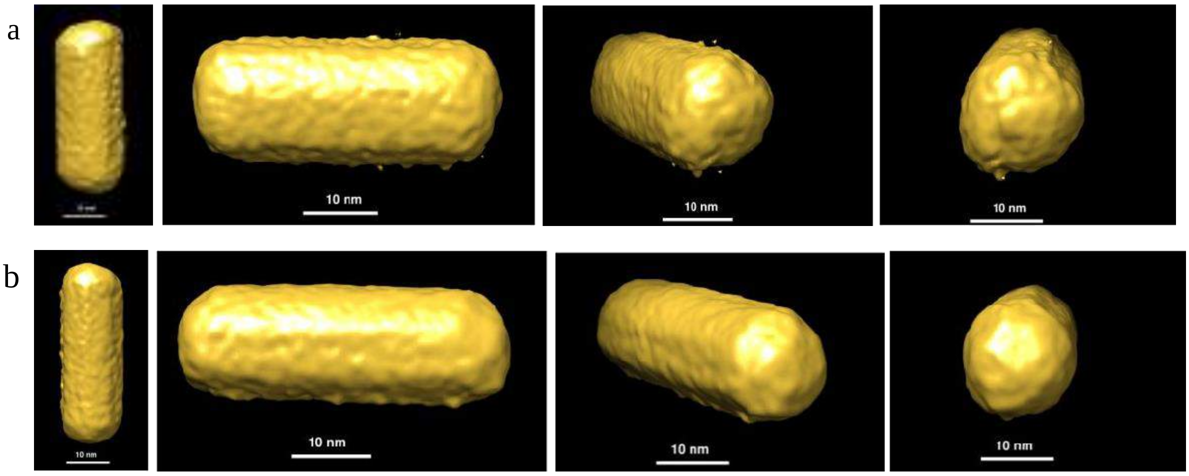

Figure S2. The morphology of AuNR@CTAB and AuNR$^+$. Panel **a** presents the TEM tomographic reconstructed images of AuNR@CTAB from different directions and panel **b** contains corresponding images of AuNR$^+$. We see no significant alteration between the two image panels.

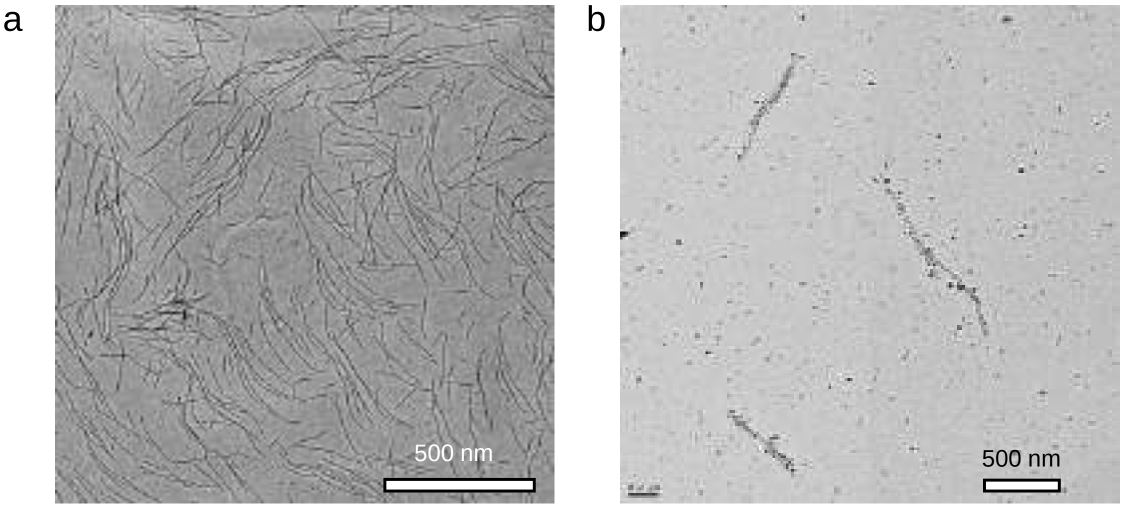

Figure S3. TEM images of a) TMV in presence of 0.002 mM MUTAB which shows that MUTAB did not cause any arrangement in TMVs at the experimental condition, and b) TMV-AuNR$^+$ in presence of low (0.5 μg/mL) TMV concentration. The TMV-AuNR$^+$ units coexist with well-dispersed excess AuNR$^+$s.

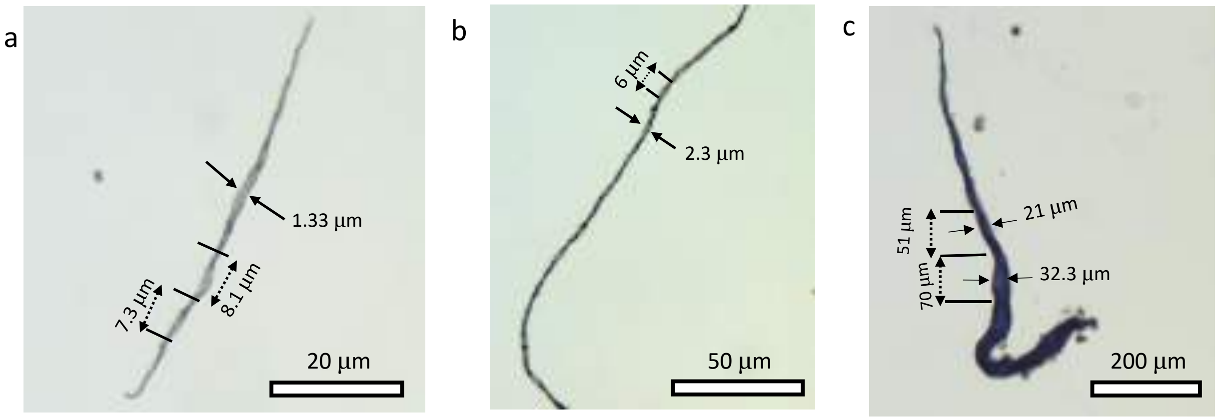

Figure S4. Optical microscopic images showing the width and pitch of TMV-AuNR$^+$ system at low to high TMV concentration- a) 6 μg/mL, b) 12 μg/mL and c) 15 μg/mL.

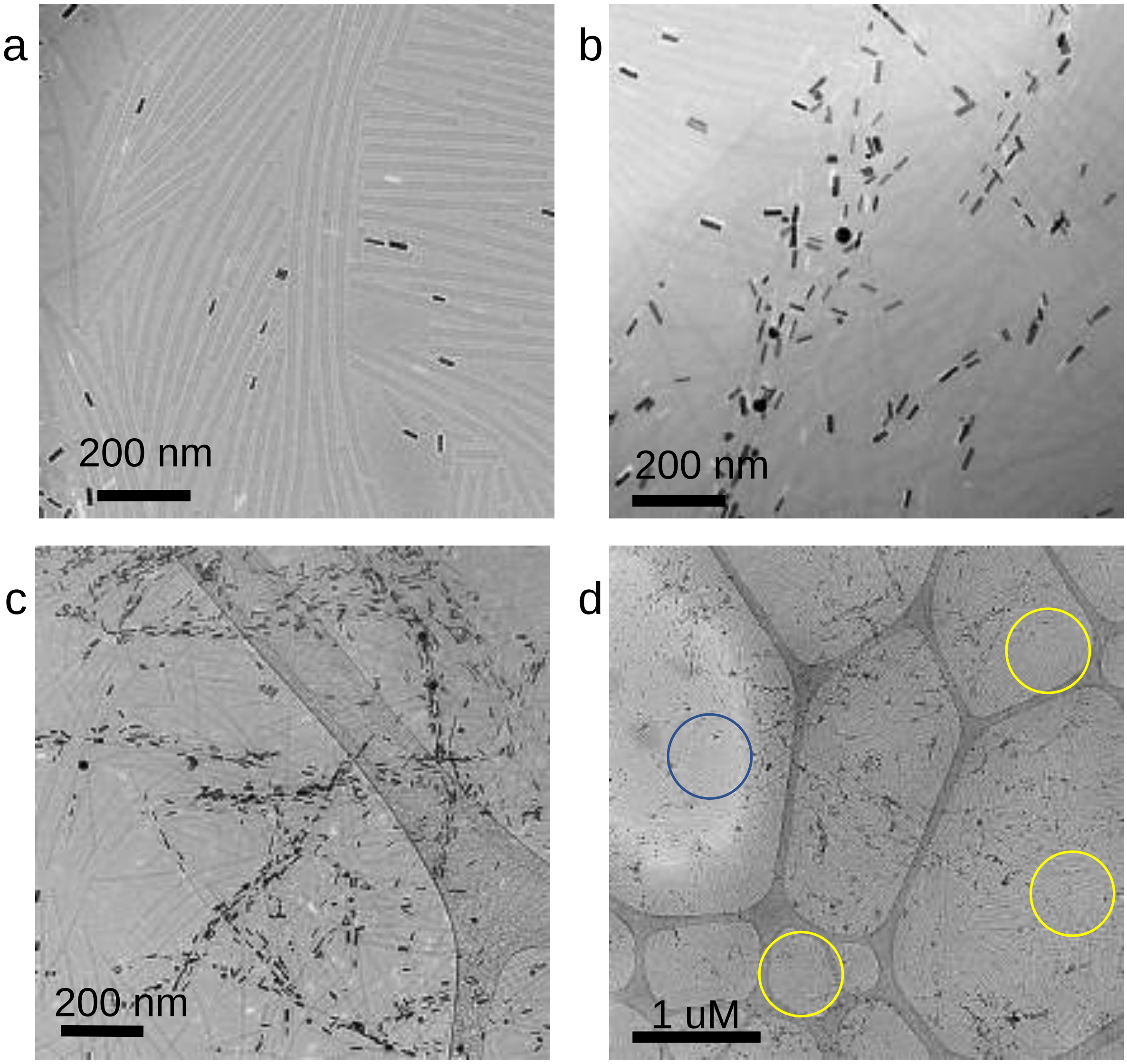

Figure S5. Cryo-TEM images of TMV-AuNR$^+$ resulting from reverse addition. **a-c** Gradually higher AuNR$^+$ to TMV concentration ratio. **d** Large-area image showing the absence of long and thick wire-like structures. The area marked with blue circle shows that in a few places TMVs appear as aligned in a particular direction locally, but in almost everywhere else their arrangement is random as marked by yellow circles.

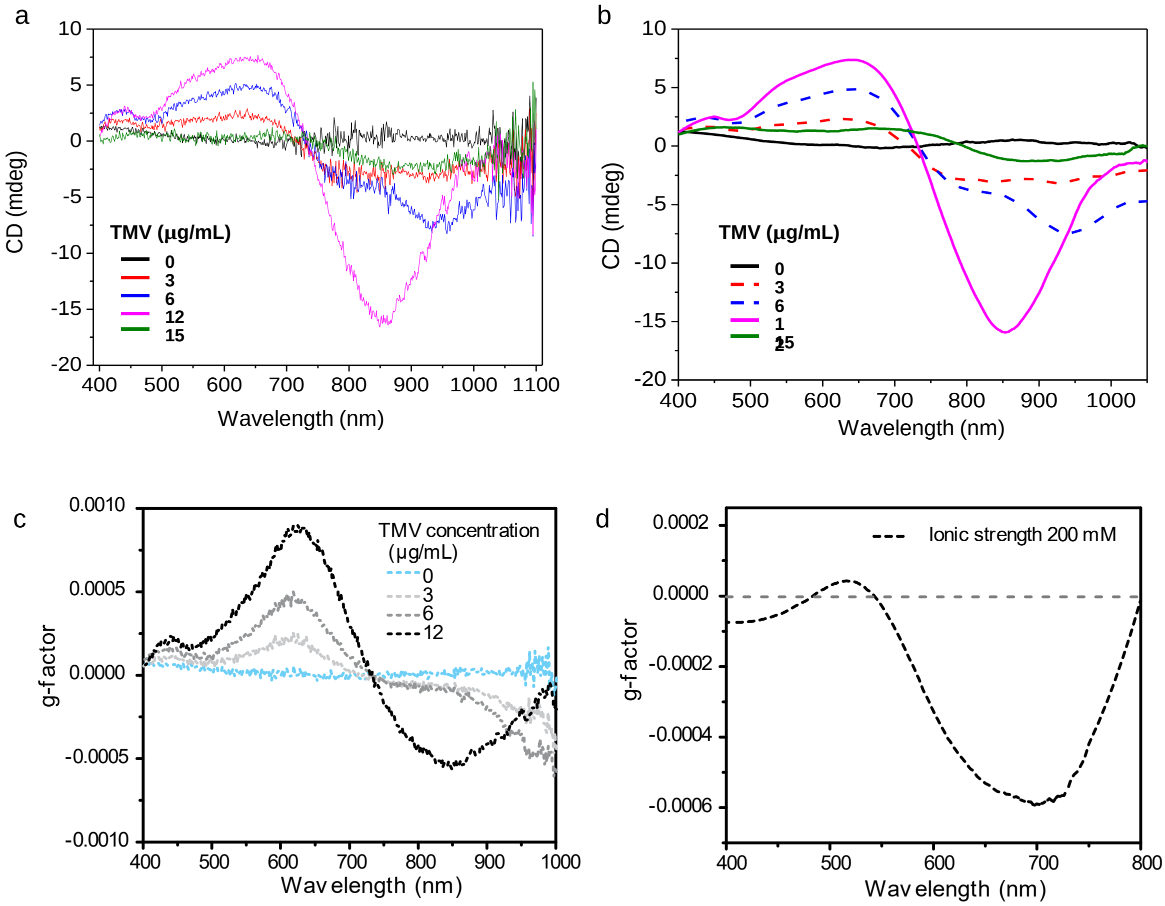

Figure S6. Experimental CD spectra at various TMV to AuNR$^+$ concentration ratio **a** without smoothening, **b** after 100-point Savitzky-Golay smoothening. Initially, with the increase in TMV concentration (up to 12 µg/mL), the CD signal gets stronger and from 12 µg/mL to 15 µg/mL, signal intensity decreases. **c** g-factor of TMV-AuNR$^+$ system and **d** that of TMV-AuNP system at 200 mM ionic strength. Intensity of the negative peak is comparable for both the systems, whereas, the positive peak is 10 times more intense in case of TMV-AuNR$^+$ system.

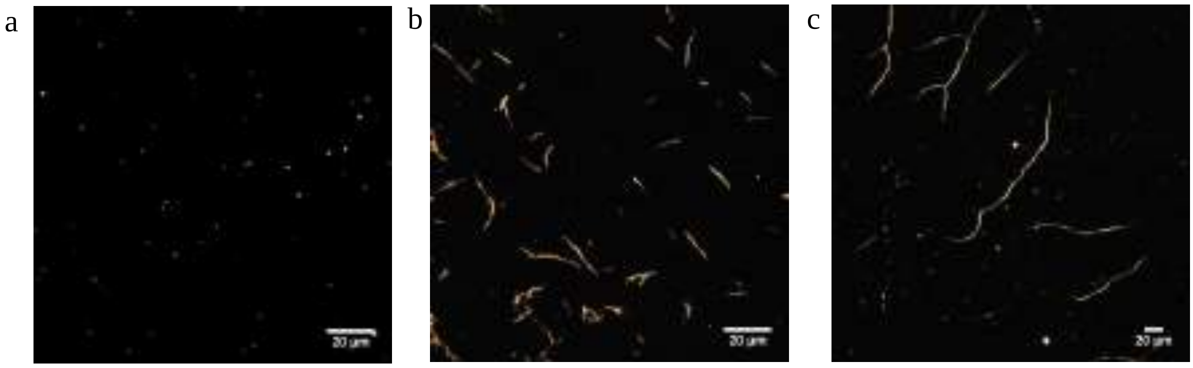

Figure S7. Dark-field optical images of TMV-AuNR$^+$ with gradually higher TMV concentration: **a** 3 ug/mL, **b** 6 ug/mL, **c** 12 ug/mL.

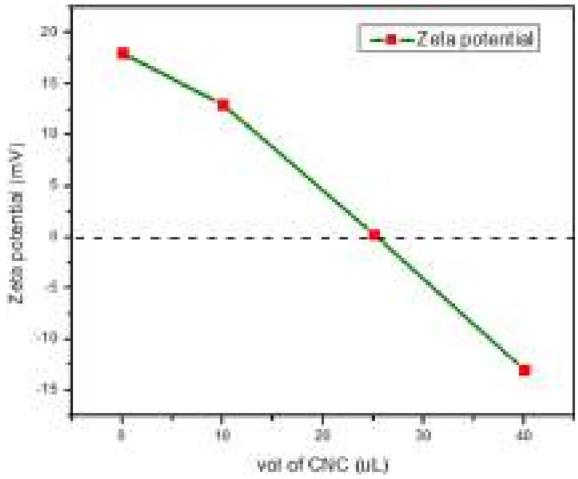

Figure S8. Change in zeta potential of CNC-AuNR$^+$ system with increasing CNC concentration. The initial value is of AuNR$^+$ alone. The value decreases as CNC is added. At a point it crosses the zero-point, suggesting that the negative surface charge of CNC is exactly neutralized by positively charged AuNR$^+$. Upon further CNC addition, zeta potential becomes more and more negative due to the conjugation of excess CNCs.

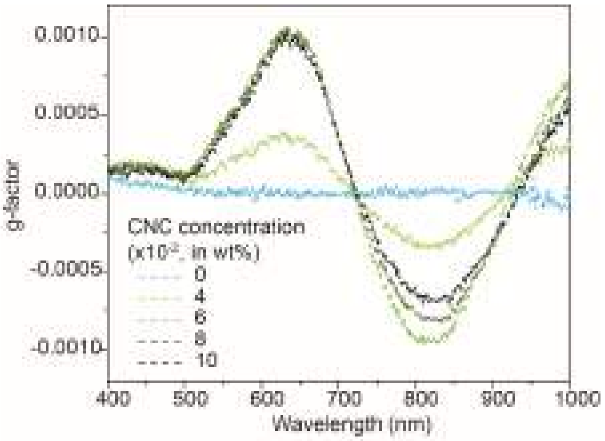

Figure S9. g-factor of CNC-AuNR$^+$ at different CNC concentration. Flattening of the absorbance spectra at high CNC concentration suppresses the negative peak intensity beyond 0.06 wt% of CNC.

ACS Sustainable Chemistry & Engineering
pubs.acs.org/journal/ascecg
Research Article

Selective Extraction of Gold by Niacin

Abhijit Nag, Md Rabiul Islam, and Thalappil Pradeep*

Cite This: https://dx.doi.org/10.1021/acssuschemeng.0c07409

Read Online

ACCESS | Metrics & More | Article Recommendations | Supporting Information

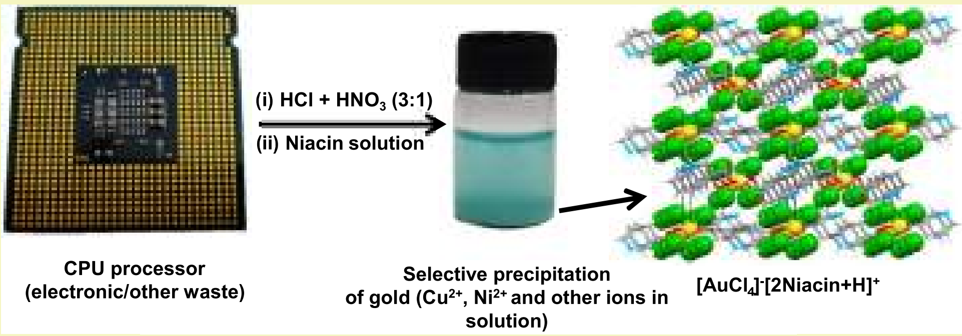

ABSTRACT: Gold recovery using a sustainable and inexpensive method has tremendous environmental and economic implications. We developed a highly cost-effective and sustainable method of gold extraction in which aqueous Au^{3+} is precipitated selectively as it is complex with the biomolecule niacin, having an overall formula, $[AuCl_4]^-[2Niacin + H]^+$, abbreviated as **I**. This selective precipitation occurs from mixtures of Au^{3+} with Ni^{2+}, Cu^{2+}, and Zn^{2+} along with commonly occurring alkali (Na^+/K^+) and alkaline earth (Mg^{2+}/Ca^{2+}) metal ions. From single-crystal studies, it was confirmed that electrostatic attraction and supramolecular interactions are the reasons for such co-precipitation, which was also confirmed by spectroscopy. Using the method, about 96.5% of gold was extracted in 2 min from electronic waste composed of Au, Cu, and Ni. This method was also employed to extract gold from nanomaterial waste generated in laboratories. Niacin, being inexpensive and renewable, costing ~US$ 6000 per ton in the local market, the method may be used for cost-effective, selective and sustainable extraction of gold from diverse raw materials.

KEYWORDS: *selective recovery of gold, gold−niacin complex, precipitation, electronic/nanowastes, sustainable chemistry*

INTRODUCTION

Noble metals are well-known in view of their exceptional physical and chemical properties.[1−9] Among them, gold is more popular since ancient times. The most universally used method for recovery of gold includes treatment of the ore with highly toxic sodium cyanide, which results in the formation of the soluble coordination complex, $Au(CN)_2^-$.[10,11] Gold is also extracted with highly toxic mercury.[12] This is currently the largest source of mercury pollution worldwide.[13,14] In this context, a sustainable, inexpensive, and efficient method for the recovery of gold from mines, as well as chemical and electronic wastes, is highly desirable.

As gold reserves are reducing day by day, it is necessary to recover gold from waste materials including nano- and electronic wastes to meet the growing demand. Gold is one of the precious metals used in electronic devices due to its corrosion resistance and high electrical conductivity. About 300 tonnes of gold are utilized every year in electronic products.[15] A recent report suggested that recovery of metals from electronic waste is more cost-effective than the mining of ores.[16]

Gold-based nanotechnology industries, such as high-efficiency compact storage devices, medical diagnostics, photovoltaics, imaging, etc., are expected to expand significantly.[17,18] The worldwide market value of gold nanoparticles (AuNPs) was projected to be 1.34 billion US dollars in 2014.[19] The market for gold-based nanotechnologies is estimated to rise drastically by 2022. As a result, about 20 000 kg of gold will enter the nanotechnology industry by this time.[19]

Many methods have been reported for the recovery of gold. Recently, Yang et al. used pyridine and *N*-bromosuccinimide to leach gold in solution, which could replace the well-known toxic methods of gold extraction like alkaline cyanide.[20] Stoddart et al. utilized different cyclodextrins where α-cyclodextrin showed efficient binding to $AuBr_4^-$ to form a precipitate.[21] Liu et al. have synthesized different types of macrocyclic tetralactam receptors, which formed host−guest complexes with square planar complexes of noble metal halides such as $AuCl_4^-$, $AuBr_4^-$, $PdCl_4^-$, etc.[22] Guo et al. selectively

Received: October 9, 2020
Revised: December 21, 2020

recovered gold using carbon nitride based on a photoreduction method.[23] Pati et al. recovered gold from nanowastes using Stoddart and co-worker's gold recovery method.[24] Recently, a green method was developed where noble metals like silver and copper were brought into solution from their metallic state using different types of carbohydrates.[25,26] Different types of covalent organic frameworks (COFs) and metal–organic frameworks (MOFs) were also used to capture gold ions selectively from aqueous solutions.[27−29] Cucurbit[6]uril was utilized to extract gold with an efficiency of 99.2% via co-precipitation.[30] Yang et al. captured gold with high adsorption capacity and selectivity using a protein membrane.[31] Love et al. used simple primary amides to extract gold selectively from electronic wastes.[32] Different types of methods used previously in the literature for gold extraction and their efficiencies are listed in Table S1.

Herein, we report the rapid co-precipitation of $[AuCl_4]^-[2Niacin + H]^+$, abbreviated as **I**, in water from gold-containing acidic mixtures by niacin. Electrostatic and supramolecular interactions such as hydrogen bonding and van der Waals (vdW) interactions are responsible for such complexation, as revealed by single-crystal studies. This phenomenon is highly selective for $AuCl_4^-$ and excludes other commonly coexisting ions such as Ni^{2+}, Fe^{3+}, Pt^{2+}, Cu^{2+}, and Zn^{2+} present in such solutions, along with alkali (Na^+/K^+) and alkaline earth (Mg^{2+}/Ca^{2+}) metal ions and Al^{3+}. X-ray photoelectron spectroscopy (XPS) and Raman studies also supported the formation of **I**. Using this method, gold was recovered from various waste samples, including electronic waste.

■ MATERIALS AND METHODS

Chemicals. Niacin, $CuCl_2{\cdot}2H_2O$, $FeCl_3{\cdot}6H_2O$, K_2PtCl_4, $HAuCl_4{\cdot}3H_2O$, $ZnCl_2$, NaCl, $AlCl_3$, and $MgCl_2$ were purchased from Sigma-Aldrich and used without further purification. Ethanol, HCl, and HNO_3 were purchased from Rankem. Milli-Q water was used throughout the experiment.

Crystallization of I. Briefly, 1 mL of $HAuCl_4$ (27 mM) and 1 mL of a saturated solution of niacin (125 mM) were mixed. NaCl (100 mg) was added to slow down the precipitation. The solution was kept for slow evaporation at room temperature. After 2 days, yellow crystals suitable for X-ray crystallographic analysis were obtained.

Crystallization of $Cu(H_2O)_4(Niacin)_2$. Briefly, 1 mL of $CuCl_2$ (27 mM) and 1 mL of a saturated solution of niacin (125 mM) were mixed. The solution was kept for slow evaporation at room temperature. After 3 days, blue crystals were obtained. The crystal structure of this system has been reported previously.[33]

Instrumentation. *X-ray Crystallography.* Single-crystal X-ray data collection was performed using a Bruker D8 VENTURE APEX3 diffractometer using Mo Kα ($\lambda = 0.71073$ Å) radiation. Indexing was performed using APEX3. The program, SAINT-v8.37A, was used for integrating the data collection frames. Absorption correction was performed by a multiscan method implemented in SADABS. The structure was solved using SHELXT-2018/2 and refined using SHELXL-2018/3 (full-matrix least-squares on $F2$) contained in WinGX v2018.3. Crystal data and refinement conditions are listed in Table S1. The crystal data have been deposited in the Cambridge Structural Database (CCDC no. 1989872).

More details on instrumentation are provided in the Supporting Information (SI).

■ RESULTS AND DISCUSSION

Niacin is nicotinic acid and is a form of vitamin B_3, an essential human nutrient. It is produced industrially, and the sales were reported to be 31 000 tons in 2014.[34] Upon addition of a saturated solution of niacin (125 mM, 2 mL) in water to an aqueous solution (1 mL, 27 mM) of $HAuCl_4$ at room temperature, a light yellow precipitate, labeled as **I**, appeared within a few minutes (Figure 1). The initial gold concentration in this experiment was about 5139 ppm. After addition of niacin, the concentration of gold was reduced to 2.9 ppm. Therefore, about 99.9% of gold was recovered using this method (Table S2). Data corresponding to the selectivity for gold using this precipitation method are presented later.

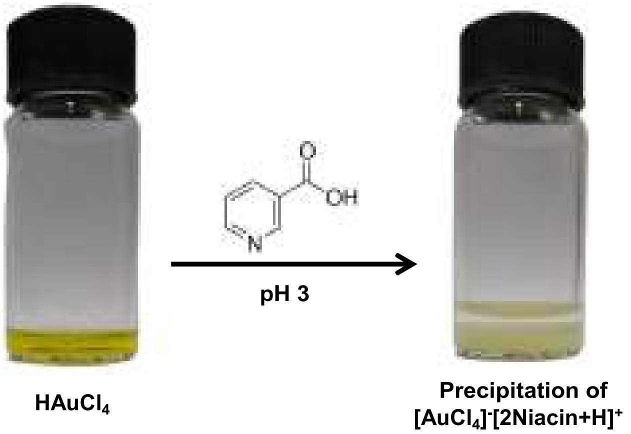

Figure 1. Formation and co-precipitation of **I** after mixing a saturated solution (2 mL) of niacin with $HAuCl_4$ (27 mM, 1 mL). The light yellow of the liquid meniscus in the bottle on the right is due to reflection from the precipitate.

The pK_a values of niacin are 2.0 and 4.85. Gold is generally extracted in acidic solutions, and the pH of the $HAuCl_4$ solution used was 1. After addition of niacin, the pH of the solution became 3. It was important to ensure that such a process occurs even at low concentrations for the process to be useful for gold recovery. It was confirmed that niacin had the ability to precipitate gold down to 320 ppb (Table S2), although complete precipitation was not observed.

Compound **I** was crystallized using slow evaporation of water. The crystal structure of **I** is presented in Figure 2A(i), where two niacin molecules interact with one $AuCl_4^-$. A simple representation of the crystal structure is shown in Figure 2A(ii). The crystal system is monoclinic with a space group $P21/n$ (Table S3 and Figure 2B). Expanded views of the unit cell in X, Y, and Z directions are presented in Figure S1. The layered structure of **I** along the Y axis is evident from Figure 3A. In the crystal, $AuCl_4^-$ and a dimer of niacin molecules (with a proton link) act as the anion and the cation, respectively. The overall formula of the complex is $[AuCl_4]^-[2Niacin + H]^+$. The proton is shared between two carboxylic groups of two niacin molecules (Figure 2A). Two pK_a values (mentioned above) support the zwitterionic structure of niacin in the crystal structure, as the pH of the solution was 3. UV–vis spectra of $[AuCl_4]^-$ (blue) and **I** (red) in dimethylformamide (DMF) were obtained (Figure S2). A characteristic transition at around 320 nm was seen in **I**, which supported the presence of $[AuCl_4]^-$ in the crystal structure. Thus, two niacin molecules are required to precipitate one molecule of $AuCl_4^-$. The required amount is about 1.25 g of niacin (equivalent to US$ 0.0084) per gram of gold.

Looking at the chemical formula, it can be confirmed that electrostatic interactions are present in the crystal structure. Strong H-bonding and vdW interactions are also responsible

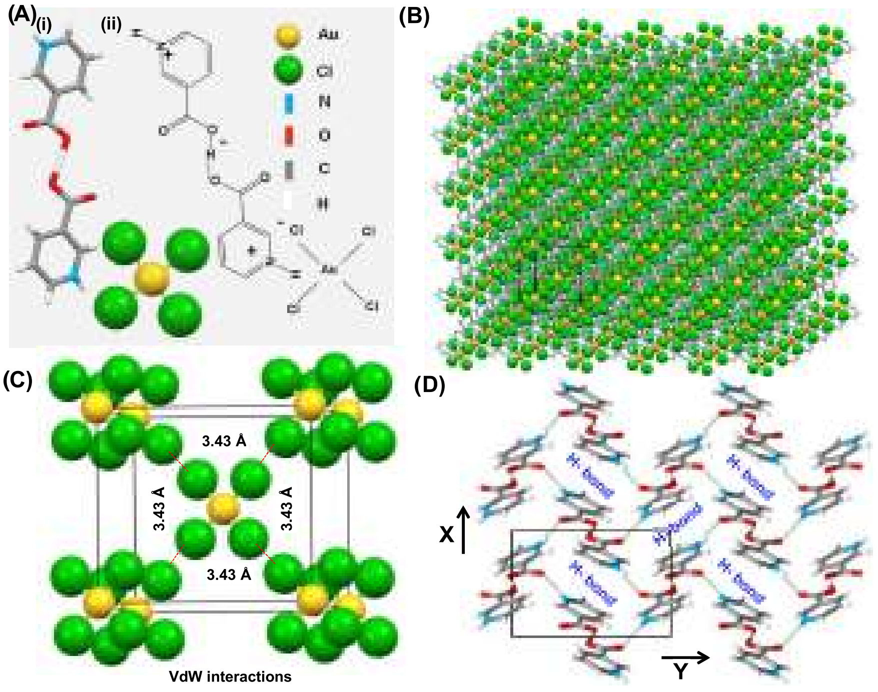

Figure 2. (A) (i) Crystal structure of **I** and (ii) Chemdraw representation of **I**. Color codes for the atoms are shown nearby. Note that the color of the H atom is white. (B) Expanded view (5 × 5 × 5) of the unit cell of **I**. (C) Van der Waals interactions between halide ions of adjacent $[AuCl_4]^-$ units. (D) H-bonding interaction between O atom of the carboxylic group and H attached to N.

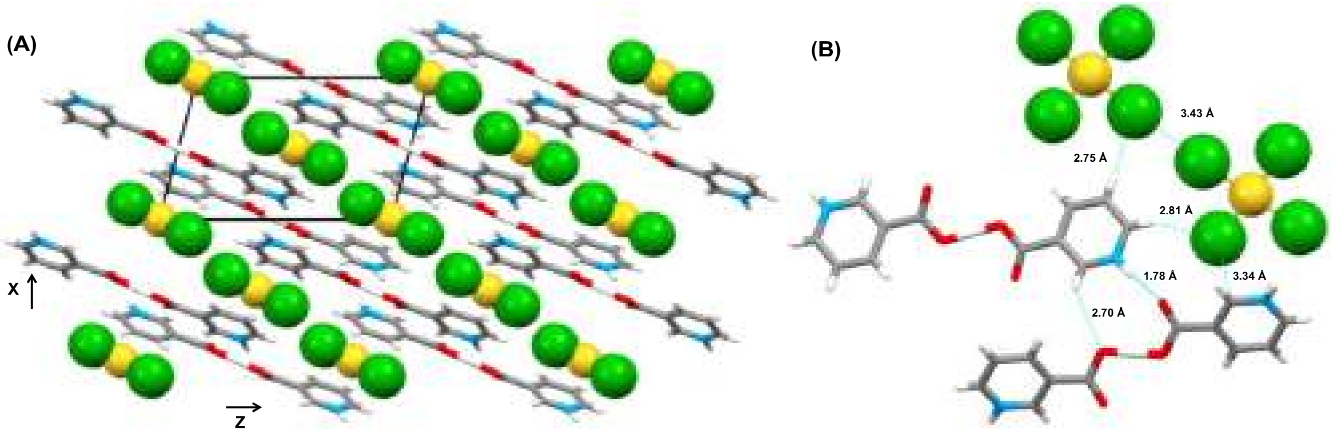

Figure 3. (A) Packing view of the crystal from the *Y* axis showing a layered structure. (B) Different noncovalent interactions such as H···Cl, Cl···Cl, Cl···C, and H···O present in the unit cell, with specific distances.

for such a complexation. VdW interactions between Cl atoms in the lattice are presented in Figure 2C, which operate in the diagonal direction of the unit cell. Similarly, H-bonding interactions between the O atom of the carboxylic group and H connected to N are presented in Figure 2D. Different types of H-bonding interactions were observed in the crystal (Figure 2D). Such kinds of self-organized and patterned structures are reminiscent of β-sheet and α-helix in proteins and also in the recently reported Au_{103} and Au_{246} nanoclusters.[35−37] Expanded views of $[AuCl_4]$ and $[2\text{Niacin} + H]^+$ in *X*, *Y*, and *Z* directions are presented in Figures S3 and S4, respectively. Different kinds of noncovalent interactions present in the crystal are shown in Figure 3B with specific distances. Noncovalent interactions between the hydrogen atoms of the aromatic ring and chlorines are also present in the crystal (Figure 3B).

To understand the distinct difference in the gold complex, the crystal structure of niacin with copper was also obtained (Figure S5). This complex dissolves in water, and its structure is already known.[33] The overall formula of the complex is $Cu(H_2O)_4(\text{Niacin-H})_2$. Here, copper formed a coordination bond with niacin through the N center of the heterocycle. There is a negative charge on the oxygen atom of the carboxylic acid group of niacin. This causes the overall charge to be zero. Such covalent bond formation is absent in **I** because gold is a soft center while N and O are hard centers in niacin. The presence of various types of noncovalent interactions that are specific in the case of $[AuCl_4]^-$ resulted in the precipitation of the complex. Complexes of niacin and such molecules with precious and transition metals have been reported,[38,39] although the structure of the gold complex and its selective precipitation have not been studied.

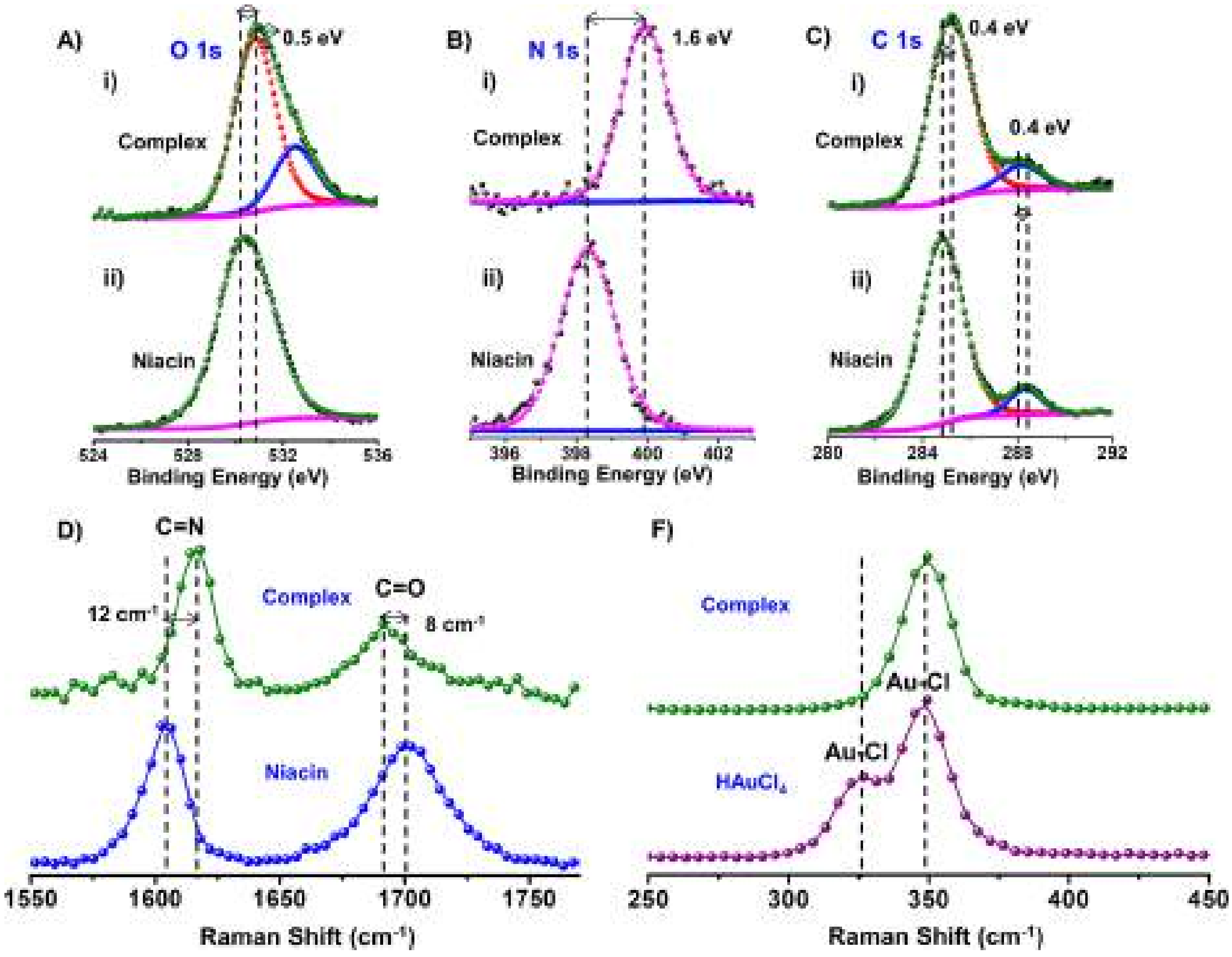

Figure 4. XPS data of oxygen (A), nitrogen (B), and carbon (C). The shift in the binding energies confirmed possible interactions in **I**. Data for pure niacin are also presented. The expanded Raman spectra of **I** are shown in Figure 3(D,F). (D) C=N and C=O stretching in **I** and niacin. About 12 and 8 cm^{-1} shifts were observed for **I** compared to niacin alone, for C=N and C=O, respectively. (F) Au−Cl stretching in **I** and $HAuCl_4$.

An XPS study was performed to reveal the interactions in the complex. Significant changes in binding energies were observed for oxygen and nitrogen in the complex, compared to free niacin. In the case of O 1s, a new peak appeared for **I** along with a ~0.5 eV chemical shift, compared to free niacin (Figure 4A), which could be due to the sharing of hydrogen between carboxylic groups of the two niacin molecules. Similarly, a chemical shift of about 1.6 eV was observed for N 1s in the complex compared to free niacin (Figure 4B). This could be due to the presence of a positive charge on N and H-bonding interactions (Figure 2D). These data confirmed the presence of strong interactions in the complex. The binding energy of C 1s was also influenced by these interactions (Figure 4C).

To get further insights into bonding, Raman spectroscopy was performed. Peak shifts of 12 and 8 cm^{-1} were observed for C=N and C=O vibrations, respectively, in **I** compared to free niacin, which is also supported by XPS and single-crystal XRD data (Figure 4D). There were two types of Au−Cl stretching for $HAuCl_4$. This is due to Au−Cl (348 cm^{-1}) in $AuCl_4^-$ and Au−Cl (326 cm^{-1}) in $AuCl_3(OH)^-$ (Figure 4F, $HAuCl_4$). Note that the spectrum of $HAuCl_4$ was measured in ambient air, which resulted in the water of hydration as the salt is hygroscopic. As the crystal structure of **I** does not have any OH attached to gold, only one Au−Cl stretching band appeared (Figure 4F). Both XPS and Raman spectroscopy are in good agreement with the single-crystal XRD data of **I**.

To test the selectivity of the process, an equimolar mixture of $HAuCl_4$, $CuCl_2$, and $ZnCl_2$ (27 mM each) was prepared by mixing the corresponding salts. After adding a saturated solution of niacin, precipitation of the gold complex occurred immediately, but copper and zinc were still in solution (Figure S6). The precipitate was examined using scanning electron microscopy/energy-dispersive spectroscopy (SEM/EDS) mapping to confirm the efficiency of the method for selectivity toward gold. SEM images revealed the formation of mesoflower-type of structures for the precipitate. SEM images of the precipitate are provided in Figure S7A,B. SEM/EDS confirmed the presence of N, O, Cl, Au, Cu, and Zn (Figure S7D). Au (10.11%), Zn (0.51%), and Cu (0.12%) were quantified by EDS mapping from the co-precipitate. About 94% pure gold was extracted using this method after one-time treatment of niacin. The elemental analysis of the precipitate is provided in Figure S7D. Elemental maps of copper, gold, and zinc are shown in Figure S7E. A detailed analysis of the solution after precipitation by inductively coupled plasma mass spectrometry (ICP MS) also confirmed the efficiency of extraction (Table S4). Similarly, niacin solution (125 mM) was added separately

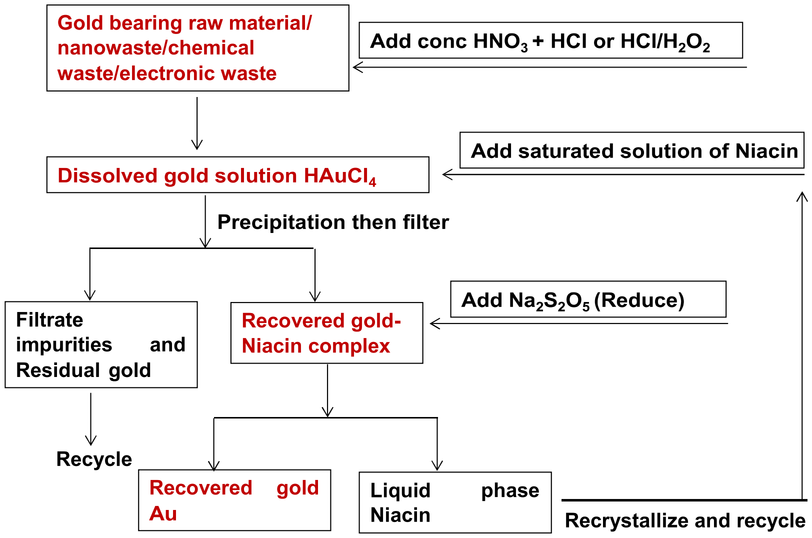

Figure 5. Gold-recovery flow chart using niacin.

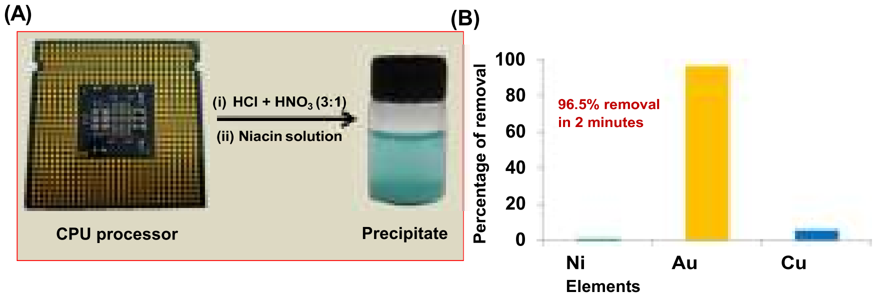

Figure 6. Recovery of gold from a central processing unit. (A) The CPU was treated with HCl and HNO_3 (3:1) to dissolve the metals. The resulting solution (blue) was treated with a saturated solution of niacin yielding a precipitate. (B) Percentage removal of various metals evaluated by ICP MS.

to 27 mM solutions of $PtCl_4$, $AlCl_3$, and $FeCl_3$ at pH 3 (Figure S8). No precipitation was observed.

A process of gold recovery using this approach is presented in Figure 5. After precipitation, **I** can be separated from impurities by filtration. The recovered **I** can be reduced using a reductant such as sodium metabisulfite ($Na_2S_2O_5$) to recover gold metal (see above). The remaining residual gold in the impurities and unused niacin (liquid phase) can be recycled. Preconcentration is necessary for precipitation when the concentration falls below 320 ppb, as mentioned earlier.

Gold was recovered from electronic waste and laboratory nanowaste. A used central processing unit (CPU) of a computer was treated with 5 mL of aqua regia (HCl and HNO_3 in a 3:1 volume ratio) to dissolve the metals (Figure 6A). The solution was heated for 2 h to remove excess acids, yielding 2 mL of a blue solution. More amounts of niacin were required to adjust the pH to 3 if excess acid was present in the solution. Note that precipitate (**I**) is soluble in HCl. To avoid such issues, excess acids were removed. The solution contained 770 ppm of Ni^{2+}, 22 320 ppm of Cu^{2+}, and 25 ppm Au^{3+} by ICP MS analysis (Table S5). A saturated solution of niacin (125 mM) in tap water (4 mL) containing common ions was added, and the pH of the solution changed to 3. After the treatment with niacin, about 96.5% of gold was recovered within 2 min (Table S5). The removal of different metals is presented in Figure 6B. Hence, it is established that niacin is highly efficient for the recovery of gold from electronic wastes.

A simulated nanowaste consisting of citrate-reduced AuNPs was synthesized. The colloidal AuNPs were precipitated using NaCl-induced aggregation, and the precipitate was dissolved using aqua regia. The niacin-based separation was carried out as before. The clear yellow solution became turbid just after addition of niacin, and the pH of the solution changed to 3. The reaction mixture was filtered through a Whatman filter paper. The precipitate was added to about 50 mM solution of $Na_2S_2O_5$ to recover gold. All stages involved in the recovery process were performed at room temperature (Figure S9).

Recovery was also attempted under certain extreme conditions. About 1 ppm of the gold solution was prepared in the presence of 160 000 ppm NaCl and 50 000 ppm $MgCl_2$. This method also has the ability to extract gold in such conditions (Table S6). This indicated that this process could be effective in collecting gold from extreme saline solutions.

The solvent can play a key role in such a process. An equimolar mixture of $HAuCl_4$ and $CuCl_2$ (27 mM) in ethanol (1 mL) was prepared. In this case, precipitation of the copper—niacin complex was observed, while gold was retained in the solution, as shown in Figure S10. Separation of $HAuCl_4$ and $CuCl_2$ can also be achieved in ethanol using niacin. Further optimization of the method and experimental parameters is ongoing in our laboratories to expand this process to more realistic applications.

https://dx.doi.org/10.1021/acssuschemeng.0c07409
ACS Sustainable Chem. Eng. XXXX, XXX, XXX−XXX

CONCLUSIONS

In summary, we discovered a method for the fast precipitation of gold in water by a simple biomolecule, niacin. The crystal structure of **I** revealed the presence of strong electrostatic, H-bonding, and vdW interactions in the crystal. Such types of interactions could be the main reason for selective precipitation of **I**. Raman spectroscopy and XPS were employed to support the single-crystal XRD data. This method is highly selective for gold. Trace amounts of gold could be recovered from complex mixtures of ions in water. This method was employed for the selective extraction of gold from electronic and chemical wastes. Extraction of gold may be achieved using HCl/H_2O_2[30] or pyridine and *N*-bromosuccinimide[20] instead of aqua regia, and Au^{3+} in the solution may be precipitated with niacin, making the process more sustainable.

ASSOCIATED CONTENT

Supporting Information

The Supporting Information is available free of charge at https://pubs.acs.org/doi/10.1021/acssuschemeng.0c07409.

Experimental details; packing of the crystal structure; separation of gold; SEM images and elemental mapping; recovery from nanowaste; crystal data and CIF files; and X-ray crystallographic data of **I** (PDF)

Gold_niacin (CIF)

Copper_niacin (CIF)

AUTHOR INFORMATION

Corresponding Author

Thalappil Pradeep − *DST Unit of Nanoscience and Thematic Unit of Excellence, Department of Chemistry, Indian Institute of Technology Madras, Chennai 600036, India;* orcid.org/0000-0003-3174-534X; Email: pradeep@iitm.ac.in; Fax: +91-44 2257-0545

Authors

Abhijit Nag − *DST Unit of Nanoscience and Thematic Unit of Excellence, Department of Chemistry, Indian Institute of Technology Madras, Chennai 600036, India*

Md Rabiul Islam − *DST Unit of Nanoscience and Thematic Unit of Excellence, Department of Chemistry, Indian Institute of Technology Madras, Chennai 600036, India*

Complete contact information is available at: https://pubs.acs.org/10.1021/acssuschemeng.0c07409

Notes

The authors declare no competing financial interest.

ACKNOWLEDGMENTS

We thank the Department of Science and Technology and Ministry of Mines, Government of India, for constantly supporting our research program. A.N. thanks IIT Madras for a doctoral fellowship.

REFERENCES

(1) Jin, R.; Zeng, C.; Zhou, M.; Chen, Y. Atomically Precise Colloidal Metal Nanoclusters and Nanoparticles: Fundamentals and Opportunities. *Chem. Rev.* **2016**, *116*, 10346−10413.

(2) Kang, X.; Zhu, M. Tailoring the Photoluminescence of Atomically Precise Nanoclusters. *Chem. Soc. Rev.* **2019**, *48*, 2422−2457.

(3) Kazan, R.; Müller, U.; Bürgi, T. Doping of Thiolate Protected Gold Clusters through Reaction with Metal Surfaces. *Nanoscale* **2019**, *11*, 2938−2945.

(4) Kerrich, R. Nature's Gold Factory. *Science* **1999**, *284*, 2101.

(5) Mathew, A.; Pradeep, T. Noble Metal Clusters: Applications in Energy, Environment, and Biology. *Part. Part. Syst. Charact.* **2014**, *31*, 1017−1053.

(6) Parker, J. F.; Fields-Zinna, C. A.; Murray, R. W. The Story of a Monodisperse Gold Nanoparticle: $Au_{25}L_{18}$. *Acc. Chem. Res.* **2010**, *43*, 1289−1296.

(7) Song, X.-R.; Goswami, N.; Yang, H.-H.; Xie, J. Functionalization of Metal Nanoclusters for Biomedical Applications. *Analyst* **2016**, *141*, 3126−3140.

(8) Yamazoe, S.; Koyasu, K.; Tsukuda, T. Nonscalable Oxidation Catalysis of Gold Clusters. *Acc. Chem. Res.* **2014**, *47*, 816−824.

(9) Yuan, X.; Luo, Z.; Yu, Y.; Yao, Q.; Xie, J. Luminescent Noble Metal Nanoclusters as an Emerging Optical Probe for Sensor Development. *Chem. - Asian J.* **2013**, *8*, 858−871.

(10) Gail, E.; Gos, S.; Kulzer, R.; Lorösch, J.; Rubo, A.; Sauer, M.; Kellens, R.; Reddy, J.; Steier, N.; Hasenpusch, W. Cyano Compounds, Inorganic. In *Ullmann's Encyclopedia of Industrial Chemistry*; Wiley-VCH Verlag GmbH & Co. KGaA, 2011.

(11) Rubo, A.; Kellens, R.; Reddy, J.; Steier, N.; Hasenpusch, W. Alkali Metal Cyanides. In *Ullmann's Encyclopedia of Industrial Chemistry*; Wiley-VCH Verlag GmbH & Co. KGaA, 2005.

(12) de Lacerda, L. D.; Salomons, W. *Mercury from Gold and Silver Mining: A Chemical Time Bomb?*; Springer: Berlin, Heidelberg, 1998.

(13) Esdaile, L. J.; Chalker, J. M. The Mercury Problem in Artisanal and Small-Scale Gold Mining. *Chem. - Eur. J.* **2018**, *24*, 6905−6916.

(14) Porcella, D. B.; Ramel, C.; Jernelov, A. Global Mercury Pollution and the Role of Gold Mining: An Overview. *Water, Air, Soil Pollut.* **1997**, *97*, 205−207.

(15) Hagelüken, C.; Corti, C. W. Recycling of Gold from Electronics: Cost-effective Use through 'Design for Recycling'. *Gold Bull.* **2010**, *43*, 209−220.

(16) Zeng, X.; Mathews, J. A.; Li, J. Urban Mining of E-Waste is Becoming More Cost- Effective Than Virgin Mining. *Environ. Sci. Technol* **2018**, *52*, 4835−4841.

(17) Roco, M. C.; Mirkin, C. A.; Hersam, M. C. Nanotechnology Research Directions for Societal Needs in 2020: Summary of International Study. *J. Nanopart. Res.* **2011**, *13*, 897−919.

(18) Wiek, A.; Gasser, L.; Siegrist, M. Systemic scenarios of nanotechnology: Sustainable governance of emerging technologies. *Futures* **2009**, *41*, 284−300.

(19) Market, G. N. *Gold Nanoparticles Market Size*. Industry Report, 2022, GMI358, Global Market Insights Inc., 2016.

(20) Yue, C.; Sun, H.; Liu, W.-J.; Guan, B.; Deng, X.; Zhang, X.; Yang, P. Environmentally Benign, Rapid, and Selective Extraction of Gold from Ores and Waste Electronic Materials. *Angew. Chem., Int. Ed.* **2017**, *56*, 9331−9335.

(21) Liu, Z.; Frasconi, M.; Lei, J.; Brown, Z. J.; Zhu, Z.; Cao, D.; Iehl, J.; Liu, G.; Fahrenbach, A. C.; Botros, Y. Y.; Farha, O. K.; Hupp, J. T.; Mirkin, C. A.; Fraser Stoddart, J. Selective Isolation of Gold Facilitated by Second-Sphere Coordination with α-Cyclodextrin. *Nat. Commun.* **2013**, *4*, No. 1855.

(22) Liu, W.; Oliver, A. G.; Smith, B. D. Macrocyclic Receptor for Precious Gold, Platinum, or Palladium Coordination Complexes. *J. Am. Chem. Soc.* **2018**, *140*, 6810−6813.

(23) Guo, Y.; Zhang, L.; Zhou, K.; Shen, Y.; Zhang, Q.; Gu, C. Selective Gold Recovery by Carbon Nitride through Photoreduction. *J. Mater. Chem. A* **2014**, *2*, 19594−19597.

(24) Pati, P.; McGinnis, S.; Vikesland, P. J. Waste Not Want Not: Life Cycle Implications of Gold Recovery and Recycling from Nanowaste. *Environ. Sci.: Nano* **2016**, *3*, 1133−1143.

(25) Baksi, A.; Gandi, M.; Chaudhari, S.; Bag, S.; Gupta, S. S.; Pradeep, T. Extraction of Silver by Glucose. *Angew. Chem., Int. Ed.* **2016**, *55*, 7777−7781.

(26) Nag, A.; Baksi, A.; Krishnapriya, K. C.; Gupta, S. S.; Mondal, B.; Chakraborty, P.; Pradeep, T. Synergistic Effect in Green Extraction

of Noble Metals and Its Consequences. *Eur. J. Inorg. Chem.* **2017**, *2017*, 3072−3079.

(27) Zhou, Z.; Zhong, W.; Cui, K.; Zhuang, Z.; Li, L.; Li, L.; Bi, J.; Yu, Y. A Covalent Organic Framework Bearing Thioether Pendant Arms for Selective Detection and Recovery of Au From Ultra-Low Concentration Aqueous Solution. *Chem. Commun.* **2018**, *54*, 9977−9980.

(28) Mon, M.; Ferrando-Soria, J.; Grancha, T.; Fortea-Pérez, F. R.; Gascon, J.; Leyva- Pérez, A.; Armentano, D.; Pardo, E. Selective Gold Recovery and Catalysis in a Highly Flexible Methionine-Decorated Metal−Organic Framework. *J. Am. Chem. Soc.* **2016**, *138*, 7864−7867.

(29) Sun, D. T.; Gasilova, N.; Yang, S.; Oveisi, E.; Queen, W. L. Rapid, Selective Extraction of Trace Amounts of Gold from Complex Water Mixtures with a Metal−Organic Framework (MOF)/Polymer Composite. *J. Am. Chem. Soc.* **2018**, *140*, 16697−16703.

(30) Wu, H.; Jones, L. O.; Wang, Y.; Shen, D.; Liu, Z.; Zhang, L.; Cai, K.; Jiao, Y.; Stern, C. L.; Schatz, G. C.; Stoddart, J. F. High-Efficiency Gold Recovery Using Cucurbit[6]uril. *ACS Appl. Mater. Interfaces* **2020**, *12*, 38768−38777.

(31) Yang, F.; Yan, Z.; Zhao, J.; Miao, S.; Wang, D.; Yang, P. Rapid Capture of Trace Precious Metals by Amyloid-Like Protein Membrane with High Adsorption Capacity and Selectivity. *J. Mater. Chem. A* **2020**, *8*, 3438−3449.

(32) Doidge, E. D.; Carson, I.; Tasker, P. A.; Ellis, R. J.; Morrison, C. A.; Love, J. B. A Simple Primary Amide for the Selective Recovery of Gold from Secondary Resources. *Angew. Chem., Int. Ed.* **2016**, *55*, 12436−12439.

(33) Anacleto, B.; Gomes, P.; Correia-Branco, A.; Silva, C.; Martel, F.; Brandão, P. Design, Structural Characterization and Cytotoxic Properties of Copper(I) and Copper(II) Complexes Formed by Vitamin B_3 Type. *Polyhedron* **2017**, *138*, 277−286.

(34) Blum, R. Vitamins, 11. Niacin (Nicotinic Acid, Nicotinamide). In *Ullmann's Encyclopedia of Industrial Chemistry*; Wiley-VCH Verlag GmbH & Co. KGaA, 2015; pp 1−9.

(35) Dunitz, J. D. Pauling's Left-Handed α-Helix. *Angew. Chem., Int. Ed.* **2001**, *40*, 4167−4173.

(36) Higaki, T.; Liu, C.; Zhou, M.; Luo, T.-Y.; Rosi, N. L.; Jin, R. Tailoring the Structure of 58-Electron Gold Nanoclusters: $Au_{103}S_2$(S-Nap)$_{41}$ and Its Implications. *J. Am. Chem. Soc.* **2017**, *139*, 9994−10001.

(37) Zeng, C.; Chen, Y.; Kirschbaum, K.; Lambright, K. J.; Jin, R. Emergence of Hierarchical Structural Complexities in Nanoparticles and Their Assembly. *Science* **2016**, *354*, 1580−1584.

(38) Al-Saif, F. A.; Refat, M. S. Ten Metal Complexes of Vitamin B_3/Niacin: Spectroscopic, Thermal, Antibacterial, Antifungal, Cytotoxicity and Antitumor Studies of Mn(II), Fe(III), Co(II), Ni(II), Cu(II), Zn(II), Pd(II), Cd(II), Pt(IV) and Au(III) Complexes. *J. Mol. Struct.* **2012**, *1021*, 40−52.

(39) Dar, A.; Moss, K.; Cottrill, S. M.; Parish, R. V.; McAuliffe, C. A.; Pritchard, R. G.; Beagley, B.; Sandbank, J. Complexes of Gold(III) with Mononegative Bidentate N,O-Ligands. *J. Chem. Soc., Dalton Trans.* **1992**, *12*, 1907−1913.

Supporting Information for Publication

Selective Extraction of Gold by Niacin

Abhijit Nag† , Md Rabiul Islam† , and Thalappil Pradeep†*

†DST Unit of Nanoscience and Thematic Unit of Excellence, Department of Chemistry,

Indian Institute of Technology Madras, Chennai-600036, India.

*Corresponding Author Email: pradeep@iitm.ac.in; Fax: + 91-44 2257-0545

SUPPORTING INFORMATION CONTENT

Total number of pages: 15

Total number of figures: 10

Total number of tables: 6

Table of Contents

Instrumentation

Inductively coupled plasma-mass spectrometry (ICP MS)

ICP MS was performed using a Perkin Elmer NexION 300X instrument equipped with Ar plasma. Before doing any sample, the instrument was calibrated with gold standard of four different concentrations (0, 10, 100 and 1000 ppb) to get a calibration curve with $R^2=0.9999$. Blank experiment (0 ppb) was performed with milli-Q water (18.3 MΩ resistance) with 5% (v/v) hydrochloric acid. Standards were also prepared in 5% hydrochloric acid. The same amount (5%) of hydrochloric acid was added to the collected samples also before analyses. For other metals also, the instrument was calibrated with the standard by the same procedure, but 5% nitric acid was used.

Scanning electron microscopy (SEM)

SEM (scanning electron microscopy) and energy dispersive analysis of X-rays (EDS) were performed using an FEI QUANTA-200 SEM.

X-ray photoelectron spectroscopy

XPS measurements were performed with an Omicron ESCA Probe Spectrometer. It consists of EA 125 energy analyzer, XM 1000 MkII X-ray source and monochromator, DAR 400 X-ray source (Al/Mg), VUV source HIS 13, CN 10 and CN 10+ charge neutralizer system, ISE 10 sputter ion source and MKS residual gas analyzer for temperature programed desorption (TPD). Polychromatic Al Kα X-rays (hν = 1486.6 eV) were used for analysis.

Table S1. Different methods for gold recovery available in the literature.

References	**Method used**	**Uptake percentage of gold**
Precious metal recovery from electronic waste by a porous porphyrin polymer[1]	Adsorption	98.8
High-efficiency gold recovery using Cucurbit[6]uril[2]	Precipitation	99.2
Selective isolation of gold facilitated by second-sphere coordination with α-cyclodextrin[3]	Precipitation	Not available
Environmentally benign, rapid, and selective extraction of gold from ores and waste electronic materials[4]	Chemical leaching	90
Rapid capture of trace precious metals by amyloid-like protein membrane with high adsorption capacity and selectivity[5]	Adsorption	99.6
A simple primary amide for the selective recovery of gold from secondary resources[6]	Solvent extraction	Not available
Selective extraction of trace amounts of gold from complex water mixtures with a metal–organic framework (MOF)/polymer composite[7]	Adsorption	99
This work	Precipitation	99.9

Table S2. ICP MS data for gold extraction at different concentrations of gold.

Initial gold concentration	Gold concentration after niacin treatment
5139 ppm	2.9 ppm
320 ppb	248 ppb

Table S3. Crystal data and structure refinement for I.

Identification code	shelx	
Empirical formula	C12 H11 Au Cl4 N2 O4	
Formula weight	585.99	
Temperature	293(2) K	
Wavelength	0.71073 Å	
Crystal system	Monoclinic	
Space group	P 21/n	
Unit cell dimensions	a = 7.2567(18) Å	a= 90°.
	b = 10.516(4) Å	b= 105.095(14)°.
	c = 11.444(4) Å	g = 90°.
Volume	843.2(5) Å^3	
Z	2	
Density (calculated)	2.308 Mg/m^3	
Absorption coefficient	9.376 mm^{-1}	
F(000)	552	
Crystal size	0.200 x 0.150 x 0.100 mm^3	
Theta range for data collection	3.580 to 29.980°.	
Index ranges	-9<=h<=10, -14<=k<=14, -15<=l<=16	
Reflections collected	14924	
Independent reflections	2426 [R(int) = 0.0557]	
Completeness to theta = 25.242°	98.9 %	
Absorption correction	Semi-empirical from equivalents	
Max. and min. transmission	0.7451 and 0.4461	
Refinement method	Full-matrix least-squares on F^2	
Data / restraints / parameters	2426 / 1 / 112	
Goodness-of-fit on F^2	1.278	
Final R indices [I>2sigma(I)]	R1 = 0.0271, wR2 = 0.0644	
R indices (all data)	R1 = 0.0354, wR2 = 0.0710	
Extinction coefficient	0.0376(16)	
Largest diff. peak and hole	0.681 and -0.928 e.Å^{-3}	

Packing in I

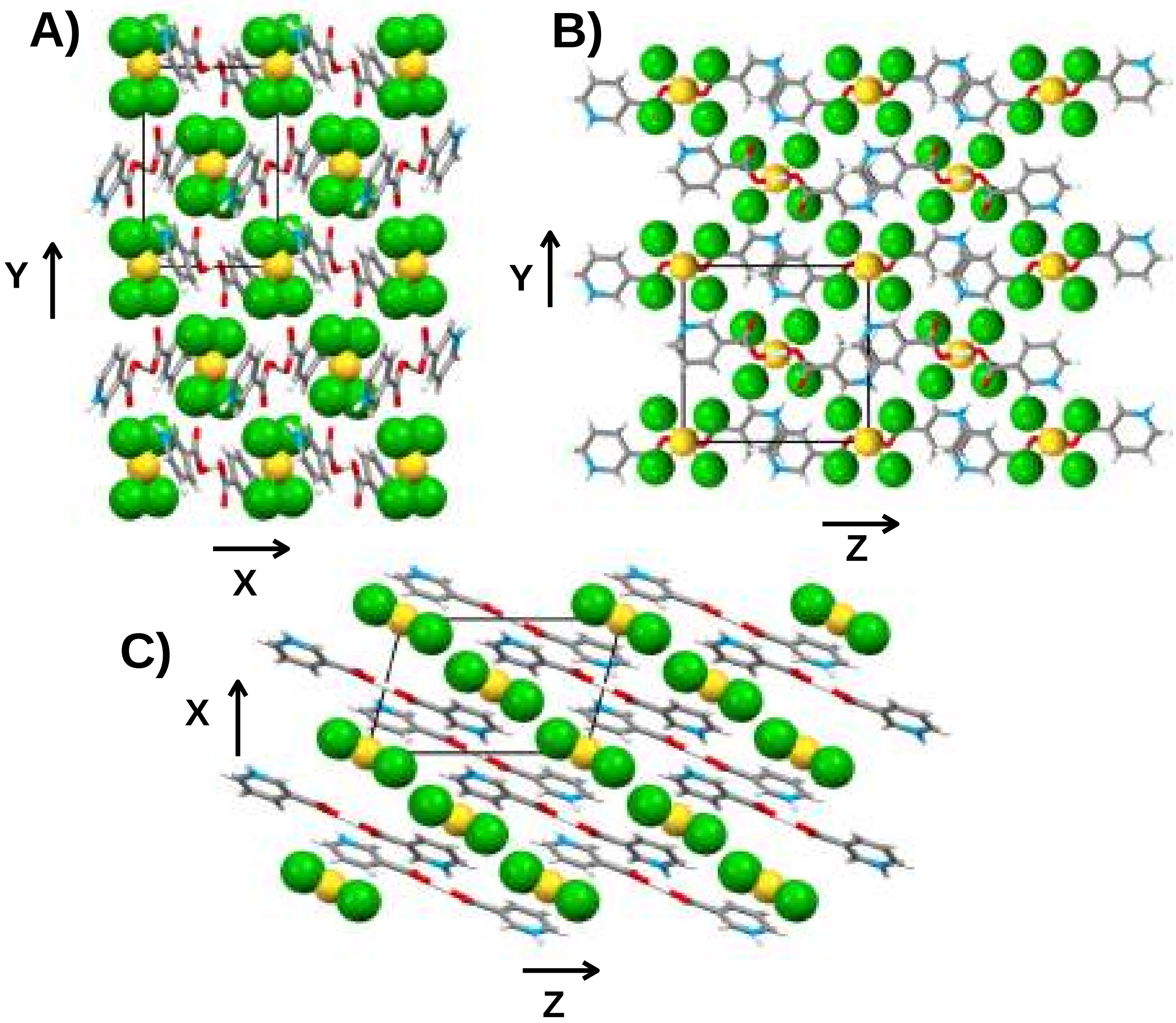

Figure S1. Packing of the crystal. Views from, **A)** Z, **B)** X and **C)** Y axes.

UV-vis spectra

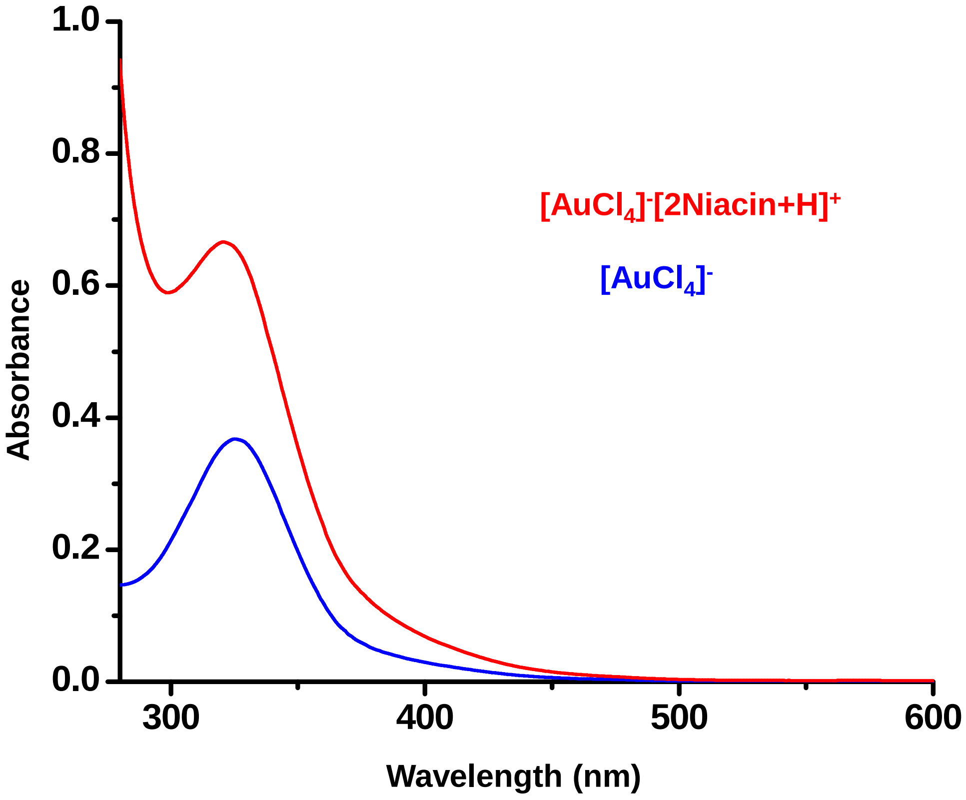

Figure S2. UV-vis spectra of $[AuCl_4]^-$ (blue) and $[AuCl_4]^-[2Niacin+H]^+$ (red) in DMF.

Packing of $AuCl_4^-$ in a crystal of I

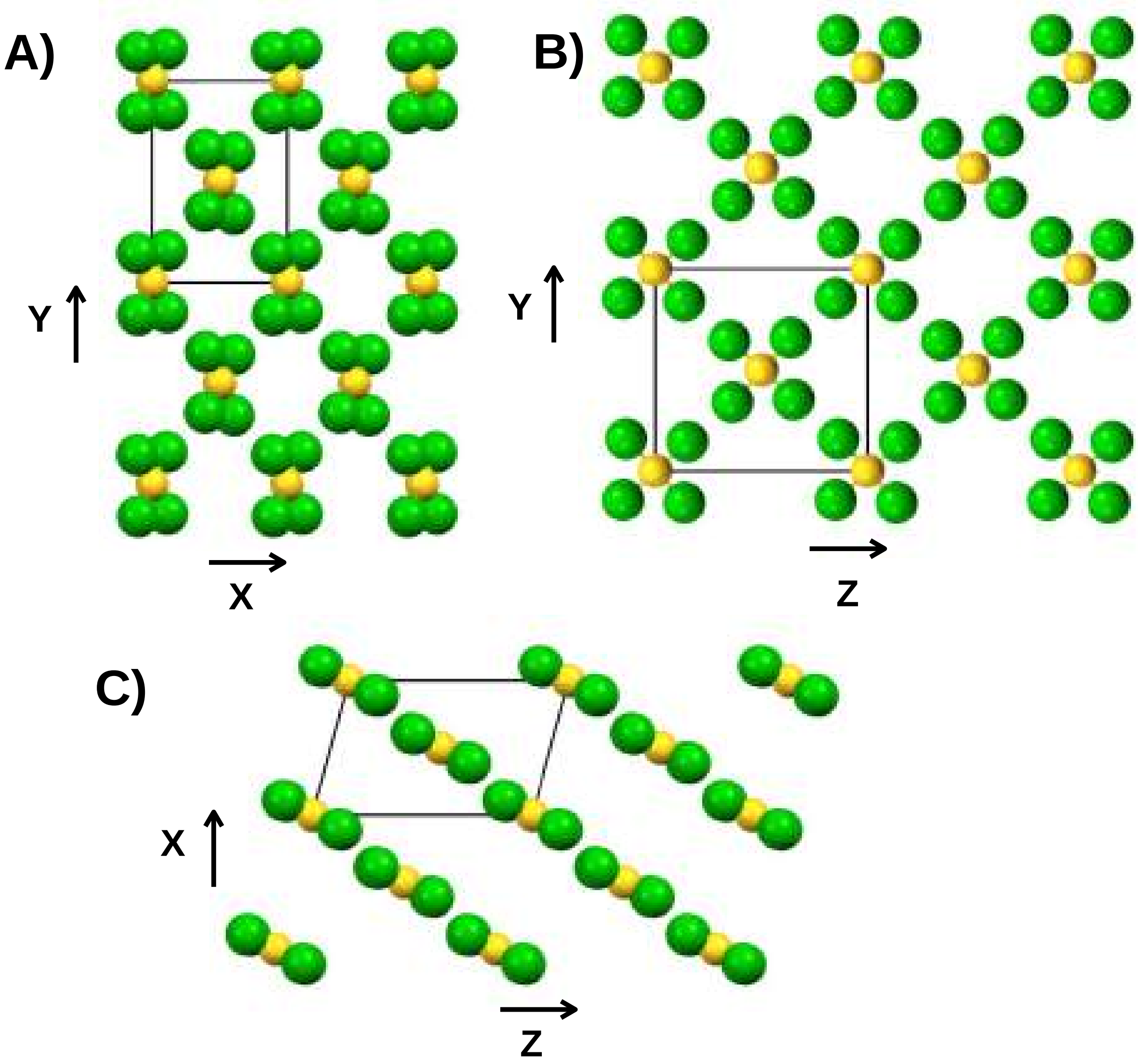

Figure S3. Packing of $AuCl_4^-$ in the crystal. Views from, **A)** Z, **B)** X and **C)** Y axes.

Packing of [2Niacin+H]$^+$ in a crystal of I

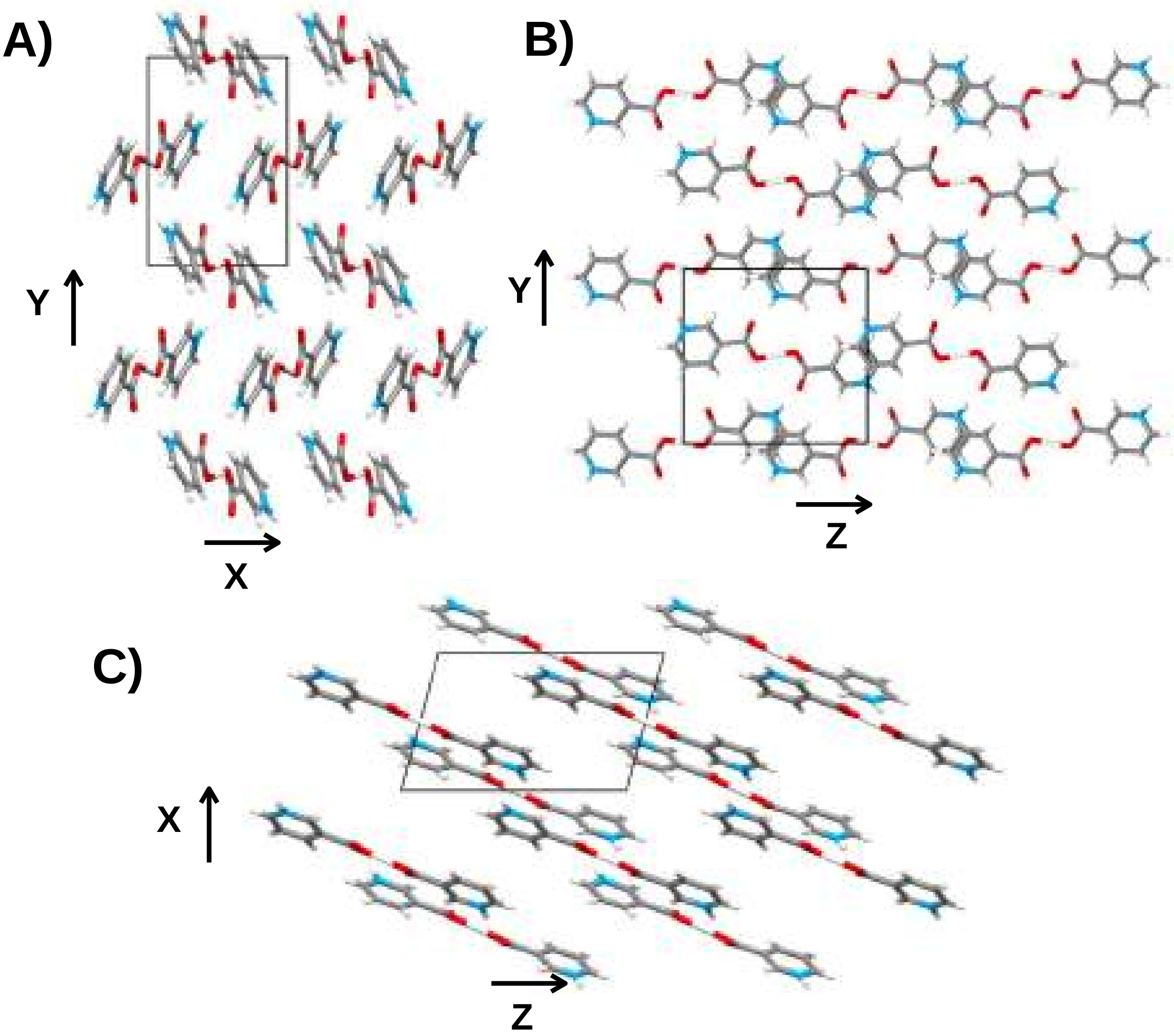

Figure S4. Packing of [2Niacin+H]$^+$ in the crystal. Views from, **A)** Z, **B)** X and **C)** Y axes.

Crystal structure of $Cu(H_2O)_4(Niacin\text{-}H)_2$

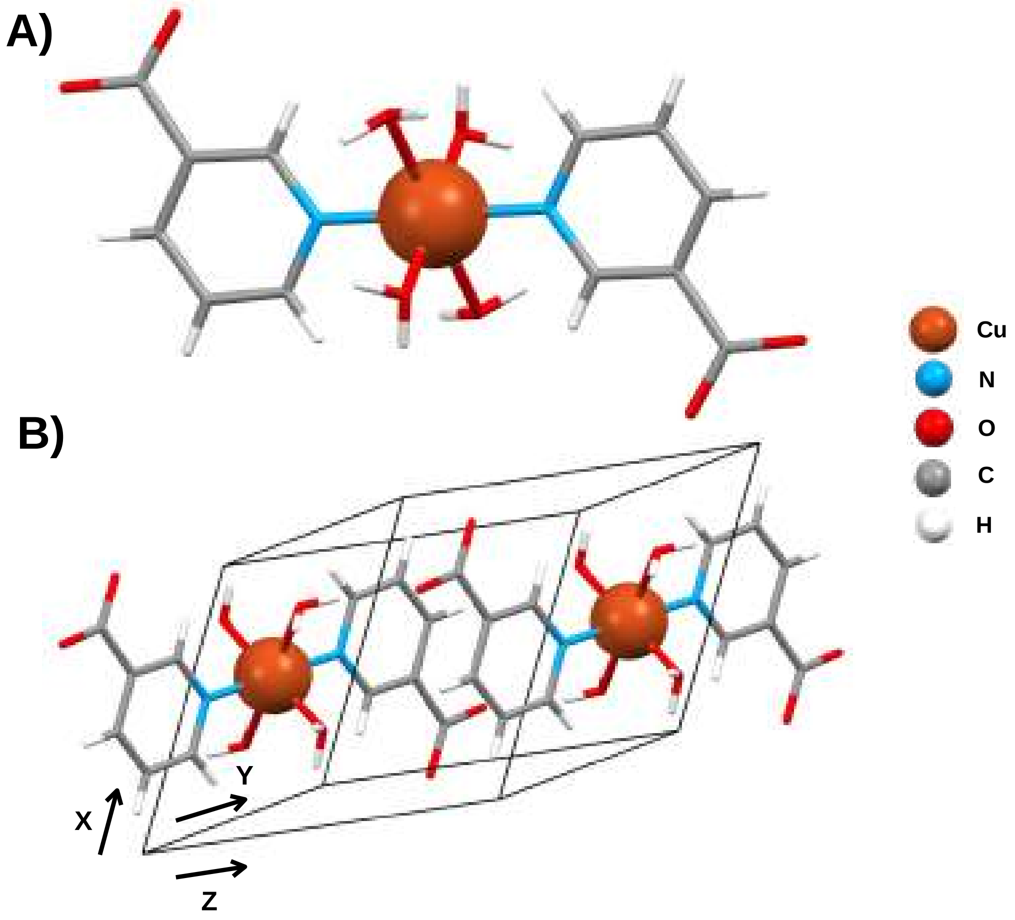

Figure S5. A) Crystal structure of $Cu(H_2O)_4(Niacin\text{-}H)_2$. Color codes for the atoms are also shown. B) Unit cell of $Cu(H_2O)_4(Niacin\text{-}H)_2$. Crystal structure of this system was reported earlier.[8]

Selectivity towards gold

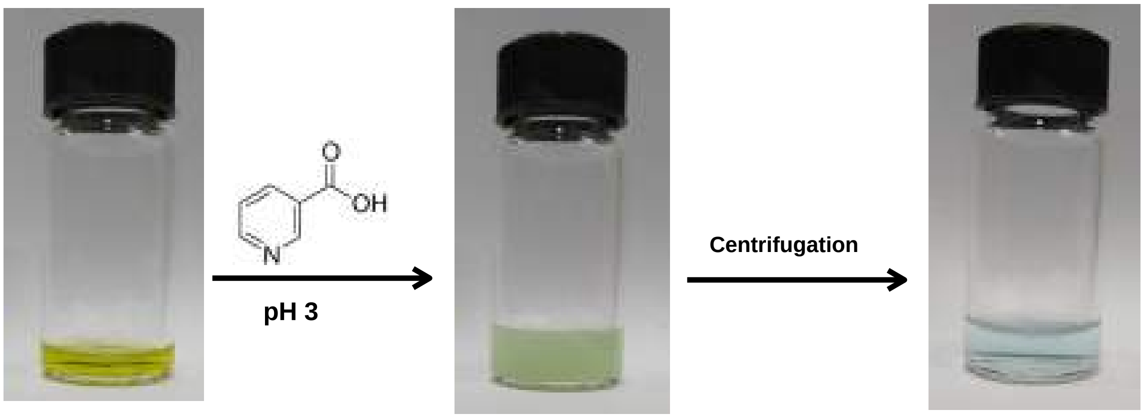

Equimolar solution of $HAuCl_4$, $CuCl_2$ & $ZnCl_2$

Precipitation of gold niacin complex

Copper & zinc solution

Figure S6. Separation of gold from an equimolar mixture of $HAuCl_4$, $CuCl_2$ and $ZnCl_2$, using saturated (125 mM) solution of niacin.

SEM/EDAX of the precipitate

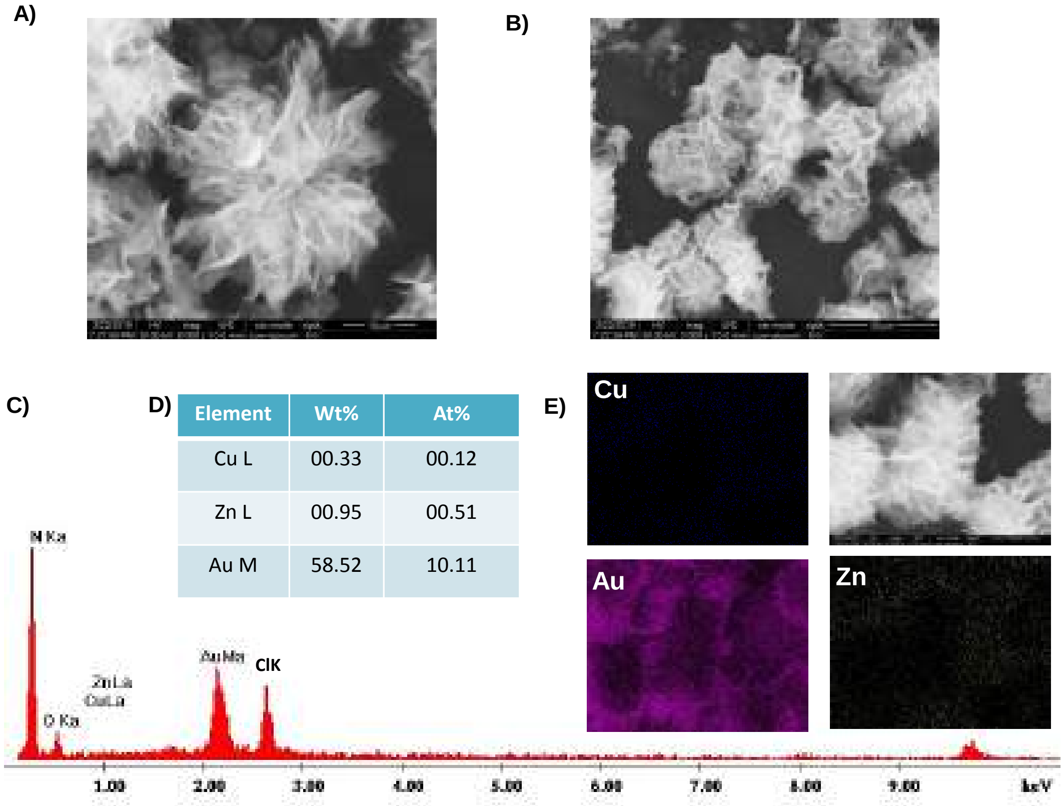

Element	Wt%	At%
Cu L	00.33	00.12
Zn L	00.95	00.51
Au M	58.52	10.11

Figure S7. A)-B) SEM images of the precipitate. C) EDS spectrum of the precipitate. D) Elemental analyses data copper, gold and zinc. E) Elemental maps corresponding to zinc, copper, and gold are shown, along with a SEM image. Scale bar is the same for all the images.

Table S4. ICP MS data for gold extraction from the mixtures of $HAuCl_4$, $CuCl_2$ and $ZnCl_2$.

Ions	Initial concentration (ppm)	Final concentration in solution after niacin treatment (ppm)
Cu^{2+}	1710	1616
Au^{3+}	5139	3.9
Zn^{2+}	1745	1639

Selectivity towards gold

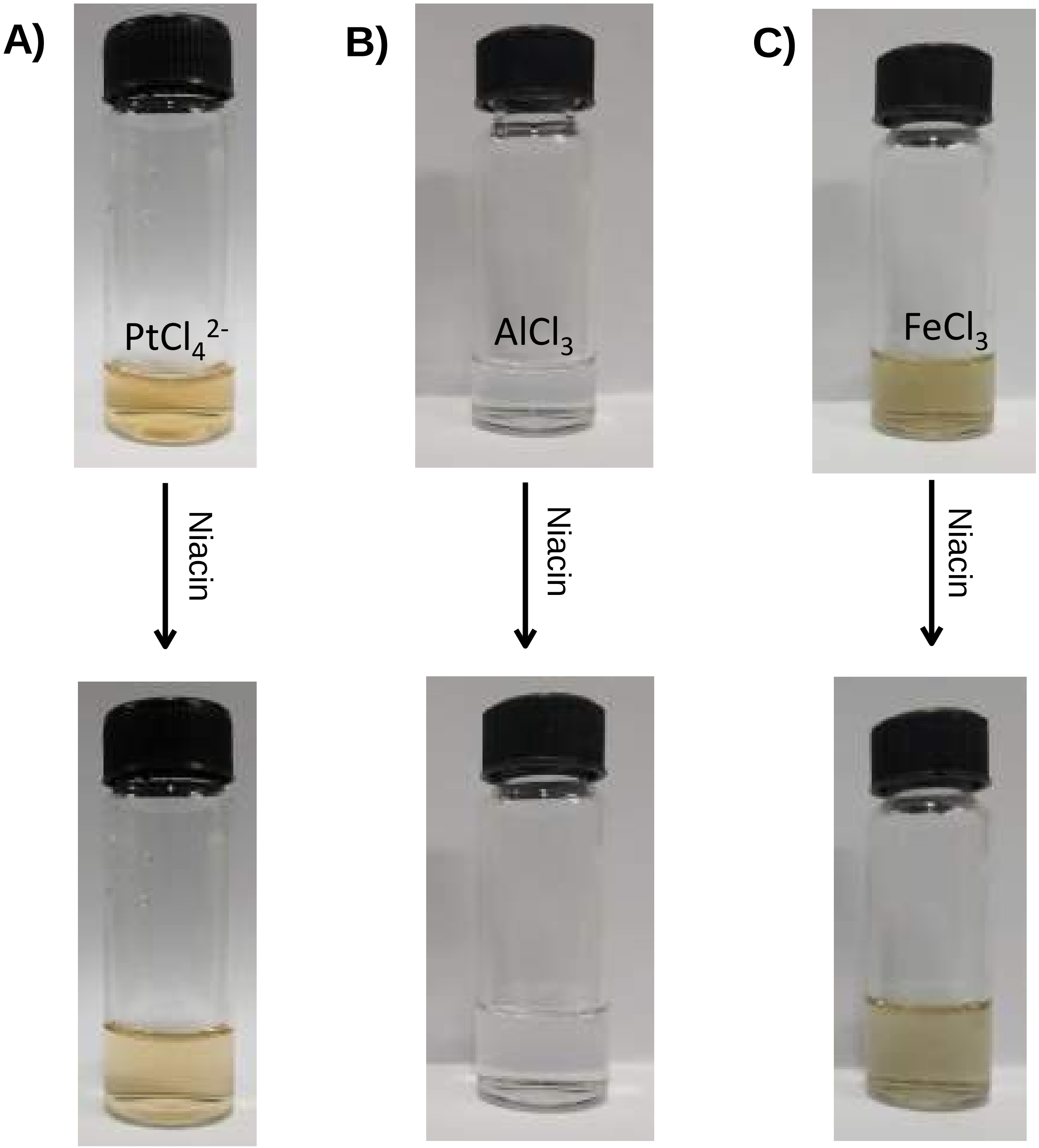

Figure S8. About 125 mM solution of niacin (2 mL) was added to 27 mM 2 mL solutions of A) $PtCl_4^{2-}$, B) $AlCl_3$ and C) $FeCl_3$ at pH 3. No precipitation was observed.

Recovery of gold from nanowaste

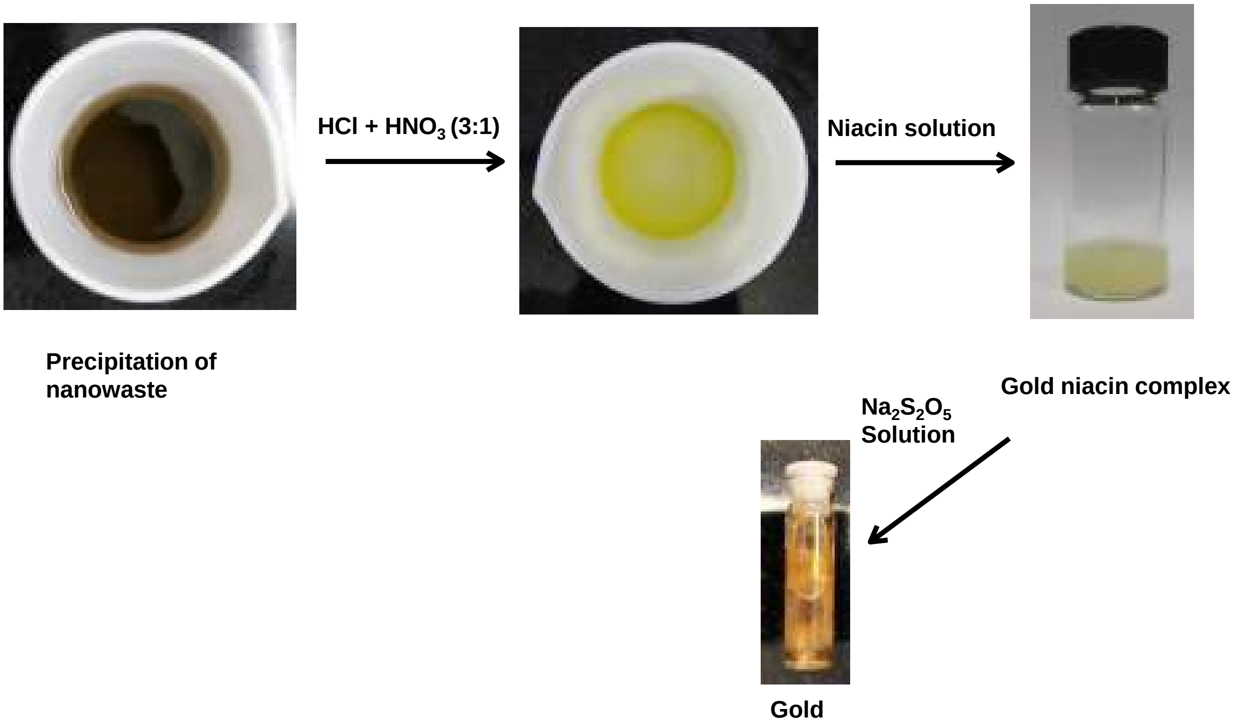

Figure S9. Schematic of the gold recovery process from gold nanowaste. Precipitation of bulk gold by reduction with $Na_2S_2O_5$ is shown.

Table S5. ICP MS data for gold extraction from electronic wastes.

Ions	Initial concentration (ppm)	Final concentration in solution after niacin treatment (ppm)
Ni^{2+}	770	760
Au^{3+}	25	0.85
Cu^{2+}	22320	21120

Table S6. ICP MS data for gold extraction in presence of NaCl and $MgCl_2$.

Initial gold concentration	Gold concentration after niacin treatment
1 ppm	344 ppb

Co-precipitation of copper-niacin in ethanol

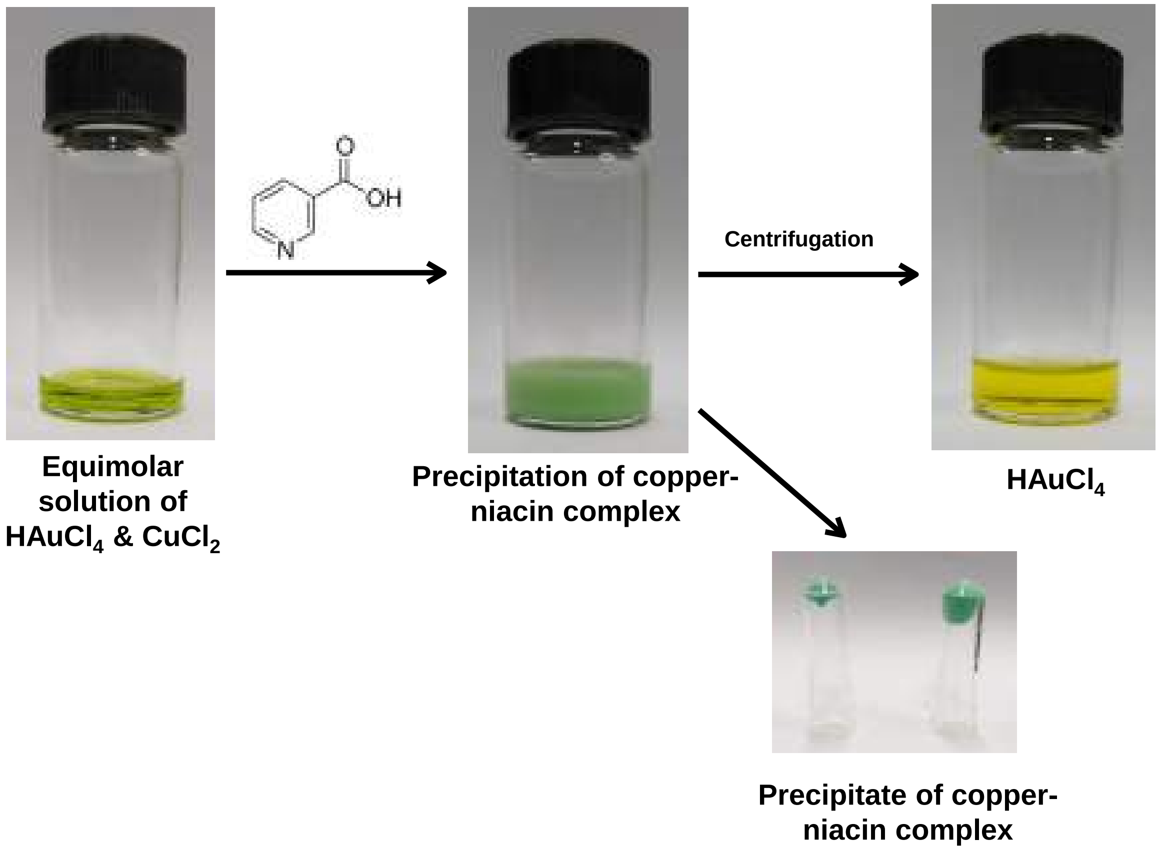

Figure S10. Co-precipitation of copper-niacin complex after addition of saturated niacin solution (1 mL) to an equimolar mixture (27 mM each) of $HAuCl_4$ and $CuCl_2$ (1 mL) in ethanol. By centrifugation, gold and copper can be separated.

References

1. Hong, Y.; Thirion, D.; Subramanian, S.; Yoo, M.; Choi, H.; Kim, H. Y.; Stoddart, J. F.; Yavuz, C. T., Precious Metal Recovery from Electronic Waste by a Porous Porphyrin Polymer. *PNAS* **2020,** *117* (28), 16174-16180.

2. Wu, H.; Jones, L. O.; Wang, Y.; Shen, D.; Liu, Z.; Zhang, L.; Cai, K.; Jiao, Y.; Stern, C. L.; Schatz, G. C.; Stoddart, J. F., High-Efficiency Gold Recovery Using Cucurbit[6]uril. *ACS Appl. Mater. Interfaces* **2020,** *12* (34), 38768-38777.

3. Liu, Z.; Frasconi, M.; Lei, J.; Brown, Z. J.; Zhu, Z.; Cao, D.; Iehl, J.; Liu, G.; Fahrenbach, A. C.; Botros, Y. Y.; Farha, O. K.; Hupp, J. T.; Mirkin, C. A.; Fraser Stoddart, J., Selective Isolation of Gold Facilitated by Second-Sphere Coordination with α-Cyclodextrin. *Nat. Commun.* **2013,** *4* (1), 1855.

4. Yue, C.; Sun, H.; Liu, W.-J.; Guan, B.; Deng, X.; Zhang, X.; Yang, P., Environmentally Benign, Rapid, and Selective Extraction of Gold from Ores and Waste Electronic Materials. *Angew. Chem. Int.Ed.* **2017,** *56* (32), 9331-9335.

5. Yang, F.; Yan, Z.; Zhao, J.; Miao, S.; Wang, D.; Yang, P., Rapid Capture Of Trace Precious Metals by Amyloid-Like Protein Membrane with High Adsorption Capacity and Selectivity. *J. Mater. Chem. A* **2020,** *8* (6), 3438-3449.

6. Doidge, E. D.; Carson, I.; Tasker, P. A.; Ellis, R. J.; Morrison, C. A.; Love, J. B., A Simple Primary Amide for the Selective Recovery of Gold from Secondary Resources. *Angew. Chem. Int. Ed.* **2016,** *55* (40), 12436-12439.

7. Sun, D. T.; Gasilova, N.; Yang, S.; Oveisi, E.; Queen, W. L., Rapid, Selective Extraction of Trace Amounts of Gold from Complex Water Mixtures with a Metal–Organic Framework (MOF)/Polymer Composite. *J. Am. Chem. Soc.* **2018,** *140* (48), 16697-16703.

8. Anacleto, B.; Gomes, P.; Correia-Branco, A.; Silva, C.; Martel, F.; Brandão, P., Design, Structural Characterization and Cytotoxic Properties of Copper(I) and Copper(II) Complexes Formed by Vitamin B3 Type. *Polyhedron* **2017,** *138*, 277-286.

Publications with other groups

ACES Asian Chemical Editorial Society
doi.org/10.1002/asia.202100475
CHEMISTRY AN ASIAN JOURNAL
Full Paper

Design of a Waste Paper-Derived Chemically 'Reactive' and Durable Functional Material with Tailorable Mechanical Property Following an Ambient and Sustainable Chemical Approach

Arpita Shome,[a] Adil M. Rather,[a, b] Angana Borbora,[a] Pillalamarri Srikrishnarka,[c] Avijit Baidya,[c] Thalappil Pradeep,*[c] and Uttam Manna*[a, d]

Abstract: Controlled tailoring of mechanical property and wettability is important for designing various functional materials. The integration of these characteristics with waste materials is immensely challenging to achieve, however, it can provide sustainable solutions to combat relevant environmental pollutions and other relevant challenges. Here, the strategic conversion of discarded and valueless waste paper into functional products has been introduced following a catalyst-free chemical approach to tailor both the mechanical property and water wettability at ambient conditions for sustainable waste management and controlling the relevant environmental pollution. In the current design, the controlled and appropriate silanization of waste paper allowed to modulate both the a) porosity and b) compressive modulus of the paper-derived sponges. Further, the association of 1,4-conjugate addition reaction between amine and acrylate groups allowed to obtain an unconventional waste paper-derived chemically 'reactive' sponge. The appropriate covalent modification of the residual reactive acrylate groups with selected alkylamines at ambient conditions provided a facile basis to tailor the water wettability from moderate hydrophobicity, adhesive superhydrophobicity to non-adhesive superhydrophobicity. The embedded superhydrophobicity in the waste paper-derived sponge was capable of sustaining large physical deformations, severe physical abrasions, prolonged exposure to harsh aqueous conditions, etc. Further, the waste paper-derived, extremely water-repellent sponges and membranes were successfully extended for proof-of-concept demonstration of a practically relevant outdoor application, where the repetitive remediation of oil spillages has been demonstrated following both selective absorption (25 times) of oils and gravity-driven filtration-based (50 times) separation of oils from oil/water mixtures at different harsh aqueous scenarios.

Introduction

In the past, mechanically durable materials have been fabricated extensively for various prospective energy and health related applications.[1–3] The strategic integration of carbon nanotubes,[4,5] graphene derivatives,[6–8] cellulose nanocrystals,[9] etc. impart the required mechanical durability for practical applications. Li *et al.*, developed ultralight, compressible covalent organic framework aerogel reinforced with reduced graphene oxide which exhibits excellent absorption and electrochemical properties.[7] Wang *et al.*, fabricated highly compressible boron nitride nanotubes aerogel reinforced with reduced graphene oxide with superior mechanical property which was impossible to attain without the reinforcement.[8] Apart from the commonly used nanomaterials,[10–12] different other approaches[13–19] – including association of elastomers, MXenes, electrodeposited nano-alloys etc. have been introduced to develop mechanically durable materials embedded with extreme liquid wettability. However, such approaches are inadequate to tailor the chemical functionality and water wettability – due to the lack of any residual chemical reactivity. In the past, chemically reactive interfaces have been designed adopting click chemistry,[20,21] azlactone ring opening reaction,[22] Schiff base reactions[23] etc. for modulating the chemical functionality, however, such reported materials are inappropriate for tuning the mechanical property. Nevertheless, the demonstration of consecutive tailoring of mechanical property and chemical functionality in the same material is rare in the relevant literature.

In the past, discarded plant bio-mass was transformed into functional material to combat potential environmental pollutions.[24,25] In that context, here, waste paper that generally poses major concerns including deforestation, water consumption and pollution, landfills, air pollution etc.[26,27] has been extended to transform into a functional material with tailorable mechanical property and chemical functionalities – following a

---

[a] A. Shome, Dr. A. M. Rather, A. Borbora, Prof. U. Manna
Bio-Inspired Polymeric Materials Lab, Department of Chemistry,
Indian Institute of Technology-Guwahati
Kamrup, Assam 781039 (India)
[b] Dr. A. M. Rather
Department of Chemical and Biochemical Engineering,
The Ohio State University
Columbus, Ohio 43210 (USA)
[c] P. Srikrishnarka, Dr. A. Baidya, Prof. T. Pradeep
Department of Chemistry,
DST Unit of Nanoscience (DST UNS) and Thematic Unit of Excellence (TUE),
Indian Institute of Technology Madras
Chennai 600036 (India)
E-mail: pradeep@iitm.ac.in
[d] Prof. U. Manna
Centre for Nanotechnology,
Indian Institute of Technology-Guwahati
Kamrup, Assam 781039 (India)
E-mail: umanna@iitg.ac.in

Supporting information for this article is available on the WWW under https://doi.org/10.1002/asia.202100475

facile and scalable chemical reaction at ambient conditions. In the past, some approaches were adopted to develop paper based functional materials – including rewritable and functional chromogenic interfcaes,[28] electrochemical devices for on-site bio-sensing,[29] energy storage devices,[30] combating electromagnetic pollution[31] and so on.

Recently, a few water-repellent papers have been successfully developed through the strategic association of bio-inspired wettability for demonstrating controlled droplet manipulation, microbial resistance, self-cleaning performances etc.[18,32–37] The direct transformation of waste paper into durable and functional materials following a facile and scalable synthesis process is yet to be introduced in the literature.[32–37] For example, Li *et al.* oxidized office paper with sodium chlorite followed by carbonization at 1000 °C under inert atmosphere to develop a compressible carbon aerogel, on which the water droplet beaded with advancing contact angle ~150°.[34] Further, Li *et al.* utilized Fe_3O_4 modified office paper adopting oxidation and pyrolysis method (200–1000 °C) for fabrication of highly salt resistant, electrically conductive carbon aerogel.[36] In another report, Yue *et al.* developed a banana peel/waste paper derived hydrophobic, compressible hybrid aerogel with water contact angle ~149° by adopting the pyrolysis approach (900 °C).[37] Furthermore, the previously reported approaches lacked the ability to tailor the compressive modulus of the synthesized materials, which could prove beneficial for obtaining the ideal substrate for repetitive and prolonged oil/water separation performance of the paper derived materials. Furthermore, some compressible spongy materials with porous network have already been demonstrated for prospective applications as thermal insulators.[38–40] In general, the existing approaches for deriving functional superhydrophobic materials from waste paper primarily depends on the high temperature pyrolysis process,[32–35,39–42] which is an energy consuming, sophisticated approach that leads to secondary pollution. Hence, a facile, economic design for converting waste paper into a chemically 'reactive' sponges with the scope to tailor both the mechanical property and chemistry would provide an avenue for a) develloping eco-friendly/economic thermal insulators, b) prospective use in efficient remediation of oil spillages and c) controlled droplet manipulation.

In this current design, different types of waste papers (i.e. tissue paper, office paper, newspaper, cardboard paper) were *reconstructed into lightweight, porous, highly compressible, covalently cross-linked, chemically 'reactive' sponges with tailorable mechanical property and chemical functionality.* The strategic condensation of the cellulosic hydroxyl groups (of waste paper) with the hydroxyl groups of an amine functionalized binder i.e. 3-(2-aminoethylamino)-propyltrimethoxysilane (AEPTMS) during the sponge fabrication process, provided a facile basis for the catalyst-free 1,4-conjugate cross-linking of the amine functionalized cellulose with dipentaerythritol pentaacrylate (5Acl). This simple cross-linking process induced the desired chemical 'reactivity' in the waste paper derived sponge. After the association of covalent cross-linking process, the residual acrylate groups in the waste paper derived sponge provided a simple basis to tailor the water wettability from hydrophobic, adhesive superhydrophobic to non-adhesive superhydrophobic (~25° to 161°) through association of the desired post covalent modification of the chemically 'reactive' sponge with the appropriate alkylamines following the same 1,4-conjugate addition reaction at ambient conditions. The embedded superhydrophobicity in the waste-paper derived spongy material could sustain various harsh physical abrasions including sand paper abrasion, sand drop test and repetitive manual compression (1000 times) with 60% strain. Moreover, the long term (30 days) exposure to UV radiation and chemically contaminated aqueous phases including extremes of pH (1 and 12), surfactant contaminated water, river and sea water failed to deter the embedded superhydrophobicity of the waste paper derived functional material. Such a durable and highly compressible superhydrophobic sponge was extended to examine its performance or suitability towards practically relevant challenging settings. As a proof of concept of demonstration, selective absorption based repetitive (25 times) cleaning of a wide range of oil/oily contaminants at chemically harsh aqueous settings with high absorption capacities (upto 4000 wt%) has been successfully demonstrated. The analogous waste paper derived membranes were also extended for repetitive (50 times) gravity-driven filtration-based separation of oils from oil/water mixtures even at chemically contaminated aqueous environments without compromising the associated anti-wetting property. Thus, such strategic association of facile and robust chemistries with the valueless waste paper at ambient conditions could be further useful for developing smart bio-interfaces, thermal insulators, open-microfluidic devices etc.

Results and Discussion

Fabrication of Waste Paper Fibers derived Mechanically Durable Sponges

In this report, waste paper has been converted into a functional material with the ability to tailor both the 1) mechanical property and 2) chemistry following a catalyst-free, facile chemical approach. In this context, we have introduced a rational and unique strategy for developing waste paper derived chemically 'reactive' deformable sponges following a facile and environment friendly fabrication procedure. The integration of AEPTMS and 5Acl as the binder and covalent cross-linker, respectively, allowed to 1) modulate the mechanical property and 2) induct chemical reactivity in the waste paper derived material as shown in Scheme 1. Further, the appropriate chemical modification of the waste paper derived chemically 'reactive' sponge with the selected alkylamines following the 1,4-conjugate addition reaction allowed to tailor the water wettability. In the recent past, Baidya *et al.* developed a fluorinated cellulose nanofiber based superhydrophobic coating, where perfluorooctyltriethoxysilane and AEPTMS were covalently integrated with the hydroxyl groups of cellulosic nanofibers.[18] The polymerization of AEPTMS imparted mechanical stability to the silane modified cellulose nanofibers in

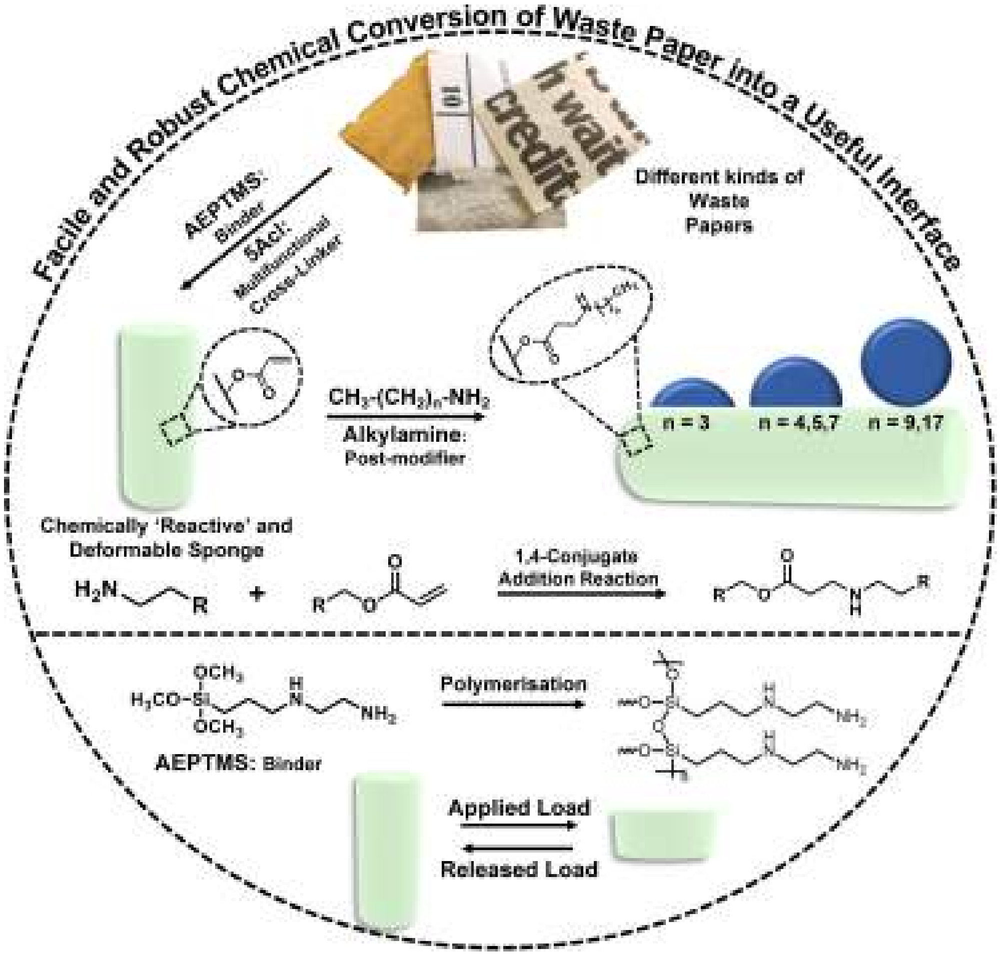

Scheme 1. Schematic illustrating the facile and robust conversion of waste papers into a deformable and chemically 'reactive' sponge. The covalent association of an amine modified silane binder i.e. 3-(2-aminoethylamino)-propyltrimethoxysilane (AEPTMS) with the hydroxyl groups of cellulose (waste paper) during the sponge fabrication process paved an avenue to tailor the mechanical property of the sponge by varying the concentration of the binder used. The catalyst-free 1,4-conjugate addition reaction between the primary amine of the binder with a multi-functional cross-linker provided a facile basis to induce residual chemical 'reactivity' in the waste paper derived sponge. The residual acrylate reactivity was exploited to alter the water wettability of the sponge following the Michael addition reaction between with alkylamines of varying chain lengths.

comparison to the unmodified one. Inspired from this report, in the current study, the association of AEPTMS and chemically 'reactive' cross-linking process with the waste paper allowed to tailor the mechanical property and water wettability respectively, in the waste paper derived sponge denoted as WPDS. Shredded pieces of a model waste paper (i.e. tissue paper) in aqueous media were stirred under room temperature for 6 hours and thereafter, this mixture was poured into cylindrical molds followed by freeze drying to obtain an inherently hydrophilic sponge (beaded water immediately soaked with contact angle of 0°), denoted as WPS$_{\text{control}}$ as shown in Figure 1A, B. WPS$_{\text{control}}$ underwent permanent deformation on application of an external load (500 g) and failed to regain its original shape as shown in Figure 1C, D. FESEM images of WPS$_{\text{control}}$ revealed compact and fibrous domains as shown in Figure 1E, F, the compact network is attributed to the distortion of the skeletal framework of the fragile WPS$_{\text{control}}$ while manual handling. However, the strategic *in situ* association of AEPTMS with this disintegrated waste paper fibers in aqueous media followed by freeze drying yielded a hydrophilic and spongy material that can regain its deformed shape after removal of the external load (500 g) as shown in Figure 1G–J. Thus, the addition of 3.25 wt% AEPTMS w.r.t. 1.96 wt% waste paper denoted as WPDS$_1$ (where 1 denotes the concentration of AEPTMS added, refer to Table S1), resulted in a highly porous interconnected spongy network as shown in Figure 1K, L. Increasing the concentration of AEPTMS further led to change in the morphology and porosity of the as prepared sponges (WPDS$_2$ and WPDS$_3$) as shown in Figure S1A–H and Table S1. This change in morphology is attributed to the polymerization of AEPTMS resulting in a polymeric network. The integration of AEPTMS with the waste paper sponge was validated through XPS analysis as shown in Figure 1M, where the additional peaks corresponding to N and Si were exhibited after AEPTMS modification. De-convoluted XPS for C 1s of waste paper sponge (WPS$_{\text{control}}$) is shown in Figure S2B, where the peaks at 284.5, 286.5 and at 287.6 eV corresponds to C–C, C–O and O–C–O respectively. After the association of AEPTMS, the

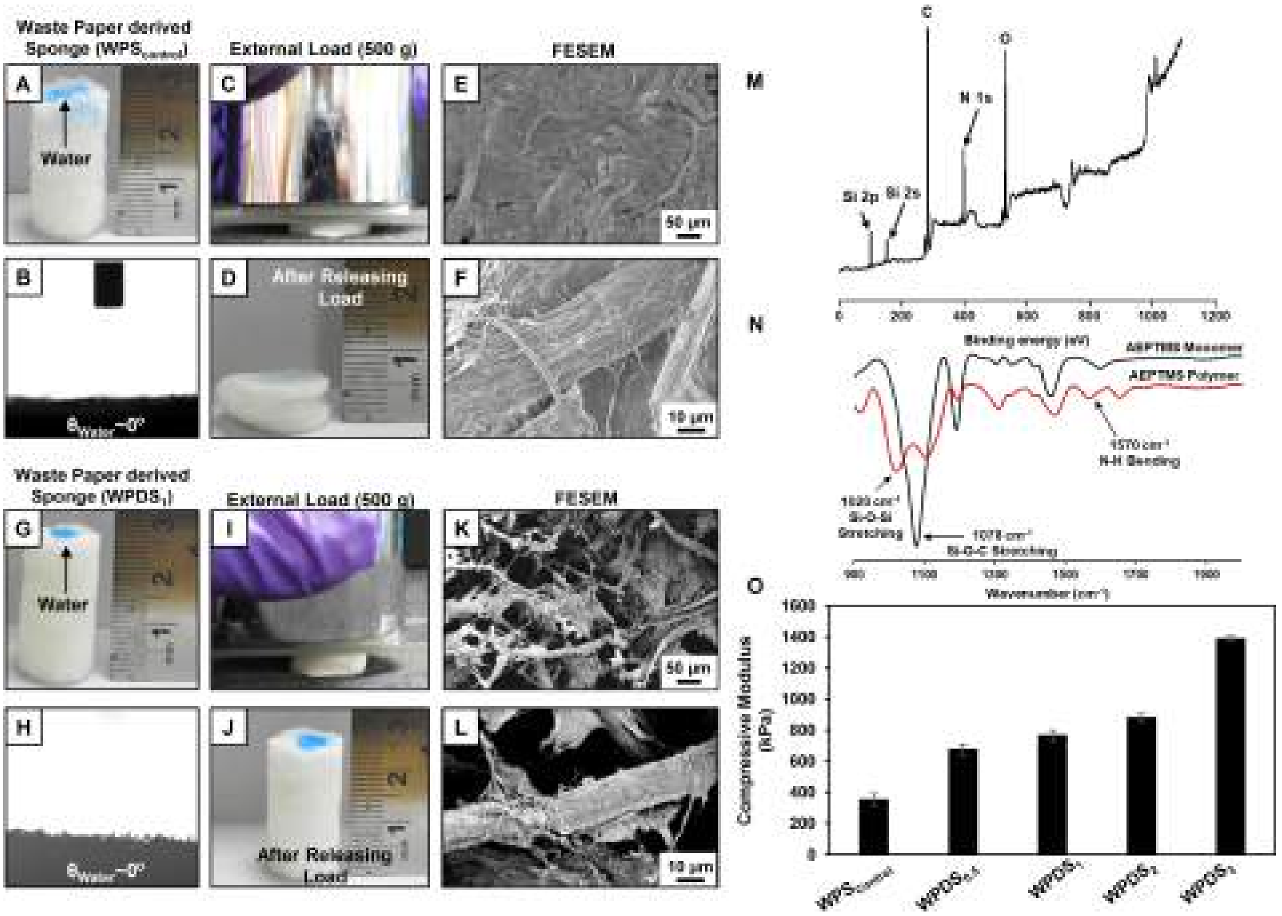

Figure 1. A–D) Digital image (A) and water contact angle image (B) illustrating the hydrophilic waste paper sponge (WPS$_{control}$) that was compressed with an external load of 500 g (C) such that WPS$_{control}$ underwent permanent deformation on releasing the load (D). E, F) FESEM images at low (E) and high (F) magnifications revealing the morphology of WPS$_{control}$. G–L) Digital image (G) and water contact angle image (H) illustrating a waste paper derived sponge that was developed by *in situ* covalent modification of waste paper with an amine modified silane binder (AEPTMS). On compressing the silane modified waste paper derived sponge, (WPDS$_1$ where 1 denotes the concentration of AEPTMS) with an external load of 500 g (I), WPDS$_1$ was capable of completely recovering its dimensions on releasing the load (J), thus, validating the role of AEPTMS in imparting mechanical durability to the sponge. K, L) FESEM images at low (K) and high (L) magnification of the silane modified waste paper derived sponge, WPDS$_1$ revealed the presence of an interconnected fibrous and porous morphology. M) XPS spectra of the AEPTMS modified waste paper sponge, WPDS$_1$ which reveals the presence of N 2p and Si 2s,2p peaks indicating the association of AEPTMS with waste paper. N) ATR-FTIR analysis of AEPTMS monomer exhibits a peak at 1078 cm^{-1} corresponding to the Si-O–C bond of the monomer (black) which depleted entirely and a new peak at 1028 cm^{-1} corresponding to the Si-O–Si bond appeared for the AEPTMS polymer which confirmed the silane polymerization process (red). O) Bar diagram accounting for the varying compressive modulus values of the sponges developed using waste paper doped with different concentrations of the binder.

relative peak intensity corresponding to C–O depleted and slightly shifted (to 286.1 eV) as shown in Figure S2E, which was attributed to the covalent bonding between Si of (AEPTMS) with the hydroxyl groups of cellulose.[18] Further, the polymerization of AEPTMS in aqueous media was confirmed through the standard FTIR analysis. The AEPTMS monomer exhibited the characteristic Si-O–C stretching peak at 1078 cm^{-1}. On polymerization of AEPTMS, the peak at 1078 cm^{-1} diminished and a new peak at 1020 cm^{-1} appeared which corresponds to the Si-O–Si stretching as shown in Figure 1N. Moreover, Energy Dispersive X-ray (EDX) analysis of the sponges confirmed the doping of AEPTMS into the sponges, where the peaks corresponding to N and Si elements were exhibited in addition to the C and O peaks of cellulose as shown in Figure S3A–D. The uniform and varying distribution of C, O, N, Si was confirmed with elemental mapping for all the AEPTMS associated sponges as shown in Figure S4A–T. Hence, EDX analysis confirmed the homogenous integration of AEPTMS with the waste paper mixture, providing a uniform skeletal network of AEPTMS all throughout the sponges. The compressive stress-strain analysis further revealed that AEPTMS modification played the major role in tailoring the compressive modulus of the sponges that were modified with different wt% AEPTMS. The compressive modulus values decrease in the order as $WPDS_3 > WPDS_2 > WPDS_1 > WPDS_{0.5} > WPS_{control}$ as shown in Figure 1O. In-plane compression test was further performed to evaluate the shape recovery of the AEPTMS associated sponge after application of different percentage of external strain. The physically deformed WPDS$_1$, which was subjected to 20%, 40% and 60% compressive strain, recovered its original shape, once the applied load was released as evident from the hysteresis curve as shown in Figure S5B. Moreover, the cyclic compressive study of $WPDS_{0.5}$, $WPDS_1$, $WPDS_2$ and $WPDS_3$ revealed that the as fabricated sponges exhibited satisfactory recovery even after 1000 cycles of compression (Figure S6B–E), except the $WPS_{control}$. A permanent physical deformation was observed for $WPS_{control}$ after the 1st cycle of compression as shown in Figure S6A. Thus, the controlled association of AEPTMS with waste paper allowed to adopt a route for tailorable and durable mechanical property.

Induction of Chemical 'Reactivity' in the Waste Paper Derived Highly Compressible Sponges

The waste paper derived functional substrates developed till date for a wide range of applications are reported in Table 1. However, the reported materials lack the covalent cross-linking network and none of the reported approaches provides an avenue to associate diverse and desired chemical functionalities (Table 1). In this work, the simple and catalyst-free 1,4-conjugate addition reaction between amine and acrylate has been adopted to associate both i) covalent cross-linkage in the sponge and ii) readily 'reactive' residual acrylate groups for post covalent modification with different nucleophiles at ambient conditions.[45,46] The XPS analysis of the deconvoluted N 2p peak (at ~400 eV, Figure 2A) of $WPDS_1$ revealed the presence of primary amine moiety in the paper sponge after addition of binder. The induction of chemical reactivity in the paper sponge was achieved through the reaction of the primary amine groups of the binder with a multifunctional acrylate cross-linker(5Acl) following the catalyst-free 1,4-conjugate addition reaction between amine and acrylate groups at ambient conditions (Scheme 1). The presence of 'reactive' acrylate groups in the waste paper sponge rendered it highly reactive at ambient conditions towards some specific nucleophiles (Figure 2B). The post covalent modification (Figure 2C) of the chemically 'reactive' waste paper sponge with amine containing small molecule, octadecylamine (ODA) transformed the hydrophilic sponge into a superhydrophobic sponge with water contact angle (WCA) ~160° as shown in Figure 2D, E. The successful modification of residual acrylate groups in the amine functionalized waste paper derived sponge was further confirmed through standard FTIR analysis.[43,44] The appearance of the peak at 1408 cm^{-1} and 1730 cm^{-1} corresponding to the C–H stretching of β carbon of the vinyl group and the carbonyl stretching respectively confirmed the presence of the multifunctional acrylate cross-linker, i.e. 5Acl. (Figure 2F, red). These FTIR signatures were not observed in the $WPDS_1$ prior to treatment with 5Acl as shown in Figure 2F (green). Interestingly, after post modification of the chemically 'reactive' waste paper derived sponge with ODA the FTIR peak intensity at 1408 cm^{-1} decreases with respect to the normalized carbonyl peak at 1730 cm^{-1} (which serves as the internal standard) as shown in Figure 2F (black). Hence, the FTIR analysis confirms the successful post modification of the paper sponge with ODA. As shown in Figure S7E, F, 3.25 wt% AEPTMS w.r.t. 1.96 wt% of waste paper (denoted as waste paper derived superhydrophobic sponge, $WPDSHS_1$) is the minimum concentration of AEPTMS required to display superhydrophobicity. However, the waste paper derived chemically 'reactive' sponge with 1.65 wt% AEPTMS (denoted as $WPDSHS_{0.5}$) after post modification displayed only hydrophobicity with water contact angle 144° as shown in Figure S7A, B. The sponges developed with concentrations above 3.25 wt% of AEPTMS (denoted as $WPDSHS_2$ and $WPDSHS_3$) successfully displayed the extreme anti-wetting property with advancing water contact angles above 150° and contact angle hysteresis below 10° as shown in Figure S7I, J, M, N and Table S2. Moreover, the presence of residual chemical reactivity provided a facile basis to tune the wettability from 25° to 161° following the 1,4-conjugate addition reaction of residual acrylates with amine containing lower analogues of ODA as shown in Figure 2G and Figure S8A–V. After the modification of chemically 'reactive' sponge with ODA, non-adhesive superhydrophobicity was noted, where a stream of water readily bounced off from the surface of $WPDSHS_1$ as shown in Figure 2H and Movie 1. Moreover, on submerging $WPDSHS_1$ underwater, a shiny interface was observed which confirms the presence of a metastable trapped air layer that is responsible for the existence of heterogeneous wettability as shown in Figure 2I. The waste paper derived superhydrophobic sponge displayed contrasting water and oil wettability, wherein the oil droplet was soaked immediately with oil contact angle 0° as shown in Figure 2J, K. Such contrast in liquid wettability is beneficial for remediation of oil spillages following both selective absorption and filtration processes. Moreover, the post treatment with 5Acl and ODA did not alter the mechanical durability as confirmed from the compressive modulus of the sponge before and after post chemical modification as shown in Figure S9A (black line), thus, re-assuring that AEPTMS is responsible for the enhanced mechanical durability of the sponges. Moreover, the porosity remained unaltered after post covalent modification as shown in Figure S9A (red line).

Irrespective of the type of waste paper, this facile fabrication procedure could be further extended for developing compressible superhydrophobic sponges using different types of waste papers, including office paper (A4 paper), newspaper and cardboard paper as shown in Figure 3A, F and Table S3. The water droplets beaded with contact angles above 150° and contact angle hysteresis below 10°. Even the mixture (1:1:1:1 weight ratio) of all the different types of waste papers (tissue paper, cardboard, newspaper and office paper) remained efficient to provide a superhydrophobic spongy material as shown in Figure 3G, H and Table S3. The compressive modulus of the synthesized superhydrophobic sponges varied based on the nature of the waste paper even though the silanization and post-covalent modification process remains unchanged. Interestingly, the compressive modulus was noticed to be maximum (1285 kPa) for the spongy material that was prepared using the mixture of waste papers. Moreover, the porosity of the different sponges decreased in the order as i.e. newspaper > office paper > cardboard paper > mixture of papers. The order of porosity and compressive modulus followed a completely opposite order as shown in Figure 3I since increased porosity reduces the cross-sectional area for stress tolerance. The maximum compressive modulus (1285 kPa) and minimum

Table 1. Illustrating the utilization of waste paper as the major constituent or substrate for remoulding into various functional material following various chemical approaches for different relevant applications. The embedded physical properties and the associated durability of the functional substrates has also been compared in the table.

Components Used	Chemistries Involved/Reaction Conditions	Major Physical Properties	Physical Durability	Chemical Durability	Applications	Ref.
Filter Paper	Electrochemical device assimilated on paper used as substrate	Electrical Conductivity	Not Performed	Not Performed	Biosensing	[27]]
Newspaper, Office Paper, Cardboard Paper, Glossy Brochure Paper	Metallic resonator pattern drawn using silver ink on the paper substrates	Electromagnetic shielding	Not Performed	Not Performed	Electromagnetic Pollution	[29]
Cellulose Filter Papers	Condensation of hydroxyl groups with fluorinated silane O_2 plasma etching/Heating (50 °C–120 °C)	Extremes of Liquid Wettability	Not Performed	Not Performed	Microfluidic Devices	[30]
Office Paper	Used as substrate without any modification	Extremes of Liquid Wettability	Not Performed	Performed only at various pH	Oil/Water Separation	[31]
Office Paper, Cardboard Paper, Newspaper	Acidic Oxidation Carbonization (at 1000 °C in N_2 atmosphere)	Extreme Water Wettability	Not Performed	Not Performed	Oil/Water Separation	[32]
Office Paper	Carbonization (at 1000 °C in N_2 atmosphere)	Electrical Conductivity, Extreme Water Wettability	Not Performed	Not Performed	Electrocatalyst Oil/Water Separation	[33]
Office Paper	Carbonization (200–1000 °C in N_2 atmosphere) O_2 Plasma	Electrical Conductivity, Magnetic, Janus Water Wettability	Not Performed	Performed only at saline conditions	Heavy metal ions, soluble organics and Oil/Water Separation	[34]
Office Paper/Banana Peel	Carbonization (at 900 °C in N_2 atmosphere)	Extreme Water Wettability	Not Performed	Performed (24 hours exposure to acidic and basic pH, salt water, river water and organic solvents	Oil/Water Separation	[35]
Office Paper	Heating (50–90 °C)	Extremes of Liquid Wettability, Photochromism	Not Performed	Not Performed	Photochromism	[39]
Waste Paper	Carbonization (at 1000 °C in N_2 atmosphere)	Electrical Conductivity Thermal Conductivity	Not Performed	Not Performed	Wearable Device	[40]
Office Paper	Hydrothermal Processing (180 °C) Carbonization (800 °C)	Electrical Conductivity	Not Performed	Not Performed	Ultracapacitor Electrodes	[41]
Office Paper	Draining, Pressing and Drying	Electrical Conductivity	Not Performed	Not Performed	Strain Sensor	[42]
Waste Paper (Tissue Paper, Office Paper, Cardboard paper and Newspaper)	1,4-Conjugate Addition Reaction	Tailorable Water Wettability and Compressive Modulus	Performed (Sand paper abrasion, sand drop test, load compression and manual squeezing)	Performed (30 days exposure to acidic and basic pH, surfactants, sea water, river water, organic solvents and UV radiation)	Oil/Water Separation	Current Work

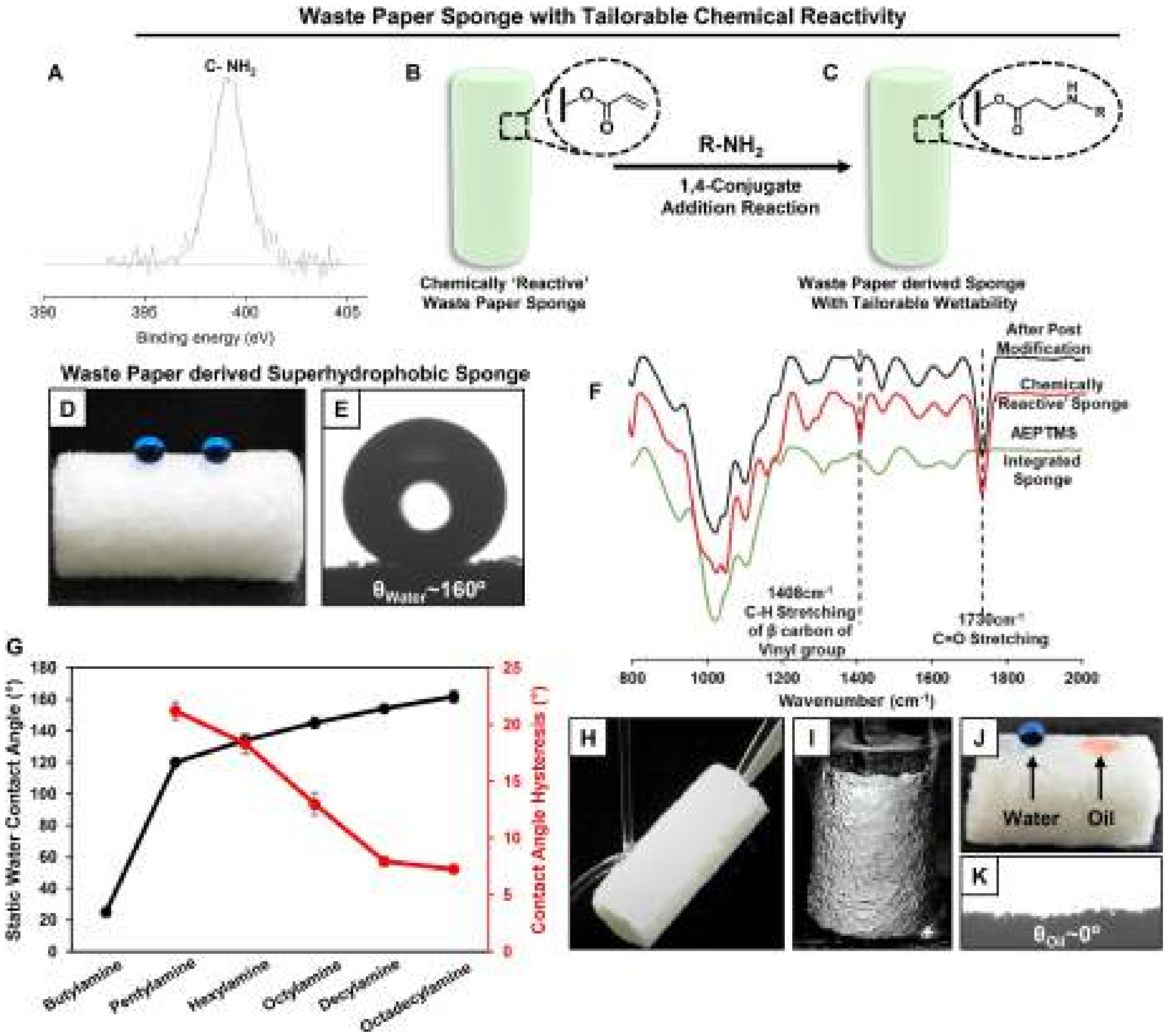

Figure 2. A) De-convulated XPS spectra of N 2p of the waste paper derived sponge that was covalently associated with AEPTMS. The peak at 400 eV indicates the presence of primary amines in the fabricated sponge owing to the presence of AEPTMS. B, C) Schematic illustrating the 1,4-conjugate addition reaction of the chemically 'reactive' waste paper derived sponge with amine containing small molecules that provides an avenue to tailor the water wettability of the sponge. D, E) Digital image (D) and water contact angle image (E) of the beaded water droplet on the waste paper derived sponge, WPDSHS$_1$ that was post modified with octadecylamine (ODA). F) ATR-FTIR analysis of the chemically 'reactive' waste paper derived sponge (red) revealed the presence of peaks at 1408 cm^{-1} and 1730 cm^{-1} which corresponds to the symmetric deformation of the C–H bond of β carbon of the vinyl group and carbonyl stretching frequency respectively. However, the AEPTMS modified waste paper derived sponge (WPDS$_1$) did not exhibit the mentioned peaks (green). The reduction in the peak intensity at 1408 cm^{-1} with respect to the normalized carbonyl peak at 1730 cm^{-1} confirmed the covalent linkage of the residual acrylate functionalities with the amine containing small molecule i. e. octadecylamine (black). G) Bar diagram representing the static water contact angles (black) and contact angle hysteresis (red) of the beaded water droplet on the waste paper derived sponge that was modified with different amine containing small molecules including butylamine, pentylamine, hexylamine, octylamine, decylamine and octadecylamine. H) Digital image demonstrating the bouncing of a stream of water from the surface of the waste paper derived superhydrophobic sponge, WPDSHS$_1$. I) The waste paper derived superhydrophobic sponge, WPDSHS$_1$ displayed a shiny interface on submerging under water which confirms the presence of a metastable air layer that confers the heterogeneous water wettability. J, K) Digital image (J) and oil contact angle image (K) displaying the presence of contrasting oil and water wettability, where the water droplet is extremely repelled by the waste paper derived superhydrophobic sponge, WPDSHS$_1$ while the oil droplet is immediately soaked.

porosity (85%) was observed for the sponge derived from the mixture of different papers as shown in Figure 3I.

Examining the Physical and Chemical Durability of the Embedded Water Repellence

The sustainability of the waste paper derived superhydrophobic sponges at severe challenging physical and chemical environments is of utmost importance for real life applicability. WPDSHS$_1$ with a) 3.25 wt% of AEPTMS, which was the minimum concentration required to exhibit superhydrophobic property

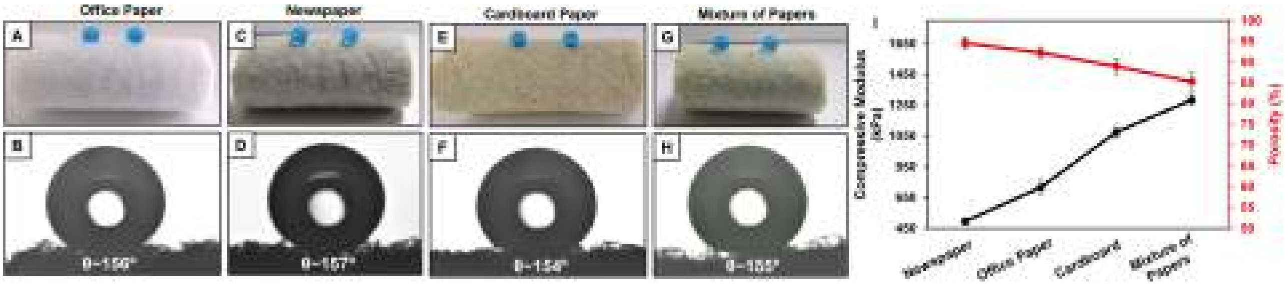

Figure 3. A–H) Digital images (A,C,E,G) and water contact angle images (B,D,F,H) of superhydrophobic sponges that were developed using different types of waste paper i.e. office paper (A,B), newspaper (C,D), cardboard paper (E,F) and a mixture of the mentioned papers (G,H). I) Plot illustrating the compressive modulus (black) and porosity (red) of the different types of waste paper derived superhydrophobic sponges.

and b) the least compressive modulus (and thus, enhanced compressibility) was chosen to investigate the durability of its water repellence behavior. To examine the impact of physical deformation on the embedded water wettability of the waste paper derived sponge, $WPDSHS_1$ gradually increasing manual compressive strain was applied on the as fabricated superhydrophobic sponge. Exposure to 60% compressive strain followed by release of the strain revealed that the sponge recovered to its original shape without perturbing the embedded extreme water repellence behavior as shown in Figure 4A. Further, imposing repetitive compressive strain using an external load of 500 g for 1000 consecutive cycles failed to perturb the embedded anti-wetting property in the sponge ($WPDSHS_1$) with advancing contact angles above 150° and contact angle hysteresises below 10° as shown in Figure 4B. Moreover, the anti-wetting property is not just limited to the surface of the sponge but was exhibited by the bulk of the prepared sponge as well as shown in Figure 4C, D, where $WPDSHS_1$ (inset image) was arbitrarily sliced into pieces to randomly expose the interior of the sponge. The freshly exposed interiors of the waste paper derived superhydrophobic sponge continued to repel the beaded water with contact angles above 155°. Next, a standard and widely accepted abrasive test, i.e., sand paper abrasion was performed on the waste paper derived superhydrophobic material (Figure 4E). An abrasive sand paper was rubbed with an applied load of 500 g in back and forth direction multiple times (Figure 4F) on $WPDSHS_1$. Although the physical integrity of the sponge was compromised (Figure 4G), the embedded water repellence on the physically abraded interface remained intact with advancing contact angle ~155° and contact angle hysteresis ~8° as shown in Figure 3G, H. Furthermore, 150 g of sand grains were poured onto the surface of $WPDSHS_1$ (tilted at 45°) from a height of 25 cm. The sand grains exposed interface of $WPDSHS_1$ displayed extreme water repellence with water contact angle ~157° and contact angle hysteresis ~6° as shown in Figure S10A–C. In addition to various severe physical abrasions, chemical durability is also vital for practical applications. In that context, $WPDSHS_1$ was exposed to severe harsh and practically relevant complex aqueous media including acidic water (pH 1), basic water (pH 12), surfactant water (SDS, DTAB), river water and seawater for a prolonged duration (30 days). The anti-wetting property was examined at regular intervals, it was concluded that the embedded bio-inspired water-repellent property remained intact with advancing water contact angle above 150° and contact angle hysteresis below 10° as shown in Figure 4I. Moreover, the prolonged (30 days) exposure to both short (254 nm) and long (365 nm) UV radiation failed to perturb the embedded water repellence, which is evident with advancing contact angle greater than 150° and contact angle hysteresis below 10° as shown in Figure S10D. Furthermore, $WPDSHS_1$ was exposed to various polar and non-polar organic solvents for 30 days, however, the embedded water repellence remained unaltered as shown in Figure S11. Hence, the abundant and valueless waste paper was successfully reconstructed into a highly compressible superhydrophobic spongy material with extremely durable embedded water repellence property – that would be sustainable for performance at harsh and hostile practical settings.

Absorption based Oil/Water Separation Performance at Challenging Environments

In the past, a few approaches were introduced to convert the valueless and highly abundant waste paper into functional materials for various applications as included in Table 1. However, most of the earlier approaches failed to demonstrate the physical and chemical durability of the waste paper derived functional materials. Some of the waste paper derived bio-inspired materials that were prepared following the carbonization process at very high temperatures were successfully extended to demonstrate the oil/water separation, however, tolerance of such materials at harsh physical and chemical settings was not examined as noted in Table 1. In contrast to the earlier reports, the current design allowed to convert waste paper into a durable superhydrophobic spongy material as discussed above. The highly compressible waste paper derived sponge with an interconnected porous network exhibited high porosity (above 95%, Figure S9A) and the presence of contrasting water/oil wettability was exploited to demonstrate the energy efficient and environment friendly separation of oil/oily contaminants from the aqueous phase.[46,47] The embedded superhydrophobicity allowed the selective infiltration of the oil phase, while higher porosity facilitated the absorption and gravity-driven filtration of the oil/oily phases. The oil absorption

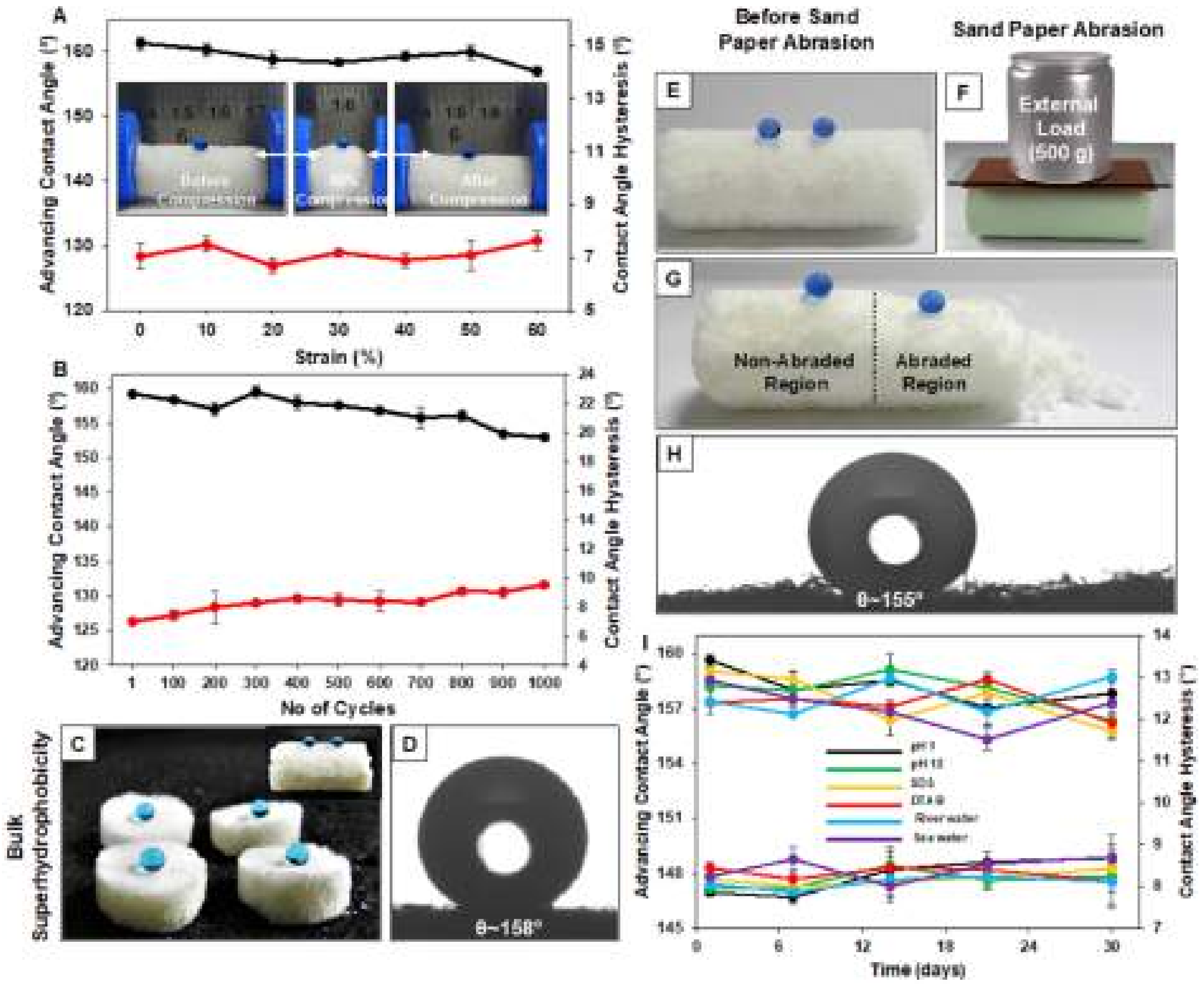

Figure 4. A) Plot accounting for the advancing contact angle (black) and contact angle hysteresis (red) of the beaded water droplet on the waste paper derived superhydrophobic sponge, $WPDSHS_1$ that was subjected to 60% manual compression. The inset images further exhibit that the embedded water repellence behaviour remains intact before (left), during (middle) and after (right) compression. B) Plot representing the advancing contact angle (black) and contact angle hysteresis (red) of the beaded water droplet on the waste paper derived superhydrophobic sponge, $WPDSHS_1$ that was repetitively deformed for 1000 cycles under 60% manual compression. C, D) Digital image (C) and contact angle image (D) of the waste paper derived superhydrophobic sponge, $WPDSHS_1$ (inset image) that was arbitrarily sliced into pieces to investigate the presence of bulk superhydrophobic property. E–H) Digital images illustrating the rubbing of a sand paper on the surface of the waste paper derived superhydrophobic sponge, $WPDSHS_1$ with a 500 g load on top (F). The freshly exposed interior of the superhydrophobic sponge continued to display unperturbed water repellence behaviour (G, H). I) Plot accounting for the advancing contact angle and contact angle hysteresis of the beaded water droplet on the waste paper derived superhydrophobic sponge, $WPDSHS_1$ that was exposed to chemically contaminated, harsh aqueous phases including pH 1 (black), pH 12 (green), SDS (yellow), DTAB (red), river water (blue), artificial sea water (violet) for 30 days.

capacities were calculated for all the waste paper derived superhydrophobic sponges ($WPDSHS_1$, $WPDSHS_2$, $WPDSHS_3$) having different porosities using the formula given below,

$$Q = \frac{M_2 - M_1}{M_1}$$

where, M_1 and M_2 is the weight of the sponge before and after oil absorption. Irrespective of the density and viscosity of the used oil/oily phases, the oil absorption capacity of $WPDSHS_1$ was found to be maximum (up to 3960 wt%) in comparison to both $WPDSHS_2$ and $WPDSHS_3$ as shown in Figure 5A. The gradual increment of AEPTMS amount in the waste paper derived superhydrophobic sponges elevated the density of the prepared sponges as noted in Table S2. The density of $WPDSHS_1$ was found to be minimum ~0.017 g/cm^3, whereas the other superhydrophobic sponges had higher density. The association of high compressibility, which allows easy compressive deformation is appropriate for repetitive absorption/desorption of oil/oily phase without compromising the physical integrity. Compressive modulus and cyclic compressibility analysis revealed that $WPDSHS_1$ is the most compressible variant with unperturbed embedded water repellence even after 1000 cycles of compression (as shown in Figure 4B). Therefore, the highly porous, durable and compressible $WPDSHS_1$ proved to be the ideal candidate for repetitive collection of the oil phase

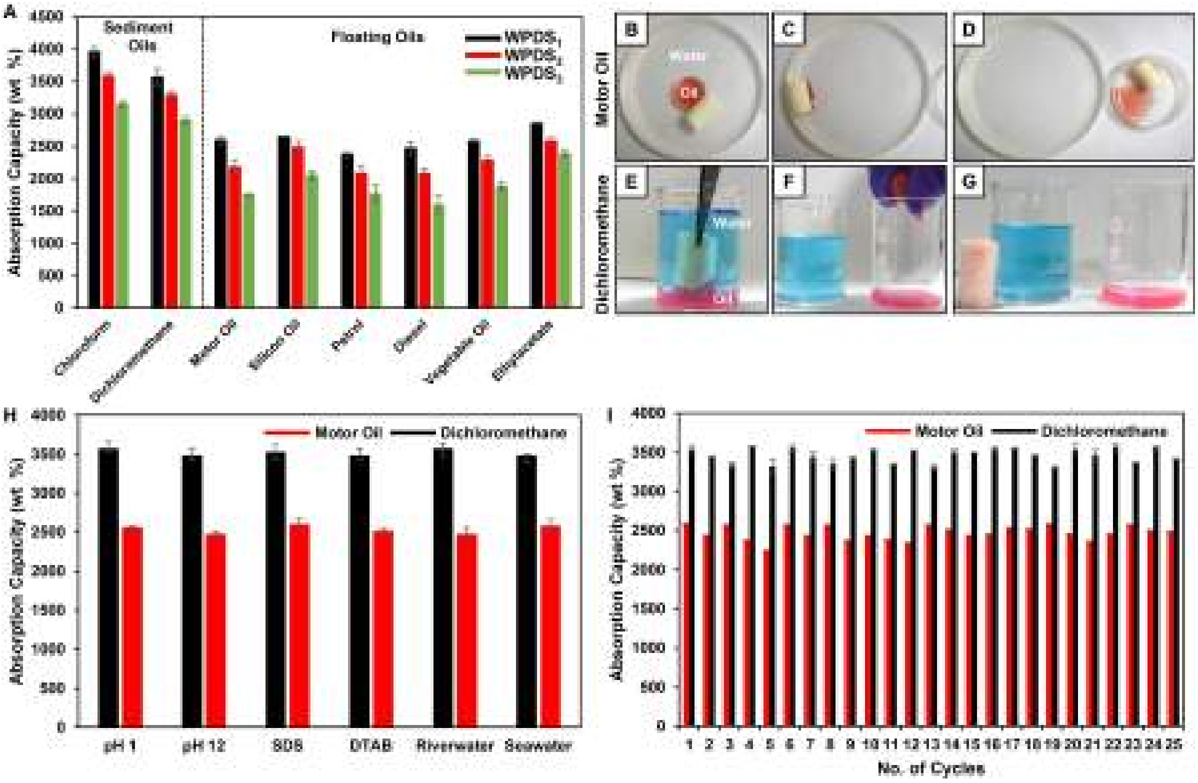

Figure 5. A) Plot accounting for the oil absorption capacities of the different waste paper derived compressible, superhydrophobic sponges i.e. WPDSHS$_1$, WPDSHS$_2$, WPDSHS$_3$ for a wide range of oils with varying densities and viscosities. B–G) Digital images illustrating the absorption based selective oil absorption of light oil i.e. motor oil (B–D) and model heavy oil i.e. dichloromethane (E–G) by the waste paper derived compressible, superhydrophobic sponge, WPDSHS$_1$ from an oil/water interface, such that the absorbed oil can be re-collected by manually squeezing the sponge (D,G). H) Plot illustrating the selective oil absorption capacity of WPDSHS$_1$ for both light (red) and heavy (black) oils at practically relevant settings where the water phase was chemically contaminated with acid, base, surfactants, salt etc. I) Plot illustrating the repetitive oil absorption capacity of WPDSHS$_1$ upto 25 cycles for both light (red) and heavy (black) oils.

selectively from the water phase with a high oil absorption capacity.

First, floating oil i.e. motor oil was placed in a petri-dish filled with water and subsequently, WPDSHS$_1$ was placed at the oil/water interface such that it rapidly and selectively absorbed only the oil phase while repelling the water phase as shown in Figure 5B–D and Movie 2. The absorbed oil was collected by manual squeezing of the sponge as shown in Figure 5D. Furthermore, the same sponge was extended for selective removal of various other floating oils including silicone oil, petrol, diesel, vegetable oil as shown in Figure S12A–P. Moreover, WPDSHS$_1$ was also extended for selective collection of model sediment oil i.e. dichloromethane (DCM; dyed pink for visual inspection) as shown in Figure 5E–G and Movie 3. The absorbed oil was collected, and no trace of water was observed even though the sponge was first in contact with the aqueous phase prior to absorption of the model heavy oil phase as shown in Figure 5G. The oil absorption capacity of WPDSHS$_1$ was further calculated for motor oil and dichloromethane in chemically harsh aqueous environments including acidic water (pH 1), basic water (pH 12), surfactant contaminated water (SDS, DTAB), river water and seawater. Remarkably, the oil absorption capacity remained unperturbed (i.e. ~2500 wt% for motor oil and ~3500 wt% for DCM) even at such extreme environments as shown in Figure 5H. Recyclability of the oil absorbents is an essential factor for real-life practical applications. The repetitive absorption-desorption ability of WPDSHS$_1$ was examined with motor oil and DCM for 25 cycles and it was observed that the oil absorption capacities remained unaltered as shown in Figure 5I. The extreme water repellence was examined after every 5 cycles of absorption-desorption for both floating and sediment oils and it was found that the anti-wetting property remained intact for both the oils with advancing water contact angle above 150° and contact angle hysteresis below 10° as shown in Figure S13A.

Gravity-driven filtration-based oil/water separation

Furthermore, this design provided a single strategy to fabricate waste paper derived superhydrophobic membranes of varying tensile strengths with analogous compositions to that of the sponges. The waste paper derived superhydrophobic membranes (WPDSHM$_1$, WPDSHM$_2$, WPDSHM$_3$) with varying compositions of AEPTMS displayed bio-mimicked extreme water repellence with advancing contact angle above 150° and contact angle hysteresis below 10° as shown in Figure S14A–F and Table S4. The tensile strength of the membranes revealed that the increase in AEPTMS content led to an increase in the tensile modulus in the order WPDSHM$_3$ > WPDSHM$_2$ > WPDSHM$_1$ as shown in Figure S14G,H. To maximize the utilization of the current design, the waste paper derived superhydrophobic membranes were extended for gravity-driven filtration-based oil/water separation. All three superhydrophobic membranes (WPDSHM$_1$, WPDSHM$_2$, WPDSHM$_3$), were individually tied to the open end of a lab made prototype to demonstrate the gravity driven selective filtration of oil/oily phase from oil/water mixture as shown in Figure 6A. Firstly, model sediment oil i.e. dichloromethane (dyed pink for visual inspection)/water (dyed blue for visual inspection) mixture was poured through the funnel at the opposite end of the tube. The oil phase selectively permeated through the WPDSHM$_1$ while the water phase remained suspended and restricted by the superhydrophobic membrane as shown in Figure 6A–C and Movie 4. Furthermore, the same approach was extended for separation of floating oil i.e. kerosene/water (dyed red for visual inspection) mixture where the oil phase selectively permeated through the membrane as shown in Figure 6D–F and Movie 5. This energy efficient separation technique was also used for separation of other floating oil/water mixtures including petrol and diesel (Figure S15A–H). The oil separation efficiency of WPDSHM$_1$ was calculated for a wide range of oils including petrol, diesel, kerosene, dichloromethane and chloroform using the formula given below,

$$\eta = (Vr/Vi) \times 100$$

where, Vr and Vi is the volume of the oil before and after separation. The oil separation efficiency remained above 97% irrespective of the densities of the oils used as shown in Figure 6G. Other membranes (WPDSHM$_2$ & WPDSHM$_3$) were also efficient for selective filtration of the oil phase but the flux of the selectively filtrated oil/oily phases was low in comparison to WPDSHM$_1$ (~25000 Lm^{-2}h^{-1} for dichloromethane and ~13500 Lm^{-2}h^{-1} for kerosene). The porosity of the superhydrophobic membranes which decreased (from ~99% to ~96%) in the order: WPDSHM$_1$ > WPDSHM$_2$ > WPDSHM$_3$ as tabulated in Table S4 affected the rate of flux of the oils. For a given oil/oily phase, the flux for the filtrated oil phase decreased in the similar order as that of porosity i.e. WPDSHM$_1$ >

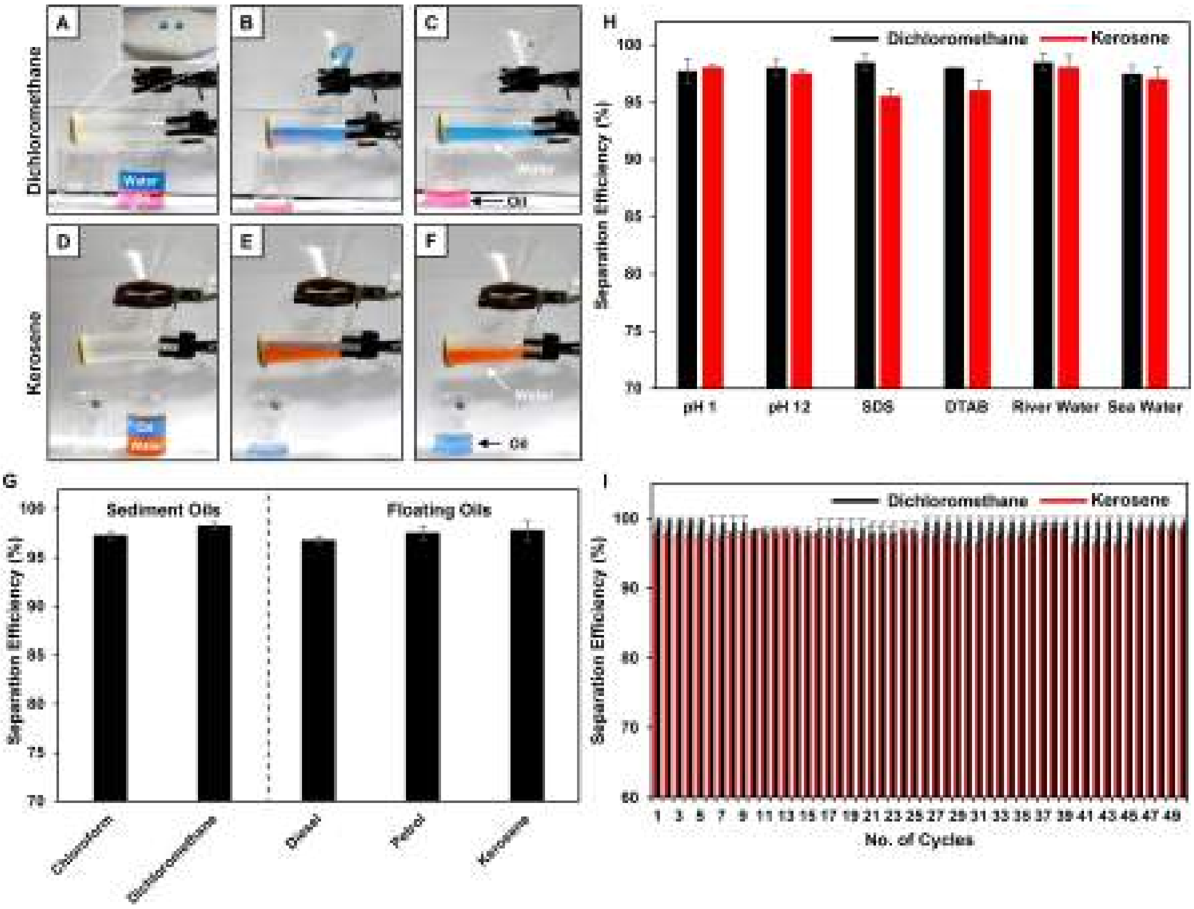

Figure 6. A–F) Digital images illustrating the gravity-driven filtration based selective passage of model sediment oil phase i.e. dichloromethane (A–C) and light oil i.e. kerosene (D–F) from an oil/water mixture through the waste paper derived superhydrophobic membrane, WPDSHM$_1$ (inset image in A). The water phase remained restricted by the extreme water-repellent membrane. G) Plot illustrating the oil separation efficiency of WPDSHM$_1$ for a wide range of oils with varying densities. H) Plot depicting the oil separation efficiency of WPDSHM$_1$ for both light (red) and heavy (black) oils at practically relevant settings where the water phase was chemically contaminated with acid, base, surfactants, salt etc. I) Plot illustrating the repetitive oil separation efficiency of WPDSHM$_1$ upto 50 cycles for both light (red) and heavy (black) oils.

$WPDSHM_2 > WPDSHM_3$ as shown in Figure S16A. Thus, $WPDSHM_1$ emerged as the best candidate for gravity-driven filtration of oil/oily phase from an oil/water mixture. Moreover, the separation efficiency was calculated at extremes of harsh aqueous media including acidic water (pH 1), basic water (pH 12), surfactant contaminated water (SDS, DTAB), river water and seawater for oil/water mixtures using both heavy (i.e. dichloromethane) and light (i.e. kerosene) oils as shown in Figure 6H, Figure S17A–L, Figure S18A–L. The oil/water separation performance remained merely perturbed even at severe settings (Figure 6H). The recycling ability of the membrane was also examined for 50 cycles of separation for both sediment (dichloromethane) and floating (kerosene) oils and the oil separation efficiency remained above 95% for 50 consecutive cycles as shown in Figure 6I. Moreover, the embedded water repellence of the membrane was examined after every 5 cycles of separation for both dichloromethane and kerosene and the anti-wetting property remained intact with advancing contact angle above 150° and contact angle hysteresis below 10° as shown in Figure S19A. Thus, such a robust and highly durable substrate involves facile fabrication and impeccable recyclability can be applied extensively for applications at practical context.

Conclusion

Here, we have reported the unconventional restructuring of discarded and valueless waste paper into a highly porous, compressible and chemically 'reactive' sponge embedded with extreme water repellence behavior. The varying concentration of the covalently integrated amine functionalized silane binder with the waste paper provided a basis to tailor the mechanical property. Further, the catalyst-free 1,4-conjugate addition reaction at ambient conditions between the labile amines of the selected binder and a multi-functional acrylate cross-linker allowed to induce chemical 'reactivity' in the waste paper derived sponge. The strategic post covalent modification of the residual acrylate functionalities in the waste paper derived sponge was extended to tailor the water wettability from hydrophobic to 3D-superhydrophobic. The as developed waste paper based superhydrophobic sponges could sustain repetitive compression (60% compressive strain) for 1000 cycles, severe physical abrasions including sand paper abrasion, sand drop test, prolonged (30 days) exposure to harsh chemical aqueous conditions including extremes of pH (1, 12), surfactant contamination (SDS, DTAB), river water, seawater and UV irradiation for 30 days without compromising the embedded anti-wetting property. These highly compressible, physically and chemically durable waste paper derived sponges were successfully extended for repetitive (25 times) absorption-based separation of viscous oils from the aqueous phase without compromising the embedded water repellence and physical integrity even at chemically harsh aqueous settings. Furthermore, the waste paper derived membranes were utilized for repetitive (50 times) gravity-driven filtration-based oil/water remediation at chemically harsh aqueous settings without compromising the embedded lotus-leaf inspired anti-wetting property. Such an approach of converting waste paper into functional materials could be further useful for developing various other functional interfaces.

Experimental Section

Materials: Dipentaerythritol penta-acrylate (5Acl, MW ~ 524.21 g/mol), silicone oil (CAS No. 63148-58-3), methylene blue (CAS No. 122965-43-9), rhodamine 6G (CAS No. 989-38-8), Nile red (CAS No. 7385-67-3), octadecylamine, decylamine, octylamine, hexylamine, pentylamine, butylamine, 3-(2-aminoethylamino)-propyltrimethoxysilane (CAS No. 1760-24-3), sodium dodecyl sulfate (SDS), dodecyl trimethyl ammonium chloride (DTAB) were obtained from Sigma-Aldrich (Bangalore, India). Chloroform, tetrahydrofuran, dichloromethane was procured from FINAR. Ethyl acetate was procured from RANKEM (Maharashtra, India). Sodium chloride, magnesium chloride, calcium chloride, magnesium sulphate, and sodium hydroxide were purchased from Merck Specialties Private Limited. Hydrochloric acid was purchased from Fischer Scientific (Hyderabad, India). Ethanol was purchased from Changshu Hongsheng Fine Chemical Co. Ltd. Adhesive tape, calibration weights, vegetable oil, tissue paper, sand paper were purchased from Amazon, India. Motor Oil (Castrol GTX 20 W-50), kerosene oil, petrol and diesel were purchased from Indian Oil petrol pump. Newspaper, cardboard paper, office paper was purchased from a local store in IIT Guwahati. Sand grains were collected from a construction site at IIT Guwahati and rinsed with water, dried prior to use. River water was procured from Brahmaputra River, Guwahati (Assam, India).

General Considerations: All the glass wares were washed with acetone prior to use. Contact angle measurements were carried out using a KRUSS Drop Shape Analyzer-DSA25 with an automatic liquid dispenser at ambient conditions. The contact angles were measured using 5 μl water droplet at three different locations for each sample. Labconco Freezone Freeze Dryer was used for lyophilization of the sponges. Scanning electron microscope images were acquired using the Sigma Carl Zeiss scanning electron microscope. The samples were sputtered with gold prior to imaging. ATR-FTIR spectra was recorded using the Perkin Elmer instrument at ambient conditions. To identify the chemical oxidation states of the elements, XPS was performed by using an ESCA probe TPD spectrometer, Omicron Nanotechnology with a polychromatic Al Kα (hν = 1486.6 eV) X-ray source with a step size of 0.1 eV per second. The binding energy (B.E) of all the elements was calibrated with respect to C 1s (284.8 eV). Compressive and tensile measurements were carried out using a 5 kN electromechanical Universal Testing Machine. Digital images were acquired using a Canon Power shot SX420 IS digital camera. Milli-Q grade water was used for all experiments.

The porosity measurements were calculated using the widely adapted standard formula,

$$\mathit{Porosity}\ (\%) = \left(1 - \frac{\rho}{\rho s}\right) \times 100$$

Where, ρ and ρ_s is the volumetric mass density of the porous sponge and solid sponge respectively.[49,50]

Fabrication of chemically 'reactive' waste paper derived sponges followed by post covalent chemical modification: To fabricate the waste-paper derived sponges, 1.96 wt% of waste paper was shredded into pieces and dispersed in 30 mL of water under constant stirring for 1 hour followed by addition of 3-(2-aminoethylamino)-propyltrimethoxysilane (AEPTMS) in desired amounts (1.65 wt%, 3.25 wt%, 4.79 wt%, 6.29 wt%) which are denoted as $WPDS_{0.5}$, $WPDS_1$, $WPDS_2$, $WPDS_3$ respectively. Here, tissue paper was selected as the model waste paper for performing all the experiments. The AEPTMS added waste paper mixture was kept under continuous stirring at room temperature for 6 hours to ensure uniform mixing. Thereafter, the mixture was poured into cylindrical molds and glass petri-dish for fabricating the sponges and membranes respectively. The molds were frozen in liquid N_2 and subsequently, lyophilized at −101 °C for 36 hours. Afterwards, the dried sponges/membranes were further treated with an ethanolic solution of dipentaerythritol penta-acrylate (1.325 g 5Acl in 10 mL ethanol) for 3 hours followed by thorough washing in ethanol for 15 mins and THF each. Thereafter, the sponges were subjected to post covalent modification with amine containing small molecules i.e. butylamine (30 mg/mL), pentylamine (30 mg/mL), hexylamine (30 mg/mL), octylamine (30 mg/mL), decylamine (30 mg/mL) and octadecylamine (5 mg/mL) for 12 hours. Then, the samples were thoroughly washed with THF and subsequently dried at ambient conditions.

Physical and Chemical Durability Tests: To examine the durability of the embedded anti-wetting property of the waste paper derived superhydrophobic sponges, various harsh physical and chemical challenges were imposed as described in detail below.

Sand Paper Abrasion: In this test, the waste paper derived compressible, superhydrophobic sponge, $WPDSHS_1$ (length ~5 cm) was rubbed manually with a sand paper for 20 times back and forth with a 500 g load on top to inflict severe damage to the sponge. Thereafter, the embedded anti-wetting property on the freshly exposed interior of the sponge was examined through contact angle measurements and digital images.

Bulk Superhydrophobicity: The presence of three-dimensional water wettability in the waste paper derived sponge ($WPDSHS_1$) was examined by arbitrarily slicing the sponge into pieces to expose the interiors. Subsequently, the anti-wetting property was examined using contact angle measurements.

Sand Drop Test: In this test, 150 g of sand grains were poured from a height of 25 cm on the waste paper derived superhydrophobic sponge, $WPDSHS_1$ (length ~4 cm) which was pre-tilted at 45°. Thereafter, the embedded anti-wetting property was examined on the abraded surface of the sponge using contact angle measurements and digital images.

UV Irradiation: The waste paper derived compressible superhydrophobic sponge, $WPDSHS_1$ was subjected to both short (254 nm) and long (365 nm) UV irradiation for 30 days. The embedded water-repellent property was examined at regular intervals through contact angle measurements and digital images.

Chemical Durability: The waste paper derived superhydrophobic sponge, $WPDSHS_1$ was exposed to various harsh chemically complex aqueous phases including acidic water (pH 1), basic water (pH 12), surfactant contaminated water (SDS, 1 mM and DTAB, 1 mM), river water (Brahmaputra River, Assam, India) and artificial seawater. Artificial seawater was prepared by mixing $MgCl_2$ (0.226 g), $MgSO_4$ (0.325 g), NaCl (2.673 g) and $CaCl_2$ (0.112 g) in 100 mL of de-ionized water in a volumetric flask. Similarly, the waste paper derived superhydrophobic sponge, $WPDSHS_1$ was exposed to various polar and non-polar organic solvents including methanol, ethanol, tetrahydrofuran, dimethyl sulfoxide, acetone, chloroform, hexane, dichloromethane for 30 days and subsequently, the embedded water repellence was examined at regular intervals through contact angle measurements.

Absorption Based Oil/Water Separation: The waste paper derived compressible superhydrophobic sponges were exploited successfully for absorption-based collection of oils of varying densities and viscosities from an oil/water interface. Briefly, 1 mL of the oil (dyed with Nile red for petrol, diesel, silicone and vegetable oil for visual inspection) was placed in a petri-dish filled with water. Then, the waste paper derived superhydrophobic sponge was placed at the oil/water interface such that it selectively absorbed only the oil phase. The absorbed oil was recovered by manually squeezing the sponge. Furthermore, this absorption-based selective separation was extended for model heavy oil i.e. dichloromethane, DCM (dyed with Nile red). Briefly, 5 mL of DCM was poured in a beaker filled with 15 mL of water followed by immersion of the superhydrophobic sponge into the oil/water mixture such that sediment oil phase was selectively absorbed. The absorbed oil was recovered by manual squeezing of the sponge.

Gravity-Driven Filtration based Oil/Water Separation: The waste paper derived superhydrophobic membranes were further extended for gravity-driven selective filtration of various light and heavy oils from an oil/water mixture. A lab made proto-type was developed using a 50 mL falcon tube where one end of the tube was tied with the waste paper derived superhydrophobic membrane and a hole was made at the closed end of the tube to pour the oil/water mixture with the help of a funnel. Water was dyed with methylene blue and rhodamine 6G as required and dichloromethane (model heavy oil) was dyed with Nile red. To demonstrate the gravity-driven filtration-based oil/water separation, an equal amount of oil and water (20 mL each) was poured through the funnel at the closed end such that the oil phase selectively permeated through the superhydrophobic membrane, while the water phase remained restricted by the water-repellent membrane.

Acknowledgements

We acknowledge the financial support from Science and Engineering Research Board (CVD/2020/000018), Government of India. We thank CIF and Department of Chemistry, Indian Institute of Technology-Guwahati, for their generous assistance in executing various experiments and for the infrastructure. Ms. Arpita Shome and Mr. Adil Majeed Rather thanks IIT Guwahati for their PhD fellowship. Angana Borbora thanks MoE and Council of Scientific & Industrial Research (CSIR, India) for the PhD scholarship. Pillalamarri Srikrishnarka and Avijit Baidya thanks IIT Madras for their PhD fellowship.

Conflict of Interest

The authors declare no conflict of interest.

Keywords: Waste paper · mechanically tailorable · chemically reactive · facile chemistry · tunable water wettability

[1] Y. Wu, B. O. Okesola, J. Xu, I. Korotkin, A. Berardo, I. Corridori, F. Luigi, P. Di Brochetti, J. Kanczler, J. Feng, W. Li, Y. Shi, V. Farafonov, Y. Wang, R. F. Thompson, M.-M. Titirici, D. Nerukh, S. Karabasov, R. O. C. Oreffo, J. C. Rodriguez-Cabello, G. Vozzi, H. S. Azevedo, N. M. Pugno, W. Wang, A. Mata *Nat. Commun.* **2020**, *11*, 1182–1193.

[2] X. Cao, J. Zhang, S. Chen, R. J. Varley, K. Pan, *Adv. Funct. Mater.* **2020**, *30*, 2003618–2003627.

[3] Y. Hu, Z. Chen, H. Zhou, L. Zhong, X. Peng, R.-C. Sun, *Adv. Funct. Mater.* **2019**, *29*, 1904472–1904499.
[4] M. Jian, K. Xia, Q. Wang, Z. Yin, H. Wang, C. Wang, H. Xie, M. Zhang, Y. Zhang, *Adv. Funct. Mater.* **2017**, *27*, 1606066–1606074.
[5] L. Han, K. Liu, M. Wang, K. Wang, L. Fang, H. Chen, J. Zhou, X. Lu, *Adv. Funct. Mater.* **2018**, *28*, 1704195–1704206.
[6] D. Jiang, J. Zhang, S. Qin, Z. Wang, K. A. S. Usman, D. Hegh, J. Liu, W. Lei, J. M. Razal, *ACS Nano* **2021**, *15*, 5000–5010.
[7] C. Li, J. Yang, P. Pachfule, S. Li, M.-Y. Ye, J. Schmidt, A. Thomas, *Nat. Commun.* **2020**, *11*, 4712–4719.
[8] M. Wang, T. Zhang, D. Mao, Y. Yao, X. Zeng, L. Ren, Q. Cai, S. Mateti, L. H. Li, X. Zeng, G. Du, R. Sun, Y. Chen, J. B. Xu, C.-P. Wong, *ACS Nano* **2019**, *13*, 7402–7409.
[9] H. Zhuo, Y. Hu, Z. Chen, X. Peng, L. Liu, Q. Luo, J. Yi, C. Liu, L. Zhong, *J. Mater. Chem. A* **2019**, *7*, 8092–8100.
[10] M. Sun, C. Boo, W. Shi, J. Rolf, E. Shaulsky, W. Cheng, D. L. Plata, J. Qu, M. Elimelech, *Adv. Funct. Mater.* **2019**, *29*, 1903125–1903138.
[11] A. Das, J. Deka, A. M. Rather, B. K. Bhunia, P. P. Saikia, B. B. Mandal, K. Raidongia, U. Manna, *ACS Appl. Mater. Interfaces* **2017**, *9*, 42354–42365.
[12] P. Wang, B. Sun, Y. Liang, H. Han, X. Fan, W. Wang, Z. Yang, *J. Mater. Chem. A* **2018**, *6*, 10404–10410.
[13] P. Wang, W. Wei, Z. Li, W. Duan, H. Han, Q. Xie, *J. Mater. Chem. A* **2020**, *8*, 3509–3516.
[14] W. T. Cao, W. Feng, Y. Y. Jiang, C. Ma, Z. F. Zhou, M. G. Ma, Y. Chen, F. Chen, *Mater. Horiz.* **2019**, *6*, 1057–1065.
[15] Q. Liu, D. Chen, Z. Kang, *ACS Appl. Mater. Interfaces* **2015**, *7*, 1859–1867.
[16] Q. Zhou, W. Wu, S. Zhou, T. Xing, G. Sun, G. Chen, *Chem. Eng. J.* **2020**, *382*, 122988–122999.
[17] F. Geyer, C. Scho"necker, H. J. Butt, D. Vollmer, *Adv. Mater.* **2017**, *29*, 1603524–1603530.
[18] Baidya, M. A. Ganayee, S. J. Ravindran, K. C. Tam, S. K. Das, R. H. A. Ras, T. Pradeep, *ACS Nano* **2017**, *11*, 11091–11099.
[19] B. Wu, J. Lyu, C. Peng, D. Jiang, J. Yang, J. Yang, S. Xing, L. Sheng, *Chem. Eng. J.* **2020**, *387*, 124066–124074.
[20] X. Du, M. Wang, A. Welle, F. Behboodi-Sadabad, Y. Wang, P. A. Levkin, Z. Gu, *Adv. Funct. Mater.* **2018**, *28*, 1803765–1803772.
[21] A. Shome, A. M. Rather, A. Ghosal, B. K. Bunia, B. B. Mandal, U. Manna, *ACS Sustainable Chem. Eng.* **2019**, *7*, 7502–7509.
[22] A. Das, A. Shome, U. Manna, *J. Mater. Chem. A* **2021**, *9*, 824–856.
[23] R. Gao, S. Xiao, W. Gan, Q. Liu, H. Amer, T. Rosenau, J. Li, Y. Lu, *ACS Sustainable Chem. Eng.* **2018**, *6*, 9047–9055.
[24] Z. Xia, J. Li, J. Zhang, X. Zhang, X. Zheng, J. Zhang, *J. Bioresour. Bioprod.* **2020**, *5*, 79–95.
[25] X. Miao, J. Lin, F. Bian, *J. Bioresour. Bioprod.* **2020**, *5*, 26–36.
[26] K. Pivnenko, D. Laner, T. F. Astrup, *Environ. Sci. Technol.* **2016**, *50*, 12302–12311.
[27] J. Y. Keränen, E. Retulainen, *BioResources* **2016**, *11*, 10404–10418.
[28] M. I. Khazi, W. Jeong, J.-M. Kim, *Adv. Mater.* **2018**, *30*, 1705310–1705332.
[29] H. Yu, Z. Chen, Y. Liu, O. Alkhamis, Z. Song, Y. Xiao, *Angew. Chem. Int. Ed.* **2020**, *60*, 2993–3000.
[30] F. Brunetti, A. Operamolla, S. Castro-Hermosa, G. Lucarelli, V. Manca, G. M. Farinola, T. M. Brown, *Adv. Funct. Mater.* **2019**, *29*, 1806798–1806831.
[31] Z. Wang, X. Fu, Z. Zhang, Y. Jiang, M. Waqar, P. Xie, K. Bi, Y. Liu, X. Yin, R. Fan, *J. Cleaner Prod.* **2019**, *234*, 588–596.
[32] C Li, M. Boban, S. A. Snyder, S. P. R. Kobaku, G. Kwon, G. Mehta, A. Tuteja, *Adv. Funct. Mater.* **2016**, *26*, 6121–6131.
[33] L. Li, J. Zhu, Z. Zeng, *ACS Appl. Mater. Interfaces* **2020**, *12*, 55894–55902.
[34] L. Li, B. Li, H. Sun, J. Zhang, *J. Mater. Chem. A* **2017**, *5*, 14858–14864.
[35] T.-N. Ye, W.-J. Feng, B. Zhang, M. Xu, L.-B. Lv, J. Su, X. Wei, K.-X. Wang, X.-H. Li, J.-S. Chen, *J. Mater. Chem. A* **2015**, *3*, 13926–13932.
[36] L. Li, T. Hu, A. Li, J. Zhang, *ACS Appl. Mater. Interfaces* **2020**, *12*, 32143–32153.
[37] X. Yue, T. Zhang, D. Yang, F. Qiu, Z. Li, *J. Cleaner Prod.* **2018**, *199*, 411–419.
[38] W. Sakuma, S. Yamasaki, S. Fujisawa, T. Kodama, J. Shiomi, K. Kanamori, T. Saito, *ACS Nano* **2021**, *15*, 1436–1444.
[39] Y. Kobayashi, T. Saito, A. Isogai, *Angew. Chem. Int. Ed.* **2014**, *53*, 10394–10397; *Angew. Chem.* **2014**, *126*, 10562–10565.
[40] C. Jia, L. Li, Y. Liu, B. Fang, H. Ding, J. Song, Y. Liu, K. Xiang, S. Lin, Z. Li, W. Si, B. Li, X. Sheng, D. Wang, X. Wei, H. Wu, *Nat. Commun.* **2020**, *11*, 3732–3745.
[41] G. Zhang, G. Chen, F. Yang, Z. Guo, *Nanoscale Adv.* **2020**, *2*, 4813–4821.
[42] Y.-Q. Li, W.-B. Zhu, X.-G. Yu, P. Huang, S.-Y. Fu, N. Hu, K. Liao, *ACS Appl. Mater. Interfaces* **2016**, *8*, 33189–33196.
[43] D. Puthusseri, V. Aravindan, B. Anothumakkool, S. Kurungot, S. Madhavi, S. Ogale, *Small* **2014**, *10*, 4395–4402.
[44] H. Liu, H. Xiang, Y. Ma, Z. Li, Q. Meng, H. Jiang, H. Wu, P. Li, H. Zhou, W. Huang, *ACS Sustainable Chem. Eng.* **2018**, *6*, 15749–15755.
[45] M. R. Weatherspoon, M. B. Dickerson, G. Wang, Y. Cai, S. Shian, S. C. Jones, S. R. Marder, K. H. Sandhage, *Angew. Chem. Int. Ed.* **2007**, *46*, 5724–5727; *Angew. Chem.* **2007**, *119*, 5826–5829.
[46] J. Ford, S. R. Marder, S. Yang, *Chem. Mater.* **2009**, *21*, 476–483.
[47] D. W. Wei, H. Wei, A. C. Gauthier, J. Song, Y. Jin, H. Xiao, *J. Bioresour. Bioprod.* **2020**, *5*, 1–15.
[48] D. Lv, G. Tang, L. Chen, M. Zhang, J. Cui, R. Xiong, C. Huang, *ACS Appl. Polym. Mater.* **2020**, *2*, 5686–5697.
[49] Z. Zhang, G. Sèbe, D. Rentsch, T. Zimmermann, P. Tingaut, *Chem. Mater.* **2014**, *26*, 2659–2668.
[50] S. Zhou, P. Liu, M. Wang, H. Zhao, J. Yang, F. Xu, *ACS Sustainable Chem. Eng.* **2016**, *4*, 6409–6416.

Manuscript received: May 4, 2021
Revised manuscript received: June 1, 2021
Accepted manuscript online: June 1, 2021
Version of record online: June 22, 2021

CHEMISTRY
AN ASIAN JOURNAL

Supporting Information

Design of a Waste Paper-Derived Chemically 'Reactive' and Durable Functional Material with Tailorable Mechanical Property Following an Ambient and Sustainable Chemical Approach

Arpita Shome, Adil M. Rather, Angana Borbora, Pillalamarri Srikrishnarka, Avijit Baidya, Thalappil Pradeep,* and Uttam Manna*

Table of Contents

Facile conversion of waste paper into a deformable and chemically ‘reactive’ sponge. The covalent association of a binder with waste paper paved an avenue to tailor the mechanical property and the catalyst-free 1,4-conjugate addition reaction between the primary amine of the binder with a multi-functional cross-linker provided a facile basis to induce residual chemical ‘reactivity’.

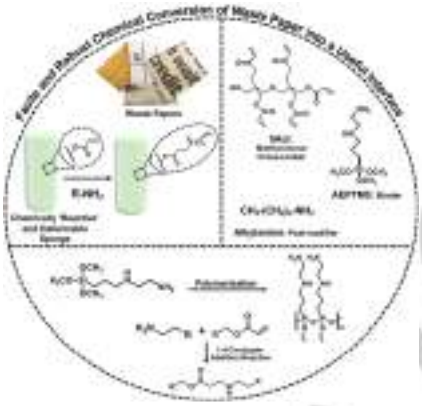

Arpita Shome, [a] *Adil M Rather,* [a], [b] *Angana Borbora,* [a] *Pillalamarri Srikrishnarka,* [c] *Avijit Baidya,* [c], [e] *Thalappil Pradeep**[c] *and Uttam Manna** [a], [d]

Page No. – Page No.

Design of Waste Paper Derived Chemically ‘Reactive’ & Durable Functional Material with Tailorable Mechanical Property Following an Ambient & Sustainable Chemical Approach

Movie 1: Video graphic evidence of bouncing of a stream of water jet from the surface of the waste-paper derived superhydrophobic sponge

Movie 2: Demonstration of the absorption based selective separation of light oil (i.e. motor oil) from an oil/water interface using the waste-paper derived superhydrophobic sponge

Movie 3: Demonstration of the absorption based selective separation of model heavy oil (i.e. dichloromethane) from an oil/water interface using waste-paper derived superhydrophobic sponge

Movie 4: Demonstration of the gravity-driven filtration based selective separation of light oil (i.e. kerosene) from an oil/water mixture through the waste-paper derived superhydrophobic sponge

Movie 5: Demonstration of the gravity-driven filtration based selective separation of model heavy oil (i.e. dichloromethane) from an oil/water mixture through the waste-paper derived superhydrophobic sponge

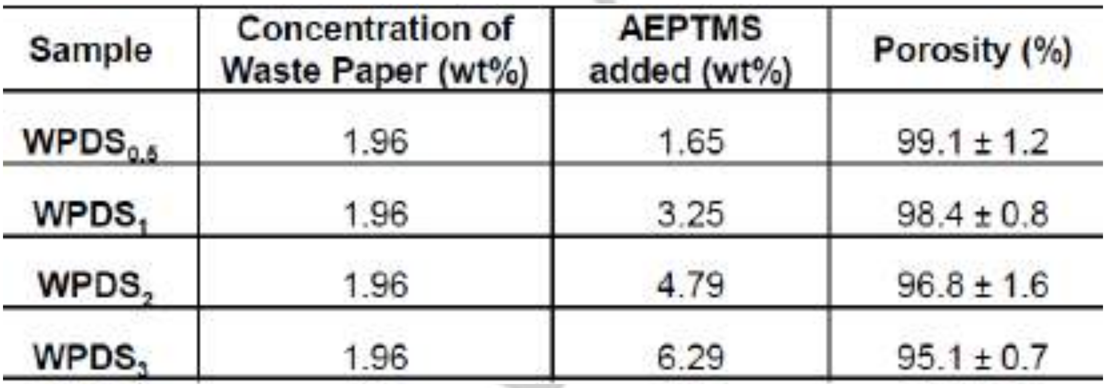

Sample	Concentration of Waste Paper (wt%)	AEPTMS added (wt%)	Porosity (%)
$WPDS_{0.5}$	1.96	1.65	99.1 ± 1.2
$WPDS_1$	1.96	3.25	98.4 ± 0.8
$WPDS_2$	1.96	4.79	96.8 ± 1.6
$WPDS_3$	1.96	6.29	95.1 ± 0.7

Table S1 accounting for the concentration of waste paper and AEPTMS used for developing the waste paper derived sponges with varying porosities.

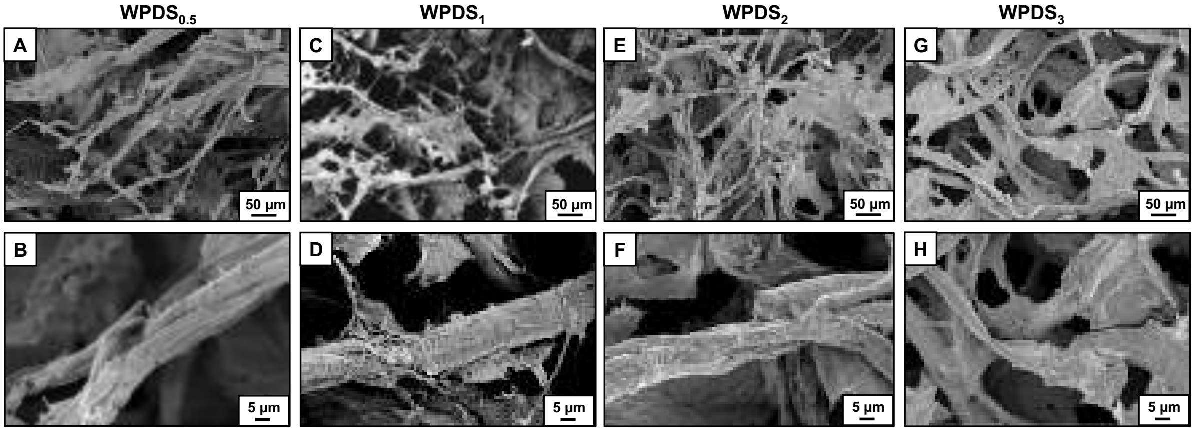

Figure S1. A-H) FESEM images at low (A, C, E, G) and high (B, D, F, H) magnifications exhibiting the interconnected, fibrous and porous morphology of the waste paper derived sponges doped with different concentrations of the binder, AEPTMS.

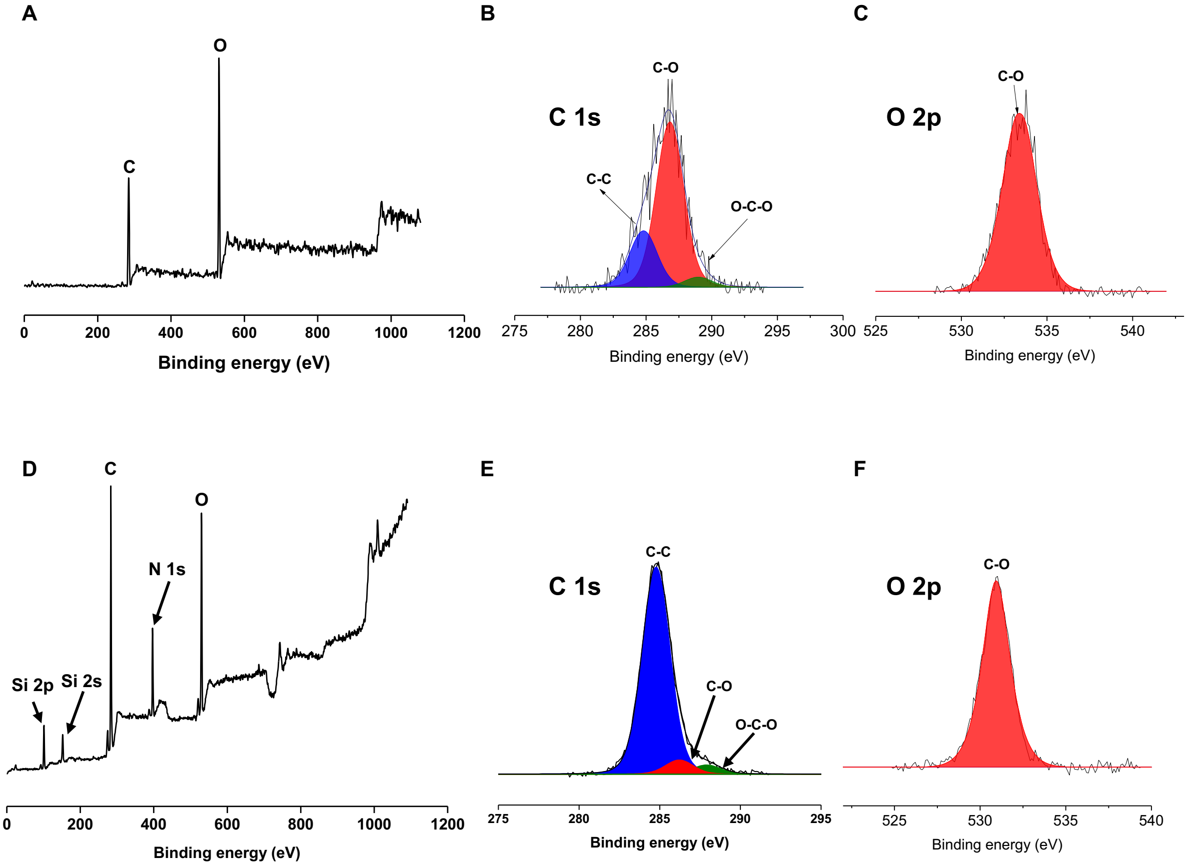

Figure S2. A) XPS spectra of waste paper derived sponge, $WPS_{control}$. B,C) De-convoluted XPS spectra of C 1s (B) and O 2p (C) of the waste paper derived sponge, $WPS_{control}$ respectively. D) XPS spectra of waste paper derived sponge,$WPDS_1$ E-H) De-convoluted XPS spectra of C 1s (E), O 2p (F), N 2p (G) and Si 2p (H) of the waste paper derived sponge,$WPDS_1$ respectively.

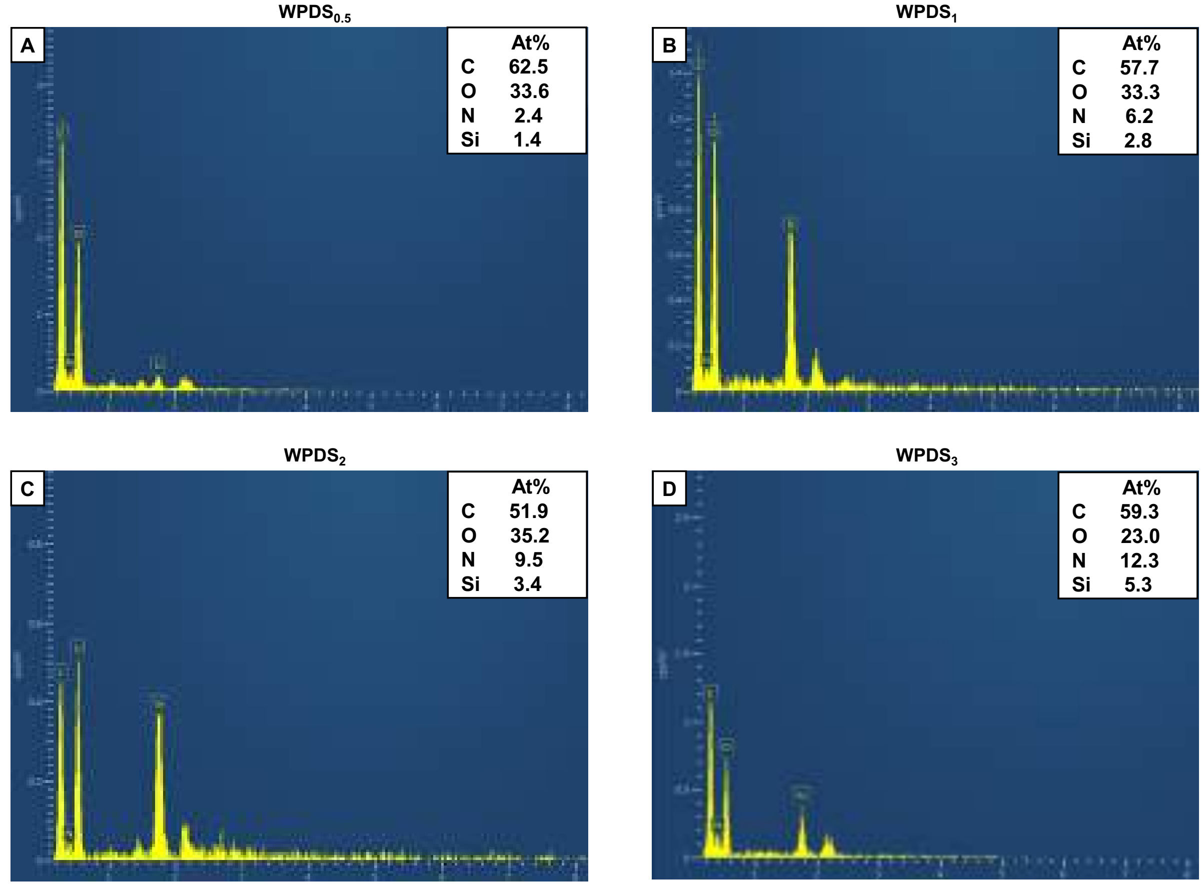

Figure S3. A-D) Energy dispersive X-ray spectral analysis of the waste paper derived sponges doped with different concentrations of the binder (AEPTMS) i.e. WPDS$_{0.5}$ (A), WPDS$_1$ (B), WPDS$_2$ (C) and WPDS$_3$ (D).

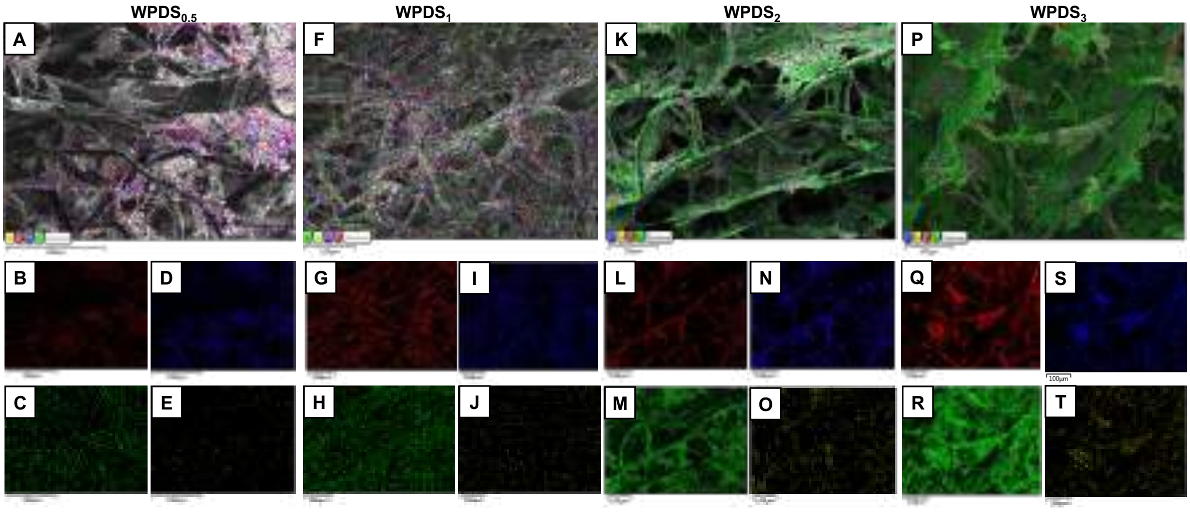

Figure S4. A-D) Energy dispersive X-ray mapping images of the waste paper derived sponges i.e. WPDS$_{0.5}$ (A-E), WPDS$_1$ (F-J), WPDS$_2$ (K-O) and WPDS$_3$ (P-T). The color codes for the elements are C (red), O (blue), Si (green) and N (yellow).

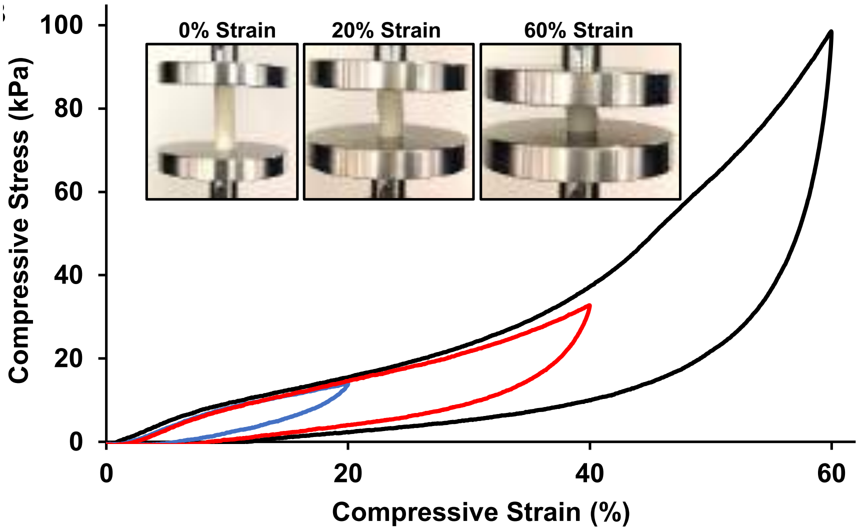

Figure S5. Plot illustrating the cyclic stress-strain analysis of $WPDS_1$ under different percentage of strain.

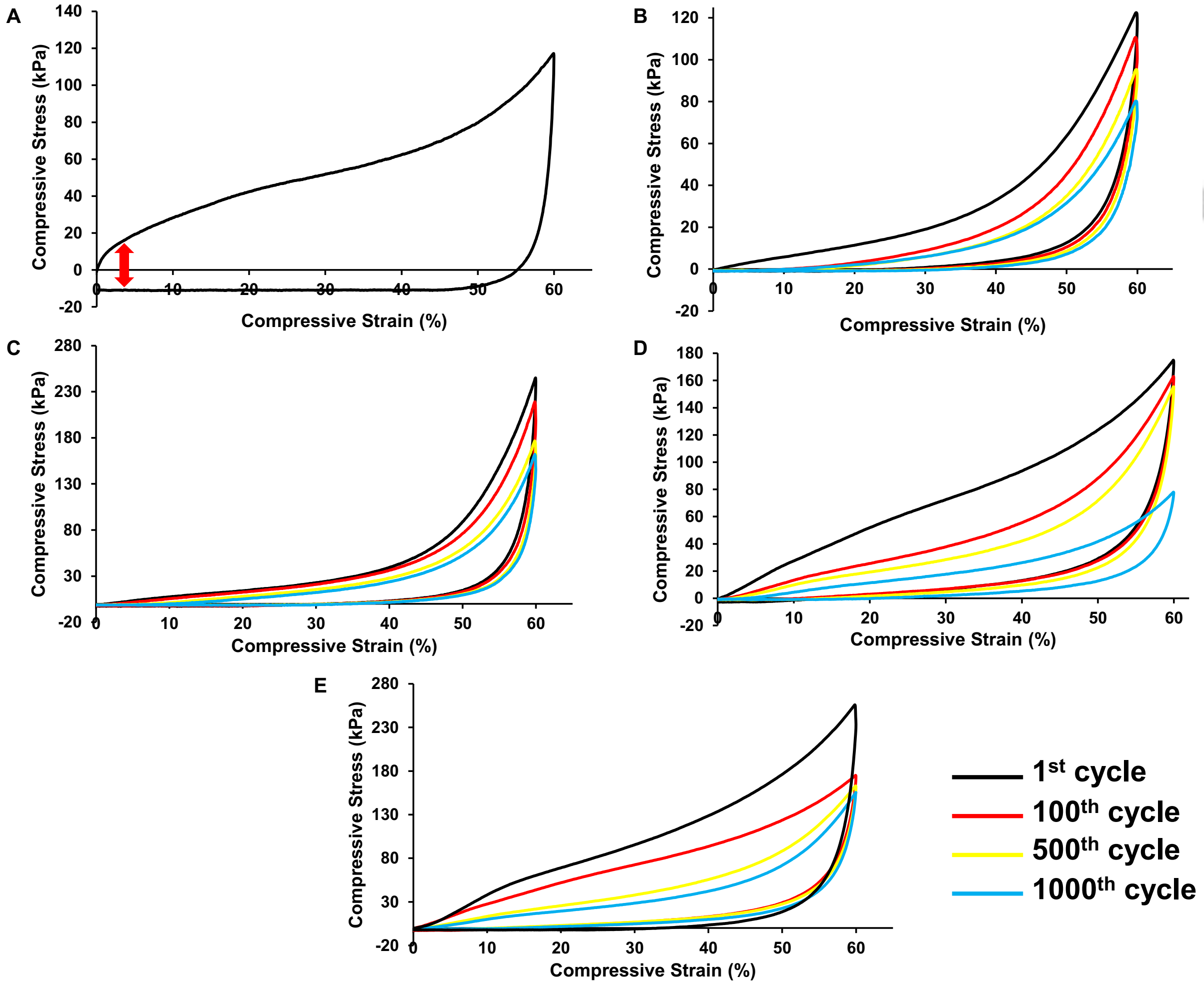

Figure S6. A-E) Plot accounting for the cyclic compression analysis of the waste paper derived sponge, WPS$_{control}$ (A) and the waste paper derived sponges doped with different concentrations of the binder (AEPTMS) i.e. WPDS$_{0.5}$ (B), WPDS$_1$ (C), WPDS$_2$ (D) and WPDS$_3$ (E).

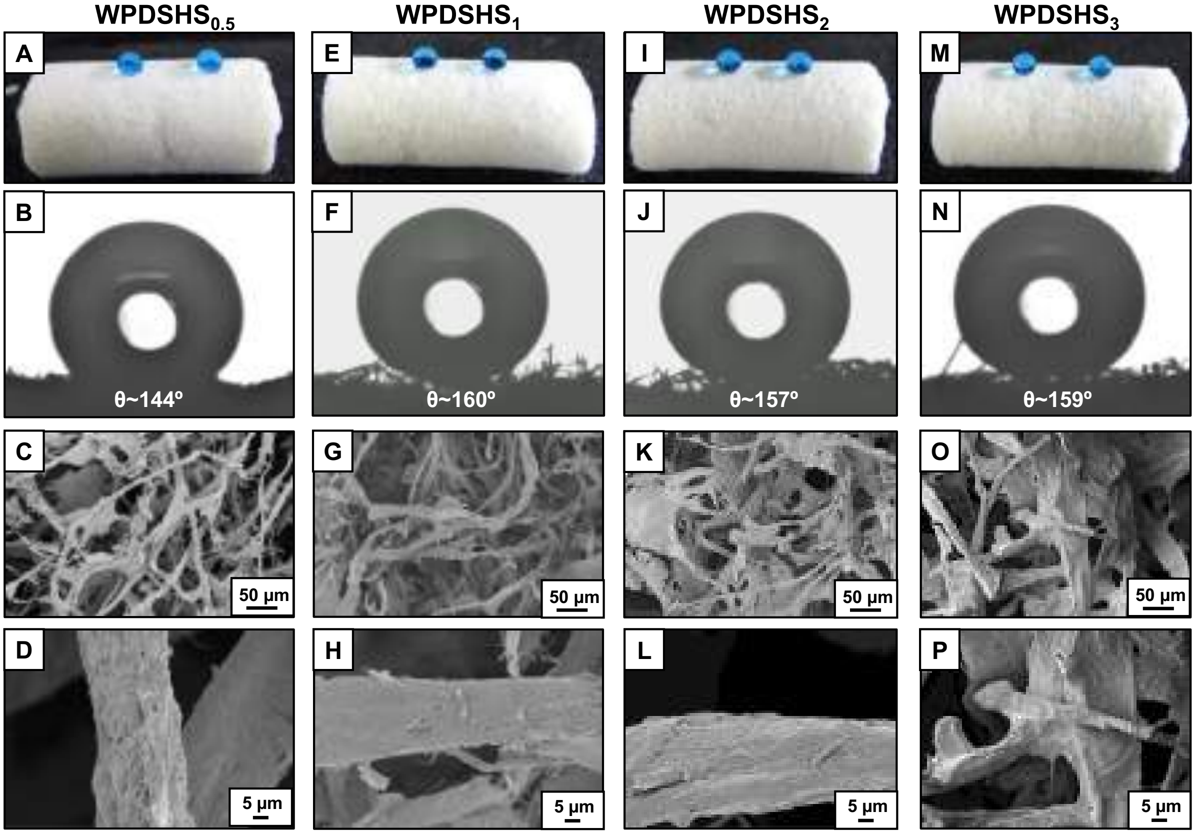

Figure S7. A-N) Digital images (A, E, I, M) and water contact angle images (B, F, J, N) of the beaded water droplet on the waste paper derived sponges that was post covalently modified with octadecylamine. C-P) FESEM images at low (C, G, K, O) and high (D, H, L, P) magnifications exhibiting the morphology of the waste paper derived sponges (doped with different concentrations of binder, AEPTMS) after post covalent modification.

Sample	Advancing Contact Angle (°)	Contact Angle Hysteresis (°)	Density (g/cm^3)
WPDSHS$_{0.5}$	146.4±1.1	15.3±1.5	0.015 ± 0.9
WPDSHS$_1$	159.4±1.2	7.3±0.4	0.017 ± 1.2
WPDSHS$_2$	158.7±0.6	7.5±0.6	0.018 ± 0.6
WPDSHS$_3$	157.2±0.6	7.6±1.4	0.022 ± 1.5

Table S2. Accounting for the advancing contact angle, contact angle hysteresis and density of the beaded water droplet on the waste paper derived sponges after post covalent modification.

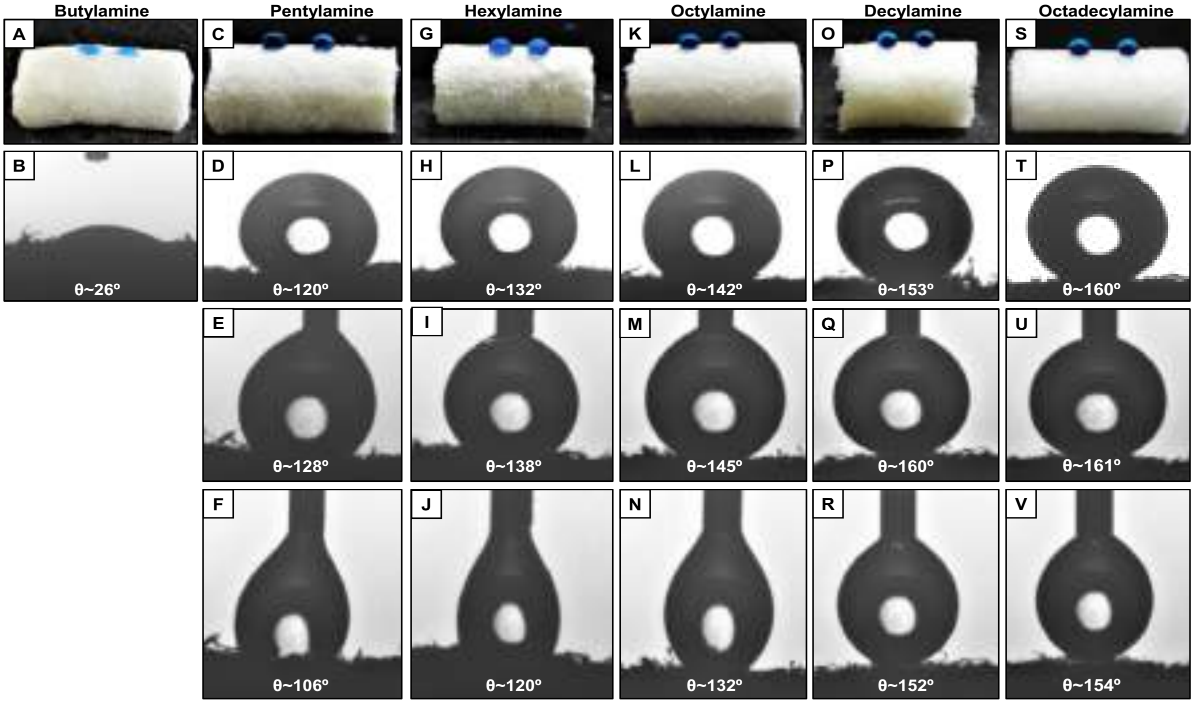

Figure S8. A-V) Digital images and contact angle images of the beaded water droplet on the waste paper derived sponge, WPDS$_1$ that was post covalently modified with butylamine (A-B), pentylamine (C-F), hexylamine (G-J), octylamine (K-N), decylamine (O-R) and octadecylamine (S-V).

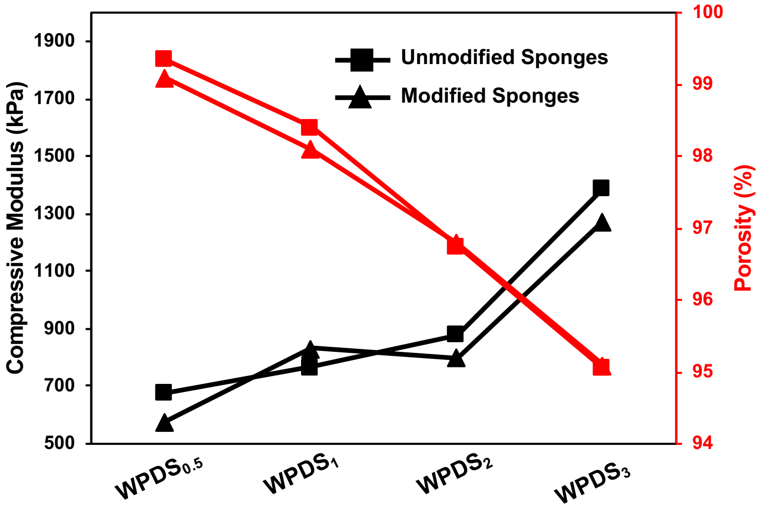

Figure S9. A) Plot illustrating the compressive modulus (black) and porosity (red) of the waste paper derived superhydrophobic sponges before and after post covalent modification to alter the wettability.

Sample	Advancing Contact Angle (°)	Contact Angle Hysteresis (°)
Office Paper	158.4 ± 0.6	7.5 ± 1.3
Newspaper	159.2 ± 1.1	7.3 ± 0.9
Cardboard Paper	157.8 ± 1.2	7.8 ± 1.1
Mixture of Papers	156.7 ± 0.8	8.21± 1.4

Table S3 accounting for the advancing contact angle and contact angle hysteresis of the beaded water droplet on the different types of waste paper derived superhydrophobic sponges.

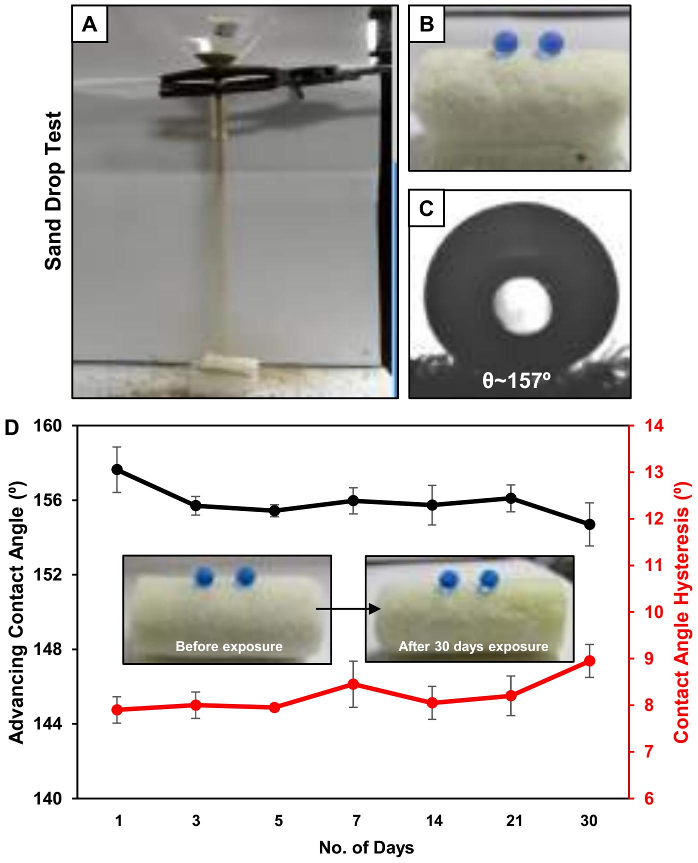

Figure S10. A-C) Digital image (A, B) and contact angle image (C) illustrating the sand drop test (A) followed by examination of water repellence after sand drop test (B-C) on the waste paper derived superhydrophobic sponge, WPDSHS$_1$. D) Plot accounting for the advancing contact angle (black) and contact angle hysteresis (red) of the beaded water droplet on the waste paper derived superhydrophobic sponge, WPDSHS$_1$ after 30 days exposure to UV radiation.

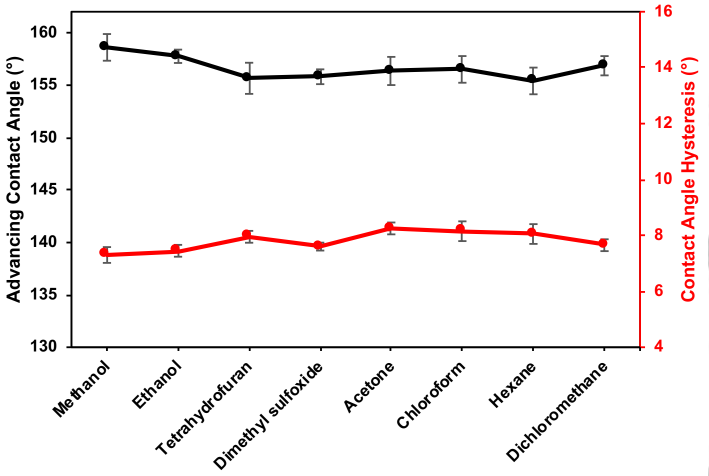

Figure S11. Plot accounting for the advancing contact angle (black) and contact angle hysteresis (red) of the beaded water droplet on the waste paper derived superhydrophobic sponge, WPDSHS$_1$ after 30 days exposure to different polar and non-polar organic solvents.

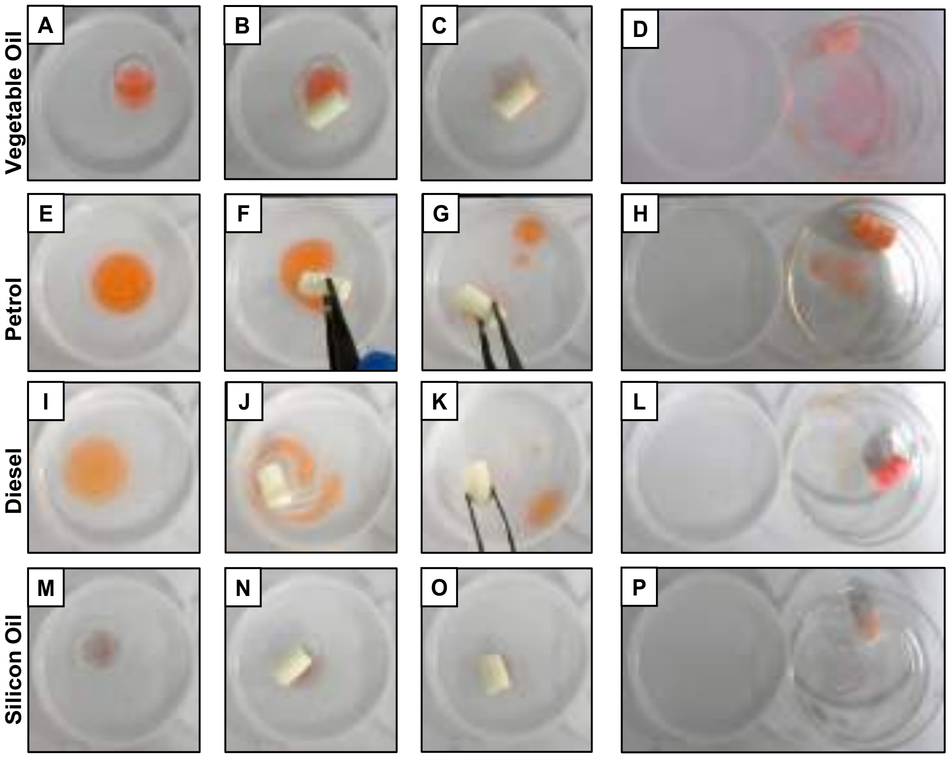

Figure S12. A-P) Digital images illustrating the absorption based selective separation of vegetable oil (A-D), petrol (E-H), diesel (I-L) and silicon oil (M-P) using the waste paper derived superhydrophobic sponge, WPDSHS$_1$ from an oil/water interface.

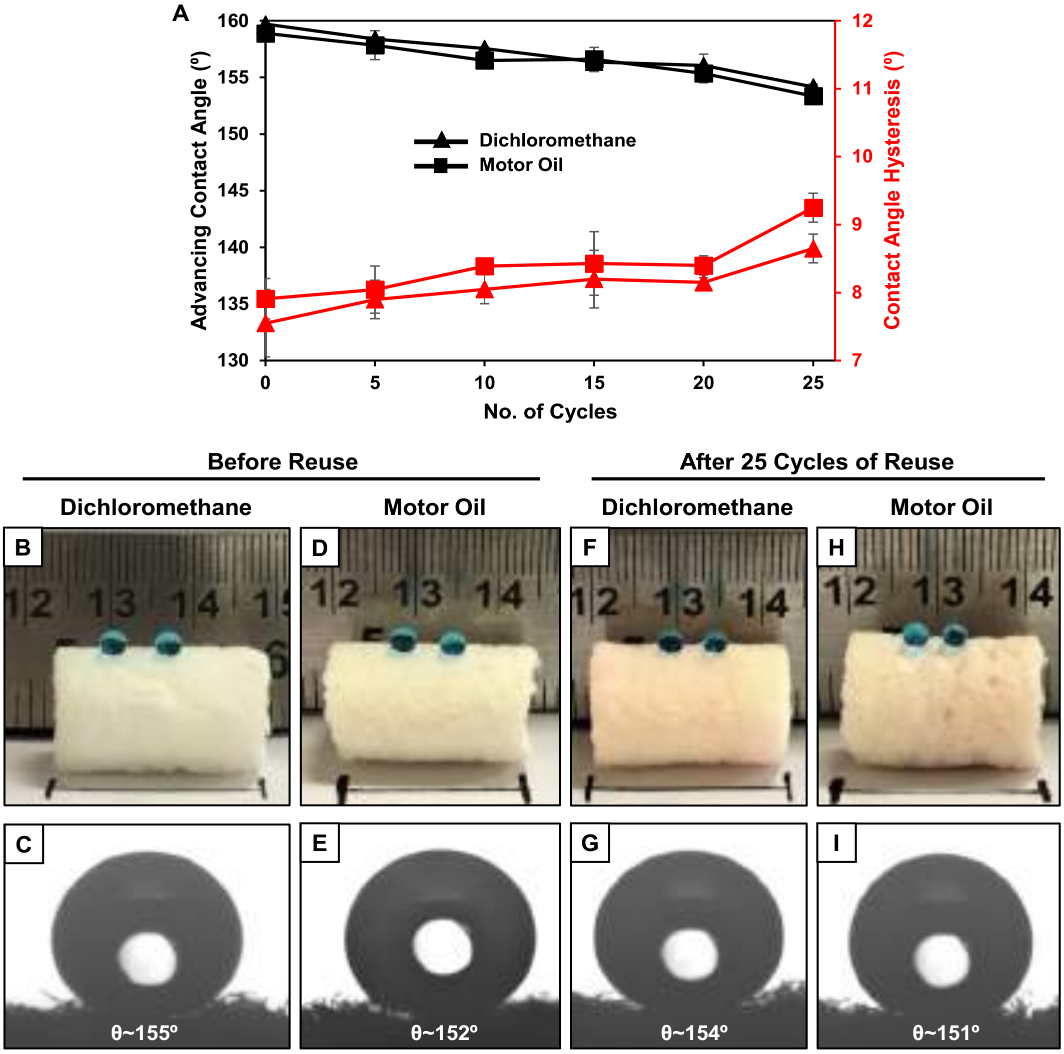

Figure S13. A) Plot accounting for the advancing contact angle (black) and contact angle hysteresis (red) of the beaded water droplet on the waste paper derived superhydrophobic sponge, WPDSHS$_1$ that was used repetitively for 25 times of selective absorption of both light (motor oil) and heavy (dichloromethane) oils from an oil/water mixture. B-I) Digital images (B, D, F, H) and contact angle images (C, E, G, I) of the waste paper derived superhydrophobic sponge, WPDSHS$_1$ before (B-E) and after (F-I) 25 times of use for selective absorption of light (motor oil) and heavy oils (dichloromethane) from an oil/water mixture.

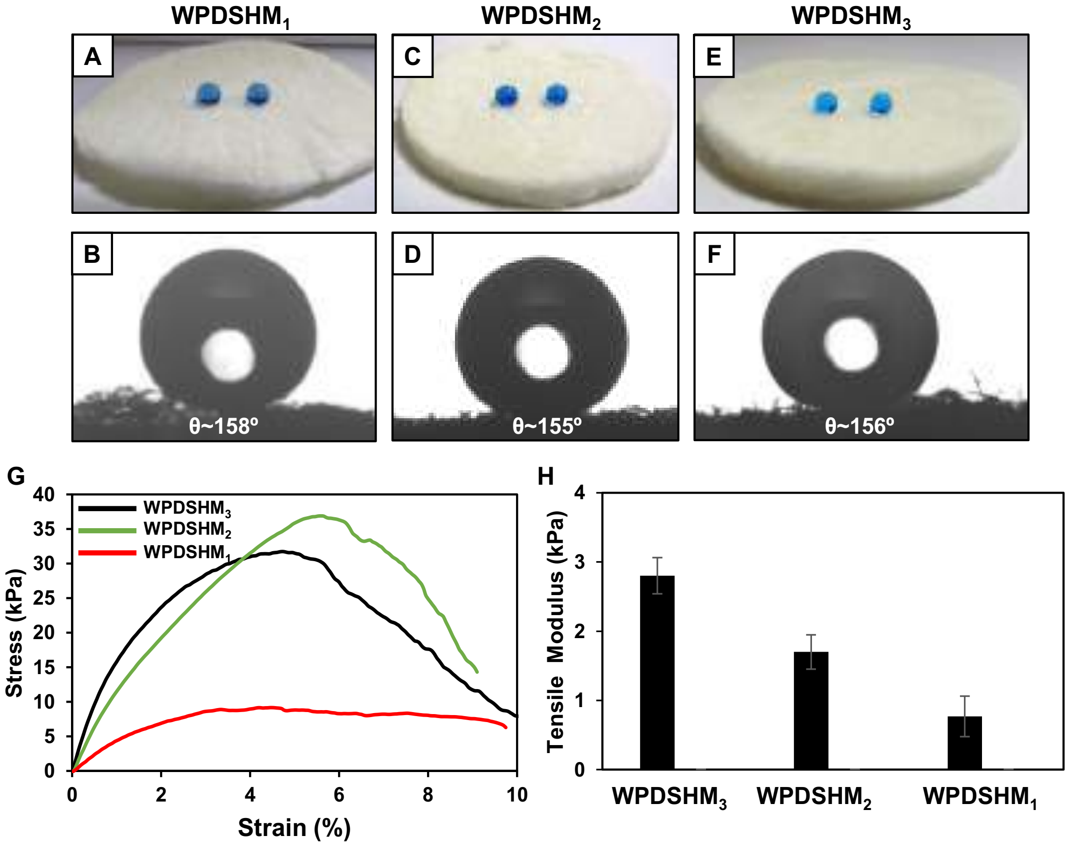

Figure S14. A-F) Digital images (A, C, E) and contact angle images (B, D, F) of the beaded water droplet on the waste paper derived superhydrophobic membranes that were developed using different concentrations of the silane binder (AEPTMS). G) Plot illustrating the tensile stress-strain analysis of the waste paper derived superhydrophobic membranes. H) Bar diagram accounting for the tensile modulus of the waste paper derived superhydrophobic membranes.

Sample	Advancing Contact Angle (°)	Contact Angle Hysteresis (°)	Porosity (%)
WPDSHM$_1$	158.4 ± 1.3	7.3 ± 0.7	99.3 ± 1.2
WPDSHM$_2$	156.6 ± 1.5	7.5 ± 0.8	97.5 ± 0.9
WPDSHM$_3$	157.9 ± 0.7	7.4 ± 1.1	96.1 ± 0.5

Table S4 accounts for the advancing water contact, contact angle hysteresis and porosity of the waste paper derived superhydrophobic membranes that were developed with different concentrations of AEPTMS.

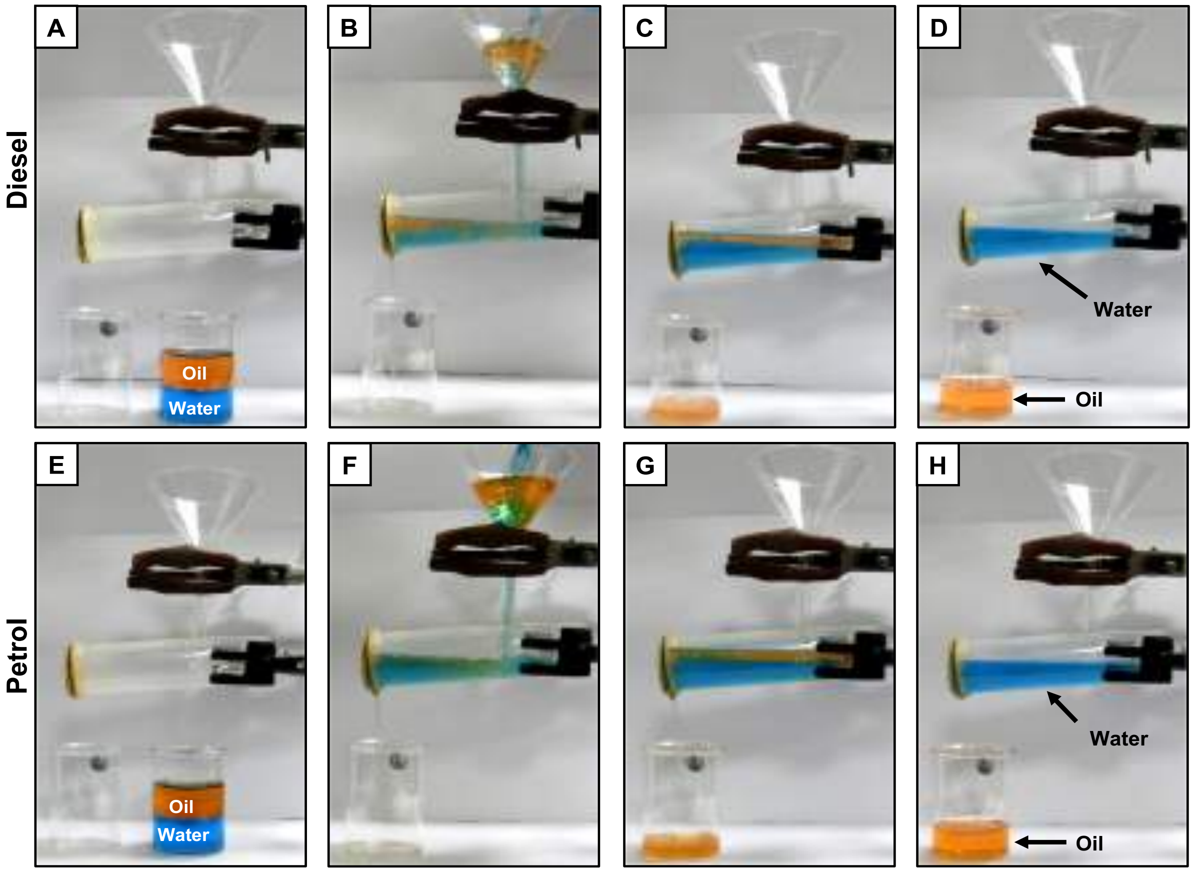

Figure S15. A-H) Digital images illustrating the gravity-driven filtration based selective separation of diesel (A-D) and petrol (E-H) by the waste paper derived superhydrophobic membrane, WPDSHM₁ from an oil/water mixture.

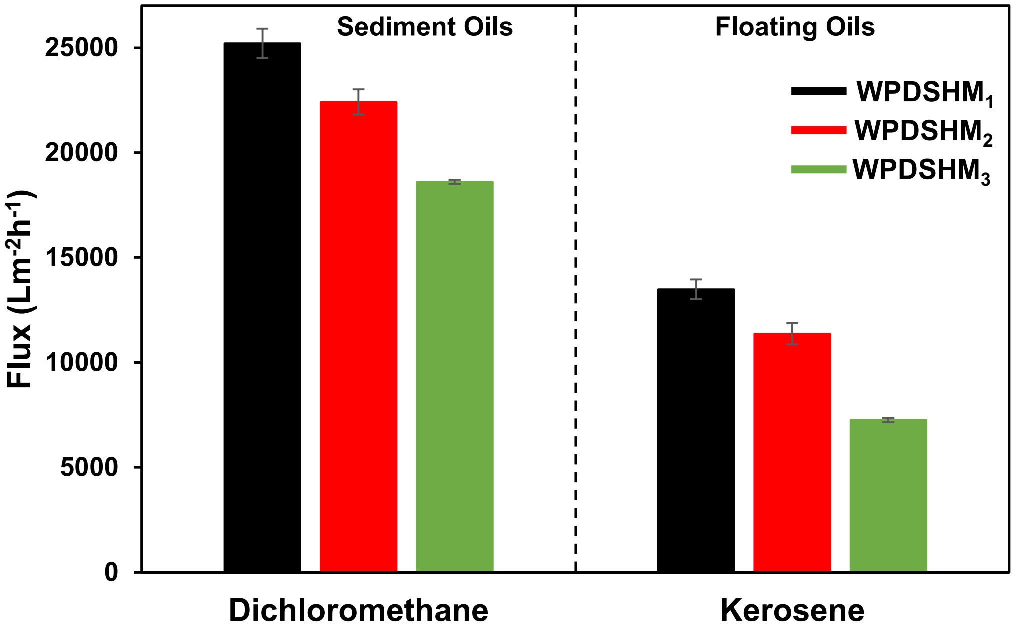

Figure S16. A) Plot accounting for the rate of flux of model sediment and floating oils through the waste paper derived superhydrophobic membranes with varying porosities.

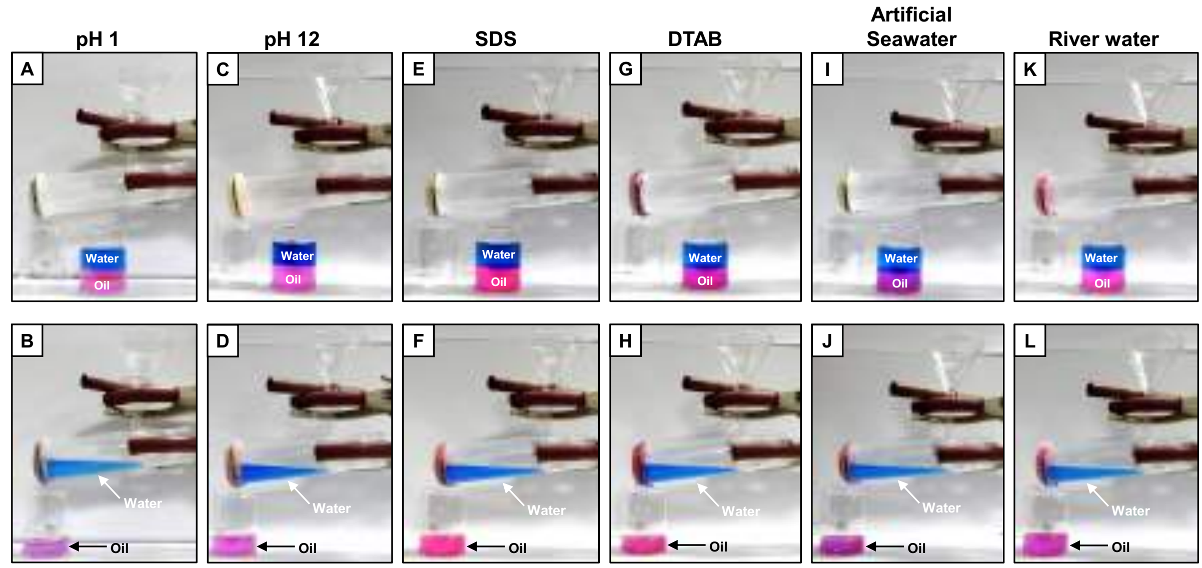

Figure S17. A-L) Digital images illustrating the gravity-driven filtration based selective separation of model heavy oil phase i.e. dichloromethane (dyed pink for visual inspection) by the waste paper derived superhydrophobic membrane, WPDSHM$_1$ from an oil/water mixture where the aqueous phase is chemically contaminated i.e. acidic water (A-B), basic water (C-D), surfactant contaminated (E-H), artificial sea water (I-J) and river water (K-L).

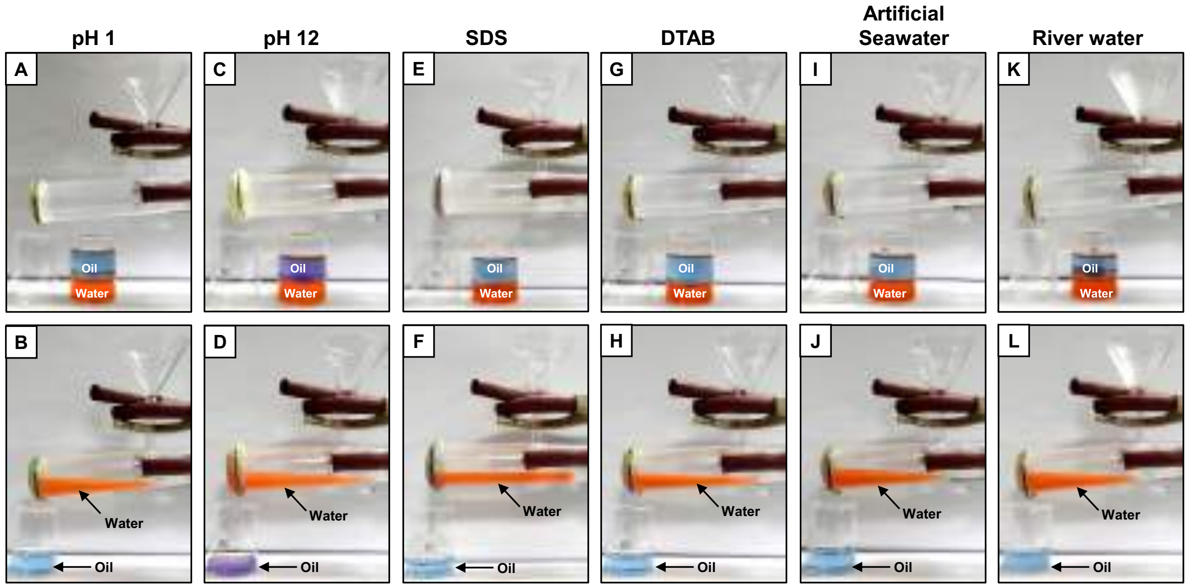

Figure S18. A-L) Digital images illustrating the gravity-driven filtration based selective separation of the light oil phase i.e. kerosene by the waste paper derived superhydrophobic membrane, WPDSHM$_1$ from an oil/water mixture where the aqueous phase is chemically contaminated i.e. acidic water (A-B), basic water (C-D), surfactant contaminated (E-H), artificial sea water (I-J) and river water (K-L).

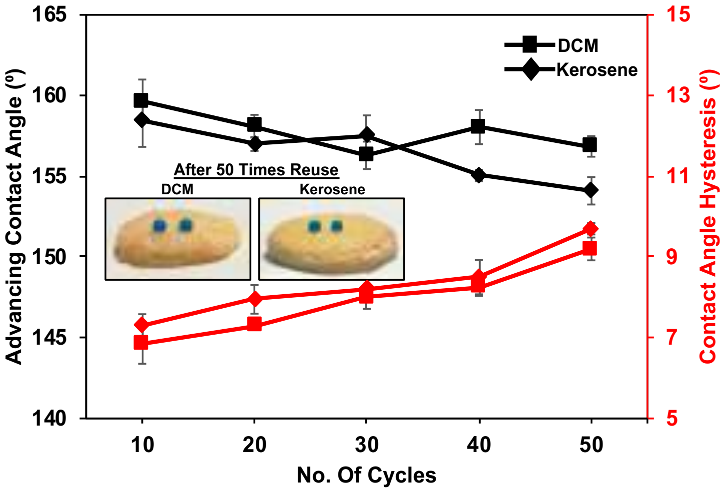

Figure S19. A) Plot accounting for the advancing contact angle (black) and contact angle hysteresis (red) of the beaded water droplet on the waste paper derived superhydrophobic membrane, WPDSHM$_1$ that was repetitively used (50 times) for separation of both light (kerosene) and heavy (dichloromethane) oils from an oil/water mixture. Inset images exhibit the intact water repellence property and physical integrity of the membrane after reuse.

JACS
JOURNAL OF THE AMERICAN CHEMICAL SOCIETY

pubs.acs.org/JACS

Article

Kinetics of Intercluster Reactions between Atomically Precise Noble Metal Clusters $[Ag_{25}(DMBT)_{18}]^-$ and $[Au_{25}(PET)_{18}]^-$ in Room Temperature Solutions

Marco Neumaier,*[,||] Ananya Baksi,[||] Patrick Weis, Erik K. Schneider, Papri Chakraborty, Horst Hahn, Thalappil Pradeep,* and Manfred M. Kappes*

Cite This: https://doi.org/10.1021/jacs.1c01140

Read Online

ABSTRACT: The kinetics of intercluster metal atom exchange reactions between solvated $[Ag_{25}(DMBT)_{18}]^-$ and $[Au_{25}(PET)_{18}]^-$ (DMBT and PET are 2,4-dimethylbenzenethiol and 2-phenylethanethiol, respectively, both $C_8H_{10}S$) were probed by electrospray ionization mass spectrometry and computer-based modeling. Anion mass spectra and collision induced dissociation (CID) measurements show that both cluster monomers and dimers are involved in the reactions. We have modeled the corresponding kinetics assuming a reaction mechanism in which metal atom exchange occurs through transient dimers. Our kinetic model contains three types of generic reactions: dimerization of monomers, metal atom exchange in the transient dimers, and dissociation of the dimers to monomers. There are correspondingly 377 discrete species connected by in total 1302 reactions (i.e., dimerization, dissociation and atom exchange reactions) leading to the entire series of monomeric and dimeric products $[Ag_mAu_{25-m}]^-$ ($m = 1-24$) and $[Ag_mAu_{50-m}]^{2-}$ ($m = 0-50$), respectively. The rate constants of the corresponding reactions were fitted to the experimental data, and good agreement was obtained with exchange rate constants which scale with the probability of finding a silver or gold atom in the respective monomeric subunit of the dimer, i.e., reflecting an entropic driving force for alloying. Allowing the dimerization rate constant to scale with increasing gold composition of the respective reactants improves the agreement further. The rate constants obtained are physically plausible, thus strongly supporting dimer-mediated metal atom exchange in this intercluster reaction system.

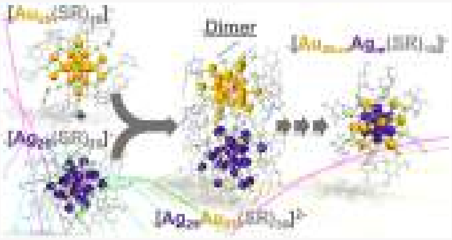

■ INTRODUCTION

Intercluster reactions[1−8] in homogeneous solution constitute an emerging area in the field of atomically precise nanoclusters[9−20] with great potential for the controlled formation of transition metal nanoalloys.[21−24] Reactions between different coinage metal clusters have been studied, focusing on the identification of intermediates and products via electrospray ionization mass spectrometry (ESI MS) of liquid reaction mixtures. In the first documented case, the reaction between solvated $[PPh_4^+]_4[Ag_{44}(SR)_{30}]^{4-}$ and $[TOA]^+[Au_{25}(SR)_{18}]^-$ clusters (TOA refers to tetraoctylammonium cations, SR refers to thiolate) resulted in the formation of mixed $[Ag_mAg_{25-m}(SR)_{18}]^-$($m$ = 0−20) nanoalloy clusters (i.e., having the same overall metal nuclearity).[7] In another example, reactions between solvated $Ag_{29}(BDT)_{12}(PPh_3)_4$ "superatoms" and $Cu_{12}S_6(DPPPT)_4$ clusters (BDT and DPPPT are 1,3-benzenedithiolate and bis(diphenylphosphino)pentane, respectively) have recently been shown to lead to extensive copper−silver exchange without significantly changing the structure type of the various $Ag_{29-x}Cu_x$ species formed as mixing progressed.[4] Intercluster reactions have also been reported between a coinage metal cluster and other transition metal cluster species, e.g., between $[Au_{25}(SR)_{18}]^-$ and $Ir_9(SR)_6$ clusters leading to the formation of a new bimetallic, neutral $Ir_3Au_{22}(SR)_{18}$ cluster.[5] Recently, a trimetallic dithiol protected $MAu_xAg_{28-x}(BDT)_{12}(PPh_3)_4$ (M = Ni, Pd, or Pt and x = 1−12) cluster was formed by intercluster reactions.[6]

On the basis of MS and density functional theory (DFT) calculations, Pradeep and co-workers proposed that the reaction between $[Ag_{44}(SR)_{30}]^{4-}$ and $[Au_{25}(SR)_{18}]^-$ proceeds via ligand interaction between two solvated clusters in close proximity.[7] Shortly thereafter, Bürgi et al. used a different approach to support this picture. They showed that in the "$Au_{38}(SR)_{24}$ + $Au_{38-x}Ag_x(SR)_{24}$" reaction system, separation of the two reagents by a dialysis membrane impermeable to the solvated clusters but still permeable to their smaller building blocks (<1000 Da) prevented the nanoalloying reaction completely, on the experimental time scale.[25] This implies that metal exchange via oxidative dissolution/readsorption of small component building blocks, an alternative mechanism,

Received: February 1, 2021

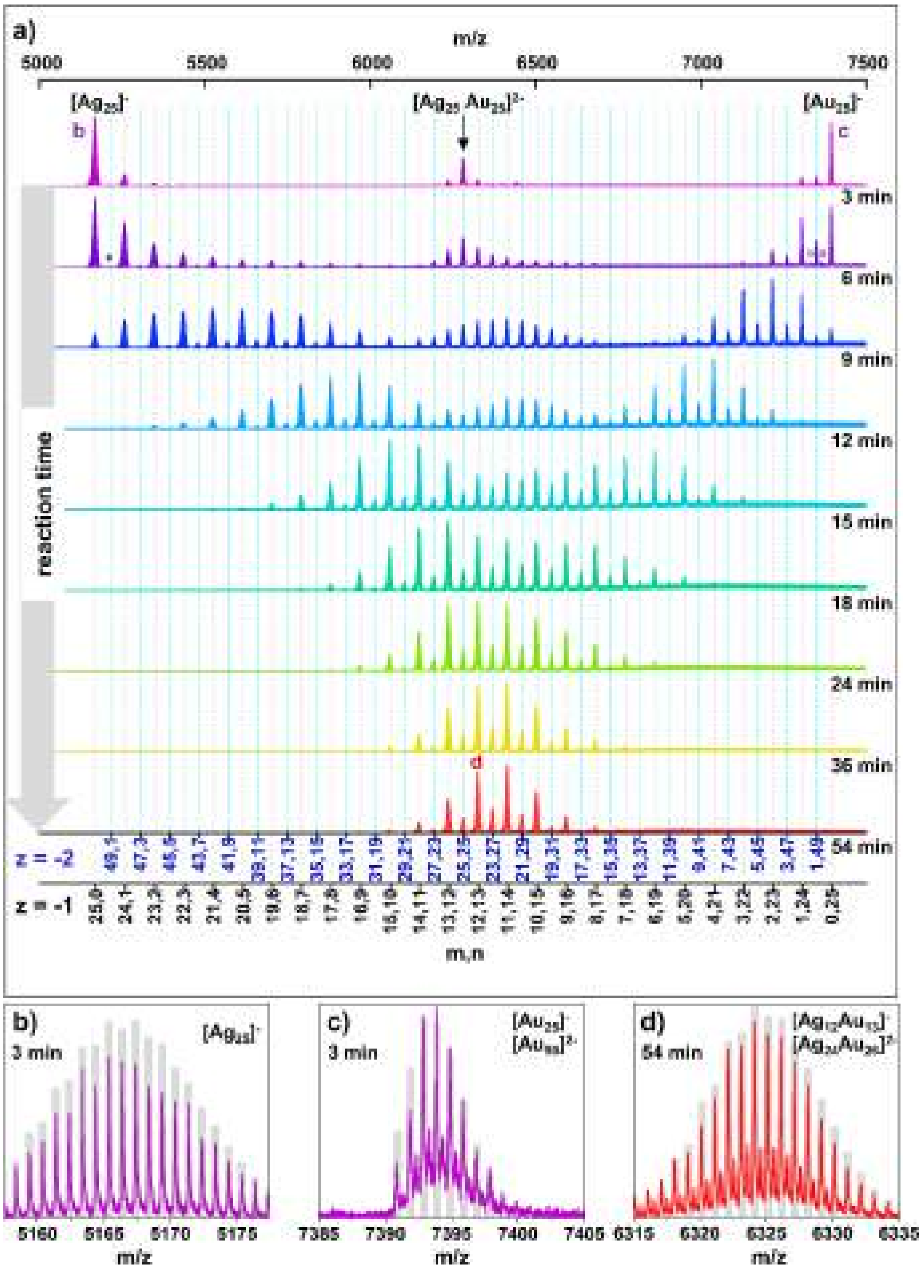

Figure 1. (a) Time dependent changes in the mass spectra of a 1:1 (40:40 nmol L^{-1}) mixture of $[Au_{25}(PET)_{18}]^-$ and $[Ag_{25}(DMBT)_{18}]^-$ over a 54 min time scale after mixing. Pairs of integers m,n label either $[Ag_mAu_n]^-$ cluster monoanions (black scale) or $[Ag_mAu_n]^{2-}$ cluster dianions (blue scale). Gray grid lines are spaced by 89 u (the mass difference of Au and Ag) to guide the eye. The peaks on the gray grid lines correspond to both monomers $[Ag_mAu_{25-m}]^-$ and the corresponding doubly charged dimers $[Ag_{2m}Au_{50-2m}]^{2-}$ with even number of silver and gold atoms of the same m/z. Note that due to the resolved isotopic patterns, the relative intensities of both species can be deconvoluted. The cyan colored grid lines (also spaced by 89 u) correspond to doubly charged dimers with odd numbers (total) of silver and gold atoms. The peak labeled with an asterisk in the mass spectrum taken at 6 min reaction time refers to $[Ag_{49}Au]^{2-}$. Peaks marked with a circle at 6 min correspond to triply charged trimers $[AgAu_{74}(SR)_{54}]^{3-}$ and $[Ag_2Au_{73}(SR)_{54}]^{3-}$. The peaks labeled with "b", "c", and "d" correspond to the clusters shown in the zoom plots b–d. (b) Isotopic distribution of $[Ag_{25}]^-$ after a reaction time of 3 min. Only peaks separated by 1 u are observed which shows that doubly charged $[Ag_{50}]^{2-}$ clusters are not present. Gray bars refer to the calculated (natural) isotopic pattern of $[Ag_{25}]^-$. (c) (Ligand-associated) Isotopic distribution of $[Au_{25}]^-$ after a reaction time of 3 min. In addition to $[Au_{25}]^-$, $[Au_{50}]^{2-}$ clusters are also present as indicated by additional peaks between the singly spaced $[Au_{25}]^-$ signals. Gray bars correspond to the calculated isotopic distribution of $[Au_{25}]^-$. (d) Isotopic distribution of $[Ag_{12}Au_{13}]^-$ after a reaction time of 54 min with underlying signal of doubly charged $[Ag_{24}Au_{26}]^{2-}$. Gray bars refer to the calculated isotopic distribution of $[Ag_{12}Au_{13}]^-$.

was not kinetically competitive with the dimer mediated process.

What is the driving force for dimer-mediated nanoalloying? In a recent study, equal amounts of isotopically pure $[^{107}Ag_{25}(SR)_{18}(PPh_4)]^-$ and $[^{109}Ag_{25}(SR)_{18}(PPh_4)]^-$ were reacted in room temperature solution to form a purely statistical distribution of $[^{107}Ag_{25-x}{}^{109}Ag_x(SR)_{18}]^-$ isotopologue products.[26] Here the driving force was clearly entropic with essentially no enthalpic contributions. By contrast, enthalpic contributions might be expected to become more important when alloying two different metals by an intercluster reaction. We recently found in the "$[Au_{25}(PET)_{18}]^-$ + $[Ag_{44}(FTP)_{30}]^{4-}$" reaction system (FTP is 4-fluorothiophenol), that although metal atom exchange starts from the outside of the M_{44} unit, i.e., in the staples, the introduced gold atoms can subsequently insert themselves into the cluster cores. Such swapping rearrangement occurs in what is presumably a thermally activated "nanogymnastic fashion" to form the most stable isomers in a matter of minutes.[27] How the initial metal exchange between two individual, negatively charged, ligand-interleaved, and staple-protected clusters starts is presently an open question. So far the picture is based only on DFT calculations of plausible intermediates.[8,28] To help clarify this further, it would be useful to provide some first order kinetic data for the three most important mechanistic steps in the overall intercluster reaction: dimer formation, metal atom exchange, and dimer dissociation. This is the motivation for the present study.

Of particular interest for the mechanistic understanding are reactions between isostructural clusters. Arguably, the simplest case concerns the eight-electron superatom[29−31] species $[Au_{25}(SR)_{18}]^-$ and $[Ag_{25}(SR)_{18}]^-$. Their reaction leads to the formation of all possible alloy clusters while always preserving 25 metal atoms and 18 ligands in the mixed monomer clusters.[28] Here we show systematic, time-resolved anion mass spectrometry measurements for the intercluster exchange reaction between $[Ag_{25}(DMBT)_{18}]^-$ and $[Au_{25}(PET)_{18}]^-$ in solution on a time scale of up to 60 min after mixing—resolving both the changing monomer compositions and concentrations and also probing those of the transiently formed dimers. Additional CID studies as a function of reaction time reveal that the fragmentation behavior of dimers qualitatively changes as the reaction proceeds and that the stability of the mixed dimers increases with mixing degree within the component monomers.

Note that specific electrospray conditions can also lead to some dimer formation in gas phase. In fact, the formation of dimers of $[Au_{25}(SR)_{18}]^-$ clusters was first studied under controlled electrospray conditions.[32] However, there are meanwhile multiple reports strongly indicating the existence of such dimers in solution and solid phase too. For example, Liu et al. reported $Ag_2Au_{50}(PET)_{36}$ dimers in solution which showed distinct optical and electronic properties, compared to those of the $Au_{25}(SR)_{18}$ clusters also present.[33] The crystal structure of this dimer was also solved. Linear polymers of $Au_{25}(SBu)_{18}$ clusters were also observed in the crystalline state.[34] Cations are known to induce dimerization of $Ag_{29}(BDT)_{12}$ clusters as well.[35] All such studies clearly indicate that the formation of dimers of clusters is not limited to selected mass spectrometric conditions but that extensive dimerization may occur spontaneously in solution or solid state as well.

In this study we have used mass spectrometry to probe dimerization induced intercluster reactions in room temperature solutions under conditions in which ion densities were too low to allow for additional dimer formation in gas phase. On the basis of the mass spectrometric data, we have modeled the kinetics of this intercluster reaction using several different mechanistic schemes which require the exchange reaction to take place *exclusively* within transiently formed dimers. The best fitting model was able to qualitatively and quantitatively describe the experimental observations. The resulting rate constants turned out to provide physically reasonable constraints on the time scales of the underlying processes.

To our knowledge this is the first quantitative kinetics study for any intercluster/nanoalloying reaction in solution. The level of agreement between best fitting simulation and experimental data extending over time scales of more than 50 min following mixing strongly supports the dimer mediated reaction hypothesis. We demonstrate that multiple, sequential dimerization and dissociation steps are involved in the chemistry, and we determine the magnitudes of the associated rate constants and from this obtain insights into the underlying atomic scale rearrangements.

■ RESULTS AND DISCUSSION

Mass Spectrometry and Collision Induced Dissociation. *ESI-MS.* Both $[Au_{25}(PET)_{18}]^-$ [36,37] and $[Ag_{25}(DMBT)_{18}]^-$ [38] were synthesized following previously reported methods (see the Supporting Information). The kinetics of the "$[Ag_{25}(DMBT)_{18}]^-$ + $[Au_{25}(PET)_{18}]^-$" reaction system was monitored using a high resolution Bruker timsTOF mass spectrometer system equipped with an ESI source. This ensures a typical mass resolution exceeding 25 000 which is sufficient to resolve the isotopic patterns of both singly negatively charged monomers and doubly negatively charged dimers (m/z 5000−7500; see Figure 1), which are the only metal containing species observable by ESI-MS with significant abundance. Prior to the kinetics measurements, ESI conditions were optimized such that intensities of $[Au_{25}(PET)_{18}]^-$ and $[Ag_{25}(DMBT)_{18}]^-$ were comparable for similar cluster concentrations for quantitative analyses. As dimers are more prone to fragmentation than monomers, mild electrospray conditions were chosen. The optimized measurement conditions and parameters are given in the Supporting Information (which also includes a description of the cluster synthesis and ESI mass spectra of the pure cluster solutions in Figure S1).

A typical series of averaged mass spectra of a 1:1 (40:40 nmol L^{-1}) mixture of $[Ag_{25}(DMBT)_{18}]^-$ and $[Au_{25}(PET)_{18}]^-$ taken at different reaction times is shown in Figure 1a. From previous studies it is known that in addition to metal atom exchanges, ligand exchange reactions can also occur in monothiolate-protected clusters reactions.[39−43] As the isomeric ligands DMBT and PET share the same mass and as the same number of 18 and 36 ligands is always maintained in the monomers and dimers, respectively, the DMBT-PET exchange cannot be followed by MS alone.

However, the energy changes upon ligand exchange are rather small. For the hypothetical ligand exchange reaction $[Ag_{25}(DMBT)_{18}]^-$ + $[Au_{25}(PET)_{18}]^-$ → $[Au_{25}(DMBT)_{18}]^-$ + $[Ag_{25}(PET)_{18}]^-$ we calculate (DFT, BP-86) an endothermicity of 1.26 eV, i.e., less than 0.1 eV per ligand. In similar test calculations for the single-metal exchanged clusters $[AgAu_{24}(DMBT/PET)_{18}]^-$ and $[Ag_{24}Au(DMBT/PET)_{18}]^-$ we found a negligible ligand influence on the respective isomer order (see Supporting Information for more details and Tables S1 and S2).

Therefore, in the following we will ignore the role of the ligands and from this point on we will label all species only according to the number of their silver and gold atoms. The dominant peaks visible in the spectrum after 3 min shown in Figure 1a belong to the monomers $[Ag_{25}]^-$ (m/z 5167) and $[Au_{25}]^-$ (m/z 7394) and to the dimer $[Ag_{25}Au_{25}]^{2-}$ (m/z 6280). Note that several isomers of $[Ag_{25}Au_{25}]^{2-}$ can exist in principle. For example, smaller amounts of both $[AgAu_{24}]^-$

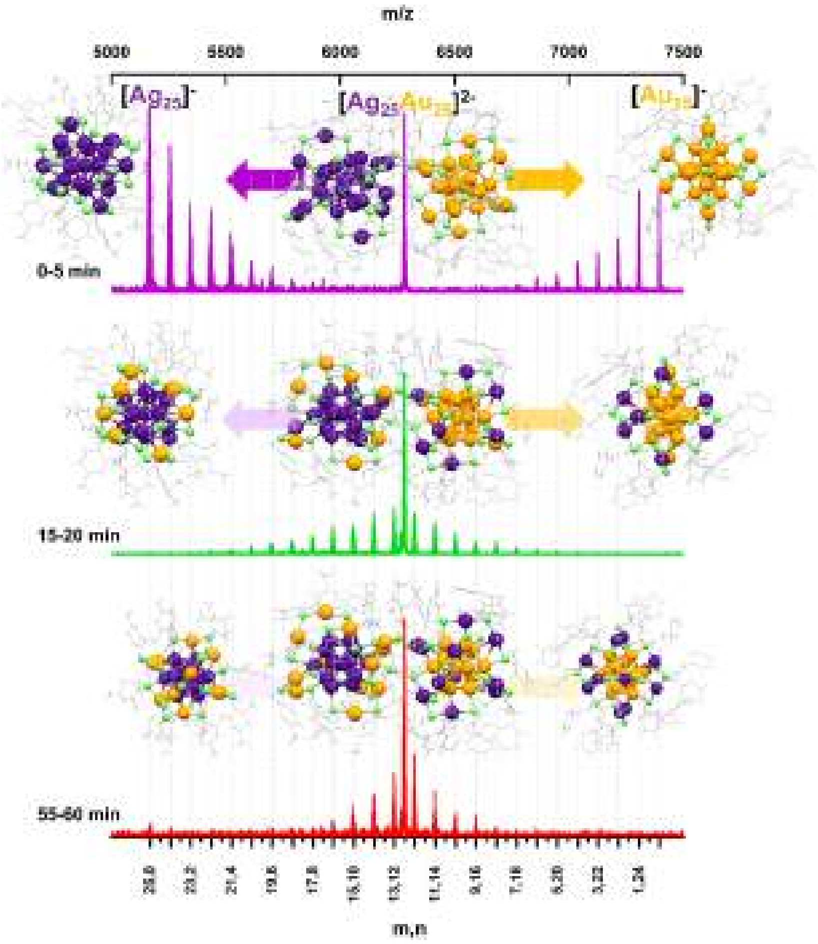

Figure 2. Collision induced dissociation of $[Au_{25}Ag_{25}]^{2-}$ (m/z = 6280) clusters at 30 eV laboratory collision energy after different reaction times measured on a Waters Synapt G2Si HDMS mass spectrometer. After short reaction times of up to 5 min, the formed $[Au_{25}Ag_{25}]^{2-}$ isomers dissociate primarily to $[Ag_{25}]^-$ and $[Au_{25}]^-$ as well as to a lesser degree to more mixed monomer $[Ag_mAu_{25-m}]^-$ anions, e.g., $[Ag_{21}Au_4]^-$ and $[Ag_4Au_{21}]^-$. After long reaction times of up to 60 min, the main fragments are well mixed $[Ag_{13}Au_{12}]^-$ and $[Ag_{12}Au_{13}]^-$ ions pointing to a higher mixing degree of the formed $[Au_{25}Ag_{25}]^{2-}$ isomers. The integrated intensity of the fragments decreases with reaction time which can be explained with a higher stability of the more mixed $[Au_{25}Ag_{25}]^{2-}$ cluster isomers like $[(Ag_{12}Au_{13})(Ag_{13}Au_{12})]^{2-}$. The concentration and mixing ratio of the $[Ag_{25}]^-$ and $[Au_{25}]^-$ clusters were chosen like in the kinetics experiment, i.e., 40:40 nmol L^{-1}.

and $[Ag_{24}Au]^-$ monomers are already present after short reaction times. Therefore, a fraction of the $[Ag_{25}Au_{25}]^{2-}$ signal is also due to $[(Ag_{24}Au)(AgAu_{24})]^{2-}$. Note that the round brackets refer to the two monomeric subunits of the corresponding doubly charged dimer.

Expanding on previous reports[1,28,32] of the initially formed dimer $[(Ag_{25})(Au_{25})]^{2-}$, we have recorded the time-dependent intensities of all dimers $[Ag_mAu_{50-m}]^{2-}$ with m = 0−49 together with those of the singly charged reaction products $[Ag_mAu_{25-m}]^-$ (m = 1−24), i.e., up to the fully mixed $[Ag_{13}Au_{12}]^-$ (m/z 6236) and $[Ag_{12}Au_{13}]^-$ (m/z 6325) clusters. Note that we use the notation $[Ag_mAu_{50-m}]^{2-}$ with m = 0−49 (i.e., without round brackets) to indicate all possible isomeric dimer dianions each of which comprises only monomers with 25 metal atom nuclearity. Closer inspection of the mass spectra shows that dimerization is clearly favored when gold is present in the monomers (note that dimerization is also observed in comparably concentrated pure $[Au_{25}(PET)_{18}]^-$ solutions (data not shown)). While $[Ag_{50}]^{2-}$ dimers are not present after 3 min (Figure 1b), $[Au_{50}]^{2-}$ dimers are clearly detected (Figure 1c) with comparable intensities to $[Ag_{25}Au_{25}]^{2-}$. In addition, the dianion $[AgAu_{49}]^{2-}$ shows a ~15-fold higher intensity compared to $[Ag_{49}Au]^{2-}$ (peak labeled with an asterisk in Figure 1a). Dianionic species with an even number of gold and silver atoms $[Ag_{2m}Au_{50-2m}]^{2-}$ share the same m/z ratio as monoanionic species $[Ag_mAu_{25-m}]^-$, and their peaks overlap. Therefore, only dimers $[Ag_{2m-1}Au_{50-(2m-1)}]^{2-}$ with odd numbers of silver and gold atoms (i.e., peaks lying on the cyan colored grid lines) are directly visible in Figure 1a. We note, however, that in all cases we can clearly differentiate between monomers and dimers due to the resolved isotopic patterns (Figure 1b−d). On the gold side also less intense signals of triply charged trimers are visible, i.e., $[Ag_mAu_{75-m}(SR)_{54}]^{3-}$ with m = 1−5, which however were not further taken into account in this analysis due to their low intensity (see Figure S2).

After a longer reaction time, the dimer distribution centered around $[Ag_{25}Au_{25}]^{2-}$ broadens and other dimers such as $[Ag_{27}Au_{23}]^{2-}$ (m/z 6191) and $[Ag_{23}Au_{27}]^{2-}$(m/z 6370) appear (Figure 1a, 12 min). At the same time, more mixed monomers grow successively from the silver and gold sides of the mass spectra until an equilibrium state is reached after ~45 min with $[Ag_{11}Au_{14}]^-$ and $[Ag_{12}Au_{13}]^-$ (Figure 1a and Figure 1d) being the dominant monomer species plus smaller contributions of monomers $[Ag_mAu_{25-m}]^-$ with m = 8−15 and dimers $[Ag_mAu_{50-m}]^{2-}$ with m = 18−28 (Figure 1a). The slight

Scheme 1. Illustration of the Different Reactions Considered[a]

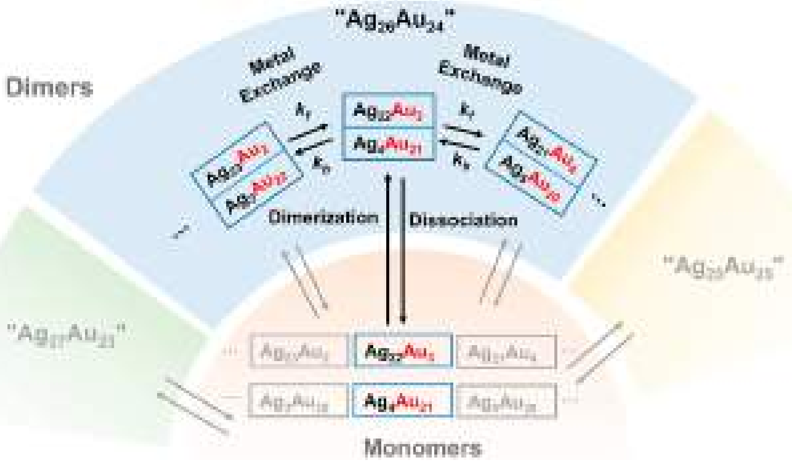

[a]Any combination of two monomers $[Ag_mAu_{25-m}]^-$ and $[Ag_nAu_{25-n}]^-$ can react to form a dimer with the sum formula $[Ag_{m+n}Au_{50-m-n}]^{2-}$ but still consisting of the well-defined monomeric subunits $[(Ag_mAu_{25-m})]^-$ and $[(Ag_nAu_{25-n})]^-$. Each dimer can isomerize via (multiple) metal atom exchanges between the monomeric subunits and separate into the respective monomers potentially at any time. Exchange rate constants k_f and k_b refer to reactions that increase (k_f) or decrease (k_b) the entropy in the dimers, respectively. As an example, we show the m,n combinations 22,3 and 4,21 for illustration. The two monomers $[Ag_{22}Au_3]^-$ and $[Ag_4Au_{21}]^-$ dimerize to form initially $[(Ag_{22}Au_3)(Ag_4Au_{21})]^{2-}$. This dimer can isomerize by metal exchange either to $[(Ag_{21}Au_4)(Ag_5Au_{20})]^{2-}$ or to $[(Ag_{23}Au_2)(Ag_3Au_{22})]^{2-}$. The isomerized dimers can undergo further metal exchange or dissociate to monomers.

asymmetry toward a higher gold content with respect to a perfect 1:1 cluster ratio where $[Ag_{12}Au_{13}]^-$ and $[Ag_{13}Au_{12}]^-$ should be the dominant species can be most likely traced back to weighing and dilution errors (the concentrations of 40 nmol L^{-1} were reached by a two-step dilution). For $[Ag_{25}]^-$:$[Au_{25}]^-$ mixing ratios differing from 1:1 the equilibrium distribution is shifted according to the silver:gold atom ratio. Hence, for a mixing ratio of $[Ag_{25}]^-$:$[Au_{25}]^-$ = 5:3 (100:60 nmol L^{-1}) the equilibrium distribution is approximately centered at around $[Ag_{16}Au_9]^-$, i.e., $\frac{5\cdot 25}{3\cdot 25+5\cdot 25}\cdot 25 \approx 16$ Ag and $\frac{3\cdot 25}{3\cdot 25+5\cdot 25}\cdot 25 \approx 9$ Au atoms (Figure S9b). As monoanion:dianion ratios (e.g., $[Ag_{12}Au_{13}]^-$:$[Ag_{24}Au_{26}]^{2-}$) stay constant after ~25 min, we conclude that from then on dimers and monomers are in dynamic equilibrium. Consequently, formation of stable dianions consisting of coalesced monomeric subunits (not able to dissociate back to monomers) can be ruled out. Otherwise, all monomers would end up in these stable dimers or in even higher oligomers, which is clearly not the case on a time scale of up to ~60 min.

Collision Induced Dissociation (CID). CID measurements were carried out using a Waters Synapt G2Si HDMS mass spectrometer equipped with an ESI source. To obtain a first order measure of reaction-time-dependent changes in the constituents of dimers with a given m/z ratio, we collided mass selected ions with nitrogen in a collision cell held at 0.02 mbar keeping the collision energy (E_{lab} = 30 eV) constant while measuring the corresponding fragment ion mass spectra. The fragments always contain 25 metal atoms indicating that the dimers consist of two weakly bound monomeric subunits with 25 metal atoms each. As an example, the CID of $[Ag_{25}Au_{25}]^{2-}$ (m/z 6280; see Figure 2) at different reaction times results in different fragmentation patterns. Initially, the dominant fragments are $[Ag_{25}]^-$, $[Au_{25}]^-$ plus smaller contributions of mixed clusters with up to about six exchanged metal atoms. After longer reaction times the fully mixed monomers $[Ag_{13}Au_{12}]^-$ and $[Au_{12}Ag_{13}]^-$ dominate. Obviously, for a given dimer composition, various isomers coexist confirming that the dimers are active participants in the reaction. The decreased fragmentation efficiency of $[Ag_{25}Au_{25}]^{2-}$ after longer reaction times points to a higher stability of late $[Ag_{25}Au_{25}]^{2-}$ species (e.g., $[(Ag_{12}Au_{13})(Ag_{13}Au_{12})]^{2-}$) compared to $[Ag_{25}Au_{25}]^{2-}$ species that are formed in the beginning of the reaction (e.g., $[(Ag_{25})(Au_{25})]^{2-}$ or $[(Ag_{24}Au)(AgAu_{24})]^{2-}$). Nevertheless, these "more mixed" dimers such as $[(Ag_{12}Au_{13})(Ag_{13}Au_{12})]^{2-}$ are apparently still able to dissociate back to the respective monomers in solution (for which a dynamic dimer—monomer equilibrium is observed).

Kinetic Model. Next we fit the experimental data, which comprises reaction-time-dependent mass spectral signal intensities (assumed to be directly proportional to solution concentrations of the corresponding anionic species) for several initial $[Ag_{25}]^-$:$[Au_{25}]^-$ composition ratios. For this, we use three related kinetics models (simulations 1—3) that have common key mechanistic assumptions. Due to the complexity and the large number of reactions involved, we stress at the outset that we do not aim to simulate the experiment quantitatively. Instead, we want to compare the model with the experimental findings, narrow down the range of rate constants which still provide a reasonable description, and finally check the physical plausibility.

Key Assumptions. All simulations are based on the sequence of events shown in Scheme 1. We start with the most simple assumptions and then continuously improve the agreement with the experiment by refining the input parameters. The exchange kinetics was modeled by standard matrix algebra suites in MATLAB (see the Supporting Information, Scheme S1, and Figure S4 for more details) and by solving all kinetic differential equations numerically.

The key assumptions of our model are the following.

(1) Monomers always contain 25 metal atoms, and dimers contain 50 metal atoms reflecting the experimental findings.

(2) Two monomers $[Ag_mAu_{25-m}]^-$ and $[Ag_nAu_{25-n}]^-$ can dimerize with a bimolecular rate constant k_{dim}, and the

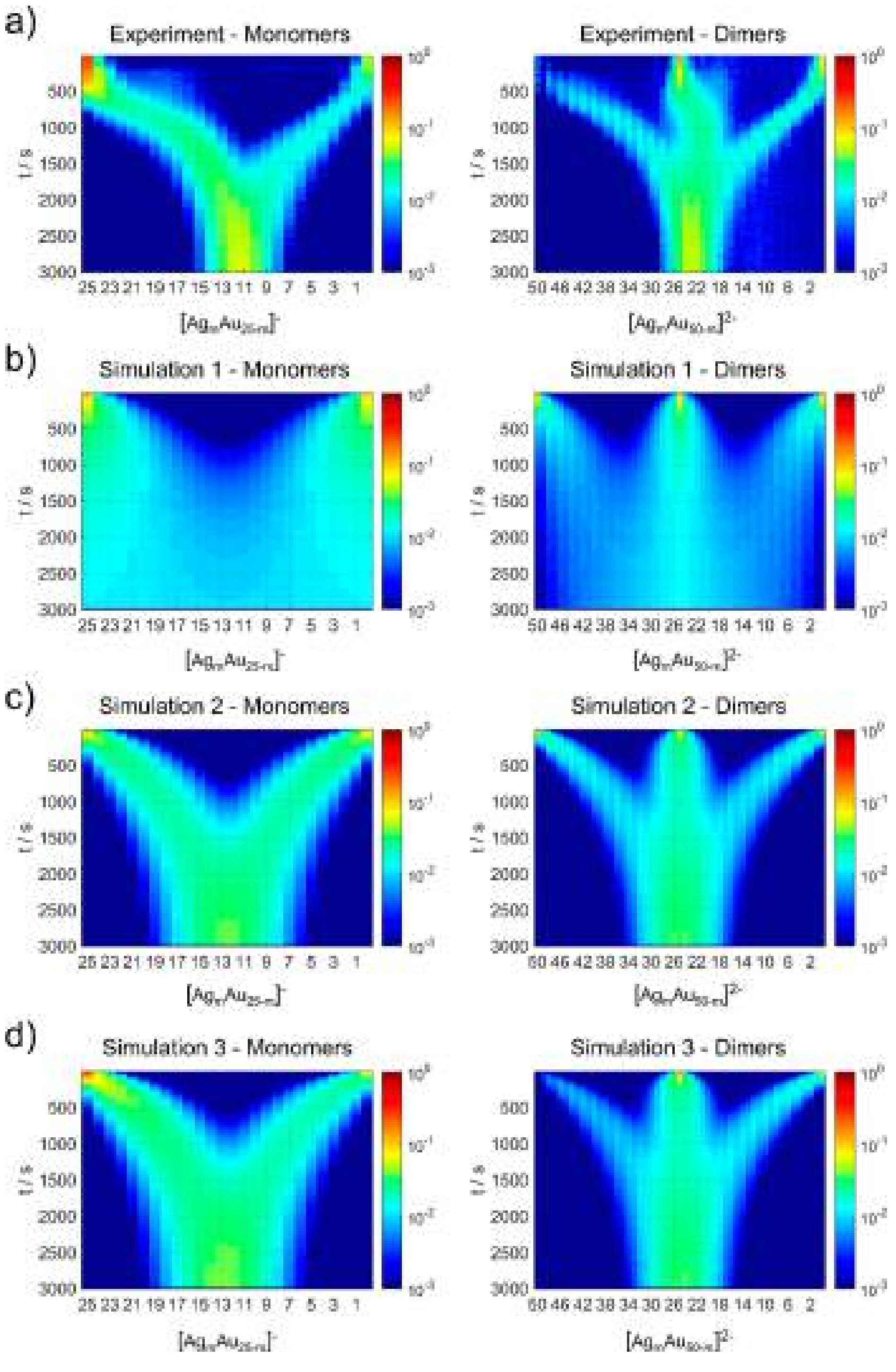

Figure 3. Contour plots of monoanionic monomer and dianionic dimer intensities for the exchange reaction between $[Ag_{25}]^-$ and $[Au_{25}]^-$. (a) Experiment (mixing ratio 40:40 nmol L^{-1}). (b) Simulation 1 (best fitting rate constants): $k_{dim} = 3.2 \times 10^{-3}$ L $nmol^{-1}$ s^{-1}, $k_{diss} = 3.2 \times 10^{-2}$ s^{-1}, and $k_{ex} = 3.2 \times 10^{-2}$ s^{-1}. (c) Simulation 2 (best fit): $k_{dim} = 1 \times 10^{-2}$ L $nmol^{-1}s^{-1}$, $k_{diss} = 1 \times 10^{-1}$ s^{-1}, and $k_{ex} = 3.2 \times 10^{-2}$ s^{-1} (scaled by the probability factors from eqs 2 and 3). (d) Simulation 3 (like simulation 2 but additionally k_{dim} was scaled by the factor f_{Au}): optimum rate constants are $k_{dim} = 1 \times 10^{-2}$ L $nmol^{-1}s^{-1}$, $k_{diss} = 5.6 \times 10^{-2}$ s^{-1}, and $k_{ex} = 3.2 \times 10^{-2}$ s^{-1}. Starting concentrations of all simulations were chosen as in the experiment, i.e., $c([Au_{25}]^-_{t=0}) = 40$ nmol L^{-1}, $c([Au_{25}]^-_{t=0}) = 40$ nmol L^{-1} (all other species were set to concentration zero). Note that in the case of pure gold cluster solutions, dimers were already present at time zero. However, as the dimerization proceeds much faster than the metal exchange, the presence of dimers at zero time can be neglected in the simulations.

formed dimers can dissociate back with a unimolecular rate constant k_{diss}.

(3) Dimers always comprise two monomeric subunits consisting of 25 atoms which can exchange single metal atoms with a unimolecular rate constant k_{ex} (and can eventually dissociate). As a consequence, for each dimeric species with composition $[Ag_{m+n}Au_{50-m-n}]^{2-}$, there are several topologically different isomers: $[(Ag_{m-x}Au_{25-m+x})(Ag_{n+x}Au_{25-n-x})]^{2-}$ (where m and n each range from 0–25, $x \leq m$, and $x \leq (25 - n)$). We

Table 1. Summary of Simulations 1−3 As Discussed in the Text[a]

simulation	P_{ex}	f_{Au}	k_{dim}, L nmol^{-1} s^{-1}	k_{diss}, s^{-1}	k_{ex}, s^{-1}	k_{dim}:k_{diss}
1	constant	constant (=1)	3.2×10^{-3}	3.2×10^{-2}	3.2×10^{-2}	0.10
2	variable	constant (=1)	1×10^{-2}	1×10^{-1}	3.2×10^{-2}	0.10
3	variable	variable	1×10^{-2}	5.6×10^{-2}	3.2×10^{-2}	0.18

[a] The respective rate constants are obtained from a least squares fit. Overall, simulation 3 agrees best with experiment. This simulation includes an increased dimerization rate for gold rich clusters (via f_{Au}). See text for details.

allow exchange of metal atoms only within these transient dimers.

In order to compare experiment and simulation, we deconvolute the mass spectra into monomers and dimers, respectively (see the Supporting Information and Figure S3 for more details). The experimental ion intensities of monoanions and dianions for a 40:40 nmol L^{-1} mixing ratio of $[Ag_{25}]^-$ and $[Au_{25}]^-$ clusters are shown as a contour plot in Figure 3a. Each ion intensity was normalized to the total ion signal in order to account for instabilities of the ion source (see Supporting Information).

Simulation 1. In a first step we assume that the rate constants for dimerization, dissociation, and metal atom exchange are independent of the cluster composition; i.e., the kinetics is defined by only three rate constants k_{dim}, k_{diss}, and k_{ex}. Note that this is somewhat unphysical since the exchange rate constant is independent of the relative gold/silver content, but it is the most basic assumption that we can make. Simulated concentrations were treated like the experimental data (see Supporting Information) and have therefore been normalized to the sum of all ion concentrations. For all simulations a "dead time" of 20 s was chosen; i.e., at time zero in Figure 3a the reaction is assumed to have already proceeded for 20 s after mixing. Note that the choice of this "dead time" is not critical with respect to the overall kinetics as it mainly affects the time dependence of the starting species $[Ag_{25}]^-$, $[Au_{25}]^-$, and $[(Ag_{25})(Au_{25})]^{2-}$.

To find the best possible agreement between simulation and experiment, we simulated the kinetics for 13 exponentially equidistant rate constants in the range of 10^{-4} to 1 (in units of s^{-1} or L nmol^{-1} s^{-1}, respectively) resulting in 2197 ($13 \times 13 \times 13$) possible combinations.

As the dimer:monomer ratios can be affected to some degree by the mass spectrometer settings, we have chosen not the relative ion intensities but the time $t_{max,i}$ when each species i passes through its maximum concentration (as measured by ESI-MS signal) as the most robust target feature that has to be reproduced by the model. Therefore, the mean squared deviation between model and experiment was calculated with eq 1 for each simulation,

$$\chi^2 = \sum_{i=1}^{77} (t_{max,i}^{sim} - t_{max,i}^{exp})^2 \qquad (1)$$

where 77 is the total number of ion species (26 monoanions: $[Ag_mAu_{25-m}]^-$, $m = 0{-}25$ and 51 dianions $[Ag_mAu_{50-m}]^{2-}$, $m = 0{-}50$). Note that in the simulation all possible 351 dimer isomers $[(Ag_{m-x}Au_{25-m+x})(Ag_{n+x}Au_{25-n-x})]^{2-}$ (m and n each range from 0−25, $x \leq m$, and $x \leq (25-n)$) have been taken into account and summed up afterward to the corresponding $[Ag_{m+n}Au_{50-m-n}]^{2-}$ ($m + n = 0{-}50$) species to allow comparison with the experiment. The number of possible dimers (351) can be determined by calculating all possible combinations of the 26 monomer species (see Supporting Information). The simulations with the lowest χ^2 values were further inspected by eye to choose the simulation with the best possible agreement in terms of both $t_{max,i}$ and relative ion intensities.

For simulation 1, a rather poor agreement was found independent of the choice of rate constants. The best possible level of agreement is shown in Figure 3b for the parameters $k_{dim} = 3.2 \times 10^{-3}$ L nmol^{-1} s^{-1}, $k_{diss} = 3.2 \times 10^{-2}$ s^{-1}, and $k_{ex} = 3.2 \times 10^{-2}$ s^{-1} (see Table 1). Compared to the experiment, the predicted cluster distributions at long reaction times are much broader and the distribution widens early. For very long reaction times (>3000 s, not shown), the monomers become evenly distributed and the dimer distribution is only determined by the number of possible isomers with a maximum of 13 for $[Ag_{25}Au_{25}]^{2-}$. The reason is the composition independent exchange rate constant k_{ex}, which leads to an even partitioning of all clusters in the equilibrium. The experimental data show that this is clearly not the case. Obviously, the model lacks a "driving force" that drags the clusters toward a narrower composition distribution.

Simulation 2. In simulation 2, we continue to keep the rate constants for the dimerization and dissociation steps constant (i.e., independent of Ag:Au composition of the respective species) but now scale the exchange rate constant according to the probability of finding a silver or gold atom in the respective monomer subunit of the dimer. We assume that all metal atoms can be exchanged independent of their position in the subunit (i.e., core, icosahedral shell, or staple atoms can be exchanged with the same probability). As an example, for a $[(Ag_{25})(Au_{25})]^{2-}$ dimer consisting of the two monoanionic subunits $[Ag_{25}]^-$ and $[Au_{25}]^-$, the probability factor for silver/gold exchange according to the scheme $[(Ag_{25})(Au_{25})]^{2-} \rightarrow [(Ag_{24}Au)(AgAu_{24})]^{2-}$ is 1. If the $[Ag_{25}Au_{25}]^{2-}$ dimer consists of the subunits $[Ag_{24}Au]^-$ and $[AgAu_{24}]^-$, the combined probability factor is $\frac{24}{25}\cdot\frac{24}{25} = 0.9216$ in the direction where the dimer becomes more mixed, $[(Ag_{24}Au)(AgAu_{24})]^{2-} \rightarrow [(Ag_{23}Au_2)(Ag_2Au_{23})]^{2-}$, and $\frac{1}{25}\cdot\frac{1}{25} = 0.0016$ in the direction $[(Ag_{24}Au)(AgAu_{24})]^{2-} \rightarrow [(Ag_{25})(Au_{25})]^{2-}$ where the dimer becomes less mixed. The remaining probability of 0.0768 corresponds to the "null" reaction where two gold or two silver atoms are swapped between the monomeric subunits. The differences in the probability factors can be interpreted as an entropic driving force that drags the cluster distribution toward a state with higher entropy, while the composition of the clusters in equilibrium is controlled by the mixing ratio of $[Ag_{25}]^-$ and $[Au_{25}]^-$, i.e., $[Ag_{13}Au_{12}]^-$ and $[Ag_{12}Au_{13}]^-$ for a 1:1 mixture. For the general case, $[(Ag_mAu_{25-m})(Ag_nAu_{25-n})]^{2-}$ (with $m > n$), the combined probabilities for the forward and backward metal exchange reactions are given by

$$P_f^{ex} = \frac{m}{25}\cdot\frac{25-n}{25} \qquad (2)$$

$$P_{\mathrm{b}}^{\mathrm{ex}} = \frac{n}{25} \cdot \frac{25 - m}{25} \tag{3}$$

We define the forward reaction, occurring with k_f, where the silver atom is always transferred from the silver richer subunit of the dimer to the silver poorer subunit. Accordingly, the gold atom is transferred from the gold richer subunit to the gold poorer subunit. Note that by that definition the forward mixing reaction always leads to a higher total entropy in the products compared to the educts while the opposite is true for the backward reaction. As an example, for the dimer $[(Ag_{22}Au_3)(Ag_4Au_{21})]^{2-}$ the forward reaction produces $[(Ag_{21}Au_4)(Ag_5Au_{20})]^{2-}$ and the backward reaction leads to $[(Ag_{23}Au_2)(Ag_3Au_{22})]^{2-}$. For a quantitative calculation of the reaction entropy and the apparently less significant reaction energies as determined by explorative DFT calculations, see the Supporting Information.

Accordingly, in simulation 2 we scale the exchange rate constant k_{ex} by $P_{\mathrm{f}}^{\mathrm{ex}}$ and $P_{\mathrm{b}}^{\mathrm{ex}}$, resulting in 600 individual rate constants for the metal atom exchange reactions.

Analogous to simulation 1, the best fitting parameter set was determined which is shown in Figure 3c for $k_{\mathrm{dim}} = 1 \times 10^{-2}$ L nmol^{-1} s^{-1}, $k_{\mathrm{diss}} = 1 \times 10^{-1}$ s^{-1}, and $k_{\mathrm{ex}} = 3.2 \times 10^{-2}$ s^{-1} (see Table 1). The exchange rate constant k_{ex} has the biggest influence on the kinetic development of the clusters determining $t_{\mathrm{max,i}}^{\mathrm{exp}}$ while k_{dim} and k_{diss} mainly determine the intensities of monoanions and dianions. This holds true as long as k_{dim} does not become too small and rate determining. Therefore, χ^2 values of simulations with $k_{\mathrm{ex}} = 3.2 \times 10^{-2}$ s^{-1}, k_{dim}:k_{diss} ratio of 0.1, and k_{dim} in the range of 1.8×10^{-3} to 1×10^{-1} L nmol^{-1} s^{-1} agree well within a standard deviation of 1%. In Figure S5 we contrast the experimentally observed kinetics of $[Ag_{25}Au_{25}]^{2-}$ to the integrated $[Ag_{25}Au_{25}]^{2-}$ concentration of the model. In addition, we show the normalized concentrations of all 13 $[(Ag_{25-x}Au_x)(Ag_xAu_{25-x})]^{2-}$ isomers (not individually accessible to MS) from simulation 2. The experiment and the simulation have in common that the integrated signal of $[Ag_{25}Au_{25}]^{2-}$ traverses a minimum with $[(Ag_{25})(Au_{25})]^{2-}$ being the dominant species in the beginning of the reaction and $[(Ag_{13}Au_{12})(Ag_{12}Au_{13})]^{2-}$ close to the equilibrium.

Given the few assumptions in the model, the qualitative agreement with the experiment is surprisingly good and allows the conclusion that the metal atom exchange proceeds more slowly in higher entropy dimers. Because of the statistical Bernoulli approach (eqs 2 and 3) the equilibrium distributions of the monomers and dimers of simulation 2 equal a binomial distribution. As shown in Figure S6, the experimental equilibrium distributions are somewhat narrower than the binomial distributions.

In contrast to the experimental data, the kinetics of the silver and gold sides in simulation 2 is exactly equal and symmetric. In the experiment, the monoanions generally show higher intensities on the silver side, especially at the beginning of the reaction, which can partially be explained by the better ability of gold clusters to form dimers.

Simulation 3 is based on simulation 2, but we now account for the unequal ability of the monomers to form dimers based on their composition. In contrast to $[Au_{25}]^-$, we do not observe (homo)dimers of $[Ag_{25}]^-$. It is still an open question which parameters dominate the ability to form dimers (e.g., attractive van der Waals forces between the clusters,[28,32] π−π interactions[28] or metallophilic[44−46] interactions between the metal atoms in the staples[28,32] (including possibly gold dimer and/or gold nanowire formation via a "twist-and-lock" mechanism[8,34]). On the basis of recent DFT-based calculations, including relativistic semicore pseudopotentials, the dimer binding energies of $[Au_{50}]^{2-}$ and $[(Ag_{25})(Au_{25})]^{2-}$ are 2.5 and 2.1 eV, respectively, while $[Ag_{50}]^{2-}$ exhibits a significantly lower binding energy of only 0.97 eV.[8] This generally points to a better dimerization ability if gold is present in the monomers. On the other hand, the isotope exchange experiment of pure $[Ag_{25}(DMBT)_{18}]^-$ clusters[26] can only be explained by silver homo dimers as reaction intermediates. Possibly they are too weakly bound to survive the ionization process in our experiment. Recent NMR studies by Salassa et al. have shown that DMBT ligand exchange is occurring in room temperature $[Ag_{25}(DMBT)_{18}]^-$ solutions.[47] This intercluster ligand exchange can only take place through the formation of transient dimers, strongly supporting the assumption that intercluster metal exchange through transient dimers occurs in pure $[Ag_{25}(DMBT)_{18}]^-$ solutions as well.

In order to account for the asymmetry between gold and silver, in simulation 3 we loosely scale the dimerization rate constant k_{dim} by a factor f_{Au}, which accounts for the fraction of gold atoms in the reactants. As an example, for $[Ag_8Au_{17}]^- + [Ag_{15}Au_{10}]^-$, f_{Au} amounts to $\frac{17 + 10}{50} = 0.54$. The best agreement for simulation 3 with the experiment is obtained for the rate constants $k_{\mathrm{dim}} = 1 \times 10^{-2}$ L nmol^{-1} s^{-1}, $k_{\mathrm{diss}} = 5.6 \times 10^{-2}$ s^{-1}, and $k_{\mathrm{ex}} = 3.2 \times 10^{-2}$ s^{-1} (see Table 1 and Figure 3d). Other values of k_{dim} and k_{diss} give almost identical results as long the k_{dim}:k_{diss} ratio is kept at around ∼0.2. With the rate constants from simulation 2, the dimer-to-monomer ratio deviates by 40% between simulation and experiment. Simulation 3 is almost identical to simulation 2, except that (like in the experiment) the cluster distribution is now asymmetric with respect to the silver and gold sides, which is most obvious at short reaction times. In simulation 3 there are more gold rich dimers present, $[Ag_{50}]^{2-}$ is not formed, and there are less gold rich monomers present as a larger fraction of these is converted to dimers. Overall, the qualitative agreement with the experimental data has improved. Note that the choice of f_{Au} regarding the dimerization of pure $[Ag_{25}]^-$ clusters (for which f_{Au} equals zero in simulation 3) is uncritical with respect to the overall kinetics which is most obvious when comparing simulation 3 with simulation 2 ($f_{\mathrm{Au}} = 1$ for all dimerization steps). A comparison of other measured and simulated mixing ratios based on simulation 3 showing consistently good agreement is presented in Figures S7−S9. In Figure S10 we show the composition of the modeled $[Ag_{25}Au_{25}]^{2-}$ isomers at five time intervals including the three time intervals from the CID experiment (Figure 2) and contrast the findings to the experimental CID data where $[Ag_{25}Au_{25}]^{2-}$ was brought to collision with nitrogen to further support our modeling. Note that for all simulations shown, the optimized rate constants from simulation 3 were applied.

We next discuss our findings (based on simulation 3) in more detail and try to constrain the rate constants to narrower limits.

The exchange rate constant k_{ex} has the strongest impact on the kinetic development of the intercluster reaction defining $t_{\mathrm{max},i}^{\mathrm{exp}}$, whereas k_{dim} and k_{diss} mainly determine the intensities of monoanions and dianions. Hence, on the basis of our model, k_{ex} can be roughly restricted to the range 2×10^{-2} s^{-1} < k_{ex} < 5×10^{-2} s^{-1}. For a good agreement with the experimental data, the rate constants for dimerization and dissociation can be varied to some extent, but preferably, the k_{dim}:k_{diss} ratio must lie in the range 0.1−0.3. Only then the experimentally observed equilibrium monomer-to-dimer ratio of ∼1 is reproduced.

The dimerization rate constant cannot be arbitrarily small as it then becomes rate determining and the formation of mixed clusters proceeds too slowly. For good agreement with the experiment, $k_{\mathrm{dim}} \cdot c([\mathrm{M}_{25}]^-)$ must be at least of the order of the exchange rate constant k_{ex}. Hence, for a cluster concentration of 40 nmol L^{-1} and $k_{\mathrm{ex}} = 3.2 \times 10^{-2}\ \mathrm{s}^{-1}$, k_{dim} should be higher than $\sim 1 \times 10^{-3}$ L nmol^{-1} s^{-1}. In contrast to this lower limit, there exists no upper limit for k_{dim} kineticswise, i.e., in terms of $t_{\mathrm{max},i}$. If k_{dim} is increased, the predicted dimer-to-monomer ratio increases and deviates from the experimentally observed approximately 1:1 ratio (Figure 3a). Therefore, k_{diss} has to be adjusted bearing in mind the k_{dim}:k_{diss} ratio from Table 1.

Similar considerations apply to the dissociation rate constant k_{diss}. If k_{diss} is too small, early dimers like $[(\mathrm{Ag}_{25})(\mathrm{Au}_{25})]^{2-}$ or $[\mathrm{Au}_{50}]^{2-}$ are almost frozen out and monomeric product ions are formed insufficiently and on time scales that are not in line with the experimental findings. Hence, within our model, k_{diss} must be greater than or equal to $\sim 1 \times 10^{-2}\ \mathrm{s}^{-1}$. Similar to the case of k_{dim}, an upper limit for k_{diss} cannot really be given (as it also depends on k_{dim}).

Plausibility of Rate Constant Values. The physical upper limit for the dimerization rate constant of near-spherical, neutral molecules in solution is the diffusion limited case for which the rate constant is given by

$$k_{\mathrm{D}} = \frac{8}{3}\frac{k_{\mathrm{B}}T}{\eta}N_{\mathrm{A}} \tag{4}$$

where k_{B} is the Boltzmann constant, T is the temperature, N_{A} is the Avogadro constant, and η is the dynamic viscosity of the solvent (DMF).[48] With $\eta = 0.799 \times 10^{-3}$ Pa·s [49] and $T = 298$ K, k_{D} amounts to 8.3 L nmol^{-1} s^{-1}, which is approximately 3 orders of magnitude larger than typical dimerization rate constants from our simulations. In the case of charged molecules the diffusion limited rate constant of eq 4 must be multiplied by the Debye factor f_{Debye} which accounts for the Coulomb interaction between the ions.[50−52]

$$f_{\mathrm{Debye}} = \frac{q_{\mathrm{A}}q_{\mathrm{B}}}{4\pi\varepsilon_0\varepsilon_{\mathrm{r}}Rk_{\mathrm{B}}T}\left[\exp\left(\frac{q_{\mathrm{A}}q_{\mathrm{B}}}{4\pi\varepsilon_0\varepsilon_{\mathrm{r}}Rk_{\mathrm{B}}T}\right) - 1\right]^{-1} \tag{5}$$

Here q_{A} and q_{B} are the charges of the ions, ε_0 is the vacuum permittivity, ε_{r} is the relative permittivity of the solvent (DMF, $\varepsilon_{\mathrm{r}} = 38.4$),[53] and R is the reaction distance which we assume to be twice the radius of the $[\mathrm{Au}_{25}]^-$ cluster ($r = 6.35$ Å).[37] As shown in Figure S11, f_{Debye} equals 0.53 at a distance of 12.7 Å and the diffusion limited rate constant reduces to 4.4 L nmol^{-1} s^{-1} which is still a factor of ∼500 higher than the deduced dimerization rate constant estimated from our model (a deviation that we rationalize as due to finite activation energies for dimerization).

There is very little experimental data on the dimerization of other solvated, equicharged, aryl-terminated clusters in the 1 nm size range to compare with. Biopolymer anions whose dimerization may also involve $\pi-\pi$ interactions are better studied in this regard. For example, oligoribonucleotides with a chain length between four and seven nucleotides combine with a bimolecular rate constant of 2×10^{-3} L nmol^{-1} s^{-1}, and typical dissociation rates of double stranded dye-labeled oligomers consisting of 10 base pairs were determined to $\sim 1 \times 10^{-2}\ \mathrm{s}^{-1}$.[54,55] The (dimer) dissociation rate decreases strongly with increasing oligomer size at a given temperature.[54] Gotoh et al. found a dissociation rate constant of 1.2×10^{-4} s^{-1} for a 20-mer oligonucleotide.[56] Our determined rate constants for dimerization and dimer dissociation are in surprisingly good agreement with these numbers, despite the different systems, concentrations, and solvents (perhaps fortuitously).

According to eq 6, k_{diss} directly determines the average lifetime τ of the cluster dimers for which we may estimate an upper limit of ∼100 s.

$$\tau = \frac{1}{k_{\mathrm{diss}}} \tag{6}$$

The number of exchange reactions during the lifetime τ of the dimer dianion can be estimated by Poisson statistics,

$$P(k) = \frac{(k_{\mathrm{ex}}\tau)^k\ \mathrm{e}^{-(k_{\mathrm{ex}}\tau)}}{k!} \tag{7}$$

where $P(k)$ is the probability of k exchange reactions to occur during the lifetime τ of the dimer and k_{ex} is the exchange rate constant. With $\tau = 0.056^{-1}$ s ≈ 18 s, on average 0.5 exchanges occur in the dimers, and with the upper limit $\tau = 0.01^{-1}$ s = 100 s, on average 3.2 exchanges occur.

Although the overall agreement between the simulations and experiment is good in terms of kinetics, the observed experimental equilibrium distributions are somewhat narrower compared to the corresponding binomial distributions from the simulation. Similar observations have been made by Zhang et al. when doping silver atoms into $\mathrm{Au}_{38}(\mathrm{SC}_2\mathrm{H}_4\mathrm{Ph})_{24}$ clusters.[25] It was found that a cluster distribution centered around $\mathrm{Ag}_{6.5}\mathrm{Au}_{38-6.5}$ became significantly sharper over a time scale of 3 h. The authors argued that not all possible 38 positions in the cluster are occupied by silver atoms with the same probability. On the basis of our own DFT calculations (see the Supporting Information) and on the basis of findings by Krishnadas et al.,[28] the staple and icosahedral center positions in a $\mathrm{M}_{25}(\mathrm{SR}_{18})$ cluster are preferentially occupied by gold atoms while the 12 icosahedron core positions are preferentially occupied by silver atoms. These results are largely in line with the X-ray structure analysis of $\mathrm{Au}_{18.8}\mathrm{Ag}_{6.2}(\mathrm{SCH}_2\mathrm{CH}_2\mathrm{Ph})_{18}$ where approximately equal partitioning of silver and gold in the icosahedral core was found, while gold atoms clearly favored the staple and the icosahedron central position.[57]

In a recent study it was proposed on the basis of DFT calculations that the metal atom exchange in the "$[\mathrm{Au}_{25}(\mathrm{PET})_{18}]^-$ + $[\mathrm{Ag}_{25}(\mathrm{DMBT})_{18}]^-$" system takes place in a two-step fashion where first exchange of staple metal atoms takes place followed by swapping of heterometal atoms into the icosahedral M_{13}-kernel.[8] Conceivably, such stabilizing intracluster rearrangement processes occur on a time scale that is (significantly) longer than that of metal exchange as inferred here. This could explain why the kinetics and (near) equilibrium composition distributions observed on time scales of >30 min appear mainly entropically driven but are narrower than binomial distributions in detail.

Note that if no intracluster rearrangement took place at all, only the staple atoms could participate in metal atom exchange, i.e., only 48% ($=\frac{12}{25} \cdot 100\%$) of the silver atoms of

https://doi.org/10.1021/jacs.1c01140
J. Am. Chem. Soc. XXXX, XXX, XXX−XXX

Ag_{25}^- would be available for the doping of the Au_{25}^- cluster. Hence, for a mixing ratio of Ag_{25}:Au_{25} of 3:5, the cluster equilibrium distribution would be centered around $Ag_{4.5}Au_{20.5}^-$ $(\frac{3\cdot 12}{3\cdot 25+5\cdot 25}\cdot 25 \approx 4.5)$ and not around $Ag_9Au_{16}^-$ as observed in the experiment. This simple consideration clearly shows that also metal atoms in the icosahedral shell (and center) must participate in the reaction over the 60 min time scale probed.

CONCLUSIONS

We have explored the kinetics of intercluster metal exchange reactions between $[Ag_{25}(DMBT)_{18}]^-$ and $[Au_{25}(PET)_{18}]^-$ in room temperature solutions by probing the solution composition with high resolution electrospray ionization mass spectrometry over a time scale of 60 min from the beginning of the reaction. For the cluster concentrations probed (40−100 nmol L^{-1}), anion mass spectra show significant amounts of both cluster monomers and dimers, with changing overall Ag:Au compositions that track synchronously with reaction time before finally approaching a dynamic equilibrium. We have modeled the corresponding kinetics assuming that the mass spectra essentially reflect the solution composition. Consistent with previous literature on related intercluster reactions, we have assumed a reaction mechanism in which metal atom exchange can only occur during transient dimer formation. Specifically, our simple kinetic model contains three generic reactions: dimerization of monomers, metal atom exchange in the transient dimer, and dimer dissociation. In detail, there are multiple isomeric forms to consider. If one takes this accurately into account, there are potentially 377 species involved and 1302 reactions occurring for which the rate constants are unknown a priori. We have therefore attempted to constrain the range of possible rate constants by comparing the predictions of our kinetic model with experiment under a number of further simplifying assumptions (simulations 1−3). Best agreement with measurements for several different starting composition ratios was obtained by simulation 3, where

(i) metal atom exchange rates were allowed to scale with the probability of finding a silver or gold atom in the respective subunit of the dimer, where this is equivalent to an entropic driving force (by way of assuming all possible substitutional isomers in the 50 atom dimers contribute equally to the exchange process), and

(ii) the dimerization rate constants were allowed to scale with increasing gold composition of the respective educts.

The rate constants then obtained are physically plausible also when compared to measurements of the dimerization and dimer dissociation rates of oligoribonucleotides. Like the aryl-ligand interleaved transient dimer formation invoked here, these solution reactions also involve association/dissociation of two negatively charged educts. Altogether, our kinetic study strongly supports dimer mediated metal atom exchange in this intercluster reaction system. It points to future research using structure sensitive gas-phase methods such as energy resolved CID, high resolution ion mobility spectrometry, or trapped ion electron diffraction to explore a range of remaining issues, e.g., (i) What is the detailed reaction path leading to a transient dimer configuration able to exchange metal atoms? (ii) How does this depend on the type of terminating ligands? (iii) To what extent are the ligands then involved in mediating the actual metal atom exchange? (iv) Once the exchange has occurred, what is the kinetics of site-specific metal atom interdiffusion processes between staple, icosahedral core and center positions?

ASSOCIATED CONTENT

Supporting Information

The Supporting Information is available free of charge at https://pubs.acs.org/doi/10.1021/jacs.1c01140.

> Full experimental methods description (synthesis, high resolution mass spectrometry, collision induced dissociation measurements), DFT calculations, kinetics simulations, CID simulation and reaction distance dependence of Debye factor (PDF)

AUTHOR INFORMATION

Corresponding Authors

Marco Neumaier − *Institute of Nanotechnology, Karlsruhe Institute of Technology, 76344 Eggenstein-Leopoldshafen, Germany*; orcid.org/0000-0002-3810-3377; Email: marco.neumaier@kit.edu

Thalappil Pradeep − *DST Unit of Nanoscience and Thematic Unit of Excellence, Indian Institute of Technology Madras, 600 036 Chennai, India*; orcid.org/0000-0003-3174-534X; Email: pradeep@iitm.ac.in

Manfred M. Kappes − *Institute of Nanotechnology, Karlsruhe Institute of Technology, 76344 Eggenstein-Leopoldshafen, Germany; Institute of Physical Chemistry, Karlsruhe Institute of Technology, 76131 Karlsruhe, Germany*; orcid.org/0000-0002-1199-1730; Email: manfred.kappes@kit.edu

Authors

Ananya Baksi − *Institute of Nanotechnology, Karlsruhe Institute of Technology, 76344 Eggenstein-Leopoldshafen, Germany*; orcid.org/0000-0003-3328-4399

Patrick Weis − *Institute of Physical Chemistry, Karlsruhe Institute of Technology, 76131 Karlsruhe, Germany*; orcid.org/0000-0001-7006-6759

Erik K. Schneider − *Institute of Physical Chemistry, Karlsruhe Institute of Technology, 76131 Karlsruhe, Germany*

Papri Chakraborty − *Institute of Nanotechnology, Karlsruhe Institute of Technology, 76344 Eggenstein-Leopoldshafen, Germany; Institute of Physical Chemistry, Karlsruhe Institute of Technology, 76131 Karlsruhe, Germany*

Horst Hahn − *Institute of Nanotechnology, Karlsruhe Institute of Technology, 76344 Eggenstein-Leopoldshafen, Germany*; orcid.org/0000-0001-9901-3861

Complete contact information is available at: https://pubs.acs.org/10.1021/jacs.1c01140

Author Contributions

[‖]M.N. and A.B. have contributed equally.

Notes

The authors declare no competing financial interest.

ACKNOWLEDGMENTS

M.M.K., H.H., and T.P. thank DFG/DST for support of an Indo-German collaborative project (Grants KA 972/11-1, HA 1344/47-1, and DST/INT/FRG/DFG/P-01/2020). M.M.K. thanks KIT for funding of the timsTOFMS used in this study. P.W. and M.M.K. thank the DFG funded collaborative research center “3MET” (TRR 88, Subproject C6) for funding which led to development of data analysis methods also used in this project. T.P. acknowledges funding for the Centre of Excellence on Molecular Materials and Functions under the Institution of Eminence scheme of IIT Madras.

REFERENCES

(1) Krishnadas, K. R.; Baksi, A.; Ghosh, A.; Natarajan, G.; Som, A.; Pradeep, T. Interparticle Reactions: An Emerging Direction in Nanomaterials Chemistry. *Acc. Chem. Res.* **2017**, *50*, 1988−1996.

(2) Chakraborty, I.; Pradeep, T. Atomically Precise Clusters of Noble Metals: Emerging Link between Atoms and Nanoparticles. *Chem. Rev.* **2017**, *117*, 8208−8271.

(3) Krishnadas, K. R.; Baksi, A.; Ghosh, A.; Natarajan, G.; Pradeep, T. Manifestation of Geometric and Electronic Shell Structures of Metal Clusters in Intercluster Reactions. *ACS Nano* **2017**, *11*, 6015−6023.

(4) Baksi, A.; Schneider, E. K.; Weis, P.; Chakraborty, I.; Fuhr, O.; Lebedkin, S.; Parak, W. J.; Kappes, M. M. Linear Size Contraction of Ligand Protected Ag_{29} Clusters by Substituting Ag with Cu. *ACS Nano* **2020**, *14*, 15064−15070.

(5) Bhat, S.; Baksi, A.; Mudedla, S. K.; Natarajan, G.; Subramanian, V.; Pradeep, T. $Au_{22}Ir_3(PET)_{18}$: An Unusual Alloy Cluster through Intercluster Reaction. *J. Phys. Chem. Lett.* **2017**, *8*, 2787−2793.

(6) Khatun, E.; Chakraborty, P.; Jacob, B. R.; Paramasivam, G.; Bodiuzzaman, M.; Dar, W. A.; Pradeep, T. Intercluster Reactions Resulting in Silver-Rich Trimetallic Nanoclusters. *Chem. Mater.* **2020**, *32*, 611−619.

(7) Krishnadas, K. R.; Ghosh, A.; Baksi, A.; Chakraborty, I.; Natarajan, G.; Pradeep, T. Intercluster Reactions between $Au_{25}(SR)_{18}$ and $Ag_{44}(SR)_{30}$. *J. Am. Chem. Soc.* **2016**, *138*, 140−148.

(8) Huang, B.; Pei, Y. On the Mechanism of Inter-Cluster Alloying Reactions: Two-Stage Metal Exchange of $[Au_{25}(PET)_{18}]^-$ and $[Ag_{25}(DMBT)_{18}]^-$ Clusters. *J. Mater. Chem. A* **2020**, *8*, 10242−10251.

(9) Yang, J.; Jin, R. New Advances in Atomically Precise Silver Nanoclusters. *ACS Mater. Lett.* **2019**, *1*, 482−489.

(10) Kurashige, W.; Niihori, Y.; Sharma, S.; Negishi, Y. Precise Synthesis, Functionalization and Application of Thiolate-Protected Gold Clusters. *Coord. Chem. Rev.* **2016**, *320*−*321*, 238−250.

(11) Jin, R.; Zeng, C.; Zhou, M.; Chen, Y. Atomically Precise Colloidal Metal Nanoclusters and Nanoparticles: Fundamentals and Opportunities. *Chem. Rev.* **2016**, *116*, 10346−10413.

(12) Maity, P.; Xie, S.; Yamauchi, M.; Tsukuda, T. Stabilized Gold Clusters: From Isolation toward Controlled Synthesis. *Nanoscale* **2012**, *4*, 4027.

(13) Yao, Q.; Wu, Z.; Liu, Z.; Lin, Y.; Yuan, X.; Xie, J. Molecular Reactivity of Thiolate-Protected Noble Metal Nanoclusters: Synthesis, Self-Assembly, and Applications. *Chem. Sci.* **2021**, *12*, 99−127.

(14) Aikens, C. M. Electronic and Geometric Structure, Optical Properties, and Excited State Behavior in Atomically Precise Thiolate-Stabilized Noble Metal Nanoclusters. *Acc. Chem. Res.* **2018**, *51*, 3065−3073.

(15) Häkkinen, H. Atomic and Electronic Structure of Gold Clusters: Understanding Flakes, Cages and Superatoms from Simple Concepts. *Chem. Soc. Rev.* **2008**, *37*, 1847.

(16) Comby-Zerbino, C.; Bertorelle, F.; Dugourd, P.; Antoine, R.; Chirot, F. Structure and Charge Heterogeneity in Isomeric $Au_{25}(MBA)_{18}$ Nanoclusters -Insights from Ion Mobility and Mass Spectrometry. *J. Phys. Chem. A* **2020**, *124*, 5840−5848.

(17) Price, R. C.; Whetten, R. L. All-Aromatic, Nanometer-Scale, Gold-Cluster Thiolate Complexes. *J. Am. Chem. Soc.* **2005**, *127*, 13750−13751.

(18) Alhilaly, M. J.; Huang, R. W.; Naphade, R.; Alamer, B.; Hedhili, M. N.; Emwas, A. H.; Maity, P.; Yin, J.; Shkurenko, A.; Mohammed, O. F.; Eddaoudi, M.; Bakr, O. M. Assembly of Atomically Precise Silver Nanoclusters into Nanocluster-Based Frameworks. *J. Am. Chem. Soc.* **2019**, *141*, 9585−9592.

(19) Pollitt, S.; Truttmann, V.; Haunold, T.; Garcia, C.; Olszewski, W.; Llorca, J.; Barrabés, N.; Rupprechter, G. The Dynamic Structure of $Au_{38}(SR)_{24}$ Nanoclusters Supported on CeO_2 upon Pretreatment and CO Oxidation. *ACS Catal.* **2020**, *10*, 6144−6148.

(20) Wang, S.; Song, Y.; Jin, S.; Liu, X.; Zhang, J.; Pei, Y.; Meng, X.; Chen, M.; Li, P.; Zhu, M. Metal Exchange Method Using Au_{25} Nanoclusters as Templates for Alloy Nanoclusters with Atomic Precision. *J. Am. Chem. Soc.* **2015**, *137*, 4018−4021.

(21) Ferrando, R.; Jellinek, J.; Johnston, R. L. Nanoalloys: From Theory to Applications of Alloy Clusters and Nanoparticles. *Chem. Rev.* **2008**, *108*, 845−910.

(22) Calvo, F. Thermodynamics of Nanoalloys. *Phys. Chem. Chem. Phys.* **2015**, *17*, 27922−27939.

(23) Peng, L.; Ringe, E.; Van Duyne, R. P.; Marks, L. D. Segregation in Bimetallic Nanoparticles. *Phys. Chem. Chem. Phys.* **2015**, *17*, 27940−27951.

(24) Ferrando, R. Symmetry Breaking and Morphological Instabilities in Core-Shell Metallic Nanoparticles. *J. Phys.: Condens. Matter* **2015**, *27*, 013003.

(25) Zhang, B.; Salassa, G.; Bürgi, T. Silver Migration between $Au_{38}(SC_2H_4Ph)_{24}$ and Doped $Ag_xAu_{38-x}(SC_2H_4Ph)_{24}$ Nanoclusters. *Chem. Commun.* **2016**, *52*, 9205−9207.

(26) Chakraborty, P.; Nag, A.; Natarajan, G.; Bandyopadhyay, N.; Paramasivam, G.; Panwar, M. K.; Chakrabarti, J.; Pradeep, T. Rapid Isotopic Exchange in Nanoparticles. *Sci. Adv.* **2019**, *5*, eaau7555.

(27) Baksi, A.; Schneider, E. K.; Weis, P.; Krishnadas, K. R.; Ghosh, D.; Hahn, H.; Pradeep, T.; Kappes, M. M. Nanogymnastics: Visualization of Intercluster Reactions by High-Resolution Trapped Ion Mobility Mass Spectrometry. *J. Phys. Chem. C* **2019**, *123*, 28477−28485.

(28) Krishnadas, K. R.; Baksi, A.; Ghosh, A.; Natarajan, G.; Pradeep, T. Structure-Conserving Spontaneous Transformations between Nanoparticles. *Nat. Commun.* **2016**, *7*, 13447.

(29) Kappes, M. M.; Kunz, R. W.; Schumacher, E. Production of Large Sodium Clusters (Na_x, $x \leq 65$) by Seeded Beam Expansions. *Chem. Phys. Lett.* **1982**, *91*, 413−418.

(30) Knight, W. D.; Clemenger, K.; De Heer, W. A.; Saunders, W. A.; Chou, M. Y.; Cohen, M. L. Electronic Shell Structure and Abundances of Sodium Clusters. *Phys. Rev. Lett.* **1984**, *52*, 2141−2143.

(31) Walter, M.; Akola, J.; Lopez-Acevedo, O.; Jadzinsky, P. D.; Calero, G.; Ackerson, C. J.; Whetten, R. L.; Gronbeck, H.; Hakkinen, H. A Unified View of Ligand-Protected Gold Clusters as Superatom Complexes. *Proc. Natl. Acad. Sci. U. S. A.* **2008**, *105*, 9157−9162.

(32) Baksi, A.; Chakraborty, P.; Bhat, S.; Natarajan, G.; Pradeep, T. $[Au_{25}(SR)_{18}]_2^{2-}$: A Noble Metal Cluster Dimer in the Gas Phase. *Chem. Commun.* **2016**, *52*, 8397−8400.

(33) Liu, X.; Saranya, G.; Huang, X.; Cheng, X.; Wang, R.; Chen, M.; Zhang, C.; Li, T.; Zhu, Y. $Ag_2Au_{50}(PET)_{36}$ Nanocluster: Dimeric Assembly of $Au_{25}(PET)_{18}$ Enabled by Silver Atoms. *Angew. Chem., Int. Ed.* **2020**, *59*, 13941−13946.

(34) De Nardi, M.; Antonello, S.; Jiang, D. E.; Pan, F.; Rissanen, K.; Ruzzi, M.; Venzo, A.; Zoleo, A.; Maran, F. Gold Nanowired: A Linear $(Au_{25})_n$ Polymer from Au_{25} Molecular Clusters. *ACS Nano* **2014**, *8*, 8505−8512.

(35) Chakraborty, P.; Baksi, A.; Mudedla, S. K.; Nag, A.; Paramasivam, G.; Subramanian, V.; Pradeep, T. Understanding Proton Capture and Cation-Induced Dimerization of $[Ag_{29}(BDT)_{12}]^{3-}$ Clusters by Ion Mobility Mass Spectrometry. *Phys. Chem. Chem. Phys.* **2018**, *20*, 7593−7603.

(36) Heaven, M. W.; Dass, A.; White, P. S.; Holt, K. M.; Murray, R. W. Crystal Structure of the Gold Nanoparticle $[N(C_8H_{17})_4]$-$[Au_{25}(SCH_2CH_2Ph)_{18}]$. *J. Am. Chem. Soc.* **2008**, *130*, 3754−3755.

(37) Zhu, M.; Aikens, C. M.; Hollander, F. J.; Schatz, G. C.; Jin, R. Correlating the Crystal Structure of A Thiol-Protected Au_{25} Cluster and Optical Properties. *J. Am. Chem. Soc.* **2008**, *130*, 5883−5885.

(38) Joshi, C. P.; Bootharaju, M. S.; Alhilaly, M. J.; Bakr, O. M. $[Ag_{25}(SR)_{18}]^-$: The "Golden" Silver Nanoparticle. *J. Am. Chem. Soc.* **2015**, *137*, 11578−11581.

(39) Niihori, Y.; Kikuchi, Y.; Kato, A.; Matsuzaki, M.; Negishi, Y. Understanding Ligand-Exchange Reactions on Thiolate-Protected

Gold Clusters by Probing Isomer Distributions Using Reversed-Phase High-Performance Liquid Chromatography. *ACS Nano* **2015**, *9*, 9347−9356.

(40) Caragheorgheopol, A.; Chechik, V. Mechanistic Aspects of Ligand Exchange in Au Nanoparticles. *Phys. Chem. Chem. Phys.* **2008**, *10*, 5029−5041.

(41) Niihori, Y.; Kurashige, W.; Matsuzaki, M.; Negishi, Y. Remarkable Enhancement in Ligand-Exchange Reactivity of Thiolate-Protected Au_{25} Nanoclusters by Single Pd Atom Doping. *Nanoscale* **2013**, *5*, 508−512.

(42) Shibu, E. S.; Muhammed, M. A. H.; Tsukuda, T.; Pradeep, T. Ligand Exchange of $Au_{25}SG_{18}$ Leading to Functionalized Gold Clusters: Spectroscopy, Kinetics, and Luminescence. *J. Phys. Chem. C* **2008**, *112*, 12168−12176.

(43) Baghdasaryan, A.; Martin, K.; Lawson Daku, L. M.; Mastropasqua Talamo, M.; Avarvari, N.; Bürgi, T. Ligand Exchange Reactions on the Chiral Au_{38} Cluster: CD Modulation Caused by the Modification of the Ligand Shell Composition. *Nanoscale* **2020**, *12*, 18160−18170.

(44) Schmidbaur, H. The Aurophilicity Phenomenon: A Decade of Experimental Findings, Theoretical Concepts and Emerging Applications. *Gold Bull.* **2000**, *33*, 3−10.

(45) Schmidbaur, H.; Schier, A. Aurophilic Interactions as a Subject of Current Research: An up-Date. *Chem. Soc. Rev.* **2012**, *41*, 370−412.

(46) Schmidbaur, H.; Schier, A. Argentophilic Interactions. *Angew. Chem., Int. Ed.* **2015**, *54*, 746−784.

(47) Salassa, G.; Krishnadas, K. R.; Pupier, M.; Viger-Gravel, J.; Bürgi, T. Role of Intercluster and Interligand Dynamics of $[Ag_{25}(DMBT)_{18}]^-$ Nanoclusters by Multinuclear Magnetic Resonance Spectroscopy. *J. Phys. Chem. C* **2021**, *125*, 2524−2530.

(48) Hasinoff, B. B. Simultaneous Diffusion and Chemical Activation Control of the Kinetics of the Binding of Carbon Monoxide to Ferroprotoporphyrin IX in Glycerol-Water Mixtures of High Viscosity. *Can. J. Chem.* **1977**, *55*, 3955−3960.

(49) Han, K. J.; Oh, J. H.; Park, S. J.; Gmehling, J. Excess Molar Volumes and Viscosity Deviations for the Ternary System N,N-Dimethylformamide + N-Methylformamide + Water and the Binary Subsystems at 298.15 K. *J. Chem. Eng. Data* **2005**, *50*, 1951−1955.

(50) Takahashi, K.; Bartels, D. M.; Cline, J. A.; Jonah, C. D. Reaction Rates of the Hydrated Electron with NO_2^-, NO_3^-, and Hydronium Ions as a Function of Temperature from 125 to 380 °C. *Chem. Phys. Lett.* **2002**, *357*, 358−364.

(51) Hemmes, P. On the Possibility of Like-Charged Ion Pairing in Solution. *J. Am. Chem. Soc.* **1972**, *94*, 75−76.

(52) Rice, S. A.; Butler, P. R.; Pilling, M. J.; Baird, J. K. A Solution of the Debye-Smoluchowski Equation for the Rate of Reaction of Ions in Dilute Solution. *J. Chem. Phys.* **1979**, *70*, 4001−4007.

(53) Hunger, J.; Buchner, R.; Kandil, M. E.; May, E. F.; Marsh, K. N.; Hefter, G. Relative Permittivity of Dimethylsulfoxide and N,N-Dimethylformamide at Temperatures from (278 to 328) K and Pressures from (0.1 to 5) MPa. *J. Chem. Eng. Data* **2010**, *55*, 2055−2065.

(54) Craig, M. E.; Crothers, D. M.; Doty, P. Relaxation Kinetics of Dimer Formation by Self Complementary Oligonucleotides. *J. Mol. Biol.* **1971**, *62*, 383−401.

(55) Morrison, L. E.; Stols, L. M. Sensitive Fluorescence-Based Thermodynamic and Kinetic Measurements of DNA Hybridization in Solution. *Biochemistry* **1993**, *32*, 3095−3104.

(56) Gotoh, M. A New Approach to Determine the Effect of Mismatches on Kinetic Parameters in DNA Hybridization Using an Optical Biosensor. *DNA Res.* **1995**, *2*, 285−293.

(57) Kumara, C.; Aikens, C. M.; Dass, A. X-Ray Crystal Structure and Theoretical Analysis of $Au_{25\text{-}x}Ag_x(SCH_2CH_2Ph)_{18}^-$ Alloy. *J. Phys. Chem. Lett.* **2014**, *5*, 461−466.

Supporting information

Kinetics of Intercluster Reactions between Atomically Precise Noble Metal Clusters $[Ag_{25}(DMBT)_{18}]^{-}$ and $[Au_{25}(PET)_{18}]^{-}$ in Room Temperature Solutions

Marco Neumaier[1*†], Ananya Baksi[1†], Patrick Weis[2], Erik K. Schneider[2], Papri Chakraborty[1,2], Horst Hahn[1], Thalappil Pradeep[3*] and Manfred M. Kappes[1,2*]

[1]*Institute of Nanotechnology, Karlsruhe Institute of Technology, 76344 Eggenstein-Leopoldshafen, Germany*

[2]*Institute of Physical Chemistry, Karlsruhe Institute of Technology, 76131 Karlsruhe, Germany*

[3]*DST Unit of Nanoscience and Thematic Unit of Excellence, Indian Institute of Technology Madras, 600 036 Chennai, India*

*Email: marco.neumaier@kit.edu, manfred.kappes@kit.edu, pradeep@iitm.ac.in

†Contributed equally

Materials and synthesis of clusters

Materials. Silver nitrate ($AgNO_3$), dichloromethane (DCM), phenylethanethiol (PET), 2,4-dimethylbenzenethiol (DMBT), 1,3-benzenedithiol (BDT) and sodium borohydride ($NaBH_4$) were purchased from Sigma Aldrich. Chloroauric acid ($HAuCl_4{\cdot}3H_2O$) was prepared in the lab from pure gold and aqua regia.

Synthesis of $[TOA]^+[Au_{25}(PET)_{18}]^-$. The cluster was synthesized following the previously reported method.[1–3] About 40 mg of $HAuCl_4{\cdot}3H_2O$ was dissolved in 7.5 mL tetrahydrofuran (THF) and 65 mg of tetraoctylammoniumbromide (TOABr) was added. The mixture was stirred for 15 min. The color changed from golden yellow to orange red confirming successful complexation. 68 µL of PET was directly added and the mixture was stirred for another hour for Au-PET thiolate formation. The yellow thiolates were then reduced using 39 mg of $NaBH_4$ in ice-cold water. The color of the mixture changed to brown indicating reduction of the thiolates. The solution was stirred for another 5 h for complete conversion and size focusing to achieve high yield of $[Au_{25}(PET)_{18}]^-$. After 5 h, the as-synthesized cluster was dried using a rotary evaporator and excess methanol was added to precipitate the clusters and to remove the free thiol and excess thiolates. The procedure was repeated several times to get a clean cluster sample. The resulting sample contains a small quantity of larger clusters. To remove the larger clusters, the methanol washed clusters were extracted in acetone and centrifuged for a few times. The supernatant solution was collected leaving behind a smaller quantity of precipitate consisting of larger clusters. The acetone solution was then vacuum dried and the cluster was dissolved in DCM and centrifuged at 10000 rpm. The supernatant solution was collected which consisted of pure $[TOA]^+[Au_{25}(PET)_{18}]^-$ clusters. The purified cluster was characterized by UV-vis absorption spectroscopy, where characteristic peaks at 675 nm and 450 nm confirmed the formation of Au_{25} clusters. The sample was crystallized from solution in a mixture of toluene/ethanol kept at room temperature. This sample was used for detailed characterization by ESI-MS and intercluster reactions.

Synthesis of $[PPh_4]^+[Ag_{25}(DMBT)_{18}]^-$. The synthesis followed a reported method with slight modification.[4] A quantity of 38 mg $AgNO_3$ was dissolved in a mixture of 2 mL methanol and 17 mL DCM. About 90 μL of 2,4-DMBT was added to the mixture to form yellow insoluble thiolates (Ag-S complex) and the mixture was kept at 0 ^oC for 15–17 min while stirring. Afterwards 6 mg of PPh_4Br dissolved in 0.5 mL of methanol was added followed by the dropwise addition of 15 mg of $NaBH_4$ in 0.5 mL of ice–cold water. The reaction mixture was kept for 7–8 h while stirring. After that, stirring was discontinued and the solution was held at 4 ^oC for about two days. For purification of the cluster, the sample was centrifuged to remove any insoluble impurities and DCM was removed by rotary evaporation. The precipitate was washed twice with methanol. After that, the cluster was redissolved in DCM and again centrifuged to remove any further insoluble contaminants. DCM was again removed by rotary evaporation and the purified cluster was obtained in the powder form. Dark black crystals of the cluster were obtained from a DCM/hexane mixture kept at 4^oC over a period of around seven days. The cluster was redissolved in DCM, characterized by UV-vis and then used for ESI-MS (see Figure S1).

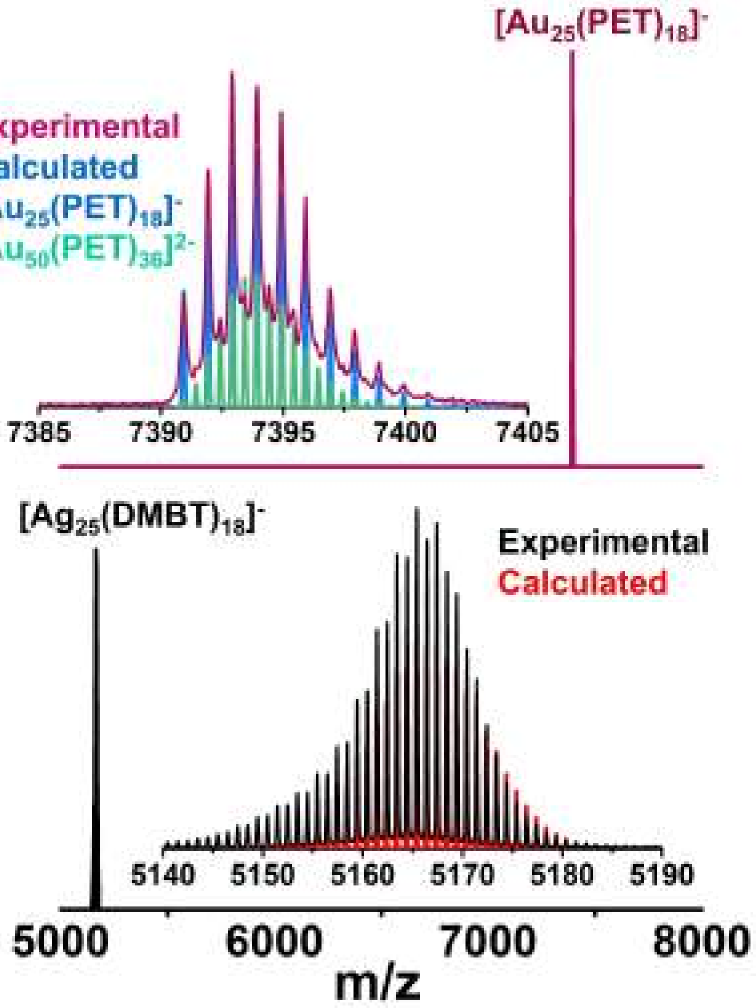

Figure S1. Mass spectra of pure [Au$_{25}$(PET)$_{18}$]$^-$ and [Ag$_{25}$(DMBT)$_{18}$]$^-$ clusters with isotopically resolved patterns and the corresponding calculated isotope distributions. Note that for [Au$_{25}$(PET)$_{18}$]$^-$ dimers are present also in the pure cluster solution.

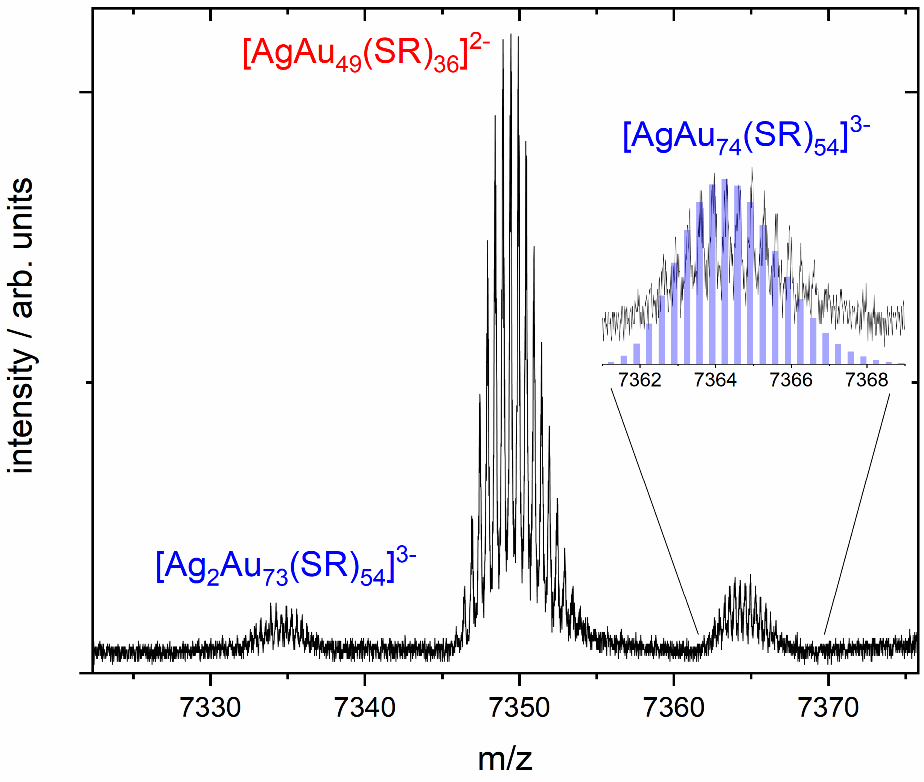

Figure S2. Integrated signal between 0 – 6 min reaction time ([Ag$_{25}$]$^{-}$:[Au$_{25}$]$^{-}$ ratio = 40:40 nmol L^{-1}). Next to the dianion [AgAu$_{49}$(SR)$_{36}$]$^{2-}$ trimer signals are apparent with about tenfold less intensity compared to [AgAu$_{49}$(SR)$_{36}$]$^{2-}$. The inset shows the calculated spectrum of the triply charged trimer [AgAu$_{74}$(SR)$_{54}$]$^{3-}$ ion (blue bars) together with the experimental signal.

Mass spectrometry and collision induced dissociation

High resolution mass spectra as a function of reaction time after mixing were recorded on a Bruker timsTOF-MS in Karlsruhe at a mass resolution exceeding 25000. Briefly, the timsTOF comprises an electrospray ion source (ESI), a trapped ion mobility spectrometer (TIMS), a quadrupole mass filter (QMS), a collision cell (which is a second quadrupole) as well as an orthogonally accelerated time-of-flight mass spectrometer with a reflectron (oa-ReTOF). TIMS is a high resolution variant of ion mobility spectrometry allowing isomer separation based on collision cross section. For (low) intensity reasons we operated the timsTOF in the "TIMS-off" mode in this study, i.e. without isomer separation. Typical measurement conditions were as follows: sample concentration: 40–100 nmol L^{-1} in DMF, flow rate: 3 µL min^{-1}, capillary voltage: 4.5 kV, nebulizer: 0.3 bar, dry gas: 2 L min^{-1}, dry temperature: 300 °C, ion energy: 1 eV, collision energy: 1 eV, transfer time: 200 µs, pre-pulse storage time: 20 µs and scan time: 1 ms. Different mixing ratios of $[Au_{25}(PET)_{18}]^-$ and $[Ag_{25}(DMBT)_{18}]^-$ were mixed and injected directly into the mass spectrometer to avoid delay in the measurement. Considering the sample transfer time, a "dead time" of about 20 – 40 s between starting the reaction by mixing and completing the first mass spectral scan is possible in all experiments.

Collision induced dissociation (CID) studies were carried out in Chennai using a Waters Synapt G2Si mass spectrometer system, comprising an ESI source, a quadrupole mass filter for mass-preselection, a travelling wave ion mobility spectrometer (not used in this study), a collision cell and a ReTOF mass analyzer with a specified resolution of 50000. For the CID studies, the $[Ag_{25}Au_{25}]^{2-}$ parent ions were mass selected in the QMS and collided with nitrogen at 0.02 mbar with a laboratory frame collision energy of 30 eV. The fragments were analyzed in the ReTOF. Again, the mass resolution is high enough to allow isotopic resolution of all species.

Data analysis

For best accuracy each mass spectrum was smoothed by a 5 point moving average procedure and recalibrated linearly with respect to calculated m/z values of $[Ag_{25}(SR)]_{18}^-$ and $[Au_{25}(SR)]_{18}^-$. As monoanions $[Ag_mAu_{25-m}]^-$ share the same m/z ratio as dianions $[Ag_{2m}Au_{50-2m}]^{2-}$, their intensities have to be deconvoluted, see Figure S1 as an example. The integer (larger) peaks correspond to both monoanion and dianion isotopologues while the (smaller) half integer peaks (marked with an asterisk) correspond to dianionic dimers only. Therefore, we integrate first the half integer peaks and multiply the result by a factor of 2 to get the dianion intensity (using the fact that the isotopologue distribution is quite wide and almost Gaussian-shaped). The monoanion intensities are obtained by integrating the integer peaks and subtracting the corresponding dianion intensities. Each ion intensity was normalized to the sum of all ions (strictly speaking the sum of all monomers and the monomeric subunits in the dimers) I_{total}:

$$I_{total} = \sum_{i=1}^{26} I_i^{monoanion} + 2 \cdot \sum_{j=1}^{51} I_j^{dianion} \quad (1)$$

No systematic behavior of I_{total} was found and for some measurement series I_{total} was constant within ~10% on a timescale of up to 60 min. On this basis we can rule out significant dark reaction channels not accessible to mass spectrometry and conclude that the kinetics followed by mass spectrometry largely resemble the kinetics in solution.

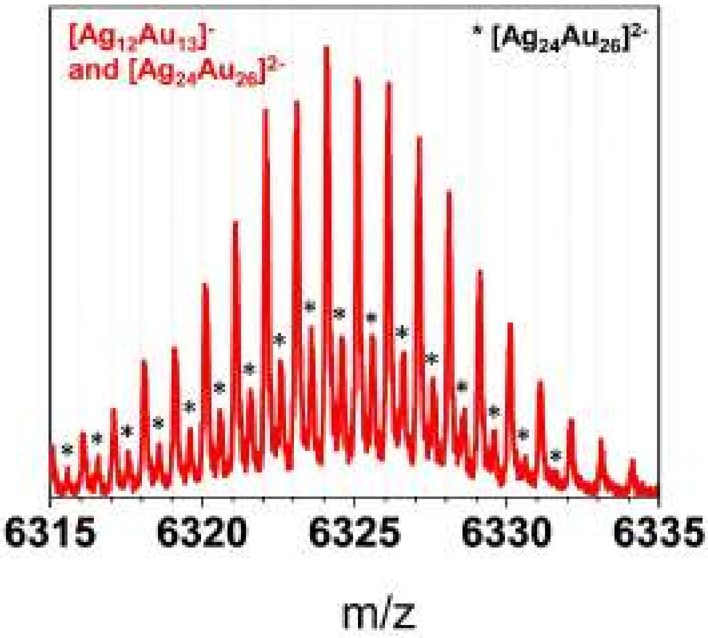

Figure S3. Isotopic distribution for $[Ag_{12}Au_{13}]^-$ with underlying dianion signal of $[Ag_{24}Au_{26}]^{2-}$. The spectrum was taken for a $[Ag_{25}]^-$:$[Au_{25}]^-$ ratio of 40:40 nmol L^{-1} and after a reaction time of 54 min. Peaks marked with an asterisk belong to the dianion $[Ag_{24}Au_{26}]^{2-}$ only.

Kinetic Model

The exchange kinetics was modeled by standard matrix algebra suites in MATLAB and solving all kinetic differential equations numerically. According to reaction scheme 1 (see main text for details) all 26 monoanions can form dimers which in turn can dissociate to the monomers. The number of possible dimerization and dissociation steps is given by the number of possible combinations of monoanions with repetition

$$C(n,r) = \frac{(n+r-1)!}{r!(n-1)!} = 351 \qquad (2)$$

where n=26 is the number of monoanions and r=2 is the sample size, i.e. reaction partners. Note that for dianions aside from $[Ag_{50}]^{2-}$ and $[Au_{50}]^{2-}$ several constitutional isomers exist with $[Ag_{25}Au_{25}]^{2-}$ being the dimer with a maximum of 13 possible isomers ranging from $[(Ag_{25})(Au_{25})]^{2-}$, over $[(Ag_{18}Au_{7})(Ag_{7}Au_{18})]^{2-}$, to fully mixed $[(Ag_{12}Au_{13})(Ag_{13}Au_{12})]^{2-}$. In total there exist 351 different dianionic species. Note that different isomers of the monomeric subunits (i.e. with well-defined structures where e.g. gold atoms preferably occupy the staple and core positions and silver atoms the icosahedral shell) were not taken into account.

When we allow metal atom exchange exclusively in the dianions the number of physically meaningful exchange reactions amounts to 600. Therefore, the reaction is determined by 1302 (=351+351+600) elementary reactions in total and can be written as

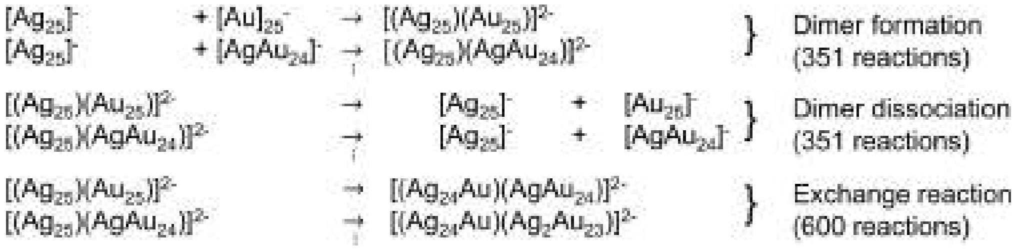

Scheme S1. Reaction scheme based on the kinetic model. The kinetics of the intercluster reaction between $[Ag_{25}]^{-}$ and $[Au_{25}]^{-}$ is described by 1302 reactions.

From the reactions in scheme S1 the stoichiometric matrix **α** can be calculated.

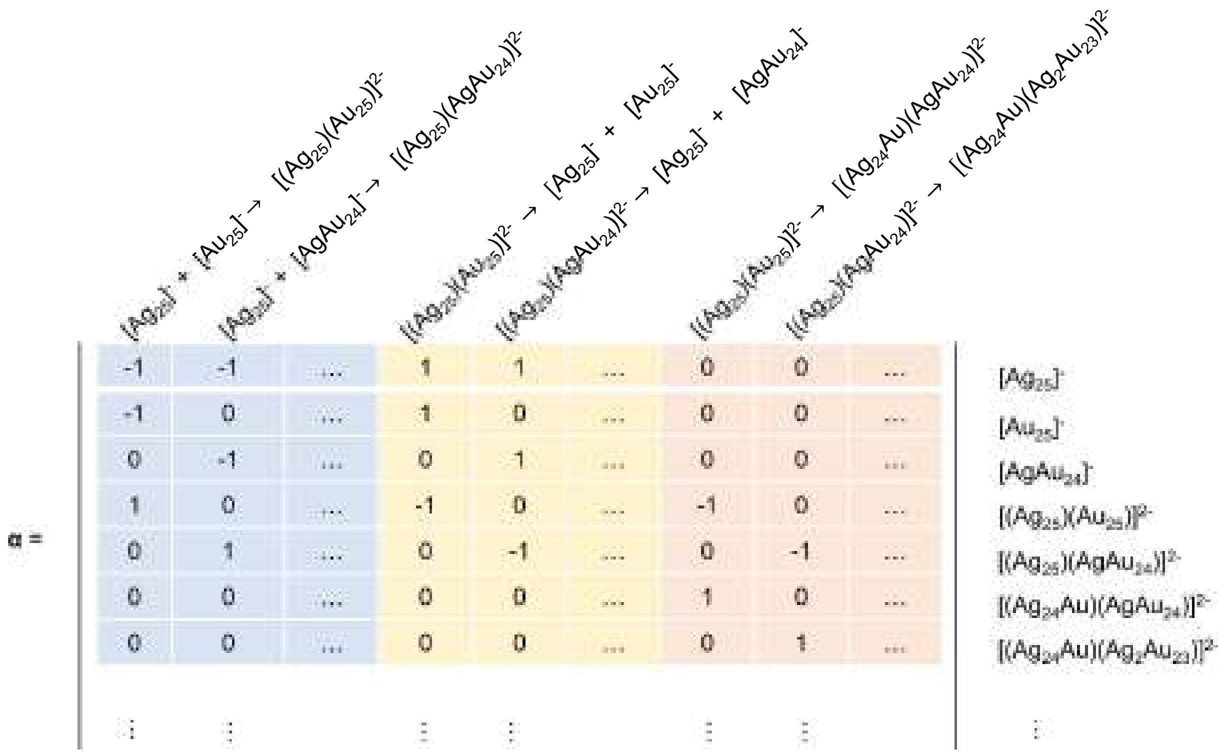

$$\boldsymbol{\alpha} = \begin{array}{ccccccccc|l}
[Ag_{25}]^- + [Au_{25}]^- \rightarrow [(Ag_{25})(Au_{25})]^{2-} & [Ag_{25}]^- + [AgAu_{24}]^- \rightarrow [(Ag_{25})(AgAu_{24})]^{2-} & & [(Ag_{25})(Au_{25})]^{2-} \rightarrow [Ag_{25}]^- + [Au_{25}]^- & [(Ag_{25})(AgAu_{24})]^{2-} \rightarrow [Ag_{25}]^- + [AgAu_{24}]^- & & [(Ag_{25})(Au_{25})]^{2-} \rightarrow [(Ag_{24}Au)(AgAu_{24})]^{2-} & [(Ag_{25})(AgAu_{24})]^{2-} \rightarrow [(Ag_{24}Au)(Ag_2Au_{23})]^{2-} & & \\
-1 & -1 & \cdots & 1 & 1 & \cdots & 0 & 0 & \cdots & [Ag_{25}]^- \\
-1 & 0 & \cdots & 1 & 0 & \cdots & 0 & 0 & \cdots & [Au_{25}]^- \\
0 & -1 & \cdots & 0 & 1 & \cdots & 0 & 0 & \cdots & [AgAu_{24}]^- \\
1 & 0 & \cdots & -1 & 0 & \cdots & -1 & 0 & \cdots & [(Ag_{25})(Au_{25})]^{2-} \\
0 & 1 & \cdots & 0 & -1 & \cdots & 0 & -1 & \cdots & [(Ag_{25})(AgAu_{24})]^{2-} \\
0 & 0 & \cdots & 0 & 0 & \cdots & 1 & 0 & \cdots & [(Ag_{24}Au)(AgAu_{24})]^{2-} \\
0 & 0 & \cdots & 0 & 0 & \cdots & 0 & 1 & \cdots & [(Ag_{24}Au)(Ag_2Au_{23})]^{2-} \\
\vdots & \vdots & & \vdots & \vdots & & \vdots & \vdots & & \vdots
\end{array}$$

Figure S4. Stoichiometric matrix **α** according to the reactions in scheme S1. Number of columns correspond to the number of elementary reactions (=1302) and number of rows equals the number of species participating in the reaction (=377). The matrix elements represent stoichiometric factors, which are -1 if one unit of the corresponding species is consumed in the reaction, 1 if one unit of the species is produced and 0 if the species does not participate in the reaction. The blue and yellow columns represent the 351 dimerization and dissociation reactions, respectively. The red columns represent the 600 intra-cluster exchange reactions.

The number of columns in **α** correspond to the number of elementary reactions (=1302) and the number of rows equal the number of participating species (=377). The matrix elements in **α** represent stoichiometric factors of a definite species at a given elementary step which are positive in case of products, negative in case of reactants and zero if the species does not participate in the reaction.

By introducing the rate vector $\vec{r}$ with the corresponding concentrations *c* of the clusters

$$\vec{r} = \begin{pmatrix} k_{dim} \cdot c([\mathrm{Ag}_{25}]^-) \cdot c([\mathrm{Au}_{25}]^-) \\ k_{dim} \cdot c([\mathrm{Ag}_{25}]^-) \cdot c([\mathrm{AgAu}_{24}]^-) \\ \vdots \\ k_{diss} \cdot c([(\mathrm{Ag}_{25})(\mathrm{Au}_{25})]^{2-}) \\ k_{diss} \cdot c([(\mathrm{Ag}_{25})(\mathrm{AgAu}_{24})]^{2-}) \\ \vdots \\ k_{ex}P_{ex,1} \cdot c([(\mathrm{Ag}_{25})(\mathrm{Au}_{25})]^{2-}) \\ k_{ex}P_{ex,2} \cdot c([(\mathrm{Ag}_{25})(\mathrm{AgAu}_{24})]^{2-}) \\ \vdots \end{pmatrix} \tag{3}$$

the 377 differential reaction equations are given by

$$\frac{dC(t)}{dt} = \boldsymbol{\alpha} \cdot \vec{r} \tag{4}$$

and are solved numerically in MATLAB by using the Ordinary Differential Equations (ODE) solver ODE45. Simulated concentrations were treated like the experimental data (to allow easy comparison) and have been normalized to the sum of all ion concentrations (counting the dianions twice to account for the monomeric subunits, see above). Time zero was assumed to equal the “dead time” of ~20 s of the experiment.

Calculation of mixing entropy

For the dimer $[(\mathrm{Ag}_{22}\mathrm{Au}_3)(\mathrm{Ag}_4\mathrm{Au}_{21})]^{2-}$ the forward mixing reaction produces $[(\mathrm{Ag}_{21}\mathrm{Au}_4)(\mathrm{Ag}_5\mathrm{Au}_{20})]^{2-}$ and the backward mixing reaction leads to $[(\mathrm{Ag}_{23}\mathrm{Au}_2)(\mathrm{Ag}_3\mathrm{Au}_{22})]^{2-}$. Based on equation 5 and the number of structural isomers W for each monomeric subunit (SU), the configurational entropy change for the forward reaction is 1.04 $\mathrm{J \cdot K^{-1} \cdot mol^{-1}}$ and for the backward reaction it is -1.24 $\mathrm{J \cdot K^{-1} \cdot mol^{-1}}$.

$$\Delta S = \frac{1}{25} \cdot R \cdot \left(\ln W_{SU1,product} + \ln W_{SU2,product} - \ln W_{SU1,educt} - \ln W_{SU2,educt} \right) \tag{5}$$

The number of structural isomers W can be calculated from the binomial coefficient $\binom{n}{k}$ where n is the number of metal atoms per subunit (n=25) and k is the number of silver or gold atoms in the respective subunit (k=0–25). The total mixing entropy for the formation of $[(\mathrm{Ag}_{12}\mathrm{Au}_{13})(\mathrm{Ag}_{13}\mathrm{Au}_{12})]^{2-}$ is 10.28 $\mathrm{J \cdot K^{-1} \cdot mol^{-1}}$.

DFT Calculations

Method. The quantum chemical calculations were performed with the TURBOMOLE package[5] with the BP86-functional[6,7] and def-SVP basis set[8]. We used the published crystal structure coordinates[4,9] of $Ag_{25}(DMBT)_{18}$ and $Au_{25}(PET)_{18}$ as starting points, removed the counterions and optimized the geometries without symmetry restrictions. The mixed clusters were obtained by exchanging gold and silver atoms and reoptimizing the structure.

Results.

(A) Metal atom exchange

In a first step we investigated the exchange of one metal atom, i.e. the reaction

$$[\mathrm{Ag_{25}(DMBT)_{18}}]^{-}+[\mathrm{Au_{25}(PET)_{18}}]^{-} \rightarrow [\mathrm{Ag_{24}Au(DMBT)_{18}}]^{-}+[\mathrm{Ag\,Au_{24}(PET)_{18}}]^{-} \qquad (6)$$

In both pure $[Au_{25}(PET)_{18}]^{-}$ and $[Ag_{25}(DMBT)_{18}]^{-}$ clusters, the metal atoms have topologically the same arrangements: 12 atoms form an icosahedron, one atom is in its core and another 12 atoms form 6 “staples” and are bound to the DMBT and PET molecules covering the cluster. Therefore, we assume that the mixed clusters also have these topologies. For the mixed $[AgAu_{24}(PET)_{18}]^{-}$ clusters 3 isomers have to be considered: The extra metal atom can either be in the core, in the icosahedron or on the staple. It turns out that in the most stable structure of $[AgAu_{24}(PET)_{18}]^{-}$ the silver atom replaces one gold atom on the icosahedron (core: +0.31 eV, staple: +0.20 eV). In $[AuAg_{24}(DMBT)_{18}]^{-}$ the gold atom is in the core (icosahedron: +0.27 eV, staple: +0.28 eV). With these optimized isomers the mixing reaction (7) is exothermic by 0.5 eV. These findings are in line with the calculations by Krishnadas et al.[10] Since the number of possible isomers quickly increases with the number of exchanged metal atoms we did not try to follow all steps but focused on the limiting case of complete mixing, i.e. exchange of 12 atoms:

$$[\mathrm{Ag_{25}(DMBT)_{18}}]^{-}+[\mathrm{Au_{25}(PET)_{18}}]^{-} \rightarrow [\mathrm{Ag_{13}Au_{12}(DMBT)_{18}}]^{-}+[\mathrm{Ag_{12}Au_{13}(PET)_{18}}]^{-} \qquad (7)$$

Even so, there are still a large number of isomers possible for the mixed clusters $[Ag_{13}Au_{12}(DMBT)_{18}]^{-}$ and $[Ag_{12}Au_{13}(PET)_{18}]^{-}$. The obvious limiting cases are the isomers with 12 atoms of the same element on staple and icosahedron, respectively (see Table S1, isomers I and II). In the case $[Ag_{12}Au_{13}(PET)_{18}]^{-}$ the isomer with a Au atom in the core, 12 Ag atoms on the icosahedron and the remaining 12 Au atoms on the staples is the lowest energy isomer that we found. Swapping the elements in icosahedron and staple is highly unfavourable (isomer II, +1.04 eV), moving the Au atom from the core to the icosahedron (isomer III) increases the energy by 0.11 eV. We also calculated several isomers with a “statistical” distribution, i.e.

similar numbers of Au and Ag atoms in icosahedron and staples (isomers IV-VII). They are between 0.41 eV and 0.87 eV higher in energy. Therefore we are confident that isomer I represents the global minimum for $[Ag_{12}Au_{13}(PET)_{18}]^-$. For $[Ag_{13}Au_{12}(DMBT)_{18}]^-$ we performed similar calculations. We found that the isomer with one Au atom in the core, 12 Ag atoms on the icosahedron and one Ag plus 11 Au atoms on the staples (isomer III) to be the lowest in energy. With these lowest energy structures we obtain for reaction (7) an exothermicity of 1.69 eV.

Table S1. Relative energies for isomers of $[Ag_{12}Au_{13}(PET)_{18}]^-$ and $[Ag_{13}Au_{12}(DMBT)_{18}]^-$.

$[Ag_{12}Au_{13}(PET)_{18}]^-$	core	icosahedron	staple	relative Energy [eV]
I	**Au**	**12 Ag**	**12 Au**	**0**
II	Au	12 Au	12 Ag	1.27
III	Ag	11 Ag, 1Au	12 Au	0.11
IV	Au	6 Ag, 6 Au	6 Ag, 6 Au	0.41
V	Au	6 Ag, 6 Au	6 Ag, 6 Au	0.56
VI	Au	6 Ag, 6 Au	6 Ag, 6 Au	0.63
VII	Ag	5 Ag, 7Au	6 Ag, 6 Au	0.87
$[Ag_{13}Au_{12}(DMBT)_{18}]^-$				
I	Ag	12 Ag	12 Au	0.40
II	Ag	12 Au	12 Ag	1.04
III	**Au**	**12 Ag**	**1 Ag, 11 Au**	**0**
IV	Ag	6 Ag, 6 Au	6 Ag, 6 Au	0.56
V	Ag	6 Ag, 6 Au	6 Ag, 6 Au	0.72
VI	Ag	6 Ag, 6 Au	6 Ag, 6 Au	0.66
VII	Au	6Ag, 6 Au	7 Ag, 5 Au	0.34

(B) Ligand exchange

What role do the different ligands DMBT vs. PET play in the nanoalloying chemistry?

In order to shed some light into this issue we compared the DFT-energies of $[Ag_{25}(DMBT)_{18}]^-$ and $[Au_{25}(PET)_{18}]^-$ with those of the (experimentally not accessible) ligand-exchanged clusters $[Au_{25}(DMBT)_{18}]^-$ and $[Ag_{25}(PET)_{18}]^-$ (obtained by replacing all Ag by Au atoms and vice versa and optimizing the geometries).

For the hypothetical exchange reaction:

$$[Ag_{25}(DMBT)_{18}]^- + [Au_{25}(PET)_{18}]^- \rightarrow [Au_{25}(DMBT)_{18}]^- + [Ag_{25}(PET)_{18}]^- \qquad (8)$$

we calculate an endothermicity of 1.26 eV, i.e. less than 0.1 eV for each ligand exchange. Note that in reaction (8) we assumed the most basic ligand exchange being well aware that there can be partial ligand exchange or ligand exchange at some specific sites on the cluster surface favouring the formation of the dimers.

Does the ligand shell alter the order of topological isomers?

As a test case we reinvestigated the three isomers of $[Ag_{24}Au(SR)_{18}]^{-}$ and $[AgAu_{24}(SR)_{18}]^{-}$ (SR=PET and DMBT), now as function of the ligand. The relative energies are summarized in Table S2.

Table S2. Relative energies for isomers of $[Ag_{24}Au(SR)_{18}]^{-}$ and $[AgAu_{24}(SR)_{18}]^{-}$ (SR=PET and DMBT) as function of the ligand.

	$[AgAu_{24}PET_{18}]^{-}$	$[AgAu_{24}DMBT_{18}]^{-}$
Ag icosahedron	0.00 eV	0.00 eV
Ag staple	0.20 eV	0.20 eV
Ag core	0.31 eV	0.29 eV
	$[Ag_{24}AuPET_{18}]^{-}$	$[Ag_{24}AuDMBT_{18}]^{-}$
Au core	0.00 eV	0.00 eV
Au icosahedron	0.30 eV	0.27 eV
Au staple	0.31 eV	0.28 eV

From this we conclude that the impact of the ligands on the relative energies of the isomers is negligible in this case. We assume that this is the case for all mixed clusters.

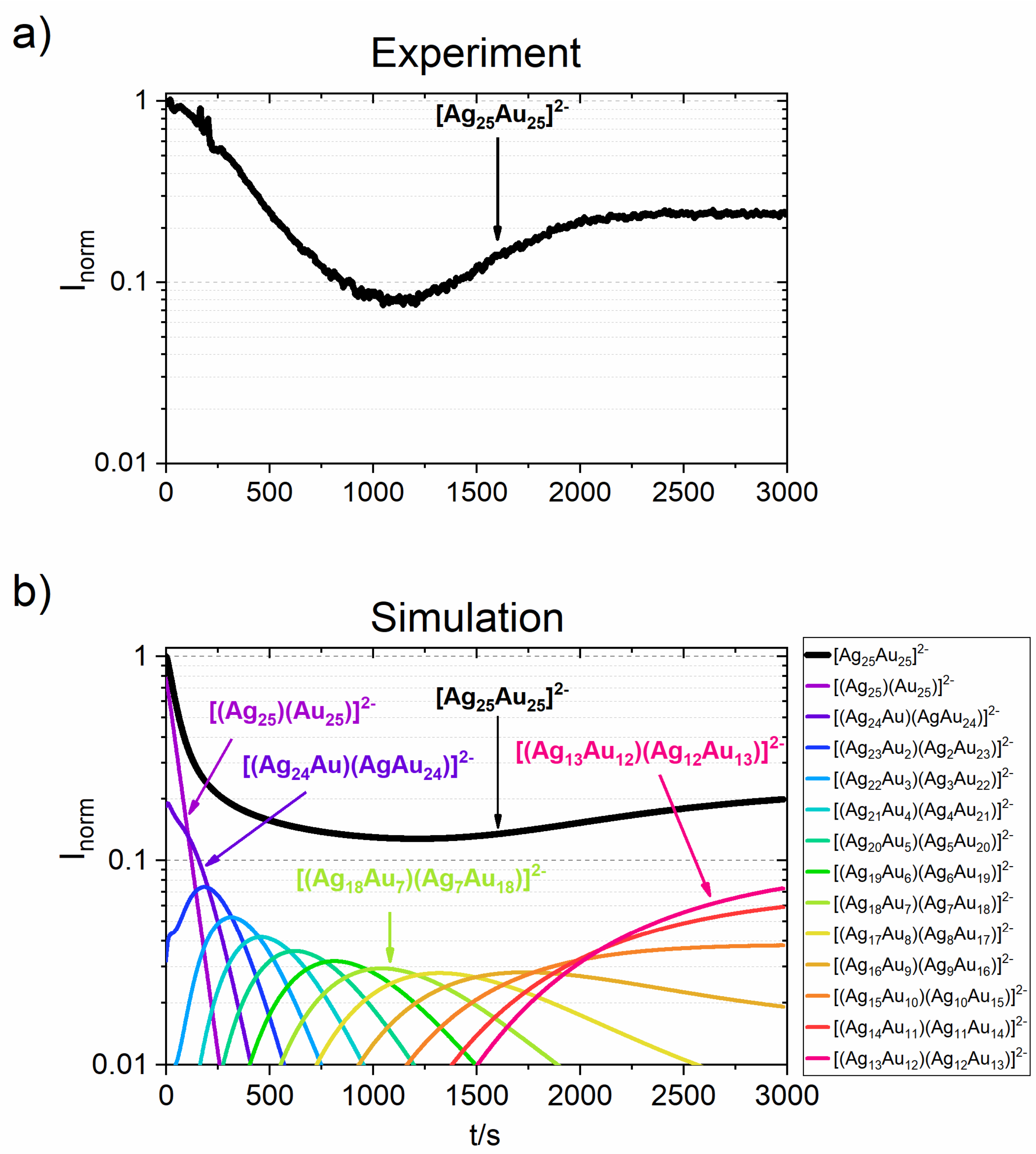

Figure S5. Time dependence of normalized $[Ag_{25}Au_{25}]^{2-}$ solution concentration as observed in a) experiment by ESI-MS (40:40 nmol L^{-1} ratio of Ag_{25}:Au_{25}) and b) in simulation 2. The intensity of $[Ag_{25}Au_{25}]^{2-}$ in the experiment was normalized to 1 at time zero. In the simulation the integrated signal $[Ag_{25}Au_{25}]^{2-}$ was normalized to 1 after a reaction time of 20s, which is the estimated “dead time” of the experiment. Colored lines in b) refer to isomers of $[Ag_{25}Au_{25}]^{2-}$ starting from $[(Ag_{25})(Au_{25})]^{2-}$ (purple) to fully mixed $[(Ag_{13}Au_{12})(Ag_{12}Au_{13})]^{2-}$ (pink) clusters. The experiment and the simulation have in common that the integrated signal of $[Ag_{25}Au_{25}]^{2-}$ shows a minimum before an equilibrium is reached after ~2500 s in the experiment and after ~3500 s (not shown) in the simulation.

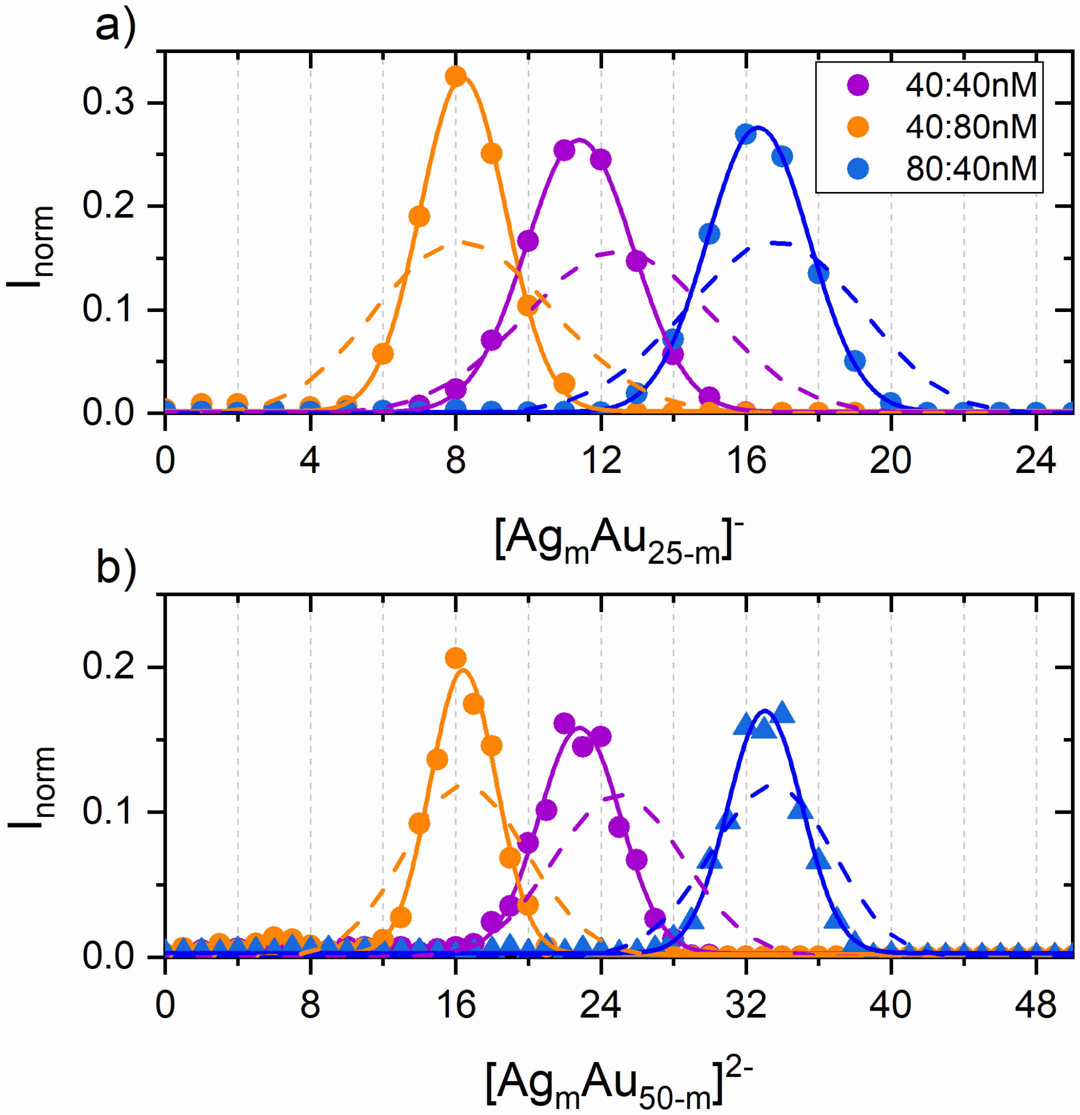

Figure S6. Experimental equilibrium distributions after 54 min for a) monoanions and b) dianions for three different mixing ratios of $[Ag_{25}]^-$:$[Au_{25}]^-$ clusters. The dashed lines show the expected binomial distributions.

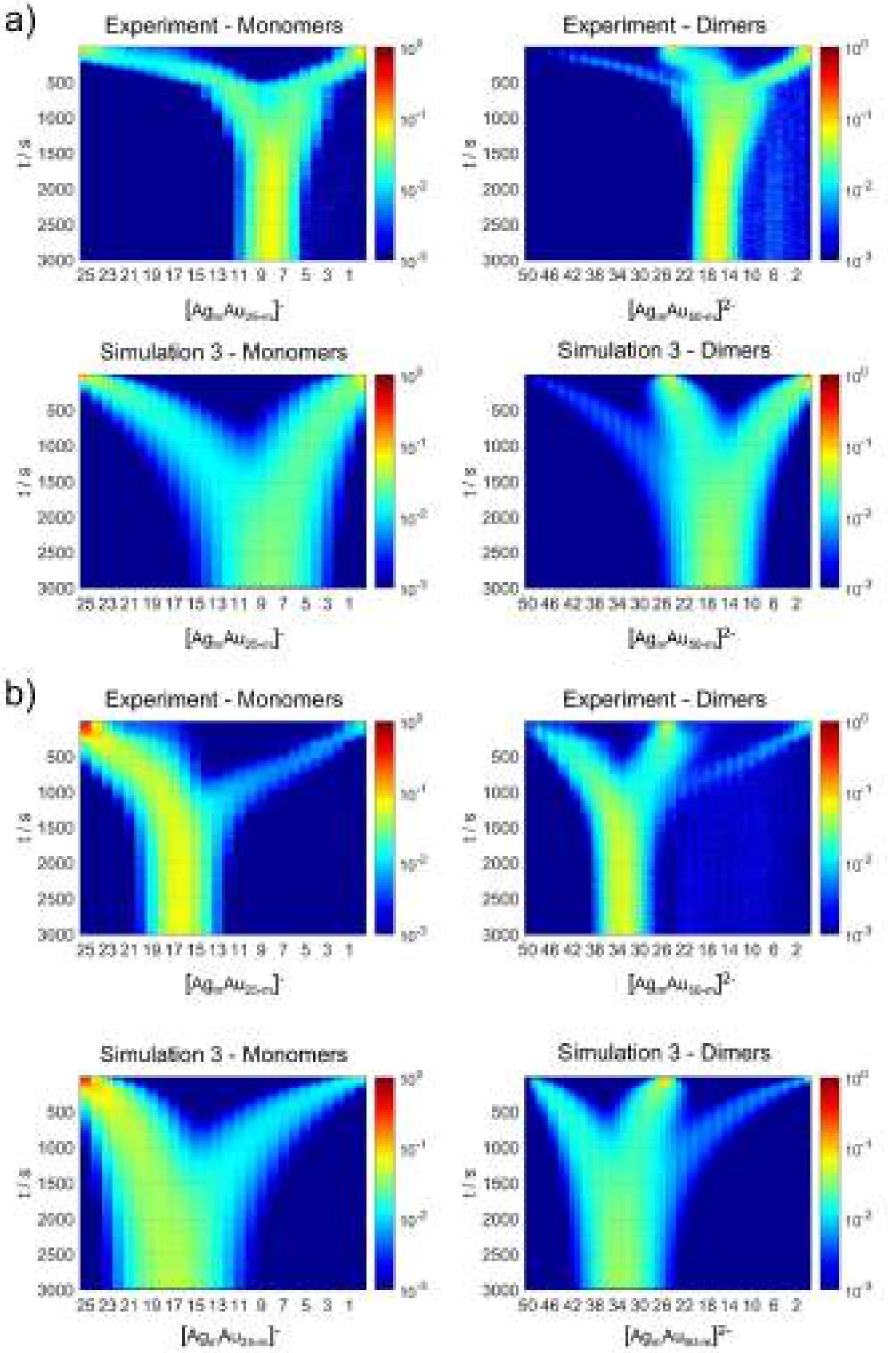

Figure S7. Contour plots of monomers and dimers for the exchange reaction between $[Ag_{25}]^-$ and $[Au_{25}]^-$ for a mixing ratio of $[Ag_{25}]^-$: $[Au_{25}]^-$ of a) 40:80 nmol L^{-1} and b) 80:40 nmol L^{-1} for experiment (top) and simulation (bottom). For all simulations the optimized rate constants from simulation 3 were applied, i.e. $k_{dim} = 1{\cdot}10^{-2}$ L nmol^{-1}s^{-1} , $k_{diss} = 5.6{\cdot}10^{-2}$ s^{-1} and $k_{ex} = 3.2{\cdot}10^{-2}$ s^{-1}. Starting conditions of all simulations were chosen as in the experiment.

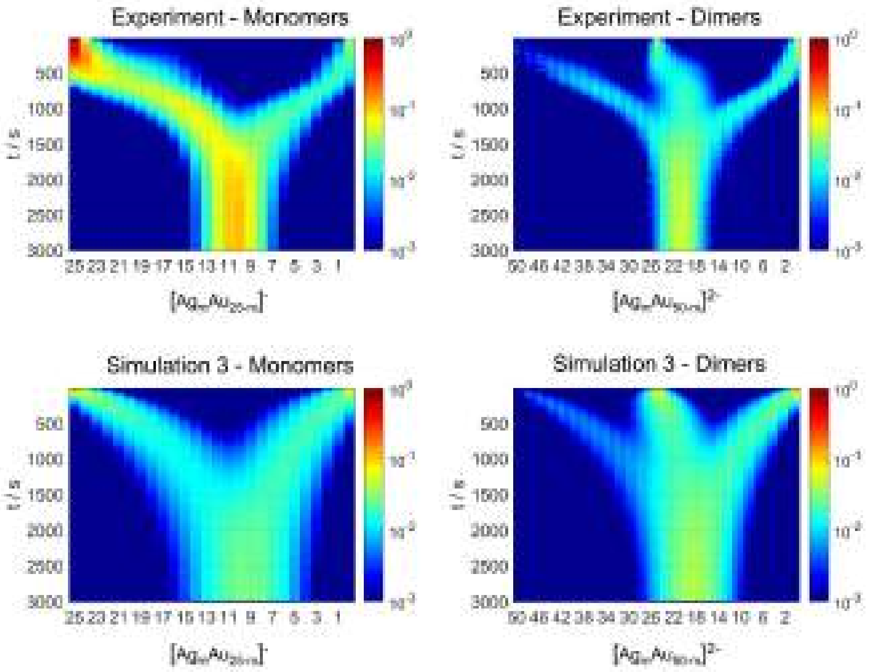

Figure S8. Contour plots of monomers and dimers for the exchange reaction between $[Ag_{25}]^-$ and $[Au_{25}]^-$ for a mixing ratio of $[Ag_{25}]^-$: $[Au_{25}]^-$ of 60:100 nmol L^{-1} for experiment (top) and simulation (bottom). For all simulations the optimized rate constants from simulation 3 were applied, i.e. $k_{dim} = 1 \cdot 10^{-2}$ L nmol^{-1} s^{-1}, $k_{diss} = 5.6 \cdot 10^{-2}$ s^{-1} and $k_{ex} = 3.2 \cdot 10^{-2}$ s^{-1}. Starting conditions of all simulations were chosen as in the experiment.

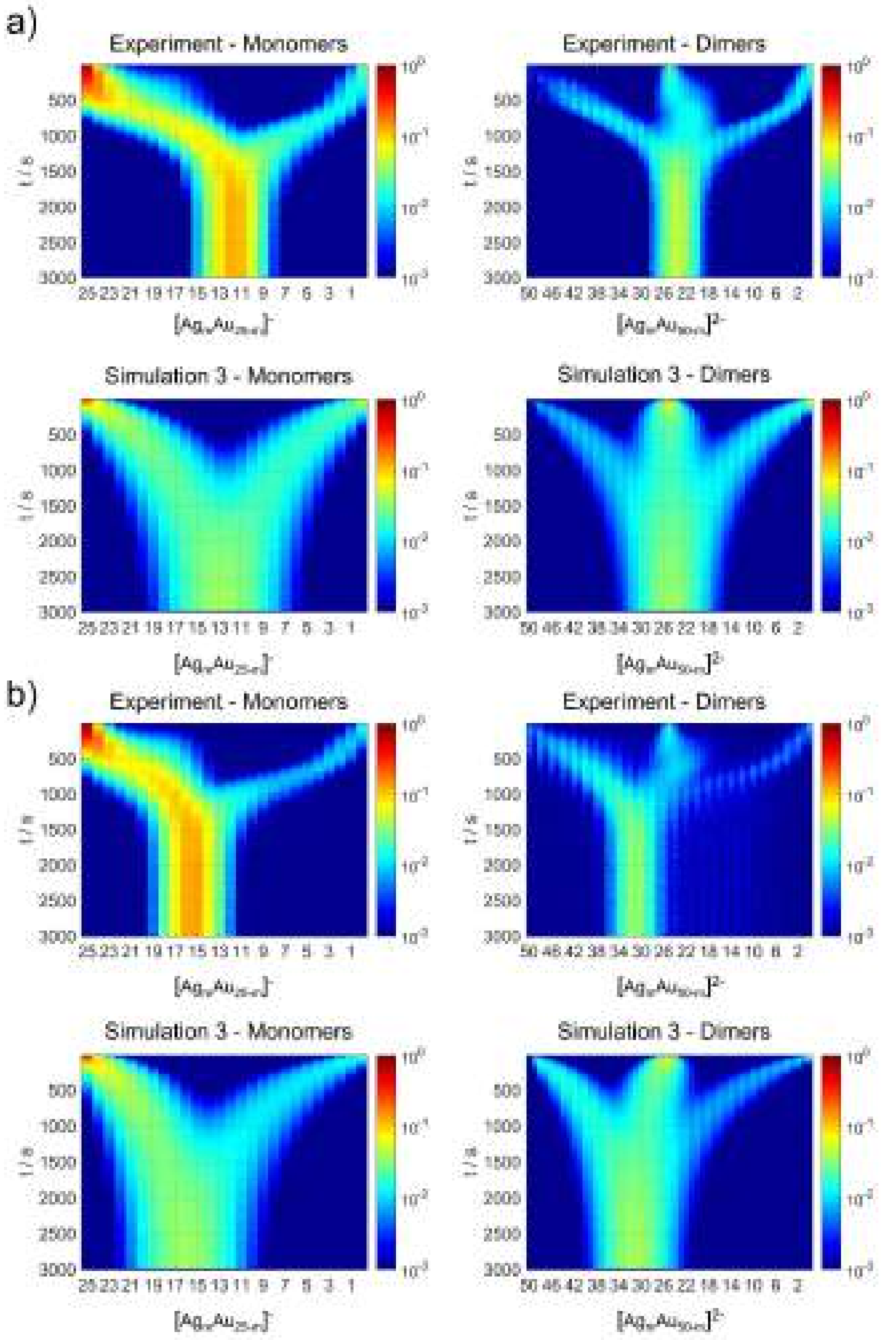

Figure S9. Contour plots of monomers and dimers for the exchange reaction between $[Ag_{25}]^-$ and $[Au_{25}]^-$ for a mixing ratio of $[Ag_{25}]^-$: $[Au_{25}]^-$ of a) 50:50 nmol L^{-1} and b) 100:60 nmol L^{-1} for experiment (top) and simulation (bottom). For all simulations the optimized rate constants from simulation 3 were applied, i.e. $k_{dim} = 1\cdot10^{-2}$ L nmol^{-1} s^{-1}, $k_{diss} = 5.6\cdot10^{-2}$ s^{-1} and $k_{ex} = 3.2\cdot10^{-2}$ s^{-1}. Starting conditions of all simulations were chosen as in the experiment.

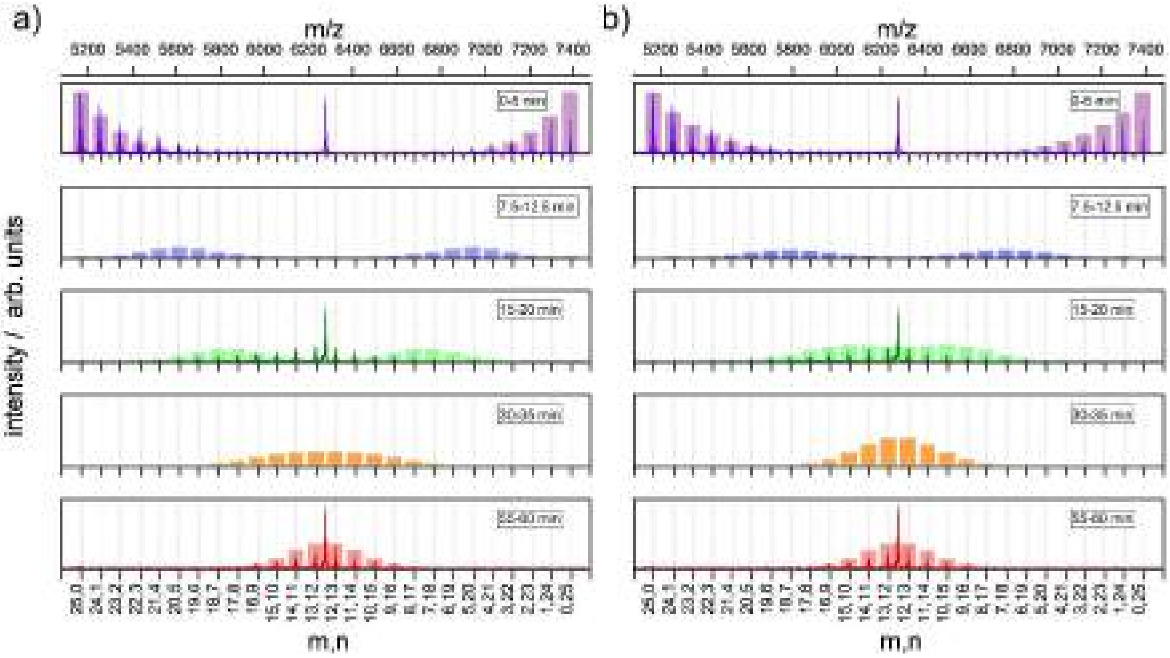

Figure S10. a) Modelled composition of $[Ag_{25}Au_{25}]^{2-}$ isomers (bar plots) based on simulation 3 at five different time intervals ($k_{dim} = 1{\cdot}10^{-2}$ L nmol^{-1} s^{-1}, $k_{diss} = 5.6{\cdot}10^{-2}$ s^{-1} and $k_{ex} = 3.2{\cdot}10^{-2}$ s^{-1}, mixing ratio 40:40 nmol L^{-1}) together with experimental data (spectrum in the 0–5 min, 15–20 min and 55–60 min time interval) from the CID experiment. Bars correspond to the simulated monomeric subunit constituents of the $[Ag_{25}Au_{25}]^{2-}$ dimers at the respective reaction time intervals. As an example, during the 0–5 min reaction time window, the dominant $[Ag_{25}Au_{25}]^{2-}$ isomer consists of $[Ag_{25}]^{-}$ and $[Au_{25}]^{-}$ subunits in good agreement with the experimental data. After a reaction time of 15–20 min the dominant $[Ag_{25}Au_{25}]^{2-}$ isomer in simulation 3 is $[(Ag_{18}Au_{7})(Au_{7}Ag_{18})]^{2-}$, while in the experiment $[(Ag_{13}Au_{12})(Au_{12}Ag_{13})]^{2-}$ is already present, i.e. the experimental kinetics proceeds somewhat faster. b) The same plot as in a) but with $k_{ex} = 5{\cdot}10^{-2}$ s^{-1} (which is still within our estimated range of k_{ex}). This leads to a better agreement for the 15–20 min CID experiment. Note however that the CID data were recorded on a different instrument (Synapt mass spectrometer; IIT Madras) compared to the kinetics data (tims-TOFMS; KIT) which serve as the basis for our determined rate constants. Another reason for the deviation could be further Ag/Au mixing as a result of collisional heating before dissociation.

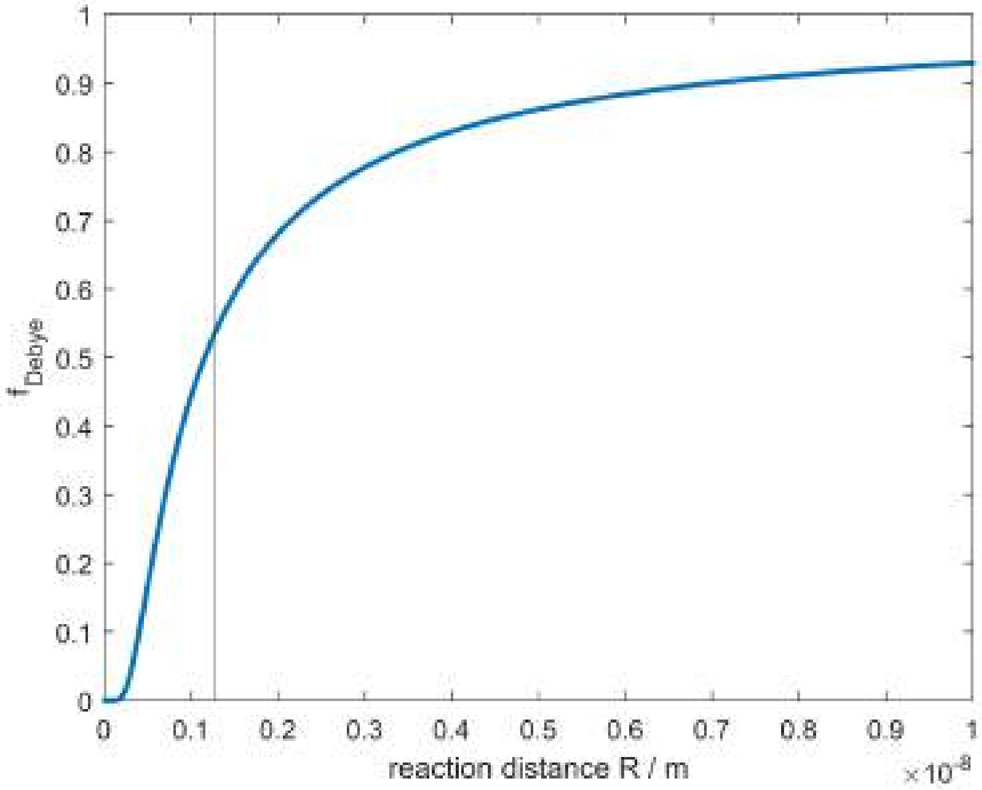

Figure S11: Debye factor f_{Debye} according to equation 6 as a function of the reaction distance R. For $[M_{25}]^-$ (M = Ag or Au) clusters the reaction distance is assumed to be twice the radius of $[Au_{25}]^-$ which corresponds to R=12.7Å (denoted by the black vertical line).

References

(1) Zhu, M.; Lanni, E.; Garg, N.; Bier, M. E.; Jin, R. Kinetically Controlled, High-Yield Synthesis of Au_{25} Clusters. *J. Am. Chem. Soc.* **2008**, *130*, 1138–1139.

(2) Wu, Z.; Suhan, J.; Jin, R. One-Pot Synthesis of Atomically Monodisperse, Thiol-Functionalized Au_{25} Nanoclusters. *J. Mater. Chem.* **2009**, *19*, 622–626.

(3) Krishnadas, K. R.; Ghosh, A.; Baksi, A.; Chakraborty, I.; Natarajan, G.; Pradeep, T. Intercluster Reactions between $Au_{25}(SR)_{18}$ and $Ag_{44}(SR)_{30}$. *J. Am. Chem. Soc.* **2016**, *138*, 140–148.

(4) Joshi, C. P.; Bootharaju, M. S.; Alhilaly, M. J.; Bakr, O. M. $[Ag_{25}(SR)_{18}]^-$: The “Golden” Silver Nanoparticle. *J. Am. Chem. Soc.* **2015**, *137*, 11578–11581.

(5) Furche, F.; Ahlrichs, R.; Hättig, C.; Klopper, W.; Sierka, M.; Weigend, F. Turbomole. *Wiley Interdiscip. Rev. Comput. Mol. Sci.* **2014**, *4*, 91–100.

(6) Becke, A. D. Density-Functional Exchange-Energy Approximation with Correct Asymptotic Behavior. *Phys. Rev. A* **1988**, *38*, 3098–3100.

(7) Perdew, J. P. Density-Functional Approximation for the Correlation Energy of the Inhomogeneous Electron Gas. *Phys. Rev. B* **1986**, *33*, 8822–8824.

(8) Weigend, F.; Ahlrichs, R. Balanced Basis Sets of Split Valence, Triple Zeta Valence and Quadruple Zeta Valence Quality for H to Rn: Design and Assessment of Accuracy. *Phys. Chem. Chem. Phys.* **2005**, *7*, 3297.

(9) Heaven, M. W.; Dass, A.; White, P. S.; Holt, K. M.; Murray, R. W. Crystal Structure of the Gold Nanoparticle $[N(C_8H_{17})_4][Au_{25}(SCH_2CH_2Ph)_{18}]$. *J. Am. Chem. Soc.* **2008**, *130*, 3754–3755.

(10) Krishnadas, K. R.; Baksi, A.; Ghosh, A.; Natarajan, G.; Pradeep, T. Structure-Conserving Spontaneous Transformations between Nanoparticles. *Nat. Commun.* **2016**, *7*, 13447.

Coordinates of calculated structures

Ag$_{25}$DMBT$_{18}$
349

Ag	14.77088	17.52654	14.62452
Ag	17.62927	18.71260	15.20890
Ag	19.37684	16.09222	16.20866
Ag	17.24119	13.69534	16.39037
Ag	13.35763	16.46562	17.01561
Ag	11.72964	18.55536	15.20580
Ag	13.25717	18.51471	12.34170
Ag	14.84712	15.26213	12.43878
Ag	16.37838	16.53777	16.89824
Ag	14.74882	16.74503	19.71691
Ag	11.62638	15.12354	19.16660
Ag	12.48428	13.60533	16.40057
Ag	14.91248	12.01770	16.00589
Ag	12.14393	10.66326	15.11291
Ag	10.25314	13.59989	14.45172
Ag	12.46410	15.83023	14.13095
Ag	16.26599	13.03004	13.56693
Ag	17.72246	10.89783	15.22844
Ag	16.66401	11.17241	18.22891
Ag	14.87257	14.22570	18.08871
Ag	13.28942	12.99775	13.63178
Ag	15.16096	12.78332	10.64406
Ag	17.89549	14.33145	11.46449
Ag	17.20397	15.86994	14.15633
Ag	14.82993	14.76511	15.28109
S	15.52127	19.94647	14.98741
S	20.02788	18.36357	15.49282
S	19.74915	13.68417	16.59394
S	11.84279	20.19258	13.39085
S	14.84878	17.33234	10.94898
S	11.09278	17.61057	17.37163
S	17.08783	17.26126	19.23114
S	12.56534	16.68157	20.79200
S	10.23230	13.84401	17.61336
S	14.36533	9.65168	15.24029
S	9.80069	11.20861	14.78894
S	9.94310	15.97029	13.87075
S	17.95302	9.39982	17.16070
S	15.11024	12.27024	19.74628
S	18.34550	11.68726	12.98022
S	12.84830	12.27881	11.22646
S	17.32419	12.90566	9.52898
S	19.34415	15.83688	12.77224
C	19.67593	9.50833	17.66575
C	20.67545	9.87342	16.73947
C	20.05222	9.10827	18.97996
C	22.03145	9.84907	17.09343
C	21.42370	9.09880	19.30271
C	19.02716	8.70399	20.01185
C	22.43218	9.46402	18.38806
C	23.88834	9.47101	18.79864
C	14.39267	8.19599	16.29724
C	15.15395	7.11283	15.80542
C	13.71384	8.06889	17.54074

C	15.25146	5.91318	16.52345
C	13.83043	6.84525	18.23273
C	12.89722	9.18753	18.12798
C	14.58840	5.75601	17.75629
C	14.68988	4.47496	18.55650
C	18.00693	10.30981	11.87153
C	16.72859	9.72868	11.75906
C	19.07605	9.82073	11.06763
C	16.49192	8.67943	10.85808
C	18.80483	8.76284	10.17837
C	20.46086	10.41952	11.14342
C	17.52831	8.17750	10.04725
C	17.28942	7.05728	9.05750
C	12.71573	10.54159	10.76529
C	12.42568	10.20678	9.41197
C	12.84777	9.51041	11.71625
C	12.28658	8.84317	9.07799
C	12.27462	11.26567	8.34720
C	12.69931	8.16540	11.35347
C	12.41653	7.80376	10.01995
C	12.27909	6.35152	9.61609
C	9.32586	10.47232	13.21835
C	9.02864	9.08091	13.16555
C	9.15002	11.26518	12.06528
C	8.56123	8.54972	11.94665
C	9.20480	8.18630	14.36935
C	8.68185	10.70436	10.86960
C	8.38006	9.33024	10.78710
C	7.91607	8.70507	9.48978
C	9.36510	15.97063	12.16948
C	8.05008	15.51052	11.87390
C	10.15855	16.50397	11.13135
C	7.60261	15.59126	10.53774
C	7.14342	14.95005	12.94292
C	9.68087	16.57970	9.81744
C	8.38801	16.11753	9.49372
C	7.86097	16.20631	8.07747
C	10.23652	20.19167	12.58105
C	10.11100	20.71299	11.26277
C	9.08171	19.77489	13.27751
C	8.82000	20.78366	10.69924
C	11.31040	21.17257	10.47023
C	7.81473	19.85937	12.68680
C	7.66006	20.36421	11.37956
C	6.29970	20.41982	10.71919
C	10.86488	18.98478	18.51111
C	9.61302	19.02458	19.16407
C	11.83270	19.98975	18.78853
C	9.30601	20.04229	20.07744
C	11.48854	20.99942	19.71172
C	13.18879	20.00085	18.13854
C	10.24152	21.05622	20.36634
C	9.91786	22.18419	21.32298
C	17.10559	19.01946	19.62546
C	16.89765	20.00357	18.64090
C	17.37574	19.41974	20.96771
C	16.94127	21.36810	18.96109
C	17.41178	20.79821	21.25533

C	17.60975	18.40811	22.06451
C	17.19558	21.79341	20.27921
C	17.22036	23.26114	20.64865
C	20.50410	19.52847	16.77990
C	20.20875	20.89477	16.57008
C	21.26750	19.14704	17.91874
C	20.65089	21.87754	17.46387
C	21.69096	20.16338	18.80139
C	21.64079	17.71324	18.19937
C	21.40058	21.52734	18.60567
C	21.84900	22.57199	19.60405
C	20.39750	13.57909	18.26506
C	19.56287	13.34020	19.37737
C	21.80354	13.69085	18.45937
C	20.09337	13.21735	20.66794
C	22.30457	13.57321	19.77282
C	22.74545	13.91923	17.30167
C	21.48118	13.33604	20.89066
C	22.06228	13.18894	22.28040
C	15.88246	11.96438	21.35058
C	15.86484	10.62837	21.81300
C	16.44924	12.97739	22.17198
C	16.40035	10.28492	23.06191
C	16.97762	12.59639	23.42428
C	16.50017	14.41823	21.74126
C	16.96958	11.26830	23.89630
C	17.53002	10.92367	25.25940
C	12.88924	15.98051	22.41722
C	13.13323	16.87265	23.49916
C	12.86648	14.59033	22.65459
C	13.34164	16.31856	24.78019
C	13.16780	18.36992	23.30099
C	13.07739	14.07355	23.93932
C	13.31963	14.93288	25.03169
C	13.56244	14.37835	26.41869
C	15.79173	21.03259	13.57735
C	15.20547	22.32926	13.60678
C	16.59412	20.65751	12.47806
C	15.45792	23.19629	12.52160
C	14.34088	22.78807	14.75652
C	16.82735	21.54661	11.42118
C	16.26031	22.83878	11.42132
C	16.51920	23.80436	10.28432
C	19.67289	17.20538	11.64898
C	21.00359	17.71174	11.57519
C	18.67961	17.74091	10.80386
C	21.27252	18.73573	10.64453
C	22.10794	17.17260	12.45251
C	18.98680	18.75366	9.88229
C	20.29344	19.27166	9.78302
C	20.64971	20.34327	8.77452
C	17.16411	13.84597	8.00726
C	18.24533	14.63620	7.52196
C	16.00695	13.69850	7.21013
C	18.09453	15.26793	6.26945
C	19.52807	14.80304	8.29812
C	15.89107	14.33833	5.97001
C	16.93609	15.14724	5.47746

C	16.80593	15.87872	4.15937
C	14.16406	17.67376	9.31281
C	14.39885	18.96913	8.79560
C	13.44818	16.72814	8.53233
C	13.93139	19.33670	7.52739
C	12.99303	17.13260	7.25762
C	13.17338	15.33404	9.02556
C	13.21610	18.41908	6.72942
C	12.73289	18.79422	5.34485
C	9.39136	12.43501	18.34880
C	8.08979	12.18166	17.85747
C	9.91630	11.61324	19.38260
C	7.31378	11.13477	18.36785
C	9.10440	10.56910	19.87739
C	11.28675	11.83370	19.95800
C	7.80874	10.30448	19.39502
C	6.96573	9.19105	19.97836
H	20.37978	10.17837	15.72140
H	22.78961	10.13552	16.34421
H	21.71532	8.78700	20.32194
H	18.36806	7.88878	19.63807
H	18.35318	9.55461	20.26961
H	19.51715	8.36180	20.94860
H	24.56198	9.42335	17.91552
H	24.13270	8.61383	19.46457
H	24.14323	10.40156	19.35807
H	15.67948	7.22285	14.84312
H	15.85808	5.08648	16.11535
H	13.29945	6.74534	19.19663
H	13.52204	10.09071	18.31124
H	12.43764	8.88582	19.09262
H	12.07189	9.50448	17.44394
H	15.20870	3.67659	17.98325
H	13.68544	4.08944	18.84429
H	15.25921	4.62835	19.50259
H	15.90521	10.09341	12.39498
H	15.47579	8.25592	10.78817
H	19.63428	8.38514	9.55322
H	20.86938	10.38013	12.17830
H	20.44841	11.49467	10.85342
H	21.16343	9.88472	10.46829
H	16.25701	6.65522	9.14243
H	17.99864	6.21230	9.21326
H	17.42685	7.40486	8.00740
H	13.08019	9.76385	12.76336
H	12.06254	8.58606	8.02685
H	11.49579	12.01057	8.62264
H	12.00673	10.81411	7.36793
H	13.22028	11.84160	8.21682
H	12.80911	7.38740	12.12854
H	11.82979	6.24875	8.60464
H	11.64179	5.78681	10.33279
H	13.26892	5.83846	9.59314
H	9.38737	12.34204	12.10940
H	8.32528	7.47111	11.90561
H	8.64717	8.57164	15.25204
H	10.27466	8.13374	14.68052
H	8.85895	7.15249	14.15392

H	8.55344	11.35253	9.98635
H	7.26330	7.82252	9.66838
H	8.78340	8.35595	8.88171
H	7.35021	9.43077	8.86529
H	11.17128	16.87443	11.36874
H	6.58472	15.22717	10.30782
H	7.57080	14.02551	13.39943
H	6.14413	14.69747	12.52788
H	7.00945	15.66997	13.78108
H	10.33039	17.00647	9.03422
H	6.89590	15.66626	7.96562
H	8.57954	15.77382	7.34525
H	7.69017	17.26478	7.77154
H	9.18424	19.37719	14.30096
H	8.72166	21.18861	9.67589
H	11.91704	21.91625	11.03332
H	11.00018	21.62535	9.50425
H	11.99763	20.32314	10.24171
H	6.93158	19.52136	13.25542
H	6.27825	21.15330	9.88365
H	5.50347	20.70033	11.44367
H	6.01805	19.42736	10.29577
H	8.87432	18.23621	18.94632
H	8.31976	20.04585	20.57340
H	12.24116	21.77846	19.92805
H	13.11900	20.07488	17.02817
H	13.74737	19.05635	18.34566
H	13.80943	20.84510	18.50353
H	9.04081	21.93947	21.96045
H	9.67695	23.12635	20.77620
H	10.77558	22.41144	21.99452
H	16.69279	19.69988	17.60134
H	16.77538	22.11021	18.16151
H	17.62261	21.10613	22.29563
H	16.71075	17.76839	22.22363
H	17.85177	18.91018	23.02585
H	18.43926	17.71287	21.80767
H	17.25357	23.90696	19.74503
H	18.10237	23.51152	21.28004
H	16.31470	23.55140	21.23120
H	19.62707	21.18489	15.67935
H	20.40740	22.93615	17.26800
H	22.28283	19.86673	19.68581
H	22.22003	17.26834	17.35959
H	20.73671	17.07274	18.33455
H	22.25209	17.63128	19.12280
H	22.01373	23.55875	19.11822
H	22.79332	22.27644	20.11172
H	21.08252	22.72290	20.40014
H	18.47447	13.24961	19.21926
H	19.41017	13.02598	21.51297
H	23.39529	13.66863	19.92403
H	22.68357	13.08709	16.56477
H	23.79714	14.00178	17.65137
H	22.48775	14.84458	16.73793
H	21.49196	13.78479	23.02790
H	23.12286	13.52016	22.31830
H	22.03268	12.12850	22.62393

H	15.42254	9.84839	21.17174
H	16.37579	9.23117	23.38982
H	17.41942	13.38573	24.05836
H	15.47447	14.82979	21.59568
H	17.03180	14.54363	20.77339
H	17.01221	15.04685	22.49860
H	17.73963	9.83592	25.35136
H	16.81748	11.19241	26.07434
H	18.47617	11.47230	25.46473
H	12.69170	13.90434	21.81068
H	13.52676	17.01087	25.62136
H	13.96752	18.66929	22.58534
H	13.34896	18.89538	24.26338
H	12.21513	18.74581	22.86619
H	13.05833	12.98077	24.08975
H	13.61344	15.18700	27.17954
H	14.52048	13.81085	26.46645
H	12.75658	13.67337	26.72452
H	17.05255	19.65556	12.45216
H	15.00663	24.20438	12.54845
H	13.41681	22.17056	14.83253
H	14.03420	23.84835	14.62595
H	14.87110	22.69164	15.73072
H	17.47494	21.22286	10.58871
H	15.98631	24.76761	10.43699
H	16.18489	23.38628	9.30730
H	17.60513	24.03245	10.18122
H	17.64747	17.35661	10.85906
H	22.30472	19.12680	10.58877
H	22.23159	16.07374	12.32179
H	21.87788	17.33934	13.52971
H	23.07635	17.66661	12.22137
H	18.18809	19.13425	9.22272
H	21.27691	21.14271	9.22935
H	19.74068	20.82268	8.35149
H	21.23029	19.92391	7.91933
H	15.18876	13.05512	7.57378
H	18.93260	15.88407	5.89773
H	19.98753	13.82021	8.54644
H	19.35230	15.32138	9.27097
H	20.26667	15.40374	7.72613
H	14.97211	14.20265	5.37426
H	17.79929	16.15763	3.74561
H	16.22129	16.82126	4.27708
H	16.27722	15.26265	3.39828
H	14.95410	19.69497	9.41255
H	14.12591	20.35733	7.15445
H	12.43369	16.39743	6.65182
H	14.12347	14.77933	9.20433
H	12.57396	14.75551	8.29284
H	12.62576	15.33360	9.99270
H	12.37139	19.84569	5.30798
H	11.90337	18.13519	5.00776
H	13.54994	18.70514	4.59044
H	7.68917	12.82361	17.05682
H	6.30454	10.95999	17.95586
H	9.51432	9.93224	20.68203
H	11.37226	12.85307	20.40754

H	12.08109	11.78106	19.18220
H	11.52541	11.08966	20.74641
H	6.36926	8.67430	19.19385
H	6.24071	9.57935	20.73256
H	7.59195	8.42775	20.48929

$Au_{25}PET_{18}$

349

Au	12.52666	15.34445	12.15412
Au	15.65562	16.52948	13.03461
Au	17.43579	13.43367	13.75694
Au	14.82838	11.10913	13.53645
Au	11.05591	14.02736	14.46309
Au	9.57283	16.70357	12.81880
Au	10.99696	16.36594	9.44567
Au	12.66229	13.38418	9.80075
Au	14.11908	13.94307	14.37415
Au	12.46893	14.10836	17.42111
Au	9.37719	12.30827	16.62987
Au	9.98117	11.36342	13.33849
Au	12.48070	9.61323	12.86629
Au	9.34980	8.42692	11.99139
Au	7.57009	11.52426	11.27080
Au	10.17583	13.84840	11.49552
Au	13.94922	10.93516	10.55846
Au	15.42887	8.25663	12.20738
Au	14.00859	8.59703	15.58163
Au	12.34363	11.57952	15.22761
Au	10.89120	11.01650	10.64978
Au	12.53614	10.85272	7.60107
Au	15.63052	12.64791	8.39279
Au	15.02984	13.58656	11.68643
Au	12.50387	12.47936	12.51372
S	13.51522	17.53363	12.77953
S	17.88107	15.69055	13.14125
S	17.18338	11.14302	14.36268
S	9.64588	17.85116	10.73054
S	12.42067	15.09342	8.01605
S	9.34388	15.74417	14.98149
S	14.69048	14.57228	16.70833
S	10.26253	13.80981	18.26278
S	8.26912	10.88259	15.08395
C	13.66167	18.59030	11.25738
H	14.34578	18.10028	10.53477
H	12.64532	18.60026	10.80815
C	14.10653	20.03297	11.56840
H	13.39404	20.47686	12.29853
H	13.99490	20.60945	10.62014
C	15.52726	20.18356	12.07779
C	16.62246	20.10081	11.18932
H	16.44186	19.93669	10.11248
C	17.94074	20.22746	11.65659
H	18.78001	20.15949	10.94414
C	18.18959	20.44376	13.02392
H	19.22459	20.54976	13.39080
C	17.10949	20.52680	13.91931
H	17.28840	20.68988	14.99528
C	15.79193	20.39612	13.44728
H	14.95065	20.45781	14.15802
C	18.65069	16.48288	14.63469
H	18.61225	17.57745	14.44769
H	18.03365	16.26349	15.52982

C	20.10097	16.00296	14.83156
H	20.09579	14.89834	14.97212
H	20.67807	16.20766	13.90274
C	20.76157	16.67838	16.01892
C	21.48635	17.88003	15.86192
H	21.60328	18.31098	14.85227
C	22.06443	18.52739	16.96686
H	22.63057	19.46275	16.81967
C	21.92591	17.98299	18.25552
H	22.38060	18.48818	19.12422
C	21.20794	16.78651	18.42815
H	21.09846	16.34609	19.43343
C	20.63211	16.14317	17.31959
H	20.07668	15.20024	17.46385
C	17.02613	11.24137	16.20743
H	16.19518	11.93299	16.45497
H	16.73805	10.21979	16.54097
C	18.34025	11.68850	16.87324
H	19.17000	11.03660	16.52257
H	18.57095	12.71946	16.51584
C	18.27442	11.66455	18.38990
C	19.06428	10.76434	19.13772
H	19.74465	10.07668	18.60632
C	18.99873	10.73444	20.54193
H	19.62659	10.02317	21.10473
C	18.13435	11.60609	21.22582
H	18.07930	11.58390	22.32723
C	17.33975	12.50731	20.49389
H	16.65922	13.19758	21.02048
C	17.40914	12.53669	19.09089
H	16.77920	13.24873	18.52827
C	7.93916	17.59974	10.04157
H	7.98359	17.93578	8.98349
H	7.70957	16.51394	10.06355
C	6.88754	18.39249	10.83783
H	7.16508	19.46962	10.84903
H	6.90922	18.03967	11.89446
C	5.49529	18.21738	10.25969
C	4.88192	19.24018	9.50526
H	5.41782	20.19367	9.35448
C	3.60138	19.06520	8.95231
H	3.13963	19.88084	8.37018
C	2.91076	17.85679	9.14387
H	1.90422	17.71754	8.71455
C	3.51065	16.82735	9.89157
H	2.97497	15.87655	10.05265
C	4.79000	17.00608	10.44284
H	5.25227	16.19110	11.02619
C	11.31672	14.36938	6.70735
H	11.75311	13.37159	6.47763
H	10.31063	14.19735	7.13692
C	11.24536	15.22321	5.42767
H	12.27622	15.38510	5.04104
H	10.71261	14.60556	4.66673
C	10.53238	16.55491	5.56874
C	11.24983	17.76901	5.60150
H	12.34926	17.74648	5.51624
C	10.58544	19.00011	5.73726

H	11.16734	19.93710	5.75987
C	9.18531	19.03824	5.84370
H	8.66145	20.00328	5.94935
C	8.45659	17.83574	5.81031
H	7.35631	17.85258	5.88461
C	9.12455	16.60776	5.67193
H	8.53837	15.67324	5.63298
C	10.04831	17.03255	16.11661
H	10.21647	16.51156	17.08397
H	11.02932	17.37463	15.72953
C	9.06489	18.20649	16.28666
H	8.90420	18.68501	15.29483
H	8.08148	17.79871	16.61105
C	9.55022	19.23893	17.28739
C	9.43376	19.00820	18.67690
H	8.97142	18.07050	19.03132
C	9.89086	19.95405	19.60904
H	9.78638	19.75425	20.68901
C	10.47342	21.15622	19.16845
H	10.82661	21.90257	19.89968
C	10.59953	21.39829	17.78969
H	11.05180	22.33849	17.43110
C	10.14466	20.44602	16.86095
H	10.24481	20.64394	15.77982
C	14.85962	16.41719	16.82645
H	15.73969	16.67249	16.19656
H	13.97413	16.89810	16.36458
C	15.06346	16.87727	18.28258
H	14.14704	16.63081	18.86492
H	15.89835	16.29337	18.73002
C	15.36562	18.36175	18.38121
C	16.69881	18.82767	18.37939
H	17.52765	18.10004	18.33381
C	16.98651	20.20171	18.44123
H	18.03650	20.53972	18.44553
C	15.94006	21.13880	18.50367
H	16.16265	22.21805	18.55446
C	14.60797	20.68914	18.50369
H	13.77575	21.41082	18.55397
C	14.32511	19.31426	18.44284
H	13.27485	18.97629	18.44843
C	10.43667	12.80079	19.81316
H	10.96172	11.85270	19.57530
H	11.08034	13.39253	20.49885
C	9.06301	12.52363	20.45179
H	8.55134	13.49282	20.64409
H	8.43637	11.96604	19.71991
C	9.19382	11.73351	21.74083
C	9.22540	10.32167	21.72336
H	9.11320	9.78982	20.76277
C	9.38734	9.58703	22.90996
H	9.40458	8.48496	22.87192
C	9.52214	10.25341	24.14028
H	9.64764	9.67796	25.07276
C	9.49173	11.65833	24.17369
H	9.59186	12.19137	25.13444
C	9.32954	12.38843	22.98429
H	9.30155	13.49161	23.01946

C	8.71401	9.17673	15.65944
H	8.30460	8.49290	14.88392
H	9.81897	9.07499	15.65968
C	8.12610	8.85632	17.04531
H	8.59175	9.54747	17.78631
H	7.03588	9.07593	17.04213
C	8.36220	7.41363	17.45374
C	7.29238	6.49825	17.55247
H	6.26555	6.84713	17.34707
C	7.51425	5.15704	17.91122
H	6.66102	4.46166	17.98686
C	8.81859	4.70314	18.17090
H	8.99611	3.65072	18.44947
C	9.89537	5.60308	18.07301
H	10.92429	5.25910	18.27241
C	9.66948	6.94431	17.72068
H	10.52292	7.64276	17.65476
S	11.49107	7.42353	12.24180
S	7.12492	9.26772	11.88787
S	7.82292	13.81489	10.66538
S	15.35747	7.11018	14.29633
S	12.58573	9.86996	17.01186
S	15.65802	9.21396	10.04379
S	10.31481	10.39129	8.31597
S	14.74212	11.15018	6.75785
S	16.74084	14.07010	9.94047
C	11.34999	6.36609	13.76379
H	10.66847	6.85549	14.48927
H	12.36805	6.35617	14.20907
C	10.90455	4.92334	13.45383
H	11.61262	4.48127	12.71831
H	11.02322	4.34557	14.40046
C	9.48044	4.77179	12.95426
C	8.39187	4.84783	13.85145
H	8.58023	5.00760	14.92763
C	7.07034	4.71995	13.39382
H	6.23649	4.78250	14.11311
C	6.81148	4.50915	12.02751
H	5.77392	4.40222	11.66822
C	7.88485	4.43289	11.12348
H	7.69806	4.27399	10.04824
C	9.20572	4.56494	11.58585
H	10.04161	4.50855	10.86832
C	6.35075	8.47555	10.39673
H	6.38683	7.38111	10.58492
H	6.96656	8.69230	9.50011
C	4.90126	8.95886	10.20239
H	4.90915	10.06321	10.05975
H	4.32596	8.75758	11.13305
C	4.23557	8.28310	9.01809
C	3.50329	7.08670	9.18016
H	3.38481	6.66010	10.19147
C	2.91973	6.43916	8.07821
H	2.34774	5.50802	8.22942
C	3.06018	6.97809	6.78749
H	2.60113	6.47284	5.92112
C	3.78569	8.16929	6.60977
H	3.89670	8.60547	5.60281

C	4.36695	8.81285	7.71536
H	4.92813	9.75176	7.56707
C	7.98138	13.71739	8.82062
H	8.80994	13.02290	8.57304
H	8.27331	14.73819	8.48803
C	6.66551	13.27593	8.15463
H	5.83871	13.93188	8.50466
H	6.42985	12.24637	8.51292
C	6.73068	13.29773	6.63788
C	5.93928	14.19592	5.88927
H	5.25937	14.88438	6.42021
C	6.00202	14.22220	4.48487
H	5.37261	14.93163	3.92147
C	6.86536	13.34910	3.80152
H	6.91820	13.36842	2.69995
C	7.66209	12.45044	4.53427
H	8.34196	11.75916	4.00814
C	7.59544	12.42463	5.93747
H	8.22670	11.71417	6.50059
C	17.06501	7.36096	14.98333
H	17.02179	7.02414	16.04121
H	17.29448	8.44681	14.96189
C	18.11600	6.56922	14.18521
H	17.83998	5.49169	14.17509
H	18.09165	6.92157	13.12849
C	19.50911	6.74676	14.76055
C	20.12427	5.72653	15.51704
H	19.58935	4.77301	15.67112
C	21.40547	5.90402	16.06767
H	21.86868	5.09037	16.65142
C	22.09499	7.11234	15.87152
H	23.10203	7.25354	16.29903
C	21.49325	8.13922	15.12181
H	22.02801	9.08995	14.95726
C	20.21322	7.95803	14.57296
H	19.74945	8.77099	13.98802
C	13.69077	10.59463	18.31932
H	13.25376	11.59181	18.55039
H	14.69573	10.76818	17.88777
C	13.76609	9.74056	19.59858
H	12.73667	9.58191	19.99039
H	14.30449	10.35676	20.35672
C	14.47376	8.40632	19.45476
C	13.75218	7.19445	19.43201
H	12.65358	7.22086	19.52649
C	14.41141	5.96076	19.29454
H	13.82635	5.02558	19.27990
C	15.81044	5.91773	19.17625
H	16.33026	4.95064	19.06938
C	16.54331	7.11796	19.19983
H	17.64289	7.09721	19.11644
C	15.88052	8.34853	19.34009
H	16.47003	9.28123	19.37163
C	14.95065	7.92625	8.90980
H	14.78200	8.44726	7.94252
H	13.96963	7.58547	9.29803
C	15.93243	6.75110	8.73858
H	16.09295	6.27176	9.73006

H	16.91619	7.15771	8.41389
C	15.44506	5.72010	7.73739
C	15.56598	5.94945	6.34804
H	16.03331	6.88491	5.99424
C	15.10705	5.00505	5.41533
H	15.21530	5.20364	4.33551
C	14.51788	3.80585	5.85520
H	14.16303	3.06069	5.12356
C	14.38726	3.56520	7.23380
H	13.92998	2.62721	7.59183
C	14.84401	4.51602	8.16310
H	14.74021	4.31921	9.24409
C	10.14214	8.54681	8.19700
H	9.26319	8.29278	8.82898
H	11.02791	8.06402	8.65634
C	9.93365	8.08802	6.74112
H	10.84904	8.33306	6.15656
H	9.09874	8.67378	6.29617
C	9.62833	6.60420	6.64237
C	8.29418	6.14103	6.64413
H	7.46686	6.87038	6.68993
C	8.00362	4.76760	6.58203
H	6.95294	4.43175	6.57773
C	9.04811	3.82838	6.51945
H	8.82327	2.74960	6.46851
C	10.38112	4.27527	6.51949
H	11.21182	3.55184	6.46902
C	10.66686	5.64954	6.58061
C	14.56737	12.16275	5.20984
H	14.04353	13.11075	5.45067
H	13.92237	11.57337	4.52338
C	15.94059	12.44047	4.57053
H	16.44983	11.47135	4.37151
H	16.56960	12.99238	5.30471
C	15.80928	13.23896	3.28672
C	15.78228	14.65076	3.31322
H	15.89865	15.17613	4.27688
C	15.61951	15.39350	2.13179
H	15.60580	16.49534	2.17703
C	15.47931	14.73541	0.89763
H	15.35312	15.31716	-0.03082
C	15.50525	13.33064	0.85520
H	15.40087	12.80409	-0.10867
C	15.66829	12.59242	2.03948
H	15.69272	11.48940	1.99708
C	16.29588	15.77741	9.36944
H	16.70863	16.45921	10.14495
H	15.19105	15.88039	9.37319
C	16.87929	16.10040	7.98222
H	16.40842	15.41328	7.24082
H	17.96885	15.87746	7.98033
C	16.64612	17.54538	7.58027
C	17.71806	18.45857	7.48400
H	18.74439	18.10608	7.68565
C	17.49879	19.80225	7.13302
H	18.35359	20.49590	7.05943
C	16.19506	20.26079	6.87849
H	16.01957	21.31522	6.60632

C	15.11625	19.36296	6.97346
H	14.08784	19.71054	6.77764
C	15.33952	18.01927	7.31807
H	14.48454	17.32251	7.38198
H	11.71783	5.98531	6.57513

$Ag_1Au_{24}PET_{18}$_Ag_in_core

349

Au	12.51257	15.33570	12.15114
Au	15.66944	16.51337	13.02760
Au	17.43849	13.43126	13.75032
Au	14.81156	11.10482	13.53072
Au	11.06620	14.01726	14.46669
Au	9.57365	16.70528	12.80733
Au	10.99444	16.37304	9.45101
Au	12.66117	13.36821	9.80472
Au	14.12037	13.93966	14.35677
Au	12.46194	14.10908	17.42208
Au	9.38140	12.32316	16.64026
Au	9.98667	11.36491	13.33335
Au	12.48572	9.62291	12.87280
Au	9.33052	8.44279	11.99883
Au	7.56134	11.52577	11.27718
Au	10.18584	13.85357	11.49856
Au	13.93247	10.94427	10.55871
Au	15.42198	8.25329	12.22045
Au	14.00720	8.59090	15.57774
Au	12.33814	11.59442	15.22359
Au	10.88138	11.01994	10.66889
Au	12.53535	10.85035	7.60270
Au	15.61691	12.63321	8.38374
Au	15.01512	13.58888	11.69286
Ag	12.49958	12.47979	12.51387
S	13.53222	17.52056	12.78298
S	17.89783	15.68306	13.12949
S	17.17617	11.14771	14.36567
S	9.63860	17.86199	10.72513
S	12.41938	15.10167	8.02657
S	9.34472	15.74582	14.96684
S	14.68203	14.56383	16.70772
S	10.25954	13.82369	18.27711
S	8.27638	10.89522	15.09877
C	13.67677	18.57897	11.26209
H	14.35712	18.08823	10.53639
H	12.65907	18.59202	10.81588
C	14.12614	20.02040	11.57286
H	13.41843	20.46459	12.30741
H	14.01091	20.59864	10.62606
C	15.54990	20.16699	12.07477
C	16.63973	20.08928	11.17924
H	16.45265	19.93222	10.10244
C	17.96087	20.21283	11.63925
H	18.79581	20.14770	10.92147
C	18.21799	20.42193	13.00617
H	19.25514	20.52732	13.36710
C	17.14337	20.49907	13.90866
H	17.32883	20.65544	14.98450
C	15.82293	20.37079	13.44400
H	14.98610	20.42727	14.16040
C	18.66024	16.47362	14.62789
H	18.62451	17.56836	14.44145
H	18.03710	16.25460	15.51888

C	20.10852	15.99147	14.83368
H	20.10043	14.88690	14.97482
H	20.69205	16.19470	13.90862
C	20.76231	16.66595	16.02535
C	21.50729	17.85540	15.87086
H	21.64598	18.27709	14.86005
C	22.07839	18.50213	16.97988
H	22.65955	19.42855	16.83477
C	21.91309	17.96879	18.26994
H	22.36314	18.47283	19.14175
C	21.17454	16.78448	18.44015
H	21.04276	16.35340	19.44678
C	20.60595	16.14177	17.32759
H	20.03479	15.20802	17.47012
C	17.01669	11.25326	16.20959
H	16.18421	11.94428	16.45397
H	16.73010	10.23227	16.54622
C	18.32923	11.70445	16.87599
H	19.16101	11.05520	16.52528
H	18.55694	12.73605	16.51832
C	18.26428	11.68067	18.39269
C	19.06088	10.78603	19.14006
H	19.74798	10.10531	18.60839
C	18.99401	10.75328	20.54412
H	19.62873	10.04784	21.10659
C	18.12083	11.61586	21.22837
H	18.05963	11.58660	22.32930
C	17.32271	12.51454	20.49714
H	16.64030	13.20248	21.02437
C	17.39277	12.54619	19.09420
H	16.75820	13.25456	18.53212
C	7.93317	17.60167	10.03566
H	7.97537	17.94286	8.97914
H	7.71114	16.51418	10.05251
C	6.87620	18.38321	10.83585
H	7.14823	19.46165	10.85520
H	6.89778	18.02294	11.88993
C	5.48600	18.20545	10.25361
C	4.87074	19.22968	9.50261
H	5.40434	20.18514	9.35617
C	3.59152	19.05335	8.94708
H	3.12870	19.86973	8.36684
C	2.90395	17.84231	9.13300
H	1.89683	17.70343	8.70494
C	3.50687	16.81051	9.87496
H	2.97512	15.85623	10.02833
C	4.78476	16.99071	10.42916
H	5.24905	16.17422	11.00877
C	11.31916	14.38536	6.71085
H	11.76015	13.39182	6.47201
H	10.31393	14.20406	7.13865
C	11.24302	15.24958	5.43827
H	12.27308	15.41975	5.05307
H	10.71331	14.63553	4.67231
C	10.52348	16.57648	5.58979
C	11.23582	17.79285	5.64414
H	12.33596	17.77560	5.56726
C	10.56561	19.01957	5.79035

H	11.14370	19.95835	5.82980
C	9.16451	19.05102	5.88580
H	8.63616	20.01247	6.00115
C	8.44071	17.84638	5.82977
H	7.33974	17.85820	5.89414
C	9.11456	16.62281	5.68088
H	8.53215	15.68697	5.62180
C	10.04854	17.03454	16.10179
H	10.22169	16.51221	17.06759
H	11.02754	17.37996	15.71253
C	9.06325	18.20583	16.27862
H	8.90079	18.68983	15.28980
H	8.08073	17.79418	16.60107
C	9.54661	19.23350	17.28537
C	9.46129	18.97967	18.67323
H	9.02789	18.02615	19.02193
C	9.91364	19.92212	19.61104
H	9.83194	19.70487	20.68960
C	10.46177	21.14318	19.17822
H	10.81405	21.88540	19.91407
C	10.55586	21.40873	17.80129
H	10.97848	22.36495	17.44886
C	10.10626	20.45964	16.86661
H	10.18348	20.67493	15.78694
C	14.85529	16.40821	16.82591
H	15.74608	16.65911	16.20943
H	13.97899	16.89119	16.34873
C	15.03816	16.87329	18.28332
H	14.11256	16.63052	18.85256
H	15.86507	16.28965	18.74547
C	15.34141	18.35763	18.38028
C	16.67528	18.82092	18.40591
H	17.50334	18.09122	18.38623
C	16.96450	20.19488	18.46275
H	18.01481	20.53085	18.48968
C	15.91891	21.13453	18.49212
H	16.14264	22.21390	18.53495
C	14.58614	20.68745	18.46747
H	13.75462	21.41115	18.49561
C	14.30173	19.31268	18.41168
H	13.25084	18.97688	18.39766
C	10.43884	12.80742	19.82261
H	10.96052	11.85946	19.57713
H	11.08740	13.39406	20.50805
C	9.06781	12.52944	20.46647
H	8.56023	13.49845	20.67044
H	8.43540	11.98012	19.73331
C	9.20351	11.72655	21.74711
C	9.22467	10.31476	21.71562
H	9.09977	9.79317	20.75096
C	9.39228	9.56722	22.89333
H	9.40066	8.46550	22.84416
C	9.54390	10.22052	24.12867
H	9.67557	9.63510	25.05405
C	9.52329	11.62523	24.17617
H	9.63590	12.14795	25.14120
C	9.35483	12.36826	22.99564
H	9.33334	13.47119	23.04237

C	8.71996	9.18981	15.67588
H	8.31263	8.50600	14.89918
H	9.82497	9.08802	15.67885
C	8.12926	8.86791	17.06033
H	8.59240	9.55936	17.80264
H	7.03879	9.08612	17.05479
C	8.36655	7.42529	17.46853
C	7.29785	6.50826	17.56476
H	6.27073	6.85603	17.35888
C	7.52122	5.16674	17.92152
H	6.66872	4.47040	17.99659
C	8.82599	4.71408	18.18113
H	9.00536	3.66017	18.45285
C	9.90130	5.61631	18.08833
H	10.93006	5.27403	18.29143
C	9.67402	6.95770	17.73760
H	10.52649	7.65760	17.67385
S	11.46837	7.43636	12.24119
S	7.10244	9.27411	11.89898
S	7.82223	13.80954	10.66216
S	15.35945	7.09836	14.30392
S	12.58382	9.86304	17.00287
S	15.65237	9.21352	10.06157
S	10.31549	10.39732	8.31868
S	14.73733	11.13399	6.74635
S	16.72458	14.05815	9.92600
C	11.32795	6.37827	13.76262
H	10.64964	6.86906	14.49020
H	12.34692	6.36558	14.20586
C	10.87832	4.93649	13.45383
H	11.58304	4.49295	12.71602
H	10.99853	4.35833	14.40007
C	9.45234	4.78824	12.95875
C	8.36674	4.86697	13.85933
H	8.55887	5.02609	14.93494
C	7.04345	4.74216	13.40589
H	6.21194	4.80731	14.12767
C	6.77985	4.53101	12.04053
H	5.74096	4.42566	11.68464
C	7.85023	4.45207	11.13317
H	7.65977	4.29241	10.05869
C	9.17286	4.58167	11.59122
H	10.00630	4.52359	10.87101
C	6.33851	8.48474	10.40070
H	6.37350	7.38986	10.58646
H	6.96128	8.70381	9.50947
C	4.89056	8.96825	10.19582
H	4.89900	10.07374	10.06208
H	4.30551	8.75890	11.11855
C	4.23873	8.30205	8.99844
C	3.49734	7.10904	9.14251
H	3.36061	6.67764	10.14948
C	2.92788	6.47059	8.02788
H	2.34871	5.54168	8.16493
C	3.09174	7.01560	6.74251
H	2.64341	6.51775	5.86628
C	3.82661	8.20362	6.58273
H	3.95660	8.64425	5.58001

C	4.39344	8.83811	7.70087
H	4.96195	9.77469	7.56657
C	7.98404	13.70505	8.81841
H	8.81654	13.01375	8.57487
H	8.27166	14.72611	8.48283
C	6.67245	13.25470	8.14971
H	5.84068	13.90559	8.49742
H	6.44262	12.22390	8.50826
C	6.74133	13.27602	6.63315
C	5.94871	14.17099	5.88197
H	5.26092	14.85356	6.41039
C	6.01933	14.20079	4.47801
H	5.39075	14.90943	3.91270
C	6.89033	13.33297	3.79761
H	6.94990	13.35555	2.69644
C	7.68668	12.43601	4.53287
H	8.37188	11.74824	4.00906
C	7.61273	12.40718	5.93564
H	8.24326	11.69762	6.50077
C	17.06648	7.35892	14.98962
H	17.02600	7.02180	16.04751
H	17.28974	8.44609	14.96822
C	18.12109	6.57327	14.19025
H	17.84988	5.49451	14.17827
H	18.09546	6.92732	13.13415
C	19.51332	6.75590	14.76614
C	20.13180	5.73803	15.52313
H	19.60022	4.78263	15.67725
C	21.41234	5.92003	16.07375
H	21.87744	5.10889	16.65951
C	22.09845	7.13000	15.87582
H	23.10591	7.27395	16.30143
C	21.49310	8.15475	15.12612
H	22.02492	9.10698	14.96067
C	20.21321	7.96952	14.57829
H	19.74593	8.78142	13.99468
C	13.68540	10.58484	18.31445
H	13.24267	11.57813	18.55116
H	14.68940	10.76719	17.88415
C	13.76597	9.72479	19.58956
H	12.73695	9.55001	19.97545
H	14.29242	10.34383	20.35380
C	14.49336	8.40176	19.44136
C	13.79007	7.17943	19.40690
H	12.69090	7.18871	19.49780
C	14.46830	5.95659	19.26468
H	13.89719	5.01303	19.23985
C	15.86849	5.93510	19.15414
H	16.40324	4.97663	19.04355
C	16.58325	7.14590	19.18945
H	17.68342	7.14228	19.11193
C	15.90141	8.36555	19.33366
H	16.47690	9.30665	19.37399
C	14.94725	7.92641	8.92565
H	14.77529	8.44966	7.96013
H	13.96746	7.58248	9.31429
C	15.93018	6.75326	8.74813
H	16.09541	6.27117	9.73743

H	16.91218	7.16251	8.42100
C	15.44075	5.72447	7.74547
C	15.51688	5.97717	6.35687
H	15.95194	6.92855	6.00438
C	15.05180	5.03697	5.42303
H	15.12175	5.25545	4.34390
C	14.50322	3.81779	5.86057
H	14.14762	3.07426	5.12765
C	14.41753	3.55371	7.23833
H	13.98883	2.60163	7.59457
C	14.88051	4.50026	8.16903
H	14.81348	4.28445	9.24927
C	10.14217	8.55275	8.20197
H	9.25365	8.30174	8.82169
H	11.02030	8.07046	8.67646
C	9.95478	8.08654	6.74553
H	10.87890	8.32812	6.17338
H	9.12681	8.67012	6.28518
C	9.65075	6.60219	6.65126
C	8.31672	6.13914	6.62972
H	7.48883	6.86900	6.65022
C	8.02720	4.76509	6.57683
H	6.97678	4.42908	6.55478
C	9.07255	3.82521	6.54642
H	8.84851	2.74587	6.50430
C	10.40544	4.27205	6.56755
H	11.23683	3.54821	6.53992
C	10.69015	5.64690	6.61944
C	14.55757	12.15070	5.20121
H	14.03847	13.09983	5.44762
H	13.90651	11.56551	4.51690
C	15.92812	12.42528	4.55497
H	16.43237	11.45497	4.34902
H	16.56363	12.97198	5.28742
C	15.79227	13.22975	3.27535
C	15.77369	14.64155	3.30832
H	15.90001	15.16189	4.27347
C	15.60708	15.39061	2.13143
H	15.60004	16.49228	2.18183
C	15.45429	14.73887	0.89540
H	15.32467	15.32549	-0.02950
C	15.47147	13.33417	0.84657
H	15.35686	12.81263	-0.11886
C	15.63867	12.58961	2.02631
H	15.65714	11.48668	1.97855
C	16.28395	15.76488	9.35081
H	16.69665	16.44694	10.12619
H	15.17929	15.87039	9.35214
C	16.87084	16.08533	7.96439
H	16.39535	15.40272	7.22174
H	17.95859	15.85385	7.96325
C	16.64985	17.53264	7.56385
C	17.73067	18.43480	7.46287
H	18.75439	18.07115	7.65771
C	17.52362	19.78116	7.11479
H	18.38515	20.46610	7.03842
C	16.22350	20.25340	6.86698
H	16.05747	21.31016	6.59793

C	15.13604	19.36643	6.96546
H	14.11050	19.72485	6.77425
C	15.34702	18.02011	7.30767
H	14.48533	17.33193	7.37444
H	11.74109	5.98269	6.63026

$Ag_1Au_{24}PET_{18}$_Ag_in_icosahedron
349

Ag	12.46424	15.33834	12.14229
Au	15.54410	16.54944	13.06282
Au	17.38598	13.46559	13.73962
Au	14.80708	11.09648	13.54235
Au	11.03963	14.01553	14.44116
Au	9.60432	16.69409	12.80234
Au	11.02410	16.34437	9.41578
Au	12.60959	13.36342	9.81423
Au	14.09092	13.96114	14.34869
Au	12.43965	14.09604	17.40937
Au	9.35422	12.28825	16.62562
Au	9.98426	11.32159	13.35768
Au	12.49679	9.57731	12.88870
Au	9.31009	8.44065	12.00417
Au	7.52050	11.54841	11.26881
Au	10.12670	13.75463	11.52559
Au	13.94527	10.92751	10.57963
Au	15.42186	8.24162	12.22234
Au	13.99417	8.57997	15.59973
Au	12.34254	11.57298	15.23137
Au	10.89236	10.96060	10.66265
Au	12.52688	10.80686	7.61230
Au	15.60469	12.65421	8.38852
Au	14.96903	13.62829	11.66810
Au	12.48345	12.46761	12.51614
S	13.40892	17.57404	12.89160
S	17.78159	15.72211	13.09297
S	17.16102	11.17504	14.35306
S	9.70023	17.83927	10.71327
S	12.42408	15.04556	7.99183
S	9.35296	15.75734	14.97216
S	14.66386	14.54411	16.70293
S	10.23070	13.80464	18.24828
S	8.25927	10.84544	15.08671
C	13.53116	18.70352	11.42197
H	14.18091	18.23701	10.65339
H	12.50152	18.75554	11.00708
C	14.01102	20.12503	11.77664
H	13.33875	20.54341	12.55818
H	13.86466	20.74674	10.86189
C	15.45494	20.23855	12.22609
C	16.50835	20.17289	11.28698
H	16.27823	20.04611	10.21453
C	17.84779	20.27213	11.69728
H	18.65329	20.21407	10.94597
C	18.16021	20.44793	13.05745
H	19.21159	20.53789	13.37943
C	17.12258	20.51210	14.00319
H	17.35159	20.64355	15.07390
C	15.78385	20.40424	13.58827
H	14.97634	20.44707	14.33845
C	18.60446	16.53417	14.54656
H	18.54792	17.62665	14.35141
H	18.02714	16.31812	15.46860
C	20.06604	16.06841	14.68641

H	20.07864	14.96187	14.81049
H	20.60765	16.29323	13.74100
C	20.76086	16.73442	15.85936
C	21.45482	17.95341	15.69664
H	21.51968	18.40668	14.69208
C	22.06677	18.59058	16.78913
H	22.60794	19.53988	16.63722
C	21.99362	18.01867	18.07123
H	22.47540	18.51568	18.92997
C	21.30653	16.80506	18.24962
H	21.24856	16.34301	19.24957
C	20.69669	16.17190	17.15337
H	20.16619	15.21516	17.30139
C	17.01338	11.26825	16.19903
H	16.17980	11.95413	16.45353
H	16.73442	10.24389	16.53143
C	18.32869	11.72230	16.85768
H	19.16146	11.08037	16.49585
H	18.54770	12.75789	16.50646
C	18.27485	11.68633	18.37465
C	19.08395	10.79303	19.11004
H	19.76840	10.11735	18.56864
C	19.03205	10.75481	20.51464
H	19.67779	10.05211	21.06791
C	18.15996	11.60854	21.21124
H	18.11426	11.57838	22.31290
C	17.34468	12.50119	20.49161
H	16.65659	13.17616	21.02812
C	17.40242	12.54076	19.08837
H	16.75841	13.24746	18.53503
C	7.98957	17.61651	10.02292
H	8.03944	17.95623	8.96628
H	7.74349	16.53426	10.04089
C	6.95007	18.42166	10.82249
H	7.23912	19.49579	10.83109
H	6.97199	18.06991	11.87944
C	5.55382	18.26028	10.24986
C	4.94864	19.28775	9.49513
H	5.49347	20.23559	9.34081
C	3.66453	19.12448	8.94684
H	3.20950	19.94309	8.36359
C	2.96190	17.92392	9.14433
H	1.95218	17.79449	8.71947
C	3.55373	16.89000	9.89220
H	3.00882	15.94528	10.05776
C	4.83685	17.05671	10.43835
H	5.29307	16.23801	11.02127
C	11.30115	14.32943	6.69476
H	11.72121	13.32349	6.46996
H	10.29487	14.17580	7.13080
C	11.23642	15.17625	5.41016
H	12.26765	15.32167	5.01807
H	10.69209	14.56105	4.65546
C	10.54268	16.51876	5.54490
C	11.27591	17.72386	5.55311
H	12.37423	17.68614	5.45921
C	10.62839	18.96537	5.67548
H	11.22221	19.89509	5.67714

C	9.22990	19.02322	5.79375
H	8.71917	19.99661	5.88644
C	8.48577	17.82971	5.78731
H	7.38644	17.86225	5.87060
C	9.13695	16.59121	5.66360
H	8.53923	15.66335	5.65019
C	10.08476	17.04036	16.09658
H	10.25877	16.51838	17.06238
H	11.06477	17.37046	15.69630
C	9.11648	18.22513	16.27709
H	8.96283	18.71608	15.29032
H	8.12754	17.82692	16.59675
C	9.61385	19.24046	17.28954
C	9.50339	18.98987	18.67617
H	9.04333	18.04685	19.01927
C	9.96609	19.92162	19.61966
H	9.85887	19.71010	20.69711
C	10.55467	21.12615	19.19352
H	10.91689	21.85923	19.93374
C	10.67626	21.38705	17.81786
H	11.13360	22.32903	17.47062
C	10.21217	20.45056	16.87775
H	10.30904	20.66324	15.79919
C	14.86607	16.38211	16.85995
H	15.75944	16.63207	16.24690
H	13.99683	16.88936	16.39557
C	15.05915	16.81041	18.32725
H	14.13054	16.57026	18.89261
H	15.87699	16.20228	18.77422
C	15.38754	18.28674	18.45906
C	16.72881	18.72888	18.47222
H	17.54495	17.98772	18.41607
C	17.04073	20.09599	18.56323
H	18.09655	20.41497	18.57654
C	16.01085	21.04996	18.64251
H	16.25222	22.12372	18.71774
C	14.67105	20.62421	18.62787
H	13.85159	21.35963	18.68846
C	14.36404	19.25612	18.53728
H	13.30789	18.93702	18.53122
C	10.40742	12.80345	19.80375
H	10.93100	11.85368	19.56937
H	11.05359	13.39832	20.48431
C	9.03542	12.53168	20.44814
H	8.53301	13.50325	20.65242
H	8.39959	11.98586	19.71534
C	9.16786	11.72905	21.72930
C	9.18710	10.31720	21.69924
H	9.06416	9.79480	20.73481
C	9.35052	9.57076	22.87825
H	9.35850	8.46899	22.83025
C	9.49899	10.22508	24.11347
H	9.62415	9.64037	25.04023
C	9.48187	11.62987	24.15927
H	9.59428	12.15355	25.12379
C	9.31789	12.37178	22.97745
H	9.29996	13.47480	23.02256
C	8.70275	9.14706	15.68450

H	8.30174	8.45428	14.91243
H	9.80783	9.04824	15.69554
C	8.10444	8.83942	17.06877
H	8.56167	9.53986	17.80630
H	7.01351	9.05499	17.05473
C	8.34308	7.40176	17.49306
C	7.27571	6.48395	17.59604
H	6.24885	6.82718	17.38142
C	7.50022	5.14723	17.96963
H	6.64884	4.45003	18.04906
C	8.80488	4.70023	18.23942
H	8.98464	3.65106	18.52856
C	9.87923	5.60254	18.13704
H	10.90846	5.26345	18.34316
C	9.65063	6.93950	17.77061
H	10.50223	7.63981	17.70077
S	11.43965	7.41642	12.26395
S	7.08781	9.28915	11.87932
S	7.77581	13.83871	10.65314
S	15.34628	7.09603	14.31303
S	12.58044	9.86988	17.02638
S	15.66361	9.21381	10.06496
S	10.31465	10.31624	8.33661
S	14.72824	11.13310	6.76940
S	16.69906	14.09159	9.93102
C	11.28680	6.36356	13.78802
H	10.61210	6.86302	14.51287
H	12.30483	6.34226	14.23294
C	10.82319	4.92583	13.48152
H	11.53128	4.46960	12.75477
H	10.92487	4.35168	14.43233
C	9.40193	4.79178	12.96907
C	8.30513	4.89466	13.85349
H	8.48434	5.06642	14.92937
C	6.98683	4.77921	13.38337
H	6.14632	4.86098	14.09291
C	6.73937	4.55561	12.01698
H	5.70426	4.45831	11.64802
C	7.82098	4.45392	11.12540
H	7.64346	4.28467	10.05017
C	9.13864	4.57296	11.60028
H	9.98109	4.49635	10.89238
C	6.33564	8.50088	10.37490
H	6.36897	7.40603	10.56118
H	6.96532	8.72033	9.48856
C	4.88913	8.98394	10.15906
H	4.89839	10.08978	10.02750
H	4.29683	8.77286	11.07671
C	4.24661	8.31934	8.95580
C	3.48936	7.13583	9.09530
H	3.33534	6.71019	10.10222
C	2.92535	6.49998	7.97637
H	2.33540	5.57736	8.10981
C	3.10934	7.03909	6.69129
H	2.66275	6.54510	5.81200
C	3.86145	8.21689	6.53578
H	4.00765	8.65268	5.53319
C	4.42431	8.84776	7.65796

H	5.00868	9.77493	7.52638
C	7.96096	13.72099	8.81197
H	8.79420	13.02521	8.58438
H	8.25690	14.73812	8.47165
C	6.65620	13.27084	8.12989
H	5.82590	13.93737	8.45021
H	6.40960	12.24998	8.50496
C	6.75164	13.26068	6.61474
C	5.99078	14.15617	5.83202
H	5.31217	14.86675	6.33483
C	6.08163	14.15223	4.42888
H	5.47743	14.86187	3.83880
C	6.94207	13.24973	3.78106
H	7.01342	13.24188	2.68041
C	7.71051	12.35506	4.54811
H	8.39116	11.64382	4.05035
C	7.61549	12.35927	5.94994
H	8.22276	11.64929	6.53947
C	17.05178	7.35844	15.00175
H	17.00900	7.02409	16.06043
H	17.27569	8.44535	14.97859
C	18.10794	6.57002	14.20715
H	17.84130	5.49007	14.20667
H	18.07762	6.91347	13.14766
C	19.50078	6.76429	14.77748
C	20.12231	5.75941	15.54925
H	19.59272	4.80553	15.71881
C	21.40278	5.95271	16.09614
H	21.87166	5.15024	16.69075
C	22.08478	7.16222	15.88172
H	23.09043	7.31655	16.30797
C	21.47700	8.17362	15.11601
H	22.00639	9.12458	14.93614
C	20.19789	7.97639	14.57047
H	19.72951	8.77710	13.97243
C	13.68867	10.59397	18.33105
H	13.25095	11.59073	18.56254
H	14.69267	10.76844	17.89751
C	13.76733	9.74108	19.61088
H	12.73853	9.57814	20.00253
H	14.30287	10.36016	20.36872
C	14.48173	8.41035	19.46810
C	13.76592	7.19520	19.43886
H	12.66632	7.21678	19.52242
C	14.43189	5.96450	19.30730
H	13.85135	5.02657	19.28900
C	15.83196	5.92800	19.19956
H	16.35707	4.96333	19.09682
C	16.55903	7.13166	19.22786
H	17.65931	7.11598	19.15346
C	15.88948	8.35922	19.36216
H	16.47423	9.29488	19.39576
C	14.96847	7.93207	8.91693
H	14.79907	8.46025	7.95375
H	13.98856	7.58145	9.29905
C	15.95844	6.76507	8.73863
H	16.10509	6.26614	9.72254
H	16.94557	7.18283	8.43885

C	15.49284	5.75197	7.70902
C	15.60099	6.02558	6.32659
H	16.03648	6.98553	5.99875
C	15.16714	5.09537	5.36803
H	15.26893	5.32686	4.29416
C	14.61248	3.86815	5.77422
H	14.27503	3.13546	5.02205
C	14.49331	3.58403	7.14551
H	14.06217	2.62424	7.47729
C	14.92738	4.51958	8.10096
H	14.83430	4.28810	9.17600
C	10.16395	8.46925	8.22412
H	9.28128	8.20906	8.84857
H	11.05019	7.99832	8.69486
C	9.97504	8.00029	6.76886
H	10.90216	8.23154	6.19727
H	9.15321	8.59003	6.30535
C	9.65643	6.51873	6.67872
C	8.31757	6.07027	6.64999
H	7.49774	6.80929	6.66622
C	8.01325	4.69953	6.59522
H	6.95934	4.37508	6.56670
C	9.04837	3.74822	6.57107
H	8.81280	2.67152	6.52485
C	10.38586	4.18039	6.60288
H	11.20928	3.44720	6.58355
C	10.68552	5.55207	6.65615
C	14.54635	12.12888	5.21148
H	14.01504	13.07520	5.44241
H	13.90699	11.52794	4.52981
C	15.91879	12.41098	4.57225
H	16.43459	11.44367	4.38135
H	16.54284	12.97209	5.30366
C	15.78557	13.19961	3.28261
C	15.76137	14.61161	3.29817
H	15.88249	15.14400	4.25738
C	15.59638	15.34540	2.11146
H	15.58438	16.44759	2.14797
C	15.45184	14.67795	0.88284
H	15.32304	15.25269	-0.04962
C	15.47639	13.27285	0.85112
H	15.37101	12.73906	-0.10865
C	15.64061	12.54359	2.04074
H	15.66262	11.44022	2.00705
C	16.25404	15.79700	9.35506
H	16.65073	16.47893	10.13862
H	15.14862	15.89505	9.34099
C	16.85717	16.12772	7.97833
H	16.40124	15.44209	7.22623
H	17.94777	15.91054	7.99220
C	16.62115	17.57376	7.58189
C	17.68805	18.49477	7.50779
H	18.71303	18.14923	7.72769
C	17.46495	19.83862	7.15978
H	18.31668	20.53712	7.09703
C	16.16156	20.29051	6.89177
H	15.98184	21.34718	6.63122
C	15.08788	19.38435	6.96311

H	14.06060	19.72476	6.74964
C	15.31528	18.04067	7.30446
H	14.46370	17.33904	7.35694
H	11.74007	5.87590	6.67573

$Ag_1Au_{24}PET_{18}$_Ag_in_staple

349

Au	12.51750	15.36443	12.14137
Au	15.65579	16.53770	13.05010
Au	17.43970	13.43561	13.75916
Au	14.82335	11.16484	13.54420
Au	11.05654	14.04567	14.45841
Au	9.57852	16.71967	12.79196
Au	11.00689	16.37535	9.42536
Au	12.67015	13.38665	9.78793
Au	14.11021	13.98511	14.37072
Au	12.47140	14.13445	17.42420
Au	9.37598	12.33974	16.63484
Au	9.98823	11.38560	13.34415
Au	12.47394	9.63690	12.87940
Au	9.37891	8.43166	11.99998
Au	7.58550	11.52282	11.25659
Au	10.18395	13.85990	11.47212
Au	13.96352	10.92832	10.55655
Ag	15.26298	8.49289	12.18837
Au	14.01308	8.60199	15.55507
Au	12.34099	11.61805	15.24106
Au	10.89561	11.02508	10.65183
Au	12.55205	10.87179	7.59853
Au	15.63958	12.68363	8.39090
Au	15.01891	13.61624	11.67525
Au	12.50815	12.49493	12.50665
S	13.51886	17.54504	12.77427
S	17.88196	15.70155	13.17980
S	17.18636	11.13661	14.33557
S	9.65043	17.86286	10.70158
S	12.43221	15.09746	8.00291
S	9.34398	15.76517	14.95555
S	14.69147	14.60407	16.70814
S	10.26509	13.83976	18.26703
S	8.26811	10.91513	15.08687
C	13.68158	18.60135	11.25351
H	14.37393	18.11160	10.53870
H	12.67033	18.61108	10.79289
C	14.12281	20.04379	11.57078
H	13.40003	20.48825	12.29034
H	14.02575	20.62016	10.62090
C	15.53598	20.19263	12.10135
C	16.64422	20.11067	11.22916
H	16.47940	19.94969	10.14934
C	17.95551	20.23428	11.71649
H	18.80538	20.16670	11.01669
C	18.18410	20.44676	13.08794
H	19.21365	20.55007	13.47060
C	17.09080	20.52931	13.96725
H	17.25388	20.68974	15.04613
C	15.78032	20.40167	13.47516
H	14.92851	20.46307	14.17321
C	18.62516	16.47174	14.69787
H	18.59338	17.56879	14.52480
H	17.99005	16.24193	15.57764

C	20.06979	15.98483	14.91753
H	20.05827	14.87801	15.04011
H	20.66764	16.20265	14.00504
C	20.70592	16.63842	16.13023
C	21.45479	17.82906	16.00701
H	21.60860	18.26789	15.00574
C	22.01039	18.45584	17.13518
H	22.59623	19.38280	17.01427
C	21.82468	17.90133	18.41348
H	22.26173	18.39024	19.30039
C	21.08218	16.71543	18.55255
H	20.93561	16.26699	19.54947
C	20.52919	16.09266	17.42095
H	19.95431	15.15784	17.53937
C	17.04982	11.20672	16.18383
H	16.22950	11.90423	16.44961
H	16.75230	10.18384	16.50473
C	18.37567	11.62953	16.84181
H	19.19154	10.96208	16.48801
H	18.62369	12.65577	16.48255
C	18.31626	11.60981	18.35888
C	19.08915	10.69395	19.10528
H	19.75160	9.99009	18.57253
C	19.03040	10.66972	20.50987
H	19.64453	9.94571	21.07154
C	18.18999	11.56301	21.19565
H	18.14040	11.54537	22.29738
C	17.41186	12.47962	20.46523
H	16.74961	13.18638	20.99321
C	17.47450	12.50316	19.06180
H	16.85779	13.22804	18.50102
C	7.94532	17.60266	10.01166
H	7.98904	17.93900	8.95365
H	7.72120	16.51571	10.03314
C	6.88895	18.38969	10.80730
H	7.16160	19.46806	10.81992
H	6.91064	18.03590	11.86358
C	5.49857	18.20879	10.22653
C	4.88480	19.22701	9.46619
H	5.41867	20.18131	9.31326
C	3.60632	19.04653	8.91031
H	3.14409	19.85869	8.32371
C	2.91824	17.83713	9.10485
H	1.91342	17.69347	8.67297
C	3.51858	16.81227	9.85842
H	2.98476	15.86084	10.02196
C	4.79595	16.99643	10.41249
H	5.25878	16.18496	11.00023
C	11.32869	14.37379	6.69377
H	11.76796	13.37794	6.46128
H	10.32385	14.19731	7.12448
C	11.25205	15.23041	5.41629
H	12.28169	15.39654	5.02816
H	10.71997	14.61277	4.65492
C	10.53501	16.55936	5.56188
C	11.24889	17.77536	5.60225
H	12.34858	17.75630	5.51961
C	10.58068	19.00389	5.74229

H	11.15983	19.94241	5.77064
C	9.18020	19.03750	5.84573
H	8.65338	20.00050	5.95510
C	8.45495	17.83312	5.80477
H	7.35445	17.84656	5.87644
C	9.12678	16.60771	5.66220
H	8.54347	15.67163	5.61716
C	10.04592	17.05374	16.09204
H	10.22168	16.53016	17.05666
H	11.02312	17.40302	15.70188
C	9.05575	18.22055	16.27067
H	8.88805	18.70292	15.28191
H	8.07612	17.80459	16.59643
C	9.53674	19.25175	17.27499
C	9.45500	18.99977	18.66338
H	9.02499	18.04560	19.01448
C	9.90591	19.94532	19.59878
H	9.82869	19.72883	20.67782
C	10.44725	21.16834	19.16292
H	10.79575	21.91413	19.89698
C	10.53854	21.43167	17.78538
H	10.95828	22.38826	17.43057
C	10.09043	20.47952	16.85315
H	10.16354	20.69388	15.77302
C	14.85235	16.44905	16.83912
H	15.73802	16.71201	16.22041
H	13.96978	16.92905	16.37072
C	15.03846	16.90242	18.29970
H	14.11704	16.64810	18.87079
H	15.87146	16.32052	18.75309
C	15.33172	18.38798	18.40843
C	16.66243	18.86037	18.43172
H	17.49555	18.13695	18.39892
C	16.94204	20.23570	18.50216
H	17.99007	20.57896	18.52631
C	15.88998	21.16745	18.54791
H	16.10629	22.24768	18.60503
C	14.56032	20.71130	18.52308
H	13.72378	21.42873	18.56036
C	14.28549	19.33521	18.45409
H	13.23697	18.99204	18.44064
C	10.44013	12.83253	19.81859
H	10.96290	11.88310	19.58106
H	11.08658	13.42422	20.50167
C	9.06714	12.56021	20.46065
H	8.55718	13.53110	20.64890
H	8.43848	11.99993	19.73257
C	9.19845	11.77654	21.75362
C	9.22690	10.36458	21.74381
H	9.11226	9.82770	20.78634
C	9.38869	9.63614	22.93425
H	9.40357	8.53385	22.90225
C	9.52648	10.30895	24.16073
H	9.65177	9.73833	25.09620
C	9.49937	11.71410	24.18648
H	9.60192	12.25217	25.14416
C	9.33733	12.43798	22.99329
H	9.31177	13.54139	23.02248

C	8.70686	9.21024	15.67013
H	8.29475	8.52418	14.89810
H	9.81146	9.10475	15.67107
C	8.11817	8.89862	17.05770
H	8.58663	9.59176	17.79509
H	7.02877	9.12228	17.05394
C	8.34911	7.45715	17.47331
C	7.27548	6.54720	17.58051
H	6.24951	6.89977	17.37712
C	7.49259	5.20665	17.94456
H	6.63643	4.51567	18.02702
C	8.79580	4.74801	18.20152
H	8.96974	3.69572	18.48277
C	9.87623	5.64272	18.09619
H	10.90424	5.29531	18.29429
C	9.65514	6.98339	17.73864
H	10.51161	7.67756	17.66693
S	11.51664	7.42282	12.27876
S	7.15340	9.26750	11.88669
S	7.82996	13.81257	10.64473
S	15.31520	7.12639	14.21447
S	12.60612	9.88640	16.99660
S	15.67575	9.26551	9.90288
S	10.33521	10.39161	8.31896
S	14.75355	11.19015	6.75121
S	16.74518	14.09877	9.94805
C	11.35486	6.39197	13.81750
H	10.66308	6.89506	14.52354
H	12.36641	6.38951	14.27759
C	10.91140	4.94492	13.52602
H	11.62773	4.48895	12.80716
H	11.01779	4.38377	14.48396
C	9.49303	4.78754	13.01212
C	8.39437	4.87623	13.89576
H	8.57080	5.04931	14.97187
C	7.07803	4.74392	13.42459
H	6.23605	4.81659	14.13336
C	6.83467	4.51600	12.05818
H	5.80123	4.40535	11.68827
C	7.91826	4.42700	11.16757
H	7.74358	4.25446	10.09239
C	9.23388	4.56331	11.64340
H	10.07785	4.49654	10.93632
C	6.38101	8.45890	10.40357
H	6.42539	7.36627	10.60024
H	6.99273	8.67309	9.50357
C	4.92753	8.93039	10.21020
H	4.92693	10.03332	10.05673
H	4.35722	8.73413	11.14498
C	4.26235	8.23805	9.03523
C	3.53984	7.03784	9.21224
H	3.42887	6.62032	10.22819
C	2.95698	6.37486	8.11914
H	2.39266	5.44099	8.28196
C	3.08844	6.90178	6.82253
H	2.63016	6.38420	5.96308
C	3.80402	8.09666	6.63002
H	3.90766	8.52357	5.61830

C	4.38466	8.75570	7.72679
H	4.93834	9.69717	7.56685
C	7.99177	13.70991	8.80050
H	8.82761	13.02286	8.55684
H	8.27400	14.73233	8.46463
C	6.68209	13.25227	8.13331
H	5.84770	13.90123	8.47835
H	6.45615	12.22174	8.49501
C	6.75238	13.26884	6.61675
C	5.95994	14.16071	5.86179
H	5.27413	14.84744	6.38739
C	6.02912	14.18301	4.45760
H	5.39903	14.88776	3.88913
C	6.89973	13.31186	3.78099
H	6.95748	13.32790	2.67961
C	7.69735	12.41927	4.52019
H	8.38299	11.72967	3.99938
C	7.62436	12.39750	5.92312
H	8.25629	11.69179	6.49145
C	17.04600	7.35015	14.84644
H	17.06397	6.94611	15.88103
H	17.27296	8.43622	14.88593
C	18.06736	6.62418	13.95205
H	17.78979	5.54990	13.87033
H	18.00720	7.05488	12.92611
C	19.48038	6.75746	14.48999
C	20.10753	5.69154	15.16980
H	19.56801	4.73531	15.28664
C	21.40566	5.82773	15.69162
H	21.87772	4.97895	16.21525
C	22.10098	7.03961	15.54307
H	23.12139	7.14820	15.94781
C	21.48778	8.11156	14.86989
H	22.02663	9.06570	14.74272
C	20.19061	7.97149	14.34978
H	19.71769	8.81979	13.82539
C	13.70994	10.60248	18.30988
H	13.28332	11.60559	18.53453
H	14.72076	10.76116	17.88625
C	13.76358	9.75193	19.59252
H	12.72869	9.60477	19.97416
H	14.29988	10.36550	20.35437
C	14.45981	8.41033	19.46134
C	13.72790	7.20465	19.44716
H	12.62930	7.24140	19.53848
C	14.37699	5.96418	19.32320
H	13.78408	5.03389	19.31546
C	15.77587	5.90817	19.20940
H	16.28773	4.93588	19.11181
C	16.51879	7.10224	19.22402
H	17.61835	7.07131	19.14325
C	15.86625	8.33950	19.35104
H	16.46362	9.26735	19.37583
C	14.91632	7.93511	8.85469
H	14.71836	8.39451	7.86228
H	13.94558	7.61673	9.28679
C	15.88784	6.74531	8.72222
H	16.06337	6.31057	9.73138

H	16.86844	7.13283	8.36502
C	15.38816	5.66915	7.77620
C	15.43957	5.85915	6.37639
H	15.85836	6.79813	5.97437
C	14.97495	4.87076	5.49354
H	15.02849	5.03927	4.40456
C	14.45077	3.66528	5.99456
H	14.09249	2.88548	5.30167
C	14.38993	3.46299	7.38400
H	13.98363	2.52089	7.78959
C	14.85117	4.45824	8.26335
H	14.80216	4.29098	9.35324
C	10.17783	8.54490	8.21463
H	9.29542	8.29011	8.84142
H	11.06342	8.07329	8.68597
C	9.98539	8.06921	6.76209
H	10.90726	8.30644	6.18461
H	9.15570	8.64971	6.30088
C	9.67951	6.58445	6.68042
C	8.34468	6.12339	6.66665
H	7.51796	6.85462	6.68576
C	8.05264	4.74954	6.62350
H	7.00154	4.41538	6.60692
C	9.09644	3.80784	6.59590
H	8.87068	2.72862	6.56024
C	10.43010	4.25260	6.61139
H	11.26066	3.52772	6.58833
C	10.71727	5.62732	6.65311
C	14.57105	12.20064	5.20312
H	14.04541	13.14787	5.44327
H	13.92712	11.60921	4.51731
C	15.94333	12.48091	4.56258
H	16.45523	11.51259	4.36642
H	16.57076	13.03613	5.29566
C	15.81140	13.27557	3.27658
C	15.78315	14.68742	3.29863
H	15.89823	15.21576	4.26082
C	15.62124	15.42636	2.11469
H	15.60683	16.52835	2.15639
C	15.48298	14.76438	0.88238
H	15.35765	15.34316	-0.04805
C	15.50987	13.35949	0.84440
H	15.40709	12.82982	-0.11794
C	15.67211	12.62513	2.03116
H	15.69752	11.52200	1.99231
C	16.31190	15.80933	9.37773
H	16.71534	16.48838	10.16057
H	15.20740	15.91438	9.36643
C	16.91435	16.13439	7.99924
H	16.45701	15.44522	7.25132
H	18.00467	15.91576	8.01322
C	16.68060	17.57831	7.59421
C	17.74881	18.49786	7.51877
H	18.77321	18.15116	7.73941
C	17.52819	19.84062	7.16506
H	18.38006	20.53940	7.10826
C	16.22679	20.29157	6.88616
H	16.05019	21.34515	6.61147

C	15.15167	19.38732	6.96007
H	14.12519	19.72913	6.74489
C	15.37640	18.04476	7.30797
H	14.52446	17.34308	7.35631
H	11.76897	5.96086	6.65989

Ag$_{12}$Au$_{13}$PET$_{18}$_I
349

Ag	12.52056	15.30216	12.14424
Au	15.50937	16.52431	13.06865
Au	17.37204	13.40093	13.74501
Ag	14.83860	11.20121	13.52054
Ag	11.05634	14.03487	14.40502
Au	9.60057	16.60829	12.84168
Au	11.09187	16.25818	9.40496
Ag	12.62399	13.35812	9.82271
Ag	14.08056	13.96432	14.35276
Au	12.49593	14.11103	17.34321
Au	9.38406	12.23503	16.55008
Ag	10.03544	11.37451	13.39261
Ag	12.48410	9.66145	12.88583
Au	9.49635	8.43819	11.96148
Au	7.63415	11.56109	11.28431
Ag	10.16695	13.76201	11.51105
Ag	13.95033	10.92975	10.62651
Au	15.40206	8.35394	12.18960
Au	13.91158	8.70648	15.62662
Ag	12.38239	11.60696	15.20944
Ag	10.92710	10.99955	10.67778
Au	12.51150	10.85547	7.68765
Au	15.62402	12.73209	8.48160
Ag	14.97154	13.58777	11.63817
Au	12.50312	12.48195	12.51590
S	13.38013	17.56025	12.94335
S	17.72970	15.65919	13.06965
S	17.23676	11.12449	14.41192
S	9.78440	17.73273	10.74566
S	12.46012	15.02298	7.90203
S	9.26240	15.72913	15.01943
S	14.74294	14.57037	16.73620
S	10.26387	13.81192	18.11653
S	8.23969	10.75420	15.09744
C	13.49329	18.74402	11.51632
H	14.11332	18.29546	10.71320
H	12.45375	18.82999	11.13262
C	14.00980	20.14173	11.91155
H	13.36838	20.54143	12.72802
H	13.84889	20.80146	11.02610
C	15.46829	20.21320	12.32089
C	16.49129	20.15168	11.34824
H	16.22669	20.05390	10.28079
C	17.84420	20.21898	11.71898
H	18.62492	20.17026	10.94137
C	18.20127	20.35463	13.07282
H	19.26352	20.41785	13.36397
C	17.19444	20.41276	14.05161
H	17.45840	20.51333	15.11753
C	15.84159	20.33917	13.67602
H	15.05835	20.38160	14.45140
C	18.57487	16.46860	14.51388
H	18.50875	17.56194	14.32715
H	18.01572	16.24112	15.44443
C	20.04114	16.00932	14.62205

H	20.06095	14.90418	14.75782
H	20.55848	16.22547	13.66125
C	20.76265	16.68943	15.77062
C	21.46615	17.89784	15.57414
H	21.51960	18.33159	14.56034
C	22.10268	18.54826	16.64461
H	22.65055	19.48910	16.46653
C	22.04556	18.00011	17.93777
H	22.54671	18.50742	18.77922
C	21.34964	16.79689	18.14958
H	21.30438	16.35298	19.15834
C	20.71519	16.15053	17.07534
H	20.17846	15.20171	17.24950
C	17.08306	11.25126	16.25466
H	16.23485	11.92180	16.50275
H	16.82573	10.22721	16.60599
C	18.38365	11.74199	16.91812
H	19.23118	11.11530	16.56442
H	18.58156	12.77910	16.55909
C	18.32172	11.71605	18.43479
C	19.11813	10.81902	19.17955
H	19.80239	10.13699	18.64578
C	19.05453	10.78530	20.58373
H	19.68735	10.07656	21.14417
C	18.18577	11.65024	21.27066
H	18.13354	11.62636	22.37219
C	17.38329	12.54693	20.54170
H	16.69822	13.23080	21.07079
C	17.45049	12.57973	19.13866
H	16.81409	13.28757	18.57776
C	8.07985	17.58886	10.02149
H	8.16032	17.95061	8.97407
H	7.79681	16.51571	10.01008
C	7.05552	18.41046	10.82384
H	7.38594	19.47151	10.87141
H	7.04053	18.02654	11.86972
C	5.66600	18.32189	10.21938
C	5.11157	19.39998	9.49691
H	5.69245	20.33274	9.39013
C	3.83275	19.30531	8.92058
H	3.41747	20.16296	8.36439
C	3.08476	18.12358	9.05610
H	2.07944	18.04801	8.60847
C	3.62560	17.03983	9.77147
H	3.04491	16.10939	9.88873
C	4.90328	17.13830	10.34641
H	5.31904	16.28131	10.90415
C	11.29806	14.32436	6.63109
H	11.71252	13.32464	6.37201
H	10.30729	14.15478	7.09662
C	11.17752	15.18813	5.36104
H	12.19282	15.34729	4.93419
H	10.60926	14.58039	4.61805
C	10.47955	16.52214	5.54332
C	11.20821	17.72946	5.58671
H	12.30534	17.69989	5.47881
C	10.55704	18.96279	5.76110
H	11.14727	19.89447	5.78956

C	9.15961	19.01038	5.89738
H	8.64620	19.97741	6.03205
C	8.41993	17.81486	5.85491
H	7.32161	17.83954	5.95221
C	9.07464	16.58455	5.67763
H	8.48008	15.65561	5.63074
C	9.94668	17.05587	16.12319
H	10.07971	16.56865	17.11326
H	10.94484	17.37007	15.75545
C	8.98481	18.25546	16.22881
H	8.86027	18.70380	15.21805
H	7.98477	17.87956	16.54036
C	9.46934	19.30916	17.20742
C	9.28859	19.14052	18.59899
H	8.77194	18.23829	18.97025
C	9.74839	20.10375	19.51184
H	9.59259	19.95263	20.59355
C	10.39936	21.26170	19.04915
H	10.75355	22.02283	19.76459
C	10.59043	21.44196	17.66831
H	11.09867	22.34618	17.29268
C	10.13161	20.47263	16.75957
H	10.28295	20.62236	15.67661
C	14.92500	16.40826	16.91866
H	15.84134	16.67017	16.34555
H	14.07415	16.91649	16.42183
C	15.05755	16.83684	18.39266
H	14.11226	16.58132	18.92277
H	15.86668	16.23894	18.86788
C	15.35807	18.31758	18.53810
C	16.69117	18.78178	18.58656
H	17.52027	18.05404	18.54731
C	16.97778	20.15359	18.68920
H	18.02726	20.49071	18.73185
C	15.93057	21.09038	18.74318
H	16.15252	22.16786	18.82500
C	14.59875	20.64287	18.69341
H	13.76608	21.36455	18.73593
C	14.31716	19.27012	18.59137
H	13.26723	18.93279	18.55728
C	10.41491	12.86369	19.70830
H	10.94145	11.90667	19.51296
H	11.04920	13.48070	20.38014
C	9.03133	12.61203	20.33587
H	8.52139	13.58845	20.49177
H	8.41211	12.03492	19.61287
C	9.14088	11.86042	21.64973
C	9.18083	10.44886	21.67318
H	9.09154	9.88986	20.72579
C	9.32247	9.74958	22.88343
H	9.34667	8.64699	22.87777
C	9.42821	10.45181	24.09665
H	9.53776	9.90396	25.04763
C	9.38941	11.85685	24.08917
H	9.46707	12.41772	25.03601
C	9.24750	12.55157	22.87622
H	9.21272	13.65506	22.87882
C	8.75159	9.06221	15.65674

H	8.30970	8.37062	14.90661
H	9.85633	8.97077	15.59458
C	8.25176	8.72214	17.07308
H	8.76160	9.40310	17.79320
H	7.16294	8.93867	17.13731
C	8.51537	7.27358	17.44109
C	7.46009	6.34078	17.53463
H	6.42432	6.68176	17.36319
C	7.70774	4.99209	17.84490
H	6.86567	4.28294	17.91840
C	9.02370	4.54855	18.06072
H	9.22146	3.49024	18.30091
C	10.08593	5.46624	17.96862
H	11.12352	5.13113	18.13518
C	9.83425	6.81471	17.66456
H	10.67603	7.52766	17.60266
S	11.62555	7.40218	12.08764
S	7.27583	9.30265	11.95834
S	7.76990	13.83731	10.61717
S	15.21532	7.22925	14.28522
S	12.54588	9.94293	17.13085
S	15.74203	9.23268	10.01203
S	10.26364	10.39791	8.29345
S	14.74364	11.15583	6.91476
S	16.76777	14.21264	9.93509
C	11.51147	6.21929	13.51536
H	10.89085	6.66844	14.31770
H	12.55072	6.13348	13.89987
C	10.99511	4.82131	13.12088
H	11.63655	4.42136	12.30454
H	11.15627	4.16211	14.00665
C	9.53665	4.74926	12.71159
C	8.51361	4.80997	13.68423
H	8.77816	4.90691	14.75177
C	7.16074	4.74246	13.31335
H	6.37997	4.79046	14.09096
C	6.80379	4.60737	11.95943
H	5.74156	4.54445	11.66813
C	7.81067	4.54984	10.98065
H	7.54676	4.44941	9.91471
C	9.16346	4.62369	11.35638
H	9.94678	4.58179	10.58104
C	6.43462	8.49386	10.51144
H	6.50149	7.40039	10.69716
H	6.99579	8.72279	9.58245
C	4.96810	8.95157	10.39988
H	4.94762	10.05581	10.25707
H	4.45034	8.74104	11.36170
C	4.24820	8.26363	9.25497
C	3.54544	7.05592	9.45831
H	3.49128	6.62850	10.47476
C	2.91089	6.39807	8.39120
H	2.36334	5.45807	8.57465
C	2.96958	6.93773	7.09454
H	2.47000	6.42458	6.25570
C	3.66495	8.14005	6.87587
H	3.71157	8.57725	5.86425
C	4.29727	8.79392	7.94679

H	4.83401	9.74171	7.76714
C	7.92564	13.70949	8.77474
H	8.77676	13.04210	8.52804
H	8.17928	14.73426	8.42287
C	6.62790	13.21289	8.10997
H	5.77640	13.83232	8.46688
H	6.43727	12.17287	8.46450
C	6.68943	13.24645	6.59344
C	5.88605	14.14074	5.85286
H	5.19574	14.81421	6.38969
C	5.95037	14.18241	4.44891
H	5.31207	14.88880	3.89174
C	6.82679	13.32838	3.75806
H	6.88053	13.35943	2.65678
C	7.63560	12.43398	4.48281
H	8.32629	11.75822	3.95061
C	7.56764	12.39316	5.88559
H	8.20918	11.68740	6.44325
C	16.92044	7.36500	15.00955
H	16.83856	7.00116	16.05614
H	17.20811	8.43689	15.02325
C	17.94065	6.54031	14.20511
H	17.60811	5.47978	14.16089
H	17.95238	6.92199	13.15839
C	19.33255	6.62694	14.80438
C	19.88717	5.54832	15.52589
H	19.30362	4.61781	15.63768
C	21.16935	5.63961	16.09522
H	21.58450	4.78165	16.65102
C	21.92068	6.81848	15.95351
H	22.92903	6.89099	16.39478
C	21.37955	7.90298	15.23945
H	21.96267	8.83131	15.11768
C	20.09838	7.80793	14.67164
H	19.68222	8.66553	14.11512
C	13.71042	10.63958	18.40061
H	13.29994	11.64153	18.65742
H	14.70212	10.80403	17.93524
C	13.82659	9.77753	19.67221
H	12.81039	9.62281	20.09852
H	14.39661	10.38412	20.41480
C	14.51980	8.44070	19.49214
C	13.78708	7.23575	19.45152
H	12.69026	7.26902	19.56143
C	14.43394	6.00005	19.27787
H	13.84058	5.07030	19.25189
C	15.83097	5.94767	19.13934
H	16.34093	4.97887	19.00428
C	16.57469	7.14078	19.17928
H	17.67283	7.11229	19.08088
C	15.92429	8.37348	19.35581
H	16.52198	9.30052	19.40031
C	15.05345	7.90822	8.90822
H	14.92171	8.39625	7.91838
H	14.05443	7.59684	9.27604
C	16.01175	6.70588	8.80155
H	16.13390	6.25516	9.81154
H	17.01323	7.07932	8.49172

C	15.52503	5.65590	7.82003
C	15.71135	5.82576	6.42934
H	16.23332	6.72622	6.06126
C	15.25012	4.86613	5.51343
H	15.41108	5.01779	4.43255
C	14.59159	3.71086	5.97208
H	14.23502	2.95315	5.25422
C	14.39495	3.52945	7.35199
H	13.88161	2.62682	7.72453
C	14.85530	4.49516	8.26383
H	14.69906	4.34475	9.34600
C	10.07738	8.56063	8.10932
H	9.16062	8.30070	8.68267
H	10.92713	8.04970	8.60525
C	9.94222	8.13392	6.63498
H	10.88774	8.38678	6.10404
H	9.13461	8.73510	6.16132
C	9.63571	6.65456	6.48814
C	8.30056	6.19643	6.43836
H	7.47477	6.92797	6.47682
C	8.00759	4.82600	6.33537
H	6.95655	4.49390	6.29223
C	9.05051	3.88443	6.28197
H	8.82373	2.80798	6.19997
C	10.38435	4.32589	6.33263
H	11.21352	3.60016	6.29025
C	10.67234	5.69729	6.43513
C	14.59076	12.10526	5.32384
H	14.06270	13.06123	5.52023
H	13.95718	11.48789	4.65166
C	15.97362	12.35987	4.69588
H	16.48804	11.38500	4.54517
H	16.58980	12.94340	5.41633
C	15.86124	13.10449	3.37829
C	15.81416	14.51569	3.34790
H	15.89877	15.07974	4.29272
C	15.67077	15.20832	2.13406
H	15.64122	16.31079	2.13428
C	15.57010	14.49967	0.92415
H	15.45949	15.04234	-0.02968
C	15.61549	13.09488	0.93857
H	15.54181	12.52902	-0.00562
C	15.75903	12.40681	2.15511
H	15.79829	11.30346	2.15809
C	16.25651	15.90494	9.37625
H	16.69844	16.59648	10.12639
H	15.15176	15.99653	9.43835
C	16.75598	16.24491	7.95976
H	16.24901	15.56101	7.24041
H	17.84562	16.03234	7.89629
C	16.48644	17.69182	7.58953
C	17.53705	18.63003	7.49807
H	18.57399	18.29514	7.67448
C	17.28330	19.97672	7.18402
H	18.12181	20.69024	7.11185
C	15.96576	20.41276	6.96261
H	15.76323	21.46934	6.71882
C	14.90809	19.48971	7.05329

H	13.86929	19.81896	6.88268
C	15.16585	18.14328	7.36121
H	14.32757	17.42617	7.42279
H	11.72384	6.02968	6.46944

$Ag_{12}Au_{13}PET_{18}$_II

349

Au	12.56519	15.33962	12.14111
Ag	15.54364	16.37676	13.00758
Ag	17.22941	13.43408	13.66401
Au	14.82658	11.12556	13.56857
Au	11.07049	14.07541	14.44262
Ag	9.78143	16.55305	12.78465
Ag	11.08999	16.15704	9.57454
Au	12.65596	13.35870	9.76672
Au	14.14319	13.95659	14.37653
Ag	12.44639	14.02682	17.21910
Ag	9.52658	12.42286	16.47772
Au	9.98908	11.38907	13.38443
Au	12.43543	9.62106	12.88737
Ag	9.45805	8.58271	12.02092
Ag	7.77233	11.52497	11.36437
Au	10.17464	13.83528	11.46085
Au	13.93098	10.88558	10.58647
Ag	15.21931	8.40781	12.24443
Ag	13.91107	8.80433	15.45400
Au	12.34535	11.60279	15.26285
Au	10.85869	11.00378	10.65260
Ag	12.55576	10.93466	7.81008
Ag	15.47423	12.53853	8.55097
Au	15.01262	13.57057	11.64457
Au	12.50069	12.48033	12.51473
S	13.43562	17.58182	12.68525
S	17.87869	15.72251	13.15971
S	17.18620	11.07345	14.32604
S	9.78902	17.86713	10.73272
S	12.45837	14.96887	7.89930
S	9.33836	15.72239	15.04906
S	14.75785	14.62712	16.66907
S	10.30208	13.79753	18.34504
S	8.17233	10.99839	15.01573
C	13.66200	18.52440	11.09882
H	14.37199	17.98014	10.44286
H	12.67002	18.53547	10.59822
C	14.13077	19.97309	11.34258
H	13.39395	20.47942	12.00492
H	14.08541	20.49203	10.35664
C	15.52712	20.11327	11.91779
C	16.66288	19.97530	11.08921
H	16.53154	19.78001	10.01054
C	17.95908	20.08707	11.61830
H	18.83090	19.97544	10.95222
C	18.14435	20.34294	12.98862
H	19.16205	20.43498	13.40420
C	17.02335	20.48158	13.82508
H	17.15275	20.67770	14.90264
C	15.72807	20.36601	13.29151
H	14.85407	20.47367	13.95553
C	18.53381	16.46818	14.72751
H	18.47944	17.57119	14.60422
H	17.88022	16.18699	15.57913
C	19.98567	16.02340	14.99527

H	20.00638	14.91480	15.09789
H	20.60794	16.27609	14.10840
C	20.56002	16.67435	16.23969
C	21.29082	17.87989	16.15925
H	21.47699	18.33151	15.16917
C	21.78832	18.50532	17.31500
H	22.36125	19.44407	17.22689
C	21.56144	17.93442	18.57943
H	21.95339	18.42184	19.48802
C	20.83576	16.73401	18.67652
H	20.65659	16.27252	19.66207
C	20.34118	16.11286	17.51731
H	19.77961	15.16658	17.60454
C	17.10401	11.20639	16.17449
H	16.26127	11.87352	16.44867
H	16.88126	10.18811	16.56287
C	18.42582	11.73235	16.76509
H	19.26752	11.10577	16.39711
H	18.59542	12.76222	16.37146
C	18.41899	11.74702	18.28319
C	19.20705	10.83952	19.02386
H	19.85150	10.12298	18.48594
C	19.18478	10.83936	20.42967
H	19.80989	10.12174	20.98739
C	18.36773	11.74925	21.12214
H	18.34856	11.75150	22.22495
C	17.57522	12.65793	20.39731
H	16.93110	13.37728	20.93074
C	17.60028	12.65654	18.99233
H	16.97110	13.37285	18.43404
C	8.07101	17.64175	10.07186
H	8.08739	17.98340	9.01455
H	7.82169	16.55888	10.08855
C	7.03339	18.43466	10.88892
H	7.32999	19.50644	10.92004
H	7.05352	18.06154	11.93852
C	5.63558	18.29692	10.31437
C	5.05372	19.33082	9.54960
H	5.61746	20.26727	9.39352
C	3.77055	19.18857	8.99338
H	3.33438	20.01264	8.40334
C	3.04414	18.00233	9.19239
H	2.03520	17.88926	8.76097
C	3.61165	16.96213	9.95047
H	3.04776	16.02884	10.11772
C	4.89427	17.10835	10.50413
H	5.33195	16.28506	11.09483
C	11.25766	14.23501	6.68356
H	11.65064	13.22745	6.42083
H	10.27781	14.08836	7.17891
C	11.11196	15.08424	5.40605
H	12.11543	15.21783	4.94336
H	10.50842	14.47870	4.69025
C	10.44659	16.43370	5.59784
C	11.20545	17.62198	5.65312
H	12.30114	17.56501	5.54166
C	10.58567	18.86905	5.84229
H	11.19869	19.78522	5.88292

C	9.18977	18.94976	5.97941
H	8.70119	19.92761	6.12674
C	8.42008	17.77407	5.92406
H	7.32292	17.82549	6.02345
C	9.04384	16.52950	5.73407
H	8.42680	15.61579	5.67813
C	10.05901	17.02679	16.15676
H	10.24779	16.53866	17.13717
H	11.02903	17.37547	15.74738
C	9.06508	18.19505	16.30865
H	8.89120	18.65161	15.30894
H	8.08828	17.78267	16.64803
C	9.53946	19.25631	17.28452
C	9.49789	19.02463	18.67834
H	9.10716	18.06341	19.05518
C	9.93750	20.00064	19.58745
H	9.89301	19.79957	20.67125
C	10.42572	21.23412	19.11953
H	10.76463	22.00360	19.83333
C	10.47626	21.47752	17.73632
H	10.85426	22.44186	17.35655
C	10.04079	20.49482	16.83003
H	10.08129	20.69399	15.74524
C	14.82911	16.48239	16.74434
H	15.70834	16.78668	16.13589
H	13.92812	16.91098	16.26023
C	14.97564	16.97632	18.19699
H	14.04898	16.72098	18.75910
H	15.81060	16.42159	18.67987
C	15.24425	18.46876	18.27034
C	16.56845	18.95985	18.28740
H	17.41179	18.24768	18.27992
C	16.82832	20.34033	18.32021
H	17.87135	20.69874	18.34015
C	15.76303	21.25811	18.33420
H	15.96407	22.34247	18.36175
C	14.44010	20.78298	18.31614
H	13.59307	21.48867	18.32954
C	14.18462	19.40166	18.28471
H	13.14075	19.04433	18.27702
C	10.56640	12.62644	19.75964
H	11.02887	11.68979	19.38237
H	11.28235	13.10892	20.46020
C	9.23893	12.31852	20.48114
H	8.76456	13.27822	20.78459
H	8.54618	11.83023	19.75905
C	9.44317	11.43201	21.69542
C	9.46458	10.02511	21.57186
H	9.29084	9.56500	20.58373
C	9.69304	9.20355	22.68865
H	9.69977	8.10732	22.56743
C	9.90632	9.77590	23.95474
H	10.08328	9.13231	24.83275
C	9.88766	11.17449	24.09388
H	10.04906	11.63422	25.08375
C	9.65852	11.99149	22.97401
H	9.63976	13.08911	23.09267
C	8.48843	9.27494	15.62720

H	7.99394	8.59407	14.90088
H	9.57963	9.07541	15.60109
C	7.93084	9.05814	17.04585
H	8.46748	9.74599	17.73978
H	6.85759	9.34967	17.06699
C	8.08763	7.62124	17.50789
C	6.97924	6.74981	17.57382
H	5.97811	7.13221	17.31001
C	7.13143	5.41034	17.97284
H	6.24946	4.74941	18.02077
C	8.40273	4.91488	18.30988
H	8.52508	3.86416	18.62210
C	9.51713	5.77087	18.24709
H	10.51977	5.39353	18.50975
C	9.36071	7.11004	17.85111
H	10.24245	7.77438	17.80968
S	11.56623	7.37804	12.34417
S	7.12293	9.23622	11.86689
S	7.81517	13.88581	10.70334
S	15.21158	7.09355	14.29623
S	12.54262	9.99189	17.12966
S	15.66377	9.23917	9.98055
S	10.24424	10.33357	8.35977
S	14.69981	11.16365	6.68337
S	16.82819	13.96364	10.01246
C	11.33938	6.43597	13.93081
H	10.62957	6.98068	14.58661
H	12.33134	6.42460	14.43145
C	10.87004	4.98743	13.68729
H	11.60679	4.48062	13.02524
H	10.91498	4.46869	14.67336
C	9.47375	4.84763	13.11184
C	8.33785	4.98592	13.94018
H	8.46899	5.18118	15.01886
C	7.04173	4.87451	13.41080
H	6.16981	4.98632	14.07671
C	6.85669	4.61872	12.04044
H	5.83905	4.52706	11.62463
C	7.97782	4.47974	11.20423
H	7.84859	4.28365	10.12664
C	9.27302	4.59489	11.73809
H	10.14714	4.48688	11.07427
C	6.46980	8.49120	10.29800
H	6.52426	7.38815	10.42090
H	7.12436	8.77287	9.44729
C	5.01817	8.93570	10.02855
H	4.99725	10.04433	9.92630
H	4.39480	8.68245	10.91448
C	4.44576	8.28494	8.78312
C	3.71528	7.07911	8.86216
H	3.52704	6.62763	9.85191
C	3.22058	6.45330	7.70542
H	2.64781	5.51435	7.79243
C	3.44994	7.02412	6.44140
H	3.06058	6.53616	5.53200
C	4.17503	8.22500	6.34574
H	4.35585	8.68660	5.36054
C	4.66678	8.84656	7.50594

H	5.22772	9.79331	7.41983
C	7.89876	13.75404	8.85486
H	8.74173	13.08709	8.58095
H	8.12192	14.77259	8.46739
C	6.57749	13.22866	8.26260
H	5.73534	13.85435	8.63108
H	6.40796	12.19805	8.65429
C	6.58553	13.21678	6.74447
C	5.79705	14.12477	6.00486
H	5.15079	14.83907	6.54358
C	5.82145	14.12847	4.59909
H	5.19576	14.84622	4.04220
C	6.64101	13.22161	3.90560
H	6.66257	13.22278	2.80283
C	7.43348	12.31205	4.62936
H	8.07897	11.59453	4.09511
C	7.40623	12.30986	6.03430
H	8.03542	11.59288	6.59173
C	16.92959	7.31926	14.95695
H	16.91328	6.97761	16.01426
H	17.17867	8.40218	14.94026
C	17.96740	6.52654	14.13994
H	17.67167	5.45449	14.10988
H	17.94643	6.89878	13.09005
C	19.36539	6.66585	14.71370
C	19.94872	5.63285	15.47857
H	19.38619	4.69574	15.63501
C	21.23184	5.77686	16.03446
H	21.66928	4.95339	16.62440
C	21.95670	6.96398	15.83506
H	22.96544	7.07857	16.26655
C	21.38779	8.00323	15.07675
H	21.95052	8.93713	14.90901
C	20.10526	7.85523	14.52335
H	19.66652	8.67772	13.93230
C	13.74265	10.72566	18.34607
H	13.34921	11.73295	18.60907
H	14.72267	10.87283	17.85122
C	13.88797	9.87590	19.62328
H	12.88390	9.73901	20.08371
H	14.48823	10.48262	20.34083
C	14.55781	8.52862	19.43169
C	13.80274	7.33802	19.37375
H	12.70662	7.39152	19.48257
C	14.42683	6.09304	19.18488
H	13.81678	5.17498	19.14232
C	15.82328	6.01681	19.05073
H	16.31524	5.04063	18.90356
C	16.58916	7.19486	19.10868
H	17.68668	7.14695	19.01154
C	15.96113	8.43729	19.29845
H	16.57516	9.35288	19.35626
C	14.94386	7.93487	8.87222
H	14.75486	8.42332	7.89200
H	13.97399	7.58555	9.28141
C	15.93829	6.76713	8.71978
H	16.11337	6.31094	9.71945
H	16.91455	7.17990	8.37929

C	15.46325	5.70545	7.74467
C	15.50354	5.93663	6.35073
H	15.89289	6.89815	5.97324
C	15.06384	4.95999	5.44235
H	15.10705	5.16080	4.35845
C	14.57698	3.72630	5.91111
H	14.23868	2.95604	5.19786
C	14.52759	3.48344	7.29446
H	14.15066	2.51894	7.67490
C	14.96299	4.46684	8.20003
H	14.92265	4.26840	9.28495
C	10.17376	8.47831	8.28403
H	9.29553	8.17330	8.89356
H	11.07567	8.05013	8.76679
C	10.02576	7.98480	6.83139
H	10.95133	8.24153	6.26813
H	9.18941	8.53862	6.34986
C	9.75915	6.49200	6.75786
C	8.43565	5.99898	6.74274
H	7.59125	6.70987	6.75216
C	8.17778	4.61814	6.70937
H	7.13522	4.25830	6.69116
C	9.24439	3.70194	6.69277
H	9.04495	2.61731	6.66460
C	10.56666	4.17900	6.70892
H	11.41465	3.47449	6.69333
C	10.82014	5.56068	6.74109
C	14.43505	12.33481	5.26891
H	13.97211	13.27120	5.64624
H	13.71938	11.85205	4.56826
C	15.76238	12.64351	4.54748
H	16.23713	11.68410	4.24368
H	16.45497	13.13186	5.26968
C	15.55763	13.53031	3.33349
C	15.53518	14.93714	3.45757
H	15.70878	15.39702	4.44584
C	15.30586	15.75894	2.34113
H	15.29830	16.85512	2.46276
C	15.09279	15.18690	1.07487
H	14.91505	15.83068	0.19716
C	15.11260	13.78838	0.93520
H	14.95145	13.32889	-0.05483
C	15.34258	12.97114	2.05471
H	15.36224	11.87357	1.93563
C	16.50989	15.68709	9.40212
H	17.00431	16.36805	10.12840
H	15.41850	15.88550	9.42930
C	17.06597	15.90534	7.98309
H	16.53001	15.21675	7.28937
H	18.13974	15.61582	7.96099
C	16.90611	17.34214	7.52177
C	18.01275	18.21577	7.45550
H	19.01491	17.83504	7.71783
C	17.85754	19.55531	7.05788
H	18.73817	20.21801	7.00969
C	16.58496	20.04859	6.72251
H	16.46022	21.09941	6.41156
C	15.47232	19.19032	6.78547

H	14.46870	19.56591	6.52403
C	15.63174	17.85111	7.18006
H	14.75136	17.18496	7.22161
H	11.86350	5.91950	6.74768

Ag$_{12}$Au$_{13}$PET$_{18}$_III

349

Ag	12.52287	15.31799	12.17197
Au	15.51968	16.52082	13.10237
Au	17.38203	13.40364	13.76969
Ag	14.84046	11.19392	13.54771
Ag	11.00936	14.00358	14.39132
Au	9.60385	16.60757	12.81228
Au	11.11635	16.26440	9.38241
Ag	12.68848	13.43757	9.83867
Ag	14.03993	13.94151	14.38166
Au	12.48697	14.10008	17.34808
Au	9.39576	12.23039	16.52482
Ag	10.02990	11.33347	13.30477
Ag	12.49881	9.65488	12.85235
Au	9.46849	8.44669	11.95901
Au	7.59534	11.55891	11.30754
Ag	10.17834	13.78466	11.48967
Ag	14.03358	10.96746	10.64491
Au	15.43238	8.36921	12.17282
Au	13.90889	8.69550	15.59984
Ag	12.34109	11.57396	15.18956
Au	11.02913	11.05745	10.58209
Ag	12.52192	10.94957	7.83935
Au	15.63453	12.75949	8.48152
Ag	15.00217	13.61487	11.67126
Au	12.51924	12.48884	12.51141
S	13.38854	17.55688	13.00971
S	17.74194	15.66009	13.08952
S	17.23687	11.12988	14.44137
S	9.80165	17.73514	10.71801
S	12.48657	15.03590	7.87126
S	9.24605	15.73689	14.99148
S	14.74024	14.53828	16.74829
S	10.24834	13.81331	18.10110
S	8.27455	10.74359	15.06350
C	13.48427	18.75526	11.59351
H	14.09142	18.31334	10.77704
H	12.43953	18.84762	11.22581
C	14.01017	20.14748	11.99558
H	13.38599	20.53745	12.83004
H	13.83114	20.81845	11.12216
C	15.47698	20.21437	12.37529
C	16.47918	20.16806	11.38040
H	16.19236	20.08466	10.31755
C	17.83951	20.23342	11.72321
H	18.60348	20.19768	10.92849
C	18.22504	20.35157	13.07086
H	19.29314	20.41321	13.34011
C	17.23919	20.39410	14.07155
H	17.52550	20.48185	15.13280
C	15.87878	20.32239	13.72381
H	15.11228	20.35288	14.51621
C	18.58544	16.46923	14.53543
H	18.51902	17.56260	14.34898
H	18.02537	16.24165	15.46537
C	20.05182	16.01089	14.64598

H	20.07266	14.90620	14.78474
H	20.57003	16.22520	13.68519
C	20.77039	16.69528	15.79385
C	21.45778	17.91314	15.59858
H	21.50136	18.35109	14.58610
C	22.09013	18.56806	16.66871
H	22.62566	19.51615	16.49155
C	22.04475	18.01521	17.96039
H	22.54253	18.52624	18.80158
C	21.36515	16.80251	18.17090
H	21.32967	16.35469	19.17832
C	20.73476	16.15166	17.09693
H	20.21010	15.19590	17.27006
C	17.08151	11.25410	16.28422
H	16.23210	11.92309	16.53238
H	16.82554	10.22893	16.63311
C	18.38012	11.74566	16.95069
H	19.22996	11.12315	16.59517
H	18.57538	12.78504	16.59670
C	18.31608	11.71236	18.46721
C	19.12136	10.82126	19.20950
H	19.81487	10.14992	18.67414
C	19.05456	10.77969	20.61333
H	19.69455	10.07590	21.17185
C	18.17355	11.63043	21.30235
H	18.11805	11.59960	22.40354
C	17.36249	12.52139	20.57589
H	16.66796	13.19431	21.10665
C	17.43307	12.56219	19.17325
H	16.78973	13.26506	18.61410
C	8.10043	17.58975	9.98525
H	8.18600	17.94939	8.93753
H	7.81735	16.51669	9.97495
C	7.07305	18.41346	10.78153
H	7.39909	19.47622	10.82041
H	7.05980	18.03790	11.83045
C	5.68373	18.31423	10.17826
C	5.12658	19.38233	9.44317
H	5.70533	20.31503	9.32482
C	3.84756	19.27793	8.86896
H	3.42984	20.12802	8.30310
C	3.10228	18.09630	9.01931
H	2.09693	18.01303	8.57311
C	3.64598	17.02235	9.74724
H	3.06746	16.09209	9.87601
C	4.92391	17.13043	10.31998
H	5.34206	16.28117	10.88775
C	11.30754	14.29680	6.63756
H	11.72519	13.29605	6.38684
H	10.32700	14.12852	7.12465
C	11.15905	15.13282	5.35169
H	12.16477	15.27950	4.89856
H	10.57268	14.51049	4.63546
C	10.46928	16.47276	5.52116
C	11.20495	17.67661	5.53843
H	12.30076	17.63955	5.42035
C	10.56202	18.91585	5.70050
H	11.15726	19.84470	5.70696

C	9.16635	18.97289	5.85100
H	8.65938	19.94462	5.97598
C	8.42001	17.78091	5.83499
H	7.32296	17.81301	5.94382
C	9.06635	16.54448	5.66947
H	8.46638	15.61827	5.64252
C	9.95521	17.05736	16.08702
H	10.04897	16.58469	17.08853
H	10.97189	17.32818	15.73496
C	9.03609	18.29338	16.14878
H	8.94712	18.72059	15.12491
H	8.01748	17.96299	16.45057
C	9.54413	19.35172	17.10963
C	9.23039	19.29201	18.48600
H	8.58866	18.47385	18.85688
C	9.71340	20.25929	19.38272
H	9.45107	20.19505	20.45239
C	10.52218	21.31155	18.91760
H	10.89616	22.07618	19.61920
C	10.84674	21.38247	17.55143
H	11.47791	22.20481	17.17426
C	10.36410	20.40956	16.65954
H	10.62184	20.47243	15.58826
C	14.94396	16.37271	16.94174
H	15.86368	16.62685	16.37061
H	14.09933	16.89482	16.44884
C	15.08213	16.78681	18.41945
H	14.13138	16.54533	18.94615
H	15.87866	16.16899	18.89064
C	15.41280	18.25961	18.57922
C	16.75538	18.69617	18.62486
H	17.56944	17.95255	18.57086
C	17.07065	20.06031	18.74386
H	18.12709	20.37513	18.78323
C	16.04310	21.01720	18.81821
H	16.28722	22.08865	18.91419
C	14.70225	20.59728	18.77127
H	13.88489	21.33520	18.82966
C	14.39182	19.23208	18.65203
H	13.33497	18.91692	18.61928
C	10.37928	12.86764	19.69654
H	10.91221	11.91230	19.51084
H	11.00127	13.48788	20.37688
C	8.98718	12.61179	20.30320
H	8.46945	13.58616	20.44532
H	8.38277	12.02726	19.57361
C	9.07961	11.86788	21.62279
C	9.12696	10.45676	21.65446
H	9.05666	9.89221	20.70876
C	9.25221	9.76470	22.87061
H	9.28208	8.66224	22.87131
C	9.33392	10.47395	24.08159
H	9.43027	9.93173	25.03722
C	9.28800	11.87871	24.06590
H	9.34709	12.44499	25.01086
C	9.16259	12.56622	22.84705
H	9.12196	13.66950	22.84303
C	8.77657	9.05288	15.63532

H	8.34009	8.35976	14.88344
H	9.88157	8.95811	15.58441
C	8.26143	8.72186	17.04825
H	8.76923	9.40216	17.77060
H	7.17356	8.94602	17.10150
C	8.51138	7.27307	17.42521
C	7.44796	6.34968	17.51902
H	6.41592	6.69812	17.34042
C	7.68291	5.00078	17.83819
H	6.83467	4.29892	17.91087
C	8.99406	4.54754	18.06307
H	9.18174	3.48929	18.31148
C	10.06427	5.45584	17.97064
H	11.09828	5.11264	18.14313
C	9.82527	6.80458	17.65782
H	10.67303	7.51038	17.59597
S	11.60515	7.41989	12.05399
S	7.23951	9.29622	11.97135
S	7.77178	13.83114	10.63476
S	15.23402	7.23497	14.26198
S	12.51837	9.90465	17.10442
S	15.78763	9.25388	9.99849
S	10.19668	10.39307	8.30484
S	14.74694	11.19382	6.90907
S	16.77929	14.23810	9.94435
C	11.52271	6.21690	13.46664
H	10.91013	6.64936	14.28415
H	12.56796	6.13315	13.83479
C	11.01141	4.82042	13.05957
H	11.63661	4.44242	12.22031
H	11.20185	4.14672	13.92853
C	9.54375	4.73863	12.68597
C	8.54613	4.75868	13.68626
H	8.83756	4.83182	14.74862
C	7.18493	4.68156	13.34950
H	6.42462	4.69813	14.14840
C	6.79399	4.57730	12.00232
H	5.72532	4.50677	11.73751
C	7.77526	4.56030	10.99638
H	7.48517	4.48351	9.93533
C	9.13650	4.64379	11.33816
H	9.89900	4.63361	10.54150
C	6.41312	8.49424	10.51243
H	6.48759	7.39960	10.68839
H	6.97827	8.73692	9.58939
C	4.94330	8.93989	10.39493
H	4.91390	10.04515	10.26229
H	4.42079	8.71542	11.35106
C	4.23772	8.25581	9.23886
C	3.54928	7.03715	9.42550
H	3.49490	6.59848	10.43715
C	2.92930	6.38242	8.34798
H	2.39333	5.43331	8.51839
C	2.98811	6.93644	7.05736
H	2.49968	6.42585	6.21041
C	3.66922	8.14974	6.85528
H	3.71625	8.59796	5.84851
C	4.28710	8.80039	7.93657

H	4.81292	9.75659	7.76982
C	7.92153	13.68127	8.79290
H	8.74803	12.98096	8.55354
H	8.20871	14.69308	8.42950
C	6.60559	13.22225	8.13685
H	5.77716	13.87692	8.48506
H	6.37887	12.19512	8.50710
C	6.66434	13.22987	6.61988
C	5.88634	14.13586	5.86654
H	5.21849	14.83877	6.39395
C	5.94763	14.15255	4.46188
H	5.32946	14.86896	3.89484
C	6.79555	13.26107	3.78295
H	6.84663	13.27213	2.68116
C	7.57880	12.35439	4.52046
H	8.24636	11.64868	3.99755
C	7.51404	12.33862	5.92394
H	8.13543	11.62331	6.49225
C	16.93215	7.37432	15.00155
H	16.84208	7.00653	16.04611
H	17.21601	8.44720	15.02164
C	17.96179	6.55540	14.20323
H	17.63105	5.49473	14.14995
H	17.98406	6.94258	13.15870
C	19.34738	6.64020	14.81720
C	19.89358	5.56001	15.54281
H	19.30864	4.62942	15.64618
C	21.16937	5.64984	16.12650
H	21.57842	4.79041	16.68455
C	21.92248	6.82886	15.99563
H	22.92553	6.90048	16.44896
C	21.38966	7.91490	15.27769
H	21.97450	8.84316	15.16391
C	20.11484	7.82127	14.69549
H	19.70508	8.67987	14.13582
C	13.66790	10.61950	18.37783
H	13.24115	11.61476	18.63426
H	14.65818	10.79973	17.91525
C	13.79385	9.75824	19.64919
H	12.77863	9.58561	20.07099
H	14.35031	10.37378	20.39465
C	14.51081	8.43393	19.46978
C	13.79840	7.21746	19.41417
H	12.70001	7.23210	19.51175
C	14.46722	5.99359	19.23992
H	13.88946	5.05448	19.20173
C	15.86634	5.96491	19.11614
H	16.39356	5.00545	18.98087
C	16.58996	7.16969	19.17138
H	17.68931	7.15994	19.08395
C	15.91762	8.39051	19.34840
H	16.49966	9.32679	19.40536
C	15.08553	7.94104	8.88852
H	14.95830	8.43442	7.90051
H	14.08491	7.63498	9.25680
C	16.03601	6.73289	8.77700
H	16.15259	6.27612	9.78491
H	17.04052	7.10205	8.47197

C	15.54659	5.69078	7.78847
C	15.74107	5.86523	6.39947
H	16.27243	6.76277	6.03775
C	15.27762	4.91260	5.47734
H	15.44474	5.06773	4.39791
C	14.60935	3.75983	5.92795
H	14.25023	3.00807	5.20515
C	14.40543	3.57358	7.30617
H	13.88556	2.67223	7.67265
C	14.86751	4.53247	8.22433
H	14.70602	4.37791	9.30512
C	10.07953	8.54539	8.16916
H	9.19225	8.24710	8.76922
H	10.96481	8.07701	8.64466
C	9.92532	8.09859	6.70172
H	10.85504	8.36150	6.14783
H	9.09790	8.67953	6.23675
C	9.64022	6.61306	6.57400
C	8.31140	6.13498	6.54725
H	7.47571	6.85477	6.59167
C	8.03738	4.75961	6.45939
H	6.99084	4.41175	6.43362
C	9.09321	3.83297	6.39836
H	8.88119	2.75273	6.32750
C	10.42083	4.29445	6.42625
H	11.26017	3.58096	6.37752
C	10.68994	5.67079	6.51365
C	14.55511	12.15956	5.33429
H	14.04499	13.12086	5.55303
H	13.89251	11.55780	4.67531
C	15.91542	12.41035	4.65601
H	16.41661	11.43276	4.48057
H	16.56077	12.98363	5.35872
C	15.76134	13.16484	3.34857
C	15.70465	14.57613	3.33100
H	15.81394	15.13302	4.27760
C	15.52121	15.27790	2.12779
H	15.48557	16.38018	2.13803
C	15.38887	14.57868	0.91539
H	15.24586	15.12838	-0.03006
C	15.44351	13.17414	0.91678
H	15.34574	12.61555	-0.02960
C	15.62721	12.47704	2.12283
H	15.67379	11.37399	2.11529
C	16.26238	15.93163	9.39495
H	16.71429	16.62238	10.13978
H	15.15848	16.02431	9.47100
C	16.74346	16.27295	7.97224
H	16.22740	15.58967	7.25900
H	17.83226	16.06063	7.89499
C	16.46882	17.72001	7.60664
C	17.51584	18.66282	7.52045
H	18.55403	18.33101	7.69548
C	17.25705	20.00991	7.21229
H	18.09271	20.72724	7.14482
C	15.93802	20.44163	6.99081
H	15.73179	21.49821	6.75010
C	14.88394	19.51398	7.07593

H	13.84392	19.83960	6.90576
C	15.14687	18.16723	7.37804
H	14.31157	17.44624	7.43371
H	11.73698	6.01827	6.53072

Ag$_{12}$Au$_{13}$PET$_{18}$_IV
349

Ag	12.51620	15.32963	12.12487
Au	15.62540	16.53644	13.04230
Ag	17.23621	13.38460	13.53941
Au	14.85819	11.20629	13.48496
Ag	11.16761	14.11649	14.47421
Au	9.70335	16.70284	12.78843
Ag	11.10887	16.03882	9.49401
Au	12.53527	13.30613	9.79285
Ag	14.18620	14.03976	14.28952
Au	12.55403	14.21114	17.35008
Ag	9.61613	12.35740	16.46706
Au	10.06518	11.41905	13.48213
Ag	12.48714	9.63185	12.90276
Au	9.37870	8.42360	11.98538
Ag	7.76791	11.57462	11.49001
Au	10.14566	13.75483	11.54513
Ag	13.83665	10.84622	10.55478
Au	15.29920	8.25801	12.24077
Ag	13.89487	8.92457	15.53457
Au	12.46934	11.65730	15.23686
Ag	10.81932	10.92197	10.73924
Au	12.45035	10.75091	7.67846
Ag	15.38947	12.60291	8.56167
Au	14.94020	13.54049	11.54639
Au	12.50235	12.48104	12.51474
S	13.48059	17.54007	12.87552
S	17.85222	15.70129	13.10017
S	17.22379	11.04579	14.26938
S	9.88616	17.78859	10.66973
S	12.42279	14.82449	7.80767
S	9.35149	15.79410	14.95636
S	14.78212	14.67434	16.66557
S	10.35872	13.90217	18.21603
S	8.23822	10.88146	15.08658
C	13.59713	18.70239	11.42972
H	14.25950	18.26175	10.65644
H	12.56824	18.75282	11.01205
C	14.05801	20.12034	11.82187
H	13.36501	20.51791	12.59590
H	13.92699	20.75845	10.91603
C	15.49044	20.23312	12.30641
C	16.56524	20.20020	11.39014
H	16.35920	20.10088	10.30988
C	17.89441	20.29468	11.83356
H	18.71755	20.26591	11.09987
C	18.17482	20.42881	13.20527
H	19.21830	20.50949	13.55388
C	17.11567	20.46089	14.12844
H	17.31916	20.56044	15.20772
C	15.78707	20.36137	13.67998
H	14.96246	20.38242	14.41208
C	18.59408	16.39742	14.65442
H	18.55779	17.50310	14.55381
H	17.96932	16.11039	15.52532
C	20.04444	15.91221	14.84063

H	20.04553	14.80120	14.91751
H	20.63199	16.17296	13.93261
C	20.68819	16.52168	16.07241
C	21.45337	17.70492	15.98332
H	21.61560	18.16828	14.99449
C	22.01419	18.29381	17.12925
H	22.61237	19.21596	17.03459
C	21.81713	17.70808	18.39178
H	22.25783	18.16730	19.29268
C	21.05821	16.52910	18.49690
H	20.90167	16.05587	19.48070
C	20.50060	15.94417	17.34766
H	19.91287	15.01466	17.44172
C	17.15430	11.22633	16.11486
H	16.31240	11.89705	16.38269
H	16.93456	10.21686	16.52785
C	18.48016	11.76218	16.68733
H	19.31993	11.13870	16.30982
H	18.63932	12.79091	16.28628
C	18.49604	11.78143	18.20546
C	19.31083	10.88842	18.93507
H	19.95815	10.18138	18.38811
C	19.30988	10.88911	20.34098
H	19.95579	10.18299	20.88963
C	18.48805	11.78567	21.04511
H	18.48430	11.78755	22.14810
C	17.66969	12.68026	20.33161
H	17.02164	13.38939	20.87379
C	17.67317	12.67785	18.92634
H	17.02144	13.38222	18.37877
C	8.16836	17.63242	9.98175
H	8.23926	17.91544	8.90930
H	7.86072	16.56687	10.05105
C	7.16242	18.52796	10.72806
H	7.50915	19.58431	10.69192
H	7.15314	18.22408	11.79962
C	5.76713	18.41356	10.14249
C	5.23618	19.42294	9.31090
H	5.83919	20.32507	9.10737
C	3.95395	19.29944	8.74783
H	3.55780	20.10384	8.10488
C	3.17779	18.15715	9.00728
H	2.16975	18.05913	8.57017
C	3.69441	17.14179	9.83262
H	3.09122	16.24346	10.04721
C	4.97603	17.26901	10.39309
H	5.37381	16.46565	11.03706
C	11.18044	14.09508	6.63443
H	11.54055	13.06808	6.39904
H	10.20541	13.98948	7.15006
C	11.03191	14.91383	5.33762
H	12.03042	15.01797	4.85697
H	10.40662	14.30190	4.64617
C	10.39324	16.27951	5.50490
C	11.17107	17.45688	5.50793
H	12.26296	17.38050	5.37351
C	10.57435	18.71849	5.67433
H	11.20158	19.62596	5.67021

C	9.18350	18.82529	5.84246
H	8.71307	19.81471	5.97097
C	8.39520	17.66055	5.84032
H	7.30157	17.73192	5.96367
C	8.99569	16.40152	5.67150
H	8.36375	15.49642	5.65702
C	9.97378	17.10868	16.10923
H	10.11551	16.60002	17.08726
H	10.96243	17.47075	15.76107
C	8.96487	18.26649	16.23355
H	8.82888	18.73215	15.23217
H	7.97832	17.84467	16.52971
C	9.40046	19.31694	17.23861
C	9.26129	19.08995	18.62666
H	8.81632	18.14229	18.97679
C	9.67426	20.05164	19.56306
H	9.55262	19.85407	20.64166
C	10.23505	21.26625	19.12844
H	10.55341	22.02506	19.86295
C	10.38341	21.50510	17.75138
H	10.81908	22.45488	17.39744
C	9.97247	20.53698	16.81852
H	10.09025	20.73207	15.73864
C	14.93654	16.51682	16.83528
H	15.84073	16.79763	16.25254
H	14.06938	17.00477	16.34662
C	15.07084	16.94836	18.30808
H	14.14427	16.65042	18.84922
H	15.91157	16.38633	18.77186
C	15.30520	18.44091	18.45318
C	16.61517	18.96498	18.51377
H	17.47669	18.27552	18.48398
C	16.83713	20.34880	18.61768
H	17.86948	20.73427	18.67064
C	15.74769	21.23682	18.66025
H	15.91966	22.32333	18.74317
C	14.43813	20.72905	18.59935
H	13.57262	21.41126	18.63434
C	14.22116	19.34482	18.49680
H	13.18840	18.95885	18.45508
C	10.57420	12.83398	19.72054
H	11.10097	11.89958	19.43194
H	11.21935	13.39406	20.43074
C	9.21085	12.51371	20.36318
H	8.68652	13.46789	20.59380
H	8.58335	11.97149	19.62017
C	9.36301	11.68349	21.62438
C	9.41909	10.27369	21.56103
H	9.31259	9.77078	20.58433
C	9.59851	9.50366	22.72254
H	9.63380	8.40386	22.64822
C	9.72740	10.13191	23.97333
H	9.86638	9.52880	24.88617
C	9.67366	11.53429	24.05230
H	9.76915	12.03759	25.02945
C	9.49346	12.29980	22.88797
H	9.44680	13.40061	22.95918
C	8.66979	9.16561	15.64567

H	8.19074	8.47739	14.91605
H	9.76827	9.02522	15.57472
C	8.17465	8.87794	17.07546
H	8.70543	9.56550	17.77374
H	7.09060	9.11726	17.14439
C	8.41494	7.43477	17.47913
C	7.35470	6.50474	17.53372
H	6.32900	6.84417	17.30792
C	7.58559	5.15995	17.87231
H	6.74024	4.45217	17.91297
C	8.88887	4.71844	18.15856
H	9.07298	3.66354	18.42315
C	9.95591	5.63348	18.10598
H	10.98346	5.29911	18.32735
C	9.72067	6.97751	17.77110
H	10.56590	7.68818	17.73699
S	11.52422	7.42125	12.15014
S	7.15161	9.25808	11.92920
S	7.77998	13.91351	10.76072
S	15.11610	7.17302	14.35977
S	12.58036	10.13790	17.22135
S	15.65059	9.16626	10.07264
S	10.22231	10.28850	8.36327
S	14.64539	11.05999	6.81189
S	16.76766	14.07828	9.94250
C	11.40910	6.25659	13.59415
H	10.74658	6.69549	14.36829
H	12.43816	6.20638	14.01142
C	10.94930	4.83885	13.19996
H	11.64230	4.44314	12.42497
H	11.08137	4.19938	14.10471
C	9.51674	4.72552	12.71596
C	8.44239	4.75589	13.63284
H	8.64894	4.85359	14.71315
C	7.11307	4.66096	13.18998
H	6.29029	4.68775	13.92416
C	6.83205	4.52894	11.81819
H	5.78846	4.44794	11.46999
C	7.89073	4.49936	10.89439
H	7.68674	4.40148	9.81506
C	9.21948	4.59930	11.34233
H	10.04372	4.58027	10.60976
C	6.40859	8.56246	10.37528
H	6.44406	7.45675	10.47584
H	7.03318	8.84897	9.50409
C	4.95858	9.04893	10.18970
H	4.95839	10.16001	10.11368
H	4.37096	8.78796	11.09762
C	4.31419	8.44098	8.95751
C	3.54919	7.25754	9.04565
H	3.38744	6.79312	10.03406
C	2.98824	6.66961	7.89930
H	2.39030	5.74723	7.99323
C	3.18478	7.25667	6.63730
H	2.74398	6.79820	5.73607
C	3.94330	8.43598	6.53314
H	4.09933	8.91028	5.54978
C	4.50107	9.01993	7.68282

H	5.08855	9.94969	7.58954
C	7.85104	13.73448	8.91518
H	8.69134	13.06162	8.64772
H	8.07420	14.74371	8.50343
C	6.52425	13.20315	8.34062
H	5.68596	13.82920	8.71716
H	6.36115	12.17477	8.74098
C	6.51055	13.18455	6.82245
C	5.69821	14.07916	6.09205
H	5.05133	14.78707	6.63839
C	5.70143	14.07930	4.68614
H	5.05749	14.78674	4.13687
C	6.52289	13.18179	3.98279
H	6.52834	13.18047	2.87982
C	7.33891	12.28570	4.69709
H	7.98679	11.57593	4.15552
C	7.33313	12.28725	6.10234
H	7.98322	11.58184	6.65053
C	16.83389	7.32784	15.04798
H	16.76246	7.04481	16.12041
H	17.14252	8.39311	14.97881
C	17.83909	6.43116	14.30203
H	17.48949	5.37568	14.33553
H	17.85143	6.73693	13.23105
C	19.23337	6.54056	14.89100
C	19.75989	5.52745	15.72085
H	19.15423	4.62617	15.92021
C	21.04104	5.64618	16.28741
H	21.43369	4.83891	16.92890
C	21.82051	6.78746	16.03340
H	22.82765	6.88179	16.47340
C	21.30839	7.80647	15.20975
H	21.91425	8.70399	14.99937
C	20.02786	7.68393	14.64569
H	19.63363	8.49007	14.00301
C	13.82192	10.86699	18.39560
H	13.46128	11.89369	18.63142
H	14.79721	10.97325	17.88058
C	13.96991	10.04746	19.69200
H	12.97064	9.94011	20.17037
H	14.59195	10.66052	20.38535
C	14.61297	8.68381	19.52499
C	13.83825	7.50441	19.51611
H	12.74553	7.57771	19.64538
C	14.43910	6.24464	19.35075
H	13.81425	5.33551	19.35034
C	15.83105	6.14179	19.18931
H	16.30479	5.15381	19.06183
C	16.61620	7.30862	19.19678
H	17.71055	7.24033	19.07827
C	16.01159	8.56581	19.36457
H	16.64101	9.47258	19.38321
C	15.02514	7.85310	8.91989
H	14.88392	8.36232	7.94208
H	14.03593	7.49290	9.26843
C	16.03166	6.69335	8.79450
H	16.16580	6.22561	9.79516
H	17.01936	7.11356	8.49991

C	15.59480	5.64575	7.78699
C	15.73820	5.87425	6.39962
H	16.18717	6.82094	6.05200
C	15.32454	4.91522	5.46080
H	15.44968	5.11390	4.38281
C	14.75859	3.70189	5.89227
H	14.43973	2.94510	5.15589
C	14.60559	3.46175	7.26860
H	14.16576	2.51297	7.62006
C	15.01730	4.42720	8.20389
H	14.89596	4.23104	9.28318
C	10.06572	8.44634	8.19249
H	9.16089	8.16666	8.77479
H	10.93196	7.95683	8.68123
C	9.93092	8.01580	6.71941
H	10.85966	8.30883	6.17931
H	9.09380	8.58259	6.25487
C	9.68801	6.52468	6.57346
C	8.37492	6.00868	6.51083
H	7.51761	6.70341	6.53990
C	8.14449	4.62634	6.40587
H	7.10982	4.24742	6.35137
C	9.22848	3.73164	6.36426
H	9.04997	2.64625	6.28046
C	10.54106	4.23132	6.42722
H	11.40228	3.54364	6.39293
C	10.76652	5.61413	6.53086
C	14.42935	12.12967	5.30851
H	13.90251	13.06367	5.59823
H	13.78411	11.57017	4.59792
C	15.79247	12.45085	4.66582
H	16.31690	11.49703	4.43397
H	16.42008	12.99236	5.40925
C	15.63980	13.28248	3.40560
C	15.58366	14.69221	3.47056
H	15.69044	15.19404	4.44780
C	15.40379	15.46355	2.31000
H	15.36847	16.56326	2.38559
C	15.27449	14.83670	1.05854
H	15.13516	15.44084	0.14643
C	15.32827	13.43443	0.97797
H	15.23247	12.93223	0.00028
C	15.50895	12.66760	2.14136
H	15.55565	11.56687	2.06887
C	16.33624	15.79407	9.38310
H	16.81577	16.48243	10.11226
H	15.23781	15.93467	9.45454
C	16.83066	16.08118	7.95295
H	16.29987	15.39301	7.25529
H	17.91478	15.84227	7.88367
C	16.58954	17.52401	7.54855
C	17.64925	18.45461	7.49340
H	18.67515	18.11591	7.71938
C	17.41759	19.79906	7.15396
H	18.26251	20.50731	7.11286
C	16.11405	20.23963	6.86742
H	15.92933	21.29425	6.60215
C	15.04754	19.32401	6.92061

H	14.01979	19.65763	6.69905
C	15.28354	17.98033	7.25634
H	14.43870	17.26920	7.29087
H	11.80162	5.99358	6.57416

Ag$_{12}$Au$_{13}$PET$_{18}$_V
349

Au	12.63307	15.29503	12.12585
Ag	15.43051	16.37622	13.09502
Au	17.39431	13.40175	13.77503
Ag	14.77150	11.09480	13.65296
Au	10.95998	14.03491	14.32630
Ag	9.74096	16.51930	12.81360
Au	11.05533	16.31308	9.42350
Ag	12.79447	13.38539	9.79710
Au	14.03501	13.85725	14.44761
Ag	12.42986	14.02612	17.17087
Au	9.34121	12.24650	16.54939
Ag	9.93431	11.40862	13.27493
Au	12.37245	9.66818	12.89874
Ag	9.57703	8.58436	11.93016
Au	7.61202	11.55811	11.25235
Ag	10.23445	13.86794	11.37313
Au	14.04714	10.92897	10.69952
Ag	15.26425	8.44346	12.21217
Au	13.95029	8.65059	15.60265
Ag	12.21218	11.57881	15.22935
Au	10.97237	11.10588	10.57810
Ag	12.57794	10.93832	7.85485
Au	15.66677	12.71749	8.47745
Ag	15.07272	13.55339	11.75061
Au	12.50332	12.48164	12.51311
S	13.32894	17.59227	12.77651
S	17.76119	15.67014	13.14184
S	17.19805	11.11512	14.40934
S	9.73816	17.79693	10.74375
S	12.47389	15.08443	7.95650
S	9.30260	15.72835	15.08206
S	14.76731	14.57066	16.71888
S	10.22393	13.78090	18.15175
S	8.20450	10.81332	15.03817
C	13.60326	18.60697	11.24449
H	14.34343	18.10028	10.59230
H	12.63198	18.62429	10.70522
C	14.04438	20.04903	11.56605
H	13.27981	20.51860	12.22425
H	14.02734	20.60943	10.60253
C	15.41844	20.17802	12.19485
C	16.58235	20.11495	11.39681
H	16.48795	19.98896	10.30401
C	17.85899	20.21611	11.97435
H	18.75373	20.16683	11.33121
C	17.99548	20.38492	13.36403
H	18.99706	20.47116	13.81853
C	16.84587	20.44701	14.17084
H	16.93746	20.57341	15.26271
C	15.57100	20.34302	13.58819
H	14.67448	20.39032	14.22825
C	18.52699	16.46989	14.63211
H	18.44054	17.56553	14.46596
H	17.94000	16.21149	15.53721
C	20.00079	16.05229	14.80188

H	20.04489	14.94688	14.92835
H	20.55273	16.29198	13.86635
C	20.65138	16.74121	15.98684
C	21.33521	17.96682	15.83117
H	21.42842	18.40736	14.82323
C	21.90257	18.62598	16.93479
H	22.43679	19.58006	16.78830
C	21.79413	18.06968	18.22129
H	22.24101	18.58382	19.08882
C	21.11725	16.84921	18.39285
H	21.03227	16.39887	19.39615
C	20.55230	16.19431	17.28545
H	20.02962	15.23263	17.42892
C	17.08273	11.23190	16.25638
H	16.26317	11.93159	16.51985
H	16.79635	10.21598	16.60808
C	18.40994	11.67773	16.89813
H	19.22773	11.00979	16.55016
H	18.64788	12.69947	16.52002
C	18.35652	11.68238	18.41529
C	19.11639	10.76595	19.17419
H	19.76867	10.04541	18.65119
C	19.05632	10.76082	20.57898
H	19.66046	10.03617	21.15061
C	18.22773	11.67436	21.25242
H	18.17702	11.67159	22.35425
C	17.46292	12.59212	20.50946
H	16.81046	13.31493	21.02799
C	17.52675	12.59629	19.10591
H	16.91965	13.32039	18.53360
C	8.01692	17.60710	10.07714
H	8.03031	18.01095	9.04244
H	7.77017	16.52567	10.03355
C	6.99325	18.35385	10.95098
H	7.29169	19.42195	11.04020
H	7.02331	17.92078	11.97729
C	5.58851	18.25153	10.38498
C	4.99411	19.33516	9.70377
H	5.55347	20.28199	9.60526
C	3.70319	19.22828	9.15762
H	3.25678	20.09048	8.63342
C	2.98250	18.02858	9.28272
H	1.96775	17.94318	8.85872
C	3.56312	16.93921	9.95696
H	3.00424	15.99445	10.06588
C	4.85322	17.04986	10.50134
H	5.30072	16.18798	11.02607
C	11.35628	14.33231	6.67481
H	11.80271	13.34274	6.43108
H	10.36224	14.14231	7.12503
C	11.23776	15.17622	5.39098
H	12.25625	15.34635	4.97624
H	10.69095	14.54830	4.64867
C	10.51549	16.50088	5.54464
C	11.22521	17.71922	5.59174
H	12.32475	17.70470	5.50828
C	10.55236	18.94413	5.73999
H	11.12797	19.88467	5.77341

C	9.15179	18.97178	5.84545
H	8.62136	19.93209	5.96069
C	8.43106	17.76506	5.79888
H	7.33073	17.77379	5.87316
C	9.10739	16.54310	5.64790
H	8.52754	15.60510	5.59822
C	10.10700	17.03630	16.12766
H	10.30336	16.56806	17.11626
H	11.07867	17.33684	15.68407
C	9.16273	18.24606	16.27691
H	8.99138	18.69419	15.27296
H	8.17603	17.87625	16.63583
C	9.68998	19.30192	17.23092
C	9.63568	19.10151	18.62920
H	9.19522	18.16943	19.02413
C	10.12270	20.07231	19.51954
H	10.06615	19.89642	20.60716
C	10.67231	21.27014	19.02765
H	11.04769	22.03642	19.72647
C	10.73630	21.48242	17.63985
H	11.16226	22.41885	17.24140
C	10.25305	20.50457	16.75281
H	10.30442	20.67979	15.66433
C	14.88735	16.42230	16.80344
H	15.78440	16.70278	16.20932
H	14.00737	16.88130	16.30877
C	15.03025	16.90581	18.26067
H	14.08480	16.68565	18.80608
H	15.83295	16.31399	18.75408
C	15.36008	18.38488	18.35011
C	16.70353	18.81962	18.38983
H	17.51622	18.07260	18.38449
C	17.02181	20.18723	18.44168
H	18.07886	20.49997	18.47813
C	15.99636	21.14936	18.45223
H	16.24240	22.22381	18.49523
C	14.65482	20.73089	18.41069
H	13.83856	21.47209	18.42063
C	14.34102	19.36208	18.36018
H	13.28289	19.05028	18.33358
C	10.41666	12.80913	19.72180
H	10.93005	11.84999	19.50177
H	11.07568	13.40975	20.38558
C	9.05401	12.55353	20.39395
H	8.54895	13.52990	20.56555
H	8.41407	11.97848	19.68776
C	9.20081	11.80059	21.70305
C	9.24414	10.38898	21.72467
H	9.13058	9.83044	20.77956
C	9.41888	9.68884	22.93015
H	9.44445	8.58625	22.92301
C	9.55542	10.39007	24.14088
H	9.69069	9.84163	25.08820
C	9.51410	11.79510	24.13552
H	9.61530	12.35534	25.08055
C	9.33902	12.49044	22.92726
H	9.30202	13.59390	22.93177
C	8.66694	9.10292	15.58597

H	8.22896	8.42695	14.81939
H	9.77094	8.99215	15.55467
C	8.12148	8.76526	16.98605
H	8.61234	9.44489	17.72042
H	7.03263	8.98907	17.01594
C	8.36482	7.31649	17.36631
C	7.30440	6.38565	17.41062
H	6.27882	6.72805	17.18850
C	7.53423	5.03751	17.73666
H	6.68852	4.32976	17.76989
C	8.83710	4.59289	18.01951
H	9.02074	3.53544	18.27410
C	9.90438	5.50840	17.97654
H	10.93165	5.17182	18.19610
C	9.67037	6.85611	17.65537
H	10.51576	7.56718	17.63178
S	11.67924	7.36968	12.24908
S	7.24644	9.28993	11.88674
S	7.80780	13.84472	10.61804
S	15.26627	7.16600	14.28213
S	12.53226	9.87957	17.06983
S	15.70269	9.23380	9.94354
S	10.23981	10.39608	8.30595
S	14.78452	11.18265	6.87523
S	16.80249	14.15187	9.98835
C	11.40502	6.35599	13.78177
H	10.66531	6.86342	14.43393
H	12.37648	6.33860	14.32069
C	10.96326	4.91388	13.46140
H	11.72724	4.44368	12.80295
H	10.98090	4.35410	14.42527
C	9.58871	4.78457	12.83374
C	8.42545	4.84880	13.63265
H	8.52075	4.97636	14.72519
C	7.14834	4.74657	13.05635
H	6.25415	4.79667	13.70019
C	7.01068	4.57554	11.66705
H	6.00874	4.48835	11.21354
C	8.15962	4.51252	10.85935
H	8.06707	4.38447	9.76776
C	9.43498	4.61760	11.44076
H	10.33098	4.56942	10.80002
C	6.47545	8.48891	10.39985
H	6.56213	7.39342	10.56688
H	7.05922	8.74609	9.49232
C	5.00119	8.90705	10.23561
H	4.95717	10.01231	10.10786
H	4.45330	8.66908	11.17396
C	4.34440	8.21705	9.05471
C	3.66164	6.99146	9.21528
H	3.57466	6.55150	10.22403
C	3.08724	6.33178	8.11563
H	2.55388	5.37783	8.26601
C	3.18747	6.88748	6.82820
H	2.73488	6.37304	5.96382
C	3.86344	8.10774	6.65174
H	3.94198	8.55760	5.64769
C	4.43549	8.76317	7.75518

H	4.95713	9.72485	7.60795
C	7.92005	13.72806	8.77081
H	8.73983	13.02921	8.50573
H	8.20454	14.74430	8.41859
C	6.59182	13.28093	8.13212
H	5.77375	13.94621	8.48453
H	6.35722	12.25777	8.50855
C	6.63968	13.28030	6.61477
C	5.87163	14.19442	5.86134
H	5.21759	14.90999	6.38893
C	5.92580	14.20343	4.45637
H	5.31527	14.92614	3.88908
C	6.75670	13.29626	3.77718
H	6.80282	13.30211	2.67516
C	7.52964	12.38085	4.51462
H	8.18388	11.66298	3.99150
C	7.47163	12.37274	5.91843
H	8.08470	11.65026	6.48638
C	16.98767	7.35362	14.94880
H	16.97362	6.95004	15.98360
H	17.23604	8.43470	14.99207
C	18.01010	6.60490	14.07521
H	17.70943	5.53745	13.98580
H	17.98121	7.03812	13.04893
C	19.41495	6.70405	14.64151
C	20.00719	5.61854	15.32161
H	19.44592	4.67275	15.41920
C	21.29844	5.72220	15.86761
H	21.74317	4.85853	16.39082
C	22.02161	6.92052	15.74355
H	23.03663	7.00336	16.16739
C	21.44307	8.01181	15.07062
H	22.00386	8.95553	14.96260
C	20.15265	7.90436	14.52637
H	19.70686	8.76766	14.00251
C	13.65034	10.63078	18.35176
H	13.20653	11.62200	18.59358
H	14.64540	10.81717	17.90238
C	13.76503	9.78845	19.63697
H	12.74583	9.62387	20.05219
H	14.31495	10.41503	20.37811
C	14.48067	8.45995	19.48547
C	13.76490	7.24500	19.44247
H	12.66559	7.26517	19.52769
C	14.43148	6.01644	19.29609
H	13.85123	5.07865	19.26600
C	15.83171	5.98164	19.18837
H	16.35721	5.01845	19.07451
C	16.55845	7.18490	19.23105
H	17.65862	7.17044	19.15511
C	15.88837	8.41053	19.38016
H	16.47285	9.34580	19.42678
C	14.89602	7.92655	8.89875
H	14.69987	8.39474	7.91007
H	13.92411	7.62752	9.34288
C	15.83852	6.71544	8.74942
H	16.00927	6.26705	9.75336
H	16.82572	7.08383	8.39045

C	15.30977	5.66035	7.79539
C	15.36554	5.86015	6.39709
H	15.80811	6.79125	6.00219
C	14.87754	4.88989	5.50670
H	14.93541	5.06523	4.41906
C	14.32534	3.69324	5.99858
H	13.94925	2.92733	5.29974
C	14.25968	3.48166	7.38641
H	13.83167	2.54616	7.78486
C	14.74399	4.45895	8.27349
H	14.69143	4.28421	9.36199
C	10.11693	8.54469	8.22039
H	9.22009	8.26535	8.81539
H	10.99675	8.08408	8.71382
C	9.97159	8.06222	6.76307
H	10.91666	8.28146	6.21662
H	9.16905	8.65537	6.27098
C	9.63975	6.58363	6.67317
C	8.29576	6.15061	6.63334
H	7.48403	6.89867	6.63903
C	7.97570	4.78341	6.58102
H	6.91825	4.47205	6.54455
C	8.99992	3.81998	6.57009
H	8.75251	2.74587	6.52666
C	10.34201	4.23673	6.61177
H	11.15729	3.49445	6.60156
C	10.65755	5.60511	6.66277
C	14.59285	12.15402	5.30478
H	14.07985	13.11348	5.52429
H	13.93382	11.55350	4.64093
C	15.95592	12.40870	4.63315
H	16.46047	11.43202	4.46191
H	16.59590	12.98346	5.33954
C	15.81020	13.16157	3.32389
C	15.76748	14.57320	3.30211
H	15.88057	15.13177	4.24727
C	15.59391	15.27331	2.09645
H	15.56883	16.37591	2.10348
C	15.45794	14.57203	0.88568
H	15.32362	15.12045	-0.06179
C	15.49861	13.16699	0.89120
H	15.39781	12.60671	-0.05385
C	15.67251	12.47167	2.09965
H	15.70900	11.36820	2.09527
C	16.33908	15.86170	9.43971
H	16.77606	16.53827	10.20634
H	15.23498	15.97178	9.47009
C	16.88570	16.19880	8.03993
H	16.39441	15.51979	7.30527
H	17.97424	15.97344	8.01078
C	16.64499	17.64789	7.65923
C	17.70718	18.57676	7.61564
H	18.73185	18.23253	7.83909
C	17.48025	19.92514	7.28862
H	18.32733	20.63126	7.25593
C	16.17853	20.37199	7.00396
H	15.99717	21.42961	6.74845
C	15.10950	19.45852	7.04627

H	14.08317	19.79695	6.82517
C	15.34062	18.11055	7.36850
H	14.49391	17.40103	7.39150
H	11.71608	5.91554	6.68948

Ag$_{12}$Au$_{13}$PET$_{18}$_VI

349

Ag	12.53225	15.31120	12.12741
Ag	15.44817	16.38981	13.00410
Ag	17.20532	13.42206	13.62092
Ag	14.79399	11.10038	13.51519
Ag	11.03740	14.04789	14.37850
Ag	9.70420	16.46779	12.82670
Ag	11.05861	16.17581	9.54558
Ag	12.63257	13.35809	9.74498
Ag	14.10414	13.91648	14.33865
Ag	12.49371	13.95390	17.18647
Ag	9.47753	12.45331	16.44638
Ag	9.93428	11.40515	13.31524
Au	12.34845	9.64947	12.87677
Au	9.30717	8.45130	12.02843
Au	7.53999	11.58098	11.21955
Au	10.16770	13.79820	11.43361
Au	13.92160	10.87943	10.61684
Au	15.42217	8.28346	12.16607
Au	13.94508	8.63922	15.55625
Au	12.31486	11.60038	15.18365
Au	10.92513	11.02022	10.59592
Au	12.48517	10.82048	7.58163
Au	15.61068	12.62684	8.38578
Au	14.94305	13.57312	11.60744
Au	12.47542	12.49018	12.49044
S	13.32623	17.56821	12.86488
S	17.77663	15.71010	13.04150
S	17.18138	11.09654	14.32348
S	9.74433	17.80265	10.78993
S	12.47392	15.05891	7.90441
S	9.25030	15.65566	15.08138
S	14.80106	14.52975	16.66443
S	10.33822	13.79742	18.29483
S	8.12740	11.02726	15.01714
C	13.49249	18.66250	11.36983
H	14.18060	18.19027	10.63893
H	12.48367	18.71041	10.90638
C	13.95812	20.08936	11.72317
H	13.24513	20.52417	12.45818
H	13.86716	20.69506	10.79093
C	15.37494	20.19879	12.25193
C	16.47790	20.14518	11.37075
H	16.30465	20.03474	10.28588
C	17.79361	20.23540	11.85438
H	18.63864	20.19155	11.14696
C	18.03155	20.38602	13.23232
H	19.06394	20.46460	13.61304
C	16.94401	20.43772	14.12133
H	17.11513	20.54917	15.20510
C	15.62949	20.34237	13.63269
H	14.78218	20.38016	14.33758
C	18.52301	16.48143	14.55618
H	18.45928	17.58189	14.41588
H	17.92006	16.21535	15.44882
C	19.98837	16.04033	14.74330

H	20.01633	14.93375	14.86417
H	20.55506	16.27696	13.81563
C	20.63753	16.71351	15.93813
C	21.34792	17.92530	15.79306
H	21.46201	18.36519	14.78692
C	21.91524	18.57136	16.90437
H	22.47020	19.51476	16.76582
C	21.78032	18.01543	18.18846
H	22.22678	18.51934	19.06223
C	21.07645	16.80895	18.34975
H	20.96987	16.35895	19.35113
C	20.51154	16.16724	17.23462
H	19.96753	15.21651	17.37107
C	17.10180	11.24222	16.17009
H	16.25340	11.90018	16.44960
H	16.88859	10.22234	16.56059
C	18.41676	11.78046	16.76572
H	19.26663	11.17658	16.37897
H	18.56596	12.82029	16.39001
C	18.42235	11.76511	18.28376
C	19.26058	10.88295	18.99977
H	19.93452	10.20990	18.44208
C	19.25016	10.85215	20.40544
H	19.91567	10.15593	20.94338
C	18.39412	11.70496	21.12303
H	18.38281	11.68214	22.22579
C	17.55206	12.58835	20.42301
H	16.87818	13.26434	20.97617
C	17.56609	12.61827	19.01824
H	16.89820	13.31411	18.47899
C	8.03126	17.61905	10.10316
H	8.06188	18.00432	9.06127
H	7.76949	16.54003	10.07069
C	6.99277	18.38789	10.94146
H	7.29927	19.45449	11.01850
H	6.99870	17.97305	11.97548
C	5.59968	18.28740	10.34776
C	5.03165	19.36117	9.62899
H	5.60283	20.30007	9.52311
C	3.75249	19.25498	9.05567
H	3.32692	20.10988	8.50290
C	3.01660	18.06547	9.19021
H	2.01091	17.98077	8.74497
C	3.57046	16.98569	9.90149
H	2.99932	16.04922	10.01836
C	4.84888	17.09610	10.47296
H	5.27515	16.24227	11.02748
C	11.31438	14.35566	6.63325
H	11.71367	13.35210	6.36519
H	10.31670	14.19721	7.08820
C	11.20457	15.22815	5.36729
H	12.22255	15.37931	4.94335
H	10.62984	14.63443	4.61823
C	10.52293	16.56833	5.56487
C	11.26751	17.76316	5.65735
H	12.36593	17.71894	5.57048
C	10.63108	19.00055	5.85475
H	11.23385	19.92176	5.92484

C	9.23191	19.06526	5.96424
H	8.73034	20.03538	6.11901
C	8.47601	17.88287	5.87236
H	7.37649	17.92157	5.94967
C	9.11672	16.64834	5.67334
H	8.51057	15.72948	5.58967
C	9.94814	16.98761	16.17241
H	10.11804	16.51986	17.16622
H	10.92795	17.32597	15.77738
C	8.96176	18.16667	16.28753
H	8.80218	18.60018	15.27525
H	7.97853	17.76943	16.62575
C	9.43658	19.24635	17.24243
C	9.33527	19.06890	18.64105
H	8.89386	18.13750	19.03648
C	9.77912	20.06059	19.53104
H	9.68622	19.90219	20.61890
C	10.33291	21.25615	19.03820
H	10.67403	22.03901	19.73640
C	10.44478	21.44521	17.64997
H	10.87617	22.37882	17.25079
C	10.00340	20.44719	16.76384
H	10.09217	20.60380	15.67487
C	14.89720	16.37719	16.83672
H	15.79372	16.69860	16.26296
H	14.01580	16.84675	16.35474
C	15.01899	16.80464	18.31240
H	14.08953	16.50653	18.84845
H	15.85658	16.23981	18.77875
C	15.25811	18.29607	18.46289
C	16.57128	18.81469	18.50194
H	17.42963	18.12229	18.45333
C	16.80118	20.19694	18.60730
H	17.83615	20.57729	18.64242
C	15.71634	21.08924	18.67363
H	15.89429	22.17471	18.75802
C	14.40388	20.58716	18.63370
H	13.54157	21.27233	18.68571
C	14.17906	19.20418	18.52901
H	13.14364	18.82391	18.50292
C	10.56675	12.63813	19.72621
H	10.99436	11.67920	19.36540
H	11.30293	13.10579	20.41571
C	9.23414	12.38710	20.45967
H	8.79949	13.36631	20.75974
H	8.51718	11.92052	19.74688
C	9.41729	11.50161	21.67812
C	9.39886	10.09404	21.56120
H	9.20653	9.63414	20.57641
C	9.61154	9.27162	22.68041
H	9.58760	8.17510	22.56411
C	9.84809	9.84377	23.94253
H	10.01294	9.19962	24.82250
C	9.86865	11.24296	24.07515
H	10.04868	11.70262	25.06183
C	9.65563	12.06087	22.95269
H	9.66841	13.15915	23.06611
C	8.47025	9.31690	15.64728

H	7.94225	8.62513	14.95537
H	9.55731	9.10550	15.57306
C	7.97775	9.11220	17.09254
H	8.55515	9.79709	17.75635
H	6.91114	9.42043	17.16166
C	8.13494	7.67610	17.55615
C	7.01793	6.82172	17.67961
H	6.01129	7.21890	17.46265
C	7.16814	5.48153	18.07689
H	6.27919	4.83495	18.17110
C	8.44634	4.96708	18.35442
H	8.56723	3.91576	18.66536
C	9.56928	5.80575	18.23483
H	10.57735	5.41383	18.45165
C	9.41487	7.14585	17.84085
H	10.30346	7.79682	17.75579
S	11.41630	7.40042	12.36099
S	7.10381	9.33012	11.85857
S	7.77971	13.86593	10.59246
S	15.27482	7.15086	14.25414
S	12.57089	9.91522	17.03404
S	15.69643	9.24303	10.00875
S	10.26571	10.32905	8.29176
S	14.69245	11.14001	6.75703
S	16.76099	14.02794	9.92309
C	11.20779	6.43162	13.93385
H	10.52373	6.97895	14.61388
H	12.21460	6.41668	14.40453
C	10.72387	4.98867	13.68882
H	11.43256	4.48641	12.99368
H	10.80382	4.45825	14.66674
C	9.30602	4.85697	13.16600
C	8.20239	5.02146	14.03243
H	8.37356	5.23465	15.10213
C	6.88707	4.91352	13.55242
H	6.04134	5.04566	14.24787
C	6.64958	4.63468	12.19451
H	5.61663	4.54332	11.81812
C	7.73818	4.46992	11.32108
H	7.56830	4.25569	10.25262
C	9.05304	4.58206	11.80542
H	9.90113	4.45447	11.11172
C	6.36942	8.51997	10.35557
H	6.39862	7.42811	10.55889
H	7.01002	8.72568	9.47376
C	4.92643	9.00131	10.11460
H	4.93906	10.10330	9.95429
H	4.32546	8.81545	11.03207
C	4.29337	8.30692	8.92309
C	3.54574	7.12018	9.08538
H	3.39051	6.71546	10.10070
C	2.99275	6.45494	7.97818
H	2.40788	5.53186	8.12944
C	3.17987	6.96620	6.68217
H	2.74469	6.44712	5.81168
C	3.92117	8.14760	6.50422
H	4.06858	8.56242	5.49296
C	4.47172	8.80893	7.61499

H	5.04557	9.74000	7.46576
C	7.93295	13.75419	8.74800
H	8.77289	13.07249	8.50213
H	8.20277	14.77680	8.40229
C	6.62548	13.28226	8.08520
H	5.78880	13.93233	8.42200
H	6.40403	12.25490	8.45795
C	6.70181	13.28288	6.56894
C	5.94717	14.19754	5.80272
H	5.28301	14.91224	6.31873
C	6.02755	14.20812	4.39902
H	5.42722	14.93110	3.82137
C	6.87116	13.30171	3.73458
H	6.93760	13.30858	2.63362
C	7.63074	12.38585	4.48513
H	8.29525	11.66903	3.97379
C	7.54701	12.37644	5.88758
H	8.15002	11.65313	6.46504
C	16.97777	7.35369	14.96871
H	16.91053	7.00623	16.02181
H	17.22783	8.43565	14.95914
C	18.01903	6.54647	14.17368
H	17.71796	5.47590	14.14592
H	18.01685	6.91291	13.12139
C	19.41011	6.68222	14.76553
C	19.99785	5.63194	15.50239
H	19.44147	4.68706	15.63151
C	21.27923	5.76874	16.06429
H	21.72081	4.93220	16.63226
C	21.99642	6.96557	15.89910
H	23.00385	7.07437	16.33503
C	21.42194	8.02215	15.16939
H	21.97862	8.96409	15.02908
C	20.14149	7.88187	14.60955
H	19.69859	8.71770	14.04063
C	13.73656	10.62034	18.30048
H	13.29792	11.60126	18.58815
H	14.71339	10.82410	17.81998
C	13.89567	9.73336	19.55024
H	12.88931	9.52462	19.97691
H	14.44094	10.34790	20.30422
C	14.64930	8.43480	19.33621
C	13.96814	7.20620	19.20344
H	12.86707	7.19255	19.26530
C	14.67115	6.00642	18.99894
H	14.11743	5.05778	18.89712
C	16.07414	6.01478	18.92449
H	16.62852	5.07426	18.76738
C	16.76665	7.23180	19.05643
H	17.86809	7.25097	19.00585
C	16.05999	8.42870	19.26063
H	16.61746	9.37465	19.37480
C	15.01929	7.94504	8.86647
H	14.85146	8.46500	7.89858
H	14.04025	7.58849	9.24505
C	16.02133	6.78597	8.70377
H	16.18291	6.31000	9.69655
H	17.00089	7.20857	8.38618

C	15.55948	5.74495	7.70043
C	15.63976	5.99480	6.31164
H	16.05453	6.95500	5.95865
C	15.20655	5.03949	5.37786
H	15.28152	5.25484	4.29847
C	14.68533	3.80861	5.81565
H	14.34995	3.05560	5.08297
C	14.59705	3.54661	7.19360
H	14.19517	2.58292	7.54990
C	15.02690	4.50861	8.12448
H	14.95614	4.29525	9.20497
C	10.15971	8.47588	8.23607
H	9.27121	8.21473	8.85147
H	11.04724	8.04163	8.73912
C	10.01121	7.95346	6.79454
H	10.93933	8.19745	6.22993
H	9.17776	8.49863	6.29868
C	9.74520	6.45950	6.75215
C	8.42335	5.96372	6.71799
H	7.57842	6.67352	6.69044
C	8.16789	4.58201	6.71246
H	7.12666	4.21932	6.67840
C	9.23557	3.66763	6.74388
H	9.03802	2.58233	6.73785
C	10.55659	4.14735	6.77946
H	11.40511	3.44355	6.80052
C	10.80746	5.52971	6.78324
C	14.52035	12.16422	5.21626
H	14.00815	13.11542	5.46957
H	13.86697	11.58524	4.52899
C	15.89464	12.42998	4.57448
H	16.39949	11.45690	4.38382
H	16.52650	12.98562	5.30339
C	15.76813	13.21652	3.28272
C	15.73136	14.62824	3.29614
H	15.83398	15.16348	4.25583
C	15.57676	15.35861	2.10595
H	15.55597	16.46069	2.14050
C	15.45408	14.68810	0.87658
H	15.33457	15.26039	-0.05860
C	15.48901	13.28323	0.84752
H	15.39854	12.74699	-0.11239
C	15.64402	12.55728	2.04040
H	15.67616	11.45411	2.00875
C	16.40308	15.74969	9.33244
H	16.84342	16.41608	10.10568
H	15.30447	15.90741	9.31959
C	17.01490	16.03140	7.94839
H	16.53215	15.34874	7.21108
H	18.09690	15.77516	7.96713
C	16.82964	17.47686	7.52487
C	17.91694	18.37661	7.50423
H	18.92218	18.01219	7.77804
C	17.73860	19.72240	7.13855
H	18.60434	20.40608	7.12572
C	16.46164	20.19494	6.79025
H	16.31833	21.25059	6.50437
C	15.36816	19.31016	6.80907

H	14.36100	19.67034	6.53955
C	15.55051	17.96506	7.17137
H	14.68466	17.27872	7.18126
H	11.84972	5.89115	6.80474

Ag$_{12}$Au$_{13}$PET$_{18}$_VII
349

Au	12.64198	15.26386	12.14164
Au	15.64980	16.52734	13.00122
Au	17.41357	13.42929	13.79401
Au	14.79076	11.09341	13.59015
Au	11.09327	14.04029	14.42152
Au	9.58288	16.64663	12.85414
Au	11.05285	16.30173	9.47759
Au	12.67111	13.31640	9.83861
Au	14.07160	13.90741	14.39945
Au	12.50559	14.08535	17.44282
Au	9.38598	12.31188	16.64626
Au	10.02408	11.40878	13.39002
Au	12.48209	9.62624	12.86000
Ag	9.44182	8.60280	12.05282
Ag	7.75963	11.56978	11.39977
Ag	10.18809	13.82911	11.51636
Ag	13.94231	10.89960	10.61152
Ag	15.32171	8.46190	12.18354
Ag	13.95185	8.71405	15.43354
Ag	12.33841	11.57524	15.26571
Ag	10.87126	11.03294	10.68719
Ag	12.48580	10.98227	7.82040
Ag	15.50194	12.47704	8.56149
Ag	15.04179	13.52495	11.70960
Ag	12.50760	12.45038	12.52521
S	13.52479	17.54335	12.68198
S	17.86336	15.67397	13.14426
S	17.17365	11.14645	14.41097
S	9.72737	17.79617	10.77638
S	12.42270	15.03490	7.99416
S	9.31338	15.69443	15.01159
S	14.73160	14.54156	16.74169
S	10.29522	13.80579	18.27187
S	8.23900	10.90205	15.11910
C	13.72382	18.53475	11.12230
H	14.41248	18.00288	10.43441
H	12.71661	18.54666	10.65254
C	14.19301	19.97960	11.38499
H	13.48274	20.46383	12.09120
H	14.10090	20.52280	10.41517
C	15.61256	20.12109	11.90044
C	16.71207	19.98527	11.02387
H	16.53615	19.78579	9.95228
C	18.02926	20.10418	11.49614
H	18.87155	19.99467	10.79264
C	18.27273	20.36541	12.85650
H	19.30702	20.46592	13.22689
C	17.18836	20.50085	13.74024
H	17.36328	20.70029	14.81076
C	15.87168	20.37781	13.26349
H	15.02686	20.48233	13.96504
C	18.61625	16.48877	14.63550
H	18.58305	17.58013	14.43009
H	17.98775	16.28518	15.52636
C	20.06265	16.00855	14.85774

H	20.05339	14.90649	15.01727
H	20.65159	16.19588	13.93277
C	20.71026	16.70227	16.04181
C	21.44187	17.89811	15.87326
H	21.57386	18.31083	14.85788
C	22.00799	18.56247	16.97429
H	22.57985	19.49286	16.81824
C	21.85050	18.04114	18.27025
H	22.29616	18.55951	19.13584
C	21.12569	16.85051	18.45434
H	21.00196	16.42776	19.46552
C	20.56175	16.19014	17.34968
H	20.00108	15.25174	17.50320
C	17.02727	11.23489	16.25723
H	16.18778	11.91248	16.51569
H	16.76097	10.20685	16.58912
C	18.33797	11.69990	16.91819
H	19.17548	11.06282	16.55912
H	18.54996	12.73669	16.56653
C	18.27711	11.66465	18.43486
C	19.05709	10.74798	19.17282
H	19.72843	10.05700	18.63436
C	18.99303	10.70650	20.57677
H	19.61293	9.98276	21.13237
C	18.14044	11.58271	21.26968
H	18.08692	11.55146	22.37095
C	17.35519	12.49961	20.54728
H	16.68316	13.19258	21.08116
C	17.42275	12.54023	19.14455
H	16.79964	13.26324	18.58842
C	8.02492	17.60511	10.05836
H	8.09554	17.95883	9.00756
H	7.77112	16.52378	10.06157
C	6.98536	18.41149	10.85642
H	7.29167	19.48028	10.89398
H	6.98173	18.03641	11.90562
C	5.59581	18.28775	10.25817
C	5.01404	19.34909	9.53251
H	5.57374	20.29381	9.41726
C	3.73452	19.22316	8.96377
H	3.29764	20.06815	8.40474
C	3.01325	18.02640	9.11074
H	2.00748	17.92601	8.66903
C	3.58161	16.95906	9.82950
H	3.02174	16.01703	9.95566
C	4.86011	17.08851	10.39636
H	5.29846	16.24410	10.95607
C	11.25483	14.34743	6.72016
H	11.68305	13.36254	6.43019
H	10.27389	14.15283	7.19595
C	11.10944	15.23977	5.47244
H	12.11865	15.43089	5.04429
H	10.55137	14.63710	4.71820
C	10.38129	16.55198	5.69088
C	11.08602	17.76829	5.81286
H	12.18636	17.76148	5.73876
C	10.40735	18.98116	6.02207
H	10.97930	19.91984	6.11499

C	9.00541	18.99860	6.11233
H	8.47014	19.94943	6.27372
C	8.28937	17.79410	5.99105
H	7.18833	17.79562	6.05344
C	8.97183	16.58404	5.78171
H	8.39621	15.64807	5.67547
C	9.99663	16.99897	16.14320
H	10.16237	16.48576	17.11510
H	10.97730	17.34763	15.76129
C	9.00116	18.16488	16.29794
H	8.84198	18.63415	15.30160
H	8.01936	17.75038	16.61909
C	9.46940	19.21094	17.29298
C	9.37950	18.97627	18.68382
H	8.95170	18.02466	19.04447
C	9.81818	19.93652	19.60999
H	9.73516	19.73333	20.69115
C	10.35533	21.15695	19.16218
H	10.69436	21.91415	19.88889
C	10.45409	21.40347	17.78207
H	10.86957	22.35841	17.41795
C	10.01855	20.43659	16.85903
H	10.09694	20.63809	15.77676
C	14.86800	16.39137	16.82515
H	15.76533	16.64653	16.22026
H	13.99190	16.84710	16.32119
C	15.01395	16.89419	18.27401
H	14.08138	16.64954	18.83096
H	15.84117	16.33680	18.76671
C	15.28946	18.38573	18.33664
C	16.61431	18.87328	18.37396
H	17.45536	18.15850	18.38881
C	16.87795	20.25326	18.39819
H	17.92146	20.60910	18.43375
C	15.81558	21.17422	18.38293
H	16.01952	22.25816	18.40388
C	14.49161	20.70287	18.34413
H	13.64710	21.41176	18.33508
C	14.23271	19.32219	18.32137
H	13.18836	18.96704	18.29699
C	10.45682	12.79209	19.82117
H	10.96748	11.83751	19.57807
H	11.10933	13.37404	20.50674
C	9.07923	12.53548	20.45949
H	8.57712	13.51154	20.64188
H	8.44800	11.97719	19.73210
C	9.19896	11.75703	21.75682
C	9.23363	10.34522	21.75228
H	9.13400	9.80436	20.79543
C	9.38318	9.62201	22.94743
H	9.40280	8.51971	22.91981
C	9.50265	10.29998	24.17304
H	9.61825	9.73330	25.11214
C	9.46949	11.70504	24.19332
H	9.55760	12.24707	25.15018
C	9.31966	12.42380	22.99544
H	9.28921	13.52720	23.02007
C	8.63346	9.18520	15.69855

H	8.19692	8.51333	14.92738
H	9.73498	9.04861	15.69915
C	8.04184	8.88574	17.08781
H	8.53261	9.56302	17.82495
H	6.95893	9.13864	17.08697
C	8.23554	7.43683	17.49604
C	7.14179	6.54770	17.57052
H	6.12772	6.92285	17.34880
C	7.32446	5.19951	17.92503
H	6.45347	4.52470	17.98058
C	8.61247	4.71288	18.20619
H	8.75931	3.65500	18.48171
C	9.71240	5.58683	18.13382
H	10.72816	5.21619	18.35199
C	9.52600	6.93500	17.78446
H	10.39708	7.61337	17.73694
S	11.55380	7.40650	12.24081
S	7.12264	9.29650	11.97425
S	7.80086	13.88945	10.67410
S	15.31931	7.11113	14.21004
S	12.52305	9.82861	17.06630
S	15.76776	9.30964	9.94119
S	10.18712	10.39312	8.35977
S	14.63790	11.14239	6.70740
S	16.84578	13.90136	9.99629
C	11.38678	6.40091	13.79623
H	10.71104	6.92257	14.50468
H	12.39914	6.36508	14.25314
C	10.89828	4.96525	13.51741
H	11.60372	4.48030	12.80682
H	10.98015	4.40949	14.48076
C	9.47901	4.85211	12.99489
C	8.37800	4.97490	13.87153
H	8.55294	5.14026	14.94912
C	7.06091	4.88383	13.39209
H	6.21738	4.98267	14.09558
C	6.81928	4.66308	12.02440
H	5.78529	4.58523	11.64800
C	7.90515	4.54043	11.14043
H	7.73155	4.37222	10.06439
C	9.22152	4.63615	11.62417
H	10.06751	4.54058	10.92285
C	6.41727	8.54024	10.43197
H	6.45647	7.43862	10.57178
H	7.05687	8.79748	9.56244
C	4.96754	9.00671	10.19251
H	4.96336	10.11398	10.07466
H	4.36214	8.77707	11.09717
C	4.35325	8.34851	8.97116
C	3.59770	7.16121	9.08619
H	3.42165	6.73001	10.08718
C	3.06308	6.52853	7.95113
H	2.47173	5.60425	8.06624
C	3.27673	7.07380	6.67324
H	2.85616	6.58046	5.78078
C	4.02651	8.25605	6.54182
H	4.19546	8.69767	5.54539
C	4.55828	8.88443	7.68041

H	5.13903	9.81617	7.56652
C	7.90103	13.72741	8.83041
H	8.74621	13.05865	8.56699
H	8.13046	14.74188	8.43467
C	6.58838	13.19901	8.22095
H	5.74089	13.81854	8.58752
H	6.41977	12.16592	8.60664
C	6.60574	13.19600	6.70288
C	5.79345	14.08345	5.96382
H	5.12294	14.77452	6.50337
C	5.82445	14.09650	4.55814
H	5.17899	14.79739	4.00216
C	6.67544	13.21979	3.86366
H	6.70266	13.22820	2.76097
C	7.49210	12.33117	4.58675
H	8.16211	11.63690	4.05184
C	7.45794	12.31940	5.99146
H	8.10630	11.61901	6.54838
C	17.02423	7.34862	14.90093
H	17.00211	6.96635	15.94417
H	17.25328	8.43503	14.93146
C	18.08883	6.60904	14.06878
H	17.81606	5.53296	13.99653
H	18.07246	7.01849	13.03281
C	19.47629	6.75651	14.66535
C	20.06867	5.71142	15.40648
H	19.52144	4.76007	15.52722
C	21.34170	5.86146	15.98348
H	21.78658	5.02835	16.55402
C	22.04710	7.06699	15.82988
H	23.04810	7.18630	16.27779
C	21.46886	8.11851	15.09607
H	22.01636	9.06709	14.96406
C	20.19654	7.96429	14.52119
H	19.75118	8.79611	13.94858
C	13.65516	10.52695	18.36367
H	13.23480	11.51839	18.64381
H	14.65477	10.71161	17.92306
C	13.76680	9.63702	19.61725
H	12.74651	9.45575	20.02342
H	14.31667	10.23182	20.38404
C	14.48276	8.31639	19.41005
C	13.76890	7.10487	19.29594
H	12.66887	7.12094	19.37206
C	14.43767	5.88578	19.09131
H	13.85847	4.95093	19.00423
C	15.83905	5.85663	18.99606
H	16.36594	4.90102	18.83550
C	16.56452	7.05608	19.10949
H	17.66534	7.04573	19.04308
C	15.89163	8.27210	19.31567
H	16.47441	9.20432	19.41594
C	15.09362	7.97905	8.83434
H	14.93206	8.45089	7.84103
H	14.11118	7.63180	9.21471
C	16.08801	6.80630	8.72344
H	16.24402	6.37187	9.73594
H	17.07086	7.21032	8.39207

C	15.62481	5.72568	7.76396
C	15.72253	5.91065	6.36607
H	16.15345	6.84854	5.97447
C	15.28748	4.91886	5.47193
H	15.37660	5.08379	4.38473
C	14.74648	3.71542	5.95955
H	14.41127	2.93301	5.25805
C	14.63935	3.51818	7.34699
H	14.21948	2.57764	7.74231
C	15.07154	4.51650	8.23751
H	14.98621	4.35351	9.32584
C	10.10909	8.54167	8.22212
H	9.21413	8.22348	8.80023
H	10.99365	8.09061	8.71592
C	9.99552	8.07948	6.75636
H	10.92430	8.37195	6.21595
H	9.15482	8.62590	6.27427
C	9.76891	6.58281	6.64403
C	8.46015	6.05371	6.59901
H	7.59658	6.74118	6.61158
C	8.24156	4.66717	6.53376
H	7.21000	4.27813	6.49298
C	9.33336	3.78118	6.51452
H	9.16414	2.69230	6.46202
C	10.64157	4.29383	6.56008
H	11.50918	3.61367	6.54313
C	10.85521	5.68099	6.62419
C	14.41443	12.30711	5.27986
H	13.98385	13.26409	5.64224
H	13.68235	11.84095	4.58501
C	15.75087	12.56176	4.55464
H	16.18939	11.58351	4.25694
H	16.46242	13.02946	5.27207
C	15.57398	13.44683	3.33498
C	15.59379	14.85446	3.45075
H	15.78179	15.31491	4.43611
C	15.38820	15.67610	2.32960
H	15.41319	16.77270	2.44490
C	15.15742	15.10310	1.06683
H	14.99827	15.74664	0.18537
C	15.13533	13.70380	0.93543
H	14.95984	13.24345	-0.05174
C	15.34130	12.88668	2.05975
H	15.32756	11.78832	1.94729
C	16.49780	15.61534	9.37877
H	17.02220	16.30295	10.07744
H	15.40986	15.82277	9.45247
C	16.99345	15.83347	7.93655
H	16.41655	15.15603	7.26477
H	18.05987	15.52471	7.86678
C	16.83959	17.27449	7.48721
C	17.95866	18.12756	7.37405
H	18.96407	17.72598	7.58856
C	17.81210	19.47199	6.98992
H	18.70270	20.11735	6.90313
C	16.53541	19.99214	6.71596
H	16.41729	21.04678	6.41537
C	15.41039	19.15494	6.82614

H	14.40344	19.55138	6.61235
C	15.56116	17.81056	7.20671
H	14.67093	17.16091	7.28485
H	11.88749	6.06949	6.65473

Ag$_{13}$Au$_{12}$DMBT$_{18}$_I
349

Ag	14.64468	17.63002	14.54625
Au	17.70070	19.07714	15.20382
Au	19.82240	16.19061	16.04418
Ag	17.37079	13.94795	16.24338
Ag	13.33908	16.46652	16.98509
Au	11.55714	18.84425	15.21899
Au	13.29878	18.64676	12.08123
Ag	14.82053	15.34125	12.38565
Ag	16.36715	16.72387	16.76451
Au	14.70898	16.87891	19.74989
Au	11.54867	15.00828	19.26451
Ag	12.58784	13.58364	16.30844
Ag	15.14365	12.13656	15.95327
Au	12.32252	10.54664	15.03853
Au	10.12598	13.42785	14.27858
Ag	12.44637	15.84638	14.13616
Ag	16.40781	13.21925	13.43655
Au	18.04864	10.85527	15.23914
Au	16.41444	11.25235	18.52247
Ag	14.99815	14.33118	17.99593
Ag	13.39809	13.01817	13.58307
Au	14.99375	12.82867	10.49605
Au	18.10229	14.60014	11.13332
Ag	17.20653	16.10600	14.08422
Ag	14.88591	14.86358	15.19682
S	15.52238	20.02198	15.06788
S	20.00079	18.45098	15.26592
S	19.89870	13.89424	16.66384
S	11.94573	20.20216	13.29820
S	14.80558	17.36748	10.77131
S	11.04186	17.64033	17.18733
S	16.96075	17.42839	19.15652
S	12.53224	16.61748	20.71930
S	10.35348	13.77785	17.63240
S	14.57771	9.78563	14.99816
S	10.00913	11.12673	14.93320
S	9.89808	15.76662	13.87729
S	17.76217	9.69566	17.30235
S	14.99692	12.53667	19.93668
S	18.44120	11.70489	13.06044
S	12.75412	12.36008	11.15634
S	17.22105	12.94949	9.64728
S	19.26887	16.12163	12.52481
C	19.35720	9.61686	18.14524
C	20.51649	10.18311	17.57809
C	19.44571	8.88247	19.35907
C	21.76264	10.02698	18.19743
C	20.71665	8.75112	19.95695
C	18.23033	8.26800	20.01057
C	21.88581	9.30826	19.40460
C	23.22709	9.16316	20.08970
C	14.71043	8.16144	15.76871
C	15.42772	7.20634	15.01421
C	14.18102	7.80315	17.03797
C	15.62704	5.90723	15.49885

C	14.39035	6.48178	17.48776
C	13.42986	8.78247	17.89747
C	15.10772	5.51869	16.75064
C	15.34163	4.12857	17.30173
C	18.12533	10.27533	12.00101
C	16.81816	9.81768	11.74253
C	19.23440	9.63030	11.38878
C	16.59396	8.73407	10.88189
C	18.97391	8.54333	10.52820
C	20.65563	10.07520	11.64665
C	17.67243	8.07936	10.25204
C	17.43878	6.93680	9.28713
C	12.57625	10.64683	10.60485
C	12.19561	10.38859	9.25881
C	12.76034	9.57018	11.49440
C	12.01236	9.04489	8.86804
C	12.00672	11.50067	8.25530
C	12.56966	8.24729	11.07430
C	12.18955	7.95884	9.74708
C	11.98415	6.53087	9.28889
C	9.34928	10.16840	13.55208
C	8.97957	8.81682	13.78722
C	9.12330	10.75253	12.28961
C	8.38117	8.10537	12.72635
C	9.22069	8.14654	15.11862
C	8.52378	10.01630	11.26034
C	8.13998	8.67425	11.46080
C	7.51133	7.87078	10.34325
C	9.24095	15.96455	12.21284
C	7.93543	15.49521	11.89067
C	9.96434	16.71154	11.26074
C	7.43515	15.76797	10.60002
C	7.08605	14.74214	12.88500
C	9.43063	16.97851	9.99313
C	8.15509	16.49778	9.63357
C	7.58769	16.74454	8.25231
C	10.38451	20.39566	12.41110
C	10.37818	21.14953	11.20626
C	9.17549	19.89999	12.93984
C	9.13425	21.37289	10.57851
C	11.64798	21.69141	10.59537
C	7.95917	20.14619	12.29140
C	7.91608	20.89031	11.09411
C	6.60401	21.14675	10.38524
C	10.66428	18.83826	18.48082
C	9.41625	18.65878	19.11685
C	11.52735	19.88394	18.90504
C	9.01009	19.50187	20.15899
C	11.08068	20.72107	19.95001
C	12.88350	20.10180	18.29390
C	9.83618	20.55966	20.59047
C	9.38947	21.50953	21.68117
C	17.02271	19.17622	19.60763
C	16.53213	20.17950	18.74775
C	17.61423	19.54107	20.84945
C	16.61186	21.53318	19.10196
C	17.67171	20.91245	21.17790
C	18.17115	18.50841	21.80048

C	17.18015	21.92676	20.33152
C	17.23601	23.38437	20.73553
C	20.81595	19.37769	16.59017
C	20.08628	20.10725	17.54823
C	22.23659	19.39730	16.61632
C	20.74464	20.84988	18.53683
C	22.86693	20.15124	17.62885
C	23.06579	18.64757	15.60080
C	22.15327	20.88224	18.59797
C	22.86755	21.66659	19.67749
C	20.40288	13.88415	18.39343
C	19.50715	13.45798	19.39503
C	21.74659	14.19872	18.73991
C	19.91875	13.34619	20.72982
C	22.12375	14.09073	20.09496
C	22.75385	14.63942	17.70660
C	21.23829	13.67098	21.10663
C	21.67944	13.58319	22.55188
C	15.72899	12.21397	21.56159
C	15.57654	10.90713	22.07902
C	16.37289	13.20512	22.34831
C	16.05970	10.56851	23.34953
C	16.84622	12.83030	23.62583
C	16.55741	14.61681	21.86159
C	16.70724	11.53126	24.15192
C	17.20521	11.19031	25.54015
C	12.83374	15.91636	22.35325
C	13.20886	16.80041	23.40154
C	12.63991	14.54634	22.62105
C	13.37343	16.25590	24.69243
C	13.43586	18.27288	23.15616
C	12.80998	14.04120	23.91598
C	13.18124	14.89040	24.97947
C	13.38119	14.34276	26.37578
C	15.63280	21.23999	13.74213
C	14.95037	22.47594	13.90561
C	16.38258	21.00354	12.57061
C	15.05304	23.43005	12.86995
C	14.14237	22.78620	15.14309
C	16.47060	21.97783	11.56915
C	15.80289	23.21410	11.69859
C	15.89947	24.26818	10.61682
C	19.59261	17.52614	11.43520
C	20.94594	17.93122	11.25851
C	18.56464	18.19713	10.74631
C	21.20480	19.01744	10.39867
C	22.08519	17.21168	11.94141
C	18.86275	19.26382	9.88458
C	20.18917	19.70079	9.69919
C	20.52443	20.86239	8.78817
C	17.22625	13.68107	7.99572
C	18.47456	13.83267	7.32958
C	16.03132	14.00555	7.32547
C	18.45946	14.32236	6.00730
C	19.78294	13.48923	7.99921
C	16.05390	14.48701	6.00951
C	17.27383	14.66067	5.32533
C	17.31198	15.21994	3.91952

C	14.18603	17.64603	9.09291
C	14.65048	18.81034	8.44129
C	13.29836	16.76947	8.41710
C	14.24647	19.11896	7.13654
C	12.91565	17.10806	7.09918
C	12.76427	15.51979	9.06076
C	13.36666	18.26594	6.43712
C	12.93838	18.58058	5.01981
C	9.48564	12.38660	18.37575
C	8.11051	12.30300	18.06480
C	10.08162	11.39233	19.19686
C	7.32218	11.25391	18.55536
C	9.25663	10.35504	19.68120
C	11.54117	11.43016	19.54941
C	7.88289	10.25897	19.38246
C	7.03525	9.14510	19.95869
H	20.43169	10.75642	16.63997
H	22.65428	10.48126	17.73243
H	20.78997	8.18043	20.90014
H	17.65017	7.64704	19.29205
H	17.53119	9.05624	20.37816
H	18.51859	7.63484	20.87685
H	24.01862	8.84068	19.37650
H	23.18747	8.42007	20.91553
H	23.56192	10.13224	20.52668
H	15.83232	7.49807	14.03129
H	16.19384	5.18346	14.88757
H	13.97155	6.19717	18.46999
H	14.07341	9.65589	18.15857
H	13.08344	8.30988	18.84079
H	12.54303	9.20067	17.36555
H	15.43589	3.37659	16.48768
H	14.51431	3.80772	17.97207
H	16.28294	4.08091	17.89860
H	15.96404	10.31214	12.23181
H	15.55742	8.40349	10.69830
H	19.83431	8.03615	10.05514
H	20.90568	10.02359	12.73028
H	20.81299	11.13451	11.34390
H	21.37811	9.44045	11.08930
H	16.55229	6.33142	9.57757
H	18.31793	6.25766	9.23344
H	17.24958	7.31207	8.25380
H	13.06185	9.77290	12.53485
H	11.71662	8.84255	7.82260
H	11.28675	12.26492	8.62272
H	11.64338	11.10468	7.28263
H	12.96551	12.04031	8.07439
H	12.71895	7.42914	11.79978
H	11.62555	6.48594	8.23789
H	11.23901	6.00233	9.92587
H	12.92914	5.94318	9.34651
H	9.42860	11.79845	12.11932
H	8.08723	7.05530	12.90559
H	8.77630	8.72804	15.95702
H	10.31169	8.06997	15.33824
H	8.79517	7.12044	15.13304
H	8.35795	10.49753	10.28138

H	7.10314	6.90508	10.71227
H	8.25533	7.63847	9.54653
H	6.68048	8.42863	9.85552
H	10.96074	17.10364	11.53068
H	6.42481	15.39914	10.34555
H	7.55112	13.76723	13.16645
H	6.07388	14.53867	12.47404
H	6.97958	15.30982	13.83642
H	10.02296	17.57028	9.27475
H	6.48513	16.60138	8.22982
H	8.02545	16.04561	7.50113
H	7.80818	17.77625	7.89921
H	9.19767	19.31211	13.87246
H	9.12382	21.95766	9.64112
H	12.24013	22.28153	11.32990
H	11.42545	22.33622	9.71844
H	12.31720	20.86573	10.25536
H	7.02815	19.74282	12.72495
H	6.72457	21.86839	9.54858
H	5.83667	21.55593	11.08061
H	6.18406	20.20607	9.96016
H	8.76248	17.83728	18.78141
H	8.03224	19.33358	20.64307
H	11.74919	21.53642	20.28065
H	12.81956	20.26847	17.19330
H	13.53004	19.20230	18.42833
H	13.40137	20.96747	18.75674
H	8.75584	20.99579	22.43755
H	8.78434	22.35016	21.26603
H	10.25602	21.96225	22.21067
H	16.08502	19.89894	17.78141
H	16.22383	22.29291	18.40192
H	18.12684	21.19799	22.14357
H	17.38085	17.79837	22.13344
H	18.60996	18.99125	22.70025
H	18.95705	17.88908	21.31388
H	17.51040	24.03686	19.87697
H	17.97493	23.55744	21.54778
H	16.24676	23.74048	21.10782
H	18.98503	20.09018	17.52079
H	20.14086	21.40507	19.27447
H	23.97135	20.16597	17.65364
H	22.85154	18.99410	14.56515
H	22.84225	17.55643	15.61732
H	24.15157	18.78136	15.79583
H	22.50225	22.71720	19.72886
H	23.96491	21.69592	19.50456
H	22.69878	21.21829	20.68402
H	18.47304	13.19309	19.11546
H	19.19682	12.99676	21.48738
H	23.16514	14.34197	20.36644
H	22.82721	13.90715	16.87190
H	23.76079	14.77038	18.15803
H	22.45118	15.60541	17.23763
H	21.25730	14.41911	23.15753
H	22.78611	13.63265	22.64695
H	21.33567	12.63694	23.02608
H	15.06700	10.14872	21.46284

H	15.93181	9.53666	23.72080
H	17.35148	13.60089	24.23507
H	15.57630	15.12032	21.70026
H	17.08811	14.65302	20.88622
H	17.13368	15.22045	22.59335
H	17.56587	10.13983	25.59927
H	16.39737	11.30012	26.30202
H	18.03891	11.85692	25.85153
H	12.35663	13.87345	21.79589
H	13.66363	16.93911	25.51080
H	14.29241	18.44076	22.46159
H	13.65159	18.80825	24.10560
H	12.55264	18.74633	22.67238
H	12.65804	12.96364	24.09736
H	13.57544	15.15385	27.11000
H	14.24545	13.64005	26.41295
H	12.48886	13.77466	26.72403
H	16.91262	20.04537	12.44902
H	14.52575	24.39274	12.99624
H	13.28511	22.08424	15.25207
H	13.73553	23.81947	15.10376
H	14.75706	22.68338	16.06573
H	17.07737	21.76713	10.67181
H	15.29028	25.16438	10.86393
H	15.54511	23.88035	9.63443
H	16.95096	24.60620	10.46858
H	17.51868	17.86911	10.86684
H	22.25478	19.33514	10.26302
H	22.11793	16.13831	11.64758
H	21.96993	17.22608	13.04731
H	23.06120	17.67661	11.68258
H	18.04053	19.75598	9.33684
H	20.91889	21.73213	9.36333
H	19.63027	21.21100	8.22814
H	21.30581	20.58824	8.04340
H	15.07088	13.87671	7.84912
H	19.42706	14.43834	5.48676
H	19.78054	12.44661	8.38900
H	19.96867	14.14864	8.88001
H	20.63458	13.60273	7.29506
H	15.10145	14.73768	5.51260
H	18.23189	14.90802	3.37835
H	17.29776	16.33531	3.92738
H	16.43328	14.88869	3.32326
H	15.33307	19.48418	8.98375
H	14.62219	20.03904	6.65579
H	12.22354	16.42822	6.57062
H	13.58571	14.83568	9.37334
H	12.09492	14.96300	8.37292
H	12.19192	15.74202	9.98736
H	12.59730	19.63571	4.92010
H	12.10713	17.92176	4.68766
H	13.77914	18.44445	4.30018
H	7.66315	13.07879	17.42255
H	6.25143	11.21081	18.29012
H	9.71907	9.58209	20.32118
H	11.80726	12.37296	20.08227
H	12.18067	11.42281	18.63862

H	11.83278	10.57194	20.18987
H	6.17789	8.89796	19.29485
H	6.60945	9.42876	20.95032
H	7.62758	8.21652	20.11301

$Ag_{13}Au_{12}DMBT_{18}$_II

349

Au	14.76234	17.59661	14.64375
Ag	17.72588	18.74599	15.24811
Ag	19.35770	16.18015	16.29109
Au	17.24740	13.62997	16.40906
Au	13.35407	16.40948	17.04916
Ag	11.82508	18.63778	15.16395
Ag	13.25881	18.50779	12.30001
Au	14.92882	15.32500	12.34057
Au	16.41170	16.54599	16.90696
Ag	14.71548	16.69112	19.72681
Ag	11.84454	15.07330	19.31181
Au	12.46470	13.51241	16.27536
Au	14.94264	11.97254	15.89437
Ag	12.03223	10.72354	15.04025
Ag	10.34299	13.48559	14.21180
Au	12.51501	15.93852	14.01023
Au	16.32717	13.08841	13.43475
Ag	17.70548	10.88508	15.19497
Ag	16.64100	11.10650	18.15228
Au	14.83898	14.16819	18.08717
Au	13.31028	13.00811	13.51056
Ag	15.19134	12.84216	10.56848
Ag	17.88114	14.40977	11.31164
Au	17.26028	15.97809	14.16904
Ag	14.85560	14.77422	15.22682
S	15.58912	19.95416	14.99137
S	20.13136	18.43432	15.59968
S	19.71088	13.73905	16.59099
S	11.84408	20.23039	13.29921
S	14.89748	17.37361	10.88810
S	11.14908	17.61017	17.29291
S	17.06979	17.22560	19.21618
S	12.60918	16.69713	20.97207
S	10.42362	13.87251	17.70342
S	14.24161	9.64934	15.24554
S	9.66564	11.15637	14.62745
S	10.03345	15.90059	13.78263
S	17.97714	9.34464	17.10026
S	15.04037	12.18445	19.66632
S	18.34803	11.68828	12.93935
S	12.85418	12.32273	11.14497
S	17.34582	12.93634	9.40458
S	19.30963	15.85962	12.71196
C	19.69327	9.48358	17.61338
C	20.69093	9.88115	16.69778
C	20.07132	9.07427	18.92475
C	22.04530	9.87659	17.05814
C	21.44114	9.08476	19.25407
C	19.04775	8.64241	19.94679
C	22.44708	9.48064	18.34939
C	23.90090	9.50965	18.76704
C	14.29176	8.33421	16.47026
C	15.12024	7.24075	16.13461
C	13.54590	8.30600	17.68161

C	15.21944	6.12475	16.97618
C	13.67141	7.16637	18.50381
C	12.64382	9.43489	18.09799
C	14.49330	6.06671	18.18203
C	14.59468	4.87796	19.11350
C	17.97841	10.33273	11.81511
C	16.68611	9.78827	11.68421
C	19.04521	9.81940	11.02362
C	16.43457	8.74817	10.77723
C	18.75836	8.77025	10.12929
C	20.44403	10.38245	11.11870
C	17.46845	8.22000	9.97980
C	17.21308	7.10819	8.98482
C	12.74590	10.56666	10.75884
C	12.49838	10.18255	9.40976
C	12.85354	9.57205	11.74933
C	12.37397	8.80737	9.12227
C	12.37632	11.20256	8.30432
C	12.71849	8.21448	11.43255
C	12.47735	7.80326	10.10528
C	12.35592	6.33674	9.75119
C	9.24380	10.38871	13.05944
C	8.93564	8.99863	13.03022
C	9.11204	11.15344	11.88105
C	8.50050	8.44110	11.81117
C	9.06938	8.13300	14.26035
C	8.67795	10.56648	10.68522
C	8.36372	9.19367	10.62742
C	7.93196	8.54130	9.33234
C	9.43418	16.00683	12.09165
C	8.09998	15.59728	11.80828
C	10.22163	16.56182	11.06184
C	7.62754	15.74659	10.48702
C	7.20003	15.02197	12.87535
C	9.71825	16.70591	9.76346
C	8.40572	16.29540	9.44945
C	7.85181	16.46183	8.05070
C	10.21359	20.18882	12.54687
C	10.03666	20.69106	11.22686
C	9.08844	19.76181	13.28499
C	8.72717	20.73593	10.70535
C	11.20371	21.15791	10.39136
C	7.80190	19.81962	12.73514
C	7.59654	20.30797	11.42850
C	6.21420	20.33680	10.81361
C	10.95561	18.87777	18.55276
C	9.76251	18.79324	19.30508
C	11.88182	19.92426	18.81844
C	9.47048	19.73257	20.30275
C	11.55512	20.85090	19.83052
C	13.17667	20.05739	18.06631
C	10.36487	20.78579	20.58306
C	10.05446	21.82919	21.63542
C	17.07833	18.99110	19.57452
C	16.84630	19.96203	18.58406
C	17.36172	19.40551	20.90986
C	16.87956	21.32966	18.89109
C	17.38621	20.78662	21.18384

C	17.61930	18.40582	22.01250
C	17.14666	21.77037	20.20149
C	17.15549	23.24154	20.55773
C	20.57206	19.57940	16.91321
C	20.25916	20.94621	16.73332
C	21.32856	19.18267	18.05216
C	20.68017	21.91387	17.65328
C	21.72962	20.18334	18.96241
C	21.71381	17.74662	18.30323
C	21.42388	21.54775	18.79419
C	21.84994	22.57574	19.81947
C	20.33941	13.55742	18.26355
C	19.49733	13.28843	19.36204
C	21.74562	13.65138	18.46414
C	20.02384	13.11344	20.64828
C	22.24098	13.48430	19.77409
C	22.69117	13.91673	17.31719
C	21.41164	13.21381	20.87988
C	21.98621	13.01449	22.26580
C	15.83839	11.94619	21.27339
C	15.81780	10.61801	21.76012
C	16.41909	12.96978	22.06937
C	16.35849	10.29494	23.01184
C	16.95341	12.60812	23.32547
C	16.47976	14.40178	21.61438
C	16.93756	11.29069	23.82478
C	17.49305	10.97064	25.19573
C	12.98953	15.97833	22.57440
C	13.22217	16.86065	23.66747
C	13.01445	14.58458	22.79229
C	13.46075	16.29499	24.93796
C	13.21717	18.36063	23.48868
C	13.25637	14.05572	24.06651
C	13.48317	14.90585	25.16944
C	13.75195	14.33887	26.54672
C	15.78952	20.98493	13.53017
C	15.17510	22.26900	13.52662
C	16.57841	20.58557	12.42995
C	15.38569	23.10020	12.40525
C	14.32646	22.75488	14.67738
C	16.76501	21.43771	11.33464
C	16.16936	22.71675	11.30031
C	16.38210	23.64399	10.12257
C	19.66625	17.25981	11.63613
C	20.99133	17.78616	11.62944
C	18.70601	17.78086	10.74473
C	21.28690	18.81995	10.71753
C	22.06634	17.25453	12.54675
C	19.03970	18.80491	9.84597
C	20.34135	19.34440	9.81307
C	20.72833	20.42658	8.82769
C	17.18951	13.87929	7.88567
C	18.28228	14.64968	7.39314
C	16.02156	13.76165	7.09929
C	18.13231	15.29303	6.14660
C	19.57625	14.78266	8.15745
C	15.90697	14.41126	5.86415
C	16.96363	15.20142	5.36577

C	16.83440	15.94570	4.05468
C	14.17879	17.62979	9.24816
C	14.41714	18.90852	8.69096
C	13.43992	16.67128	8.50759
C	13.92892	19.24717	7.42300
C	12.96525	17.04694	7.23076
C	13.16505	15.29169	9.03694
C	13.19113	18.31533	6.66275
C	12.69026	18.65608	5.27566
C	9.53509	12.45436	18.36504
C	8.30390	12.16980	17.73021
C	9.93409	11.67812	19.48766
C	7.47988	11.13018	18.17533
C	9.07797	10.63767	19.91019
C	11.20235	11.95106	20.25058
C	7.85451	10.33897	19.28061
C	6.96043	9.22951	19.78992
H	20.39316	10.19551	15.68327
H	22.80209	10.18695	16.31702
H	21.73394	8.76365	20.27009
H	18.40469	7.82000	19.56113
H	18.35718	9.47906	20.20640
H	19.53815	8.29990	20.88333
H	24.57983	9.46149	17.88790
H	24.15237	8.66253	19.44298
H	24.14152	10.44905	19.31807
H	15.69449	7.27472	15.19491
H	15.88023	5.28871	16.68963
H	13.09262	7.14315	19.44455
H	13.20696	10.39050	18.18783
H	12.16225	9.22384	19.07539
H	11.82996	9.61425	17.35315
H	15.15225	4.03932	18.64392
H	13.58965	4.49810	19.40623
H	15.12567	5.14391	20.05711
H	15.86528	10.18081	12.30659
H	15.40929	8.35017	10.69365
H	19.58619	8.37075	9.51562
H	20.84755	10.31259	12.15415
H	20.45994	11.46255	10.84801
H	21.13720	9.84230	10.43823
H	16.16978	6.73273	9.05658
H	17.89863	6.24516	9.14718
H	17.37208	7.45407	7.93718
H	13.05322	9.86764	12.79161
H	12.18335	8.51160	8.07482
H	11.58419	11.95147	8.52724
H	12.14231	10.71567	7.33348
H	13.32342	11.77880	8.18365
H	12.80559	7.46640	12.23924
H	11.93745	6.19510	8.73119
H	11.69867	5.79664	10.46876
H	13.34724	5.82678	9.77673
H	9.35599	12.22925	11.90684
H	8.25510	7.36395	11.78966
H	8.47425	8.53380	15.11119
H	10.12598	8.09863	14.61509
H	8.73905	7.09196	14.05551

H	8.58445	11.19222	9.78143
H	7.27926	7.65926	9.51339
H	8.81355	8.18453	8.74957
H	7.37676	9.25184	8.68125
H	11.24958	16.89051	11.29463
H	6.59614	15.41779	10.26419
H	7.62046	14.08042	13.30207
H	6.19119	14.79594	12.46823
H	7.08594	15.72215	13.73326
H	10.36438	17.14414	8.98386
H	6.86157	15.96870	7.94124
H	8.53416	16.02729	7.28572
H	7.72160	17.53773	7.78962
H	9.23213	19.37846	14.30913
H	8.58867	21.12697	9.68109
H	11.80964	21.92530	10.92265
H	10.85767	21.58452	9.42556
H	11.90236	20.31796	10.16404
H	6.94293	19.47445	13.33584
H	6.15680	21.05346	9.96531
H	5.43958	20.62373	11.55889
H	5.92876	19.33336	10.41922
H	9.06015	17.96946	19.09900
H	8.53229	19.64012	20.87682
H	12.27322	21.66475	20.03512
H	13.00552	20.19281	16.97127
H	13.80043	19.13763	18.16087
H	13.77553	20.91630	18.43381
H	9.26019	21.48290	22.33176
H	9.69730	22.77994	21.17387
H	10.95368	22.08142	22.24021
H	16.63377	19.64288	17.55125
H	16.69365	22.06233	18.08713
H	17.60656	21.10617	22.21865
H	16.72750	17.76037	22.18908
H	17.86833	18.91875	22.96625
H	18.45335	17.71641	21.75340
H	17.17768	23.87948	19.64824
H	18.03700	23.50790	21.18314
H	16.24861	23.52662	21.14110
H	19.67840	21.24717	15.84575
H	20.42377	22.97343	17.48001
H	22.31535	19.87409	19.84669
H	22.31522	17.33119	17.46383
H	20.81358	17.09291	18.39975
H	22.30635	17.64699	19.23722
H	22.00971	23.57424	19.35646
H	22.79154	22.27952	20.33191
H	21.07314	22.70242	20.60993
H	18.40928	13.21931	19.19395
H	19.33637	12.89517	21.48324
H	23.33177	13.56755	19.93171
H	22.62269	13.11626	16.54626
H	23.74318	13.97346	17.67079
H	22.44556	14.86907	16.79372
H	21.42037	13.59251	23.03055
H	23.05047	13.33181	22.31788
H	21.94287	11.94387	22.57431

H	15.37081	9.82707	21.13534
H	16.33026	9.24747	23.35897
H	17.40408	13.40752	23.94019
H	15.45657	14.82810	21.49819
H	16.97908	14.50281	20.62741
H	17.02619	15.03342	22.34450
H	17.70893	9.88577	25.30586
H	16.77372	11.24706	26.00219
H	18.43415	11.52868	25.39809
H	12.85351	13.90600	21.93951
H	13.63471	16.98039	25.78721
H	13.99331	18.68643	22.75915
H	13.40620	18.87812	24.45399
H	12.24683	18.71932	23.07872
H	13.27115	12.96072	24.20076
H	13.80520	15.13983	27.31557
H	14.71620	13.78064	26.57567
H	12.95756	13.62255	26.85691
H	17.06280	19.59564	12.43685
H	14.91565	24.09997	12.40585
H	13.42521	22.11385	14.80754
H	13.98159	23.79698	14.50350
H	14.88383	22.72505	15.64032
H	17.40065	21.09799	10.49974
H	15.83154	24.60068	10.25102
H	16.03605	23.18207	9.16970
H	17.46040	23.89058	9.98701
H	17.68036	17.37535	10.74796
H	22.31408	19.22772	10.71194
H	22.22243	16.16161	12.40254
H	21.78621	17.39926	13.61530
H	23.03228	17.77421	12.36782
H	18.26860	19.17661	9.14949
H	21.31294	21.23735	9.31773
H	19.83358	20.88812	8.35714
H	21.36346	20.02204	8.00476
H	15.19382	13.13377	7.46811
H	18.97887	15.89480	5.77033
H	20.01877	13.78810	8.38934
H	19.41968	15.29000	9.13979
H	20.32039	15.37633	7.58499
H	14.97904	14.29938	5.27742
H	17.82876	16.20957	3.63339
H	16.26837	16.89800	4.18490
H	16.28725	15.34554	3.29386
H	14.99068	19.64630	9.27660
H	14.12295	20.25683	7.02093
H	12.38628	16.30105	6.65732
H	14.11656	14.73417	9.20206
H	12.54156	14.70331	8.33283
H	12.64640	15.31419	10.01935
H	12.34111	19.71059	5.21373
H	11.84739	17.99815	4.97108
H	13.49390	18.53448	4.51147
H	7.99794	12.78095	16.86610
H	6.53210	10.92851	17.64668
H	9.38926	10.03230	20.78080
H	11.16796	12.96255	20.72298

H	12.10312	11.94215	19.60037
H	11.35428	11.20580	21.05991
H	6.46852	8.68446	18.95405
H	6.14614	9.62838	20.44018
H	7.52903	8.48904	20.39349

$Ag_{13}Au_{12}DMBT_{18}$_III

349

Ag	14.71274	17.65497	14.59615
Au	17.74146	19.05457	15.25209
Au	19.80111	16.13550	16.14181
Ag	17.32028	13.89782	16.37744
Ag	13.32501	16.54925	17.02212
Au	11.46562	18.84743	15.24478
Au	13.27334	18.62498	12.16756
Ag	14.87963	15.32043	12.42872
Ag	16.39540	16.72867	16.84571
Au	14.69038	16.92731	19.81841
Au	11.50611	15.07161	19.31185
Ag	12.50282	13.69939	16.37663
Ag	15.00943	12.14633	16.04839
Au	12.28884	10.55399	15.08229
Au	10.13963	13.44066	14.26922
Ag	12.46756	15.92309	14.12946
Ag	16.34067	13.13894	13.58581
Au	18.05772	10.91493	15.18029
Au	16.46881	11.27090	18.50204
Ag	14.93739	14.38816	18.08806
Ag	13.32251	13.06387	13.66783
Au	15.04750	12.83314	10.56469
Ag	17.81480	14.55716	11.39626
Ag	17.23871	16.04988	14.14925
Au	14.86823	14.88935	15.27467
S	15.57914	20.03544	15.07489
S	20.02822	18.39143	15.35915
S	19.84128	13.84054	16.76797
S	11.78320	20.14017	13.26785
S	14.87186	17.41583	10.89995
S	11.03215	17.69775	17.26282
S	16.94543	17.46716	19.22968
S	12.50981	16.66088	20.77594
S	10.27558	13.85958	17.68886
S	14.54907	9.80034	15.03799
S	9.98453	11.17097	15.02309
S	9.95345	15.75139	13.71078
S	17.78971	9.73005	17.22994
S	15.03971	12.52655	19.93184
S	18.43796	11.78667	13.00239
S	12.77563	12.51392	11.21757
S	17.24824	12.92166	9.62717
S	19.30954	16.02704	12.65257
C	19.40116	9.61047	18.03477
C	20.56039	10.14335	17.43627
C	19.50175	8.87284	19.24597
C	21.81791	9.95262	18.02269
C	20.78363	8.70683	19.81022
C	18.28847	8.28674	19.92660
C	21.95295	9.23185	19.22706
C	23.30539	9.05529	19.88195
C	14.68350	8.17072	15.79708
C	15.38356	7.21384	15.02862
C	14.17425	7.81201	17.07417

C	15.58422	5.91257	15.50634
C	14.38505	6.48854	17.51770
C	13.44247	8.79344	17.94787
C	15.08406	5.52346	16.76598
C	15.31831	4.12950	17.30704
C	18.11893	10.38272	11.91028
C	16.83497	9.81779	11.78029
C	19.19827	9.87682	11.13696
C	16.60401	8.76418	10.88524
C	18.93087	8.81585	10.24683
C	20.59272	10.44882	11.24508
C	17.65088	8.24750	10.09405
C	17.40114	7.14409	9.08848
C	12.45986	10.82139	10.66850
C	11.88624	10.61278	9.38434
C	12.73921	9.71547	11.49573
C	11.61977	9.28506	8.98591
C	11.57288	11.76136	8.45469
C	12.45861	8.41031	11.07118
C	11.89196	8.17007	9.80183
C	11.59040	6.76070	9.33968
C	9.25583	10.17351	13.70495
C	8.85424	8.84565	14.01287
C	9.00951	10.70585	12.42356
C	8.20453	8.10457	13.00357
C	9.11409	8.23039	15.36701
C	8.35987	9.94117	11.44648
C	7.94307	8.62191	11.71995
C	7.25964	7.78655	10.65909
C	9.43800	15.79601	11.98597
C	8.12851	15.37015	11.62463
C	10.28101	16.36151	11.00761
C	7.73711	15.50885	10.27598
C	7.16788	14.79347	12.63567
C	9.85355	16.50137	9.68058
C	8.57159	16.06551	9.28659
C	8.11689	16.18086	7.84733
C	10.23607	20.14392	12.33516
C	10.19695	20.82839	11.09017
C	9.06269	19.56652	12.86099
C	8.95786	20.89909	10.41901
C	11.42944	21.45278	10.48159
C	7.84997	19.66048	12.16758
C	7.77526	20.32936	10.92810
C	6.47019	20.41013	10.16659
C	10.69017	18.93335	18.53048
C	9.45425	18.78444	19.19681
C	11.57402	19.97953	18.90824
C	9.07964	19.65977	20.22433
C	11.16046	20.84716	19.94182
C	12.91643	20.16837	18.25804
C	9.92804	20.71679	20.61242
C	9.51892	21.69631	21.69175
C	17.00883	19.22138	19.65411
C	16.54747	20.21349	18.76600
C	17.57072	19.60212	20.90482
C	16.62704	21.57226	19.10037
C	17.62841	20.97801	21.21306

C	18.09632	18.58080	21.88560
C	17.16467	21.98157	20.33852
C	17.21871	23.44484	20.72169
C	20.83574	19.32053	16.68613
C	20.10507	20.08555	17.61531
C	22.25569	19.30500	16.74291
C	20.76093	20.82943	18.60476
C	22.88347	20.06028	17.75593
C	23.08581	18.51508	15.75912
C	22.16821	20.82596	18.69693
C	22.87953	21.60922	19.77924
C	20.38382	13.82589	18.48583
C	19.49261	13.47007	19.51795
C	21.75113	14.07339	18.79215
C	19.93188	13.36306	20.84451
C	22.15691	13.97192	20.13923
C	22.75309	14.43659	17.72394
C	21.27635	13.62250	21.18146
C	21.74940	13.54091	22.61694
C	15.75696	12.20491	21.56332
C	15.63541	10.88678	22.05988
C	16.36388	13.20236	22.37121
C	16.11472	10.54291	23.33023
C	16.83376	12.82161	23.64844
C	16.51545	14.62595	21.90772
C	16.72623	11.51146	24.15379
C	17.21873	11.16362	25.54223
C	12.80402	15.94050	22.40307
C	13.17844	16.81095	23.46283
C	12.60898	14.56731	22.65359
C	13.34416	16.24961	24.74635
C	13.40189	18.28709	23.23722
C	12.78024	14.04522	23.94159
C	13.15273	14.88044	25.01570
C	13.35242	14.31484	26.40484
C	15.69891	21.20374	13.70698
C	14.96621	22.41837	13.79799
C	16.51059	20.95841	12.57937
C	15.08500	23.34367	12.73824
C	14.09129	22.73743	14.98719
C	16.61154	21.90418	11.55157
C	15.89680	23.11972	11.61066
C	16.01119	24.14576	10.50375
C	19.63634	17.39147	11.52515
C	20.99538	17.76522	11.30929
C	18.61486	18.06534	10.82670
C	21.26366	18.80748	10.40001
C	22.12865	17.05609	12.01183
C	18.92039	19.09159	9.91879
C	20.25275	19.48724	9.68948
C	20.59884	20.60166	8.72470
C	17.11309	13.66890	7.99487
C	18.17231	14.46136	7.46862
C	16.00728	13.35566	7.17438
C	18.05135	14.92860	6.14278
C	19.40092	14.80397	8.27401
C	15.92306	13.83360	5.86071
C	16.94520	14.64058	5.32004

C	16.84516	15.20171	3.91844
C	14.39604	17.84418	9.20518
C	14.70375	19.15478	8.77483
C	13.77242	16.93733	8.30903
C	14.40051	19.57667	7.47342
C	13.48751	17.39474	7.00283
C	13.41251	15.53340	8.71302
C	13.78666	18.69709	6.55721
C	13.48663	19.12777	5.13750
C	9.45474	12.44255	18.43635
C	8.06997	12.34716	18.17619
C	10.09422	11.44022	19.21344
C	7.31408	11.27829	18.67496
C	9.30198	10.38107	19.70522
C	11.56538	11.49077	19.51180
C	7.91897	10.27307	19.45754
C	7.10797	9.13604	20.04129
H	20.46720	10.71726	16.49933
H	22.70947	10.38058	17.53313
H	20.86599	8.13401	20.75136
H	17.67735	7.67893	19.22250
H	17.61654	9.09099	20.31022
H	18.58250	7.64727	20.78623
H	24.09123	8.79971	19.13679
H	23.28732	8.25221	20.65058
H	23.63195	9.99349	20.38795
H	15.77420	7.50549	14.04010
H	16.13711	5.18761	14.88385
H	13.98242	6.20384	18.50659
H	14.08948	9.66959	18.19049
H	13.11909	8.32359	18.90075
H	12.54283	9.20790	17.43513
H	15.34396	3.37328	16.49155
H	14.52649	3.83041	18.02807
H	16.29370	4.06063	17.84405
H	16.00708	10.20314	12.39679
H	15.58476	8.35121	10.79665
H	19.76739	8.42016	9.64301
H	20.97088	10.40693	12.29113
H	20.61449	11.52209	10.94947
H	21.30136	9.89440	10.59245
H	16.61508	6.44018	9.43970
H	18.32353	6.55742	8.88402
H	17.05196	7.55907	8.11371
H	13.18453	9.88105	12.49005
H	11.17652	9.12010	7.98710
H	10.89592	12.50377	8.93273
H	11.09728	11.39755	7.51833
H	12.49614	12.32235	8.18220
H	12.68398	7.56731	11.74684
H	11.08811	6.75365	8.34838
H	10.92866	6.22913	10.06070
H	12.52025	6.15290	9.24966
H	9.33790	11.73367	12.19612
H	7.88528	7.07353	13.24026
H	8.71392	8.86423	16.18973
H	10.20829	8.12817	15.55760
H	8.65705	7.22042	15.44212

H	8.17991	10.38149	10.45104
H	6.81701	6.86158	11.08791
H	7.97791	7.47703	9.86472
H	6.44538	8.35283	10.15377
H	11.28535	16.71192	11.30141
H	6.72324	15.17304	9.99174
H	7.54766	13.83246	13.05713
H	6.17238	14.60338	12.17990
H	7.03953	15.47488	13.50608
H	10.53349	16.95964	8.94250
H	7.01918	16.03289	7.75057
H	8.61195	15.41856	7.20116
H	8.36788	17.17695	7.41891
H	9.10968	19.03513	13.82591
H	8.92227	21.42984	9.45073
H	11.95396	22.11853	11.20262
H	11.17221	22.04312	9.57624
H	12.17188	20.67434	10.18470
H	6.94678	19.19656	12.59963
H	6.54160	21.10579	9.30266
H	5.63708	20.75812	10.81803
H	6.17416	19.41164	9.77002
H	8.78551	17.96077	18.89868
H	8.10946	19.51770	20.73149
H	11.84583	21.66159	20.23777
H	12.82484	20.31661	17.15699
H	13.55469	19.26299	18.39130
H	13.45772	21.03504	18.69132
H	8.88373	21.21130	22.46551
H	8.92852	22.54373	21.26943
H	10.40339	22.13725	22.20112
H	16.12315	19.91979	17.79333
H	16.26343	22.32301	18.37795
H	18.06183	21.27632	22.18484
H	17.29328	17.88088	22.20985
H	18.51611	19.07462	22.78851
H	18.88976	17.94896	21.42810
H	17.50778	24.08389	19.85793
H	17.94548	23.62810	21.54262
H	16.22479	23.80832	21.07397
H	19.00446	20.09389	17.56572
H	20.15619	21.41485	19.31781
H	23.98719	20.04835	17.80389
H	22.89116	18.83699	14.71171
H	22.84263	17.42861	15.80108
H	24.17101	18.63507	15.96594
H	22.51603	22.66037	19.82928
H	23.97777	21.63590	19.61124
H	22.70602	21.16094	20.78515
H	18.43908	13.25809	19.26863
H	19.21138	13.06919	21.62677
H	23.21754	14.16927	20.37891
H	22.76565	13.68319	16.90497
H	23.77704	14.52304	18.14688
H	22.48995	15.40630	17.23948
H	21.39715	14.41599	23.21202
H	22.85916	13.52262	22.68288
H	21.36026	12.62946	23.12327

H	15.15393	10.12351	21.42730
H	16.01166	9.50255	23.68501
H	17.31185	13.59658	24.27369
H	15.52320	15.11011	21.75582
H	17.04464	14.69028	20.93300
H	17.07806	15.23082	22.64900
H	17.61476	10.12529	25.58794
H	16.39815	11.23193	26.29529
H	18.02493	11.85298	25.87556
H	12.32377	13.90536	21.82022
H	13.63393	16.92222	25.57360
H	14.25856	18.46606	22.54560
H	13.61551	18.81039	24.19380
H	12.51800	18.76479	22.75892
H	12.62906	12.96526	24.10890
H	13.54994	15.11606	27.14888
H	14.21453	13.60904	26.43224
H	12.45879	13.74505	26.74695
H	17.07809	20.01635	12.51228
H	14.52001	24.29040	12.80971
H	13.25320	22.01001	15.08069
H	13.65096	23.75354	14.89567
H	14.66535	22.68525	15.93971
H	17.26908	21.68798	10.69190
H	15.39284	25.04495	10.71458
H	15.67801	23.73134	9.52466
H	17.06398	24.48420	10.36776
H	17.56199	17.77607	10.98177
H	22.31852	19.09460	10.23539
H	22.15358	15.97390	11.74987
H	22.01000	17.10227	13.11697
H	23.10906	17.50491	11.74110
H	18.09737	19.58228	9.37113
H	21.01912	21.48768	9.25531
H	19.70366	20.94393	8.16223
H	21.36394	20.28065	7.98141
H	15.20693	12.71554	7.58089
H	18.86987	15.55029	5.73796
H	19.92069	13.89147	8.64289
H	19.14394	15.40396	9.17972
H	20.12098	15.39712	7.67158
H	15.04659	13.56897	5.24382
H	17.84909	15.39529	3.48145
H	16.29139	16.16981	3.91024
H	16.30149	14.50999	3.23772
H	15.17977	19.85025	9.48551
H	14.64650	20.60837	7.16741
H	13.00224	16.68995	6.30461
H	14.31868	14.93224	8.95302
H	12.86604	15.01036	7.90075
H	12.78150	15.51307	9.62725
H	13.20695	20.20326	5.08633
H	12.65521	18.53590	4.69649
H	14.37383	18.99083	4.47523
H	7.58858	13.12966	17.56754
H	6.23394	11.22797	18.45253
H	9.79886	9.60003	20.30842
H	11.83965	12.42653	20.05269

H	12.17017	11.50905	18.57726
H	11.89181	10.62447	20.12381
H	6.23326	8.88633	19.40137
H	6.71023	9.39633	21.05078
H	7.71931	8.21473	20.16018

$Ag_{13}Au_{12}DMBT_{18}$_IV

349

Ag	14.73669	17.65561	14.58387
Au	17.80124	19.10035	15.21880
Ag	19.53118	16.12455	16.04021
Au	17.35048	13.83743	16.32896
Ag	13.45873	16.59781	17.03896
Au	11.43414	18.83933	15.28589
Ag	13.03539	18.45541	12.33330
Au	14.85362	15.32454	12.42311
Ag	16.50159	16.75066	16.79165
Au	14.82216	16.95987	19.76043
Ag	11.78261	15.06729	19.11993
Au	12.59696	13.68246	16.38255
Ag	15.05120	12.10687	15.96601
Au	12.07262	10.55733	14.97769
Ag	10.25020	13.51649	14.52400
Au	12.48846	15.94506	14.16006
Ag	16.27188	13.07508	13.46281
Au	17.98894	10.84225	15.26954
Ag	16.54074	11.51748	18.42404
Au	15.02232	14.35454	18.05388
Ag	13.27708	13.03656	13.64250
Au	15.05772	12.83240	10.56530
Ag	17.75264	14.64793	11.43009
Au	17.23501	16.03637	14.11362
Ag	14.90698	14.87396	15.25384
S	15.61549	20.01819	14.96464
S	20.08177	18.47348	15.52121
S	19.85060	13.72478	16.50250
S	11.55288	20.14582	13.29600
S	14.79081	17.44550	10.99321
S	11.15289	17.70693	17.35150
S	17.07767	17.49337	19.15259
S	12.64607	16.69147	20.72362
S	10.30836	13.90441	17.54120
S	14.35186	9.85283	15.01566
S	9.76107	11.11996	14.83888
S	9.99506	15.87012	13.86208
S	17.75005	9.68961	17.34350
S	14.97864	12.59017	19.96484
S	18.35919	11.67007	13.06805
S	12.78240	12.45478	11.19376
S	17.28404	12.95793	9.68570
S	19.35460	16.05040	12.70524
C	19.37984	9.55066	18.09752
C	20.54987	9.92002	17.40497
C	19.48252	8.95587	19.38775
C	21.81496	9.70804	17.97119
C	20.76961	8.76193	19.92629
C	18.25935	8.54566	20.17089
C	21.95001	9.12601	19.24650
C	23.30704	8.91798	19.88316
C	14.52493	8.26487	15.84964
C	15.23943	7.28482	15.12869
C	14.02764	7.96615	17.14756

C	15.46354	6.01255	15.67330
C	14.26296	6.67340	17.65837
C	13.28807	8.98370	17.97206
C	14.97361	5.68129	16.95144
C	15.20346	4.31483	17.56042
C	18.11151	10.20206	12.04454
C	16.82783	9.76893	11.66513
C	19.26046	9.49725	11.58658
C	16.66351	8.65118	10.83301
C	19.05996	8.37839	10.75445
C	20.65890	9.91721	11.97588
C	17.78024	7.93543	10.35984
C	17.62575	6.73520	9.45021
C	12.53289	10.74787	10.65402
C	11.95180	10.51542	9.37714
C	12.88194	9.65482	11.47147
C	11.75239	9.17772	8.97442
C	11.56226	11.64972	8.45922
C	12.66541	8.33833	11.04249
C	12.09755	8.07428	9.77877
C	11.88368	6.65375	9.30173
C	9.15872	10.43311	13.28544
C	8.85508	9.04522	13.20878
C	8.88256	11.27082	12.18633
C	8.27853	8.56114	12.01703
C	9.13845	8.10613	14.35642
C	8.30379	10.75713	11.01782
C	7.99270	9.38677	10.91108
C	7.40755	8.81266	9.63924
C	9.42169	15.83136	12.16105
C	8.06986	15.46798	11.89778
C	10.24841	16.23680	11.09267
C	7.61655	15.51844	10.56256
C	7.13225	15.04368	13.00243
C	9.76312	16.28817	9.78021
C	8.43176	15.92501	9.48827
C	7.89860	15.99210	8.07313
C	9.95590	20.05034	12.46790
C	9.84019	20.58367	11.15445
C	8.81259	19.55058	13.12483
C	8.56431	20.58654	10.55356
C	11.03508	21.12216	10.40526
C	7.56111	19.57087	12.49652
C	7.41281	20.08882	11.19357
C	6.06935	20.07788	10.49706
C	10.84072	18.96489	18.60588
C	9.62635	18.82782	19.31069
C	11.72636	20.03061	18.92405
C	9.27434	19.73215	20.32258
C	11.33684	20.92494	19.94261
C	13.04490	20.21127	18.22453
C	10.12513	20.80516	20.65405
C	9.75110	21.81303	21.72041
C	17.15017	19.25951	19.52259
C	16.68265	20.22693	18.61486
C	17.71365	19.67165	20.76443
C	16.75422	21.59457	18.91959
C	17.76819	21.05217	21.03945

C	18.23793	18.67449	21.77070
C	17.29427	22.03394	20.14341
C	17.35743	23.50319	20.50237
C	20.73647	19.39944	16.92049
C	20.17757	20.64306	17.28249
C	21.89755	18.93027	17.59626
C	20.74453	21.41808	18.30131
C	22.43958	19.73554	18.61966
C	22.54569	17.61195	17.25470
C	21.88921	20.97595	18.99545
C	22.48449	21.78772	20.12532
C	20.48452	13.70144	18.18396
C	19.63459	13.67847	19.30906
C	21.89533	13.65950	18.37010
C	20.15880	13.62487	20.60687
C	22.38936	13.61659	19.69048
C	22.84927	13.64899	17.19860
C	21.55241	13.59773	20.82292
C	22.12223	13.52142	22.22306
C	15.82736	12.31613	21.54090
C	15.70189	11.01490	22.07987
C	16.52598	13.30886	22.27992
C	16.26037	10.68506	23.32287
C	17.08040	12.94110	23.52448
C	16.67298	14.71805	21.77736
C	16.96695	11.64713	24.07165
C	17.56242	11.31992	25.42422
C	12.95229	15.97996	22.34879
C	13.32028	16.84744	23.41475
C	12.76771	14.60449	22.59743
C	13.48569	16.28289	24.69673
C	13.53591	18.32574	23.19679
C	12.93944	14.07746	23.88367
C	13.30394	14.91121	24.96128
C	13.51338	14.34208	26.34754
C	15.68569	21.14133	13.55654
C	14.91086	22.33209	13.61338
C	16.50013	20.88621	12.43370
C	14.98795	23.22285	12.52074
C	14.03417	22.66184	14.79805
C	16.55904	21.79915	11.37318
C	15.79859	22.98796	11.39458
C	15.86498	23.97652	10.25020
C	19.61387	17.46500	11.62350
C	20.93181	17.99811	11.51769
C	18.58090	18.00268	10.82857
C	21.14955	19.04908	10.60423
C	22.07671	17.45730	12.34088
C	18.83785	19.04266	9.92268
C	20.13109	19.58671	9.79073
C	20.43217	20.68829	8.79688
C	17.19397	13.69616	8.04741
C	18.30724	14.41406	7.52671
C	16.07174	13.46165	7.22262
C	18.22458	14.89103	6.20128
C	19.55110	14.66903	8.34189
C	16.02528	13.94835	5.91068
C	17.10365	14.68292	5.37471

C	17.04573	15.24646	3.97157
C	14.22730	17.82451	9.31450
C	14.46196	19.15157	8.88294
C	13.61244	16.89966	8.43106
C	14.09217	19.56948	7.59800
C	13.25582	17.35573	7.14198
C	13.34378	15.47468	8.82765
C	13.48019	18.67273	6.69683
C	13.10600	19.10355	5.29499
C	9.49386	12.46636	18.24509
C	8.13779	12.30210	17.87948
C	10.09654	11.53406	19.13111
C	7.37991	11.23640	18.37786
C	9.30293	10.47167	19.61484
C	11.53091	11.66171	19.55573
C	7.95153	10.29618	19.26090
C	7.13374	9.15619	19.82834
H	20.45967	10.38201	16.40793
H	22.71469	10.00491	17.40541
H	20.84818	8.29916	20.92667
H	17.59764	7.87630	19.57664
H	17.64104	9.43182	20.45077
H	18.54337	8.02301	21.10926
H	24.12610	9.01996	19.13880
H	23.39292	7.91124	20.35045
H	23.49647	9.66724	20.68681
H	15.62720	7.53404	14.12763
H	16.03064	5.26653	15.09014
H	13.87378	6.43547	18.66518
H	13.92814	9.87239	18.17946
H	12.96388	8.55557	18.94395
H	12.38845	9.36968	17.43786
H	15.73450	3.63973	16.85554
H	14.24354	3.82430	17.84210
H	15.81624	4.37893	18.48893
H	15.94232	10.31482	12.02764
H	15.64321	8.34379	10.54682
H	19.95030	7.83022	10.39637
H	20.79757	9.88481	13.08039
H	20.87155	10.96510	11.66786
H	21.41770	9.25290	11.50891
H	16.55544	6.49539	9.27333
H	18.11061	5.82887	9.88010
H	18.09818	6.91303	8.45652
H	13.33418	9.83612	12.45914
H	11.30367	8.99454	7.98123
H	10.84839	12.34704	8.95104
H	11.09658	11.26469	7.52645
H	12.44815	12.26440	8.17942
H	12.94300	7.50534	11.71104
H	11.24948	6.61886	8.38977
H	11.39385	6.03068	10.08322
H	12.85076	6.15721	9.05291
H	9.12949	12.34464	12.25131
H	8.03822	7.48450	11.95494
H	8.66441	8.45928	15.29919
H	10.23213	8.04778	14.56602
H	8.77239	7.08057	14.13484

H	8.09565	11.43929	10.17634
H	6.77909	7.91794	9.84249
H	8.21273	8.49719	8.93507
H	6.78094	9.55920	9.10379
H	11.29386	16.51987	11.30718
H	6.56893	15.23075	10.35876
H	7.50179	14.12955	13.52503
H	6.11707	14.82799	12.60532
H	7.04624	15.82856	13.78723
H	10.43685	16.61883	8.97153
H	6.88594	15.54004	7.99569
H	8.56458	15.45814	7.35823
H	7.82318	17.04542	7.71598
H	8.91462	19.13990	14.14294
H	8.47251	21.00060	9.53325
H	11.57788	21.89555	10.99358
H	10.72933	21.56773	9.43458
H	11.77793	20.31730	10.19058
H	6.68332	19.17209	13.03343
H	6.04121	20.79499	9.64782
H	5.24337	20.33944	11.19516
H	5.83805	19.06753	10.08563
H	8.95320	17.99354	19.05512
H	8.32014	19.60015	20.86141
H	12.02343	21.75364	20.19206
H	12.91418	20.32399	17.12325
H	13.69612	19.31652	18.36602
H	13.59193	21.09567	18.61255
H	8.90845	21.44998	22.34806
H	9.43526	22.78374	21.27097
H	10.60844	22.03358	22.39480
H	16.25131	19.90946	17.65337
H	16.38114	22.32736	18.18369
H	18.20326	21.37388	22.00327
H	17.43110	17.99140	22.12077
H	18.66698	19.19085	22.65646
H	19.02435	18.02384	21.32780
H	17.07837	24.14567	19.63962
H	18.37768	23.80224	20.83350
H	16.66285	23.74880	21.33922
H	19.28083	21.00307	16.75250
H	20.28120	22.38498	18.56107
H	23.34009	19.36836	19.14427
H	22.82003	17.55091	16.17757
H	21.85084	16.76000	17.45119
H	23.46320	17.44831	17.85920
H	22.39473	22.88040	19.93630
H	23.56069	21.55283	20.27700
H	21.96364	21.58180	21.09006
H	18.54307	13.70738	19.15178
H	19.46649	13.60096	21.46539
H	23.48468	13.59167	19.83580
H	22.67496	12.76552	16.54385
H	23.90530	13.62511	17.54433
H	22.71429	14.54205	16.54708
H	21.62118	14.24083	22.90883
H	23.21182	13.74250	22.23464
H	21.98361	12.50660	22.66453

H	15.15058	10.25204	21.50582
H	16.14623	9.65840	23.71243
H	17.62624	13.71510	24.09381
H	15.68012	15.21701	21.69043
H	17.12147	14.75461	20.76165
H	17.30347	15.32710	22.45824
H	17.62948	10.22227	25.58583
H	16.94721	11.73952	26.25479
H	18.58526	11.74413	25.53585
H	12.49421	13.93936	21.76274
H	13.76827	16.95442	25.52744
H	14.38472	18.51151	22.49775
H	13.75578	18.84352	24.15512
H	12.64664	18.80260	22.72805
H	12.79493	12.99594	24.04676
H	13.63176	15.14520	27.10655
H	14.42733	13.70508	26.38722
H	12.65967	13.69931	26.65972
H	17.10246	19.96448	12.39637
H	14.38920	24.15024	12.56385
H	13.21195	21.91964	14.91341
H	13.57036	23.66480	14.68174
H	14.61275	22.64687	15.74888
H	17.22027	21.57889	10.51756
H	15.20471	24.85263	10.42827
H	15.55231	23.51091	9.28748
H	16.90071	24.35900	10.10040
H	17.55636	17.60308	10.91676
H	22.17163	19.46160	10.52345
H	22.23197	16.36961	12.15996
H	21.87180	17.57308	13.42969
H	23.02249	17.99086	12.10443
H	18.00951	19.42572	9.30251
H	21.07727	21.47806	9.24309
H	19.50129	21.17395	8.43252
H	20.97133	20.29602	7.90262
H	15.22887	12.87586	7.62485
H	19.08627	15.45380	5.79984
H	19.99981	13.72199	8.71661
H	19.33027	15.28675	9.24556
H	20.31690	15.20791	7.74456
H	15.13331	13.74939	5.29159
H	18.05673	15.51626	3.59668
H	16.42126	16.16948	3.93218
H	16.59705	14.52138	3.25627
H	14.93549	19.86281	9.58035
H	14.28274	20.61345	7.29394
H	12.77677	16.63521	6.45548
H	14.29119	14.92719	9.03648
H	12.80481	14.92817	8.02597
H	12.74338	15.40471	9.75960
H	12.69329	20.13676	5.28007
H	12.34697	18.42585	4.84713
H	13.99222	19.09888	4.61743
H	7.68005	13.02784	17.18788
H	6.32557	11.13137	18.06803
H	9.77382	9.74522	20.30122
H	11.71307	12.62479	20.09169

H	12.21961	11.67839	18.68191
H	11.83791	10.83450	20.22844
H	6.42450	8.74648	19.07528
H	6.52300	9.48708	20.70160
H	7.78091	8.32253	20.17758

$Ag_{13}Au_{12}DMBT_{18}$_V

349

Au	14.78132	17.67624	14.61980
Ag	17.60988	18.90890	15.45758
Au	19.76633	16.10769	16.25483
Ag	17.25148	13.80513	16.47629
Au	13.19786	16.45182	16.91096
Ag	11.61267	18.68671	15.11232
Au	13.26398	18.73182	12.19359
Ag	15.13704	15.48407	12.38297
Au	16.26180	16.62957	16.98628
Ag	14.63889	16.84078	19.65313
Au	11.63170	15.06546	19.40905
Ag	12.45988	13.60566	16.17571
Au	14.97456	12.12995	15.92546
Ag	12.34171	10.77506	14.95177
Au	10.16008	13.48633	14.15930
Ag	12.57514	16.02213	13.92072
Au	16.52082	13.29295	13.53412
Ag	17.74604	10.96704	15.24228
Au	16.58025	11.13900	18.37367
Ag	14.73313	14.29442	18.05098
Au	13.44640	13.21254	13.46545
Ag	15.18635	12.89497	10.69480
Au	18.01104	14.65954	11.08187
Ag	17.35447	16.09656	14.33431
Ag	14.88874	14.89028	15.22821
S	15.47757	20.06676	15.12466
S	19.99394	18.41439	15.62190
S	19.77844	13.75309	16.68172
S	11.74057	20.24878	13.24581
S	14.95759	17.60645	10.95711
S	10.92168	17.53522	17.13187
S	17.00901	17.41070	19.24936
S	12.51523	16.71966	20.87860
S	10.44500	13.83593	17.75574
S	14.58750	9.76764	14.99050
S	9.94781	11.21240	14.88034
S	10.04831	15.81811	13.63836
S	17.86509	9.49444	17.21139
S	15.09472	12.39305	19.75247
S	18.47096	11.77892	13.03469
S	12.79578	12.57153	11.12193
S	17.34265	12.95906	9.52534
S	19.22145	16.08683	12.55968
C	19.56323	9.52785	17.81058
C	20.61426	9.87864	16.93796
C	19.86242	9.06643	19.12261
C	21.95130	9.78006	17.34466
C	21.21851	8.98709	19.50096
C	18.77922	8.66651	20.09421
C	22.27879	9.33845	18.64274
C	23.71696	9.27376	19.10811
C	14.63735	8.26977	15.98344
C	15.40439	7.21952	15.43072
C	13.96682	8.07211	17.22212

C	15.50908	5.98231	16.07965
C	14.09325	6.81304	17.84491
C	13.15219	9.15370	17.87538
C	14.85159	5.75463	17.30465
C	14.96826	4.43424	18.03553
C	18.06090	10.42388	11.92186
C	16.74279	9.96239	11.73803
C	19.12425	9.82436	11.18802
C	16.46303	8.92092	10.84053
C	18.80870	8.77926	10.29814
C	20.55211	10.29511	11.33866
C	17.49352	8.30996	10.09979
C	17.20773	7.20062	9.11008
C	12.53802	10.84453	10.67579
C	12.01070	10.55638	9.38562
C	12.80549	9.78543	11.56511
C	11.77440	9.20599	9.05096
C	11.70310	11.65033	8.39015
C	12.55489	8.45581	11.20406
C	12.03207	8.13878	9.93278
C	11.75308	6.70360	9.54200
C	9.29074	10.23170	13.51888
C	8.92525	8.88307	13.78249
C	9.05992	10.78324	12.24161
C	8.32751	8.14460	12.73979
C	9.17066	8.24408	15.12862
C	8.46142	10.02088	11.23101
C	8.07963	8.68301	11.46232
C	7.44689	7.85316	10.36638
C	9.49389	15.89707	11.92617
C	8.17047	15.49637	11.58933
C	10.32859	16.44720	10.93184
C	7.75923	15.63762	10.24651
C	7.21697	14.93852	12.61743
C	9.88295	16.58858	9.61145
C	8.58576	16.17650	9.24137
C	8.09974	16.32497	7.81551
C	10.16308	20.18089	12.37521
C	10.05379	20.74959	11.07660
C	9.01508	19.66907	13.01517
C	8.77927	20.76981	10.47190
C	11.24916	21.31332	10.34796
C	7.76499	19.70748	12.38526
C	7.62425	20.25946	11.09529
C	6.28155	20.27459	10.39763
C	10.61271	18.72885	18.43922
C	9.41825	18.51929	19.16558
C	11.45853	19.81928	18.78091
C	9.04986	19.37533	20.21092
C	11.05563	20.66129	19.83850
C	12.75302	20.07972	18.06396
C	9.86247	20.47169	20.56420
C	9.46010	21.42990	21.66472
C	16.98502	19.17419	19.61628
C	16.38863	20.12138	18.76243
C	17.61234	19.61200	20.81948
C	16.38689	21.48619	19.08726
C	17.58435	20.98843	21.11918

C	18.29214	18.64065	21.75514
C	16.97680	21.94717	20.28096
C	16.93594	23.40886	20.67266
C	20.68633	19.35098	16.99882
C	19.95039	20.39918	17.58918
C	22.02519	19.11283	17.41639
C	20.51314	21.20188	18.58949
C	22.55704	19.93322	18.43336
C	22.87640	18.03287	16.79681
C	21.83167	20.97871	19.03644
C	22.43779	21.82739	20.13296
C	20.39571	13.60177	18.36853
C	19.51657	13.43335	19.45697
C	21.80034	13.58523	18.58908
C	20.00630	13.26070	20.75841
C	22.26017	13.42223	19.91272
C	22.78455	13.73109	17.45387
C	21.39372	13.25760	21.01077
C	21.92834	13.05987	22.41280
C	15.75245	12.14338	21.41901
C	15.65758	10.83374	21.94046
C	16.29691	13.17886	22.22491
C	16.09196	10.53799	23.23981
C	16.72786	12.84538	23.52711
C	16.42129	14.59479	21.73120
C	16.63663	11.54480	24.06223
C	17.08368	11.25520	25.47913
C	12.91024	16.03914	22.49625
C	13.35835	16.93486	23.50703
C	12.71946	14.67634	22.80575
C	13.58968	16.41334	24.79750
C	13.58351	18.40073	23.22254
C	12.95893	14.19297	24.09786
C	13.39776	15.05670	25.12359
C	13.65795	14.53447	26.51993
C	15.74528	21.16770	13.72719
C	15.07993	22.42568	13.72760
C	16.62838	20.84697	12.67383
C	15.34472	23.31603	12.66469
C	14.12188	22.82506	14.82510
C	16.87010	21.75745	11.63780
C	16.22977	23.01486	11.61241
C	16.49105	24.00045	10.49337
C	19.64069	17.53207	11.56254
C	20.97803	18.02035	11.61507
C	18.71108	18.13563	10.69218
C	21.31636	19.11111	10.78876
C	22.02418	17.38338	12.49760
C	19.08920	19.20950	9.87197
C	20.40231	19.71977	9.90507
C	20.83287	20.86351	9.01166
C	17.05907	13.62691	7.87560
C	18.05634	14.37932	7.19208
C	15.87980	13.25991	7.19272
C	17.79664	14.75888	5.85847
C	19.36329	14.76409	7.83874
C	15.65820	13.64832	5.86507
C	16.61289	14.42071	5.17376

C	16.37021	14.88906	3.75567
C	14.46386	17.90896	9.24339
C	14.73551	19.20157	8.73943
C	13.86154	16.93837	8.40229
C	14.41500	19.54257	7.41916
C	13.55965	17.31382	7.07404
C	13.55029	15.54662	8.88180
C	13.82052	18.59736	6.55649
C	13.50373	18.94210	5.11718
C	9.53853	12.43932	18.44183
C	8.21374	12.30123	17.96918
C	10.04351	11.51213	19.39176
C	7.38848	11.26560	18.42327
C	9.18213	10.48314	19.83192
C	11.44602	11.60064	19.92431
C	7.85959	10.33407	19.37215
C	6.96552	9.23108	19.89680
H	20.37215	10.23309	15.92164
H	22.75229	10.05163	16.63547
H	21.45373	8.62321	20.51745
H	18.09096	7.91340	19.64929
H	18.14328	9.54052	20.37129
H	19.21350	8.24694	21.02679
H	24.40305	8.97746	18.28404
H	23.84733	8.54938	19.94168
H	24.06299	10.26759	19.47781
H	15.92676	7.38587	14.47449
H	16.11860	5.18244	15.62485
H	13.56985	6.65822	18.80586
H	13.77473	10.05267	18.08852
H	12.71087	8.80301	18.83178
H	12.31646	9.49912	17.21844
H	15.42185	3.65028	17.39130
H	13.97499	4.06388	18.37600
H	15.60692	4.52609	18.94484
H	15.92442	10.41622	12.32034
H	15.41910	8.58502	10.72074
H	19.63468	8.31651	9.72761
H	20.90252	10.21189	12.39244
H	20.65408	11.36883	11.06131
H	21.23734	9.70194	10.69514
H	16.15752	6.84652	9.19014
H	17.87740	6.32473	9.26800
H	17.36479	7.54080	8.05990
H	13.22915	10.00593	12.55874
H	11.36153	8.98346	8.05017
H	10.98803	12.39446	8.80702
H	11.27117	11.23018	7.45634
H	12.61962	12.22442	8.12198
H	12.77360	7.65456	11.93072
H	11.35194	6.63214	8.50798
H	11.01061	6.23371	10.22695
H	12.67428	6.07911	9.59074
H	9.36137	11.82540	12.04409
H	8.04087	7.09697	12.94393
H	8.71632	8.83645	15.95416
H	10.26137	8.18310	15.35424
H	8.75759	7.21320	15.16364

H	8.29245	10.47905	10.24154
H	7.01295	6.91075	10.76526
H	8.19446	7.57418	9.58778
H	6.63521	8.41069	9.84721
H	11.34201	16.78560	11.20836
H	6.73671	15.31431	9.97962
H	7.58297	13.96770	13.02894
H	6.20882	14.77232	12.18074
H	7.12094	15.62037	13.49159
H	10.56182	17.02564	8.85953
H	7.05312	15.96865	7.70041
H	8.73312	15.74498	7.10569
H	8.13426	17.38721	7.48186
H	9.10816	19.23061	14.02317
H	8.69062	21.21063	9.46270
H	11.79139	22.06275	10.96650
H	10.94485	21.79322	9.39326
H	11.99205	20.51465	10.11279
H	6.88609	19.29052	12.90602
H	6.28426	20.95293	9.51711
H	5.46768	20.60330	11.08195
H	6.00703	19.25706	10.03411
H	8.77615	17.66460	18.89788
H	8.11598	19.18132	20.76653
H	11.71743	21.50367	20.10864
H	12.59678	20.26962	16.97458
H	13.42899	19.19347	18.11883
H	13.28879	20.95020	18.49624
H	8.77231	20.94883	22.39409
H	8.93162	22.32274	21.25433
H	10.34453	21.80587	22.22464
H	15.92058	19.78860	17.82311
H	15.91362	22.20065	18.39177
H	18.06798	21.32591	22.05400
H	17.57494	17.88339	22.14620
H	18.74497	19.17088	22.62054
H	19.09305	18.07005	21.23439
H	16.71636	24.05933	19.79855
H	17.90018	23.74493	21.11525
H	16.14550	23.60444	21.43518
H	18.91383	20.58535	17.26210
H	19.90498	22.00827	19.03228
H	23.59517	19.74404	18.76069
H	22.95062	18.15666	15.69330
H	22.43261	17.02342	16.96262
H	23.90267	18.03696	17.22193
H	22.25021	22.91153	19.96300
H	23.53663	21.67789	20.20654
H	22.00067	21.57690	21.12769
H	18.43010	13.42688	19.27166
H	19.29117	13.12456	21.58757
H	23.35124	13.42019	20.08828
H	22.64055	12.93206	16.69282
H	23.83151	13.68326	17.82363
H	22.64618	14.69563	16.91485
H	21.44141	13.75116	23.13702
H	23.02531	13.23354	22.46179
H	21.73616	12.02428	22.77804

H	15.23883	10.03708	21.30445
H	16.00299	9.50502	23.61890
H	17.16413	13.64829	24.14769
H	15.41719	15.05095	21.56633
H	16.95655	14.64992	20.76016
H	16.96119	15.23095	22.46289
H	17.20243	10.16414	25.65502
H	16.34519	11.63213	26.22533
H	18.05496	11.74634	25.71173
H	12.38275	13.99037	22.01221
H	13.93290	17.10921	25.58406
H	14.38596	18.55145	22.46281
H	13.87652	18.94683	24.14492
H	12.67045	18.87872	22.80192
H	12.80523	13.12061	24.30694
H	13.97183	15.34742	27.20938
H	14.46118	13.76161	26.52080
H	12.75047	14.05518	26.95337
H	17.13831	19.86981	12.66603
H	14.83535	24.29635	12.67059
H	13.23968	22.14587	14.85386
H	13.74972	23.86069	14.66964
H	14.60170	22.77114	15.82820
H	17.58192	21.47794	10.84279
H	15.93528	24.95050	10.64732
H	16.18314	23.58853	9.50484
H	17.57379	24.25064	10.41415
H	17.67439	17.76227	10.66080
H	22.35359	19.49067	10.82965
H	22.12120	16.29454	12.28762
H	21.74872	17.47416	13.57289
H	23.01524	17.86411	12.34921
H	18.34101	19.65386	9.19292
H	21.40399	21.63361	9.57749
H	19.95931	21.36483	8.54177
H	21.49592	20.51147	8.18669
H	15.12875	12.64575	7.71765
H	18.57066	15.34141	5.32707
H	19.89280	13.87523	8.24840
H	19.20264	15.45080	8.70343
H	20.03283	15.27254	7.11283
H	14.72728	13.33851	5.35901
H	17.31995	14.97703	3.18387
H	15.88452	15.89307	3.73987
H	15.70021	14.19407	3.20355
H	15.19482	19.94653	9.40973
H	14.62855	20.56311	7.05643
H	13.09864	16.55700	6.41528
H	14.48184	14.99023	9.13557
H	13.01378	14.96380	8.10547
H	12.92980	15.55316	9.80311
H	13.12352	19.98316	5.01922
H	12.73914	18.25698	4.69050
H	14.41062	18.86623	4.47224
H	7.83489	13.02809	17.23286
H	6.35719	11.18663	18.03713
H	9.57565	9.75703	20.56607
H	11.61530	12.56869	20.45283

H	12.20064	11.57920	19.10839
H	11.66880	10.77284	20.62943
H	6.33684	8.79409	19.08933
H	6.26755	9.60980	20.68064
H	7.55561	8.40733	20.35401

Ag$_{13}$Au$_{12}$DMBT$_{18}$_VI

349

Au	14.71152	17.68881	14.59325
Au	17.82218	19.04381	15.32933
Au	19.76220	16.07261	16.28909
Au	17.19814	13.87296	16.42273
Au	13.27769	16.61838	17.00373
Au	11.37246	18.94840	15.17883
Au	13.22272	18.65748	12.16608
Au	14.89647	15.41480	12.47072
Au	16.25219	16.73589	16.93121
Au	14.59389	17.01905	19.90557
Au	11.45871	15.20776	19.38860
Au	12.44325	13.69320	16.33942
Ag	14.89659	12.15739	16.01888
Ag	12.20313	10.75808	15.20304
Ag	10.22557	13.36537	14.36093
Ag	12.44703	16.05264	14.05368
Ag	16.29007	13.21134	13.57007
Ag	17.65200	11.04830	15.25224
Ag	16.67276	11.38721	18.25770
Ag	14.80631	14.42921	18.15804
Ag	13.25809	13.12590	13.62197
Ag	15.09707	12.98837	10.66891
Ag	17.85255	14.53915	11.46301
Ag	17.23768	16.12182	14.27338
Ag	14.79669	14.89949	15.29282
S	15.67278	20.00413	14.97430
S	20.08253	18.36946	15.67975
S	19.71753	13.71970	16.67815
S	11.70036	20.20216	13.18664
S	14.85480	17.46900	10.90120
S	11.00602	17.76443	17.19403
S	16.86076	17.47421	19.26307
S	12.42191	16.78932	20.88614
S	10.28360	14.00403	17.71538
S	14.46837	9.81621	15.12177
S	9.78917	11.05605	15.04904
S	9.95567	15.73171	13.82168
S	17.90957	9.56452	17.20532
S	15.04551	12.42703	19.74402
S	18.30487	11.79817	12.99338
S	12.76789	12.47502	11.22825
S	17.28181	13.05216	9.57247
S	19.31138	16.00420	12.79291
C	19.64562	9.59305	17.66156
C	20.63744	9.85194	16.69163
C	20.03800	9.21287	18.97746
C	21.99945	9.73284	17.00109
C	21.41539	9.11258	19.25668
C	19.02161	8.91674	20.05316
C	22.41567	9.36395	18.29601
C	23.88218	9.26784	18.65684
C	14.61555	8.29412	16.06962
C	15.38875	7.28368	15.45612
C	14.01702	8.04701	17.33539

C	15.58100	6.04311	16.07776
C	14.22613	6.78424	17.92786
C	13.18669	9.08005	18.04679
C	15.00147	5.76908	17.33198
C	15.21432	4.44468	18.03295
C	17.91665	10.42881	11.89180
C	16.61782	9.89674	11.77377
C	18.97105	9.89192	11.09877
C	16.34663	8.85062	10.87866
C	18.66502	8.84002	10.21387
C	20.37832	10.43469	11.18266
C	17.36771	8.30350	10.07781
C	17.09110	7.18890	9.09135
C	12.59661	10.74393	10.76357
C	12.32722	10.41805	9.40344
C	12.66658	9.70866	11.71707
C	12.14880	9.06010	9.06564
C	12.22805	11.48216	8.33788
C	12.48705	8.36905	11.34965
C	12.22862	8.01647	10.00874
C	12.07203	6.56804	9.59809
C	9.25819	10.09571	13.62366
C	8.93700	8.72101	13.80485
C	9.07009	10.69186	12.35918
C	8.42757	8.00788	12.70029
C	9.13509	8.03038	15.13342
C	8.56301	9.95350	11.28234
C	8.22929	8.59238	11.43375
C	7.71101	7.77958	10.26752
C	9.34130	15.78680	12.13466
C	8.03727	15.29511	11.84037
C	10.09520	16.39800	11.11022
C	7.56161	15.42279	10.51770
C	7.16942	14.65387	12.89593
C	9.59082	16.51478	9.80951
C	8.30912	16.02236	9.48585
C	7.75495	16.15389	8.08325
C	10.16661	20.17498	12.23427
C	10.13449	20.85423	10.98603
C	8.99583	19.58140	12.74683
C	8.90346	20.90627	10.29949
C	11.36785	21.48962	10.39021
C	7.79074	19.65656	12.03784
C	7.72283	20.31950	10.79510
C	6.43164	20.36780	10.00787
C	10.73966	18.97554	18.50314
C	9.54848	18.80194	19.24022
C	11.62924	20.03498	18.83224
C	9.21935	19.67000	20.28992
C	11.26477	20.88852	19.89434
C	12.92618	20.24929	18.10305
C	10.07446	20.73577	20.63483
C	9.72341	21.70310	21.74527
C	16.95290	19.25041	19.58365
C	16.52464	20.19972	18.63906
C	17.49508	19.68220	20.82740
C	16.61261	21.57313	18.91133
C	17.56439	21.06813	21.07000

C	17.98304	18.69961	21.86612
C	17.12791	22.03418	20.13859
C	17.19368	23.51053	20.46665
C	20.75689	19.29425	17.07925
C	20.08500	20.42051	17.59235
C	22.04304	18.95159	17.58228
C	20.65793	21.19879	18.60625
C	22.58614	19.75392	18.60641
C	22.82292	17.77266	17.05759
C	21.92085	20.87466	19.14052
C	22.53027	21.68306	20.26516
C	20.30999	13.54330	18.37172
C	19.41789	13.46265	19.45960
C	21.70979	13.43025	18.59413
C	19.89180	13.27241	20.76450
C	22.15332	13.25515	19.92175
C	22.70418	13.49256	17.45949
C	21.27503	13.16829	21.01937
C	21.79187	12.94665	22.42445
C	15.80991	12.12844	21.35348
C	15.81377	10.78620	21.80009
C	16.35024	13.13893	22.19550
C	16.34014	10.43532	23.05027
C	16.87349	12.75028	23.44835
C	16.38470	14.58558	21.78517
C	16.87862	11.41777	23.90625
C	17.41375	11.06559	25.27770
C	12.72679	16.05788	22.50790
C	13.02839	16.93445	23.58497
C	12.62061	14.67133	22.73517
C	13.21430	16.36548	24.86250
C	13.15018	18.42666	23.38548
C	12.81075	14.14097	24.01713
C	13.11264	14.98243	25.10869
C	13.33491	14.40928	26.49133
C	15.82788	21.09353	13.54686
C	15.09905	22.31417	13.56230
C	16.66855	20.78824	12.45636
C	15.25236	23.18728	12.46347
C	14.19386	22.69486	14.71026
C	16.80330	21.68461	11.38917
C	16.09444	22.90525	11.37141
C	16.24945	23.87861	10.22247
C	19.64668	17.37433	11.67360
C	20.97936	17.87672	11.60212
C	18.66041	17.91192	10.82133
C	21.25873	18.89151	10.66460
C	22.07860	17.33582	12.48507
C	18.97919	18.90926	9.88683
C	20.28968	19.41671	9.78553
C	20.66222	20.45897	8.75233
C	17.16389	13.93747	8.01604
C	18.26937	14.68672	7.51928
C	16.01610	13.78705	7.20558
C	18.15372	15.27190	6.24076
C	19.53809	14.86529	8.31568
C	15.93388	14.38246	5.94098
C	17.00516	15.14759	5.43499

C	16.91275	15.83014	4.08764
C	14.29168	17.77995	9.20698
C	14.63797	19.03831	8.66512
C	13.56215	16.85022	8.42237
C	14.26154	19.38891	7.36207
C	13.20217	17.23617	7.11218
C	13.18519	15.49007	8.94147
C	13.53185	18.48835	6.55795
C	13.14332	18.84421	5.13901
C	9.38081	12.60937	18.41071
C	8.02615	12.52144	18.02000
C	9.92851	11.62855	19.27949
C	7.21030	11.48086	18.47940
C	9.07587	10.59655	19.72724
C	11.36329	11.67241	19.72133
C	7.72237	10.49713	19.35083
C	6.84025	9.38867	19.88356
H	20.32813	10.14272	15.67327
H	22.75035	9.92617	16.21554
H	21.71849	8.81663	20.27737
H	18.30853	8.12402	19.73458
H	18.40223	9.81486	20.28478
H	19.51734	8.59109	20.99286
H	24.51533	9.10984	17.75660
H	24.07779	8.43236	19.36503
H	24.23974	10.20248	19.14970
H	15.84621	7.48444	14.47361
H	16.19768	5.27718	15.57652
H	13.75660	6.58984	18.90958
H	13.77783	9.99806	18.26572
H	12.79532	8.68661	19.00856
H	12.31479	9.40759	17.42986
H	15.67475	3.69429	17.35458
H	14.25662	4.02063	18.41094
H	15.88894	4.55270	18.91419
H	15.80561	10.29516	12.40312
H	15.31576	8.46471	10.80650
H	19.48339	8.42675	9.59638
H	20.77830	10.38111	12.22035
H	20.41058	11.50912	10.89145
H	21.06339	9.87070	10.51316
H	16.04499	6.82380	9.17616
H	17.77000	6.31995	9.25058
H	17.24180	7.52757	8.04002
H	12.86843	9.95697	12.77179
H	11.93013	8.81141	8.01134
H	11.46847	12.25178	8.59963
H	11.96402	11.04019	7.35313
H	13.19387	12.02789	8.22622
H	12.55226	7.58838	12.12680
H	11.64121	6.47640	8.57747
H	11.41000	6.01468	10.30108
H	13.05199	6.03585	9.59335
H	9.33299	11.75438	12.22083
H	8.17164	6.94213	12.84291
H	8.59448	8.55478	15.95256
H	10.21028	8.02436	15.42917
H	8.78374	6.97701	15.09289

H	8.43141	10.44911	10.30543
H	7.13172	6.89382	10.60888
H	8.54916	7.40350	9.63505
H	7.05384	8.38592	9.60578
H	11.09345	16.80263	11.35170
H	6.55144	15.03667	10.28904
H	7.63210	13.71925	13.29566
H	6.16903	14.39325	12.48834
H	7.03366	15.32395	13.77437
H	10.21119	16.99656	9.03465
H	6.77860	15.63284	7.97898
H	8.44997	15.72444	7.32638
H	7.59840	17.22167	7.80354
H	9.03868	19.05338	13.71363
H	8.87114	21.43985	9.33265
H	11.86621	22.17660	11.11002
H	11.11771	22.06135	9.47104
H	12.12888	20.71979	10.12004
H	6.88807	19.18368	12.46068
H	6.45045	21.16807	9.23621
H	5.55592	20.54861	10.66976
H	6.24578	19.40242	9.48213
H	8.87819	17.96626	18.98205
H	8.27916	19.51645	20.84712
H	11.95494	21.71066	20.15492
H	12.75993	20.42292	17.01386
H	13.57510	19.34433	18.16775
H	13.48849	21.10948	18.52214
H	8.96295	21.27588	22.43458
H	9.30343	22.65305	21.33859
H	10.61727	21.97661	22.34838
H	16.10927	19.85968	17.67828
H	16.27230	22.29390	18.14789
H	17.98222	21.40735	22.03527
H	17.15342	18.05181	22.23090
H	18.42179	19.22813	22.73978
H	18.75194	18.01296	21.44774
H	17.04456	24.13673	19.56095
H	18.17288	23.78863	20.91715
H	16.40713	23.79897	21.20262
H	19.09226	20.68417	17.19351
H	20.10249	22.07123	18.98992
H	23.58542	19.48764	18.99546
H	22.93560	17.81019	15.95087
H	22.29400	16.81557	17.28204
H	23.83427	17.72608	17.51471
H	22.24792	22.75690	20.19736
H	23.64021	21.61805	20.26236
H	22.18320	21.31825	21.26076
H	18.33549	13.55843	19.27026
H	19.16860	13.20362	21.59487
H	23.24096	13.17809	20.10112
H	22.52287	12.67491	16.72719
H	23.74541	13.40156	17.83720
H	22.62020	14.44456	16.88816
H	21.31539	13.64343	23.14996
H	22.89247	13.09186	22.48430
H	21.57130	11.91288	22.77886

H	15.39292	10.00690	21.14388
H	16.33228	9.37645	23.36242
H	17.30502	13.53755	24.09212
H	15.35719	14.98969	21.63622
H	16.91685	14.73068	20.82011
H	16.88621	15.21059	22.55345
H	17.70347	9.99409	25.34015
H	16.65271	11.24688	26.07315
H	18.30583	11.67662	25.53988
H	12.39161	14.00451	21.88872
H	13.44702	17.04248	25.70409
H	13.99068	18.67528	22.69620
H	13.33039	18.94537	24.35142
H	12.23463	18.85244	22.91793
H	12.72940	13.05098	24.16585
H	13.48761	15.20967	27.24683
H	14.23091	13.74731	26.51491
H	12.46951	13.79053	26.82073
H	17.23063	19.84083	12.44837
H	14.68937	24.13763	12.47297
H	13.34732	21.97908	14.81405
H	13.76348	23.70778	14.55692
H	14.73877	22.68678	15.68086
H	17.48356	21.42500	10.56028
H	15.61937	24.78303	10.36426
H	15.95900	23.41522	9.25191
H	17.30574	24.21595	10.11400
H	17.62417	17.54073	10.88353
H	22.29088	19.28426	10.61789
H	22.20528	16.23792	12.34990
H	21.84003	17.49423	13.56164
H	23.04764	17.83314	12.26327
H	18.18609	19.28694	9.21875
H	21.27570	21.27554	9.19576
H	19.75987	20.92074	8.29645
H	21.26266	20.01791	7.92218
H	15.17971	13.17320	7.57860
H	19.01307	15.85098	5.85782
H	19.97774	13.88642	8.61072
H	19.34982	15.42015	9.26600
H	20.29689	15.43441	7.73761
H	15.02078	14.24566	5.33640
H	17.91856	16.07487	3.68225
H	16.34381	16.78704	4.15780
H	16.38665	15.19496	3.34052
H	15.19975	19.75094	9.29132
H	14.53900	20.38137	6.96623
H	12.63138	16.51553	6.49990
H	14.09315	14.88633	9.17288
H	12.58058	14.92679	8.20109
H	12.60720	15.54747	9.88850
H	12.85452	19.91493	5.04980
H	12.28987	18.22820	4.78113
H	13.98946	18.67576	4.43188
H	7.61639	13.28715	17.34152
H	6.15693	11.43410	18.15276
H	9.50140	9.82740	20.39645
H	11.58248	12.60758	20.28900

H	12.05783	11.69025	18.85270
H	11.62336	10.80476	20.36243
H	6.13695	9.01620	19.10608
H	6.21875	9.73883	20.74142
H	7.44052	8.52524	20.24407

Ag$_{13}$Au$_{12}$DMBT$_{18}$_VII
349

Ag	14.72648	17.71232	14.57858
Ag	17.59504	18.95618	15.22642
Ag	19.47621	16.26132	16.16110
Ag	17.34862	13.85252	16.31068
Ag	13.32514	16.50001	16.94806
Ag	11.63194	18.60096	15.22288
Ag	12.98304	18.59861	12.37538
Ag	14.98200	15.36081	12.29098
Ag	16.40342	16.68156	16.84805
Ag	14.85749	16.78901	19.60052
Ag	11.77451	15.04091	19.16315
Ag	12.51180	13.59219	16.21704
Ag	15.06477	12.07636	15.92645
Au	12.23035	10.59860	14.92737
Au	10.12045	13.49616	14.13235
Au	12.52412	15.95260	14.03788
Au	16.43497	13.17084	13.49997
Au	18.07213	10.78360	15.25851
Au	16.44353	11.18641	18.48272
Au	14.92075	14.26610	17.96863
Au	13.44288	13.08554	13.50498
Au	15.11451	12.85435	10.46150
Au	18.13303	14.64526	11.14752
Au	17.24282	16.11143	14.12325
Au	14.89853	14.89788	15.19034
S	15.43336	20.10163	15.03718
S	19.99153	18.57810	15.50039
S	19.85116	13.85033	16.47995
S	11.49568	20.23667	13.39663
S	14.75579	17.58249	11.07071
S	11.05025	17.55976	17.36111
S	17.18225	17.43292	19.11790
S	12.70361	16.64129	20.74637
S	10.36810	13.84395	17.57329
S	14.46930	9.77475	14.95241
S	9.92528	11.21609	14.82749
S	10.03557	15.82117	13.59844
S	17.74922	9.58311	17.28483
S	15.02263	12.48946	19.88317
S	18.41197	11.68234	13.08519
S	12.82587	12.61513	11.08921
S	17.37451	12.90576	9.68715
S	19.26095	16.18556	12.57110
C	19.33442	9.44432	18.13875
C	20.51415	9.98142	17.59089
C	19.38872	8.68159	19.33912
C	21.75196	9.76514	18.21321
C	20.64901	8.49011	19.93857
C	18.14703	8.09780	19.96922
C	21.84247	9.01492	19.40152
C	23.16724	8.79456	20.09880
C	14.53806	8.18857	15.80521
C	15.23020	7.17538	15.10748
C	13.98413	7.91099	17.08516
C	15.38105	5.89485	15.65746

C	14.14645	6.60904	17.60176
C	13.26088	8.95671	17.88759
C	14.83588	5.58591	16.91876
C	14.98367	4.21051	17.53332
C	18.06049	10.25665	12.02836
C	16.74615	9.85878	11.72520
C	19.16431	9.55377	11.46947
C	16.50737	8.77558	10.86574
C	18.88821	8.47009	10.61269
C	20.59272	9.93865	11.77891
C	17.57689	8.06254	10.28996
C	17.33952	6.90124	9.34828
C	12.47320	10.91838	10.57281
C	11.85058	10.71579	9.31098
C	12.77128	9.81450	11.39437
C	11.55608	9.39030	8.92690
C	11.51527	11.86707	8.39189
C	12.45821	8.51179	10.98466
C	11.84565	8.27475	9.73636
C	11.52454	6.86706	9.28258
C	9.21303	10.24894	13.48003
C	8.87442	8.89074	13.73203
C	8.89987	10.83396	12.23776
C	8.22121	8.17562	12.70792
C	9.19882	8.22119	15.04571
C	8.24648	10.09305	11.24389
C	7.89445	8.74588	11.46121
C	7.21830	7.92810	10.38224
C	9.55399	15.88643	11.86311
C	8.20414	15.60579	11.51125
C	10.46488	16.29654	10.86935
C	7.83390	15.74176	10.15669
C	7.18644	15.17377	12.53864
C	10.05885	16.43765	9.53540
C	8.73014	16.15855	9.15313
C	8.28222	16.32440	7.71684
C	9.84807	20.08859	12.69147
C	9.59675	20.59503	11.38546
C	8.77788	19.57516	13.45563
C	8.27172	20.55691	10.90384
C	10.70228	21.15514	10.52377
C	7.47347	19.55291	12.94570
C	7.19536	20.04324	11.65325
C	5.79553	19.98932	11.08085
C	10.78368	18.85874	18.57536
C	9.56813	18.77764	19.29005
C	11.68980	19.91930	18.85375
C	9.23760	19.72908	20.26476
C	11.32442	20.85931	19.83983
C	13.00685	20.05257	18.14125
C	10.11232	20.79476	20.55681
C	9.76325	21.84891	21.58628
C	17.16390	19.19103	19.50705
C	16.62463	20.15141	18.63095
C	17.73701	19.61588	20.74201
C	16.62681	21.51462	18.96097
C	17.72155	20.99177	21.04302
C	18.34856	18.63192	21.71109

C	17.17081	21.96263	20.17980
C	17.16338	23.42657	20.56477
C	20.56243	19.60820	16.85819
C	19.97004	20.87152	17.07313
C	21.68659	19.22376	17.64208
C	20.46843	21.74922	18.04300
C	22.16024	20.13061	18.61344
C	22.37057	17.89203	17.46114
C	21.57681	21.39238	18.83781
C	22.09852	22.31574	19.91698
C	20.51498	13.71534	18.14390
C	19.68384	13.48696	19.26063
C	21.92547	13.78470	18.32553
C	20.22295	13.34455	20.54546
C	22.43519	13.64614	19.63367
C	22.86486	13.98644	17.15957
C	21.61494	13.42748	20.75754
C	22.20386	13.25746	22.14144
C	15.81868	12.25507	21.49881
C	15.64884	10.98321	22.08878
C	16.53143	13.26332	22.19871
C	16.18909	10.69278	23.34936
C	17.06112	12.93700	23.46564
C	16.71970	14.64605	21.63772
C	16.91110	11.66977	24.06353
C	17.48533	11.38600	25.43487
C	13.06724	15.93462	22.35686
C	13.54075	16.79223	23.39050
C	12.82651	14.57341	22.64142
C	13.75037	16.23656	24.66997
C	13.81285	18.25605	23.14017
C	13.04442	14.05444	23.92378
C	13.51277	14.88032	24.96705
C	13.76954	14.31898	26.34866
C	15.61697	21.22304	13.64203
C	14.92060	22.46381	13.67909
C	16.46560	20.93495	12.55155
C	15.11767	23.36793	12.61286
C	13.99827	22.82846	14.81799
C	16.64129	21.85902	11.51363
C	15.96788	23.09911	11.52381
C	16.16524	24.10339	10.40811
C	19.53198	17.62339	11.50935
C	20.83790	18.18948	11.47357
C	18.51568	18.14174	10.68303
C	21.06315	19.26329	10.58779
C	21.96299	17.66740	12.33553
C	18.78224	19.20240	9.80452
C	20.06512	19.78299	9.73880
C	20.37766	20.90720	8.77427
C	17.40060	13.48290	7.97596
C	18.63118	13.87961	7.38269
C	16.23580	13.40901	7.18438
C	18.62064	14.22291	6.01404
C	19.92164	13.93504	8.16272
C	16.26506	13.74972	5.82607
C	17.46213	14.17604	5.21489
C	17.49424	14.58578	3.75853

C	14.34294	18.06216	9.37962
C	14.50085	19.43179	9.06017
C	13.91090	17.15760	8.37395
C	14.23520	19.90864	7.77007
C	13.65850	17.67245	7.08255
C	13.72138	15.69065	8.65097
C	13.81039	19.03197	6.74913
C	13.55598	19.53101	5.34312
C	9.52465	12.42436	18.27936
C	8.17031	12.27506	17.90000
C	10.09869	11.49152	19.18439
C	7.38859	11.22723	18.40058
C	9.28141	10.44930	19.67367
C	11.53052	11.59863	19.62389
C	7.93172	10.29066	19.30545
C	7.08521	9.17742	19.88466
H	20.45482	10.57975	16.66685
H	22.66263	10.19611	17.76404
H	20.69580	7.89622	20.86925
H	17.55519	7.50495	19.23665
H	17.46978	8.90323	20.34023
H	18.40563	7.44435	20.82971
H	24.02278	9.04990	19.43752
H	23.28932	7.73733	20.42526
H	23.25397	9.42868	21.01162
H	15.65773	7.40565	14.11794
H	15.93187	5.12385	15.09133
H	13.71328	6.38942	18.59470
H	13.93641	9.81262	18.12219
H	12.88169	8.54085	18.84457
H	12.40012	9.38717	17.32342
H	15.50806	3.51225	16.84611
H	13.99363	3.76319	17.78040
H	15.56582	4.24687	18.48271
H	15.89959	10.40170	12.17456
H	15.46538	8.49203	10.63972
H	19.74273	7.92245	10.17534
H	20.80802	9.85491	12.86847
H	20.80062	10.99593	11.50114
H	21.30707	9.28569	11.23265
H	16.25580	6.68260	9.23916
H	17.83924	5.97254	9.70758
H	17.74314	7.11256	8.33118
H	13.25364	9.97796	12.37139
H	11.07277	9.22817	7.94653
H	10.85508	12.61211	8.88919
H	11.00924	11.50612	7.47065
H	12.43222	12.42309	8.08928
H	12.69316	7.66885	11.65682
H	10.87505	6.86541	8.38077
H	11.00488	6.29173	10.08096
H	12.44995	6.30002	9.02639
H	9.17447	11.88659	12.05564
H	7.94966	7.12222	12.90234
H	8.79861	8.79782	15.90952
H	10.30152	8.15487	15.20145
H	8.78417	7.19118	15.08348
H	8.00959	10.57617	10.28055

H	6.59015	7.11789	10.81347
H	7.96798	7.44141	9.71475
H	6.56956	8.55949	9.73653
H	11.50938	16.50902	11.15458
H	6.78791	15.51782	9.87960
H	7.47339	14.20511	13.01225
H	6.18094	15.05470	12.08111
H	7.11449	15.91025	13.36977
H	10.79297	16.77109	8.78238
H	7.26075	15.91621	7.55648
H	8.97074	15.80792	7.01085
H	8.26346	17.39853	7.41995
H	8.97806	19.19049	14.46983
H	8.07532	20.95117	9.89031
H	11.25778	21.96688	11.04430
H	10.29978	21.55745	9.56941
H	11.45879	20.37378	10.27673
H	6.65868	19.14564	13.56876
H	5.66778	20.70718	10.24144
H	5.02775	20.22265	11.85161
H	5.56028	18.97346	10.68513
H	8.87838	17.94607	19.07304
H	8.28202	19.63752	20.80973
H	12.03045	21.68079	20.05637
H	12.87517	20.16548	17.03918
H	13.63545	19.14129	18.28090
H	13.58443	20.92400	18.51352
H	8.91172	21.52880	22.22514
H	9.47179	22.81144	21.10353
H	10.62539	22.07128	22.25406
H	16.19160	19.83133	17.67049
H	16.19759	22.23804	18.24646
H	18.16467	21.31869	22.00148
H	17.59460	17.89628	22.07278
H	18.77684	19.15477	22.59347
H	19.15579	18.03623	21.22943
H	16.81960	24.06657	19.72374
H	18.17615	23.77751	20.86705
H	16.48512	23.61911	21.42850
H	19.10059	21.16616	16.46186
H	19.98032	22.72849	18.18433
H	23.03342	19.83113	19.22118
H	22.70690	17.74065	16.41089
H	21.67718	17.04807	17.69195
H	23.25290	17.80064	18.12973
H	21.99830	23.38463	19.62530
H	23.17001	22.12065	20.14206
H	21.53295	22.18499	20.86963
H	18.59417	13.41369	19.10840
H	19.54317	13.16320	21.39553
H	23.52958	13.70852	19.77575
H	22.75657	13.17282	16.40716
H	23.92302	14.01320	17.49878
H	22.64780	14.93242	16.61339
H	21.64520	13.85035	22.89998
H	23.26821	13.57697	22.17608
H	22.16497	12.19323	22.47268
H	15.08341	10.21159	21.54122

H	16.04701	9.68700	23.78177
H	17.61885	13.72116	24.00841
H	15.74244	15.17723	21.55745
H	17.15198	14.62628	20.61540
H	17.38359	15.25750	22.28322
H	17.51988	10.29532	25.64558
H	16.87415	11.85977	26.23871
H	18.51833	11.78689	25.53785
H	12.46391	13.91508	21.83566
H	14.11386	16.90370	25.47235
H	14.61778	18.39788	22.38126
H	14.12506	18.77085	24.07427
H	12.91612	18.77233	22.73032
H	12.85132	12.98444	24.11189
H	13.96846	15.12491	27.08751
H	14.65215	13.63740	26.35033
H	12.90341	13.72436	26.71749
H	17.00368	19.97360	12.51851
H	14.58148	24.33328	12.64590
H	13.12617	22.13679	14.86515
H	13.60702	23.86162	14.69742
H	14.51532	22.75881	15.80142
H	17.32706	21.60489	10.68748
H	15.55735	25.01957	10.57071
H	15.87618	23.67993	9.41887
H	17.23133	24.41650	10.32402
H	17.50162	17.71115	10.72741
H	22.07521	19.70575	10.55662
H	22.13063	16.57923	12.17176
H	21.72890	17.79579	13.41742
H	22.91003	18.20708	12.11921
H	17.97107	19.57431	9.15566
H	20.98397	21.70553	9.25779
H	19.45031	21.37432	8.37836
H	20.96293	20.54097	7.89816
H	15.29561	13.06880	7.64859
H	19.57414	14.53687	5.55325
H	20.12876	12.97087	8.67906
H	19.87839	14.71082	8.96449
H	20.78006	14.17017	7.49812
H	15.33694	13.68127	5.23267
H	18.53123	14.59715	3.35862
H	17.07493	15.60953	3.61720
H	16.88973	13.89849	3.12573
H	14.83470	20.12756	9.84797
H	14.36161	20.98432	7.55587
H	13.32366	16.96584	6.30219
H	14.67864	15.20646	8.94909
H	13.33548	15.16066	7.75433
H	13.01604	15.51262	9.49092
H	13.04930	20.52172	5.34507
H	12.92117	18.82380	4.76631
H	14.50861	19.65537	4.77583
H	7.73473	13.00175	17.19543
H	6.33583	11.13689	18.08007
H	9.73065	9.72642	20.37851
H	11.73054	12.57857	20.12098
H	12.23045	11.56308	18.76052

H	11.80700	10.78919	20.33107
H	6.37471	8.76809	19.13239
H	6.47279	9.53551	20.74605
H	7.71154	8.33701	20.25570

Ag$_{24}$Au$_{1}$DMBT$_{18}$_Au_in_core
349

Ag	14.77020	17.54086	14.62672
Ag	17.62339	18.72086	15.21657
Ag	19.38242	16.07237	16.21527
Ag	17.25377	13.71036	16.38706
Ag	13.33587	16.47310	17.01662
Ag	11.70406	18.55114	15.22178
Ag	13.25123	18.51224	12.33438
Ag	14.83829	15.28428	12.42870
Ag	16.37056	16.54787	16.91639
Ag	14.75035	16.74734	19.71035
Ag	11.61654	15.10778	19.16760
Ag	12.47429	13.60372	16.39810
Ag	14.91304	12.00848	15.99139
Ag	12.14942	10.66347	15.10681
Ag	10.24451	13.59329	14.43715
Ag	12.44329	15.82780	14.13405
Ag	16.28327	13.03800	13.55742
Ag	17.71743	10.90336	15.22617
Ag	16.63790	11.18178	18.24454
Ag	14.87357	14.21414	18.09641
Ag	13.29515	12.99550	13.60768
Ag	15.16492	12.79870	10.64195
Ag	17.92914	14.34527	11.47060
Ag	17.21139	15.87939	14.14635
Au	14.82942	14.77076	15.27824
S	15.51434	19.95226	14.97815
S	20.01641	18.35251	15.51540
S	19.75575	13.66203	16.59074
S	11.83814	20.17938	13.40211
S	14.84300	17.33993	10.93216
S	11.07910	17.61293	17.39402
S	17.08871	17.28621	19.23204
S	12.56731	16.66306	20.78769
S	10.22849	13.83162	17.60651
S	14.36922	9.64578	15.23660
S	9.80467	11.20171	14.77872
S	9.92941	15.96721	13.87261
S	17.92032	9.41207	17.16551
S	15.09005	12.28035	19.76864
S	18.34804	11.68866	12.97666
S	12.85144	12.27629	11.21127
S	17.33310	12.93298	9.53787
S	19.35846	15.86040	12.78515
C	19.64045	9.50230	17.68336
C	20.64994	9.86350	16.76591
C	20.00394	9.09189	18.99748
C	22.00277	9.82618	17.12920
C	21.37333	9.06968	19.33016
C	18.96859	8.68892	20.01949
C	22.39108	9.43150	18.42516
C	23.84462	9.42990	18.84486
C	14.39533	8.19275	16.29706
C	15.15085	7.10572	15.80406
C	13.72064	8.07030	17.54274
C	15.24807	5.90787	16.52443

C	13.83708	6.84795	18.23769
C	12.90780	9.19192	18.12926
C	14.59049	5.75602	17.76128
C	14.70308	4.48027	18.56817
C	18.00496	10.31679	11.86240
C	16.72459	9.74132	11.74547
C	19.07398	9.82576	11.05957
C	16.48598	8.69484	10.84175
C	18.80117	8.76960	10.16874
C	20.45969	10.42238	11.13599
C	17.52264	8.18970	10.03329
C	17.28205	7.07139	9.04178
C	12.73118	10.53625	10.75759
C	12.46288	10.19424	9.40127
C	12.84809	9.51016	11.71555
C	12.32746	8.82908	9.07266
C	12.33130	11.24703	8.32800
C	12.70422	8.16318	11.35782
C	12.44189	7.79450	10.02219
C	12.31212	6.34035	9.62279
C	9.33298	10.45564	13.21176
C	9.03104	9.06519	13.16927
C	9.16530	11.23959	12.05118
C	8.56902	8.52498	11.95193
C	9.19483	8.18073	14.38229
C	8.70161	10.67034	10.85801
C	8.39637	9.29611	10.78523
C	7.93805	8.66335	9.48951
C	9.34927	15.98321	12.17180
C	8.04003	15.51005	11.87168
C	10.13295	16.54431	11.14102
C	7.58863	15.60607	10.53768
C	7.14303	14.91974	12.93271
C	9.65112	16.63536	9.82976
C	8.36427	16.15988	9.50091
C	7.83768	16.25605	8.08497
C	10.23534	20.19469	12.58557
C	10.11895	20.72528	11.27032
C	9.07488	19.77865	13.27333
C	8.83135	20.80283	10.69940
C	11.32394	21.18887	10.48868
C	7.81176	19.87083	12.67594
C	7.66625	20.38344	11.37044
C	6.30906	20.44772	10.70428
C	10.86289	18.98834	18.53427
C	9.61806	19.02700	19.20154
C	11.83118	19.99555	18.79831
C	9.31889	20.04613	20.11521
C	11.49394	21.00883	19.72090
C	13.18165	20.00570	18.13696
C	10.25433	21.06525	20.38838
C	9.93175	22.19952	21.33776
C	17.09246	19.04671	19.61620
C	16.86385	20.02443	18.62987
C	17.37435	19.45532	20.95322
C	16.89733	21.39051	18.94366
C	17.40004	20.83555	21.23459
C	17.63367	18.45119	22.05131

C	17.16177	21.82419	20.25730
C	17.16716	23.29366	20.62044
C	20.50360	19.50553	16.80895
C	20.18096	20.87021	16.63195
C	21.30438	19.11715	17.91942
C	20.63422	21.84461	17.52926
C	21.73863	20.12502	18.80656
C	21.70477	17.68436	18.16581
C	21.42264	21.48739	18.64244
C	21.88565	22.52275	19.64378
C	20.40055	13.55424	18.26334
C	19.56406	13.31896	19.37492
C	21.80680	13.66032	18.45865
C	20.09267	13.19757	20.66633
C	22.30600	13.54426	19.77305
C	22.75109	13.88057	17.30129
C	21.48051	13.31384	20.89059
C	22.05803	13.17666	22.28284
C	15.88199	11.99197	21.36710
C	15.85977	10.66065	21.84423
C	16.46840	13.00825	22.16911
C	16.41030	10.32567	23.08845
C	17.01358	12.63543	23.41724
C	16.52397	14.44430	21.72364
C	17.00109	11.31307	23.90368
C	17.57502	10.97588	25.26297
C	12.89794	15.96270	22.41182
C	13.14601	16.85507	23.49255
C	12.87845	14.57234	22.64896
C	13.36116	16.30107	24.77259
C	13.17903	18.35232	23.29428
C	13.09629	14.05579	23.93256
C	13.34160	14.91545	25.02409
C	13.58093	14.36085	26.41174
C	15.78355	21.03050	13.56153
C	15.19657	22.32688	13.58527
C	16.58535	20.65022	12.46380
C	15.44623	23.18794	12.49462
C	14.33434	22.79211	14.73421
C	16.81609	21.53358	11.40158
C	16.24713	22.82491	11.39507
C	16.50222	23.78390	10.25163
C	19.67979	17.22273	11.65137
C	21.00815	17.73500	11.57461
C	18.68578	17.74280	10.79784
C	21.27427	18.74793	10.63131
C	22.11392	17.20993	12.45866
C	18.99048	18.74429	9.86298
C	20.29463	19.26742	9.76015
C	20.64791	20.33190	8.74303
C	17.18212	13.88412	8.02170
C	18.27827	14.65126	7.53309
C	16.01657	13.76826	7.23198
C	18.13499	15.29072	6.28355
C	19.56881	14.78599	8.30279
C	15.90839	14.41481	5.99465
C	16.96937	15.20018	5.49820
C	16.84809	15.93947	4.18355

C	14.14174	17.66537	9.29942
C	14.38617	18.95130	8.76379
C	13.40087	16.72114	8.54117
C	13.90342	19.31140	7.49913
C	12.92956	17.11829	7.27001
C	13.11234	15.33761	9.05541
C	13.16210	18.39542	6.72352
C	12.66157	18.76133	5.34263
C	9.38690	12.42018	18.33732
C	8.08676	12.16749	17.84210
C	9.90906	11.59739	19.37165
C	7.30923	11.12014	18.34931
C	9.09636	10.55180	19.86199
C	11.27701	11.81842	19.95258
C	7.80151	10.28857	19.37668
C	6.95627	9.17607	19.95858
H	20.36385	10.17572	15.74726
H	22.76844	10.11017	16.38663
H	21.65509	8.75056	20.34987
H	18.30287	7.88456	19.63410
H	18.30237	9.54450	20.28143
H	19.44932	8.33277	20.95582
H	24.52134	9.26571	17.97774
H	24.05443	8.63996	19.59923
H	24.13061	10.40564	19.30354
H	15.67188	7.21187	14.83888
H	15.85034	5.07838	16.11544
H	13.30984	6.75178	19.20395
H	13.53492	10.09425	18.30878
H	12.45023	8.89358	19.09587
H	12.08192	9.50902	17.44603
H	15.08261	3.63832	17.94957
H	13.72149	4.17543	18.99524
H	15.40523	4.60205	19.42603
H	15.90088	10.10875	12.37939
H	15.46811	8.27631	10.76767
H	19.63114	8.38848	9.54636
H	20.86753	10.38316	12.17113
H	20.44932	11.49731	10.84500
H	21.16191	9.88578	10.46191
H	16.24738	6.67436	9.12261
H	17.98660	6.22285	9.19938
H	17.42506	7.41921	7.99250
H	13.06424	9.76923	12.76476
H	12.11851	8.56673	8.01972
H	11.55003	11.99541	8.58654
H	12.07784	10.79025	7.34734
H	13.28054	11.81957	8.20896
H	12.80085	7.38939	12.13877
H	11.83731	6.23102	8.62370
H	11.70211	5.76816	10.35672
H	13.30776	5.84028	9.57267
H	9.40508	12.31616	12.08808
H	8.33143	7.44652	11.91814
H	8.63249	8.57627	15.25745
H	10.26217	8.12682	14.70175
H	8.84637	7.14643	14.17360
H	8.57887	11.31172	9.96895

H	7.34980	7.73702	9.66972
H	8.80867	8.38317	8.85134
H	7.30827	9.36014	8.89351
H	11.14097	16.92513	11.38246
H	6.57525	15.23202	10.30395
H	7.58179	13.99138	13.37054
H	6.14531	14.66391	12.51592
H	7.00360	15.62228	13.78464
H	10.29237	17.08508	9.05255
H	6.82501	15.80690	7.99403
H	8.50552	15.73247	7.36333
H	7.76855	17.31543	7.74647
H	9.17014	19.37521	14.29526
H	8.74046	21.21274	9.67737
H	11.92843	21.92721	11.06100
H	11.02059	21.64917	9.52407
H	12.01133	20.33990	10.25839
H	6.92432	19.53206	13.23744
H	6.31090	21.14083	9.83499
H	5.52033	20.78668	11.41228
H	5.99803	19.44495	10.32875
H	8.87913	18.23596	18.99441
H	8.34008	20.04569	20.62577
H	12.24630	21.79124	19.92532
H	13.10219	20.07387	17.02679
H	13.74360	19.06322	18.34406
H	13.80382	20.85272	18.49255
H	9.16056	21.90311	22.08162
H	9.53543	23.08820	20.79150
H	10.83366	22.53736	21.89429
H	16.65210	19.71398	17.59375
H	16.71606	22.12749	18.14253
H	17.62128	21.15007	22.27069
H	16.74455	17.80131	22.22371
H	17.88094	18.96031	23.00762
H	18.46889	17.76530	21.78768
H	17.27941	23.93500	19.71974
H	17.99435	23.54084	21.32252
H	16.21689	23.59387	21.12178
H	19.56834	21.16607	15.76417
H	20.36838	22.90225	17.35910
H	22.36098	19.82289	19.66793
H	22.26881	17.26248	17.30392
H	20.81327	17.02837	18.31194
H	22.33995	17.59528	19.07231
H	22.03393	23.51634	19.16661
H	22.84232	22.22716	20.12762
H	21.13518	22.65942	20.45749
H	18.47587	13.22825	19.21521
H	19.40807	13.00831	21.51071
H	23.39699	13.63523	19.92509
H	22.68533	13.04736	16.56592
H	23.80292	13.95777	17.65184
H	22.49937	14.80642	16.73570
H	21.52089	13.82141	23.01451
H	23.13376	13.45594	22.30938
H	21.97589	12.12938	22.65642
H	15.40207	9.87775	21.21745

H	16.38089	9.27564	23.42785
H	17.47404	13.42700	24.03494
H	15.49912	14.86341	21.59381
H	17.03832	14.55565	20.74479
H	17.05582	15.07583	22.46468
H	17.88464	9.90976	25.32275
H	16.82959	11.14701	26.07518
H	18.46185	11.60376	25.50080
H	12.70258	13.88618	21.80542
H	13.55093	16.99339	25.61271
H	13.97738	18.65237	22.57729
H	13.36149	18.87799	24.25630
H	12.22548	18.72752	22.86087
H	13.08136	12.96290	24.08265
H	13.75378	15.17142	27.15200
H	14.46907	13.68853	26.43242
H	12.71370	13.75810	26.76684
H	17.04494	19.64871	12.44298
H	14.99368	24.19559	12.51636
H	13.41286	22.17189	14.81853
H	14.02350	23.85018	14.59566
H	14.86821	22.70624	15.70739
H	17.46291	21.20591	10.57006
H	15.96688	24.74664	10.39870
H	16.16796	23.35854	9.27774
H	17.58743	24.01418	10.14590
H	17.65561	17.35352	10.85479
H	22.30504	19.14233	10.57205
H	22.24771	16.11148	12.33426
H	21.87832	17.38041	13.53407
H	23.07889	17.71090	12.22813
H	18.19216	19.11059	9.19499
H	21.19827	21.17964	9.21035
H	19.73944	20.74494	8.25421
H	21.30372	19.92671	7.93708
H	15.18485	13.14481	7.59934
H	18.98537	15.88771	5.90850
H	20.00733	13.79207	8.54473
H	19.40951	15.30414	9.27864
H	20.31743	15.37234	7.72894
H	14.98257	14.30337	5.40468
H	17.84501	16.20003	3.76637
H	16.28284	16.89300	4.30737
H	16.30388	15.33701	3.42247
H	14.96014	19.67658	9.36401
H	14.10648	20.32483	7.11135
H	12.34647	16.38585	6.68348
H	14.05651	14.77567	9.24241
H	12.50574	14.75437	8.33236
H	12.56570	15.35709	10.02290
H	12.33618	19.82396	5.29335
H	11.80215	18.12587	5.03642
H	13.45764	18.62904	4.57233
H	7.68835	12.81043	17.04115
H	6.30114	10.94581	17.93436
H	9.50527	9.91199	20.66481
H	11.36016	12.83805	20.40216
H	12.07467	11.76596	19.18030

H	11.51256	11.07476	20.74226
H	6.34929	8.66990	19.17534
H	6.24097	9.56303	20.72267
H	7.58190	8.40440	20.45759

$Ag_{24}Au_{1}DMBT_{18}$_Au_in_icosahedron
349

Au	14.75200	17.53698	14.66575
Ag	17.65258	18.72449	15.23026
Ag	19.36861	16.06924	16.21409
Ag	17.24305	13.73691	16.37634
Ag	13.33940	16.47533	17.04335
Ag	11.74009	18.60271	15.21857
Ag	13.27810	18.52803	12.32297
Ag	14.83380	15.29582	12.42297
Ag	16.37623	16.54952	16.92188
Ag	14.73737	16.75128	19.73312
Ag	11.60592	15.13309	19.17381
Ag	12.46794	13.61912	16.39955
Ag	14.89871	12.05031	15.98769
Ag	12.16025	10.68350	15.11439
Ag	10.25519	13.57266	14.43889
Ag	12.45200	15.87428	14.12509
Ag	16.25590	13.06544	13.54690
Ag	17.69303	10.92643	15.23085
Ag	16.63137	11.20292	18.22502
Ag	14.86487	14.23811	18.09062
Ag	13.27315	13.02559	13.61916
Ag	15.15754	12.81996	10.63637
Ag	17.91273	14.35159	11.46509
Ag	17.19540	15.89126	14.14981
Ag	14.81598	14.77756	15.27904
S	15.53638	19.94827	14.99276
S	20.03913	18.34862	15.53529
S	19.75382	13.65694	16.58619
S	11.85357	20.20121	13.37338
S	14.84644	17.34148	10.90313
S	11.08151	17.63386	17.36699
S	17.07518	17.27800	19.24985
S	12.55221	16.68051	20.80490
S	10.21236	13.87116	17.60741
S	14.38839	9.67550	15.22459
S	9.80362	11.18747	14.80893
S	9.93990	15.94376	13.87637
S	17.92758	9.42949	17.16529
S	15.07437	12.28421	19.75235
S	18.33199	11.70931	12.98474
S	12.84396	12.30092	11.21059
S	17.32738	12.93541	9.53012
S	19.34112	15.86822	12.77799
C	19.64986	9.53790	17.67049
C	20.65020	9.89648	16.74188
C	20.02560	9.14146	18.98552
C	22.00595	9.86935	17.09500
C	21.39764	9.12846	19.30739
C	19.00041	8.74372	20.01974
C	22.40633	9.48761	18.39126
C	23.86314	9.49594	18.79926
C	14.42627	8.22127	16.28318
C	15.19604	7.14390	15.79064
C	13.74577	8.08688	17.52458

C	15.30027	5.94373	16.50591
C	13.87049	6.86264	18.21494
C	12.91645	9.19626	18.11145
C	14.63759	5.78030	17.73860
C	14.75970	4.50287	18.54137
C	17.99442	10.33186	11.87559
C	16.71421	9.75651	11.75531
C	19.06674	9.83667	11.07974
C	16.47889	8.70671	10.85466
C	18.79664	8.77879	10.19012
C	20.45384	10.42898	11.16425
C	17.51843	8.19890	10.05156
C	17.28105	7.07830	9.06189
C	12.72111	10.56201	10.75450
C	12.46018	10.22004	9.39668
C	12.82951	9.53548	11.71336
C	12.32471	8.85510	9.06729
C	12.33587	11.27305	8.32280
C	12.68585	8.18874	11.35490
C	12.43163	7.82040	10.01757
C	12.30227	6.36644	9.61738
C	9.32766	10.42464	13.25142
C	9.02224	9.03462	13.22648
C	9.16096	11.19455	12.08126
C	8.55537	8.48094	12.01701
C	9.18968	8.16412	14.44914
C	8.69364	10.61197	10.89611
C	8.38299	9.23804	10.84122
C	7.91817	8.59174	9.55456
C	9.35584	15.97062	12.17752
C	8.04584	15.49903	11.87815
C	10.13502	16.54253	11.14920
C	7.58950	15.60641	10.54679
C	7.15168	14.90219	12.93801
C	9.64857	16.64385	9.84046
C	8.36127	16.16925	9.51200
C	7.83089	16.27432	8.09817
C	10.24767	20.20998	12.56540
C	10.12425	20.73780	11.24956
C	9.09099	19.79270	13.25897
C	8.83362	20.81516	10.68559
C	11.32580	21.19698	10.46009
C	7.82473	19.88489	12.66845
C	7.67202	20.39735	11.36364
C	6.31068	20.46456	10.70627
C	10.86121	18.98817	18.53088
C	9.61754	19.01134	19.20117
C	11.82603	19.99482	18.81002
C	9.31588	20.01482	20.13120
C	11.48791	20.99012	19.75153
C	13.17413	20.02241	18.14400
C	10.24913	21.03112	20.42179
C	9.92539	22.14661	21.39285
C	17.08675	19.03830	19.63476
C	16.86776	20.01641	18.64644
C	17.36474	19.44662	20.97259
C	16.90809	21.38258	18.95876
C	17.39651	20.82699	21.25277

C	17.61374	18.44191	22.07251
C	17.16908	21.81596	20.27328
C	17.18308	23.28580	20.63459
C	20.52431	19.49132	16.83862
C	20.22060	20.86041	16.66228
C	21.30613	19.08931	17.95775
C	20.67302	21.82604	17.56948
C	21.74008	20.08865	18.85460
C	21.68734	17.65116	18.20299
C	21.44200	21.45524	18.69181
C	21.90351	22.48103	19.70360
C	20.40279	13.55976	18.25725
C	19.56782	13.33091	19.37174
C	21.80920	13.66831	18.45051
C	20.09824	13.21609	20.66293
C	22.31028	13.55889	19.76476
C	22.75146	13.88423	17.29074
C	21.48657	13.33269	20.88449
C	22.06648	13.19874	22.27607
C	15.87256	11.97531	21.34373
C	15.85673	10.63822	21.80451
C	16.45419	12.98455	22.15857
C	16.40797	10.29076	23.04499
C	16.99941	12.59937	23.40280
C	16.50221	14.42632	21.73089
C	16.99309	11.27095	23.87286
C	17.56678	10.91988	25.22873
C	12.88090	15.96802	22.42426
C	13.13107	16.85241	23.51104
C	12.85930	14.57600	22.65178
C	13.34645	16.28921	24.78700
C	13.16679	18.35093	23.32302
C	13.07757	14.05021	23.93153
C	13.32518	14.90190	25.02883
C	13.56378	14.33743	26.41261
C	15.78568	20.99498	13.54988
C	15.19599	22.29060	13.55346
C	16.58025	20.59318	12.45450
C	15.43691	23.13014	12.44451
C	14.34446	22.77927	14.70082
C	16.80043	21.45514	11.37308
C	16.22920	22.74533	11.34595
C	16.47371	23.68132	10.18150
C	19.67450	17.22332	11.63897
C	21.00275	17.73798	11.57433
C	18.68985	17.73464	10.76923
C	21.27770	18.74551	10.62778
C	22.09897	17.22209	12.47537
C	19.00350	18.73089	9.83171
C	20.30737	19.25718	9.74177
C	20.67089	20.31464	8.72095
C	17.18724	13.89081	8.01595
C	18.29262	14.64655	7.53017
C	16.02042	13.79202	7.22588
C	18.15683	15.29298	6.28338
C	19.58452	14.76290	8.30076
C	15.91953	14.44554	5.99164
C	16.98996	15.21981	5.49804

C	16.87757	15.96505	4.18594
C	14.14459	17.66006	9.27081
C	14.39503	18.94180	8.72716
C	13.39865	16.71608	8.51690
C	13.91578	19.29676	7.45987
C	12.93158	17.10735	7.24242
C	13.10405	15.33702	9.03906
C	13.17094	18.37997	6.68851
C	12.67248	18.74094	5.30558
C	9.35990	12.46623	18.33695
C	8.05341	12.23025	17.85022
C	9.88205	11.62968	19.36029
C	7.26997	11.18589	18.35451
C	9.06271	10.58886	19.84952
C	11.25757	11.83180	19.93039
C	7.76223	10.34103	19.37101
C	6.91205	9.22970	19.94794
H	20.35463	10.19739	15.72260
H	22.76448	10.15012	16.34393
H	21.68917	8.81863	20.32718
H	18.33771	7.93011	19.64890
H	18.33003	9.59739	20.27665
H	19.49043	8.40199	20.95664
H	24.53358	9.32338	17.92887
H	24.08153	8.71605	19.56160
H	24.14923	10.47826	19.24353
H	15.72234	7.25946	14.82938
H	15.91096	5.12113	16.09555
H	13.33765	6.75661	19.17711
H	13.53125	10.10548	18.29854
H	12.45766	8.88826	19.07450
H	12.08981	9.50570	17.42551
H	15.13837	3.66388	17.91821
H	13.78190	4.19363	18.97378
H	15.46699	4.62477	19.39505
H	15.88801	10.12636	12.38451
H	15.46144	8.28737	10.77913
H	19.62847	8.39652	9.57092
H	20.85366	10.39239	12.20260
H	20.44922	11.50290	10.86934
H	21.15931	9.88773	10.49731
H	16.24769	6.67805	9.14370
H	17.98845	6.23235	9.22051
H	17.42241	7.42498	8.01198
H	13.03806	9.79449	12.76414
H	12.12219	8.59295	8.01305
H	11.55642	12.02424	8.57859
H	12.08453	10.81703	7.34124
H	13.28747	11.84238	8.20719
H	12.77618	7.41483	12.13647
H	11.83204	6.25768	8.61605
H	11.68832	5.79475	10.34842
H	13.29766	5.86542	9.57172
H	9.40648	12.27018	12.10380
H	8.31338	7.40307	11.99729
H	8.62966	8.56947	15.32125
H	10.25789	8.11413	14.76613
H	8.84078	7.12748	14.25326

H	8.57291	11.24220	9.99883
H	7.34199	7.66033	9.74705
H	8.78510	8.31738	8.90894
H	7.27457	9.27765	8.96062
H	11.14198	16.92570	11.39110
H	6.57495	15.23511	10.31369
H	7.59150	13.97125	13.36917
H	6.15287	14.64896	12.52226
H	7.01433	15.59958	13.79452
H	10.28627	17.10146	9.06496
H	6.81548	15.83113	8.00830
H	8.49371	15.75009	7.37233
H	7.76684	17.33551	7.76449
H	9.19259	19.38802	14.27982
H	8.73717	21.22438	9.66375
H	11.93195	21.93913	11.02579
H	11.01839	21.65123	9.49388
H	12.01316	20.34713	10.23341
H	6.94031	19.54627	13.23484
H	6.31047	21.15184	9.83237
H	5.52868	20.81298	11.41723
H	5.99115	19.46112	10.33975
H	8.88169	18.22040	18.98319
H	8.33605	20.00535	20.63966
H	12.23908	21.76994	19.96998
H	13.08934	20.10644	17.03517
H	13.74169	19.07985	18.33377
H	13.79275	20.86747	18.51074
H	9.15507	21.83489	22.13141
H	9.52731	23.04494	20.86398
H	10.82711	22.47507	21.95529
H	16.65738	19.70515	17.61028
H	16.73533	22.12011	18.15625
H	17.61335	21.14143	22.28983
H	16.72055	17.79666	22.24134
H	17.85935	18.95032	23.02961
H	18.44646	17.75152	21.81285
H	17.30795	23.92515	19.73411
H	18.00625	23.52732	21.34329
H	16.23097	23.59417	21.12738
H	19.62473	21.16672	15.78655
H	20.42265	22.88751	17.39965
H	22.34729	19.77596	19.72294
H	22.25790	17.22661	17.34684
H	20.78692	17.00458	18.33461
H	22.30970	17.55122	19.11717
H	22.06410	23.47619	19.23379
H	22.85321	22.17509	20.19469
H	21.14649	22.61874	20.51101
H	18.47923	13.24127	19.21424
H	19.41485	13.03175	21.50935
H	23.40132	13.65227	19.91520
H	22.68952	13.04430	16.56275
H	23.80314	13.97015	17.63976
H	22.49390	14.80348	16.71720
H	21.53395	13.84907	23.00622
H	23.14352	13.47320	22.29914
H	21.98031	12.15349	22.65444

H	15.40381	9.86082	21.16756
H	16.38437	9.23639	23.37108
H	17.45260	13.38599	24.03210
H	15.47507	14.84017	21.60252
H	17.01900	14.55280	20.75506
H	17.02765	15.05214	22.48131
H	17.88471	9.85555	25.27478
H	16.81807	11.07401	26.04135
H	18.44793	11.55162	25.47715
H	12.68127	13.89603	21.80364
H	13.53803	16.97534	25.63178
H	13.96476	18.65436	22.60707
H	13.35137	18.86965	24.28841
H	12.21342	18.73085	22.89332
H	13.06107	12.95634	24.07409
H	13.74598	15.14228	27.15683
H	14.44586	13.65703	26.42682
H	12.69218	13.74059	26.76709
H	17.04197	19.59245	12.45116
H	14.98490	24.13820	12.45035
H	13.42831	22.15551	14.81128
H	14.02441	23.83106	14.53802
H	14.89014	22.72405	15.66948
H	17.44147	21.11227	10.54343
H	15.94396	24.64877	10.31665
H	16.12589	23.23852	9.22028
H	17.55854	23.90441	10.05837
H	17.66029	17.34208	10.81516
H	22.30835	19.14153	10.57781
H	22.23567	16.12290	12.36110
H	21.85112	17.40026	13.54682
H	23.06578	17.72280	12.25209
H	18.21297	19.08926	9.15026
H	21.21156	21.16827	9.18888
H	19.76783	20.72017	8.21611
H	21.33954	19.90555	7.92761
H	15.18156	13.17679	7.59062
H	19.01407	15.88157	5.91066
H	20.01089	13.76284	8.53898
H	19.43111	15.27937	9.27839
H	20.34019	15.34248	7.72924
H	14.99168	14.34910	5.40230
H	17.87747	16.21854	3.77153
H	16.32020	16.92284	4.31244
H	16.32959	15.37018	3.42158
H	14.97000	19.66843	9.32478
H	14.12300	20.30741	7.06690
H	12.34804	16.37320	6.65839
H	14.04601	14.77432	9.23474
H	12.49882	14.75019	8.31779
H	12.55391	15.36451	10.00439
H	12.34691	19.80338	5.25201
H	11.81352	18.10436	5.00037
H	13.46955	18.60623	4.53672
H	7.65511	12.88397	17.05788
H	6.25714	11.02448	17.94592
H	9.47039	9.94035	20.64599
H	11.35656	12.84710	20.38637

H	12.04699	11.77656	19.14965
H	11.49243	11.07966	20.71216
H	6.29808	8.73394	19.16347
H	6.20279	9.61521	20.71840
H	7.53465	8.44979	20.43784

Ag$_{24}$Au$_{1}$DMBT$_{18}$_Au_in_staple
349

Ag	14.72463	17.53140	14.57965
Au	17.68875	18.88923	15.19215
Ag	19.39321	15.98312	16.20907
Ag	17.25086	13.75471	16.38171
Ag	13.35620	16.50331	16.99643
Ag	11.70188	18.55419	15.17379
Ag	13.22480	18.51319	12.28662
Ag	14.84919	15.29924	12.43166
Ag	16.38240	16.62287	16.86734
Ag	14.74079	16.78986	19.70570
Ag	11.62830	15.15404	19.14964
Ag	12.49980	13.62698	16.39578
Ag	14.92548	12.05273	15.99930
Ag	12.16922	10.67595	15.11674
Ag	10.25629	13.57857	14.46117
Ag	12.44759	15.82426	14.12339
Ag	16.29112	13.08787	13.56219
Ag	17.72023	10.94298	15.23735
Ag	16.65448	11.20886	18.23119
Ag	14.89155	14.28257	18.07339
Ag	13.31179	13.01068	13.62838
Ag	15.17904	12.81476	10.64430
Ag	17.92713	14.36596	11.46028
Ag	17.21084	15.94866	14.14372
Ag	14.83979	14.79940	15.27239
S	15.55838	19.93838	14.92874
S	19.97779	18.28923	15.53379
S	19.76511	13.58114	16.59767
S	11.79950	20.17675	13.34174
S	14.83592	17.34881	10.90240
S	11.08861	17.64676	17.36271
S	17.07946	17.29895	19.22514
S	12.55455	16.72017	20.77381
S	10.23934	13.87009	17.59645
S	14.39584	9.67392	15.24124
S	9.81569	11.18647	14.80545
S	9.92560	15.94546	13.87110
S	17.92235	9.42330	17.15989
S	15.10259	12.32580	19.73577
S	18.36817	11.73473	12.99433
S	12.86829	12.29425	11.22441
S	17.34139	12.94699	9.52704
S	19.36668	15.86349	12.78119
C	19.64506	9.49624	17.66902
C	20.65429	9.82585	16.73968
C	20.01092	9.09977	18.98719
C	22.00911	9.76985	17.09437
C	21.38168	9.05900	19.31108
C	18.97583	8.73088	20.02220
C	22.39946	9.38856	18.39347
C	23.85536	9.36346	18.80441
C	14.41953	8.21207	16.28963
C	15.17268	7.12716	15.78895
C	13.74607	8.08210	17.53572

C	15.26909	5.92429	16.50148
C	13.86140	6.85525	18.22228
C	12.93501	9.20076	18.13071
C	14.61284	5.76514	17.73779
C	14.71703	4.48184	18.53400
C	18.03151	10.36141	11.87984
C	16.75275	9.78259	11.76016
C	19.10308	9.87297	11.07878
C	16.51798	8.73693	10.85449
C	18.83372	8.81879	10.18452
C	20.48862	10.46908	11.16220
C	17.55676	8.23622	10.04598
C	17.31984	7.12003	9.05120
C	12.74708	10.55552	10.76581
C	12.47036	10.21580	9.41084
C	12.87363	9.52744	11.72081
C	12.33855	8.85084	9.07955
C	12.32531	11.27102	8.34167
C	12.73275	8.18093	11.36063
C	12.46327	7.81452	10.02568
C	12.33468	6.36070	9.62461
C	9.34498	10.43912	13.23877
C	9.04836	9.04731	13.19655
C	9.17283	11.22222	12.07845
C	8.58441	8.50581	11.98073
C	9.22172	8.16281	14.40825
C	8.70844	10.65133	10.88613
C	8.40656	9.27651	10.81429
C	7.94617	8.64124	9.52053
C	9.34087	15.93539	12.17209
C	8.03215	15.45463	11.88166
C	10.12177	16.48040	11.13050
C	7.57942	15.52535	10.54665
C	7.13734	14.88197	12.95421
C	9.63906	16.54576	9.81797
C	8.35315	16.06131	9.49899
C	7.82220	16.13488	8.08330
C	10.18776	20.15744	12.54303
C	10.04926	20.66982	11.22275
C	9.04130	19.73552	13.25010
C	8.75374	20.72692	10.66793
C	11.23952	21.13346	10.41887
C	7.76974	19.80641	12.66776
C	7.60198	20.30239	11.35874
C	6.23635	20.34355	10.70828
C	10.88009	19.03624	18.48705
C	9.63497	19.09226	19.15187
C	11.85765	20.03686	18.74514
C	9.34487	20.12044	20.05876
C	11.53059	21.05769	19.66237
C	13.20713	20.03213	18.08115
C	10.29097	21.12982	20.32912
C	9.98453	22.26907	21.27795
C	17.11584	19.04988	19.65077
C	16.93380	20.05287	18.67979
C	17.37451	19.42485	21.00259
C	16.99116	21.41134	19.02353
C	17.42508	20.79791	21.31361

C	17.58238	18.39284	22.08531
C	17.23364	21.81181	20.35169
C	17.27028	23.27283	20.74600
C	20.54970	19.41709	16.82181
C	20.30176	20.79688	16.64788
C	21.33821	18.97988	17.92140
C	20.81133	21.74161	17.54632
C	21.83373	19.96086	18.80738
C	21.66469	17.52759	18.16561
C	21.58736	21.33818	18.65230
C	22.10910	22.34287	19.65564
C	20.40211	13.50271	18.27525
C	19.55482	13.32333	19.38931
C	21.81018	13.57396	18.47379
C	20.07533	13.22088	20.68578
C	22.30112	13.47804	19.79285
C	22.76468	13.73805	17.31543
C	21.46529	13.30068	20.91254
C	22.03480	13.17616	22.30929
C	15.86602	12.01148	21.34287
C	15.83919	10.67443	21.80217
C	16.43385	13.01929	22.16964
C	16.36728	10.32504	23.05250
C	16.95504	12.63245	23.42329
C	16.49271	14.46100	21.74318
C	16.93811	11.30334	23.89192
C	17.48947	10.95183	25.25699
C	12.87609	16.02291	22.40105
C	13.12010	16.91708	23.48128
C	12.85082	14.63328	22.64172
C	13.32527	16.36567	24.76403
C	13.15755	18.41379	23.27960
C	13.05929	14.11911	23.92785
C	13.30058	14.98066	25.01876
C	13.53738	14.42886	26.40792
C	15.75186	21.05646	13.52607
C	15.11244	22.32488	13.59326
C	16.53300	20.72238	12.39973
C	15.28963	23.21124	12.50850
C	14.26920	22.73692	14.77637
C	16.69219	21.63166	11.34652
C	16.06937	22.89773	11.37940
C	16.24787	23.88346	10.24446
C	19.69309	17.24707	11.67623
C	21.02327	17.75421	11.60240
C	18.69539	17.79686	10.84558
C	21.28771	18.79363	10.68784
C	22.13272	17.19789	12.46277
C	18.99775	18.82493	9.93966
C	20.30366	19.34479	9.84177
C	20.65383	20.43507	8.85129
C	17.17831	13.89527	8.01049
C	18.26028	14.68405	7.52448
C	16.01726	13.75641	7.21762
C	18.10674	15.32224	6.27557
C	19.54616	14.84413	8.29693
C	15.89859	14.40249	5.98103
C	16.94468	15.20954	5.48777

C	16.81151	15.94810	4.17393
C	14.14208	17.67171	9.26610
C	14.37823	18.95897	8.73008
C	13.41478	16.71974	8.50402
C	13.90178	19.31241	7.46115
C	12.95079	17.10959	7.22804
C	13.13713	15.33420	9.01874
C	13.17556	18.38801	6.68122
C	12.68268	18.74713	5.29582
C	9.39448	12.46659	18.33790
C	8.08855	12.22039	17.85472
C	9.92205	11.64112	19.36734
C	7.31071	11.17670	18.36892
C	9.10822	10.60056	19.86633
C	11.29817	11.85322	19.93200
C	7.80818	10.34288	19.39198
C	6.96365	9.23275	19.97944
H	20.36669	10.12633	15.71794
H	22.77471	10.02663	16.34186
H	21.66487	8.75018	20.33360
H	18.29608	7.92986	19.65497
H	18.32376	9.60067	20.27251
H	19.45672	8.38448	20.96208
H	24.52670	9.25239	17.92508
H	24.07011	8.52951	19.50869
H	24.14350	10.30921	19.32082
H	15.69345	7.23907	14.82429
H	15.86958	5.09650	16.08649
H	13.33455	6.75331	19.18827
H	13.56180	10.10292	18.31215
H	12.48071	8.89730	19.09735
H	12.10632	9.52031	17.45198
H	15.19880	3.67338	17.94276
H	13.71633	4.11672	18.85849
H	15.32393	4.62319	19.45852
H	15.92760	10.14578	12.39465
H	15.50159	8.31495	10.77948
H	19.66513	8.44182	9.56151
H	20.89126	10.42936	12.19935
H	20.48001	11.54425	10.87194
H	21.19389	9.93278	10.49104
H	16.28648	6.71938	9.13090
H	18.02716	6.27333	9.20637
H	17.46161	7.47128	8.00287
H	13.09561	9.78451	12.76930
H	12.12437	8.59010	8.02726
H	11.54302	12.01524	8.60896
H	12.06576	10.81590	7.36180
H	13.27090	11.84825	8.21659
H	12.83784	7.40562	12.13901
H	11.88515	6.25316	8.61373
H	11.70176	5.79336	10.34302
H	13.32780	5.85397	9.60151
H	9.41035	12.29932	12.11438
H	8.34864	7.42685	11.94804
H	8.65992	8.55420	15.28561
H	10.29041	8.11513	14.72399
H	8.87866	7.12661	14.19990

H	8.58304	11.29197	9.99696
H	7.31586	7.74360	9.70427
H	8.81598	8.31327	8.90430
H	7.35792	9.35368	8.90134
H	11.12908	16.86768	11.36417
H	6.56667	15.14480	10.32069
H	7.57849	13.96245	13.40807
H	6.13972	14.61663	12.54320
H	6.99772	15.59954	13.79347
H	10.27911	16.98146	9.03187
H	6.85135	15.60314	7.98273
H	8.53356	15.68331	7.35533
H	7.66200	17.19025	7.76179
H	9.15395	19.34463	14.27514
H	8.64497	21.12475	9.64283
H	11.84500	21.88440	10.97358
H	10.91905	21.57884	9.45282
H	11.93105	20.28761	10.18990
H	6.89348	19.46432	13.24451
H	6.20837	21.05793	9.85668
H	5.44602	20.64080	11.43267
H	5.95103	19.34179	10.31007
H	8.88859	18.30703	18.94940
H	8.36385	20.13555	20.56484
H	12.29119	21.83287	19.86424
H	13.12411	20.09109	16.97082
H	13.76335	19.08746	18.29451
H	13.83595	20.87787	18.42807
H	9.13283	22.02362	21.94860
H	9.71185	23.19882	20.72469
H	10.86133	22.51866	21.91596
H	16.74724	19.76571	17.63252
H	16.84664	22.16923	18.23454
H	17.62701	21.08582	22.36143
H	16.67280	17.76356	22.22425
H	17.82091	18.87590	23.05724
H	18.40453	17.68987	21.82596
H	17.34846	23.93261	19.85510
H	18.13164	23.49724	21.41436
H	16.34801	23.57047	21.29822
H	19.70219	21.12793	15.78412
H	20.60107	22.81251	17.38171
H	22.44488	19.62230	19.66304
H	22.21093	17.07563	17.30781
H	20.74060	16.91890	18.31235
H	22.29262	17.40623	19.07320
H	22.29852	23.33211	19.18408
H	23.05579	21.99933	20.12702
H	21.37375	22.50771	20.47775
H	18.46474	13.26507	19.22803
H	19.38263	13.07546	21.53216
H	23.39367	13.54177	19.94734
H	22.68573	12.88220	16.60811
H	23.81604	13.80510	17.66958
H	22.53451	14.64925	16.71801
H	21.48864	13.82165	23.03325
H	23.10874	13.46191	22.34092
H	21.95740	12.13051	22.68892

H	15.39592	9.89826	21.15698
H	16.33574	9.27057	23.37751
H	17.39805	13.41792	24.06134
H	15.46926	14.87807	21.59728
H	17.02549	14.58716	20.77603
H	17.00668	15.08460	22.50335
H	17.72034	9.86739	25.33709
H	16.76175	11.19442	26.06681
H	18.42142	11.51699	25.48109
H	12.67595	13.94569	21.79908
H	13.51048	17.05963	25.60382
H	13.95881	18.71000	22.56433
H	13.33829	18.94129	24.24096
H	12.20620	18.79033	22.84248
H	13.03833	13.02671	24.08071
H	13.61706	15.24095	27.16257
H	14.47848	13.83370	26.45302
H	12.71329	13.74999	26.72470
H	17.03279	19.74197	12.35299
H	14.79763	24.19889	12.56048
H	13.35005	22.11161	14.85053
H	13.95054	23.79771	14.68704
H	14.82143	22.61233	15.73470
H	17.32447	21.34596	10.48868
H	15.67887	24.82111	10.42384
H	15.89992	23.45898	9.27510
H	17.31886	24.15943	10.10850
H	17.66396	17.41051	10.89870
H	22.31980	19.18529	10.63269
H	22.26115	16.10339	12.30281
H	21.90493	17.33413	13.54447
H	23.09832	17.70217	12.24229
H	18.19544	19.21684	9.29114
H	21.27251	21.23287	9.32060
H	19.74189	20.91344	8.43330
H	21.24063	20.03458	7.99133
H	15.19793	13.11492	7.58185
H	18.94549	15.93723	5.90342
H	20.00426	13.85913	8.53907
H	19.37460	15.35788	9.27309
H	20.28417	15.44588	7.72519
H	14.97641	14.27352	5.38888
H	17.80414	16.22409	3.75641
H	16.23217	16.89297	4.29921
H	16.27585	15.33839	3.41259
H	14.94125	19.69032	9.33327
H	14.09779	20.32717	7.07312
H	12.38254	16.36945	6.63666
H	14.08587	14.78164	9.21028
H	12.53876	14.74459	8.29406
H	12.58713	15.34952	9.98442
H	12.33599	19.80300	5.24524
H	11.84003	18.09483	4.97869
H	13.48987	18.63336	4.53417
H	7.68622	12.86502	17.05706
H	6.29806	11.00719	17.96316
H	9.52033	9.96048	20.66730
H	11.39576	12.87366	20.37647

H	12.08601	11.79172	19.15019
H	11.53709	11.11026	20.72130
H	6.35647	8.72260	19.19885
H	6.24838	9.62289	20.74198
H	7.58984	8.46364	20.48167

Editorials

NANO · MICRO
small
www.small-journal.com

Special Issue on “Nanoclusters”: A Glimpse into the Efforts to Redefine Matter at the Nanoscale

Thalappil Pradeep

Matter at the nanoscale is being redefined. One of the most evident aspects of this evolution is centred on nanoclusters (NCs) or atomically precise clusters (APCs), and most of the work in this area is on APCs of noble metals, and especially clusters of gold. Just to give an indication, of the over 572 papers published with “atomically precise cluster” in the title or abstract (as listed by the Web of Science as of March 31, 2021), 405 were on gold, 86 on silver and 81 on other materials. Among those APCs of gold, the most studied cluster is $Au_{25}L_{18}^{-}$, with ligands (L) such as glutathione and phenylethane thiol.

This speaks simultaneously about the limitations and opportunities in the area, on the need to discover new clusters and new ligands. Visible gaps include missing nuclearities, alloys, cluster adducts, polymers, and assemblies. A somewhat deeper exploration of the literature reveals the absence of well-defined principles for cluster synthesis of all nuclearities, their stabilities, transformations, etc. It is also clear that NCs can be formed by any kind of matter, and greater efforts are needed to diversify into oxides, chalcogenides, pnictides and others. While the synthesis, identification, and structures of APCs have been central aspects of recent research, their properties as individual clusters and assembled solids are becoming important. Luminescence has been the most explored property, while mechanical, electrical, and magnetic properties are slowly gaining attention.

The complexity of NCs is increasing, both compositional and structural, in terms of core and ligand. Complex structures result in new properties such as chirality. Assemblies can also result in complexities, and they too can be chiral. Ligand arrangements and multiple possibilities in structures can result in isomers. These pose challenges in synthesis, separation, crystallisation, and understanding of structures. In addition, as many clusters are similar in size and are prepared with the same or compatible ligands, it is possible for them to co-crystallize in different ways. As a diverse family of clusters are available now and as several of them are of similar size and shape, this possibility can produce very new materials with a combination of properties of the participating clusters. Assemblies can arise in several other ways as well: between NCs themselves, between NCs and nanoparticles, and also between NCs and molecules.

As more and more NCs, their crystals, assemblies, and properties are explored, a detailed understanding of structure-property relations becomes a central aspect of their study. At the same time, all-electron computations become complex and often impossible on larger NCs and newer methods have to be developed. Not only the standard requirements of electronic energy levels and optical spectra, but also complex questions associated with conformations of ligands over the cluster surface, solvent-accessible sites, mechanisms of transformation and the associated energetics are important to understand. As assemblies become more important, there is a need to have them computed as well.

These knowledge gaps and clear possibilities necessitate the introduction of new methodologies to explore NC science. Recently, the area has seen the induction of many gas phase spectroscopy techniques to understand their electronic structure, chemical reactivity, shape, isomers, etc. Photophysics of NCs is being explored and excited states are being studied with greater time resolution. Carrier dynamics at varied timescales present new opportunities for NCs in photochemistry and energy transfer. Other stimuli such as pressure and temperature reveal new aspects of their properties.

As this area expands, properties translating to applications are becoming evident. It is being realised that APCs are indeed molecules. Composition, geometric and electronic structures, chemical properties, reactivity and associated kinetics and thermodynamics are consistent with this description. The size and shape of several such molecules are similar to biomolecules, and both resemble each other in terms of organisation and hierarchy. Combining APCs with biomolecules and complex entities such as viruses using chemical principles can produce even more diverse systems with new properties useful for biology.

For quite some time, the principal focus of NCs has been on luminescence, especially in the near-infrared region, in view of potential applications in biolabeling and imaging. This subject area is dominated by protein- and DNA-protected clusters. The other recognised application of NCs is in the area of catalysis, where several oxidation reactions have been identified. A deeper understanding of such processes requires films of NCs, explored with finer tools of imaging and spectroscopy.

All of these directions pertaining to the research of NCs are captured to varying degrees in this special issue. Many of the important practitioners of the area as well as several younger researchers present their work here. In 9 review-type articles and 20 original research papers, this special issue captures many of the emerging directions. An aspect particularly important to note is the participation of nearly all regions of the world and its associated diversity.

I am sure that young researchers in the area will see new pointers from these papers. For others from the larger area of small matter, new connections will be established.

I am immensely thankful to the editorial team of *Small*, especially Dr. Lisa Smith, who took care of every aspect of this special issue. I am thankful to the journal and the publisher for recognising the area in the form of a special issue.

I hope that you will enjoy reading this collection.

Thalappil Pradeep

DOI: 10.1002/smll.202102931

Thalappil Pradeep is an Institute Professor at the Indian Institute of Technology Madras, Chennai, India. He is the Deepak Parekh Institute Chair Professor and is also a Professor of Chemistry. He studied at the University of Calicut, Indian Institute of Science, UC Berkeley, and Purdue. His research interests are in molecular and nanoscale materials and he develops instrumentation for such studies. In addition to the work on advanced materials, he is involved in the development of affordable technologies for drinking water purification and some of them have been commercialized. Visit http://www.dstuns.iitm.ac.in/pradeep-research-group.php for more information.

ACS Sustainable Chemistry & Engineering
pubs.acs.org/journal/ascecg
Editorial

Expectations for Perspectives in *ACS Sustainable Chemistry & Engineering*

Cite This: *ACS Sustainable Chem. Eng.* 2021, 9, 16528−16530

Read Online
ACCESS | Metrics & More | Article Recommendations

■ INTRODUCTION AND NEED FOR THIS EDITORIAL

ACS Sustainable Chemistry & Engineering (*ACS SCE*) Editors are dedicated in their efforts to provide guidance to prospective contributors on manuscript content and expectations. For example, we have recently published editorials that articulate the expectations for scope and content of the journal in specific topic areas and provide guidance on effective ways to incorporate sustainability metrics in manuscripts.[1−14] These editorials provide insights into how the scope and the coverage of topics have evolved as the field of sustainable chemistry and engineering expands and grows in new directions. As an editorial team, we believe that thought leadership is key to the success of our field and the journal. Thus, perspective articles that focus on a specific topic, where authors share fresh and new ideas, are extremely beneficial to the readers of *ACS SCE*. Thoughtful and creative perspectives have significant potential to catalyze new development and stimulate constructive discussion on a given topic. Such perspectives are different from classical reviews that focus on the development of a specific field over a certain period. This editorial delineates the critical factors and qualities that a forward-looking *ACS SCE* perspectives article should deliver.

■ REVIEWS VS PERSPECTIVES: CLARIFYING THE STRUCTURE

General guidance on writing effective review articles has been previously described in editorials by other ACS journals.[16,17] It is our expectation that *ACS SCE* perspectives go beyond reviewing a research topic and *critique* the reviewed literature in the context of sustainable chemistry and engineering: delineating research gaps, highlighting debate and disagreement, and emphasizing the remaining challenges. This distinguishing feature is clearly spelled out in the *ACS SCE* Author Guidelines as follows: “Perspectives are thoroughly documented assessments of selected areas of the sustainable chemistry and engineering research literature.” Perspectives should preferably project significant advances and opportunities in emerging or rapidly evolving topics in sustainable chemistry and engineering. They should clearly discuss potential sustainability advantages of the reviewed topic as well as the fundamental and practical challenges that must be addressed for the timely implementation of sustainable processes and products. Thus, in addition to the traditional criteria used to evaluate review articles such as (a) the current importance of the topic under review, (b) thoroughness of the literature coverage, and (c) overall clarity of presentation, the following two additional characteristics must also be evident in *ACS SCE* perspectives: (d) critical, thoughtful assessment of sustainability-related aspects in the reviewed literature and (e) clear identification of future research needs and directions for further advancing green and sustainable chemistry and engineering. Perspectives that do not meet these criteria will be deemed out of scope and, therefore, unsuitable for consideration in *ACS SCE*.

■ BEYOND A GOOD REVIEW: ELEMENTS OF AN *ACS SCE* PERSPECTIVE

What Makes the Cut at *ACS SCE* When It Comes to Perspective Submissions? We encourage authors to apply life cycle and/or systems thinking to identify any sustainability-related challenges such as, but not limited to, the material intensity, energy intensity, CO_2 footprint, water usage, toxicity of chemicals, and environmental impact that are associated with a reviewed topic. We recommend authors to consult recent scope and metrics editorials to understand the sustainability considerations associated with various topics (e.g., catalysis, materials, clean and renewable energy, energy conversion, storage materials and devices, green synthesis of chemicals, feedstock CO_2 footprint, biomass processing, biobased chemicals and solvents, electrochemistry, waste recycling, and more) covered by *ACS SCE*.[3−11] Identifying research gaps and needs in the field based on a detailed analysis and exposure of sustainability hotspots would be a vital contribution of *ACS SCE* perspectives. For example, if a life cycle analysis is lacking in the literature that prevents one from making an informed sustainability assessment of a process or product, highlighting such a drawback in the perspectives will be useful to direct research. Such analysis could be based on easily accessible metrics such as E-factor, material intensity, atom economy, and more. *ACS SCE* perspectives that contain a compelling account of scientific and sustainability attributes of the reviewed topic will not only satisfy the desired quality features but also have a high probability of paving the way for future scientific and technological advances. We refer prospective authors to a sampling of recent articles,[18−23]

Received: November 19, 2021
Published: December 13, 2021

where they will gain a better understanding of the attributes of published *ACS SCE* perspectives.

What Does *Not* Make the Cut? A high standard of scientific writing is expected as it is essential to clearly articulate sustainability assessment and discussions without ambiguity. Manuscripts that do not adhere to such standards will be returned without review. In addition, we provide here examples of content that are more likely to be rejected after editorial review. Perspectives that address the degradation of pollutants will *not* be considered, as the scope of our journal allows us to accommodate manuscripts that concentrate on pollution prevention rather than pollutant treatment.[15] However, perspectives that deal with conversion of waste to value-added products to promote a circular economy are welcome. In such cases, waste recycling strategies must address the sustainability of the overall process (even if it is qualitative) to warrant further consideration and provide an indication of the practicality in terms of scale and adequacy of final use. Perspectives that highlight well-established biobased materials and/or their applications will be considered unsuitable unless critical discussions that focus on advances related to sustainability aspects in the life cycle for the product (e.g., resource, process, product) are provided. Perspectives that highlight advances in green and sustainable nanotechnology, especially those pertaining to synthesis of nanomaterials, may not pass the editorial review stage if a critical treatment of aspects such as use of sustainable raw materials and greener processes (based on energy sources, processing solvents, and more) is lacking. It is of utmost importance to note that the use of biobased or derived materials and/or solvents does *not* automatically guarantee sustainability. Perspectives must analyze the performance of such systems and conduct critical comparisons, preferably using sustainability metrics, with respect to benchmarks or existing technologies. Similarly, it is important to present advances in catalysts and materials for applications in energy conversion, storage, and utilization in terms of their activity, stability, efficiency, cyclability, performance, and cost considerations that identify improvements in sustainability. Through such rigorous analysis and discussion of published data, we seek a clear articulation of new insights introduced by the perspective not previously addressed by published reviews/perspectives.

ACS SCE strongly encourages perspectives authors to submit an outline of their proposed perspective to Executive Editor Bala Subramaniam at subramaniam-office@sustain.acs.org for feedback prior to submitting a fully developed version. Such a proposal should show clear evidence of the desired attributes stated herein to solicit feedback that either encourages or discourages the submission of a full version of the perspective manuscript. We will strive to provide such feedback within 2 weeks. Please note that an encouragement to submit a full version does not guarantee its acceptance. Rather, it means that the submitted full version is more likely to be sent for external review if it possesses the requisite attributes and clearly addresses any feedback. If authors choose to submit a full version without an approved proposal, please note that it may still take one to 2 weeks to make the initial decision on whether the perspective article fits the journal scope. All authors should note that the opportunity to provide feedback on a proposed perspective is reserved only for perspectives and *not* for regular articles. All questions on the content of this editorial should also be submitted to Executive Editor Bala Subramaniam at subramaniam-office@sustain.acs.org.

CLOSING

We hope that the guidelines presented here will help authors to develop compelling and thought-provoking perspectives that enhance the impact of their contributions in the broader context of sustainability. Such perspectives, in turn, should cultivate and promote a critical sustainability mindset among our audience. *ACS SCE* welcomes perspectives from all researchers and practitioners of the field. Where appropriate, we encourage authors to consider assembling an international team with complementary aptitude or expertise to critically cover and assess the science, technology, and sustainability aspects of the reviewed topic. As always, we are interested in hearing feedback and suggestions from contributors and readers.

David T. Allen, Editor-in-Chief orcid.org/0000-0001-6646-8755
D. Julie Carrier, Associate Editor orcid.org/0000-0003-3322-4660
Jingwen Chen, Associate Editor orcid.org/0000-0002-5756-3336
Nicholas Gathergood, Associate Editor orcid.org/0000-0002-9398-9799
Jeannette M. Garcia, Associate Editor orcid.org/0000-0002-8336-4592
Jinlong Gong, Associate Editor orcid.org/0000-0001-7263-318X
Hongxian Han, Associate Editor orcid.org/0000-0002-2522-1817
King Kuok (Mimi) Hii, Associate Editor orcid.org/0000-0002-1163-0505
Bing-Joe Hwang, Associate Editor orcid.org/0000-0002-3873-2149
Asha Liza James, Development Editor
Mihir Jha, Development Editor
Peter Licence, Executive Editor orcid.org/0000-0003-2992-0153
Andrew C. Marr, Associate Editor orcid.org/0000-0001-6798-0582
Michael Meier, Associate Editor orcid.org/0000-0002-4448-5279
Audrey Moores, Associate Editor orcid.org/0000-0003-1259-913X
Ryuhei Nakamura, Associate Editor orcid.org/0000-0003-0743-8534
Thalappil Pradeep, Associate Editor orcid.org/0000-0003-3174-534X
Liane Rossi, Associate Editor orcid.org/0000-0001-7679-0852
Bert Sels, Associate Editor orcid.org/0000-0001-9657-1710
Bala Subramaniam, Executive Editor orcid.org/0000-0001-5361-1954
Michael K. C. Tam, Associate Editor orcid.org/0000-0002-7603-5635
Lin Zhuang, Associate Editor orcid.org/0000-0002-5642-6735
Julio F. Serrano, Managing Editor orcid.org/0000-0002-7803-808X

AUTHOR INFORMATION

Complete contact information is available at:
https://pubs.acs.org/10.1021/acssuschemeng.1c07865

Notes

Views expressed in this editorial are those of the authors and not necessarily the views of the ACS.

REFERENCES

(1) Allen, D. T.; Licence, P.; Subramaniam, B.; Williams, R. M. ACS Sustainable Chemistry & Engineering Welcomes Expanded Editorial Boards with New Initiatives. *ACS Sustainable Chem. Eng.* **2021**, *9* (1), 1−2.

(2) Allen, D. T.; Carrier, D. J.; Chen, J.; Gathergood, N.; Gong, J.; Han, H.; Kuok (Mimi) Hii, K.; Hwang, B.-J.; Licence, P.; Meier, M.; Moores, A.; Nakamura, R.; Pradeep, T.; Sels, B.; Subramaniam, B.; Tam, M. K. C.; Zhang, L.; Zhuang, L.; Williams, R. M.; Anastas, P. T. The Evolution of ACS Sustainable Chemistry & Engineering. *ACS Sustainable Chem. Eng.* **2020**, *8*, 1.

(3) Tam, M. K. C.; Meier, M. A. R.; Zhang, L.; Allen, D. T.; Licence, P.; Subramaniam, B. Expectations for Papers on Sustainable Materials in ACS Sustainable Chemistry & Engineering. *ACS Sustainable Chem. Eng.* **2020**, *8*, 1703−1704.

(4) Kuok (Mimi) Hii, K.; Moores, A.; Pradeep, T.; Sels, B.; Allen, D. T.; Licence, P.; Subramaniam, B. Expectations for Manuscripts on Catalysis in ACS Sustainable Chemistry & Engineering. *ACS Sustainable Chem. Eng.* **2020**, *8*, 4995−4996.

(5) Pradeep, T.; Allen, D. T.; Licence, P.; Subramaniam, B. Expectations for Manuscripts with Nanoscience and Nanotechnology Elements in ACS Sustainable Chemistry & Engineering. *ACS Sustainable Chem. Eng.* **2020**, *8*, 7751−7752.

(6) Allen, D. T.; Chen, J.; Licence, P.; Subramaniam, B. Expectations for Manuscripts on Industrial Ecology in ACS Sustainable Chemistry & Engineering. *ACS Sustainable Chem. Eng.* **2020**, *8*, 9599−9600.

(7) Carrier, D. J.; Allen, D. T.; Gathergood, N.; Han, H.; Licence, P.; Meier, M. R.; Moores, A.; Pradeep, T.; Sels, B.; Subramaniam, B.; Tam, M. K. C.; Zhang, L. Expectations for Manuscripts on Biomass Feedstocks and Processing in ACS Sustainable Chemistry & Engineering. *ACS Sustainable Chem. Eng.* **2020**, *8*, 11031−11032.

(8) Allen, D. T.; Gathergood, N.; Licence, P.; Subramaniam, B. Expectations for Manuscripts Contributing to the Field of Solvents in ACS Sustainable Chemistry & Engineering. *ACS Sustainable Chem. Eng.* **2020**, *8*, 14627−14629.

(9) Han, H.; Gong, J.; Hwang, B.-J.; Nakamura, R.; Zhuang, L.; Allen, D. T.; Licence, P.; Subramaniam, B. Expectations for Papers on Photochemistry, Photoelectrochemistry, and Electrochemistry for Energy Conversion and Storage in ACS Sustainable Chemistry & Engineering. *ACS Sustainable Chem. Eng.* **2020**, *8*, 3038−3039.

(10) Allen, D. T.; Carrier, D. J.; Chen, J.; Gathergood, N.; Gong, J.; Han, H.; Kuok (Mimi) Hii, K.; Hwang, B.-J.; James, A. L.; Licence, P.; Meier, M.; Moores, A.; Nakamura, R.; Pradeep, T.; Sels, B.; Subramaniam, B.; Tam, M. K. C.; Zhang, L.; Zhuang, L.; Williams, R. M. Expectations for Manuscripts in ACS Sustainable Chemistry & Engineering: Scope Summary and Call for Creativity. *ACS Sustainable Chem. Eng.* **2020**, *8* (43), 16046−16047.

(11) Chen, J.; Zhang, S.; Allen, D. T.; Subramaniam, B.; Licence, P. Expectations for Manuscripts Contributing to the Field on Management of Synthetic Chemicals in ACS Sustainable Chemistry & Engineering. *ACS Sustainable Chem. Eng.* **2021**, *9* (9), 3376−3378.

(12) Subramaniam, B.; Licence, P.; Moores, A.; Allen, D. T. Shaping Effective Practices for Incorporating Sustainability Assessment in Manuscripts Submitted to ACS Sustainable Chemistry & Engineering: An Initiative by the Editors. *ACS Sustainable Chem. Eng.* **2021**, *9* (11), 3977−3978.

(13) Debecker, D. P.; Kuok (Mimi) Hii, K.; Moores, A.; Rossi, L. M.; Sels, B.; Allen, D. T.; Subramaniam, B. Shaping Effective Practices for Incorporating Sustainability Assessment in Manuscripts Submitted to ACS Sustainable Chemistry & Engineering: Catalysis and Catalytic Processes. *ACS Sustainable Chem. Eng.* **2021**, *9* (14), 4936−4940.

(14) Meier, M. A.; Tam, M. K. Shaping Effective Practices for Incorporating Sustainability Assessment in Manuscripts Submitted to ACS Sustainable Chemistry & Engineering: Biomaterials. *ACS Sustainable Chem. Eng.* **2021**, *9* (22), 7400−7402.

(15) Allen, D. T.; Carrier, D. J.; Gong, J.; Gathergood, N.; Han, H.; Hwang, B.-J.; Licence, P.; Meier, M.; Moores, A.; Pradeep, T.; Qiu, J.; Sels, B.; Subramaniam, B.; Tam, M. K. C.; Zhang, L.; Williams, R. M. Why Wasn't My ACS Sustainable Chemistry & Engineering Manuscript Sent Out for Review? *ACS Sustainable Chem. Eng.* **2019**, *7*, 1−2.

(16) Skrabalak, S. E. Writing Effective Review Articles. *Chem. Mater.* **2021**, *33* (9), 3021.

(17) Alvaro, E.; Zwicky, D. A. Improving the Quality of Literature Reviews in Chemistry: Tools and Techniques. *J. Chem. Health Saf.* **2021**, *28* (5), 303−310.

(18) Sheldon, R. A. Metrics of green chemistry and sustainability: past, present, and future. *ACS Sustainable Chem. Eng.* **2018**, *6* (1), 32−48.

(19) Onwukamike, K. N.; Grelier, S.; Grau, E.; Cramail, H.; Meier, M. A. R. Critical Review on Sustainable Homogeneous Cellulose Modification: Why Renewability Is Not Enough. *ACS Sustainable Chem. Eng.* **2019**, *7*, 1826−1840.

(20) Xie, W.; Li, T.; Tiraferri, A.; Drioli, E.; Figoli, A.; Crittenden, J. C.; Liu, B. Toward the next generation of sustainable membranes from green chemistry principles. *ACS Sustainable Chem. Eng.* **2021**, *9*, 50−75.

(21) Arshad, F.; Li, L.; Amin, K.; Fan, E. S.; Manurkar, N.; Ahmad, A.; Yang, J. B.; Wu, F.; Chen, R. J. A Comprehensive Review of the Advancement in Recycling the Anode and Electrolyte from Spent Lithium Ion Batteries. *ACS Sustainable Chem. Eng.* **2020**, *8* (36), 13527−13554.

(22) Zhang, M.; Xin, D.; Zheng, X.; Chen, Q.; Zhang, W.-H. Toward Greener Solution Processing of Perovskite Solar Cells. *ACS Sustainable Chem. Eng.* **2020**, *8*, 13126−13138.

(23) Elsamadony, M.; Elreedy, A.; Mostafa, A.; Fujii, M.; Gescher, J.; Shakeri Yekta, S.; Schnurer, A.; Gaillard, J. F.; Pant, D. Perspectives on Potential Applications of Nanometal Derivatives in Gaseous Bioenergy Pathways: Mechanisms, Life Cycle, and Toxicity. *ACS Sustainable Chem. Eng.* **2021**, *9* (29), 9563−9589.

ACS Sustainable Chemistry & Engineering

pubs.acs.org/journal/ascecg

Editorial

Nanotechnology for Sustainability in *ACS Sustainable Chemistry & Engineering*: Some Pointers

Cite This: *ACS Sustainable Chem. Eng.* 2021, 9, 14327−14329

Read Online

ACCESS | Metrics & More | Article Recommendations

Nanotechnology refers to the construction and manipulation of matter at the nanoscale. Such matter with characteristic dimensions in the range of 1−100 nm at least along one of its axes, exhibiting new properties with functional attributes, can be utilized for creating macroscopic objects, devices, and products for new applications. These properties, for example, could enable catalysis by single atoms or spectroscopy with single nanowires. Various other relevant material characteristics are critical for other properties including thermal resistance, superhydrophobicity, scratch resistance, efficient water transport, sensors for diverse analytes, molecular encapsulation, and charge collection toward the design of novel products and devices expected to generate a sizable market. All these functions could be accomplished with extremely small quantities of materials, as in the case of a molecularly thin coating functioning as a superhydrophobic windshield or a few nanometer diameter particles functioning as catalysts. This undoubtedly makes nanotechnology an important enabler of sustainability[1] in materials and resources, while enhancing quality of life for a growing world population with increasing demand for energy and materials. By incorporating principles of Green Chemistry, nanomaterials can be synthesized and utilized in a responsible manner with reduced environmental impact. Applications of such materials and their properties will take the world closer to the United Nations Sustainable Development Goals (UNSDGs). Signs of these are already visible in several areas, including access to clean water.[2]

Although constituent materials become small in dimension, they exhibit new properties because of confinement of electrons in them, certainly different from their bulk counterparts. A familiar example is gold nanoparticles, which can be blue or wine red in solution and alternatively nonluminescent or brightly red luminescent upon examination with an ultraviolet lamp. Nanoparticles of TiO_2 can make reactive oxygen species, and this phenomenon is used, for example, in wastewater treatment or in self-cleaning coatings and/or formulations. Furthermore, heterojunction nanomaterials, comprising various nanomaterials, have unlimited potential in renewable energy systems because of their unique and controllable interface effects. For instance, heterojunction nanomaterials often exhibit improved catalytic activity as compared to single-component nanomaterials. The charge transfer or complementary redox characteristics of heterojunctions can promote improved activity and efficiency for specific chemical reactions.[3] As nanoparticle dimensions are comparable to cell constituents, i.e., proteins and their aggregates, they can enter biological systems. This action can be made selective, targeted, and simpler by appropriate functionalization. This is both beneficial (as in cancer therapy) or harmful (as in toxicity). These aspects can make nanoparticles stay in the environment and living systems for long times, leading to unintended outcomes, with speciation of nanosystems in the environment becoming an increasingly relevant topic for future research.[4] Thus, nanotechnology presents both opportunities and risks which contributed to various discussions on the safety of manufactured nanomaterials by national and international bodies.[5]

ACS Sustainable Chemistry & Engineering (*ACS SCE*) realizes the importance of nanomaterials and nanotechnology in making the world better and more sustainable through various initiatives including the powerful vision outlined in the UNSDGs. Our response to UNSDGs is outlined in a recent editorial.[6] Simultaneously, we have been publishing cutting edge research in diverse areas including new materials, sensors, energy harvesting, conversion and storage, water purification, recycling, thermal barriers, fire retardation, permeability control, superhydrophobicity, molecular delivery, efficient agriculture, therapy, smart devices, and many others which are all important in realizing the dream of a sustainable world.

While new research outcomes in all these areas are welcome, there are several others in which new insights are needed. We point out a few of them as follows:

(a) Detailed understanding of materials and functions using computational approaches is welcome. We realize that materials and processes, and consequently their computational aspects, are complex in view of the structural and functional connections in "large" nanosystems. Another related aspect is the impact of the activity/function on the material/device over a substantial period. Often research papers examine a few or tens of cycles of operation, say for example, in a catalytic cycle. While this may be appropriate and even adequate for certain areas, hundreds of cycles (or long-term stability, e.g., in flow systems) and impacts of operations on nanomaterials may be necessary in other areas

Received: October 14, 2021
Published: November 1, 2021

https://doi.org/10.1021/acssuschemeng.1c07031

including energy storage or industrial processes. Computational insights into materials during operation is essential.[7]

(b) Another significant need relates to a greater appreciation of phenomena at other length scales. Although nanomaterials are indeed useful, more traditional materials at the microscale may be better in properties and performance.[8] This points to the need to explore nanomaterials along with other materials to understand and appreciate the power of materials at all length scales, particularly in relation to new applications. This is particularly important for bulk materials with inherent nanostructures such as cellulose, clays, and zeolites.

(c) Materials, especially metals and metal oxides at the nanoscale, are not adequately explored using the principles of Green Chemistry.[9] The reason appears to be that in most such papers synthesis is attempted from the perspective of novel phenomena and end use is not either clear or appropriately addressed. *ACS SCE* encourages the use of sustainability metrics in the synthesis of nanomaterials of any kind. Authors can see more information in some of our recent editorials.[10−12]

(d) Manufacturing with principles of Green Chemistry involving, for example, atom economy, efficient solvent use, reduced waste, and reduced energy consumption would imply that processes become akin to biology. However, making more of the same nanoparticles using bacterial and other cells or biomachinery would not be welcome for our journal. At the same time, there are several open challenges in “bioenabled synthesis” such as shape tunability, monodispersity, unique functions of end products, mechanisms of particle growth, and fate of biomolecules and biomachinery because of particle synthesis. Exploring these aspects will make biosynthesis more structured.

(e) Although nanomaterials are energetic, often due to the increased surface energy of the materials, they also need energy for their synthesis. Although processes involving nanomaterials may save energy due to the utilization of their inherent metastability, the overall energy advantages of nanotechnology considering production, utilization, regeneration, and reuse of nanomaterials, devices, and products need to be assessed realistically.

(f) Nanotechnology is highly interdisciplinary. We welcome manuscripts in which multiple subject areas contribute to the problem being addressed.

(g) Newer synthetic and processing methods may be brought in, such as droplet synthesis, flow synthesis, nanoskiving, mechanochemistry, interfacial synthesis, and aqueous synthesis so that multiple aspects of sustainability and efficiency are addressed.

(h) Novel nanostructures could be designed for sustainable chemistry processes, such as core−shell nanostructures, van der Waals heterostructures, and hierarchical structures as well as hollow and porous structures, with additional implications in terms of properties and applications.

(i) Expand the application of nanoscale metals and their oxide materials in renewable energy systems including photocatalysis, electrocatalysis, and optoelectronic devices. The tunable photoelectric properties of metallic nanomaterials can achieve the expectation of efficiency and energy savings.

ACS SCE discourages submissions in the following areas: (i) Reports on green synthesis of new materials with incremental advances such as changing a plant source will not be considered. New insights from such papers are rather limited. An example is the “green” synthesis of carbon materials, especially carbon dots, by hydrothermal methods using plant-based raw materials. (ii) Inorganic and organic materials derived from plant and animal parts, extracts, and components are diverse. However, the synthetic approaches follow very similar routes leading to similar products. Well-known methods for doping and composite preparation are then added to create new materials. While diversity in raw materials can generate new results, the novelty in such scientific findings is rather limited. (c) Reports on processing waste materials, especially plastics, leading to new nanomaterials are welcome, only if overall environmental sustainability is considered. (d) Similarly, waste-to-wealth approaches to make materials are encouraged only if they lead to sustainability in resource management or produce new materials with novel properties using principles of sustainability.

We hope that these guidelines contribute to greater appreciation of nanotechnology in sustainable chemistry and engineering. We believe that adoption of these guidelines will result in more impactful publications and thereby move us a step closer to a more sustainable future.

Thalappil Pradeep, Associate Editor orcid.org/0000-0003-3174-534X

Zhenxing Li, Early Career Board orcid.org/0000-0002-4020-7490

Rafael Luque, Editorial Advisory Board orcid.org/0000-0003-4190-1916

AUTHOR INFORMATION

Complete contact information is available at: https://pubs.acs.org/10.1021/acssuschemeng.1c07031

Notes

Views expressed in this editorial are those of the authors and not necessarily the views of the ACS.

REFERENCES

(1) See for example Hyeon, T.; Manna, L.; Wong, S. S. Sustainable Nanotechnology. *Chem. Soc. Rev.* **2015**, *44*, 5755−5757.

(2) Nagar, A.; Pradeep, T. Clean water Through Nanotechnology: Needs, Gaps, and Fulfillment. *ACS Nano* **2020**, *14*, 6420−6435.

(3) Li, Z.; Hu, M.; Wang, P.; Liu, J.; Yao, J.; Li, C. Heterojunction Catalyst in Electrocatalytic Water Splitting. *Coord. Chem. Rev.* **2021**, *439*, 213953.

(4) Biswas, P.; Wu, C. Y. Nanoparticles and the Environment. *J. Air Waste Manage. Assoc.* **2005**, *55*, 708−746.

(5) For example, see Environment Directorate Joint Meeting of the Chemicals Committee and the Working Party on Chemicals, Pesticides and Biotechnology; OECD. https://www.oecd.org/officialdocuments/publicdisplaydocumentpdf/?cote=env/jm/%20mono(2020)38&doclanguage=en (accessed October 2021).

(6) Anastas, P.; Nolasco, M.; Kerton, F.; Kirchhoff, M.; Licence, P.; Pradeep, T.; Subramaniam, B.; Moores, A. The Power of the United Nations Sustainable Development Goals in Sustainable Chemistry and Engineering Research. *ACS Sustainable Chem. Eng.* **2021**, *9*, 8015−8017.

(7) Zhan, C.; Lian, C.; Zhang, Y.; Thompson, M. W.; Xie, Y.; Wu, J.; Kent, P. R. C.; Cummings, P. T.; Jiang, De-En.; Wesolowski, D. J. Computational Insights into Materials and Interfaces for Capacitive Energy Storage. *Adv. Sci.* **2017**, *4*, 1700059.

(8) Mukherjee, S.; Kumar, A. A.; Sudhakar, C.; Kumar, R.; Ahuja, T.; Mondal, B.; Srikrishnarka, P.; Philip, L.; Pradeep, T. Sustainable and Affordable Composites Built Using Microstructures Performing Better Than Nanostructures for Arsenic Removal. *ACS Sustainable Chem. Eng.* **2019**, *7*, 3222−3233.

(9) Gilbertson, L. M.; Zimmerman, J. B.; Plata, D. L.; Hutchison, J. E.; Anastas, P. T. Designing Nanomaterials to Maximize Performance and Minimize Undesirable Implications Guided by the Principles of Green Chemistry. *Chem. Soc. Rev.* **2015**, *44*, 5758−5777.

(10) Allen, D. T.; Carrier, D. J.; Gong, J.; Hwang, B.-J.; Licence, P.; Moores, A.; Pradeep, T.; Sels, B.; Subramaniam, B.; Tam, M. K. C.; Zhang, L.; Williams, R. M. Advancing the Use of Sustainability Metrics in ACS Sustainable Chemistry & Engineering. *ACS Sustainable Chem. Eng.* **2018**, *6*, 1.

(11) Subramaniam, B.; Licence, P.; Moores, A.; Allen, D. T. Shaping Effective Practices for Incorporating Sustainability Assessment in Manuscripts Submitted to ACS Sustainable Chemistry & Engineering: An Initiative by the Editors. *ACS Sustainable Chem. Eng.* **2021**, *9*, 3977−3978.

(12) Meier, M. A. R.; Tam, M. K. C. Shaping Effective Practices for Incorporating Sustainability Assessment in Manuscripts Submitted to ACS Sustainable Chemistry & Engineering: Biomaterials. *ACS Sustainable Chem. Eng.* **2021**, *9*, 7400−7402.

ACS Sustainable Chemistry & Engineering

pubs.acs.org/journal/ascecg

Editorial

ACS Sustainable Chemistry & Engineering Welcomes Manuscripts on Alternative Feedstocks

Cite This: *ACS Sustainable Chem. Eng.* 2021, 9, 4702−4703

Read Online

ACCESS | Metrics & More | Article Recommendations

This editorial highlights key research challenges associated with the use of feedstocks for sustainable transformations, with a particular focus on food and forest materials, areas in which *ACS Sustainable Chemistry & Engineering* welcomes manuscripts. This editorial complements previous editorials on circular processing of plastics[1] and e-wastes.[2]

Energy, chemicals, and polymers are still mostly produced from building blocks derived from petroleum, coal, and natural gas. As the demand for these commodities continues to increase, there is a need to develop sustainable production routes from renewable biobased resources. In the United States Department of Energy 2016 Billion-Ton Report, feedstock availability in the United States is projected to include up to one billion tons per year of crop residues, herbaceous energy crops, woody crops, algae, and urban construction residues. In addition to residues considered in the Billion-Ton Report, energy and commodity feedstocks could include carbon-rich materials such as marine and freshwater feedstocks, as well as food, textile, plastic, and water treatment wastes, as outlined below.

Typical marine feedstocks could consist of macroalgae and halobacteria, as well as residues from fishery and seafood industries.[3] Freshwater biomass could include cyanobacteria, fish residues, and predominantly water-cultured crops, such as water hyacinth.[4] These feedstocks and residues are sources of bioactive compounds, such as lipids, proteins, polysaccharides, and pigments, that find use in commercial sectors with high volume−low value (human food and animal feed) to low volume−high value (cosmetic, nutraceutical, pharmaceutical, and biomedicine) products.

Landfilled textiles and food wastes are significant and could be diverted if these carbon streams were refashioned into feedstocks instead of refuse. In the United States, textile waste in municipal solid waste (MSW) has increased by ∼40% over the past two decades, with approximately 11 million tons landfilled annually.[5] Textile wastes may include cotton and synthetic blends and ornamentation within garments.[6] Pretreatment methods can regenerate cellulose within the fabrics for use in conventional upgrading schemes for cellulose (i.e., biorefinery applications), but insights into unconventional uses with garment-based carbon are needed. Food waste is another significant feedstock alternative as it is produced globally at large rates with approximately 95% of food waste sent to the landfill.[5] Plastic wastes, which have been addressed in a separate editorial,[1] are often mixed with food wastes and other landfilled wastes. Synergistic methods for recycling the polymers, polymer−inorganic composites, and inorganic materials co-mingled with food wastes should be explored, since the recycling or upcycling of textile and plastics wastes is often limited due to the mixed nature of these materials. Residues from wastewater treatment plants are other sources of carbon feedstock. However, their use is challenging. Regional and large-scale studies on water−energy nexus in urban water systems and research on practical experiences are still missing.[7]

Carbon-rich wastes have potential for conversion to liquid fuels, to commodity and specialty chemicals, and also to methane. Often, an important hurdle to their use is point-source collection and consumer acceptance. However, it is critical that all feedstocks—whether stemming from renewable or nonrenewable sources—should be examined in the context of a circular economy. Their use should not be assessed simply on the fact that they are possibly derived from renewable resources but also on their potential for integration within downstream or upstream operations or processes that are respectful of economic constraints and environmental ramifications. To date, many research efforts have focused on developing feedstock conversion processes which are not integrated within the circularity of the operations and which have neglected the complexity of the mixtures in which these materials are embedded.

Broadly, the topical area of integration of novel or traditional feedstocks into upstream/downstream biorefinery or transformation operations respecting circularity will be welcomed. Specific cases addressing acute feedstock processing challenges that are current barriers to circularity will also be of interest. Manuscripts that address wholistically the integration of feedstocks in the circular economy will be welcomed. We look forward to your feedback and your manuscript submissions in these areas.

Abigail S. Engelberth, Early Career Board orcid.org/0000-0002-8150-0562

Wei Niu, Early Career Board orcid.org/0000-0003-3826-1276

Sónia P. M. Ventura, Early Career Board orcid.org/0000-0001-9049-4267

Received: March 20, 2021
Published: April 5, 2021

Sankar Nair, Editorial Advisory Board orcid.org/0000-0001-5339-470X
Marcelo A. Nolasco, Editorial Advisory Board
D. Julie Carrier, Associate Editor orcid.org/0000-0003-3322-4660

AUTHOR INFORMATION

Complete contact information is available at:
https://pubs.acs.org/10.1021/acssuschemeng.1c01929

Notes

REFERENCES

(1) Bakshi, B. R.; Shonnard, D.; Allen, D. T. ACS Sustainable Chemistry & Engineering Invites Contributions to a Virtual Special Issue on The Circular Economy of Plastics. *ACS Sustainable Chem. Eng.* **2021**, *9*, 1425−1426.

(2) Zhang, L.; Pradeep, T.; Licence, P.; Subramaniam, B.; Allen, D. T. ACS Sustainable Chemistry & Engineering Welcomes Manuscripts on Advanced E-Waste Recycling. *ACS Sustainable Chem. Eng.* **2021**, *9*, 3624−3625.

(3) Kerton, F.; Liu, Y.; Omari, K.; Hawboldt, K. Green chemistry and the ocean-based biorefinery. *Green Chem.* **2013**, *15*, 860−871.

(4) Guna, V.; Ilangovan, M.; Anantha Prasad, M. G.; Reddy, N. Water hyacinth: A unique source for sustainable materials and products. *ACS Sustainable Chem. Eng.* **2017**, *5* (6), 4478−4490.

(5) Breunig, H.; et al. Bioenergy potential from food waste in California. *Environ. Sci. Technol.* **2017**, *51* (3), 1120−1128.

(6) *Facts and Figures about Materials, Waste and Recycling. Textiles: Material-Specific Data*. U.S. Environmental Protection Agency. https://www.epa.gov/facts-and-figures-about-materials-waste-and-recycling/textiles-material-specific-data (accessed March 2021).

(7) Chrispim, M.; Scholz, M.; Nolasco, M. Phosphorus recovery from municipal wastewater treatment: Critical review of challenges and opportunities for developing countries. *J. Environ. Manage.* **2019**, *248*, 109268.

ACS Sustainable Chemistry & Engineering
pubs.acs.org/journal/ascecg
Editorial

The Power of the United Nations Sustainable Development Goals in Sustainable Chemistry and Engineering Research

Cite This: *ACS Sustainable Chem. Eng.* 2021, 9, 8015−8017
Read Online

In 2015, the United Nations (UN) unveiled an ambitious plan, the Sustainable Development Goals (SDGs), aimed at providing guidelines, applicable universally to all nations, for equitable and responsible development, respectful of humans and ecosystems.[1] The SDGs plan sets a clear agenda to be achieved by 2030 (Agenda 2030), composed of 17 goals and 169 targets, that promotes economic growth, environmental protection, social inclusion, and human well-being.[2] This framework has been adopted by many governmental agencies, foundations, and companies in order to articulate specific actions in the broader context of sustainable development.[3,4] The global scientific community has also established connections to the SDGs, highlighting the central role that sustainable chemistry and engineering must play to realize them.[5,6] In particular, the SDGs are a powerful way to focus on how chemicals are used.[7] The central role and impact of advanced technologies on global well-being and sustainability are further recognized by the declaration of a United Nations International Year of Basic Sciences for Sustainable Development in 2022.[8]

Time-bound action based on specific policies in different regions is critical for achieving Agenda 2030. For example, the successes of India, China, and Brazil, among the most populous countries, in achieving the SDGs will hugely contribute to the global outcomes. Efforts are underway to quantify progress, such as the SDG India Index.[9] Directed actions to achieve the SDGs will be region specific. For example, it has been suggested that combating environmental pollution will be key in achieving the SDGs in China.[10] Advances in science, technology, and education are critical to successfully address the various challenges and achieve the SDGs.

Within *ACS Sustainable Chemistry & Engineering* (*ACS SCE*), we encourage authors to connect their research to the SDGs (Figure 1), identifying societal, environmental, and health-related benefits within submitted manuscripts where appropriate. The editors of *ACS SCE* are currently publishing a series of editorials on effective practices to incorporate sustainability assessments in submitted papers.[11] We believe that the SDGs offer an opportunity to assess reported discoveries in a uniform and easily recognizable way. Specifically, sustainability advances reported in manuscripts can be used to benchmark progress against published 2030 SDG targets. This approach provides a framework to guide and trigger advances in sustainable chemistry and engineering, in a way similar to the 12 Principles of Green Chemistry[12] and the 12 Principles of Green Engineering.[13] It must be noted that all these frameworks call for a holistic view of sustainability, whereby advances should lead to progress in all criteria, not in just one or a few at the expense of others. We encourage authors to adopt such an approach when critically assessing their reported advances.

Figure 1. United Nations Sustainable Development Goals (SDGs).

We also welcome perspective-type manuscripts on the topic of the SDGs in the context of chemistry and engineering research, education, chemistry enterprise, public agencies, etc. While several such articles have appeared since the launch of the SDGs, the global crisis caused by the COVID-19 pandemic is reinforcing the urgency to work toward these goals. COVID-19 has had a major impact on human health and well-being (Goal 3) globally, yet the difference in the abilities of nations to effectively respond to the pandemic is revealing disparities across the globe in a number of SDG areas such as poverty (Goal 1), hunger (Goal 2), education (Goal 4), clean water and sanitation (Goal 6), and economic growth (Goal 8). Our ability to produce and consume responsibly has been drastically affected by disrupted supply chains, impaired mobility for people and goods, and increased reliance on disposables (Goal 12). The use of disposable masks, alongside already widespread use of single use plastics, is impacting habitats both on land and in the ocean (Goals 14 and 15). Some governments have seized this opportunity to cast ambitious plans for a post pandemic economic recovery to provide a boost to clean and affordable energy (Goal 7),

Received: June 4, 2021
Published: June 21, 2021

industry, innovation, and infrastructures (Goal 9), sustainable cities and communities (Goal 11), and climate change research (Goal 13). Similar to the strategy required to combat the global challenges posed by COVID-19, the achievement of Agenda 2030 also calls for a systemic, holistic, concerted, and global effort.

Clearly, many good practices have already been implemented, and progress is beginning to have a demonstrable impact. For example, eliminating open defecation by 2020 and providing clean water on tap (Goal 6) for every home in India by 2024, directly impacting the lives of 1.39 billion Indians, will be heartening accomplishments in this direction. At the global scale, the realization of water and sewage treatment methods will be essential to secure supplies of potable water. The chemical industry is not only the enabler of clean water, it also delivers many of the platform products that our daily lives depend upon, such as fertilizers (Goal 2), medicines (Goal 3), and materials for clothing and buildings (Goals 11 and 12). Thus, it will play a central role in meeting the SDGs. The growing global population, associated with fast urbanization, has contributed to some of the world's important challenges. The demand for everyday products is expected to double by 2030,[14] and the resulting expansion in chemical manufacturing must not worsen the environment's well-being and human health. At present, industry relies almost exclusively on fossil-based carbon sources for raw materials and energy. Its energy consumption results in greenhouse gas emissions that are approximately a third of those emitted by the transportation sector.[15] To lessen this burden, it is imperative that the chemical industry also deploys renewable and recycled carbon sources, both for raw materials and energy. Efforts toward such a transition are already underway. Examples include the use of biomass as feedstocks and, more recently, the electrification of the industry using renewable power[16] and plastics upcycling.[17] Chemical manufacturing is also accompanied by generation of end-of-use wastes, which must be reused or recycled to implement a circular economy.[18] Examples include converting the wastes into energy and materials,[19] which contribute to decarbonization (Goals 7 and 11). *ACS SCE* welcomes manuscripts that address advances on these topics, in the areas of catalysis (including photo- and electro-catalysis), energy materials, biomaterials, and resource-efficient chemical transformations.

Sustainability education (Goal 4) is essential to achieving the SDGs. Teaching chemistry and engineering from a systems thinking perspective will enable future chemists and engineers to consider the consequences of the choices they make in designing chemical products and processes from the beginning,[20] rather than deal with unintended consequences after their manifestation. Sharing examples of green chemistry and engineering applications of the SDGs with students as well as the general public will demonstrate that science and engineering can provide the solutions to global challenges. This has been exemplified by the rapid development of safe and effective COVID-19 vaccines. Equally important to the attainment of the SDGs is a workforce trained to embrace diversity, equity, and inclusion, as well as in collaborative partnerships to tackle the grand sustainability challenges of our times.

As we reflect on the role of the journal, *ACS SCE*, in advancing the SDGs, we should reflect on the role of chemistry and engineering itself. It was perhaps first said by Ronald Breslow[21] that "Chemistry is the central science." If that is indeed true, then we need to ask ourselves, "Central to what?" Is it merely central because it interacts with other disciplines? Is it central because it interconnects with other industry sectors? Or is it something bigger? Is chemistry central to our ability to understand and solve the greatest challenges of our generation, the same challenges that have been outlined by the UN's SDGs? In other words, sustainable chemistry and engineering are not merely important to the more obviously applicable SDGs such as production and consumption but rather also equally indispensable to those essential but less obviously related goals such as equity, equality, and justice. Achieving the broad range of goals will require building metaphorical bonds between the elements of our scientific and technological discoveries in catalysis, materials, and solvent systems to the humanitarian elements of education, economics, and social policy.[22] Through this approach, we can recognize that our technical understanding and creativity needs to link to broader societal mechanisms if we are to meet these important humanitarian goals at a global scale.

At *ACS SCE*, we strongly believe that sustainable chemistry and engineering will play a central role and serve as a hub to connect other disciplines in achieving Agenda 2030 in a holistic way. We are pleased to contribute to this mammoth effort.

Paul Anastas, Chair, Editorial Advisory Board orcid.org/0000-0003-4777-5172
Marcelo Nolasco, Editorial Advisory Board
Francesca Kerton, Memorial University of Newfoundland orcid.org/0000-0002-8165-473X
Mary Kirchhoff, ACS Green Chemistry Institute orcid.org/0000-0002-9527-6979
Peter Licence, Executive Editor orcid.org/0000-0003-2992-0153
Thalappil Pradeep, Associate Editor orcid.org/0000-0003-3174-534X
Bala Subramaniam, Executive Editor orcid.org/0000-0001-5361-1954
Audrey Moores, Associate Editor orcid.org/0000-0003-1259-913X

AUTHOR INFORMATION

Complete contact information is available at:
https://pubs.acs.org/10.1021/acssuschemeng.1c03762

Notes

REFERENCES

(1) United Nations, General Assembly. Sustainable Development Goals. *SDGs Transform Our World 2030*, 2015.

(2) Stafford-Smith, M.; Griggs, D.; Gaffney, O.; Ullah, F.; Reyers, B.; Kanie, N.; Stigson, B.; Shrivastava, P.; Leach, M.; O'Connell, D. Integration: the key to implementing the Sustainable Development Goals. *Sustainability science* **2017**, *12* (6), 911−919.

(3) Axon, S.; James, D. The UN Sustainable Development Goals: How can sustainable chemistry contribute? A view from the chemical industry. *Current Opinion in Green and Sustainable Chemistry* **2018**, *13*, 140−145.

(4) O'Riordan, T. J. UN sustainable development goals: How can sustainable/green chemistry contribute? The view from the agrochemical industry. *Current Opinion in Green and Sustainable Chemistry* **2018**, *13*, 158−163.

(5) Anastas, P. T.; Zimmerman, J. B. The United Nations sustainability goals: How can sustainable chemistry contribute? *Current Opinion in Green and Sustainable Chemistry* **2018**, *13*, 150−153.

(6) Noce, A. M.*How Chemistry Can Help Meet the UN's Sustainable Development Goals*; C&E News, 2018; Vol. *96*, p 22.

(7) Poliakoff, M.; Licence, P.; George, M. W. UN sustainable development goals: How can sustainable/green chemistry contribute? By doing things differently. *Current Op. Green and Sustainable Chem.* **2018**, *13*, 146−149.

(8) International Year of Basic Sciences for Sustainable Development. *United Nations*. https://www.iybssd2022.org (accessed May 18, 2021).

(9) SDG India Index & Dashboard 2019−20, 2019. *NITI Ayog*, November 2, 2019. https://niti.gov.in/sites/default/files/SDG-India-Index-2.0_27-Dec.pdf (accessed May 13, 2021).

(10) Yu, S.; Sial, M. S.; Tran, D. K.; Badulescu, A.; Thu, P. A.; Sehleanu, M. Adoption and Implementation of Sustainable Development Goals (SDGs) in China, Agenda 2030. *Sustainability* **2020**, *12*, 6288.

(11) Subramaniam, B.; Licence, P.; Moores, A.; Allen, D. T. *ACS Sustainable Chem. Eng.* **2021**, *9* (11), 3977−3978.

(12) Anastas, P. T.; Warner, J. C. Principles of Green Chemistry. In *Green Chemistry: Theory and Practice*; Oxford University Press, 1998; pp 29−56.

(13) Anastas, P. T.; Zimmerman, J. B. Peer Reviewed: Design through the 12 Principles of Green Engineering. *Environ. Sci. Technol.* **2003**, *37* (5), 94A−101A.

(14) Global Chemicals Outlook II, 2019. *United Nations Environment Programme*. https://wedocs.unep.org/bitstream/handle/20.500.11822/28113/GCOII.pdf (accessed Jan 12, 2020).

(15) World GHG Emissions Flow Chart, 2010. *ECOFYS*. https://ingmarschumacher.files.wordpress.com/2013/05/asn-ecofys-2013-world-ghg-emissions-flow-chart-2010.pdf (accessed Jan 25, 2021).

(16) Barton, J. L. Electrification of the chemical industry. *Science* **2020**, *368*, 1181−1182.

(17) Liu, S.; Kots, P. A.; Vance, B. C.; Danielson, A.; Vlachos, D. G. Plastic waste to fuels by hydrocracking at mild conditions. *Sci. Adv.* **2021**, *7*, eabf8283.

(18) Keijer, T.; Bakker, V.; Slootweg, J. C. Circular chemistry to enable a circular economy. *Nat. Chem.* **2019**, *11* (3), 190−195.

(19) Cano, V.; Cano, J.; Nunes, S. C.; Nolasco, M. A. Electricity generation influenced by nitrogen transformations in a microbial fuel cell: assessment of temperature and external resistance. *Renewable Sustainable Energy Rev.* **2021**, *139*, 110590.

(20) Mahaffy, P. G.; Ho, F. M.; Haack, J. A.; Brush, E. J. Can Chemistry Be a Central Science without Systems Thinking?, Editorial of Special Issue on Reimagining Chemistry Education: Systems Thinking, and Green and Sustainable Chemistry. *J. Chem. Educ.* **2019**, *96* (12), 2679−2681.

(21) Breslow, R. *Chemistry Today and Tomorrow: The Central, Useful, and Creative Science*; American Chemical Society: Washington, DC, 1997.

(22) Anastas, P. T.; Zimmerman, J. B. The periodic table of the elements of green and sustainable chemistry. *Green Chem.* **2019**, *21* (24), 6545−6566.

ACS Sustainable Chemistry & Engineering

pubs.acs.org/journal/ascecg

Editorial

Lab to Market: Where the Rubber Meets the Road for Sustainable Chemical Technologies

Cite This: *ACS Sustainable Chem. Eng.* 2021, 9, 2987−2989

Read Online

ACCESS | Metrics & More | Article Recommendations

Global chemical industry sales exceeded 5 trillion U.S. dollars in 2017 and are expected to double by 2030.[1] The chemical industry is among the most energy intensive industrial sectors and has greenhouse gas emissions totaling roughly a third of the greenhouse gas emissions of the transportation sector.[2] Raw materials for the chemical industry along with the energy required for their extraction and further processing are predominantly derived from fossil sources. Without transitioning to more sustainable technologies and raw materials, the required expansion of the global chemicals enterprise will exacerbate sustainability challenges. However, expansion of the industry also presents a significant opportunity to promote *sustainability and a circular economy*. Further, the accelerated increase in global environmental and safety regulations for new and existing chemicals and materials is also driving governmental actions aimed at technologies that are inherently safer and sustainable.[3,4] Despite the COVID-19-induced shrinkage of industrial production in 2020, the global chemical industry could be poised to invest in sustainable chemical manufacturing.[5] New technologies based on renewable sources of energy and raw materials, that are less resource intensive, are urgently needed to minimize harm to the environment and human health.

Sustainable manufacturing of chemicals can be based on plant-based biomass, abundantly available CO_2 and end-of-use waste to promote a circular economy (Figure 1). The future chemical industry can also be powered by renewable sources of power such as solar and wind energy, and renewable hydrogen to eliminate the carbon footprint caused by fossil-based energy sources. Fortunately, plant/waste-based biomass, solar, and wind energies are abundantly available to make this grand vision a reality. Major challenges include the development of new, practically viable technologies to make chemicals and fuels from these emerging feedstocks, finding processes that minimize resource consumption, and mapping a transition for the existing industry to evolve to a new, sustainable configuration.

Fundamentally, biomass resources are physically and chemically different from fossil fuels. While crude oils can be cracked and distilled into various gas and liquid components in an oil refinery and natural gas liquids can be cryogenically separated in gas processing plants, different separation technologies are needed to convert solid and involatile liquid biomass into useful chemicals in biorefineries. Chemically, biomass resources also tend to contain oxygenates, rather than hydrocarbons. Hence, while fossil fuels are transformed into valuable feedstocks largely by selective oxidation of C−H and C=C bonds (generally exothermic processes), transformations of biomass require the exact opposite—to reduce or transform C−O bonds—for which there are very few truly "green" and sustainable methods. This means that the infrastructure and network of processes required for a chemical industry based on biomass processing will be very different from those that exist currently. Mapping pathways to accomplish the transformation with biomass and other emerging feedstocks (CO_2, plastic wastes, etc.) will be challenging. Another challenge will be navigation of the notorious "Valley of Death" between early and late "technology readiness levels" (TRLs) for innovative technologies. Technologies must be demonstrated, economically and environmentally, at appropriate scales to be viable for large-scale commodity level production. These demonstrations will require closer collaboration between the private and public sectors such as governments, academia, and industry to deliver technological solutions. These public−private partnerships will share the greater risks that are invariably associated with transformative technologies.

Despite these challenges, steps in the transition to a sustainable chemical industry are already being taken. Some of these steps have been showcased by the Presidential Green Chemistry Challenge Awards, established by the United States Environmental Protection Agency in 1995 (now known as the Green Chemistry Challenge Awards), that highlight scientific and technical advances in green chemistry. The winning technologies have impacted a broad range of everyday products, including pharmaceuticals, foods, packaging, cosmetics, clothing, and electronics.[6] They are reported to have annually eliminated nearly 360 thousand metric tons of hazardous chemicals, saved 21 billion gallons of water, and cut CO_2 equivalent emissions by approximately 3.5 million metric tons.[7] While these achievements are significant, they only represent proof of viability as there is still ample room to shrink the industry's environmental footprint, such as the billions of metric tons of CO_2 emitted by the chemical industry annually.[1]

Received: February 10, 2021
Published: March 1, 2021

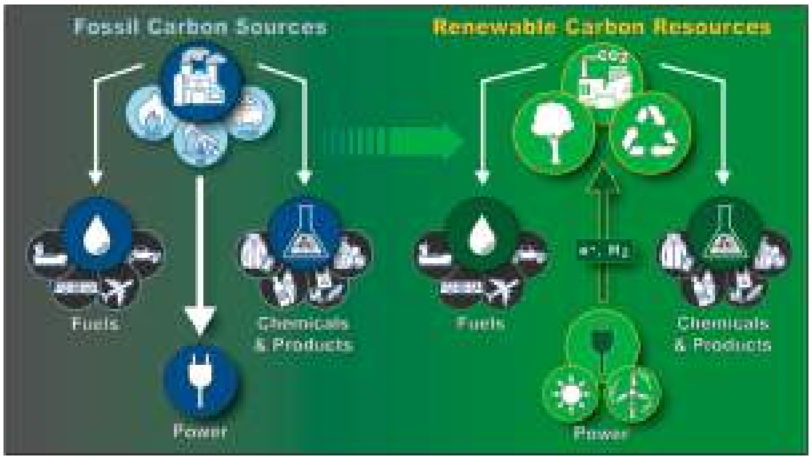

Figure 1. Transition to the grand vision: Distributed biorefineries where chemicals and fuels are made from renewable carbon sources powered by renewable energy.

Since measuring progress is critical in maintaining momentum in transitioning to sustainable chemical manufacturing, it is significant that many major chemical manufacturers now routinely track performance using sustainability metrics. The ACS Green Chemistry Institute reported a survey on how quantitative sustainability metrics are used in chemical manufacturing as well as future needs to translate promising green chemistry ideas into industrial technologies.[8] Major chemical and product manufacturers such as Dow,[9] BASF,[10] DuPont,[11] and Procter & Gamble[12] have used metrics and tools developed within their organizations to reduce the environmental footprints of their existing products and processes. The extent of these reductions may be seen in the annual sustainability reports posted at the company websites.

Beyond the evidence of major manufacturers measuring their sustainability performance, another reason to be optimistic is growth in sales for renewable chemicals. The global market size was $65 billion in 2019[13] and is projected to grow 10% annually and top $126 billion by 2026. While the market size is still a small fraction of the overall chemical industry output, it is significant enough to attract further investment.

All of these advances are driven by innovation. *ACS Sustainable Chemistry & Engineering* (*ACS SCE*) plans to publish a Virtual Special Issue (VSI) later this year titled *Industrial Sustainability*, featuring successful lab-to-market transitions of sustainable chemical technologies. As part of the VSI or otherwise, we invite case studies, which could be normal *ACS SCE* manuscripts such as research articles, features, or perspectives. Contributions are also invited that would be 1000−2000 word manuscripts to describe how barriers to commercialization were overcome in moving sustainable chemistry and engineering innovations from lab scale to commercialization. Manuscripts should identify various techno-economic barrier(s), successful practices for overcoming these barrier(s), and a description of how the experience might benefit other commercialization activities. The content should preferably address the following aspects: (a) brief description of the lab-scale innovation with appropriate literature and patent references, (b) technoeconomic, LCA, and risk/benefit analysis behind the business decision to commercialize, (c) key R&D studies and their scales that helped advance the TRL of the concept toward eventual commercialization, (d) partnerships across the product value chain that were critical to successful commercialization, (e) time from concept to commercialization, (f) estimate of the overall investment for a manufacturing plant of a given capacity, and (g) lessons learned from practices in other sectors or businesses. While all of this content is welcome, it is not necessary that every manuscript address all of these aspects. Figures that show the various production scales and key partners at each scale (producers of feedstock, energy, catalyst, chemical precursors, products, etc.) as well as quantitative sustainability analysis showing beneficial economic and environmental profiles would be appropriate. Manuscripts that are judged to be commercial promotions without generalizable findings are discouraged.

Please note that the foregoing guidelines are meant as suggestions. Authors are encouraged to add other aspects as appropriate. If you wish to specifically contribute to the VSI in preparation, please email us at your early convenience. We look forward to receiving manuscripts in the important area of translational sustainable chemistry and engineering.

We are aware that many of the challenges in bridging the gap between lab to market have not been addressed adequately in this limited space. Our editors will be revisiting this issue of global significance in future editorials.

Bala Subramaniam, Executive Editor orcid.org/0000-0001-5361-1954

David Allen, Editor-in-Chief orcid.org/0000-0001-6646-8755

King Kuok (Mimi) Hii, Associate Editor orcid.org/0000-0002-1163-0505

Juan Colberg, Guest Editor, Industrial Sustainability Virtual Special Issue

Thalappil Pradeep, Associate Editor orcid.org/0000-0003-3174-534X

AUTHOR INFORMATION

Complete contact information is available at:
https://pubs.acs.org/10.1021/acssuschemeng.1c00980

Notes

Views expressed in this editorial are those of the authors and not necessarily the views of the ACS.

REFERENCES

(1) *Global Chemical Outlooks II*, 2019. United Nations Environment Programme. https://wedocs.unep.org/bitstream/handle/20.500.11822/28113/GCOII.pdf (accessed Jan 12, 2020).

(2) *World GHG Emissions Flow Chart*, 2010. ECOFYS. https://ingmarschumacher.files.wordpress.com/2013/05/asn-ecofys-2013-world-ghg-emissions-flow-chart-2010.pdf (accessed Jan 25, 2021).

(3) *Communication from the Commission to the European Parliament, the Council, The European Economic and Social Committee and the Committee of the Regions. Chemicals Strategy for Sustainability Towards a Toxic-Free Environment-Brussels*, Oct14, 2020. European Commission. https://ec.europa.eu/environment/pdf/chemicals/2020/10/Strategy.pdf (accessed Jan 31, 2021).

(4) *S.999, Sustainable Chemistry Research and Development Act of 2019*, 116th Congress (2019−2020). https://www.congress.gov/bill/116th-congress/senate-bill/999 (accessed Jan 31, 2020).

(5) Bomgardner, M. M. US Chemical Industry Will Bounce Back This Year. *C&EN's World Chemical Outlook 2021*; January 10, 2021, Vol. *99*, Issue 2, p 31.

(6) *Green Chemistry Challenge Winners*. U.S. Enviromental Protection Agency. www.epa.gov/greenchemistry/presidential-green-chemistry-challenge-winners (accessed Jan 25, 2021).

(7) *Information About the Green Chemistry Challenge*. U.S. Enviromental Protection Agency. www.epa.gov/greenchemistry/information-about-presidential-green-chemistry-challenge (accessed Dec 27, 2019).

(8) Giraud, R. J.; Williams, P. A.; Sehgal, A.; Ponnusamy, E.; Phillips, A. K.; Manley, J. H. Implementing green chemistry in chemical manufacturing: a survey. *ACS Sustainable Chem. Eng.* **2014**, *2*, 2237−42.

(9) *Science and Sustainability*. DOW. www.dow.com/en-us/science-and-sustainability/ (accessed Jan 25, 2021).

(10) *Global Sustainability*. BASF. www.basf.com/en/company/sustainability.html (accessed Jan 25, 2021).

(11) *Sustainability*. DuPont. www.dupont.com/corporate-functions/sustainability.html (accessed Jan 25, 2021).

(12) *Environmental Sustainability*. Proctor & Gamble. https://us.pg.com/environmental-sustainability/ (accessed Jan 25, 2021).

(13) *Global Renewable Chemicals Market Share Will Reach USD 126 Billion by end of 2026: Facts & Factors*. Global News Wire. https://www.globenewswire.com/news-release/2020/11/10/2123412/0/en/Global-Renewable-Chemicals-Market-Share-Will-Reach-USD-126-Billion-by-end-of-2026-Facts-Factors.html (accessed Feb 2021).

https://dx.doi.org/10.1021/acssuschemeng.1c00980
ACS Sustainable Chem. Eng. 2021, 9, 2987−2989

General Articles

Sanjay Bajpai (1965–2021)

Dr Sanjay Bajpai, Scientist-G, Department of Science and Technology (DST), Government of India, who successfully implemented creative national and international R&D programmes, passed away on 12 May 2021. He was born on 19 February 1965. He pursued B.Tech. in Mechanical Engineering from Malaviya National Institute of Technology, Jaipur, followed by MBA from University of Rajasthan, Jaipur and subsequently earned Ph.D. for the work on 'Alternative fuels for internal combustion engines' from IIT-Delhi.

After a brief stint in industry, Sanjay joined as Scientist-B in DST in 1991. His outstanding accomplishments ensured elevation to various levels, becoming Head of Technology Mission Division – Water and Energy. During three decades of dedicated service, he conceptualized and steered various schemes, particularly state S&T mechanisms through application of appropriate technology development and commercialization endeavours. While implementing the State Council of S&T programme and being a visionary, he identified water and energy sectors, where DST had to work in mission mode. As a true *Karma Yogi*, he translated his vision into action keeping synergy of thoughts with all his colleagues and laid the foundation for Water and Energy programmes with clear focus on societal interventions and industry linkages, where appropriate. He started field-specific initiatives in the areas of water, bio-fuels and clean energy, with outcomes impacting people. His acumen in relating technology for societal relevance was the reason for assigning the Winning, Augmentation and Renovation for Water (WAR for Water) programme, spearheaded by T. Ramasami, the then Secretary of DST, on the directions of Supreme Court of India, to come out with technological solutions for addressing various water challenges. His proactive approach and inclusiveness enabled in finding sustainable solutions, through establishment of appropriate drinking water facilities/units in 300 much needed villages, benefiting over 1.60 million people, across the country, which have been replicated by various states, NGOs and a few corporates. This unique approach led to international collaborations, viz. Dutch India Water Alliance for Leadership Initiative (DIWALI), through a consortium of knowledge institutions and enterprises from The Netherlands and India, between India and European Union, and a new Indigo initiative between DST and R&D institutions of Belgium, Finland, France, The Netherlands, Germany and Spain, in designing solutions to meet the utility price envelope of countries similar to Indian situation. He was the brain behind the Indo-UK projects on Water Quality Research programme, which focused mainly on fate and management of emerging contaminants. He was also instrumental in starting Water Innovation Centers under Water Technology Initiatives to carry out collaborative research with many institutions/groups to come up with sustainable solutions and technologies for various water-related challenges.

Sanjay shaped a strong eco-system for R&D and technology demonstration in launching Clean Energy Research Initiative, with initial focus on Solar Energy. Seeing its success, it was expanded to cover programmes related to Methanol, Desalination, Clean coal, Building energy research, Materials for energy storage, Carbon capture storage and utilization, etc., by leveraging international collaborations. These enabled India to occupy a leadership position among 23 nations under Mission Innovation. He accelerated Clean Energy Innovation with enhanced funding, greater public–private partnership and knowledge sharing. In the process, India became the first country in developing collaborative programmes for Smart Grid and Off Grid in mounting demand-driven convergent solutions, in consortia mode, reaching advanced technology readiness levels.

Sanjay's interventions resulted in several papers, technical reports, Indian and US patents, and successful demonstration of various technologies; some of them leading to commercialization. As part of various technical committees, he ably mentored many young researchers in taking up challenging tasks and projects of great relevance. He also played a stellar role in spearheading many unique programmes of contemporary interest and guided policy makers in formulating significant initiatives of national importance. The worthy contributions of Sanjay and his team received many honours, to name a few, National Urban Water Award by the Union Ministry of Urban Development, Grand Challenges: Top Solutions Award by Technology Review – Massachusetts Institute of Technology (USA), National Award for Excellence in Ground Water by the Union Ministry of Water Resources, FICCI-HSBC Water-Innovation Award by FICCI, Hydrology Research Promotion Award by the Association of Hydrologists of India, Make in India Award by Indian Desalination Association and Global Water Award by Energy and Environment Foundation and Aqua Excellence Award by Aqua Foundation. Sanjay was a Fellow of Indian National Academy of Engineering and conferred with Honorary Fellowship of Association of Hydrologists of India.

Sanjay has been instrumental in shaping DST's foray in water and energy technologies and has led mission programmes in both these domains. He has conceptualized, crafted and implemented research, development and demonstration programmes in these domains for accelerated innovations. While quantifying the impact of his work on the S&T landscape of India may not be accurate, one may state the following. Under his direct supervision, over 1100 individual R&D projects, 4 Centers of Excellence, 2 of them jointly with Institutions in USA under India-US bilateral cooperation, in Clean Solar Energy, 2 Solar Hubs and 10 Water Quality, Management and Testing Centers, amounting to Rs 1350 crore, were sanctioned over the last 14 years.

Fifty five Post-doctoral Fellowships for young faculty/scientists and 65 Internships for doctoral students were awarded in the areas of Solar Energy, Water Technology and Energy Efficiency in Buildings for pursuing research in some of the leading Universities/Institutions in USA. This contributed to the work of 800 researchers in 350 S&T institutions and NGOs across the country. Many of these projects were across disciplines and multi-institutional, having strong industry participation leading to technology development for adoption by the industry. He was instrumental in leveraging crucial multilateral collaborations in the areas of clean energy and water under the aegis of Mission Innovation, Accelerating Carbon Capture Utilisation and Storage Technologies and European Union, along with establishing significant bilateral interactions in the areas of water and clean energy with UK, The Netherlands, Sweden, France and USA. In addition, he facilitated formulation of schemes and annual budgetary plans for all the 28 State S&T Councils for which DST extended core support to the tune of Rs 450 crore for taking up various activities of local relevance. The mechanisms he created, with the support of younger colleagues, ensured that the allocated funds reach the investigators quickly. This made a large difference for the investigator; there was always an individual who was considerate to the needs of R&D and the Society. He made significant contribution to development of National Cooling Action Plan. He was instrumental in conceptualizing and launching Global Cooling Prize as part of Mission Innovation Challenge on Affordable Heating and Cooling Challenge.

Sanjay will be fondly remembered by scientific fraternity as the true champion of S&T face of India. He brought together many researchers across academia, R&D labs and industry, in taking up some of the challenges faced across the globe. He was concerned about the development of S&T in less endowed institutions and therefore created channels for them wherever opportunity arose. Despite health concerns faced over the last decade, he ensured that ‘the show must go on’, which was in fact his working principle at office. While on leave or even when in hospital, he used to respond to the mails/messages/calls of S&T fraternity, or queries from his colleagues and offer guidance in processing the proposals for sanction, so as not to keep the matter pending. He was approachable to all. Compassion and ever willing positive attitude were his hall marks with a lasting SMILE (characterized by simplicity, modesty, integrity, leadership and empathy) in the service of the nation.

With his sad demise, DST has lost one of its most capable officers who represented India’s emerging S&T management face.

Sanjay leaves behind his mother, wife, two daughters and a son.

ASHUTOSH SHARMA[1]
RAJIV K. TAYAL[1]
AKHILESH GUPTA[1,*]
NEELIMA ALAM[1]
G. V. RAGHUNATH REDDY[1]
VINEET SAINI[1]
J. B. V. REDDY[1]
RANJITH KRISHNA PAI[1]
LIGY PHILIP[2]
PRASADA RAJU[3]
T. PRADEEP[4]

[1]*Department of Science and Technology,*
New Delhi 110 016, India
[2]*Department of Civil Engineering,*
Indian Institute of Technology Madras,
Chennai 600 036, India
[3]*Indistrial Consultancy and Sponsored Research,*
Indian Institute of Technology Madras,
Chennai 600 036, India
(former Scientist, DST)
[4]*Department of Chemistry,*
Indian Institute of Technology Madras,
Chennai 600 036, India
**e-mail: akhilesh.g@nic.in*

Edited by S. K. Satheesh, and printed & published by G. Madhavan for Current Science Association, Bengaluru 560 080.
Typeset by WINTECS Typesetters, Bengaluru and Printed at Lotus Printers Pvt Ltd, Bengaluru (Ph: 2320 9909)

Water Security Through Advanced Materials

by Prof Thalappil Pradeep, Professor at the Indian Institute of Technology Madras, and Sritama Mukherjee.

Thalappil Pradeep is an Institute Professor at the Indian Institute of Technology Madras, Chennai, India. He works on advanced materials and affordable clean water. His pesticide removal technology is estimated to have reached about 10 million people. His arsenic removal technology, approved for national implementation, is delivering arsenic free water to about 1.2 million people every day. Sritama Mukherjee holds a M.Sc. in chemistry from Pondicherry Central University, Puducherry and is currently finishing her Ph.D. under the guidance of Prof. T. Pradeep in the Department of Chemistry, Indian Institute of Technology Madras, Chennai. In this article they assess the importance of advanced materials to achieving water security.

Water is connected to every aspect of life, including its origin. The security of a society is intimately linked to the availability of its water resources. The world experiences an ever-increasing demand for fresh water, and planners are in a fix as to how the water needs of tomorrow can be met, keeping pace with the rapid increase in urbanization and migration. Availability of an affordable, adequate quality of water is a prerequisite to create any economic activity. Considering the specific case of India, it has just 4% of the global freshwater resources but 18% of the world's population. The World Bank predicts that achieving a growth rate of 8% or above for India will be possible only with a robust water management system. India (and the world) is increasingly becoming urban. The city population has risen rapidly: from 28% in 2000 to 33% in 2016. Highly populous countries like India and China, while increasing their industrial productivity in chemical, pharmaceutical, agrochemical, automotive, petrochemical, semiconductor, and other sectors, are experiencing a rapid decline in their water resources, which are further burdened by unprocessed industrial waste. In a rapidly interconnected world, negative impacts of industrial production cannot be localized. A difficult knot of complications arise when these emerging issues blend with the existing global problems that can only be solved through technological advances, disciplined approaches for responsible use of resources, and compassion in order to create sustainable solutions. Therefore, to achieve water security would require significant advances in treating, purifying, and assessing toxicity in water, combined with sustainable economic and technological development across the world, especially in less-developed countries.

> "Recent advances in the field of nanoscience provide many possible solutions to alleviate these issues, particularly for reducing scarcity and for sensing and removing contaminants."

An AMRIT unit attached to traditional hand pump in Nadia district of West Bengal (2015). Image courtesy of Prof Thalappil Pradeep

The impact of poor water quality is alarming. Water scarcity affects more than 40% of the global population. About 2 billion people do not have safe drinking water services. Over 2.2 million people die every year due to multiple water quality issues such as microbial pollution, heavy metal contamination, etc. About 80% of wastewater goes into waterways without adequate treatment. Over 200 million people are affected due to fluoride, 220 million due to arsenic, several million due to nitrate, cadmium, chromium, perchlorate, etc. In conjunction with such statistics, we need to remember that consuming water containing a low dose (over 10 ppb) of arsenic for over 5 years can cause irreversible changes in people resulting in hyperpigmentation, while chronic exposure impacts the reproductive system, heart, etc., and can even lead to cancer. These being the facts, it is unpardonable that access to clean water is not a core priority for all nations.

Clean water challenges are highly interdisciplinary. Understanding the multifaceted issues and solving them require the inputs of those across the fields of science, academia and politics. Recent advances in the field of nanoscience provide many possible solutions to alleviate these issues, particularly for reducing scarcity and for

> “The impact of poor water quality is alarming. Water scarcity affects more than 40% of the global population. About 2 billion people do not have safe drinking water services. Over 2.2 million people die every year due to multiple water quality issues such as microbial pollution, heavy metal contamination.”

sensing and removing contaminants. In recent years, carbon-based nanomaterials such as graphene and its derivatives, carbon nanotubes (CNTs), carbon nanofibers (CNFs), nanoporous carbon, fullerenes, graphitic carbon nitride and several other inorganic and organic materials have been used extensively as adsorbents, catalytic oxidants, membranes, disinfectants, and also for sensing and monitoring due to their extraordinary surface properties, electronic structure, ease of chemical modification, large specific surface area, controlled structural varieties, high chemical stability, porosity, low density, ease of regeneration, and reusability. Metal and metal oxide NPs have also been reported for various water purification and quality monitoring purposes. Nanomaterials, such as MoS_2 nanosheets for disinfection, CNF films for biocidal activity, silver nanobrushes for atmospheric water harvesting, and ferrihydrite for heavy-metal removal are debuting commercial applications in the water sector. Some of them have reached people in the form of affordable and easy-to-operate devices such as filtration-incorporated hand pumps, community plants, desalination units, and atmospheric water generators.

Our efforts have been to find appropriate and most advanced materials to scavenge specific contaminants in water, unaffected by the presence of others, in the most cost-effective fashion, sustainably. In the course of this, we discovered new nanostructured materials with large adsorption capacities for arsenite and arsenate ions in water to make practically viable solutions. Advanced spectroscopic and structural tools allowed us to understand the materials and processes in greater detail to appreciate their power in practical situations. Stability, toxicity, environmental lifetime and such other aspects of relevance were studied. These materials prepared in quantities were tested in the laboratory conditions for extended periods and with large volumes of water of the order of tens of kiloliters. Today these products and solutions, collectively referred to as AMRIT, acronym for Anion and Metal Removal by Indian Technology, are instrumental in ensuring arsenic-free water for over 12 million people (a simple installation connected to a hand pump is shown in the picture below). Similarly, there are filters that remove pesticides from drinking water using nanochemistry. That technology had already reached over 75 million people by 2016, when implementation data were last collected, reducing pesticide levels from over 20 times the safety standard, present in several parts of India, to concentrations substantially below it. Such solutions do not require electricity and are affordable, even for those living in the poorest parts of the world.

Alternate methods of microbial disinfection, desalination, water harvesting, recycling, contaminant sensing, and monitoring are debuting the marketplace. For example, capacitive deionization (CDI) is another promising and emerging direction for desalination, due to its relatively low input capital, high-energy efficiency, scalability, and minimal maintenance requirements, despite being limited by feedwater's total dissolved solids (TDS) and volume of treatment possible today. Research on further modification of CDI technology utilizing ion-exchange membranes has enabled researchers to overcome the operational limitation by eliminating the discharging cycle, enabling self-regeneration, and improving ion adsorption capacity, providing practically unlimited surface area for ion adsorption resulting in up to 80-90% salt removal efficiency with the electrode[18] Another active sustainable technology emerging is water harvesting from the atmosphere and some of them have been translated to commercial atmospheric water generators (AWGs). These AWGs extract moisture primarily by condensation or adsorption mechanism, or a combination of both. The energy efficiency of AWGs (amount of energy consumed per liter of water generated) renders them fit for regions with relative humidity (RH) > 40%. Hence, AWGs have proven to be a viable alternative in coastal regions where lack of sufficient resources has deterred the installation of desalination plants. Emerging advanced materials have the potential of taking up humidity during night and releasing the harvested water during the day, by absorbing sunlight, enabling the creation of clean water solutions with sustainable energy.

With various affordable and sustainable solutions for clean water that have been discussed above, there are huge opportunities available through diverse nanotechnologies for achieving water security in developing countries. We expect that the future applications of surface science and engineering for atmospheric water harvesting will focus on combining nanoengineered structures with unique wetting gradients that would not require additional energy input, other than solar-heat-enabled processes. Bio-mimicked structures can particularly help the AWG market flourish in arid North African and Middle East countries, specific regions of which are suffering from water scarcity today. The development of next-generation membranes could contribute to achieving the set target of reducing desalination costs from US $2.00 to US $0.50 per m^3 (as per the U.S. Department of Energy). One possible direction is the development of aquaporin membranes that offer the required selectivity. With synthetic water channels like CNTs, 2-D porous sheets of graphene oxide or MoS_2 or aligned peptides forming pores that mimic aquaporins can enhance salt rejection and cost-effective upscaling of the processes. Achieving higher sensitivity and creating a compact and cost-effective sensor accessory will enable the integration of such devices with smartphones and will facilitate point-of-use applications and creation of an interconnected network[22] Hydroinformatics is an emerging branch that possesses global visibility of resources for planning, designing, analysis and quantification, and therefore would enable decision-makers to efficiently manage aquatic resources and the environment. These potential opportunities call for higher governmental investment in infrastructure, awareness, education and adequate focus on water-related research activities, especially in developing countries. Increasing participation of people would give rise to numerous solutions to the clean water problem and also would generate more employment, ultimately paving the way to achieving far greater water security.

DESHABHIMANI WEEKLY December 5 2021 www.deshabhimani.com
5 ഡിസംബർ 2021

ദേശാഭിമാനി
വാരിക

കർഷകസമരത്തിന്റെ രാഷ്ട്രീയമാനങ്ങൾ
ടി പി കുഞ്ഞിക്കണ്ണൻ

കർഷക മുന്നേറ്റവും ഗോഡിമീഡിയയും
ശ്രീജിത്ത് ദിവാകരൻ

അഞ്ച് കവിതകൾ/ കുഴൂർ വിത്സൺ
മൂന്നു മക്കൾ/ സുറാബ്

അറിവിന്റെ അഴലും ആഴവും
ശാസ്ത്രത്തിന്റെ ജനപക്ഷം

ഡോ. ടി പ്രദീപും
ഡോ. ഗഗൻദീപ് കാങ്ങും
സംസാരിക്കുന്നു

ഡോ. ടി പ്രദീപ്

ജ്ഞാനസമൂഹമെന്നതുകൊണ്ട് നാമുദ്ദേശിക്കുന്നത് ജ്ഞാനം സമൂഹക്ഷേമത്തിനായി ഉപയോഗിക്കുന്ന സമൂഹത്തെയാണ്. ജ്ഞാനം മനുഷ്യരിൽ പ്രവർത്തിക്കുന്നു. ജ്ഞാനസമൂഹം വിവരസമൂഹത്തിൽ നിന്നും വ്യത്യസ്തമാണ്. വിവരം നാളിതുവരെയുള്ള സമൂഹങ്ങളൊക്കെയും ക്രയവിക്രയം ചെയ്തിട്ടുണ്ട്. അങ്ങനെയാണ് അവ വളർന്നതുതന്നെ.

കേരളം ജ്ഞാന സമൂഹത്തിലേക്ക് വളരുമ്പോൾ

ജ്ഞാനസമൂഹ നിർമിതിയുടെ ആണിക്കല്ലാണ് ഉന്നത വിദ്യാഭ്യാസം. ബിസിനസ് കാർഡിൽ പതിച്ച ഡിഗ്രികളുടെ എണ്ണത്തെയല്ല വിദ്യാഭ്യാസമായി നാം കരുതേണ്ടത്. ‘ഉടുപ്പിൽ തുന്നിച്ചേർക്കും ഉന്നതവിദ്യാഭ്യാസം എത്ര താഴ്ത്തീലാ നമ്മെ’ എന്ന് കവി. ആ ഡിഗ്രികൾ ആവശ്യം തന്നെ. അത് കുറഞ്ഞ അളവിൽ അറിവും, കൂടുതൽ അഭ്യാസവും ഉൾച്ചേരുന്നതായതുകൊണ്ട് വിദ്യാഭ്യാസത്തിന്റെ ആത്യന്തിക ലക്ഷ്യമായ സാമൂഹ്യനീതി അതുവഴി സംഭവിക്കുന്നില്ല. എല്ലാവർക്കും ബിരുദം കിട്ടിയാൽ മാത്രം ജ്ഞാനസമൂഹ നിർമിതി സാധ്യമാകില്ല. അങ്ങനെ ആകുമായിരുന്നെങ്കിൽ എല്ലാ പരീക്ഷകളിലും നൂറു ശതമാനം വിജയം ഉറപ്പാക്കുകയും, സ്കൂൾ പാസായവരെയെല്ലാം ഡിഗ്രി വരെയെങ്കിലും പഠിപ്പിക്കാനുള്ള സ്ഥാപനങ്ങൾ ഉണ്ടാക്കുകയും ചെയ്താൽ ജ്ഞാനസമൂഹം വളരെ പെട്ടെന്നുതന്നെ ഉണ്ടാക്കാനാകും.

അങ്ങനെ സംഭവിച്ചാൽ ചായപ്പീടികകളിലും തുന്നൽക്കടകളിലും ഡിഗ്രിക്കാർ ജോലിക്കുവരും. ആ ഡിഗ്രിക്കാരെക്കൊണ്ടുതുന്നൽ ജോലി ചെയ്യാനായില്ലയെങ്കിൽ തുന്നൽ ജോലി ഉണ്ടാകില്ല. തുന്നാൻ ആളില്ലെങ്കിൽ പുതിയ തുന്നൽ രീതികൾ വരും. തുന്നൽക്കടകൾ അപ്രത്യക്ഷമാകും, വസ്ത്രങ്ങൾ റെഡിമെയ്ഡുകൾ മാത്രമാകും. അവ യന്ത്രങ്ങൾ കൊണ്ട് നിർമിച്ചുവെന്നും വരും. ഇത് എല്ലാ രംഗത്തും വന്നുചേരും. കൃഷി തൊട്ട് അടുക്കളവരെ അടിമുടി മാറ്റപ്പെടും.

ജ്ഞാനസമൂഹമെന്നതുകൊണ്ട് നാമുദ്ദേശിക്കുന്നത് ജ്ഞാനം സമൂഹക്ഷേമത്തിനായി ഉപയോഗിക്കുന്ന സമൂഹത്തെയാണ്. ജ്ഞാനം മനുഷ്യരിൽ പ്രവർത്തിക്കുന്നു. ജ്ഞാനസമൂഹം വിവരസമൂഹത്തിൽ നിന്നും വ്യത്യസ്തമാണ്. വിവരം നാളിതുവരെയുള്ള സമൂഹങ്ങളൊക്കെയും ക്രയവിക്രയം ചെയ്തിട്ടുണ്ട്. അങ്ങനെയാണ് അവ വളർന്നതു തന്നെ. വിവരത്തെ അറിവായി മാറ്റപ്പെടുമ്പോഴാണ് പുതിയ കണ്ടെത്തലുകളും വികസനസാധ്യതകളും രൂപപ്പെടുന്നത്. ഒരു രാസസമവാക്യം അറിവാണ്. ആ അറിവുകൊണ്ട് ഒരു വസ്തു മറ്റൊന്നാകുന്നത് എങ്ങനെ എന്നറിയാം. അത്തരം അറിവുകളെക്കൊണ്ട് പദാർഥവിജ്ഞാനം കൈവരുമ്പോൾ പുതിയ രാസസമവാക്യങ്ങളും പുതിയ രാസക്രിയകളുണ്ടാക്കാനുള്ള വഴികളും നാമറിയുന്നു. ആ ജ്ഞാനം പുതിയ പോളിമർ ഉണ്ടാക്കാനും വൈക്കോലിൽ നിന്ന് ആൾക്കഹോളുണ്ടാക്കാനും കഴിയുന്ന പുതിയ വിജ്ഞാനമായി വികസിക്കുന്നു. ആ പുതിയ വിജ്ഞാനം പുതിയ സാങ്കേതിക വിദ്യയായി സമൂഹ നിർമിതിക്ക് വഴി

വെക്കുന്നു.

ജ്ഞാനസമൂഹം അന്നേവരെയുള്ള അറിവിനെ ഉപയോഗിക്കുന്നതോടൊപ്പം പുതിയ അറിവുകളെ ഉല്പാദിപ്പിക്കുകയും ചെയ്യുന്നു. അത് സാങ്കേതികവിദ്യകളിൽ മാത്രമല്ല ഭാഷയിൽ, തത്വശാസ്ത്രത്തിൽ, സാമൂഹ്യ ശാസ്ത്രത്തിൽ, ലളിതകലകളിൽ എന്നിങ്ങനെ എല്ലാറ്റിലും മാറ്റമുണ്ടാക്കുന്നു. സമൂഹത്തിന്റെ നിലനില്പിനുതന്നെ വിജ്ഞാനം അനുപേക്ഷണീയമായി വരുന്നു. അങ്ങനെ ജ്ഞാനസമ്പാദനം അത്യന്താപേക്ഷിതമായി വരുന്നു. ജ്ഞാനസമ്പാദനത്തിന്റെ ഇടങ്ങൾ ജ്ഞാനനിർമിതിയിലേക്ക് അനിവാര്യമായി മാറ്റപ്പെടുന്നു. അങ്ങനെ കലാശാലകളെ പുനർനിർവചിക്കേണ്ട അവസ്ഥ വരുന്നു.

നമ്മുടെ കലാലയങ്ങളിൽ നിന്ന് ജ്ഞാനനിർമിതി വലിയൊരർഥത്തിൽ കൈമോശം വന്നിരിക്കുന്നു. കേരളത്തിന്റെ തനതായ പ്രശ്നങ്ങളെ ഇവിടെത്തന്നെയാണ് മനസ്സിലാക്കേണ്ടത്. ആ പ്രശ്നങ്ങളുടെ ദുരീകരണവും ഇവിടെത്തന്നെയാണ് നടക്കേണ്ടത്. അത് സംഭവിക്കണമെങ്കിൽ ഇവിടെ അതിനു കഴിയുന്ന ജ്ഞാനസമൂഹങ്ങൾ രൂപപ്പെടണം. അവയ്ക്ക് കാര്യ

ക്ഷമമമായി പ്രവർത്തിക്കാവുന്ന സംവിധാനങ്ങൾ വരണം. ആ ജ്ഞാനസമൂഹങ്ങൾ ഉല്പാദിപ്പിക്കുന്ന അറിവുകളെ ഉപയോഗിക്കാനുള്ള അന്തരീക്ഷം രൂപപ്പെടണം. അത് ആവശ്യപ്പെടുന്ന വിവിധങ്ങളായ സംവിധാനങ്ങളുടെ സംഘാതങ്ങൾ തന്നെ രൂപപ്പെടണം. അതിന് ഉൾക്കാഴ്‌ചയുള്ള നേതൃത്വം ആവശ്യമുണ്ട്.

കേരളീയ സമൂഹത്തിന്റെ, ഇന്ത്യൻ സമൂഹത്തിന്റെതന്നെ ജ്ഞാനസമൂഹത്തിലേക്കുള്ള യാത്രയിലെ നിർണായകമായ പുഴുക്കുത്തുകളെക്കുറിച്ച് സൂചിപ്പിക്കേണ്ടത് അത്യാവശ്യമാണ്. ഇന്ത്യൻ സമൂഹത്തിന്റെ ശാപമെന്ന് ചിന്തകരൊക്കെയും ചൂണ്ടിക്കാട്ടിയ ജാതിതന്നെയാണ് നമ്മുടെ ഒന്നാമത്തെ ശത്രു. അത് പല രീതിയിൽ നമുക്കിടയിൽ പ്രവർത്തിക്കുന്നു. അത് മനുഷ്യരെ ജനനത്തിൽത്തന്നെ വ്യത്യസ്‌തരാക്കുന്നു. ജാതി നിർമാർജനത്തിന്റെ ഐതിഹാസികമായ സമരങ്ങൾ ശതാഭിഷിക്തമായിരിക്കുന്നു. എങ്കിലും ജാതി ജീവിച്ചുകൊണ്ടിരിക്കുന്നു. ജാതിയുടെ തിരിച്ചറിയൽ കാർഡുകൾ നാം ശരീരത്തിൽ പേറിക്കൊണ്ടിരിക്കുന്നു. അത് നമ്മുടെ ഭാഷയിൽ, ഉടുപ്പിൽ, ഭക്ഷണത്തിൽ, കല്യാണങ്ങളിൽ അങ്ങനെ എല്ലാറ്റിലും പ്രതിഫലിക്കുന്നു.

ജ്ഞാനസമൂഹം മലയാളിയെ മനുഷ്യനാക്കാൻ വഴിവെക്കുന്നു. നമ്പൂതിരിയെ മനുഷ്യനാക്കാൻ തുടങ്ങിവെച്ച ശ്രമങ്ങൾക്ക് തൊണ്ണൂറ് ആണ്ടായിരിക്കുന്നു. ‘അടുക്കളയിൽ നിന്ന് അരങ്ങത്തേക്ക്’ ആദ്യമായി അവതരിപ്പിച്ചത് 1929 ലാണ്. ഈ ശ്രമങ്ങളൊക്കെയും വലിയ മാറ്റങ്ങൾക്ക് വഴിതുറന്നുവെങ്കിലും ജാതി നശിച്ചില്ല. കാരണം, എനിക്കു തോന്നുന്നത് ഈ സംരഭങ്ങളൊക്കെയും ജാതിയിൽ അന്തർലീനമായ സമ്പദ്‌വ്യവസ്ഥയുടെ ശ്രേണീകരണത്തെ ഇല്ലായ്‌മ ചെയ്യാൻ മതിയായില്ല എന്നതാണ്. വിദ്യാഭ്യാസവും തൊഴിലവസരങ്ങളും വിദേശവാസവും വലിയ മാറ്റങ്ങൾക്ക് വഴി തുറന്നുവെങ്കിലും നമ്മുടെ ജീവിതം ജ്ഞാനസമൂഹം ആവശ്യപ്പെടുന്ന രീതിയിലേക്ക് മാറ്റപ്പെടുകയുണ്ടായില്ല. വിദ്യാഭ്യാസം കൊണ്ട് ജ്ഞാനസമൂഹം രൂപപ്പെട്ടില്ല എന്നുതന്നെ പറയാം.

നമ്മുടെ ആചാരങ്ങളുടെ പട്ടിക നോക്കുക!

(1) ഒരു ജ്ഞാനസമൂഹത്തിലെ വിവാഹത്തിന് നൂറു പവന്റെ തിളക്കമാവശ്യമില്ല. സ്വർണക്കടകളാൽ അലംകൃതമായ തെരുവുകൾ അമേരിക്കയിലോ യൂറോപ്പിലോ കാണാൻ കഴിയുകയില്ല. ഇന്ത്യൻ വീടുകളിൽ ശേഖരിച്ചു

ലി ക്വാൻ യു

വെച്ചിരിക്കുന്ന സ്വർണത്തിന്റെ അളവ് ഇരുപത്തിയയ്യായിരം ടൺ ആണെന്ന് പറയാം. സ്വർണത്തിന്റെ രൂപത്തിൽ ഒരു ലക്ഷം കോടി ഡോളർ നമ്മുടെ വീടുകളിൽ സംഭരിച്ചുവെച്ചിരിക്കുകയാണ്.

(2) സ്ത്രീധന മരണങ്ങൾ ജ്ഞാനസമൂഹത്തിൽ ഉണ്ടാകരുത്. പട്ടിണി മരണങ്ങൾ ഇല്ല എന്നു നാം അഭിമാനിക്കുന്നു. സ്ത്രീധന മരണങ്ങൾ അതിലുമെത്രയോ നികൃഷ്ടമാണ്. എങ്കിലും ഇത് സംഭവിച്ചുകൊണ്ടിരിക്കുന്നു. നാമത് നിസ്സംഗരായി കണ്ടുകൊണ്ടിരിക്കുന്നു.

(3) ജ്ഞാനസമൂഹത്തിൽ കഴിവ് മാത്രമായിരിക്കണം വളർച്ചയുടെ അളവുകോൽ. എങ്കിലും അറിവില്ലാത്തവരുടെ ഒരു പറ്റമായി അറിവിന്റെ ഗിരിശൃംഖങ്ങളായിരിക്കേണ്ട സർവകലാശാലകൾ കൂടി മാറ്റപ്പെട്ടിരിക്കുന്നു.

(4) ജ്ഞാനസമൂഹം അഴിമതി കുറഞ്ഞതും നിയമവാഴ്ച ഉള്ളതുമായിരിക്കണം. പക്ഷേ, നമ്മുടെ വഴികളിലൊക്കെയും അഴിമതി പതിയിരിക്കുന്നു.

എങ്ങനെയാണ് ഒരു ജ്ഞാനസമൂഹം സാധ്യമാകുക? ഉദാഹരണങ്ങളിലേക്ക് നോക്കുക നന്നായിരിക്കും. 1930 കളിൽ കുറെ മീൻപിടുത്തക്കാരുടെയും കച്ചവടക്കാരുടെയും ഗ്രാമമായിരുന്നു സിംഗപ്പൂർ. 1965 ലാണ് സിംഗപ്പൂരിന് സ്വാതന്ത്ര്യം ലഭിച്ചത്. ലി ക്വാൻ യു എന്ന ആദ്യത്തെ പ്രധാനമന്ത്രി, ആ രാജ്യം രാഷ്ട്രപിതാവെന്ന് കൊണ്ടാടുന്ന വിഖ്യാതനായ രാഷ്ട്രതന്ത്രജ്ഞൻ, ആ രാജ്യത്തിന്റെ വികസനത്തിന് അനിവാര്യമായ മൂന്ന് ആണിക്കല്ലുകളെക്കുറിച്ച് പറഞ്ഞു. അവ ഇവയാണ്. മെറിറ്റോക്രസി, ഹോണസ്റ്റി, പ്രാഗ്മാറ്റിസം. അർഹത, സത്യസന്ധത, പ്രായോഗികത എന്നിങ്ങനെ ഈ തത്വങ്ങളെ മൊഴിമാറ്റം ചെയ്യാം. മെറിറ്റോക്രസി എന്നാൽ കഴിവിന്റെ അംഗീകാരം. കഴിവ് മാത്രമാണ് തൊഴിലിന്റെ, ജോലിക്കയറ്റത്തിന്റെ അളവുകോൽ. അത് കുടുംബമഹിമയോ ജാതിയോ മതമോ വംശീതയോ അല്ല. മെറിറ്റോക്രസി എല്ലാ രംഗത്തേക്കും വ്യാപിക്കുന്നു. വൈസ് ചാൻസലറെ തെരഞ്ഞെടുക്കുമ്പോൾ ജാതിയോ മതമോ തെരഞ്ഞെടുപ്പിന്റെ മാന

സിംഗപ്പൂർ നഗരക്കാഴ്ച

ദണ്ഡമല്ല. ഹോണസ്റ്റി എന്നാൽ തൊഴിലിനോടുള്ള പ്രതിബദ്ധത, ആത്മാർഥത, സത്യസന്ധത എന്നിവയൊക്കെ ഇതിൽ പ്രതിഫലിക്കുന്നു. സത്യസന്ധത കൈമോശം വന്ന ഒരാളെയും വെച്ചുപൊറുപ്പിക്കയില്ല. അയാൾക്ക് സ്വാതന്ത്ര്യവും ജീവിതം തന്നെയും നഷ്ടമായേക്കാം. പ്രാഗ്മാറ്റിസം എന്നതുകൊണ്ട് രാഷ്ട്ര നിർമിതിയുടെ പ്രത്യയശാസ്ത്രം അന്ധമായ വിശ്വാസമല്ല പ്രായോഗികതയാണ് എന്ന് അടിവരയിടുന്നു. രാഷ്ട്രത്തിൽ വ്യത്യസ്തമായ പാർട്ടികളുണ്ടാകാം, അവർക്ക് വ്യത്യസ്തമായ അഭിപ്രായങ്ങളും. എന്നാൽ രാഷ്ട്ര നിർമിതിയുടെ കാര്യത്തിൽ അവയുടെ അന്തസത്തയിൽ എല്ലാവരും ഒരേ അഭിപ്രായം ഉള്ളവരാണ്. അതുകൊണ്ട്, വ്യത്യസ്ത പാർട്ടികളിലുള്ളവർ കൂടി മന്ത്രിസഭയുടെ ഭാഗമാകും. അവസരങ്ങളുടെ വീതിച്ചെടുക്കലല്ല, കഠിനമായ ജോലികൾ കഴിവുള്ളവരെ കണ്ടെത്തി ഏല്പിക്കുകയാണ് പതിവ്. അതുകൊണ്ട്, ഏറ്റവും കഴിവുറ്റവരുടെ കൂട്ടായ്മയായാണ് മന്ത്രിസഭ വികസിക്കുന്നത്. അതുകൊണ്ട് കഴിഞ്ഞ അമ്പതു വർഷം കൊണ്ട് സിംഗപ്പൂരിന്റെ പ്രതിശീർഷ വരുമാനം ഇരുപത് ഇരട്ടിയായി വർധിച്ചു. ഇന്നത് അമേരിക്കയുടെ പ്രതിശീർഷ വരുമാനത്തിന്റെ തൊട്ടുതാഴെയാണ്.

ഒരു സംസ്ഥാനത്തിനുമാത്രം ജ്ഞാനസമൂഹമായി മാറാൻ കഴിയുമോ? സാമൂഹിക, രാഷ്ട്രീയ അന്തരീക്ഷത്തിനനുസരിച്ച് പ്രാദേശിക മാറ്റങ്ങൾ പല രാഷ്ട്രങ്ങളിലുമുണ്ടായിട്ടുണ്ട്. അമേരിക്കയിൽ മൊത്തത്തിൽ ഭരണ സംവിധാനം ഏകീകൃതമാണെങ്കിലും വളർച്ചയുടെ ഗിരിശൃംഗങ്ങളിലെത്തിനില്ക്കുന്നത് കിഴക്കും പടിഞ്ഞാറുമുള്ള ന്യൂയോർക്കും കാലിഫോർണിയയുമാണ്. അതിനുള്ള കാരണം മനുഷ്യവിഭവമാണ്. അന്യരാജ്യങ്ങളിൽ നിന്നുവന്ന അനന്തമായ കഴിവുകളുള്ള മനുഷ്യരുടെ വലിയ സംഘാതങ്ങളാണ് ഈ സംസ്ഥാനങ്ങളുടെ വികസനത്തിന്റെ അടിത്തറയായി മാറിയത്. അവർക്ക് വരാനും വളരാനുമുള്ള വഴി തുറന്നിടുകവഴി അമേരിക്ക അനന്തമായ അവസരങ്ങളുടെ രാജ്യമായി മാറി.

കഴിവുള്ളവർക്ക് അവസരങ്ങൾ കൊടുക്കുന്നതുവഴി രാജ്യം മനുഷ്യവികാസത്തിലേക്കുള്ള നിതാന്ത പ്രയാണത്തിലേക്കു വഴി തുറക്കുന്നു. എല്ലാവർക്കും വളരാനുള്ള അവസരമുണ്ടെങ്കിൽ രാജ്യം വളർച്ചയിലേക്ക് മുന്നേറുക തന്നെ ചെയ്യും.

പ്രൊഫ. എം മുരളീധരൻ

പക്ഷേ, നാം കൊച്ചു കൊച്ചു കാര്യങ്ങളിൽ അഭിരമിക്കുകയാണ്. അഭിരമിച്ചുകൊണ്ടേയിരിക്കുകയാണ്. ഇതൊരു രോഗാവസ്ഥയെ സൂചിപ്പിക്കുന്നു. കഴിഞ്ഞകാല സംഭവങ്ങളെ ശ്രദ്ധിച്ചു കാണുമ്പോൾ ഒരു കാര്യം വ്യക്തമാണ്. വലിയ സാമൂഹ്യ വികാസത്തിന് സാധ്യമാകുന്ന വിഷയങ്ങൾ ചിലതെല്ലാം കഴിഞ്ഞ മാസങ്ങളിൽ തീക്ഷ്ണമായി നമുക്ക് മുമ്പിലെത്തി. സ്ത്രീധനവും അതിന്റെ വിപത്തും, കള്ളപ്പണവും ആസൂത്രിത അഴിമതിയും, വ്യാവസായിക സൗഹൃദവും ഉദ്യോഗസ്ഥ രാഷ്ട്രീയ ബന്ധവും, സ്ത്രീ പീഡനവും സ്ത്രീ സൗഹൃദ സമൂഹവും, ഭിന്നശേഷി സൗഹൃദവും മറ്റ് ന്യൂനപക്ഷ നിലപാടുകളും എന്നിങ്ങനെ വ്യത്യസ്തമായ വിഷയങ്ങൾ. അവയിലെല്ലാം ഒരു വലിയ മാറ്റത്തിന്റെ കാറ്റ് സമൂഹം പ്രതീക്ഷിച്ചിരുന്നു. എന്തുകൊണ്ട് വലിയ മാറ്റങ്ങൾ സാധ്യമാകുന്നില്ല? ഒരഞ്ചു വർഷക്കാലത്തെ അനുഭവങ്ങളെ ഒരുമിച്ച് കാണുമ്പോൾ ചില വലിയ കാര്യങ്ങൾ ശ്രദ്ധിക്കേണ്ടതുണ്ട്. കേരളം അഭിമുഖീകരിക്കുന്ന മുഖ്യമായ വിഷയങ്ങൾ ഇവയാണ്. (1) പരിസ്ഥിതി സുരക്ഷ: ഒരു സംസ്ഥാനത്തിന്റെ ഒരു ദശാബ്ദക്കാലത്തെ അധ്വാനം മുഴുവൻ നാലു ദിവസത്തെ മഴയിൽ ഒഴുകിപ്പോകുന്ന കാഴ്ചയാണ് നാം കണ്ടത്. ഇനിയൊരിക്കലും അത് സംഭവിച്ചു കൂട. (2) ആരോഗ്യ സുരക്ഷ: മഹാമാരികളുടെ ഒരു നിരതന്നെ നമ്മെ വിറപ്പിച്ചുകൊണ്ട് കടന്നു

പോയി; കടന്നുപോയിക്കൊണ്ടിരിക്കുന്നു. ഇനിയൊരു മഹാമാരി നമ്മുടെ സമൂഹത്തിൽ വിള്ളലുണ്ടാക്കിക്കൂടാ. (3) തൊഴിൽ സുരക്ഷ: അന്യസംസ്ഥാനങ്ങളിൽ നിന്നും വിദേശ രാഷ്ട്രങ്ങളിൽ നിന്നും മലയാളി തിരിച്ചെത്തിക്കൊണ്ടിരിക്കുന്നു. പുതിയ തൊഴിലവസരങ്ങളും പുത്തൻ സാങ്കേതികവിദ്യയും കണ്ടെത്തിയില്ലെങ്കിൽ സാമൂഹ്യവ്യവസ്ഥ താളം തെറ്റുമെന്നു തന്നെ പറയാം. (4) സാമൂഹ്യ സുരക്ഷ: നവോത്ഥാനത്തിന്റെ സുഗന്ധം ഇവിടെ നിന്ന് അപ്രത്യക്ഷമായിരിക്കുന്നു. സമൂഹത്തിന്റെ പുഴുക്കുത്തുകൾ പല രീതിയിൽ പ്രത്യക്ഷപ്പെട്ടുകൊണ്ടിരിക്കുന്നു. ശക്തമായ നിയമ നിർമാണവും നിയമവാഴ്ചക്കുള്ള സംവിധാനവും ഉണ്ടായിരിക്കണം. സ്ത്രീപഡനവും സ്ത്രീധന കൊലപാതകങ്ങളും സ്വർണ കള്ളക്കടത്തും ഉണ്ടാകാൻ പാടില്ലാത്ത വിധം നിയമസുരക്ഷയും ദുരാചാരങ്ങളുടെ ദുരീകരണവും ഉണ്ടാകേണ്ടിയിരിക്കുന്നു. (5) സ്ഥാപന സുരക്ഷ: നാം മുമ്പുണ്ടാക്കിയ സ്ഥാപനങ്ങളെല്ലാം മൂല്യച്യുതിയുടെ അഗാധതകളിലാണ്. നമ്മുടെ സർവകലാശാലകളും ഗവേഷണ സ്ഥാപനങ്ങളും അവയുടെ പ്രഖ്യാപിത ലക്ഷ്യങ്ങളിൽ നിന്ന് ബഹുദൂരം പിന്നോട്ട് പോയിരിക്കുന്നു. പ്രഗത്ഭരായ കർമകുശലർ നമ്മുടെ സ്ഥാപനങ്ങളിൽ നിന്നും അപ്രത്യക്ഷരായിരിക്കുന്നു. ഇതിനൊക്കെയുള്ള പോംവഴിയാണ് ജ്ഞാനസമൂഹം.

ഒരിക്കൽ ഐൻസ്റ്റീൻ പറഞ്ഞതായി കേട്ടിട്ടുള്ള ഒരു കഥയുണ്ട്. വർഷങ്ങൾക്കുമുമ്പ് പ്രശസ്തമായ ഒരു ദേശമുണ്ടായിരുന്നു. അവിടെ വലിയ കച്ചവട സ്ഥാപനങ്ങളും ഉല്പാദന സ്ഥാപനങ്ങളും വിദ്യാലയങ്ങളും മറ്റും ഉണ്ടായിരുന്നു. ജനങ്ങൾ സമ്പദ്സമൃദ്ധിയിലായിരുന്നു. ആ പ്രശസ്തമായ ദേശത്തെക്കുറിച്ച് കേട്ടറിഞ്ഞ് ഒരാൾ അവിടെയെത്തി. തങ്ങളുടെ അഭിവൃദ്ധി അതിഥിക്കുമുമ്പിൽ തുറന്നുവെക്കാൻ അവർക്ക് വലിയ ഉത്സാഹമായിരുന്നു. അതൊക്കെ കണ്ടതിനുശേഷം അദ്ദേഹം അവരോട് ചോദിച്ചു. 'നിങ്ങളുടെ ഈ സമൃദ്ധി കണ്ട് ഞാൻ സന്തോഷിക്കുന്നു. പക്ഷേ, ഈ സമൃദ്ധി നിങ്ങളെങ്ങനെയാണ് സംരക്ഷിക്കുക?' അവർ പറഞ്ഞു: 'അതിന് ഞങ്ങൾക്ക് പോലീസുണ്ട്. പട്ടാളമുണ്ട്.' 'അവരല്ല നിങ്ങളുടെ സമുദ്ധി സംരക്ഷിക്കുന്നത്'. അയാൾ തുടർന്ന് ചോദിച്ചു. 'വേറെയാരുണ്ട്?' തങ്ങൾക്കൊരു കർദിനാളുണ്ടെന്നും അദ്ദേഹം തങ്ങളുടെ സമൃദ്ധി സംരക്ഷിക്കുമെന്നും അവർ പറഞ്ഞു. 'അവർക്ക് ഇതൊന്നും സംരക്ഷിക്കാൻ കഴിയില്ല.' അദ്ദേഹം തുടർന്നു. 'വേറെയാരുണ്ട്?' അവർ പലരുടെയും പേരുകൾ പറഞ്ഞു. പണക്കാർ, കച്ചവടക്കാർ, ജഡ്ജിമാർ, വക്കീലന്മാർ തുടങ്ങി ഒട്ടേറെപ്പേർ. 'നിങ്ങളെ സംരക്ഷിക്കുന്നവർ അവരൊന്നുമല്ല.' അദ്ദേഹം പറഞ്ഞു. പിന്നെയാരാണ് ഞങ്ങളെ സംരക്ഷിക്കുന്നതെന്ന ജനങ്ങളുടെ ചോദ്യത്തിന് മറുപടിയായി അദ്ദേഹം പറഞ്ഞു. 'നിങ്ങളുടെ സമൂഹം സംരക്ഷിക്കേണ്ടത് ഇവിടത്തെ അധ്യാപകരാണ്. ഈ നഗരത്തിന്റെ ഗുരുവാരാണ്?' അങ്ങനെ അവർക്ക് മനസ്സിലായി. തങ്ങളെ സംരക്ഷിക്കുന്നത് ആരാണെന്ന്, തങ്ങൾ സംരക്ഷിക്കേണ്ടത് വിദ്യാലയങ്ങളെ യും സർവകലാശാലകളെയുമാണെന്ന്.

ഓരോ രാജ്യവും, ലോകംതന്നെയും വികസിച്ചത് ആശയങ്ങളെക്കൊണ്ടാണ്. ഇക്കാണുന്ന നഗരങ്ങളാക്കെയും ഉണ്ടായത് ആശയങ്ങളും അധ്വാനവും ചേർന്നാണ്. ആശയം തന്നെയും ഒരധ്വാനമാണ്. നഗരങ്ങളുടെ വികസനത്തിന് മനുഷ്യരാശിയുടെ നീണ്ട വഴിത്താരയിൽ എത്രയോ ചുരുങ്ങിയ കാലയളവിന്റെ ചരിത്രം മാത്രമേ ഉള്ളു. ആറ്റങ്ങളുണ്ടെന്ന അറിവിന് ഇരുനൂറ് വർഷത്തെ ചരിത്രം മാത്രമേയുള്ളു. നാളിതുവരെയുള്ള വൈദ്യുതിയുടെ ചരിത്രം നൂറ്റിയിരുപത് വർഷത്തിലൊതുങ്ങുന്നു. ഡിഎൻഎ കണ്ടെത്തിയത്, തന്മാത്രകളാണ് രോഗഹേതുവെന്നും അവക്കുള്ള പ്രതിവിധികളും തന്മാത്രകളാണെന്നും ഉള്ള അറിവിന്, എഴുപത് വർഷത്തെ ചരിത്രമേയുള്ളു. നോക്കു, അമ്പത് വർഷം കൊണ്ട് എന്തൊക്കെ മാറ്റങ്ങളാണ് സംഭവിച്ചത്? മൊബൈൽ ഫോണും ഇന്റർനെറ്റും നമ്മുടെ ജീവിതത്തെ മാറ്റിമറിച്ചത് കഴിഞ്ഞ ഒരു ദശാബ്ദം കൊണ്ടാണ്. ഇനിയൊരു ഇരുപത്തിയഞ്ച് വർഷത്തിനുള്ളിൽ സാങ്കേതിക വിപ്ളവങ്ങളുടെ ഒരു പെരുമഴ തന്നെ സംഭവിക്കാൻ പോകുന്നുവെന്ന് പറയാം. 2030കളിൽ മനുഷ്യൻ ചന്ദ്രനിലേക്ക് ദിവസേനെ യാത്ര ചെയ്തുവെന്ന് വരാം. ബഹിരാകാശ യാത്ര വിദേശയാത്ര പോലെ സുപരിചിതമായെന്നും വരാം!

കഴിവുള്ളവർക്ക് അവസരങ്ങൾ കൊടുക്കുന്നതു വഴി രാജ്യം മനുഷ്യവികാസത്തിലേക്കുള്ള നിതാന്ത പ്രയാണത്തിലേക്കു വഴി തുറക്കുന്നു. എല്ലാവർക്കും വളരാനുള്ള അവസരമുണ്ടെങ്കിൽ രാജ്യം വളർച്ചയിലേക്ക് മുന്നേറുകതന്നെ ചെയ്യും.

ഒന്നോർത്തു നോക്കുക. അറവു മൃഗങ്ങളില്ലാതെ ഇറച്ചി തയ്യാറാക്കുന്ന ഫാക്ടറികളെപ്പറ്റി, അടുക്കള അപ്രത്യക്ഷമാകുന്ന വീടുകളെപ്പറ്റി, നൂറ്റിയിരുപതികളിലെത്തി നില്ക്കുന്ന മനുഷ്യായുസിനെപ്പറ്റി, ശരീരത്തിന്റെ തന്നെ ഭാഗമായ യന്ത്രസംവിധാനങ്ങളെപ്പറ്റി, യാത്ര ആവശ്യമില്ലാത്ത ലോകത്തെപ്പറ്റി, സ്വീകരണ മുറിയിൽ ഡിജിറ്റൽ രൂപത്തിൽ വന്നെത്തുന്ന അതിഥിയെപ്പറ്റി, ആശുപത്രികളിലും ഹോട്ടലുകളിലും വീടുകളിലും ഫാക്റ്ററികളിലും അക്ഷീണം ജോലി ചെയ്യുന്ന ഹ്യൂമനോയിഡുകളെപ്പറ്റി. ലോകം അതിശീഘ്രം മാറുകയാണ്. ഈ മാറ്റം കാണാതെ, സ്വർണക്കടത്തിലും കള്ളപ്പണത്തിലും ആണ്ടു മുങ്ങുന്ന സമൂഹത്തെ കാണുമ്പോൾ സൂരി നമ്പൂതിരിപ്പാടിന്റെ ലോകം കേരളത്തിൽ നിന്നും പടിയിറങ്ങിയിട്ടില്ല എന്ന് ഇടയ്ക്കിടെ ഓർമ്മിക്കാനിടവരുന്നു. അതോടൊപ്പം നാമറിയേണ്ടത്, ആ ലോകം നമ്മുടെ അയൽപക്കത്ത് ചരിത്രവിസ്മൃതിയിൽ ആണ്ടുപോയ്ക്കൊണ്ടിരിക്കുകയാണ് എന്ന് കൂടിയാണ് ●

(തൃശൂരിൽ നടന്ന പ്രൊഫ. എം മുരളീധരൻ സ്മാരക പ്രഭാഷണത്തിന്റെ സംഗ്രഹിത രൂപം. **തയ്യാറാക്കിയത്: ആരതി ശങ്കർ)**

ഡോ. ടി പ്രദീപ്

ഡോ. ടി പ്രദീപ്/കെ എൽ ജോസ്

കേരളത്തിന്റെ ഉൾനാടൻ ഗ്രാമങ്ങളിലൊന്നായ പന്താവൂരിൽനിന്ന് ശാസ്ത്രലോകത്തിന്റെ അനന്ത വിസ്മയങ്ങളിലേക്ക് പറന്നുയർന്ന ഈ മലയാളി ശാസ്ത്രജ്ഞന്റെ പ്രതീക്ഷകളും ഉത്കണ്ഠകളും ചിന്താലോകത്തിന്റെ വൈവിധ്യവും ആഴവും ചില കമ്പനങ്ങൾ സൃഷ്ടിക്കും...

നാനോ കണത്തിലെ രൂപഭദ്രത

‘അനന്തവും അജ്ഞാതവും അവർണനീയവു’മായ പ്രപഞ്ചരഹസ്യങ്ങളെ നിർധാരണം ചെയ്യുന്ന ശാസ്ത്രജ്ഞരുടെ ലോകം കേരളീയ പൊതുമണ്ഡലത്തിന്റെ ഇരുൾനിറഞ്ഞ ഭാഗമാണ്. ശാസ്ത്രമേഖലയിലെ പ്രതിഭാശാലികൾ മലയാളിജീവിതത്തിലെ അജ്ഞാത ഭൂഖണ്ഡങ്ങളാണ്.

ലാളിത്യത്തിന്റെയും അറിവിന്റെയും മാതൃകാജീവിതരൂപങ്ങളെ ‘ദന്തഗോപുരവാസി’കളായി ചിത്രീകരിക്കാനാണ് നമുക്കിഷ്ടം. മനുഷ്യജീവിതത്തിന്റെ ചാലകശക്തികളായ ശാസ്ത്രലോകത്തിന്റെ ഉപാസകരെ അറിഞ്ഞാദരിക്കുന്നതിൽ നാം പലപ്പോഴും കുറ്റകരമായ അനാസ്ഥ പുലർത്തുന്നു.

ശാസ്ത്രീയ വിജ്ഞാനത്തിന്റെ മഹാവിസ്ഫോടനങ്ങളാണ് പ്രപഞ്ചജീവിതത്തിന്റെ ഗതിവിഗതികളെ നിയന്ത്രിക്കുന്നതെന്ന തിരിച്ചറിവിലേക്ക് നാമുണരേണ്ടിയിരിക്കുന്നു. ഇത്തരം ഉണർച്ചകൾ ‘ജ്ഞാനസമൂഹ’മെന്ന ആഗ്രഹത്തിലേക്കടുക്കാൻ നമ്മെ സഹായിക്കുകതന്നെ ചെയ്യും.

ഗണിതജ്ഞനും ജ്യോതിശ്ശാസ്ത്രജ്ഞനുമായ സംഗമഗ്രാമ മാധവനിൽനിന്ന് ആരംഭിക്കുന്ന ശാസ്ത്രജ്ഞപരമ്പര മലയാളി ജീവിതത്തിന്റെ പൂർവാർജിത സമ്പാദ്യമാണ്. ബൊട്ടാണിക്കൽ സർവെ ഓഫ് ഇന്ത്യ യാഥാർഥ്യമാക്കിയ ഇ കെ ജാനകിഅമ്മാൾ, സി വി രാമനുമൊത്ത് പ്രവർത്തിച്ചിരുന്ന ഏക വനിതാ ശാസ്ത്രജ്ഞയായ അന്നാമാണി, ഹരിതവിപ്ലവത്തിന്റെ പിതാവെന്നറിയപ്പെടുന്ന എം എസ് സ്വാമിനാഥൻ തുടങ്ങിയ ഒട്ടേറെ മലയാളി ശാസ്ത്രപ്രതിഭകൾ നമ്മുടെ ഓർമകളിൽ പ്രകാശം വിതറുന്നവരാണ്.

പശ്ചിമഘട്ടമേറിയും വളരുന്ന കേരളത്തിന്റെ ശാസ്ത്രഖ്യാതി പരത്തുന്ന പ്രതിഭകളിലൊരാളാണ് പ്രൊഫ. ടി പ്രദീപ്. പദാർഥ വിജ്ഞാനീയത്തിലും പ്രത്യേകിച്ച് ‘നാനോ സാങ്കേതിക വിദ്യ’യിൽ സങ്കീർണഗവേഷണങ്ങൾക്ക് നേതൃത്വം നല്കുന്ന പ്രദീപ് ചെന്നൈ ഐഐടിയിൽ ഇൻസ്റ്റിറ്റ്യൂട്ട് പ്രൊഫസറും ദീപക് പരേഖ് ചെയർ പ്രൊഫസറുമാണ് (ഇൻസ്റ്റിറ്റ്യൂട്ട് പ്രൊഫസർ എന്നത് ഐഐടികളിൽ നല്കുന്ന ഏറ്റവുമുയർന്ന അധ്യാപക പദവിയാണ്).

ബാംഗ്ലൂരിലെ ഇന്ത്യൻ ഇൻസ്റ്റിറ്റ്യൂട്ട് ഓഫ് സയൻസിൽനിന്ന് ഭൗതിക രസതന്ത്രത്തിൽ ഡോക്ടറേറ്റ് കരസ്ഥമാക്കിയ അദ്ദേ

ഹം കാലിഫോർണിയ സർവകലാശാല, ബെർക്കിലി, പർഡ്യൂ സർവകലാശാല, ഇന്ത്യാന എന്നിവിടങ്ങളിലെ പോസ്റ്റ് ഡോക്റ്ററൽ ഫെലോയായിരുന്നു. അന്താരാഷ്ട്ര പ്രശസ്തങ്ങളായ ഒട്ടേറെ സർവകലാശാലകളിൽ വിസിറ്റിങ് പ്രൊഫസറായ അദ്ദേഹം ഉന്നത നിലവാരമുള്ള ഒട്ടേറെ ശാസ്ത്ര ഗ്രന്ഥങ്ങളുടെയും പ്രബന്ധങ്ങളുടെയും രചയിതാവാണ്. തന്റെ ശാസ്ത്രഗവേഷണ സംഭാവനകളെ ആധാരമാക്കി പത്മശ്രീ (2020), ശാന്തിസ്വരൂപ് ഭട്നാഗർ അവാർഡ് (2008), നിക്കേയ് ഏഷ്യ പ്രൈസ് (2020), രസതന്ത്രത്തിനുള്ള TWAS പ്രൈസ് (2018) തുടങ്ങി ഒട്ടേറെ പുരസ്കാരങ്ങൾ ഡോ. ടി പ്രദീപ് കരസ്ഥമാക്കിയിട്ടുണ്ട് (പ്രദിപിനെക്കുറിച്ചുള്ള കൂടുതൽ വിവരങ്ങൾ https: // pradeepresearch.org/ ൽ ലഭ്യമാകും).

കഴിഞ്ഞ കേരളപ്പിറവി ദിനത്തിൽ പ്രൊഫ. പ്രദീപുമായി സൂം മീറ്റിങ് വഴി നടത്തിയ അഭിമുഖ സംഭാഷണത്തിലെ പ്രസക്തഭാഗങ്ങളാണിത്. കേരളത്തിന്റെ ഉൾനാടൻ ഗ്രാമങ്ങളിലൊന്നായ പന്താവൂരിൽനിന്ന് ശാസ്ത്രലോകത്തിന്റെ അനന്തതയിലേക്ക് പടർന്ന ഈ മലയാളിയുടെ പ്രതീക്ഷകളും ഉത്കണ്ഠകളും നമുക്ക് പങ്കുവെയ്ക്കാം. കേരളത്തിന്റെ വിദ്യാഭ്യാസ മേഖല, പ്രതിസന്ധികൾ, തന്റെ ഗവേഷണാനുഭവങ്ങൾ, കിനാവുകൾ, മനുഷ്യന്റെ സ്വത്വപ്രതിസന്ധികൾ തുടങ്ങി ഒട്ടേറെ മേഖലകളിലേക്ക് വ്യാപരിക്കുന്ന ഈ ശാസ്ത്രജ്ഞന്റെ ചിന്താലോകത്തിന്റെ വൈവിധ്യവും ആഴവും ചില കമ്പനങ്ങൾ സൃഷ്ടിക്കും.

? ശാസ്ത്രാഭിമുഖ്യത്തെക്കുറിച്ചുള്ള സംവാദങ്ങൾ മഹാമാരിക്കാലത്ത് ഏറെ സജീവമായി. മാനവപുരോഗതിയുടെ അനിവാര്യഘടകമായി ശാസ്ത്രാവബോധം വിലയിരുത്തപ്പെടുന്നു. എന്നാൽ വലിയ വികസനക്കുതിപ്പുകൾ നടത്തിയ രാഷ്ട്രങ്ങൾ പോലും ഇക്കാര്യത്തിൽ പലപ്പോഴും പുറകോട്ടുനടക്കുന്നു. വാക്സിൻ സംശയാലുത്വം മൂലം പ്രതിരോധക്കുത്തിവെയ്പിന് വിസമ്മതിക്കുന്ന ആയിരങ്ങളെ അമേരിക്കയിൽപോലും കാണാൻ സാധിക്കും. ശാസ്ത്രാഭിമുഖ്യത്തിന്റെ കാര്യത്തിൽ കേരളത്തിന്റെ സ്ഥാനമെന്താണ്. ഇന്ത്യയിലെ ഇതര ഭൂവിഭാഗങ്ങളെ അപേക്ഷിച്ച് കേരളത്തിന് എന്തെങ്കിലും സവിശേഷതയുണ്ടോ.

= ശാസ്ത്രാഭിമുഖ്യവും രാഷ്ട്രത്തിന്റെ സാമ്പത്തിക പുരോഗതിയും തമ്മിൽ പ്രത്യക്ഷത്തിൽ ഒരു ബന്ധവുമില്ല. വികസിത രാഷ്ട്രങ്ങൾക്ക് കൂടുതൽ ശാസ്ത്രാഭിരുചി ഉണ്ടെന്ന് പറയുന്നതിൽ അർഥമില്ല. സമ്പത്തിന്റെ വർധന ഉപഭോഗതൃഷ്ണയെ വർധിപ്പിക്കുന്നു. സമ്പന്നരാഷ്ട്രങ്ങൾ ശാസ്ത്രീയ കണ്ടുപിടുത്തങ്ങളുടെ സൗകര്യങ്ങൾ ഉപയോഗപ്പെടുത്തുമ്പോൾത്തന്നെ അവരുടെ ജീവിതത്തിന്റെ ഭാഗമായി ശാസ്ത്രം മാറുന്നില്ല. അമേരിക്കയിലും യൂറോപ്യൻ രാഷ്ട്രങ്ങളിലും വാക്സിനേഷനു വിധേയരാകാൻ വിസമ്മതിക്കുന്ന ജനതതി ഇതിന്റെ തെളിവാണ്.

എന്നാൽ ഇന്ത്യയിലെത്തുമ്പോൾ കാര്യങ്ങൾ കുറെക്കൂടി പരിതാപകരമാണ്. ശാസ്ത്രപുരോഗതി ആർജിക്കുമ്പോൾത്തന്നെ ശാസ്ത്രാവബോധത്തിന് പുറംതിരിഞ്ഞുനില്ക്കുന്ന രാജ്യമാണ് നമ്മുടേത്. ഏറ്റവും നൂതനമായ ശാസ്ത്രസാങ്കേതികവിദ്യ ഉപയോഗിച്ച് നാം തെരയുന്നത് നമ്മുടെ ഗ്രഹനിലയും ഭാഗ്യനിർഭാഗ്യങ്ങളുമാണ്. കേരളീയ സമൂഹത്തിലും ഇത്തരം പ്രവണതകൾ ദൃശ്യമാണ്.

ജാനകി അമ്മാൾ

ശാസ്ത്രപുരോഗതി ആർജിക്കുമ്പോൾത്തന്നെ ശാസ്ത്രാവബോധത്തിന് പുറംതിരിഞ്ഞു നിൽക്കുന്ന രാജ്യമാണ് നമ്മുടേത്. ഏറ്റവും നൂതനമായ ശാസ്ത്രസാങ്കേതികവിദ്യ ഉപയോഗിച്ച് നാം തെരയുന്നത് നമ്മുടെ ഗ്രഹനിലയും ഭാഗ്യനിർഭാഗ്യങ്ങളുമാണ്. കേരളീയ സമൂഹത്തിലും ഇത്തരം പ്രവണതകൾ ദൃശ്യമാണ്.

സി വി രാമൻ

ജാതീയതയുടെ വലിയ മേൽക്കോയ്മക്ക് നമ്മൾ കീഴ്പ്പെട്ടിരിക്കുന്നു. ജാതീയതയും ശാസ്ത്രവും ഒരുമിച്ചുപോകുന്നതല്ല. ശാസ്ത്രമെന്നത് നിരന്തരമായ ചോദ്യങ്ങളും ഉത്തരങ്ങളുടെ പുതുക്കലുമാണ്. മാറ്റമില്ലാത്ത ആചാരങ്ങളാലും വിശ്വാസത്താലും ബന്ധിതമാകുന്ന മതാത്മകജീവിതമാണ് നാം പിന്തുടരുന്നത്. വിശ്വാസജീവിതത്തിൽ അഭിരമിക്കുന്ന ജനതയ്ക്ക് ശാസ്ത്രാഭിമുഖ്യം ഉണ്ടാകുക എളുപ്പമല്ല.

ഇന്ത്യയിലെ മധ്യവർഗം ആചാരബന്ധിതമായ ജീവിതമൂല്യങ്ങളോട് ശാസ്ത്രീയ കണ്ടെത്തലുകളെ ഇഴചേർക്കുന്നു. പാശ്ചാത്യ/ആധുനിക ശാസ്ത്രസാങ്കേതികവിദ്യയുടെ ഉപഭോക്താക്കളാവുമ്പോൾത്തന്നെ ജാതീയ ശ്രേണികൾ നമ്മുടെ സാമൂഹിക അടയാളങ്ങളായി തുടരുന്നു.

? ശാസ്ത്രത്തെ സാമാന്യവൽക്കരിക്കുന്നതിൽ ശാസ്ത്രസാഹിത്യത്തിന് നിർണായകമായ പങ്കുണ്ട്. വിഖ്യാത ശാസ്ത്രജ്ഞരായ ആൽബർട് ഐൻസ്റ്റീൻ, സ്റ്റീഫൻ ഹാക്കിങ്, ഫ്രെഡ് ഹോയിൽ തുടങ്ങിയവരുടെ സാമാന്യജനതക്കായുള്ള രചനകൾ ഉദാഹരണങ്ങളാണ്. കാൾ സാഗനും സി പി സ്നോയും ഏറെ ജനപ്രിയരായ ശാസ്ത്രസാഹിത്യ രചയിതാക്കളാണ്. ഓക്സ്ഫോർഡ് സർവകലാശാലയിൽ ‘പബ്ലിക് അണ്ടർസ്റ്റാന്റിങ്

ഓഫ് സയൻസി'ൽ പ്രൊഫസർ പദവിയിലിരുന്നാണ് റിചാർഡ് ഡോക്കിൻസ് വളരെ പ്രചാരം സിദ്ധിച്ച തന്റെ രചനകൾ നിർവഹിച്ചത്. കേരള സാഹിത്യ അക്കാദമിയുടെ പുരസ്കാരം നേടിയ 'കുഞ്ഞുകണങ്ങൾക്ക് വസന്തം' തുടങ്ങിയ പുസ്തകങ്ങളും ഒട്ടേറെ ലേഖനങ്ങളും പ്രദീപിന്റെ ഈ രംഗത്തെ മികച്ച സംഭാവനകളാണ്. 'ദന്തഗോപുരവാസി'കളെന്നു വിശേഷിപ്പിക്കപ്പെടുന്ന ശാസ്ത്രസമൂഹത്തെയും ശാസ്ത്രസംഭാവനകളെയും സാമാന്യവൽക്കരിക്കുന്ന ഇന്ത്യൻ/കേരളീയ മാതൃകകൾ വളരെ കുറവാണ്. എന്താണ് പ്രതിബന്ധം.

പഞ്ചാബിലെ ആർസെനിക്, അയേൺ റിമൂവൽ പ്ലാന്റിന്റെ ആകാശദൃശ്യം

= ഭാഷ ഒരു പ്രധാന തടസ്സമായി നിൽക്കുന്നു. യൂറോപ്യൻ രാജ്യങ്ങളിൽ അവരുടെ തദ്ദേശീയ ഭാഷയിലാണ് അവർ ശാസ്ത്രം പഠിക്കുന്നത്. എന്നാൽ ഇവിടെ ഇംഗ്ലീഷിലാണ് നാം ശാസ്ത്രം പഠിക്കുന്നത്. പാശ്ചാത്യ ലോകത്ത് അവർ പഠിക്കുന്ന ശാസ്ത്രഭാഷയും ജനതയിലേക്ക് പകരുന്ന ഭാഷയും ഒന്നുതന്നെയാണ്. മലയാളത്തിൽ ശാസ്ത്ര സാഹിത്യമെഴുതുമ്പോൾ നാം ഇംഗ്ലീഷിൽ പഠിച്ച ശാസ്ത്രം മാറ്റിയെഴുതേണ്ടിവരുന്നു. കേവലം മൊഴിമാറ്റത്തിന്റെ പ്രശ്നം മാത്രമല്ലിത്. ഒരു പുത്തൻ ശാസ്ത്രഭാഷയ്ക്കാവശ്യമായ പദാവലികൾ നാം കണ്ടെത്തേണ്ടിയിരിക്കുന്നു. ഇതിനെ ഭേദിച്ചു കടന്ന അപൂർവം പ്രതിഭാശാലികൾക്കൊരുദാഹരണമാണ് ഡോ. കെ ഭാസ്കരൻനായർ. അദ്ദേഹത്തിന്റെ ശാസ്ത്രലേഖനങ്ങൾ അക്കാലത്ത് എഴുതിയിരുന്ന കുട്ടികൃഷ്ണമാരാരുടെ സാഹിത്യപ്രബന്ധങ്ങൾക്ക് ഒപ്പം നില്ക്കുന്നവയാണ്.

കവിതാവിമർശനത്തിന്റെ ഭാഷാരീതിയിലാണ് ഭാസ്കരൻനായർ ശാസ്ത്ര സാഹിത്യം രചിച്ചത്. ഡോ. ഭാസ്കരൻനായരുടെ ഔന്നത്യത്തോളമെത്തുന്ന രചനകൾ പില്ക്കാലത്ത് ഉണ്ടായില്ല എന്നത് യാഥാർഥ്യമാണ്. ശാസ്ത്രീയ വിജ്ഞാനത്തിന്റെ നൂതനപദാവലികൾ കണ്ടെത്തുന്ന കാര്യത്തിൽ നാം വിജയിച്ചില്ല.

മലയാളത്തിൽ നാം 'വാക്സിനേഷൻ' എന്ന പദം വ്യാപകമായി ഉപയോഗിക്കുമ്പോൾ തമിഴിലത് 'തടുപ്പൂശി' (തടുക്കുന്ന സൂചി) യായി മാറുന്നു. അവിടത്തെ ജനത അത് സ്വീകരിച്ചു. ഇക്കാര്യത്തിൽ നാം മലയാളികൾ ഏറെ പിറകിലാണ്. കണ്ടെത്തിയ ശാസ്ത്രസാങ്കേതിക പദാവലികൾ തന്നെ ഗ്രന്ഥങ്ങളിൽ ഉറങ്ങുന്നു. അത് ജനതയുടെ വ്യവഹാരഭാഷയായില്ല. ഒ വി വിജയന്റെ 'ഖസാക്കിന്റെ ഇതിഹാസ'ത്തെ പോലെ ഭാഷയുടെ സുഗന്ധം നിറയുന്ന ഒരു ശാസ്ത്രഗ്രന്ഥം നമുക്കുണ്ടോ? അതായത് ജനതയുടെ ഹൃദയത്തെ തൊടുന്നരീതിയിൽ ശാസ്ത്രമെഴുതാൻ നമുക്കാവുന്നില്ല.

? നൊബേൽ പുരസ്കാരങ്ങളുടെ കാലമാണല്ലോ. ഈ പുരസ്കാരവേള എപ്പോഴും വിവാദങ്ങളാൽ നിറയാറുണ്ട്. നൊബേൽ പുരസ്കാരങ്ങളിൽ ജിയോപൊളിറ്റിക്സിന്റെ സ്വാധീനമുണ്ടാവാറുണ്ടെന്ന് പറയപ്പെടുന്നു. ശാസ്ത്രീയ മേഖലകളിൽ ഏഷ്യൻ, ആഫ്രിക്കൻ പ്രതിഭകളെ നിരന്തരം അവഗണിക്കാറുണ്ട്. അങ്ങനെ നിരന്തരം അവഗണിക്കപ്പെട്ട പ്രതിഭകളിൽ ഒരാളായിരുന്നു മലയാളിയായ പ്രൊഫ. ഇ സി ജി സുദർശൻ. 'ടാക്കിയോൺ കണിക'യുമായി ബന്ധപ്പെട്ട ഗവേഷണ മേഖലയിൽ വ്യാപരിച്ചിരുന്ന ഡോ. സുദർശൻ 80 കളിൽ തൃശൂർ സെന്റ് തോമസ് കോളേജ് സന്ദർശിച്ചപ്പോൾ നാമിരുവരും ചേർന്നാണ് അദ്ദേഹത്തെ ഇന്റർവ്യൂ ചെയ്തത്. ഓർക്കുന്നോ അക്കാലം. നൊബേൽ പുരസ്കാരത്തിന്റെ രാഷ്ട്രീയത്തെക്കുറിച്ച് എന്താണഭിപ്രായം.

= ഡോ. സുദർശന്റെ സെന്റ് തോമസ് കോളേജ് സന്ദർശനവും അദ്ദേഹവുമായി നാം നടത്തിയ അഭിമുഖവും ഞാനോർക്കുന്നു. നൊബേൽ സമ്മാന വിവാദത്തെ ഞാൻ വേറൊരു തലത്തിലൂടെയാണ് കാണുന്നത്. നൊബേൽ പുരസ്കാരത്തിനു പരിഗണിക്കാവുന്ന ഉന്നതരായ എത്ര പ്രതിഭാശാലികളെ നാം സ്വ

ഷ്ടിച്ചിട്ടുണ്ട്? നമുക്ക് തൊള്ളായിരത്തിലധികം സർവകലാശാലകളുണ്ട്. അവിടെ നടക്കുന്ന ഗവേഷണത്തിലൂടെ ലോകം അംഗീകരിക്കുന്ന എത്ര ഗവേഷകർ ഉയർന്നുവരുന്നുണ്ട്? ടാഗോറിനോളം വലുതായ എത്ര എഴുത്തുകാർ നമുക്കുണ്ട്? ഈ വിഖ്യാത പുരസ്കാരം ലഭിക്കാതെ പോയ ഒട്ടേറെ മഹാപ്രതിഭകളുണ്ട്. ഗാന്ധിജിയും ടോൾസ്റ്റോയിയും ഉദാഹരണങ്ങളാണ്.

രസതന്ത്രത്തിന്റെ മേഖലയിൽ മൂലകങ്ങളുടെ ആവർത്തനപ്പട്ടികയുടെ പിതാവെന്നറിയപ്പെടുന്ന മെൻഡലിയേവ്, രാസസംയുക്തങ്ങളിലെ ബന്ധനത്തെ നിർവചിച്ച ജി എൻ ലൂയിസ് തുടങ്ങി ഒട്ടേറെപ്പേർക്ക് നൊബേൽ സമ്മാനം ലഭിച്ചിട്ടില്ല. അന്തർദേശീയ രാഷ്ട്രീയത്തിന്റെ വിവിധ താല്പര്യങ്ങൾ ചില ഘട്ടങ്ങളിൽ സ്വാധീനം ചെലുത്തിയിട്ടുണ്ടാവാം. അന്തർദേശീയ നിലവാരമുള്ള ശാസ്ത്ര ഗവേഷണ സ്ഥാപനങ്ങൾ കൂടുതൽ ഉയർന്നുവരുന്നതോടെ നമ്മുടെയും നിലവാരം മെച്ചപ്പെട്ടേക്കാം.

അത്തരം നിലവാരമുള്ള ഒരു സ്ഥാപനമെങ്കിലും കേരളത്തിലുണ്ടോ എന്ന് നാം പരിശോധിക്കേണ്ടതുണ്ട്. ഇത്തരം സ്ഥാപനങ്ങൾ പടുത്തുയർത്തുന്നതിന് വലിയ മൂലധനനിക്ഷേപം ആവശ്യമാണ്. രണ്ടായിരമോ മൂവായിരമോ കോടികൾ നിക്ഷേപിച്ച് ഇത്തരം സ്ഥാപനങ്ങൾ ആരംഭിച്ചാലും അതിന്റെ ഗുണഫലങ്ങൾ പെട്ടെന്ന് പ്രതിഫലിക്കണമെന്നില്ല. പക്ഷേ, നാം കാണേണ്ടത്, വമ്പിച്ച മൂലധനനിക്ഷേപത്തിലൂടെ അമേരിക്ക നടത്തിയ റോക്കറ്റ് വിക്ഷേപണങ്ങൾ അവരെ ലോക ജേതാക്കളാക്കിമാറ്റി എന്നതുകൂടിയാണ്. ശാസ്ത്രീയ ഗവേഷണത്തിനായി നാം നിക്ഷേപിക്കുന്ന കോടികളിലൂടെ നാമാർജിക്കുന്ന ഗവേഷണഫലങ്ങൾ സമൂഹത്തെ മാറ്റുന്നു. പതിറ്റാണ്ടുകൾകൊണ്ട് ഇന്ത്യ ഒട്ടേറെ മുന്നോട്ടുപോയിട്ടുണ്ട് എന്നത് വസ്തുതയാണ്. എങ്കിലും ഇനിയുമേറെ ദൂരം താണ്ടേണ്ടതുണ്ട്.

? ഇത്തരമൊരു ചർച്ചയിൽ ഉയർന്നുവരാവുന്ന പേരുകളിലൊന്നാണ് ഡോ. താണു പത്മനാഭൻ. ഒരു വാരികയുടെ മുഖചിത്രമായി അദ്ദേഹത്തെ മലയാളികൾ ആഘോഷിക്കുമ്പോഴാണ് രംഗബോധമില്ലാത്ത കോമാളിയെപ്പോലെ ആ ശാസ്ത്രപ്രതിഭയുടെ മരണം സംഭവിക്കുന്നത്. ദേശീയ പ്രശസ്തിയുള്ള രണ്ട് മലയാളി ശാസ്ത്രജ്ഞർ എന്ന നിലയിൽ ഏതെങ്കിലും തരത്തിലുള്ള പാരസ്പര്യം നിങ്ങൾ തമ്മിലുണ്ടായിരുന്നോ. ഡോക്ടർ താണു പത്മനാഭനെയും താങ്കളെയും കേരളത്തിലെ സർവകലാശാലകളിലേക്ക് വൈസ് ചാൻസലർമാരാകാൻ ക്ഷണിച്ചുവെന്നും നിങ്ങളത് തിരസ്കരിച്ചുവെന്നും ചില അടക്കംപറച്ചിലുകളുണ്ട്. എന്തെങ്കിലും വാസ്തവമുണ്ടോ. ഉണ്ടെങ്കിൽ തിരസ്കാരത്തിന്റെ കാരണം.

= ഡോ. താണു പത്മനാഭനുമായി ഗാഢസൗഹൃദം ഉണ്ടായിരുന്നുവെന്ന് പറയാൻ കഴിയില്ല. പലവട്ടം കാണുകയും സംസാരിക്കുകയും സെമിനാറുകളിൽ ഒരുമിച്ച് പങ്കെടുക്കുകയും ചെയ്തിട്ടുണ്ട്. അദ്ദേഹത്തിന്റെയും എന്റെയും ഗവേഷണമേഖലകൾ വ്യത്യസ്തമായിരുന്നു. വിസിയാകാനുള്ള നിർദേശത്തെ അദ്ദേഹം മറ്റൊരവസരത്തിൽ പരിഗണിക്കാമെന്ന് പറഞ്ഞതായി കേട്ടിട്ടുണ്ട്.

എന്നെ സംബന്ധിച്ചിടത്തോളം ഇത്തരമൊരു നിർദേശം ഉത്തരവാദിത്തപ്പെട്ടവരിൽനിന്ന് വന്നിരുന്നു. ആ സമയത്ത് ഞാനത് സ്വീകരിച്ചില്ല. മൂന്നുവർഷത്തെ വൈസ് ചാൻസലർ പദവികൊണ്ട് വിദ്യാഭ്യാസരംഗത്ത് ഗുണപരമായ എന്തെങ്കിലും ചെയ്യാനാകുമെന്നോ അടിസ്ഥാനപരമായ മാറ്റം വരുത്താനാകുമെന്നോ ഞാൻ കരുതുന്നില്ല. കേരളത്തിന്റെ ഉന്നതവിദ്യാഭ്യാസരംഗത്തിന്റെ/സർവകലാശാലകളുടെ അലകും പിടിയും മാറ്റേണ്ട സാഹചര്യമാണ്. മതവും ജാതിസംഘടനകളും കേരളത്തിലെ ഉന്നതവിദ്യാഭ്യാസരംഗത്തെ നിർണായക സ്വാധീനങ്ങളാണ്. അവയിൽ മാറ്റങ്ങളുണ്ടാക്കുക എന്നത് സങ്കീർണമായ പ്രശ്നമാണ്. വിസിയുടെ സ്വാതന്ത്ര്യവും, ഇടപെടൽ സാധ്യതകളും വളരെ പരിമിതമാണ്. സാമ്പത്തികമായ ചില ഘടകങ്ങളുമുണ്ട്.


അന്നാമാണി

ശാസ്ത്രാഭിമുഖ്യവും രാഷ്ട്രത്തിന്റെ സാമ്പത്തിക പുരോഗതിയും തമ്മിൽ പ്രത്യക്ഷത്തിൽ ഒരു ബന്ധവുമില്ല. വികസിത രാഷ്ട്രങ്ങൾക്ക് കൂടുതൽ ശാസ്ത്രാഭിരുചി ഉണ്ടെന്ന് പറയുന്നതിൽ അർത്ഥമില്ല. സമ്പത്തിന്റെ വർദ്ധന ഉപഭോഗതൃഷ്ണയെ വർദ്ധിപ്പിക്കുന്നു.


ഐൻസ്റ്റീൻ

ചെന്നൈ ഐഐടിയിൽ ഞങ്ങളുടെ ബജറ്റ് വിഹിതം 1200 കോടി രൂപയാണ്. ഗവേഷണത്തിനുമാത്രം 600 കോടി രൂപ ചെലവഴിക്കുന്നു. കോഴിക്കോട് സർവകലാശാലയിൽ ഗവേഷണത്തിനായി ചെലവഴിക്കുന്നത് 20 കോടി രൂപയാണ്. സാമ്പത്തിക ഘടകങ്ങളിൽ മാത്രമല്ല ഇടപെടുന്ന മനുഷ്യരുടെ ഗുണപരത, മത്സരശേഷി തുടങ്ങിയ മേഖലകളിലും രണ്ടു സ്ഥാപനങ്ങളും തമ്മിൽ അന്തരമേറെയുണ്ട്. അതിനാൽ ഞാൻ ആ നിർദേശങ്ങൾ സ്വീകരിക്കുകയുണ്ടായില്ല.

ഇത്തരം സ്ഥാപനങ്ങളിൽ അനുഭവിക്കുന്ന മറ്റുചില പ്രശ്നങ്ങൾക്കൂടി നാം പരിഗണിക്കേണ്ടതുണ്ട്. വിഖ്യാതനായ ഒരു ശാസ്ത്രജ്ഞനോ ഉന്നതനായ ഒരു അക്കാദമീഷ്യനോ സർവകലാശാല തലവനാകുമ്പോൾ അവർക്ക് പ്രവർത്തിക്കാൻ, പ്രോജക്ടുകൾ തയ്യാറാക്കാൻ ആവശ്യമായ ഇടം നാം നല്കണം. കക്ഷി- രാഷ്ട്രീയ ഇടപെടലുകൾ, ഉദ്യോഗസ്ഥ ലോബികൾ ഒരുപക്ഷേ, ആദരണീയനായ ഒരു പ്രൊഫസറുടെ വലിയ തടസ്സങ്ങളായി മാറാറുണ്ട്. മനുഷ്യരെ അവരുടെ കഴിവുകളുടെ അടിസ്ഥാനത്തിൽ മനസ്സിലാക്കാൻ ശ്രമിക്കണം. ഉന്നതനായ ഒരു ശാസ്ത്രഗവേഷകന് ലോകത്തെവിടെയും സ്വീകാര്യതയുണ്ട്. നിങ്ങളയാളുടെ പ്രവൃത്തികൾക്ക് തടസ്സം നിന്നാൽ അയാൾക്ക് സർവകലാശാല വിടാവുന്നതാണ്. നഷ്ടം നമുക്കായിരിക്കും. കാരണം അയാൾ ചിലപ്പോൾ ഒരു സർവകലാശാലയെക്കാൾ വലുതായിരിക്കും. ഐസക്ന്യൂട്ടനും ആൽബർട്ട് ഐൻസ്റ്റീനും അങ്ങനെയായിരുന്നു.

? നമ്മുടെ സർവകലാശാലകളുടെ പ്രശ്നങ്ങൾ എന്തൊക്കെയാണ്. ഇതരസംസ്ഥാന സർവകലാശാലകളുമായി താരതമ്യം ചെ

യ്യാമോ. വിദ്യാഭ്യാസം സാർവത്രികമാക്കുന്നതിൽ വിജയം കൈവരിച്ചുവെങ്കിലും ഇന്ത്യയിൽത്തന്നെ ആദ്യസ്ഥാനങ്ങളിൽ നിൽക്കുന്ന ഉന്നത വിദ്യാഭ്യാസ സ്ഥാപനങ്ങൾ നമുക്കില്ല എന്നുതന്നെ പറയാം. അന്തർദേശീയമായി പരിഗണിക്കുമ്പോൾ നാം പിന്നെയും പുറകിലാവും. എന്താണ് പ്രശ്നം.

= പ്രശ്നത്തിന്റെ കേന്ദ്രബിന്ദു നമ്മുടെ ഗുണപരത ഉയരണമെന്നതാണ്. ഇതിന് എളുപ്പവഴികളില്ല. വിദ്യാഭ്യാസത്തിന്റെ ആത്യന്തിക ലക്ഷ്യം മനുഷ്യന്റെ സർവതോന്മുഖമായ വികാസമാണ്. ആ തരത്തിലുള്ള ഒരന്തരീക്ഷം ഉന്നതവിദ്യാഭ്യാസമേഖലയിൽ ഇന്നില്ല. കേരളത്തിൽ എയിഡഡ് കോളേജുകളിൽ ശമ്പളം നല്കുന്നത് സർക്കാർ. നിയമനം നടത്തുന്നത് ജാതിനേതൃത്വത്താൽ നയിക്കപ്പെടുന്ന മാനേജ്മെന്റ്.

നടത്തിപ്പുകാരുടെ ജാതിയിൽ പെടുന്നവരായിരിക്കും ബഹുഭൂരിപക്ഷം അധ്യാപകരും. ഇതെങ്ങനെ സാധ്യമാകുന്നു. വലിയതോതിലുള്ള വക്രീകരണം നടന്നിരിക്കുന്നു. ജാതിപരിഗണനയുടെ അടിസ്ഥാനത്തിൽമാത്രം അധ്യാപക ജോലിക്ക് വരുന്നവർക്ക് എങ്ങനെ വിശ്വമാനവികതയുടെ അതിരുകളില്ലാത്ത ലോകത്തെ കാണാനാകും.

ഈ ഘടനയിൽ മാറ്റംവരുത്താൻ ശ്രമിച്ചാൽ വലിയ എതിർപ്പുകളുണ്ടാകും. വിദ്യാഭ്യാസമേഖലയിലെ മൂലധനനിക്ഷേപം നിയമനങ്ങളിലൂടെ തിരിച്ചെടുക്കാമെന്ന് അനുഭവത്തിലൂടെ പഠിച്ച ഈ ലോബി തന്നെയായിരിക്കും മാറ്റത്തിന്റെ എതിർപ്പുകാർ.

ലോകം അതിവേഗം മാറുകയാണ്. വിദ്യാഭ്യാസവും തൊഴിലും തമ്മിലുള്ള പാരസ്പര്യത്തെ മനസ്സിലാക്കണം. വിദ്യാഭ്യാസം digital platform ലേക്ക് മാറുകയാണ്. പക്ഷേ, കോഴിക്കോട് സർവകലാശാലയിൽ കൊമേഴ്സിൽ ഡിഗ്രി കോഴ്സ് ചെയ്യുന്ന വിദ്യാർഥിക്ക് എന്തുകൊണ്ട് കേരള സർവകലാശാലയിൽ സയൻസിന് തുടർപഠനം ചെയ്യാൻ കഴിയുന്നില്ല. മറ്റൊരുകാര്യം നമ്മുടെ തെരഞ്ഞെടുപ്പാണ്. 12-ാം ക്ലാസ്സിൽ പഠിക്കുന്ന ഒരു കൗമാരക്കാരന് എന്തറിയാം അനന്തമായ ലോകത്തെപ്പറ്റി? സയൻസ് തെരഞ്ഞെടുത്ത അവന് ഇരുപത്തഞ്ചാം വയസ്സിൽ മ്യൂസിക്കോ ആർട്ടോ പഠിക്കണമെങ്കിൽ അയാൾക്കതിന് കഴിയണം. 17-ാമത്തെ വയസ്സിൽ ഡോക്ടറാവാൻ തീരുമാനിച്ച വിദ്യാർഥിക്ക് അത് തിരുത്തി എൻജിനീയറാവാൻ അവസരം നല്കണം.

ലോകത്ത് പലയിടത്തും ഇത്തരം മാറ്റങ്ങൾ പ്രകടമാണ്. ഐഐടി ചെന്നൈയിൽനിന്ന് ബിടെക്ക് കഴിഞ്ഞവരിൽ ചിലർ മികച്ച ന്യൂറോ സർജന്മാരായി മാറിയിട്ടുണ്ട്. പക്ഷേ, അവർക്കത് സാധ്യമായത് അവർ അമേരിക്കയിൽ പോയതുകൊണ്ടാണ്. സദൃശമായ വലിയ മാറ്റങ്ങൾ നമ്മുടെ യൂണിവേഴ്സിറ്റികളിൽ ഉണ്ടാകണം. അത്തരം തിരുത്തൽ പ്രക്രിയയിലൂടെ മാത്രമേ സമൂഹത്തെ മാറ്റാൻ കഴിയുന്ന ഊർജം പ്രസരിക്കുന്ന വലിയ അക്കാദമിക വ്യക്തിത്വങ്ങൾ ഉണ്ടാകൂ.

കേരളം താരതമ്യം ചെയ്യേണ്ടത് കർണാടകത്തെയോ പഞ്ചാബിനെയോ ആകരുത്. അന്തർദേശീയ തലത്തിൽ ഒന്നാം സ്ഥാനത്തുനില്ക്കുന്ന സ്ഥാപനങ്ങളോടാണ് നാം മത്സരിക്കേണ്ടത്. കേരളത്തിന്റെ സമ്പത്ത് പ്രതിഭാധനരായ മനുഷ്യരാണ്. ഇൻഫോസിസും ബൈജൂസ് ആപ്പും സൃഷ്ടിച്ചവർ മലയാളികളാണ്. നമുക്ക് ലോകത്തിന്റെ സർവക

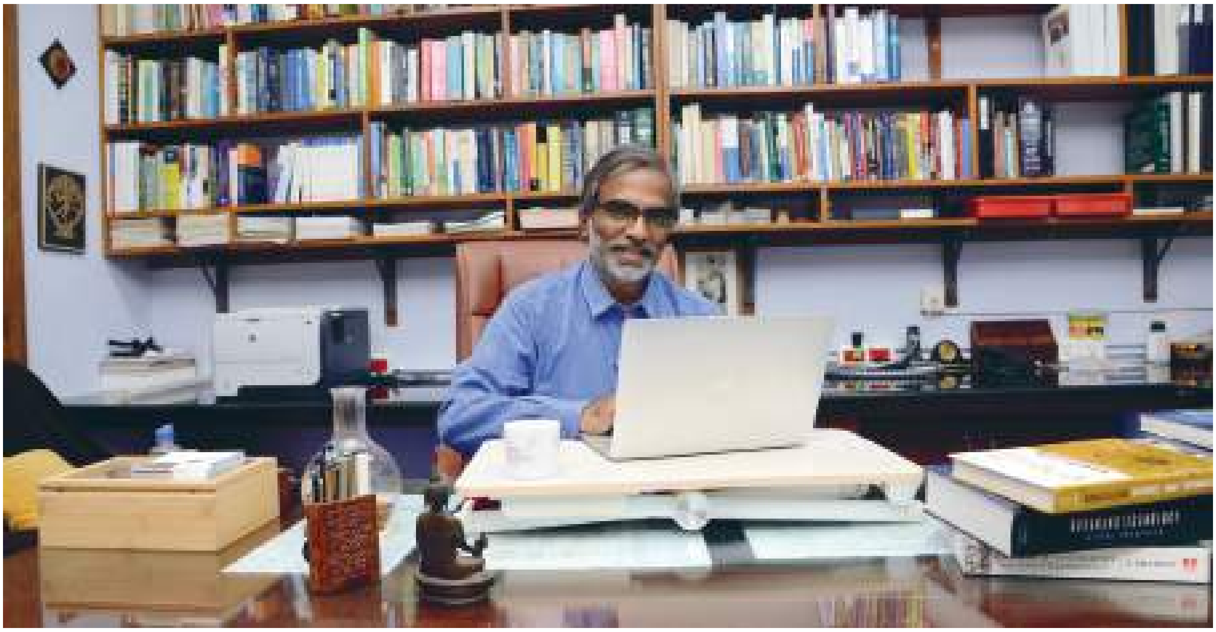

ഡോ. ടി പ്രദീപ്

ലാശാലയാകാൻ കഴിയും. കെട്ടിടങ്ങളും മൂലധനവും മാത്രം പോര. അറിവിനെ ആരാധിക്കുന്ന ഒരു ജനസമൂഹമായി നാം മാറണം.

? ജ്ഞാനസമൂഹത്തെക്കുറിച്ചുള്ള ചർച്ച കേരളത്തിൽ സജീവമാണ്. കേരളത്തെ ജ്ഞാനസമൂഹമായി പരിവർത്തനപ്പെടുത്തുന്നതിനുള്ള സാധ്യതകൾ...

= ജ്ഞാനസമൂഹമെന്നത് ക്ഷേമസമൂഹം കൂടിയാണ്. അത്തരമൊരു ക്ഷേമസമൂഹമായ് മാറുന്നതിന് കേരളത്തിന് സാധ്യതകളുണ്ട്. വിദ്യാഭ്യാസമാണ് കേരള വികസനത്തിന്റെ അടിത്തറ എന്നു നാം മനസ്സിലാക്കണം. മികച്ച വിദ്യാഭ്യാസസ്ഥാപനങ്ങൾ ഉണ്ടാകണം. മറ്റുപല രാജ്യങ്ങളിൽനിന്നും വിദ്യാഭ്യാസ ആവശ്യങ്ങൾക്കായി ആളുകൾ കേരളത്തിലേക്ക് വരണം. എന്നാലിപ്പോൾ സ്ഥിതി മറിച്ചാണ്.

കേരളത്തിൽ മികച്ച ഒരു ലാംഗ്വേജ് കോഴ്സ് പോലും ചെയ്യാനുള്ള സ്ഥാപനങ്ങൾ ഇല്ല. അത്തരം ഘട്ടങ്ങളിൽ മലയാളികൾ ഡൽഹിയിലേക്കോ ഹൈദരാബാദിലേക്കോ പോകുന്നു. ഈ അവസ്ഥാന്തരത്തെ നാം തിരിച്ചറിയണം. കേരളത്തെ ലോകത്തിന്റെ എഡ്യുക്കേഷൻ ഹബ്ബ് ആക്കി മാറ്റണം. അന്താരാഷ്ട്ര സമൂഹത്തിന് വരാൻപറ്റുന്ന ഒരു സമൂഹമായി നാം മാറണം. മോറൽ പോലീസിങ് ഉണ്ടാകരുത്. യുവതക്കാവശ്യമായ സ്വാതന്ത്ര്യം നല്കണം. ഓരോ രംഗത്തും ഇടത്തരം പ്രതിഭകളെ വാഴ്ത്തുന്നതിനുപകരം ഉയർന്ന മാനങ്ങളുള്ള പ്രഗത്ഭമതികളെ സൃഷ്ടിക്കണം. എന്തായാലും കേരളം മാറണമെങ്കിൽ ഒറ്റവഴിയെയുള്ളൂ. അത് വിദ്യാഭ്യാസത്തിന്റെ വഴിയാണ്.

തുറന്ന സമീപനവും നിരന്തരമായ ചോദ്യം ചെയ്യലുകളും ജ്ഞാനസമൂഹമായി മാറുന്നതിനുള്ള അനുപേക്ഷണീയ ഘടകങ്ങളാണ്.

? സർവകലാശാലകളുടെ ഗുണനിലവാരം അവയുടെ അക്കാദമിക സ്വാതന്ത്ര്യത്തെ ആശ്രയിച്ചിരിക്കുന്നു. സ്വയംഭരണം, യോഗ്യത അടിസ്ഥാനമാക്കിമാത്രമുള്ള തെരഞ്ഞെടുപ്പ് എന്നിവ മേൽക്കൈ നേടുമ്പോൾ സംവരണത്തിന്റെ (ജാതി/സാമ്പത്തിക പിന്നോക്കാവസ്ഥ) ഇടമെന്താണ്.

= പലതരം അസമത്വങ്ങളിൽ നിലനില്ക്കുന്ന ആളുകളെ പരിരക്ഷിക്കുന്നതിന് ഭരണഘടന ശ്രമിക്കുന്നു. ഇത് തുടരേണ്ടത് തന്നെയാണെന്ന കാര്യത്തിൽ സംശയമില്ല. അന്തിമഘട്ട തെരഞ്ഞെടുപ്പിന്റെ കാര്യത്തിൽ പക്ഷേ, കാര്യം വ്യത്യസ്തമാണ്. ഏറ്റവും ഉന്നതരായ രണ്ട് ഭൗതികശാസ്ത്രജ്ഞരെ തെരഞ്ഞെടുക്കേണ്ട ഘട്ടത്തിൽ ഏറ്റവും മികച്ചവരെ തന്നെ നാം തെരഞ്ഞെടുക്കണം. അവിടെവരെ എത്തുന്നതിന് ആളുകളെ സജ്ജരാക്കുന്നതിൽ സംവരണവഴികൾ ശരിയാണ്. അന്തിമഘട്ടത്തിൽ സാധ്യമാണോ?

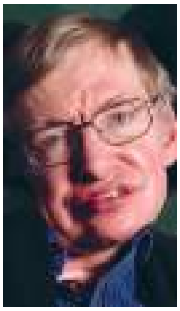

സ്റ്റീഫൻ ഹോക്കിങ്

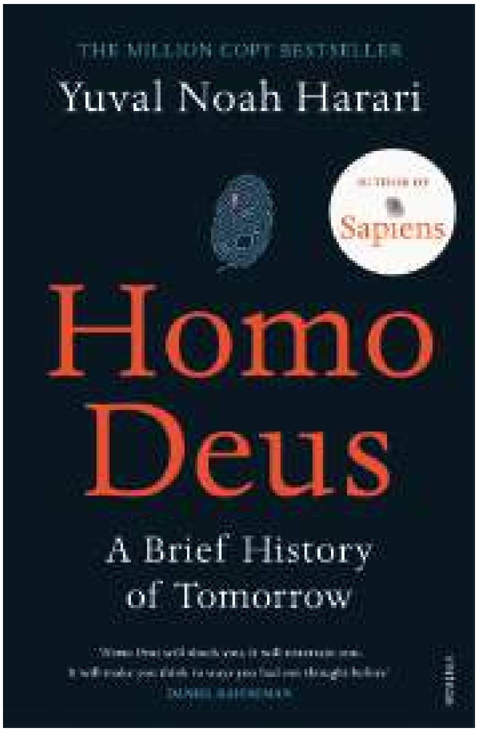

മികച്ച അസ്ട്രോഫിസിസ്റ്റിനെ തെരഞ്ഞെടുക്കുന്ന വേളയിൽ സംവരണം വേണമെന്ന വാദം ശരിയാണോ? സൂക്ഷ്മതലത്തിലേക്ക് വരുമ്പോൾ ഇത് പ്രശ്നം സൃഷ്ടിക്കും. ഗിരിശൃംഗങ്ങളാൽ നിറയേണ്ട സർവകലാശാലകളിൽ മൊട്ടക്കുന്നുകൾ നിറയും. ഐഎസ്ആർഒയിൽ റോക്കറ്റ് സാങ്കേതികവിദ്യ ഏറ്റവും നന്നായറിയുന്ന ആളെയാണ് നിയമിക്കേണ്ടത്. സാമാന്യ സംവരണത്തിന്റെ ഭരണഘടനാ നിർദേശങ്ങൾ പാലിക്കുമ്പോൾ തന്നെ ഏറ്റവും ഉയർന്നതലത്തിൽ മറ്റുപരിഗണനകൾ ഒഴിവാക്കി ഏറ്റവും മികച്ച വ്യക്തിയെ നാം നിശ്ചയിക്കണം. ജാതി, വരുമാനം തുടങ്ങിയ എല്ലാ സംവരണങ്ങളും ഈ ഘട്ടത്തിൽ ഒഴിവാക്കണം.

കാൾ സാഗൻ

എല്ലാവർക്കും അവസരസമത്വവും മത്സരക്ഷമതയും ഉറപ്പാക്കുന്നതിനാണ് നാം ശ്രമിക്കേണ്ടത്. സംവരണതത്വം പാലിക്കുന്നതിന് കൂടുതൽ വിസിമാരെ സൃഷ്ടിക്കുന്നതിനായി കൂടുതൽ സർവകലാശാലകൾ ഉണ്ടാക്കുക എന്ന രീതിയിലേക്ക് നാം മാറുന്നു. എല്ലാ വിഷയങ്ങൾക്കും വെവ്വേറെ സർവകലാശാലകൾ ഉണ്ടാക്കാൻ ശ്രമിച്ചാൽ അവയുടെ ലക്ഷ്യം വഴിമാറും. സർവകലാശാലകൾക്കുപകരം സ്റ്റഡിസെന്ററുകൾ ഉയരും.

? ഐഐടികൾ അടക്കമുള്ള ഇന്ത്യയിലെ ഉന്നതവിദ്യാഭ്യാസ സ്ഥാപനങ്ങളിലും പല കേന്ദ്ര സർവകലാശാലകളിലും ദളിത്/പിന്നോക്കജാതി തിരസ്കാരങ്ങളെ സംബന്ധിച്ച് ഒട്ടേറെ വാർത്തകൾ പുറത്തുവരുന്നു. താങ്കളുടെ സ്ഥാപനമായ ചെന്നൈ ഐഐടിയിലും അംബേദ്ക്കർ/പെരിയോർ കൂട്ടായ്മകളുമായി ബന്ധപ്പെട്ട് ഇത്തരം വാർത്തകൾ വന്നിരുന്നു. വിവിധങ്ങളായ കാരണങ്ങളാൽ ഇത്തരം സ്ഥാപനങ്ങളിലെ യുവഗവേഷകരുടെ ആത്മഹത്യാവാർത്തകളും മാധ്യമശ്രദ്ധ നേടുന്നു. ശാസ്ത്രജ്ഞനെന്നനിലയിൽ ലോകത്തിലെ വിവിധ സർവകലാശാലകളുമായി അടുത്തബന്ധം പുലർത്തുന്ന പ്രദീപ് എങ്ങനെയാണ് ഈ ഇന്ത്യൻ സാഹചര്യത്തെ വിലയിരുത്തുന്നത്.

= സർവകലാശാലകൾ സമൂഹത്തിന്റെ കണ്ണാടികളാണ്. അസമതകളും ഉച്ചനീചത്വങ്ങളും സാമൂഹിക യാഥാർഥ്യങ്ങളാണ്. അതിവിടെയും പ്രതിഫലിക്കുന്നു. വിവിധ ആവശ്യങ്ങൾക്കായി ക്യൂവിൽ നില്ക്കുന്ന സാധാരണക്കാരനുമുന്നിലൂടെ ‘ക്യൂ’ പാലിക്കാതെ ആവശ്യങ്ങൾ നേടിയെടുക്കുന്ന

ഉന്നതരെ നാം കാണുന്നില്ലേ? രാഷ്ട്രീയ പ്രമുഖൻ, ഐഎഎസുകാരൻ, സ്വാധീനമുള്ള മറ്റൊരാൾ എന്നിങ്ങനെയുള്ളവർക്ക് അത്തരം ‘വരി’കളൊന്നും ബാധകമല്ല. ഐഐടികളിലും ഇത്തരം വേർതിരിവുകൾ കാണും.

ഐഐടി പ്രൊഫസറായതുകൊണ്ട് ഒരാൾ നായരോ അയ്യങ്കാരോ ആകാതിരിക്കുന്നില്ല. വിദ്യാഭ്യാസവിചക്ഷണരിലും ശാസ്ത്രജ്ഞരിലും ജാത്യാഭിമാനം നിലനിൽക്കുന്നു. ഒരു വ്യക്തി എന്നനിലയിൽ എനിക്കിതിൽ സങ്കടമുണ്ട്. ഞാനിവിടെ ഐഐടിയിൽ വരുന്ന വേളയിൽ വിദ്യാർഥികളുടെ ഹാജർ പുസ്തകത്തിൽ ജനറൽ, എസ്‌സി, എസ്‌ടി എന്ന രീതിയിൽ രേഖപ്പെടുത്താറുണ്ട്. ഇതൊരു ജാതിവിവേചനമാണെന്ന് ആർക്കും തോന്നിയിരുന്നില്ല. ഫാക്കൽറ്റി മീറ്റിങ്ങുകളിൽ വിദ്യാർഥികളുടെ വിജയപരാജയങ്ങൾ ചർച്ചചെയ്യുമ്പോൾ അവയ്ക്കുള്ള കാരണമായി ഇത്തരം കാറ്റഗറികൾ ഉയർന്നുവരാറുണ്ട്.

പിന്നീട് ആ രീതി ഒഴിവാക്കപ്പെട്ടു. പരിശോധകന്റെ മനസ്സിൽ രൂഢമായ ജാതിവാസനയുടെ പ്രതിഫലനമായിരുന്നു ഈ രീതി. സംവരണം പാലിച്ചുവരുന്നവരും ഇത്തരം വിലയിരുത്തൽ രീതികളിൽനിന്ന് മുക്തരല്ല. ഇതൊരു സാമൂഹ്യ യാഥാർഥ്യമാണ്.

? ‘നാനോ സാങ്കേതികവിദ്യ’ വിഭാഗത്തിലെ ഇന്ത്യയിലെ പ്രഗത്ഭനായ രസതന്ത്രജ്ഞന്റെ തുടക്കം പന്താവൂർ എന്ന ചെറുഗ്രാമത്തിൽനിന്നായിരുന്നു. പൊന്നാനി പരിസരത്തെ പന്താവൂർ, മൂക്കുതല സർക്കാർ ഹൈസ്കൂളുകളിൽ പഠനം. അധ്യാപകരായ മാതാപിതാക്കൾ. ഓർമകളിൽ നിറയുന്ന ബാല്യം, കൗമാരക്കാലം വിവരിക്കാമോ.

= ഇടശ്ശേരിക്കവിതയിൽ സൂചിപ്പിച്ചതുപോലെ പ്രകൃതിപാഠശാലയിൽനിന്ന് മനുഷ്യരുടെ പാഠശാലയിലേക്ക് പ്രവേശിക്കുന്ന ചെറുബാല്യക്കാരനെ ഞാനോർക്കുന്നു. പ്രഥമ വിദ്യാലയത്തിൽനിന്ന് കുതറി വീട്ടിലേക്കോടാൻ കരച്ചിലോടെ ശ്രമിക്കുന്ന കുട്ടി. പന്താവൂരിലെ പ്രൈമറി വിദ്യാലയത്തിൽനിന്ന് മൂക്കുതല ഹൈസ്കൂളിലേക്ക് എന്റെ പഠനം മാറുന്നു. വീട്ടിൽനിന്ന് 4-5 കിലോമീറ്റർ ദൈർഘ്യമുള്ള വിദ്യാലയത്തിലേക്ക് കൂട്ടുകാരോടൊത്ത് പാടത്തും പറമ്പിലും നടന്ന അക്കാലം. ചെറുജലാശയങ്ങളിൽ മീൻപിടിച്ചും പാടത്തെ വെള്ളം പാറ്റിയും ഞങ്ങൾ നടത്തിയ യാത്രകൾ ആഘോഷങ്ങളായിരുന്നു. പഠനവും അങ്ങനെയായിരുന്നു.


സി പി സ്നോ

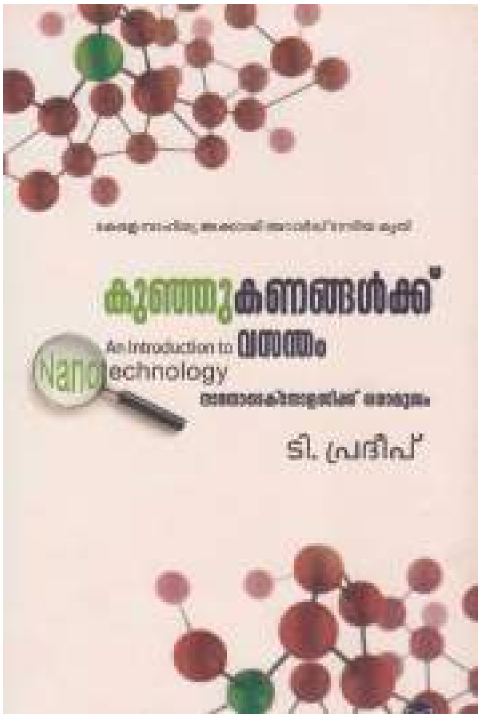

എന്റെ സമവയസ്കരായ എല്ലാ മലയാളികളെയും പോലെ ഞാനും സമഭാവനയുള്ള സമൂഹത്തിന്റെ ലാളനയേറ്റു വളർന്നവനാണ്. എല്ലാവരും പഠിച്ചത് അയൽപക്ക വിദ്യാലയങ്ങളിലായിരുന്നു. അന്നത്തെ പഠനകാലത്തേക്ക് തിരിഞ്ഞുനോക്കുമ്പോൾ എനിക്കോർമവരുന്നത് ഭാഷയുടെ സുഗന്ധമാണ്. അച്ഛൻ ഭാഷാധ്യാപകനായിരുന്നുവെന്നത് വലിയൊരു പ്രചോദനമായിരുന്നു. എന്തായാലും സ്കൂൾ എന്ന് പറയുമ്പോൾ എന്നിൽ നിറയുന്നത് ഭാഷയാണ്. വാക്കുകളും വാചകങ്ങളും സ്വപ്നങ്ങളും നിറയുന്ന ഭാഷ. ആശാന്റെ സീതാകാവ്യവും ഭാരതപര്യടനവും തുടങ്ങിയ ഉന്നതമൂല്യമുള്ള ഗ്രന്ഥങ്ങൾ ഇപ്പോഴും ബാക്കിയാവുന്നു.

? ബിരുദതലം മുതൽ ഞാനറിയുന്ന പ്രദീപ് അക്കാലത്തെ ജനാധിപത്യ വിദ്യാർഥി പ്രസ്ഥാനത്തിലെ ഉശിരൻ പ്രവർത്തകനായിരുന്നു. മാഗസിൻ എഡിറ്ററടക്കമുള്ള ഉത്തരവാദിത്തങ്ങൾ നിർവഹിച്ച കോളേജ് യൂണിയൻ ഭാരവാഹിയായിരുന്നു. അക്കാലത്ത് കണ്ട കിനാവുകളിൽ എന്തുണ്ട് ബാക്കി.

= ഇതൊരു സങ്കീർണമായ ചോദ്യമാണ്. യൗവനത്തിൽ റൊമാന്റിക് ആവാത്ത മനുഷ്യനുണ്ടാകില്ല. ആശയങ്ങളാണ് നമ്മെ രൂപപ്പെടുത്തുന്നത്. ആശയങ്ങൾ തന്നെയായിരുന്നു നമ്മുടെ ഊർജസ്രോതസ്സുകൾ. അന്നത്തെ കാലത്തെ ആശയങ്ങളുടെ ഒരു റൊമാന്റിക് സ്റ്റേറ്റ് എന്ന് വേണമെങ്കിൽ വിശേഷിപ്പിക്കാം. പക്ഷേ, എന്നിലിപ്പോഴുള്ളത് ഗാന്ധിജിയാണ്. ഗാന്ധിജി ഇന്ത്യയെ മനസ്സിലാക്കിയോളം മറ്റാരെങ്കിലും മനസ്സിലാക്കിയിട്ടുണ്ടോ. ഒരുപക്ഷേ, ബുദ്ധനുണ്ടാകും. പക്ഷേ, എനിക്കറിയാവുന്ന കമ്മ്യൂണിസ്റ്റ് പ്രസ്ഥാനം ഗാന്ധിജിയെ വിലയിരുത്തുന്നതിൽ പരാജയമായിരുന്നു. ഗാന്ധിജിയുടെ മൂല്യം പുനർനിർണയം ചെയ്യേണ്ടിയിരിക്കുന്നു. ഞാനറിയുന്ന ഗാന്ധിജിയിൽ ഇടതുപക്ഷവും അംബേദ്ക്കറിസവുമുണ്ട്.

സുസ്ഥിരമായൊരു വികസനസങ്കല്പനം ഗാന്ധിജിയിലുണ്ട്. ജനാധിപത്യത്തിന്റെ സൂക്ഷ്മരൂപങ്ങളുടെ കലവറയാണ് ഗാന്ധിയൻ ചിന്ത. ഉദാഹരണത്തിന് ന്യൂനപക്ഷ കരുതൽ. 80 കളിലെ കാല്പനികനായ യുവാവ് ലോകത്തെ ഒരു പ്രത്യേക വീക്ഷണത്തിലൂടെ ദർശിച്ചപ്പോൾ അത് വളരെ ആകർഷകമായി തോന്നി. ഇന്നത്തെ വീക്ഷണം കൂടുതൽ ബഹുസ്വരമാണ്. ലോകത്തെ മാറ്റിയത് തത്വശാസ്ത്രം അഥവാ പ്രത്യയശാസ്ത്രമാണെന്നാണ് അന്ന് കരുതിയത്. ഇന്ന് തോന്നുന്നു ലോകത്തെ മാറ്റുന്നത് ശാസ്ത്രമാണെന്ന്. ശാസ്ത്രമെന്ന് പറയുമ്പോൾ രസതന്ത്രവും ഊർജതന്ത്രവും മാത്രമല്ല, മറിച്ച് എല്ലാ മേഖലകളെയും സ്പർശിക്കുന്ന

ഒന്നാണത്. അതിന്റെ വാതായനങ്ങൾ വിശാലമാണ്. എന്നെ രൂപപ്പെടുത്തിയത് അന്നത്തെ കാലവും ചിന്തകളുമാണ്. എന്റെ അടിത്തറയാണത്. അതാണെന്നിൽ അവശേഷിക്കുന്നതും.

? നിളയും ഇടശ്ശേരിയും അക്കിത്തവും എംടിയും കവിതയും നിറയുന്ന പൊന്നാനി പശ്ചാത്തലത്തിലെ പഴയ സാഹിത്യകുതുകിയുടെ വർത്തമാന താല്പര്യങ്ങളെന്താണ്. ഐൻസ്റ്റീനും നീൽസ്ബോറിനുമൊപ്പം സോറൻ കീർക്കെഗാറിനെ ഉദ്ധരിച്ച് താങ്കൾ നടത്തിയ ഒരു സമീപകാല പ്രഭാഷണത്തിന്റെ പശ്ചാത്തലത്തിലാണീ ചോദ്യം.

= ഭാഷ നമ്മുടെ മുലപ്പാലാണ്. സാഹിത്യം അതിന്റെ ഭാഗമാണ്. ശാസ്ത്രവും മറ്റും നമ്മൾ ജീവിതത്തിലൂടെ ആർജിച്ചെടുക്കുന്നതാണ്. ഇതൊരുമിക്കുമ്പോഴാണ് നമുക്ക് സാമൂഹിക പ്രതിബദ്ധത കൈവരുന്നത്. ഇതെല്ലാം എന്നിൽ ബാക്കിയാകുന്നതുകൊണ്ടാണ് സാമൂഹികാവബോധം നിലനിർത്തി എനിക്ക് ശാസ്ത്രഗവേഷണം നടത്താൻ കഴിയുന്നത്. അല്ലെങ്കിൽ എനിക്കത് ഉപരിപ്ലവമായി ചെയ്യാമായിരുന്നു. ഇതിനാലാണ് ശാസ്ത്രം വായിക്കുമ്പോൾ എനിക്ക് സോറൻ കീർക്കെഗാറിനെ ഓർമവരുന്നത്. കുട്ടികൃഷ്ണമാരാരെ വായിച്ചതിനാൽ 'മോളിക്യുലർ സ്ട്രക്ച്ചർ' വിശകലനം നടത്തുമ്പോൾ പഴയ രൂപഭദ്രതാവാദം ഓർമവരുന്നു. അതിനാൽ സാമൂഹ്യക്ഷേമമെന്നത് സയൻസിന്റെ ഭാഗമായി ചെയ്യേണ്ടതാണെന്ന വിശ്വാസം എന്നെ നിയന്ത്രിക്കുന്നു.

മലയാളം പഠിക്കുമ്പോൾത്തന്നെ നമുക്ക് ശാസ്ത്രജ്ഞനാകാൻ കഴിയണം. സംഗീതം പഠിക്കുന്ന വിദ്യാർഥിക്ക് രസതന്ത്രത്തിൽ ബിരുദമെടുക്കാനാകണം. ഇത് രണ്ടും ഉപേക്ഷിച്ചോ നിലനിർത്തിയോ വേണമെങ്കിലയാൾക്ക് മെഡിക്കൽ ബിരുദമെടുക്കാനാകണം. അതാണ് പുതിയ സാധ്യതകൾ. മാതൃഭാഷാ പഠനത്തിന്റെ പ്രസക്തി ഇവിടെയാണ് വരുന്നത്.

ഗ്രഹാം കുക്ക്സ്, ഡോ. സി എൻ ആർ റാവു എന്നിവർക്കൊപ്പം ഡോ. ടി പ്രദീപ്

താണു പത്മനാഭൻ

സർക്കാർ ഉത്തരവുകൾ മാത്രം പോര. അത് നമ്മുടെ സ്വത്വത്തിന്റെ പ്രകാശനമാണെന്ന് നാം തിരിച്ചറിയണം.

? ശാസ്ത്രഗവേഷണമാണ് തന്റെ നിയോഗമെന്ന് പ്രദീപ് തിരിച്ചറിഞ്ഞതെപ്പോഴായിരുന്നു. പ്രചോദനമായ വലിയ മാതൃകകൾ... ഡോ. സി എൻ ആർ റാവുമായുള്ള ബന്ധം വിശദീകരിക്കാമോ.

= എം എസ് സി കഴിഞ്ഞ ഇടവേളയിലാണ് റിസർച്ചിനെ കുറിച്ചാലോചിക്കുന്നത്. കാലിക്കറ്റ് യൂണിവേഴ്സിറ്റി സെന്ററിൽ ഇതുമായി ബന്ധപ്പെട്ട് ചില ആലോചനകൾക്കായി ചെന്നപ്പോഴാണ് ഇന്ത്യൻ ഇൻസ്റ്റിറ്റ്യൂട്ട് ഓഫ് സയൻസ് എന്റെ ചിന്തയിലേക്ക് ഗൗരവതരമായി കടന്നുവന്നത്. ഐ എസ് സി യിൽ എത്തിയപ്പോഴാണ് ശാസ്ത്രത്തിന്റെ അത്ഭുതവും ആനന്ദവും എന്നെ കീഴ്പ്പെടുത്തുന്നത്. ശാസ്ത്രീയ കണ്ടെത്തലുകൾ ഒരു ലഹരിയായി എന്നിൽ പടർന്നതും ഇക്കാലത്താണ്. അവിടെ ഞാനടുത്തറിഞ്ഞ മഹാപ്രതിഭകൾ. ഡോ. സി എൻ ആർ റാവു, ഡോ. എം വിജയൻ തുടങ്ങിയവർ.

നൊബേൽ സമ്മാനമൊഴികെ എല്ലാ പുരസ്കാരങ്ങളും നേടിയിട്ടുള്ള, അതിപ്രശസ്തങ്ങളായ 80 ലധികം സർവകലാശാലകളിൽനിന്ന് ഓണററി ഡോക്ടറേറ്റ് നേടിയിട്ടുള്ള ഡോ. സി എൻ ആർ റാവുവിന്റെ കഠിനപ്രയത്നവും അർപ്പണബോധവും ഊർജവും എന്നേയും ബാധിച്ചു. സയൻസ് എന്നത് വലിയ ആഹ്ലാദമുണ്ടാക്കുന്നതാണെന്ന് ഞാൻ തിരിച്ചറിഞ്ഞു. കാലിഫോർണിയ സർവകലാശാലയിലെ ബെർക്കിലിയിൽ എന്റെ ഗവേഷണങ്ങൾക്ക് ഊർജം പകർന്ന പ്രൊഫ. ഡേവിഡ് എ ഷർളി, പ്രൊഫ. ആർ ഗ്രഹാം കുക്ക്സ് തുടങ്ങിയവർ എന്റെ ധൈഷണികവ്യാപാരങ്ങൾക്ക് തെളിമയേകി. ഡോ. ഗ്ലെൻ ടി സീബോർഡിന്റെ സാമീപ്യം ബെർക്കിലിയിൽവെച്ച് ഞാനനുഭവിച്ചിരുന്നു.

ഒമ്പത് ട്രാൻസ് യുറേനിക്ക് മൂലകങ്ങൾ കണ്ടുപിടിച്ച രസതന്ത്രത്തിൽ നൊബേൽ സമ്മാനം ലഭിച്ച വ്യക്തിയാണ് അദ്ദേഹം. ഇത്തരം മഹാപ്രതിഭകളുടെ ആല

ങ്കാരികമായി പറഞ്ഞാൽ ഹിമാലയങ്ങളുടെ സാന്നിധ്യം എന്നെ ആനന്ദിപ്പിച്ചു. ഇതാണെന്റെ വഴിയെന്ന് ഞാൻ തിരിച്ചറിഞ്ഞു. ദീർഘഭാഷണങ്ങൾ ശാസ്ത്രത്തെക്കുറിച്ചായി മാറി. എൻവിയും എംടിയും ജിയും പിയും ഇടശ്ശേരിയും എഴുതിയ പുസ്തകങ്ങൾ എനിക്കുതന്ന അതേ ആഹ്ലാദം മഹത്തായ ശാസ്ത്രഗ്രന്ഥങ്ങൾ നല്കി. ശാസ്ത്രലോകത്തെ മഹാപ്രതിഭകൾ എന്റെ യാത്രയിലെ പ്രകാശസ്തംഭങ്ങളായിമാറി.

? അമേരിക്കയിലെ അക്കാദമിക ജീവിതം എങ്ങനെയായിരുന്നു. ഏഷ്യൻ, ആഫ്രിക്കൻ വിദ്യാർഥികളും ഗവേഷകരും വംശീയാധിക്ഷേപത്തിന് വിധേയരാകുന്നുണ്ടോ. ഒരു വ്യക്തിയെന്നരീതിയിൽ നിറത്തിന്റേയും ദേശത്തിന്റേയും പേരിലുള്ള വിവേചനം അനുഭവിച്ചിട്ടുണ്ടോ.

= വംശീയ ചേരിതിരിവ് ശാസ്ത്രമേഖലയിൽ നേരിട്ട് കാണാനായില്ല എന്നുതന്നെ പറയാം. തെരുവുകളിലും കഫേകളിലും ഞാനത് കണ്ടിട്ടുണ്ട്. അമേരിക്കയേക്കാൾ കൂടുതൽ അത് ദൃശ്യമാകുന്നത് യുകെയിലാണ്. ശാസ്ത്രമേഖലയിൽ ഒരുപക്ഷേ, വളരെ ആന്തരികമായി ഇത്തരം വിവേചനങ്ങൾ ഉണ്ടായിട്ടുണ്ടാകാം. ഏതായാലും ഇന്ന് ചേരുന്ന അന്തർദേശീയ തലത്തിലുള്ള ഒത്തുചേരലുകളിലും കമ്മിറ്റികളിലും ഇതിനെതിരെ പ്രതിരോധമുണ്ട്. അത്തരം കമ്മിറ്റികളുടെ ആദ്യ അജണ്ടയായി എല്ലാത്തരം ദേശീയ വംശീയ ചേരിതിരുവകളിൽനിന്ന് മുക്തമായ നിലപാടെടുക്കണമെന്ന പ്രതിജ്ഞയെടുക്കേണ്ടതുണ്ട്. പക്ഷേ, ഇത്തരമൊരു നിലപാടിലേക്ക് മറ്റുള്ളവരെ പ്രേരിപ്പിക്കുന്ന നമ്മളുടെ അവസ്ഥയെന്താണ്?

മനുഷ്യൻ എന്നത് ഡിഎൻഎയാണെന്ന വസ്തുത നാം വിസ്മരിക്കുന്നു. 65000 വർഷങ്ങൾ പിന്നോക്കം പോയാൽ ഇന്ത്യക്കാരൻ എന്താണ്? അപ്പോൾ എവിടെ ജാതിയും ദേശവും? നമ്മുടെ ഭക്ഷണവും വസ്ത്രവും എങ്ങനെ രൂപപ്പെട്ടു? എല്ലാം വലിയ കലർപ്പുകളാണ്. പരശതം മിശ്രണങ്ങളിലൂടെ രൂപപ്പെട്ടതാണവ. പുറത്തേക്കൊന്ന് നോക്കിയാൽ നമ്മുടെ സങ്കുചിതമായ എല്ലാ കെട്ടുപാടുകളും ഇല്ലാതാകും. കാഴ്ചപ്പാടുകളിലും വിശ്വാസങ്ങളിലും അഴിച്ചുപണികൾക്ക് നാം തയ്യാറല്ല.

യൂറോപ്യൻ സമൂഹത്തിന്റെ വിമോചനത്തിന്റെ അടിത്തറയായത് ഇത്തരം പൊളിച്ചെഴുത്തുകളായിരുന്നു. സ്കാൻഡിനേവിയൻ രാജ്യങ്ങളിലേക്ക് നോക്കൂ. അവിടെ നിങ്ങളുടെ മതം ഒരു പരിഗണനയേയല്ല. ശ്രീനാരായണ ഗുരുവിനെപ്പോലുള്ളവർ നേതൃത്വം നല്കിയ വലിയ നവോത്ഥാനപ്രസ്ഥാനങ്ങളിലൂടെ കടന്നുപോയ കേരളം അണുവിടമാറിയിട്ടില്ല എന്നതിന്റെ ഏറ്റവും പുതിയ ഉദാഹരണമായിരുന്നു സമീപകാല ശബരിമല പ്രശ്നം. ശുദ്ധി, അശുദ്ധി, ആചാരം തുടങ്ങിയ പ്രശ്നങ്ങളിൽ കേരളീയ സമൂഹം വിഭജിതമാകുന്നത് ഇരുപത്തിയൊന്നാം നൂറ്റാണ്ടിലാണെന്ന വസ്തുത നാം ഓർക്കേണ്ടതുണ്ട്.

? പ്രദീപിന്റെ സവിശേഷ പഠ

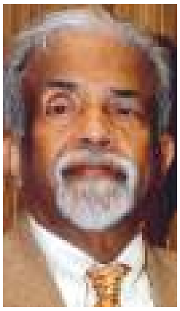

ഇ സി ജി സുദർശൻ

ബാംഗ്ലൂരിലെ ഇന്ത്യൻ ഇൻസ്റ്റിറ്റ്യൂട്ട് ഓഫ് സയൻസ്

2008ലെ ശാന്തിസ്വരൂപ് ഭട്നാഗർ അവാർഡ് മുൻ പ്രധാനമന്ത്രി മൻമോഹൻ സിങ്ങിൽ നിന്ന് ഏറ്റുവാങ്ങുന്നു

രാഷ്ട്രപതി രാംനാഥ് കോവിന്ദിൽ നിന്ന് പത്മശ്രീ സ്വീകരിക്കുന്നു

മലയാളത്തിൽ നാം 'വാക്സിനേഷൻ' എന്ന പദം വ്യാപകമായി ഉപയോഗിക്കുമ്പോൾ തമിഴിലത് 'തടുപ്പൂശി' (തടുക്കുന്ന സൂചി) യായി മാറുന്നു. അവിടത്തെ ജനത അത് സ്വീകരിച്ചു. ഇക്കാര്യത്തിൽ നാം മലയാളികൾ ഏറെ പിറകിലാണ്. കണ്ടെത്തിയ ശാസ്ത്ര സാങ്കേതിക പദാവലികൾ തന്നെ ഗ്രന്ഥങ്ങളിൽ ഉറങ്ങുന്നു. അത് ജനതയുടെ വ്യവഹാര ഭാഷയായില്ല.

നമേഖലയാണല്ലോ നാനോ ടെക്നോളജി. ശാസ്ത്രകുതുകികളായ സാധാരണക്കാർക്കായി 'കുഞ്ഞുകണങ്ങളുടെ വസന്തത്തി'ൽ നടത്തുന്ന പ്രധാന ഇടപെടലുകൾ ലഘുവായി ലളിതമായി വിശദീകരിക്കാമോ.

= തന്മാത്രകൾ തമ്മിലുള്ള രാസപ്രതിപ്രവർത്തനത്തെ spectroscropy എന്ന ശാസ്ത്രമേഖല ഉപയോഗിച്ച് അപഗ്രഥിക്കുകയാണ് കുറേനാളുകളായി ഞാൻ ചെയ്തുകൊണ്ടിരിക്കുന്നതെന്ന് സാമാന്യമായി പറയാം. പദാർഥ വിജ്ഞാനീയം, ശാസ്ത്രീയ വിശകലനങ്ങളെ പ്രായോഗിക പദ്ധതികളാക്കി മാറ്റിത്തീർക്കൽ, ഇവക്കാവശ്യമായ നവീന ഉപകരണങ്ങളുടെ നിർമ്മിതി ഇതൊക്കെയാണ് എന്റെയും ടീമിന്റെയും ഗവേഷണവഴികൾ. നവീനമായ ഉല്പന്നങ്ങളും കണ്ടുപിടുത്തങ്ങളും സാമാന്യജനതക്ക് ലഭ്യമാക്കാനുതകുന്ന ഒട്ടേറെ പുത്തൻ സംരംഭങ്ങളും സ്വതന്ത്രമായ ഒരു റിസർച്ച് ഓർഗനൈസേഷനും രൂപീകൃതമായിട്ടുണ്ട്.

ആറ്റം → തന്മാത്ര → പാർട്ടിക്കിൾ (മെറ്റീരിയൽ) എന്ന രീതിയിലാണ് പദാർഥം വികസിക്കുന്നത്. അതായത് ആറ്റവും തന്മാത്രയും കഴിഞ്ഞാൽ ആയിരമോ പതിനായിരമോ ആറ്റങ്ങൾ ചേരുന്ന ഒരു കണത്തെയാണ് നാനോ പാർട്ടിക്കിൾ എന്നുപറയുന്നത്.

പദാർഥത്തിന്റെ ചില ഗുണങ്ങൾ ഈ കണികകളിൽ കാണാം. നാനോ പാർട്ടിക്കിളിനെക്കാൾ ചെറുതും തന്മാത്രകളെക്കാൾ വലുതുമായ പത്തോ നൂറോ ആറ്റങ്ങൾ കൂടിച്ചേർന്ന സംഘാതങ്ങളെയാണ് ക്ലസ്റ്റേഴ്സ് എന്നുപറയുന്നത്. ഇത്തരം ക്ലസ്റ്റേഴ്സിൽ ഉണ്ടാകുന്ന രാസീയ മാറ്റങ്ങളാണ് പദാർഥങ്ങളെ രാസത്വരകങ്ങളാക്കുന്നത്.

കുട്ടികൃഷ്ണ മാരാർ

പദാർഥങ്ങളുടെ സവിശേഷ ഗുണങ്ങൾ (propertise of mtater) ഉരുത്തിരിയുന്നത് ഈ പദാർഥ കണങ്ങളിലാണ്. ഇത്തരം ചില പുതുകണങ്ങളെ ഞങ്ങളുടെ ലാബ് കണ്ടെത്തുകയും അത് മോളിക്യൂലർ ക്ലസ്റ്റർ മെറ്റീരിയൽസ് എന്ന ശാസ്ത്രവിഭാഗമായി മാറുകയും ചെയ്തിട്ടുണ്ട്.

A + B = C + D എന്ന രീതിയിൽ ഒരു രാസസമവാക്യം പദാർഥകണികകളിൽ സാധ്യമാകുമോ എന്ന് ഞങ്ങൾ പരിശോധിച്ചു. പദാർഥങ്ങളുടെ കണങ്ങൾ തന്മാത്രകൾ തന്നെയാണ് എന്ന പുത്തൻ അറിവിനുകാരണം ഞങ്ങളുടെ ഗ്രൂപ്പിന്റെ ഗവേഷണ പ്രവർത്തനങ്ങളാണ്. പദാർഥങ്ങളുടെ കണങ്ങളിലുള്ള രാസക്രിയകൾ ഞങ്ങൾ കണ്ടെത്തി. ഇതു വളരെ പ്രധാനപ്പെട്ട ഒരു കണ്ടെത്തലാണ്. ആറ്റിക്കുറുക്കി പറയുകയാണെങ്കിൽ പദാർഥങ്ങളുടെ കണങ്ങളെല്ലാം തന്മാത്രകളാണ് എന്ന കണ്ടെത്തലാണ് കഴിഞ്ഞ 10 വർഷക്കാലത്തെ ഞങ്ങളുടെ ഗവേഷണത്തിന്റെ നേട്ടം.

ഖരാവസ്ഥയിലുള്ള വെള്ളത്തിന്റെ രാസഘടനയെക്കുറിച്ച് പഠിക്കുന്നതിനായി നവീനമായൊരു ഉപകരണം ഞങ്ങൾ വികസിപ്പിച്ചു. ഈ ഉപകരണമുപയോഗിച്ച് വളരെ താണ ഊർജനിലയിൽ, വളരെ താണ ഊഷ്മാവിൽ

[10 കെൽവിൻ (-263^{0}C)] ഖരാവസ്ഥയിലുള്ള വെള്ളത്തെ (ഹിമം) നിലനിർത്തി അതിന്റെ അതിലോലമായ OH ബോണ്ടിന്മേൽ ഞങ്ങൾ അയോൺ കൊളീഷൻ നടത്തി. ഇതിനാവശ്യമായ പ്രത്യേക ഉപകരണങ്ങൾ ഉണ്ടാക്കി. എന്താണീ കണ്ടുപിടുത്തത്തിന്റെ മർമ്മം?

ബഹിരാകാശത്ത് ഇത്തരത്തിലുള്ള ഖരാവസ്ഥയിലുള്ള കണങ്ങളുണ്ട്. കോസ്മിക് രശ്മികൾ ഖരാവസ്ഥയിലുള്ള കണങ്ങളിൽ ഇടിക്കും. ബഹിരാകാശത്ത് സാന്നിധ്യമറിയിച്ച മീഥേൻ തന്മാത്രകളും ഖരാവസ്ഥയിലുള്ള ജലത്തിന്റെ തന്മാത്രകളും തമ്മിൽ അതിസൂക്ഷ്മമായ പ്രവർത്തനത്തിലൂടെ മീഥേൻ ഹൈഡ്രേറ്റിനെ ഉല്പാദിപ്പിക്കുന്നതായി ഞങ്ങൾ പരീക്ഷണശാലകളിലെ പ്രവർത്തനങ്ങളാൽ തെളിയിച്ചു. മീഥേൻ ഹൈഡ്രേറ്റ് എന്നത് വെള്ളത്തിന്റെ തന്മാത്രകളുടെ ഒരു

ഡോ. ടി പ്രദീപ് ഭാര്യ ശുഭ, മക്കളായ രഘു, ലയ എന്നിവർക്കൊപ്പം

കൂടിനകത്ത് മീഥേൻ അടക്കം ചെയ്തിരിക്കുന്നു എന്നാണ്.

5 വർഷമെടുത്ത ഗവേഷണ പദ്ധതിയിലൂടെയാണ് ഞങ്ങളിത് ശാസ്ത്രീയമായി തെളിയിച്ചത്. ഈ കണ്ടുപിടുത്തം മറ്റ ചില സാധ്യതകളിലേക്ക് വിരൽചൂണ്ടുന്നു. ഹൈഡ്രേറ്റ് എന്ന 'കൂടിനകത്ത്' മീഥേൻ ഇരിക്കുമ്പോൾ അതിനകത്തേക്ക് കോസ്മിക് രശ്മികളോ മറ്റു പ്രകാശകിരണങ്ങളോ വന്നാൽ മീഥേൻ തന്മാത്ര transform ചെയ്യപ്പെടാം. അങ്ങനെ വന്നാൽ അതിനകത്തുള്ള കാർബൺ തന്മാത്ര ഒന്നോ രണ്ടോ മൂന്നോ കാർബൺ ഉള്ള തന്മാത്രകളായിമാറാം.

ഈ കാർബൺ തന്മാത്രയും നൈട്രജൻ തന്മാത്രയും തമ്മിൽ രാസപ്രവർത്തനത്തിലൂടെ അമിനോ ആസിഡ് ഉണ്ടാകാം. അമിനോ ആസിഡ് ഉണ്ടാകുക എന്നതിനർഥം ബഹിരാകാശത്ത് ജീവനുണ്ടാകാം എന്നതാണ്. സയൻസ് ഫിക്ഷനെ വെല്ലുന്ന ഇത്തരമൊരു സാധ്യതയാണ് ഇപ്പോഴത്തെ ഗവേഷണത്തിന്റെ മുഖ്യകേന്ദ്രം. മനുഷ്യഭാവനയെ എക്കാലത്തും പ്രചോദിപ്പിച്ചിരുന്ന 'ബഹിരാകാശത്തും ജീവൻ' എന്നത് നാളത്തെ ശാസ്ത്രം യാഥാർഥ്യമാക്കിയേക്കാം.

? നിങ്ങളുടെ ഗവേഷണപദ്ധതിയിലൂടെ ജലത്തിലെ രാസമാലിന്യങ്ങളെ നിർമാജനം ചെയ്യുന്ന ചില കണ്ടുപിടുത്തങ്ങൾ നടത്തിയതായി അറിഞ്ഞിട്ടുണ്ട്. വികസിതവും വികസ്വരവുമായ രാഷ്ട്രങ്ങൾ ഒരേപോലെ അനുഭവിക്കുന്ന പ്രശ്നമാണ് ജലത്തിലെ രാസമാലിന്യം. കുടിവെള്ളത്തിൽനിന്ന് രാസമാലിന്യം വേർപെടുത്തുന്നതിനായി നിങ്ങൾ കണ്ടെത്തിയ 'നാനോ ഫിൽട്ടേഴ്സി'ന്റെ സാമൂഹിക പ്രത്യാഘാതങ്ങൾ എന്തൊക്കെയാണ്. വിശദീകരിക്കാമോ.

ഇടശ്ശേരി

= ഏകദേശം ഇരുപത് വർഷങ്ങൾക്കുമുമ്പാണ് കുടിവെള്ളത്തിൽ വ്യാപകമായി രാസമാലിന്യവും കീടനാശിനികളും അടങ്ങിയിട്ടുണ്ടെന്ന മാധ്യമവാർത്തകൾ എന്റെ ശ്രദ്ധയിൽപ്പെടുന്നത്. എന്റെ അന്വേഷണത്തിൽ അനുവദനീയ അളവിനെക്കാൾ 30 ഇരട്ടി കീടനാശിനികൾ ജലത്തിലുണ്ടെന്ന് മനസ്സിലായി. നാനോ കണങ്ങൾ മൂലമുള്ള ചില പ്രവർത്തനങ്ങളിലൂടെ ഇതൊഴിവാക്കാമെന്ന് ഞങ്ങൾ കണ്ടെത്തി.

ഇതിന്റെ പ്രയോഗസാധ്യത മനസ്സിലാക്കി ഈ സാങ്കേതിക വിദ്യ വികസിപ്പിച്ച് അതിന്റെ പേറ്റന്റ് എടുത്തു. ഇതാണ് എന്റെ ആദ്യ പേറ്റന്റ്. ഈ സാങ്കേതികവിദ്യ കൈമാറ്റത്തിലൂടെ റോയൽറ്റി ഇനത്തിൽ എന്റെ സ്ഥാപനത്തിന് 450 ലക്ഷം രൂപ ലഭിച്ചു. അതിനർഥം ആ സാങ്കേതികവിദ്യമൂലം 500 കോടി രൂപയെങ്കിലും ഉണ്ടായെന്നതാണ്. ഇതൊരു മൂർത്തമായ കാര്യം. ഇതുമൂലം സമൂഹത്തിനുണ്ടാകുന്ന ഇതരഗുണഫലങ്ങളാണ് പ്രാധാന്യമർഹിക്കുന്നത്. 80കൾ മുതൽ ഇന്ത്യയിലെ ചില ഭാഗങ്ങളിൽ കുടിവെള്ളത്തിൽ ആഴ്സെനിക്കുണ്ടെന്ന് നമുക്കറിയാം. ഇത് നിർമാർജനം ചെയ്യുന്ന രീതികൾ വളരെ ചെലവേറിയതാകയാൽ ഗവൺമെന്റുകൾക്ക് അത് താങ്ങാവുന്നതായിരുന്നില്ല.

ഞങ്ങൾ പുതിയ സാങ്കേതികവിദ്യകൾ വികസിപ്പിച്ചു. താരതമ്യേന ചെലവുകുറഞ്ഞതിനാൽ ഞങ്ങൾ കണ്ടെത്തിയ ആഴ്സനിക് നിർമാർജനത്തിനുള്ള സാങ്കേതികവിദ്യ ഇന്ത്യാ ഗവൺമെന്റ് അംഗീകരിച്ചു. 15 ലക്ഷത്തിലധികം ജനങ്ങൾ ഇന്നതിന്റെ ഗുണഭോക്താക്കളാണ്. ജലത്തിലെ കീടനാശിനി നിർമാർജനസാങ്കേതികവിദ്യ ഒരു കോടിയോളം മനുഷ്യർക്ക് പ്രയോജനകരമായി ഭവിച്ചു. രണ്ടും ചേർന്നാൽ 1.15 കോടി മനുഷ്യർ ഈ സാങ്കേതികവിദ്യകളുടെ ഗുണഭോക്താക്കളാണ്. ശാസ്ത്ര സാങ്കേതികവിദ്യകൾ സാമൂഹ്യ ക്ഷേമത്തിൽ ഇടപെടുന്നതിന്റെ ഒരു ചെറിയ ഉദാഹരണമാണിത്.

ഈ സാങ്കേതികവിദ്യയുടെ നടപ്പാക്കൽ, വിപണനം തുടങ്ങിയവക്കായി ഊർജസ്വലതയുള്ള യുവാക്കളുടെ, ശാസ്ത്രാഭിരുചിയുള്ള യുവതയുടെ എന്റർപ്രണർ എക്കോസിസ്റ്റം രൂപീകരിക്കപ്പെട്ടു എന്നതും ശ്രദ്ധേയമാണ്.

? നിങ്ങളുടെ ഗവേഷണത്തിന്റെ ഭാഗമായ് സ്വർണം പരീക്ഷണശാലയിൽ ഉണ്ടാക്കാമെന്ന് കണ്ടെത്തിയതായി മാധ്യമവാർത്തകൾ ഉണ്ടായിരുന്നു. അങ്ങനെയെങ്കിൽ വ്യാവസായികാടിസ്ഥാനത്തിലുള്ള സ്വർണനിർമിതി സാധ്യതകൾ ഈ ഗവേഷണഫലത്തിനുണ്ടോ.

= ഇതൊരു മുഖ്യധാരാ ഗവേഷണ പദ്ധതിയായിരുന്നില്ല. മുഖ്യധാരാ ഗവേഷണത്തിന്റെ ഒരു ഉപോല്പന്നമായിരുന്നു ഈ കണ്ടെത്തൽ. ആഴ്സനിക് മണ്ണിലും വെള്ളത്തിലുമുണ്ട്. ആഴ്സനിക് സാന്നിധ്യമുള്ള വെള്ളം കുടിക്കുന്നതു മൂലം കൃഷിയിടങ്ങളിൽനിന്നുള്ള വിളകളിലൂടെ അത് നമ്മുടെ ഭക്ഷണത്തിൽ കലരുന്നു. നെല്ലിൽ, പാലിൽ, അരിയിൽ തുടങ്ങി പലയിടത്തും ഇതിന്റെ സാന്നിധ്യമുണ്ടാവാം.

വിവിധയിനം അരിയിനങ്ങളെ ഞങ്ങൾ പിന്തുടർന്നപ്പോൾ ആഴ്സനിക്കിനൊപ്പം സ്വർണവും വെള്ളിയും ഇവയിൽ ഞങ്ങൾ കണ്ടെത്തി. മണ്ണിൽ ഉള്ളതിന്റെ നൂറുമടങ്ങ് enriched ആയ ലോഹ സാന്നിധ്യം ഞങ്ങൾ അരിയിൽ കണ്ടു. അരിയുടെയും തവിടിന്റെയും ഇടയിലാണ് ഇവയൂടെ ഇരിപ്പ്. ഏതാനും വർഷങ്ങളെടുത്ത് 600ലധികം വിവിധ നെല്ലിനങ്ങളെ ഞങ്ങൾ ലാബിൽ പലതലമുറ കൃഷിചെയ്ത് അവയിലെ അരിയിനങ്ങളെ നിരീക്ഷണത്തിന് വിധേയമാക്കി.

ഞങ്ങളുടെ കണ്ടെത്തൽ ശ്രദ്ധേയമായിരുന്നു. അരിയിൽ ആഴ്സനിക്ക് ശേഖരമുള്ളപ്പോൾ തന്നെ ചിലയിനം അരിയിനങ്ങൾക്ക് അവയെ തിരസ്കരിക്കാനുള്ള കഴിവുമുണ്ടായിരുന്നു. മണ്ണിൽ ആഴ്സനിക് സാന്നിധ്യമുള്ളപ്പോൾത്തന്നെ അവിടെ വിളയുന്ന അരിയിൽ അവയുടെ അസാന്നിധ്യം! ഇതാണ് വിചിത്രമായ പ്രകൃതി പ്രതിഭാസം. ഈ വൈവിധ്യം തിരിച്ചറിയാൻ കെല്പുള്ള ചില ഗോത്രവർഗങ്ങളുമുണ്ടെന്ന് ഞങ്ങൾ കണ്ടെത്തി. അത്തരം അരിയെ അവർ പ്രത്യേകതരം ഔഷധ കൂട്ടുകൾക്കായി ഉപയോഗിക്കുന്നതു കണ്ടു.

നാനോ പാർട്ടിക്കിൾ ഉപയോഗിച്ച് ആഴ്സനിക് വേർതിരിച്ചെടുക്കുന്ന അതേരീതിയിൽ സിൽവറും സ്വർണവും വേർതിരിക്കാൻ കഴിയുമെന്നത് ഒരു സാധ്യതയാണ്. അത്തരം ഗവേഷണം ഞങ്ങളുടെ മേഖലയല്ലാത്തതുകൊണ്ട് അതൊരു സാധ്യത മാത്രമായി അവശേഷിക്കുന്നു. ഇങ്ങനെ കാണുന്ന ലോഹങ്ങളിൽ സ്വർണം മാത്രമല്ല ചിലപ്പോൾ യുറേനിയവും ഉണ്ടാകാറുണ്ട്.

ആഴ്സനിക് സാന്നിധ്യമില്ലാത്ത പ്രദേശങ്ങളിൽ ഉദാഹരണത്തിന് തമിഴ്നാട്ടിൽ അരിയിൽ ഞങ്ങൾ ആഴ്സനിക് സാന്നിധ്യം കണ്ടിട്ടുണ്ട്. ഇതെങ്ങനെ മണ്ണിലും ജലത്തിലുമില്ലാതെ അരിയിൽമാത്രം വരാനിടയായതിന്റെ കാരണം ഞങ്ങളന്വേഷിച്ചു. അത് വളപ്രയോഗത്തിലൂടെയാവാം എന്ന അറിവ് ഞങ്ങളെ അത്ഭുതപ്പെടുത്തി. ഇങ്ങനെ ഈ ഗവേഷണപദ്ധതിയിലൂടെ സംഭ്രമജനകമായ ഒട്ടേറെ അറിവുകൾ ഞങ്ങളുടെ റിസർച്ച് ഗ്രൂപ്പിനുണ്ടായി.

? കോവിഡ് മഹാമാരി എല്ലാ മേഖലകളെയും പോലെ ശാസ്ത്രഗവേഷണമേഖലയെയും ബാധിച്ചിരിക്കുമല്ലോ. എന്തായിരുന്നു അതിന്റെ പ്രതിഫലനങ്ങൾ.

= ഗവേഷണസ്ഥാപനങ്ങളുടെയും പരീക്ഷണശാലകളുടെ യും പ്രവർത്തനം ഏകദേശം 2 വർഷത്തോളം മന്ദീഭവിച്ചു. എല്ലാ മേഖലകളിലും ഉണ്ടായ പ്രവർത്തനമരവിപ്പിലൂടെ ഞങ്ങളും കടന്നുപോയി. സർക്കാരുകളുടെ അജണ്ടകൾ മാറിയതിനാൽ റിസർച്ച് ഫണ്ടിങ് കുറഞ്ഞു. അത് തികച്ചും സ്വാഭാവികമാണ്. ആഗോളതലത്തിൽത്തന്നെ ഗവേഷണം സ്തംഭിച്ചു. ഈ ആലസ്യകാലം ഞങ്ങളുടെ പ്രവർത്തനരീതികളെ മാറ്റിമറിച്ചു. സമയക്രമം താറുമാറായി. ശാസ്ത്ര സാങ്കേതിക ഗവേഷണങ്ങൾ 2 വർഷത്തോളം നിശ്ചലമാകുക എന്നതിനർഥം ഗവേഷണത്തിന്റെ വേഗം മന്ദീഭവിച്ചു എന്നതാണ്. എല്ലാം ക്രമത്തിലാവാൻ ഒരുപക്ഷേ, വർഷങ്ങളെടുത്തേക്കും.

ഡോ. എം വിജയൻ

നോബൽ പുരസ്കാരം ലഭിക്കാതെ പോയ ഒട്ടേറെ മഹാപ്രതിഭകളുണ്ട്. ഗാന്ധിജിയും ടോൾസ്റ്റോയിയും ഉദാഹരണങ്ങളാണ്. രസതന്ത്രത്തിന്റെ മേഖലയിൽ മൂലകങ്ങളുടെ ആവർത്തനപ്പട്ടികയുടെ പിതാവെന്നറിയപ്പെടുന്ന മെൻഡലിയേവ്, രാസസംയുക്തങ്ങളിലെ ബന്ധനത്തെ നിർവചിച്ച ജി എൻ ലൂയിസ് തുടങ്ങി ഒട്ടേറെപ്പേർക്ക് നോബൽ സമ്മാനം ലഭിച്ചിട്ടില്ല.

സോറൻ കിർകെഗർ

? പ്രമുഖ ചരിത്രകാരനും ശാസ്ത്രസാഹിത്യ രചയിതാവുമായ യുവാൽ നോവ ഹരാരിയുടെ രണ്ട് സമീപകാല ഗ്രന്ഥങ്ങളുണ്ട്. ഹോമോദിയൂസ്: എ ബ്രീഫ് ഹിസ്റ്ററി ഓഫ് ടുമാറോ (2017), 21 ലെസ്സൻസ് ഓഫ് 21-ാം സെഞ്ച്വറി (2018). ഇവയിലൂടെ അദ്ദേഹം നിരീക്ഷിക്കുന്നത് മനുഷ്യവർഗത്തിന്റെ മുഖമുദ്രയായ മനുഷ്യത്വം, വിമോചകമൂല്യങ്ങളോടുള്ള ആഭിമുഖ്യം എന്നിവ ശാസ്ത്ര സാങ്കേതിക പുരോഗതിമൂലം മന്ദീഭവിക്കുമെന്നാണ്. ഒരു സമ്പൂർണ ആൽഗൊരിതമായി മനുഷ്യൻ പരിണമിക്കുന്നതും നിർമിത ബുദ്ധി പ്രയോഗങ്ങൾ മേൽക്കൈനേടുന്നതും ഭാവി മാനവചരിത്രത്തിന്റെ ഇരുണ്ട കാലമായി ഒട്ടേറെ നിരീക്ഷകർ വിലയിരുത്തുന്നു. ഭരണകൂടങ്ങളുടെ സമഗ്രാധിപത്യ പ്രവണതകൾ കൂടുതൽ വെളിവാക്കപ്പെടുന്നതിനും സാധാരണപൗരരുടെ നിരീക്ഷണവലയം ശക്തിപ്പെടുന്നതിനും ഇത് തീർച്ചയായും വഴിയൊരുക്കും. സാമൂഹ്യ പ്രതിബദ്ധതയുള്ള ശാസ്ത്രജ്ഞൻ എന്നനിലയിൽ ഈ പ്രവണതകളെ പ്രദീപ് എങ്ങിനെ നിരീക്ഷിക്കുന്നു.

= ഭരണകൂടങ്ങൾ എല്ലാവരെയും നിരീക്ഷിക്കുകയാണ്. മുമ്പ് ഒരാളുടെ കൊടുക്കൽ വാങ്ങൽ പ്രക്രിയകൾ മാത്രമാണ് നിരീക്ഷണ വിധേയമായിരുന്നത്. നിരീക്ഷകന്റെ പങ്ക് ഇന്ന് കൂടുതൽ വിപുലീകൃതമാണ്. അക്കൗണ്ടിങ് നിരീക്ഷകൻ ഇന്ന് ഒരു വ്യക്തിയുടെ മുഴുവൻ ശാരീരികവും മാനസികവുമായ പെരുമാറ്റങ്ങളുടെ നിരീക്ഷകനായി മാറിയിരിക്കുന്നു. ഒരു സാങ്കേതികവിദ്യ ഭീമന് സ്വതന്ത്രവ്യക്തികളുടെ പ്രവർത്തനങ്ങളെ നിയന്ത്രിക്കുന്നതിനും വഴിതിരിച്ചുവിടുന്നതിനും കഴിയും. എഐ, ബിഗ് ഡാറ്റ തുടങ്ങിയവക്ക് തീർച്ചയായും ചില ഇരുണ്ട

വശങ്ങളുണ്ട്. സമഗ്രാധിപത്യത്തിന്റെ ലോകത്തേക്ക് പോകാനുള്ള സാധ്യത തള്ളാനാവില്ല. ഇതെന്റെ മേഖലയല്ലാത്തതിനാൽ ആഴത്തിലുള്ള വിശകലനത്തിന് മുതിരുന്നില്ല.

ഇതിനെ പ്രതിരോധിക്കാൻ ജനാഭിമുഖ്യമുള്ള ശാസ്ത്ര സാങ്കേതികവിദ്യക്ക് കഴിയുമെന്നാണ് ഞാൻ പ്രതീക്ഷിക്കുന്നത്. നമ്മുടെ നിലപാടുകളാണ് പ്രശ്നം. എല്ലാവരുടെയും അടുത്തേക്ക് വിദ്യാഭ്യാസം എത്തിക്കുന്നതിനുള്ള സാങ്കേതികവിദ്യകളുടെ സാധ്യതകൾ നാം ഉപയോഗപ്പെടുത്തണം. അറിവ് ഉണ്ടാക്കുന്ന അസ്വാതന്ത്ര്യത്തെ സ്വാതന്ത്ര്യമാക്കി മാറ്റുന്നതും അറിവാണെന്ന് നാം തിരിച്ചറിയണം. സമഗ്രാധിപത്യത്തിന്റെ ഭാഗത്തേക്ക് ലോകം തിരിയുമ്പോഴും ജനാധിപത്യത്തിന്റെ സുന്ദരമായ ഇടം സൃഷ്ടിക്കുന്നതിനുള്ള സാധ്യതകൾ അവശേഷിക്കുന്നു.

എല്ലാവർക്കും ജലവും ഭക്ഷണവും ഔഷധവും നല്കുന്നതിനുള്ള സാങ്കേതിക സാധ്യതകൾ ഉപയോഗപ്പെടുത്തണം. ഗ്ലോബൽ കണക്ടിവിറ്റി എല്ലാവരുടെയും അവകാശമാണ്. സാങ്കേതികവിദ്യയുടെ സാധ്യതകൾ അനന്തമാണ്. മനുഷ്യപക്ഷത്തുനിന്നുള്ള വികസനസങ്കല്പനത്തിന് ഊന്നൽ നല്കണം.

? ഇവിടെ മറ്റൊരു പ്രശ്നമുദിക്കുന്നു. നമ്മുടെ ഗവേഷണം ദരിദ്രജനവിഭാഗത്തെ അവഗണിക്കുന്നുണ്ടോ. പോഷകാഹാരക്കുറവ്, ദാരിദ്ര്യം, പകർച്ചവ്യാധികൾ, അടിസ്ഥാന ജീവനോപാധികളുടെ വികസനം തുടങ്ങിയ മേഖലകളെ നമ്മുടെ ഗവേഷണമേഖല ഗൗരവത്തോടെ പരിഗണിക്കുന്നില്ലേ. ഉദാഹരണങ്ങൾ ധാരാളമുണ്ട്. ഉന്നതശാസ്ത്രഗവേഷണ മേഖല സ്ത്രീകളെ മാറ്റിനിർത്തുന്നുണ്ടോ. വിശദീകരിക്കാമോ... ഇന്ത്യയുടെ ശാപമായി വിലയിരുത്തപ്പെടുന്ന സവർണാവർണ ഭേദം ഈ മേഖലയിലുണ്ടോ.

= ഞാൻ നേരത്തെ സൂചിപ്പിച്ചതുപോലെ സാമൂഹ്യയാഥാർഥ്യങ്ങളുടെ പ്രതിഫലനം ഇവിടെയുമുണ്ടാകും. സ്ത്രീകളുടെ അസാന്നിധ്യവും അങ്ങനെ ദർശിക്കണം. സമൂഹത്തിലെ ചൂഷിതമേഖലകൾ, അസമതകൾ പ്രതിഫലിക്കുന്ന കണ്ണാടികളാണ് ഈ മേഖലയെന്ന എന്റെ മുൻപ്രസ്താവന ഞനാവർത്തിക്കുന്നു. ഇതെങ്ങനെ ലഘൂകരിക്കാമെന്ന് പരിശോധിക്കണം.

നിയമപരിരക്ഷ കൊണ്ടുമാത്രം ഇത് നടപ്പാവില്ല. ശാസ്ത്രത്തിലും സാമൂഹ്യവിഷയങ്ങളിലും പുരോഗമനപക്ഷപാതിത്വം പുലർത്തുന്ന ആണുങ്ങൾ വീട്ടിലെങ്ങനെ പെരുമാറുന്നു? ആണധികാരത്തിന്റെ ഒട്ടേറെ പുത്തൻഗാഥകൾ നാം നിരന്തരം കേൾക്കുന്നു. ഞാൻ വ്യക്തിപരമായി ഇത്തരമൊരു മേഖലയിലൂടെ ചിലപ്പോഴൊക്കെ കടന്നുപോയിട്ടുണ്ട്. ബ്രാഹ്മണനായിരുന്നുവെങ്കിൽ കുറച്ചുകൂടി നന്നായേനെ എന്ന് ഞാൻ ചിന്തിച്ച സന്ദർഭങ്ങളുണ്ടായിട്ടുണ്ട്. ഇരുപത്തിയഞ്ചിലോ മുപ്പതിലോ നിൽക്കുന്ന ഒരു ഗവേഷകന് തീർച്ചയായും ഇത്തരം അനുഭവങ്ങൾ ഉണ്ടാകാം. മാംസാഹാരം കഴിച്ചതിന്റെ പേരിൽ അവഹേളിക്കപ്പെട്ട വിദ്യാർഥികൾ ഐഐടി ഹോസ്റ്റലിലുണ്ട്.

? മലയാളികളുടെ മാതൃഭൂമിയിലേക്ക് തിരിച്ചെത്തി നമുക്കീ സംഭാഷണം അവസാനിപ്പിക്കാം. നവോത്ഥാനത്തിലൂടെ കടന്നുപോയ മലയാളി സമൂഹത്തിന്റെ വർത്തമാനാവസ്ഥയോടുള്ള പ്രതികരണം. ജാതിയും ആചാരങ്ങളും മുറുകെപ്പിടിച്ച് പുതുകേരളം സൃഷ്ടിക്കാമെന്ന് വ്യാമോഹിക്കുന്നവർ ഇവിടെ ധാരാളമുണ്ട്. ജനസംഖ്യാനുപാതികമായി നോക്കിയാൽ ഇന്ത്യയിലേറ്റവും കൂടുതൽ സ്വർണാഭരണങ്ങൾ സൂക്ഷിക്കുന്നത് മലയാളികളാണെന്ന് പ്രദീപിന്റെ ഒരു സമീപകാല പ്രഭാഷണത്തിലുണ്ടായിരുന്നു. നവകേരള നിർമിതിയുടെ സാധ്യതകൾ എന്തൊക്കെയാണ്.

= ശാസ്ത്രം എന്നത് പ്രതീക്ഷയാണ്. കൂടുതൽ മെച്ചപ്പെട്ടൊരു ഭാവി സ്വപ്നം കാണുന്നവർക്ക് അത് സാക്ഷാത്കരിക്കാനുള്ള ‘tool’ ശാസ്ത്രമാണ്. എല്ലാവർക്കും വിദ്യാഭ്യാസം, തൊഴിൽ, ഭക്ഷണം, മരുന്ന്, കണക്ടിവിറ്റി തുടങ്ങിയ പ്രതീക്ഷകളെ യാഥാർഥ്യമാക്കുന്നത് ശാസ്ത്രമാണ്.

> **ലോകത്ത് പലയിടത്തും മാറ്റങ്ങൾ പ്രകടമാണ്. ഐഐടി ചെന്നൈയിൽനിന്ന് ബിടെക്ക് കഴിഞ്ഞവരിൽ ചിലർ മികച്ച ന്യൂറോ സർജന്മാരായി മാറിയിട്ടുണ്ട്. പക്ഷെ അവർക്കത് സാധ്യമായത് അവർ അമേരിക്കയിൽ പോയതുകൊണ്ടാണ്. സദൃശമായ വലിയ മാറ്റങ്ങൾ നമ്മുടെ യൂണിവേഴ്സിറ്റികളിൽ ഉണ്ടാകണം. അത്തരം തിരുത്തൽ പ്രക്രിയയിലൂടെ മാത്രമേ സമൂഹത്തെ മാറ്റാൻ കഴിയുന്ന ഊർജം പ്രസരിക്കുന്ന വലിയ അക്കാദമിക വ്യക്തിത്വങ്ങൾ ഉണ്ടാകൂ.**

നമ്മുടെ ആയുർദൈർഘ്യത്തിന്റെ വർധന, ശിശുമരണനിരക്കിലുണ്ടായ കുറവ് എന്നിവ സംഭവിച്ചത് പ്രതീക്ഷകളുടെ ശാസ്ത്രം ജനങ്ങളിലെത്തിയതുകൊണ്ടാണ്. പക്ഷേ, കോവിഡ് വാക്സിൻ സ്വീകരിക്കാൻ ആശുപത്രിയിലെത്തുമ്പോഴും നമ്മൾ നായരും തീയനും പട്ടികജാതിക്കാരനുമാകുന്നതാണ് പ്രശ്നം. ബുദ്ധിയെ സ്വാധീനിച്ചതുപോലെ ഹൃദയങ്ങളെ സ്വാധീനിക്കുന്ന ഗുണമേന്മയേറിയ വിദ്യാഭ്യാസം സാധ്യമാകണം.

നാരായണഗുരുവിനും രണ്ടാം മഹായുദ്ധത്തിനുശേഷവും കേരളം വളർന്നപ്പോഴും ഒട്ടേറെ അപച്യുതികളിലേക്ക് നാം തിരിച്ചുപോയി. മോചനമാണ് പുതിയ വിദ്യാഭ്യാസം. പക്ഷേ, ഗർത്തങ്ങൾ നമ്മെ കാത്തിരിക്കുകയാണ്. ജാതിചേരിതിരിവുകൾ, പരമ്പരാഗത ആചാരങ്ങൾ തുടങ്ങിയവ. പുത്തൻവെല്ലുവിളികളെ പുരോഗമനപ്രസ്ഥാനങ്ങൾ ഏറ്റെടുക്കണം. സിംഗപ്പൂർ, ഫിൻലന്റ്, വിയറ്റ്നാം, സ്കാൻഡിനേവിയൻ രാജ്യങ്ങൾ തുടങ്ങിയവയിൽ നമുക്ക് പകർത്താവുന്ന ഒട്ടേറെ മാതൃകകൾ ഉണ്ട്. ശാസ്ത്രബോധമുള്ള കർമോത്സുകതയുള്ള നമ്മുടെ മനുഷ്യസമ്പത്തിനെ ലക്ഷ്യബോധത്തോടെ നാം പ്രയോജനപ്പെടുത്തണം. ഫ്യൂഡൽ, പാട്രിയാർക്കൽ മൂല്യങ്ങളിൽനിന്ന് കുതറിമാറുന്നതിന് വലിയ സാമൂഹ്യമാറ്റങ്ങൾ ഉണ്ടാകേണ്ടിയിരിക്കുന്നു. Remitted economyയെ മാത്രം ആശ്രയിക്കാതെ വിശാലമായ ആകാശത്തേക്ക് പറന്നുപോകുന്ന യുവതയുടെ കർമശേഷി മലയാളനാട്ടിൽ നിലനിർത്താൻ കഴിഞ്ഞാൽ കേരളം മാറും. ശാസ്ത്രത്തിന്റെ അനന്തമായ ശോഭനമായ ഭാവിയുടെ ചിറകിലേറി ‘മലയാളിയുടെ മാതൃഭൂമിക്ക്’ കുതിക്കാനാകുമെന്ന് ഞാൻ വിശ്വസിക്കുന്നു ●

Book Chapter

Chapter 3

C0015 Nanosensors for water quality monitoring

Tanvi Gupte[a,b] **and Thalappil Pradeep**[a,*]
[a] *DST Unit of Nanoscience (DST UNS) and Thematic Unit of Excellence, Department of Chemistry, Indian Institute of Technology Madras, Chennai, India,*
[b] *Department of Metallurgical and Materials Engineering, Indian Institute of Technology, Chennai, India*
[*] *Corresponding author: e-mail address: pradeep@iitm.ac.in*

s0010 Significance of water quality monitoring

p0010 Water is the essence of life on earth. Yet, availability of water of appropriate quality in adequate quantity is an ever-increasing concern due to a number of issues, including pollution of water bodies. Robust technologies are being developed for water quality monitoring and purification. Identification and quantitation of contaminant(s) are essential aspects of controlling water pollution. According to UNICEF and WHO, the proportion of population in the least developed countries using limited water services has doubled between 2000 and 2017 [1]. Organic pollutants, pharmaceuticals, heavy metals, pathogens, explosives, pesticides, and other such water contaminants have posed an acute threat to the ecosystem worldwide. Key findings of the WHO report attribute 3.3% of deaths and 4.6% of disability-adjusted life years to the effects of inadequate water, sanitation, and hygiene, for the year 2016 at a global scale [2].

p0015 Hence, one of the global targets for UN Sustainable Development Goals (SDGs) is the availability of safe and affordable drinking water for all by 2030. Some of the significant challenges for achieving these goals are increasing population, climate change, expanding cities, rapid industrial development, improper waste management, eutrophication of water bodies, etc. In these emerging global development conditions, prompt pollutant recognition has become a need of the hour.

p0020 Water quality plays a significant role in human health and economic growth, from household to global scale. Hence, the accurate and timely evaluation of its quality is essential for initiating remedial strategies to ensure that the contaminants are at acceptable levels and prevent them from causing environmental catastrophes [3]. Water quality monitoring provides information for regulatory measures and surveillance. Water is expected to contain small amounts of contaminants, and in fact, some of them such as essential and trace minerals are important for life. However, certain toxic substances pose a threat to human health even at low concentrations. The maximum acceptable level of each contaminant is different. Therefore, the development of sensitive water quality sensors for the detection of trace pollutants is essential.

s0015 Water quality sensors

p0025 A sensor is broadly defined as a device that detects events or changes in its physical environment. The information is relayed as data to other devices, such as a computer. Water quality sensors are essential for ensuring availability and accessibility for quality water for human activities ranging from drinking to agricultural and industrial purposes. The sensors could be located at the point of use or at the water treatment facilities, or within the water distribution system. The information from such sensors is vital for water management issues such as meeting the required regulations for water quality, industrial and municipal wastewater treatment (e.g., monitoring specific, target compounds), agricultural irrigation, identification of noncompliant water bodies, and establishing an early warning system (e.g., leakage detection).

p0030 Monitoring water quality requires qualitative and quantitative measurement of various pollutants. However, developing such a sensor is a challenging task due to diversity and complexity of the water samples and trace amounts of contaminants that need to be detected. In addition, several aspects of the water such as temperature, pH, dissolved solids and gases, etc. can have an impact on the chemical state and concentration of the contaminants. Hence, physical, chemical, and biological parameters need to be taken into consideration for water quality monitoring. Physical parameters include color, suspended particles, turbidity, density, conductivity, temperature, and total dissolved solids. Chemical parameters may be organic and

Separation Science and Technology, Volume 15. https://doi.org/10.1016/B978-0-323-90763-7.00010-X

inorganic (pH, dissolved oxygen, hardness, disinfectants, phosphates, nitrogen content, micronutrients, and other inorganic metal contaminants). Biological parameters include various micro-organisms such as algae, bacteria, and pathogens [4]. Current sensing technologies are mainly based on colorimetry, electrochemistry, or lab-based spectroscopic methods. Traditional methods for water quality monitoring are largely dependent on laboratory analysis, complex instrumentation, and computing infrastructure. They require frequent calibration and are often not suitable for continuous sampling [4]. Thus, there is a high demand for sensitive, simple, cost-effective, and portable *in situ* operating sensors for real time monitoring of water quality. Incorporation of nanotechnology and innovative techniques in fabrication of sensors is proving to be a promising tool. Sensors for monitoring water quality are essential emerging field in nanosensor technology research. Nanosensors with the capabilities to provide quantitative information comparable to conventional analysis methods along with the advantage of miniaturization of devices are an effective alternative.

s0020 Nanosensors

p0035 Nanosensors are sensing devices that utilize nanomaterials as recognition elements to detect changes. In recent years, nanomaterials-based sensors are gaining popularity. They provide high sensitivity, specificity, large surface area to volume ratio, quantum confinement effects, rapid detection, and tunable magnetic, electrical, and optical properties [5]. They have wide applications in detecting toxic gases, food packaging, healthcare diagnostics, and water quality monitoring. This chapter focuses on the recent advances and techniques in nanosensing technology, emphasizing research toward real-life applications that can replace traditional water quality evaluation methods.

p0040 Types of water quality nanosensors based on the signal transduction mechanism employed for sensing are discussed in this chapter. These include electrochemical, optical, and magnetic nanosensors. Biomimetic and hybrid nanosensing technologies are also mentioned briefly. Various suitable nanomaterial platforms such as noble metal nanostructures, quantum dots, magnetic nanoparticles (MNP), metal–organic frameworks (MOFs), clusters, enzymes, molecularly imprinted polymers, aptamers, carbon nanomaterials, etc., are also discussed concurrently. Table 1 enlists applications of various nanosensors discussed in the chapter for monitoring water quality.

s0025 Electrochemical nanosensors

p0045 Electrochemical nanosensors are sensing devices that measure the change in current, voltage, conductance or impedance resulting from a reaction, using nanomaterials as recognition elements that convert the signal to digital information. Typically, an electrochemical sensor consists of three electrodes-working, a reference, and a counter (auxiliary) electrode. The working electrode serves as the surface where the reaction/process of interest occurs. Different electrochemical techniques are amperometry, voltammetry, potentiometry, impedance spectroscopy, and conductometry (capacitive and resistive). Due to the different detection mechanisms involved, information on various aspects of an electrochemical reaction is gained from different techniques [6]. Electrochemical sensing methods are sensitive and reliable due to their advantages such as low cost, lower limit of detection, quick response, and portability. They are promising candidates for making real-time and in-process monitoring and detection of trace amounts of water pollutants feasible [7,8].

p0050 The geometry, design, and configuration of the working electrode (WE) play an important role in electrochemical sensors [9]. A combination of nanotechnology and electrochemistry can produce robust and reliable electrical instruments for monitoring environmental contaminants [10]. Usually, the WE is miniaturized to provide portability for on-field sensing. A nanoelectrode (NE) or a WE electrode modified using nanomaterial platforms and surface modifications provide improved conductivity, sensitivity, and surface area to detect target contaminant(s) [7]. Screen printing is a fabrication technique that promotes miniaturization of electrochemical sensing devices. A screen printed electrode (SPE) integrates the three electrodes on an insulated solid substrate made of polyvinyl chloride, polyethyleneterephthalate, ceramic, etc.) [11]. SPE is typically fabricated by layer by layer deposition of ink onto the substrate. The technique involves an ink-blocking stencil supported on a woven mesh. The ink and other printable modifiers are pumped across the stencil by a roller or squeegee. The ink is usually allowed to solidify by thermal treatment between printing of successive ink layers. Commonly used inks include carbon, platinum, gold and silver [12]. The thickness of SPE is usually a few microns which is easily controlled by number of ink layers and amount of printed ink [11]. Suitable modifiers such as catalyst, nanomaterials, metallic nanocomposites, organic compounds, etc. may be used along with the ink (bulk modified recognition systems) or included on the electrode surface. This increases the effective surface area, absorption capability, electrical conductivity, selectivity and sensitivity [9,13]. The modifications for SPE may also be in the form of specific electrode design or a suitable solid substrate [9]. Fig. 1A shows typical design of a SPE used in electrochemical sensing.

t0010 **TABLE 1** Applications of various nanosensors for monitoring water quality.

Sr. No	Transduction mechanism	Sensor material	Analyte	Limit of detection	References
1.	Electrochemical	Choline oxidase enzyme and MWCNT	Pb^{2+}	0.0083 ppb	[16]
		Graphene conjugated with CdSe QDs, HRP-labeled AuNPs and specific monoclonal antibody on GCE	Hg^{2+}	0.06 ppb	[17]
		HS-$(CH_2)_2$-$[OCH_2CH_2]_6$-OCH self-assembled monolayer on aptasensor	Ampicillin and sulfadimethoxine drugs	10 pM and 1 nM, respectively	[18]
		Immobilized aptamers and IC-DNA-labeled AuNPs on rGO and Au dendritic nanostructures	Hg^{2+}, Cd^{2+}, and As^{3+}	2.0, 0.62, and 0.17 pM, respectively	[37]
		DNA-modified Fe_3O_4@Au MNPs on magnetic GCE	Ag^{+} and Hg^{2+}	3.4 nM (0.37 ppb) and 1.7 nM (0.34 ppb), respectively	[41]
		Polypyrrole on pencil graphite electrode	Dibutyl phthalate	4.5 nM	[21]
		CuO-TiO_2 hybrid nanocomposite on GCE	Methyl parathion	1.21 ppb	[22]
		Poly(3,4-ethylene-dioxythiophene) nanorods/GO nanocomposite on GCE	Hg^{2+}	2.78 nM (0.55 ppb)	[23]
		Amorphous carbon and Bi NPs on SPE	Pb^{2+} and Cd^{2+}	3.8 and 2.2 ppb, respectively	[45]
		N-methyl-2-pyrrolidone (NMP) exfoliated graphene nanosheets on GCE	Hydroquinone, catechol, 4-chlorophenol, and 4-nitrophenol	0.012, 0.015, 0.01, and 0.04 μM, respectively	[47]
		Vertically aligned two-dimensional (2D) MoS_2	Pb^{2+}	0.3 ppb	[50]
		Fe_3O_4 NPs hybridized with S-MWCNTs that were combined with poly (2,6-pyridine dicarboxylic acid) on GCE	Omeprazole	15 nM	[24]
		AuNPs/α-MnO_2	As^{3+}	0.019 ppb	[55]
2.	Optical	4-mercaptopyridine functionalized Au NPs	Hg^{2+}	8 nM (1.60 ppb)	[60]
		Monoclonal cholera toxin antibody-conjugated AuNPs that were modified with mercaptopropionic acid	Cholera toxin	10 nM	[58]
		Silver dendrite SERS substrate	Ferbam pesticide	0.861 ppm	[64]
		Tetraphenylporphyrin tetrasulfonic acid (TPPS) and black phosphorus QDs	Hg^{2+}	0.39 nM (0.078 ppb)	[67]
		Nitrogen-doped carbon QDs	Humic substances	0.2 mg/L	[69]

Continued

TABLE 1 Applications of various nanosensors for monitoring water quality.—cont'd

Sr. No	Transduction mechanism	Sensor material	Analyte	Limit of detection	References
		Fe_3O_4 microspheres and Au NPs using SERS	16 PAHs	100–5 nM	[73]
		Gold-coated magnetic nanosphere–anti-*E. coli* antibody complex and Raman label	*E. coli*	8 cfu/mL	[71]
		Core–shell MOF@Ag NPs on SPCE	PAHs	pM	[88]
3.	Magnetic nanosensors	Schiff base/silica/magnetite as preconcentration phase	Pb^{2+}, Cd^{2+} and Cu^{2+},	0.14, 0.19 and 0.12 $\mu g\,L^{-1}$, respectively	[89]
	Biomimetic and hybrid nanosensing	Plant with lead-sensitive DNA and CNTs in leaves	Pb^{2+}	—	[90]
		Nanoswimmer: PEDOT/Au bilayer microtubes with catalase enzyme	Mercury, copper, herbicide-aminotriazole, and pesticide-NaN_3	Micromolar levels	[93]

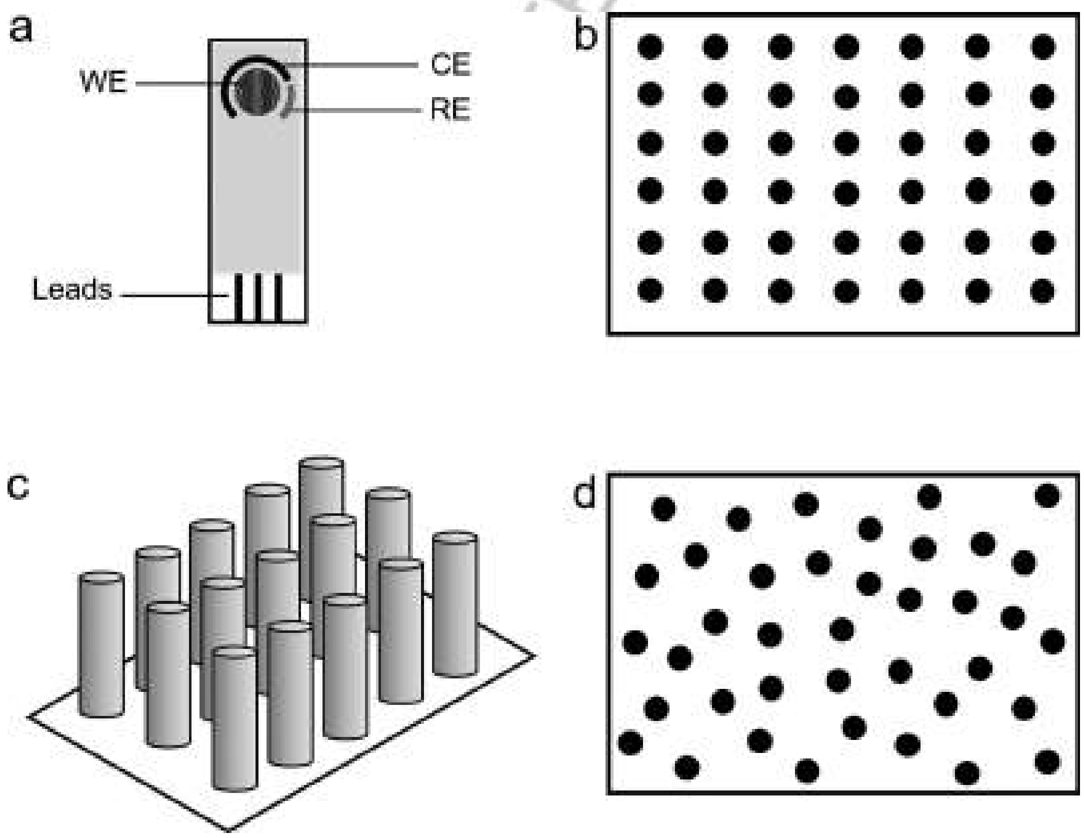

f0010 **FIG. 1** Examples of typical geometries of a few electrochemical electrodes: (A) screen-printed electrode (SPE), (B) square nanoelectrode array (NEA), (C) three-dimensional nanowire NEA, (D) randomly arranged NE ensemble (NEE). WE: working electrode, CE: counter electrode, and RE: reference electrode.

This fabrication technique produces mechanically stable, cost-effective and disposable electrodes. SPEs can easily be used with miniaturized, portable electrochemical sensing instruments for on-field detection of water contaminants [12].

p0055 Electrochemical nanosensors can also be in the form of an individual NE, an electrode with at least one dimension (e.g., radius for discs or nanowires and thickness for lines) of approximately 50 nm. Typical geometries of NE are NE arrays (NEA) and NE ensemble (NEE), as shown in Fig. 1B–D. NEA are perfectly ordered sets of NE that have single as well as multianalyte measurement capability (Fig. 1B and C). NEE are randomly arrange groups of NE that can be used to obtain spatial distribution measurements for a single analyte (Fig. 1D) [6,14]. Multiplexed designs offer the possibility of differently modifying individual electrodes in an array to detect different target analytes [9].

p0060 Different nanomaterial platforms used for electrode modification include biorecognition elements (e.g., enzymes [15,16], nucleic acids, cells, antibodies [17], aptamers [18], microorganisms, etc.) [19], molecularly imprinted polymer (MIP) [20,21], nanocomposites [22,23], nanoparticles [24], nanostructures [25], carbon nanomaterials such as carbon nanotubes [15,26–28], carbon nanofibers, graphene, etc. Using nanomaterials in electrochemical sensing provides advantages such as greater mass transport, high current densities, low background charging current, and enhanced surface-to-volume ratio [14,20]. This results in higher sensitivity and lower detection limits [14].

p0065 The electrode surface modification can be in the form of adsorption, covalent bonding, electrochemical deposition, and electrochemical polymerization. In the adsorption type of modification, noncovalent interactions exist between the electrode surface and the modifier, mainly as coatings, chemical adsorption, or self-assembled monolayers. Electrochemical deposition and polymerization surface modification methods involve applying a voltage to the WE in an electrolyte containing the preferred modifier. This results in the formation of polymeric or metallic films on the surface. In the case of SPE, the preferred material is added in the ink [9].

p0070 Electrochemical nanosensors have been used for detection of various water contaminants such as heavy metals (e.g., Pb^{2+}, Cd^{2+}, As^{3+}, etc.) [7,25,28], pharmaceuticals [20,24], pesticides [22,29], etc. Moreover, portable and low-cost potentiostats are now widely available commercially that are useful for *in situ*/online/point-of-care analysis [9]. Some of the widely used nanomaterial platforms employed in electrochemical nanosensors are described in brief in the following subsections.

s0030 *Electrochemical biosensors*

p0075 Electrochemical biosensors are a class of nanosensors that use various biorecognition elements such as enzymes, antibodies, aptamers, nucleic acids, cells, etc. to detect analytes electrochemically. Fig. 2 shows the schematic of a typical electrochemical biosensor comprising a biorecognition element (which allows selective detection of specific analyte(s)) and other components like transducer, amplifier, processor, and display. Enzyme, antibody, aptamer, and DNA-based electrochemical biosensors to detect water contaminants with suitable examples are briefly described.

s0035 Enzyme

p0080 Enzymes have been widely used for the detection of heavy metal ions as the interaction causes a change in the structure and properties of the enzyme. This leads to activation or inhibition effect on an enzyme activity in the presence of specific ions. Commonly used enzymes in electrochemical metal ion sensors include oxidase, peroxidase, and urease [30]. An amperometric choline biosensor was developed to detect Pb^{2+} using choline oxidase enzyme (ChOx) and multiwalled carbon nanotubes (MWCNT). In the presence of Pb^{2+} ions, the enzyme activity (oxidization of choline into betaine) was inhibited, causing a decrease in the choline oxidation current. The detection limit was 0.04 nM (0.0083 ppb) with high selectivity for Pb^{2+} ions, and the detection was successful in tap water samples [16].

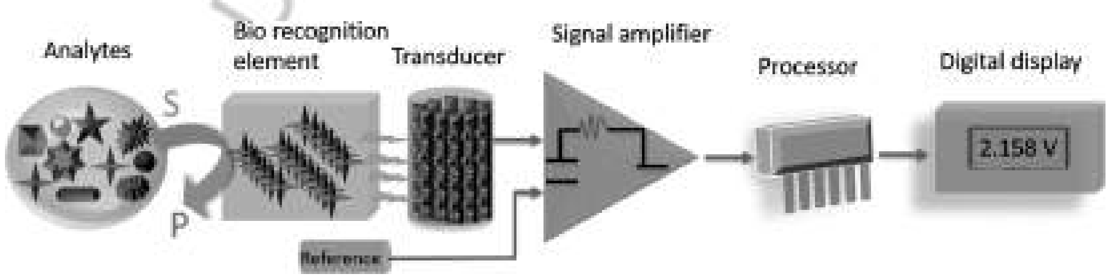

f0015 **FIG. 2** Schematic illustration showing the key components of an electrochemical biosensor. Here, the biorecognition element converts the substrate (S) to the product (P). The transducer converts the biological response into an electrical signal. The output is then amplified and processed by a transistor processor, and finally, the output is displayed on a computer. *From H.S. Magar, M.E. Ghica, M.N. Abbas, C.M.A. Brett, Highly sensitive choline oxidase enzyme inhibition biosensor for Lead ions based on multiwalled carbon nanotube modified glassy carbon electrodes, Electroanalysis 29 (7) (2017) 1741–1748. doi:10.1002/elan.201700111.*

s0040 Antibody

p0085 Antibody-based electrochemical nanosensors are centered around the conformational modifications produced by the bio-recognition interaction between the antibody and the antigen which are detected by a transducer. They are also termed electrochemical immunosensors. The immunochemical reactions are converted into an electrical signal such as current, potential difference, or resistivity change. The antibody is usually immobilized onto the electrode surface. An antibody (Ab) monomer is a globular plasma protein made of four polypeptide chains—two light chains (~25 kDa each) and two heavy chains (~50 kDa each) which are connected by disulfide bonds. Each of these chains has a constant and a variable region and form a characteristic "Y" shape. The variable regions determine the selectivity and binding to specific antigens or analytes. Various immobilization techniques include microcontact printing, direct spotting, covalent binding, and adsorption to a conductive polymer matrix [31]. The performance of these sensors is usually enhanced by modifying the working electrode with electrically conductive nanomaterials. This helps in the amplification of their signal and immobilization of more antibodies [32]. In the case of heavy metal ion detection, the change in the current on the electrode surface due to oxidation and reduction of selectively adsorbed species is quantified. An ultrasensitive electrochemiluminescent (ECL) immunoassay for mercury detection was developed based on graphene conjugated with CdSe quantum dots, horseradish peroxidase (HRP)-labeled gold nanoparticles (AuNPs), and specific monoclonal antibody (mAb) against Hg^{2+}. The detection was performed using a glassy carbon electrode (GCE) and cyclic voltammetry. The immunosensor exhibited good stability, accuracy, and acceptable reproducibility in environmental samples with a detection limit of 0.06 ppb [17]. The high specificity and sensitivity aspects of antibody-based electrochemical sensors have been helpful for the detection of contaminants such as pharmaceuticals [33,34], toxic microorganisms such as microalgae [35], pesticides, etc. However, immunosensors have certain drawbacks, including the high production costs of antibodies, instability, and difficulty with multiplexing [32].

s0045 Aptamer

p0090 Electrochemical aptamer-based nanosensor platforms have received significant attention in the past decade. Aptamers are single-stranded oligonucleotides or peptides that show high affinity and specificity to their targets [36]. These are usually immobilized on an electrode substrate. Aptamer-based nanosensors interact in two ways with the target analyte. The interaction can result in structural modification or a change in both flexibility and conformation of the immobilized aptamer. In the first type of interaction, the electron transfer resistance between the electrode surface and the redox-active species in the solution is altered. In the second case, the sensing is based on either an increase or a decrease in the redox current. Aptamers can be labeled with electrochemical and fluorescent reporter tags and are stable in a wide range of experimental conditions [36]. Yang et al. reported a signaling-probe displacement electrochemical aptasensor (EAS). The sensing mechanism in signaling-probe displacement sensor is based on the theoretical assumption that the target analyte will cause displacement and release of the signaling probe (ferrocene in this experiment) from the electrode surface, leading to a decrease in the current signal. The researchers passivated the aptasensor surface with HS-$(CH_2)_2$-$[OCH_2CH_2]_6$-OCH self-assembled monolayer which enabled picomolar detection of antibacterial drugs (ampicillin and sulfadimethoxine). This is the first reported EAS that works well for both hydrophilic and lipophilic targets. They also demonstrated the efficacy in lake water samples [18]. Tang et al. developed an aptasensor array using a multichannel disposable screen-printed carbon electrode (SPCE) for the simultaneous detection of three heavy metal ions (Hg^{2+}, Cd^{2+}, and As^{3+}) by open circuit potential (OCP) technology. The sensor had an internal calibration DNA sequence (IC-DNA) to correct the background signal generated by the detection system. The array was first modified with reduced graphene oxide (rGO) and dendritic gold nanostructures followed by immobilization of aptamers and IC-DNA-labeled AuNPs. The aptasensor array showed high sensitivity toward Hg^{2+}, Cd^{2+}, and As^{3+} with detection limits of 2.0, 0.62, and 0.17 pM, respectively, without mutual interference or interference from other ions. Moreover, the array was successful in simultaneous detection of the three ions in real water samples, and the results accurately matched with the data obtained from inductively coupled plasma mass spectrometry [37].

s0050 Deoxyribonucleic acid (DNA)

p0095 DNA as a bio-recognition element for water quality assessment has vast potential due to its properties such as selectivity, sensitivity, biodegradability, cost-effectiveness, portability, and easy manipulation [38,39]. Also, for certain analytes, electrochemical DNA nanosensors produce direct electronic signals overcoming the need for expensive signal converting instruments. Moreover, these sensors work efficiently in turbid or colored samples too [39]. Also, various strategies exist to amplify signals of electrochemical DNA biosensors to achieve ultrasensitivity. For example, nicking enzyme-assisted amplification by using various endonucleases. This strategy allows rapid exponential amplification of a target nucleic acid. Other techniques utilize core-shell nanoparticles and nanocomposites (e.g., AuNPs, graphene, carbon nanotubes (CNTs)) for surface modification and signal amplification [38]. Electrochemical DNA sensors are utilized for sensing heavy metal ions, pharmaceuticals, and microorganisms (e.g., coliform bacteria, *E. coli*). Detection of heavy metal ions depends on selective and specific binding of the ions with distinct DNA bases, resulting in a stable DNA-duplex [39]; for example, thymine-Hg^{2+}-thymine (T-Hg^{2+}-T) mismatch, cytosine-Ag^{+}-cytosine (C-Ag^{+}-C) mismatch, and Pb^{2+}-stabilized G-quadruplex [38]. Heavy metal ions may also facilitate the cleavage of deoxyribozymes (DNAzymes) [39]. DNAzymes are artificial single-stranded DNA sequences that can cleave RNA. They possess a substrate and an enzyme strand. The substrate strand has a ribonucleoside adenosine at the cleavage site, while the enzyme strand shows catalytic activity in the presence of the analyte [40]. An electrochemical DNA sensor was developed based on DNA-modified Fe_3O_4@Au magnetic nanoparticles (MNPs) on magnetic glassy carbon electrode for detection of heavy metal ions. Two electrochemically active species, ferrocene (Fc) and methylene blue (MB) were used as labels for the simultaneous detection of Ag^{+} and Hg^{2+} by square wave voltammetry. The detection limit was in the nanomolar range for both the ions, and the sensor worked efficiently in lake and drinking water. The developed biosensor can be translated into a universal platform for the detection of other heavy metal ions [41].

s0055 *Electrochemical molecularly imprinted polymer (MIP) nanosensors*

p0100 Molecularly imprinted polymers (MIPs) are also termed as plastic antibodies or bio-mimetic receptors. They are produced by the template-induced formation of specific recognition sites in a polymer. The synthesis of MIPs includes components such as monomers, cross-linkers, initiators, and solvents. The monomers polymerize in the presence of the target/imprint molecule, which acts as a template to form recognition sites. Removal of the imprint molecule yields a highly cross-linked polymeric scaffold with selective, non-covalent-binding sites/cavities for the target analyte [9]. MIPs can be synthesized in various ways, such as polymerization (bulk, suspension, or precipitation), self-assembled electropolymerization, soft lithography, and spin coating [21]. The affinity and selectivity properties of synthesized receptors are comparable to the natural receptors. They possess several advantageous properties such as enhanced stability, robustness, low-cost and straightforward production, scalability, and ease of adapting the template-target molecule system to practical applications in assays and sensors, thus making them a viable alternative to natural receptors [9,42]. These are also compatible with SPEs [42]. MIP sensors are applied to the determination of heavy metals, biomolecules, pharmaceuticals, explosives, etc. [9,42]. Currently, nanoparticles (NPs) and nanostructured coatings are being widely explored for MIP sensing technology [42]. Bolat et al. developed a MIP nanosensor for the quantification of dibutyl phthalate (DBP). DBP is one of the widely used phthalate esters (PEs), which are emergent pollutants for water, soil, and atmosphere. The synthesis of the sensor was a single-step process involving electrochemical polymerization of pyrrole on the pencil graphite electrode (PGE) surface. Electrochemical impedance spectroscopy (EIS) was used for the detection of DBP with a detection limit of 4.5 nM [21]. Despite widespread research and several advantageous features of MIP nanosensors, there are a few fundamental problems that need to be addressed before commercial applications are feasible. Some of the issues include improved stability, cost-effectiveness, repeatability, accuracy, calibration, portability, and multianalyte detection in complex real water samples.

s0060 *Nanomaterials-based electrochemical nanosensors*

p0105 Significant advancements have been made in nanomaterials-based electrochemical sensor platforms, resulting in new technologies to ensure environmental and human safety. To develop highly sensitive electrochemical nanosensors, researchers have utilized various nanomaterials such as nanocomposites, nanoparticles, metal-oxides, two-dimensional (2D), and carbon nanomaterials to modify the surfaces of the electrodes for the detection of environmental pollutants.

s0065 Nanocomposites

p0110 Nanocomposites are multiphase solid materials with at least one component having nanoscale dimensions (termed nanofillers). The constituent materials possess significantly different physical or chemical properties; however, their combination yields a material with distinct characteristics, which differ from those of individual components. Commonly used nanofillers are 0D particles (fullerene), 1D nanofibers (carbon nanotubes), and 2D nanosheets (graphene and its oxygenated derivatives, boron nitride) [43]. A diverse range of nanocomposites can be fabricated by combining nanofillers with semiconducting nanoparticles, metals, metal oxides, polymers, quantum dots, hydrogels, and biomolecules. Nanocomposites constitute emerging electrochemical and fluorescent sensing platforms [44]. Nanocomposite-based electrochemical sensors are robust, highly sensitive, low cost, portable, decentralized, reliable, rapid, and can exhibit detection limits in the picomolar range. An example of such a sensor involves CuO-TiO_2 hybrid nanocomposites on the GCE for the sensitive and selective detection of methyl parathion (an organophosphorus pesticide) with a limit of detection of 1.21 ppb. The sensor showed efficient sensing ability in the presence of interfering materials and groundwater samples [22]. Conducting polymers have also been extensively investigated for their use in nanocomposite electrochemical sensors. Polymer nanocomposites are comprised of copolymer/polymer matrix or nanofillers dispersed in the polymer matrix. They offer distinct properties such as high electrical conductivity, rapid electrode kinetics, high chemical stability in aqueous solutions, and environmental stability. They have a wide range of applications in analyzing several pollutants (e.g., pesticides, heavy metals, nitrite, nitroaromatic compounds, phenolic compounds, hydrazine, etc.). The most commonly used methods for synthesizing polymer nanocomposites are in situ polymerization, direct mixing of polymer and nanofillers (melt-mixing and solution-mixing), sol–gel, and electrochemical synthesis [10]. Researchers have developed an electrochemical Hg^{2+} sensor using a poly(3,4-ethylene-dioxythiophene) nanorods/GO nanocomposite-modified GCE (PEDOT/GO/GCE). PEDOT polymer with nanorod-like structures attached to the surface of GO nanosheets helped enhance the nanocomposite's electroactive sites. Differential pulse stripping voltammetry (DPSV) was used for the analysis. The detection limit reported was 2.78 nM (0.55 ppb) at a signal-to-noise ratio of 3. The applicability of the developed sensor was successfully demonstrated in tap water samples [23]. Major challenges with polymeric nanocomposite-based electrochemical sensors are dispersing nanofillers in the polymer matrix uniformly and enabling a strong interaction at their interface. The dispersion issue can be addressed by surfactants, physical treatment, and chemical functionalization of the surface of nanofillers [23]. Researchers have also used disposable, miniaturized SPEs for nanocomposite based electrochemical water sensors. Niu et al. synthesized a nanocomposite made of bismuth nanoparticles and amorphous carbon. Ink was prepared by milling the prepared nanocomposite to a specific particle size distribution suitable for screen printing. High surface area imparted by porous carbon and Bi NPs enabled the detection of trace concentrations of Pb^{2+} and Cd^{2+} ions (3.8 and 2.2 ppb, respectively) using square wave anodic stripping voltammetry technique (SWASV). The performance of these SPEs was successfully tested in tap water and wastewater from an urban wastewater treatment plant [45].

s0070 Two-dimensional (2D) nanomaterials

p0115 Two-dimensional (2D) nanomaterials such as graphite-carbon nitride ($g\text{-}C_3N_4$) nanosheet, boron nitride (BN) nanosheet, graphene, and various transition metal dichalcogenides (TMDs) (MoS_2, $MoSe_2$, WS_2, etc.) possess unique chemical and physical properties, which have been explored to monitor the environmental pollutants [46]. 2D nanomaterials have high surface area, chemical stability, good electrical conductivity, easy functionalization, and mechanical strength. In several instances, nanohybrids are fabricated by introducing metal oxides, noble metal NPs, or organic compounds on the surface of 2D nanomaterials to obtain sensors with better synergistic properties. Several 2D nanomaterials-based electrochemical sensors have been developed for the detection of heavy metal ions (e.g., Pb^{2+}, Cd^{2+}), pharmaceuticals (e.g., metronidazole, kanamycin), pesticides (e.g., chlorpyrifos, carbofuran), organic compounds (e.g., 4-chlorophenol, 4-nitrophenol, bisphenol A), bacteria (e.g., *S. aureus*, *S. arlettae*, *E. coli*, *S. oneidensis*, *Salmonella*), etc. [46]. Wu et al. developed a sensor to detect phenols using single-step *N*-methyl-2-pyrrolidone (NMP) exfoliated graphene nanosheets on GCE as a sensing platform. Such NMP-exfoliated graphene nanosheets exhibited enhanced electrochemical activity compared to multistep chemical oxidation synthesis. Moreover, the electrochemical performance was further improved after anodization due to increased oxygen-related active defect sites and amplified effective surface area resulting from increased surface roughness. The developed sensor showed detection limits of 0.012, 0.015, 0.01, and 0.04 μM for hydroquinone, catechol, 4-chlorophenol, and 4-nitrophenol, respectively [47]. Similarly, many MoS_2 (TMD) based nanomaterials have also been used as sensors to analyze water contaminants. For example, MoS_2/polyaniline nanocomposite to determine chloramphenicol [48], Ag nanoprism@MoS_2 for sensing disinfection by-product trichloroacetamide in drinking water [49], vertically aligned two-dimensional (2D) MoS_2 (edge exposed) nanofilm for lead ion (Pb^{2+}) detection [50], etc.

s0075 Carbon nanomaterials

p0120 Electrochemical sensors have been fabricated with carbon-based nanomaterials such as carbon nanotubes, graphene, graphene oxide, carbon nanofibers, and nanocrystalline diamond for highly sensitive and selective detection of various water contaminants. Carbon nanomaterials offer unique physical, chemical and electrical properties like large surface area, high carrier mobility, low residual current, flexibility, readily renewable surface, and ambipolar electric field effect [51]. Geometrical advantage of these materials ensures the exposure of maximum surface atoms, which facilitates binding of a substantial fraction of analytes. Carbon nanomaterials are usually coupled with biorecognition elements, metal oxides, nanoparticles, noble metals, etc. to enhance selectivity, specificity, and sensitivities. Their applications include sensing various water contaminants such as heavy metals, pesticides, pathogens, nitroaromatic explosives, and antibiotics [51]. An electrochemical omeprazole sensor based on shortened multiwalled carbon nanotubes (S-MWCNT) was developed.

Fe_3O_4 nanoparticles were hybridized with S-MWCNTs, which were combined with electro-polymerized poly (2,6-pyridine dicarboxylic acid) on GCE for nanomolar detection of omeprazole [24]. Recently, a rapid, fully integrated, inexpensive electrochemical sensor array was reported for in situ water quality monitoring. Simultaneous monitoring of pH (57.5 mV/pH), free chlorine (186 nA/ppm), temperature (16.9 mV/°C), heavy metal ($<$10 ppb), and on-demand monitoring of acetaminophen and 17β-estradiol ($<$10 nM) was successfully achieved. The researchers merged nanomaterials and CNT-based sensors on microscopic glass slides. The sensor had a custom-made readout circuit, a potentiostat, and an Android app. The integrated system was efficient in monitoring tap, swimming pool, and lake water. Moreover, it can be easily modified to integrate other sensors, enabling multiplexing capability to monitor a range of water quality parameters [52].

p0125 In general, carbon nanomaterial-based sensors enable highly selective and sensitive detection of pollutants without the need for labeling or amplification techniques [51].

s0080 Nanoparticles and nanostructures

p0130 Electrochemical sensors made using nanoparticle-modified electrodes possess high surface area, improved mass-transport and electron transfer rates, high signal-to-noise ratio, and low solution resistance [53]. Metal, metal oxide, polymeric, and noble metal NPs can improve binding of analytes and performance of electrochemical sensor for the quantification of environmental samples. NPs also exhibit notably different characteristics from bulk materials (e.g., bulk Au vs AuNP). Particle size and size distribution of NPs are essential for their performance as an electrochemical sensor as it determines the degree of diffusion-layer overlap [54]. NPs are often used in conjunction with other materials such as polymers, carbon-based nanomaterials, biorecognition elements, etc. Au NPs have been widely used to modify bulk electrodes. Au NP-modified electrodes eliminate the memory effect and interferences of other ions and improve the sensitivity and detection limits [53]. An efficient and antiinterference electrochemical sensor for As^{3+} detection was developed with AuNPs/α-MnO_2. The reported limit of detection was 0.019 ppb, and the sensor was successfully employed for detection of As^{3+} in a real water sample [55].

s0085 Optical nanosensors

p0135 Optical sensors are dependent on the changes in the optical properties of water. Such sensors are generally preferred for sensing applications as they provide low detection limits, rapid response, selectivity, are unaffected by electromagnetic noise, and have multiplexing potential [56,57]. They can be colorimetric (visible color change), fluorescent, chemiluminescent, surface plasmon resonance sensors, fiber optic sensors, etc. Various nanomaterial platforms employed in optical sensing include noble metals (e.g., gold [58–62] and silver nanostructures [63–66]), quantum dots [67–70], magnetic nanoparticles (MNPs) [71–73], metal–organic frameworks [74–80], core – shell nanocages [81], and clusters [57].

s0090 *Noble metals*

p0140 Noble metal nanostructures possess plasmonic behavior due to their distinct localized surface plasmon resonance (LSPR), which provides the basis for the fabrication of visual and spectroscopic optical sensors. Plasmonic gold (AuNPs) and silver nanoparticles (AgNPs) possess high extinction coefficients leading to distinct color when dispersed in solution [82]. The LSPR of AuNPs and AgNPs is sensitive to the shape, composition, size, refractive index, pH of the surrounding environment, and aggregation properties of these plasmonic NPs [3,83,84]. Two types of optical signal transduction methods utilize LSPR: surface-enhanced Raman spectroscopy (SERS) and colorimetric (absorption) methods. The LSPR plays a role in enhancing the electromagnetic field near the NPs when coupled with the wavelength of incident light. This enables surface-enhanced Raman spectroscopy (SERS) based detection. It is possible to achieve multiplex analysis and sensitivity to the level of single molecule and single pathogen detection by SERS. When a molecule is in close proximity or adsorbed on AuNPs or AgNPs, its Raman cross section is enhanced several folds due to SERS [3]. For colorimetric detection, the change in refractive index of solution upon introduction of analyte molecule results in a shift in LSPR peak. This effect on the refractive index of the medium could be attributed to aggregation or conjugation of NPs. The interaction between the analyte and NPs exists in the form of hydrogen bonding, donor-acceptor reaction, and electrostatic interaction. Aggregation-induced decrease in the interparticle distance leads to overlap between the plasmon fields of neighboring NPs, prompting a red shift of the LSPR band and a strong visible color change. The change in color is from red to blue for AuNPs and yellow to brown for AgNPs. This property has enabled visual detection and label-free plasmonic sensing [82].

p0145 Depending on the application of the sensor, the NPs can be modified with suitable functional groups. Usually, AuNPs are functionalized using thiol, phosphine, disulfide, or isocyanide. Thiol groups can also be used to functionalize AgNPs. Noble metal nanoparticle sensors have their application to detect bacteria, fungi, viruses, inorganic anions, heavy metal ions, and pesticides [82]. A portable and cost-effective fiber-optic sensor was developed for Hg^{2+} detection using 4-mercaptopyridine (4-MPY)-functionalized Au nanoparticles (AuNPs/4-MPY). A plasmonic coupling structure was generated by self-assembly of 4-MPY on Au film surface to capture Hg^{2+} followed by introduction of AuNPs/4-MPY. This coupling produced changes in LSPR wavelength leading to highly sensitive and selective detection of Hg^{2+} with a detection limit of 8 nM (1.60 ppb). It was tested for Hg^{2+} detection in tap water and has practical potentials for on-site monitoring [60]. A colorimetric assay was developed for sensitive detection of cholera toxin using monoclonal cholera toxin antibody-conjugated AuNPs. The AuNP surface was modified with mercaptopropionic acid (MPA) before conjugating with antibody. The toxin binds with antibody-conjugated AuNPs resulting in a network of aggregated NPs. This leads to discernible color change, and the red shift can be detected by UV–Visible spectroscopy. The assay showed high specificity and a detection limit of 10 nM. They also demonstrated the feasibility of the assay to detect cholera toxin in tap and lake water. This method can be extended to any target toxin for which specific antibodies are available [58]. Integrating a SERS sensor into a portable Raman device could facilitate economic, on-site pollutant detection [3,64]. Such an instrument quantifying SERS was fabricated using a silver dendrite SERS substrate for ferbam (pesticide) detection. It showed results in semi-quantitative, layman's format (without showing the spectra), and its use could also be extended to other target molecules [64].

s0095 Quantum dots (QDs)

p0150 Quantum dots (QDs) are nanoscale semiconductor particles with distinct optical and electronic properties having diameters ranging between 1 and 6 nm. Although they are crystals, they behave like atoms due to their bound, discrete electronic states and show quantum confinement effects. Symmetric emission profiles with narrow bandwidths and size tunability of their emission color contribute to their application as excellent fluorophores for sensors [85]. Their optoelectronic properties depend on the composition, size, shape, and surface chemistry [86]. A ratiometric fluorescence sensor was developed for the selective detection of Hg^{2+} using tetraphenylporphyrin tetrasulfonic acid (TPPS) and black phosphorus quantum dots (BP QDs). Ratiometric fluorescence assays depend on the measurement of the ratio of two signals, hence minimizing the influence of instrument and environmental conditions. The sensing was based on two phenomenons. Inhibition of the inner filter effect originating between BP QDs and TPPS in the presence of Hg^{2+} results in restoration of fluorescence of BP QDs. At the same time, Hg^{2+} causes quenching of the red fluorescence of TPPS due to its coordination with Mn^{2+}. They also tested tap and river water samples with a detection limit of 0.39 nM (0.078 ppb) [67]. Yu et al. developed a sensor to detect humic substances (HS), a key component of dissolved organic matter (DOM) using nitrogen-doped carbon quantum dots. HS are present in the aqueous environment (0.2–20 mg/L) and can influence the dissolution, transformation, and bioavailability of heavy metals. Hence their quantification is essential. The sensor was effective in a wide pH range of 3–12 with a detection range of 0–100 mg/L and detection limit of 0.2 mg/L (more efficient than the frequently used modified Lowry method). They validated the feasibility of the sensor in natural surface water samples. They also fabricated a carbon dot-based portable test paper for successful quantification of HS, which, when coupled with a light-emitting diode lamp, can be used for on-site detection [69].

s0100 Magnetic nanoparticles (MNPs)

p0155 Fig. 3 shows the applications of MNP-based SERS analysis of water pollutants. Several advantages are high and controllable enhancement factor, extraction and preconcentration of pollutants (due to adsorption and magnetism properties), effective magnetic separation, high selectivity (with suitable coating or specific capture molecules). MNPs can be used as substrates or Raman tags (MNPs labeled with specific Raman reporters) for SERS-based detection [87]. A magnetic substrate was developed comprising Fe_3O_4 microspheres and Au NPs to detect the 16 EPA priority polycyclic aromatic hydrocarbons (PAHs) using SERS. The 16 PAHs were easily differentiated based on their characteristic SERS peaks with a 100–5 nM detection limit. Moreover, the substrate was successfully tested for sensing PAHs in river water. Additionally, it can be used for on-site monitoring of PAHs as the quantitative detection was conducted using a portable Raman spectrometer. The method can be used to identify chemically similar hydrophobic contaminant molecules whose effective separation may be difficult [73]. MNPs have also been utilized in the detection of pathogens in water. A method to enumerate *E. coli* was developed using a combination of immunomagnetic separation (IMS) and SERS. Upon interaction with *E. coli*, a sandwich structure was formed comprising of gold-coated magnetic nanosphere–anti-*E. coli* antibody complex and Raman label (gold nanorods coated with 5,5-dithiobis-(2-nitrobenzoic acid) (DTNB)). The assay was selective, and the limit of detection (LOD) was 8 cfu/mL. *E. coli* detection was successful in real water sample analysis, and the results were comparable with the classical counting methods [71].

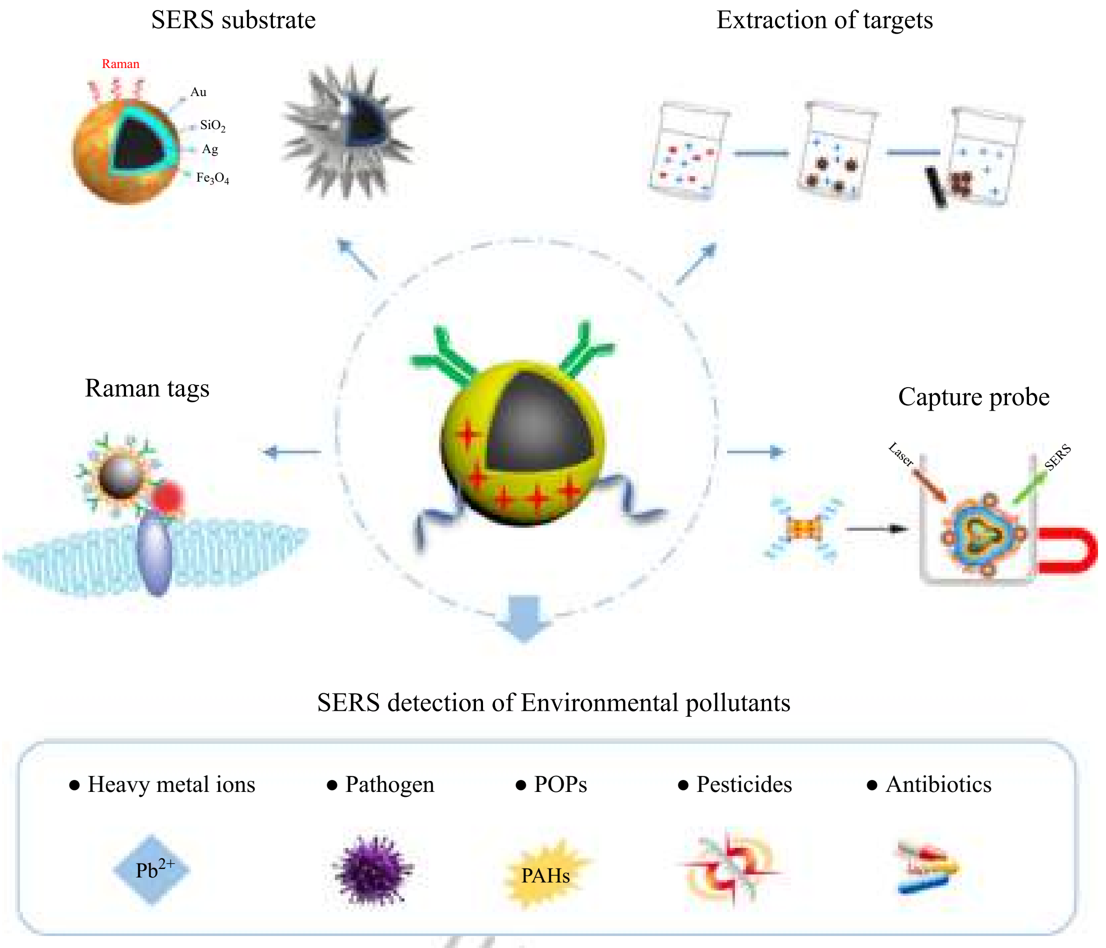

f0020 **FIG. 3** Schematic of the applications of MNPs in SERS-based detection of environmental pollutants. SERS: surface-enhanced Raman scattering, POPs: persistent organic pollutants, PAHs: polycyclic aromatic hydrocarbons. *From H. Wei, K. Rodriguez, S. Renneckar, W. Leng, P.J. Vikesland, Preparation and evaluation of nanocellulose–gold nanoparticle nanocomposites for SERS applications, Analyst 140 (2015) 5640–5649. doi:10.1039/c5an00606f.*

s0105 *Metal–organic frameworks (MOFs)*

p0160 MOFs are a class of porous structures comprising metal ions or metal clusters and organic ligands, which are considered a promising platform for sensing and adsorption applications. They have unique optoelectronic properties, high porosity, long fluorescence lifetime, large surface area, and structural diversity. Fluorophores can be easily introduced into the pores of MOFs by ligand modifications, making them excellent candidates for optical detection [75]. Their luminescent properties are influenced by their structure, pore surfaces, their host-guest chemistry, coordination environment, etc. [80]. Fluorescent MOFs have demonstrated their quick and sensitive sensing capability to detect heavy-metal ions [80], pharmaceuticals (e.g., tetracycline [76], sulfamethazine (SMZ) [77], nitrofurantoin (NFT) [75], etc.), explosives [75,78] (e.g., 2,4,6-trinitrophenol (TNP), 4-nitrophenol (4-NP), etc.), pathogens (*Bacillus anthracis* [74], *Staphylococcus arlettae* (*S. arlettae*) [79], etc.), PAHs [88], etc. Several MOFs demonstrate excellent adsorption property, which plays a vital role in the preconcentration of the analyte. Hence, MOFs not only have potential in selective detection of contaminants and monitoring water quality but also in contaminant removal and wastewater treatment. Wang et al. synthesized two highly porous, stable isostructural Zr(IV)-based MOFs with excellent fluorescent and adsorption properties. Both the MOFs efficiently and selectively detected ppb levels of nitrofurazone (NZF) and nitrofurantoin (NFT) antibiotics as well as explosives such as 2,4,6-trinitrophenol (TNP) and 4-nitrophenol (4-NP). The electron and energy transfers in the host – guest system played a vital role in their exceptional quenching efficiency [75]. Another concept for MOF-based highly sensitive SERS detection includes encapsulation of NPs within MOFs. The NPs serve as SERS "hot spots" and the adsorption property of the MOF enables preconcentration of target molecules near these "hot spots" resulting in enhancement of SERS sensitivity. Utilizing this principle, Li et al. synthesized core–shell MOF@Ag NPs composite on a screen-printed carbon electrode via *in situ* electrodeposition. The prepared substrate was reusable and highly sensitivity for detection of PAHs at concentrations as low as hundreds of pM [88].

s0110 Magnetic nanosensors

p0165 Sensors based on magnetic nanoparticles (MNPs) have application in environmental water contaminants detection due to their capability to magnetize under an applied magnetic field [56]. Their general formula is MFe_2O_4 ($M = Fe, Co, Cu, Mn$, etc.) such as maghemite (γ-Fe_2O_3), magnetite (Fe_3O_4), and cobalt oxide (Co_3O_4) [89]. They offer several advantages such as extraction and preconcentration of the target analyte from the complex water samples [56,87]. Second, MNPs are reusable as they can be isolated by the application of an external magnetic field [89]. Additionally, their biocompatibility permits immobilization of biorecognition elements (e.g., protein, antibody, enzyme, aptamer) on their surfaces, which can enhance their specificity toward environmental pollutants [87]. MNPs show a finite-size effect or high surface-to-volume ratio and are nonporous (no diffusion limitations), enabling higher surface adsorption capacity [89]. However, pure magnetic particles tend to form aggregates. Hence, the magnetic core is often coated with a suitable protective coating. Silica, gold, and water-soluble polymers are commonly used for protection and rendering versatility in surface modification [56,89]. Once the target analyte is magnetically isolated, it is usually detected using various optical or standard spectroscopic tools [56]. Applications of MNPs using optical nanosensor-based detection of environmental pollutants have already been discussed in this chapter. A magnetic nanocomposite based on Schiff base/silica/magnetite as a preconcentration phase was developed for the trace determination of Pb^{2+}, Cd^{2+}, and Cu^{2+}. Iron oxide-silica magnetic particles were modified with a Schiff base ($Fe_3O_4/SiO_2/L$). The developed magnetic solid phase is easily retrievable from large volumes of aqueous solutions. The separated metal ions were subsequently analyzed by flame atomic absorption spectrometry (FAAS). The detection limits were 0.14, 0.19 and 0.12 $\mu g\,L^{-1}$ for Pb^{2+}, Cd^{2+} and Cu^{2+}, respectively. The established method was successfully applied to analyze seven different natural water samples, and satisfactory results were obtained [89]. Currently, magnetic nanosensors are limited by portability and instrument availability issues [56].

s0115 Novel nanosensing technologies

p0170 Novel nanosensors which do not classify under conventional nanosensing technologies based on electrochemical, optical, or magnetic signal transduction are described here briefly. This section includes nanosensors that are hybrid (whose function and signal transduction involves interaction between synthetic and nonsynthetic components) or biomimicking (in terms of design, physical or chemical properties). Researchers are exploring alternative techniques that are not entirely dependent on complex materials and devices to assess water quality.

p0175 The hybridization approach that involves combining synthetic procedures or materials with natural systems is an emerging field. Researchers from the Parson school of design have developed an *in vivo*, plant-based novel water monitoring device named Argus. It is a living plant with DNA nanosensors (lead-sensitive DNA and CNTs) in the leaves capable of real-time detection of Pb^{2+} in water. The nanosensors are injected inside the leaf of a plant and stay within the intercellular space. It shows fluorescence when excited at 535 nm. Due to plants' natural property of water uptake, the impurities in water reach the leaf. The working principle involves breaking double-stranded DNA into single-stranded DNA (ssDNA) in the presence of Pb^{2+}. The ssDNA binds strongly to the walls of single-walled CNTs that cause quenching of fluorescence. The plants provide an optical readout of lead in water, with a concentration-dependent reduction in fluorescence. Such sensors can be modified appropriately for the detection of other elements for continuous water monitoring. It can also be used in domestic set-up apart from the industrial environment. This could be as simple as watering a house plant regularly to determine the chemical levels in the water [90].

p0180 Another novel nanosensor technology that has attracted significant attention is nanorobots also termed nanomotors or nanoswimmers. Nanorobots are locomotive machines of nanoscale dimensions that are designed to perform directed tasks via self or an externally controlled propulsion mechanism. Their movement can be influenced by chemical, magnet, light, ultrasound, or electrical agents [91]. They possess immense potential in environmental detection and remediation applications. This concept is equivalent to the use of live aquatic organisms for water quality testing. Various materials have been investigated for the fabrication of nanorobots. One of the most unique and incomparable advantage over other sensing technologies is their movement ability in complex mediums. This property enables the active attachment of nanorobots to the target and enhances the mass transfer in solution [92]. Also, the stirring action due to the motion of nanorobots can improve the detection sensitivity and amplify signals [91,92]. The sensing mechanism could be based on chemical changes due to nanorobots motion, electrochemical, fluorescent, electrochemiluminescent (ECL), or colorimetric [92]. Based on the principle of nanorobots, researchers have developed an enzyme-powered nanoswimmer for water-quality testing. It was fabricated by template-based electrodeposition of PEDOT/Au bilayer microtubes. Catalase enzyme was cross-linked to the Au layer. The biocatalytic decomposition of the hydrogen peroxide fuel at the enzymatic layer generates the oxygen bubbles at the tail end of the fish. The thrust thus generated leads to swimming motion. Exposure of the nanoswimmers to chemical stress (e.g., heavy metals-mercury and copper, herbicide-aminotriazole, and pesticide-NaN_3) causes inhibition of the activity of catalase, leading to a lower bubble frequency. Thus, the biocatalytic bubble propulsion mechanism gets impaired. Time-dependent optical tracking of changes in the speed and lifetime (survival) of the nanoswimmer, offers a simple and real-time visualization of pollutant-induced changes. Thus, pollutants that are known to inhibit the catalase activity can be efficiently detected down to the micromolar levels by this novel sensing technology [93].

s0120 Challenges and concerns

p0185 Nanomaterials allow sensors to achieve very low limits of detection with enhanced analytical performance. However, the advancement in the field of nanosensors for water quality monitoring comes with certain challenges. Water is a highly variable and complex matrix. The global water quality can vary substantially due to differences in hardness, alkalinity, and inorganic and organic contaminants [94]. Hence, the sensors must function efficiently, and the detection limits must be tested across this broad range of water quality conditions.

p0190 Moreover, strategic planning and design of nanosensor research are essential for minimizing health risks associated with unintended releases of nanomaterials used in nanosensors to prevent hazardous environmental implications. Conventionally researchers focus on performance efficiency and price for material selection. However, the choice for optimum material must be made considering the environmental and ecological health impacts as well [95]. The toxicity of nanoscale materials is often different from their bulk counterparts and is dependent on their size, shape and charge. Teratogenicity, DNA damage, and decreased cell mitochondrial membrane potential are few of the toxic effects caused by nanomaterials. Hence, they must be used with caution and their exposure to ecosystem must be minimum. Also, the materials must meet the quality criteria and be compatible with mass manufacturing methods. This helps in ensuring robustness and translation from laboratory-scale prototypes to commercial applications. Ideally, the developed nanosensor should be sustainable, scalable, and nontoxic that still elicits the desired functionality.

p0195 Real-time, on-site water analysis preferably requires simultaneous monitoring of multiple contaminants using a single sensor. Developing nanosensors with multiplexing (multianalyte) determination capabilities along with resistance to various interferences are significant challenges retarding commercial applications.

s0125 Future outlook

p0200 The global nanosensors market generated revenue worth USD 432 million in 2019, with electrochemical nanosensors accounting for the largest market share [96]. Significant progress has been made in the design and development of nanotechnology-enabled sensors across different industries. However, extensive research is awaited for the fabrication of automated, compact, on-site water monitoring devices that are preferably integrated with mobile phone. Such devices would enable *in situ* operations and online, remote, real-time analysis. This advancement will lead to immediate notification and initiation of quick remedial action for averting potential large-scale environmental damage. Also, disposable testing strip-based sensors would enable residential water quality testing.

p0205 The field of nanosensors for water quality monitoring is still inted electrodes for environmental monitoring of heat infancy, and very few such sensor devices have made it to market (e.g., graphene nanosheets based sensor by NanoAffix Science LLC). Extensive collaborative efforts between multidisciplinary science and engineering domains are need of the hour for the design and fabrication of easy-to-use environmental sensors. The potential impact of nanosensors in water quality monitoring is expected to be profound.

References

[1] UNICEF & WHO, Progress on Household Drinking Water, Sanitation and Hygiene 2000–2017. Special Focus on Inequalities, 2019. https://washdata.org/sites/default/files/documents/reports/2019-07/jmp-2019-wash-households.pdf.

[2] WHO, Safer Water, Better Health, World Health Organization, Geneva, 2019. Update https://apps.who.int/iris/bitstream/handle/10665/329905/9789241516891-eng.pdf.

[3] H. Wei, S.M.H. Abtahi, P.J. Vikesland, Plasmonic colorimetric and SERS sensors for environmental analysis, Environ. Sci. Nano 2 (2015) 120–135,- https://doi.org/10.1039/c4en00211c.

[4] P. Kruse, Review on water quality sensors, J. Phys. D Appl. Phys. 51 (2018) 203002, https://doi.org/10.1088/1361-6463/aabb93.

[5] N. Bhardwaj, S.K. Bhardwaj, D. Bhatt, D.K. Lim, K.H. Kim, A. Deep, Optical detection of waterborne pathogens using nanomaterials, TrAC - Trends Anal. Chem. 113 (2019) 280–300, https://doi.org/10.1016/j.trac.2019.02.019.

[6] D. Wei, M.J.A. Bailey, P. Andrew, T. Ryhänen, Electrochemical biosensors at the nanoscale, Lab Chip 9 (15) (2009) 2123–2131, https://doi.org/10.1039/b903118a.

[7] B. Maleki, M. Baghayeri, M. Ghanei-Motlagh, et al., Polyamidoamine dendrimer functionalized iron oxide nanoparticles for simultaneous electrochemical detection of pb 2+ and cd 2+ ions in environmental waters, Meas J. Int. Meas Confed. 140 (2019) 81–88, https://doi.org/10.1016/j.measurement.2019.03.052.

[8] Z. Keivani, M. Shabani-Nooshabadi, H. Karimi-Maleh, An electrochemical strategy to determine thiosulfate, 4-chlorophenol and nitrite as three important pollutants in water samples via a nanostructure modified sensor, J. Colloid Interface Sci. 507 (2017) 11–17, https://doi.org/10.1016/j.jcis.2017.07.098.

[9] A. Garciá-Miranda Ferrari, P. Carrington, S.J. Rowley-Neale, C.E. Banks, Recent advances in portable heavy metal electrochemical sensing platforms, Environ. Sci. Water Res. Technol. 6 (10) (2020) 2676–2690, https://doi.org/10.1039/d0ew00407c.

[10] S. Tajik, H. Beitollahi, F.G. Nejad, et al., Recent developments in polymer nanocomposite-based electrochemical sensors for detecting environmental pollutants, Ind. Eng. Chem. Res. 60 (3) (2021) 1112–1136, https://doi.org/10.1021/acs.iecr.0c04952.

[11] X. Liu, Y. Yao, Y. Ying, J. Ping, Recent advances in nanomaterial-enabled screen-printed electrochemical sensors for heavy metal detection, TrAC Trends Anal. Chem. 115 (2019) 187–202, https://doi.org/10.1016/J.TRAC.2019.03.021.

[12] J. Barton, M.B.G. García, D.H. Santos, et al., Screen-printed electrodes for environmental monitoring of heavy metal ions: a review, Microchim. Acta 183 (2) (2015) 503–517, https://doi.org/10.1007/S00604-015-1651-0.

[13] H. Beitollahi, S.Z. Mohammadi, M. Safaei, S. Tajik, Applications of electrochemical sensors and biosensors based on modified screen-printed electrodes: a review, Anal. Methods 12 (12) (2020) 1547–1560, https://doi.org/10.1039/c9ay02598g.

[14] N. Karimian, P. Ugo, Recent advances in sensing and biosensing with arrays of nanoelectrodes, Curr. Opin. Electrochem. 16 (2019) 106–116, https://doi.org/10.1016/j.coelec.2019.04.026.

[15] K.B. Male, S. Hrapovic, J.M. Santini, J.H.T. Luong, Biosensor for Arsenite using Arsenite oxidase and multiwalled carbon nanotube modified electrodes, Anal. Chem. 79 (20) (2007) 7831–7837, https://doi.org/10.1021/AC070766I.

[16] H.S. Magar, M.E. Ghica, M.N. Abbas, C.M.A. Brett, Highly sensitive choline oxidase enzyme inhibition biosensor for Lead ions based on multiwalled carbon nanotube modified glassy carbon electrodes, Electroanalysis. 29 (7) (2017) 1741–1748, https://doi.org/10.1002/elan.201700111.

[17] F. Cai, Q. Zhu, K. Zhao, A. Deng, J. Li, Multiple signal amplified electrochemiluminescent immunoassay for Hg2+ using graphene-coupled quantum dots and gold nanoparticles-labeled horseradish peroxidase, Environ. Sci. Technol. 49 (8) (2015) 5013–5020, https://doi.org/10.1021/acs.est.5b00690.

[18] Z. Yang, X. Ding, Q. Guo, et al., Second generation of signaling-probe displacement electrochemical aptasensor for detection of picomolar ampicillin and sulfadimethoxine, Sens. Actuators B 253 (2017) 1129–1136, https://doi.org/10.1016/j.snb.2017.07.119.

[19] K. Mondal, A. Sharma, Recent advances in electrospun metal-oxide nanofiber based interfaces for electrochemical biosensing, RSC Adv. 6 (97) (2016) 94595–94616, https://doi.org/10.1039/c6ra21477k.

[20] G. Ozcelikay, S. Kurbanoglu, A. Yarman, F.W. Scheller, S.A. Ozkan, Au-Pt nanoparticles based molecularly imprinted nanosensor for electrochemical detection of the lipopeptide antibiotic drug daptomycin, Sens. Actuators B 320 (2020), https://doi.org/10.1016/j.snb.2020.128285, 128285.

[21] G. Bolat, Y.T. Yaman, S. Abaci, Molecularly imprinted electrochemical impedance sensor for sensitive dibutyl phthalate (DBP) determination, Sens. Actuators B 299 (2019) 127000, https://doi.org/10.1016/j.snb.2019.127000.

[22] X. Tian, L. Liu, Y. Li, et al., Nonenzymatic electrochemical sensor based on CuO-TiO2 for sensitive and selective detection of methyl parathion pesticide in ground water, Sens. Actuators B 256 (2018) 135–142, https://doi.org/10.1016/j.snb.2017.10.066.

[23] Y. Zuo, J. Xu, X. Zhu, et al., Poly(3,4-ethylenedioxythiophene) nanorods/graphene oxide nanocomposite as a new electrode material for the selective electrochemical detection of mercury (II), Synth. Met. 220 (2016) 14–19, https://doi.org/10.1016/j.synthmet.2016.05.022.

[24] K. Deng, X. Liu, C. Li, Z. Hou, H. Huang, An electrochemical omeprazole sensor based on shortened multi-walled carbon nanotubes-Fe3O4 nanoparticles and poly(2, 6-pyridinedicarboxylic acid), Sens. Actuators B 253 (2017) 1–9, https://doi.org/10.1016/j.snb.2017.06.117.

[25] T. Gupte, S.K. Jana, J.S. Mohanty, et al., Highly sensitive As3+ detection using electrodeposited nanostructured MnO x and phase evolution of the active material during sensing, ACS Appl. Mater. Interfaces 11 (31) (2019) 28154–28163, https://doi.org/10.1021/acsami.9b06023.

[26] L. Xiao, G.G. Wildgoose, R.G. Compton, Sensitive electrochemical detection of arsenic (III) using gold nanoparticle modified carbon nanotubes via anodic stripping voltammetry, Anal. Chim. Acta 620 (1–2) (2008) 44–49, https://doi.org/10.1016/j.aca.2008.05.015.

[27] X. Li, H. Zhou, C. Fu, F. Wang, Y. Ding, Y. Kuang, A novel design of engineered multi-walled carbon nanotubes material and its improved performance in simultaneous detection of cd(II) and pb(II) by square wave anodic stripping voltammetry, Sens. Actuators B 236 (2016) 144–152, https://doi.org/10.1016/j.snb.2016.05.149.

[28] G. Liu, Y. Lin, Y. Tu, Z. Ren, Ultrasensitive voltammetric detection of trace heavy metal ions using carbon nanotube nanoelectrode array, Analyst 130 (7) (2005) 1098–1101, https://doi.org/10.1039/b419447k.

[29] D. Sahoo, A. Mandal, T. Mitra, K. Chakraborty, M. Bardhan, A.K. Dasgupta, Nanosensing of pesticides by zinc oxide quantum dot: an optical and electrochemical approach for the detection of pesticides in water, J. Agric. Food Chem. 66 (2) (2018) 414–423, https://doi.org/10.1021/acs.jafc.7b04188.

[30] L. Cui, J. Wu, H. Ju, Electrochemical sensing of heavy metal ions with inorganic, organic and bio-materials, Biosens. Bioelectron. 63 (2015) 276–286, https://doi.org/10.1016/j.bios.2014.07.052.

[31] E.K. Wujcik, H. Wei, X. Zhang, et al., Antibody nanosensors: a detailed review, RSC Adv. 4 (82) (2014) 43725–43745, https://doi.org/10.1039/c4ra07119k.

[32] T.O. Hara, B. Singh, Electrochemical biosensors for detection of pesticides and heavy metal toxicants in water: recent trends and Progress, ACS ES&T Water. 1 (3) (2021) 462–478, https://doi.org/10.1021/acsestwater.0c00125.

[33] W. Chen, Q. Zhu, Q. Tang, K. Zhao, A. Deng, J. Li, Ultrasensitive detection of diclofenac based on electrochemiluminescent immunosensor with multiple signal amplification strategy of palladium attached graphene oxide as bioprobes and ceria doped zinc oxide as substrates, Sens. Actuators B 268 (2018) 411–420, https://doi.org/10.1016/j.snb.2018.04.106.

[34] Z. Zhang, M. Yang, X. Wu, et al., A competitive immunosensor for ultrasensitive detection of sulphonamides from environmental waters using silver nanoparticles decorated single-walled carbon nanohorns as labels, Chemosphere 225 (2019) 282–287, https://doi.org/10.1016/j.chemosphere.2019.03.033.

[35] S. Oloketuyi, E. Mazzega, J. Zavašnik, et al., Electrochemical immunosensor functionalized with nanobodies for the detection of the toxic microalgae Alexandrium minutum using glassy carbon electrode modified with gold nanoparticles, Biosens. Bioelectron. 154 (2020), https://doi.org/10.1016/j.bios.2020.112052, 112052.

[36] F. Li, Z. Yu, X. Han, R.Y. Lai, Electrochemical aptamer-based sensors for food and water analysis: a review, Anal. Chim. Acta 1051 (2019) 1–23, https://doi.org/10.1016/j.aca.2018.10.058.

[37] W. Tang, Z. Wang, J. Yu, F. Zhang, P. He, Internal calibration potentiometric Aptasensors for simultaneous detection of Hg2+, Cd2+, and As3+ based on a screen-printed carbon electrodes Array, Anal. Chem. 90 (14) (2018) 8337–8344, https://doi.org/10.1021/acs.analchem.7b04150.

[38] J. Sun, Y. Gan, T. Liang, et al., Signal enhancement of electrochemical DNA biosensors for the detection of trace heavy metals, Curr. Opin. Electrochem. 17 (2019) 23–29, https://doi.org/10.1016/j.coelec.2019.04.007.

[39] M.R. Saidur, A.R.A. Aziz, W.J. Basirun, Recent advances in DNA-based electrochemical biosensors for heavy metal ion detection: a review, Biosens. Bioelectron. 90 (2017) 125–139, https://doi.org/10.1016/j.bios.2016.11.039.

[40] D. Soukarié, V. Ecochard, L. Salomé, DNA-based nanobiosensors for monitoring of water quality, Int. J. Hyg. Environ. Health 226 (2020) 113485, https://doi.org/10.1016/j.ijheh.2020.113485.

[41] P. Miao, Y. Tang, L. Wang, DNA modified Fe3O4@au magnetic nanoparticles as selective probes for simultaneous detection of heavy metal ions, ACS Appl. Mater. Interfaces 9 (4) (2017) 3940–3947, https://doi.org/10.1021/acsami.6b14247.

[42] O.S. Ahmad, T.S. Bedwell, C. Esen, A. Garcia-Cruz, S.A. Piletsky, Molecularly imprinted polymers in electrochemical and optical sensors, Trends Biotechnol. 37 (3) (2019) 294–309, https://doi.org/10.1016/j.tibtech.2018.08.009.

[43] X. Sun, C. Huang, L. Wang, et al., Recent Progress in graphene/polymer nanocomposites, Adv. Mater. 33 (6) (2021) 2001105, https://doi.org/10.1002/adma.202001105.

[44] S.K. Krishnan, E. Singh, P. Singh, M. Meyyappan, H.S. Nalwa, A review on graphene-based nanocomposites for electrochemical and fluorescent biosensors, RSC Adv. 9 (16) (2019) 8778–8781, https://doi.org/10.1039/c8ra09577a.

[45] Niu P, Fernández-Sánchez C, Gich M, Navarro-Hernández C, Fanjul-Bolado P, Roig A. Screen-Printed Electrodes Made of a Bismuth Nanoparticle Porous Carbon Nanocomposite Applied to the Determination of Heavy Metal Ions. Springer. doi:https://doi.org/10.1007/s00604-015-1684-4.

[46] S. Su, S. Chen, C. Fan, Recent advances in two-dimensional nanomaterials-based electrochemical sensors for environmental analysis, Green Energy Environ. 3 (2) (2018) 97–106, https://doi.org/10.1016/j.gee.2017.08.005.

[47] C. Wu, Q. Cheng, K. Wu, Electrochemical functionalization of N -Methyl-2-pyrrolidone-exfoliated graphene nanosheets as highly sensitive analytical platform for phenols, Anal. Chem. 87 (6) (2015) 3294–3299, https://doi.org/10.1021/ac504309j.

[48] H.Y. Chen, J. Wang, L. Meng, T. Yang, K. Jiao, Thin-layered MoS2/polyaniline nanocomposite for highly sensitive electrochemical detection of chloramphenicol, Chin. Chem. Lett. 27 (2) (2016) 231–234, https://doi.org/10.1016/j.cclet.2015.09.018.

[49] X. Fang, Z. Zeng, Q. Li, et al., Ultrasensitive detection of disinfection byproduct trichloroacetamide in drinking water with ag nanoprism@MoS2 heterostructure-based electrochemical sensor, Sens. Actuators B 332 (2021) 129526, https://doi.org/10.1016/j.snb.2021.129526.

[50] J.H. Hwang, M.A. Islam, H. Choi, et al., Improving electrochemical Pb2+ detection using a vertically aligned 2D MoS2 nanofilm, Anal. Chem. 91 (18) (2019) 11770–11777, https://doi.org/10.1021/acs.analchem.9b02382.

[51] P. Ramnani, N.M. Saucedo, A. Mulchandani, Carbon nanomaterial-based electrochemical biosensors for label-free sensing of environmental pollutants, Chemosphere 143 (2016) 85–98, https://doi.org/10.1016/j.chemosphere.2015.04.063.

[52] A.U. Alam, D. Clyne, H. Jin, N.X. Hu, M.J. Deen, Fully integrated, simple, and low-cost electrochemical sensor Array for in situ water quality monitoring, ACS Sensors. 5 (2) (2020) 412–422, https://doi.org/10.1021/acssensors.9b02095.

[53] M. Li, H. Gou, I. Al-Ogaidi, N. Wu, Nanostructured sensors for detection of heavy metals: a review, ACS Sustain. Chem. Eng. 1 (7) (2013) 713–723, https://doi.org/10.1021/sc400019a.

[54] L. Rassaei, F. Marken, M. Sillanpää, M. Amiri, C.M. Cirtiu, M. Sillanpää, Nanoparticles in electrochemical sensors for environmental monitoring, TrAC - Trends Anal. Chem. 30 (11) (2011) 1704–1715, https://doi.org/10.1016/j.trac.2011.05.009.

[55] M. Yang, X. Chen, T.J. Jiang, Z. Guo, J.H. Liu, X.J. Huang, Electrochemical detection of trace arsenic(III) by nanocomposite of nanorod-like α-MnO2 decorated with ∼5 nm au nanoparticles: considering the change of arsenic speciation, Anal. Chem. 88 (19) (2016) 9720–9728, https://doi.org/10.1021/acs.analchem.6b02629.

[56] P.J. Vikesland, K.R. Wigginton, Nanomaterial enabled biosensors for pathogen monitoring - a review, Environ. Sci. Technol. 44 (10) (2010) 3656–3669, https://doi.org/10.1021/es903704z.

[57] G.N. Liu, R.D. Xu, R.Y. Zhao, et al., Hybrid copper iodide cluster-based pellet sensor for highly selective optical detection of o-nitrophenol and tetracycline hydrochloride in aqueous solution, ACS Sustain. Chem. Eng. 7 (23) (2019) 18863–18873, https://doi.org/10.1021/acssuschemeng.9b03963.

[58] S.A. Khan, J.A. DeGrasse, B.J. Yakes, T.R. Croley, Rapid and sensitive detection of cholera toxin using gold nanoparticle-based simple colorimetric and dynamic light scattering assay, Anal. Chim. Acta 892 (2015) 167–174, https://doi.org/10.1016/j.aca.2015.08.029.

[59] Y. Kim, R.C. Johnson, J.T. Hupp, Gold nanoparticle-based sensing of “spectroscopically silent” heavy metal ions, Nano Lett. 1 (4) (2001) 3–5, https://doi.org/10.1021/nl0100116.

[60] H. Yuan, W. Ji, S. Chu, et al., Mercaptopyridine-functionalized gold nanoparticles for fiber-optic surface plasmon resonance hg 2+ sensing, ACS Sensors. 4 (3) (2019) 704–710, https://doi.org/10.1021/acssensors.8b01558.

[61] L. Bao, P. Sheng, J. Li, S. Wu, Q. Cai, S. Yao, Surface enhanced Raman spectroscopic detection of polycyclic aromatic hydrocarbons (PAHs) using a gold nanoparticles-modified alginate gel network, Analyst 137 (17) (2012) 4010–4015, https://doi.org/10.1039/c2an35589b.

[62] J. Li, L. Yang, Y. Ruan, et al., Dual-mode optical Nanosensor based on gold nanoparticles and carbon dots for visible detection of as(III) in water, ACS Appl. Nano. Mater. 3 (8) (2020) 8224–8231, https://doi.org/10.1021/acsanm.0c01647.

[63] Y. Bhattacharjee, D. Chatterjee, A. Chakraborty, Mercaptobenzoheterocyclic compounds functionalized silver nanoparticle, an ultrasensitive colorimetric probe for hg(II) detection in water with picomolar precision: a correlation between sensitivity and binding affinity, Sens. Actuators B 255 (2018) 210–216, https://doi.org/10.1016/j.snb.2017.08.066.

[64] J. Zheng, S. Pang, T.P. Labuza, L. He, Semi-quantification of surface-enhanced Raman scattering using a handheld Raman spectrometer: a feasibility study, Analyst 138 (23) (2013) 7075–7078, https://doi.org/10.1039/c3an01450a.

[65] Z. Zhou, J. Lu, J. Wang, et al., Trace detection of polycyclic aromatic hydrocarbons in environmental waters by SERS, Spectrochim. Acta - Part A Mol. Biomol. Spectrosc. 234 (2020) 118250–118256, https://doi.org/10.1016/j.saa.2020.118250.

[66] R. Hu, R. Tang, J. Xu, F. Lu, Chemical nanosensors based on molecularly-imprinted polymers doped with silver nanoparticles for the rapid detection of caffeine in wastewater, Anal. Chim. Acta 1034 (2018) 176–183, https://doi.org/10.1016/j.aca.2018.06.012.

[67] W. Gu, X. Pei, Y. Cheng, et al., Black phosphorus quantum dots as the Ratiometric fluorescence probe for trace mercury ion detection based on inner filter effect, ACS Sensors. 2 (4) (2017) 576–582, https://doi.org/10.1021/acssensors.7b00102.

[68] Y. Zhang, J.Y. Xiao, Y. Zhu, et al., Fluorescence sensor based on biosynthetic CdSe/CdS quantum dots and liposome carrier signal amplification for mercury detection, Anal. Chem. 92 (5) (2020) 3990–3997, https://doi.org/10.1021/acs.analchem.9b05508.

[69] Y.F. Guan, B.C. Huang, C. Qian, H.Q. Yu, Quantification of humic substances in natural water using nitrogen-doped carbon dots, Environ. Sci. Technol. 51 (24) (2017) 14092–14099, https://doi.org/10.1021/acs.est.7b04430.

[70] A. Mehta, A. Mishra, S. Kainth, S. Basu, Carbon quantum dots/TiO2 nanocomposite for sensing of toxic metals and photodetoxification of dyes with kill waste by waste concept, Mater. Des. 155 (2018) 485–493, https://doi.org/10.1016/j.matdes.2018.06.015.

[71] B. Guven, N. Basaran-akgul, E. Temur, U. Tamer, SERS-based sandwich immunoassay using antibody coated magnetic nanoparticles for Escherichia coli enumeration, Analyst 136 (2011) 740–748, https://doi.org/10.1039/c0an00473a.

[72] S. Tang, Y. Li, H. Huang, et al., Efficient enrichment and self-assembly of hybrid nanoparticles into removable and magnetic SERS substrates for sensitive detection of environmental pollutants, ACS Appl. Mater. Interfaces 9 (8) (2017) 7472–7480, https://doi.org/10.1021/acsami.6b16141.

[73] J. Du, J. Xu, Z. Sun, C. Jing, Au nanoparticles grafted on Fe3O4 as effective SERS substrates for label-free detection of the 16 EPA priority polycyclic aromatic hydrocarbons, Anal. Chim. Acta 915 (2016) 81–89, https://doi.org/10.1016/j.aca.2016.02.009.

[74] M. Wu, Y. Zhuang, J. Liu, W. Chen, X. Li, R.J. Xie, Ratiometric fluorescence detection of 2,6-pyridine dicarboxylic acid with a dual-emitting lanthanide metal-organic framework (MOF), Opt. Mater. (Amst). 106 (2020) 110006, https://doi.org/10.1016/j.optmat.2020.110006.

[75] B. Wang, X.L. Lv, D. Feng, et al., Highly stable Zr(IV)-based metal-organic frameworks for the detection and removal of antibiotics and organic explosives in water, J. Am. Chem. Soc. 138 (19) (2016) 6204–6216, https://doi.org/10.1021/jacs.6b01663.

[76] Y. Zhou, Q. Yang, D. Zhang, N. Gan, Q. Li, J. Cuan, Detection and removal of antibiotic tetracycline in water with a highly stable luminescent MOF, Sens. Actuators B 262 (2018) 137–143, https://doi.org/10.1016/j.snb.2018.01.218.

[77] X.D. Zhu, K. Zhang, Y. Wang, et al., Fluorescent metal-organic framework (MOF) as a highly sensitive and quickly responsive chemical sensor for the detection of antibiotics in simulated wastewater, Inorg. Chem. 57 (3) (2018) 1060–1065, https://doi.org/10.1021/acs.inorgchem.7b02471.

[78] X.J. Zhang, F.Z. Su, D.M. Chen, et al., A water-stable Eu III -based MOF as a dual-emission luminescent sensor for discriminative detection of nitroaromatic pollutants, Dalton Trans. 48 (5) (2019) 1843–1849, https://doi.org/10.1039/c8dt04397c.

[79] N. Bhardwaj, S.K. Bhardwaj, J. Mehta, M.K. Nayak, A. Deep, Bacteriophage conjugated IRMOF-3 as a novel opto-sensor for: *S. arlettae*, New J. Chem. 40 (9) (2016) 8068–8073, https://doi.org/10.1039/c6nj00899b.

[80] L. Wen, X. Zheng, K. Lv, C. Wang, X. Xu, Two amino-decorated metal-organic frameworks for highly selective and quantitatively sensing of HgII and CrVI in aqueous solution, Inorg. Chem. 54 (15) (2015) 7133–7135, https://doi.org/10.1021/acs.inorgchem.5b00098.

[81] S. Mukherjee, M. Shah, K. Chaudhari, et al., Smartphone-based fluoride-specific sensor for rapid and affordable colorimetric detection and precise quantification at sub-ppm levels for field applications, ACS Omega. 5 (39) (2020) 25253–25263, https://doi.org/10.1021/acsomega.0c03465.

[82] V. Brahmkhatri, P. Pandit, P. Rananaware, A. D'Souza, M.D. Kurkuri, Recent progress in detection of chemical and biological toxins in water using plasmonic nanosensors, Trends Environ. Anal. Chem. 30 (2021) e00117, https://doi.org/10.1016/j.teac.2021.e00117.

[83] H. Wei, K. Rodriguez, S. Renneckar, W. Leng, P.J. Vikesland, Preparation and evaluation of nanocellulose–gold nanoparticle nanocomposites for SERS applications, Analyst 140 (2015) 5640–5649, https://doi.org/10.1039/c5an00606f.

[84] L.S. Lawson, W. Chan, T. Huser, A highly sensitive nanoscale pH-sensor using au nanoparticles linked by a multifunctional Raman- active reporter molecule, Nanoscale 6 (2014) 7971–7980, https://doi.org/10.1039/c3nr06277e.

[85] M. Chern, J.C. Kays, S. Bhuckory, A.M. Dennis, Sensing with photoluminescent semiconductor quantum dots, Methods Appl. Fluoresc. 7 (1) (2019) 1–36, https://doi.org/10.1088/2050-6120/aaf6f8.

[86] U. Resch-Genger, M. Grabolle, S. Cavaliere-Jaricot, R. Nitschke, T. Nann, Quantum dots versus organic dyes as fluorescent labels, Nat. Methods 5 (9) (2008) 763–775, https://doi.org/10.1038/nmeth.1248.

[87] D. Song, R. Yang, F. Long, A. Zhu, Applications of magnetic nanoparticles in surface-enhanced Raman scattering (SERS) detection of environmental pollutants, J. Environ. Sci. (China) 80 (2019) 14–34, https://doi.org/10.1016/j.jes.2018.07.004.

[88] D. Li, X. Cao, Q. Zhang, et al., Facile in situ synthesis of core–shell MOF@ag nanoparticle composites on screen-printed electrodes for ultrasensitive SERS detection of polycyclic aromatic hydrocarbons, J. Mater. Chem. A 7 (23) (2019) 14108–14117, https://doi.org/10.1039/C9TA03690C.

[89] H. Bagheri, A. Afkhami, M. Saber-Tehrani, H. Khoshsafar, Preparation and characterization of magnetic nanocomposite of Schiff base/silica/magnetite as a preconcentration phase for the trace determination of heavy metal ions in water, food and biological samples using atomic absorption spectrometry, Talanta 97 (2012) 87–95, https://doi.org/10.1016/j.talanta.2012.03.066.

[90] MIT Media Lab, Overview Argus: Water monitoring through nanosensors inside living plants, MIT Media Lab, 2021. Accessed April 1, https://www.media.mit.edu/projects/argus-sensors-inside-plants/overview/.

[91] H. Zhou, C.C. Mayorga-Martinez, S. Pané, L. Zhang, M. Pumera, Magnetically driven micro and nanorobots, Chem. Rev. 121 (2021) 4999–5041, https://doi.org/10.1021/acs.chemrev.0c01234.

[92] L. Kong, J. Guan, M. Pumera, Micro- and nanorobots based sensing and biosensing, Curr. Opin. Electrochem. 10 (2018) 174–182, https://doi.org/10.1016/j.coelec.2018.06.004.

[93] J. Orozco, V. García-Gradilla, M. D'Agostino, W. Gao, A. Cortés, J. Wang, Artificial enzyme-powered microfish for water-quality testing, ACS Nano 7 (1) (2013) 818–824, https://doi.org/10.1021/nn305372n.

[94] P.J. Vikesland, Nanosensors for water quality monitoring, Nat. Nanotechnol. 13 (8) (2018) 651–660, https://doi.org/10.1038/s41565-018-0209-9.

[95] M.M. Falinski, D.L. Plata, S.S. Chopra, T.L. Theis, L.M. Gilbertson, J.B. Zimmerman, A framework for sustainable nanomaterial selection and design based on performance, hazard, and economic considerations, Nat. Nanotechnol. 13 (8) (2018) 708–714, https://doi.org/10.1038/s41565-018-0120-4.

[96] GMI Research, Nanosensors Market Industry Report: Size, Opportunities & Forecast 2020–2027, GMI Research, 2020. Published 2020. Accessed March 31, 2021, https://www.gmiresearch.com/report/global-nanosensors-market/.

Patents

Indian Patents (Granted)

1. A method of ionization on a 2d-nanostructured surface, T. Pradeep, Pallab Basuri, Sourav Kanti Jana and Biswajit Mondal, application no. 202141004464, dated February 02, 2021, issued as patent no. 383701, dated December 03, 2021.

2. Ambient microdroplet annealing method for converting polydispersed nanoparticles to their monodispersed analogues, T. Pradeep, Angshuman Ray Chowdhuri, B. K. Spoorthi, Biswajit Mondal, Paulami Bose and Sandeep Bose application no. 202041056735, dated December 28, 2020, issued as patent no. 377934, dated September 27, 2021.

3. A green method for preparing robust and sustainable cellulose-polyaniline based nanocomposite for effective removal of fluoride from water and a purifier thereof, T. Pradeep and Sritama Mukherjee, application no. 201941046691, dated November 15, 2019, issued as patent no. 376317, dated September 2, 2021.

4. Patterned metallic nanobrushes for capture of atmospheric humidity, Thalappil Pradeep, Depanjan Sarkar, Anindita Mahapatra, Anirban Som and Avijit Baidya, application no. 201641044759, dated December 29, 2016, issued as patent no. 375956, dated August 31, 2021.

5. Method for selective extraction of gold by niacin, Thalappil Pradeep and Abhijit Nag, application no. 202041047984, dated November 03, 2020, issued as patent no. 374251, dated August 10, 2021.

6. A portable water filtration device for removing impurities from water using contaminant - specific purification cartridges, T. Pradeep, Ramesh Kumar and Anupam Chandra, application no. 201741047404, dated December 30 , 2017, issued as patent no. 373947 dated August 5, 2021.

7. A method to make unprotected naked clusters of metals of precise composition in air without mass selection, T. Pradeep, Ananya Baksi, Atanu Ghosh, Md Bodiuzzaman, Papri Chakraborty, Depanjan Sarkar, Pallab Basuri and Madhuri Jash, application no. 201641035574, dated October 18, 2016, issued as patent no. 369127, dated June 11, 2021.

8. Removal of lead from waste water using nanoscale MoS2, T. Pradeep, Biswajit Mondal, Ananthu Mahendranath, Anirban Som, Sandeep Bose, Tripti Ahuja, Avula Anil Kumar and Jyotirmoy Ghosh, application no. 201741044447, dated December 11, 2017, issued as patent no. 365164, dated April 22, 2021.

9. A process for low temperature, low pressure synthesis of gas hydrates, T. Pradeep, Jyotirmoy Ghosh, Rabin Rajan J. Methikkalam, Radha Gobinda Bhuin, Gopi Ragupathy, Nilesh Choudhary and Rajnish Kumar, application no. 201841049836, dated December 29, 2018, issued as patent no. 356814, dated January 27, 2021.

10. Aqueous composition for durable and extremely efficient water repelling superhydrophobic materials at ambient condition thereof, T. Pradeep, Avijit Baidya, Azhar Ganayee and Jakka Ravindran Swathy, application no. 201741036772, dated October 17, 2017, complete specification filed on October 16, 2018, issued as patent no. 356023, dated January 18, 2021.

11. Method for creating nanopores in MoS_2 nanosheets by chemical drilling for disinfection of water under visible light, T. Pradeep, Depanjan Sarkar, Anirban Som, Biswajit Mondal and Jakka Ravindran Swathy, application no. 201741037148, dated October 20, 2017, issued as patent no. 356015, dated January 18, 2021.

12. Method of making nanoparticles of precise isotopic composition by rapid isotopic exchange, T. Pradeep, Papri Chakraborti and Esma Khatun, application no. 201741037349, dated October 23, 2017, complete specification filed on October 23, 2018, issued as patent no. 355248, dated January 4, 2021.

Indian Patents (Applied)

1. A luminescence-based method of detecting arsenic using atomically precise noble metal nanocluster and phosphine, T. Pradeep and Sritama Mukherjee, application no. 202141038227, dated August 24, 2021.
2. An electrode system for detection of free chlorine with differential oxidant response, T. Pradeep, Kamalesh Chaudhari, Tullio Servida, Vishnu Kannan, and B. K. Spoorthi, application no. 202141031970, dated July 15, 2021.
3. A compact, modular and scalable continuous-flow greywater sink for potable and non-potable uses, T. Pradeep, Ankit Nagar, and Md Rabiul Islam, application no. 202141054715, dated November 26, 2021.
4. Synthesis of copper sulfide nanostructures in brass coated steel cords used in radial tires under ambient conditions, T. Pradeep, A. Sreekumaran Nair, Arijit Jana, and C. M. Cherian, application no. 202141047183, dated December 15, 2021.

PCT (Applied)

1. A point-of-care (poc) amperometric device for selective arsenic, T. Pradeep, Sourav Kanti Jana, Kamalesh Chaudhari, Md Rabiul Islam, application no. PCT/IN2021/050496, dated December 9, 2021.
2. Method for selective extraction of gold by niacin, T. Pradeep, Abhijit Nag, application no. PCT/IN2021/051021, dated October 27, 2021.

Selected media
Reports

News

THE HINDU BusinessLine

OXYGEN INNOVATIONS

Coming, DIY oxygen kits, using off-the-shelf materials

TV Jayan | New Delhi | Updated on April 26, 2021

Pradeep's research student Srikrishnarka Pillalamarri demonstrating the prototype oxygen generator

Researchers at IIT Madras have fabricated a DIY kit that can generate oxygen sufficient for a patient in home care.

As the acute shortage of medical oxygen leaves hospitals across the country gasping, scientists at several laboratories are trying to put together a kit that can help deliver the live-saving gas for critical patients at home or hospitals.

ET THE ECONOMIC TIMES English Edition | 31 May, 2021, 10:40 AM IST | E-Paper

INCUBATING DEEP TECH

With 240 startups valued at ₹10.5k cr incubated over 8 years, IIT Madras is India's hi-tech haven *by* **Dia Rekhi & Ainoor Peermohamed**

VAYUJAL TECHNOLOGIES

QNU LABS

EPLANE COMPANY

THE HINDU

TAMIL NADU

In Thoothukudi district, swipe a card to get potable water

R. Sujatha

CHENNAI, APRIL 01, 2021 17:03 IST
UPDATED: APRIL 01, 2021 17:04 IST

THE HINDU

of mammals

Nanosheets help in the detection of uric acid in urine, alcohol in breath

Research Matters
Research based news stories & highlights in science, engineering, technology & humanities in India.

Prof Subramaniam Chandramouli receives the prestigious Swarnajayanti Fellowship for 2021

Read time: 4 mins
Mumbai Dec 8, 2021, (Research Matters):

An Alumnus of PRG

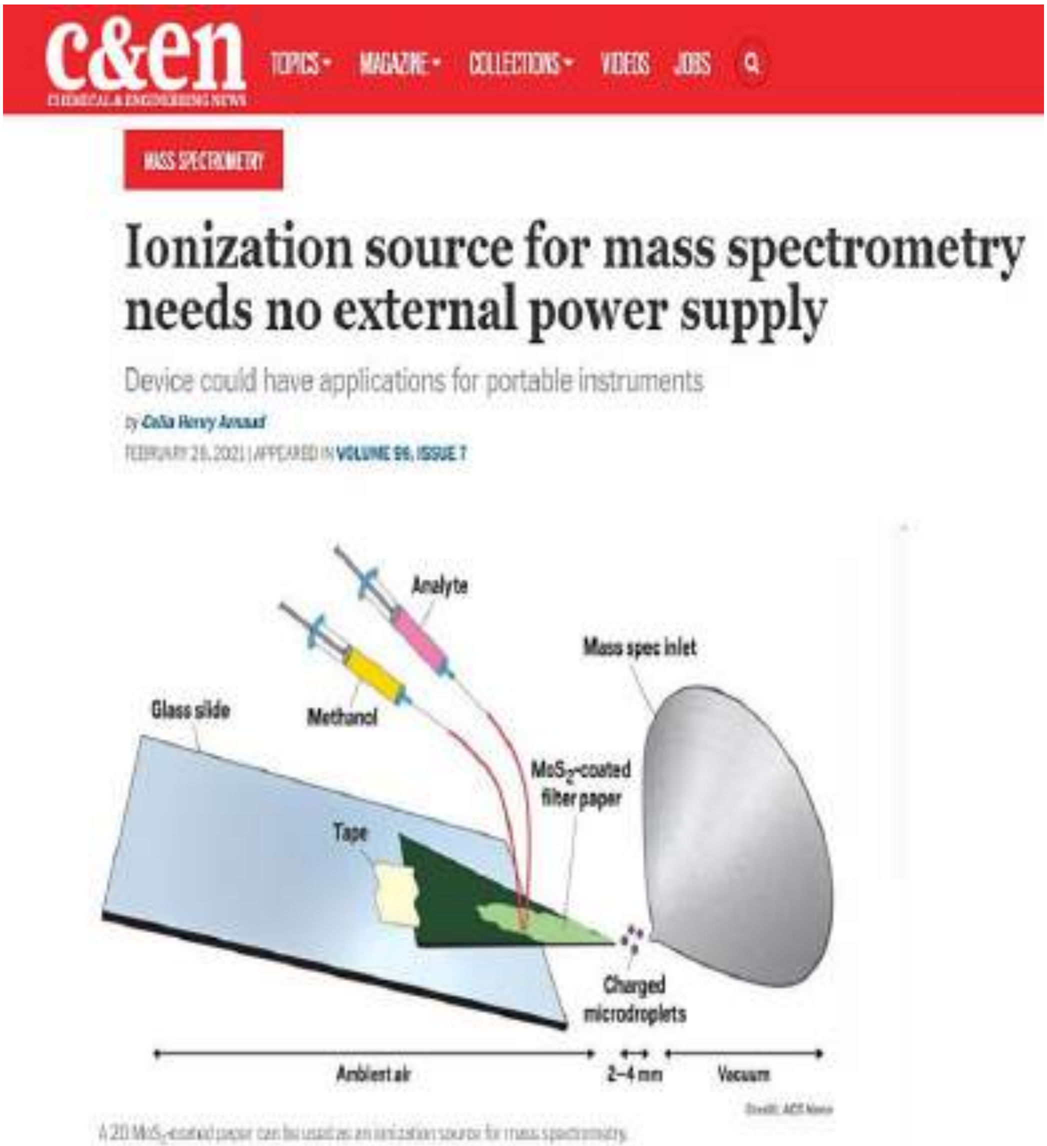

MASS SPECTROMETRY

Ionization source for mass spectrometry needs no external power supply

Device could have applications for portable instruments

by Celia Henry Arnaud

FEBRUARY 28, 2021 | APPEARED IN VOLUME 99, ISSUE 7

Credit: ACS Nano

A 2D MoS_2-coated paper can be used as an ionization source for mass spectrometry.

INDIA NARRATIVE

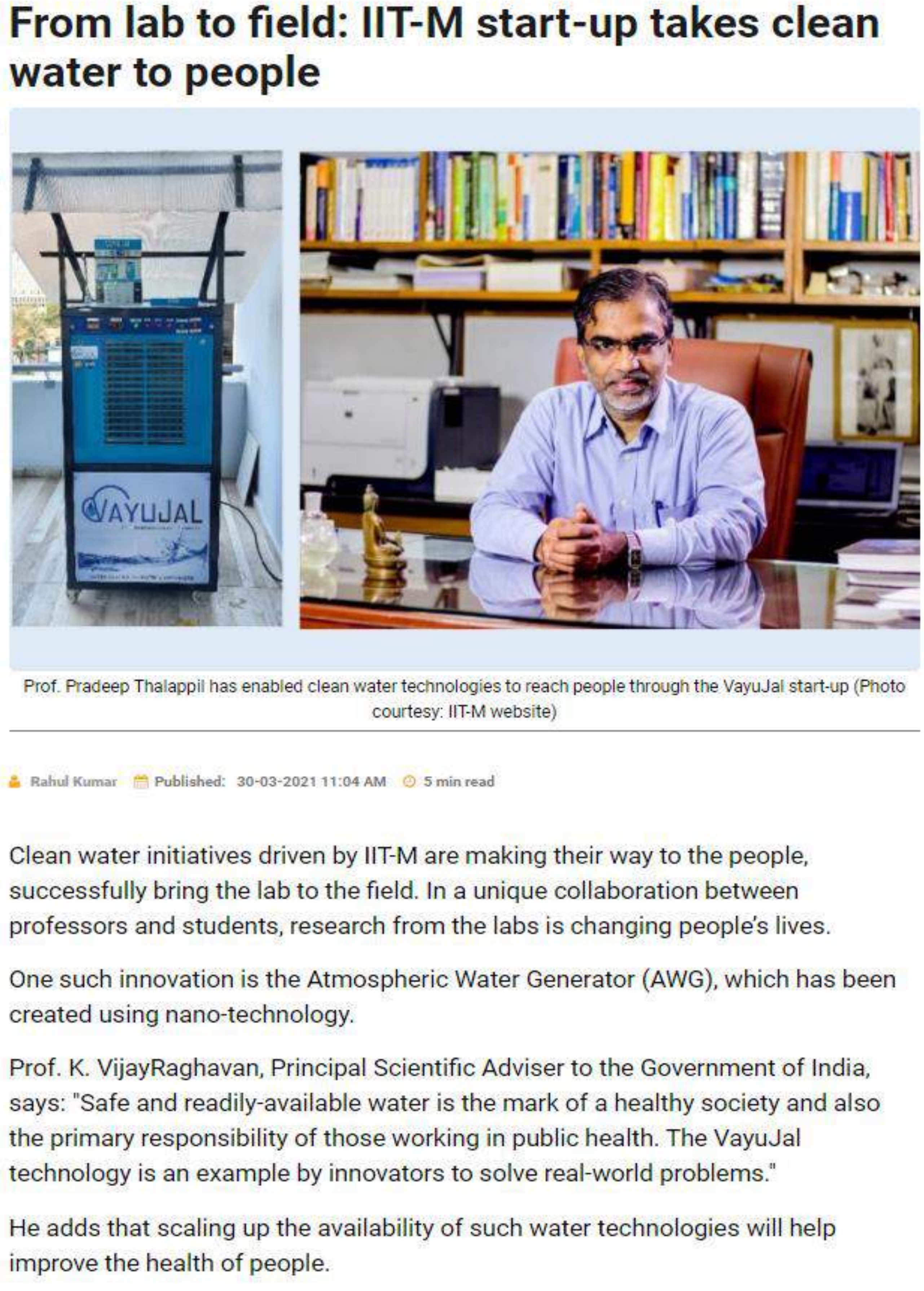

From lab to field: IIT-M start-up takes clean water to people

Prof. Pradeep Thalappil has enabled clean water technologies to reach people through the VayuJal start-up (Photo courtesy: IIT-M website)

Rahul Kumar Published: 30-03-2021 11:04 AM 5 min read

Clean water initiatives driven by IIT-M are making their way to the people, successfully bring the lab to the field. In a unique collaboration between professors and students, research from the labs is changing people's lives.

One such innovation is the Atmospheric Water Generator (AWG), which has been created using nano-technology.

Prof. K. VijayRaghavan, Principal Scientific Adviser to the Government of India, says: "Safe and readily-available water is the mark of a healthy society and also the primary responsibility of those working in public health. The VayuJal technology is an example by innovators to solve real-world problems."

He adds that scaling up the availability of such water technologies will help improve the health of people.

Pradeep Research Group 2021

Acknowledgements
Students and Collaborators

Funding

Department of Science & Technology
Government of India